

平成 24 (2012) 年度 研究成果
著書・総説・発表論文等

著書・総説・発表論文等リスト

著書・総説・解説

1. 増川一, 北島正治, 櫻井英博, 井上和仁
「ラン藻の窒素固定酵素ニトロゲナーゼを利用した大規模な水素生産構想」
微細藻類によるエネルギー生産と事業展開 (竹山春子監修), **2012**, CMC 出版, pp.80-87.
2. N. Maru, D. Uemura
「Chapter 10, Sea-Originated Cytotoxic Substances in Advances in Food and Nutrition Research」
Marine Medicinal Foods Implications and Applications: Animals and Microbes
2012, 65, 171-184, (Ed. Se-Kwon Kim) Elsevier
3. O. Ohno, K. Suenaga, D. Uemura
Chapter 11 「Secondary Metabolites with New Medicinal Functions from Marine Organisms in Advances in Food and Nutrition Research」
Marine Medicinal Foods Implications and Applications: Animals and Microbes
2012, 65, 185-193, (Ed. Se-Kwon Kim) Elsevier
4. M. Kita, T. Inuzuka, N. Maru, D. Uemura
Chapter 12 「Bioactive Molecules from Symbiotic Marine Dinoflagellates」
Marine Pharmacognosy: Trends and Applications
2012, *in press*, (Ed. Kim) CRC Press
5. 上村大輔
サイエンス・インタビュー 科学の今、そして未来「生物が作り出す毒から探る知られざる生命のしくみ」
自然と科学の情報誌ミルシル
2012, 5 (3月), 3-5 国立科学博物館
6. 上村大輔
特集日本の化学：その元気度は？ (天然物化学) 「そこに「オリジナリティー」はあるか?!」
化学
2012, 67 (4), 28-30

7. 堀 久男
「世界の化学品規制・ルールの解釈とその違反回避のための実務」
第6章7節、「有機フッ素化合物 (PFOS/PFOA)」、技術情報協会、2012年
12月28日刊行
8. 濱田嘉昭、菅原正 (編著)
「現代化学」
2013、放送大学教育振興会
9. 庄田耕一郎、栗原顕輔、菅原 正
「人工細胞(原始細胞モデル)の化学的構築」
2013、遺伝 66、pp. 365-373.
10. T. Sugawara, K. Kurihara, K. Suzuki
「Constructive Approach Towards Protocells」
2013, Engineering of Chemical Complexity, World Scientific Lecture Notes in
Complex Systems (Eds. A.S. Mikhailov, G. Ertl), World Scientific, pp. 359-374.
11. T. Sugawara, A. Miyazaki
Engineering of Chemical Complexity, World Scientific Lecture Notes in Complex
Systems (Eds. A.S. Mikhailov, G. Ertl)
「Constructive Approach Towards Protocells」
2013, Multifunctional Molecular Materials (Ed. L. Ouahab), Pan Stanford Pub., pp.
359-374.
12. 西本右子
「透明性を損なわないフィルム・コーティング剤への機能付与」第9章第8
節
高分子の水・湿度が関係した劣化の原因究明とその対策
(技術情報協会) (2012)
13. 西本右子
「各種機能水の分析法」
クリーンテクノロジー、**22**, 10, 35-38 (2012)
14. T. Yokozawa, Y. Nanashima, H. Kohno, R. Suzuki, M. Nojima, and Y. Ohta

Catalyst-transfer condensation polymerization for precision synthesis of π -conjugated polymers.

Pure Appl. Chem., **2013**, 85, 573-587.

15. 野嶋雅貴, 太田佳宏, 横澤勉
触媒移動型連鎖縮合重合の新展開
ケミカルエンジニアリング, **2012**, 57, 649-655.

発表論文

1. M. Kitashima, H. Masukawa, H. Sakurai, and K. Inoue
Flexible Plastic Bioreactors for Photobiological Hydrogen Production by Hydrogenase-Deficient Cyanobacteria
Biosci. Biotech. Biochem., **2012**, 76, 831-833.
2. T. Abe, F. P. Sahin, K. Akiyama, T. Naito, M. Kishigami, K. Miyamoto, Y. Sakakibara, D. Uemura
Construction of a Metagenomic Library for the Marine Sponge *Halichondria okadai*
Biosci. Biotechnol. Biochem., **2012**, 76, 633-639.
3. K. Yuki, M. Ikeda, K. Miyamoto, O. Ohno, K. Yamada, D. Uemura
Isolation of 9-Hydroxy-10E, 12Z-octadecadienoic Acid, an Inhibitor of Fat Accumulation from *Valeriana fauriei*
Biosci. Biotechnol. Biochem., **2012**, 76, 1233-1235.
4. T. Abe, A. Kukita, K. Akiyama, T. Naito, D. Uemura
Isolation and Structure of a Novel Biindole Pigment Substituted with an Ethyl Group from a Metagenomic Library Derived from the Marine Sponge *Halichondria okadai*
Chem. Lett., **2012**, 41, 728-729.
5. H. Takamura, K. Tsuda, Y. Kawakubo, I. Kadota, D. Uemura
Stereoselective synthesis of the C94-C104 fragment of symbiodinolide
Tetrahedron Letters, **2012**, 53, 4317-4319.

6. M. Kobayashi, H. Kawashima, K. Takemori, H. Ito, A. Murai, S. Masuda, K. Yamada, D. Uemura, F. Horio
Ternatin, a cyclic peptide isolated from mushroom, and its derivative suppress hyperglycemia and hepatic fatty acid synthesis in spontaneously diabetic KK-A^y mice
Biochem. Biophys. Res. Commun., **2012**, 427, 299-304.

7. I. Okamoto, T. Ono, R. Sameshima and A. Ono.
Metal ion-binding properties of DNA duplexes containing thiopyrimidine base pairs
Chem. Commun., **2012**, 48, 4347-4349.

8. T. Uchiyama, T. Miura, H. Takeuchi, T. Dairaku, T. Komuro, T. Kawamura, Y. Kondo, L. Benda, V. Sychrovsky, P. Bour, I. Okamoto, A. Ono and Y. Tanaka.
Raman spectroscopic detection of the T-Hg^{II}-T base pair and the ionic characteristics of mercury
Nucleic Acids Research, **2012**, 40, 5766-5774.

9. T. Funai, Y. Miyazaki, M. Aotani, E. Yamaguchi, O. Nakagawa, S. Wada, H. Torigoe, A. Ono, and H. Urata.
Ag^I Ion Mediated Formation of a C–A Mismatch by DNA Polymerases
Angew. Chem. Int. Ed., **2012**, 51, 6464–6466

10. H. Torigoe, I. Okamoto, T. Dairaku, Y. Tanaka, A. Ono, T. Kozasa.
Thermodynamic and structural properties of the specific binding between Ag⁺ ion and C:C mismatched base pair in duplex DNA to form C-Ag-C metal-mediated base pair
Biochimie, **2012**, 94, 2431-2440.

11. H. Torigoe, Y. Miyakawa, A. Ono, T. Kozasa.
Positive cooperativity of the specific binding between Hg²⁺ ion and T:T mismatched base pairs in duplex DNA
Thermochimica Acta, **2012**, 532, 28– 35

12. Y. Takino, N. Yoshinari, T. Kawamoto, and T. Konno
Thiolato-bridged Au^I₂Cu^I₂ and Cu^I₄ Metallorings Derived from Benzothiazoline: Can Gold(I) Plus Copper(I) Make Silver(I)?

Chem. Lett. **2012**, *41*, 834-836.

13. Y. Miyazaki, Y. Kataoka, W. Mori, and T. Kawamoto
Synthesis, crystal structures and properties of novel heterobimetallic Cd-Pt and Zn-Pt coordination polymers using nicotinic acid
Inorg. Chem. Commun. **2012**, *25*, 14-17.
14. T. Kawamoto, N. Suzuki, T. Ono, D. Gong, and T. Konno
Chirality transfer based on reversible C-C bond formation/breaking in nickel(II) complexes
Chem. Commun. **2013**, *49*, 668-670.
15. A. Yoshida, W. Shen, T. Eda, R. Watanabe, T. Ito, S. Naito
NO_x storage/reduction over alkali-metal-nitrate impregnated titanate nanobelt catalysts and investigation of alkali metal cation migration using XPS
Catalysis Today, **2012**, *184*, 78-82.
16. A. Yoshida, Y. Mori, T. Ikeda, K. Azemoto, S. Naito
Enhancement of catalytic activity of Ir/TiO₂ by partially reduced titanium oxide in aerobic oxidation of alcohols
Catalysis Today, **2013**, *203*, 153-157.
17. 吉田 暁弘, 奥山 高志, 齋藤 直樹, 内藤 周弐
炭素材料と水素化リチウムからなる新規水素吸蔵材料の開発とその水素吸蔵機構
触媒, **2012**, *54*, 90-92.
18. K. Nomiya, Y. Mouri, Y. Sakai and S. Matsunaga,
Reaction products of titanium(IV) sulfate with the two, dimeric precursors, 1,2,3-tri-titanium(IV)- and 1,2-di-titanium(IV)-substituted α -Keggin polyoxometalates (POMs), under acidic conditions. A tetra-titanium(IV) oxide cluster and one coordinated sulfate ion grafted on a di-lacunary Keggin POM
Inorg. Chem. Commun. **2012**, *19*, 10-14.
19. N. C. Kasuga, R. Yoshikawa, Y. Sakai and K. Nomiya,
Syntheses, Structures, and Antimicrobial Activities of Remarkably Light-Stable, and Water-Soluble Silver Complexes with Amino Acid Derivatives, Silver(I) *N*-Acetylmethioninates

- Inorg. Chem.* **2012**, *51*, 1640-1647.
20. T. Yoshida, K. Nomiya and S. Matsunaga,
Novel intercluster compound between
heptakis{triphenylphosphinegold(I)}dioxonium cation and α -Keggin
polyoxometalate anion
Dalton Trans. **2012**, *41*, 10085-10090.
21. S. Hikichi, K. Hanaue, T. Fujimura, H. Okuda, J. Nakazawa, Y. Ohzu, C. Kobayashi,
and M. Akita
Characterization of Nickel(II)-Acylperoxo Species Relevant to Catalytic Alkane
Hydroxylation by Nickel Complex with *m*CPBA
Dalton Trans. **2013**, *42*, 3346–3356.
22. T. Akashi, J. Nakazawa, and S. Hikichi
Iron complex immobilized catalyst based on β -ketiminate ligand: Alkene
oxygenation activity depending on the morphology of silica support and the
structures of base additives
J. Mol. Catal. A: Chem., **2013**, *371*, 42–47.
23. H. Hori, T. Sakamoto, T. Tanabe, M. Kasuya, A. Chino, Q. Wu, K. Kannan
Metal-induced decomposition of perchlorate in pressurized hot water
Chemosphere **2012**, *89*, 737-742.
24. J. Shinji, B.-J. Kang, T. Okutsu, K. Banzai, T. Ohira, N. Tsutsui, M. N. Wilder
Changes in crustacean hyperglycemic hormones in Pacific whiteleg shrimp
Litopenaeus vannamei subjected to air-exposure and low-salinity stresses.
Fish. Sci. **2012**, *78*, 833-840.
25. N. Tsutsui, A. Nagakura, C. Nagai, T. Ohira, H. Nagasawa
The effects of sinus gland peptides in ex vivo vitellogenin gene expression in the
ovaries of the kuruma prawn, *Marsupenaeus japonicus*.
Fish. Sci. **2013**, *79*, 33-38.
26. K. Suzuki, R. Aboshi, K. Kurihara, and T. Sugawara
Adhesion and Fusion of Two Kinds of Phospholipid Hybrid Vesicles Controlled by

Surface Charges of Vesicular Membranes

Chem. Lett. **2012**, *41*, 789-791.

27. K. Suzuki, K. Kurihara, Y. Okura, T. Toyota, and T. Sugawara
pH-Induced Switchable Vesicular Aggregation of Zwitterionic Phospholipids and Anionic Phospholipids
Chem. Lett. **2012**, *41*, 1084-1086.
28. H. Sato, S. Ushiyama, M. Sogo, M. Aoki, K-i. Shudo, T. Sugawara, S. Yanagisawa, Y. Morikawa, and S. Masuda
Local electronic properties at organic–metal interfaces: thiophene derivatives on Pt(111) *Phys. Chem. Chem. Phys.* **2012**, *14*, 15412-15420.
29. M. Iwasaka, Y. Miyashita, Y. Mizukawa, K. Suzuki, T. Toyota, and T. Sugawara
Bi-axial alignment control of guanine crystals by diamagnetic orientation
Appl. Phys. Exp. **2013**, *6*, 037002(4 pages).
30. T. Matsubara, R. Takahashi, and S. Asai
ONIOM Study of the Mechanism of Olefin Hydrogenation by the Wilkinson's Catalyst: Reaction Paths and Energy Surfaces of Trans and Cis Form
Bull. Chem. Soc. Jpn. **2013**, *86*, 243-254.
31. N. Watanabe, H. Kino, S. Watanabe, H. K. Ijuin, M. Yamada, M. Matsumoto
Synthesis of bicyclic dioxetanes tethering a fluororescer through an ω -carbamoyl-substituted linker and their highperformance chemiluminescence in an aqueous system
Tetrahedron, **2012**, *68*, 6079-6087.
32. N. Watanabe, K. Matsumoto, T. Tanaka, H. Suzuki, H. K. Ijuin, M. Matsumoto
N-Acyl group-directed color modulation in the *t*-BuOK-mediated chemiluminescent decomposition of hydroxyarylsubstituted dioxetanes fused with a pyrrolidine ring
Tetrahedron Lett. **2012**, *53*, 5309-5313.
33. N. Watanabe, M. Hamano, S. Todaka, T. Asaeda. H. K. Ijuin, M. Matsumoto
Diphenylparabanic Acid as a Synthon for the Synthesis of α -Diketones and

α -Ketocarboxylic Acids

J. Org. Chem., **2012**, 77, 632-639.

34. M. Tanimura, N. Watanabe, H. K. Ijuin, and M. Matsumoto
Base-Induced Chemiluminescent Decomposition of Bicyclic Dioxetanes Bearing a (Benzothiazol-2-yl)-3-hydroxyphenyl Group: A Radiationless Pathway Leading to Marked Decline of Chemiluminescence Efficiency".
J. Org. Chem., **2012**, 77, 4725-4731.
35. H. Hagiwara, N. Watanabe, H. K. Ijuin, M. Yamada, M. Matsumoto
Synthesis of bicyclic dioxetanes bearing a 4-(benzimidazol-2-yl)-3-hydroxy phenyl group and their base-induced chemiluminescent decomposition in an aprotic medium and in an aqueous medium
Heterocycles, **2013**, 87, 65-78.
36. H. Kawashima, N. Watanabe, H. K. Ijuin, M. Matsumoto
Magnesium methoxide-induced chemiluminescent decomposition of bicyclic dioxetanes bearing a 2'-alkoxy-2-hydroxy-1,1'-binaphthyl-7-yl moiety
Luminescence, in press.
37. S. Ito, M. Watanabe, M. Saito and H. Yamamura
Crystal structure and electrical properties of new brownmillerite-type composition $\text{Ba}_2\text{In}_{2-x}(\text{Zn,Zr})_x\text{O}_5$ system
Trans. Mater. Res. Soc. Japan, **2012**, 37, 393-397.
38. Y. Sugiyama, T. Kariwa, T. Sakurada, S. Okamoto
Remarkable Activation of an Alkyne [2 + 2 + 2] Cycloaddition Catalyst, 2-Iminomethylpyridine (Dipimp)/ $\text{CoCl}_2 \cdot 6\text{H}_2\text{O}/\text{Zn}$, by a Phthalate Additive
Synlett, **2012**, 23, 2549-2553.
39. H. Takemoto, H. Kawakami, M. Saito, and H. Yamamura,
Lattice distortion and thermoelectric property for $\text{Zn}_{1-(x+y)}\text{Ga}_x\text{In}_y\text{O}$ ($x + y = 0.007$, $0 \leq x \leq 0.007$, $0 \leq y \leq 0.007$)
Trans. Mater. Res. Soc. Japan, **2012**, 37, 399-403.
40. H. Takemoto, M. Saito, and H. Yamamura,

Influence of average ionic radius of dopants in Zn site on thermal conductivity and dimensionless figure of merit for $Zn_{1-(x+y)}Ga_xIn_yO$ ($0.0 \leq x + y \leq 0.007$)

Trans. Mater. Res. Soc. Japan, **2012**, 37, 429-433.

プロシーディング

1. 櫻井英博、増川 一、北島正治、井上和仁
シアノバクテリアによる光生物学的水素生産実用化に向けた研究開発：バイオリアクターの低コスト化と培養気相
第32回水素エネルギー協会大会（2012）、広島
2. 40th Annual Conference of North American Thermal Analysis Society,
Orlando, Florida, USA (2012)
Yuko NISHIMOTO
Detection of Water State in Methylcellulose Thermo Reversible Hydrogels
using Melting of a Eutectic

報告書・紀要

1. 北島正治、井上和仁
シアノバクテリアのニトロゲナーゼを利用した水素の光生物学的生産性に関する研究
Science Journal of Kanagawa University, **2012**, 23, 83-87.
2. 野宮健司、吉田拓也、伊能小百合、保田裕太、力石紀子、松永 諭
Keggin型ヘテロポリアニオンと金(I)多核クラスターからなる新規クラスター間化合物の合成
Science Journal of Kanagawa University, **2012**, 23, 21-25.

微細藻類によるエネルギー生産と事業展望

Technology of Microalgal Energy Production and its Business Prospect

監修：竹山春子

Supervisor : Haruko Takeyama

シーエムシー出版

第10章 ラン藻の窒素固定酵素ニトロゲナーゼを利用した大規模な水素生産構想

増川 一*¹, 北島正治*², 櫻井英博*³, 井上和仁*⁴

1 はじめに

地表に到達する太陽光エネルギーは、人類が消費する化石燃料エネルギーの6,000倍を超えるほど膨大である(表1)。しかし、そのエネルギー密度は、地球表面で平均して年間で1,500 kWh・m⁻²程度と低く、経済性の確保が課題である。化石燃料代替のエネルギーとして、地球温暖化の軽減に相当程度の貢献をするためには、将来得られるエネルギー資源が量的に大きくなければならない。約68億人の人類が摂取する食物エネルギー(1日2,000 kcal)と比較して、消費する化石燃料エネルギーは、世界平均でその約20倍、日本は約50倍、米国は約100倍に達するほど莫大である(表1)。したがって、陸上エネルギー作物から現在の食料生産と同程度のエネルギーが新規に得られたとしても、化石燃料消費のわずか5%を満たすに過ぎない。このように、陸上バイオマスには量的限界があるので、経済性を確保した光生物学的なエネルギー生産を実現

表1 太陽光エネルギーと社会的エネルギー消費

		数量 (10 ¹⁸ J/year)	比率	
			対 [A]	対 [B]
世界 (IEA)	一次エネルギー消費 (2008) [A]	513	1.00	1.23
	(うち化石エネルギー消費 (2008) [B])	417	0.81	1.00
	光合成純生産	4,200	8.2	10
	太陽光エネルギー	2,700,000	5,300	6,500
	食物の摂取エネルギー	20.8	0.041	0.050
日本 (資源エネルギー庁)	一次エネルギー消費 (2008) [A]	23.2	1.00	1.18
	(うち化石エネルギー消費 (2008) [B])	19.6	0.84	1.00
	太陽光エネルギー (陸地)	2,100	89	107
	太陽光エネルギー (含200海里水域)	33,000	1,400	1,700
	食物の摂取エネルギー	0.39	0.017	0.02

*1 Hajime Masukawa (独)科学技術振興機構 さきがけ研究者; 神奈川大学 光合成水素生産研究所 客員研究員

*2 Masaharu Kitashima 神奈川大学 総合理学研究所 客員研究員

*3 Hidehiro Sakurai 神奈川大学 光合成水素生産研究所 客員教授

*4 Kazuhito Inoue 神奈川大学 理学部 生物科学科 教授, 光合成水素生産研究所 所長

するためには、海洋面など広大な面積を利用した大規模な水素生産のシステムの構築が必要だと考える^{1~3)}。

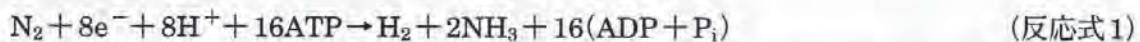
2 ラン藻による水素生産

2.1 ニトロゲナーゼとヒドロゲナーゼ

ラン藻（シアノバクテリア）は、葉緑体を持つ高等植物や真核藻類と同様に水を電子供与体として、酸素発生型の光合成を行う原核生物である。ラン藻の水素生産に利用出来る酵素は、ヒドロゲナーゼまたはニトロゲナーゼであり、後者は一部のものだけが持っている⁴⁾。

ニトロゲナーゼは、空気中の窒素ガスをアンモニアへと固定する酵素で、マメ科植物の根に共生する根粒菌など、一部の原核生物のみが活性を持つ。水を電子供与体として利用出来る光合成生物のうち、ニトロゲナーゼを持つのは、ラン藻の一部に限られ、クロレラ、クラミドモナス、ユーグレナ等の真核光合成生物は持たない。

ニトロゲナーゼによる窒素（N₂）固定反応では、アンモニア生成に伴う必然的な副産物として水素が発生する。

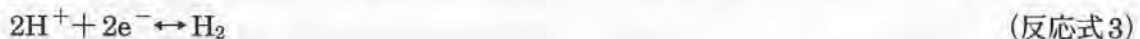


上式では、電子の約3/4が窒素固定（N₂還元）に、残りの約1/4が水素発生（H⁺還元）に使われる。窒素ガスが存在しないアルゴン（Ar）気相下などでは、投入された全ての電子が水素生産に向かう。



反応に必要な電子は、直接的には還元型フェレドキシン（鉄硫黄タンパク質）またはフラボドキシン（フラビン蛋白質）から供給される。ニトロゲナーゼは、上記反応式に示されるように大量のATP（生体内の高エネルギー物質）を消費するので、理論的な最大エネルギー変換効率は低い（通常のC3型光合成の約60%）、ヒドロゲナーゼと異なり酸素存在下でも不可逆的に水素を生産できる点が、大規模生産時の省力化にとっての利点となる（表2）。

ヒドロゲナーゼは、水素の発生または吸収を触媒する酵素で、次の反応を触媒する。



生理的条件下で、上記のように可逆的に反応を触媒できるものは、双方向性（可逆的）ヒドロゲナーゼ（ラン藻のものはNiFe型ヒドロゲナーゼ、緑藻のものはFeFe型ヒドロゲナーゼ）と呼ばれ、水素生産への利用が可能である。その電子供与体は還元型フェレドキシンまたはNADPHである。これに対し、水素の吸収だけを触媒するものは、取込み型ヒドロゲナーゼ（Hup）と呼ばれる。

表2 水素生産に利用されるヒドロゲナーゼとニトロゲナーゼ

反応式	長所	短所
ヒドロゲナーゼ $2H^+ + 2e^- \rightleftharpoons H_2$	<ul style="list-style-type: none"> ・理論的最大エネルギー変換効率が高い 	<ul style="list-style-type: none"> ・可逆反応であり、水素の再吸収（夜間、曇天下）の抑制が必要 ・酵素が酸素感受性であるため、水素生産の時期と酸素発生型光合成の時期とを時間的に分けることが必要
ニトロゲナーゼ N ₂ 存在下 $N_2 + 8e^- + 8H^+ + 16ATP \rightarrow 2NH_3 + H_2 + 16(ADP + P_i)$ Ar気相下 $2H^+ + 2e^- + 4ATP \rightarrow H_2 + 4(ADP + P_i)$	<ul style="list-style-type: none"> ・不可逆反応であり、一方向的に水素発生が起こる（水素吸収が起こらない） ・ラン藻ではニトロゲナーゼを酸素から保護する機能を発達させているので、好気的な培養気相中でも水素生産が可能 	<ul style="list-style-type: none"> ・理論的最大エネルギー変換効率が低い

光合成微生物では、各種光合成細菌、ラン藻、緑藻など多くのものがヒドロゲナーゼを持つ。ニトロゲナーゼと比較して、ヒドロゲナーゼは反応にATPを必要としないので理論的最大エネルギー変換効率が高い。しかし、酸素発生型光合成生物のヒドロゲナーゼを利用して水素生産を行わせる場合は、酵素が正逆両方向の反応を触媒するため（反応式3）、夜間や曇天下では水素の再吸収が起こるので、その対策が必要となる。窒素ガスを常にフローさせながら水素を収穫する方法もあるが、低濃度の水素しか得られない。ところが、緑藻クラミドモナスでは、第1段階で通常の光合成を行わせたのち、第2段階で細胞を嫌氣的気相下で硫黄欠乏培地に移して光照射を続けると、酸素発生を伴う通常の光合成活性が低下し、次いで、前段階で蓄積した糖質を分解して水素を連続光下で3-5日程度生産出来る。このようにして、酸素発生期から嫌氣的水素生産期へと培養条件を変えることで時間的に分離できるので、ヒドロゲナーゼを利用した水素生産研究も盛んにおこなわれている⁵⁾。水素生産における両酵素の長所・短所を表2に示す。ニトロゲナーゼを利用した水素生産は、理論的最大エネルギー変換効率の点ではヒドロゲナーゼ利用系より低い。遺伝子工学的手法による改良を積み重ね、エネルギー変換効率を高めていけば、その長所（表2）から水素生産の省力化、低コスト化、大規模化の可能性が開けると期待される。

2.2 ヘテロシスト形成型ラン藻のニトロゲナーゼを利用した光生物学的水素生産

ニトロゲナーゼはヒドロゲナーゼと同様に酸素感受性が高く、酸素発生を伴う光合成に基づく水素生産を行う場合には、いかにして両反応を両立させるかが課題になるが、ラン藻自身が様々な方法でその問題を解決しており、酸素共存下でも水素生産を維持している⁴⁾。Anabaena, Nostoc 属等のラン藻は、硝酸塩類などの窒素栄養源が欠乏した条件下では、通常の酸素発生型光合成を行う栄養細胞の一部が、約10-20細胞の間隔で異型細胞（ヘテロシスト）へと分化し、

2.3 取り込み型ヒドロゲナーゼの遺伝子破壊による水素生産性増大

ヘテロシスト形成型ラン藻は、通常ヒドロゲナーゼも持っており、ニトロゲナーゼによって生産された水素は再吸収されてしまう。しかし、ヒドロゲナーゼを遺伝子工学的に不活性化することによって得られる改変株は、酸素存在下でも水素を再吸収しないので、発生した水素の収穫は数週間に一度程度おこなえば十分であり、海洋面上などでの大規模な水素生産の省力化が可能となる。

Nostoc/Anabaena sp. PCC 7120 株は、窒素固定ラン藻として初めて全ゲノム塩基配列が明らかにされた株である。この株は、取り込み型 (Hup) および双方向性 (Hox) の2種類のヒドロゲナーゼ遺伝子を持つ。これら2種類のヒドロゲナーゼ遺伝子を遺伝子工学的に分断破壊したところ、光合成に基づく水素生産活性は、野生株の4-7倍に向上した⁶⁾。次に、窒素固定ラン藻13株について、アセチレン還元法で測定したニトロゲナーゼ活性の比較を行い、活性の高い株として *Nostoc* sp. PCC 7422 株を選抜した。この株は、Hox 活性がほとんどなく、Hup 活性のみが高かったため、後者の遺伝子の塩基配列を明らかにし、それを遺伝子工学的に分断破壊した株 (*Nostoc* sp. PCC 7422 Δ Hup) を作成した。この改良株は、気相をアルゴン置換した密閉ガラス容器内で、光合成による酸素発生を伴いながら、水素の蓄積が出来る (図2)、その濃度は培養気相の30% (v/v) にまで達した⁷⁾。

さらに、この改良株は、低濃度の窒素ガスを含む密閉ガラス容器内において、以下のように長期にわたる水素の繰り返し収穫が可能であった。改変株を、窒素栄養源を含む培地 (BG11) で、5%二酸化炭素を添加した空気下で光合成的に培養した後に、窒素栄養源を含まない培地 (BG11₀) に移した。培養気相中の窒素ガス濃度がゼロに近い場合、細胞の活性維持に必要な窒素栄養が確保できないために、水素生産活性は次第に低下していく。逆に、窒素ガス濃度が高い場合には、窒素固定が活発に行われることによって速やかに窒素栄養が充足され、その結果ニト

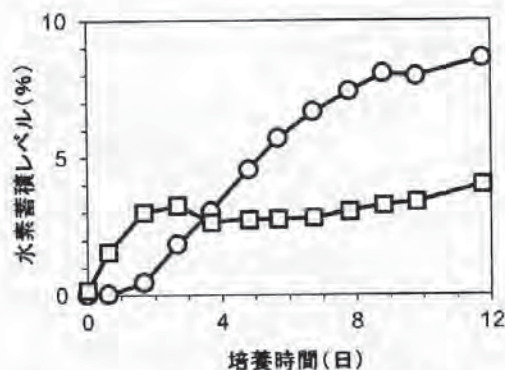


図2 改良ラン藻による水素の蓄積

○：水素，□：酸素，初期気相：95% Ar + 5% CO₂。
ヒドロゲナーゼ活性を除去したラン藻改良株 (*Nostoc* sp. PCC 7422 Δ Hup) は、窒素栄養欠乏培地に移すと、酸素共存下でも水素を長期間にわたり蓄積できる。

ロゲナーゼ活性が低下するために水素生産の高い活性が持続しない。しかし、窒素ガス濃度1%という条件下では、この変異株は、高い水素生産活性のまま、窒素固定を低レベルながら行うことができるので、活性維持に必要な窒素栄養を合成でき、培地を交換することなく高い水素生産活性を60日間以上持続できた。(Kitashima *et al.*, 論文投稿準備中)。

3 ニトロゲナーゼへの変異導入による水素生産性の向上

3.1 ニトロゲナーゼ活性中心金属クラスター配位子ホモクエン酸の除去

上記のような低濃度の窒素ガス気相中では、ニトロゲナーゼ反応で窒素固定に配分される電子は僅かで、大部分の電子が水素生産に使われる。その結果、反応式1の場合と比べて水素生産活性が上昇すると同時に、窒素栄養が充足されない状態が持続するため、水素生産の高活性が持続するようになる。このように電子配分比率を水素生産に有利に変更する方法は、培養気相の最適化の他に、遺伝子工学的手法でニトロゲナーゼに変異を導入することによってもある程度可能である。以下にその研究例を紹介する。

ニトロゲナーゼは鉄、硫黄、モリブデン (Mo) から成る金属クラスターを触媒部位に持ち、そこで窒素固定および水素発生が起こる。その金属クラスターのMoに、有機酸であるホモクエン酸が配位しており、ホモクエン酸は効率的な窒素固定を行うためには必須である。従属栄養細菌 *Klebsiella* の研究から、ホモクエン酸濃度を低下させれば、上記のような水素生産活性の上昇と持続化の効果が期待されることから、取り込み型ヒドロゲナーゼ破壊株 (Δ Hup) を親株として、ホモクエン酸合成能力を部分的に欠損 (*nifV1* 遺伝子破壊) させた変異株を作成した (注: *Nostoc/Anabaena* sp. PCC 7120 株はこの遺伝子を2個 (*nifV1* と *nifV2*) 持つ)。その変異株では、空気下の培養条件で水素生産の高い活性が部分的だが持続するようになり、培養液全体の水素生産性は Δ Hup の約2倍まで向上した⁸⁾。

3.2 ニトロゲナーゼ活性中心近傍のアミノ酸残基置換

ニトロゲナーゼが窒素固定反応を行う上で、活性中心金属クラスターだけでなく、その近傍にあるアミノ酸残基も重要であることが知られている。ニトロゲナーゼの立体構造⁹⁾ を基に、活性中心部位から5 Å以内に位置する複数のアミノ酸残基の中から6つの残基を標的として選び、別の残基に置換した変異株を合計49株作成した。そのうちのいくつかは、空気下でもAr気相中と同程度の高い水素生産活性を示し、 Δ Hup 株と比較した場合、クロロフィル当たりの水素生産活性は空気下で3-4倍向上した (図3)。一方、これらの変異株の窒素固定活性は著しく低下しており、反応における電子の大部分が水素生産に向かうように電子配分比率が変更されたと示唆される。その結果、窒素ガス気相中でも水素生産の高活性が長期にわたり持続するようになった¹⁰⁾。

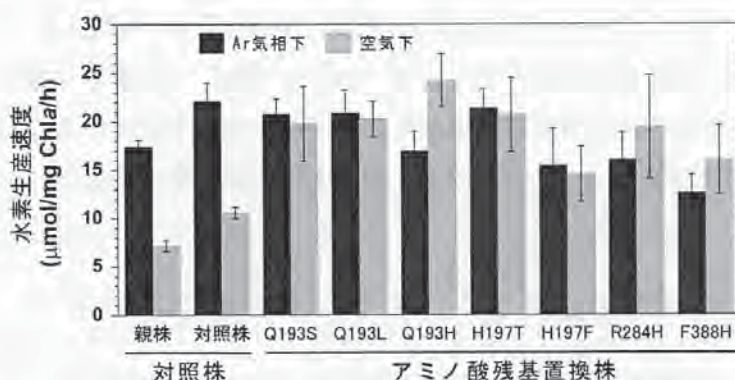


図3 ニトロゲナーゼ活性中心近傍アミノ酸残基置換の水素生産活性
 黒棒グラフ：Ar気相下，灰色棒グラフ：空気下。野生型ニトロゲナーゼを持つ対照株の空気下の水素生産活性は，窒素ガスによる阻害のためAr気相下の活性と比べて低下する。一方，いくつかのアミノ酸残基置換株は，空気下でもAr気相下と同程度の水素生産活性を示した。さらに，そのうちのいくつかは，対照株のAr気相下の活性に匹敵する活性を空気下で示す。水素生産活性の測定方法：細胞懸濁液を2-3時間光照射し，その間に生産された水素量をガスクロマトグラフを用いて測定した。

4 更なる水素生産性の向上に向けた改良の必要性

Δ Hup株の光から水素へのエネルギー変換効率は，実験室の弱光下では1%以上（太陽光換算，Ar気相で1週間にわたる水素生産）に達する⁷⁾。しかし，同様の変異株で，屋外で報告されている効率の最高値は0.1%（空気+2% CO₂気相，屋外で1日以上にわたる水素生産）¹¹⁾に過ぎない。水素生産の実用化に資するラン藻の開発には，ニトロゲナーゼの水素生産性を更に向上させる改良に加えて，光合成系や様々な代謝系の改良が必要である。今後，解決すべき課題として，ニトロゲナーゼが水素発生よりも窒素固定を最大化するように進化してきた結果だと考えられる低い分子活性（代謝回転数6.4/s），強光下での光利用効率の低下（強光阻害），培地中および細胞内の窒素化合物によるニトロゲナーゼ発現・活性の低下などが挙げられる。その他に，ヘテロシスト形成型ラン藻に特徴的な改良として，ヘテロシスト頻度の増加（最適化）やニトロゲナーゼ反応に必要な還元力源（スクロース）の合成およびヘテロシストへの供給の強化なども必要だと考えられる。筆者らの当面の目標は，これらの改良を積み重ねることで，屋外での（光→水素）エネルギー変換効率0.5%の達成を目指し，さらに将来の実用化のためには，1%以上にまで効率を高めることが目標となる。

5 おわりに

日本は，国土面積は狭いが，世界第6位の排他的経済水域を持つので，その水域を，更には外国の水域や公海をエネルギー生産の場として利用することが考えられる。将来的には，ラン藻が

太陽光をエネルギー変換効率1.2%で水素に変換し、関連工学的技術の進歩により、エネルギー回収率50%で精製された水素が目的港まで運搬できれば、世界の海洋の2%の海域（オーストラリア大陸の85%相当）を利用することにより人類が消費する化石燃料エネルギー（現在レベル）の50%を代替できると試算される。エネルギー変換効率の更なる向上、利用海域の拡大により、更に大きな代替エネルギー源となる可能性を持つ。ラン藻を海上培養し水素を光生物的に大規模生産する技術の実用化には、水素の分離、精製、貯蔵、利用（燃料電池）等の工学的技術の発展や社会的インフラの整備が課題であるが、現在、NEDO、ALCA等により水素関連技術研究の推進が図られており、その成果が期待される。ラン藻のニトロゲナーゼを利用した水素生産は、エネルギー変換効率は低いが、省力化、低コスト化、大規模化に適しているので、再生可能エネルギーの大規模生産につながる有力な候補であると考えられる。

文 献

- 1) 櫻井英博, 増川一, 燃料電池, 6, 46 (2006)
- 2) H. Sakurai and H. Masukawa, *Mar. Biotechnol.*, 9, 128 (2007)
- 3) H. Sakurai *et al.*, "Recent Advances in Phototrophic Prokaryotes", p.291, Springer (2010)
- 4) P. Tamagnini *et al.*, *Microbiol. Mol. Biol. Rev.*, 66, 1 (2002)
- 5) M. L. Ghirardi *et al.*, *Annu. Rev. Plant Biol.*, 58, 71 (2007)
- 6) H. Masukawa *et al.*, *Appl. Microbiol. Biotechnol.*, 58, 618 (2002)
- 7) F. Yoshino *et al.*, *Mar. Biotechnol.*, 9, 101 (2007)
- 8) H. Masukawa *et al.*, *Appl. Environ. Microbiol.*, 73, 7562 (2007)
- 9) O. Einsle *et al.*, *Science*, 297, 1696 (2002)
- 10) H. Masukawa *et al.*, *Appl. Environ. Microbiol.*, 76, 6741 (2010)
- 11) A. A. Tsygankov *et al.*, *Biotechnol. Bioeng.*, 80, 777 (2002)

**世界の化学品規制・ルール の解釈と
その違反回避のための実務**

(株)技術情報協会

2013年12月発刊 抜刷

第6章

化学物質管理を取り巻く現況・課題・今後の行方と企業対応法

第7節 有機フッ素化合物 (PFOS/PFOA)

1. PFOS/PFOA とは何か

炭素・フッ素結合を有する化学物質を有機フッ素化合物と言うが、その中にペルフルオロアルキルスルホン酸類と言われる一連の物質群がある。これは一般式 $C_nF_{2n+1}SO_3H$ (n は 1 以上の整数) で表される。また、類似した物質群にペルフルオロカルボン酸類というものがあり、こちらは一般式 $C_nF_{2n+1}COOH$ (n は 1 以上の整数) で表される。ペルフルオロアルキルスルホン酸類の代表的な化学種が PFOS (ペルフルオロオクタンスルホン酸, Perfluorooctanesulfonic acid, $C_8F_{17}SO_3H$) である。PFOS は本来、英語の Perfluorooctanesulfonate の略で、ペルフルオロオクタンスルホン酸 ($C_8F_{17}SO_3H$) が解離した陰イオン ($C_8F_{17}SO_3^-$) を意味するが、最近のストックホルム条約のホームページでは混乱を防ぐためか PFOS (Perfluorooctanesulfonic acid) と記述している。もちろん酸でも水中では解離して $C_8F_{17}SO_3^-$ になるので $C_8F_{17}SO_3H$ およびその塩の総称が PFOS と考えて良い。一方ペルフルオロカルボン酸類の代表物質は PFOA (ペルフルオロオクタン酸, Perfluorooctanoic acid, $C_7F_{15}COOH$) である。図 1 に PFOS, PFOA および環境水中でしばしば存在が報告されているペルフルオロアルキルスルホン酸類, ペルフルオロカルボン酸類, およびそれらの誘導体の構造を示す。

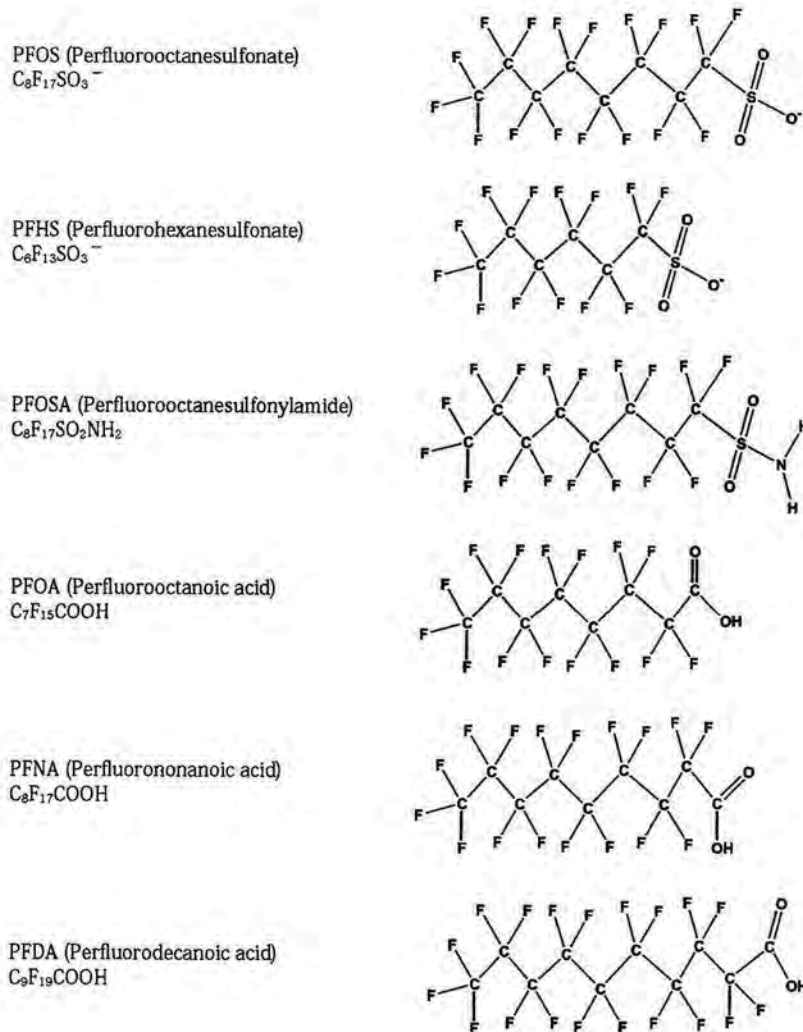


図 1

PFOSをはじめとするペルフルオロアルキルスルホン酸類は完全な人工物質で自然起源はない。一方、ペルフルオロカルボン酸類については、長い間自然起源はないと言われてきたが、近年、トリフルオロ酢酸 (CF_3COOH) が人間活動のほとんどない南極近辺の深海で検出されたため^{1,2)}、少なくともトリフルオロ酢酸については自然起源が存在するのではと考えられている。

このような物質群はフッ素系界面活性剤の主要な構成成分である。フッ素系界面活性剤は耐熱性 (500℃程度でも使える)、耐薬品性 (強酸、強アルカリ溶液中でも分解しない)、界面活性 (通常の界面活性剤では泡が消えるような媒体中でも泡を作ることができる)、有効性 (50～100 ppm 程度の少量の添加で効果がある)、光透過性 (光吸収しない、反射しない) といった特異的な性質を持っている^{3,4)}。このため PFOS は 2000 年に公表された米国の調査では撥水剤、カーペット、繊維、皮、ボードの保護剤、塗料、撥水・撥油紙、半導体リソグラフィー用の処理剤 (反射防止剤、酸発生剤、波うち防止剤)、フォトグラフィー用の処理剤、メッキ浴ミスト防止剤、航空機用油圧液体 (作動油)、消火剤、電子部品の表面処理剤、殺虫剤等の用途が挙げられていた⁵⁾。また、我が国では経済産業省が 2007 年に発表した調査結果によると半導体 (反射防止膜およびフォトレジスト)、フォトマスク (半導体および液晶ディスプレイ用)、写真感光剤、メッキ (クロムメッキ等)、泡消火剤、医療機器 (カテーテルおよび留置針)、電気電子部品 (プリンター、複写用転写ベルト、ゴムローラー等) といった用途があった⁶⁾。一方 PFOA はフッ素樹脂製造用の補助剤 (乳化剤)、消火剤、潤滑剤、グリース、ワックス、塗料、接着剤への添加、電子部品の表面処理剤等に使用されていた⁷⁻⁹⁾。

ところが 2000 年 5 月 16 日に、PFOS の製造に関して圧倒的なシェアを占めていた 3M 社が PFOS の生体蓄積性が明らかになったために製造をフェーズアウト (段階的に中止) するという発表を行い、その環境影響が懸念され始めた。これ以降、PFOS、さらには PFOA が環境水中や野生生物中に存在しているという発表が相次ぎ¹⁰⁾、環境分析の研究が進むにつれてペルフルオロノナン酸 (PFNA, $\text{C}_8\text{F}_{17}\text{COOH}$)、ペルフルオロデカン酸 (PFDA, $\text{C}_9\text{F}_{19}\text{COOH}$)、ペルフルオロウンデカン酸 ($\text{C}_{10}\text{F}_{21}\text{COOH}$, PFUA) といったペルフルオロアルキル基 ($\text{C}_n\text{F}_{2n+1}-$) が長いペルフルオロカルボン酸類 (長鎖ペルフルオロカルボン酸類) が北極圏の野生動物に PFOA 以上に蓄積していることも明らかとなった¹¹⁾。このため世界的に規制が検討されるようになったのである。

2. 規制の経緯

2000 年 5 月 16 日に 3M 社が PFOS の製造を 2003 年以降中止すると発表した 5 ヶ月後、米国環境保護庁 (EPA) は 2000 年 10 月 18 日付の官報で PFOS およびその関連物質を significant new use rule (SNUR, 重要新規利用規制) に指定することを提案した¹²⁾。SNUR とは化学物質のリスクが正当に評価できないにもかかわらず、人や環境にリスクをもたらす恐れや相当量の環境への排出もしくは人への暴露の恐れがあると判断された場合に、化学物質の製造、輸入等を制限・禁止する規則で、米国の化学物質規制法である Toxic Substances Control Act (TSCA, 健康あるいは環境に相当なリスクをもたらす化学物質および混合物を規制することを目的とした法律) に基づき交付される規則である。2002 年 11 月 21 日には経済協力開発機構 (OECD) が PFOS に関するリスクアセスメントを発表したが¹³⁾、同じころ米国では 2002 年 4 月 10 日に 13 物質¹⁴⁾、続いて 2003 年 1 月 8 日に 75 物質の PFOS 関連物質に対する SNUR の適用が開始された¹⁵⁾。これにより米国ではこれらの物質の製造・輸入が許可制となった。但し半導体レジストやフォトグラフィックフィルム、航空機用油圧作動油等は代替困難なため適用除外となった。このような状況を受けて我が国でも PFOS は 2002 年 12 月に化学物質の審査および製造等の規制に関する法律 (化審法) の第二種監視化学物質となった。米国では 2007 年 11 月にはさらに PFOS 関連物質 183 種について SNUR の適用が追加された¹⁶⁾。2006 年 12 月には EU が PFOS 濃度 0.005% 以上の物質もしくは調製品、0.1% 以上の半製品や成型品の上市を 2008 年 6 月 27 日以降禁止する 2006/122/EC 指令を発した¹⁷⁾。この指令が対象とする化学構造は一般式 $\text{C}_8\text{F}_{17}\text{SO}_2\text{Y}$ ($\text{Y} = \text{OH}$, 金属塩 ($\text{O}-\text{M}^+$), ハロゲン化物, アミド, その他ポリマーを含む誘導体) で表される全物質である。構造式は単純だが対象物質数は相当多いことになる。なお、この指令には必要な用途に関する除外規定があり、フォトリソグラフィー用のフォトレジスト、反射防止膜、フィルム、紙、あるいはプリント基板用のフォトグラフィックコーティング、メッキ浴ミスト防止剤、航空機用油圧作動油が挙げられている。また、消火剤については 2006 年 12 月 27 日より前に上市されたもの

は 2011 年 6 月 27 日までは使用できることになっていた。さらに EU は 2007 年 11 月 27 日に PIC すなわちロッテルダム条約 (The Rotterdam Convention on the Prior Informed Consent Procedure for Certain Hazardous Chemicals and Pesticides in International Trade : 国際条約の対象となる特定の化学物質および駆除剤についての事前のかつ情報に基づく同意の手続きに関するロッテルダム条約) に基づく規則 (PIC 規制) の対象物質に PFOS を追加した¹⁸⁾。カナダ環境省は 2006 年 12 月 16 日付けの官報で PFOS 関連物質の製造、使用、販売、販売のための提供および輸入を原則禁止する規制を提案した¹⁹⁾。ここで言う PFOS 関連物質とはペルフルオロオクタンスルホン酸とその塩、および $C_8F_{17}SO_2$ 、 $C_8F_{17}SO_3$ 、 $C_8F_{17}SO_2N$ 基を有する物質である。ここでも除外規定としてメッキ関係 (法が施行されてから 5 年間)、半導体や電子デバイス、フォトグラフィックフィルム、プリント基板が挙げられていた。2007 年 6 月には英国²⁰⁾ とドイツ²¹⁾ が飲料水ガイドライン ($0.3\mu\text{g/L}$) を設定した。

さらに 2005 年 6 月には残留性有機汚染物質に関するストックホルム条約 (POPs 条約) での規制の検討が開始され、2009 年 5 月の第 4 回締約国会議 (COP4) において附属書 B 物質 (製造、使用、輸出入の制限) への追加が決定した²²⁾。同時に PFOS の原料であるペルフルオロオクタンスルホニルフルオリド ($C_8F_{17}SO_2F$ 、ペルフルオロオクタンスルホン酸フルオリド、PFOSF) も附属書 B 物質へ追加された。このため我が国においてもこの条約の履行のために PFOS は 2009 年 10 月に化審法第一種特定化学物質 (原則として製造・輸入が禁止) への指定が決定し (施行は 2010 年 4 月)、3 用途 (エッチング剤、半導体用レジスト製造、業務用写真フィルムの製造) に限り例外的な使用が認められた²³⁾。同時に PFOSF も第一種特定化学物質に指定された。また PFOS はこれより前の 2008 年 11 月には化学物質排出把握管理促進法 (化管法) の第一種指定化学物質に指定され、環境中への排出量および移動量が 2010 年度分より国に届け出されることになった。2010 年 9 月には環境省が PFOS 含有廃棄物の処理に関する技術的留意事項 (ガイドライン) を発表した²⁴⁾。ここでは分解処理後の排水中の PFOS 濃度は $2\mu\text{g/L}$ を超えないよう定められている。これは筆者の知る限り、世界における排水中の PFOS 基準値の最初の例である。また、環境省のガイドラインでは焼却温度は当初は 1100°C 以上と定められたが現実の多くの焼却炉が対応できなかったため燃焼実験の結果を踏まえて 2011 年 3 月には 850°C 以上に改訂された。

一方 PFOS よりも産業界での重要性が高い PFOA については 2002 年 12 月に PFOS と共に化審法の第二種監視化学物質となったものの、有害性に関して不明な点が多いため PFOS よりも規制の検討は遅れていた。EPA は 2005 年 1 月にリスクアセスメントのドラフトを公表したが、不完全な点が多かったためかいまだに正式版が公表されていない²⁵⁾。代わりに EPA は 2006 年 1 月に世界の主要フッ素企業 8 社に自主削減プログラム (PFOA Stewardship program) を提案した²⁶⁾。これは製品中の、あるいは工場から排出される PFOA および長鎖ペルフルオロカルボン酸類および PFOA 前駆体を 2010 年までに 2000 年のレベルの 95% に削減し、2015 年までに自主的にゼロにする計画であり、2006 年 3 月までに全社が参加に同意し、現在も進行中である。このうち、PFOA 前駆体については当初は対象とする化学種が明確でなく、EPA は参加企業と協議して決めるとしていたが、テロマー製造プロセスにおけるテロマーアルコールやテロマーアイオダイド (ヨウ化物)、さらには製品中に残存し、PFOA に変化する物質である²⁷⁾。

2006 年 11 月には EPA と米国のフッ素企業が工場近郊の飲料水について、浄化あるいは代替水源に責任を持つ PFOA のレベルとして $0.5\mu\text{g/L}$ という数値を設定することで合意した²⁸⁾。2006 年 12 月にはノースカロライナ州が地下水中の暫定許容濃度を $2\mu\text{g/L}$ に設定し²⁹⁾、2009 年 1 月には EPA の水質局が暫定的な健康基準値として $0.4\mu\text{g/L}$ を設定した³⁰⁾。2007 年 6 月には英国²⁰⁾ とドイツ²¹⁾ が PFOS と同時に飲料水ガイドライン ($0.3\mu\text{g/L}$) を設定しており、水質に関連する基準値が出来つつある。我が国においても 2009 年 4 月に PFOS/PFOA は水道水に関する要監視項目に指定されている。また、炭素数 14 ~ 17 の長鎖ペルフルオロカルボン酸類は、2007 年 5 月に化審法第一種監視化学物質になっている。

3. 今後の規制動向

以上示したように PFOS については先進国を中心に製造や使用に関する厳しい規制が制定され、ストックホルム条約での本格的な規制も開始されたため使用の削減が急速に進行している。また、PFOA についても自主的な削減が進行し

ており、EPAの自主削減プログラムも順調に推移している³¹⁾。このためリスク評価の対象はPFOS/PFOAからこれらの類縁物質さらには代替物質へと移りつつある。例えばストックホルム条約のCOPの下部組織である残留性有機汚染物質検討委員会(Persistent Organic Pollutants Review Committee, POPRC: ポップロック)は2010年4月にPFOS代替物質の使用に関するガイドラインのドラフトを発表し³²⁾、2011年10月に開催されたPOPRC7の結果を受けて代替物質の使用状況に関する情報を提出するよう呼びかけている³³⁾。このドラフトには代替物質として短鎖ペルフルオロアルキルスルホン酸類、短鎖ペルフルオロアルキルケトンおよびエーテル類、フルオロテロマー、フルオロフォスフェート、フルオロポリエーテル、さらにはシロキサンやシリコンポリマーといったケイ素化合物が挙げられている。また、EPAもPFOA代替物質について2008年6月以降、100種を超える物質を審査しており、規制検討の方針として、毒性はもとより、考えられる最終的な分解生成物、生分解性、光分解性等のデータが重要であることを述べている³⁴⁾。

文 献

- 1) H. Frank, E. H. Christoph, O. Holm-Hansen, J. L. Bulliste, Environ. Sci. Technol. 36, 12-15 (2002)
- 2) B. F. Scott, R. W. Macdonald, K. Kannan, A. Fisk, A. Witter, N. Yamashita, L. Duhram, C. Spencer, D. C. G. Muir, Environ. Sci. Technol. 39, 6555-6560 (2005)
- 3) 角田光雄監修, 機能性界面活性剤, 第5章 深津隆, 占野尚之, フッ素系界面活性剤とその応用, シーエムシー, p. 96-108 (2000)
- 4) フッ素製品市場の実態と展望, シーエムシー, p. 137-148 (2001)
- 5) USEPA, PerfluorooctylSulfonates ; Proposed Significant New Use Rule, Federal Register, Vol. 65, No. 202, 62319-62333 (2000)
- 6) 経済産業省, PFOS製造禁止に伴うPFOSの使用と代替可能性に関する結果について
http://www.meti.go.jp/policy/chemical_management/03kanri/c05temp4.htm
- 7) OECD, Results of Survey on Production and Use of PFOS, PFAS and PFOA, Related Substances and Products/Mixtures Containing These Substances. OECD Environment, Health and Safety Publications Series of Risk Management No. 19, 13-Jan-2005
[http://www.oecd.org/olis/2005doc.nsf/43bb6130e5e86e5fc12569fa005d004c/9dccc1c0ae173bbdc1256f88005917c6/\\$FILE/JT00176885.PDF](http://www.oecd.org/olis/2005doc.nsf/43bb6130e5e86e5fc12569fa005d004c/9dccc1c0ae173bbdc1256f88005917c6/$FILE/JT00176885.PDF)
- 8) OECD, Results of the 2006 Survey on Production and Use of PFOS, PFAS, PFOA, PFCA, their Related Substances and Products/Mixtures Containing these Substances. OECD Environment, Health and Safety Publications Series of Risk Management No.22, 06-Dec-2006
[http://appli1.oecd.org/olis/2006doc.nsf/43bb6130e5e86e5fc12569fa005d004c/ec0131054df5f681c125723c003b1323/\\$FILE/JT03219292.PDF](http://appli1.oecd.org/olis/2006doc.nsf/43bb6130e5e86e5fc12569fa005d004c/ec0131054df5f681c125723c003b1323/$FILE/JT03219292.PDF)
- 9) 環境省環境保健部環境安全課, 平成16年度(2004年度)版「化学物質と環境」第2章, 平成15年度暴露量調査結果: 物質群別の調査結果, ペルフルオロオクタン酸
http://www.env.go.jp/chemi/kurohon/http2004/sec2_2_1.html#7
- 10) J. P. Giesy, K. Kannan, Environ. Sci. Technol., 36, 146A-152A (2002)
- 11) J. W. Martin, M. M. Smithwick, B. M. Braue, P. F. Hoekstra, D. C. G. Muir and S. A. Mabury, Environ. Sci. Technol. 38 (2004) 373-380
- 12) USEPA, PerfluorooctylSulfonates; Proposed Significant New Use Rule, Federal Register, October 18, Vol. 65, No.202, 62319-62333 (2000)
- 13) OECD, Hazard Assessment of PerfluorooctaneSulfonate (PFOS) and its Salts, Organisation for Economic Co-operation and Development, Environment Directorate, Joint Meeting of the Chemicals Committee and the Working Party on Chemicals, Pesticides and Biotechnology, ENV/JM/RD (2002)17FINAL, (2002)

- 14) USEPA, PerfluoroalkylSulfonates ; Significant New Use Rule, Federal Register, March 11, 2002, Vol. 67, No.47, 11007-11013 (2002)
- 15) USEPA, PerfluoroalkylSulfonates ; Significant New Use Rule, Federal Register, December 9, Vol. 67, No. 236, 72854-72867 (2002)
- 16) USEPA, PerfluoroalkylSulfonates ; Significant New Use Rule, Federal Register, October 9, Vol. 72, No.194, 57222-57235 (2007)
- 17) Directive 2006/122/EC of the European Parliament and of the Council of 12 December, Official Journal of the European Union, L372/32-34, 27. 12. 2006
http://eur-lex.europa.eu/LexUriServ/site/en/oj/2006/l_372/l_37220061227en00320034.pdf
- 18) Commission Regulation (EC) No 1376/227 of 23 November 2007, amending Annex I to Regulation (EC) No 304/2003 of the European Parliament and of the Council concerning the export and import of dangerous chemicals. Official Journal of the European Union, L307/14-17
http://eur-lex.europa.eu/LexUriServ/site/en/oj/2007/l_307/l_30720071124en00140017.pdf
- 19) Department of the Environment, PerfluorooctaneSulfonate and its Salts and Certain Other Compounds Regulations, Canada Gazette, Official Newspaper of the Government of Canada, Vol. 140, No. 50, December 16, 2006
<http://canadagazette.gc.ca/partI/2006/20061216/html/regle2-e.html>
- 20) Drinking Water Inspectorate, Guidance on the Water Supply (Water Quality Regulations 2000/2001 Specific to PFOS (PerfluorooctaneSulfonate) and PFOA (Perfluorooctanoic Acid) Concentrations in Drinking Water
<http://www.dwi.gov.uk/regs/infolett/2007/info0507.shtm>
- 21) Statement by the Drinking Water Commission of the German Ministry of Health at the Federal Environment Agency June 21, 2006 (revised July 13, 2006)
<http://www.umweltbundesamt.de/uba-info-presse-e/hintergrund/pft-in-drinking-water.pdf>
- 22) Stockholm Convention on Persistent Organic Pollutants (POPs)
<http://chm.pops.int/Convention/Media/PressReleases/COP4Geneva9May2009/tabid/542/Default.aspx>
- 23) 経済産業省, 第一種特定化学物質－エッセンシャルユースと取扱上の技術基準について
http://www.meti.go.jp/policy/chemical_management/kasinhou/about/class1specified_kijun.html
- 24) 環境省廃棄物・リサイクル対策部, PFOS 含有廃棄物の処理に関する技術的留意事項
<http://www.env.go.jp/recycle/misc/pfos/tptc.pdf>
- 25) USEPA, Perfluorooctanoic Acid (PFOA) and Fluorinated Telomers
<http://www.epa.gov/oppt/pfoa/pubs/pfoarisk.html>
- 26) USEPA, 2010/2015 PFOA Stewardship Program
<http://www.epa.gov/oppt/pfoa/pubs/stewardship/index.html>
- 27) 日本弗素樹脂工業会, ふっ素樹脂およびテロマー製品製造メーカーからのお知らせ, PFOA 排出量の削減活動についてのお知らせ その2
<http://www.jfia.gr.jp/>
- 28) USEPA, EPA Reaches Agreement with DuPont to Protect Drinking Water Near W. Va. Plant
http://www.epa.gov/region03/enforcement/dupont_order.pdf
- 29) Department of Environment and Natural Resources. Division of Water Quality, Subchapter 2L Section .0100, .200, .300. Classifications and Water Quality Standards Applicable to the Groundwaters of North Carolina. Last Amended on December 7, 2006
http://h2o.enr.state.nc.us/admin/rules/documents/WEBversioncomp2Lw-PFOAInterim_dec06.pdf
- 30) Division of Water Supply, State of New Jersey, Perfluorooctanoic acid (PFOA) in Drinking Water

- <http://www.nj.gov/dep/watersupply/pfoa.htm>
- 31) USEPA, Perfluorooctanoic Acid (PFOA) and Fluorinated Telomers, 2011 Annual Progress Reports,
<http://www.epa.gov/oppt/pfoa/pubs/stewardship/preports5.html>
 - 32) Stockholm Convention on Persistent Organic Pollutants. Invitation to submit comments on draft guidance document on alternatives to PFOS and derivatives
<http://chm.pops.int/Convention/POPsReviewCommittee/POPRCMeetings/POPRC5/POPRC5Followupcommunications/PFOSalternativesguidanceInvitationforcomments/tabid/741/Default.aspx>
 - 33) Invitation to submit information on alternatives to the use of perfluorooctane sulfonic acid (PFOS) in open application to the POPs Review Committee
<http://chm.pops.int/Implementation/NewPOPs/DecisionSC419Informationrequest/PFOSinopenapplication/tabid/2496/Default.aspx>
 - 34) USEPA, Perfluorooctanoic Acid (PFOA) and Fluorinated Telomers, New Chemical Review of Alternatives for PFOA and Related Chemicals
<http://www.epa.gov/oppt/pfoa/pubs/altnewchems.html>

各種機能水の評価法について

電解水、磁気処理水、超音波処理水を例に

神奈川大学 西本 右子

● はじめに

機能水は各種の希薄水溶液に物理的・化学的な処理を施すことで、機能が付加された溶液と考えることができよう。機能水の例を表1に示した。原水に純水でない水道水や地下水などが用いられているため、処理と機能との関連に明確な再現性が得られていないことが多い。また、処理の持続時間、処理に対する水温や溶存気体等の影響が無視できないことが多く、発現した機能の分析法も充分確立されているとは言いがたい。以下には純水から調製した水溶液を例に分析した結果を中心に示す。

表1 機能水の例

機能水の例	処理の例
電解水	電気分解
アルカリイオン水	電気分解
磁化水	磁気処理
超音波処理水	超音波処理(照射)
鉱物・セラミック処理水	鉱物、セラミックスとの接触
純水、RO水、脱イオン水、蒸留水、超純水	不純物等の除去
上記の複合処理水	上記の複合処理

表2 電解水の例

電解水の名称の例	pH	調製方法	主な有効成分
強酸性電解水	2.7以下	隔膜を有する電解装置でNaClを電解助剤とした電解で得られた陽極水	HClO
弱酸性電解水	2.7~5.0		HClO+ClO ⁻
微酸性電解水	5.0~6.5	隔膜のない電解装置で2~6%塩酸を電解後水道水で希釈	
電解次亜水	7.5~		NaClO
強アルカリ電解水	11付近	陰極水	NaOH, H ₂
アルカリイオン水	9~11	隔膜を有する電解装置で乳酸カルシウムを電解助剤とした電解で得られた陰極水	Ca(OH) ₂ , H ₂

● 電解水の場合(1)~(6)

電解水は電解助剤としてNaClを添加して水道水を電気分解して得られた溶液を指すことが多いが、添加する電解助剤、電解装置の構造(陽極水と陰極水を隔膜で仕切るか)、電解の電流・電圧によって性状の異なるいくつかの水溶液の総称といえる。名称も充分統一されているとはいえない。表2に電解水の例を示した。機能水学会の名称に準じるが、議論の余地はある。

ここではCl⁻を含む水溶液を電気分解した際に生じるCl₂が水に溶けて生成した次亜塩素酸(HClO)を含有する電解水についての分析、評価法を中心に述べる。これらの電解水は即効的な殺菌効果を示すため、評価法は遊離有効塩素が中心となる。

陽極での反応は以下の式で表される。



生じたCl₂は以下の式(3)に示される

ように、水中でHClOを生じる。



HClOは以下の式(4)に示す平衡関係にあるので、HClOとClO⁻の割合はpHで決まる。

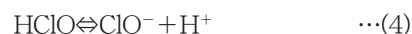


図1には電解水のpHを変化させた際のUVスペクトルを示した。232 nmの吸収はHClO、292 nmの吸収はClO⁻によるものである。pHの上昇に伴い232 nmの吸収強度が減少し、292 nmの吸収強度が増加する。255 nm付近には等吸収点が観測される。遊離有効塩素としてHClOとClO⁻の分別定量ができる方法である。図2にはこの方法で求めたHClO、ClO⁻、及びその総量をプロットした。また電解操作を施さずに試薬から調製した水溶液も性状、殺菌効果共に差異がないことが確認された。

HClOは反応性が高く、一般にシステイン(Cys)やメチオニン(Met)のような含硫アミノ酸を酸化し、タンパク質のトリプトファン(Trp)、チロシン(Tyr)、ヒスチジン(His)残基も酸化して三次構造を解くことが知られている。電解操作を施さずに試薬から調製した水溶液も性状、殺菌効果共に差異がないことが確認されているため、pH2.5~pH12の電解水モデル溶液を用いて、グリシン(Gly)、Cys、グルタ

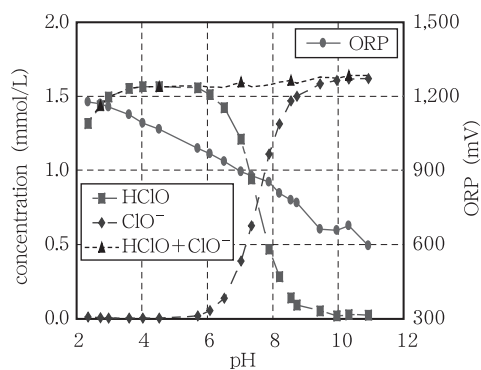
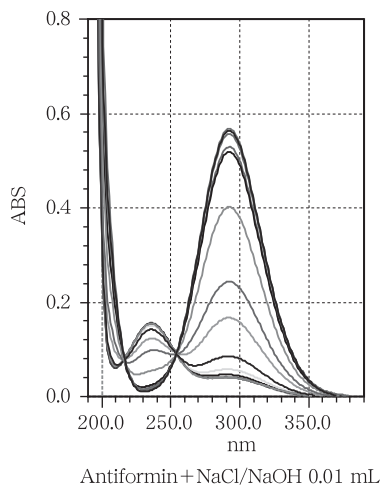


図1 電解水の有効塩素量とその組成に対するpHの影響



比1:1) の¹³C NMRの結果を示した。アミノ基部分での変化が大きく、アルカリ側では相互作用が弱くなった。*S. aureus*, *E. coli*, *P. aeruginosa*を用いて行った殺菌効果試験結果より、アルカリ側ほど即効的な殺菌効果を示さなくなることがわかり、¹³C NMRの結果と相関がみられた。

図3にpH3においてGSH及びその構成アミノ酸で含硫アミノ酸であるL-Cysと非含硫アミノ酸であるL-Gluの溶存状態を円二色性 (CD) スペクトルで測定した結果を示した。HClO濃度に伴ってピーク形状が変化したが、L-Cysではモル比1:5、L-Gluでは1:3を超えるとアミノ酸のCDピークが観測されなくなり、GSHでは1:5を超えるとピーク形状が変化しなくなった。L-CysのCDピーク強度のモル比に対する変化も併せて示した。アミノ酸濃度にかかわらず傾向は同様であり、ピーク強度変化に屈曲点が観測された。非含硫アミノ酸ではこのような屈曲点は観測されず、1:3ではほぼゼロとなった。図4にはHClOとGSH、L-Cys、L-Gluの混合溶液を用いた殺菌効果試験結果を示した。CDスペクトルにおいてピーク形状の変化が観測されなくなったモル比以上では即効的な殺菌効果が観測され、遊離型有効塩素が存在していることがわかる。

電解水ではOHラジカル等の活性酸素種の存在も指摘されているが、不明な点も多い。図5にはスピントラップ剤にDMPO (5, 5'-dimethyl-1-pyrroline-N-oxide) を用いたESR測定結果を示した。スピントラップ剤にPBN (α -phenyl-N-tert-butyl-nitron), DEPMPO (5-diethoxy-phosphoryl-5-methyl-1-pyrroline-N-oxide), 4PD-MPO (5, 5'-dimethyl-4-phenyl-1-pyrroline-N-oxide) を用いた結果と比較検討した結果、pH3、6、9.5ではスーパーオキシド (O_2^-) が観測され、pH12ではOHラジカルといくつかの活性酸素種が重なったピークが観測され

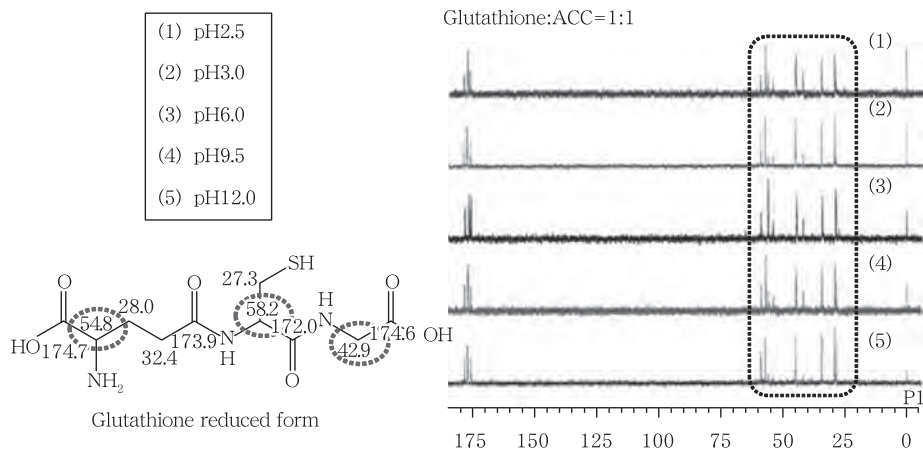


図2 電解水の有効塩素量とその組成に対するpHの影響

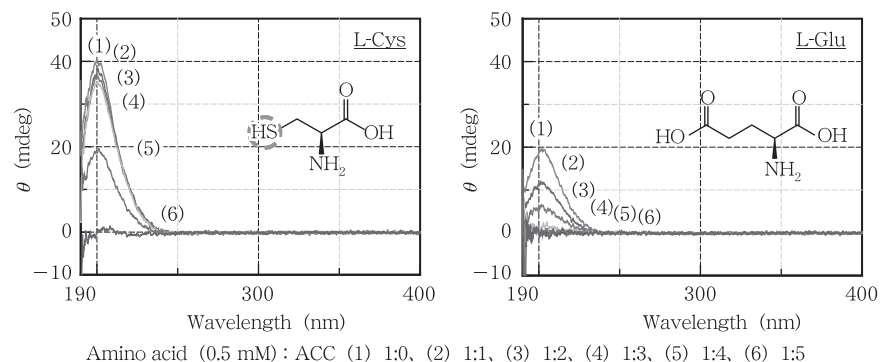


図3 L-Cys及びL-GluのCDスペクトルに対するHClOの影響

ミン酸 (Glu) のトリペプチドであり、動植物界に広く存在するグルタチオン

(GSH) への作用を¹³C NMRによって検討した。図2にはGSHとHClO (モル

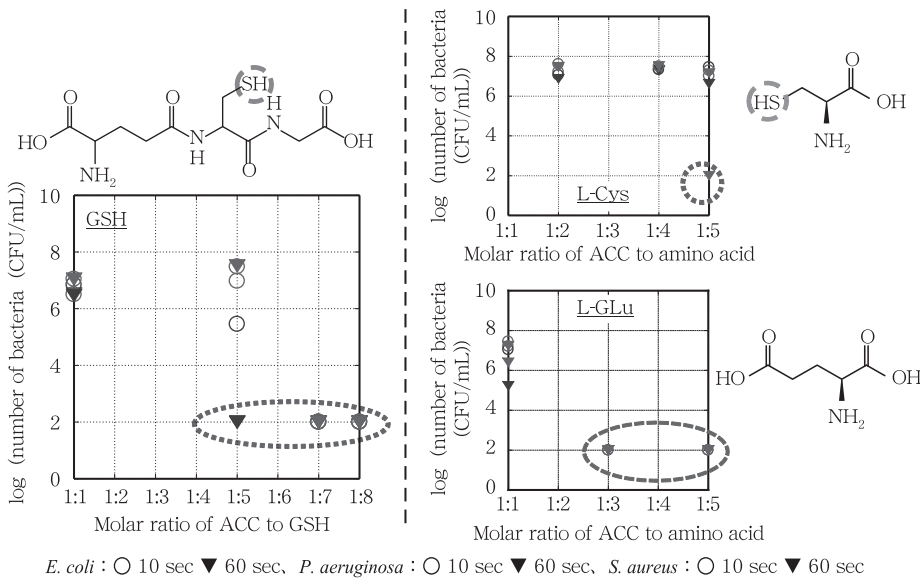


図4 殺菌効果試験結果 (GSH or Amino acid) : ACC

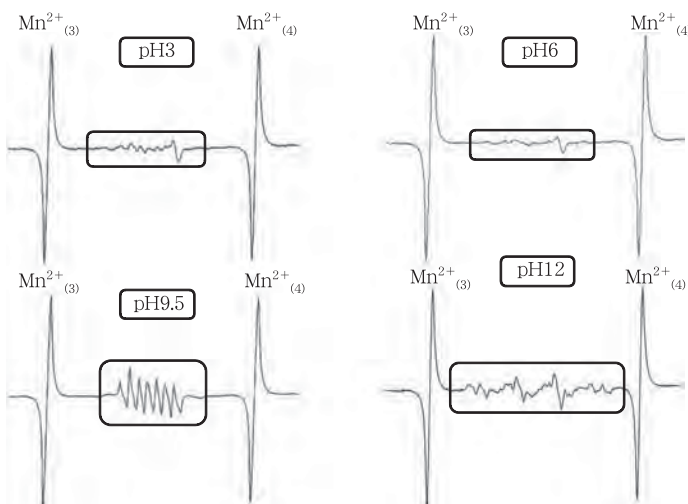


図5 電解水モデル溶液のDMPOスピントラップ法によるESR (NaCl 20 mmol/L, NaClO 5 mmol/Lに調製、pH3、pH6、pH9.5、pH12)

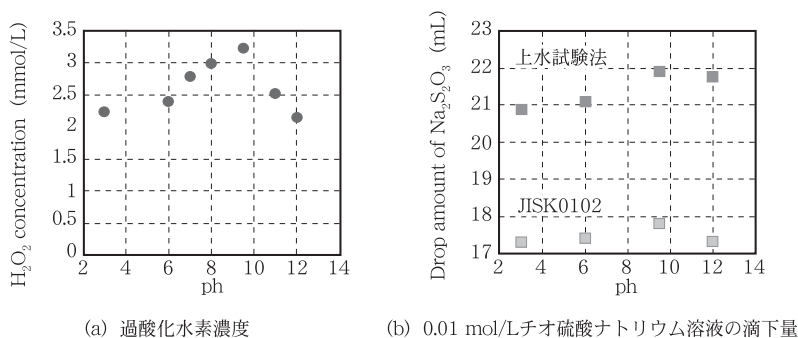


図6 電解水モデル溶液中のH₂O₂と酸化性物質の濃度に対するpHの影響

る。また発生量はpH9.5付近が多いこともわかった。アルコールデヒドロゲナーゼカタラーゼ法による過酸化水素濃度及び残留塩素測定に用いられるヨウ素滴定結果からもpH9.5付近において極大値となり、酸化性物質の生成もpH9.5付近が多いことがわかる。図6に結果を示した。図には酸化条件の異なる上水試験法の結果とJIS K 0.102の結果を併せて示した。電解水モデル溶液は電解水と溶存酸素量のみが異なるため、モデル溶液を酸素飽和水から調製し、検討したが、結果に差異はみられず溶存酸素量の影響は観測されることが確認された。

● 磁気処理水の場合⁽⁷⁾⁽⁸⁾

NaCl水溶液では磁場中で凍結させると塩と水の共晶の融解ピークが変化する。図7に0.35Tの磁場中で凍結させた0.1 mol/L NaCl水溶液の共晶の融解ピーク (DSC測定結果) を示した。脱気していない試料では融解ピークはダブルピークとなり低温側にピークが現れる。この低温側のピークは磁場強度に依存して融解温度が変化する。図8にはD-Asnを2 mmol/L含有する場合の例を示した。

溶液状態で磁気処理を施すとOHラジカルの増加が観測される。図9は10 mmol/LのNaCl、KCl、CaCl₂、MgCl₂水溶液をねじ口試験管に入れ、中心磁

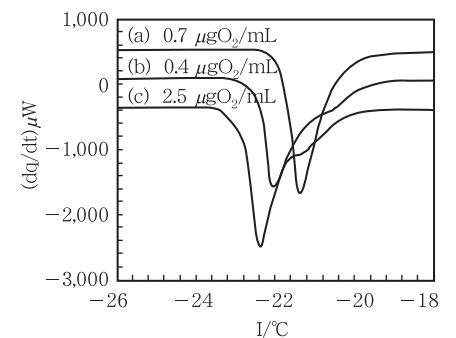


図7 NaCl水溶液 (0.1 mol/L) における塩と水の共晶に対する溶存酸素の影響 (DSC)

場が80 mTと120 mTの磁石で30回処理した溶液のOHラジカルの変化と*E. Coli*に対する抗菌試験の結果を示した。OHラジカルの発生量が多いほど菌数が少なくなっており、磁気処理の抗菌作用への関与が考えられた。

● 超音波処理の場合⁽⁹⁾

水と任意の割合で混合することができるエタノールと1-プロパノールを取り上げて、超音波処理の影響を検討した。これらのアルコールは水と共晶を形成する。そこで共晶の融解過程、近赤外吸収スペクトル、¹⁷O NMRから評価した。図10にモル分率0.2以下のエタノール水溶液の近赤外スペクトル(純水との差スペクトル)を示した。エ

タノール濃度の増加に伴い950 nm、1,150 nmの吸収(水素結合に関与しない水)が減少し、1,180 nm付近の吸収(水素結合に関与する水)が増加している。超音波処理による共晶の融解定の変化を図10に示した。処理条件は80 W、10分である。

希薄なエタノール水溶液ではエタノール1分子に直接水和する水分子は17、1-プロパノール水溶液では15といわれている。アルコール分子が完全に水和されているモル分率0.05においては、超音波処理の影響が小さく、モル分率0.1の方が大きく観測されている。超音波処理による水和構造の不安定化を反映して共晶の融解熱量が減少したと考えられた。

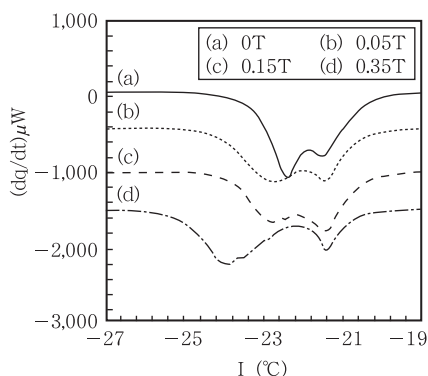


図8 D-Asnを2 mmol/L含有する0.1 mol/L NaCl水溶液の共晶の融解過程に対する磁場の影響

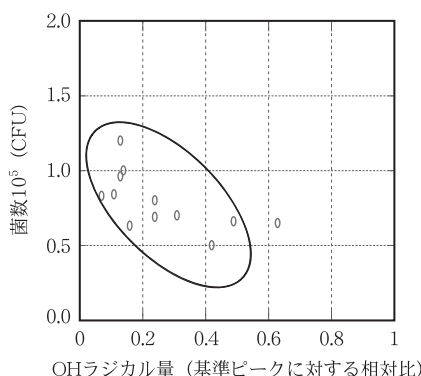


図9 塩の水溶液の磁気処理によるOHラジカル量と*E. coli*に対する抗菌試験結果

＜参考文献＞

- (1) 西本右子・森下裕子・貝塚美保子：いわゆる機能水と呼ばれる強酸性電解水の評価、分析化学、45, pp.701-706 (1996)
- (2) 野村浩康・香田忍・米森重明・下平哲司・三宅晴久・西本右子：強酸性電解水の物理化学と殺菌機構、日本手術医学会誌、19, pp.11-19 (1998)
- (3) 岩沢篤郎・中村良子・重山かの・丹羽友和・西本右子：強酸性電解水の有効塩素測定法、防菌防微誌、30, pp.627-633 (2002)
- (4) 岩沢篤郎・中村良子・丹羽友和・西本右子：強酸性電解水の殺菌効果に対するpHの影響防菌防微誌、30, pp.635-643 (2002)
- (5) 岩沢篤郎・中村良子・井上啓・丹羽友和・西本右子：強酸性電解水の殺菌効果に対するpH及び共存塩濃度の影響、防菌防微誌、32, pp.301-306 (2004)
- (6) 西本右子・井上啓：電解水の安定性に対するpHおよび温度の影響、機能水研究、2, pp.71-74 (2004)
- (7) Shizuo Fujiwara and Yuko Nishimoto : Magnetic Field Effect on Freezing of Aqueous Sodium Chloride Solution in Presence of Oxygen, Analytical Sciences, 8, pp.873-874 (1992)
- (8) 岩沢篤郎・高橋法子・中村良子・西本右子：低濃度塩水溶液に紫外線照射・磁気処理した後の活性酸素生成と殺菌効果について、防菌防微誌、36, pp.285-291 (2008)
- (9) Yuko NISHIMOTO and Youichi KANEKI : Detection of water-polar solvent interaction using melting of a eutectic, ThermochimicaActa, 399, pp.139-144 (2003)
- (10) 岩沢篤郎・原野綾・滝山由貴・中村良子・西本右子：次亜塩素酸の殺菌効果に対するpHの影響、防菌防微誌、37, pp.243-252 (2009)
- (11) 岩沢篤郎・安富真央・中村良子・西本右子：次亜塩素酸と含硫アミノ酸との相互作用と殺菌効果、防菌防微誌、38, pp.69-74 (2010)
- (12) 安富真央・岩沢篤郎・西本右子：4種のアミノ酸とグルタチオンに対する次亜塩素酸の作用と殺菌効果、防菌防微誌、39, pp.673-677 (2011)

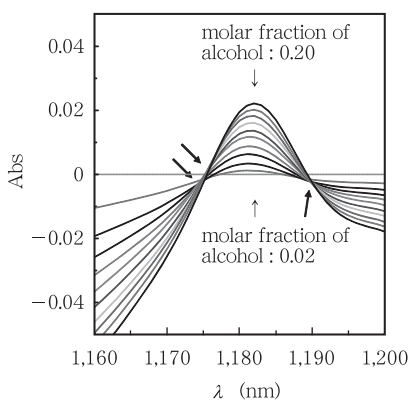
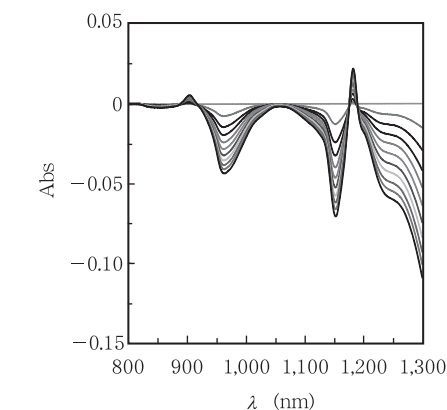


図10 エタノール水溶液の近赤外スペクトルエタノールモル分率：0.02～0.20

筆者紹介

西本右子

神奈川大学 理学部化学科 教授
〒259-1293
神奈川県平塚市土屋2946
TEL : 0463-59-4111
FAX : 0463-58-9684
E-mail : y24moto@kanagawa-u.ac.jp

Catalyst-transfer condensation polymerization for precision synthesis of π -conjugated polymers*

Tsutomu Yokozawa[‡], Yutaka Nanashima, Haruhiko Kohno, Ryosuke Suzuki, Masataka Nojima, and Yoshihiro Ohta

Department of Materials and Life Chemistry, Kanagawa University, Rokkakubashi, Kanagawa-ku, Yokohama 221-8686, Japan

Abstract: Catalyst-transfer condensation polymerization, in which the catalyst activates the polymer end-group, followed by reaction with the monomer and transfer of the catalyst to the elongated polymer end-group, has made it feasible to control the molecular weight, polydispersity, and end-groups of π -conjugated polymers. In this paper, our recent progress of Kumada–Tamao Ni catalyst-transfer coupling polymerization and Suzuki–Miyaura Pd catalyst-transfer coupling polymerization is described. In the former polymerization method, the polymerization of Grignard pyridine monomers was investigated for the synthesis of well-defined n-type π -conjugated polymers. *Para*-type pyridine monomer, 3-alkoxy-2-bromo-5-chloromagnesiopyridine, afforded poly(pyridine-2,5-diyl) with low solubility in the reaction solvent, whereas *meta*-type pyridine monomer, 2-alkoxy-5-bromo-3-chloromagnesiopyridine, yielded soluble poly(pyridine-3,5-diyl) with controlled molecular weight and low polydispersity. In Suzuki–Miyaura catalyst-transfer coupling polymerization, *t*-Bu₃PPd(Ph)Br was an effective catalyst, and well-defined poly(*p*-phenylene) and poly(3-hexylthiophene) (P3HT) were obtained by concomitant use of CsF/18-crown-6 as a base in tetrahydrofuran (THF) and a small amount of water.

Keywords: catalysis; catalysts; conjugated polymers; coupling reactions; Kumada; nickel; organic semiconductors; palladium catalyst-transfer; Suzuki.

INTRODUCTION

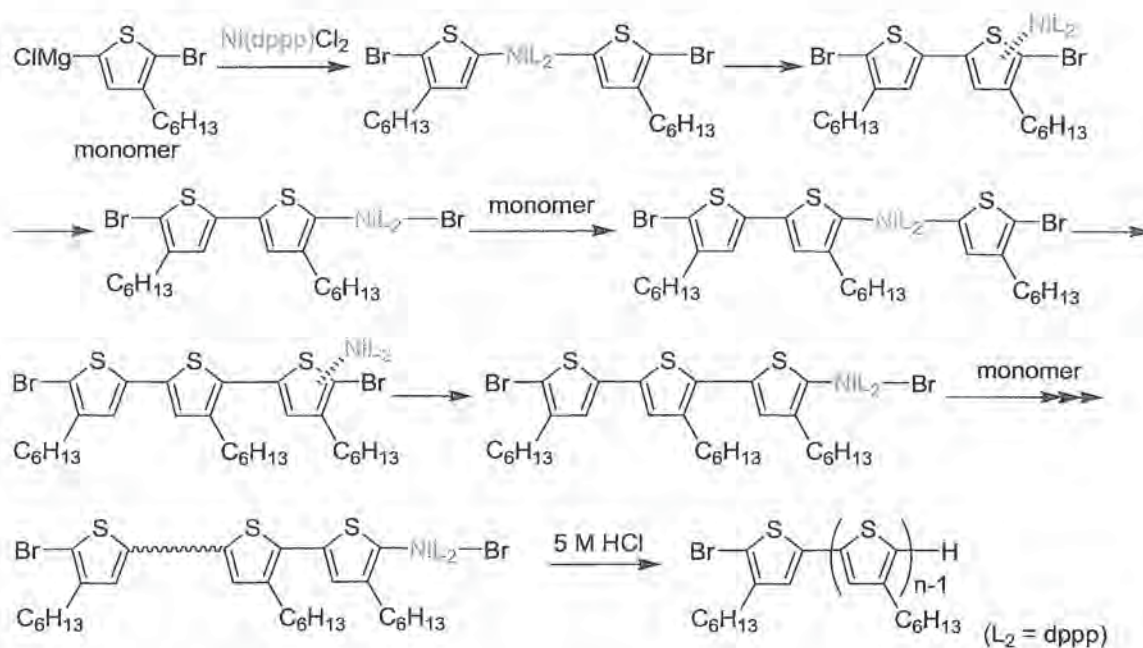
π -Conjugated polymers containing aromatic rings in the backbone are an attractive class of materials owing to their potential organic electronic materials and devices such as field effect transistors (FETs), organic light-emitting diodes (OLEDs), and photovoltaic cells. These polymers have generally been synthesized by condensation polymerization such as electrochemical polymerization [1] and metal-mediated polycondensation [2–4]. Therefore, the molecular weight of those polymers is generally difficult to control within narrow molecular weight distribution. However, uncontrolled molecular weight and broad molecular weight distribution do not stem inherently from the reaction type of condensation polymerization, i.e., condensation steps with elimination of a small molecule species, but from a polymerization mechanism for step-growth polymerization, in which all the end-groups of monomers and oligomers in the reaction mixture equally react with each other. Accordingly, if the mechanism of con-

*Pure Appl. Chem. 85, 493–587 (2013). A collection of invited papers based on presentations at the 14th International Conference on Polymers and Organic Chemistry (POC 2012), Doha, Qatar, 6–9 January 2012.

[‡]Corresponding author: E-mail: yokozt01@kanagawa-u.ac.jp

condensation polymerization could be converted from step-growth to chain-growth, π -conjugated polymers with defined molecular weight and narrow molecular weight distribution would be obtained.

This change of mechanism in condensation polymerization is evidently not impossible. We have developed chain-growth condensation polymerization and succeeded in synthesizing well-defined condensation polymers such as polyamides, polyethers, and polyesters. These polymerizations involve selective activation of the polymer end-groups as a result of differences in substituent effects between the monomer and the polymer [5,6]. Condensation polymerization with a catalyst can involve another mechanism for chain-growth condensation polymerization. That is catalyst-transfer mechanism, in which the catalyst activates the polymer end-group, followed by reaction with the monomer and transfer of the catalyst to the elongated polymer end-group, in a similar manner to biological condensation polymerization. We [7–9] and McCullough [10,11] have independently established this mechanism for the Ni-catalyzed condensation polymerization leading to poly(3-hexylthiophene) (P3HT). Thus, Ni(dppp)Cl₂ (dppp = 1,3-diphenylphosphinopropane) reacts with 2 equiv of Grignard thiophene monomer, and the coupling reaction occurs with concomitant generation of a zero-valent Ni complex. The Ni(0) complex does not diffuse to the reaction mixture but is inserted into the intramolecular C–Br bond. Another monomer reacts with this Ni, followed by the coupling reaction and transfer of the Ni catalyst to the next C–Br bond. Growth would continue in such a way that the Ni catalyst moves to the polymer end-group (Scheme 1).



Scheme 1

Since then, the catalyst-transfer condensation polymerization for poly(3-alkylthiophene)s (P3ATs) have been extensively developed. For example, block and gradient cop3ATs with different alkyl side chains and block copolymers of P3AT and vinyl polymers were synthesized [12,13]. External Ni-initiators [14–18] were formed and applied to the production of P3AT brushes from a substrate surface [14,16,19–21]. Furthermore, the mechanism has been thoroughly investigated [22–25]. We have investigated catalyst-transfer condensation polymerization for the synthesis of other π -conjugated polymers by not only Ni-catalyzed Kumada–Tamao coupling polymerization but also Pd-catalyzed Suzuki–Miyaura coupling polymerization. In this paper, our recent progress of study about catalyst-transfer condensation polymerization is described.

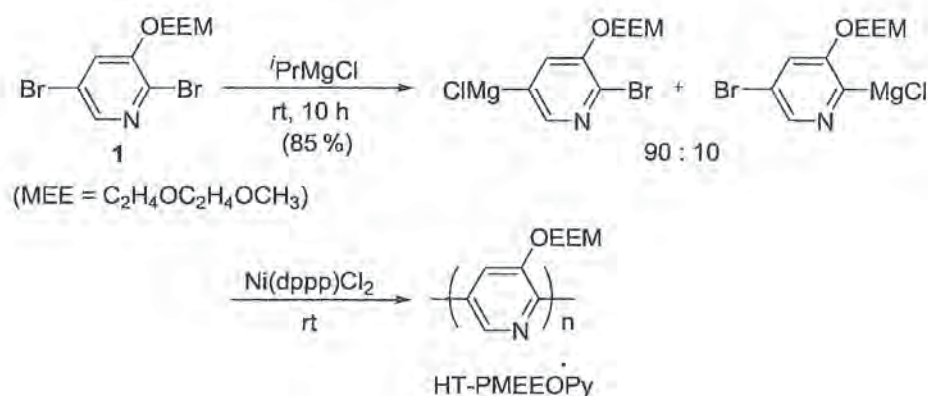
KUMADA–TAMAO COUPLING POLYMERIZATION

Kumada–Tamao catalyst-transfer condensation polymerization yields not only P3ATs but also poly(*p*-phenylene)s [26], poly(*m*-phenylene)s [27], poly(*N*-alkylpyrrole)s [28,29], polyfluorenes [29,30], and poly(bithienylmethylene)s [31] in a controlled manner. However, Kumada–Tamao catalyst-transfer condensation polymerization has been limited to the polymerization of donor monomers for the synthesis of p-type π -conjugated polymers. The polymerization of acceptor monomers has the following difficulties: (1) some electron-withdrawing groups such as carbonyl group in acceptor monomers are not tolerable for the formation of Grignard monomer; (2) the solubility of n-type π -conjugated polymers is generally lower than that of p-type ones because acceptor aromatics have stronger π – π stacking interaction than donor aromatics do; (3) the weaker π -donation of n-type polymer backbone to a Ni(0) catalyst may not sufficiently assist intramolecular catalyst transfer on the basis of the fact that well-defined π -conjugated block copolymers were obtained by the successive polymerization from a monomer with low π -donor ability to a monomer with high π -donor ability [28,32]. Kiriy and Huck have recently advanced this field and synthesized well-defined n-type π -conjugated copolymers by unusual coupling polymerization of an anion radical of a thiophene-naphthalenediimide-thiophene monomer, generated from the corresponding dibromomonomer and zinc, with a Ni catalyst [33], which proceed in chain-growth polymerization manner presumably involving catalyst-transfer mechanism. However, the Kumada–Tamao catalyst-transfer condensation polymerization of acceptor monomer consisting of a single arene has not been reported. We have set out to explore the polymerization of simple acceptor monomers by focusing on the polymerization of pyridine monomers, which can be formed from dihalopyridine with alkyl Grignard reagent without decomposition of the monomer under this condition [34].

Poly(3-alkoxypyridine-2,5-diyl)

Polypyridine substituted with an *n*-alkoxy group is expected to have low solubility, because polyalkylpyridines are not soluble in general organic solvents such as THF, a reaction solvent for Kumada–Tamao coupling polymerization [34]. We have found that di- and trioxaalkyl groups are effective for increasing the solubility of aromatic polyester [35] and polythiophene [36]. Therefore, we decided to examine the effect of introducing methoxyethoxyethoxy (MEEO) groups into polypyridine [37].

Monomer precursor **1** was converted to a Grignard-type monomer by treatment with 1 equiv of isopropylmagnesium chloride (ⁱPrMgCl) in THF at room temperature for 10 h (conversion of **1** = 85 %). The bromine of **1** at the 5-position was predominantly, but not exclusively, converted to a chloromagnesium group. Polymerization of Grignard monomers, generated from **1** with ⁱPrMgCl, was carried out by addition of 1.8 mol % Ni(dppp)Cl₂ to the reaction mixture, as in the case of the polymerization of Grignard alkylthiophene monomers [7], but a yellow solid was unexpectedly precipitated within 1 h (Scheme 2). The obtained poly{3-(2-[2-(methoxyethoxy)ethoxy]pyridine-2,5-diyl)} (PMEEOPy) was soluble in halogenated solvents, such as dichloromethane and chloroform, although it was poorly soluble in THF, the polymerization solvent. The weight-average molecular weight (M_w) and molecular weight distribution (M_w/M_n) of PMEEOPy was as high as 25 000 and 1.33, respectively, as determined by means of gel permeation chromatography (GPC)-multiangle laser light scattering (MALLS) analysis in CHCl₃. The head-to-tail (HT) content of PMEEOPy was estimated to be 95 % by means of comparison of the ¹H NMR spectra with those of tail-to-tail (TT) and head-to-head (HH) model compounds.



Scheme 2

A solution of HT-PMEEOPy in CHCl₃ was found to emit blue light when the solution was irradiated with UV light at 254 nm. The UV–vis spectra of HT-PMEEOPy and HH-PMEEOPy, which was prepared by means of Yamamoto coupling polymerization of another monomer with Ni(COD)₂ (COD = 1,5-cyclooctadiene) [38], as well as a model compound of repeat unit **2**, 3-MEEO-pyridine, in CHCl₃ are depicted in Fig. 1A. The absorption maxima (λ_{max}) of HT-PMEEOPy and HH-PMEEOPy were observed at 392 and 330 nm, respectively, i.e., at much longer wavelength than that of **2**. The λ_{max} of HT-PMEEOPy is at 62 nm longer wavelength than that of HH-PMEEOPy, implying that the planarity of HT-PMEEOPy is higher than that of HH-PMEEOPy, resulting in a longer conjugation length. Figure 1B shows photoluminescence (PL) spectra of solutions of HT-PMEEOPy and HH-PMEEOPy in CHCl₃. The PL maxima ($\lambda_{\text{max, em}}$) of HT-PMEEOPy and HH-PMEEOPy were observed at 440 and 414 nm upon irradiation at 392 and 330 nm, respectively.

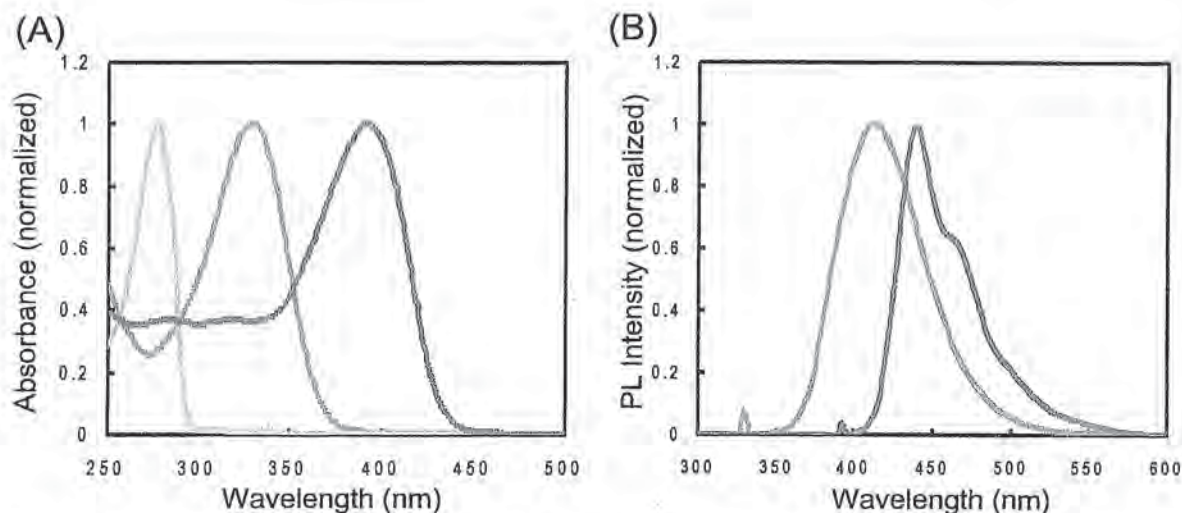


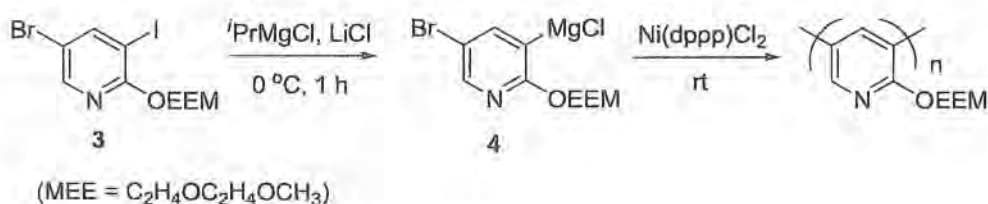
Fig. 1 (A) UV–vis spectra and (B) PL spectra of 3-MEEO-pyridine **2** as a model compound of repeat unit (green line), HH-PMEEOPy (orange line), and HT-PMEEOPy (blue line) in chloroform solution ($\sim 10^{-5}$ M).

Poly(2-alkoxypyridine-3,5-diyl)

Since PMEEOPy was precipitated during polymerization, we could not investigate the chain-growth polymerization behavior. Only if the polymer is soluble in the reaction solvent would we be able to establish whether this acceptor monomer unit undergoes Kumada–Tamao catalyst-transfer condensation polymerization. Therefore, we changed the polymerization position of this monomer unit from the 2,5-position (*para* type) to the 3,5-position (*meta* type) while retaining the same side chain (MEEO

group), although the obtained polypyridine, *m*-PMEEOPy, is not conjugated between the repeat units in the polymer [39].

We used 5-bromo-3-iodo-2-[2-(2-methoxyethoxy)ethoxy]pyridine (**3**) as a monomer precursor, which was quantitatively converted to a Grignard-type monomer **4** by treatment with 1.0 equiv of *i*PrMgCl in THF at 0 °C for 1 h. The polymerization of **4** was then carried out by addition of 1.8 mol % of Ni(dppp)Cl₂. However, the polymerization proceeded slowly (69 % conversion in 63 h), and the GPC profiles of the products showed a broad molecular weight distribution, although the peak shifted toward the higher-molecular-weight region with time. This polymerization behavior presumably arises from aggregation of Grignard monomer **4** due to coordination of the nitrogen of the pyridine ring to the magnesium. Accordingly, the polymerization of **4** with Ni(dppp)Cl₂ was carried out in the presence of LiCl (2 equiv to **4**) in a similar manner to the Kumada–Tamao catalyst-transfer condensation polymerization of *p*-phenylene monomer [26] (Scheme 3). As a result, the polymerization proceeded much faster, and the GPC chromatogram peak became narrow.



Scheme 3

When the M_n and M_w/M_n values of the crude *m*-PMEEOPy (without purification by precipitation or fractionation) were plotted against monomer conversion, the M_n value increased in proportion to conversion, and the M_w/M_n ratio was 1.34 or below over the whole conversion range (Fig. 2A), indicating chain-growth polymerization behavior. Furthermore, the M_n value also linearly increased in proportion to the feed ratio of monomer precursor **3** to the Ni catalyst (Fig. 2B). The matrix-assisted laser desorption/ionization time-of-flight (MALDI-TOF) mass spectrum of *m*-PMEEOPy obtained by polymerization for 5 min (conversion of **4** = 25 %, M_n = 4000, M_w/M_n = 1.34) contained one major series of peaks and one minor series of peaks (Fig. 3). The major peaks correspond to the Na⁺ adducts of *m*-PMEEOPy

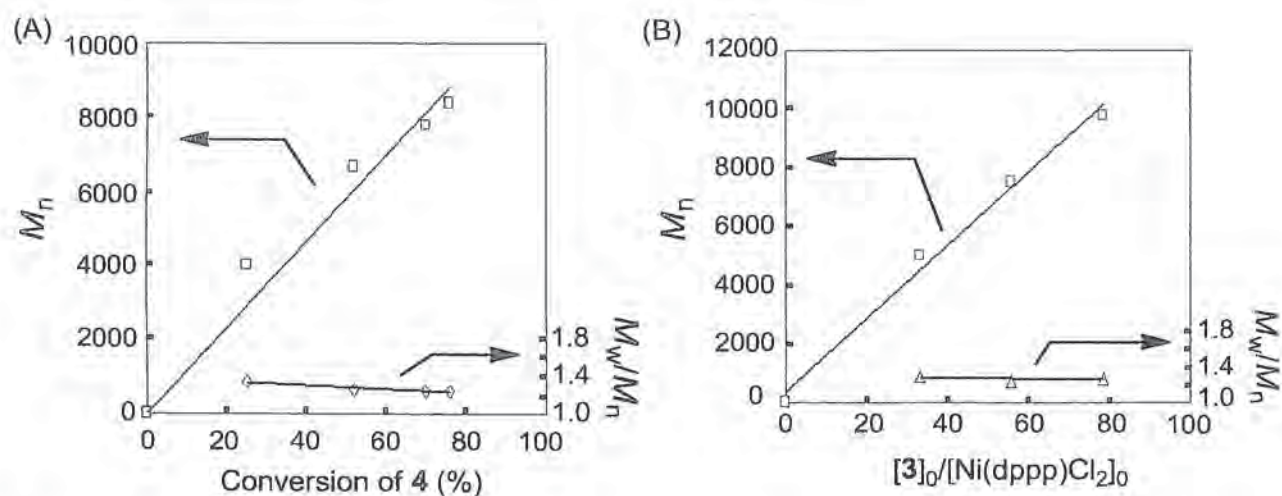


Fig. 2 (A) M_n and M_w/M_n values of *m*-PMEEOPy as a function of monomer conversion in the polymerization of **4** with 1.8 mol % of Ni(dppp)Cl₂ in the presence of 2.0 equiv of LiCl in THF ($[3]_0 = 0.1$ mol/L) at room temperature. (B) M_n and M_w/M_n values of *m*-PMEEOPy as a function of the feed ratio of **3** to Ni(dppp)Cl₂.

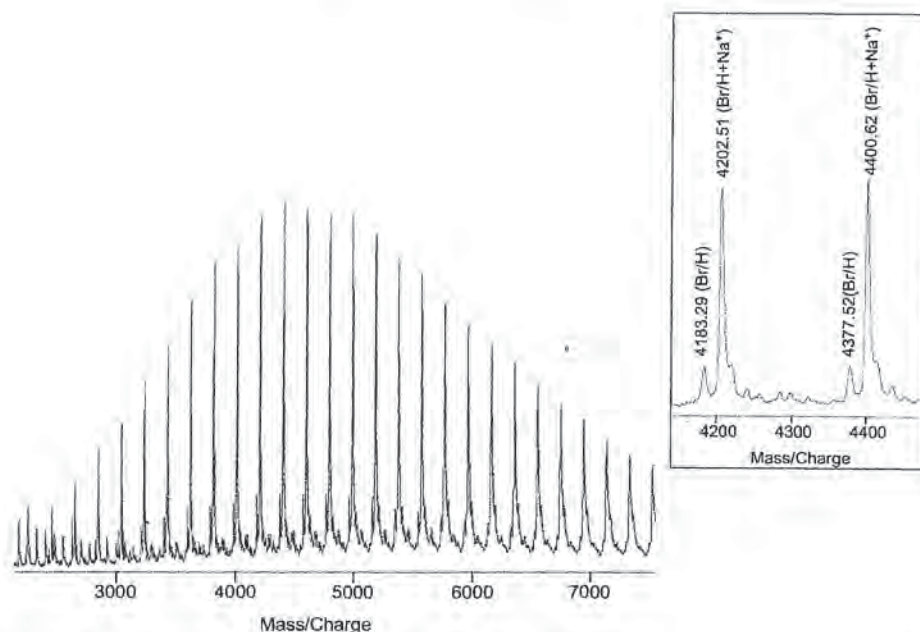
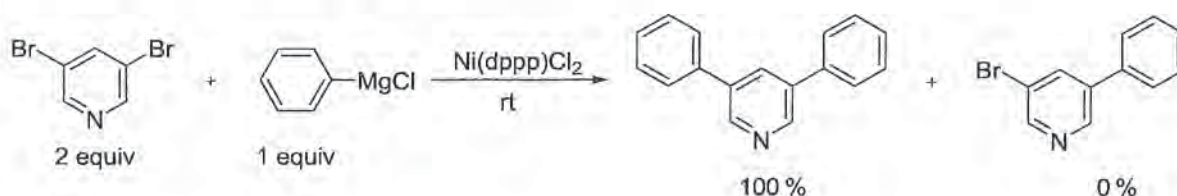


Fig. 3 MALDI-TOF mass spectra of *m*-PMEEOPy obtained by the polymerization of **4** with 1.8 mol % of Ni(dppp)Cl₂ in the presence of 2.0 equiv of LiCl in THF at room temperature for 5 min (conversion of **4** = 25 %, $M_n = 4000$, $M_w/M_n = 1.34$).

with bromine at one end and hydrogen at the other (designated as Br/H). For example, the 21-mer of this distribution is expected to produce a signal at m/z 195.2×21 (repeat unit) + 79.9 (Br) + 1.0 (H) + 23.0 (Na⁺) = 4203.1 Da, and indeed, a signal is observed at 4202.5 Da. The minor peaks correspond to *m*-PMEEOPy with Br/H ends. The polymerization behavior and the MALDI-TOF mass spectrum strongly support the involvement of a catalyst-transfer polymerization mechanism.

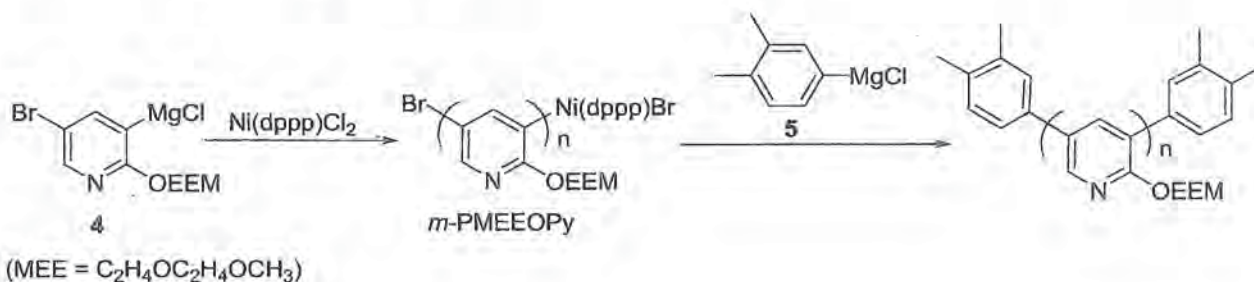
We further examined whether the Ni catalyst intramolecularly would move on the pyridine ring by means of a model reaction, as McCullough conducted in the investigation of the catalyst-transfer polymerization of thiophene monomer [10]. Thus, 3,5-dibromopyridine was reacted with half equiv of phenylmagnesium chloride in the presence of a catalytic amount of Ni(dppp)Cl₂ in THF at ambient temperature. The products were analyzed by gas chromatograph (GC), GC-mass spectrum (GC-MS), and ¹H NMR spectrum, and it turned out that only 3,5-diphenylpyridine was quantitatively formed (Scheme 4). This result indicated that successive coupling reaction took place via intramolecular transfer of Ni(0) catalyst on the pyridine ring, even though the π -donation ability of pyridine is weaker than that of donor monomers such as thiophene.



Scheme 4

Functionalization of the polymer end-groups was conducted by using Grignard reagent. Thus, **4** was polymerized with 1.99 mol % Ni(dppp)Cl₂ in the presence of 2.0 equiv of LiCl in THF at room temperature for 1 h (conversion of **4** = 80 %, $M_n = 7800$, $M_w/M_n = 1.22$), and then an excess of 3,4-dimethylphenylmagnesium chloride **5** (3,4-Me₂C₆H₃MgCl) was added to the reaction mixture

(Scheme 5). The mixture was stirred for a further 3 h, and then the reaction was quenched with 5 M HCl. End-group analysis of the obtained polymer ($M_n = 7870$, $M_w/M_n = 1.23$) was performed by MALDI-TOF MS (Fig. 4). The spectrum of an aliquot taken before addition of the Grignard reagent showed the peaks of the Na^+ cation adduct of *m*-PMEEOPy with Br/H end-groups and the non-cation adducts (Fig. 4A), whereas after the reaction with the Grignard reagent, the spectrum showed a new series of peaks, the values of which corresponded to Na^+ adducts of *m*-PMEEOPy with $\text{Me}_2\text{C}_6\text{H}_3/\text{Me}_2\text{C}_6\text{H}_3$ end-groups. Consequently, it turns out that aryl groups can be introduced at both ends of *m*-PMEEOPy by using the aryl Grignard reagent, as in the case of end-functionalization of P3ATs with Grignard reagents [9,40].



Scheme 5

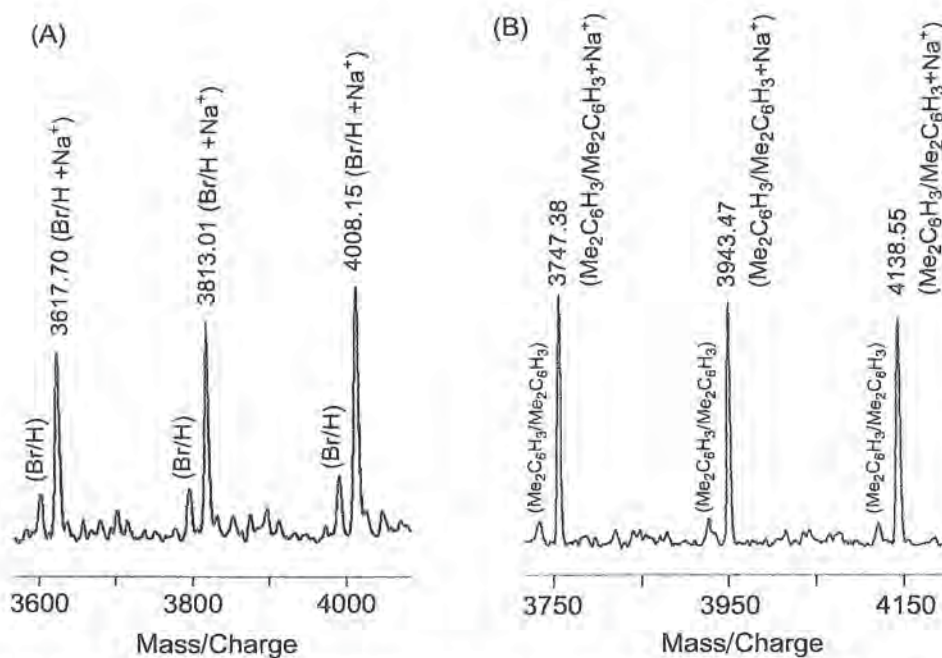
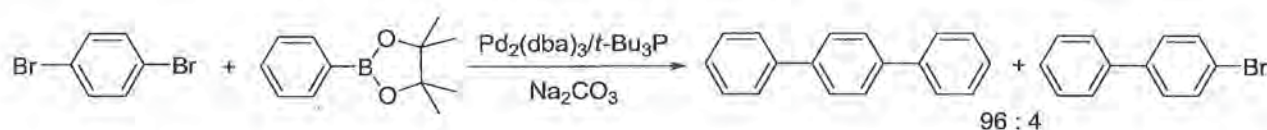


Fig. 4 MALDI-TOF mass spectra of *m*-PMEEOPy obtained by (A) the polymerization of 4 with 1.99 mol % of $\text{Ni}(\text{dppp})\text{Cl}_2$ in the presence of 2.0 equiv of LiCl in THF at room temperature for 1 h (conversion of 4 = 80 %, $M_n = 7800$, $M_w/M_n = 1.22$) and (B) subsequent reaction with 3,4-dimethylphenylmagnesium chloride ($M_n = 7870$, $M_w/M_n = 1.23$).

SUZUKI-MIYAUURA COUPLING POLYMERIZATION

Suzuki–Miyaura cross-coupling is widely used for organic synthesis and polymer synthesis because this reaction can be carried out in the presence of water and is less subject to steric hindrance of reagents and substrates. Therefore, we had started investigation of Suzuki–Miyaura catalyst-transfer condensation polymerization from model reactions: the Suzuki–Miyaura coupling reaction of dibromobenzenes

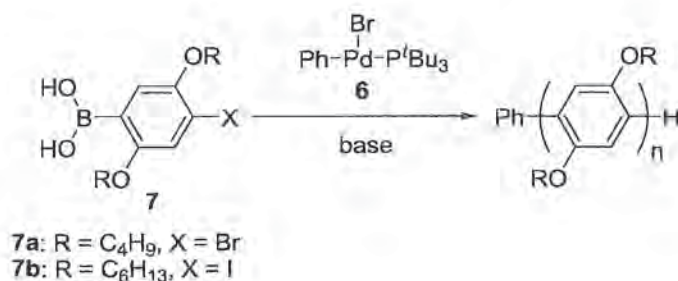
with phenylboronic acid ester with various Pd catalysts, and we found that *t*-Bu₃P was the best ligand to afford selectively diphenyl-substituted benzene via intramolecular transfer of the catalyst (Scheme 6) [41]. However, the same results that the Pd catalyst with *t*-Bu₃P ligand facilitates successive coupling reaction of dihaloarenes with boronic acids or esters were reported before our submission [42,43]. We then carried out the polymerization of a bromofluoreneboronic acid ester monomer with *t*-Bu₃PPd(Ph)Br (**6**), which had been a reported Pd complex [44], to obtain well-defined polyfluorenes via the catalyst-transfer mechanism [45]. This polymerization method was applied to the production of polyfluorene brushes from a substrate surface [46] and to the synthesis of hyperbranched polymers with 100 % degree of branching [47]. We have investigated the polymerization of other monomers leading to π -conjugated polymers.



Scheme 6

Poly(*p*-phenylene)s

In a preliminary study, the polymerization of bromophenylene boronic acid monomer **7a** with a Pd complex initiator **6** was attempted under the same conditions of the polymerization for polyfluorene using Na₂CO₃ as a typical base for Suzuki–Miyaura coupling reaction, but afforded polyphenylene with broad molecular weight distribution [45]. Therefore, we investigated the polymerization of iodo-phenylene boronic acid monomer **7b** with **6** under various conditions (Scheme 7) [48].



Scheme 7

The polymerization of **7b** with **6** ($[\mathbf{7b}]_0/[\mathbf{6}]_0 = 20$) was carried out by using various bases in THF at room temperature. We first used K₃PO₄. However, K₃PO₄ was not soluble in THF, and then **7b** remained unreacted even in 96 h. The obtained polymer had low molecular weight. When tetrabutylammonium fluoride (TBAF), which is soluble in THF, was used, **7b** remained and low-molecular-weight polymer was obtained. The use of CsF with a small amount of water for dissolving CsF gave similar results. However, addition of 18-crown-6 to the former reaction mixture accelerated the polymerization, and **7b** was consumed for 4 h. Furthermore, the molecular weight distribution became narrower up to 1.26. However, when the polymerization was carried out at higher monomer feed ratio ($[\mathbf{7b}]_0/[\mathbf{6}]_0 = 60$), the polydispersity became broad up to 1.84. The polymerization temperature was then decreased to 0 °C, resulting in narrower polydispersity ($M_w/M_n = 1.47$). Under this condition, the molecular weight of poly**7b** increased linearly in proportion to the conversion of **7b** while retaining low polydispersity ($M_w/M_n < 1.25$) in the polymerization at $[\mathbf{7b}]_0/[\mathbf{6}]_0 = 30$ (Fig. 5A). The molecular weight also proportionally increased by the $[\mathbf{7b}]_0/[\mathbf{6}]_0$ ratio up to 21 500 (Fig. 5B). Furthermore, MALDI-TOF mass spectra of the obtained poly**7b** showed that the polymer end-groups were controlled: a phenyl

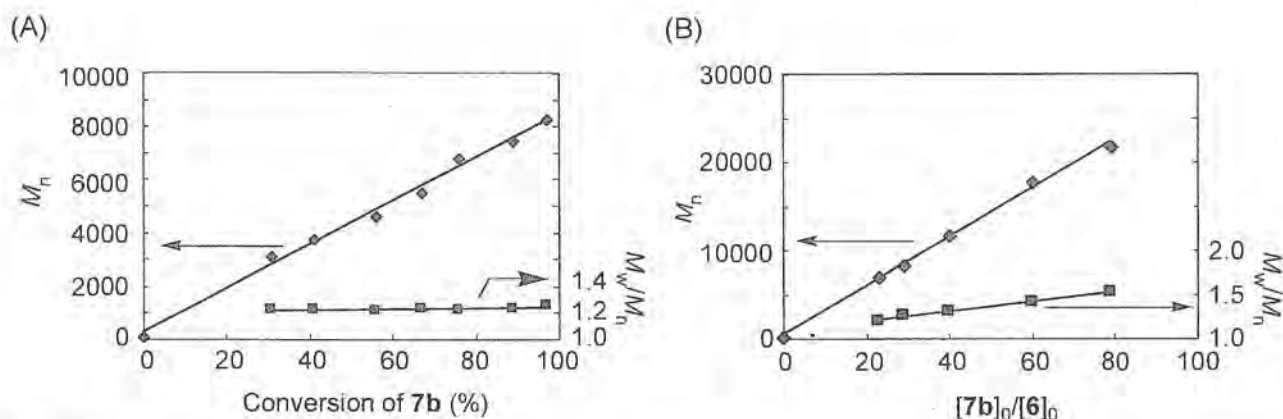


Fig. 5 M_n and M_w/M_n values of poly**7b** as a function of (A) monomer conversion, obtained by the polymerization of **7b** with **6** ($[7b]_0/[6]_0 = 30$), and (B) the feed ratio of **7b** to **6**. All the polymerizations were carried out in the presence of 4 equiv of CsF and 8 equiv of 18-crown-6 in THF ($[7b]_0 = 8.0$ mM) and water (water/THF = 1/17 (v/v)) at 0 °C. M_n and M_w/M_n values were determined by GPC based on polystyrene standards.

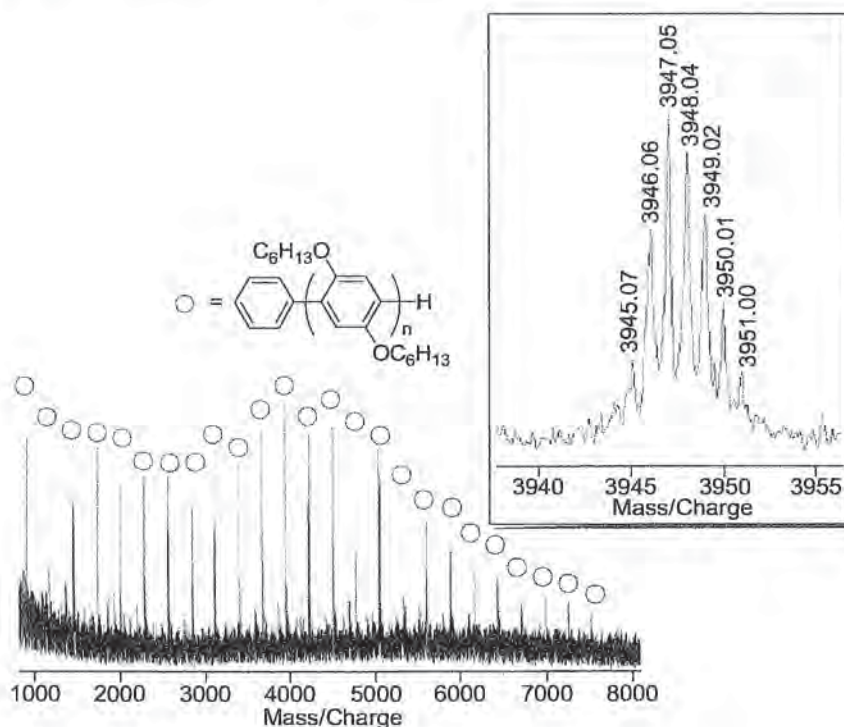
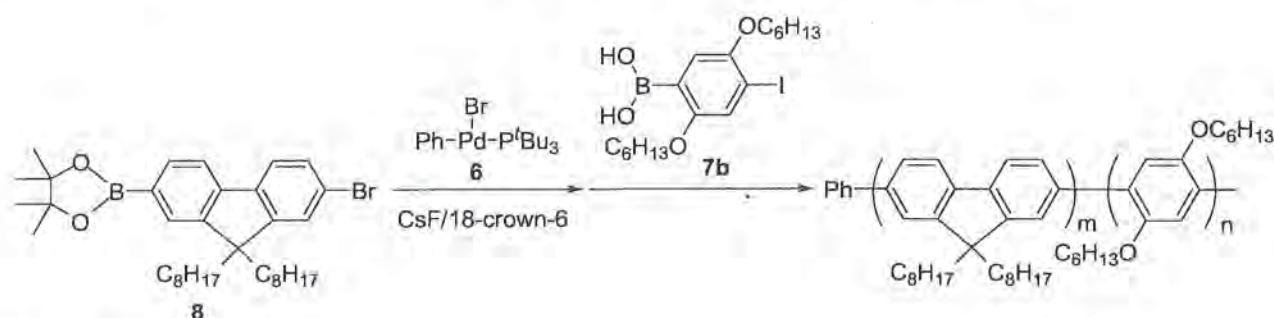


Fig. 6 MALDI-TOF mass spectra of the polymer obtained at $[7b]_0/[6]_0 = 20$.

group, derived from **6**, at one end and a hydrogen atom at the other end (Fig. 6). For example, the exact mass of a single isotope of the 14-mer with Ph/H is expected to produce a signal at 3944.99 Da, and in fact a signal was observed at 3945.07 Da, as shown in the magnified spectrum in Fig. 6. These results indicated that the polymerization of **7b** also proceeds in a chain-growth polymerization manner via catalyst-transfer mechanism.

Since we have two monomers that undergo Suzuki–Miyaura catalyst-transfer condensation polymerization, block copolymer of polyfluorene and poly(*p*-phenylene) was synthesized. The fluorene monomer **8** was polymerized first in the presence of 5.0 mol % of **6** and CsF/18-crown-6 in THF containing a small amount of water at 0 °C to afford well-defined poly**8** ($M_n = 7300$, $M_w/M_n = 1.19$). Then 1.0 equiv of *p*-phenylene monomer **7b** was added to the reaction mixture, and the second polymeriza-

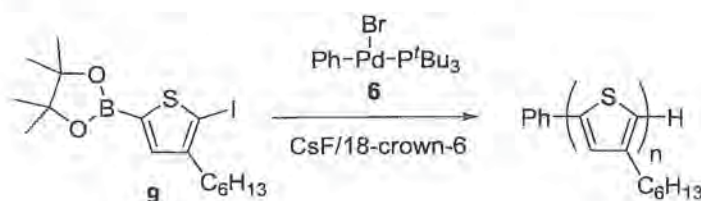
tion was conducted at the same temperature to afford the objective block copolymer with a narrow molecular weight distribution ($M_n = 13\,000$, $M_w/M_n = 1.29$) (Scheme 8). When the block copolymerization was carried out in reverse order, the polydispersity became broad ($M_w/M_n = 1.45$).



Scheme 8

Poly(3-hexylthiophene)

Suzuki–Miyaura coupling polymerizations leading to P3ATs were investigated [49–52], but well-controlled P3ATs have not been synthesized yet. Accordingly, thiophene monomer **9** was polymerized with **6** ($[9]_0/[6]_0 = 20$) under conditions similar to the case of poly(*p*-phenylene) (Scheme 9) [53]. The GPC chromatogram of the product shifted toward the higher-molecular-weight region with increasing reaction time, and monomer **9** was consumed in 24 h to afford P3HT with relatively low polydispersity ($M_w/M_n = 1.34$). The MALDI-TOF mass spectrum of P3HT, obtained after reaction for 24 h followed by quenching with 6 M HCl, contained only one series of peaks, which correspond to the polymer with a phenyl group at one end and a hydrogen atom at the other end (designated as Ph/H) (Fig. 7). For example, the exact mass of a single isotope of the 27-mer with Ph/H is expected to produce a signal at 4562.21 Da, and in fact a signal was observed at 4561.73 Da, as shown in the magnified spectrum in Fig. 7. Furthermore, the Ph/H end-groups were confirmed by the ^1H NMR spectrum, and the average value of degree of polymerization, estimated from the integral ratio of the repeat unit to the end-group, was 20, which agreed with the feed ratio. The MALDI-TOF mass spectrum of the product obtained at 15 min also contains one series of peaks due to P3HT with Ph/H, indicating that polymers with other end-groups, such as polymers from self-condensation of **9**, were not formed in the initial stage. Since the Ph and H end-groups are thought to be derived from the Ph group of **6** and the Pd complex end-group by quenching, respectively, the results of the MALDI-TOF mass spectra and the ^1H NMR spectrum of the obtained P3HT indicate that the polymerization of **9** with **6** involves the catalyst-transfer polymerization mechanism.



Scheme 9

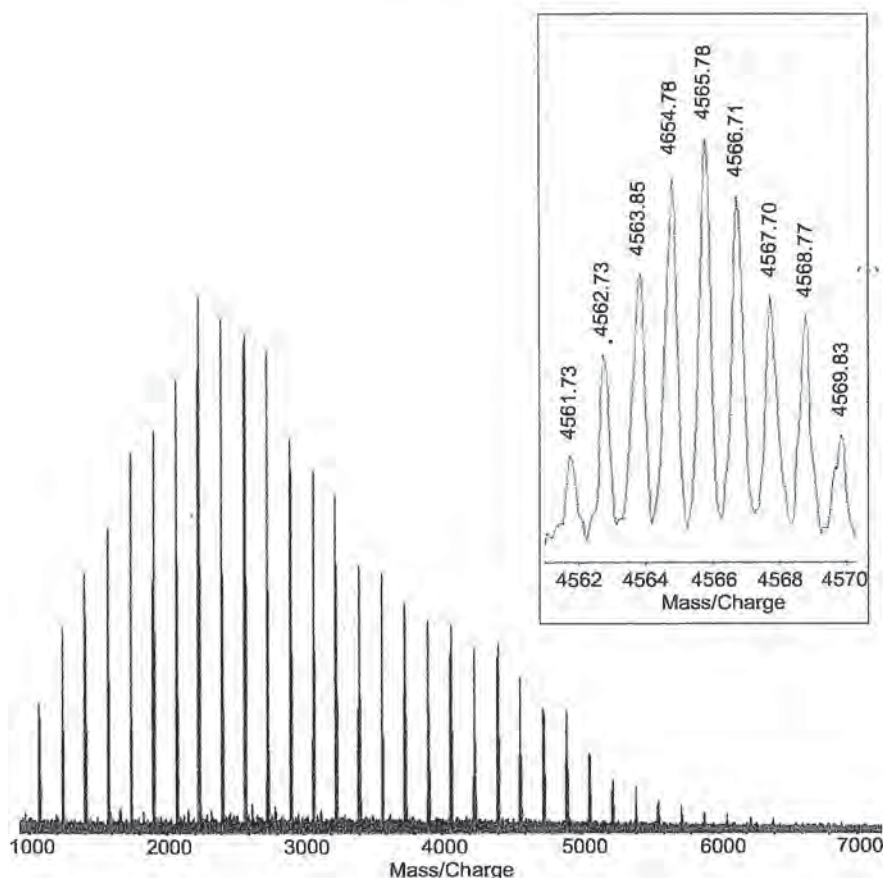


Fig. 7 MALDI-TOF mass spectra of the polymer obtained at $[9]_0/[6]_0 = 20$.

Regarding the regioregularity of P3HT, the ^1H NMR spectra showed only signals corresponding to head-to-tail, head-to-tail triad (designated as HT–HT), and other triad signals such as TT–HH, HT–HH, and TT–HT were not observed, as shown in Fig. 8 attached with the reported ^1H NMR spectrum of P3HT [54]. Therefore, the regioregularity is over 99 %, which suggests that no exchange reaction occurs between the boronic ester moiety and the iodine atom in monomer **9** in the polymerization with **6** at low temperature.

The polymerization of **9** with **6** was then carried out with various feed ratios ($[9]_0/[6]_0$) under the same polymerization conditions. The M_n values of the polymer increased linearly in proportion to $[9]_0/[6]_0$ until $[9]_0/[6]_0$ was 58, but the M_n value at $[9]_0/[6]_0 = 78$ was lower than the expected value. The polydispersity gradually increased with increasing $[9]_0/[6]_0$ ratio (Fig. 9), implying that side reactions took place in the case of polymerization at high $[9]_0/[6]_0$ ratio. Accordingly, the polymer obtained at $[9]_0/[6]_0 = 42$ was analyzed by means of MALDI-TOF MS. Again, the main series of peaks was due to the polymer with Ph/H, but another series of small peaks was also observed in the low m/z region. More detailed analysis of the by-product is required, but at least it can be said that P3HT without a Ph group derived from **6** is formed at a high $[9]_0/[6]_0$ ratio. This side reaction implies involvement of chain transfer of the catalyst to the monomer to some extent in the case of polymerization at a high $[9]_0/[6]_0$ ratio.

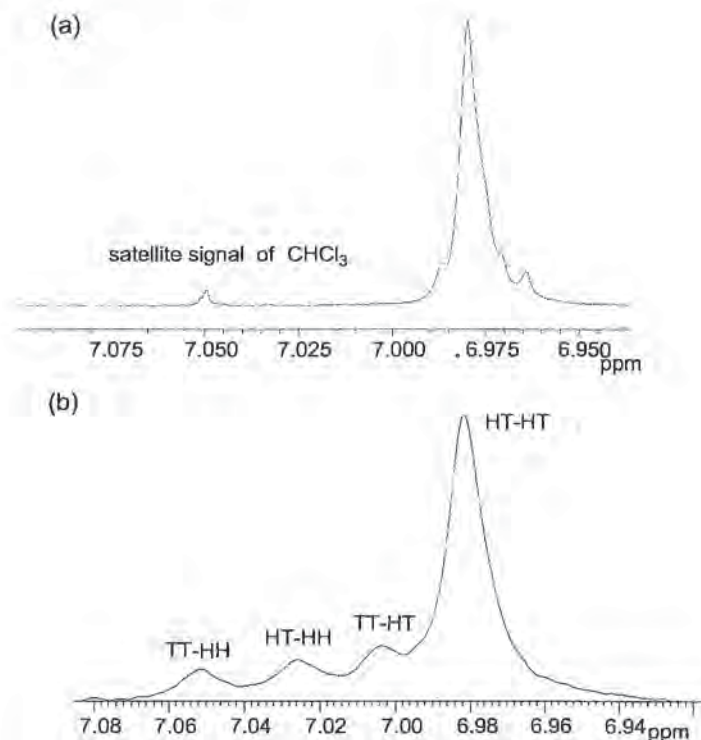


Fig. 8 (a) ^1H NMR spectrum of the polymer obtained at $[\mathbf{9}]_0/[\mathbf{6}]_0 = 20$; (b) ^1H NMR spectrum of P3HT in CDCl_3 , reported in ref. [38].

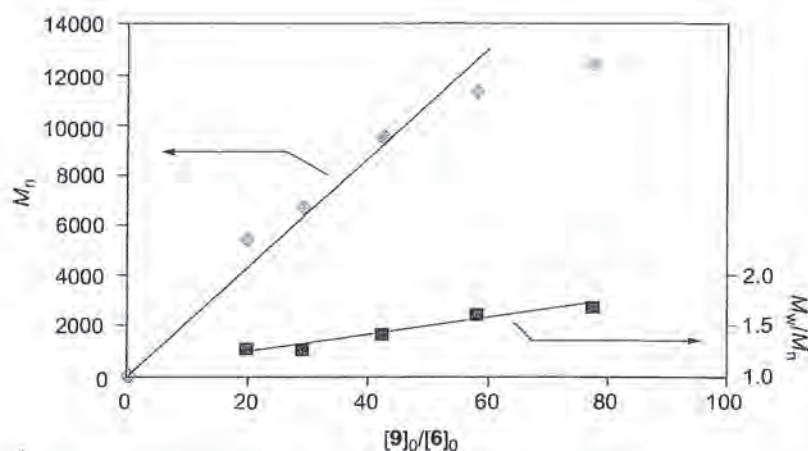
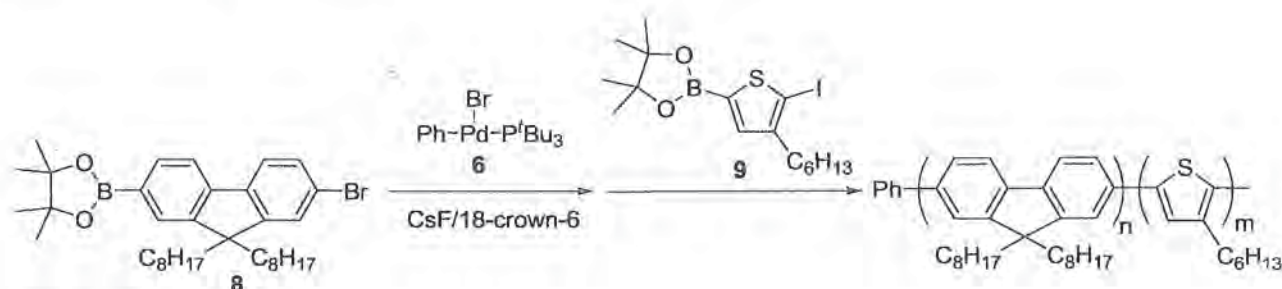


Fig. 9 M_n and M_w/M_n values of P3HT as a function of the feed ratio of $\mathbf{9}$ to $\mathbf{6}$. M_n and M_w/M_n values were determined by GPC based on polystyrene standards.

We tried to synthesize block copolymers of P3HT and polyfluorene possessing a lower donor ability than P3HT. McCullough and co-workers have reported similar block copolymers synthesized by means of Kumada–Tamao coupling polymerization, in which thiophene Grignard monomer has to be added to the reaction mixture of polyfluorene as a prepolymer in the middle stage of polymerization before loss of the pseudo living polymerization character [55].

Because successive catalyst-transfer Suzuki–Miyaura coupling polymerizations should be conducted from a monomer with low π -donor ability to a monomer with high π -donor ability, as mentioned in the previous section [48], the fluorene monomer $\mathbf{8}$ was polymerized first in the presence of $\mathbf{6}$ ($[\mathbf{8}]_0/[\mathbf{6}]_0 = 20$) and CsF/18-crown-6 at 0°C for 4 h to afford well-defined polyfluorene (conversion of

$\mathbf{8}$ = 99 %, $M_n = 10\,100$, $M_w/M_n = 1.37$). Then 1.0 equiv of thiophene monomer $\mathbf{9}$ was added to the reaction mixture, and the second polymerization was conducted at 0 °C for 72 h (Scheme 10). The GPC elution curve shifted toward the higher-molecular-weight region, and the obtained polymer showed $M_n = 14\,700$ and $M_w/M_n = 1.50$. These results indicate that the second monomer $\mathbf{9}$ was polymerized in a chain-growth polymerization manner from the polymer end group of the first polymer to yield diblock copolymer of polyfluorene and P3HT in almost quantitative yield. In the polymerization in the reverse order, surprisingly, the polymerization of $\mathbf{8}$ in the second stage hardly proceeded, and a large amount of $\mathbf{8}$ remained even 163 h after addition of $\mathbf{8}$ to the reaction mixture of P3HT as a prepolymer. The ^1H NMR spectrum of the product showed strong signals of the P3HT repeat unit and weak signals assignable to an oligofluorene segment attached to P3HT, which is different from the signals of the polyfluorene segment of polyfluorene-*b*-P3HT.



Scheme 10

CONCLUSION

We have expanded the variety of monomers for catalyst-transfer condensation polymerization leading to π -conjugated polymers. Poly(pyridine-3,5-diyl) was obtained in a controlled manner by means of Ni-catalyzed Kumada–Tamao coupling polymerization of 3-alkoxy-2-bromo-5-chloromagnesiopyridine, and well-defined poly(*p*-phenylene) and P3HT were obtained also by Pd-catalyzed Suzuki–Miyaura coupling polymerization of the corresponding boronic acid and boronic acid ester monomers. All π -conjugated block copolymers were further synthesized by successive polymerization of these different monomers in one pot. Future research efforts will be directed toward the development of catalyst-transfer condensation polymerization for the synthesis of well-defined block copolymers consisting of *p*- and *n*-type π -conjugated polymers and of well-defined, low-band-gap, donor–acceptor alternating π -conjugated polymers, both of which are promising organic electrical materials for photovoltaic devices.

REFERENCES

1. T. A. Skotheim, R. L. Elsenbaumer, J. R. Reynolds (Eds.). *Handbook of Conducting Polymers*, 2nd ed., revised and expanded, Marcel Dekker (1997).
2. G. Barbarella, M. Melucci, G. Sotgiu. *Adv. Mater.* **17**, 1581 (2005).
3. T. Yamamoto. *Macromol. Rapid Commun.* **23**, 583 (2002).
4. F. Babudri, G. M. Farinola, F. Naso. *J. Mater. Chem.* **14**, 11 (2004).
5. T. Yokozawa, A. Yokoyama. *Chem. Rev.* **109**, 5595 (2009).
6. A. Yokoyama, T. Yokozawa. *Macromolecules* **40**, 4093 (2007).
7. A. Yokoyama, R. Miyakoshi, T. Yokozawa. *Macromolecules* **37**, 1169 (2004).
8. R. Miyakoshi, A. Yokoyama, T. Yokozawa. *Macromol. Rapid Commun.* **25**, 1663 (2004).
9. R. Miyakoshi, A. Yokoyama, T. Yokozawa. *J. Am. Chem. Soc.* **127**, 17542 (2005).

10. E. E. Sheina, J. S. Liu, M. C. Iovu, D. W. Laird, R. D. McCullough. *Macromolecules* **37**, 3526 (2004).
11. M. C. Iovu, E. E. Sheina, R. R. Gil, R. D. McCullough. *Macromolecules* **38**, 8649 (2005).
12. T. Yokozawa. In *Conjugated Polymer Synthesis* (Y. Chujo, ed.), pp. 35–58. Wiley-VCH, Weinheim (2010) and references therein.
13. J. R. Locke, A. J. McNeil. *Macromolecules* **43**, 8709 (2010).
14. V. Senkovskyy, N. Khanduyeva, H. Komber, U. Oertel, M. Stamm, D. Kuckling, A. Kiriy. *J. Am. Chem. Soc.* **129**, 6626 (2007).
15. H. A. Bronstein, C. K. Luscombe. *J. Am. Chem. Soc.* **131**, 12894 (2009).
16. V. Senkovskyy, R. Tkachov, T. Beryozkina, H. Komber, U. Oertel, M. Horecha, V. Bocharova, M. Stamm, S. A. Gevorgyan, F. C. Krebs, A. Kiriy. *J. Am. Chem. Soc.* **131**, 16445 (2009).
17. A. Smeets, K. Van den Bergh, J. De Winter, P. Gerbaux, T. Verbiest, G. Koeckelberghs. *Macromolecules* **42**, 7638 (2009).
18. V. Senkovskyy, M. Sommer, R. Tkachov, H. Komber, W. T. S. Huck, A. Kiriy. *Macromolecules* **43**, 10157 (2010).
19. N. Khanduyeva, V. Senkovskyy, T. Beryozkina, V. Bocharova, F. Simon, M. Nitschke, M. Stamm, R. Grotzschel, A. Kiriy. *Macromolecules* **41**, 7383 (2008).
20. N. Khanduyeva, V. Senkovskyy, T. Beryozkina, M. Horecha, M. Stamm, C. Uhrich, M. Riede, K. Leo, A. Kiriy. *J. Am. Chem. Soc.* **131**, 153 (2009).
21. S. K. Sontag, N. Marshall, J. Locklin. *Chem. Commun.* 3354 (2009).
22. E. L. Lanni, A. J. McNeil. *J. Am. Chem. Soc.* **131**, 16573 (2009).
23. S. D. Boyd, A. K. Y. Jen, C. K. Luscombe. *Macromolecules* **42**, 9387 (2009).
24. R. Tkachov, V. Senkovskyy, H. Komber, J.-U. Sommer, A. Kiriy. *J. Am. Chem. Soc.* **132**, 7803 (2010).
25. E. L. Lanni, A. J. McNeil. *Macromolecules* **43**, 8039 (2010).
26. R. Miyakoshi, K. Shimono, A. Yokoyama, T. Yokozawa. *J. Am. Chem. Soc.* **128**, 16012 (2006).
27. K. Ohshimizu, A. Takahashi, T. Higashihara, M. Ueda. *J. Polym. Sci., Part A: Polym. Chem.* **49**, 2709 (2011).
28. A. Yokoyama, A. Kato, R. Miyakoshi, T. Yokozawa. *Macromolecules* **41**, 7271 (2008).
29. M. C. Stefan, A. E. Javier, I. Osaka, R. D. McCullough. *Macromolecules* **42**, 30 (2009).
30. L. Huang, S. P. Wu, Y. Qu, Y. H. Geng, F. S. Wang. *Macromolecules* **41**, 8944 (2008).
31. S. Wu, Y. Sun, L. Huang, J. Wang, Y. Zhou, Y. Geng, F. Wang. *Macromolecules* **43**, 4438 (2010).
32. R. Miyakoshi, A. Yokoyama, T. Yokozawa. *Chem. Lett.* **37**, 1022 (2008).
33. V. Senkovskyy, R. Tkachov, H. Komber, M. Sommer, M. Heuken, B. Voit, W. T. S. Huck, V. Kataev, A. Petr, A. Kiriy. *J. Am. Chem. Soc.* **133**, 19966 (2011).
34. T. Yamamoto, T. Nakamura, H. Fukumoto, K. Kubota. *Chem. Lett.* **30**, 502 (2001).
35. K. Iwashita, A. Yokoyama, T. Yokozawa. *J. Polym. Sci., Part A: Polym. Chem.* **43**, 4109 (2005).
36. I. Adachi, R. Miyakoshi, A. Yokoyama, T. Yokozawa. *Macromolecules* **39**, 7793 (2006).
37. Y. Nanashima, A. Yokoyama, T. Yokozawa. *J. Polym. Sci., Part A: Polym. Chem.* **50**, 1054 (2012).
38. T. Yamamoto, T. Maruyama, Z.-H. Zhou, T. Ito, T. Fukuda, Y. Yoneda, F. Begum, T. Ikeda, S. Sasaki. *J. Am. Chem. Soc.* **116**, 4832 (1994).
39. Y. Nanashima, A. Yokoyama, T. Yokozawa. *Macromolecules* **45**, 2609 (2012).
40. M. Jeffries-El, G. Sauve, R. D. McCullough. *Macromolecules* **38**, 10346 (2005).
41. Unpublished results.
42. C.-G. Dong, Q.-S. Hu. *J. Am. Chem. Soc.* **127**, 10006 (2005).
43. S. K. Weber, F. Galbrecht, U. Scherf. *Org. Lett.* **8**, 4039 (2006).
44. J. P. Stambuli, C. D. Incarvito, M. Bühl, J. F. Hartwig. *J. Am. Chem. Soc.* **126**, 1184 (2004).
45. A. Yokoyama, H. Suzuki, Y. Kubota, K. Ohuchi, H. Higashimura, T. Yokozawa. *J. Am. Chem. Soc.* **129**, 7236 (2007).

46. T. Beryozkina, K. Boyko, N. Khanduyeva, V. Senkovskyy, M. Horecha, U. Oertel, F. Simon, M. Stamm, A. Kiriya. *Angew. Chem., Int. Ed.* **48**, 2695 (2009).
47. W. Huang, L. Su, Z. Bo. *J. Am. Chem. Soc.* **131**, 10348 (2009).
48. T. Yokozawa, H. Kohno, Y. Ohta, A. Yokoyama. *Macromolecules* **43**, 7095 (2010).
49. S. Guillerez, G. Bidan. *Synth. Met.* **93**, 123 (1998).
50. M. Jayakannan, X. Lou, J. L. J. van Dongen, R. A. J. Janssen. *J. Polym. Sci., Part A: Polym. Chem.* **43**, 1454 (2005).
51. I. A. Liversedge, S. J. Higgins, M. Giles, M. Heeney, I. McCulloch. *Tetrahedron Lett.* **47**, 5143 (2006).
52. W. Li, Y. Han, B. Li, C. Liu, Z. Bo. *J. Polym. Sci., Part A: Polym. Chem.* **46**, 4556 (2008).
53. T. Yokozawa, R. Suzuki, M. Nojima, Y. Ohta, A. Yokoyama. *Macromol. Rapid Commun.* **32**, 801 (2011).
54. G. Barbarella, A. Bongini, M. Zambianchi. *Macromolecules* **27**, 3039 (1994).
55. A. E. Javier, S. R. Varshney, R. D. McCullough. *Macromolecules* **43**, 3233 (2010).

触媒移動型連鎖縮合重合の新展開

野嶋 雅貴^{*1}・太田 佳宏^{*2}・横澤 勉^{*3}

Masataka Nojima · Yoshihiro Ohta · Tsutomu Yokozawa

■ ^{*1} 神奈川大学工学研究科応用化学専攻 博士後期課程
 神奈川大学工学部物質生命化学科 ^{*2} 特別助手 博士(工学) ^{*3} 教授 工学博士 ■

1. はじめに

1977年に導電性高分子が発見されて以来¹⁾, π 共役系高分子を用いた電界効果型有機トランジスタ (OFET) や有機発光ダイオード (OLED), ポリマー太陽電池 (PSC) のような有機デバイスへの実用化に向けた研究が盛んに行われるようになった。 π 共役系高分子は, 芳香族化合物の酸化重合, または芳香族ハロゲン化物と芳香族有機金属化合物との遷移金属触媒カップリング重合²⁾によって合成されている。後者の方法において, McCullough^{3a)}と Rieke⁴⁾らはアルキル基を導入したチオフェンを結合位置を制御して重合し, 導電性や移動度の高い可溶性ポリアルキルチオフェンを得た。しかし, 遷移金属触媒を用いるカップリング重合は重縮合であるため精密に分子量や分子

量分布を制御することは本質的に不可能と考えられていた。著者らは McCullough らが報告したポリ(3-ヘキシルチオフェン) (P3HT) を与える Ni 触媒縮合重合^{3b)}を参考に, プロモヨードチオフェンに対して正確に 1 当量のイソプロピルマグネシウムクロライドを作用させてチオフェン Grignard モノマー **1** を発生させ, これに触媒量の Ni(dppp)Cl₂ (dppp = 1,3-ビス(ジフェニルホスフィノ)プロパン) を加えて室温で重合させたところ, 分子量分布が狭い, 位置規則性の高い P3HT が得られることを見出した⁵⁾。分子量は Ni 触媒の量で制御でき, 本重合はリビング重合と同等な連鎖重合であることを明らかにし, その重合機構は Ni 触媒が成長末端へと移動するまったく新しい種類の連鎖縮合重合(触媒移動型連鎖縮合重合)であることを見出した(図 1)。

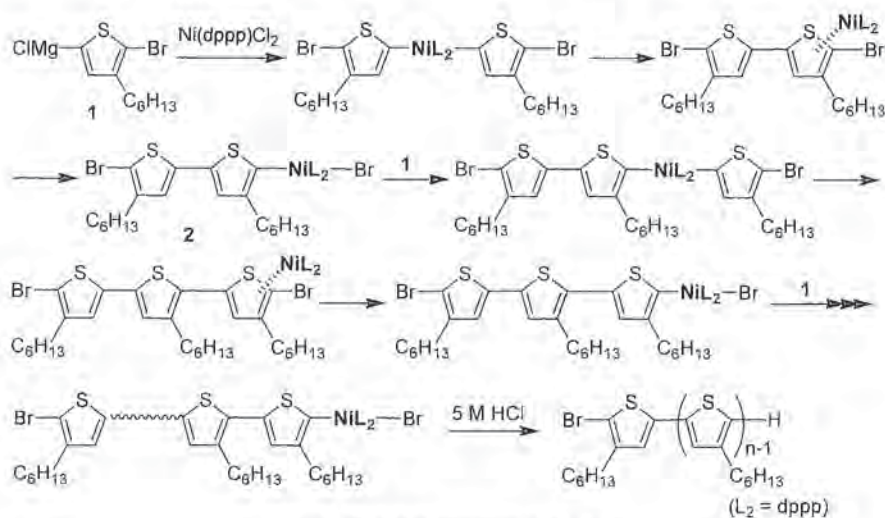
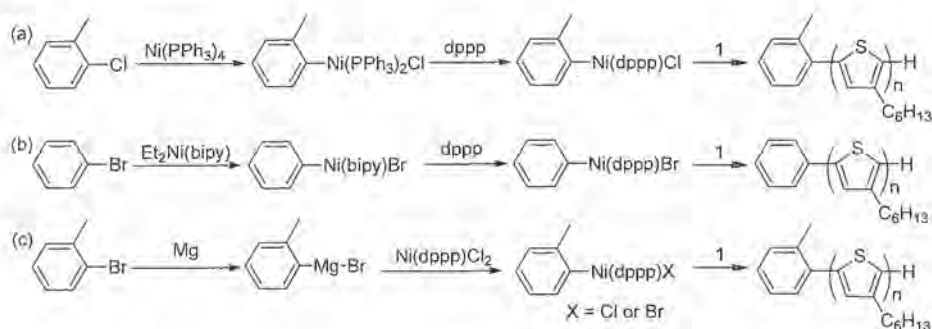


図 1 触媒移動型連鎖縮合重合機構



式 1

すなわち、開始反応として Ni(II)触媒に 2 分子の 1 が反応して二量体が生成すると、その際に発生した Ni(0)触媒は系中に拡散せずに分子内移動して二量体の C-Br 結合に挿入し、新たな Ni(II)錯体 2 が生成する。続いて 2 にモノマー 1 が反応してカップリング反応が起きると、同様に新たな末端の C-Br 結合に Ni 錯体が挿入する。これを繰り返して Ni 触媒が成長末端へと移動して連鎖重合が進行する^{6,7)}。その後、McCullough らも同様な重合系を報告するとともに⁸⁾、低分子反応においても Ni(0)錯体が芳香環上を分子内移動する現象が報告されている⁹⁾。本稿では、近年の触媒移動型連鎖縮合重合の発展を紹介する。

2. 重合開始剤

前節では重合系中で生成する 2 が Ni(II)錯体開始剤として作用したが、最近ではチオフェン二量体由来しない Ni(II)錯体開始剤を調製できるようになり、開始末端の一次構造の精密制御が可能になった。Kiriy らはプロモベンゼンと Ni(PPh₃)₄ から PhNi(PPh₃)₂-Br を系中で発生させ、これを開始剤として用いて 1 の重合を行った。しかし、1 の連鎖重合の最適な配位子は dppp であるため、得られるポリマーの位置規則性は高いものの分子量分布が広く、また、末端構造は完全には制御できなかった¹⁰⁾。その後、Luscombe らが 2-クロロトルエン (Tol-Cl) と Ni(PPh₃)₄ から Tol-Ni(PPh₃)₂-Cl を系中で発生させた後、dppp との配位子交換によって Tol-Ni(dppp)-Cl を調製し、これを 1 の重合に用いると、分子量分布が狭く、かつ片末端にトリル基ともう一方の末端に H が導入されたポリチオフェンが得られることを見出している (式 1 (a))¹¹⁾。また、Kiriy らも同様に Ph-Ni(bipy)-

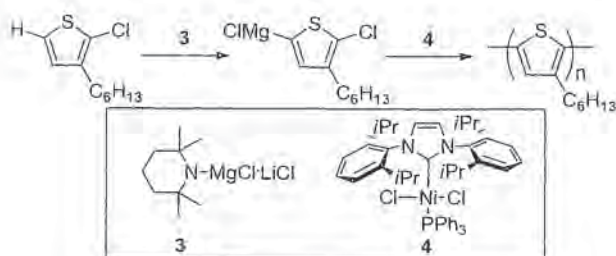
Br (bipy = 2,2'-ビピリジン) と dppp の配位子交換によって Ph-Ni(dppp)-Br を合成している (式 1 (b))¹²⁾。さらに、配位子交換を必要としない、より簡便な開始剤の調製法も報告した (式 1 (c))。すなわち、*o*-Tol-MgBr と Ni(dppp)Cl₂ を反応させるとトランスメタル化が 1 回だけ起きて *o*-Tol-Ni(dppp)-X (X = Cl, Br) が生じ、これを開始剤として用いることができる。*o*-Tol-Ni(dppp)-X にもう 1 分子の *o*-Tol-MgBr がトランスメタル化しないのは Ni 錯体上の *o*-トリル基の立体障害によるものと説明している¹³⁾。

また、6. で述べるが、著者らも Kiriy らとほぼ同時期に単離できる Pd 開始剤を用いた鈴木・宮浦カップリング重合を行っている。

3. チオフェンモノマー調製法

小澤らは、2-プロモ-3-ヘキシルチオフェンの Pd 触媒による脱ハロゲン化水素重縮合が位置規則性の高い P3HT を与えることを報告した¹⁴⁾。この重合における連鎖重合性の記述はないが、有機金属モノマーの調製を必要としない点から注目された。森らは TMPMgCl-LiCl 3 を用いて 2-プロモ-3-ヘキシルチオフェンの 5 位の水素を Grignard 化して 1 を調製し、重合を行っている¹⁵⁾。同様に 2-クロロ-3-ヘキシルチオフェンにおいても 3 を用いて Grignard モノマーを調製し、触媒に NiCl₂(PPh₃)IPr 4 を用いると触媒移動型連鎖縮合重合が進行する (式 2)¹⁶⁾。これは 4 がモノマーの C-Cl 結合へ高い活性を示すためである。

上田らは非常に嵩高い有機亜鉛試薬 Bu₄ZnLi₂ を用いてモノマーを調製し、重合を行っている¹⁷⁾。Bu₄ZnLi₂ は塩基性は低いが金属-ハロゲン交換反応には高い活性を示すため¹⁸⁾、水酸基のような



式2

Grignard 試薬と反応する官能基が存在しても保護することなく重合が可能である(式3)。

4. 重合機構

Kiriy らは、*p*-ジブロモベンゼンから調製した開始剤5を用いて重合を行うと、4-ブロモフェニル基が末端に導入されたポリマーの他に、フェニレン基が主鎖内部に導入されたポリマーも生成すると報告している(式4)。すなわち、Ni 錯体は成長末端方向だけでなく、主鎖上の長い距離を分子内移動し、開始末端の4位のC-Br結合からも重合が進行することを明らかにした(Random Walking)¹⁹⁾。さらに図1で述べた、開始剤を用いない重合においてもRandom Walking は起こり、チオフェン環が5位同士で連結したユニット(tail to tail)は高分子末端だけではなく、ポリマー内部にも生成することも明らかにした^{20, 21)}。

重合における配位子の影響も盛んに研究されている。McNeil らは配位子に1,3-ビス(ジフェニルホスフィノ)エタン(dppe)を用いると、重合成長速度が触媒濃度に1次、モノマー濃度に0次であり、重合の律速段階は還元的脱離であることを明らかにした²²⁾。また、LiCl は重合速度、分子量分

布に影響していない。一方、配位子にdpppを用いると律速段階はトランスメタル化であり、LiCl は重合速度に影響を与える²³⁾。また、電子供与性の高いアルキルホスフィン配位子を有するNi 触媒を用いて重合を行えばNi⁰-arene π 錯体がより安定化すると考え、図2に示した触媒を用いて重合を検討している²⁴⁾。その結果、メチル置換のNi(dmpe)Cl₂とシクロヘキシル置換のNi(dcpe)Cl₂は重合能がなかったのに対し、エチル置換のNi(depe)Cl₂は優れた触媒として働き、重合の律速段階はNi(dppe)Cl₂と同様に還元的脱離であることを明らかにした。また、カルベン配位子のPd 触媒によるGrignard 型モノマーの重合も最近報告している²⁵⁾。

5. 他の共役系高分子

著者らはこの触媒移動型連鎖縮合重合が他のπ共役系高分子の合成にも適用できるか検討した。その結果、LiCl 存在下、触媒にNi(dppe)Cl₂を用いるとモノマー6からポリ(*p*-フェニレン)(PPP)が²⁵⁾、過剰のdppp 存在下、触媒にNi(dppp)Cl₂を用いるとモノマー7からポリピロールが制御して合成できることを見出した(式5(a), (b))²⁶⁾。

さらに、この重合法によって制御されたπ共役系高分子のブロック共重合体の合成も可能である。

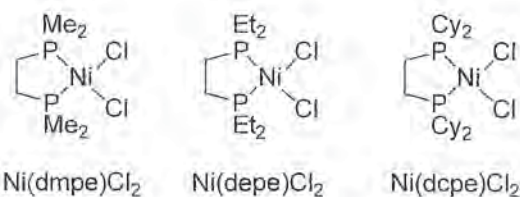
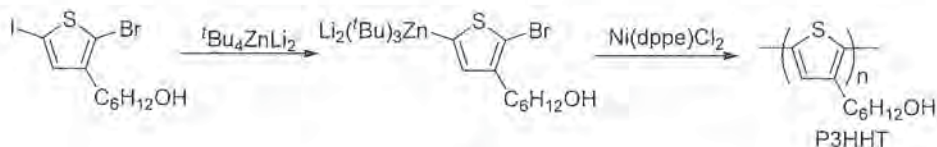
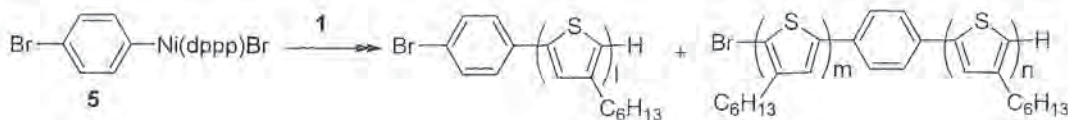


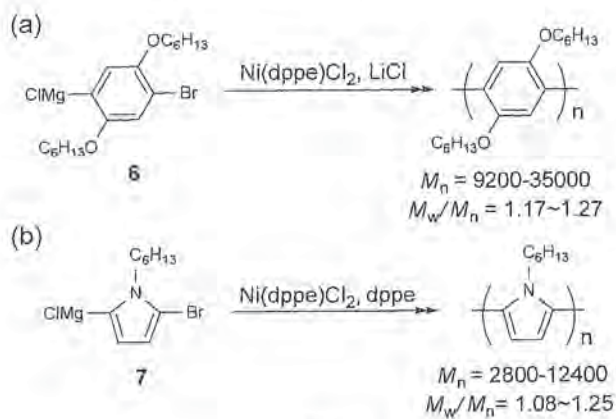
図2 種々のアルキルホスフィン配位子を有するNi 触媒



式3



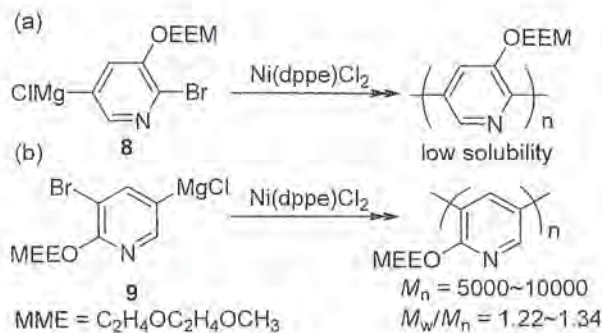
式4



式5

P3HTとPPPのブロック共重合体の合成では、1を重合した後にフェニレンモノマー6を加えたところ、PPPの単独重合体を含む分子量分布の広いポリマーが得られた。一方、6を重合した後に1を加えた結果、分子量分布の狭いブロック共重合体を得られた(図3)²⁷⁾。前者の重合法において制御ができなかった原因は、Ni触媒に対するモノマーの配位能力がベンゼン環(第二モノマー6)よりもチオフェン環(第一モノマー1)のほうが高いので、6の重合時に触媒がP3HT末端からブロモフェニレン末端に円滑に移動しなかったためと考えられる。

ここまで述べたポリマーはすべてドナー性ポリマー(p型 π 共役系高分子)であるが、近年アクセプター性ポリマー(n型 π 共役系高分子)の合成も検討されている。著者らはポリピリジンの合成を検討した結果、側鎖にメトキシエトキシエトキシ(MEEO)基を有する2,5-置換モノマー8の重合では得られるポリマーの溶解性が低く、連鎖重合性を評価できなかった。一方、3,5-置換モノマー9の重合においては分子量分布の狭いポリピリジン



式6

が得られた(式6)²⁸⁾。

さらに6位にメトキシエトキシプロピル(MEP)基を有する2,5-置換モノマー10の重合では、得られるポリマーの溶解性は向上したが、分子量分布の広いポリマーが得られた。また、両末端が臭素であるポリマーが重合初期から主に生成していたことから重合中に不均化が起きていることが明らかになった。おそらくピリジンの窒素原子に隣接する炭素上にNi成長末端が存在することによって2本のポリマーから成る配位錯体を形成しやすく、頻繁に不均化が起きていると思われる(式7)²⁹⁾。

一方、Kiryらはナフタレンジイミド構造を有するアクセプター性ポリマーの合成を報告している³⁰⁾。このアクセプターモノマーの電子吸引力と共役の広がりのため亜鉛を作用させるとラジカルアニオンが発生し、これがNi触媒によって連鎖重合し、分子量分布の狭いポリマーを与える(式8)。

6. 他のカップリング重合: 鈴木・宮浦カップリング重合

筆者らは触媒移動型連鎖縮合重合の一般性を明

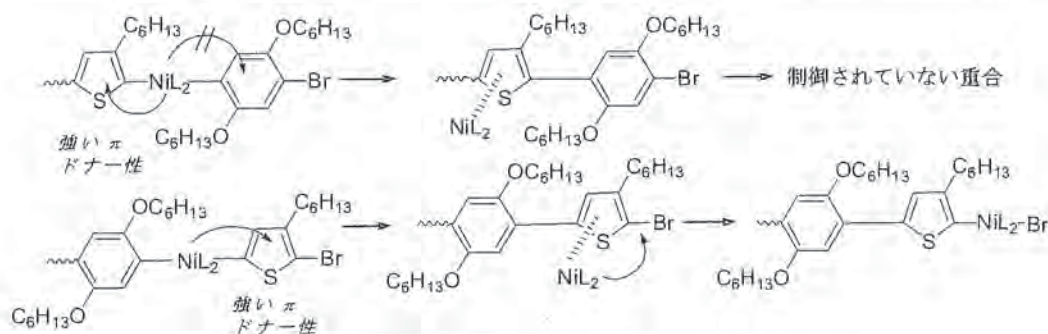
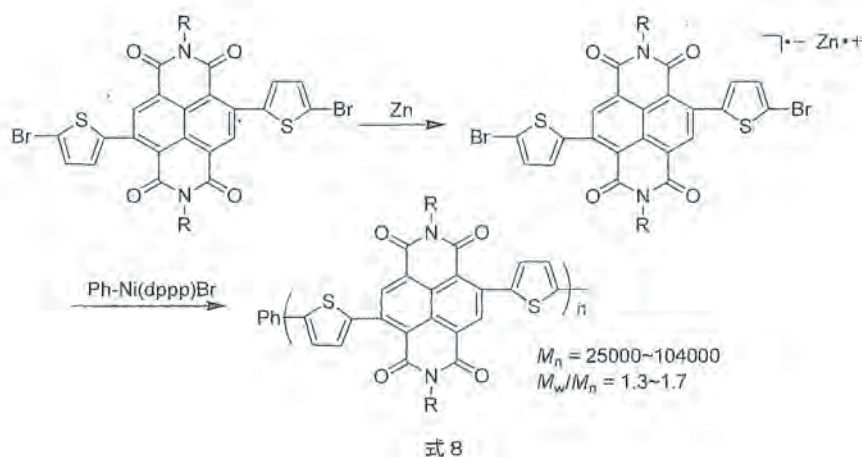
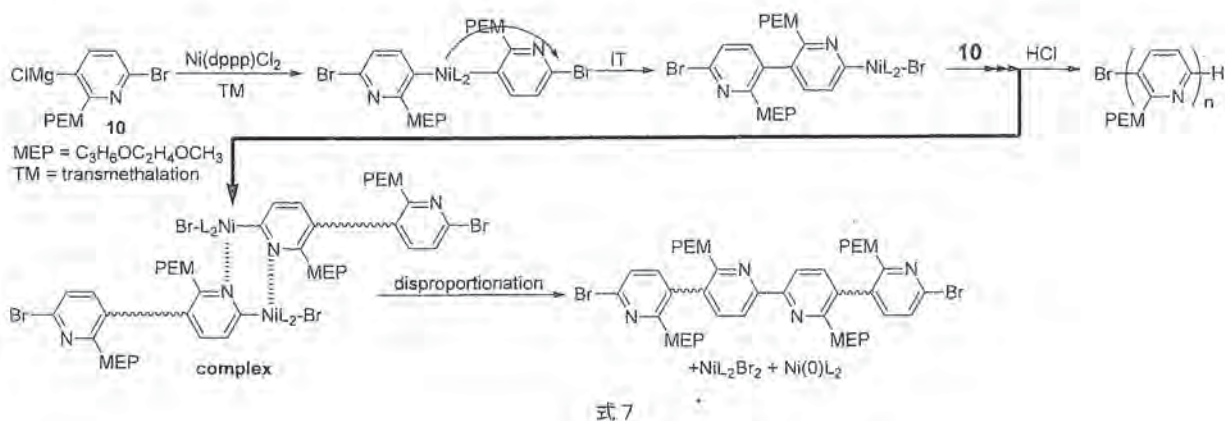


図3 ブロック共重合体におけるモノマーの重合順序の重要性

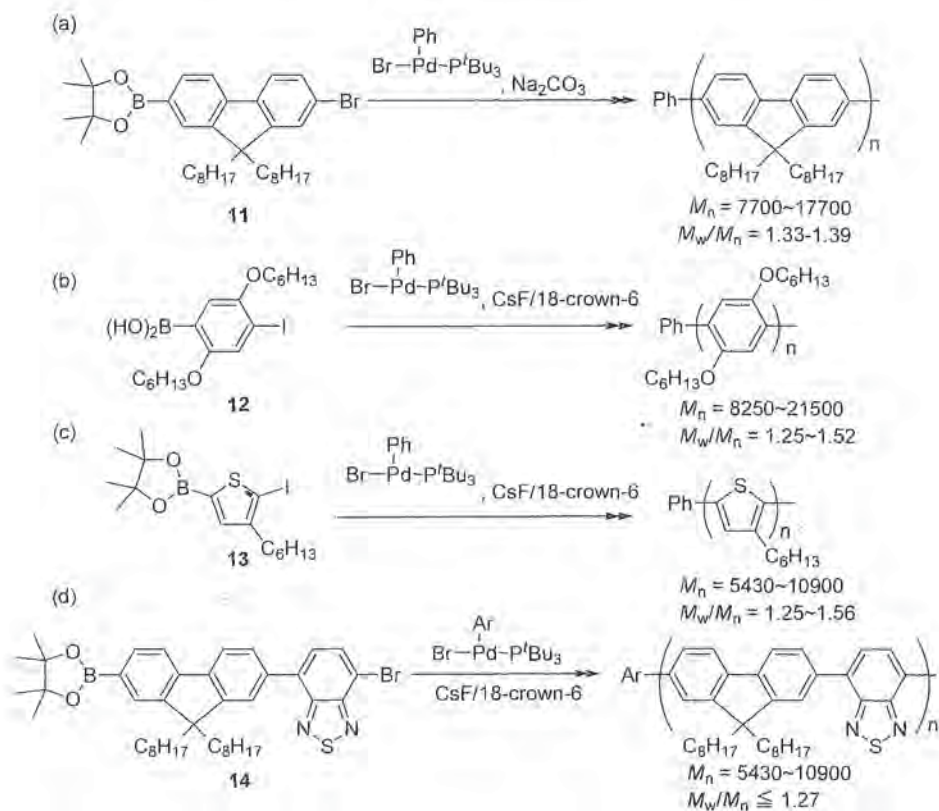


らかにするためPd触媒による鈴木・宮浦カップリング重合についても検討した。まずモデル反応としてジブロモベンゼンにフェニルホウ素酸エステルを種々のPd触媒存在下で反応させ、触媒の分子内移動により生成する二置換体を選択的に与えるPd触媒を探索した。その結果、Pd₂(dba)₃に*t*-Bu₃Pを配位子として加えると高い選択性で二置換体が生成することを見出したが、ほぼ同じ結果が他研究者によって報告された^{31,32}。Pd触媒の重合では開始種として機能するAr-Pd(II)-Br錯体を容易に単離して用いることができるため、*t*-Bu₃PPd(Ph)Brを開始剤として用いてフルオレンモノマー11をNa₂CO₃存在下で重合させた。重合は室温で進行し、末端に開始剤由来のPh基が結合したポリフルオレンが分子量分布1.39以下で得られた(式9(a))³³。さらにポリフェニレンおよびP3HTにおいても塩基としてCsFを18-crown-6と共に用いて重合を行うと分子量分布の狭いポリマーを得ることができた(式9(b), (c))^{34,35}。しかしながらピリジンモノマーの重合においてはNi

触媒を用いた時と同様に、不均化が起きた²⁹。さらにHuckらはアクセプター性モノマーとしてフルオレン-ベンゾチアジアゾール二芳香環モノマー14の重合を報告している(式9(d))³⁶。

7. 終わりに

π共役系高分子をリビング重合のように合成できる触媒移動型連鎖縮合重合について、ポリチオフェンを与える熊田・玉尾カップリング重合の最近の発展、他のπ共役系高分子の合成、さらに鈴木・宮浦カップリング重合への展開を述べた。ドナー性ポリマーだけでなく、アクセプター性ポリマーの合成においてもこの重合法が適用できることが明らかになり、触媒移動型連鎖縮合重合はπ共役高分子の一般的な合成手法になりつつある。一方、ドナー・アクセプター低バンドギャップπ共役系高分子は、太陽電池としてのより高い性能を目指して日進月歩で進化している。今後、ドナー・アクセプターモノマーを含めたさまざまなモノマーの触媒移動型連鎖縮合重合に適用可能な



式9

一般性の高い触媒、およびカップリング反応を開発すれば、太陽電池や電界効果型トランジスタの開発に優れた材料を提供できるであろう。

参考文献

- 1) H. Shirakawa, E.J. Louis, A.G. MacDiarmid, C.K. Chiang, and A.J. Heeger, *J. Chem. Soc., Chem. Commun.*, 1977, **16**, 578
- 2) T. Yamamoto, *Macromol. Rapid Commun.*, 2002, **23**, 583
- 3) a) R.D. McCullough and S.P. Williams, *J. Am. Chem. Soc.*, 1993, **115**, 11608. b) J. Liu, R.S. Loewe, and R.D. McCullough, *Macromolecules*, 1999, **32**, 5777
- 4) T.A. Chen and R.D. Rieke, *J. Am. Chem. Soc.*, 1992, **114**, 10087
- 5) A. Yokoyama, R. Miyakoshi, and T. Yokozawa, *Macromolecules*, 2004, **37**, 1169
- 6) R. Miyakoshi, A. Yokoyama, and T. Yokozawa, *J. Am. Chem. Soc.*, 2005, **127**, 17542
- 7) T. Yokozawa and A. Yokoyama, *Chem. Rev.*, 2009, **109**, 5595
- 8) M.C. Iovu, E.E. Sheina, R.R. Gil, and R.D. McCullough, *Macromolecules*, 2005, **38**, 8649
- 9) O.V. Zenkina, A. Karton, D. Freeman, L.J.W. Shimon, J.M.L. Martin, and M.E. van der Boom, *Inorg. Chem.*, 2008, **47**, 5114
- 10) V. Senkovskyy, N. Khanduyeva, H. Komber, U. Oertel, M. Stamm, D. Kuckling, and A. Kiriy, *J. Am. Chem. Soc.*, 2007, **129**, 6626
- 11) H.A. Bronstein and C.K. Luscombe, *J. Am. Chem. Soc.*, 2009, **131**, 12894
- 12) V. Senkovskyy, R. Tkachov, T. Beryozkina, H. Komber, U. Oertel, M. Horecha, V. Bocharove, M. Stamm, S.A. Gevorgyan, F.C. Krebs, and A. Kiriy, *J. Am. Chem. Soc.*, 2009, **131**, 16445
- 13) V. Senkovskyy, M. Sommer, R. Tkachov, H. Komber, W.T.S. Huck, and A. Kiriy, *Macromolecules*, 2010, **43**, 10157
- 14) Q. Wang, R. Takita, Y. Kikuzaki, and F. Ozawa, *J. Am. Chem. Soc.*, 2010, **132**, 11420
- 15) S. Tamba, S. Tanaka, Y. Okubo, H. Meguro, S. Okamoto, and A. Mori, *Chem. Lett.*, 2011, **40**, 398
- 16) S. Tamba, K. Shono, A. Sugi, and A. Mori, *J. Am. Chem. Soc.*, 2011, **133**, 9700
- 17) T. Higashihara, E. Goto, and M. Ueda, *ACS Macro Lett.*, 2012, **1**, 167
- 18) M. Uchiyama, T. Furuyama, M. Kobayashi, Y. Matsumoto, and K. Tanaka, *J. Am. Chem. Soc.*, 2006, **128**, 8404
- 19) R. Tkachov, V. Senkovskyy, H. Komber, J.-U. Sommer, and A. Kiriy, *J. Am. Chem. Soc.*, 2010, **132**, 7803
- 20) M. Verswyvel, F. Monnaie, and G. Koeckelberghs, *Macromolecules*, 2011, **44**, 9489
- 21) P. Khon, S. Huettner, H. Komber, V. Senkovskyy, R. Tkachov, R. Tkachov, A. Kiriy, R.H. Friend, U. Steiner, W.T. S. Huck, J.-U. Sommer, and M. Sommer, *J. Am. Chem. Soc.*, 2012, **134**, 4790
- 22) E.L. Lanni and A.J. McNeil, *J. Am. Chem. Soc.*, 2009, **131**, 16573
- 23) E.L. Lanni and A.J. McNeil, *Macromolecules*, 2010, **43**, 8039
- 24) E.L. Lanni, J.R. Locke, C.M. Glieave, and A.J. McNeil, *Macromolecules*, 2011, **44**, 5136
- 25) R. Miyakoshi, K. Shimono, A. Yokoyama, and T. Yokozawa, *J.*

- Am. Chem. Soc.*, 2006, **128**, 16012
- 26) A. Yokoyama, A. Kato, R. Miyakoshi, and T. Yokozawa, *Macromolecules*, 2008, **41**, 7271
- 27) R. Miyakoshi, A. Yokoyama, and T. Yokozawa, *Chem. Lett.*, 2008, **37**, 1022
- 28) Y. Nanashima, A. Yokoyama, and T. Yokozawa, *Macromolecules*, 2012, **45**, 2609
- 29) Y. Nanashima, R. Shibata, R. Miyakoshi, A. Yokoyama, and T. Yokozawa, *J. Polym. Sci., Part A: Polym. Chem.*, 2012, **50**, 3628
- 30) V. Senkovskyy, R. Tkachov, H. Komber, M. Sommer, M. Heuken, B. Voit, W. T. S. Huck, V. Kataev, A. Petr, and A. Kiriya, *J. Am. Chem. Soc.*, 2011, **133**, 19966
- 31) C.-G. Dong and Q.-S. Hu, *J. Am. Chem. Soc.*, 2005, **127**, 10006
- 32) S.K. Weber, F. Galbrecht, and U. Scherft, *Org. Lett.*, 2006, **8**, 4039
- 33) A. Yokoyama, H. Suzuki, Y. Kubota, K. Ohuchi, H. Higashimura, and T. Yokozawa, *J. Am. Chem. Soc.*, 2007, **129**, 7236
- 34) T. Yokozawa, H. Kohno, Y. Ohta, and A. Yokoyama, *Macromolecules*, 2010, **43**, 7095
- 35) T. Yokozawa, R. Suzuki, M. Nojima, Y. Ohta, and A. Yokoyama, *Macromol. Rapid Commun.*, 2011, **32**, 801
- 36) E. Elmakem, A. Kiriya, and W.T.S. Huck, *Macromolecules*, 2011, **44**, 9057

■好評発売中■

改訂 化学装置材料耐食表

幡野 佐一著 B5判 本文345頁 定価7,560円

本書の耐食表は、温度と処理物質の濃度に関してA級およびB級の2段階において材料記号を挙げ、特に重要な材料については腐食速度の変化を図示しました。また、必要に応じてその他の支配条件をできるだけ付記して予備選択の資料に供してあるのも特徴です。

- I 概説…はじめに／構造材料の内部組織と特性との関係／構造材料の機械的性質／腐食の開始／腐食環境／新しい化学装置材料／構造材料の選び方
- II 材料の物理的および機械的性質表…化学装置用主要材料の代表番号表／1. 鉄および銅／2. 高ケイ素铸铁／3. 高ニッケル铸铁／4. 高クロム铸铁／5. マルテンサイト系ステンレス鋼／6. フェライト系ステンレス鋼／7. オーステナイト系ステンレス鋼／8. Fe-Cr-Ni 合金(特殊オーステナイト鋼)／9. Fe-Cr-Al 合金／11. 高マンガン铸鋼／16. 銅および銅合金／17. Cu-Ni 合金／21. アルミニウムおよびアルミニウム合金／22. マグネシウムおよびマグネシウム合金／26. ニッケル／27. Ni-Cr-Fe 合金／28. Ni-Cu 合金／30. Ni-Mo-Fe-Cr 合金／31. Ni-Cr-Cu-Mo 合金／32. Ni-Si 合金／33. コバルト合金／36. 鉛および鉛合金／37. すず／38. 亜鉛／41. 貴金属、白金属およびバナジウム族金属／45. タングステン／46. チタンおよびチタン合金／47. ジルコニウムおよびジルコニウム合金／48. モリブデン／49. クロム／51. ケイ酸塩類製品／52. コンクリート／53. 硫黄セメント／56. 炭素および黒鉛製品／57. アスベスト／61. 合成樹脂／62. アスファルト／66. 天然ゴムおよび合成ゴム類／許容力図／鋼管の概略使用範囲／低温用鉄鋼材料／高温用金属材料
- III 耐食表…耐食表の記号の読み方／塩酸および塩化水素／ハロゲン／ハロゲン化炭化水素／無機塩化物／フッ素／硫酸／硫化水素、亜硫酸、硫黄、その他／亜硫酸塩および硫酸塩／硝酸／硫硝混酸／リン酸／その他のリン酸および化合物／その他の無機酸および無機化合物／水酸化ナトリウム／アンモニア／アルカリ性化合物および物質／炭酸塩および硝酸塩／酸化剤／水に対する金属材料の耐食性／酢酸および無水酢酸／クエン酸／その他の有機酸／炭化水素／アルコール類およびフェノール／アミン類、ピリジン類／アルデヒドおよびケトン／炭水化物および食品／高温および低温／超低温冷媒と適材、ハロゲンガス／海水
- IV 単位反応装置の型式と構造材料の工業的実例…アルキル化／ハロゲン化／脱ハロゲン化／エステル化／アミド化／還元によるアミド化／ニトロ化／スルホン化／酸化／水素添加／加水分解／総合および脱水縮合／重化／発酵／その他の反応
- 付録(I)…金属材料の特性等 40頁 付録(II)…高分子材料の選定と適用目安等 119頁

発行／化学工業社 <http://www.kako-sha.co.jp>

Note

Flexible Plastic Bioreactors for Photobiological Hydrogen Production by Hydrogenase-Deficient Cyanobacteria

Masaharu KITASHIMA,¹ Hajime MASUKAWA,^{2,3} Hidehiro SAKURAI,^{2,†} and Kazuhito INOUE^{1,2}¹Department of Biological Sciences, Kanagawa University, Tsuchiya, Hiratsuka, Kanagawa 259-1293, Japan²Research Institute for Photobiological Hydrogen Production, Kanagawa University, Tsuchiya, Hiratsuka, Kanagawa 259-1293, Japan³PRESTO, Japan Science and Technology Agency (JST), 4-1-8 Honcho, Kawaguchi, Saitama 332-0012, Japan

Received October 26, 2011; Accepted January 17, 2012; Online Publication, April 7, 2012

[doi:10.1271/bbb.110808]

Uptake hydrogenase mutant cells of the cyanobacterium *Nostoc* sp. PCC 7422 photobiologically produced H₂ catalyzed by nitrogenase for several days in H₂-barrier transparent plastic bags, and accumulated H₂ in the presence of O₂ evolved by photosynthesis. Their H₂ production activity was higher in the sealed flexible bags than in stoppered serum bottles of fixed gas volume.

Key words: bioreactor; cyanobacteria; hydrogen; hydrogen barrier film; photosynthesis

This paper describes the use of transparent flexible H₂-barrier plastic bags as culture vessels for small-scale laboratory experiments in place of stoppered serum bottles for the accumulation of H₂ photobiologically produced by cyanobacteria. Some cyanobacteria produce H₂ by the action of nitrogenase accompanied by photosynthetic O₂ evolution.^{1–4)} Plastic bags allow evaluation of H₂ production activity under ambient pressure accompanied by the emission and absorption of various gases.

Bags made from two types of gas barrier films were used: Besela film (donated by Kureha, Tokyo) composed of a poly-acrylate gas-barrier layer, and GL film (donated by Toppan, Tokyo) composed of an Al₂O₃-deposited gas-barrier layer. These films were laminated with a layer of biaxially oriented nylon (ONy) (15–25 μm), followed by either cast polypropylene (CPP) or low-density polyethylene (LDPE) (45–65 μm) on the inner surface, yielding four types of bags: Be-P and Be-E (Besela), and Gl-P and Gl-E (GL), with CPP and LDPE respectively (some of these should be available from GL Science, Tokyo). LDPE and CPP films withstand vapor heat treatment at 100 and 120 °C respectively. Although the Be-P and Gl-P bags look hazy, chemical actinometry⁵⁾ indicated that all of them transmit more than 90% of incident visible light. In the following experiments, the bags were equipped with a laboratory-made gas-sampling device (Fig. 1)⁶⁾ for sampling and exchange of gases. The concentrations of H₂, O₂, CO₂, He, and Ne were determined by gas chromatography (detector, TCD; column, Rt-Msieve 5A PLOT, 0.32 mm × 30 m, Restek, Bellefonte, PA). The gas volume in the bag was calculated by adding a known amount of He or Ne to it followed by gas determination.

The permeation of H₂ in the variously treated bags to

the outside air was determined for several days under ambient atmosphere (about 1 atm, at about 25 °C) with an initial H₂ concentration of about 5–10% in Ar. From the data, the permeability P_{mS} (cm³ m⁻² atm⁻¹ day⁻¹) were calculated by eq. (1):

$$Vdq/dt = -P_m S p, \quad (1)$$

where V = total gas volume (approximated to be constant, as the change was less than 1% throughout the experiments), q = H₂ mole fraction, t = time, S = membrane surface area, p and p₀ = H₂ partial pressure at time t and time zero respectively. Under these H₂ diffusion conditions, the numerical values of q and p are the same, and this yields P_{mS} (Table 1) from eq. (2):

$$V \ln p = -P_m S t + V \ln p_0 \quad (2)$$

Nitrogenase is an O₂-sensitive N₂ fixation enzyme limited to some prokaryotes that catalyzes the unidirectional production of H₂ as the inevitable by-product of the nitrogenase reaction.^{1,3)} In the absence of N₂, all the electrons are allocated to H₂ production. In cyanobacteria that have nitrogenase, the saccharides produced by O₂-evolving photosynthesis usually serve as the source of electrons for the nitrogenase reaction.^{1,3)} Although cyanobacteria have developed various responses alleviating the damaging effects of O₂ on nitrogenase, these responses are not always be enough completely to mitigate the O₂ effects. Stewart and Pearson⁷⁾ reported that *in vivo* nitrogenase activities (acetylene reduction) of *Anabaena flos-aquae* and *Nostoc muscorum* cells were inhibited by O₂ when the concentration exceeded 20% (v/v). The *Nostoc* sp. PCC 7422 mutant (Δ Hup) cells, which were used in the study too, whose uptake hydrogenase gene (*hupL*) had been knocked out, accumulated photobiologically produced H₂ up to about 30% (v/v) in the presence of evolved O₂.⁸⁾ The inhibitory effect of O₂ on this mutant was evident from the experiments in which the mutant cells were incubated in serum bottles with a starting gas phase of 20% O₂–75% Ar–5% CO₂: the concentration of the accumulated H₂ after 7 d was about 16% less than that of the culture with a starting gas phase that contained no O₂ (95% Ar–5% CO₂).⁸⁾

Nostoc sp. PCC 7422 Δ Hup mutant cells⁸⁾ 2 d after transfer to a combined nitrogen-free BG11₀ medium for

† To whom correspondence should be addressed. Fax: +81-463-58-9684; E-mail: sakurai@waseda.jp

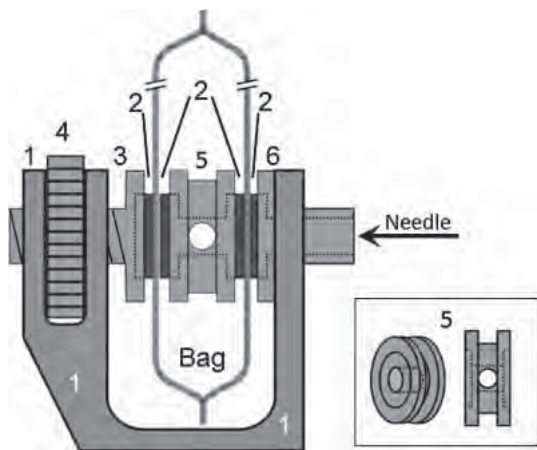


Fig. 1. Gas Sampling Device Made from Plastic.

About $35 \times 45 \times 18$ mm in size. 1, vice; 2, butyl rubber septum (gas barrier); 3, push bolt; 4, screw driving ring; 5, inner pad; 6, stopper with through hole; 7, needle. The plastic material for 1, 3, 4, 5, and 6 is PPS (polyphenylene sulfide).

Table 1. H_2 Permeability of Various Treated Barrier Membranes

Treatment	Bags	$P_m:H_2$ permeability ($\text{cm}^3 \text{m}^{-2} \text{d}^{-1} \text{atm}^{-1}$)
None	Be-E	87
	Be-P	44
	Gl-E	49
	Gl-P	44
$100^\circ\text{C} \times 20$ min 3 times	Be-E	22
	Be-P	53
	Gl-E	29
	Gl-P	48
$120^\circ\text{C} \times 20$ min autoclave	Be-E	89
	Be-P	67
	Gl-P	41

For types of membranes, see the text. The P_m values fluctuated even with the same type of the membrane according to the production lot and with the same type of heat treatment, and hence should be taken as reference values.

nitrogenase induction were put into either open serum bottles without caps or taller serum bottles of the same diameter capped with butyl rubber septa, and both types of bottles were put into untreated Be-E plastic bags. The bags containing open bottles were heat sealed. The initial gas volume was about the same for all the bottles. The time course of H_2 accumulation for the two types of containers was almost the same for the first 3 d, but after 5 d the sealed bags accumulated higher amounts of H_2 than the closed bottles (Fig. 2). The decrease in H_2 concentration in the gas phase due to H_2 dissolved in the culture media was estimated on the basis of H_2 solubility to be only about 0.04% (v/v) greater in the capped bottles than in the sealed bags after 9 d due to elevated H_2 partial pressure. These results strongly suggest that the higher O_2 partial pressure in the capped bottles as compared to the open plastic bags decreased nitrogenase-based H_2 production activity more strongly than in the latter, in agreement with a previous report.⁸⁾

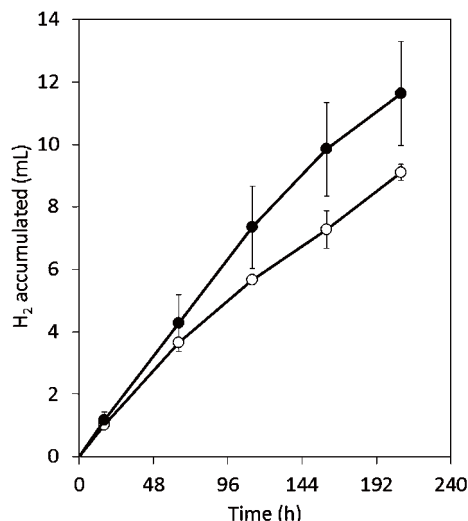


Fig. 2. Time Course of Accumulation of H_2 in Open and Capped Bottles.

Cyanobacteria at 2 d after transfer to BG110. Bags were untreated Be-E type. Initial gas composition: 94% Ar, 5% CO_2 , and 1% N_2 . Cyanobacteria culture volume: 50 mL in open bottles (3.7 cm outer diameter, 7.6 cm in height) or capped bottles (3.7 cm \times 11.6 cm). Initial gas volume: about 45–55 mL for the former and 50 mL for the latter. Light (a 12 h light and 12 h dark cycle) from fluorescent lamps illuminating both sides of the bottles at the surface of the bags: total photosynthetically active flux density of $100 \mu\text{mol photons m}^{-2} \text{sec}^{-1}$. Gas samples were taken at the end of the light period. H_2 in sealed bags (●) and in capped bottles (○). Each point is the average of triplicate samples.

Gas-barrier plastic bags are suitable for measuring biological activities accompanying gas emission and absorption, such as H_2 production, methane production, and photosynthesis under ambient pressure. Flat surface bags are suitable for determining the efficiency of light energy conversion to H_2 . The size of the bag can easily be changed by heat sealing. The bags can also accommodate various structured materials such as a latex biomimetic leaf coated with purple photosynthetic bacteria in Besela bags for photobiological H_2 production.⁹⁾

Amos¹⁰⁾ estimated the cost of hydrogenase-based photobiological H_2 production by the green alga *Chlamydomonas*, and pointed out that the product price of the bioreactor accounts for a significant portion of the overall cost. If the price of the bioreactor exceeds \$100 per m^2 , then the system is not economically viable. Prince and Ksheshgi¹¹⁾ enumerated various technical issues that must be addressed to make photobiologically produced H_2 economically viable, and one issue identified is a need to develop inexpensive bioreactors. H_2 -barrier plastic membranes were found here to be potentially viable materials for inexpensive large-scale bioreactors floating on the sea surface^{3,4)} in future real-world use. Although many of the relevant technologies are in the early stages of development, the medium-term target price of H_2 produced by cyanobacteria is estimated to be 26.4 cents per kWh.⁴⁾

Using an H_2 permeability (P_m) value of $50 \text{ cm}^3 \text{m}^{-2} \text{atm}^{-1} \text{d}^{-1}$ (Table 1), the leakage of H_2 from the plastic bioreactor was estimated to be 1.5 L m^{-2} over 60 d (compared with H_2 production: 912 L m^{-2}) as follows: Cyanobacteria produce H_2 at 1.2% efficiency

in ΔH (a high heating value of 286 kJ/mol) vs. total solar radiation of 5.4 MJ m⁻² year⁻¹, leading to an H₂ production rate of 176 kJ (15.2 L (25 °C)) m⁻² d⁻¹. The amount of O₂ produced is half that of H₂. The initial gas phase (5% CO₂ plus 1% N₂ in Ar) is 500 L m⁻², and H₂ accumulates after 60 d to a concentration of 49% (912/(500 + 912 + 456) = 0.49). H₂ leakage from both sides of the bioreactor over 60 d = $2 \times 50 \times 10^{-3} \times 0.245 \times 60 \approx 1.5$ (L m⁻²), and this can be reduced further by increasing the thickness of the barrier layer if necessary.

Acknowledgment

This work was supported in part by a Grant-in-Aid for Scientific-Research (21380200) from MEXT Japan (to HS), by PRESTO, JST (to HM), and by a donation from LiteraMed, K.K. (to KI).

References

- 1) Tamagnini P, Axelsson R, Lindberg P, Oxelfelt F, Wunschiers R, and Lindblad P, *Microbiol. Mol. Biol. Rev.*, **66**, 1–20 (2002).
- 2) Masukawa H, Mochimaru M, and Sakurai H, *Appl. Microbiol. Biotechnol.*, **58**, 618–624 (2002).
- 3) Sakurai H and Masukawa H, *Mar. Biotechnol.*, **9**, 128–145 (2007).
- 4) Sakurai H, Masukawa H, Kitashima M, and Inoue K, *Adv. Exp. Med. Biol.*, **675**, 291–303 (2010).
- 5) Hatchard CG and Parker CA, *Proc. R. Soc. Lond. A*, **235**, 518–536 (1956).
- 6) Waseda University and Kanagawa University, Japan Kokai Tokkyo Koho, 2011-085571 (April 28, 2011).
- 7) Stewart WDP and Pearson HW, *Proc. R. Soc. Lond. B*, **175**, 293–311 (1970).
- 8) Yoshino H, Ikeda H, Masukawa H, and Sakurai H, *Mar. Biotechnol.*, **9**, 101–112 (2007).
- 9) Gosse JL, Engel BJ, Hui JCH, Harwood CS, and Flickinger MC, *Biotechnol. Prog.*, **26**, 907–918 (2010).
- 10) Amos WA, *NREL Report*, NREL/MP-560-35593, www.nrel.gov/docs/fy04osti/35593.pdf (2004) (Accessed on October 23, 2011).
- 11) Prince RC and Kheshgi HS, *Crit. Rev. Microbiol.*, **31**, 19–31 (2005).

Construction of a Metagenomic Library for the Marine Sponge *Halichondria okadai*

Takahiro ABE,^{1,4,†} Fatma Pinar SAHIN,² Kiyotaka AKIYAMA,³ Takayuki NAITO,³ Mizoe KISHIGAMI,⁴ Kenji MIYAMOTO,⁴ Yasufumi SAKAKIBARA,⁴ and Daisuke UEMURA^{1,4,†}

¹Department of Chemistry, Faculty of Science, Kanagawa University, 2946 Tsuchiya, Hiratsuka, Kanagawa 259-1293, Japan

²Department of Pharmaceutical Botany, Faculty of Pharmacy, Hacettepe University, 06100, Sıhhiye, Ankara, Turkey

³Molecular Neuroscience Unit, Okinawa Institute of Science and Technology, 12-22 Suzaki, Uruma, Okinawa 904-2234, Japan

⁴Department of Biosciences and Informatics, Faculty of Science and Technology, Keio University, 3-14-1 Hiyoshi, Yokohama, Kanagawa 223-8522, Japan

Received July 19, 2011; Accepted January 11, 2012; Online Publication, April 7, 2012

[doi:10.1271/bbb.110533]

Symbionts of the marine sponge *Halichondria okadai* are promising as a source of natural products. Metagenomic technology is a powerful tool for accessing the genetic and biochemical potential of bacteria. Hence, we established a method of recovering bacterial-enriched metagenomic DNA by stepwise centrifugation. The metagenomic DNA was analyzed by ultrafast 454-pyrosequencing technology, and the results suggested that more than three types of bacterial DNA, Alphaproteobacteria, Actinobacteria, and Cyanobacteria, had been recovered, and that eukaryotic genes comprised only 0.02% of the metagenomic DNA. These results indicate that stepwise centrifugation and real-time quantitative PCR were effective for separating sponge cells and symbiotic bacteria, and that we constructed a bacteria-enriched metagenomic library from a marine sponge, *H. okadai*, selectively for the first time.

Key words: metagenomic library; *Halichondria okadai*; fosmid; 454-pyrosequencing; sponge

Many structurally unique compounds and significant biologically active compounds have been isolated from various marine invertebrates.^{1,2)} In particular, sponges, members of the porifera, are rich sources of many natural products. The marine sponge *Halichondria okadai* is generally found in tidal pools on the Pacific coast of Japan. It has an irregular round shape with a few large oscules, and is slightly hard. We have isolated halichondrin B, which exhibits strong cytotoxicity toward B16 melanoma cells, from *H. okadai*, and have analyzed its structure.^{3,4)} Erubrin (E7389), the right-side fragment of halichondrin B, has been accepted as a therapeutic drug (HALAVEN) for the treatment of breast cancer by the U.S. FDA (<http://www.fda.gov/default.htm>). Halichlorine, an alkaloid, has also been

isolated from *H. okadai*. It inhibits the production of blood vessel cell adhesion molecule (VCAM-1).^{5–7)} Okadaic acid, a polyether that inhibits phosphatase, has also been isolated from this sponge.⁸⁾ Since, many other natural products, including Alteramide A, Neohalicholactone and so on, have been isolated from this sponge,^{9,10)} *H. okadai* is promising as a source of natural products.

Recent research suggests that marine sponges harbor various microbial symbionts, and that the bacterial population may be as high as 40–60% of the sponge biomass.^{11,12)} Furthermore, many bioactive compounds in sponges are produced by these symbionts. For example, cytotoxic macrolide swinholide A is produced by both the marine sponge *Theonella swinhoei* and its symbiotic Cyanobacteria.¹³⁾ Hence, the exploitation of bacterial symbionts of marine sponges might be an effective approach to harvesting large amounts of natural products. Although microorganisms have potential as sources of bioactive compounds, only a small proportion of bacteria have been isolated from the environment.^{14,15)} Hence, to use symbiotic bacteria efficiently as sources of natural products, a metagenomic approach is appropriate. Recently, several natural products have been isolated using metagenomic libraries derived from soil.^{16,17)} These metagenomic libraries were used directly as sources of natural products by screening of clones that produce bioactive compounds by heterologous expression of metagenomic DNA. On the other hand, when construct a metagenomic library from a marine sponge, contamination by the eukaryotic genomic DNA of sponge of metagenomic DNA decreases the efficiency of heterologous expression of the symbiotic bacterial genomic DNA in *E. coli*. Hence, strict separation of symbiotic bacteria and sponge cells is very important in the construction of a metagenomic library.

[†] To whom correspondence should be addressed. Takahiro ABE, Tel: +81-46-359-4111; E-mail: abtaka@kanagawa-u.ac.jp; Daisuke UEMURA, Tel: +81-46-359-4111; E-mail: uemurad@kanagawa-u.ac.jp

Abbreviations: PCR, polymerase chain reaction; DNA, deoxyribonucleic acid; RNA, ribonucleic acid; rRNA, ribosomal RNA; COG, clusters of orthologous groups of proteins; Q-PCR, real-time quantitative PCR; VCAM, vessel cell adhesion molecule; PKS, polyketide synthase; NRPS, non-ribosomal peptide synthase; Tris, tris-hydroxymethyl-aminomethane; EDTA, ethylenediaminetetraacetic acid; CTAB, cetyl trimethyl ammonium bromide; NCBI, National Center for Biotechnology Information; nr, non-redundant database

In this study, we established a method of extracting bacterial-enriched metagenomic DNA by stepwise centrifugation and real-time quantitative PCR (Q-PCR), and then confirmed the quality of the metagenomic DNA by dataset analysis. Finally, we constructed a fosmid library with metagenomic DNA from a marine sponge, *H. okadai*, for the first time.

Materials and Methods

Sponge collection and separation of bacterial symbionts. The marine sponge *Halichondria okadai* was collected from tidal pools on the coast of Hayama, Kanagawa, Japan. The sponges were stored on ice until used, within 6 h. They were diced into small pieces and crushed manually into a cell suspension on ice with TEN buffer (3.5% sodium chloride, 10 mM tris-hydroxymethyl-aminomethane, 50 mM ethylenediaminetetraacetic acid, pH 8.5). First, the sediment and cell suspension were separated with a large nylon mesh (20 μ m). Then the sponge cells and bacteria were separated by step-wise centrifugation (Fig. 1). The cell suspension was transferred to two ultracentrifuge tubes. One cell suspension was centrifuged at 8,000 *g* for 15 min at 4 °C in a HIMAC CR20G2 centrifuge (Hitachi, Tokyo) (fraction 1). The other cell suspension was first centrifuged at 500 *g* for 5 min at 4 °C (fraction 2). The supernatant was then transferred to another tube and centrifuged at 1,000 *g* for 15 min at 4 °C (fraction 3). Next, the supernatant of the 1,000-*g* fraction was transferred to another tube and centrifuged at 3,000 *g* for 15 min at 4 °C (fraction 4). The supernatant of the 3,000-*g* fraction was then transferred to another tube and centrifuged at 8,000 *g* for 15 min at 4 °C (fraction 5). Finally, the various precipitates (fractions 1–5) were resuspended in TEN buffer and centrifuged at 8,000 *g* (20 min, 4 °C) by way of washing, twice each. The genomic DNA of fraction 1 was used for PCR amplification of 16S rRNA, and that of fraction 5 was used in both the construction of a metagenomic library and second-generation ultrafast sequencing.

DNA isolation. Genomic DNA was extracted and purified following the instructions in a commercial genomic DNA extraction kit (for example, Genomic-tips 20/G, Qiagen, Frankfurt), and the protocol used to recover genomic DNA, described by Piel *et al.*, was modified as follows.^{18,19} The precipitates were resuspended and lysed in 20 mL of guanidine solution (60% guanidine thiocyanate, 0.5% sodium dodecyl sulfate, 10 mM EDTA) during incubation at 65 °C. An equivalent volume of CTAB buffer (4% cetyl trimethyl ammonium bromide, 20 mM EDTA pH 8.0, 100 mM Tris-HCl pH 8.0, 1.4 M NaCl) and 50 μ L of mercaptoethanol were added, and the sample was incubated for 2 h at 65 °C. After lysis, genomic DNA was extracted 2–3 times with phenol-chloroform and chloroform, and precipitated with isopropanol. The precipitate was dissolved in TE buffer and incubated at 37 °C with RNase A (Toyobo, Osaka) overnight, and then precipitated with isopropanol and dissolved in TE again. The amounts of DNA were determined using a UV spectrophotometer at 260 nm (UVmini-1240, Shimadzu, Kyoto).

Bacterial diversity in metagenomic DNA determined by specific PCR amplification of 16S rRNA. PCR amplification of 16S rRNA from

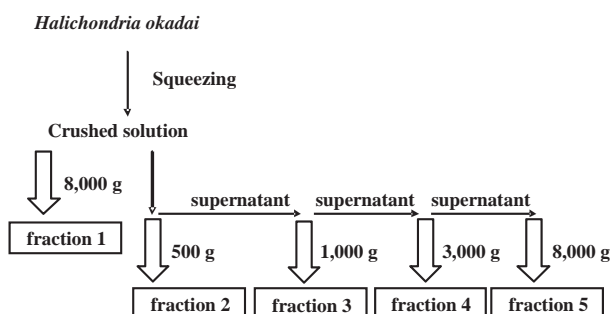


Fig. 1. Scheme for Concentration of the Bacterium from the Sponge Used in This Study.

metagenomic DNA was carried out with primers 16SrRNAF: 5'-GTGCCAGCAGCCGCGTAATAC-3' and 16SrRNAR: 5'-TACAA-GGCCCGGAACGTATTACAC-3' (Operon, Tokyo), using *Ex Taq* polymerase (Takara-Bio, Kyoto). These primers refer to *Roseovarius nubinhibens* (NR_028728), *Streptomyces* sp. (AB498686), *Staphylococcus capitis* (AB009937), *Synechocystis* sp. (AB364260), and *Escherichia coli* (AB269763), and they were designed so that they would be located outside the V1 and V8 regions of the bacterial 16S rRNA. Thermocycling consisted of 2 min of denaturation at 95 °C, followed by 30 cycles of 30 s at 95 °C, 30 s at 55 °C, and 90 s at 72 °C. The terminal elongation step was extended by 15 min, and the reaction mixtures were cooled to 4 °C upon completion. Amplicon size and integrity were examined by standard agarose gel electrophoresis and ethidium bromide staining. Amplicons were extracted using the GFX PCR DNA and Gel Band Purification Kit (GE Healthcare Japan, Tokyo). The purified PCR products were cloned to pT7-blue T vector (Takara-Bio) with a Mighty mix-DNA ligation kit (Takara-Bio) and transferred into *E. coli*, DH5- α competent cells. The 16S rRNA clones were cultured with Luria-Bertani (LB) broth supplemented with ampicillin (100 mg/L), and the clones were extracted using a GenElute Plasmid Miniprep Kit (Sigma-Aldrich, St. Louis, MO) following the manufacturer's instructions. Eighty-three positive clones were randomly selected and sequenced with a BigDye Terminator Cycle Sequencing Kit (Applied Biosystems, Norwalk, CT) with primers pT7blue-SF: 5'-CAGGTCGACTCTAGAGGATC-3' and pT7blue-SR: 5'-GACGGCCAGTGAATTTCGAGC-3' (Operon), using an ABI 3730xl DNA Analyzer (ABI). The sequence results were analyzed by Genetyx software (Genetyx, Tokyo) and compared with known sequences in the GenBank database using the BLASTN search program (<http://www.ncbi.nlm.nih.gov/>) to determine approximate phylogenetic affiliations. Chimeric genes were then compared with related 16S rRNA. A phylogenetic tree was constructed by the neighbor-joining method²⁰ based on distance matrix data by the phylogenetic program ClustalX2 (available at <http://www.clustal.org/>).²¹ Evolutionary distances were calculated using the Kimura model.²² The topology of the phylogenetic tree was evaluated by bootstrap analysis carried out with 1,000 replications.²³ 16S rRNA alignment was achieved by including the phyla Proteobacteria, Actinobacteria, Cyanobacteria, and Firmicutes. A sequence belonging to archaea was used as out group (Fig. 3).

Cloning of the 18S rRNA of *H. okadai*. PCR amplification of the 18S rRNA genes of *H. okadai* was performed with primers designed based on the conserved regions of the 18S rRNA of the marine sponges *H. melanodocia* (AY737639) and *Axinella corrugata* (AY737637). Thus 18S rRNA F: 5'-CCTGGTTGATCCTGCCAGTAGC-3' corresponded to the 1n to 17n bases of the 18S rRNA of *H. melanodocia*, and to the 1n to 24n bases of the 18S rRNA of *A. corrugata*, and 18S rRNA R: 5'-CTACAGAAACCTTGTACGAC-3' corresponded to the 1,759n to 1,779n bases of the 18S rRNA of *H. melanodocia*, and to the 1,769n to 1,789n bases of the 18S rRNA of *A. corrugata* (Operon), using genomic DNA extracted from fraction 1 with *Ex Taq* polymerase. These purified PCR products were cloned, and several positive clones were selected randomly and sequenced with primers pT7blue-SF and pT7blue-SR. The sequence results were analyzed by Genetyx software and compared with known sequences in the GenBank database using the BLASTN search program to determine approximate phylogenetic affiliations.

Quantitative real-time PCR. Cloned 18S rRNA was used as template for a single reaction of Q-PCR. The copy number of the 18S rRNA gene was determined by assuming that based on the molecular weights of the plasmid, which harbored partial 18S rRNA, 1 pg of plasmid equals 1.0×10^5 copies. To prepare a standard curve for Q-PCR, 1, 0.1, 0.01, 0.001, and 0.0001 pg of the purified plasmid was used in identical PCR reactions. Q-PCR was performed using SYBR PremiEx Taq and a Thermal Cycler Dice Real Time System (Takara-Bio).

Pyrosequencing and analysis of metagenomic GS-FLX data. Metagenomic DNA extracted from fraction 5 was used as starting material for pyrosequencing. Approximately 15 μ g of genomic DNA was sequenced by three runs on a Roche GS-FLX pyrosequencer

Table 1. Closest Phylogenetic Affiliations of Partial 16S rRNAs Retrieved from Selected Clones

Clone	Identity	Closest homolog (BLASTN)	Accession no.
2	98.0	Uncultured alphaproteobacteria (HOC32)	AB054166
4	98.5	Mucus bacterium 81	AY654839
47	96.1	Alphaproteobacterium EXT2	AB274734
70	93.5	Uncultured alphaproteobacterium	GQ346733
74	98.6	Uncultured alphaproteobacterium	AB491826
7	99.5	Uncultured bacterium	HM344756
13	99.2	Uncultured bacterium	HM835849
45	99.8	Uncultured bacterium	HM329350

(Roche, Mannheim, Germany). Genomic DNA was dissolved in TE buffer, and its purity was ensured by checking that the A260/A280 wavelength ratio was from 1.8 to 2.0. The resulting data were assembled using Newbler assembly software v1.1.02.15 (Roche). Functional annotation of the protein-coding regions was achieved using the BLASTX algorithm, which was used to query the NCBI non-redundant database (nr) and the clusters of orthologous groups database (COG).^{24–27} Comparisons of the metagenomic sequence data to the NCBI-nr and COG databases were performed at a cutoff e-value of 10^{-5} . Manual editing was performed using Genetyx software.

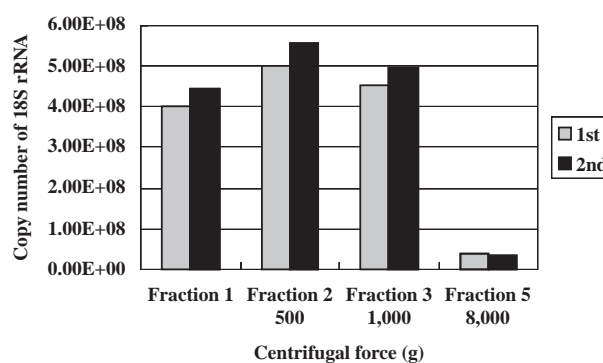
Construction of metagenomic fosmid libraries. A metagenome library was constructed following the manufacturer's instructions using a commercial fosmid library construction kit (CopyControl Fosmid Library Production Kit, Epicentre, Madison, WI). Extracted metagenomic DNA was ligated into the fosmid vector pCC1FOS (Epicentre), and the ligated vectors were packaged into lambda phages and used to transfect *E. coli* EPI300 (Epicentre). The resulting infected cells were spread onto LB medium containing 12.5 µg/mL of chloramphenicol. All the fosmid clones were stored in a deep freezer in LB medium supplemented with a mixture of chloramphenicol (12.5 µg/mL) and 10% glycerol (v/v). Induction of the fosmids to give a high copy number was achieved by the addition of induction solution (Epicentre) and incubation of the cultures at 37 °C for 5 h. After induction, the cells were collected, and the various fosmid DNAs were isolated by the alkaline lysis miniprep method.²⁸

Nucleotide sequence accession number. The DNA sequence of the continuous 18S, 28S, and 5.8S rRNAs of *H. okadae* (contig00027) is available from the GenBank database under accession no. AB511881.

Results

Genomic DNA isolation and measurement of 18S rRNA by Q-PCR assay

To measure the concentrations of eukaryotic genomic DNA in the various fractions, the copy numbers of the 18S rRNA were determined using a LightCycler system under the conditions described in "Materials and Methods." First, to design primers for Q-PCR, we extracted genomic DNA from precipitates of *H. okadae* by the CTAB method described in "Materials and Methods." Next, 18S rRNA was cloned. A blast search suggested that the clone was 18S rRNA of *H. okadae*, which shows high homology to that of the marine sponge *Halichondria melanodocia* (AY737639, 99.8%). A 10-fold dilution series of purified 18S rRNA PCR products ranging from 1×10^{-6} to 1 pg/µL was examined by Q-PCR. Genomic DNA samples were then extracted from precipitates collected by graded centrifugation under the conditions described in "Materials and Methods," and the copy numbers of the 18S rRNA segments were determined in duplicate by Q-PCR. The copy number of 18S rRNA per 1 ng of genomic DNA of the fractions collected at high speed decreased dynamically (Fig. 2). The quantity of 18S rRNA clones

**Fig. 2.** Quantification and Comparison of 18S rRNA Copies in Centrifuged Pellets of *H. okadae*.

The Q-PCR data were created using four fraction samples (crushed solution, pellets at 500 g, pellets at 1,000 g, pellets at 8,000 g), twice (1st, 2nd).

in the deposition collected at low speed (500 g) (fraction 2) was greater than that in the crushed-sponge solution (fraction 1). This is because the sponge cells were concentrated by centrifugation at low speed. On the other hand, for precipitates collected at high speed (8,000 g), the amount of 18S rRNA clones greatly decreased (fraction 5). This suggests that contaminating sponge cells were largely eliminated by low-speed centrifugation (3,000 g), and that the pellets collected from the supernatant at the higher speed (8,000 g) were enriched bacterial pellets.

Bacterial community composition

Before we evaluated the metagenomic DNA used in library construction, the composition and structure of the bacterial community of *H. okadae* were examined by PCR analysis. We cloned 16S rRNA and sequenced 83 random clones. This revealed that 76 clones (91.6%) showed high homology (97.0–99.0%) to each other, and this group was represented by clone2. First, a blast search in the NCBI database revealed that all of the clones show highest homology to uncultured bacteria (Table 1). Next, to examine the phylogenetic relation between these clones in further detail, cloned 16S rRNA (clones 2, 4, 7, 13, 45, 47, 70, and 74) was aligned with those of representatives of various bacteria using the ClustalX2 program (Fig. 3). This revealed that the dominant phylum was Alphaproteobacteria (clones 2, 4, 47, 70, and 74). Clone2 showed very high homology with the 16S rRNA genes of uncultured Alphaproteobacteria, HOC32 (98.2%), previously isolated from *H. okadae*, at a position apart from the four other clones. Two clones (clone13 and clone45) belonged to Actinobacteria, and clone7 belonged to Firmicutes. This PCR

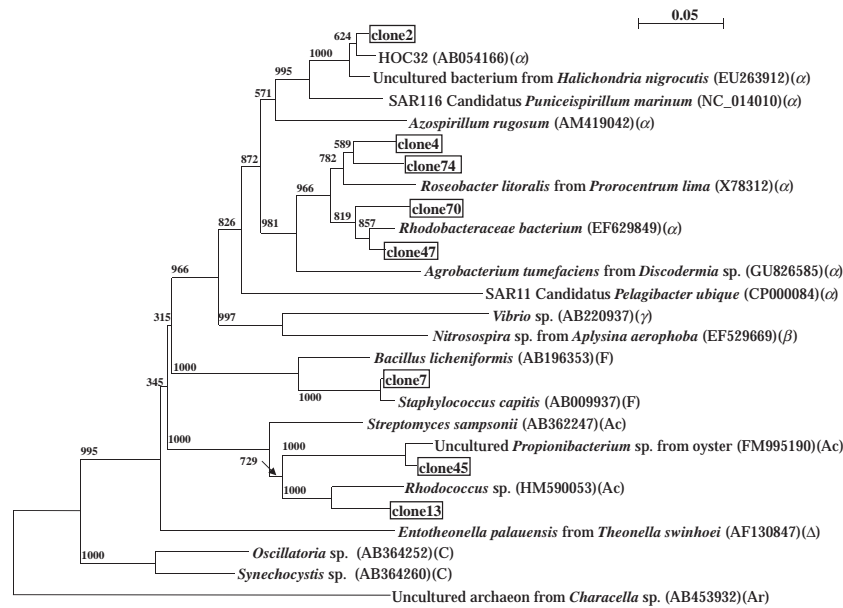


Fig. 3. Neighbor-Joining Tree for Bacterial 16S rRNA.

Bootstrap values calculated from 1,000 resamplings by neighbor-joining are shown at the various nodes. Clones derived from *H. okadai* are boxed. α , alphaproteobacteria; β , betaproteobacteria; γ , gammaproteobacteria; Δ , deltaproteobacteria; Ac, actinobacteria; F, firmicutes; C, cyanobacteria; Ar, archaea.

analysis revealed that Alphaproteobacteria are the overwhelming dominant population in the marine sponge *H. okadai*. Next, to assess the quality of the constructed library, bacteria-enriched metagenomic DNA was estimated by pyrosequencing of the metagenomic DNA, which yielded about 230,000 readings (50 Mb) with an average read length of 220 bases assembled into 17,069 contigs. These contigs were committed to the NCBI-nr database and assigned to either prokaryote (best BLASTX expectation value $\leq 10^{-5}$ to a prokaryotic entry) or eukaryote (best BLASTX expectation value $\leq 10^{-2}$ to a eukaryotic entry). Based on this analysis, at least 50.7% of the contigs in the metagenomic data set showed highest homology to genes that encode prokaryotic proteins. Very few contigs were homologous to eukaryotic proteins (0.02%), and the other contigs were considered not to be assignable. Further analysis revealed that Alphaproteobacteria was also the largest group in the metagenomic library (74.5%), followed by Actinobacteria (3.5%) and Cyanobacteria (3.3%) (Table 2). A further detailed analysis indicated that the Alphaproteobacteria category consisted mainly of uncultured Alphaproteobacteria, Rhodobacterales, Rhizobiales, and Rhodospirillales (Table 3). Rhizobiales are known to be symbionts of plants in general. This indicates that a combination of graded centrifugation and Q-PCR can be used to construct a bacterial-rich genomic library efficiently, and that the metagenomic library is rich in bacterial diversity.

Allocation of assembled contig sequences to microbial genomes

To identify the genes involved in the biosynthesis of natural products, the sequenced data sets were functionally annotated by COG category analysis based on a BLASTX search against the NCBI database, and 8,096 contigs (47.4%) were assigned to functional genes (Fig. 4). The most abundant proteins were associated with metabolism (51.7%), and the biosynthesis, trans-

Table 2. Prokaryotic Taxa Distribution in the Metagenomic DNA Based on BLAST Search against the Nr-Database

Taxon	%
Alphaproteobacteria	74.5
Betaproteobacteria	3.2
Gammaproteobacteria	6.9
Deltaproteobacteria	1.9
Zetaproteobacteria	0.1
Actinobacteria	3.5
Cyanobacteria	3.3
Planctomycetes	1.2
Firmicutes	1.0
Bacteroidetes	0.9
Chlorobi	0.5
Chloroflexi	0.3
Chlamydiae	0.2
Acidobacteria	0.2
Verrucomicrobia	0.2
Deinococci	0.1
Spirochaetes	0.1
Aquificae	0.1
Tenericutes	0.1
Incertaesedis	1.7

Table 3. Taxonomic Affiliation of Contigs of the Class Alphaproteobacteria

ORDER	%
Rhodobacterales	32.5
Unclassified alphaproteobacteria	27.8
Rhizobiales	19.3
Rhodospirillales	14.9
Sphingomonadales	2.7
Caulobacteriales	1.1
Rickettsiales	0.9
Parvularculales	0.7

port, and catabolism of secondary metabolites accounted for 1.8%. To understand better the biosynthetic pathways of natural products derived from symbiotic bacteria, we focused on secondary metabolism, and

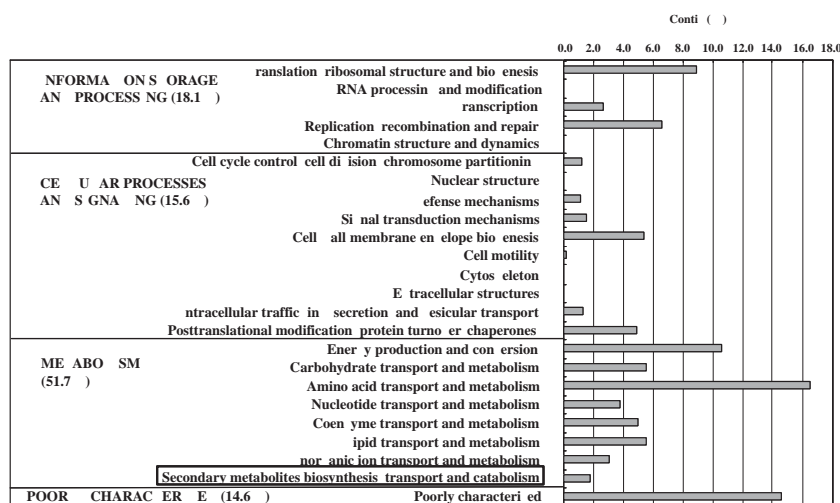


Fig. 4. Categorization of *Halichondria okadai* Metagenome Sequence Contigs According to Clusters of Orthologous Groups of Proteins (COG). The names of subcategories in the COG database are shown at the left, and the corresponding major categories are shown at the right. The numbers of readings assigned to the various major categories and their ratios are shown.

performed an advanced COG analysis using a Swiss-prot database. This revealed that 13 genes showed homology to non-ribosomal peptide synthase modules and related proteins (Table 4). These genes showed similarity to NRPS derived from Proteobacteria (30.8%), Actinobacteria (30.8%), Firmicutes (20.1%), and Cyanobacteria (15.4%).

Genomic library construction

The genomic DNA isolated by the CTAB method was larger than 25 kb, large enough to construct a fosmid library. DNA bands larger than 25 kb were recovered by subjecting the corresponding agarose slices to GFX PCR RNA and using a Gel Band Purification Kit, and the recovered genomic DNA was used to construct a fosmid library. The ligation mixture of digested genomic DNA and fosmid vector was packaged and transferred to EPI300 competent cells. As a result, 150,000 independent clones were obtained. We then confirmed that an appropriate length of genome had been inserted into these fosmids by electrophoresis of restriction enzyme-digested fosmids.

Discussion

Metagenomic analysis can be useful to understand the genetic background of the biosynthesis of natural products. Recently, it was reported that some PKS genes obtained from a metagenomic library of symbiotic bacteria were different from the genes derived from cultivable bacteria.¹⁹⁾ Thus, culture-independent analysis is preferable for the analysis of such symbionts. When one constructs a fosmid library, one must eliminate sponge cells as much as possible, because contamination by genomic DNA from the sponge is an obstacle in screening bacterial natural product-related genes from a metagenomic library. Hence, we established a method of constructing a bacteria-enriched metagenomic library from the marine sponge *H. okadai* by stepwise centrifugation and Q-PCR. Next, we investigated the quality of the metagenomic DNA to determine whether it was suitable for the construction of a metagenomic library and for the screening of natural

products. We accessed metagenomic DNA by dataset analysis, and found that the eukaryotic genome accounted for only 0.02% of total metagenomic DNA. Several genome studies have been performed on Porifera, a demosponge, and so the finding that few contigs of the metagenomic database show homology to genes derived from these projects suggests that the sponge's genome was largely removed from the metagenomic DNA.²⁹⁾ Alphaproteobacteria is the dominant group in the metagenomic library, followed by Actinobacteria and Cyanobacteria (Table 2). Various natural products have been isolated from Alphaproteobacteria, Actinobacteria, and Cyanobacteria,^{30–32)} and some might be the biogenic source of the non-ribosomal peptides.³²⁾ This suggests that the metagenomic DNA, from which the eukaryotic genome had clearly been eliminated, is a promising genetic resource for the discovery of natural products by functional screening, and that heterologous expression of metagenomic DNA using a multi-host expression system might be useful for exploiting sponges' symbiotic bacteria efficiently.

In this study, we identified 13 contigs that show homology to NRPS genes by dataset analysis (Table 4). For example, contig07303 showed homology with the gene that encodes surfactin synthase, and contig08398 showed homology with the gene that encodes saframycin Mx1 synthase.^{33,34)} To determine whether these contigs are involved in the biosynthesis of these compounds, heterologous expression of the genes is necessary. Screening of clones whose fosmid contains these contigs by colony hybridization using the contigs as probe might be an efficient approach to compiling sequencing data and to the construction of a whole cluster of NRPS genes. While various natural products have been isolated from *H. okadai*, non-ribosomal peptide has not yet been isolated from it. Hence the expression of whole clusters of NRPS-like genes in a suitable host should lead to the isolation of a non-ribosomal peptide from *H. okadai*.

Marine sponges harbor various natural products derived from secondary metabolites of symbiotic bacteria, and hence the diversity and specificity of symbiotic bacteria is an important issue in the screening

Table 4. Predicted Protein Coding Sequences in a Metagenomic Data Set Related to Secondary Metabolite Synthesis

Contig	Length (bp)	e-Value	Closest homolog (BLASTX)	Accession no.	Identity (%)
contig00219	224	6.00E-17	amino acid adenylation domain protein [<i>Paenibacillus curdlanolyticus</i> YK9]	ZP_07387014	57
contig04668	256	4.081E-14	amino acid adenylation domain protein [<i>Streptomyces flavogriseus</i> ATCC 33331]	ZP_05803229	54
contig06486	261	5.30E-06	amino acid adenylation domain-containing protein [<i>Salinispora tropica</i> CNB-440]	YP_00115962	46
contig06528	265	2.889E-12	amino acid adenylation [<i>Synechocystis</i> sp. WH 8501]	ZP_00517512	50
contig06841	260	5.00E-21	amino acid adenylation domain protein [<i>Lyngbya majuscula</i> 3L]	ZP_08431748	56
contig07303	252	2.00E-04	surfactin synthase subunit 1 [<i>Bacillus subtilis</i>]	P27206	47
contig07750	246	9.00E-10	non-ribosomal peptide synthetase [<i>Pseudomonas brassicacearum</i>]	YP_00435531	47
contig08398	276	8.00E-27	saframycin Mx1 synthetase B [<i>Myxococcus xanthus</i>]	AAC44128	70
contig08571	247	5.00E-08	peptide synthase [<i>Pseudomonas aeruginosa</i> PAb1]	ZP_06878666	55
contig08754	263	5.09E-17	non-ribosomal peptide synthetase, putative [<i>Roseobacter</i> sp. GAI101]	ZP_05099506	51
contig08780	242	6.00E-20	peptide synthetase [<i>Streptomyces</i> sp. Acta 2897]	AEA30273	62
contig08861	243	2.00E-11	hypothetical protein bcere0027_54520 [<i>Bacillus cereus</i> AH676]	ZP_04195022	51
contig11049	254	2.03E-13	putative non-ribosomal peptide synthase [<i>Bradyrhizobium</i> sp. BTAi1]	YP_00123724	50

of natural products. First, we compared the diversity of the bacterial community of *H. okadai* with those of other marine sponges.^{35–38} For sponges of the order Halichondrida, Gammaproteobacteria is the dominant bacteria in *Halichondria* sp., and Acidobacteria and Chloroflexi are the dominant groups in *Svenzea zaei*. For sponges of the order Haplosclerida, Gammaproteobacteria and Firmicutes are the dominant bacteria in *Haliclona simulans* and *Gelliodes carnosus* respectively. On the other hand, Alphaproteobacteria are the dominant bacteria in *H. panicea*, *Rhopaloeides odorabile*, and *Mycale laxissima*, of the orders Halichondrida, Dictyoceratida, and Poecilosclerida respectively.^{35,39,40} These results indicate that bacterial composition is highly varied in sponges, and that the dominance of alphaproteobacteria is not a rare characteristic.

We focused on the specificity of symbionts in the marine sponge *H. okadai*. Eighty-three clones of the 16S rRNA of *H. okadai* were analyzed by BLAST search of the NCBI database. This revealed that clone2 showed high homology to other uncultured alphaproteobacteria, HOC32 (98.2%) (AB054166), which had been cloned from *H. okadai*. Furthermore, this clone2 group is phylogenetically distant from the major marine bacteria, including SAR11, for example SAR116 (91.4%) (NC_014010).⁴¹ The fact that 1 certain bacteria were isolated from the sponge extracted separately suggested that these bacteria are sponge-specific. Indeed, it has been reported that the dominant alphaproteobacteria of *H. panicea* was a sponge-specific symbiont by sampling at different stations.³⁵ These results imply the specificity of alphaproteobacteria clone2. Furthermore, some sponge-phylum-specific symbionts have been detected by comparison of symbionts obtained from various marine sponges,⁴² but clone2 derived from *H. okadai* showed low homology to these sponge-phylum-specific alphaproteobacteria (JAWS23, JAWS8) (84.2% and 82.6%). This suggests that this symbiont of the marine sponge *H. okadai* is not a sponge-phylum-specific bacterium.

Recently, it was reported that some sponge symbionts may have co-evolved with their hosts.^{43,44} These allied sponges were isolated related species. Because the 5.8S rRNA of *H. okadai* showed high similarity to *H. panicea* (99.0%, AF062607) and sponge-specific clones had been isolated from *H. panicea*, we investigated sponge-order-specific bacteria by homology

search. We compared clone2 with the 16S rRNA clones derived from *H. panicea*, and found that the clone2 showed low homology to uncultured alphaproteobacteria in *H. panicea*, for example, HNS27 (Z88567), HNS35 (Z88568), and HNSM50 (Z88569) (86.0%, 69.8%, and 85.7%), the dominant alphaproteobacteria in *H. panicea*. This suggests that clone2 is not a sponge-order-specific bacterium.

Thus there are two methods of transmission of symbiotic bacteria in marine sponges. Usually, marine bacteria are either acquired from the surrounding sea water during filter-feeding by sponges or are transferred from parental sponges to their progeny through reproduction.⁴⁵ Sponge-species-specific symbionts are inherited by vertical transmission. Although *H. okadai*, *H. panicea*, and *H. japonica* all belong to the order Halichondrida and live in tidal pools in Japan, different natural products have been isolated from these three sponges. For example, Halichondrin B was not isolated from the latter two sponges. This can be explained by the conjecture that the symbiotic bacterium that produces natural products is sponge-species-specific. Indeed, the 16S rRNA clones derived from *H. panicea* did not show high homology to that of *H. okadai*. Hence a phylogenetic analysis and comparison of symbionts derived from *H. okadai*, *H. panicea*, and *H. japonica* sampled from the same location is necessary to determine the existence of sponge-species-specific symbionts and the relationship between these host sponges, their symbionts, and natural products. To determine this relationship, the metagenomic approach with heterologous expression and DNA analysis is effective.

In this study, we constructed a fosmid library from a marine sponge, *H. okadai*, for the first time. We eliminated the sponge genome from the recovered metagenomic DNA. A dataset analysis indicated that metagenomic DNA is a potential source for screening natural products. An analysis of bacterial diversity suggested that the metagenomic library was constructed by various bacteria, mainly Alphaproteobacteria, Actinobacteria, and Cyanobacteria. An analysis of orthologous proteins suggested that the library contains genes that are involved in non-ribosomal peptide synthesis. This analysis of the genetic profile of the metagenomic DNA should help in using uncultivable and cultivable bacteria as genomic sources in the screening of natural products.

Acknowledgments

This study was done mainly at Nagoya University and Keio University. We thank Professor Mamoru Sugita of Nagoya University and Professor Masaya Imoto of Keio University for their support. This study was supported in part by Grants-in-Aid for Creative Scientific Research (Grant no. 16GS0206, to D.U.) and Scientific Research (S) (21221009, to D.U.).

References

- 1) Uemura D, *Proc. Jpn. Acad. Ser. B, Phys. Biol. Sci.*, **86**, 190–201 (2010).
- 2) Uemura D, *Chem. Rec.*, **6**, 235–248 (2006).
- 3) Uemura D, Takahashi K, Yamamoto T, Katayama C, Tanaka J, Okumura Y, and Hirata Y, *J. Am. Chem. Soc.*, **107**, 4796–4798 (1985).
- 4) Hirata Y and Uemura D, *Pure Appl. Chem.*, **58**, 701–710 (1986).
- 5) Kuramoto M, Tong C, Yamada K, Chiba T, Hayashi Y, and Uemura D, *Tetrahedron Lett.*, **37**, 3867–3870 (1996).
- 6) Arimoto H, Hayakawa I, Kuramoto M, and Uemura D, *Tetrahedron Lett.*, **39**, 861–862 (1998).
- 7) Tsubosaka Y, Murata T, Yamada K, Uemura D, Hori M, and Ozaki H, *J. Pharmacol. Sci.*, **113**, 208–213 (2010).
- 8) Tachibana K, Scheuer P, Tsukitani Y, Kikuchi H, Engen D, Clardy J, Gopichand Y, and Schmitz F, *J. Am. Chem. Soc.*, **103**, 2469–2471 (1981).
- 9) Shigemori H, Bae AM, Yazawa K, Sasaki T, and Kobayashi J, *J. Org. Chem.*, **57**, 4317–4320 (1992).
- 10) Kigoshi H, Niwa H, Yamada K, Stout T, and Clardy J, *Tetrahedron Lett.*, **32**, 2427–2428 (1991).
- 11) Garson MJ, Zimmermann MP, Hoberg M, Larsen RM, Battershill CN, and Murphy PT, *Lipids*, **28**, 1011–1014 (1993).
- 12) Kennedy J, Marchesi JR, and Dobson AD, *Appl. Microbiol. Biotechnol.*, **75**, 11–20 (2007).
- 13) Bewley CA, Holland ND, and Faulkner DJ, *Experientia (Basel)*, **52**, 716–722 (1996).
- 14) Amann RI, Ludwig W, and Schleifer KH, *Microbiol. Rev.*, **59**, 143–169 (1995).
- 15) Torsvik V, Goksøyr J, and Daae FL, *Appl. Environ. Microbiol.*, **56**, 782–787 (1990).
- 16) Gillespie DE, Brady SF, Bettermann AD, Cianciotto NP, Liles MR, Rondon MR, Clardy J, Goodman RM, and Handelsman J, *Appl. Environ. Microbiol.*, **68**, 4301–4306 (2002).
- 17) Brady SF, Chao CJ, Handelsman J, and Clardy J, *Org. Lett.*, **3**, 1981–1984 (2001).
- 18) Piel J, Hui D, Wen G, Butzke D, Platzer M, Fusetani N, and Matsunaga S, *Proc. Natl. Acad. Sci. USA*, **46**, 16222–16227 (2004).
- 19) Kim TK and Fuerst JA, *Environ. Microbiol.*, **8**, 1460–1470 (2006).
- 20) Saitou N and Nei M, *Mol. Biol. Evol.*, **4**, 406–425 (1987).
- 21) Larkin MA, Blackshields G, Brown NP, Chenna R, McGettigan PA, McWilliam H, Valentin F, Wallace IM, Wilm A, Lopez R, Thompson JD, Gibson TJ, and Higgins DG, *Bioinformatics*, **23**, 2947–2948 (2007).
- 22) Kimura M, *J. Mol. Evol.*, **16**, 111–120 (1980).
- 23) Felsenstein J, *Evolution*, **39**, 783–791 (1985).
- 24) Tatusov RL, Koonin EV, and Lipman DJ, *Science*, **278**, 631–637 (1997).
- 25) Tatusov RL, Galperin MY, Natale DA, and Koonin EV, *Nucleic Acids Res.*, **28**, 33–36 (2000).
- 26) López GP, Brochier C, Moreira D, and Rodríguez VF, *Environ. Microbiol.*, **6**, 19–34 (2004).
- 27) Treusch AH, Kletzin A, Raddatz G, Ochsenreiter T, Quaiser A, Meurer G, Schuster SC, and Schleper C, *Environ. Microbiol.*, **6**, 970–980 (2004).
- 28) Feliciello I and Chinali G, *Anal. Biochem.*, **212**, 394–401 (1993).
- 29) Srivastava M, Simakov O, Chapman J, Fahey B, Gauthier ME, Mitros T, Richards GS, Conaco C, Dacre M, Hellsten U, Larroux C, Putnam NH, Stanke M, Adamska M, Darling A, Degnan SM, Oakley TH, Plachetzki DC, Zhai Y, Adamski M, Calcino A, Cummins SF, Goodstein DM, Harris C, Jackson DJ, Leys SP, Shu S, Woodcroft BJ, Vervoort M, Kosik KS, Manning G, Degnan BM, and Rokhsar DS, *Nature*, **466**, 720–726 (2010).
- 30) Li L, Deng W, Song J, Ding W, Zhao QF, Peng C, Song WW, Tang GL, and Liu W, *J. Bacteriol.*, **190**, 251–263 (2008).
- 31) Martens T, Gram L, Grossart HP, Kessler D, Müller R, Simon M, Wenzel SC, and Brinkhoff T, *Microb. Ecol.*, **54**, 31–42 (2007).
- 32) Dunlap WC, Battershill CN, Liptrot CH, Cobb RE, Bourne DG, Jaspars M, Long PF, and Newman DJ, *Methods*, **42**, 358–376 (2007).
- 33) Arima K, Kakinuma A, and Tamura G, *Biochem. Biophys. Res. Commun.*, **31**, 488–494 (1968).
- 34) Irschik H, Trowitzsch KW, Gerth K, Höfle G, and Reichenbach H, *J. Antibiot.*, **41**, 993–998 (1988).
- 35) Wichels A, Würtz S, Döpke H, Schütt C, and Gerdtts G, *FEMS Microbiol. Ecol.*, **56**, 102–118 (2006).
- 36) Lee ZY, He LM, Wu J, and Jiang Q, *J. Exp. Mar. Biol. Ecol.*, **329**, 75–85 (2006).
- 37) Lee OO, Chui PY, Wong YH, Pawlik JR, and Qian PY, *Appl. Environ. Microbiol.*, **75**, 6147–6156 (2009).
- 38) Li CQ, Liu WC, Zhu P, Yang JL, and Cheng KD, *Microb. Ecol.*, **62**, 800–812 (2011).
- 39) Webster NS and Hill RT, *Mar. Biol.*, **138**, 843–851 (2001).
- 40) Mohamed NM, Cicirelli EM, Kan J, Chen F, Fuqua C, and Hill RT, *Environ. Microbiol.*, **10**, 75–86 (2008).
- 41) Morris RM, Rappé MS, Cannon SA, Vergin KL, Siebold WA, Carlson CA, and Giovannoni SJ, *Nature*, **420**, 806–810 (2002).
- 42) Hentschel U, Hopke J, Horn M, Friedrich AB, Wagner M, Hacker J, and Moore BS, *Appl. Environ. Microbiol.*, **68**, 4431–4440 (2002).
- 43) Erpenbeck D, Breeuwer JAJ, van der Velde HC, and van Soest RWM, *Mar. Biol.*, **141**, 377–386 (2002).
- 44) Thacker RW and Starnes S, *Mar. Biol.*, **142**, 643–648 (2003).
- 45) Schmitt S, Angermeier H, Schiller R, Lindquist N, and Hentschel U, *Appl. Environ. Microbiol.*, **74**, 7694–7708 (2008).

Note

Isolation of 9-Hydroxy-10*E*,12*Z*-octadecadienoic Acid, an Inhibitor of Fat Accumulation from *Valeriana fauriei*

Keiji YUKI,¹ Mariko IKEDA,¹ Kenji MIYAMOTO,^{1,†} Osamu OHNO,²
Kaoru YAMADA,³ and Daisuke UEMURA^{3,†}

¹Department of Biosciences and Informatics, Keio University, 3-14-1 Hiyoshi, Yokohama 223-8522, Japan

²Department of Chemistry, Keio University, 3-14-1 Hiyoshi, Yokohama 223-8522, Japan

³Department of Chemistry, Kanagawa University, 2946 Tsuchiya, Hiratsuka 256-1293, Japan

Received January 6, 2012; Accepted February 21, 2012; Online Publication, June 7, 2012

[doi:10.1271/bbb.110994]

An EtOH extract of *Valeriana fauriei* was found to exhibit potent inhibition of fat accumulation against 3T3-L1 murine adipocytes. After performing several chromatographic steps, we successfully isolated the conjugated linoleic acid derivative, 9-hydroxy-10*E*,12*Z*-octadecadienoic acid (9-HODE). Synthesized 9-HODE and its analogs showed inhibitory activity against fat accumulation.

Key words: *Valeriana fauriei*; 3T3-L1 murine adipocytes; inhibitor; fat accumulation

Such lifestyle-related diseases as cancer, cardiovascular disease, hypertension, hyperlipidemia, and diabetes are rapidly growing epidemics in developed countries, and obesity is one of the causes.¹⁾ The Ministry of Health, Labor and Welfare in Japan has reported increasing obesity rate in the population. Although such approaches for anti-obesity as low-calorie foods have been proposed, we have focused on inhibitors of fat accumulation, because they could be applied to the development of anti-obesity drugs.

Our previous study screened the fat accumulation inhibitors from various sources. We found that the mushroom, *Coriolus versicolor*, and plant, *Valeriana fauriei*, potently inhibited fat accumulation against 3T3-L1 murine adipocytes. The highly *N*-methylated cyclic heptapeptide, (–)-ternatin, was successfully isolated from *C. versicolor* as a novel inhibitor of fat accumulation.^{2–4)} *V. fauriei* is a Chinese herbal medicine and is used to treat hysteroepilepsy and cardiac palpitations. These effects have been mediated by such terpenoid glycosides as kessoglycol diacetate and kessoglycol β -monoacetate from *V. fauriei*.^{5,6)} A novel iridoid glycoside and a sesquiterpenoid have been isolated from *V. fauriei* and showed NGF-potentiating activity.⁷⁾ However, there are no reports on the inhibition of fat accumulation. We report in this study the isolation and determination of fat accumulation inhibitors from *V. fauriei*.

To isolate the fat accumulation inhibitors, we used the assay system with 3T3-L1 murine adipocytes as described previously.²⁾ LabAssay™ Triglyceride (Wako

Pure Chemical Industries) was used to determine the amount of triglyceride in the 3T3-L1 cells, and Cell Counting Kit-8 (Dojindo Laboratories) was used to determine the cell viability. Both the fat accumulation (FA) and cell viability (CV) rates were determined by dividing the absorbance value of a sample by the absorbance of the control which had been exclusively treated with a vehicle. An FA rate of 50% and CV rate of 50% are respectively presented as the EC₅₀ and IC₅₀ values.

The rhizomes and roots of *V. fauriei* (2 kg) purchased from Tochimoto Tenkaido Co. (Japan) were extracted with 80% aqueous ethanol over 2 weeks. The concentrated extract (125 g) was partitioned between ethyl acetate and water, and the ethyl acetate layer was partitioned between 90% aqueous methanol and hexane. Since the 90% aqueous methanol layer showed inhibitory effects on fat accumulation (66% FA rate and 93% CV rate at a 100 μ g/mL conc.), the methanol fraction was separated by ODS column chromatography with stepwise elution by 70% aqueous MeOH to MeOH. The 80% aqueous MeOH fraction (73% FA rate and 93% CV rate at a 50 μ g/mL conc.) was separated by silica-gel column chromatography with stepwise elution by CHCl₃/MeOH (19/1, 9/1, and 2/1). The 9/1 CHCl₃/MeOH fraction (68% FA rate and 94% CV rate at a 50 μ g/mL conc.) showed four spots on the TLC plate [R_f = 0.63, 0.70, 0.73, and 0.80 (CHCl₃/MeOH = 9 : 1)]. These spots were separated by preparative TLC (CHCl₃/MeOH = 9 : 1) to afford an active compound (0.6 mg; 50% FA rate and 81% CV rate at a 20 μ g/mL conc.) with an R_f value of 0.70. To determine the structure, this active compound was analyzed by ¹H-NMR (300 MHz, CDCl₃), using high-resolution electrospray ionization mass spectrometry (HR-ESIMS) with a Waters LCT Premier XE and ESIMS with a Bruker Esquire 3000 Plus in the negative ESI mode. Characteristic ¹H-NMR peaks of the active compound are shown in the experimental section. Its molecular formula was determined to be C₁₈H₃₂O₃ by HR-ESIMS (m/z 295.2262 [M – H][–], as calculated for C₁₈H₃₁O₃, 295.2273). The ESI mass spectrum showed major peaks at m/z 295 ([M – H][–]), and an MS/MS analysis gave

[†] To whom correspondence should be addressed. Kenji MIYAMOTO, Fax: +81-45-566-1783; E-mail: kmiyamoto@bio.keio.ac.jp; Daisuke UEMURA, Fax: +81-463-58-9684; E-mail: uemura@kanagawa-u.ac.jp

Abbreviations: NGF, nerve growth factor; PPAR γ , peroxisome proliferator-activated receptor γ ; GPCR, G protein-coupled receptor; FA, fat accumulation; CV, cell viability

ion fragments at m/z 277 ($[(M - H_2O) - H]^-$) and 171 ($[(M - CH_3(CH_2)_4CHCHCH_2) - H]^-$). Based on these spectral data, we identified the active compound as the known but unusual fatty acid, 9-hydroxy-10*E*,12*Z*-octadecadienoic acid (9-HODE, **3**) (Fig. 1). The 1H -NMR and MS/MS peaks assigned to the active compound were in good agreement with those reported previously for 9-HODE.^{8,9} The enantiomeric excess of isolated 9-HODE was determined by an HPLC analysis after converting to the corresponding methyl ester.¹⁰ The results indicate that the absolute configuration of isolated 9-HODE was the (*R*)-enantiomer (>95% e.e.).

We next synthesized 9-HODE and its analogs by using a reported method.⁹ Methyl linoleate (**1**) was added to a mixture of SeO_2 and dichloromethane in an argon atmosphere. The reaction mixture was stirred for 24 h at room temperature, before a 10% NaCl solution was added and the mixture extracted with dichloromethane. The extract contained the 9-HODE methyl ester (**4**) and 13-hydroxy-9*Z*,11*E*-octadecadienoic acid (13-HODE) methyl ester (**6**). These compounds were purified by preparative HPLC and subsequent hydrolysis to afford racemic 9-HODE (**3**) and racemic 13-HODE (**5**), and their inhibitory activity against fat accumulation was evaluated. Figure 2A shows that synthesized 9-HODE significantly inhibited fat accumulation in 3T3-L1 cells ($EC_{50} = 20 \mu g/mL$, $IC_{50} = 29 \mu g/mL$). These results are relatively higher than those for (*R*)-9-HODE isolated from *V. fauriei* ($EC_{50} = 40 \mu g/mL$, $IC_{50} = 40 \mu g/mL$). The results indicate the stronger

activity of the (*S*)-enantiomer than that of the (*R*)-acid. Interestingly, 13-HODE showed slightly greater activity ($EC_{50} = 17 \mu g/mL$, $IC_{50} = 41 \mu g/mL$) than that of 9-HODE (Fig. 2B). The methyl esters (**4** and **6**) were also subjected to these assays, but indicated no inhibitory activity (data not shown). These results show that the structure of a conjugated diene with a hydroxyl group at the allylic position and a carboxyl group may be important for the biological activities of 9-HODE. Although the inhibitory activity of 9-HODE and 13-HODE against fat accumulation has not been previously reported, it has been reported that conjugated linoleic acid (CLA, **2**) had such biological activities such as anti-tumor and hypocholesterolemic effects.¹¹ Interestingly, we found that CLA (**2**) had weak inhibitory activity against fat accumulation ($EC_{50} = 316 \mu g/mL$, $IC_{50} = 375 \mu g/mL$) when compared with 9-HODE and 13-HODE.

It has been reported that 9-HODE and 13-HODE showed antitumoral activities.⁹ The methyl esters (**4** and **6**) had very weak activity compared with the corresponding acids. Intriguingly, 9-HODE and 13-HODE showed more potent inhibition of fat accumulation and antitumor activity than CLA, although these activities were lost by methyl esterification.

It is crucial for future applications to elucidate the mechanisms for the inhibitory activities of 9-HODE against fat accumulation. 9-HODE has been reported to act as a ligand of both $PPAR\gamma$ ¹² and G protein-coupled receptor G2A.^{13,14} $PPAR\gamma$ is a transcriptional factor belonging to the nuclear receptor super-family and is known to promote the differentiation of adipocytes. Experiments with the heterozygous mouse,¹⁵ inhibitors of $PPAR\gamma$,¹⁶ and Pro12Ala SNP in humans¹⁷ have shown a suppression of obesity by incremental serum leptin levels.¹⁸ However, it has been reported that $PPAR\gamma$ activated by troglitazone, a potent agonist, promoted the differentiation of small adipocytes and the apoptosis of large adipocytes.¹⁹ Troglitazone thus led to the miniaturization of adipocytes. It is likely that 9-HODE may activate $PPAR\gamma$ and miniaturize adipocytes in the same way as troglitazone, leading to decreased fat accumulation. G2A is a stress-inducible G protein-coupled receptor (GPCR) which is known to have such biological functions as those involving inflammatory response, proliferation, and differentiation. It has been reported that 9-HODE acted as a ligand of G2A and released a variety of cytokines.^{13,14} However, intra-

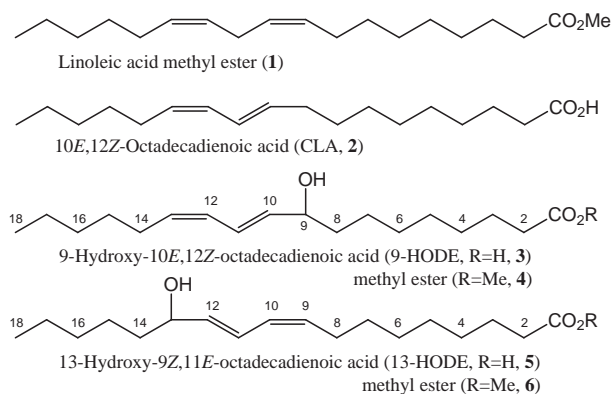


Fig. 1. Structures of Linoleic Acid Methyl Ester **1**, Conjugated Linoleic Acid **2**, Allylic Hydroxylated Derivatives **3** and **5**, and Corresponding Methyl Esters **4** and **6**.

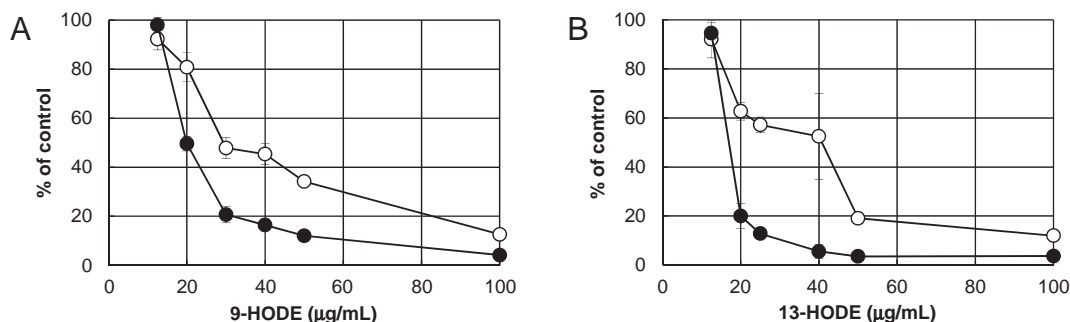


Fig. 2. Inhibitory Effects of Fat Accumulation on 3T3-L1 Murine Adipocytes.

3T3-L1 cells were treated with 9-HODE (A), 13-HODE (B), and the vehicle (control) for 1 week during differentiation. The fat accumulation (filled circles) and cell viability (unfilled circles) were then determined. Data are presented as the mean and standard deviation (SD) of four tests and are shown as a percentage of the control value.

cellular signaling mediated by G2A has not been fully elucidated. It is possible that the cytokines released by G2A played a role in the inhibition of fat accumulation after 9-HODE bound to G2A.

We successfully isolated 9-HODE in this study as an inhibitor of fat accumulation and found that 13-HODE had the same effect. The hydroxylated derivatives of conjugated linoleic acid may be potent inhibitors of fat accumulation, making it important to evaluate the activity of other analogs of 9-HODE.

Experimental

General data. ¹H-NMR spectra were recorded with a Jeol JNM AL300 FT NMR spectrometer. 9-HODE (**3**). ¹H-NMR (300 MHz, CDCl₃) δ: 0.89 (3H, t, *J* = 6.8), 1.21–1.59 (18H, m), 2.18 (2H, m), 2.35 (2H, t, *J* = 7.5), 4.15 (1H, m), 5.44 (1H, m), 5.66 (1H, dd, *J* = 6.8, 15.2), 5.97 (1H, dd, *J* = 11.2, 11.2), 6.49 (1H, dd, *J* = 11.2, 15.2).

References

- Mann CC, *Science*, **307**, 1716–1717 (2005).
- Shimokawa K, Mashima I, Asai A, Yamada K, Kita M, and Uemura D, *Tetrahedron Lett.*, **47**, 4445–4448 (2006).
- Shimokawa K, Yamada K, Kita M, and Uemura D, *Bioorg. Med. Chem. Lett.*, **17**, 4447–4449 (2007).
- Ito M, Ito J, Kitazawa H, Shimamura K, Fukami T, Tokita S, Shimokawa K, Yamada K, Kanatani A, and Uemura D, *Peptides*, **30**, 1074–1081 (2009).
- Sashida Y and Yamasaki K, “Syoyyakugaku” (in Japanese), Nankodo, Tokyo, pp. 258–260 (1997).
- Konoshima M, Sawada T, and Hata K, “Syoyyakugaku” (in Japanese), Asakura Publishing, Tokyo, pp. 234–236 (1978).
- Guo Y, Xu J, Li Y, Watanabe R, Oshima Y, Yamakuni T, and Ohizumi Y, *Chem. Pharm. Bull.*, **54**, 123–125 (2006).
- Henry DY, Gueritte-Voegelein F, Insel PA, Ferry N, Bouguet J, Potier P, Sevenet T, and Hanoune J, *Eur. J. Biochem.*, **170**, 389–394 (1987).
- Li Z, Tran VH, Duke RK, Ng MCH, Yang D, and Duke CC, *Chem. Phys. Lipids*, **158**, 39–45 (2009).
- Hübke H, Garbe L-A, and Tressl R, *Agric. Food Chem.*, **53**, 1556–1562 (2005).
- Hara K, “Kyoyakurinorusannoseikagakutoouyou” (in Japanese), Saiwai Shobo, Tokyo, pp. 14–144 (2000).
- Schild RL, Schaiff WT, Carlson MG, Cronbach EJ, Nelson DM, and Sadovsky Y, *J. Clin. Endocrinol. Metab.*, **87**, 1105–1110 (2002).
- Obinata H, Hattori T, Nakane S, Tatei K, and Izumi T, *J. Biol. Chem.*, **280**, 40676–40683 (2005).
- Ogawa A, Obinata H, Hattori T, Kishi M, Tatei K, Ishikawa O, and Izumi T, *J. Pharmacol. Exp. Ther.*, **332**, 469–478 (2010).
- Kubota N, Terauchi Y, Miki H, Tamemoto H, Yamauchi T, Komeda K, Satoh S, Nakano R, Ishii C, Sugiyama T, Eto K, Tsubamoto Y, Okuno A, Murakami K, Sekihara H, Hasegawa G, Naito M, Toyoshima Y, Tanaka S, Shiota K, Kitamura T, Fujita T, Ezaki O, Aizawa S, Nagai R, Tobe K, Kimura S, and Kadowaki T, *Mol. Cell*, **4**, 597–609 (1999).
- Yamauchi T, Waki H, Kamon J, Murakami K, Motojima K, Komeda K, Miki H, Kubota N, Terauchi Y, Tsuchida A, Kasaoka N, Yamauchi N, Ide T, Hori W, Kato S, Fukayama M, Akanuma Y, Ezaki O, Itai A, Nagai R, Kimura S, Tobe K, Kagechika H, Shudo K, and Kadowaki T, *J. Clin. Invest.*, **108**, 1001–1013 (2001).
- Hara K, Okada T, Tobe K, Yasuda K, Mori Y, Kadowaki H, Hagura R, Akanuma Y, Kimura S, Ito C, and Kadowaki T, *Biochem. Biophys. Res. Commun.*, **271**, 212–216 (2000).
- Kamon J, Yamauchi T, Terauchi Y, Kubota N, and Kadowaki T, *Folia Pharmacol. Jpn.*, **122**, 294–300 (2003).
- Okuno A, Tamemoto H, Tobe K, Ueki K, Mori Y, Iwamoto K, Umeson K, Akanuma Y, Fujiwara T, Horikoshi H, Yazaki Y, and Kadowaki T, *J. Clin. Invest.*, **101**, 1354–1361 (1998).

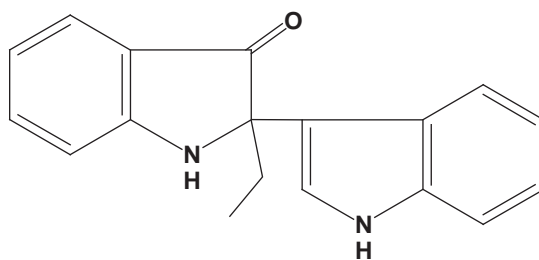
Isolation and Structure of a Novel Biindole Pigment Substituted with an Ethyl Group from a Metagenomic Library Derived from the Marine Sponge *Halichondria okadai*

Takahiro Abe,*¹ Akira Kukita,¹ Kiyotaka Akiyama,² Takayuki Naito,² and Daisuke Uemura*¹

¹Department of Chemistry, Faculty of Science, Kanagawa University, 2946 Tsuchiya, Hiratsuka, Kanagawa 259-1293

²Molecular Neuroscience Unit, Okinawa Institute of Science and Technology, 12-22 Suzaki, Uruma, Okinawa 904-2234

(Received April 5, 2012; CL-120299; E-mail: abtaka@kanagawa-u.ac.jp)



halichrome A

REPRINTED FROM

**Chemistry
Letters**

Vol.41 No.7 2012 p.728–729

CMLTAG
July 5, 2012

The Chemical Society of Japan

Published on the web June 30, 2012; doi:10.1246/cl.2012.728

Isolation and Structure of a Novel Biindole Pigment Substituted with an Ethyl Group from a Metagenomic Library Derived from the Marine Sponge *Halichondria okadai*

Takahiro Abe,^{*1} Akira Kukita,¹ Kiyotaka Akiyama,² Takayuki Naito,² and Daisuke Uemura^{*1}

¹Department of Chemistry, Faculty of Science, Kanagawa University, 2946 Tsuchiya, Hiratsuka, Kanagawa 259-1293

²Molecular Neuroscience Unit, Okinawa Institute of Science and Technology, 12-22 Suzaki, Uruma, Okinawa 904-2234

(Received April 5, 2012; CL-120299; E-mail: abtaka@kanagawa-u.ac.jp)

We screened a colored clone from a metagenomic library derived from the marine sponge *Halichondria okadai*. We isolated a yellow pigment, halichrome A (**1**), which was structurally elucidated to be a biindole, exhibited cytotoxicity against B16 melanoma cells and was substituted with an ethyl group. To the best of our knowledge, this is the first report of the isolation of a novel compound from a metagenomic library derived from a marine sponge.

Many structurally unique compounds with significant biological activity have been isolated from various marine invertebrates.¹ In particular, sponges, members of the porifera, are rich sources of many natural products. Recent research suggests that marine sponges harbor various microbial symbionts and that many bioactive compounds in sponges are produced by these symbionts.² Although microorganisms have potential as sources of bioactive compounds, only a small proportion of bacteria have been isolated from the environment.³ Hence to use symbiotic bacteria efficiently as sources of natural products, a metagenomic approach is appropriate. Recently, several natural products have been isolated using metagenomic libraries derived from soil.⁴ These metagenomic libraries were used directly as sources of natural products by screening of clones that produce bioactive compounds by heterologous expression of metagenomic DNA. We previously constructed a metagenomic library from the marine sponge *Halichondria okadai*.⁵ In this study, we screened for colored clones and found a novel compound halichrome A (**1**) (Chart 1).

A colored clone was screened for the production of pigment on Luria–Bertani (LB) agar plates and grown in a liquid-shaker culture. This culture was extracted with EtOAc and chloroform. The extract was concentrated and partitioned between EtOAc and H₂O. The EtOAc extract was subjected to fractionation with column chromatography (silica gel, toluene–EtOAc; ODS silica

gel, EtOH–H₂O) and reversed-phase HPLC (Develosil ODS-UG-5, MeOH–H₂O; YMC-pack AG-323, acetonitrile–H₂O) to give halichrome A (**1**). The cytotoxicity of halichrome A (**1**) against B16 mouse melanoma cells was determined using the MTT method.⁶ This compound showed cytotoxicity with an IC₅₀ value of 30.9 μg mL⁻¹ after 4 days.

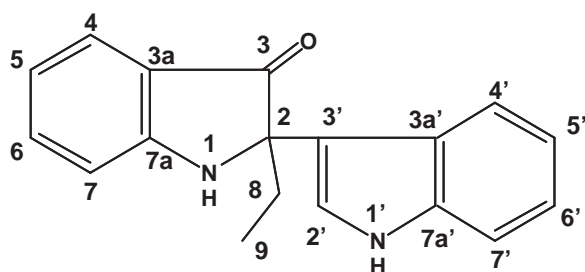
Halichrome A (**1**) was isolated as a yellow pigment soluble in both methanol and chloroform. The UV–vis absorption maxima at 402 nm with a slight inflection at shorter wavelengths indicate the presence of an indole chromophore.⁷ The molecular formula of **1** was determined to be C₁₈H₁₆N₂O by HR-ESIMS (*m/z* 299.1160, [M + Na]⁺, Δ + 0.4 mmu). The NMR data for **1** are summarized in Table 1. The ¹H NMR spectrum of **1** in chloroform-*d* showed the presence of two aromatic ring ABCD spin systems (δ 7.65, 6.85, 7.49, 6.92, and 7.50, 7.02, 7.15, 7.34), one doublet aromatic proton (δ 7.22), one methylene (δ 2.30), one methyl group (δ 0.91), and two indole NH signals (δ 5.02 and 8.11). In the ¹³C NMR spectrum, 18 carbon signals were observed, including one carbonyl carbon (δ 201.2), one methyl carbon (δ 6.1), one methylene carbon (δ 28.5), one quaternary carbon (δ 67.8), and 14 olefinic carbons (δ 159.0, 135.5, 135.0, 123.3, 123.1, 120.6, 120.5, 119.2, 118.2, 118.1, 117.1, 113.3, 110.5, and 109.6). The 9 olefinic carbon signals

Table 1. ¹³C NMR and ¹H NMR data for **1**^{a,b,c}

Position	δC	δH (mult., <i>J</i> in Hz)	HMBC (H to C)
1		5.02 (s)	2, 3, 3a, 8
2	67.8		
3	201.2		
3a	119.2		
4	123.1	7.65 (d, 7.7)	3, 7a
5	117.1	6.85 (dd, 7.2, 7.7)	3a
6	135.5	7.49 (dd, 7.2, 8.5)	7a
7	110.5	6.92 (d, 8.5)	3a
7a	159.0		
8	28.5	2.30 (m)	2, 3, 3'
9	6.1	0.91 (t, 7.3)	8
1'		8.11 (brs)	3a'
2'	120.6	7.22 (d, 2.4)	3', 3a', 7a'
3'	113.3		
3a'	123.3		
4'	118.2	7.50 (d, 8.0)	3', 7a'
5'	118.1	7.02 (dd, 8.0, 7.3)	3a'
6'	120.5	7.15 (dd, 8.0, 7.3)	7a'
7'	109.6	7.34 (d, 8.0)	3a'
7a'	135.0		

^aSolvent: CDCl₃. ^b¹H NMR (500 MHz), ¹³C NMR (125 MHz).

^cRecorded at 298 K.



halichrome A (**1**)

Chart 1.

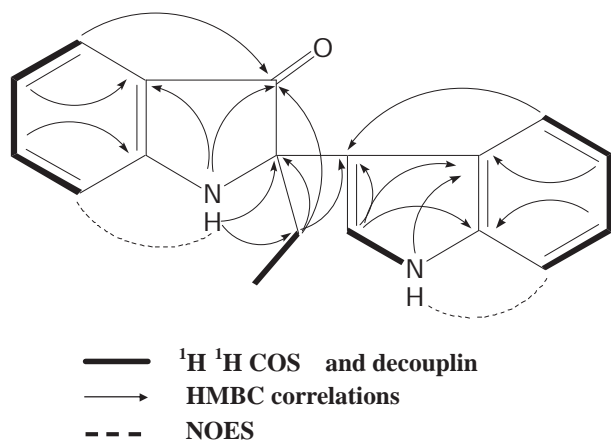


Figure 1. Selected 2D NMR^{a,b} correlations for halichrome A (**1**). ^aSolvent: CDCl₃. ^bRecorded at 298 K.

(δ 135.5, 123.1, 120.6, 120.5, 118.2, 118.1, 117.1, 110.5, and 109.6) were assigned to the methines, based on the results of an HMQC experiment. The ^1H - ^1H COSY spectrum and a decoupling experiment revealed the partial structures C4–C5–C6–C7, C4'–C5'–C6'–C7', and C8–C9, as shown in Figure 1. First, HMBC correlations at H5/C3a, H6/C7a suggested the connectivity of C3a–C4, C7a–C7, respectively. Then, the assignment of C3a and C7a were established by the similarity in the ^{13}C NMR when compared to those of ketoindole moiety of Cephalinone B.⁸ The correlations H1/C2, H1/C3, and H1/C3a in the HMBC spectrum suggested a ketoindole moiety. Furthermore, based on the HMBC correlations at H4/C3 and the NOESY correlations between H1 and H7, the ketoindole moiety should be located between N1 and C7a, as shown in Figure 1. Next, the HMBC correlations at H5'/C3a' and H6'/C7a' suggested the connectivity of C3a'–C4', and C7a'–C7', respectively. Then, the assignment of C3a' and C7a' were established by the similarity in the ^{13}C NMR when compared to those of indole moiety of Arcyriarubin B 6-O-sulfate.⁹ The decoupling of H1' and H2', and HMBC correlations at H2'/C3', H2'/C3a', H2'/C7a', and H1'/C3a' suggested an indole moiety. Furthermore, based on the HMBC correlations at H4'/C3' and the NOESY correlations between H1' and H7', the indole moiety should be located between N1' and C7a', as shown in Figure 1. Thus, these analyses showed two indole moieties and one ethyl group, and the connectivity between these partial structures was clarified by HMBC as follows. The HMBC correlations at H8/C2, H8/C3, and H1/C8 determined that the ethyl group was attached to a C2 quaternary carbon. And the HMBC correlations at H8/C3' suggest that a N1–C7a portion was connected to an N1'–C7a' portion at C2 and C3'. Consequently, the entire carbon chain was assembled and the gross structure of halichrome A (**1**) was determined to be as shown in Figure 1. The specific rotation of **1** is observed to be -0.9 (c 0.03, MeOH), and then determination of the absolute configuration at C2 is under investigation.

Many biosynthetic pathways of bacterial pigments have been investigated by a metagenomic approach. Recently, some clones that produce heterologously indigo, indirubin, and violacein were isolated from soil-derived metagenomic libraries and full or partial sequences of these gene clusters were

analyzed.^{4b,7b,10} In this study we isolated a clone that produce halichrome A. Hence sequencing of the gene clusters is in progress and analysis of the genetic information of this clone would improve the study of the open reading frames, responsible for the halichrome A biosynthesis.

In summary, halichrome A (**1**) was isolated from a metagenomic library derived from the marine sponge *H. okadae*. The gross structure of halichrome A (**1**) was revealed to be biindole substituted with an ethyl group based on 2D NMR spectra. Halichrome A (**1**) exhibits weak cytotoxicity against B16 mouse melanoma cells with an IC₅₀ value of 30.9 $\mu\text{g mL}^{-1}$. To date, some natural products have been isolated by a metagenomic approach. Most of these natural products originate from soil, marine sediment, and no example from a marine sponge has been reported. To the best of our knowledge, this is the first report of heterologous expression of a novel natural product from a metagenomic library derived from a marine sponge. These results indicate the potential of metagenomic libraries derived from marine sponges as a genetic and chemical source.

We thank Professor Kazuhito Inoue and Professor Yuko Nishimoto of Kanagawa University for their support. This study was supported in part by Grants-in-Aid for Creative Scientific Research (Grant No. 16GS0206, to D.U.) and Scientific Research (S) (No. 21221009, to D.U.).

References and Notes

- a) D. Uemura, *Proc. Jpn. Acad., Ser. B* **2010**, *86*, 190. b) D. Uemura, *Chem. Rec.* **2006**, *6*, 235.
- C. A. Bewley, N. D. Holland, D. J. Faulkner, *Cell. Mol. Life Sci.* **1996**, *52*, 716.
- a) R. I. Amann, W. Ludwig, K. H. Schleifer, *Microbiol. Rev.* **1995**, *59*, 143. b) V. Torsvik, J. Goksøyr, F. L. Daae, *Appl. Environ. Microbiol.* **1990**, *56*, 782.
- a) D. E. Gillespie, S. F. Brady, A. D. Bettermann, N. P. Cianciotto, M. R. Liles, M. R. Rondon, J. Clardy, R. M. Goodman, J. Handelsman, *Appl. Environ. Microbiol.* **2002**, *68*, 4301. b) S. F. Brady, C. J. Chao, J. Handelsman, J. Clardy, *Org. Lett.* **2001**, *3*, 1981.
- T. Abe, F. P. Sahin, K. Akiyama, T. Naito, M. Kishigami, K. Miyamoto, Y. Sakakibara, D. Uemura, *Biosci., Biotechnol., Biochem.* **2012**, *76*, 633.
- T. Mosmann, *J. Immunol. Methods* **1983**, *65*, 55.
- a) J. S. de Melo, A. P. Moura, M. J. Melo, *J. Phys. Chem. A* **2004**, *108*, 6975. b) H. K. Lim, E. J. Chung, J.-C. Kim, G. J. Choi, K. S. Jang, Y. R. Chung, K. Y. Cho, S.-W. Lee, *Appl. Environ. Microbiol.* **2005**, *71*, 7768. c) Physical properties of UV-vis absorption of **1** (in MeOH): λ/nm ($\epsilon/\text{M}^{-1}\text{cm}^{-1}$) 220 (29000), 258 (11000), and 402 nm (2000).
- P.-L. Wu, Y.-L. Hsu, C.-W. Jao, *J. Nat. Prod.* **2006**, *69*, 1467.
- K. Kamata, T. Suetsugu, Y. Yamamoto, M. Hayashi, K. Komiyama, M. Ishibashi, *J. Nat. Prod.* **2006**, *69*, 1252.
- a) I. A. MacNeil, C. L. Tiong, C. Minor, P. R. August, T. H. Grossman, K. A. Loiacono, B. A. Lynch, T. Phillips, S. Narula, R. Sundaramoorthi, A. Tyler, T. Aldredge, H. Long, M. Gilman, D. Holt, M. S. Osburne, *J. Mol. Microbiol. Biotechnol.* **2001**, *3*, 301. b) C. Guan, J. Ju, B. R. Borlee, L. L. Williamson, B. Shen, K. F. Raffa, J. Handelsman, *Appl. Environ. Microbiol.* **2007**, *73*, 3669.



Stereoselective synthesis of the C94–C104 fragment of symbiodinolide

Hiroyoshi Takamura^{a,*}, Kosuke Tsuda^a, Yohei Kawakubo^a, Isao Kadota^{a,*}, Daisuke Uemura^b

^a Department of Chemistry, Graduate School of Natural Science and Technology, Okayama University, 3-1-1 Tsushimanaka, Kita-ku, Okayama 700-8530, Japan

^b Department of Chemistry, Faculty of Science, Kanagawa University, 2946 Tsuchiya, Hiratsuka 259-1293, Japan

ARTICLE INFO

Article history:

Received 19 April 2012

Revised 28 May 2012

Accepted 1 June 2012

Available online 13 June 2012

Keywords:

Polyol marine natural product

Symbiodinolide

Achmatowicz rearrangement

Dithiane addition

ABSTRACT

Stereoselective synthesis of the C94–C104 fragment of symbiodinolide which is a polyol marine natural product with a molecular weight of 2860 has been accomplished. The synthetic route features Achmatowicz rearrangement and RuO₄-catalyzed dihydroxylation for the construction of the tetrahydropyran moiety and the dithiane addition to the aldehyde for the introduction of the side chain.

© 2012 Elsevier Ltd. All rights reserved.

Symbiodinolide (**1**, Fig. 1) is a polyol marine natural product isolated from dinoflagellate *Symbiodinium* sp.¹ This molecule exhibits voltage-dependent N-type Ca²⁺ channel-opening activity at 7 nM and COX-1 inhibition activity at 2 μM. The planar structure of **1** was elucidated by the detailed 2D NMR analysis. However, the huge and complex molecular structure of **1** featuring a molecular weight of 2860 and the presence of 61 chiral centers has hampered the complete stereochemical determination. Therefore, we are now performing the chemical degradation of the natural product^{1,2} and chemical synthesis of the fragments³ on **1** toward the complete stereostructural elucidation. With regard to the C91–C99 carbon-chain moiety, the stereochemical assignment was executed on the basis of ³J_{H,H} analysis and NOE correlations.¹ Previously, we synthesized the C79–C96 fragment by using spiroacetalization and Kotsuki coupling as the key transformations.^{3a} Herein, as a part of our synthetic and structural studies of **1**, we report the stereoselective synthetic route to the C94–C104 fragment.

Our retrosynthetic analysis of the C94–C104 fragment **2** is outlined in Scheme 1. We envisaged that the carbon-framework of **2** could be constructed through the coupling between dithiane **3** and aldehyde **4**. The vicinal oxygen-functionalized moiety at the C101 and C102 positions could be stereoselectively introduced by dihydroxylation of enone **5**. The carbon-skeleton of the methyl acetal **5** could be constructed via Achmatowicz rearrangement⁴ of optically pure alcohol **6**, which could be prepared from commercially available furfuryl alcohol.

Stereoselective construction of the tetrahydropyran part is described in Scheme 2. Treatment of furfuryl alcohol with *t*-butyl-

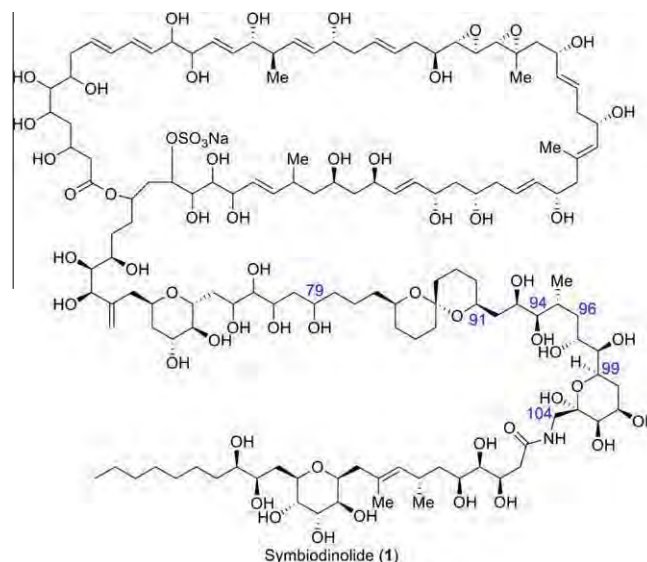
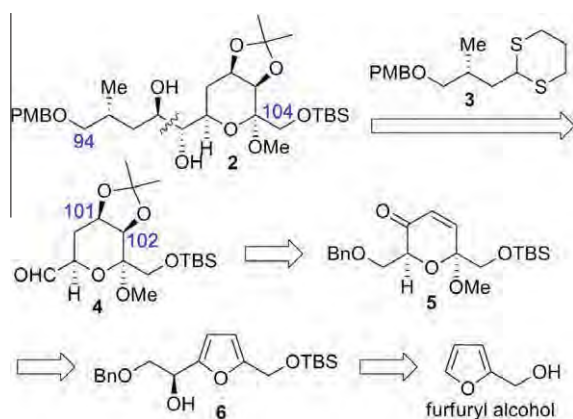


Figure 1. Structure of symbiodinolide (**1**).

dimethylsilyl chloride (TBSCl)/imidazole gave TBS ether **7** in 96% yield.⁵ Regioselective lithiation of the furan **7** with *n*-BuLi followed by the addition of 2-benzyloxy acetaldehyde **8**⁶ provided racemic alcohol **9**. Albright–Goldman oxidation⁷ of **9** and subsequent asymmetric transfer hydrogenation of the resulting furfuryl ketone with HCO₂H/Et₃N in the presence of (*S,S*)-Noyori catalyst **10** (2 mol %)⁸ afforded the chiral alcohol **6** as a single stereoisomer, as judged by the 400 MHz ¹H NMR spectra of the corresponding MTPA esters.

* Corresponding authors. Tel.: +81 86 251 7839; fax: +81 86 251 7836 (H.T.).

E-mail address: takamura@cc.okayama-u.ac.jp (H. Takamura).



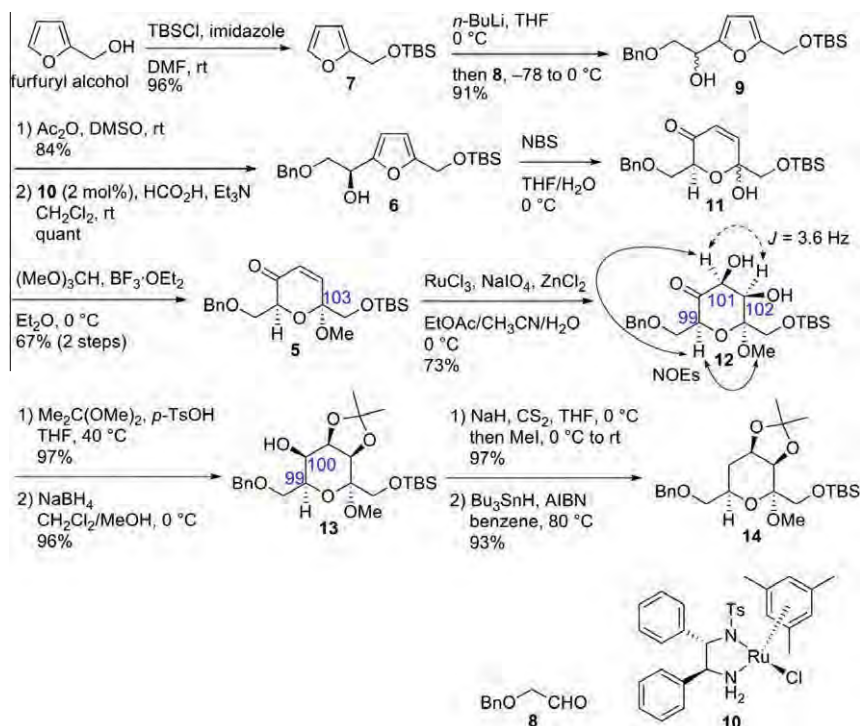
Scheme 1. Retrosynthetic analysis of the C94–C104 fragment **2**.

The absolute configuration of the resulting asymmetric center was confirmed by the modified Mosher method.⁹ Exposure of the alcohol **6** to the Achmatowicz conditions⁴ (NBS in THF/H₂O) yielded the desired rearrangement product **11** as a 1:1 diastereomeric mixture, which was unstable, therefore, treated immediately with $(\text{MeO})_3\text{CH}$ in the presence of $\text{BF}_3 \cdot \text{OEt}_2$ in Et₂O at 0 °C to give the methyl acetal **5** in 67% yield in two steps, along with its C103-epimer (10% yield in two steps). Next, we examined the stereoselective dihydroxylation of the enone **5**. When the enone **5** was subjected to the OsO_4 -dihydroxylation conditions, the reaction did not proceed at all. We speculated that this unfortunate phenomenon resulted from the electron-deficient character of the enone **5**. Therefore, the dihydroxylation of **5** was carried out with $\text{RuCl}_3/\text{NaIO}_4$ in the presence of ZnCl_2 as a Lewis acid at 0 °C, which are efficient conditions to the electron-deficient alkenes,¹⁰ to afford the desired diol **12** in 73% yield as the sole product.¹¹ The stereochemistries at the C101 to C103 positions were verified by NOE correlations and coupling constants. Thus, the observed NOEs of

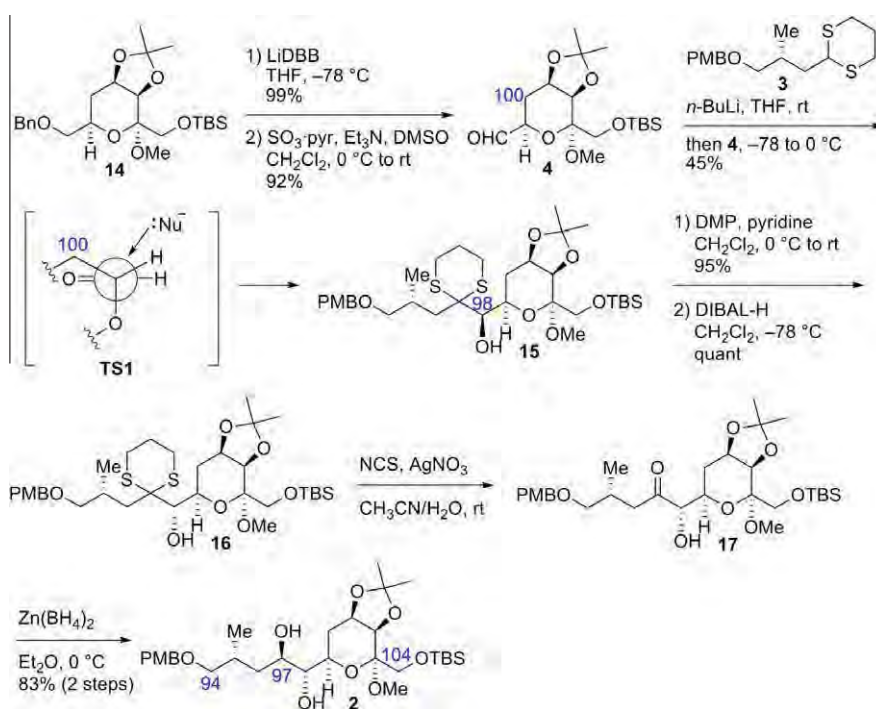
H-99/H-101 and H-99/OCH₃-103 of **12** confirmed that they were in a *syn* relationship to each other. The small magnitude of $^3J_{101,102}$ (3.6 Hz) indicated the *syn* correlation of these protons. Although the detailed conformational analysis of **5** was not carried out, the stereochemical outcome in the dihydroxylation can be rationalized by the steric repulsion between the methoxy group at the C103 position and the ruthenium reagent. After the vicinal diol moiety of **12** was protected as an acetonide, reduction with NaBH_4 proceeded stereoselectively to provide axial alcohol **13**. The resulting configuration at the C100 position was determined by the observed $^3J_{99,100}$ (5.5 Hz). The alcohol **13** was transformed into the corresponding *S*-methyl dithiocarbonate in 97% yield, which was deoxygenated under Barton–McCombie conditions¹² to afford tetrahydropyran **14** in 93% yield.

Next objective was to introduce the side chain, stereoselectively. Removal of the benzyl protective group of **14** with LiDBB^{13} and subsequent Parikh–Doering oxidation¹⁴ gave the aldehyde **4** (Scheme 3). Deprotonation of the dithiane **3**¹⁵ with *n*-BuLi at room temperature for 15 min, which were found to be the optimal conditions by the deuterium exchange experiments, and subsequent reaction of the resulting anion with the aldehyde **4** yielded alcohol **15** as a single stereoisomer.¹⁶ The stereoselectivity can be understood by a Felkin–Anh model¹⁷ as illustrated in **TS1**. Treatment of **15** with Dess–Martin periodinane (DMP)¹⁸/pyridine afforded the corresponding ketone in 95% yield, which was reduced with DIBAL-H to provide the desired alcohol **16** in quantitative yield. The dithioacetal moiety of **16** was hydrolyzed with NCS/AgNO_3 in aqueous CH_3CN ¹⁹ to afford α -hydroxy ketone **17**. Chelation-controlled reduction of **17** with $\text{Zn}(\text{BH}_4)_2$ ²⁰ furnished the desired diol as a single stereoisomer.²¹ The absolute configuration at the C97 position was confirmed by the modified Mosher method⁹ using the mono-MTPA esters derived from **2**.

In conclusion, we have synthesized the C94–C104 fragment **2** of symbiodinolide (**1**) from furfuryl alcohol, which is the key synthetic intermediate for the synthesis of the C79–C104 fragment. The synthetic route features Achmatowicz rearrangement, RuO_4 -catalyzed



Scheme 2. Synthesis of **14**.



Scheme 3. Synthesis of 2.

dihydroxylation, and coupling between the dithiane and the aldehyde. Further synthetic and structural studies on **1** are currently underway and will be reported in due course.

Acknowledgements

We appreciate the Kato Memorial Bioscience Foundation, The Research Foundation for Pharmaceutical Sciences, The Society of Synthetic Organic Chemistry, Japan (Shionogi Award in Synthetic Organic Chemistry, Japan), and The Asahi Glass Foundation for their financial supports. This research was supported by Grant-in-Aid for Scientific Research from Japan Society for the Promotion of Science (JSPS).

References and notes

- Kita, M.; Ohishi, N.; Konishi, K.; Kondo, M.; Koyama, T.; Kitamura, M.; Yamada, K.; Uemura, D. *Tetrahedron* **2007**, *63*, 6241.
- Han, C.; Yamano, Y.; Kita, M.; Takamura, H.; Uemura, D. *Tetrahedron Lett.* **2009**, *50*, 5280.
- (a) Takamura, H.; Ando, J.; Abe, T.; Murata, T.; Kadota, I.; Uemura, D. *Tetrahedron Lett.* **2008**, *49*, 4626; (b) Murata, T.; Sano, M.; Takamura, H.; Kadota, I.; Uemura, D. *J. Org. Chem.* **2009**, *74*, 4797; (c) Takamura, H.; Murata, T.; Asai, T.; Kadota, I.; Uemura, D. *J. Org. Chem.* **2009**, *74*, 6658; (d) Takamura, H.; Kadonaga, Y.; Yamano, Y.; Han, C.; Aoyama, Y.; Kadota, I.; Uemura, D. *Tetrahedron Lett.* **2009**, *50*, 863; (e) Takamura, H.; Kadonaga, Y.; Yamano, Y.; Han, C.; Kadota, I.; Uemura, D. *Tetrahedron* **2009**, *65*, 7449; (f) Takamura, H.; Kadonaga, Y.; Kadota, I.; Uemura, D. *Tetrahedron Lett.* **2010**, *51*, 2603; (g) Takamura, H.; Kadonaga, Y.; Kadota, I.; Uemura, D. *Tetrahedron* **2010**, *66*, 7569.
- Achmatowicz, O., Jr.; Bukowski, P.; Szechner, B.; Zwierzchowska, Z.; Zamojski, A. *Tetrahedron* **1971**, *27*, 1973.
- Celanire, S.; Marlin, F.; Baldwin, J. E.; Adlington, R. M. *Tetrahedron* **2005**, *61*, 3025.
- Nishizono, N.; Akama, Y.; Agata, M.; Sugo, M.; Yamaguchi, Y.; Oda, K. *Tetrahedron* **2011**, *67*, 358.
- Albright, J. D.; Goldman, L. *J. Am. Chem. Soc.* **1965**, *87*, 4214.
- (a) Fujii, A.; Hashiguchi, S.; Uematsu, N.; Ikariya, T.; Noyori, R. *J. Am. Chem. Soc.* **1996**, *118*, 2521; (b) Noyori, R.; Hashiguchi, S. *Acc. Chem. Res.* **1997**, *30*, 97.
- Ohtani, I.; Kusumi, T.; Kashman, Y.; Kakisawa, H. *J. Am. Chem. Soc.* **1991**, *113*, 4092.
- Plietker, B.; Niggemann, M. *J. Org. Chem.* **2005**, *70*, 2402.
- When the enone **5** was treated with RuCl₃/NaIO₄ in the presence of CeCl₃ at 0 °C, the diol **12** was obtained in 51% yield.
- Barton, D. H. R.; McCombie, S. W. *J. Chem. Soc., Perkin Trans. 1* **1975**, 1574.
- (a) Freeman, P. K.; Hutchinson, L. L. *J. Org. Chem.* **1980**, *45*, 1924; (b) Ireland, R. E.; Smith, M. G. *J. Am. Chem. Soc.* **1988**, *110*, 854.
- Parikh, J. R.; Doering, W. V. E. *J. Am. Chem. Soc.* **1967**, *89*, 5505.
- The dithiane **3** was prepared from commercially available methyl (S)-3-hydroxy-2-methylpropionate according to the known procedure. See: (a) Walkup, R. D.; Boatman, P. D., Jr.; Kane, R. R.; Cunningham, R. T. *Tetrahedron Lett.* **1991**, *32*, 3937; (b) Shotwell, J. B.; Roush, W. R. *Org. Lett.* **2004**, *6*, 3865.
- The absolute stereochemistry at the C98 position of **15** was elucidated by applying the modified Mosher method to the α -hydroxy ketone which was synthesized from **15** with NCS/AgNO₃ in aqueous CH₃CN.
- For a selected review, see: Mengel, A.; Reiser, O. *Chem. Rev.* **1999**, *99*, 1191.
- (a) Dess, D. B.; Martin, J. C. *J. Org. Chem.* **1983**, *48*, 4155; (b) Dess, D. B.; Martin, J. C. *J. Am. Chem. Soc.* **1991**, *113*, 7277.
- (a) Corey, E. J.; Erickson, B. W. *J. Org. Chem.* **1971**, *36*, 3553; (b) Rao, A. V. R.; Venkatswamy, G.; Javeed, S. M.; Deshpande, V. H.; Rao, B. R. *J. Org. Chem.* **1983**, *48*, 1552.
- Nakata, T.; Tanaka, T.; Oishi, T. *Tetrahedron Lett.* **1983**, *24*, 2653.
- Diol **2**: colorless oil; *R*_f = 0.40 (hexane/EtOAc=1:1); [α]_D²⁰ = -10.2 (c 0.13, CHCl₃); IR (neat) 3437, 2927 cm⁻¹; ¹H NMR (400 MHz, CDCl₃) δ 7.21 (d, *J* = 8.3 Hz, 2H), 6.84 (d, *J* = 8.3 Hz, 2H), 4.43 (s, 2H), 4.37–4.31 (m, 1H), 4.01 (dt, *J* = 10.3, 3.0 Hz, 1H), 3.97 (d, *J* = 4.9 Hz, 1H), 3.81–3.78 (m, 1H), 3.78 (s, 3H), 3.73 (d, *J* = 10.7 Hz, 1H), 3.67 (d, *J* = 10.7 Hz, 1H), 3.62–3.58 (m, 1H), 3.41 (dd, *J* = 8.9, 4.3 Hz, 1H), 3.25–3.18 (m, 2H), 3.19 (s, 3H), 2.36–2.33 (m, 1H), 2.01–1.95 (m, 1H), 1.82–1.73 (m, 3H), 1.47 (s, 3H), 1.42–1.36 (m, 1H), 1.29 (s, 3H), 0.92 (d, *J* = 6.8 Hz, 3H), 0.89 (s, 9H), 0.06 (s, 3H), 0.06 (s, 3H); ¹³C NMR (100 MHz, CDCl₃) δ 159.2, 129.6, 129.4, 113.8, 108.5, 99.9, 77.2, 76.4, 73.0, 72.1, 71.1, 71.1, 66.0, 60.3, 55.3, 47.9, 40.0, 32.2, 30.7, 29.8, 28.4, 26.5, 25.8, 18.4, -5.4, -5.5; HRMS (ESI-TOF) calcd for C₃₀H₅₂O₉SiNa (M+Na)⁺ 607.3278, found 607.3268.



ELSEVIER

Contents lists available at SciVerse ScienceDirect

Biochemical and Biophysical Research Communications

journal homepage: www.elsevier.com/locate/ybbrc

Ternatin, a cyclic peptide isolated from mushroom, and its derivative suppress hyperglycemia and hepatic fatty acid synthesis in spontaneously diabetic KK-*A^y* mice

Misato Kobayashi^a, Haruna Kawashima^a, Kumiko Takemori^b, Hiroyuki Ito^c, Atsushi Murai^a, Shun Masuda^d, Kaoru Yamada^d, Daisuke Uemura^d, Fumihiko Horio^{a,*}

^a Department of Applied Biosciences, Graduate School of Bioagricultural Sciences, Nagoya University, Nagoya 464-8601, Japan

^b Department of Food and Nutrition, Kinki University Faculty of Agriculture, Nara 631-8505, Japan

^c Department of Biomedical Engineering, Kinki University Faculty of Biology-Oriented Engineering, Wakayama 649-6493, Japan

^d Department of Chemistry, Kanagawa University, Kanagawa 259-1293, Japan

ARTICLE INFO

Article history:

Received 6 September 2012

Available online 18 September 2012

Keywords:

Ternatin
Cyclic peptide
Anti-diabetic
Blood glucose
Triglyceride
KK-*A^y* mice

ABSTRACT

(–)-Ternatin is a highly methylated cyclic heptapeptide isolated from mushroom *Coriolus versicolor*. Ternatin has an inhibitory effect on fat accumulation in 3T3-L1 adipocytes. [D-Leu⁷]ternatin, a ternatin derivative, also inhibited fat accumulation in 3T3-L1 cells, although the effectiveness of [D-Leu⁷]ternatin was lower than that of ternatin. In this study, we investigated the effects of ternatin and [D-Leu⁷]ternatin on obesity and type 2 diabetes in KK-*A^y* mice, an animal model for spontaneously developed type 2 diabetes. We continuously administered ternatin (8.5 or 17 nmol/day) or [D-Leu⁷]ternatin (68 nmol/day) to mice via a subcutaneous osmotic pump. Unexpectedly, neither ternatin nor [D-Leu⁷]ternatin affected body weight or adipose tissue weight in KK-*A^y* mice. In contrast, it was demonstrated that both ternatin and [D-Leu⁷]ternatin suppress the development of hyperglycemia. In liver, the SREBP-1c mRNA level tended to be lower or significantly decreased in mice treated with ternatin or [D-Leu⁷]ternatin, respectively. Moreover, we found that ternatin directly lowered the SREBP-1c mRNA level in Hepa1-6 hepatocyte cells. This study showed that ternatin and [D-Leu⁷]ternatin each had a preventive effect on hyperglycemia and a suppressive effect on fatty acid synthesis in KK-*A^y* mice.

© 2012 Elsevier Inc. All rights reserved.

1. Introduction

Type 2 diabetes is the leading cause of chronic kidney disease (diabetic nephropathy), blindness (diabetic retinopathy), and non-traumatic lower-limb amputations (diabetic neuropathy). The incidence of type 2 diabetes is dramatically increasing due to changes in lifestyle such as in diet and activity level [1]. The interaction between impaired insulin secretion and insulin resistance is involved in the development of type 2 diabetes. Obesity is a major risk factor for insulin resistance, type 2 diabetes, dyslipidemia, cardiovascular disease, and fatty liver. A strong link between obesity and insulin resistance has been reported in animals and human studies [2]. Therefore, the amelioration of obesity leads to both

the improvement of insulin sensitivity and the prevention of type 2 diabetes.

Various natural products, including crude extracts and isolated compounds, from plants or plant parts such as various berries [3–7], soybean [8,9], tea plant (*Camellia sinensis*) [10,11], and lotus (*Nelumbo nucifera*) [12], reportedly have physiological effects, such as the inhibition of lipase activity, the suppression of appetite, the stimulation of energy expenditure, the inhibition of adipocyte differentiation, and the regulation of lipid metabolism [13]. Numerous components from natural products can be utilized to safely treat diet-induced obesity and type 2 diabetes.

(–)-Ternatin (ternatin) is a highly methylated cyclic heptapeptide isolated from mushroom *Coriolus versicolor* [14,15]. Although ternatin had been known as an anti-bacterial or anti-microbial compound, its inhibitory effect on fat accumulation was recently shown by using 3T3-L1 adipocytes [14]. In preadipocytes at the early stage of differentiation, ternatin reduced the mRNA levels of CCAAT/enhancer binding protein- α (C/EBP- α) and sterol regulatory element binding protein-1c (SREBP-1c), and tended to suppress the peroxisome proliferative activated receptor- γ (PPAR- γ) mRNA level [16]. This suppression of preadipocyte differentiation

Abbreviations: ACC, acetyl-CoA carboxylase; C/EBP- α , CCAAT/enhancer binding protein- α ; FAS, fatty acid synthase; PPAR- γ , peroxisome proliferative activated receptor- γ ; SREBP-1c, sterol regulatory element binding protein-1c.

* Corresponding author. Address: Department of Applied Biosciences, Graduate School of Bioagricultural Sciences, Nagoya University, Furo-cho, Chikusa, Nagoya 464-8601, Japan. Fax: +81 52 789 4075.

E-mail address: horiof@agr.nagoya-u.ac.jp (F. Horio).

0006-291X/\$ - see front matter © 2012 Elsevier Inc. All rights reserved.
<http://dx.doi.org/10.1016/j.bbrc.2012.09.045>

brought about the reduction of mRNA levels of adipocyte fatty acid binding protein (aP2), lipoprotein lipase, fatty acid synthase (FAS), and acetyl-CoA carboxylase 2 (ACC2), and led to the reduction of cellular lipid accumulation [16]. In the differentiated 3T3-L1 adipocytes, ternatin treatment also reduced triglyceride synthesis, but ternatin's effectiveness in differentiated adipocytes was lower than that observed in the preadipocytes [16].

[D-Leu⁷]ternatin, a ternatin derivative, was also demonstrated to inhibit fat accumulation in 3T3-L1 cells, and the effective dose of [D-Leu⁷]ternatin was eight times that of ternatin [17]. The cytotoxicity value (IC₅₀) of [D-Leu⁷]ternatin was 12-fold higher than that of ternatin [17]. From these results, [D-Leu⁷]ternatin's inhibition of fat accumulation was lower than ternatin's, but the low toxicity of [D-Leu⁷]ternatin is beneficial. The mechanism underlying this derivative's action is thought to be similar to that of ternatin. In addition, it is unclear whether ternatin and [D-Leu⁷]ternatin have an anti-obesity effect or an anti-diabetic effect *in vivo*. From this background, in the present study we investigated whether the administration of ternatin or [D-Leu⁷]ternatin suppresses the development of obesity and type 2 diabetes in KK-A^y mice, a model for spontaneously developed type 2 diabetes.

2. Materials and methods

2.1. Animals

Four-week-old male KK-A^y mice (CLEA, Tokyo, Japan) were purchased and acclimatized for 1 week before the experiments began. All mice were maintained at a controlled temperature of 23 ± 3 °C and 55 ± 5% humidity on a 12-h light/dark cycle and allowed free access to water and a standard laboratory diet (CE-2; CLEA). The composition of the diet was as follows: protein, 254 g/kg; fat, 51 g/kg; non-nitrogenous substances, 506 g/kg; crude fiber, 35 g/kg; crude ash, 67 g/kg; energy, 15.2 MJ/kg; sufficient minerals and vitamins to maintain the health of the mice.

2.2. Administration of ternatin or [D-Leu⁷] ternatin derivative in KK-A^y mice

Ternatin was synthesized according to the method previously described [14]. [D-Leu⁷]ternatin derivative was synthesized by Peptide Institute Inc. (Osaka, Japan). Ternatin was administered to each mouse at a dose of 8.5 or 17 nmol/day via subcutaneous continuous infusion for 4 weeks using an osmotic pump. [D-Leu⁷]ternatin derivative was also administered to each mouse at a dose of 68 nmol/day. The dose of the [D-Leu⁷]ternatin derivative was calculated from the compound's inhibitory effect on fat accumulation in 3T3-L1 cells [17]. The concentration (EC₅₀) of [D-Leu⁷]ternatin derivative showing a 50% effect of the compound's maximum fat accumulation inhibition of this compound was eight times that of ternatin. These cyclic peptides were dissolved in 70% DMSO and loaded into osmotic minipumps (model 1004; Alzet, Cupertino, CA) according to the manufacturer's protocol. Control groups received pumps loaded with vehicle (70% DMSO in sterile water). An osmotic pump was surgically inserted subcutaneously into the back of each mouse.

2.3. Experimental procedure in mouse

Experiment 1: Mice were divided into three groups and subcutaneously administered vehicle (control group, 6 mice), 8.5 nmol/day ternatin (8.5 nmol ternatin group, 7 mice), or 17 nmol/day ternatin (17 nmol ternatin group, 6 mice) via the osmotic pumps. *Experiment 2:* Mice were divided into two groups and administered vehicle

(control group, 6 mice) or 68 nmol/day [D-Leu⁷]ternatin derivative ([D-Leu⁷] group, 6 mice) via the osmotic pumps.

The mice were allowed free access to drinking water and diet (CE-2; CLEA) for 4 weeks. Blood samples were collected from the tail vein once a week to measure the serum glucose concentration. Blood was collected from the tail vein at 10:00 after 1-h diet deprivation. The collected blood was kept at room temperature for 15 min for coagulation. The serum was then obtained from the coagulated blood by centrifugation at 2430g for 10 min at 4 °C. The serum was kept at -30 °C prior to use. Serum glucose was measured by the assay kit using the glucose oxidase method, Glucose II-test (Wako Pure Chemical, Osaka, Japan). At the end of the experiment, the mice were killed by decapitation, and serum, liver, and fat pad were collected. The animal care and experimental procedures were approved by the Animal Research Committee of Nagoya University and were conducted according to the Regulations for Animal Experiments at Nagoya University.

2.4. Serum components analysis

Serum triglyceride and cholesterol concentrations were, respectively measured by a Triglyceride-E test (Wako Pure Chemical) and a Cholesterol-E test (Wako Pure Chemical). A commercially available ELISA kit was used to determine the serum concentration of insulin (Morinaga Seikagaku, Kanagawa Japan).

2.5. Hepatic lipids analysis

Frozen livers were homogenized in chloroform/methanol (2:1), and liver lipids were extracted into organic solvents. A portion of this extract was dried, and the triglycerides in this dried material were measured by the Triglyceride-E test. Another portion of the extract was also used to measure total lipid content according to the method of Folch et al. [18].

2.6. RNA preparation and gene expression analysis

Total RNA was extracted from frozen tissues using TRIzol reagent (Invitrogen, Carlsbad, CA). It was then treated with DNase using a TURBO DNA-free kit (Ambion, Austin, TX). cDNA was synthesized using a High Capacity cDNA Reverse Transcription Kit (Applied Biosystems, Foster City, CA). Gene expression was quantified by real-time PCR using an ABI 7300 real-time PCR system with the Thunderbird qPCR Mix or the Thunderbird SYBR qPCR Mix (Toyobo, Tokyo, Japan). TaqMan primers and probes were used to determine mRNA levels of PPAR-γ (TaqMan Gene Expression Assays, Mm01184322_m1, Applied Biosystems) and 18S rRNA (Pre-developed TaqMan Assay Reagents, Eukaryotic 18S rRNA, Applied Biosystems). The primers for SYBR Green assay were as follows: ACC sense, 5'-TGACAGACTGATCGCAGAGAAAG-3'; ACC antisense, 5'-TGGAGA CCCCCACACA-3'; β-actin sense, 5'-AGATGACCCAGATCATGTTTGGAGA-3'; β-actin antisense, 5'-CACAGCCTGGATGGCTACGT-3' FAS antisense, 5'-TCAGCCACTTGAGTGTCTCCTC-3'; SREBP-1c sense, 5'-GGAGC CATG GATTGCACATT-3'; SREBP-1c antisense, 5'-GGCCCGGAAGTCACTGT-3'; FAS sense, 5'-GGGTTCTAGCCAGCAGAGTC-3'. The level of each mRNA was normalized to that of the corresponding 18S rRNA (KK-A^y mice) or β-actin (Hepa1-6).

2.7. Ternatin treatment in Hepa1-6 cells

Hepa1-6 cells (RBRC-RCB1638 RIKEN BRC Cell Bank, Japan) were grown in high-glucose Dulbecco's modified Eagle medium (DMEM, Wako Pure Chemical) supplemented with 10% fetal bovine serum (FBS), 100 U/ml penicillin, and 100 μg/ml streptomycin at 37 °C in a 5% CO₂-humidified incubator. To examine the cellular toxicity of ternatin, Hepa1-6 cells were treated with DMSO (vehicle) or

ternatin (1.3, 13, 130 nM, 1.3, and 13 μ M, dissolved in DMSO) for 30 h. After this culture, cell viability was assayed by a Cell Counting Kit-8 (Dojindo, Kumamoto, Japan).

To examine ternatin's effect on various mRNA levels, Hepa1-6 cells were seeded on 12-well plates (2×10^5 cells per well) on day 0. On day 1, DMSO or ternatin (1.3 and 13 nM) was added to the culture medium. Forty-eight hours after this addition, cells were harvested and used for measuring various mRNA levels.

2.8. Statistical analysis

All results are expressed as means \pm SEM. Phenotypic data were statistically analyzed by one-way ANOVA, and a subsequent Dunnett's test was carried out to compare the means of all groups (experiment 1 and Hepa1-6 cells). In experiment 2, phenotypic data were statistically analyzed by either Student's *t* test or Welch's test. When the variances of each group were equal, mean values were compared using the former test. When the variances of each group were unequal, the significance of differences was determined using the latter test. Values of $P < 0.05$ were considered statistically significant (StatView; SAS Institute, Cary, NC).

3. Results

3.1. Administration of ternatin (8.5 or 17 nmol/day) in KK-A^y mice (experiment 1)

KK-A^y mice were administered vehicle (control) or either 8.5 or 17 nmol/day ternatin. The initial body weight, final body weight, and total food intake did not differ among the three groups (Table 1). At the beginning of the experiment (5 weeks of age), the blood glucose concentration in the control group was 230 ± 9 mg/dl (Fig. 1A). The blood glucose concentrations in the control group were increased dramatically, reaching 533 mg/dl by the end of the experiment. The blood glucose concentrations at 2 and 3 weeks into the experiment were significantly lower in the 8.5 nmol ternatin group than in the control group. At 3 weeks into the experiment, the blood glucose concentration in the 17 nmol ternatin group was also significantly lower than that in the control group. The liver weight (g) tended to be lower in the 17 nmol ternatin group than in the control group (Table 1, $p = 0.084$). Liver triglyceride content and liver total lipids were significantly lower in the 17 nmol ternatin group than in the control group (Fig. 1B and C). The values of liver triglyceride content and liver total lipid content in the 8.5 nmol ternatin group were similar to those in the 17 nmol ternatin group, and the values in the 8.5 nmol ternatin group were not significantly different from those in the control group. The tissue weights of subcutaneous fat, epididymal fat, retroperitoneal fat, and mesenteric fat

in the 8.5 nmol or the 17 nmol ternatin group were not different from those in the control group (Table 1). The serum concentrations of insulin and lipids (triglycerides and cholesterol) did not differ between the control and two ternatin groups (Table 1).

Previously, it was reported that ternatin or [D-Leu⁷]ternatin derivative decreased the mRNA levels of genes regulating adipogenesis in 3T3-L1 adipocytes [16]. In the present study, the mRNA levels of PPAR- γ and SREBP-1c in the epididymal fat did not differ among these three groups (Fig. 1E). The mRNA levels of FAS or ACC tended to be lower in the 8.5 or 17 nmol ternatin group than in the control group.

In this study, 17 nmol ternatin significantly decreased liver triglyceride content and liver total lipid content (Fig. 1B and C). Therefore, we also measured the mRNA levels of PPAR- γ , SREBP-1c, FAS, and ACC in the liver (Fig. 1D). In the liver, the mRNA level of PPAR- γ , a key regulator of adipogenesis, was not changed among the three experimental groups (Fig. 1D). The SREBP-1c mRNA level in the 8.5 nmol ternatin group tended to be lower than that in the control ($p = 0.06$). However, the mRNA levels of FAS and ACC, which regulate fatty acid synthesis, were not lower in either ternatin group compared to the control group (Fig. 1D).

3.2. Administration of [D-Leu⁷]ternatin derivative (68 nmol/day) in KK-A^y mice (experiment 2)

The dose of [D-Leu⁷]ternatin derivative was eight times that of the 8.5 nmol ternatin group. The final body weight and total food intake were not different between the control and [D-Leu⁷] groups (Table 2). Liver weight was significantly lower in the [D-Leu⁷] group than in the control group (Table 2). However, the liver triglycerides and total lipid content in the [D-Leu⁷] group was not decreased compared to those in the control group (Table 2). Similar to the result in experiment 1, the [D-Leu⁷]ternatin derivative had no effect on white adipose tissue weights, such as subcutaneous fat and epididymal fat, or on serum insulin concentration (Table 2). The blood glucose concentration at 3 weeks into the experiment was significantly lower in the [D-Leu⁷] group (354 ± 30 mg/dl) than in the control group (466 ± 34 mg/dl, $p = 0.03$) (Fig. 2A).

In experiment 1, we found that the administration of ternatin tended to decrease the hepatic SREBP1c mRNA level (Fig. 1D), but not significantly, and also decreased the FAS mRNA level in epididymal fat (Fig. 1E). Therefore, we also determined the mRNA levels of lipogenic genes in liver and epididymal fat in experiment 2 (Fig. 2B and C). In liver, the SREBP-1c mRNA level was significantly lower in the [D-Leu⁷] group than in the control group (Fig. 2B). Unexpectedly, in epididymal fat, the FAS mRNA level was significantly higher in the [D-Leu⁷] group than in the control group (Fig. 2C). The [D-Leu⁷]ternatin derivative had no effect on PPAR- γ or ACC mRNA levels in both tissues.

3.3. The effect of ternatin in mouse Hepa1-6 cell line

Although data are not shown, the treatment with 1.3 and 13 nM ternatin did not show cytotoxicity in mouse Hepa1-6 cells at all. However, the higher dose of ternatin reduced the number of viable cells (27% reduction at 130 nM; 54% reduction at 1.3 μ M; and 63% reduction at 13 μ M compared to that of the control (DMSO)). The mRNA levels of SREBP-1c, ACC, and FAS in Hepa1-6 cells were measured after 1.3 and 13 nM ternatin treatment (Fig. S1). The mRNA levels of SREBP-1c and ACC were significantly decreased by 13 nM ternatin but not by 1.3 nM ternatin. The treatment with 1.3 or 13 nM ternatin did not affect the FAS mRNA level. Although data are not shown, the cellular triglyceride contents were not changed by 30 h treatment with 13 nM ternatin.

Table 1

Body composition, food intake, and serum parameters in the control, the 8.5 nmol ternatin group, and the 17.5 nmol ternatin group.

	Control	8.5 nmol ternatin	17 nmol ternatin
Initial body weight (g)	18.9 \pm 0.2	18.8 \pm 0.3	18.9 \pm 0.2
Final body weight (g)	41.4 \pm 0.9	41.4 \pm 0.6	40.2 \pm 1.3
Total food intake (g)	135.1 \pm 2.2	130.7 \pm 3.7	132.3 \pm 4.0
<i>Tissue weight (g)</i>			
Liver	2.67 \pm 0.10	2.51 \pm 0.08	2.42 \pm 0.06
Subcutaneous fat	1.10 \pm 0.14	1.02 \pm 0.14	1.04 \pm 0.10
Epididymal fat	1.33 \pm 0.05	1.34 \pm 0.05	1.29 \pm 0.05
Retroperitoneal fat	0.33 \pm 0.02	0.32 \pm 0.01	0.35 \pm 0.03
Mesenteric fat	0.64 \pm 0.03	0.64 \pm 0.05	0.59 \pm 0.07
Serum insulin (ng/mL)	13.2 \pm 3.4	10.1 \pm 2.0	10.9 \pm 1.4
Serum triglyceride (mg/dL)	292 \pm 18	349 \pm 20	316 \pm 13
Serum cholesterol (mg/dL)	141 \pm 4	128 \pm 6	141 \pm 4

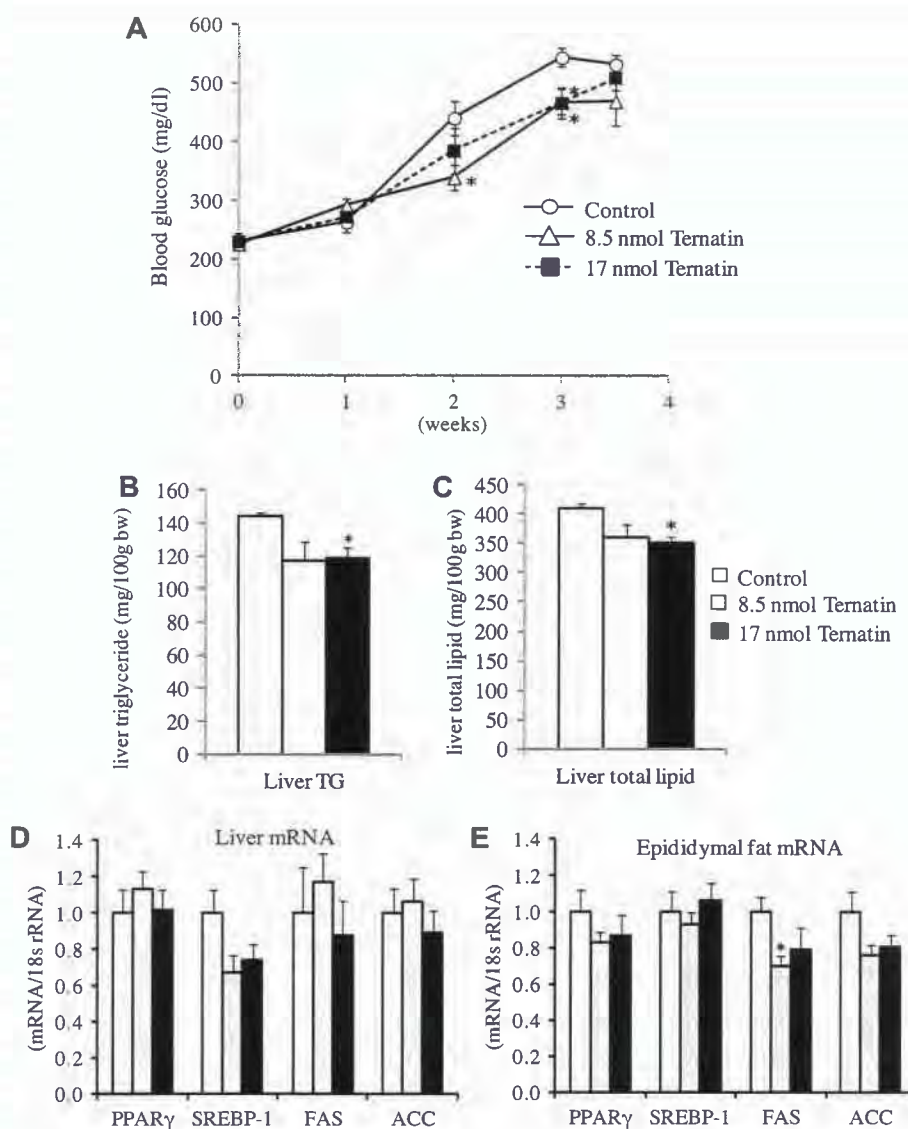


Fig. 1. The blood glucose concentrations, liver lipids, and gene expression levels in KK-*A^y* mice administered DMSO (control, $n = 6$) or ternatin (8.5 nmol ($n = 7$) and 17 nmol ($n = 6$), experiment 1). (A) Blood glucose concentrations in the control, 8.5 nmol ternatin, and 17 nmol ternatin groups. (B) Liver triglyceride content and liver total lipid content in the three groups at 4 weeks into the experiment. The liver mRNA levels (D) and the epididymal fat mRNA levels (E) of PPAR- γ , SREBP-1c, FAS, and ACC. The mRNA level of the control group was set as 1, and the relative mRNA levels of the ternatin groups were expressed as fold changes with respect to the control. The data are expressed as mean \pm SEM. * $P < 0.05$ vs control group.

4. Discussion

It has been reported that ternatin or its derivative [D-Leu⁷]ternatin suppressed the expression of lipogenic genes and inhibited fat accumulation in cultured adipocytes [14,16,17]. These data imply that ternatin or its derivative [D-Leu⁷]ternatin may be a valuable drug for the treatment of obesity. Therefore, it is necessary to demonstrate the *in vivo* effect of ternatin or its derivative. The primary aim of this study is to investigate the anti-obesity effect of ternatin or its derivative [D-Leu⁷]ternatin in an obese animal model. To investigate this effect, in the present study we selected continuous subcutaneous administration of ternatin by an osmotic pump, because we had no data on the absorption rate of ternatin or its derivative from intestine. We estimated that a dose of 8.5 or 17 nmol/day ternatin brought about its effective concentration in blood, which inhibits fat accumulation in 3T3-L1 cells [16]. Unexpectedly, in mice, ternatin or its derivative did not show any anti-obesity effect such as decreased adipose tissue weight (Tables 1 and 2). On the other hand,

Table 2

Body composition, food intake, and serum parameters in the control and the 68 nmol [D-Leu⁷]ternatin groups.

	Control	[D-Leu ⁷]
Final body weight (g)	39.6 \pm 0.5	39.7 \pm 0.7
Total food intake (g)	140.5 \pm 2.8	136.6 \pm 2.8
<i>Tissue weight (g)</i>		
Liver	2.50 \pm 0.04	2.28 \pm 0.04*
Subcutaneous fat	1.28 \pm 0.10	1.30 \pm 0.10
Epididymal fat	1.29 \pm 0.04	1.25 \pm 0.06
Serum insulin (ng/mL)	13.6 \pm 2.6	9.9 \pm 1.5
Serum triglyceride (mg/dL)	346 \pm 29	312 \pm 23
Serum cholesterol (mg/dL)	115 \pm 7	119 \pm 8
Liver TG (mg/100 g bw)	61.7 \pm 6.7	78.4 \pm 3.9
Liver total lipids (mg/100 g bw)	237 \pm 22	251 \pm 16

* $P < 0.05$ vs control group.

fortunately, we demonstrated for the first time that ternatin or its derivative had a suppressive effect on the development of

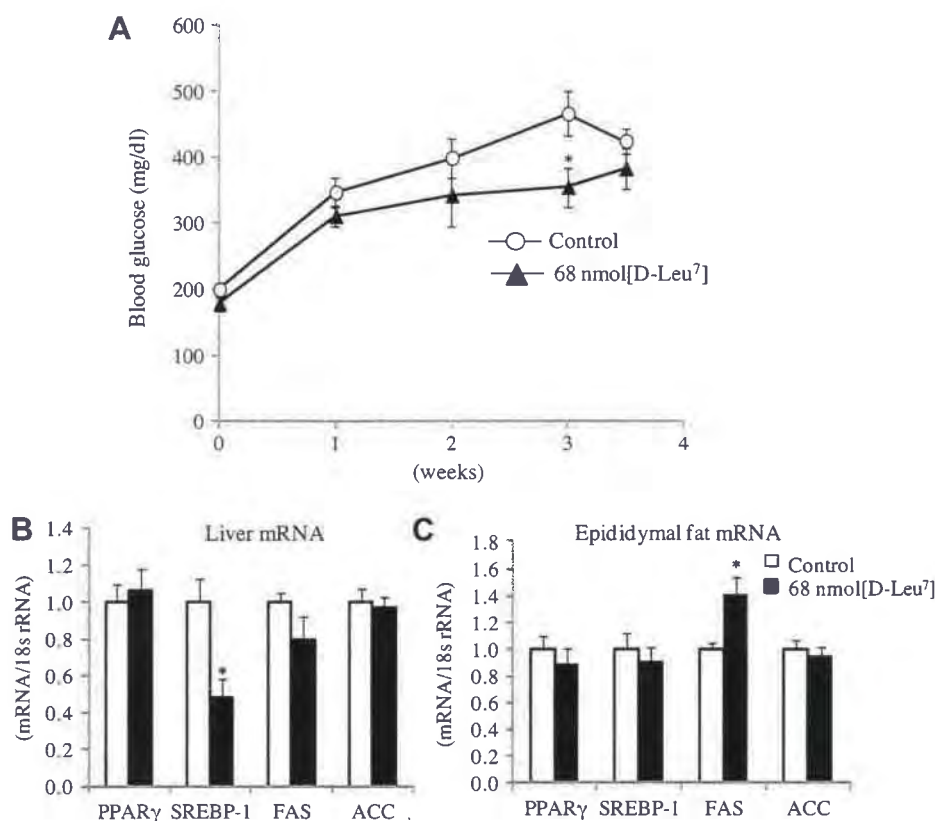


Fig. 2. Blood glucose concentrations and gene expression levels in KK-*A^y* mice administered DMSO (control, *n* = 7) or 68 nmol [D-Leu⁷]ternatin (*n* = 8) (experiment 2). (A) Blood glucose concentrations in the control or the 68 nmol [D-Leu⁷]ternatin group. The liver mRNA levels (B) and the epididymal fat mRNA levels (C) of PPAR- γ , SREBP-1c, FAS, and ACC. The mRNA level of the control group was set as 1, and the relative mRNA levels of the [D-Leu⁷]ternatin group were expressed as fold changes with respect to the control. The data are expressed as mean \pm SEM. **P* < 0.05 vs control group.

hyperglycemia (Figs. 1A and 2A). In addition, we found that ternatin suppressed the expression of SREBP-1c, which accelerates fatty acid synthesis, in liver and hepatocytes, and that this effect of ternatin might be due to its direct action (Fig. S1). This result suggested that ternatin suppresses the accumulation of liver lipids in mice.

In this study, ternatin administration showed an anti-diabetic effect but not an anti-obesity effect. However, it was reported that the oral administration of ternatin in C57BL/6 mice reduced subcutaneous and visceral fat weights [19]. The dosage of ternatin (5 mg/kg body weight/day) in C57BL/6 mice [19] was calculated as about 170 nmol/day. This dosage of ternatin in the previous C57BL/6 study was about 10–20 times that administered in this study. We speculate that this discrepancy in ternatin's effect between the present study and the previous study was caused by the differences in both the dose and manner of administration.

Ternatin or [D-Leu⁷]ternatin inhibited the fat accumulation in 3T3-L1 adipocytes [16,20]. It was speculated that this inhibitory effect was provided by the reduction in the expression of lipogenic genes, such as PPAR- γ , SREBP-1c, FAS, and ACC, and by the increase in lipolysis [16]. In this study, ternatin administration tended to reduce the FAS mRNA level in epididymal fat (Fig. 1E). However, ternatin treatment in KK-*A^y* mice did not change several adipose tissue weights or epididymal fat mRNA levels of PPAR- γ and SREBP-1c (Fig. 1E and Table 1). In a previous report, in 3T3-L1 preadipocytes, 130 nM ternatin in medium decreased lipogenic gene expression and intracellular lipid content [16]. In differentiated 3T3-L1 adipocytes, 1300 nM ternatin but not 130 nM ternatin in the medium lowered PPAR- γ and SREBP-1c mRNA levels and reduced the intracellular lipid content [16]. The effective dose of

ternatin (1300 nM) in differentiated 3T3-L1 adipocytes was much higher than its effective dose in preadipocytes [17]. As mouse adipose tissue is composed mostly of differentiated adipocytes, we suppose from the present results that ternatin hardly inhibits fat accumulation in adipose tissue of KK-*A^y* mice.

In rat primary hepatocytes, ternatin suppressed the triglyceride synthesis and enhanced fatty acid oxidation [16]. We also measured the mRNA levels of lipogenic genes in liver and found that the SREBP-1c mRNA level tended to be decreased in the ternatin groups (Fig. 1D). Consistent with this reduction of SREBP-1c mRNA level in liver, the present study demonstrated for the first time that ternatin administration reduced liver triglyceride content and liver total lipid content (Fig. 1B and C).

Similar to the results with ternatin, [D-Leu⁷]ternatin did not suppress either body weight gain or fat accumulations in subcutaneous and visceral fat (Table 2). In contrast, we demonstrated that not only ternatin but also its [D-Leu⁷]ternatin derivative had an anti-diabetic effect in KK-*A^y* mice (Fig. 2A). In liver, [D-Leu⁷]ternatin treatment also significantly decreased the SREBP-1c mRNA level (Fig. 2B). However, liver triglyceride content and liver total lipids were not decreased in mice administered [D-Leu⁷]ternatin (Table 2). At present, we cannot explain the reason why [D-Leu⁷]ternatin did not reduce liver triglyceride content. These results showed that the administration of ternatin or [D-Leu⁷]ternatin consistently suppressed the hepatic expression of the SREBP-1c gene in KK-*A^y* mice. Insulin, an activator of SREBPs, is known to increase the expression of the SREBP-1c gene and proteolytic processing of SREBP proteins [21]. Therefore, we tried to clarify whether or not ternatin directly suppresses the expression of the SREBP-1c gene in a murine

hepatocyte cell line, Hepa1-6. Consequently, we detected decreased SREBP-1c and ACC mRNA levels by ternatin treatment (13 nM) (Fig. S1). These results suggested that the hepatic expression of the SREBP-1c gene was directly suppressed by ternatin, not by the change in serum insulin concentration in KK-*A^y* mice. In addition, the reduction in serum insulin concentration in mice administered ternatin and [D-Leu⁷]ternatin might partially contribute to the decrease in the hepatic SREBP-1c mRNA level.

In conclusion, we determined the effects of ternatin and of [D-Leu⁷]ternatin on obesity and type 2 diabetes in spontaneously diabetic/obese KK-*A^y* mice. Ternatin and [D-Leu⁷]ternatin, at the dose adopted in this study, did not affect either adipose tissue weights or lipogenic genes (such as PPAR- γ and SREBP-1c) expression in adipose tissue. We revealed for the first time that ternatin and [D-Leu⁷]ternatin partially suppress hyperglycemia in KK-*A^y* mice. Interestingly, it was suggested that ternatin directly decreases hepatic TG synthesis by reducing the expression of the SREBP-1c gene. Ternatin and its derivative might improve hepatic TG metabolism, leading to the amelioration of type 2 diabetes.

Acknowledgments

This work was supported by an Adaptable and Seamless Technology transfer Program through target-driven R&D (A-STEP) (No.AS231Z03808E) from Japan Science and Technology Agency, and by a grant from The Towa foundation for food research (to F. Horio).

Appendix A. Supplementary data

Supplementary data associated with this article can be found, in the online version, at <http://dx.doi.org/10.1016/j.bbrc.2012.09.045>.

References

- [1] J.A. Yanovski, S.Z. Yanovski, Recent advances in basic obesity research, *JAMA* 282 (1999) 1504–1506.
- [2] S.E. Kahn, R.L. Hull, K.M. Utzschneider, Mechanisms linking obesity to insulin resistance and type 2 diabetes, *Nature* 444 (2006) 840–846.
- [3] M. Takikawa, S. Inoue, F. Horio, T. Tsuda, Dietary anthocyanin-rich bilberry extract ameliorates hyperglycemia and insulin sensitivity via activation of AMP-activated protein kinase in diabetic mice, *J. Nutr.* 140 (2010) 527–533.
- [4] A.S. Attele, Y.P. Zhou, J.T. Xie, J.A. Wu, L. Zhang, L. Dey, W. Pugh, P.A. Rue, K.S. Polonsky, C.S. Yuan, Antidiabetic effects of Panax ginseng berry extract and the identification of an effective component, *Diabetes* 51 (2002) 1851–1858.
- [5] L. Dey, J.T. Xie, A. Wang, J. Wu, S.A. Maleckar, C.S. Yuan, Anti-hyperglycemic effects of ginseng: comparison between root and berry, *Phytotherapy* 10 (2003) 600–605.
- [6] J.T. Xie, C.Z. Wang, M. Ni, J.A. Wu, S.R. Mehendale, H.H. Aung, A. Foo, C.S. Yuan, American ginseng berry juice intake reduces blood glucose and body weight in ob/ob mice, *J. Food Sci.* 72 (2007) S590–594.
- [7] C. Morimoto, Y. Satoh, M. Hara, S. Inoue, T. Tsujita, H. Okuda, Anti-obese action of raspberry ketone, *Life Sci.* 77 (2005) 194–204.
- [8] H. Xu, G.T. Barnes, Q. Yang, G. Tan, D. Yang, C.J. Chou, J. Sole, A. Nichols, J.S. Ross, L.A. Tartaglia, H. Chen, Chronic inflammation in fat plays a crucial role in the development of obesity-related insulin resistance, *J. Clin. Invest.* 112 (2003) 1821–1830.
- [9] C.R. Cederroth, S. Nef, Soy, phytoestrogens and metabolism: a review, *Mol. Cell. Endocrinol.* 304 (2009) 30–42.
- [10] F. Thielecke, M. Boschmann, The potential role of green tea catechins in the prevention of the metabolic syndrome – a review, *Phytochemistry* 70 (2009) 11–24.
- [11] K.A. Grove, J.D. Lambert, Laboratory, epidemiological, and human intervention studies show that tea (*Camellia sinensis*) may be useful in the prevention of obesity, *J. Nutr.* 140 (2010) 446–453.
- [12] E. Ohkoshi, H. Miyazaki, K. Shindo, H. Watanabe, A. Yoshida, H. Yajima, Constituents from the leaves of *Nelumbo nucifera* stimulate lipolysis in the white adipose tissue of mice, *Planta Med.* 73 (2007) 1255–1259.
- [13] J.W. Yun, Possible anti-obesity therapeutics from nature – a review, *Phytochemistry* 71 (2010) 1625–1641.
- [14] K. Shimokawa, I. Mashima, A. Asai, K. Yamada, M. Kita, D. Uemura, (–)-Ternatin, a highly *N*-methylated cyclic heptapeptide that inhibits fat accumulation: structure and synthesis, *Tetrahedron Lett.* 47 (2006) 4445–4448.
- [15] K. Shimokawa, I. Mashima, A. Asai, T. Ohno, K. Yamada, M. Kita, D. Uemura, Biological activity, structural features, and synthetic studies of (–)-ternatin, a potent fat-accumulation inhibitor of 3T3-L1 adipocytes, *Chem. Asian J.* 3 (2008) 438–446.
- [16] M. Ito, J. Ito, H. Kitazawa, K. Shimamura, T. Fukami, S. Tokita, K. Shimokawa, K. Yamada, A. Kanatani, D. Uemura, (–)-Ternatin inhibits adipogenesis and lipid metabolism in 3T3-L1 cells, *Peptides* 30 (2009) 1074–1081.
- [17] K. Shimokawa, Y. Iwase, K. Yamada, D. Uemura, Synthesis and inhibitory effect on fat accumulation of (–)-ternatin derivatives modified in the beta-OH-D-Leu(7) moiety, *Org. Biomol. Chem.* 6 (2008) 58–60.
- [18] J. Folch, M. Lees, G.H. Sloane Stanley, A simple method for the isolation and purification of total lipides from animal tissues, *J. Biol. Chem.* 226 (1957) 497–509.
- [19] K. Shimokawa, K. Yamada, M. Kita, D. Uemura, Convergent synthesis and in vivo inhibitory effect on fat accumulation of (–)-ternatin, a highly *N*-methylated cyclic peptide, *Bioorg. Med. Chem. Lett.* 17 (2007) 4447–4449.
- [20] K. Shimokawa, R. Miwa, K. Yamada, D. Uemura, Importance of the backbone conformation of (–)-ternatin in its fat-accumulation inhibitory activity against 3T3-L1 adipocytes, *Org. Biomol. Chem.* 7 (2009) 777–784.
- [21] M.S. Brown, J.L. Goldstein, Selective versus total insulin resistance: a pathogenic paradox, *Cell Metab.* 7 (2008) 95–96.

Cite this: *Chem. Commun.*, 2012, **48**, 4347–4349

www.rsc.org/chemcomm

COMMUNICATION

Metal ion-binding properties of DNA duplexes containing thiopyrimidine base pairs†

Itaru Okamoto,* Takashi Ono, Rimi Sameshima and Akira Ono*

Received 1st September 2011, Accepted 14th March 2012

DOI: 10.1039/c2cc15436f

Thiopyrimidine pairs in DNA duplexes were unexpectedly largely stabilized by complexation with two equivalents of Ag(I) ions and their binding properties were evaluated. The metal ion-binding properties of the thiopyrimidine base pairs differed significantly from those of unpaired bases.

In recent years, a great deal of effort has gone toward capturing certain metal ions using DNA strands. Complexes made from metal ions and DNA have been applied toward the development of new materials such as DNA-based wires and sensors capable of detecting various metal ions in aqueous solution.^{1a-e} In metal ion-mediated base pairs (metallobase pairs), the hydrogen bonds of Watson–Crick base pairs in natural DNA are replaced by metal–base bonds. Metallobase pairs in DNA duplexes may also be generated using only naturally occurring pyrimidine bases.² Thymine–thymine (T–T) and cytosine–cytosine (C–C) mismatches in duplexes selectively capture Hg(II) and Ag(I) ions to form the corresponding metal-mediated base pairs T–Hg–T and C–Ag–C. Because the binding of Hg(II) to the T–T pair is highly selective, many DNA-based sensors have been developed for selectively detecting Hg(II) ions in aqueous solutions containing various heavy metal ions.^{2b,f,3}

To develop methods for binding metal ions to DNA strands, synthetic oligodeoxyribonucleotides containing various artificial bases have been created to form specific metallobase pairs.^{1f-p} To expand the selectivity and variety of metal ions binding to nucleobases, the concept of “hard and soft acids and bases” (HSAB) is a useful guideline. In general, base pairs containing sulfur atom(s) can be expected to incorporate various heavy metal ions. However, few studies have reported on the binding of metal ions to base pairs containing sulfur atoms in DNA duplexes. Zimmermann *et al.*^{1j} described Ag(I) ion binding to an artificial base-pair having methylthio side-chains. Takezawa and collaborators⁴ reported that nucleosides having mercaptopyridione or hydroxypyridinethione bases were able to capture

Pd(II) and Ni(II) ions. In the report, they predicted that artificial bases, once incorporated into DNA strands, may efficiently and selectively capture desired metal ions.

Thiopyrimidine nucleotides are observed in RNAs in cells as minor bases.⁵ Metal ion binding properties of thiopyrimidine nucleosides and nucleotides have been examined. Thiopyrimidine nucleosides (2-thiouridine, 4-thiouridine, 2,4-dithiouridine, 5-carboxymethyl-2-thiouridine) and mononucleotides (2-thiouridine 5'-monophosphate, 4-thiouridine 5'-monophosphate) form complexes with divalent metal ions such as Ni(II), Cu(II), and Cd(II).⁶ Also, 4-thiothymine, when placed in the loop region of a DNA hairpin structure, reportedly shows an affinity for divalent heavy metal ions such as Cd(II) and Cu(II).⁷ However, the metal ion-binding properties of thiopyrimidine pairs in duplexes have not been reported. The current study investigated the metal ion-binding properties of DNA duplexes containing the thiopyrimidine–thiopyrimidine base pairs 2-thiothymine–2-thiothymine (S2–S2) and 4-thiothymine–4-thiothymine (S4–S4) by thermal denaturation and ESI-MS methods. The binding properties of the thiopyrimidine pairs in duplexes differed from those of unpaired bases.

The chemical structures of the thiopyrimidine bases and DNA duplexes containing thiopyrimidine pairs used in this study are shown in Fig. 1. Oligodeoxynucleotides (ODNs) containing S2, S4, and 4-thiouracil (SU) were prepared using commercially available phosphoramidite units.⁸ Oligodeoxyribonucleotides containing 4-methylthiouracil (MeSU) were prepared as described by Coleman and Kesicki.⁹ Details are provided in the ESI.† Because of difficulties in purification, ODNs containing MeSU were composed of a simple, thymine-rich sequence. All of the oligonucleotides were purified by reverse-phase HPLC and their identity was confirmed by MALDI-TOF MS analyses.

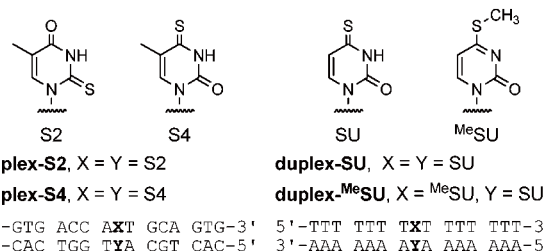


Fig. 1 Chemical structures of thiopyrimidine bases and DNA duplexes containing thiopyrimidine pairs.

Department of Material and Life Chemistry, Faculty of Engineering, Kanagawa University, 3-27-1 Rokkakubashi, Kanagawa-ku, Yokohama 221-8686, Japan. E-mail: i-okamoto@kanagawa-u.ac.jp, akiraono@kanagawa-u.ac.jp; Fax: +81-45-491-7915; Tel: +81-45-481-5661 (Ex 3887)

† Electronic supplementary information (ESI) available: Synthesis of oligonucleotides, HPLC profiles and MALDI-TOF MS spectra of these oligonucleotides, thermal denaturation profiles, ESI-TOF MS spectra and CD spectra of duplexes. See DOI: 10.1039/c2cc15436f

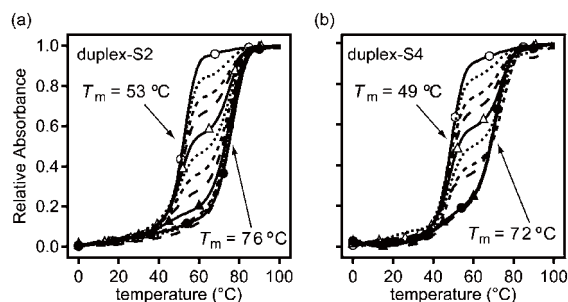


Fig. 2 Thermal denaturation experiments were performed in solutions each containing 2 μM duplex, 10 mM MOPS (pH 7.0) and 100 mM NaNO_3 in the presence of various concentrations of $\text{Ag}(\text{I})$ ions. (a) **duplex-S2** and (b) **duplex-S4**. open circles = no metal ions, open triangles = 1 equiv. $\text{Ag}(\text{I})$ ions, closed triangles = 2 equiv. $\text{Ag}(\text{I})$ ions, closed circles = 3 equiv. $\text{Ag}(\text{I})$ ions.

The metal ion-binding properties of **duplex-S2** and **duplex-S4** were evaluated by thermal denaturation. Similar to duplexes containing a T–T pair, both duplexes were stabilized by the addition of $\text{Hg}(\text{II})$ ions (for further information on the binding properties of $\text{Hg}(\text{II})$ see Fig. S4, ESI †). **Duplex-S4** was stabilized to some extent by the addition of excess $\text{Cu}(\text{II})$ ions. The same treatment, however, had no effect on the transition curve of **duplex-S2** (Fig. S10, ESI †). Thermal denaturation profiles did not change significantly in the presence of $\text{Mg}(\text{II})$, $\text{Ca}(\text{II})$, $\text{Fe}(\text{II})$, $\text{Co}(\text{II})$, $\text{Ni}(\text{II})$, $\text{Zn}(\text{II})$, $\text{Pd}(\text{II})$, $\text{Cd}(\text{II})$, or $\text{Pt}(\text{II})$ ions (Fig. S8 and S9, ESI †). In contrast, duplexes were unexpectedly and largely stabilized in the presence of $\text{Ag}(\text{I})$ ions.

Thermal denaturation profiles of **duplex-S2** and **duplex-S4** in the presence of various concentrations of $\text{Ag}(\text{I})$ are shown in Fig. 2. Both **duplex-S2** and **duplex-S4** were stabilized in the presence of two equivalents of $\text{Ag}(\text{I})$ ions ($\Delta T_m = 23^\circ\text{C}$). Additional $\text{Ag}(\text{I})$ had no effect. Thus, two equivalents of $\text{Ag}(\text{I})$ were required to fully stabilize both duplexes. In the presence of less than two equivalents of $\text{Ag}(\text{I})$ ions, two transition curves were observed in each denaturation profile for both duplexes. The origins of these transition curves are discussed below.

Fig. 3 shows ESI-MS spectra of **duplex-S2** and **duplex-S4**. In the presence of two equivalents of $\text{Ag}(\text{I})$ ions, peaks corresponding to a complex consisting of two $\text{Ag}(\text{I})$ ions and a duplex were observed (Fig. 3b and d).

The thermal denaturation profiles and the ESI-MS spectra both indicate the capture of two $\text{Ag}(\text{I})$ ions by **duplex-S2** and **duplex-S4**. The observed metal ion-binding properties of these thiopyrimidine pairs are different from those of a T–T pair, which selectively captures one $\text{Hg}(\text{II})$ ion. This is likely due to the thiocarbonyl groups, metal ion binding properties of which

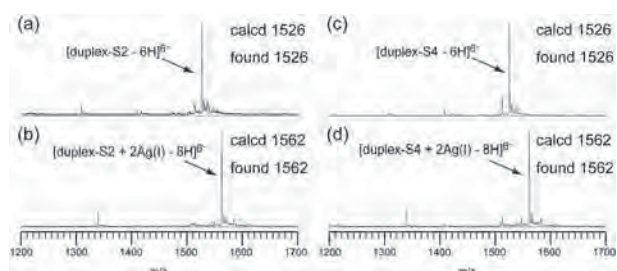


Fig. 3 ESI-MS spectra of **duplex-S2** and **duplex-S4** in the (a and c) absence and (b and d) presence of 2 equiv. of $\text{Ag}(\text{I})$ ions, respectively.

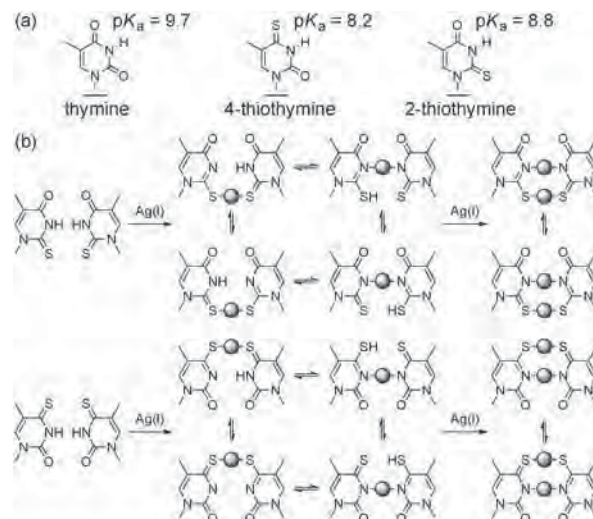


Fig. 4 (a) pK_a values and (b) proposed binding schemes of $\text{Ag}(\text{I})$ -mediated thiopyrimidine base pairs.

should be different from those of the carbonyl group of thymine. Another considerable difference between the thiopyrimidines and thymine is the relative acidity of their imino protons; pK_a values of the thiopyrimidines are smaller than that of thymine (Fig. 4a).⁵

Fig. 4b shows proposed binding schemes for the thiopyrimidine base pairs and $\text{Ag}(\text{I})$ ions. An imino or a thioenol proton of a thiopyrimidine residue, which is more acidic than the imino proton of thymine, is replaced by one $\text{Ag}(\text{I})$ ion, resulting in thiopyrimidine– $\text{Ag}(\text{I})$ –thiopyrimidine complexes (Fig. 4b). Then, another $\text{Ag}(\text{I})$ is captured by thiopyrimidine– $\text{Ag}(\text{I})$ –thiopyrimidine complexes, resulting in metallobase pairs bridged by two $\text{Ag}(\text{I})$ ions.

As mentioned above, duplexes containing the thiopyrimidine pairs were largely stabilized in the presence of $\text{Ag}(\text{I})$ ions. This is a significant deviation from the metal ion-binding properties of duplexes containing a T–T pair, on which $\text{Ag}(\text{I})$ ions have no effect. Instead, the metal ion-binding properties of the thiopyrimidine pair were more reminiscent of those of 5-fluorouracil pairs (F–F pair) in a duplex.¹⁰ Two equivalents of $\text{Ag}(\text{I})$ ions bind a F–F pair to give a F–2 $\text{Ag}(\text{I})$ –F complex.^{10,11} ESI-MS experiments showed that the binding of a second $\text{Ag}(\text{I})$ ion to form F–2 $\text{Ag}(\text{I})$ –F was relatively weak. Even in the presence of two equivalents of $\text{Ag}(\text{I})$ ions, peaks corresponding to a duplex with two $\text{Ag}(\text{I})$ ions were not observed. However, peaks corresponding to a duplex with a single $\text{Ag}(\text{I})$ ion were present.¹⁰ Megger and collaborators¹² recently reported that two $\text{Ag}(\text{I})$ ions bind Hoogsteen-type base pairs to form a metallobase pair, 1,3-dideazaadenine–2 $\text{Ag}(\text{I})$ –thymine. In their report, data from UV and CD titrations supported the binding of two $\text{Ag}(\text{I})$ ions. However, presumably due to weak $\text{Ag}(\text{I})$ ion binding, peaks corresponding to the Hoogsteen-type base pairs containing two equivalents of $\text{Ag}(\text{I})$ ions were not observed in the mass spectra. This mode of binding might be similar to that of $\text{Ag}(\text{I})$ binding in F–F pairs. Conversely, peaks corresponding to complexes consisting of two $\text{Ag}(\text{I})$ ions and a duplex containing a thiopyrimidine pair were seen in the ESI-MS spectra (Fig. 3).

Substitution of a proton with a $\text{Ag}(\text{I})$ ion in the thioenol structure, which has a relatively lower pK_a due to $\text{Ag}(\text{I})$ –N3

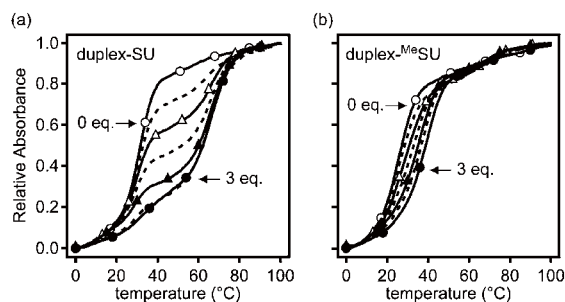


Fig. 5 Thermal denaturation experiments were performed in solutions each containing 2 μM duplex, 10 mM sodium cacodylate (pH 7), 200 mM NaClO_4 , 5 mM $\text{Mg}(\text{ClO}_4)_2$, in the presence of various concentrations of $\text{Ag}(\text{I})$ ions (0–3.0 equivalents). (a) **duplex-SU** and (b) **duplex-MeSU**. open circles = no metal ions, open triangles = 1 equiv. $\text{Ag}(\text{I})$ ions, closed triangles = 2 equiv. $\text{Ag}(\text{I})$ ions, closed circles = 3 equiv. $\text{Ag}(\text{I})$ ions.

coordination,¹³ could be a key step in the formation of stable metallobase pairs bridged by two $\text{Ag}(\text{I})$ ions (Fig. 4b). To evaluate this hypothesis, we prepared a duplex containing a 4-thiouracil–4-methylthiouracil (SU-MeSU) pair and compared its thermal denaturation profiles in the presence of various concentrations of $\text{Ag}(\text{I})$ ions (Fig. 5). To remove a predicted steric hindrance between the 5-methyl group and 4-methylthio group in 4-methylthiothymine, a uracil ring was used in these experiments. As shown in Fig. 5a, **duplex-SU**, which contained an SU-SU pair, was fully stabilized in the presence of two equivalents of $\text{Ag}(\text{I})$ ions.¹⁴ Conversely, **duplex-MeSU** was only slightly stabilized in the presence of excess $\text{Ag}(\text{I})$ ions (Fig. 5b). This indicates that the binding of a second $\text{Ag}(\text{I})$ ion is important for the stabilization of **duplex-SU**.

Consequently, a thiopyrimidine– $\text{Ag}(\text{I})$ –thiopyrimidine is not as stable as a thiopyrimidine– $2\text{Ag}(\text{I})$ –thiopyrimidine complex. Therefore, a two-phase transition was observed in denaturation profiles in the presence of less than two equivalents of $\text{Ag}(\text{I})$ ions (Fig. 2a, b, and 5a),¹⁵ the first transition corresponding to the dissociation of a free duplex and the second to the dissociation of a complex consisting of a duplex and two $\text{Ag}(\text{I})$ ions.

The above study describes the metal ion-binding properties of thiopyrimidine pairs. The binding properties of thiopyrimidine pairs were significantly different from those of unpaired bases. Thiopyrimidine-containing ODNs used in this study are commercially available and can therefore be used in a broad variety of applications in laboratories worldwide.

This study was partly supported by a Grant-in-Aid for Scientific Research (B) (21350105) and the Science Frontier “Construction and control of chemical space purposing development of new functionalized molecules and materials” (2006–2011) from the Ministry of Education, Culture, Sports, Science and Technology (MEXT), Japan.

Notes and references

- (a) J. Müller, *Nature*, 2006, **444**, 698; (b) G. H. Clever, C. Kaul and T. Carell, *Angew. Chem., Int. Ed.*, 2007, **46**, 6226–6236; (c) J. Müller, *Eur. J. Inorg. Chem.*, 2008, 3749–3763; (d) G. H. Clever and M. Shionoya, *Coord. Chem. Rev.*, 2010, **254**, 2391–2402; (e) H. Yang, K. L. Metera and H. F. Sleiman, *Coord. Chem. Rev.*, 2010, **254**, 2403–2415; (f) E. Meggers,

- P. L. Holland, W. B. Tolman, F. E. Romesberg and P. G. Schultz, *J. Am. Chem. Soc.*, 2000, **122**, 10714–10715; (g) S. Atwell, E. Meggers, G. Spraggon and P. G. Schultz, *J. Am. Chem. Soc.*, 2001, **123**, 12364–12367; (h) K. Tanaka, Y. Yamada and M. Shionoya, *J. Am. Chem. Soc.*, 2002, **124**, 8802–8803; (i) K. Tanaka, A. Tengeiji, T. Kato, N. Toyama, M. Shiro and M. Shionoya, *J. Am. Chem. Soc.*, 2002, **124**, 12494–12498; (j) N. Zimmermann, E. Meggers and P. G. Schultz, *J. Am. Chem. Soc.*, 2002, **124**, 13684–13685; (k) K. Tanaka, A. Tengeiji, T. Kato, N. Toyama and M. Shionoya, *Science*, 2003, **299**, 1212–1213; (l) C. Switzer and D. Shin, *Chem. Commun.*, 2005, 1342–1344; (m) L. Zhang and E. Meggers, *J. Am. Chem. Soc.*, 2005, **127**, 74–75; (n) K. Tanaka, G. H. Clever, Y. Takezawa, Y. Yamada, C. Kaul, M. Shionoya and T. Carell, *Nat. Nanotechnol.*, 2006, **1**, 190–194; (o) F.-A. Polonius and J. Müller, *Angew. Chem., Int. Ed.*, 2007, **46**, 5602–5604; (p) T. Ihara, T. Ishii, N. Araki, A. W. Wilson and A. Jyo, *J. Am. Chem. Soc.*, 2009, **131**, 3826–3827.
- (a) Y. Miyake, H. Togashi, M. Tashiro, H. Yamaguchi, S. Oda, M. Kudo, Y. Tanaka, Y. Kondo, R. Sawa, T. Fujimoto, T. Machinami and A. Ono, *J. Am. Chem. Soc.*, 2006, **128**, 2172–2173; (b) A. Ono, S. Cao, H. Togashi, M. Tashiro, T. Fujimoto, T. Machinami, S. Oda, Y. Miyake, I. Okamoto and Y. Tanaka, *Chem. Commun.*, 2008, 4825–4827; (c) Y. Tanaka, S. Oda, H. Yamaguchi, Y. Kondo, C. Kojima and A. Ono, *J. Am. Chem. Soc.*, 2006, **129**, 244–245; (d) Y. Tanaka, H. Yamaguchi, S. Oda, Y. Kondo, N. Nomura, C. Kojima and A. Ono, *Nucleosides, Nucleotides Nucleic Acids*, 2006, **25**, 613–624; (e) Y. Tanaka and A. Ono, *Dalton Trans.*, 2008, 4965–4974; (f) A. Ono and H. Togashi, *Angew. Chem., Int. Ed.*, 2004, **43**, 4300–4302.
- D.-L. Ma, D. S.-H. Chan, B. Y.-W. Man and C.-H. Leung, *Chem.–Asian J.*, 2011, **6**, 986–1003.
- Y. Takezawa, K. Tanaka, M. Yori, S. Tashiro, M. Shiro and M. Shionoya, *J. Org. Chem.*, 2008, **73**, 6092–6098.
- W. Saenger, *Principles of Nucleic Acid Structure*, Springer-Verlag, New York, 1987.
- (a) T. Kowalik-Jankowska, H. Kozłowski, I. Sovago, B. Nawrot, E. Sochacka and A. J. Malkiewicz, *J. Inorg. Biochem.*, 1994, **53**, 49–56; (b) T. Kowalik-Jankowska, K. Varnagy, J. Swiatek-Kozłowska, A. Jon, I. Sovago, E. Sochacka, A. Malkiewicz, J. Sychata and H. Kozłowski, *J. Inorg. Biochem.*, 1997, **65**, 257–262; (c) J. Swiatek-Kozłowska, J. Brasun, A. Dobosz, E. Sochacka and A. Glowacka, *J. Inorg. Biochem.*, 2003, **93**, 119–124; (d) A. Odani, H. Kozłowski, J. Swiatek-Kozłowska, J. Brasun, B. P. Opershall and H. Sigel, *J. Inorg. Biochem.*, 2007, **101**, 727–735; (e) J. Brasun, A. Matera, E. Sochacka, J. Swiatek-Kozłowska, H. Kozłowski, B. Opershall and H. Sigel, *J. Biol. Inorg. Chem.*, 2008, **13**, 663–674.
- O. Iranzo, H. Khalili, D. Epstein and J. Morrow, *J. Biol. Inorg. Chem.*, 2004, **9**, 462–470.
- R. S. Coleman and J. M. Siedlecki, *J. Am. Chem. Soc.*, 1992, **114**, 9229–9230.
- R. S. Coleman and E. A. Kesicki, *J. Am. Chem. Soc.*, 1994, **116**, 11636–11642.
- I. Okamoto, K. Iwamoto, Y. Watanabe, Y. Miyake and A. Ono, *Angew. Chem., Int. Ed.*, 2009, **48**, 1648–1651.
- T. Matsui, H. Miyachi, T. Baba and Y. Shigeta, *J. Phys. Chem. A*, 2011, **115**, 8504–8510.
- D. A. Megger, C. F. Guerra, J. Hoffmann, B. Brutschy, F. M. Bickelhaupt and J. Müller, *Chem.–Eur. J.*, 2011, **17**, 6533–6544.
- B. Lippart, *Prog. Inorg. Chem.*, 2005, **54**, 385–447.
- In the presence of more than two equivalents of $\text{Ag}(\text{I})$ ions, a minor denaturation curve was observed at around 40 °C. We assumed that this denaturation was due to conformational polymorphism of the duplex-SU– $2\text{Ag}(\text{I})$.
- A similar two-phase transition was observed in thermal denaturation profiles of DNA duplexes containing metal salen base pairs. G. H. Clever and T. Carell, *Angew. Chem., Int. Ed.*, 2007, **46**, 250–253.

Raman spectroscopic detection of the T-Hg^{II}-T base pair and the ionic characteristics of mercury

Tomomi Uchiyama^{1,2}, Takashi Miura², Hideo Takeuchi², Takenori Dairaku¹,
Tomoyuki Komuro^{1,2}, Takuya Kawamura¹, Yoshinori Kondo¹, Ladislav Benda³,
Vladimír Sychrovský^{3,*}, Petr Bour³, Itaru Okamoto^{4,*}, Akira Ono⁴ and
Yoshiyuki Tanaka^{1,*}

¹Laboratory of Molecular Transformation, ²Laboratory of Bio-Structural Chemistry, Graduate School of Pharmaceutical Sciences, Tohoku University, 6-3 Aza-Aoba, Aramaki, Aoba-ku, Sendai, Miyagi 980-8578, Japan, ³Department of Molecular Spectroscopy, Institute of Organic Chemistry and Biochemistry, Academy of Sciences of the Czech Republic, Flemingovo nám. 2, 16610, Praha 6, Czech Republic and ⁴Department of Material and Life Chemistry, Faculty of Engineering, Kanagawa University, 3-27-1 Rokkakubashi, Kanagawa, Yokohama, Kanagawa-ken 221-8686, Japan

Received January 10, 2012; Revised February 15, 2012; Accepted February 16, 2012

ABSTRACT

Developing applications for metal-mediated base pairs (metallo-base-pair) has recently become a high-priority area in nucleic acid research, and physicochemical analyses are important for designing and fine-tuning molecular devices using metallo-base-pairs. In this study, we characterized the Hg^{II}-mediated T-T (T-Hg^{II}-T) base pair by Raman spectroscopy, which revealed the unique physical and chemical properties of Hg^{II}. A characteristic Raman marker band at 1586 cm⁻¹ was observed and assigned to the C4=O4 stretching mode. We confirmed the assignment by the isotopic shift (¹⁸O-labeling at O4) and density functional theory (DFT) calculations. The unusually low wavenumber of the C4=O4 stretching suggested that the bond order of the C4=O4 bond reduced from its canonical value. This reduction of the bond order can be explained if the enolate-like structure (N3=C4-O4⁻) is involved as a resonance contributor in the thymine ring of the T-Hg^{II}-T pair. This resonance includes the N-Hg^{II}-bonded state (Hg^{II}-N3-C4=O4) and the N-Hg^{II}-dissociated state (Hg^{II+} N3=C4-O4⁻), and the latter contributor reduced the bond order of N-Hg^{II}. Consequently, the Hg^{II} nucleus in the T-Hg^{II}-T pair exhibited a cationic character. Natural bond orbital (NBO) analysis supports the interpretations of the Raman experiments.

INTRODUCTION

Metal-mediated nucleic acid base pairs are extensively studied molecules that are of interest because of their ability to expand the genetic code and provide new materials for nano-devices (1–15). These artificial base pairs can be made by substituting the natural nucleobases with a planar metal chelator in the DNA molecule (1–15). As an alternative, our group discovered that even the natural base, thymine, can form a stable mercury^{II}-mediated T-T base pair (T-Hg^{II}-T pair) (16–22). The RNA analogue of this molecule (U-Hg^{II}-U) also exists as a stable complex (23–25). The metal-mediated base pairs can only form with Hg^{II}, and they are used in many types of Hg^{II}-sensor (16,26–30). The DNA molecule itself has potential as a component of future nano-devices, and the introduction of a T-Hg^{II}-T pair into the sequence could enable the physical and chemical properties of such materials to be fine-tuned (31–33).

Although the T-Hg^{II}-T pair has been extensively studied since 2004 (16,17,26–33), its precise chemical structure was only revealed by ¹⁵N NMR spectroscopy in 2007 (20–22). In the NMR analysis, the thymine was ¹⁵N-labeled at N3 and incorporated into the DNA duplex **1•2**: d(CGCGTT GTCC) • d(GGACTTCGCG) (Figure 1). In the presence of the Hg^{II} ion, the thymine residues formed a T-Hg^{II}-T pair, and ¹⁵N-¹⁵N *J*-coupling across Hg^{II} (²*J*_{NN}) was detected (Figure 1c), which provided unambiguous evidence of the formation of the N3-Hg^{II}-N3 bond in the T-Hg^{II}-T pair (20–22). This *J*-coupling value was theoretically examined by density functional theory (DFT)

*To whom correspondence should be addressed. Tel: +420 220183234; Fax: +420 220183578; Email: vladimir.sychrovsky@uochb.cas.cz
Correspondence may also be addressed to Itaru Okamoto. Tel: +81 45 481 5661 (ext 3901); Email: i-okamoto@kanagawa-u.ac.jp
Correspondence may also be addressed to Yoshiyuki Tanaka. Tel./Fax: +81 22 795 5917; Email: tanaka@mail.pharm.tohoku.ac.jp

The authors wish it to be known that, in their opinion, the first two authors should be regarded as joint First Authors.

© The Author(s) 2012. Published by Oxford University Press.

This is an Open Access article distributed under the terms of the Creative Commons Attribution Non-Commercial License (<http://creativecommons.org/licenses/by-nc/3.0>), which permits unrestricted non-commercial use, distribution, and reproduction in any medium, provided the original work is properly cited.

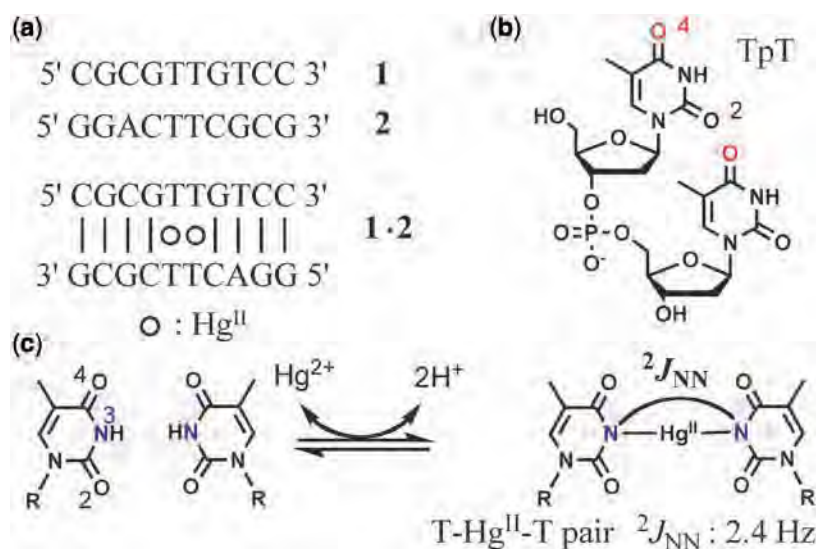


Figure 1. Sequences of DNA oligomers and the structure of the T-Hg^{II}-T pair. (a) The sequences of the DNA oligomers used for the NMR and Raman spectral measurements. (b) Chemical structure of thymidylyl (3'-5') thymidine (TpT). The numbering of each carbonyl oxygens is indicated and the labeled oxygen atoms in ¹⁸O-labeled TpT are colored in red. (c) The reaction scheme for the T-Hg^{II}-T pair formation is shown with 2-bond ¹⁵N-¹⁵N *J*-coupling (²*J*_{NN}). The numbering system for thymine is also shown, and the N3 atom is colored in blue.

calculations (34). Although various data (35–48) hinted at the chemical structure of the T-Hg^{II}-T pair prior to these studies, its chemical structure was conclusively determined by these studies (20–22,34).

However, despite elucidation of the precise chemical structure of the T-Hg^{II}-T base pair, the nature of the mercury atom in the base pair is unclear. To address this, we used Raman spectroscopy to measure the spectra of the T-Hg^{II}-T pair under different conditions. In the Raman spectra, we identified characteristic bands that were sensitive to irregular base-pair linkage that we assigned using site-specific ¹⁸O-labeling. These bands could also be interpreted using DFT calculations. Our analysis revealed several interesting properties of the N-Hg^{II} bonds, e.g. the bond order by natural bond orbital (NBO) analysis.

MATERIALS AND METHODS

DNA synthesis

DNA oligomers (CGCGTTGTCC **1** and GGACTTCGCG **2**) and non-labeled thymidylyl (3'-5') thymidine (TpT) were synthesized by the phosphoramidite method (Figure 1a and b), and purified using a reversed-phase column (COSMOSIL 5C18-AR-300; Nakalai Tesque, Kyoto, Japan). The solutions containing non-labeled TpT were evaporated under vacuum several times to remove unwanted triethylammonium acetate buffer and acetonitrile. The DNA oligomers **1** and **2** were further purified using an anion-exchange column (UNO Q-6; BIO-RAD, CA, USA) to exchange the triethylammonium counter ion with sodium. Excess NaCl was removed using a gel filtration column (TSK-GEL G3000PW; TOSOH, Tokyo, Japan) with MILLI-Q water (MILLIPORE,

MA, USA) as the mobile phase. Each oligomer was quantitated by UV absorbance at 260 nm after digestion with nuclease P1 (Yamasa, Choshi, Japan). Hg(ClO₄)₂ (Wako, Osaka, Japan) was used as the Hg^{II} source. ¹⁸O-labeled TpT at the O4 position (¹⁸O4-labeled TpT) was synthesized by the procedure shown in Supplementary Scheme S1; further details are described in the Supplementary Data.

Raman spectroscopy

To prepare the Hg^{II}-DNA complex, a solution of 2.0 mM DNA duplex **1·2** and 4.8 mM Hg(ClO₄)₂ were made, and excess Hg^{II} cations were removed using a chelating resin (Chelex 100, BIO-RAD) as described previously (20). The resulting solution was concentrated to yield the Hg^{II}-DNA complex at a final concentration of 2.0 mM for measurement purposes. To prepare the Hg^{II}-free DNA duplex, NaClO₄ was added to the 2.0 mM DNA duplex **1·2** solution to enable the final concentration of the ClO₄⁻ ion to be adjusted to 9.6 mM.

The Raman spectra of TpT were recorded using a 10 mM TpT solution containing 0–1.75 molar equivalents of Hg(ClO₄)₂ as a simple model for the system. The pH of the solution was adjusted to 6.5 by direct titration with HCl or NaOH. The Raman spectra of thymidine 5'-monophosphate (5'-TMP) were recorded under various conditions. Each sample was sealed in a glass capillary and excited with the 514.5 nm line of a Coherent Innova 70 Ar⁺ laser. The Raman scattered light was collected with a camera lens, dispersed on a Jasco NR-1800 triple spectrometer, and detected with a liquid-nitrogen-cooled CCD detector. The temperatures of the samples were maintained at 295 K. Raman scattering from the solvent was subtracted from each spectrum.

DFT calculations

The geometry of 1-methylthymine, and two possible patterns of the T-Hg^{II}-T complexes (Supplementary Figure S1) were optimized by Gaussian 03, rev. D02 (49) at the B3LYP/6-31+G(d,p) level of theory with the polarizable continuum model (PCM) of water solvent. The core electrons of the mercury atom were treated using the MWB60 relativistic pseudo-potential, while the valence electrons were treated using the MWB60 basis set. For fully optimized structures, vibrational analysis was performed and the back-scattered Raman intensities were calculated at the same level of theory. The calculated line spectra were weighted by the temperature factor (50,51) and convoluted with Lorentzian band shapes, using 5 cm⁻¹ full width at half height. ¹⁸O isotope effects were evaluated using the same force field and different oxygen masses.

The two possible topologies of the T-Hg^{II}-T complex shown in Supplementary Figure S1a and b produced almost the same spectra (Supplementary Figure S2), and the topology shown in Supplementary Figure S1a was used for comparison with experiment. Natural charges and bond orders were calculated at the B3LYP/6-31+G(d,p)/PCM(water) level with the NBO 5.0 program linked to Gaussian (49).

NMR spectra of duplex 1•2 and TpT

For the DNA duplex 1•2, 1D ¹H NMR spectra were recorded as Hg^{II}-free, Hg^{II}-bound and Hg^{II}-removed forms. We found that the Hg^{II} atoms can be removed even at temperatures below 100°C (Supplementary Figure S3). NMR spectra were also recorded for TpT to verify the complex formation of TpT with Hg^{II} (Supplementary Figures S4 and S5), and the T-Hg^{II}-T pair formations were confirmed (Supplementary Figures S3–S5).

RESULTS

Raman spectroscopic characterizations of the T-Hg^{II}-T pair

The Raman spectra of the DNA duplex 1•2 in the presence and absence of Hg(ClO₄)₂, are shown in Figure 2. Many small changes were observed in the duplex, in particular, those at 1704, 1576, 1487, 1422, 1372, 1172 and 749 cm⁻¹, caused by the complexation with Hg^{II}. In previous NMR studies (20–22), we confirmed that Hg^{II} exclusively binds to the T-T mismatch sites in the same DNA duplex 1•2 to form two successive T-Hg^{II}-T pairs, based on the observation of 2-bond ¹⁵N–¹⁵N *J*-coupling (Figure 1). Therefore, we can attribute the observed Raman spectral changes to the same Hg^{II}-binding.

Because the changes in the Raman spectra of the DNA duplex were small and were overlapped by the stronger Raman bands from the sugar-phosphate backbone and bases other than T, we used the Raman spectra of the thymidylyl (3′–5′) thymidine (TpT) for detailed studies. The spectra acquired in the presence and absence of

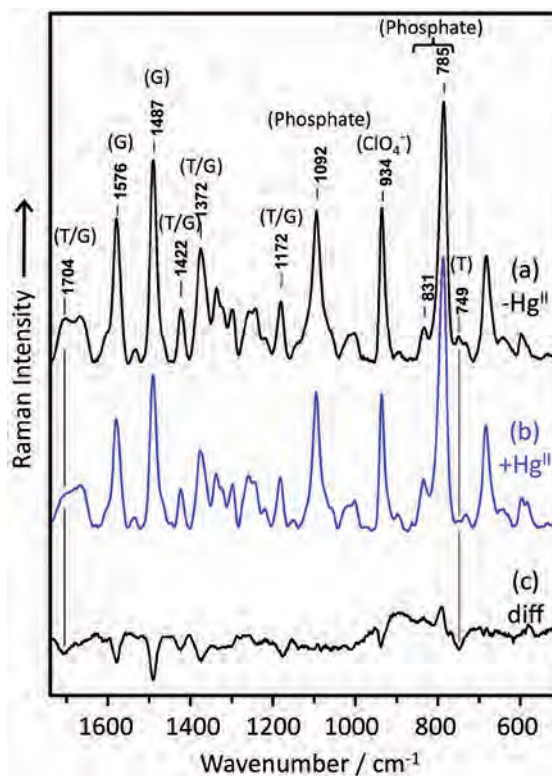


Figure 2. Raman spectra of the duplex 1•2 in the absence (a) and presence (b) of Hg^{II}, and the difference spectrum [(b)–(a)] (c) are shown. In spectrum (b), the molar ratio (Hg^{II}/duplex) was 2.0. Characteristic bands are highlighted with their wavenumber and their main origins. The band at 934 cm⁻¹ is due to ClO₄⁻. Bands at 785, 831 and 1092 cm⁻¹ were mainly due to vibration from the phosphate group. The phosphate Raman band at 1092 cm⁻¹ was used as a reference for spectral intensity. Bands at 1487 and 1576 cm⁻¹ are mainly due to guanine, and their negative peaks in spectrum (c) may be ascribed to an increase in the stacking interaction of guanosine residues upon the formation of the T-Hg^{II}-T base pair.

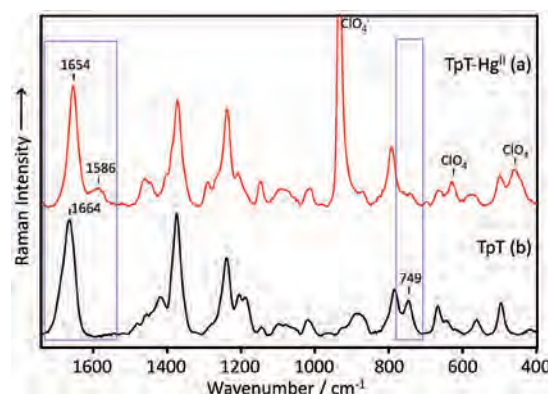


Figure 3. Raman spectra of TpT in the presence (Hg^{II}/TpT = 1.75) (a) and absence (b) of Hg^{II}. The Raman band at 934 cm⁻¹ in the spectrum of the Hg^{II}-TpT complex arises from ClO₄⁻.

Hg(ClO₄)₂ are shown in Figure 3. Clearly, the bands present at 1664 and 749 cm⁻¹ were significantly affected by the addition of Hg(ClO₄)₂, which is consistent with the duplex results.

Raman band at 749 cm⁻¹: evidence for the formation of the T-Hg^{II}-T base pair

The Raman band at 749 cm⁻¹ was perturbed upon the complexation of thymine with Hg^{II} for both the duplex **1•2** and TpT (Figures 2 and 3). We next investigated the Raman band of TpT and its Hg^{II}-complex in H₂O and D₂O (Figure 4). Upon the addition of Hg^{II} to TpT, the Raman band at 749 cm⁻¹ was suppressed (Figure 4c and d). For the Hg^{II}-free TpT in D₂O, it is shifted by 13 cm⁻¹ (Figure 4a and b). At this stage, the vibrational mode for the Raman band at 749 cm⁻¹ was found to include the contribution from the imino proton of the thymine base. To examine if the imino proton contributed to this band,

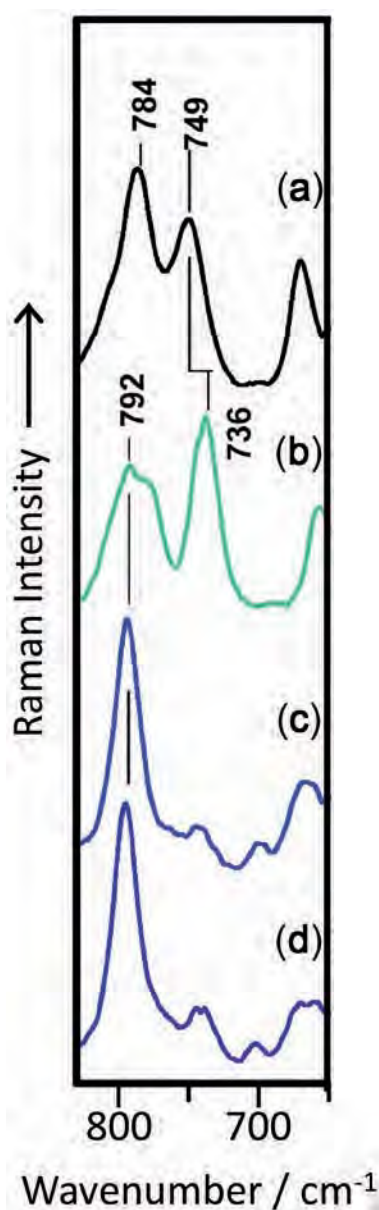


Figure 4. Raman spectra of TpT (650–830 cm⁻¹). (a) TpT alone in H₂O. (b) TpT alone in D₂O. (c) The Hg^{II}-TpT complex in H₂O. (d) The Hg^{II}-TpT complex in D₂O.

we recorded the Raman spectra of deprotonated thymidine 5'-monophosphate (5'-TMP) under strong basic conditions. The spectra obtained for 5'-TMP showed that the Raman band at 749 cm⁻¹ disappeared under strong basic conditions (Supplementary Figure S6). Thus, its absence upon the addition of Hg^{II} indicates deprotonation of N3 due to the Hg^{II}-binding. Furthermore, the spectral change that occurred at around 749 cm⁻¹ in the DNA duplex **1•2** may be similarly explained (Supplementary Figure S7). In summary, we have demonstrated the T-Hg^{II}-T pairing by the Raman spectra.

Raman bands around 1664 cm⁻¹ of TpT as a probe for thymine-Hg^{II} interaction

We observed that the Raman bands around 1664 cm⁻¹ from TpT altered upon Hg^{II}-binding. As the broad Raman band at 1664 cm⁻¹ includes contributions from both the C2=O2 and C4=O4 stretches of thymine (52,53) and these carbonyl groups are in close proximity to Hg^{II}, the Raman spectral features in this region may be useful for probing the thymine-Hg^{II} interactions. To examine the spectral changes around 1664 cm⁻¹ in detail, Hg^{II}-titration experiments of TpT were performed (Figure 5). As the concentration of Hg^{II} was increased, a shoulder band at 1685 cm⁻¹ lost intensity and a new band at 1586 cm⁻¹ emerged (Figure 5). This strongly suggests that at least one or both of the carbonyl groups C2=O2 and C4=O4 in the T-Hg^{II}-T pair were affected by Hg^{II}-binding. In addition, if the newly emerged Raman band at 1586 cm⁻¹ is assigned to the stretching mode of the carbonyl groups, it appears that quite a large perturbation occurred to the C=O double bond(s) in thymine upon Hg^{II}-complexation.

Raman spectra of ¹⁸O-labeled TpT

To determine which of the C2=O2 and C4=O4 groups of thymine was more affected by the Hg^{II}-complexation, ¹⁸O-labeled TpT at the O4 position (¹⁸O4-labeled TpT) was synthesized (Figure 1b). In Figure 6, the Raman

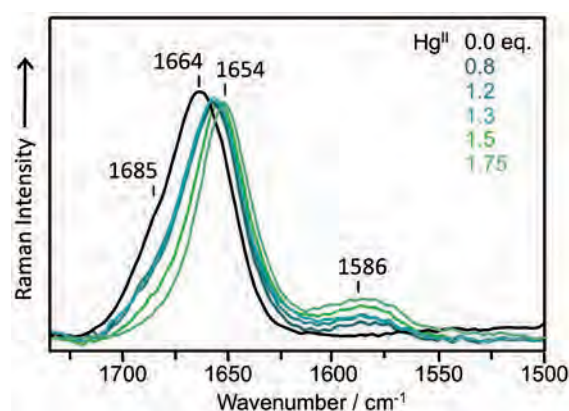


Figure 5. Hg^{II}-titration experiments of TpT by Raman spectroscopy. The molar equivalencies represented by each color are as follows: black: 0.0 eq., indigo: 0.8 eq., blue: 1.2 eq., light blue: 1.3 eq., green: 1.5 eq. and light green: 1.75 eq.

spectra of $^{18}\text{O}4$ -labeled and non-labeled TpT in the presence and absence of $\text{Hg}(\text{ClO}_4)_2$ are shown, with the main contributions provided by DFT calculations. The 1586 cm^{-1} (non-labeled) band was specifically shifted to 1570 cm^{-1} for the $^{18}\text{O}4$ -labeled TpT (Figure 6), which clearly indicates that the band originates from the vibrational mode associated with the $\text{C}4=\text{O}4$ carbonyl group.

DFT calculations of the Raman spectra

To find why the experimental wavenumber of the newly emerged Raman band at 1586 cm^{-1} (TpT) was exceptionally low for a $\text{C}=\text{O}$ stretching mode, DFT calculations of the Raman spectra for the $\text{T-Hg}^{\text{II}}\text{-T}$ base pair were performed (Figure 7). The DFT calculations reproduced the band at 1586 cm^{-1} (assignment details: Figures 6 and 7). The normal mode analysis also confirms that this band comes from the $\text{C}4=\text{O}4$ stretching vibration (Figure 8). A closer look revealed that this band was actually composed of two normal modes (Figure 8), namely, the in-phase and out-of-phase combinations of the $\text{C}=\text{O}$ stretching vibration of thymine bases in the $\text{T-Hg}^{\text{II}}\text{-T}$

pair. Both modes involve vibration of all carbonyl groups in the $\text{T-Hg}^{\text{II}}\text{-T}$ pair, but the major contribution comes from $\text{C}4=\text{O}4$.

The calculated Raman spectra of 1-methylthymine and the $\text{T-Hg}^{\text{II}}\text{-T}$ pair whose $\text{O}4$ atoms were substituted with ^{18}O are also shown in Figure 7a and c. In line with our experimental evidence, the theoretical $\text{C}4=\text{O}4$ stretching bands were shifted toward low-wavenumbers (Figure 7c and d).

The shoulder band observed at 1685 cm^{-1} in Hg^{II} -free TpT (non-labeled compound) was assigned to the $\text{C}2=\text{O}2$ stretching. Upon $^{18}\text{O}4$ -labeling, this band moved to 1660 cm^{-1} and overlapped with that of the $\text{C}5=\text{C}6$ stretching (Figure 6).

DISCUSSION

Although the wavenumber of 1586 cm^{-1} is exceptionally low for the $\text{C}4=\text{O}4$ carbonyl stretching compared to normal carbonyl stretching, the ^{18}O -isotope shift of the Raman bands demonstrated that the main contribution to the characteristic 1586 cm^{-1} band comes from the $\text{C}4=\text{O}4$ stretching mode. The DFT calculations further supported this assignment (Figure 8). The band at 1586 cm^{-1} was also observed by Morzyk-Ociepa and Michalska (48), who tentatively assigned it (based on the DFT calculations) using a deprotonated 1-methylthymine anion as a hypothetical model of the $\text{T-Hg}^{\text{II}}\text{-T}$ pair. In contrast, we have simulated the Raman spectra of the $\text{T-Hg}^{\text{II}}\text{-T}$ pair using a more realistic system that includes the heavy metal Hg^{II} (1-methylthymine- Hg^{II} (2:1) complex). Consequently, our DFT calculations further revealed that this band was composed of the collective

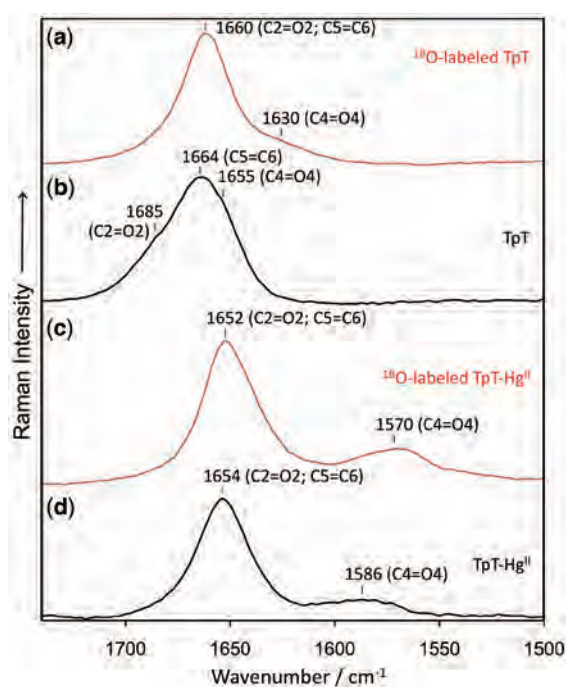


Figure 6. Raman spectra of (a) $^{18}\text{O}4$ -labeled TpT, (b) TpT, (c) $^{18}\text{O}4$ -labeled $\text{Hg}^{\text{II}}\text{-TpT}$ complex ($\text{Hg}^{\text{II}}/\text{TpT} = 1.75$) and (d) $\text{Hg}^{\text{II}}\text{-TpT}$ complex ($\text{Hg}^{\text{II}}/\text{TpT} = 1.75$). Normal modes for Hg^{II} -free 1-methylthymine (non-labeled and ^{18}O -labeled ones) are shown in Supplementary Figure S10. As a rough assignment based on the theoretical spectra (Figure 7) and the normal mode analyses (Figure 8 and Supplementary Figure S10), the main contributors to the experimental Raman bands around 1664 cm^{-1} were assigned as follows. (a) $^{18}\text{O}4$ -labeled Hg^{II} -free TpT: 1660 cm^{-1} $\text{C}2=\text{O}2$ stretching and $\text{C}5=\text{C}6$ stretching; 1630 cm^{-1} $\text{C}4=\text{O}4$ stretching. (b) Hg^{II} -free TpT: 1685 cm^{-1} $\text{C}2=\text{O}2$ stretching; 1664 cm^{-1} $\text{C}5=\text{C}6$ stretching; 1655 cm^{-1} $\text{C}4=\text{O}4$ stretching. (c) $^{18}\text{O}4$ -labeled $\text{Hg}^{\text{II}}\text{-TpT}$ complex: 1652 cm^{-1} $\text{C}2=\text{O}2$ stretching and $\text{C}5=\text{C}6$ stretching; 1570 cm^{-1} $\text{C}4=\text{O}4$ stretching. (d) $\text{Hg}^{\text{II}}\text{-TpT}$ complex: 1654 cm^{-1} $\text{C}2=\text{O}2$ stretching and $\text{C}5=\text{C}6$ stretching; 1586 cm^{-1} $\text{C}4=\text{O}4$ stretching. The assignment of the Raman bands for Hg^{II} -free TpT was principally the same as in reference (48).

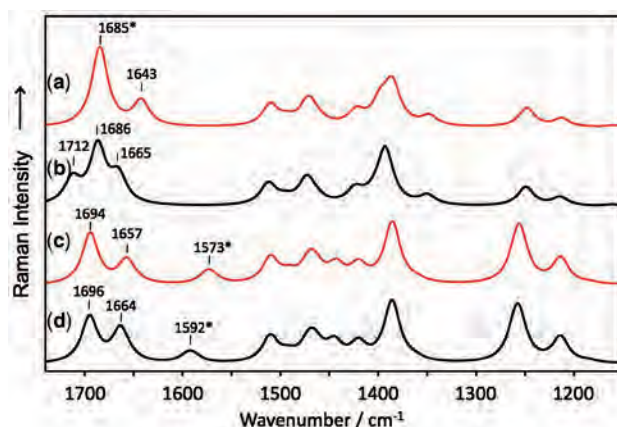


Figure 7. The high-wavenumber range of theoretical Raman spectra. (a) $^{18}\text{O}4$ -labeled 1-methylthymine; (b) non-labeled 1-methylthymine; (c) $^{18}\text{O}4$ -labeled 1-methylthymine- Hg^{II} (2:1) complex; and (d) non-labeled 1-methylthymine- Hg^{II} (2:1) complex. Throughout the calculations, 1-methylthymine was used as a model of thymidine. Major contributors to the Raman bands around the $\text{C}=\text{O}$ stretching region in the theoretical spectra are as follows: (b), 1712 cm^{-1} : $\text{C}2=\text{O}2$ stretching; 1686 cm^{-1} : $\text{C}5=\text{C}6$ stretching; 1665 cm^{-1} : $\text{C}4=\text{O}4$ stretching. (d), 1696 cm^{-1} , $\text{C}5=\text{C}6$ stretching; 1664 cm^{-1} , $\text{C}2=\text{O}2$ stretching; 1592 cm^{-1} (summation of two $\text{C}4=\text{O}4$ stretching modes in Figure 8). Asterisks indicate an apparent wavenumber due to the band overlap.

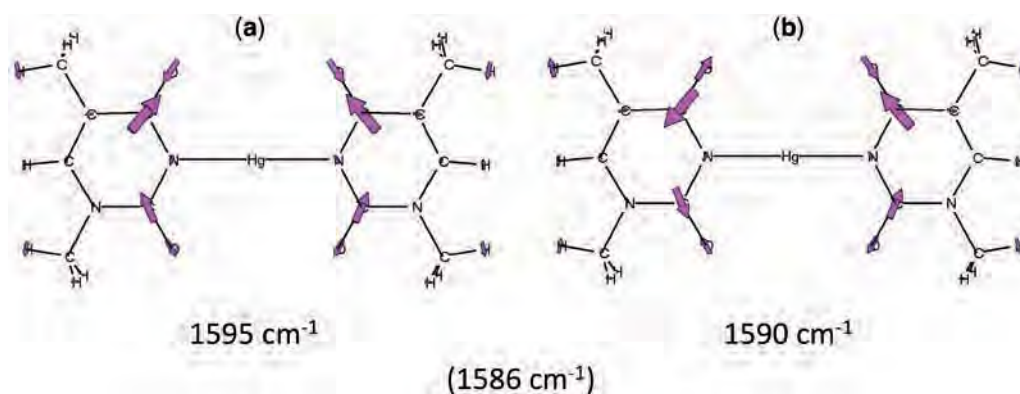


Figure 8. Normal modes for the experimental Raman bands around 1586 cm^{-1} in the $\text{T-Hg}^{\text{II}}\text{-T}$ pair. The theoretical wavenumbers (1595 and 1590 cm^{-1}) are indicated.

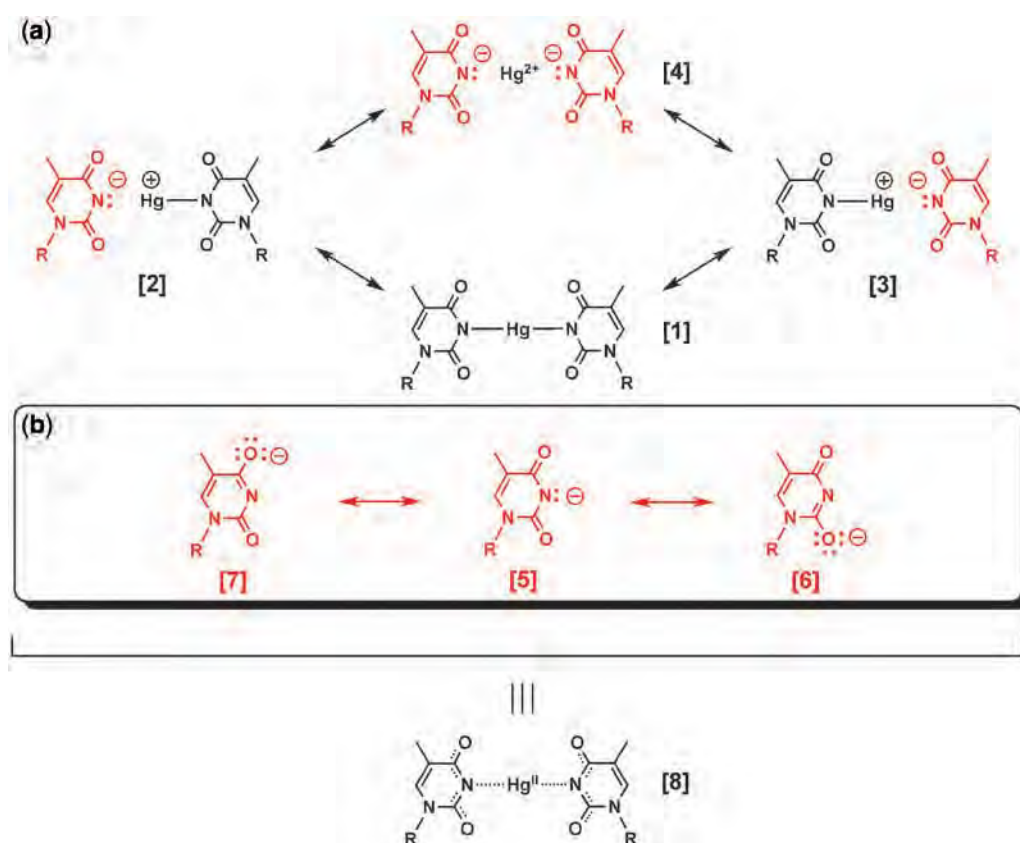


Figure 9. Resonance contributors of the $\text{T-Hg}^{\text{II}}\text{-T}$ pair. (a) Core resonance. (b) Further resonance associated with the anionic thymine **5**. The structure of **8** is the resonance hybrid (an average structure).

vibrational modes from all ‘four’ carbonyl groups in the $\text{T-Hg}^{\text{II}}\text{-T}$ base pair (Figure 8).

From a Raman spectral perspective, a lowering of the wavenumber of a carbonyl stretching mode indicates a reduced bond order of the $\text{C}=\text{O}$ bond. Hence, the resonance effect shown in Figure 9 might be responsible for this phenomenon. Within resonance contributors, the enolate-like structures **6** and **7** in Figure 9 would be

responsible for the reduced bond order. As a result, all the resonance effects shown in Figure 9 give the resonance hybrid **8** an average structure. This interpretation is consistent with the observation of the Raman band around 1588 cm^{-1} for the TpT at pH 12.4, which originates from the deprotonated thymine base at N3 and the resulting enolate-like structure of the thymine bases (Supplementary Figure S8).

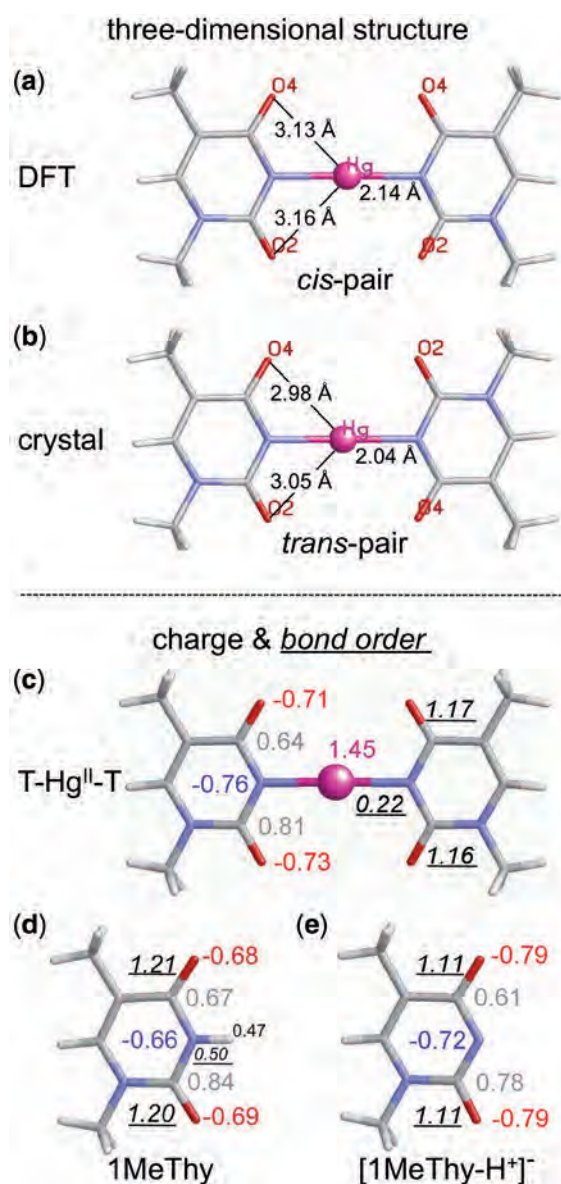


Figure 10. Results of the DFT calculations. (a) Key inter-atomic distances within the 1-methylthymine-Hg^{II} (2:1) complex. (b) Key inter-atomic distances within the crystal structure of the 1-methylthymine-Hg^{II} (2:1) complex (43). Natural charges and bond orders of (c) the T-Hg^{II}-T pair, (d) 1-methylthymine: 1MeThy and (e) deprotonated 1-methylthymine: [1MeThy-H⁺]⁻.

In addition, the same resonance effect should also reduce the effective bond order of the N-Hg^{II} bond, because in the idealized resonance contributors **2–4**, the N-Hg^{II} bond is dissociated which makes the character of the N-Hg^{II} bond ionic and weaker. The N-Hg^{II} bond is thermally cleavable even below 100°C (Supplementary Figures S3), which is indicative of an ionic character. This interpretation is consistent with our previous ¹⁵N-NMR study of T-Hg^{II}-T pairs. In that study, large down-field shifts of the ¹⁵N resonances of N3 were observed upon the complexation of thymine with Hg^{II} (20–22), and this chemical shift change was explained by

the (partially) ionic character of the N-Hg^{II} bond, based on the theory of ¹⁵N chemical shifts (21,22,54,55). However, the N-Hg^{II} bond is formally a covalent bond and, therefore, we have demonstrated that the N-Hg^{II} bonds in the T-Hg^{II}-T pair are labile covalent bonds with a significant degree of ionic character.

Next, we considered if there was any relationship between the ionicity of the N-Hg^{II} bond and the geometry of the T-Hg^{II}-T base pair calculated by the DFT method (Figure 10). The N-Hg^{II}-N linkage in the calculated geometry was essentially linear and Hg^{II}-binding to O4 seems to be weak. The calculated inter-atomic distances between the Hg atom and the keto-oxygen atoms ranged from 3.13 Å to 3.16 Å, whereas those between Hg and N3 were 2.14 Å (Figure 10a). These structural features are consistent with those observed in the crystal structure of the 1-methylthymine-Hg^{II} complex (43) (Figure 10b), namely the inter-atomic distances N3-Hg^{II}: 2.04 Å; O4-Hg^{II}: 2.98 Å; O2-Hg^{II}: 3.05 Å. This means that Hg^{II}-binding to O4 is not necessarily required for the reduction of the C4=O4 bond order.

We further characterized the bond order and the natural charge within the T-Hg^{II}-T base pair theoretically (Figure 10c–e; Supplementary Table S1). The calculated results show that the bond order of C4=O4 for the T-Hg^{II}-T pair is reduced to 1.17, from 1.21 for a neutral 1-methylthymine base (Figure 10c and d). The bond order of the N3-Hg^{II} bond becomes 0.22, which is much less than the bond order of N3-H3 (0.50; Figure 10c and d). This is consistent with our interpretation that the N-Hg^{II} bond is less covalent and rather more ionic than N-H and N-C bonds.

Consequently, the Hg^{II} atom in the T-Hg^{II}-T pair becomes cationic with a calculated natural charge of +1.45 (Figure 10c). This cationic property seems to be related to the theoretical assumption made by Voityuk (31) that the lowest unoccupied molecular orbital (LUMO) is continuously distributed around the Hg^{II} nuclei in tandem T-Hg^{II}-T base pairs. Even the LUMO orbital in a single T-Hg^{II}-T base pair possesses the same character, giving thus good pre-requisite to overlap with the density of neighboring LUMO in a consecutive T-Hg^{II}-T step (Supplementary Figure S9). This is because the Hg^{II} nucleus is the most electro-deficient part in the T-Hg^{II}-T base pairs, and may accept an additional electron. Hence, the cationic nature of the Hg^{II} nucleus is an intrinsic property of the T-Hg^{II}-T base pair.

Thus, we realistically simulated the Raman spectra, natural charges and bond orders of the T-Hg^{II}-T pair, using a model system comprising the heavy metal of Hg^{II} (1-methylthymine-Hg^{II} (2:1) complex). It is noteworthy that a metallophilic interaction between adjacent Hg^{II} nuclei in tandem U-Hg^{II}-U pairs has been recently studied (25). In combination with the findings from other theoretical studies (31,34,48), these recently proposed interactions and characteristics might be utilized to exploit the novel properties of DNA oligomers, including metal mediated base pairs like the T-Hg^{II}-T pair.

In summary, we assigned the observed Raman band at 1586 cm⁻¹ to a carbonyl stretching vibration, with the

main contribution from the C4=O4 stretching mode. The low wavenumber shift of this carbonyl vibration, measured upon adding Hg^{II}, is associated with the reduced bond order of the C4=O4 bond. This is due to the partial enolization of the thymine bases in the T-Hg^{II}-T base pair. This effect promotes a partial ionic character of the N-Hg^{II} bond and makes the Hg^{II} atom in the T-Hg^{II}-T base pair cationic. Based on the strong agreement between the experimental and theoretical data, we conclude that the Hg^{II} atom in the T-Hg^{II}-T base pairs is cationic, and that the Hg-N3 bond is less covalent and rather more ionic than N-H and N-C bonds.

SUPPLEMENTARY DATA

Supplementary Data are available at NAR Online: Supplementary Methods, Supplementary Table 1, Supplementary Scheme 1, Supplementary Figures 1–10 and Supplementary Reference [56].

ACKNOWLEDGMENTS

The authors thank Ms. Megumi Kudo for her assistance with the thermodynamics experiments.

FUNDING

Grant-in-Aid for Scientific Research (C) (18550146 and 20550145 to Y.T.) from the Ministry of Education, Culture, Sports, Science and Technology, Japan; Human Frontier Science Program (Young Investigator Grant to Y.T. and V.S.) from the Human Frontier Science Program Organization, France; Grant Agency of the Czech Republic (P205/10/0228 to V.S. and P208/11/0105 to P.B.); Intelligent Cosmos Foundation (to Y.T.); Daiichi-Sankyo Foundation of Life Science (to Y.T. and V.S.). Funding for open access charge: Human Frontier Science Program-Young Investigator Grant.

Conflict of interest statement. None declared.

REFERENCES

- Meggers,E., Holland,P.L., Tolman,W.B., Romesberg,F.E. and Schultz,P.G. (2000) A novel copper-mediated DNA base pair. *J. Am. Chem. Soc.*, **122**, 10714–10715.
- Atwell,S., Meggers,E., Spraggon,G. and Schultz,P.G. (2001) Structure of a copper-mediated base pair in DNA. *J. Am. Chem. Soc.*, **123**, 12364–12367.
- Zimmermann,N., Meggers,E. and Schultz,P.G. (2002) A novel silver(I)-mediated DNA base pair. *J. Am. Chem. Soc.*, **124**, 13684–13685.
- Zimmermann,N., Meggers,E. and Schultz,P.G. (2004) A second-generation copper(II)-mediated metallo-DNA-base pair. *Bioorg. Chem.*, **32**, 13–25.
- Weizman,H. and Tor,Y. (2001) 2,2'-bipyridine ligand: a novel building block for modifying DNA with intra-duplex metal complexes. *J. Am. Chem. Soc.*, **123**, 3375–3376.
- Tanaka,K. and Shionoya,M. (1999) Synthesis of a novel nucleoside for alternative DNA base pairing through metal complexation. *J. Org. Chem.*, **64**, 5002–5003.
- Tanaka,K., Yamada,Y. and Shionoya,M. (2002) Formation of silver(I)-mediated DNA duplex and triplex through an alternative base pair of pyridine nucleobases. *J. Am. Chem. Soc.*, **124**, 8802–8803.
- Tanaka,K., Tengeji,A., Kato,T., Toyama,N., Shiro,M. and Shionoya,M. (2002) Efficient incorporation of a copper hydroxypyridone base pair in DNA. *J. Am. Chem. Soc.*, **124**, 12494–12498.
- Tanaka,K., Tengeji,A., Kato,T., Toyama,N. and Shionoya,M. (2003) A discrete self-assembled metal array in artificial DNA. *Science*, **299**, 1212–1213.
- Switzer,C. and Shin,D. (2005) A pyrimidine-like nickel(II) DNA base pair. *Chem. Commun.*, **2005**, 1342–1344.
- Switzer,C., Sinha,S., Kim,P.H. and Heuberger,B.D. (2005) A purine-like nickel(II) base pair for DNA. *Angew. Chem. Int. Ed.*, **44**, 1529–1532.
- Clever,G.H., Kaul,C. and Carell,T. (2007) DNA-metal base pairs. *Angew. Chem. Int. Ed.*, **46**, 6226–6236.
- Müller,J. (2008) Metal-ion-mediated base pairs in nucleic acids. *Eur. J. Inorg. Chem.*, **2008**, 3749–3763.
- Johannsen,S., Korth,M.M.T., Schnabl,J. and Sigel,R.K.O. (2009) Exploring metal ion coordination to nucleic acids by NMR. *Chimia*, **63**, 146–152.
- Johannsen,S., Megger,N., Böhme,D., Sigel,R.K.O. and Müller,J. (2010) Solution structure of a DNA double helix with consecutive metal-mediated base pairs. *Nat. Chem.*, **2**, 229–234.
- Ono,A. and Togashi,H. (2004) Highly selective oligonucleotide-based sensor for mercury(II) in aqueous solutions. *Angew. Chem. Int. Ed.*, **43**, 4300–4302.
- Miyake,Y. and Ono,A. (2005) Fluorescent sensor for redox environment: a redox controlled molecular device based on the reversible mercury mediated folded structure formation of oligothymidylate. *Tetrahedron Lett.*, **46**, 2441–2443.
- Miyake,Y., Togashi,H., Tashiro,M., Yamaguchi,H., Oda,S., Kudo,M., Tanaka,Y., Kondo,Y., Sawa,R., Fujimoto,T. *et al.* (2006) Mercury(II)-mediated formation of thymine-Hg^{II}-thymine base pairs in DNA duplexes. *J. Am. Chem. Soc.*, **128**, 2172–2173.
- Tanaka,Y., Yamaguchi,H., Oda,S., Nomura,M., Kojima,C., Kondo,Y. and Ono,A. (2006) NMR spectroscopic study of a DNA duplex with mercury-mediated T-T base pairs. *Nucleosides Nucleotides Nucleic Acids*, **25**, 613–624.
- Tanaka,Y., Oda,S., Yamaguchi,H., Kondo,Y., Kojima,C. and Ono,A. (2007) ¹⁵N-¹⁵N J-coupling across Hg^{II}: Direct observation of Hg^{II}-mediated T-T base pairs in a DNA duplex. *J. Am. Chem. Soc.*, **129**, 244–245.
- Tanaka,Y. and Ono,A. (2008) Nitrogen-15 NMR spectroscopy of N-metallated nucleic acids: insights into ¹⁵N NMR parameters and N-metal bonds. *Dalton Trans.*, **2008**, 4965–4974.
- Tanaka,Y. and Ono,A. (2009) Structural Studies on Mercury(II)-mediated T-T Base-pair with NMR Spectroscopy. In: Hadjilias,N. and Sletten,E. (eds), *Metal Complexes—DNA Interactions*. Wiley, West Sussex, UK.
- Johannsen,S., Paulus,S., Düpre,N., Müller,J. and Sigel,R.K.O. (2008) Using in vitro transcription to construct scaffolds for one-dimensional arrays of mercuric ions. *J. Inorg. Biochem.*, **102**, 1141–1151.
- Kozasa,T., Miyakawa,Y., Ono,A. and Torigoe,H. (2008) The specific interaction between metal cation and mismatch base pair in duplex RNA. *Nucleic Acids Symp. Ser.*, **52**, 197–198.
- Benda,L., Straka,M., Tanaka,Y. and Sychrovský,V. (2011) On the role of mercury in the non-covalent stabilisation of consecutive U-Hg^{II}-U metal-mediated nucleic acid base pairs: metallophilic attraction enters the world of nucleic acids. *Phys. Chem. Chem. Phys.*, **13**, 100–103.
- Wang,Z., Zhang,D.Q. and Zhu,D.B. (2005) A sensitive and selective “turn on” fluorescent chemosensor for Hg(II) ion based on a new pyrene-thymine dyad. *Anal. Chim. Acta*, **549**, 10–13.
- Tang,Y.L., He,F., Yu,M.H., Feng,F.D., An,L.L., Sun,H., Wang,S., Li,Y.L. and Zhu,D.B. (2006) A reversible and highly selective fluorescent sensor for mercury(II) using poly (thiophene) that contain thymine moieties. *Macromol. Rapid Commun.*, **27**, 389–392.
- Lee,J.S., Han,M.S. and Mirkin,C.A. (2007) Colorimetric detection of mercuric ion (Hg²⁺) in aqueous media using DNA-functionalized gold nanoparticles. *Angew. Chem. Int. Ed. Engl.*, **46**, 4093–4096.

29. Liu, J. and Lu, Y. (2007) Rational design of “turn-on” allosteric DNase catalytic beacons for aqueous mercury ions with ultrahigh sensitivity and selectivity. *Angew. Chem. Int. Ed. Engl.*, **46**, 7587–7590.
30. Wang, Z., Heon Lee, J. and Lu, Y. (2008) Highly sensitive “turn-on” fluorescent sensor for Hg²⁺ in aqueous solution based on structure-switching DNA. *Chem. Commun.*, **2008**, 6005–6007.
31. Voityuk, A.A. (2006) Electronic Coupling Mediated by Stacked [Thymine-Hg-Thymine] Base Pairs. *J. Phys. Chem. B*, **110**, 21010–21013.
32. Joseph, J. and Schuster, G.B. (2007) Long-distance radical cation hopping in DNA: the effect of thymine-Hg(II)-thymine base pairs. *Org. Lett.*, **9**, 1843–1846.
33. Ito, T., Nikaido, G. and Nishimoto, S. (2007) Effects of metal binding to mismatched base pairs on DNA-mediated charge transfer. *J. Inorg. Biochem.*, **101**, 1090–1093.
34. Bagno, A. and Saielli, G.J. (2007) Metal-mediated J-coupling in DNA base pairs: Relativistic DFT predictions. *J. Am. Chem. Soc.*, **129**, 11360–11361.
35. Katz, S. (1952) The reversible reaction of sodium thymonucleate and mercuric chloride. *J. Am. Chem. Soc.*, **74**, 2238–2245.
36. Thomas, C.A. (1954) The interaction of HgCl₂ with sodium thymonucleate. *J. Am. Chem. Soc.*, **76**, 6032–6034.
37. Dove, W.F. and Yamane, T. (1960) The complete retention of transforming activity after reversal of the interaction of DNA with mercuric ion. *Biochem. Biophys. Res. Commun.*, **1960**, 608–612.
38. Yamane, T. and Davidson, N. (1961) On the complexing of deoxyribonucleic acid (DNA) by mercuric ion. *J. Am. Chem. Soc.*, **83**, 2599–2607.
39. Katz, S. (1963) Reaction of Hg(II) and double-stranded polynucleotides a step-function theory and its significance. *Biochim. Biophys. Acta*, **68**, 240–253.
40. Eichhorn, G.L. and Clark, P. (1963) Reaction of mercury(II) with nucleosides. *J. Am. Chem. Soc.*, **85**, 4020–4025.
41. Simpson, R.B. (1964) Association constants of methylmercuric+ mercuric ions with nucleosides. *J. Am. Chem. Soc.*, **86**, 2059–2065.
42. Carrabine, J.A. (1974) Stereochemistry of nucleic acids and their constituents. 16. Mercury binding to nucleic acids—crystal and molecular structures of 2:1 complexes of uracil-mercuric chloride and dihydrouracil-mercuric chloride. *Biochemistry*, **10**, 292–299.
43. Kosturko, L.D., Folzer, C. and Stewart, R.F. (1974) Crystal and molecular-structure of a 2:1 complex of 1-methylthymine-mercury(II). *Biochemistry*, **13**, 3949–3952.
44. Mansy, S. and Tobias, R.S. (1975) Heavy metal-nucleotide reactions 4. Nature of reaction between mercury(ii) and uridine or thymidine—vibrational spectroscopic studies on binding to N(3), C(4)=O, and C(5) of uracil base. *Inorg. Chem.*, **14**, 287–291.
45. Bunzel, E., Boone, C., Joly, H., Kumar, R. and Norris, A.R. (1985) Metal ion-biomolecule interactions. Part 12. ¹H and ¹³C NMR evidence for the preferred reaction of thymidine over guanosine in exchange and competition reactions with mercury(II) and methylmercury(II). *J. Inorg. Biochem.*, **25**, 61–73.
46. Gruenwedel, D.W., Cruikshank, M.K. and Smith, G.M. (1993) Effect of Hg(II) on d(GCGCATATGCGC)₂ conformation - UV absorption and circular-dichroism studies. *J. Inorg. Biochem.*, **52**, 251–261.
47. Kuklenyik, Z. and Marzilli, L.G. (1996) Site-selective binding to a DNA hairpin. relationship of sequence-dependent intra- and interstrand cross-linking to the hairpin-duplex conformational transition. *Inorg. Chem.*, **35**, 5654–5662.
48. Morzyk-Ociepa, B. and Michalska, D. (2001) Vibrational spectra of 1-methylthymine complexes with mercury(II) and potassium and ab initio calculations of the 1-MeT anion. *J. Mol. Struct.*, **598**, 133–144.
49. Frisch, M.J., Trucks, G.W., Schlegel, H.B., Scuseria, G.E., Robb, M.A., Cheeseman, J.R., Montgomery, J.A. Jr, Vreven, T., Kudin, K.N., Burant, J.C. et al. (2009), Gaussian 09, Revision A.02; Gaussian, Inc.: Wallingford CT.
50. Polavarapu, P.L. (1998) *Vibrational Spectra: Principles and Applications with Emphasis on Optical Activity*. Elsevier, Amsterdam, pp. 193–405.
51. Buděšínský, M., Daněček, P., Bednárová, L., Kapitán, J., Baumruk, V. and Bouř, P. (2008) Comparison of quantitative conformer analyses by nuclear magnetic resonance and Raman optical activity spectra for model dipeptides. *J. Phys. Chem. A*, **112**, 8633–8640.
52. Szczepaniak, K., Szczesniak, M.M. and Person, W.B. (2000) Raman and infrared spectra of thymine. A matrix isolation and DFT study. *J. Phys. Chem. A*, **104**, 3852–3863.
53. Morzyk-Ociepa, B., Nowak, M.J. and Michalska, D. (2004) Vibrational spectra of 1-methylthymine: matrix isolation, solid state and theoretical studies. *Spectrochim. Acta A*, **60**, 2113–2123.
54. Levy, G.C. and Lichiter, R.L. (1979) *Nitrogen-15 Nuclear Magnetic Resonance Spectroscopy*. Wiley, New York.
55. de Dios, A.C. (1996) Ab initio calculations of the NMR chemical shift. *Prog. Nucl. Magn. Reson. Spectr.*, **29**, 229–278.
56. Sklenář, V., Píotko, M., Leppik, R. and Saudek, V. (1993) Gradient-tailored water suppression for ¹H-¹⁵N HSQC experiments optimized to retain full sensitivity. *J. Magn. Reson. A*, **102**, 241–245.

Ag^I Ion Mediated Formation of a C–A Mismatch by DNA Polymerases**

Tatsuya Funai, Yuki Miyazaki, Megumi Aotani, Eriko Yamaguchi, Osamu Nakagawa, Shun-ichi Wada, Hidetaka Torigoe, Akira Ono, and Hidehito Urata*

DNA forms a double-stranded structure through the formation of adenine–thymine (A–T) and guanine–cytosine (G–C) Watson–Crick base pairs.^[1] The selectivity of the hydrogen bonding between bases is essential for the replication and expression of genetic information. For two decades, the development of an artificial base pair has been an area of research with the goal of expanding the genetic alphabet.^[2] Several groups have reported artificial base pairs formed by non-Watson–Crick hydrogen bonding^[3] and hydrophobic interaction based on shape complementarity.^[4] Some of these alternative base pairs, such as isoguanine–isocytosine,^[5] dκ–dX,^[6] dZ–dF,^[7] dPICS–dPICs,^[8] dImN^O–dNaO^N,^[9] and dDs–dPa^[10] pairs, were reported to be recognized and incorporated into a primer strand by DNA polymerases.

Metal-mediated base pairs are formed by the coordination of metal ions to natural or artificial bases,^[11] and have attracted considerable interest for nanodevices. Recently, Ono et al. reported that Hg^{II} and Ag^I ions specifically stabilize the thymine–thymine (T–T) and cytosine–cytosine (C–C) mismatches in oligodeoxynucleotide (ODN) duplexes through the formation of the T–Hg^{II}–T and C–Ag^I–C base pairs, respectively (Figure 1a).^[12–14] Also, the formation of a U–Hg^{II}–U base pair in RNA was reported.^[15] We focused on the biological relevance of metal-mediated base pairs and discovered that in the presence of Hg^{II} ions, DNA polymerases used thymidine 5'-triphosphate (TTP) to incorporate thymidine at the site opposite a thymine in the template strand and elongated the primer to synthesize a full-length product.^[16] Following our discovery, Park and co-workers reported the extension reactions of primer strands that have a T–T or C–C mismatch at the 3'-terminus, in the presence of

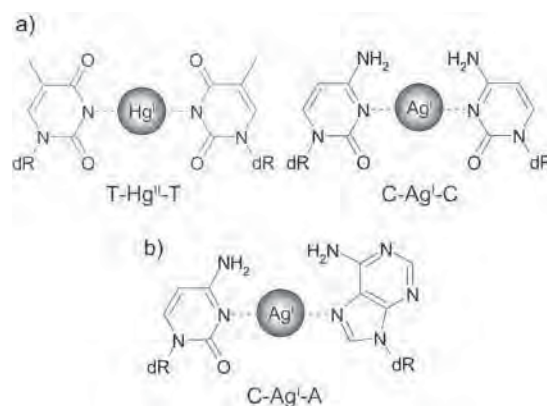


Figure 1. a) Chemical formulas of T–Hg^{II}–T and C–Ag^I–C base pairs, and b) a possible structure of the C–Ag^I–A base pair. dR = deoxyribose.

Hg^{II} or Ag^I ions, respectively.^[17] Also, an artificial Cu^{II}-mediated base pair recognized by DNA polymerases was reported.^[18] However, the Ag^I ion mediated incorporation of a deoxynucleotide into a primer strand by DNA polymerases has not yet been reported. The discovery of natural and artificial metal-mediated base pairs recognized by polymerases may increase the possibility of replicating and amplifying artificial metal-containing DNA nanodevices. Herein, we report a primer extension reaction in the presence of Ag^I ions.

The primer extension experiments were carried out using the primed template shown in Figure 2a with the Klenow fragment (KF) DNA polymerase. In the presence of dATP, dGTP, and dCTP, the extension reactions afforded the full-length product regardless of the presence or absence of Ag^I ions (Figure 2b, lanes 1 and 2). This result shows that the polymerase activity is not inhibited by Ag^I ions at the concentration of 30 μM. In the presence of dATP and dCTP, the reaction without Ag^I ions was terminated at the site opposite the C residue in the template to yield the 19-mer product (lane 3). In contrast, as Ag^I ion concentration was increased (1–50 μM), KF elongated the primer to yield the full-length 24-mer as the major product (lanes 4–9). We also used an extended primed template, which contains two C residues in the single-strand region of the template, KF also afforded the full-length product but with reduced efficiency (see Figure S1 in the Supporting Information). At higher Ag^I ion concentrations (500–1000 μM), the elongation was inhibited and the reactions produced weaker bands on the gel, probably because of the aggregation of DNA (see Figure S2 in the Supporting Information). Furthermore, KOD Dash and Taq DNA polymerases also catalyzed this reaction, meaning that this phenomenon is not specific to KF

[*] T. Funai, Y. Miyazaki, M. Aotani, E. Yamaguchi, Dr. O. Nakagawa, Dr. S. Wada, Prof. H. Urata
Osaka University of Pharmaceutical Sciences
4-20-1 Nasahara, Takatsuki, Osaka 569-1094 (Japan)
E-mail: urata@gly.oups.ac.jp

Prof. H. Torigoe
Department of Applied Chemistry, Faculty of Science, Tokyo
University of Science
1-3 Kagurazaka, Shinjuku-ku, Tokyo 162-8601 (Japan)

Prof. A. Ono
Department of Material & Life Chemistry, Faculty of Engineering,
Kanagawa University
3-27-1 Rokkakubashi, Kanagawa-ku, Yokohama 221-8686 (Japan)

[**] This work was supported in part through a Grant-in-Aid for Scientific Research from the Ministry of Education, Science, Sports and Technology (Japan).

Supporting information for this article (experimental details) is available on the WWW under <http://dx.doi.org/10.1002/anie.201109191>.

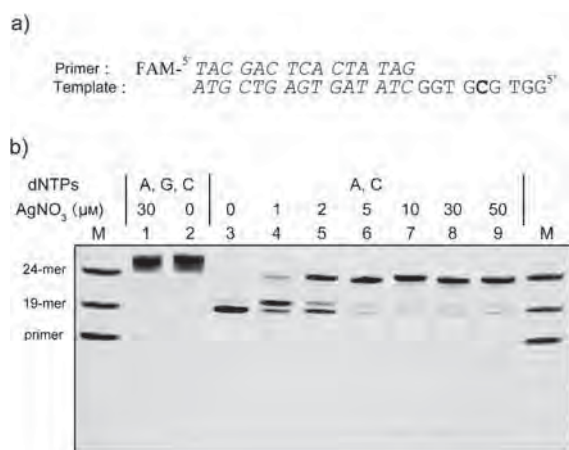


Figure 2. a) Sequences of the template and primer strands. The primer was labeled with fluorescein amidite (FAM) at the 5' end. b) Effects of Ag^I ion concentration on the primer extension reaction by the Klenow fragment (KF). The reaction mixtures (20 μL) containing 100 nM primer, 150 nM template, 20 μM dNTPs, 100 mM NaOAc, 10 mM Tris-AcOH (pH 7.9), 10 mM Mg(OAc)₂, 5 mM NH₄Cl, 0.3 units of KF, and 8 μM dithiothreitol (DTT) in the presence or absence of various concentrations of AgNO₃ were incubated at 37 °C for 1 h. The reactions were quenched by adding 100 mM DTT (0.5 μL) and a gel loading solution (2.28 μL) containing 8 M urea, 50% sucrose, and 0.2% bromophenol blue, and the mixtures were immediately heated at 90 °C for 10 min. After cooling, the mixtures were analyzed by denaturing 20% PAGE. M indicates markers for the primer, 19-mer and 24-mer.

(see Figure S3 in the Supporting Information). To exclude the effects of the counteranion (nitrate), the reactions were also carried out in the presence of Ag^I(NO₃), Na^I(NO₃), or Mg^{II}(NO₃)₂. Only Ag^I(NO₃) promoted the reaction (see Figure S4); thus, we conclude that it is the Ag^I ions that mediate the incorporation of cytosine or adenine into the site opposite the C residue in the template by KF.

Next, to confirm the kind of nucleotide incorporated into the site opposite the C residue in the template, single nucleotide insertion reactions were carried out (Figure 3). KF incorporated guanine through the formation of a Watson-Crick G-C base pair to yield the 20-mer (*n* + 1) product regardless of the presence or absence of Ag^I ions (lanes 3 and 4). In the absence of Ag^I ions, adenine, cytosine, or thymidine were not incorporated into the site opposite the C residue in the template and the primer was degraded by the 3'→5' exonuclease activity of the enzyme to afford *n* - 1, *n* - 2, and *n* - 6 products, respectively (lanes 2, 6, and 8). The 3'→5' exonuclease activity of KF competes with the polymerization activity. In the absence of the complementary dNTP (in this case dGTP), the exonuclease domain of KF seems to degrade the primer strand to yield truncated products that have the same base at the 3'-terminus as the dNTP that has been added to the reaction. Unexpectedly, in the presence of Ag^I ions, KF misincorporated adenine into the site opposite the C residue in the template (lane 1) to yield the 20-mer (*n* + 1) product together with a trace amount of the 18-mer (*n* - 1) product. However, the enzyme did not misincorporate cytosine into the same site at all (lane 5). Furthermore, even 3'→5' exonuclease-deficient KF (KF exo⁻) gave the same results (Figure S5, lanes 5 and 6). These results indicate that when

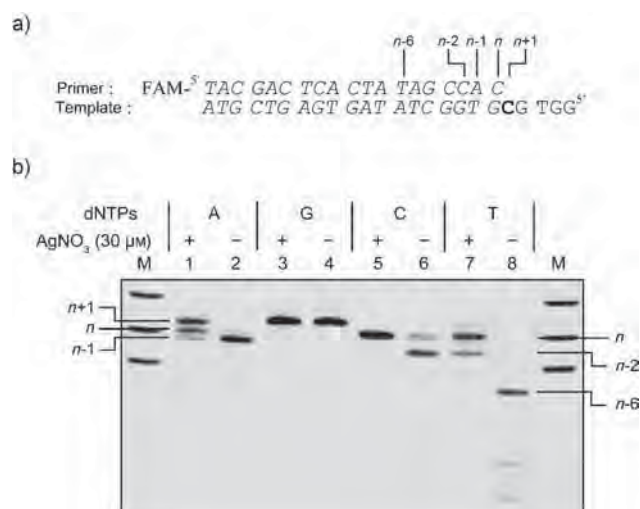


Figure 3. a) Sequences of the template and 5'-FAM-labeled primer strands. b) Single nucleotide insertions at the site opposite the C residue in the template strand were carried out by KF. The reaction conditions are the same as those indicated in Figure 2b. M indicates markers for the 15-mer, primer, and 24-mer.

dGTP was absent, KF specifically incorporated adenine into the site opposite the C residue in the template, probably through the formation of C-Ag^I-A, a silver(I)-mediated base pair. The composition of the full-length products of the Ag^I-promoted reaction was confirmed by MALDI-TOF mass spectroscopy (see Figure S6 in the Supporting Information).

To investigate the effects of other metal ions on the reaction, we performed the primer extension reaction in the presence of Mn^{II}, Fe^{II}, Fe^{III}, Co^{II}, Ni^{II}, Cu^I, Cu^{II}, Zn^{II}, Cd^{II}, Au^I, Au^{III}, Hg^{II}, Tl^I, or Pb^{II}. Figure 4 shows the relative amounts of the full-length product of the reactions catalyzed by KF. Although the reaction was not highly specific to Ag^I ions, the Ag^I ion-mediated reaction gave much higher yield than any of the other metal-mediated reactions. Some metal ions, such as Mn^{II}, Cu^I, and Cu^{II}, did catalyze the reaction but with low efficiency and reproducibility.

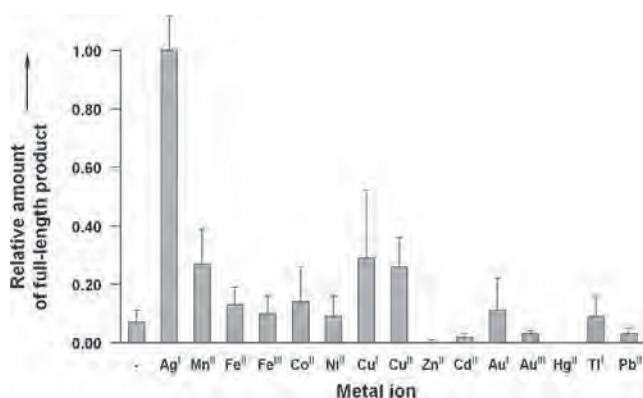


Figure 4. Effects of various metal ions on the primer extension reaction catalyzed by KF. Shown are the amounts of the full-length products of metal ion mediated reactions relative to that of Ag^I ion mediated reaction. Values are averages ± the standard deviation determined by at least five independent experiments. The reactions contained 30 μM metal ions and the other conditions are the same as those indicated in Figure 2b.

The molecular basis of the Ag^{I} -promoted selective incorporation of adenine rather than cytosine is still ambiguous. The UV melting experiments demonstrated that the C–C mismatch-containing duplex was more stable than the C–A mismatch-containing duplex by addition of Ag^{I} ions (see Table S1 in the Supporting Information). It was reported that when KF exo^- misincorporates nucleotides to form a purine–purine hydrogen-bonded mispair, the incoming dNTP rotates to the *syn* conformation to maintain the $\text{C1}'\text{--}\text{C1}'$ distance between complementary residues of canonical B-DNA, however, the purine residue in the template is maintained in the normal *anti* conformation.^[19] Thus, we investigated the incorporation of cytosine opposite an A residue in the template strand with added Ag^{I} ions (Figure 5). In the presence of dATP and dCTP, however, the reactions were terminated at the site opposite the A residue in the template strand even in the presence of Ag^{I} ions (lanes 4–9). This result may suggest that an incoming dATP rotates to the *syn* conformation and coordinates to an Ag^{I} ion with its Hoogsteen face (Figure 1b) to maintain the $\text{C1}'\text{--}\text{C1}'$ distance of B-DNA as reported in 1-deazaadenine-containing oligonucleotides.^[20] Indeed, the preferential binding of Ag^{I} -modified 1-methylcytosine to the N7 position of 9-methyladenine was reported.^[21] The *anti* to *syn* rotation of the dA residue in oligonucleotides would be energetically more disadvantageous than that of the incoming dATP. Therefore, the Ag^{I} -mediated stabilization of the C–A mismatch-containing duplex (shown by the UV melting experiments; Table S1) may be compensated by the energy required for the *anti* to *syn* rotation of the dA residue in the template strand.

In conclusion, we demonstrated that KF does not incorporate cytosine into the site opposite a C residue in the template strand even in the presence of Ag^{I} ions. Instead, adenine was shown to be incorporated opposite the C residue in the template strand by KF in the presence of Ag^{I} ions, probably through the formation of a silver(I)-mediated C– Ag^{I} –A base pair. Our findings may open up new possibilities for the discovery of additional metal-mediated base pairs recognized by DNA polymerases, leading to the construction

of a metal ion-triggered replicating system and the enzymatic preparation of metal-containing DNA nanodevices.

Received: December 28, 2011

Revised: April 16, 2012

Published online: May 29, 2012

Keywords: DNA polymerases · DNA recognition · metal ion-mediated base pairs · primer extension · silver ions

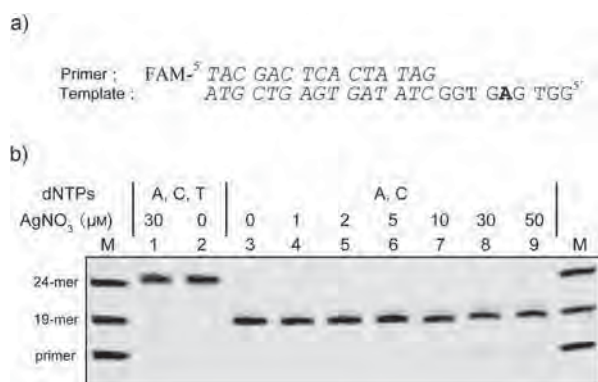


Figure 5. a) Sequences of the template and 5'-FAM-labeled primer strands. b) Effects of Ag^{I} ion concentration on the incorporation of cytosine opposite adenine in the template by KF. The reaction conditions are the same as those indicated in Figure 2b. M indicates markers for the primer, 19-mer, and 24-mer.

- [1] J. D. Watson, F. H. Crick, *Nature* **1953**, *171*, 737–738.
- [2] F. Wojciechowski, C. J. Leumann, *Chem. Soc. Rev.* **2011**, *40*, 5669–5679.
- [3] J. J. Voegel, S. A. Benner, *J. Am. Chem. Soc.* **1994**, *116*, 6929–6930.
- [4] B. A. Schweitzer, E. T. Kool, *J. Am. Chem. Soc.* **1995**, *117*, 1863–1872.
- [5] C. Switzer, S. E. Moroney, S. A. Benner, *J. Am. Chem. Soc.* **1989**, *111*, 8322–8323.
- [6] J. A. Piccirilli, T. Krauch, S. E. Moroney, S. A. Benner, *Nature* **1990**, *343*, 33–37.
- [7] K. M. Guckian, T. R. Krugh, E. T. Kool, *Nat. Struct. Biol.* **1998**, *5*, 954–959.
- [8] D. L. McMinn, A. K. Ogawa, Y. Wu, J. Liu, P. G. Schultz, F. E. Romesberg, *J. Am. Chem. Soc.* **1999**, *121*, 11585–11586.
- [9] N. Minakawa, S. Ogata, M. Takahashi, A. Matsuda, *J. Am. Chem. Soc.* **2009**, *131*, 1644–1645.
- [10] I. Hirao, M. Kimoto, T. Mitsui, T. Fujiwara, R. Kawai, A. Sato, Y. Harada, S. Yokoyama, *Nat. Methods* **2006**, *3*, 729–735.
- [11] a) G. H. Clever, C. Kaul, T. Carell, *Angew. Chem.* **2007**, *119*, 6340–6350; *Angew. Chem. Int. Ed.* **2007**, *46*, 6226–6236; b) K. Tanaka, A. Tengeiji, T. Kato, N. Toyama, M. Sionoya, *Science* **2003**, *299*, 1212–1213; c) G. H. Clever, T. Carell, *Angew. Chem.* **2007**, *119*, 254–257; *Angew. Chem. Int. Ed.* **2007**, *46*, 250–253; d) C. Switzer, S. Shinha, P. H. Kim, B. D. Heuberger, *Angew. Chem.* **2005**, *117*, 1553–1556; *Angew. Chem. Int. Ed.* **2005**, *44*, 1529–1532; e) E. Meggers, P. L. Holland, W. B. Tolman, F. E. Romesberg, P. G. Schultz, *J. Am. Chem. Soc.* **2000**, *122*, 10714–10715; f) S. Johannsen, N. Megger, D. Böhme, R. K. O. Sigel, J. Müller, *Nat. Chem.* **2010**, *2*, 229–234.
- [12] A. Ono, H. Torigoe, Y. Tanaka, I. Okamoto, *Chem. Soc. Rev.* **2011**, *40*, 5855–5866.
- [13] a) Y. Miyake, H. Togashi, M. Tashiro, H. Yamaguchi, S. Oda, M. Kudo, Y. Tanaka, Y. Kondo, R. Sawa, T. Fujimoto, T. Machinami, A. Ono, *J. Am. Chem. Soc.* **2006**, *128*, 2172–2173; b) Y. Tanaka, S. Oda, H. Yamaguchi, Y. Kondo, C. Kojima, A. Ono, *J. Am. Chem. Soc.* **2007**, *129*, 244–245.
- [14] A. Ono, S. Cao, H. Togashi, M. Tashiro, T. Fujimoto, T. Machinami, S. Oda, Y. Miyake, I. Okamoto, Y. Tanaka, *Chem. Commun.* **2008**, 4825–4827.
- [15] S. Johannsen, S. Paulus, N. Düpre, J. Müller, R. K. O. Sigel, *J. Inorg. Biochem.* **2008**, *102*, 1141–1151.
- [16] H. Urata, E. Yamaguchi, T. Funai, Y. Matsumura, S. Wada, *Angew. Chem.* **2010**, *122*, 6666–6669; *Angew. Chem. Int. Ed.* **2010**, *49*, 6516–6519.
- [17] K. S. Park, C. Jung, H. G. Park, *Angew. Chem.* **2010**, *122*, 9951–9954; *Angew. Chem. Int. Ed.* **2010**, *49*, 9757–9760.
- [18] C. Kaul, M. Müller, M. Wagner, S. Schneider, T. Carell, *Nat. Chem.* **2011**, *3*, 794–800.
- [19] A. M. Kretulskie, T. E. Spratt, *Biochemistry* **2006**, *45*, 3740–3746.
- [20] F.-A. Polonius, J. Müller, *Angew. Chem.* **2007**, *119*, 5698–5701; *Angew. Chem. Int. Ed.* **2007**, *46*, 5602–5604.
- [21] S. Menzer, M. Sabat, B. Lippert, *J. Am. Chem. Soc.* **1992**, *114*, 4644–4649.



Contents lists available at SciVerse ScienceDirect

Biochimie

journal homepage: www.elsevier.com/locate/biochi

Research paper

Thermodynamic and structural properties of the specific binding between Ag⁺ ion and C:C mismatched base pair in duplex DNA to form C–Ag–C metal-mediated base pair

Hidetaka Torigoe^{a,*}, Itaru Okamoto^b, Takenori Dairaku^c, Yoshiyuki Tanaka^c, Akira Ono^b, Tetsuo Kozasa^a^a Department of Applied Chemistry, Faculty of Science, Tokyo University of Science, 1-3 Kagurazaka, Shinjuku-ku, Tokyo 162-8601, Japan^b Department of Material & Life Chemistry, Faculty of Engineering, Kanagawa University, 3-27-1 Rokkakubashi, Kanagawa-ku, Yokohama 221-8686, Japan^c Graduate School of Pharmaceutical Sciences, Tohoku University, Aobayama, Aoba-ku, Sendai 980-8578, Miyagi, Japan

ARTICLE INFO

Article history:

Received 25 December 2011

Accepted 22 June 2012

Available online xxx

Keywords:

Metal ion–DNA interaction

Metal-mediated base pair

Ag⁺ ion

C:C mismatched base pair

Specific binding

Large binding affinity

ABSTRACT

Metal ion–nucleic acid interactions have attracted considerable interest for their involvement in structure formation and catalytic activity of nucleic acids. Although interactions between metal ion and mismatched base pair duplex are important to understand mechanism of gene mutations related to heavy metal ions, they have not been well-characterized. We recently found that the Ag⁺ ion stabilized a C:C mismatched base pair duplex DNA. A C–Ag–C metal-mediated base pair was supposed to be formed by the binding between the Ag⁺ ion and the C:C mismatched base pair to stabilize the duplex. Here, we examined specificity, thermodynamics and structure of possible C–Ag–C metal-mediated base pair. UV melting indicated that only the duplex with the C:C mismatched base pair, and not of the duplexes with the perfectly matched and other mismatched base pairs, was specifically stabilized on adding the Ag⁺ ion. Isothermal titration calorimetry demonstrated that the Ag⁺ ion specifically bound with the C:C base pair at 1:1 molar ratio with a binding constant of 10⁶ M⁻¹, which was significantly larger than those for nonspecific metal ion–DNA interactions. Electrospray ionization mass spectrometry also supported the specific 1:1 binding between the Ag⁺ ion and the C:C base pair. Circular dichroism spectroscopy and NMR revealed that the Ag⁺ ion may bind with the N3 positions of the C:C base pair without distorting the higher-order structure of the duplex. We conclude that the specific formation of C–Ag–C base pair with large binding affinity would provide a binding mode of metal ion–DNA interactions, similar to that of the previously reported T–Hg–T base pair. The C–Ag–C base pair may be useful not only for understanding of molecular mechanism of gene mutations related to heavy metal ions but also for wide variety of potential applications of metal-mediated base pairs in various fields, such as material, life and environmental sciences.

© 2012 Elsevier Masson SAS. All rights reserved.

1. Introduction

The interactions between metal ions and nucleic acids have attracted considerable interest for their involvement in structure formation and folding of nucleic acids, such as triplex, quadruplex, and RNA folding [1], and their possible roles in catalytic activity of nucleic acids, such as catalytic cofactors in ribozymes [2]. The structural and thermodynamic properties of the binding with the

perfectly matched duplex DNA have been reported for many metal ions, such as Cr³⁺ [3], Cr⁶⁺ [3], Tl⁺ [4], Fe²⁺ [5], Fe³⁺ [5], Al³⁺ [6], Mn²⁺ [7], and Cd²⁺ [8]. To understand molecular mechanism of gene mutations related to heavy metal ions [9], the study of the interaction between metal ions and the mismatched base pair duplex DNA may be important. However, few studies have been reported for the interaction of metal ions with the mismatched base pair duplex DNA. We recently found that a duplex DNA with a C:C mismatched base pair was stabilized by only the Ag⁺ ion and not by other metal ions (Mg²⁺, Ca²⁺, Mn²⁺, Fe²⁺, Fe³⁺, Co²⁺, Ni²⁺, Cu²⁺, Zn²⁺, Ru³⁺, Pd²⁺, Cd²⁺, and Pb²⁺) [10]. A C–Ag–C metal-mediated base pair (Fig. 1a) was supposed to be formed by the binding between the Ag⁺ ion and the C:C mismatched base pair in the duplex DNA. The binding of the Ag⁺ ion may stabilize the duplex DNA with the C:C mismatched base pair [10]. However, the

Abbreviations: CD, circular dichroism; ESI-MS, electrospray ionization mass spectrometry; HPLC, high-performance liquid chromatography; ITC, isothermal titration calorimetry; T_m, melting temperature.

* Corresponding author. Tel.: +81 3 5228 8259; fax: +81 3 5261 4631.

E-mail address: htorigoe@rs.kagu.tus.ac.jp (H. Torigoe).

0300-9084/\$ – see front matter © 2012 Elsevier Masson SAS. All rights reserved.
<http://dx.doi.org/10.1016/j.biochi.2012.06.024>

Please cite this article in press as: H. Torigoe, et al., Thermodynamic and structural properties of the specific binding between Ag⁺ ion and C:C mismatched base pair in duplex DNA to form C–Ag–C metal-mediated base pair, *Biochimie* (2012), <http://dx.doi.org/10.1016/j.biochi.2012.06.024>

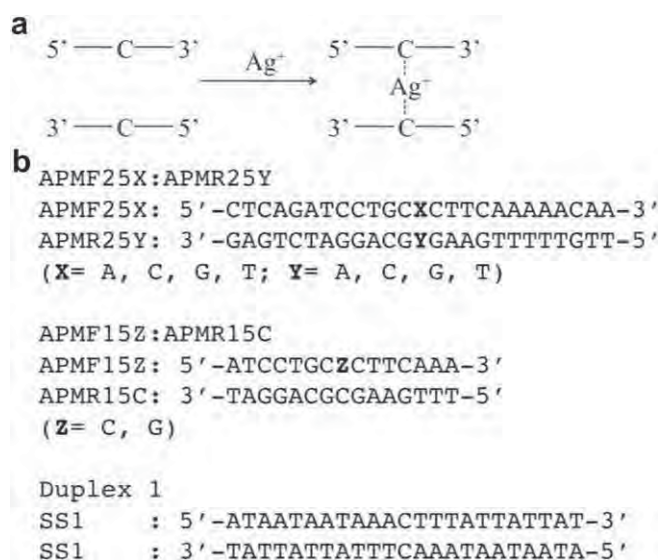


Fig. 1. (a) C–Ag–C base pair formation in duplex by the interaction between Ag^+ ion and C:C mismatched base pair. (b) Oligonucleotide sequence of the target duplexes, APMF25X:APMR25Y, APMF15Z:APMR15C and duplex 1.

mechanistic explanation for the Ag^+ ion-mediated stabilization of the duplex DNA with the C:C mismatched base pair and the possible C–Ag–C metal-mediated base pair formation was not clearly understood. Therefore, here, we have expanded our previous line of research to explore specificity, thermodynamics and structure for the interaction between the Ag^+ ion and the C:C mismatched base pair. The interaction between the Ag^+ ion and each of mismatched base pair duplex DNA or the corresponding perfectly matched duplex DNA with another base sequence was analyzed by UV melting, isothermal titration calorimetry (ITC) [11], electrospray ionization mass spectrometry (ESI-MS) [12–14], circular dichroism (CD) spectroscopy and NMR. UV melting analyses indicated that the Ag^+ ion was able to significantly stabilize the duplex with the C:C mismatched base pair without stabilizing the duplexes with the perfectly matched base pairs or the other mismatched base pairs. ITC analyses demonstrated that the Ag^+ ion specifically bound with the C:C mismatched base pair in the duplex at a 1:1 molar ratio with a binding constant of nearly 10^6 M^{-1} , which was significantly larger than those previously reported for the nonspecific interactions between metal ions and DNA (3.2×10^3 – $1.4 \times 10^5 \text{ M}^{-1}$) [3–8,15]. ESI-MS also supported the specific binding and the 1:1 molar ratio between the Ag^+ ion and the C:C mismatched base pair. CD spectroscopy and NMR study revealed that the Ag^+ ion may bind with the N3 positions of the C:C mismatched base pair without distorting the higher-order structure of the duplex. The specific formation of C–Ag–C base pair with large binding affinity would provide a binding mode of metal ion-DNA interactions, similar to that of the previously reported T–Hg–T base pair [16–19]. The C–Ag–C base pair may be useful for wide variety of potential applications of metal-mediated base pairs in various fields, such as material, life and environmental sciences. Possible applications of the C–Ag–C base pair in various fields will be discussed.

2. Materials and methods

2.1. Preparation of oligonucleotides

We synthesized DNA oligonucleotides, APMF25X: 5'-CTCA-GATCCTGCXCTTCAAAAACAA-3' (X = A, C, G, T), APMR25Y: 5'-

TTGTTTTGAAGYGCAGGATCTGAG-3' (Y = A, C, G, T), APMF15Z: 5'-ATCCTGCZCTTCAAA-3' (Z = C, G), APMR15C: 5'-TTTGAAGCGAG-GAT-3' and SS1: 5'-ATAATAATAAACTTTATTATTAT-3' (Fig. 1b), on a DNA synthesizer by using the solid-phase cyanoethyl phosphoramidite method; we then purified them with reverse-phase high-performance liquid chromatography (HPLC) on a Wakosil DNA column. The concentration of all oligonucleotides was determined by UV absorbance. Three pairs of the purified strands (APMF25X and APMR25Y, APMF15Z and APMR15C, two SS1 strands) were annealed in 5 mM potassium phosphate buffer (pH 7.0) to form the duplexes (APMF25X:APMR25Y, APMF15Z:APMR15C, duplex 1) (Fig. 1b) by heating at up to 90 °C, followed by a gradual cooling to room temperature. The annealed sample was applied on a hydroxyapatite column (BIORAD Inc.) to remove the unpaired single strands. The concentration of the duplex DNA was determined by UV absorption considering the DNA concentration ratio of 1 OD = 50 $\mu\text{g/ml}$, with a M_r of 15300 for APMF25X:APMR25Y.

2.2. UV melting

UV melting experiments were carried out on a DU-640 spectrophotometer (Beckman Inc.) equipped with a Peltier type cell holder. The cell path length was 1 cm. The UV melting profiles were measured in buffer A [10 mM sodium cacodylate-cacodylic acid (pH 6.8) and 100 mM NaNO_3] either with or without 1 μM AgNO_3 at a scan rate of 0.2 °C/min with detection at 260 nm. The first derivative was calculated from the UV melting profile. The peak temperatures in the derivative curve were designated as the melting temperature, T_m . The concentration of the duplex DNA (APMF25X:APMR25Y) used was 1 μM .

2.3. Isothermal titration calorimetry (ITC)

Isothermal titration experiments were carried out on a VP ITC system (Microcal Inc., U.S.A.) [11]. The duplex DNA (APMF25X:APMR25Y) solutions were prepared by extensive dialysis against buffer A. AgNO_3 was dissolved in the dialysis buffer. The AgNO_3 solution in buffer A was injected 30 times in 5- μl increments at 5-min intervals into the duplex DNA (APMF25X:APMR25Y) solution without changing the reaction conditions. The heat for each injection was subtracted by the heat of dilution of the injectant, which was measured by injecting the AgNO_3 solution into the same buffer. Each corrected heat was divided by the moles of AgNO_3 injected and analyzed with Microcal Origin software supplied by the manufacturer.

2.4. ESI-MS

ESI-MS measurements were performed on a time-of-flight mass spectrometer (JMS-T100; JEOL, Japan). Each aqueous solution containing the duplex DNA (APMF15Z:APMR15C) and the Ag^+ ion in 62.5 mM $\text{CH}_3\text{COONH}_4$ (pH 7.0) was diluted with CH_3OH to give 10 μM DNA in 50 mM $\text{CH}_3\text{COONH}_4$ buffer dissolved in the solvent ($\text{H}_2\text{O}:\text{CH}_3\text{OH} = 4:1$). Although the complexation between the Ag^+ ion and NH_3 in the solution can affect the activity of the Ag^+ ion, the binding between the Ag^+ ion and the C:C mismatched base pair was observed as described in the section of 3.3. The measurement conditions were as follows, needle voltage: –1.8 kV, orifice voltage: –55 V, desolvation temperature: 80–100 °C, resolution (10% valley definition): 2000, and sample flow rate: 20 $\mu\text{l/min}$.

2.5. CD spectroscopy

CD spectra were recorded at 25 °C and pH 6.8 in buffer A either with or without 1 μM AgNO_3 on a JASCO J-720 spectropolarimeter

interfaced with a microcomputer. The cell path length was 1 cm. The concentration of the duplex DNA (APMF25X:APMR25Y) used was 1 μ M.

2.6. NMR

NMR spectra were recorded at 25 °C on JEOL ECA600. 15 mM uniformly 15 N-labeled cytidine with various concentrations of the Ag^+ ion was measured in DMSO- d_6 . 1.3 mM nonlabeled duplex 1 with various concentrations of the Ag^+ ion was measured in D_2O with 100 mM NaNO_3 .

3. Results

3.1. UV melting analyses of mismatched base pair duplex DNA and the corresponding perfectly matched duplex DNA either with or without the Ag^+ ion

The thermal stability of a series of 1 μ M APMF25X:APMR25Y (X:Y = C:C, C:G and G:C) (Fig. 1b) was examined in 10 mM sodium cacodylate-cacodylic acid (pH 6.8) and 100 mM NaNO_3 either with or without 1 μ M AgNO_3 by UV melting (Figure S1). The T_m values of X:Y = C:G (66.0 °C) and X:Y = G:C (66.2 °C) with AgNO_3 were not significantly different from those without AgNO_3 (Fig. 2, Figs. S1b, S1c and Table S1). In contrast, the addition of 1 μ M AgNO_3 increased the T_m of 1 μ M X:Y = C:C by about 3.5 °C (56.9 °C \rightarrow 60.4 °C) (Fig. 2, Fig. S1a and Table S1). The increase in the T_m of X:Y = C:C by the addition of the Ag^+ ion was achieved at a molar ratio of $[\text{Ag}^+ \text{ ion}]/[\text{X:Y = C:C}] = 1$. These results indicate that the thermal stability of the C:C mismatched base pair duplex DNA was significantly increased by the addition of the Ag^+ ion at a molar ratio of $[\text{Ag}^+ \text{ ion}]/[\text{C:C mismatched base pair duplex DNA}] = 1$.

To examine the base-pair specificity of the stabilization by the addition of the Ag^+ ion, we measured the T_m values of a series of 1 μ M APMF25X:APMR25Y with 16 different base pairs, (X:Y = A:A, A:C, A:G, A:T, C:A, C:C, C:G, C:T, G:A, G:C, G:G, G:T, T:A, T:C, T:G, and T:T) (Fig. 1b), in the same buffer with or without 1 μ M AgNO_3 by UV melting (Fig. 2 and Table S1). The T_m values of the duplex DNAs with the perfectly matched base pairs (X:Y = A:T, C:G, G:C and T:A) and those of the duplex DNAs with the other kinds of mismatched base pairs (X:Y = A:A, A:C, A:G, C:A, C:T, G:A, G:G, G:T, T:C, T:G and T:T) (T_m (- Ag^+)) were not significantly changed by the addition of the Ag^+ ion (T_m (+ Ag^+)), unlike the case of X:Y = C:C ($\Delta T_m = 3.5$ °C) shown above (Fig. 2 and Table S1). These results indicate that only

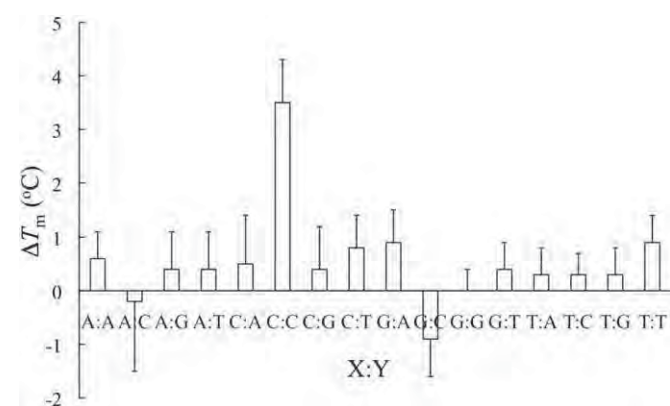


Fig. 2. Change of melting temperatures, ΔT_m , of 1 μ M duplexes [APMF25X:APMR25Y (X:Y = A:A, A:C, A:G, A:T, C:A, C:C, C:G, C:T, G:A, G:C, G:G, G:T, T:A, T:C, T:G, and T:T)] at pH 6.8 in 10 mM sodium cacodylate-cacodylic acid and 100 mM NaNO_3 upon addition of 1 μ M AgNO_3 , obtained from UV melting.

the duplex DNA with the C:C mismatched base pair was specifically stabilized by the addition of the Ag^+ ion.

To investigate whether other metal ions have the ability to stabilize the duplex DNA with the C:C mismatched base pair, we measured the T_m values of the series of 1 μ M APMF25X:APMR25Y with 16 different base pairs in 10 mM sodium cacodylate-cacodylic acid (pH 6.8) and 100 mM NaNO_3 (or NaCl) with or without each of 1.5 μ M $\text{Mn}(\text{NO}_3)_2$, $\text{Co}(\text{NO}_3)_2$, $\text{Ni}(\text{NO}_3)_2$, $\text{Zn}(\text{NO}_3)_2$, RuCl_3 , $\text{Cd}(\text{NO}_3)_2$, TlNO_3 , and $\text{Pb}(\text{NO}_3)_2$ by UV melting (Tables S2–S9). We also measured them in 10 mM sodium cacodylate-cacodylic acid (pH 6.8) and 100 mM NaClO_4 with or without 1 μ M $\text{Hg}(\text{ClO}_4)_2$ by UV melting (Table S10). The T_m values of the duplex DNAs with any kinds of base pairs including the C:C mismatched base pair were not significantly changed by the addition of each of the Mn^{2+} , Co^{2+} , Ni^{2+} , Zn^{2+} , Ru^{3+} , Cd^{2+} , Tl^+ , and Pb^{2+} ion. Although the addition of Hg^{2+} increased the T_m value of the duplex DNA with the T:T mismatched base pair by about 5.0 °C (Table S10), which was previously reported in our studies [17,19], the T_m values of the duplex DNAs with any other kinds of base pairs including the C:C mismatched base pair were not significantly altered by the addition of Hg^{2+} . These results indicate that only the Ag^+ ion stabilized the duplex DNA with the C:C mismatched base pair.

3.2. ITC analyses of the interaction between the Ag^+ ion and each of mismatched base pair duplex DNA and the corresponding perfectly matched duplex DNA

To explore the mechanism of specific stabilization of the duplex DNA with the C:C mismatched base pair by the addition of the Ag^+ ion, we examined the thermodynamic properties of the interaction between AgNO_3 and APMF25X:APMR25Y (X:Y = C:C, C:G and G:C) (Fig. 1b) in 10 mM sodium cacodylate-cacodylic acid (pH 6.8) and 100 mM NaNO_3 at 25 °C by ITC (Fig. 3). Fig. 3a shows a typical ITC profile of the interaction between AgNO_3 and X:Y = C:C at 25 °C and pH 6.8. An exothermic heat pulse was observed each time after AgNO_3 was injected into X:Y = C:C. The magnitude of each peak decreased gradually with each new injection, indicating that the Ag^+ ion specifically bound with X:Y = C:C. On the other hand, the ITC profiles of the interaction between AgNO_3 and each of X:Y = C:G and G:C at 25 °C and pH 6.8 are shown in Fig. 3b and c, respectively. Although an exothermic heat pulse was observed after each injection of AgNO_3 into X:Y = C:G or G:C, the magnitude of each peak was not significantly changed with each new injection, indicating that the Ag^+ ion nonspecifically bound with X:Y = C:G and G:C. These ITC profiles were in sharp contrast with that observed for the interaction between AgNO_3 and X:Y = C:C (Fig. 3a).

The nonspecific binding between the Ag^+ ion and each of X:Y = C:G and G:C judged from the ITC profiles (Fig. 3b and c) suggests that the Ag^+ ion may bind with the phosphate backbones of each of the perfectly matched duplex DNAs (X:Y = C:G and G:C) in a nonspecific manner due to the attraction between the positive charge of the Ag^+ ion and the negative charge of the DNA phosphate backbones. On the other hand, the specific binding between the Ag^+ ion and X:Y = C:C judged from the ITC profile (Fig. 3a) suggests that the Ag^+ ion may specifically bind with the C:C mismatched base pair of the mismatched base pair duplex DNA (X:Y = C:C) in addition to the nonspecific binding between the Ag^+ ion and the DNA phosphate backbones of X:Y = C:C. Thus, the net heat derived from the specific binding between the Ag^+ ion and the C:C mismatched base pair of the duplex DNA (X:Y = C:C) should be estimated by subtracting the heat observed for the perfectly matched duplex DNA (X:Y = C:G or G:C) from that observed for the C:C mismatched base pair duplex DNA (X:Y = C:C). Based on these considerations, in order to analyze the thermodynamic parameters of the specific binding between the Ag^+ ion and the C:C

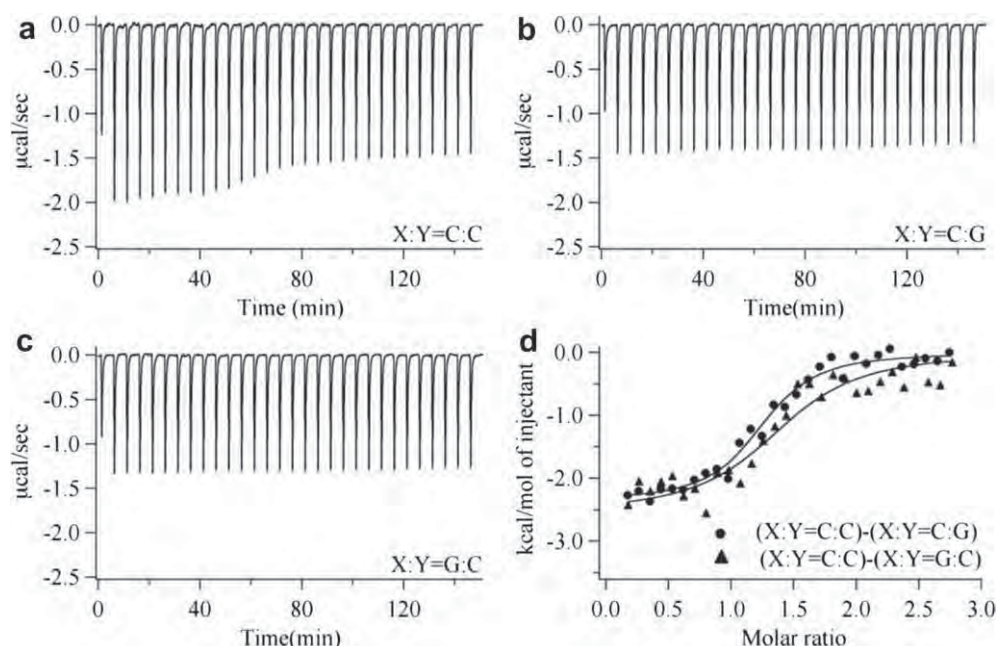


Fig. 3. Thermodynamic analyses of the interaction between the Ag^+ ion and APMF25X:APMR25Y (X:Y = C:C, C:G and G:C). (a–c) Typical ITC profile of the interaction between AgNO_3 and each of X:Y = C:C (a), X:Y = C:G (b) and X:Y = G:C (c) at 25 °C and pH 6.8 in 10 mM sodium cacodylate-cacodylic acid and 100 mM NaNO_3 . AgNO_3 solution (1 mM) was injected 30 times in 5- μl increments into each of X:Y = C:C (a), X:Y = C:G (b) and X:Y = G:C (c) solution (40 μM). Injections were administered over 12 s at 5-min intervals. (d) Titration plot against the molar ratio of $[\text{Ag}^+ \text{ ion}]/[\text{duplex DNA}]$ for (X:Y = C:C)-(X:Y = C:G) and (X:Y = C:C)-(X:Y = G:C). The data were fitted by a nonlinear least-squares method.

mismatched base pair of the duplex DNA (X:Y = C:C), the ITC profile observed for X:Y = C:G in Fig. 3b was subtracted from that observed for X:Y = C:C in Fig. 3a, and the ITC profile observed for X:Y = G:C in Fig. 3c was subtracted from that observed for X:Y = C:C in Fig. 3a. The area under each peak was integrated, and the integrated values were divided by the moles of the injected solution. The resulting values were plotted as a function of the molar ratio of $[\text{Ag}^+ \text{ ion}]/[\text{duplex DNA}]$ (Fig. 3d). The resultant titration plots were fitted to a sigmoidal curve by a nonlinear least-squares method. The stoichiometry, n , the binding constant, K_a , and the enthalpy change, ΔH , for the specific binding between the Ag^+ ion and the C:C mismatched base pair were obtained from the fitted curve [11]. The Gibbs free energy change, ΔG , and the entropy change, ΔS , were calculated from the equation, $\Delta G = -RT \ln K_a = \Delta H - T\Delta S$, where R is gas constant and T is the temperature [11].

Table 1 summarizes the thermodynamic parameters for the specific binding between the Ag^+ ion and the C:C mismatched base pair, obtained for (X:Y = C:C)-(X:Y = C:G) and (X:Y = C:C)-(X:Y = G:C). The thermodynamic parameters obtained for (X:Y = C:C)-(X:Y = C:G) and (X:Y = C:C)-(X:Y = G:C) were quite similar in magnitude. The obtained value of n was nearly 1, indicating that the Ag^+ ion bound with the C:C mismatched base pair at a molar ratio of 1:1. The nonspecific binding between the Ag^+ ion and each of X:Y = C:G and G:C may be out of the optimum range of the ITC measurements due to no significant change of the magnitude of each peak upon each new injection (Fig. 3b and c). The “ c ” value, which is the product of the duplex DNA concentration and the binding constant for the present case, should be 1–1000 for the

optimum ITC measurements [11]. Thus, the “ c ” value for the nonspecific binding may be below the value of 1. Because the duplex DNA concentration was 40 μM ($=4 \times 10^{-5} \text{ M}$), the binding constant for the nonspecific binding may be below the value of $2.5 \times 10^4 \text{ M}^{-1}$, which was about 20 times smaller than the binding constant for the specific binding between the Ag^+ ion and the C:C mismatched base pair (Table 1). Thus, the amount of the Ag^+ ion to nonspecifically bind with the phosphate backbones of the duplex DNA may be less than a few percent of that to specifically bind with the C:C mismatched base pair. The very small amount of the Ag^+ ion may not significantly affect a 1:1 binding stoichiometry. Although the sign of ΔH was negative, the sign of ΔS was positive. Because both the observed negative ΔH and positive ΔS were favorable for the specific binding between the Ag^+ ion and the C:C mismatched base pair, the specific binding between the Ag^+ ion and the C:C mismatched base pair was driven by both the negative ΔH and positive ΔS . The magnitudes of the observed K_a and ΔG were significantly larger than those previously reported for the nonspecific interaction between metal ion and DNA (3.2×10^3 – $1.4 \times 10^5 \text{ M}^{-1}$) [3–8,15], indicating that the Ag^+ ion specifically bound with the C:C mismatched base pair. To examine the concentration dependence of the obtained thermodynamic parameters, we performed the same ITC experiments using 80 μM and 120 μM target duplex DNA (Table S11) as those using 40 μM target duplex DNA (Table 1). The obtained thermodynamic parameters were quite similar in magnitude to those shown in Table 1. The concentration did not significantly affect the thermodynamic parameters for the specific binding between the Ag^+ ion and the C:C mismatched base pair.

Table 1
Thermodynamic parameters for the specific binding between the Ag^+ ion and the C:C mismatched base pair at 25 °C and pH 6.8 in 10 mM sodium cacodylate-cacodylic acid and 100 mM NaNO_3 , obtained from ITC measurements.

Profile	n	$K_a (\text{M}^{-1})$	$\Delta G (\text{kcal mol}^{-1})$	$\Delta H (\text{kcal mol}^{-1})$	$\Delta S (\text{cal mol}^{-1} \text{K}^{-1})$
(X:Y = C:C)–(X:Y = C:G)	1.06 ± 0.03	$(5.86 \pm 1.29) \times 10^5$	-7.87 ± 0.15	-2.37 ± 0.07	18.4 ± 0.7
(X:Y = C:C)–(X:Y = G:C)	1.21 ± 0.07	$(2.92 \pm 1.13) \times 10^5$	-7.45 ± 0.29	-2.55 ± 0.17	16.5 ± 1.5

Further, we examined the interaction between the Ag^+ ion and the double C:C mismatched base pair duplex, APMF25C-C:APMR25CC (Figure S2), by ITC (Figure S3). The thermodynamic parameters for the specific binding between the Ag^+ ion and the double C:C mismatched base pair were obtained from Figure S3 in the same way as those between the Ag^+ ion and the single C:C mismatched base pair. Table S12 summarizes the thermodynamic parameters for the specific binding between the Ag^+ ion and the double C:C mismatched base pair, which were based on a model of 2 binding sites. The values of n_1 and n_2 were nearly 1, indicating that 1:1 stoichiometric binding was achieved in each binding step. The magnitudes of the observed K_{a2} and ΔG_2 for the second binding between the second Ag^+ ion and the second C:C mismatched base pair were similar to those of the observed K_{a1} and ΔG_1 for the first binding between the first Ag^+ ion and the first C:C mismatched base pair. The obtained thermodynamic parameters, n , K_a , and ΔG , were quite similar in magnitude to those shown in Table 1. On the other hand, the magnitude of the negative enthalpy change for the second Ag^+ binding, ΔH_2 , was significantly larger than that for the first Ag^+ binding, ΔH_1 . In addition, although the sign of the entropy change for the first Ag^+ binding, ΔS_1 , was positive, that for the second Ag^+ binding, ΔS_2 , was negative. Therefore, the thermodynamic properties of ΔH and ΔS were quite different between the first and second Ag^+ binding.

3.3. ESI-MS of the complex between the Ag^+ ion and each of mismatched base pair duplex DNA and the corresponding perfectly matched duplex DNA

To examine the molar ratio of the binding between the Ag^+ ion and the C:C mismatched base pair, we analyzed the interaction by ESI-MS as a function of a molar ratio of $[\text{Ag}^+ \text{ ion}]/[\text{duplex DNA}]$. We measured the ESI-MS spectra of the mixture of the Ag^+ ion and a 15 base pair duplex, APMF15Z:APMR15C (Z:C = C:C and G:C) (Fig. 1b), which corresponds to the base sequence just in the middle of APMF25X:APMR25Y (X:Y = C:C and G:C), to obtain good signals and have less competing binding sites (Fig. 4). In the case of Z:C = C:C, the intensity of the peak corresponding to the free duplex ($[\text{duplex-5H}]^{5-}$) was significantly decreased, and a new peak corresponding to 1:1 complex between the Ag^+ ion and the duplex ($[\text{duplex-6H} + \text{Ag}]^{5-}$) appeared at a molar ratio of 1.0 (1.0 eq Ag for Z:C = C:C). At a molar ratio of 2.0 and 3.0 (2.0 eq Ag and 3.0 eq Ag for Z:C = C:C), the peak corresponding to the free duplex ($[\text{duplex-5H}]^{5-}$) almost disappeared, and the main peak corresponding to 1:1 complex ($[\text{duplex-6H} + \text{Ag}]^{5-}$) was maintained. In contrast, in the case of Z:C = G:C, the intensity of the peak corresponding to the free duplex ($[\text{duplex-5H}]^{5-}$) was not significantly changed, although a new small peak corresponding to 1:1 complex between the Ag^+ ion and the duplex ($[\text{duplex-6H} + \text{Ag}]^{5-}$) appeared at a molar ratio of 1.0 (1.0 eq Ag for Z:C = G:C). The peak corresponding to the free duplex ($[\text{duplex-5H}]^{5-}$) was still observed even at a molar ratio of 2.0 and 3.0 (2.0 eq Ag and 3.0 eq Ag for Z:C = G:C). These results indicate that the Ag^+ ion specifically bound with only the C:C mismatched base pair at a molar ratio of 1:1, consistent with the ITC results (Table 1). On the other hand, at a molar ratio of 2.0 and 3.0 (2.0 eq Ag and 3.0 eq Ag for Z:C = C:C and G:C) corresponding to the addition of an excess Ag^+ ion, additional peaks ($[\text{duplex-7H} + 2\text{Ag}]^{5-}$ and $[\text{duplex-8H} + 3\text{Ag}]^{5-}$) were observed for both Z:C = C:C and G:C, suggesting the extra binding sites of the Ag^+ ion by nonspecific binding with lower binding affinity. The background exothermic heat pulse observed for X:Y = C:G and G:C in ITC (Fig. 3) may be related to the nonspecific binding of the Ag^+ ion to the extra binding sites.

3.4. CD spectroscopy of mismatched base pair duplex DNA and the corresponding perfectly matched duplex DNA either with or without the Ag^+ ion

To examine the effect of the Ag^+ ion binding on the higher-order structure of duplex DNA, CD spectra of 1 μM APMF25X:APMR25Y (X:Y = C:C, C:G and G:C) (Fig. 1b) were measured in 10 mM sodium cacodylate-cacodylic acid (pH 6.8) and 100 mM NaNO_3 either with or without 1 μM AgNO_3 at 25 $^\circ\text{C}$ (Fig. 5). The CD profile of X:Y = C:C, C:G and G:C with AgNO_3 was quite similar to that observed without AgNO_3 . This result indicates that there was no significant change in the higher-order structure of X:Y = C:C, C:G and G:C on the addition of the Ag^+ ion. When a B to A-DNA conformational change is induced as previously observed by other groups upon the Ag^+ binding to the N7 position of the guanine [20], a large positive band should appear at 260 nm [21]. However, such spectral change was not observed upon the formation of the C-Ag-C complex. The higher-order structure of the mismatched base pair duplex DNA (X:Y = C:C) was not significantly distorted by the binding of the Ag^+ ion. Although we measured the CD profiles in the wavelength range of 210–320 nm, the CD profiles in the experimental buffer containing NO_3^- were quite noisy in the wavelength range of 210–250 nm due to the presence of NO_3^- . Thus, we showed the CD spectra only in the wavelength range of 250–320 nm (Fig. 5).

3.5. NMR of the complex between the Ag^+ ion and each of uniformly ^{15}N -labeled cytidine and a non-labeled duplex

Our previous NMR study of the interaction between the Ag^+ ion and the C:C mismatched base pair duplex DNA showed that one C:C mismatched base pair captured one Ag^+ ion, and the proton exchange rate between Ag^+ -free and Ag^+ -complexed duplex DNAs was slow relative to the timescale of the NMR measurement [10]. However, the binding position of the Ag^+ ion with the C:C mismatched base pair remained unclear. Thus, to reveal the binding position of the Ag^+ ion with the C:C mismatched base pair, we first measured the ^{15}N NMR and ^1H NMR spectra for the interaction between the Ag^+ ion and uniformly ^{15}N -labeled cytidine (Figs. 6 and 7). In ^{15}N -NMR spectra (Fig. 6), the N3 signal of the labeled cytidine was drastically upfield shifted by 21.8 ppm upon the binding with the Ag^+ ion at a molar ratio of $[\text{Ag}^+]/[^{15}\text{N}\text{-labeled cytidine}] = 0.5$, but the chemical shifts of the N1 and NH_2 signals were changed only by 0.39 ppm and 5.80 ppm, respectively, at the same molar ratio (Table 2). The similar chemical shift changes were also observed at a molar ratio of $[\text{Ag}^+]/[^{15}\text{N}\text{-labeled cytidine}] = 1.0$. These results indicate that the preferential binding site of the Ag^+ ion was the N3 position of the cytidine. Also, in ^1H NMR spectra (Fig. 7), the H5 and H6 signals of the labeled cytidine were downfield shifted by 0.26 ppm and 0.22 ppm, respectively, upon the binding of the Ag^+ ion with N3 of the cytidine (Table 2). Next, we measured the two-dimensional ^1H - ^1H COSY spectra for the interaction between the Ag^+ ion and a non-labeled duplex 1 (Fig. 1b) containing a C:C mismatched base pair, which was composed of two SS1 strands (Fig. 8). The H5 and H6 signals of the C:C mismatched base pair in duplex 1 were downfield shifted by 0.21 ppm and 0.25 ppm, respectively, upon the Ag^+ ion complexation (Fig. 8 and Table 2). It should be noted that these chemical shift changes were quite similar in magnitude to those observed for the H5 and H6 signals of the labeled cytidine upon the binding with the Ag^+ ion (Table 2). The NMR data suggest that the binding site of the Ag^+ ion would also be the N3 positions of the C:C mismatched base pair in duplex 1. Also, the chemical shift change for the H5 and H6 signals upon the binding with the Ag^+ ion was almost terminated at the molar equivalency of $[\text{Ag}^+ \text{ ion}]/[\text{duplex 1}] = 1.0$ (Fig. 8), indicating that the duplex 1 bound with the Ag^+ ion at a molar ratio of

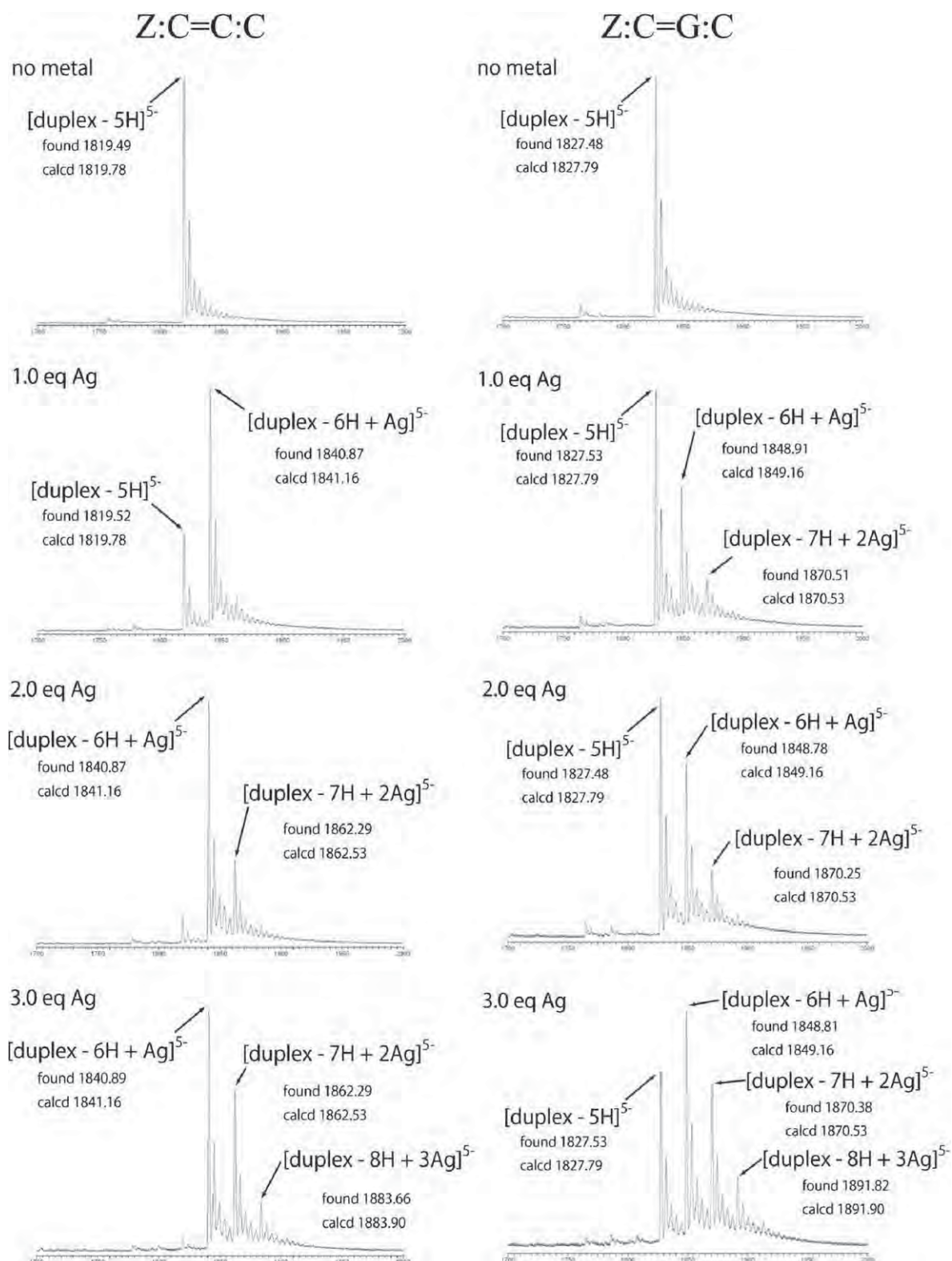


Fig. 4. ESI-MS spectra of APMF15Z:APMR15C (Z:C = C:C, G:C), corresponding to the base sequence just in the middle of APMF25X:APMR25Y (X:Y = C:C, G:C), with or without the Ag⁺ ion. Each aqueous solution containing the duplex DNA and the Ag⁺ ion in 62.5 mM CH₃COONH₄ (pH 7.0) was diluted with CH₃OH to give 10 μM DNA in 50 mM CH₃COONH₄ buffer dissolved in the solvent (H₂O:CH₃OH = 4:1).

1:1, which was consistent with the results of ITC (Table 1). These results reveal that the Ag⁺ ion may bind with the N3 positions of the two cytosine bases and bridge the two cytosine bases to form the C–Ag–C complex (Fig. 1a) in the duplex DNA.

4. Discussion

UV melting analyses showed that the addition of the Ag⁺ ion significantly increased the thermal stability of the duplex DNA with

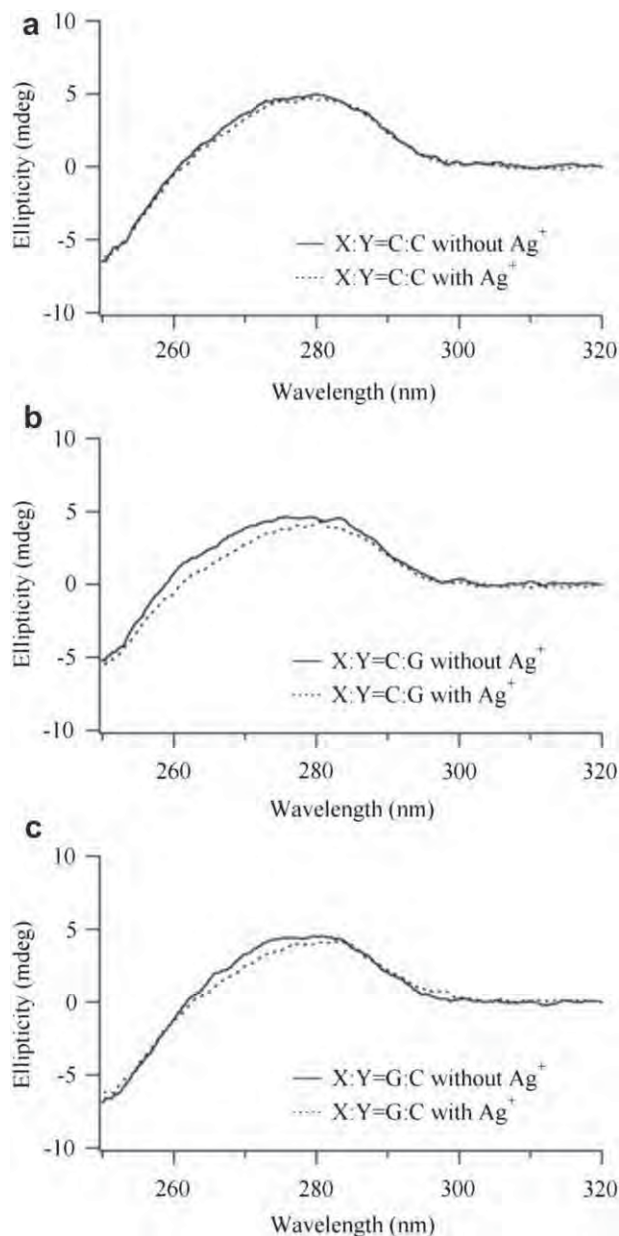


Fig. 5. CD spectra of APMF25X:APMR25Y, [X:Y = C:C (a), X:Y = C:G (b) and X:Y = G:C (c)], with or without AgNO_3 . Duplexes (1 μM) at 25 °C and pH 6.8 in 10 mM sodium cacodylate-cacodylic acid and 100 mM NaNO_3 with or without 1 μM AgNO_3 were measured at a wavelength range of 250–320 nm. The cell path length was 1 cm.

the C:C mismatched base pair (Fig. 2 and Fig. S1 and Table S1). However, the thermal stability of the duplex DNAs with the perfectly matched base pairs (X:Y = A:T, C:G, G:C and T:A) and that of the duplex DNAs with the other kinds of mismatched base pairs (X:Y = A:A, A:C, A:G, C:A, C:T, G:A, G:G, G:T, T:C, T:G and T:T) were not significantly changed by the addition of the Ag^+ ion (Fig. 2 and Table S1). Thus, only the duplex DNA with the C:C mismatched base pair was specifically stabilized by the addition of the Ag^+ ion. The base pair specificity has not been examined previously [10]. We also showed that other metal ions, such as Mn^{2+} , Co^{2+} , Ni^{2+} , Zn^{2+} , Ru^{3+} , Cd^{2+} , Tl^+ , Pb^{2+} and Hg^{2+} , did not show any notable effect on the thermal stability of the duplex DNA with the C:C mismatched base pair (Tables S2–S10). Therefore, only the Ag^+ ion was able to specifically increase the thermal stability of the duplex DNA with the C:C mismatched base pair. We previously reported that a C:C

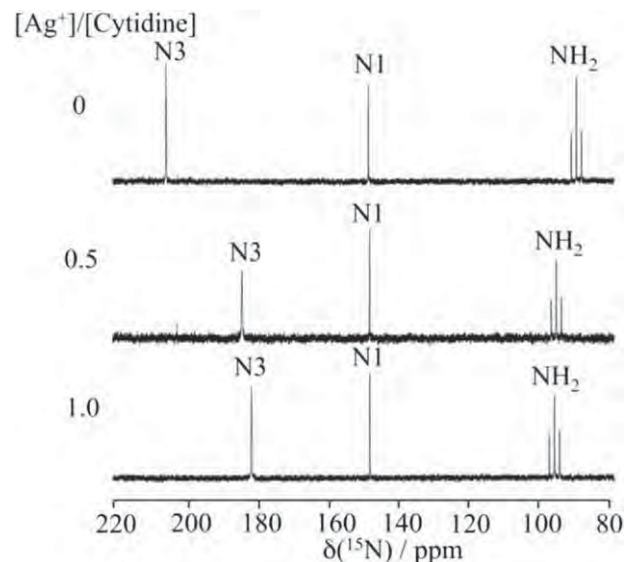


Fig. 6. ^{15}N NMR spectra of a uniformly ^{15}N -labeled cytosine mononucleoside with or without the Ag^+ ion. ^{15}N NMR spectra of 15 mM uniformly ^{15}N -labeled cytosine with various concentrations of the Ag^+ ion were measured in DMSO-d_6 at 25 °C. Molar ratios are labeled at the left side of the spectra. Resonance assignments are indicated in the spectra.

mismatched base pair duplex DNA with another base sequence was also stabilized not by other metal ions (Mg^{2+} , Ca^{2+} , Mn^{2+} , Fe^{2+} , Fe^{3+} , Co^{2+} , Ni^{2+} , Cu^{2+} , Zn^{2+} , Ru^{3+} , Pd^{2+} , Cd^{2+} , and Pb^{2+}) but by only the Ag^+ ion [10], which was consistent with the present results. Combining these results, we conclude that the combination of the Ag^+ ion and the duplex DNA with the C:C mismatched base pair is highly specific for the stabilization of the complex between metal ion and duplex DNA.

The ITC profile for the injection of the Ag^+ ion into the perfectly matched duplex DNA (X:Y = C:G and G:C) was examined in the presence of 100 mM NaNO_3 (Fig. 3b and c). A large magnitude of exothermic heat pulse was observed after each injection, and the

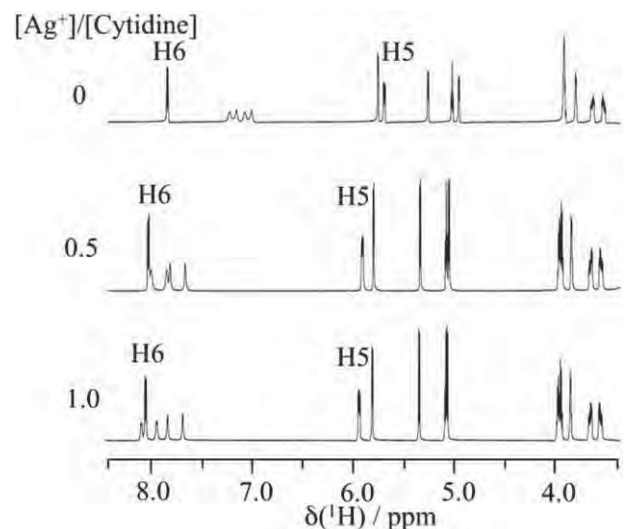


Fig. 7. ^1H NMR spectra of a uniformly ^{15}N -labeled cytosine mononucleoside with or without the Ag^+ ion. ^1H NMR spectra of 15 mM uniformly ^{15}N -labeled cytosine with various concentrations of the Ag^+ ion were measured in DMSO-d_6 at 25 °C. Molar ratios are labeled at the left side of the spectra. Resonance assignments are indicated in the spectra.

Table 2
 ^1H and ^{15}N NMR chemical shift perturbations of cytosine base in a uniformly ^{15}N -labeled cytosine mononucleoside and a nonlabeled duplex 1 upon the binding with the Ag^+ ion, obtained from ^1H NMR and ^{15}N NMR spectra.

Nucleus	Site	$[\text{Ag}^+]/[^{15}\text{N}\text{-labeled cytosine}] = 0.5$ (ppm) ^a	$[\text{Ag}^+]/[^{15}\text{N}\text{-labeled cytosine}] = 1.0$ (ppm) ^a	$[\text{Ag}^+]/[\text{Nonlabeled duplex 1}] = 1.0$ (ppm) ^a
^1H	H5	+0.25	+0.26	+0.21
	H6	+0.22	+0.22	+0.25
^{15}N	N1	-0.39	-0.42	na ^b
	N3	-21.8	-24.5	na ^b
	NH ₂	+5.80	+6.30	na ^b

^a Positive and negative values correspond to the downfield and upfield shifts, respectively.

^b Not applicable due to the absence of ^{15}N labeling of the duplex 1.

magnitude of each peak was not significantly different after each injection. To confirm that the exothermic heat pulses are derived from the nonspecific binding between the Ag^+ ion and the phosphate backbones of the perfectly matched duplex DNA, we measured the ITC profile for the injection of the Ag^+ ion into X:Y = G:C in the presence of higher salt concentration, 1 M NaNO_3 (Figure S4a). Similar to the case in the presence of 100 mM NaNO_3

(Fig. 3c), an exothermic heat pulse was observed after each injection and no significant difference in the magnitude of each peak was observed. The magnitudes of the exothermic heat pulses in the presence of 1 M NaNO_3 were significantly smaller than those observed in the presence of 100 mM NaNO_3 (Figure S4b). Before injecting the Ag^+ ion, the phosphate backbones of X:Y = G:C may bind with the Na^+ ion. The binding affinity of the Na^+ ion with the phosphate backbones of X:Y = G:C in the presence of 1 M NaNO_3 may be larger than that in the presence of 100 mM NaNO_3 . The bound Na^+ ion may be exchanged by the injected Ag^+ ion. The degree of the exchange by the Ag^+ ion in the presence of 1 M NaNO_3 may be smaller than that in the presence of 100 mM NaNO_3 due to the larger binding affinity of the Na^+ ion. Thus, the smaller magnitudes of the heat pulses upon the binding of the Ag^+ ion with the phosphate backbones were observed in the presence of 1 M NaNO_3 (Figure S4b). This suggests that the heat pulses observed upon the binding between the Ag^+ ion and the perfectly matched duplex DNA (X:Y = C:G and G:C) (Fig. 3b and c) may result from the nonspecific binding between the Ag^+ ion and the DNA phosphate backbones.

ITC analyses revealed that the Ag^+ ion specifically bound with the C:C mismatched base pair in the duplex DNA at a molar ratio of 1:1 (Fig. 3 and Table 1). ESI-MS also supported the specific binding and the molar ratio of 1:1 between the Ag^+ ion and the C:C mismatched base pair (Fig. 4). The termination of the chemical shift change for the H5 and H6 signals at the molar equivalency of $[\text{Ag}^+]/[\text{duplex 1}] = 1.0$ also indicated that the duplex 1 binds with the Ag^+ ion at a molar ratio of 1:1 (Fig. 8). The specific binding of the Ag^+ ion with the C:C mismatched base pair may result in the observed specific stabilization of the C:C mismatched base pair duplex DNA by the addition of the Ag^+ ion (Fig. 2 and Table S1). We previously reported that the Hg^{2+} ion specifically bound with the T:T mismatched base pair in the duplex DNA at a molar ratio of 1:1 to form T-Hg-T metal-mediated base pair [16–19]. Both the Hg^{2+} and Ag^+ ion have been known to bind selectively with base moieties rather than with the phosphate and sugar groups in DNA [22–29]. In the case of the T-Hg-T base pair, our previous study of ^{15}N NMR spectra of the complex between the Hg^{2+} ion and the duplex DNA containing the T:T mismatched base pair labeled with ^{15}N at the N3 position [30,31] showed that ^{15}N - ^{15}N J-coupling was observed across the Hg^{2+} ion with the coupling constant ($^2J_{\text{NN}}$) of 2.4 Hz, and the Hg^{2+} ion specifically bound with the N3 positions of the two thymine bases in place of the imino protons and bridged two thymine bases to form the T-Hg-T base pair. Analogous to the T-Hg-T base pair formation, the Ag^+ ion may specifically bind with the N3 positions of the two cytosine bases and bridge the two cytosine bases to form the C-Ag-C base pair. A similar binding mode to bind with the N3 positions was proposed for the interaction between the Ag^+ ion and artificially designed pyridine nucleobases in duplex DNA [29]. We previously analyzed the ^1H -NMR spectra of the C:C mismatched base pair duplex DNA in the absence and presence of the Ag^+ ion [10]. The proton exchange rate between the Ag^+ -free and Ag^+ -bound duplex DNAs was slow relative to the timescale of the NMR measurement [10], although the exchange rates of metal ion association–dissociation processes with DNA/RNA molecules were usually fast relative to the timescale of the NMR measurement [32]. The similar slow proton exchange rate was also observed in the ^1H -NMR study of the T-Hg-T base pair formation, where the Hg^{2+} ion bound with the N3 positions of the two thymine bases [17]. Thus, the observed slow proton exchange rate for the C-Ag-C formation suggested that the Ag^+ ion may bind with the inner N3 positions rather than with the outer O2 or N4 positions. To reveal the binding position of the Ag^+ ion with the C:C mismatched base pair more clearly, we performed more extensive NMR experiments in the present study. Our present NMR study of

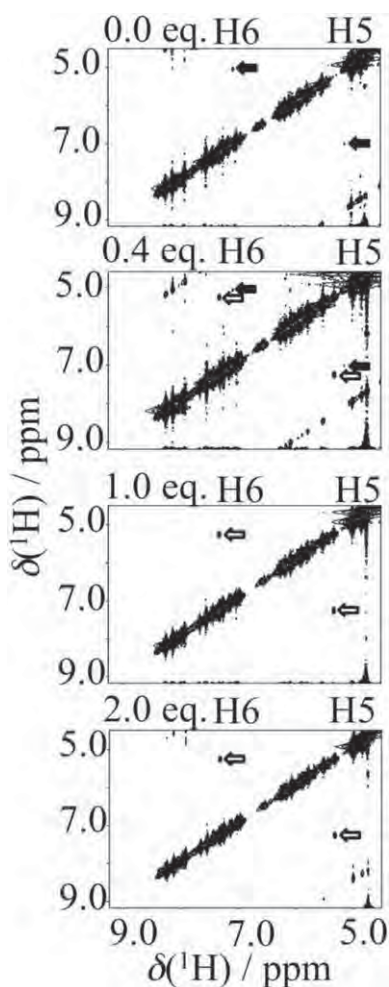


Fig. 8. ^1H - ^1H COSY spectra of a nonlabeled duplex 1 with or without the Ag^+ ion. ^1H - ^1H COSY spectra of 1.3 mM nonlabeled duplex 1 with various concentrations of the Ag^+ ion were measured in D_2O with 100 mM NaNO_3 at 25 °C. Molar equivalency of $[\text{Ag}^+]/[\text{duplex 1}]$ is labeled on top of each spectrum. H5–H6 cross peaks of Ag^+ -free and Ag^+ -bound forms are labeled with black and white arrows, respectively.

the Ag^+ ion binding with uniformly ^{15}N -labeled cytidine indicated that the preferential binding site of the Ag^+ ion was the N3 position of the cytidine (Fig. 6), and the H5 and H6 signals of the labeled cytidine were downfield shifted upon the binding of the Ag^+ ion with N3 of the cytidine (Fig. 7). The chemical shift changes for the H5 and H6 signals of the labeled cytidine upon the binding of the Ag^+ ion were quite similar in magnitude to those of the C:C mismatched base pair in duplex 1, suggesting that the binding site of the Ag^+ ion would also be the N3 positions of the C:C mismatched base pair in duplex 1 (Fig. 8 and Table 2). Taken together, we conclude that the Ag^+ ion may bind with the N3 positions of the two cytosine bases and bridge the two cytosine bases to form the C–Ag–C complex (Fig. 1a) in the duplex DNA. However, our NMR data cannot fully exclude additional binding to the exocyclic O2 or N4 positions of the cytosine bases [28]. Also, a previous infrared spectroscopic study proposed a possibility for the binding of the Ag^+ ion to the N7 position of the guanine bases in calf thymus DNA films [20].

The K_a and ΔG for the specific binding between the Ag^+ ion and the C:C mismatched base pair was nearly 10^6 M^{-1} and $-7.7 \text{ kcal mol}^{-1}$, respectively (Table 1). The magnitudes of the observed K_a and ΔG are significantly larger than those previously reported for the nonspecific interaction between metal ion and DNA (3.2×10^3 – $1.4 \times 10^5 \text{ M}^{-1}$) [3–8,15], supporting the specific binding between the Ag^+ ion and the C:C mismatched base pair. The thermodynamic properties of the specific binding have not been examined previously [10]. The observed ΔG resulted from both the observed negative ΔH and positive ΔS (Table 1). The positive ΔS for the specific binding between the Ag^+ ion and the C:C mismatched base pair measured by ITC (Table 1) includes a major contribution of a positive dehydration entropy change from the release of structured water molecules surrounding the Ag^+ ion and the DNA, and a conformational entropy change from the conformational change of duplex DNA upon binding with the Ag^+ ion [33]. The CD spectra showed that the higher-order structure of the duplex DNA was not significantly distorted by the specific binding of the Ag^+ ion (Fig. 5), suggesting no significant contribution of a conformational entropy change to the observed positive ΔS (Table 1). Thus, the observed positive ΔS (Table 1) may mainly result from the positive dehydration entropy change from the release of structured water molecules surrounding the Ag^+ ion and the DNA. In fact, a positive dehydration entropy change of the Ag^+ ion ($18 \text{ cal mol}^{-1} \text{ K}^{-1}$) [34] is similar in magnitude to the observed positive ΔS (Table 1). On the other hand, the negative ΔH for the specific binding between the Ag^+ ion and the C:C mismatched base pair measured by ITC (Table 1) reflects a major contribution from a positive dehydration enthalpy change of the Ag^+ ion ($115 \text{ kcal mol}^{-1}$) [35], and a negative binding enthalpy change from the bond formation between the Ag^+ ion and the Ag^+ ion binding positions in the two cytosine bases to form the C–Ag–C complex. Because the sign of the binding enthalpy change upon the bond formation to form the C–Ag–C complex was negative and the sign of the dehydration enthalpy change was positive, the observed negative ΔH (Table 1) might have been mainly driven by the negative binding enthalpy change upon the bond formation to form the C–Ag–C complex. Based on these, we propose a possible scheme for the specific binding between the Ag^+ ion and the C:C mismatched base pair (Fig. 9). The Ag^+ ion surrounded by structured water molecules may be dehydrated with significant contribution of the positive dehydration entropy change. The dehydrated Ag^+ ion may bind with the two cytosine bases to form the C–Ag–C complex with significant contribution from the negative binding enthalpy change.

Previous study by capillary electrophoresis reported the binding constant of $8.3 \times 10^4 \text{ M}^{-1}$ for the Ag^+ ion binding to the N7 position

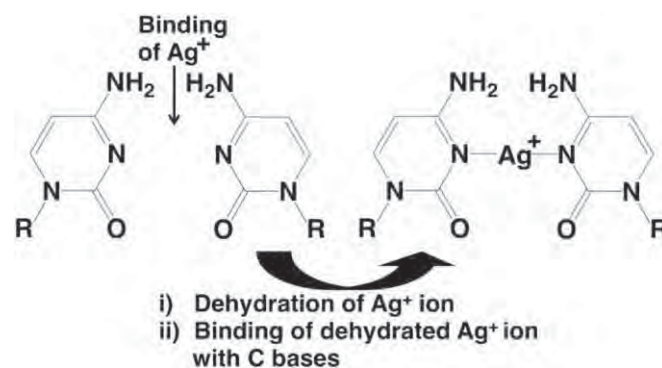


Fig. 9. Possible scheme for the specific binding between the Ag^+ ion and the C:C mismatched base pair. The Ag^+ ion surrounded by structured water molecules may be dehydrated. The dehydrated Ag^+ ion may bind with the two cytosine bases to form an N_3 – Ag – N_3 bond.

of the guanine bases in calf thymus DNA [36], which was about 10 times smaller than those obtained from the present study (nearly 10^6 M^{-1}) for the Ag^+ ion binding to the N3 positions of the C:C mismatched base pair. The number of Ag – N bond formed for the C–Ag–C complex may be larger than that formed for the Ag – G adduct, which may result in larger magnitude of the negative binding enthalpy change and provide a favorable component to the Gibbs free energy change and the binding constant.

5. Conclusions

The present study has demonstrated that the combination of the Ag^+ ion and the C:C mismatched base pair is highly specific for the metal-mediated base pair formation. The present work has also revealed that the binding constant between the Ag^+ ion and the C:C mismatched base pair is significantly larger than those for nonspecific interactions between metal ions and DNA. The specific binding between the Ag^+ ion and the C:C mismatched base pair with large binding affinity may be applied to various applications. The formation of the C–Ag–C metal-mediated base pair with the large binding affinity may enable alignment of multiple Ag^+ ions in natural C-rich duplex DNA, which may lead to construction of metallic nanowires and design of biomolecular electronic devices [37]. Further, due to the high binding specificity, the binding between the Ag^+ ion and the C:C mismatched base pair can be applied to the detection of base differences in duplex DNA, which may lead to development of efficient strategy to detect the single nucleotide polymorphisms, the most abundant form of natural genetic variation in the human genome, and promotion of customized medicine [38]. In addition, by the specific binding between the Ag^+ ion and the C:C mismatched base pair, C-rich oligonucleotides immobilized on the polymer beads can be applied to the removal of the Ag^+ ion in industrial wastewater, which may lead to advancement of convenient methods to improve the natural environment [39]. Taken together, we conclude that the specific formation of C–Ag–C base pair with large binding affinity would provide a binding mode of metal ion–DNA interactions, similar to that of the previously reported T–Hg–T base pair [16–19]. The C–Ag–C base pair may be useful for wide variety of potential applications of metal-mediated base pairs in various fields, such as material, life and environmental sciences.

Acknowledgments

We are grateful to Ms. A. Takamori for her technical assistance in the initial stage of this study. This work was partly supported by the

Casio Science Promotion Foundation; Iketani Science and Technology Foundation; Nakatani Foundation of Electronic Measuring Technology Advancement; and Tateishi Science and Technology Foundation. This work was also supported in part by Grant-in-Aid for JSPS Fellows (08J07706 to T.K.) from the Ministry of Education, Science, Sports, and Culture of Japan.

Appendix A. Supplementary material

Supplementary data associated with this article can be found, in the online version, at <http://dx.doi.org/10.1016/j.biochi.2012.06.024>.

References

- [1] J. Muller, Functional metal ions in nucleic acids, *Metallomics* 2 (2010) 318–327.
- [2] J. Schnabl, R.K. Sigel, Controlling ribozyme activity by metal ions, *Curr. Opin. Chem. Biol.* 14 (2010) 269–275.
- [3] H. Arakawa, R. Ahmad, M. Naoui, H.A. Tajmir-Riahi, A comparative study of calf thymus DNA binding to Cr(III) and Cr(VI) ions. Evidence for the guanine N-7-chromium-phosphate chelate formation, *J. Biol. Chem.* 275 (2000) 10150–10153.
- [4] A.A. Ouameur, S. Nafisi, N. Mohajerani, H.A. Tajmir-Riahi, Thallium-DNA complexes in aqueous solution. Major or minor groove binding, *J. Biomol. Struct. Dyn.* 20 (2003) 561–565.
- [5] A.A. Ouameur, H. Arakawa, R. Ahmad, M. Naoui, H.A. Tajmir-Riahi, A comparative study of Fe(II) and Fe(III) interactions with DNA duplex: major and minor grooves bindings, *DNA Cell Biol.* 24 (2005) 394–401.
- [6] J. Wu, F. Du, P. Zhang, I.A. Khan, J. Chen, Y. Liang, Thermodynamics of the interaction of aluminum ions with DNA: implications for the biological function of aluminum, *J. Inorg. Biochem.* 99 (2005) 1145–1154.
- [7] K. Utsuno, Thermodynamics of DNA condensation caused by Mn^{2+} binding, *Chem. Pharm. Bull. (Tokyo)* 56 (2008) 247–249.
- [8] Y. Li, Y.L. Xia, Y. Jiang, X.P. Yan, Extracting stoichiometry, thermodynamics, and kinetics for the interaction of DNA with cadmium ion by capillary electrophoresis on-line coupled with electrothermal atomic absorption spectrometry, *Electrophoresis* 29 (2008) 1173–1179.
- [9] D. Beyersmann, A. Hartwig, Carcinogenic metal compounds: recent insight into molecular and cellular mechanisms, *Arch. Toxicol.* 82 (2008) 493–512.
- [10] A. Ono, S. Cao, H. Togashi, M. Tashiro, T. Fujimoto, T. Machinami, S. Oda, Y. Miyake, I. Okamoto, Y. Tanaka, Specific interactions between silver(I) ions and cytosine-cytosine pairs in DNA duplexes, *Chem. Commun. (Camb)* (2008) 4825–4827.
- [11] T. Wiseman, S. Williston, J.F. Brandts, L.N. Lin, Rapid measurement of binding constants and heats of binding using a new titration calorimeter, *Anal. Biochem.* 179 (1989) 131–137.
- [12] F. Rosu, E. De Pauw, V. Gabelica, Electrospray mass spectrometry to study drug-nucleic acids interactions, *Biochimie* 90 (2008) 1074–1087.
- [13] J.S. Becker, N. Jakubowski, The synergy of elemental and biomolecular mass spectrometry: new analytical strategies in life sciences, *Chem. Soc. Rev.* 38 (2009) 1969–1983.
- [14] J.S. Brodbelt, Evaluation of DNA/Ligand interactions by electrospray ionization mass spectrometry, *Annu. Rev. Anal. Chem. (Palo Alto Calif.)* 3 (2010) 67–87.
- [15] E. Stellwagen, Q. Dong, N.C. Stellwagen, Quantitative analysis of monovalent counterion binding to random-sequence, double-stranded DNA using the replacement ion method, *Biochemistry* 46 (2007) 2050–2058.
- [16] A. Ono, H. Togashi, Highly selective oligonucleotide-based sensor for mercury(II) in aqueous solutions, *Angew. Chem. Int. Edit* 43 (2004) 4300–4302.
- [17] Y. Miyake, H. Togashi, M. Tashiro, H. Yamaguchi, S. Oda, M. Kudo, Y. Tanaka, Y. Kondo, R. Sawa, T. Fujimoto, T. Machinami, A. Ono, Mercury(II)-mediated formation of thymine-Hg(II)-thymine base pairs in DNA duplexes, *J. Am. Chem. Soc.* 128 (2006) 2172–2173.
- [18] I. Okamoto, K. Iwamoto, Y. Watanabe, Y. Miyake, A. Ono, Metal-ion selectivity of chemically modified uracil pairs in DNA duplexes, *Angew. Chem. Int. Ed. Engl.* 48 (2009) 1648–1651.
- [19] H. Torigoe, A. Ono, T. Kozasa, Hg(II) ion specifically binds with T: T mismatched base pair in duplex DNA, *Chemistry* 16 (2010) 13218–13225.
- [20] D.E. DiRico Jr., P.B. Keller, K.A. Hartman, The infrared spectrum and structure of the type I complex of silver and DNA, *Nucleic Acids Res.* 13 (1985) 251–260.
- [21] D.M. Gray, R.L. Ratliff, M.R. Vaughan, Circular dichroism spectroscopy of DNA, *Methods Enzymol.* 211 (1992) 389–406.
- [22] T. Yamane, N. Davidson, None of the spectra of the mercury (II) and silver (I) complexes of some polyribonucleotides and ribonucleic acid, *Biochim. Biophys. Acta* 55 (1962) 780–782.
- [23] R.M. Izatt, J.J. Christensen, J.H. Rytting, Sites and thermodynamic quantities associated with proton and metal ion interaction with ribonucleic acid, deoxyribonucleic acid, and their constituent bases, nucleosides, and nucleotides, *Chem. Rev.* 71 (1971) 439–481.
- [24] T. Yamane, N. Davidson, On the complexing of deoxyribonucleic acid by silver (I), *Biochim. Biophys. Acta* 55 (1962) 609–621.
- [25] M. Daune, C.A. Dekker, H.K. Schachman, Complexes of silver ion with natural and synthetic polynucleotides, *Biopolymers* 4 (1966) 51–76.
- [26] R.H. Jensen, N. Davidson, Spectrophotometric, potentiometric, and density gradient ultracentrifugation studies of the binding of silver ion by DNA, *Biopolymers* 4 (1966) 17–32.
- [27] G.L. Eichhorn, J.J. Butzow, P. Clark, E. Tarien, Interaction of metal ions with polynucleotides and related compounds. X. Studies on the reaction of silver (I) with the nucleosides and polynucleotides, and the effect of silver(I) on the zinc(II) degradation of polynucleotides, *Biopolymers* 5 (1967) 283–296.
- [28] L.G. Marzilli, T.J. Kistenmacher, M. Rossi, An extension of the role of O(2) of cytosine residues in the binding of metal ions. Synthesis and structure of 1-methylcytosine, *J. Am. Chem. Soc.* 99 (1977) 2797–2798.
- [29] K. Tanaka, Y. Yamada, M. Shionoya, Formation of silver(I)-mediated DNA duplex and triplex through an alternative base pair of pyridine nucleobases, *J. Am. Chem. Soc.* 124 (2002) 8802–8803.
- [30] Y. Tanaka, S. Oda, H. Yamaguchi, Y. Kondo, C. Kojima, A. Ono, 15N-15N J-coupling across Hg(II): direct observation of Hg(II)-mediated T-T base pairs in a DNA duplex, *J. Am. Chem. Soc.* 129 (2007) 244–245.
- [31] Y. Tanaka, A. Ono, Nitrogen-15 NMR spectroscopy of N-metallated nucleic acids: insights into 15N NMR parameters and N-metal bonds, *Dalton Trans.* (2008) 4965–4974.
- [32] Y. Tanaka, C. Kojima, E.H. Morita, Y. Kasai, K. Yamasaki, A. Ono, M. Kainosho, K. Taira, Identification of the metal ion binding site on an RNA motif from hammerhead ribozymes using (15)N NMR spectroscopy, *J. Am. Chem. Soc.* 124 (2002) 4595–4601.
- [33] D.C. Rau, V.A. Parsegian, Direct measurement of temperature-dependent solvation forces between DNA double helices, *Biophys. J.* 61 (1992) 260–271.
- [34] D.R. Rosseinsky, Electrode potentials and hydration energies - theories and correlations, *Chem. Rev.* 65 (1965) 467–490.
- [35] A.A. Rashin, B. Honig, Reevaluation of the Born model of ion hydration, *J. Phys. Chem.-US* 89 (1985) 5588–5593.
- [36] H. Arakawa, J.F. Neault, H.A. Tajmir-Riahi, Silver(I) complexes with DNA and RNA studied by Fourier transform infrared spectroscopy and capillary electrophoresis, *Biophys. J.* 81 (2001) 1580–1587.
- [37] K.M. Abu-Salah, A.A. Ansari, S.A. Alrokayan, DNA-based applications in nanobiotechnology, *J. Biomed. Biotechnol.* 2010 (2010) 715295.
- [38] C. Ding, S. Jin, High-throughput methods for SNP genotyping, *Methods Mol. Biol.* 578 (2009) 245–254.
- [39] T. Faunce, A. Watal, Nanosilver and global public health: international regulatory issues, *Nanomedicine (Lond.)* 5 (2010) 617–632.



Positive cooperativity of the specific binding between Hg^{2+} ion and T:T mismatched base pairs in duplex DNA

Hidetaka Torigoe^{a,*}, Yukako Miyakawa^a, Akira Ono^b, Tetsuo Kozasa^a

^a Department of Applied Chemistry, Faculty of Science, Tokyo University of Science, 1-3 Kagurazaka, Shinjuku-ku, Tokyo 162-8601, Japan

^b Department of Material & Life Chemistry, Faculty of Engineering, Kanagawa University, 3-27-1 Rokkakubashi, Kanagawa-ku, Yokohama 221-8686, Japan

ARTICLE INFO

Article history:

Available online 8 April 2011

Keywords:

Hg^{2+} ion
T:T mismatched base pair
Isothermal titration calorimetry
CD spectroscopy
Specific binding
Positively cooperative binding

ABSTRACT

Metal-mediated base pairs by the interaction between metal ions and artificial bases in oligonucleotides have been developed for their potential applications in nanotechnology. We recently found that a natural T:T mismatched base pair bound with Hg^{2+} ion to form a novel T–Hg–T base pair. Here, we examined the thermodynamic properties of the binding between Hg^{2+} and each of the single and double T:T mismatched base pair duplex DNAs by isothermal titration calorimetry. Hg^{2+} specifically bound with the T:T mismatched base pair at 1:1 molar ratio with 10^6 M^{-1} binding constant, which was significantly larger than those for nonspecific metal ion–DNA interactions. In the Hg^{2+} –double T:T mismatched base pair interaction, the affinity for the second Hg^{2+} binding was significantly larger than that for the first Hg^{2+} binding. The positively cooperative binding may be favorable to align multiple Hg^{2+} in duplex DNA for the application of the metal-mediated base pairs in nanotechnology.

© 2011 Elsevier B.V. All rights reserved.

1. Introduction

The interactions between metal ions and nucleic acids have attracted considerable interest not only for their involvement in biological processes, such as RNA folding [1,2] and enzymatic activity of ribozymes [3,4], but also for their wide variety of potential applications in nanotechnology including the design of biomolecular nanomachines and nanodevices [5,6]. Metal-mediated base pairs by the interaction between metal ions and artificial bases in synthetic oligonucleotides have been extensively developed for their potential applications in nanotechnology [7–15]. The metal ions were placed between the two artificial bases in duplex oligonucleotides, as shown by structural analyses of the complex between the metal ions and the artificial bases [16,17]. On the other hand, we have recently found an alternative method for generating metal-mediated base pairs in duplex DNA, based on the binding between a metal ion and a natural base in duplex DNA [18–21]. Only Hg^{2+} ion and no other metal ions bound with a natural base, thymine–thymine (T:T) mismatch, in a duplex DNA to form T–Hg–T base pair (Fig. 1a), and the binding of the Hg^{2+} ion stabilized the duplex DNA with the T:T mismatched base pair [18,19]. The thermal stability of the duplex DNA with the T–Hg–T base pair was comparable to that with the corresponding normal T:A or A:T base pair [19]. Hg^{2+} ion specifically bound with the T:T mismatched base pair, and did not bind with the perfectly matched base pairs and the

other kinds of mismatched base pairs [22,23]. Because the artificial bases are more difficult to be prepared due to time-consuming organic synthesis in comparison with the natural T:T mismatch, the T–Hg–T base pair formation (Fig. 1a) is more convenient than the base pair formation between the metal ions and the artificial bases. In spite of these convenient properties of the T–Hg–T base pair (Fig. 1a), the mechanistic explanation for the T–Hg–T base pair formation was not clearly understood. Therefore, here, we have expanded our previous line of research to explore the thermodynamic properties of the interaction between the Hg^{2+} ion and the T:T mismatched base pair. To explore the possibility for the application of multiple aligned T–Hg–T base pairs in duplex DNA to nanotechnology, we have examined the thermodynamic properties of the Hg^{2+} ion binding with not only single but also double T:T mismatched base pairs. The interaction between the Hg^{2+} ion and each of the single and double T:T mismatched base pair duplex DNA and the corresponding perfectly matched duplex DNA was analysed by isothermal titration calorimetry (ITC) [24], and circular dichroism (CD) spectroscopy. ITC analyses have demonstrated that the Hg^{2+} ion specifically bound with the T:T mismatched base pair in the duplex DNA at a molar ratio of 1:1 with a binding constant of nearly 10^6 M^{-1} . The magnitude of the observed binding constant was significantly larger than those previously reported for the nonspecific interactions between metal ion and DNA [25–31]. The specific binding between the Hg^{2+} ion and the T:T mismatched base pair was driven by both a negative enthalpy change and a positive entropy change. ITC analyses of the interaction between the Hg^{2+} ion and the double T:T mismatched base pair duplex DNA have revealed that the affinity of the second binding between the

* Corresponding author. Tel.: +81 3 5228 8259; fax: +81 3 5261 4631.
E-mail address: htorigoe@rs.kagu.tus.ac.jp (H. Torigoe).

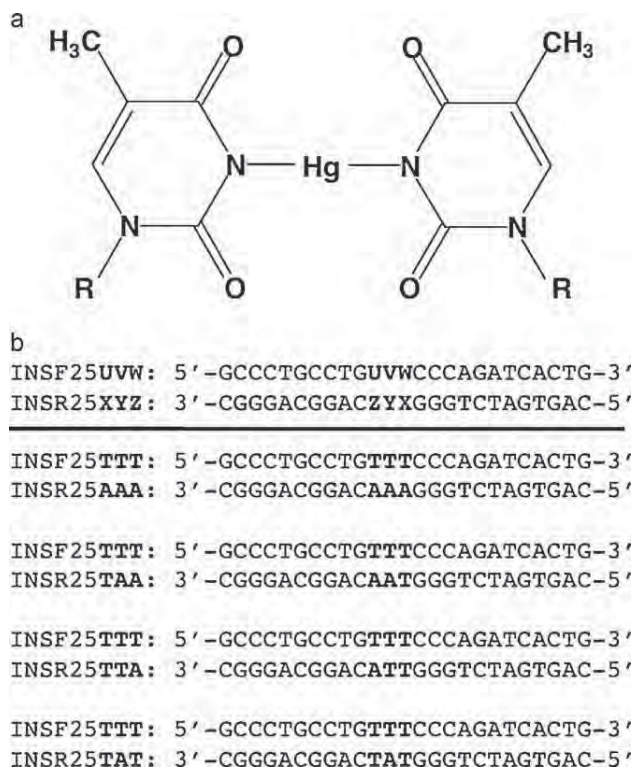


Fig. 1. (a) Structural formula of T–Hg–T base pair. (b) Oligonucleotide sequences of the target duplex INSF25UVW:INSR25XYZ used in the present study.

second Hg²⁺ ion and the second T:T mismatched base pair was significantly larger than that of the first binding between the first Hg²⁺ ion and the first T:T mismatched base pair. The positive cooperativity was observed for the specific binding between the Hg²⁺ ion and the double T:T mismatched base pairs. The positively cooperative binding would be favorable to align multiple Hg²⁺ ions in duplex DNA and support further progress in potential applications of metal-mediated base pairs in nanotechnology.

2. Experimental

2.1. Preparation of oligonucleotides

We synthesized 25-mer complementary DNA oligonucleotides, INSF25UVW: 5'-GCCCTGCCTGUVWCCCAGATCACTG-3' (UVW=TTT) (Fig. 1b) and INSR25XYZ: 5'-CAGTGATCTGGXYZCAGGCAGGGC-3' (XYZ=AAA, TAA, TTA, TAT) (Fig. 1b), on a DNA synthesizer by using the solid-phase cyanoethyl phosphoramidite method; we then purified them with reverse-phase high-performance liquid chromatography (HPLC) on a Wakosil DNA column. The concentration of all oligonucleotides was determined by UV absorbance. The purified complementary strands, INSF25UVW and INSR25XYZ, were annealed by heating at up to 90 °C, followed by a gradual cooling to room temperature. The annealed sample was applied on a hydroxyapatite column (BIORAD Inc.) to remove the unpaired single strands. The concentration of the duplex DNA (INSF25UVW:INSR25XYZ) was determined by UV absorption considering the DNA concentration ratio of 1 OD = 50 µg/ml, with a M_r of 16,500.

2.2. Isothermal titration calorimetry (ITC)

Isothermal titration experiments were carried out on a VP ITC system (Microcal Inc., U.S.A.) [24]. The duplex DNA

(INSF25UVW:INSR25XYZ) solutions were prepared by extensive dialysis against buffer A [10 mM sodium cacodylate-cacodylic acid (pH 6.8) and 100 mM NaClO₄]. Hg(ClO₄)₂ was dissolved in the dialysis buffer. The Hg(ClO₄)₂ solution in buffer A was injected 20 or 40 times in 5-µl increments at 5-min intervals into the duplex DNA (INSF25UVW:INSR25XYZ) solution without changing the reaction conditions. The heat for each injection was subtracted by the heat of dilution of the injectant, which was measured by injecting the Hg(ClO₄)₂ solution into the same buffer. Each corrected heat was divided by the moles of Hg(ClO₄)₂ injected and analysed with Microcal Origin software supplied by the manufacturer.

2.3. CD spectroscopy

CD spectra were recorded at 25 °C and pH 6.8 in buffer A either with or without Hg(ClO₄)₂ on a JASCO J-720 spectropolarimeter interfaced with a microcomputer. The cell path length was 1 cm. The concentration of the duplex DNA (INSF25UVW:INSR25XYZ) used was 1 µM.

3. Results

3.1. ITC analyses of the interaction between the Hg²⁺ ion and each of the single mismatched base pair duplex DNA and the corresponding perfectly matched duplex DNA

We examined the thermodynamic properties of the interaction between Hg(ClO₄)₂ and each of the single T:T mismatched base pair duplex DNA, INSF25TTT:INSR25TAA (Fig. 1b), and the corresponding perfectly matched duplex DNA, INSF25TTT:INSR25AAA (Fig. 1b), at 25 °C and pH 6.8 by ITC (Fig. 2) [24]. Fig. 2a shows a typical ITC profile of the interaction between Hg(ClO₄)₂ and INSF25TTT:INSR25TAA at 25 °C and pH 6.8. An exothermic heat pulse was observed each time after Hg(ClO₄)₂ was injected into INSF25TTT:INSR25TAA. The magnitude of each peak decreased gradually with each new injection, and a peak was still observed at a molar ratio of the last injection. The area under each peak was integrated, and the heat of the dilution of Hg(ClO₄)₂ measured in a separate experiment by injecting Hg(ClO₄)₂ into the same buffer was subtracted from the integrated values. The corrected heat was divided by the moles of injected solution, and the resulting values were plotted as a function of a molar ratio of [Hg²⁺ ion]/[INSF25TTT:INSR25TAA] (closed circles in Fig. 2c). The resultant titration plot was sigmoidal, indicating that the Hg²⁺ ion specifically bound with INSF25TTT:INSR25TAA. On the other hand, the ITC profile of the interaction between Hg(ClO₄)₂ and INSF25TTT:INSR25AAA at 25 °C and pH 6.8 is shown in Fig. 2b. Although an exothermic heat pulse was observed after each injection of Hg(ClO₄)₂ into INSF25TTT:INSR25AAA, the magnitude of each peak was not significantly changed with each new injection, which was in sharp contrast with the ITC profile observed for the interaction between Hg(ClO₄)₂ and INSF25TTT:INSR25TAA (Fig. 2a). The titration plot obtained from Fig. 2b (closed squares in Fig. 2c) in the same way as that obtained from Fig. 2a (closed circles in Fig. 2c) was not sigmoidal, indicating that the Hg²⁺ ion nonspecifically bound with INSF25TTT:INSR25AAA.

The nonspecific binding between the Hg²⁺ ion and INSF25TTT:INSR25AAA judged from the ITC titration plot (Fig. 2c) suggests that the Hg²⁺ ion may bind with the phosphate backbones of the perfectly matched duplex DNA (INSF25TTT:INSR25AAA) in a nonspecific manner due to the attraction between the positive charge of the Hg²⁺ ion and the negative charge of the DNA phosphate backbones. The nonspecific binding with the DNA phosphate backbones has been reported for many other metal ions, such as Mg²⁺ [32,33], Ca²⁺ [32,33], Al³⁺ [34], Ga³⁺ [34], Cr³⁺ [25], Fe³⁺ [27], Cu²⁺ [35], and Pb²⁺ [35]. On the other hand, the specific binding between the Hg²⁺ ion and INSF25TTT:INSR25TAA judged from the

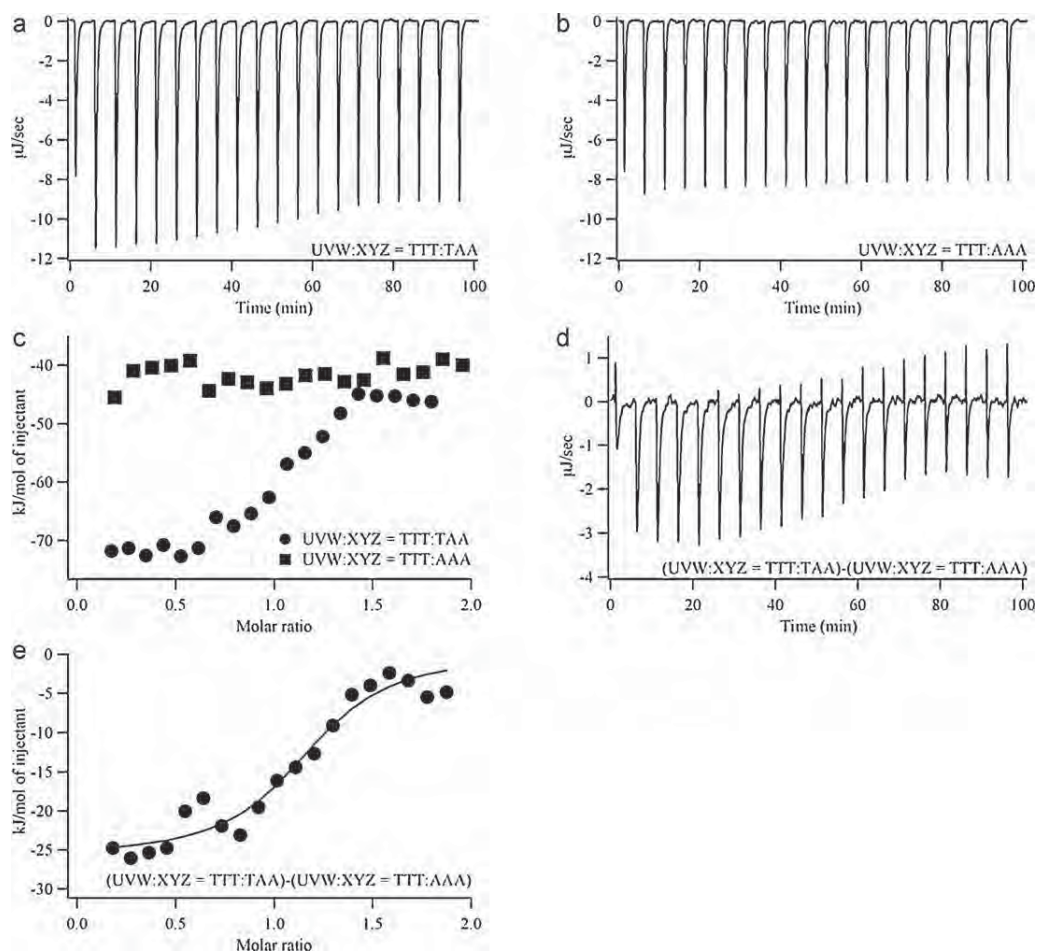


Fig. 2. Thermodynamic analyses of the interaction between the Hg^{2+} ion and each of the single T:T mismatched base pair duplex (INSF25TTT:INSR25TAA) and the corresponding perfectly matched duplex (INSF25TTT:INSR25AAA). (a and b) Typical ITC profile of the interaction between $\text{Hg}(\text{ClO}_4)_2$ and each of INSF25TTT:INSR25TAA (a) and INSF25TTT:INSR25AAA (b) at 25 °C and pH 6.8 in buffer A (see Section 2). $\text{Hg}(\text{ClO}_4)_2$ solution (1 mM in buffer A) was injected 20 times in 5- μl increments into each of INSF25TTT:INSR25TAA (a) and INSF25TTT:INSR25AAA (b) solution (40 μM in buffer A). Injections were administered over 12 s at 5-min intervals. (c) Titration plots against the molar ratio of $[\text{Hg}^{2+} \text{ ion}]/[\text{duplex DNA}]$, obtained from the ITC profiles in (a) and (b). (d) ITC profile for the specific binding between the Hg^{2+} ion and the single T:T mismatched base pair, obtained by subtracting the ITC profile observed for INSF25TTT:INSR25AAA in (b) from that observed for INSF25TTT:INSR25TAA in (a). (e) Titration plot against the molar ratio of $[\text{Hg}^{2+} \text{ ion}]/[\text{duplex DNA}]$, obtained from the ITC profile in (d). The data were fitted by a nonlinear least-squares method.

ITC titration plot (Fig. 2c) suggests that the Hg^{2+} ion may specifically bind with the single T:T mismatched base pair of the mismatched base pair duplex DNA (INSF25TTT:INSR25TAA) in addition to the nonspecific binding between the Hg^{2+} ion and the DNA phosphate backbones of INSF25TTT:INSR25TAA. Thus, the net heat derived from the specific binding between the Hg^{2+} ion and the single T:T mismatched base pair of INSF25TTT:INSR25TAA should be estimated by subtracting the heat observed for INSF25TTT:INSR25AAA from that observed for INSF25TTT:INSR25TAA. Based on these considerations, to analyse the thermodynamic parameters of the specific binding between the Hg^{2+} ion and the single T:T mismatched base pair of INSF25TTT:INSR25TAA, the ITC profile observed for INSF25TTT:INSR25AAA in Fig. 2b was subtracted from that observed for INSF25TTT:INSR25TAA in Fig. 2a to obtain that in Fig. 2d. The area under each peak in Fig. 2d was integrated, and the integrated values were divided by the moles of the injected solution. The resulting values were plotted as a function of the molar ratio of $[\text{Hg}^{2+} \text{ ion}]/[\text{duplex DNA}]$ (Fig. 2e). The resultant titration plot was fitted to a sigmoidal curve by a nonlinear least-squares method. The stoichiometry, n_1 , the binding constant, K_{a1} , and the enthalpy change, ΔH_1 , for the specific binding between the Hg^{2+} ion and the single T:T mismatched base pair were obtained from the fitted curve. The Gibbs free energy change, ΔG_1 , and the entropy change, ΔS_1 , were calculated from the equation,

$\Delta G_1 = -RT \ln K_{a1} = \Delta H_1 - T\Delta S_1$, where R is gas constant and T is the temperature.

Table 1 shows the thermodynamic parameters for the specific binding between the Hg^{2+} ion and the single T:T mismatched base pair, obtained from Fig. 2e. The obtained value of n_1 was nearly 1, indicating that the single Hg^{2+} ion bound with the single T:T mismatched base pair at a molar ratio of 1:1. Although the sign of ΔH_1 was negative, the sign of ΔS_1 was positive. Because both the observed negative ΔH_1 and positive ΔS_1 were favorable for the specific binding between the Hg^{2+} ion and the single T:T mismatched base pair, the specific binding between the Hg^{2+} ion and the single T:T mismatched base pair was driven by both the negative ΔH_1 and positive ΔS_1 . The magnitudes of the observed K_{a1} and ΔG_1 were significantly larger than those previously reported for the nonspecific interactions between metal ion and DNA [25–31], indicating that the single Hg^{2+} ion specifically bound with the single T:T mismatched base pair.

3.2. ITC analyses of the interaction between the Hg^{2+} ion and each of the continuous or interrupted double T:T mismatched base pair duplex DNA and the corresponding perfectly matched duplex DNA

To explore the possibility for the application of multiple aligned T–Hg–T base pairs in duplex DNA to nanotechnology, the inter-

Table 1

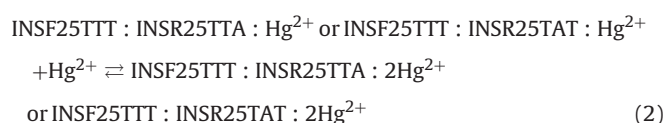
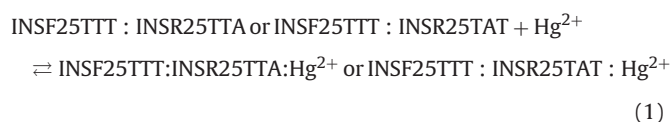
Thermodynamic parameters for the specific binding between the Hg²⁺ ion and each of the single T:T mismatched base pair and the continuous or interrupted double T:T mismatched base pairs at 25 °C and pH 6.8 in 10 mM sodium cacodylate-cacodylic acid and 100 mM NaClO₄, obtained from ITC measurements.

Binding parameters	Fig. 2e	Fig. 3g	Fig. 3h
n_1	1.16 ± 0.04	1.10 ± 0.04	1.10 ± 0.04
K_{a1} (M ⁻¹)	(5.87 ± 2.21) × 10 ⁵	(5.58 ± 2.86) × 10 ⁵	(5.15 ± 3.82) × 10 ⁵
ΔG_1 (kJ mol ⁻¹)	-32.9 ± 1.2	-32.8 ± 1.8	-32.6 ± 3.4
ΔH_1 (kJ mol ⁻¹)	-25.9 ± 1.3	-29.0 ± 9.1	-28.4 ± 3.6
ΔS_1 (J mol ⁻¹ K ⁻¹)	23.7 ± 4.4	12.9 ± 30.5	14.0 ± 12.2
n_2	na ^a	1.24 ± 0.10	1.27 ± 0.12
K_{a2} (M ⁻¹)	na ^a	(3.96 ± 2.01) × 10 ⁶	(8.01 ± 4.10) × 10 ⁶
ΔG_2 (kJ mol ⁻¹)	na ^a	-37.7 ± 1.8	-39.4 ± 1.8
ΔH_2 (kJ mol ⁻¹)	na ^a	-23.6 ± 5.3	-29.0 ± 2.8
ΔS_2 (J mol ⁻¹ K ⁻¹)	na ^a	47.2 ± 17.8	34.9 ± 9.5

^ana: not applicable as the titration plot in Fig. 2e was fitted to a model of single binding site.

action of the Hg²⁺ ion with not only single but also multiple T:T mismatched base pair duplex DNA should be investigated. To this end, we examined the thermodynamic properties of the interaction between Hg(ClO₄)₂ and each of the continuous or interrupted double T:T mismatched base pair duplex DNAs, INSF25TTT:INSR25TTA or INSF25TTT:INSR25TAT (Fig. 1b), and the corresponding perfectly matched duplex DNA, INSF25TTT:INSR25AAA (Fig. 1b), at 25 °C and pH 6.8 by ITC (Fig. 3). Fig. 3a shows a typical ITC profile of the interaction between Hg(ClO₄)₂ and INSF25TTT:INSR25TTA at 25 °C and pH 6.8. An exothermic heat pulse was observed each time after Hg(ClO₄)₂ was injected into INSF25TTT:INSR25TTA. The magnitude of each peak decreased gradually with each new injection, and a peak was still observed at a molar ratio of the last injection. The interaction between Hg(ClO₄)₂ and INSF25TTT:INSR25TAT at 25 °C and pH 6.8 also shows a similar ITC profile (Fig. 3b). The titration plots obtained from Fig. 3a (closed circles in Fig. 3d) and b (closed squares in Fig. 3d) in the same way as shown in the Section 3.1 (Fig. 2c) were sigmoidal, indicating that the Hg²⁺ ion specifically bound with INSF25TTT:INSR25TTA and INSF25TTT:INSR25TAT. On the other hand, the magnitude of each exothermic heat pulse observed after each injection of Hg(ClO₄)₂ into INSF25TTT:INSR25AAA was not significantly changed with each new injection (Fig. 3c), and the titration plot obtained from Fig. 3c (closed triangles in Fig. 3d) in the same way as shown in the Section 3.1 (Fig. 2c) was not sigmoidal, indicating the nonspecific binding between Hg²⁺ ion and INSF25TTT:INSR25AAA. The heat pulse observed in Fig. 3a and b may result from the specific binding between the Hg²⁺ ion and the continuous or interrupted double T:T mismatched base pairs of the duplex DNA (INSF25TTT:INSR25TTA or INSF25TTT:INSR25TAT) in addition to the nonspecific binding between the Hg²⁺ ion and the DNA phosphate backbones of the duplex DNA. In contrast, the heat pulse observed in Fig. 3c may correspond to only the nonspecific binding between the Hg²⁺ ion and the DNA phosphate backbones of the duplex DNA. Thus, the net heat derived from the specific binding between the Hg²⁺ ion and the continuous or interrupted double T:T mismatched base pairs of the duplex DNA (INSF25TTT:INSR25TTA or INSF25TTT:INSR25TAT) should be estimated by subtracting the heat observed for the perfectly matched duplex DNA (INSF25TTT:INSR25AAA) (Fig. 3c) from that observed for the continuous or interrupted double T:T mismatched base pair duplex DNA [INSF25TTT:INSR25TTA (Fig. 3a) or INSF25TTT:INSR25TAT (Fig. 3b)]. Based on these considerations, to analyse the thermodynamic parameters of the specific binding between the Hg²⁺ ion and the continuous double T:T mismatched base pairs of INSF25TTT:INSR25TTA, the ITC profile observed for INSF25TTT:INSR25AAA in Fig. 3c was subtracted from that observed for INSF25TTT:INSR25TTA in Fig. 3a to obtain that in Fig. 3e, and to obtain the thermodynamic parameters of the specific binding between the Hg²⁺ ion and the interrupted double T:T mismatched base pairs of INSF25TTT:INSR25TAT, the ITC profile observed for INSF25TTT:INSR25AAA in Fig. 3c was subtracted from that observed

for INSF25TTT:INSR25TAT in Fig. 3b to obtain that in Fig. 3f. The area under each peak in Fig. 3e was integrated, and the integrated values were divided by the moles of the injected solution. The resulting values were plotted as a function of the molar ratio of [Hg²⁺ ion]/[duplex DNA] (Fig. 3g). The resultant titration plot was fitted to a model of two binding sites by a nonlinear least-squares method. The model of two binding sites is based on the following two steps,



The stoichiometry, n_1 , the binding constant, K_{a1} , and the enthalpy change, ΔH_1 , for the first binding in step (1), and the stoichiometry, n_2 , the binding constant, K_{a2} , and the enthalpy change, ΔH_2 , for the second binding in step (2) were obtained from the fitted curve. The Gibbs free energy changes for the first and second binding, ΔG_1 and ΔG_2 , and the entropy changes for the first and second binding, ΔS_1 and ΔS_2 , were calculated from the equation, $\Delta G_1 = -RT \ln K_{a1} = \Delta H_1 - T\Delta S_1$ and $\Delta G_2 = -RT \ln K_{a2} = \Delta H_2 - T\Delta S_2$, where R is gas constant and T is the temperature. The titration plot (Fig. 3h) and the thermodynamic parameters of the specific binding between the Hg²⁺ ion and the interrupted double T:T mismatched base pairs of INSF25TTT:INSR25TAT were also obtained from Fig. 3f in the same way.

Table 1 shows the thermodynamic parameters for the specific binding of the Hg²⁺ ion with the continuous double T:T mismatched base pairs, obtained from Fig. 3g, and those with the interrupted double T:T mismatched base pairs, obtained from Fig. 3h, which are based on a model of two binding sites. For both cases of Fig. 3g and h, the values of n_1 and n_2 were nearly 1, indicating that the stoichiometric binding was achieved in each step of the first and second binding regardless of whether the double T:T mismatched base pairs were continuous or interrupted (Table 1). Also, for both cases of Fig. 3g and h, the magnitudes of the observed K_{a2} and ΔG_2 for the second binding between the second Hg²⁺ ion and the second T:T mismatched base pair were significantly larger than those of the observed K_{a1} and ΔG_1 for the first binding between the first Hg²⁺ ion and the first T:T mismatched base pair (Table 1). The positive cooperativity of the specific binding between the Hg²⁺ ion and the double T:T mismatched base pairs were observed for both of the continuous and interrupted double T:T mismatched base pairs (Table 1).

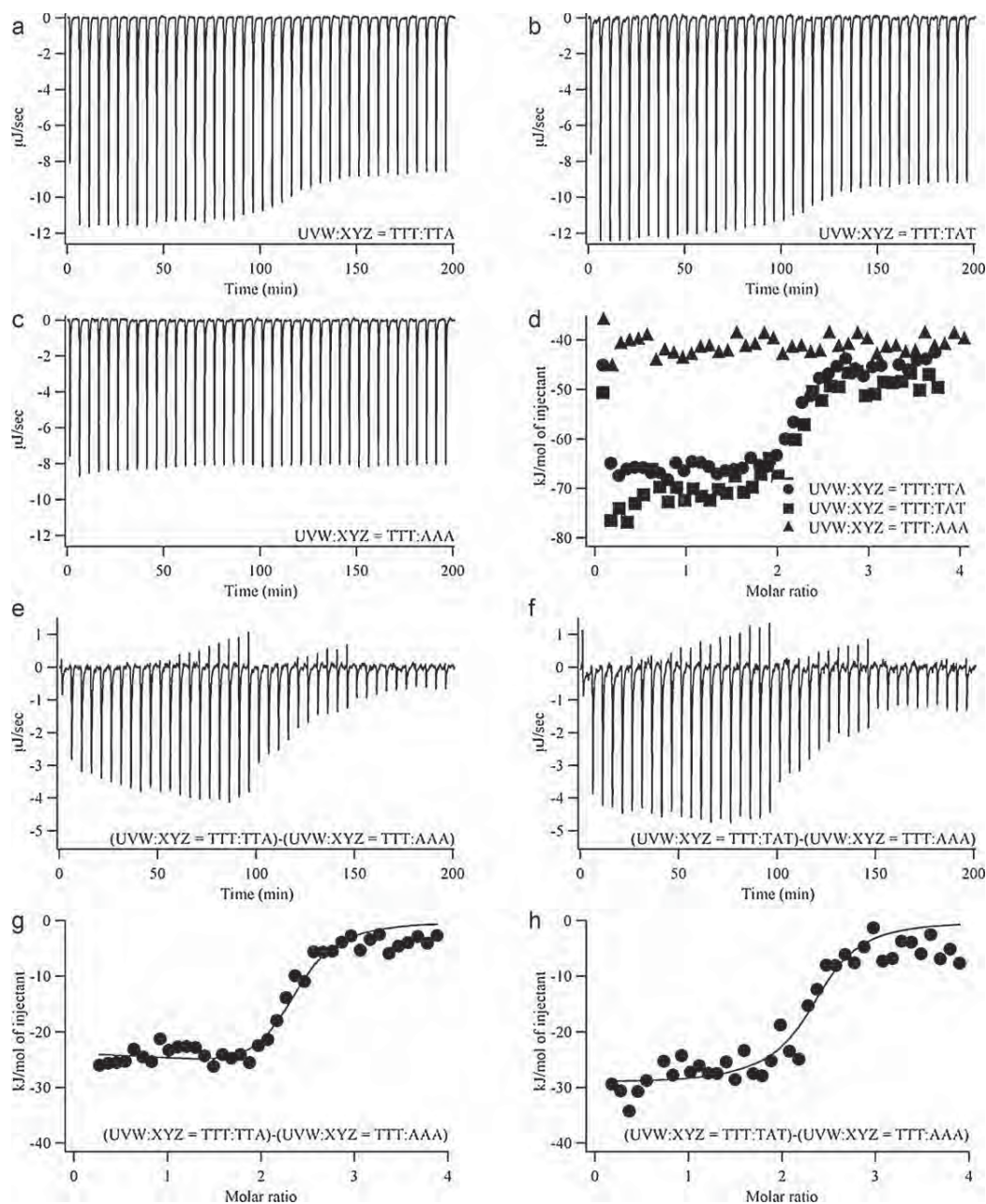


Fig. 3. Thermodynamic analyses of the interaction between the Hg^{2+} ion and each of the continuous or interrupted double T:T mismatched base pair duplexes (INSF25TTT:INSR25TTA or INSF25TTT:INSR25TAT) and the corresponding perfectly matched duplex (INSF25TTT:INSR25AAA). (a–c) Typical ITC profile of the interaction between $\text{Hg}(\text{ClO}_4)_2$ and each of INSF25TTT:INSR25TTA (a), INSF25TTT:INSR25TAT (b) and INSF25TTT:INSR25AAA (c) at 25 °C and pH 6.8 in buffer A (see Section 2). $\text{Hg}(\text{ClO}_4)_2$ solution (1 mM in buffer A) was injected 40 times in 5- μl increments into each of INSF25TTT:INSR25TTA (a), INSF25TTT:INSR25TAT (b) and INSF25TTT:INSR25AAA (c) solution (40 μM in buffer A). Injections were administered over 12 s at 5-min intervals. (d) Titration plots against the molar ratio of $[\text{Hg}^{2+} \text{ ion}]/[\text{duplex DNA}]$, obtained from the ITC profiles in (a)–(c). (e) ITC profile for the specific binding between the Hg^{2+} ion and the double continuous T:T mismatched base pair, obtained by subtracting the ITC profile observed for INSF25TTT:INSR25AAA in (c) from that observed for INSF25TTT:INSR25TTA in (a). (f) ITC profile for the specific binding between the Hg^{2+} ion and the double interrupted T:T mismatched base pair, obtained by subtracting the ITC profile observed for INSF25TTT:INSR25AAA in (c) from that observed for INSF25TTT:INSR25TAT in (b). (g) Titration plot against the molar ratio of $[\text{Hg}^{2+} \text{ ion}]/[\text{duplex DNA}]$, obtained from the ITC profile in (e). (h) Titration plot against the molar ratio of $[\text{Hg}^{2+} \text{ ion}]/[\text{duplex DNA}]$, obtained from the ITC profile in (f). The data in (g) and (h) were fitted to a model of two binding sites by a nonlinear least-squares method.

3.3. CD spectroscopy of the mismatched base pair duplex DNAs and the corresponding perfectly matched duplex DNA either with or without the Hg^{2+} ion

To examine the effect of the Hg^{2+} ion binding on the higher-order structure of duplex DNA, CD spectra of the perfectly matched duplex DNA (INSF25TTT:INSR25AAA) (Fig. 1b), the single T:T mismatched base pair duplex DNA (INSF25TTT:INSR25TAA) (Fig. 1b), and the double T:T mismatched base pair duplex DNAs

(INSF25TTT:INSR25TTA and INSF25TTT:INSR25TAT) (Fig. 1b) were measured in buffer A either with or without $\text{Hg}(\text{ClO}_4)_2$ at 25 °C and pH 6.8 (Fig. 4). The CD spectrum of INSF25TTT:INSR25AAA without $\text{Hg}(\text{ClO}_4)_2$ (Fig. 4a) may be quite different from those of INSF25TTT:INSR25TAA (Fig. 4b), INSF25TTT:INSR25TTA (Fig. 4c) and INSF25TTT:INSR25TAT (Fig. 4d) probably due to the absence of the T:T mismatched base pairs. The CD profile of INSF25TTT:INSR25AAA with $\text{Hg}(\text{ClO}_4)_2$ was quite similar to that observed without $\text{Hg}(\text{ClO}_4)_2$ (Fig. 4a). This result indicates that the

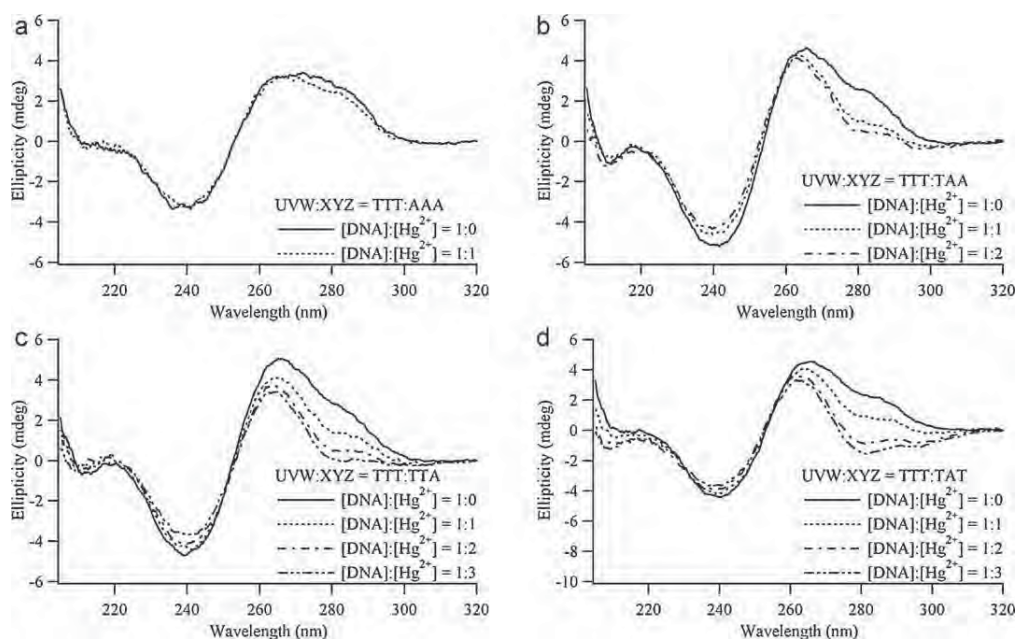


Fig. 4. CD spectra of the perfectly matched duplex, INSF25TTT:INSR25AAA (a), the single T:T mismatched base pair duplex, INSF25TTT:INSR25TAA (b), and the double T:T mismatched base pair duplexes, INSF25TTT:INSR25TTA (c) and INSF25TTT:INSR25TAT (d), with or without $\text{Hg}(\text{ClO}_4)_2$. Duplexes ($1 \mu\text{M}$) at 25°C and pH 6.8 in buffer A (see Section 2) with or without $\text{Hg}(\text{ClO}_4)_2$ were measured at a wavelength of 205–320 nm. The cell path length was 1 cm.

nonspecific binding of the Hg^{2+} ion with the phosphate backbones of the duplex DNA may not significantly change the higher-order structure of the duplex DNA. In contrast, the ellipticity of the CD profile of INSF25TTT:INSR25TAA in the 260–300 nm region was significantly decreased at the molar ratio of $[\text{Hg}^{2+}]/[\text{DNA}] = 1$ in comparison with that at the molar ratio of $[\text{Hg}^{2+}]/[\text{DNA}] = 0$ (Fig. 4b). This result indicates that the specific binding of the single Hg^{2+} ion with the single T:T mismatched base pair may significantly change the higher-order structure of the duplex DNA, unlike the nonspecific binding of the Hg^{2+} ion with the phosphate backbones of the duplex DNA. The spectral difference between $[\text{Hg}^{2+}]/[\text{DNA}] = 1$ and $[\text{Hg}^{2+}]/[\text{DNA}] = 2$ was significantly smaller in magnitude than that between $[\text{Hg}^{2+}]/[\text{DNA}] = 0$ and $[\text{Hg}^{2+}]/[\text{DNA}] = 1$ (Fig. 4b). The excess mol of Hg^{2+} may not significantly change the higher-order structure of the duplex DNA. As the molar ratio of $[\text{Hg}^{2+}]/[\text{duplex DNA}]$ was increased up to the value of 2, the ellipticity of the CD profile of INSF25TTT:INSR25TTA and INSF25TTT:INSR25TAT in the 260–300 nm region was significantly decreased (Fig. 4c and d). The change in the higher-order structure of the duplex DNA was also observed for the specific binding between the double Hg^{2+} ion and the double T:T mismatched base pairs. The spectral difference between $[\text{Hg}^{2+}]/[\text{DNA}] = 2$ and $[\text{Hg}^{2+}]/[\text{DNA}] = 3$ was significantly smaller in magnitude than that between $[\text{Hg}^{2+}]/[\text{DNA}] = 0$ and $[\text{Hg}^{2+}]/[\text{DNA}] = 1$ or that between $[\text{Hg}^{2+}]/[\text{DNA}] = 1$ and $[\text{Hg}^{2+}]/[\text{DNA}] = 2$ (Fig. 4c and d). The excess mol of Hg^{2+} may not significantly change the higher-order structure of the duplex DNA. These results clearly indicate that the higher-order structure of the T:T mismatched base pair duplex DNA was significantly changed by the specific binding of the Hg^{2+} ion with the T:T mismatched base pair.

4. Discussion

The ITC profile for the injection of the Hg^{2+} ion solution into the perfectly matched duplex (INSF25TTT:INSR25AAA) solution was examined in the presence of 100 mM NaClO_4 (Fig. 2b). A large magnitude of exothermic heat pulse was observed after each injection, and the magnitude of each peak was not significantly different after

each injection. To confirm that the large magnitudes of the exothermic heat pulses may result from the nonspecific binding of the Hg^{2+} ion with the phosphate backbones of INSF25TTT:INSR25AAA, we have measured the ITC profile for the injection of the Hg^{2+} ion solution into INSF25TTT:INSR25AAA solution in the presence of higher salt concentration, 1 M NaClO_4 (Supplementary Fig. S1). Similar to the case in the presence of 100 mM NaClO_4 , an exothermic heat pulse was observed after each injection and no significant difference in the magnitude of each peak was observed. The magnitudes of the exothermic heat pulses in the presence of 1 M NaClO_4 were significantly smaller than those observed in the presence of 100 mM NaClO_4 (Supplementary Fig. S1). Before injecting the Hg^{2+} ion solution, the phosphate backbones of INSF25TTT:INSR25AAA may bind with the Na^+ ion. The binding affinity of the Na^+ ion with the phosphate backbones of INSF25TTT:INSR25AAA in the presence of 1 M NaClO_4 may be larger than that in the presence of 100 mM NaClO_4 . The bound Na^+ ion may be exchanged by the injected Hg^{2+} ion. The degree of the exchange by the Hg^{2+} ion in the presence of 1 M NaClO_4 may be smaller than that in the presence of 100 mM NaClO_4 due to the larger binding affinity of the Na^+ ion. Thus, the smaller magnitudes of the heat pulses upon the binding of the Hg^{2+} ion with the phosphate backbones were observed in the presence of 1 M NaClO_4 . This suggests that the large magnitudes of the exothermic heat pulses in the presence of 100 mM NaClO_4 observed in Fig. 2b may result from the nonspecific binding of the Hg^{2+} ion with the phosphate backbones.

ITC analyses of the interaction between the Hg^{2+} ion and each of the single T:T mismatched base pair duplex DNA (INSF25TTT:INSR25TAA) and the corresponding perfectly matched duplex DNA (INSF25TTT:INSR25AAA) revealed that the single Hg^{2+} ion specifically bound with the single T:T mismatched base pair in the mismatched base pair duplex DNA (INSF25TTT:INSR25TAA) at a molar ratio of 1:1 (Fig. 2 and Table 1). The Hg^{2+} ion has been known to bind selectively with base moieties rather than with the phosphate and sugar groups in DNA [36–41]. In particular, the Hg^{2+} ion has a strong affinity for the N3 position of thymine bases [36–38]. A covalent and linear N3–Hg–N3 bond was observed in the crystal structure of a 1:2 complex of Hg^{2+} and 1-

methylthymine [38]. According to the literature from the 1960s, Yamane and Davidson reported that protons were released when Hg^{2+} ions bound with several natural DNAs [40]. Katz proposed the possibility of the formation of a 1:2 complex of Hg^{2+} ion and thymine bases in a double-stranded polynucleotide, $d(\text{AT})_n-d(\text{AT})_n$, with the release of protons [41]. Also, a 1:2 complex of mercury and thymine was used in nucleoside synthesis procedures, the so-called “mercury” method, a traditional synthetic method for coupling glycosyl halides and bases [42]. Thus, it is assumed that the Hg^{2+} ion may bind with the single T:T mismatched base pair in the duplex DNA through a covalent N3–Hg–N3 bond. We previously analysed the ^1H NMR spectra of the duplex DNA containing the single T:T mismatched base pair in the absence and presence of the Hg^{2+} ion [19]. We found that the imino proton resonances of the single T:T mismatched base pair disappeared in the presence of the Hg^{2+} ion, suggesting that the imino protons of the single T:T mismatched base pair were substituted with the Hg^{2+} ion [19]. We also previously examined the ^{15}N NMR spectra of the complex of the Hg^{2+} ion and the duplex DNA containing the single T:T mismatched base pair labeled with ^{15}N at the N3 position [43,44]. We found ^{15}N – ^{15}N J -coupling across the Hg^{2+} ion with the coupling constant ($^2J_{\text{NN}}$) of 2.4 Hz [43,44]. This observation clearly demonstrated the N3–Hg–N3 bond formation in the T–Hg–T complex. Taken together, we conclude that the Hg^{2+} ion specifically binds with the N3 positions of two thymine bases in place of the imino protons and bridges two thymine bases to form the T–Hg–T complex (Fig. 1a) in the duplex DNA (INSF25TTT:INSR25TAA).

The K_a and ΔG for the specific binding between the Hg^{2+} ion and the single T:T mismatched base pair was $5.87 \times 10^5 \text{ M}^{-1}$ and $-32.9 \text{ kJ mol}^{-1}$, respectively (Table 1). The magnitudes of the observed K_a and ΔG were significantly larger than those previously reported for the nonspecific interaction between metal ion and DNA [25–31], supporting the specific binding between the Hg^{2+} ion and the single T:T mismatched base pair. The observed ΔG resulted from both the observed negative ΔH and positive ΔS (Table 1). The positive ΔS for the specific binding between the Hg^{2+} ion and the single T:T mismatched base pair measured by ITC (Table 1) includes a major contribution of a dehydration entropy change from the release of structured water molecules surrounding the Hg^{2+} ion and the duplex DNA, and a conformational entropy change from the conformational change of the duplex DNA upon the binding with the Hg^{2+} ion [45]. The dehydration entropy change of the Hg^{2+} ion is largely positive ($238 \text{ J mol}^{-1} \text{ K}^{-1}$) [46,47], and that of the duplex DNA is also expected to be positive due to the release of structured water molecules from the surface of the duplex DNA. Thus, the total dehydration entropy change should be positive. On the other hand, the CD spectra showed that the higher-order structure of the single T:T mismatched base pair duplex DNA was significantly changed by the specific binding of the Hg^{2+} ion (Fig. 4b), suggesting a significant contribution of a conformational entropy change to the observed positive ΔS (Table 1). Because the magnitude of the positive dehydration entropy change (more than $238 \text{ J mol}^{-1} \text{ K}^{-1}$) discussed above may be significantly larger than that of the observed positive ΔS ($23.7 \text{ J mol}^{-1} \text{ K}^{-1}$) (Table 1), another major component of the observed ΔS , that is, the conformational entropy change should be negative. Because the positive dehydration entropy change was favorable and the negative conformational entropy change was unfavorable for the specific binding between the Hg^{2+} ion and the single T:T mismatched base pair, the observed positive ΔS (Table 1) might have been mainly driven by the positive dehydration entropy change. On the other hand, the negative ΔH for the specific binding between the Hg^{2+} ion and the single T:T mismatched base pair measured by ITC (Table 1) reflects a major contribution from a positive dehydration enthalpy change of the Hg^{2+} ion (1840 kJ mol^{-1}) [48], a positive deprotonation enthalpy change of the two thymine bases (1450 kJ mol^{-1}) [49,50] upon the binding of the Hg^{2+} ion with the

single T:T mismatched base pair, an accompanying positive protonation enthalpy change of the cacodylate buffer (1.96 kJ mol^{-1}) [51] taking up the two protons released from the two thymine bases, and a negative binding enthalpy change from the N3–Hg–N3 bond formation in the T–Hg–T complex. Because the sign of only the binding enthalpy change upon the N3–Hg–N3 bond formation was negative and the signs of the enthalpy changes from the other three contributions were positive, the observed negative ΔH (Table 1) might have been mainly driven by the negative binding enthalpy change from the N3–Hg–N3 bond formation.

ITC analyses of the interaction between the Hg^{2+} ion and each of the continuous and interrupted double T:T mismatched base pair duplex DNAs (INSF25TTT:INSR25TTA and INSF25TTT:INSR25TAT) revealed that the molar ratios n_1 and n_2 for the first and second binding were nearly 1 for both of the mismatched base pair duplex DNAs (Table 1). The stoichiometric binding was achieved in each step of the first and second binding regardless of whether the double T:T mismatched base pairs were continuous or interrupted, similar to the stoichiometric binding between the single Hg^{2+} ion and the single T:T mismatched base pair (Table 1). The magnitudes of the observed K_{a2} and ΔG_2 for the second binding between the second Hg^{2+} ion and the second T:T mismatched base pair were significantly larger than those of the observed K_{a1} and ΔG_1 for the first binding between the first Hg^{2+} ion and the first T:T mismatched base pair (Table 1). The positive cooperativity of the specific binding between the Hg^{2+} ion and the double T:T mismatched base pairs were observed for both of the continuous and interrupted double T:T mismatched base pair duplex DNAs (INSF25TTT:INSR25TTA and INSF25TTT:INSR25TAT) (Table 1). The CD spectra showed that the higher-order structure of the continuous and interrupted double T:T mismatched base pair duplex DNAs was significantly distorted by the specific binding of the Hg^{2+} ion (Fig. 4c and d). When the first Hg^{2+} ion binds with the first T:T mismatched base pair, the higher-order structure of the continuous and interrupted double T:T mismatched base pair duplex DNAs may be changed into their distorted higher-order structure, where the second Hg^{2+} ion may bind with the second T:T mismatched base pair more easily. The change in the higher-order structure of the continuous and interrupted double T:T mismatched base pair duplex DNAs induced by the binding of the first Hg^{2+} ion with the first T:T mismatched base pair may be one of the reason for the positive cooperativity of the specific binding between the Hg^{2+} ion and the double T:T mismatched base pairs. However, the detailed mechanism for the positively cooperative binding remains to be elucidated.

5. Conclusions

The present study has demonstrated that the binding affinity between the Hg^{2+} ion and the T:T mismatched base pair was significantly larger than those for previously reported nonspecific interactions between metal ions and DNA [25–31]. The specific binding between the Hg^{2+} ion and the T:T mismatched base pair was mainly driven by the positive dehydration entropy change and the negative binding enthalpy change. In the interactions between the Hg^{2+} ion and each of the continuous and interrupted double T:T mismatched base pairs, the stoichiometric binding at a molar ratio of 1:1 was achieved in each step of the first and second binding, similar to that between the single Hg^{2+} ion and the single T:T mismatched base pair. The binding affinity between the second Hg^{2+} ion and the second T:T mismatched base pair was significantly larger than that between the first Hg^{2+} ion and the first T:T mismatched base pair. The stoichiometric and positively cooperative binding between the double Hg^{2+} ions and the double T:T mismatched base pairs may be favorable to align multiple Hg^{2+} ions in duplex DNA for the application of the metal-mediated base pairs in nanotechnology. The T–Hg–T base pair formation involving the

natural bases with the large binding affinity shown in the present study may be more convenient than the formation of other previously reported metal-mediated base pairs involving the artificial bases [7–15] due to lack of time-consuming synthesis of the bases. Taken together, we conclude that the T–Hg–T base pair could be a key metal-mediated base pair and may eventually lead to progress in potential applications of metal-mediated base pairs in nanotechnology.

Acknowledgments

This research was partly supported by the Casio Science Promotion Foundation, Iketani Science and Technology Foundation, Nakatani Foundation of Electronic Measuring Technology Advancement, and Tateishi Science and Technology Foundation. This work was also supported in part by Grant-in-Aid for JSPS Fellows (08J07706 to T.K.) from the Ministry of Education, Science, Sports, and Culture of Japan.

Appendix A. Supplementary data

Supplementary data associated with this article can be found, in the online version, at doi:10.1016/j.tca.2011.03.018.

References

- [1] D.E. Draper, RNA folding: thermodynamic and molecular descriptions of the roles of ions, *Biophys. J.* 95 (2008) 5489–5495.
- [2] E.A. Aleman, R. Lamichhane, D. Rueda, Exploring RNA folding one molecule at a time, *Curr. Opin. Chem. Biol.* 12 (2008) 647–654.
- [3] J.K. Frederiksen, J.A. Piccirilli, Identification of catalytic metal ion ligands in ribozymes, *Methods* 49 (2009) 148–166.
- [4] J. Schnabl, R.K. Sigel, Controlling ribozyme activity by metal ions, *Curr. Opin. Chem. Biol.* 14 (2010) 269–275.
- [5] E. Gazit, Use of biomolecular templates for the fabrication of metal nanowires, *FEBS J.* 274 (2007) 317–322.
- [6] F.A. Aldaye, A.L. Palmer, H.F. Sleiman, Assembling materials with DNA as the guide, *Science* 321 (2008) 1795–1799.
- [7] E. Meggers, P. Holland, W. Tolman, F. Romesberg, P. Schultz, A novel copper-mediated dna base pair, *J. Am. Chem. Soc.* 122 (2000) 10714–10715.
- [8] H.Y. Weizman, Tor 2,2'-Bipyridine ligand: a novel building block for modifying DNA with intra-duplex metal complexes, *J. Am. Chem. Soc.* 123 (2001) 3375–3376.
- [9] S. Atwell, E. Meggers, G. Spraggon, P.G. Schultz, Structure of a copper-mediated base pair in DNA, *J. Am. Chem. Soc.* 123 (2001) 12364–12367.
- [10] K. Tanaka, Y. Yamada, M. Shionoya, Formation of silver(I)-mediated DNA duplex and triplex through an alternative base pair of pyridine nucleobases, *J. Am. Chem. Soc.* 124 (2002) 8802–8803.
- [11] K. Tanaka, A. Tengeiji, T. Kato, N. Toyama, M. Shiro, M. Shionoya, Efficient incorporation of a copper hydroxypyridone base pair in DNA, *J. Am. Chem. Soc.* 124 (2002) 12494–12498.
- [12] N. Zimmermann, E. Meggers, P.G. Schultz, A novel silver(i)-mediated DNA base pair, *J. Am. Chem. Soc.* 124 (2002) 13684–13685.
- [13] K. Tanaka, A. Tengeiji, T. Kato, N. Toyama, M. Shionoya, A discrete self-assembled metal array in artificial DNA, *Science* 299 (2003) 1212–1213.
- [14] M. Shionoya, K. Tanaka, Artificial metallo-DNA: a bio-inspired approach to metal array programming, *Curr. Opin. Chem. Biol.* 8 (2004) 592–597.
- [15] G.H. Clever, C. Kaul, T. Carell, DNA–metal base pairs, *Angew. Chem. Int. Ed. Engl.* 46 (2007) 6226–6236.
- [16] F.A. Polonius, J. Muller, An artificial base pair, mediated by hydrogen bonding and metal-ion binding, *Angew. Chem. Int. Ed. Engl.* 46 (2007) 5602–5604.
- [17] M.K. Schlegel, L.O. Essen, E. Meggers, Duplex structure of a minimal nucleic acid, *J. Am. Chem. Soc.* 130 (2008) 8158–8159.
- [18] A. Ono, H. Togashi, Highly selective oligonucleotide-based sensor for mercury(II) in aqueous solutions, *Angew. Chem. Int. Ed.* 43 (2004) 4300–4302.
- [19] Y. Miyake, H. Togashi, M. Tashiro, H. Yamaguchi, S. Oda, M. Kudo, Y. Tanaka, Y. Kondo, R. Sawa, T. Fujimoto, T. Machinami, A. Ono, Mercury(II)-mediated formation of thymine–Hg(II)–thymine base pairs in DNA duplexes, *J. Am. Chem. Soc.* 128 (2006) 2172–2173.
- [20] I. Okamoto, K. Iwamoto, Y. Watanabe, Y. Miyake, A. Ono, Metal-ion selectivity of chemically modified uracil pairs in DNA duplexes, *Angew. Chem. Int. Ed. Engl.* 48 (2009) 1648–1651.
- [21] A. Ono, S. Cao, H. Togashi, M. Tashiro, T. Fujimoto, T. Machinami, S. Oda, Y. Miyake, I. Okamoto, Y. Tanaka, Specific interactions between silver(I) ions and cytosine–cytosine pairs in DNA duplexes, *Chem. Commun. (Camb.)* (2008) 4825–4827.
- [22] H. Torigoe, K. Kawahashi, A. Takamori, A. Ono, Novel strategy for single nucleotide polymorphism (SNP) genotyping by heteroduplex analysis: specific stabilization of TT mismatch base pair by mercury (II) cation and CC mismatch base pair by silver (I) cation, *Nucleosides Nucleotides Nucleic Acids* 24 (2005) 915–917.
- [23] H. Torigoe, A. Ono, T. Kozasa, Hg(II) ion specifically binds with T:T mismatched base pair in duplex DNA, *Chemistry* 16 (2010) 13218–13225.
- [24] T. Wiseman, S. Williston, J.F. Brandts, L.N. Lin, Rapid measurement of binding constants and heats of binding using a new titration calorimeter, *Anal. Biochem.* 179 (1989) 131–137.
- [25] H. Arakawa, R. Ahmad, M. Naoui, H.A. Tajmir-Riahi, A comparative study of calf thymus DNA binding to Cr(III) and Cr(VI) ions. Evidence for the guanine N-7-chromium-phosphate chelate formation, *J. Biol. Chem.* 275 (2000) 10150–10153.
- [26] A.A. Ouameur, S. Nafisi, N. Mohajerani, H.A. Tajmir-Riahi, Thallium–DNA complexes in aqueous solution. Major or minor groove binding, *J. Biomol. Struct. Dyn.* 20 (2003) 561–565.
- [27] A.A. Ouameur, H. Arakawa, R. Ahmad, M. Naoui, H.A. Tajmir-Riahi, A Comparative study of Fe(II) and Fe(III) interactions with DNA duplex: major and minor grooves bindings, *DNA Cell. Biol.* 24 (2005) 394–401.
- [28] J. Wu, F. Du, P. Zhang, I.A. Khan, J. Chen, Y. Liang, Thermodynamics of the interaction of aluminum ions with DNA: implications for the biological function of aluminum, *J. Inorg. Biochem.* 99 (2005) 1145–1154.
- [29] E. Stellwagen, Q. Dong, N.C. Stellwagen, Quantitative analysis of monovalent counterion binding to random-sequence, double-stranded DNA using the replacement ion method, *Biochemistry* 46 (2007) 2050–2058.
- [30] K. Utsuno, Thermodynamics of DNA condensation caused by Mn²⁺ binding, *Chem. Pharm. Bull. (Tokyo)* 56 (2008) 247–249.
- [31] Y. Li, Y.L. Xia, Y. Jiang, X.P. Yan, Extracting stoichiometry, thermodynamics, and kinetics for the interaction of DNA with cadmium ion by capillary electrophoresis on-line coupled with electrothermal atomic absorption spectrometry, *Electrophoresis* 29 (2008) 1173–1179.
- [32] T.K. Chiu, R. E. Dickerson, 1 A crystal structures of B-DNA reveal sequence-specific binding and groove-specific bending of DNA by magnesium and calcium, *J. Mol. Biol.* 301 (2000) 915–945.
- [33] R. Ahmad, H. Arakawa, H.A. Tajmir-Riahi, A comparative study of DNA complexation with Mg(II) and Ca(II) in aqueous solution: major and minor grooves bindings, *Biophys. J.* 84 (2003) 2460–2466.
- [34] R. Ahmad, M. Naoui, J.F. Neault, S. Diamantoglou, H.A. Tajmir-Riahi, An FTIR spectroscopic study of calf-thymus DNA complexation with Al(III) and Ga(III) cations, *J. Biomol. Struct. Dyn.* 13 (1996) 795–802.
- [35] H.A. Tajmir-Riahi, M. Naoui, R. Ahmad, The effects of Cu²⁺ and Pb²⁺ on the solution structure of calf thymus DNA: DNA condensation and denaturation studied by Fourier transform infrared difference spectroscopy, *Biopolymers* 33 (1993) 1819–1827.
- [36] R.M. Izatt, J.J. Christensen, J.H. Rytting, Sites and thermodynamic quantities associated with proton and metal ion interaction with ribonucleic acid, deoxyribonucleic acid, and their constituent bases, nucleosides, and nucleotides, *Chem. Rev.* 71 (1971) 439–481.
- [37] R.B. Simpson, Association constants of methylmercuric and mercuric ions with nucleosides, *J. Am. Chem. Soc.* 86 (1964) 2059–2065.
- [38] L.D. Kosturko, C. Folzer, R.F. Stewart, The crystal and molecular structure of a 2:1 complex of 1-methylthymine–mercury (II), *Biochemistry* 13 (1974) 3949–3952.
- [39] T. Yamane, N. Davidson, None of the spectra of the mercury (II) and silver (I) complexes of some polyribonucleotides and ribonucleic acid, *Biochim. Biophys. Acta* 55 (1962) 780–782.
- [40] T. Yamane, N. Davidson, On the complexing of desoxyribonucleic acid (DNA) by mercuric ion, *J. Am. Chem. Soc.* 83 (1961) 2599–2607.
- [41] S. Katz, The reversible reaction of Hg (II) and double-stranded polynucleotides. A step-function theory and its significance, *Biochim. Biophys. Acta* 68 (1963) 240–253.
- [42] J.J. Fox, N. Yung, J. Davoll, G.B. Brown, Pyrimidine nucleosides. I. A new route for the synthesis of thymine nucleosides, *J. Am. Chem. Soc.* 78 (1956) 2117–2122.
- [43] Y. Tanaka, S. Oda, H. Yamaguchi, Y. Kondo, C. Kojima, A. Ono, 15N–15N J-coupling across Hg(II): direct observation of Hg(II)-mediated T–T base pairs in a DNA duplex, *J. Am. Chem. Soc.* 129 (2007) 244–245.
- [44] Y. Tanaka, A. Ono, Nitrogen-15 NMR spectroscopy of N-metallated nucleic acids: insights into 15N NMR parameters and N-metal bonds, *Dalton Trans.* (2008) 4965–4974.
- [45] D.C. Rau, V.A. Parsegian, Direct measurement of temperature-dependent solvation forces between DNA double helices, *Biophys. J.* 61 (1992) 260–271.
- [46] D.R. Rosseinsky, Electrode potentials and hydration energies – theories and correlations, *Chem. Rev.* 65 (1965) 467–490.
- [47] G. Chillemi, G. Mancini, N. Sanna, V. Barone, S. Della Longa, M. Benfatto, N.V. Pavel, P. D'Angelo, Evidence for sevenfold coordination in the first solvation shell of Hg(II) aqua ion, *J. Am. Chem. Soc.* 129 (2007) 5430–5436.
- [48] A.A. Rashin, B. Honig, Reevaluation of the born model of ion hydration, *J. Phys. Chem.* 89 (1985) 5588–5593.
- [49] A.K. Chandra, M.T. Nguyen, T. Uchimaru, T. Zeegers-Huyskens, Protonation and deprotonation enthalpies of guanine and adenine and implications for the structure and energy of their complexes with water: comparison with uracil, thymine, and cytosine, *J. Phys. Chem. A* 103 (1999) 8853–8860.
- [50] Y.Q. Huang, H. Kenttamaa, Theoretical estimations of the 298 K gas-phase acidities of the pyrimidine-based nucleobases uracil, thymine, and cytosine, *J. Phys. Chem. A* 107 (2003) 4893–4897.
- [51] H. Fukada, K. Takahashi, Enthalpy and heat capacity changes for the proton dissociation of various buffer components in 0.1 M potassium chloride, *Proteins* 33 (1998) 159–166.

Thiolato-bridged Au^I₂Cu^I₂ and Cu^I₄ Metallorings Derived from Benzothiazoline: Can Gold(I) Plus Copper(I) Make Silver(I)?

Yusuke Takino,¹ Nobuto Yoshinari,¹ Tatsuya Kawamoto,² and Takumi Konno*¹

¹Department of Chemistry, Graduate School of Science, Osaka University, Toyonaka, Osaka 560-0043

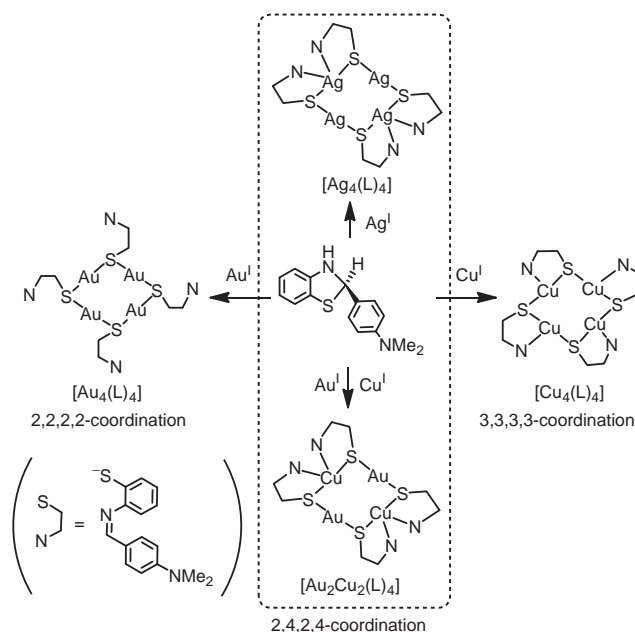
²Department of Chemistry, Faculty of Science, Kanagawa University, Hiratsuka, Kanagawa 259-1293

(Received May 31, 2012; CL-120470; E-mail: konno@chem.sci.osaka-u.ac.jp)

A thiolato-bridged Au^I₂Cu^I₂ metalloring compound, [Au₂Cu₂(L)₄] (L = (C₆H₄NMe₂)CH=N(C₆H₄)S⁻), together with an analogous Cu^I₄ compound, [Cu₄(L)₄], was newly prepared from 2-(4-dimethylaminophenyl)benzothiazoline. The Au^I₂Cu^I₂ compound was found to show structural and spectroscopic features comparable well with those of [Ag₄(L)₄], rather than those of [Au₄(L)₄] and [Cu₄(L)₄].

There has been considerable research interest in multinuclear coordination compounds of group 11 elements in recent years.¹ In particular, heterometallic compounds containing two or three kinds of group 11 metal ions are of much interest due to their fascinating structural features and unique chemical and physicochemical properties.² In general, this class of compounds can be synthesized by one-pot reactions of selected organic ligands with a mixture of group 11 metal ions or by stepwise reactions via homometallic precursors with a different group 11 metal ion. However, the former reactions commonly require troublesome separation processes because of the formation of a mixture of several homometallic and heterometallic species, while the latter reactions require well-designed, controlled reaction pathways. Thus, the finding of a coordination system that exclusively affords a single heterometallic species from a mixture of different kinds of group 11 metal ions remains a great challenge.

In our successive study on the reactivity of 2-substituted benzothiazolines toward transition-metal ions,³ we have recently synthesized thiolato-bridged tetranuclear complexes, [Au₄(L)₄] and [Ag₄(L)₄] (L = (C₆H₄NMe₂)CH=N(C₆H₄)S⁻), by the simple reactions of 2-(4-dimethylaminophenyl)benzothiazoline with gold(I) or silver(I) in chloroform in a 1:1 ratio.⁴ In addition, we have found that an analogous tetranuclear complex containing both Au^I and Ag^I ions, [Au₂Ag₂(L)₄], is selectively produced by a similar reaction with a 1:1 mixture of gold(I) and silver(I).⁴ This result prompted us to investigate whether this synthetic method is applicable to the preparation of a heterometallic complex containing both of Au^I and Cu^I. In this paper, we report that the use of a 1:1 mixture of gold(I) and copper(I), instead of a mixture of gold(I) and silver(I), indeed results in the production of an expected heterometallic complex, [Au₂Cu₂(L)₄]. The preparation of an analogous Cu^I₄ complex, [Cu₄(L)₄], from 2-(4-dimethylaminophenyl)benzothiazoline is also reported. Notably, [Au₂Cu₂(L)₄] was found to exhibit structural and spectroscopic features that are comparable well with those of [Ag₄(L)₄], rather than those of [Au₄(L)₄] and [Cu₄(L)₄] (Scheme 1). As far as we know, this is the first report that points out the possible creation of characteristics of a silver(I) compound by the introduction of a mixture of Au^I and Cu^I ions, in place of Ag^I ions.



Scheme 1. The Au^I₄, Ag^I₄, Cu^I₄, and Au^I₂Cu^I₂ metalloring structures with iminothiolates.

Treatment of a chloroform solution of 2-(4-dimethylaminophenyl)benzothiazoline, a chloroform solution of chloro(tetrahydrothiophene)gold(I), and an acetonitrile solution of tetraacetonitrilecopper(I) perchlorate in a 2:1:1 ratio in the presence of NEt₃ gave a dark orange solution, from which orange crystals (1·2CHCl₃) suitable for X-ray crystallography were isolated by slow evaporation at room temperature.⁵ X-ray fluorescence analysis of this compound revealed the presence of Au and Cu, and its elemental analysis was consistent with a formula containing iminothiolate ligands (L = (C₆H₄NMe₂)CH=N(C₆H₄)S⁻) and Au^I and Cu^I atoms in a 2:1:1 ratio.⁶ Single-crystal X-ray analysis revealed that **1** contains two Au^I and two Cu^I atoms in combination with four L ligands, with the lack of any counter ions.⁷ As shown in Figure 1, the Au^I and Cu^I atoms are alternately linked by four S atoms from four L ligands, forming a thiolato-bridged Au^I₂Cu^I₂ metalloring structure with a C_i symmetry. Each L ligand adopts a μ₂-κ¹S:κ²N,S coordination mode, in which its imine group coordinates to a Cu^I atom (av Cu–N = 2.16(5) Å) and its thiolato group bridges Au^I and Cu^I atoms (av Au–S = 2.295(18) Å, Cu–S = 2.31(3) Å). As a result, two Cu^I atoms are situated in an N₂S₂ tetrahedral geometry (N–Cu–N = 117.88(14)°, S–Cu–S = 111.10(5)°), while two Au^I atoms are in an S₂ linear geometry (S–Au–S = 176.44(4)°). The preference of linear and tetrahedral geometries for Au^I and Cu^I, as well as the high affinity of an imine group to a Cu^I center

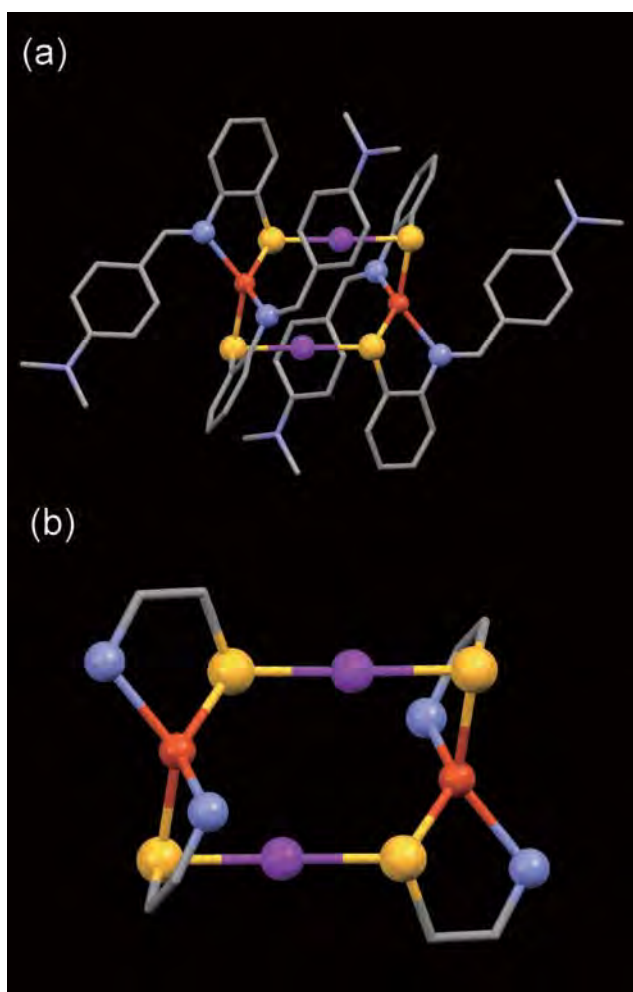


Figure 1. Perspective views of (a) **1** and (b) its core structure; Au^I: purple, Cu^I: brown, N: blue, S: yellow, C: gray. H atoms are omitted for clarity.

rather than to an Au^I center, accounts for the formation of this metalloring structure. Despite the C_i symmetric structure in crystal **1**, the ¹H NMR spectrum of **1** in CDCl₃ gave only a single set of signals for four L ligands (Figure S1a),⁵ suggestive of the flexible nature of its Au^I₂Cu^I₂S₄ metalloring framework with an averaged C_{2h} symmetry in solution.

It is possible that three heterometallic species, [Au₃Cu₁(L)₄], [Au₂Cu₂(L)₄], and [Au₁Cu₃(L)₄], besides two homometallic species, [Au₄(L)₄] and [Cu₄(L)₄], are formed from L ligands in combination with a 1:1 mixture of Au^I and Cu^I ions. In addition, two isomeric forms that are discriminated by the arrangement of Au^I and Cu^I ions, AuAuCuCu-type and AuCuAuCu-type, are possible for [Au₂Cu₂(L)₄]. However, the present reaction exclusively produced [Au₂Cu₂(L)₄] with an AuCuAuCu-type arrangement in a moderate yield of ca. 50%. Since the ¹H NMR spectrum of a reaction mixture of 2-(4-dimethylaminophenyl)benzothiazoline, triethylamine, chloro(tetrahydrothiophene)gold(I), and tetraacetonitrilecopper(I) perchlorate in a 2:2:1:1 ratio in CDCl₃/CD₃CN is indicative of the formation of a complex mixture with no obvious preference for a single species (Figure S1b),⁵ the selective isolation of **1** is attributed to its less

solubility in solution. This is different from the corresponding reaction with a mixture of gold(I) and silver(I), in which a single species of [Au₂Ag₂(L)₄] with an AuAgAuAg-type arrangement is selectively formed in solution.^{4,8} The affinity of an imine group to a Cu^I center, which is much higher than to an Ag^I center, seems to prevent the conversion of some kinetic products to the thermodynamically stable product of **1** in solution.

To obtain a homometallic Cu₄ metalloring compound, a chloroform solution of 2-(4-dimethylaminophenyl)benzothiazoline was treated with an acetonitrile solution of tetraacetonitrilecopper(I) perchlorate in a 1:1 ratio. However, this reaction did not give [Cu₄(L)₄] but produced a brown compound of [Cu₈(L)₈](ClO₄) that has been obtained by the 2:1 reaction of 2-(4-dimethylaminophenyl)benzothiazoline with copper(II) acetate in 1,2-dichloroethane.^{3c} After several trials, an orange compound **2**, which is assignable to have a neutral formula of [Cu^I(L)]_n, based on the elemental analysis and IR spectrum that is essentially the same as that of **1** (Figure S2),⁵ was obtained by the reaction of 2-(4-dimethylaminophenyl)benzothiazoline with copper(II) acetate in a 2:1 ratio in toluene.^{5,9} Although the characterization of **2** by means of the NMR spectroscopy was precluded owing to its poor solubility in common solvents and its instability in solution,¹⁰ an expected Cu₄ metalloring structure was established by single-crystal X-ray analysis.¹¹ In **2**, four Cu atoms are bridged by four S atoms from four L ligands to form a tetranuclear metalloring structure with an S_4 symmetry (Figure 2). Each Cu atom in **2** is in a +1 oxidation state, as evidenced by the lack of any counter cations. Thus, it is seen that 2-(4-dimethylaminophenyl)benzothiazoline acts not only as a ligand precursor but also as a reducing agent for copper(II).^{3c} The successful isolation of **2** by the use of toluene as a reaction medium, instead of 1,2-dichloroethane, is most likely due to the insolubility of **2** in this solvent, which leads to the precipitation of **2** prior to its conversion into [Cu₈(L)₈]⁺ in solution. Each L ligand in **2** also adopts a μ_2 - κ^1 S: κ^2 N,S coordination mode (av Cu–S = 2.211(4) Å, av Cu–N = 2.140(9) Å), like in **1**. However, in **2**, four imine groups from four L ligands bind to four different Cu^I atoms, and each Cu^I atom is situated in an NS₂ trigonal-planar geometry (S–Cu–S = 146.59(8)°, N–Cu–S = 117.9(3) and 87.8(3)°). Thus, the four bridging S atoms in **2** are situated in a square arrangement, which is distinct from an arrangement of parallelogram found in **1**.

Previously, we have shown that the homometallic Au₄^I and Ag₄^I compounds, [Au₄(L)₄] and [Ag₄(L)₄], also have a metalloring structure, in which four metal atoms are bridged by four S atoms from four L ligands, as in the case of [Cu₄(L)₄] (**2**).⁴ However, in [Au₄(L)₄], all four Au^I atoms adopt a two-coordination geometry, whereas two of four Ag^I atoms adopt a two-coordination geometry and the other Ag^I atoms have a four-coordination geometry in [Ag₄(L)₄] (Figure S3).⁵ The 2,2,2,2-coordination in [Au₄(L)₄] and the 2,4,2,4-coordination in [Ag₄(L)₄] are both different from the 3,3,3,3-coordination found in **2**, in which four Cu^I atoms are unified to have a three-coordination geometry. It should be noted that the 2,4,2,4-coordination pattern in [Ag₄(L)₄] is the same as that in [Au₂Cu₂(L)₄] (**1**). In addition, the four bridging S atoms in [Ag₄(L)₄] are in an arrangement of parallelogram like in **1**, whereas those in [Au₄(L)₄] are in a square arrangement like in **2**. Thus, the overall metalloring structure in [Ag₄(L)₄] is well comparable with that in [Au₂Cu₂(L)₄] (**1**), rather than those in

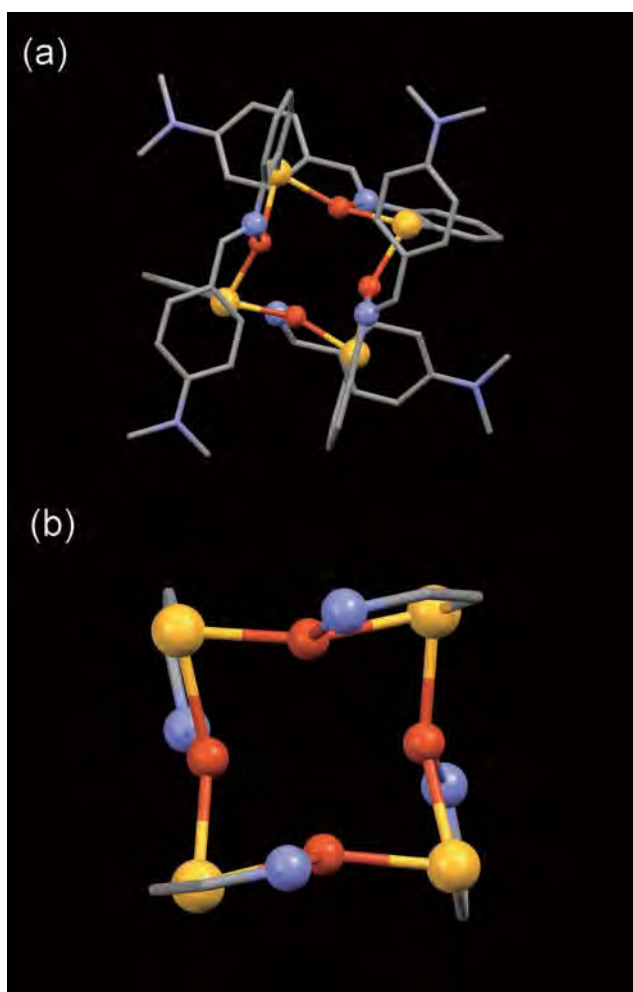


Figure 2. Perspective views of (a) **2** and (b) its core structure; Cu^I: brown, N: blue, S: yellow, C: gray. H atoms are omitted for clarity.

[Au₄(L)₄] and [Cu₄(L)₄] (**2**). Besides the structural feature, the similarity between [Ag₄(L)₄] and [Au₂Cu₂(L)₄] (**1**) was noticed in the solid-state electronic spectra. That is, the diffuse reflection spectrum of **1** is dominated by an intense band at 392 nm,¹² the peak position of which is very close to that for [Ag₄(L)₄] (390 nm), rather than those for [Au₄(L)₄] (380 nm) and **2** (402 nm) (Figure S4).⁵

In summary, we showed that a single species of [Au₂Cu₂(L)₄], in which Au^I and Cu^I atoms are alternately bridged by S atoms in a cyclic form, is selectively isolated from the reaction of 2-(4-dimethylaminophenyl)benzothiazoline with a mixture of gold(I) and copper(I). An analogous homometallic Cu₄ metal-organic compound, [Cu₄(L)₄], was also obtained by the reaction with copper(II) when toluene was used as a reaction solvent. What is the most remarkable finding is that the structural feature of [Au₂Cu₂(L)₄], as well as its electronic spectral feature, is similar to that of [Ag₄(L)₄], rather than those of [Au₄(L)₄] and [Cu₄(L)₄]. This finding indicates for the first time that a coordination compound bearing characteristics of a homometallic silver(I) species is possibly created from gold(I) and copper(I), providing a significant insight into the development

of modern “alchemy” that meets the demand of alternatives for rare metals or harmful elements.¹³

This work was supported in part by Grants-in-Aids for Science Research No. 23350026 from the Ministry of Education, Culture, Sports, Science and Technology of Japan and by Izumi Science and Technology Foundation.

References and Notes

- a) R. Mukherjee, in *Transition Metal Groups 9–12 in Comprehensive Coordination Chemistry II: From Biology to Nanotechnology*, ed. by J. A. McCleverty, T. J. Meyer, Elsevier, Oxford, **2004**, Vol. 6, Chap. 6.6, pp. 747–910. doi:10.1016/B0-08-043748-6/05086-6. b) M. C. Gimeno, A. Laguna, in *Transition Metal Groups 9–12 in Comprehensive Coordination Chemistry II: From Biology to Nanotechnology*, ed. by J. A. McCleverty, T. J. Meyer, Elsevier, Oxford, **2004**, Vol. 6, Chap. 6.7, pp. 911–1145. doi:10.1016/B0-08-043748-6/05122-7. c) C.-M. Che, S.-W. Lai, *Coord. Chem. Rev.* **2005**, *249*, 1296. d) E. R. T. Tiekink, J.-G. Kang, *Coord. Chem. Rev.* **2009**, *253*, 1627.
- a) A. Toyota, T. Yamaguchi, A. Igashira-Kamiyama, T. Kawamoto, T. Konno, *Angew. Chem., Int. Ed.* **2005**, *44*, 1088. b) Z.-N. Chen, N. Zhao, Y. Fan, J. Ni, *Coord. Chem. Rev.* **2009**, *253*, 1. c) S. Sculfort, P. Braunstein, *Chem. Soc. Rev.* **2011**, *40*, 2741. d) Y. Takemura, T. Nishida, B. Kure, T. Nakajima, M. Iida, T. Tanase, *Chem.—Eur. J.* **2011**, *17*, 10528. e) I. O. Koshevoy, C.-L. Lin, A. J. Karttunen, J. Jänis, M. Haukka, S. P. Tunik, P.-T. Chou, T. A. Pakkanen, *Chem.—Eur. J.* **2011**, *17*, 11456. f) A. C. Jahnke, K. Pröpper, C. Bronner, J. Teichgräber, S. Dechert, M. John, O. S. Wenger, F. Meyer, *J. Am. Chem. Soc.* **2012**, *134*, 2938.
- a) T. Kawamoto, K. Takeda, M. Nishiwaki, T. Aridomi, T. Konno, *Inorg. Chem.* **2007**, *46*, 4239. b) T. Kawamoto, M. Nishiwaki, Y. Tsunekawa, K. Nozaki, T. Konno, *Inorg. Chem.* **2008**, *47*, 3095. c) T. Kawamoto, M. Nishiwaki, M. Nishijima, K. Nozaki, A. Igashira-Kamiyama, T. Konno, *Chem.—Eur. J.* **2008**, *14*, 9842. d) T. Kawamoto, Y. Takino, K. Sakoda, T. Konno, *Chem. Lett.* **2010**, *39*, 1264.
- Y. Takino, K. Tsuge, A. Igashira-Kamiyama, T. Kawamoto, T. Konno, *Chem.—Asian J.* **2011**, *6*, 2931.
- Supporting Information is available electronically on the CSJ-Journal Web site, <http://www.csj.jp/journals/chem-lett/index.html>.
- Anal. Calcd for **1**·2CHCl₃: C, 41.81; H, 3.51; N, 6.29%. Found: C, 41.75; H, 3.51; N, 6.41%.
- Crystal data for **1**·2CHCl₃, Triclinic, *P* $\bar{1}$, *a* = 8.684(3) Å, *b* = 13.144(4) Å, *c* = 14.618(5) Å, α = 82.937(13)°, β = 84.632(13)°, γ = 74.993(13)°, *V* = 1596.0(9) Å³, *Z* = 1, *T* = 200(2) K, *D*_{calcd} = 1.853 g cm⁻³, 13853 reflections measured, 7218 independent (*R*_{int} = 0.0689), *R*₁ = 0.040 (*I* > 2σ(*I*)), *wR*₂ = 0.101 (all data). CCDC = 886212.
- A similar reaction of 2-(4-dimethylaminophenyl)benzothiazoline with a mixture of silver(I) perchlorate and tetraacetonitrilecopper(I) perchlorate also gave a complex mixture, which is much more complicated than that formed from chloro(tetrahydrothiophene)-gold(I) and tetraacetonitrilecopper(I) perchlorate.
- Anal. Calcd for **2**: C, 56.49; H, 4.74; N, 8.78%. Found: C, 56.71; H, 4.87; N, 8.71%.
- Compound **2** was soluble in CH₂Cl₂ only slightly, and its solution color changed from orange to dark brown within several hours. The spectrum of the brown solution was identical with that of [Cu₈(L)₈]⁺.
- Crystal data for **2**·C₇H₈, Trigonal, *I*_{41/a}, *a* = 18.98(3) Å, *b* = 18.98(3) Å, *c* = 21.08(3) Å, *V* = 7589(20) Å³, *Z* = 4, *T* = 200(2) K, *D*_{calcd} = 1.255 g cm⁻³, 9923 reflections measured, 3003 independent (*R*_{int} = 0.109), *R*₁ = 0.085 (*I* > 2σ(*I*)), *wR*₂ = 0.299 (all data). CCDC = 886213.
- The intense band is assignable as arising from π–π* transition within the conjugated 4-NMe₂-Ph-C(H)=N moiety.^{3b}
- a) K. Hayashi, S. Matsuishi, T. Kamiya, M. Hirano, H. Hosono, *Nature* **2002**, *419*, 462. b) K. Kusada, M. Yamauchi, H. Kobayashi, H. Kitagawa, Y. Kubota, *J. Am. Chem. Soc.* **2010**, *132*, 15896.



Synthesis, crystal structures and properties of novel heterobimetallic Cd–Pt and Zn–Pt coordination polymers using nicotinic acid

Yuhei Miyazaki, Yusuke Kataoka, Wasuke Mori, Tatsuya Kawamoto*

Department of Chemistry, Faculty of Science, Kanagawa University, Hiratsuka, Kanagawa 259-1293, Japan

ARTICLE INFO

Article history:

Received 1 July 2012

Accepted 14 August 2012

Available online 21 August 2012

Keywords:

Zn and Cd coordination polymers

Pt complex ligand

Crystal structure

Gas adsorption property

ABSTRACT

Two novel heterobimetallic coordination polymers, $[\text{Cd}\{\text{Pt}(\text{nic})_4\}]_n \cdot 5n\text{H}_2\text{O}$ (**Cd–Pt-1**) and $[\text{Zn}\{\text{Pt}(\text{nic})_4\}(\text{H}_2\text{O})_4]_n \cdot n\text{H}_2\text{O}$ (**Zn–Pt-1**) (nicH = nicotinic acid), were synthesized by a one-pot slow-evaporation reaction system in water. Single crystal X-ray analysis revealed that **Cd–Pt-1** and **Zn–Pt-1** are two-dimensional sheet frameworks with open pores and one-dimensional chain polymers, respectively. However, crystal structure of **Cd–Pt-1** is not robust in air. Therefore, BET surface area (pore volume) of **Cd–Pt-1** calculated by N_2 gas adsorption measurement is very low and the value is $22.5 \text{ m}^2 \text{ g}^{-1}$ ($0.00813 \text{ cm}^3 \text{ g}^{-1}$).

© 2012 Elsevier B.V. All rights reserved.

In recent years, porous coordination polymers (**PCPs**) or metal-organic frameworks (**MOFs**) with well-defined pores have attracted attention because of potential applications in gas storage [1–3], heterogeneous catalysis [4–6], magnetism [7,8] and so on. Coordination polymers can be easily prepared through self-assembly of organic ligands as linkers and metal ions as connecting nodes, and this makes it possible to construct the coordination polymers with desired properties. Since Mori and co-workers in our group reported that paddle-wheel copper coordination polymer, $[\text{Cu}_2(p\text{-BDC})_2]_n$ ($p\text{-BDC}$ = 1,4-benzendicarboxylate), can encapsulate several gases in 1997, many works concerning the applications of coordination polymers have been carried out until now [9–12].

In this research area, the immobilization of open metal sites as activity sites for specific and selective substances in coordination polymers is also very important for their applications. One general approach for immobilization of metal sites is to use complex ligands instead of organic ligands in the construction of traditional coordination polymers. Then, several heterobimetallic coordination polymers with permanent porosity have been realized for functional properties such as gas adsorption, sensing materials, heterogeneous catalyst and so on [13–18]. Specially, from a view point of the catalytic applications of coordination polymers, the use of Pt(II) or Pd(II) complex ligand will be one of the effective approaches because Pt(II) and Pd(II) complexes have been widely employed as homogeneous catalysts in catalytic reactions such as hydrogenation reaction, water photo-reduction reaction and hydrocarbon C–H bond activation. Generally, compared with homogeneous catalysis, heterogeneous coordination polymers introduced homogeneous complex catalyst units as complex

ligands resulted in the high stability and the easy separation of them from solvents because coordination polymers are insoluble in common organic solvents such as alcohols. In recent studies, our group also succeeded to synthesize and characterize some heterobimetallic coordination polymers constituted of Pd(II) and Pt(II) complex ligands using isonicotinic acid (inaH). Specifically, $[\text{Zn}\{\text{Pd}(\text{ina})_4\}]_n$ constructed from mononuclear Zn metal nodes and $[\text{Pd}(\text{ina})_4]$ complex ligands acted as not only useful heterogeneous water photo-reduction catalyst [19] but also selective H_2 gas adsorption materials versus N_2 gas [20]. There are some reports about heterobimetallic Pt(II) and Pd(II) coordination polymers [21–24], but they are still at development stages compared with the other coordination polymers. Therefore, we also have attempted to prepare novel Pt(II) and Pd(II) coordination polymers using other complex ligands.

In this paper, we report synthesis, crystal structures and properties of two novel heterobimetallic coordination polymers, $[\text{Cd}\{\text{Pt}(\text{nic})_4\}]_n \cdot 5n\text{H}_2\text{O}$ (**Cd–Pt-1**) and $[\text{Zn}\{\text{Pt}(\text{nic})_4\}(\text{H}_2\text{O})_4]_n \cdot n\text{H}_2\text{O}$ (**Zn–Pt-1**), constructed from mononuclear Cd or Zn unit as a bridging node and $[\text{Pt}(\text{nic})_4]$ as a complex ligand (Fig. 1). Although some Pt(II) heterobimetallic coordination polymers have been reported so far, there is no report about heterobimetallic coordination polymers with $[\text{Pt}(\text{nicH})_2(\text{nic})_2]$ complex ligand.

At first, $[\text{Pt}(\text{nicH})_2(\text{nic})_2]$ complex was synthesized by a solvothermal method in water solution (5.0 ml) containing of $\text{K}_2[\text{PtCl}_4]$ (0.10 mmol) and nicH (0.40 mmol) [25]. Single crystal X-ray analysis revealed that $[\text{Pt}(\text{nicH})_2(\text{nic})_2]$ was crystallized in triclinic space group $P\bar{1}$ and the asymmetric unit consists of one-half of $[\text{Pt}(\text{nicH})_2(\text{nic})_2]$. The charge balance of $[\text{Pt}(\text{nicH})_2(\text{nic})_2]$ is maintained by two *trans*-position carboxylate ions. In packing view, $[\text{Pt}(\text{nicH})_2(\text{nic})_2]$ is self-assembled by strong hydrogen bonds between carboxylate and carboxylic acid of $[\text{Pt}(\text{nicH})_2(\text{nic})_2]$ (Fig. S1). Therefore, $[\text{Pt}(\text{nicH})_2(\text{nic})_2]$ complex is largely insoluble in common solvents such as water, alcohol

* Corresponding author. Tel.: +81 463 59 4111; fax: +81 463 58 9684.
E-mail address: kaw@kanagawa-u.ac.jp (T. Kawamoto).

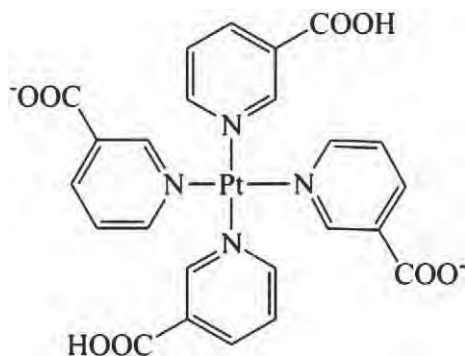


Fig 1. Structure of $[\text{Pt}(\text{nicH})_2(\text{nic})_2]$ complex ligand.

and DMF. Therefore, we tried synthesis of heterobimetallic coordination polymers using $[\text{Pt}(\text{nicH})_2(\text{nic})_2]$ complex ligand by one pot methods in water solution.

Cd-Pt-1 and **Zn-Pt-1** were synthesized by one-pot slow-evaporation reactions as follows: A mixture of $\text{K}_2[\text{PtCl}_4]$ (0.05 mmol), nicH (0.20 mmol) and $\text{Cd}(\text{NO}_3)_2$ or $\text{Zn}(\text{NO}_3)_2$ (0.10 mmol) was dissolved in distilled water (6.0 ml) at room temperature. The solution was transformed into a 20 ml sample vial and allowed to stand for 1 week. The obtained colorless block crystals were filtered, washed with distilled water and dried at room temperature. CHN elemental analysis for $[\text{Cd}\{\text{Pt}(\text{nic})_4\}]_n \cdot 6n\text{H}_2\text{O}$ (**Cd-Pt-1**): Calcd. C, 31.89; H, 3.12; N, 6.20%. Found C, 31.98; H, 3.05; N, 6.17%. Solvent content calcd (%) from the proposed formula: H_2O 12.00; found (%) determined by TGA: 12.31 and $[\text{Zn}\{\text{Pt}(\text{nic})_4\}(\text{H}_2\text{O})_4]_n \cdot n\text{H}_2\text{O}$ (**Zn-Pt-1**): Calcd. C, 34.36; H, 3.12; N, 6.68%. Found C, 34.02; H, 3.37; N, 6.46%. Solvent

content calcd (%) from the proposed formula: H_2O 10.74; found (%) determined by TGA: 8.81.

Single crystal X-ray analysis revealed that **Cd-Pt-1** is crystallized in tetragonal space group $P4/ncc$ and features two dimensional porous frameworks [26]. The asymmetric unit consists of one Cd node and a quarter $[\text{Pt}(\text{nic})_4]$ complex ligand. The coordination environment of Cd and Pt atoms is shown in Fig. 2a. The Cd atoms are coordinated by eight O atoms ($\text{Cd}-\text{O}=2.378$ and 2.454 Å) derived from carboxylate ions of $[\text{Pt}(\text{nic})_4]$ units ($\text{C}-\text{O}=1.263$ and 1.262 Å). The charge of $[\text{Cd}(\text{COO})_4]^{2-}$ units was balanced by $[\text{Pt}(\text{nic})_4]^{2+}$ complex ligand and therefore overall framework is neutral. As shown in Fig. 2b, the packing view along the c axis revealed that the structure of **Cd-Pt-1** is as wave-like two dimensional sheets and then these sheets are packed along the c axis with ABAB fashion (Fig. 2c). In addition, the two-dimensional frameworks have open pores with approximately 4.0×4.0 Å² along an a–b plane, taking into account the van der Waals radii of surface atom (Fig. 2d). The neighboring Pt–Pt distance is 9.655 Å.

Another type coordination polymer **Zn-Pt-1** is crystallized in triclinic $P-1$ and has one-dimensional zig-zag chain structure [27]. The asymmetric unit consists of one Zn metal node and one-half of $[\text{Pt}(\text{nic})_4]$ complex ligand. As shown in Fig. 3a, Zn atom is octahedrally coordinated by six O atoms; two O atoms from carboxylate ions of $[\text{Pt}(\text{nic})_4]$ complex ligand ($\text{C}-\text{O}=1.239$ and 1.277 Å, $\text{Zn}-\text{O}=2.048$ Å) and four O atoms of H_2O molecules ($\text{Zn}-\text{O}=2.072$ and 2.048 Å). Therefore, the charge of Pt(II) is balanced by non-coordinated carboxylate ions of $[\text{Pt}(\text{nic})_4]$ and that of Zn(II) by coordinated carboxylate ions. From the packing view in Fig. 3b, **Zn-Pt-1** forms a one-dimensional chain polymer structure and there are no cavities. The chain polymers are stacked along the b axis with the distance of 9.032 Å.

In these single crystal X-ray analyses, the accurate number of guest solvent H_2O molecules could not be determined because of disorder of H_2O molecules. Therefore, we determined the number of

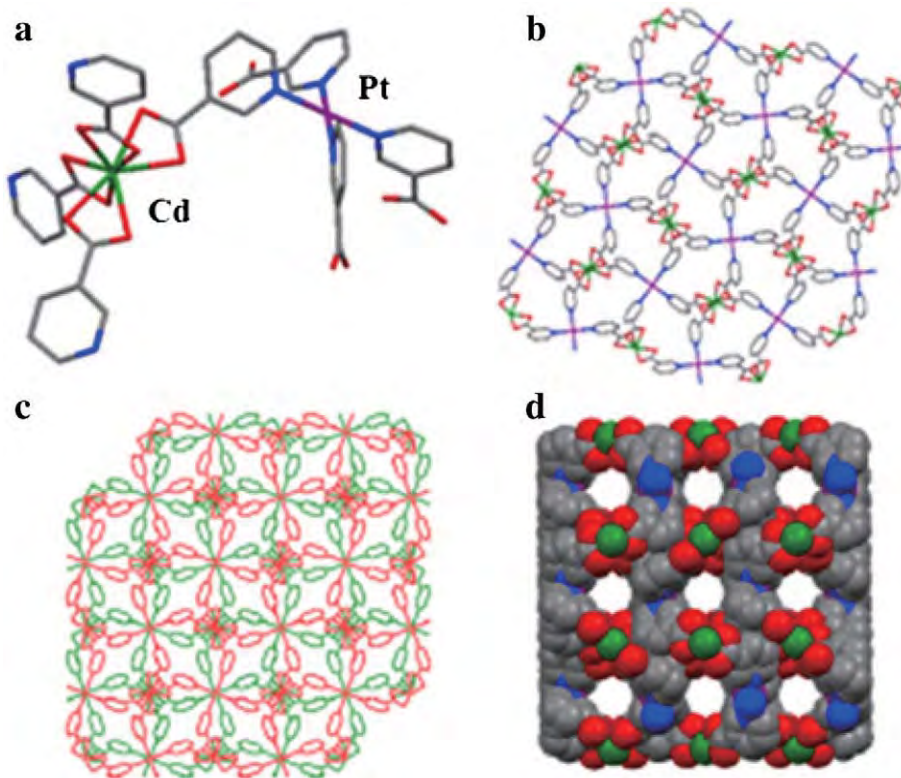


Fig. 2. Crystal structure of **Cd-Pt-1**. a) Crystal structure around Cd(II) and Pt(II) metal centers. b–c) Packing view along the c axis. d) Space filling model of two dimensional network structure along the a–b plane. Hydrogen atoms and guest H_2O molecules are omitted for clarity. Cd atoms are shown in green, Pt in purple, C in gray, N in blue and O in red.

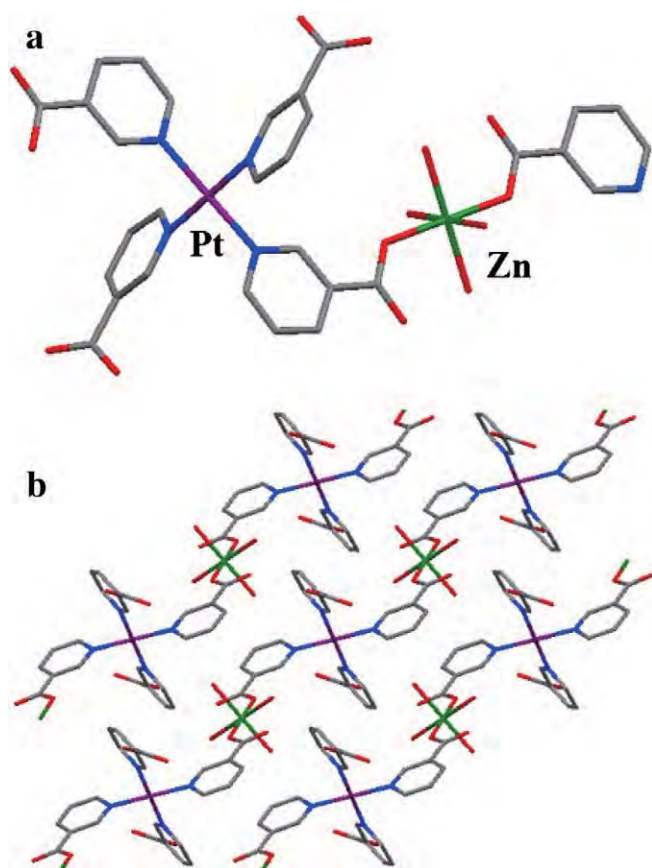


Fig. 3. Crystal structure of **Zn-Pt-1**. a) Crystal structure around Zn(II) and Pt(II) metal centers. b) Packing view along the c axis. Hydrogen atoms and guest H₂O molecules are omitted for clarity. Zn atoms are shown in green, Pt in purple, C in gray, N in blue and O in red.

solvent molecules based on elemental analysis and TGA. TGA-curves of **Cd-Pt-1** and **Zn-Pt-1** revealed the weight loss around 373 K due to the removal of solvent H₂O molecules and the decomposition of these frameworks around 573 K. From the weight of the lost H₂O molecules and elemental analysis, **Cd-Pt-1** includes five H₂O molecules for [Cd{Pt(nic)₄}] formula. **Zn-Pt-1** also includes five H₂O molecules for [Zn{Pt(nic)₄}] formula unit (four H₂O molecules coordinate to Zn atom and one H₂O molecule is non-coordinated guest molecule).

To confirm the permanent porosity of **Cd-Pt-1**, we performed N₂ and H₂ gas adsorption measurements at 77 K and 760 mm Hg [28]. As shown in Fig. 4, N₂ gas adsorption isotherm of **Cd-Pt-1** is type III in IUPAC classification being associated with non porous solids. The calculated BET surface area and pore volume are too low in comparison with traditional coordination polymers (these values are 22.5 m²/g and 0.00813 cm³/g respectively). Moreover, H₂ gas adsorption performance of **Cd-Pt-1** was not completely observed. We assumed that N₂ or H₂ gas (the kinetic diameters are 3.64 and 2.84 Å respectively) can be adsorbed into pores of **Cd-Pt-1** observed by a single crystal X-ray analysis, but the gas adsorption measurements revealed that **Cd-Pt-1** has no such ability. In the course of measurement, we also confirmed that crystals of **Cd-Pt-1** are air-sensitive and crystallinity is gradually lost by moving these crystals out of reaction solution and standing while crystals of **Cd-Pt-1** are very stable in reaction solution for a half year. XRPD measurement of samples after gas adsorption measurement also revealed that observed peaks are different from simulation peaks calculated from crystal structure (Fig. S2). Therefore, open pores of **Cd-Pt-1** may be closed due to the loss of crystalline structure by removal of guest H₂O molecules. Additionally, **Zn-Pt-1** shows also too low

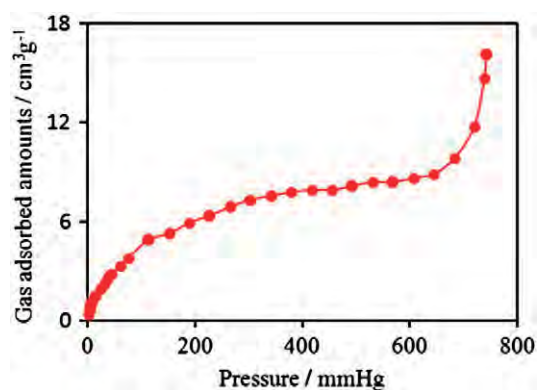


Fig. 4. N₂ gas adsorption isotherm of **Cd-Pt-1** at 77.4 K and 760 mm Hg.

surface area (BET surface area is 2.91 m²/g) owing to non-pore structure.

In summary, we synthesized and characterized two heterobimetallic coordination polymers from mononuclear Cd or Zn metal node and Pt complex ligand. From a single crystal X-ray analysis, the structure of Cd-Pt coordination polymer is ABAB packing two-dimensional sheet frameworks and Zn-Pt coordination polymer has one-dimensional zig-zag chain structure. In N₂ gas adsorption measurements, two coordination polymers showed too low BET surface area by the loss of crystal structure in Cd-Pt coordination polymer and non-porous structure in Zn-Pt coordination polymer. In this work, we succeed to prepare two kinds of coordination polymers with different topological networks by selection of metal nodes. Now, we are attempting to prepare several Pt(II) heterobimetallic coordination polymers using other metal nodes such as Cu(II), Co(II) and Ni(II).

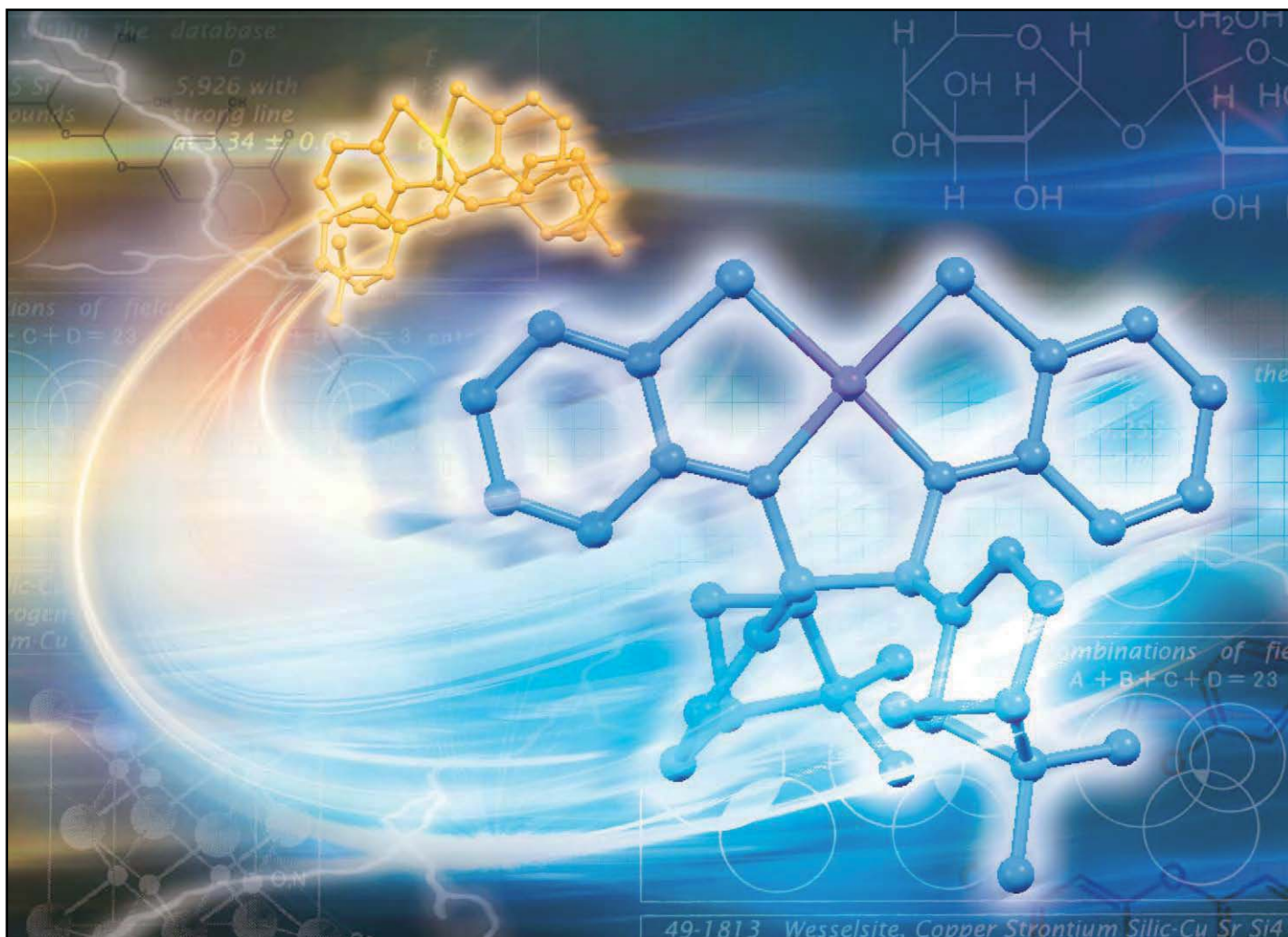
Appendix A. Supplementary material

CCDC 886315, 886316 and 886317 contain the supplemental crystallographic data for Cd-Pt-1 and Zn-Pt-1. These data can be obtained free of charge from <http://www.ccdc.cam.ac.uk/conts/retrieving.html>, or from the Cambridge Crystallographic Data Centre, 12 Union Road, Cambridge CB2 1EZ, UK; fax (+44) 1223-336-033; or e-mail: deposit@ccdc.cam.ac.uk.

References

- [1] H.K. Chae, D.Y. Siberio-Perez, J. Kim, Y. Go, M. Eddaoudi, A.J. Matzger, M. O'Keeffe, O.M. Yaghi, *Nature* 427 (2004) 523.
- [2] B. Chen, X. Zhao, A. Putkham, K. Hong, E.B. Lobkovsky, E.J. Hurtado, A.J. Fletcher, K.M. Thomas, *J. Am. Chem. Soc.* 130 (2008) 6411.
- [3] P. Kanoo, G. Mostafa, R. Matsuda, S. Kitagawa, T.K. Maji, *Chem. Commun.* 47 (2011) 8106.
- [4] C.D. Wu, W. Lin, *Angew. Chem. Int. Ed.* 119 (2007) 1093.
- [5] Y. Li, P. Song, J. Zheng, X. Li, *Chem. Eur. J.* 16 (2010) 10887.
- [6] A. Corma, H. Garcia, F.K. Llabres, I. Xamena, *Chem. Rev.* 110 (2010) 4606.
- [7] G.J. Halder, C.J. Kepert, B. Moubaraki, K.S. Murray, J.D. Cashion, *Science* 298 (2002) 1762.
- [8] Y.-Z. Zheng, M.-L. Tong, W.-X. Zhang, X.-M. Chen, *Angew. Chem. Int. Ed.* 45 (2006) 6310.
- [9] W. Mori, F. Inoue, K. Yoshida, H. Nakayama, S. Takamizawa, M. Kishita, *Chem. Lett.* (1997) 1291.
- [10] S. Naito, T. Tanibe, E. Saito, T. Miyao, W. Mori, *Chem. Lett.* (2001) 1178.
- [11] C.N. Kato, M. Hasegawa, T. Sato, A. Yoshizawa, T. Inoue, W. Mori, *J. Catal.* 230 (2005) 226.
- [12] K. Seki, W. Mori, *J. Phys. Chem. B* 106 (2002) 1380.
- [13] M.C. Das, S. Xiang, Z. Zhang, B. Chen, *Angew. Chem. Int. Ed.* 50 (2011) 10510.
- [14] M.C. Das, Q. Guo, Y. He, J. Kim, C.-G. Zhao, K. Hong, S. Xiang, Z. Zhang, K.M. Thomas, R. Krishna, B. Chen, *J. Am. Chem. Soc.* 134 (2012) 8703.
- [15] Z. Zhang, S. Xiang, K. Hong, M.C. Das, H.D. Arman, M. Garcia, J.U. Mondal, K.M. Thomas, B. Chen, *Inorg. Chem.* 51 (2012) 4947.
- [16] S.-C. Xiang, Z. Zhang, C.-G. Zhao, K. Hong, X. Zhao, D.-R. Ding, M.-H. Xie, C.-D. Wu, M.C. Das, R. Gill, K.M. Thomas, B. Chen, *Nat. Commun.* 2 (2011) 204.
- [17] R. Kitaura, G. Onoyama, H. Sakamoto, R. Matsuda, S. Noro, S. Kitagawa, *Angew. Chem. Int. Ed.* 43 (2004) 2684.

- [18] S.H. Cho, S.T. Nguyen, J.T. Hupp, T.E. Albrecht-Schmitt, Chem. Commun. (2006) 2563.
- [19] Y. Miyazaki, Y. Kataoka, Y. Kitagawa, M. Okumura, W. Mori, Chem. Lett. 39 (2010) 878.
- [20] Y. Miyazaki, Y. Kataoka, T. Kawamoto, W. Mori, Eur. J. Inorg. Chem. 5 (2012) 807.
- [21] J. Hafizovic, A. Krivokapic, K.C. Szeto, S. Jakoben, K.P. Lillerud, U. Olsbye, M. Tilser, Cryst. Growth Des. 7 (2007) 2302.
- [22] K.C. Szeto, K.O. Kongshaug, S. Jakobsen, M. Tilset, K.P. Lillerud, Dalton Trans. (2008) 2055.
- [23] R. Song, K.M. Kim, Y.S. Sohn, Inorg. Chem. 42 (2003) 821.
- [24] H. Hara, A. Kobayashi, S. Noro, H.C. Chang, M. Kato, Dalton Trans. 40 (2011) 8012.
- [25] Crystal data for [Pt(nicH)₂(nic)₂]: C₂₄H₁₈N₄O₈Pt, M_r=685.52, triclinic, space group, P-1, a=8.009(4) Å, b=8.133(5) Å, c=9.297(6) Å, α=86.97(4)° β=78.67(4)° γ=71.71(3)° V=563.8(6) Å³, Z=1, R_{int}=0.0270, D_c=2.019 g cm⁻³, μ=6.259 mm⁻¹, GOF=1.005, 5953 reflections measured, 2517 unique. The final R₁=0.0581 [I > 2σ(I)], wR₂=0.1643 (all data), CCDC=886315.
- [26] Crystal data for Cd–Pt-1: C₂₄H₁₆CdN₄O₈Pt, M_r=891.91, tetragonal, space group, P4/ncc, a=13.640(2) Å, c=17.128(3) Å, V=3186.7(9) Å³, Z=4, R_{int}=0.0294, D_c=1.659 g cm⁻³, μ=5.105 mm⁻¹, GOF=0.980, 30880 reflections measured, 1837 unique. The final R₁=0.0551 [I > 2σ(I)], wR₂=0.2315 (all data), CCDC=886316.
- [27] Crystal data for Zn–Pt-1: C₂₄H₂₈N₄O₁₄PtZn, M_r=856.97, triclinic, space group, P-1, a=7.8384(18) Å, b=9.0320(18) Å, c=9.809(2) Å, α=86.979(11)° β=83.2280(10)° γ=79.698(10)° V=678.1(3) Å³, Z=1, R_{int}=0.0459, D_c=2.098 g cm⁻³, μ=6.097 mm⁻¹, GOF=1.016, 7030 reflections measured, 2978 unique. The final R₁=0.0294 [I > 2σ(I)], wR₂=0.0634 (all data), CCDC=886317.
- [28] Gas adsorption measurements were carried out with a Micromeritics ASAP 2010 instrument and from these adsorption curves, the specific surface area was determined. Freshly prepared samples were activated at room temperature under high vacuum for 24 h prior to measurements. The adsorption isotherms for N₂ and H₂ gases were recorded at liquid N₂ temperature.

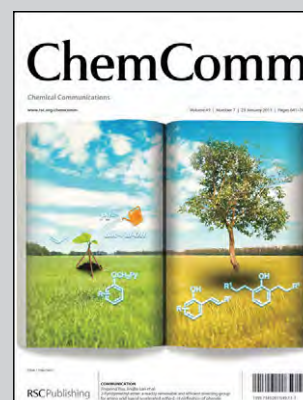


Showcasing research from the laboratories of Professor Tatsuya Kawamoto, Kanagawa University, Japan, and Professor Takumi Konno, Osaka University, Japan

Chirality transfer based on reversible C–C bond formation/breaking in nickel(II) complexes

The reaction of (1*R*)-(–)-myrtenal-derived benzothiazoline with nickel(II) acetate in ethanol exclusively gave a Schiff base-type nickel(II) complex having *M* helical configurational myrtenyl arms, which is reversibly converted to a non-innocent-type complex having additional *S,S* configurational asymmetric carbon centres.

As featured in:



See Tatsuya Kawamoto *et al.*, *Chem. Commun.*, 2013, **49**, 668.

RSC Publishing

www.rsc.org/chemcomm

Registered Charity Number 207890

COMMUNICATION

Chirality transfer based on reversible C–C bond formation/breaking in nickel(II) complexes†

Cite this: *Chem. Commun.*, 2013, **49**, 668

Received 31st August 2012,
Accepted 8th October 2012

Tatsuya Kawamoto,^a Narumi Suzuki,^a Takeshi Ono,^a Dafei Gong^b and Takumi Konno^b

DOI: 10.1039/c2cc36332a

www.rsc.org/chemcomm

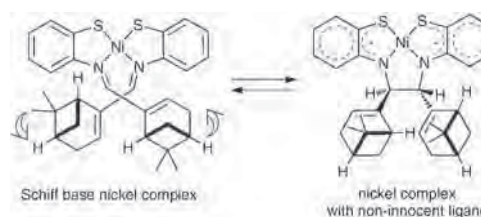
The reaction of (1*R*)-(–)-myrtenal-derived benzothiazoline with nickel(II) acetate in ethanol exclusively gave a Schiff base-type nickel(II) complex having *M* helical configurational myrtenyl arms, which is reversibly converted to a non-innocent-type complex having additional *S,S* configurational asymmetric carbon centres.

Transfer of chirality at the molecular level has been a subject of great interest in recent years because it is closely associated with the development of asymmetric catalysis and chiral recognition.¹ The formation of chiral supramolecular host systems and the chiral information transfer from a host system to guest molecules by solid–solid interaction has attracted much attention in the field of host–guest chemistry.² In coordination chemistry, considerable interest has been directed toward the chirality transfer from a tetrahedral centre of an organic ligand to an octahedral metal centre, and steric factors that govern the chiral selective formation of metal complexes have been extensively investigated.³ The chirality transfer between metal centres has also been observed in the formation of multinuclear complexes with a helical chirality.⁴ Recently, the chiral-auxiliary-mediated asymmetric synthesis based on an efficient chirality transfer was reported in an octahedral ruthenium polypyridyl system.^{5,6} Furthermore, the chirality inversion at a metal centre induced by pH change was also reported in cysteine-bound ruthenabenzene derivatives,^{5,7} and the reversible mutarotation between the solid state and solution was found in a helicate-type macrocyclic ytterbium complex.^{5,8} However, a report on chirality transfer that occurs in the course of a structural conversion between two chiral compounds has not appeared to date. Herein, we report a remarkable chirality transfer phenomenon based on a reversible C–C bond formation/breaking between two isomeric nickel(II) complexes having chiral myrtenyl groups; one is a Schiff base-type complex with a helical chirality that arises from the crossing of two myrtenyl arms and the other is a non-

innocent-type complex with two asymmetric carbon centres that are created by the imino C–C bond formation (Scheme 1).⁹

The benzothiazoline employed in this work was prepared by the reaction of 2-aminothiophenol and (1*R*)-(–)-myrtenal in ethanol. The addition of nickel(II) acetate to an ethanol solution of this benzothiazoline in a 2 : 1 (L : M) ratio gave brown powder (**1**). This product was assigned to an expected Schiff base-type nickel(II) complex having two pendent myrtenyl arms (Scheme 2)¹⁰ by means of its ¹H NMR spectrum and elemental analysis. The appearance of a half-set of ¹H NMR signals for ligands in the complex is indicative of the presence of a single *C*₂ symmetrical isomer with *P* or *M* helical configuration (Fig. 1). The absorption spectrum of **1** in CHCl₃ is characterized by a broad visible band centered at ca. 500 nm (Fig. S1, ESI†). In this region, positive–negative CD bands from the longer wavelength side are observed in the CD spectrum, consistent with the optically active nature of the complex. Unfortunately, single crystals of **1** suitable for X-ray diffraction were unable to obtain from the reaction solution or by the recrystallization of the initial product owing to its low solubility in common solvents. Thus, the determination of the chiral configuration of **1** (*P* or *M*) could not be made at this stage.

It is expected from our previous works that the Schiff base-type complex (**1**) is converted to a non-innocent-type complex,⁹ which possesses two additional asymmetric carbon centres adjacent to myrtenyl groups, *via* a simple flip of its pendent myrtenyl arms accompanied by an imino C–C bond formation (Scheme 1). In this case, the *P* and *M* configurational Schiff base-type complexes are considered to lead to *R,R* and *S,S* configurational carbon centres in the resulting non-innocent-type complex, respectively, because of the steric demand. When **1** was treated in THF at 30–40 °C for

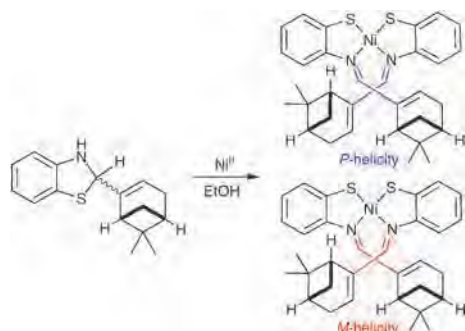


Scheme 1 Interconversion between Schiff base-type and non-innocent-type nickel(II) complexes.

^a Department of Chemistry, Kanagawa University, Hiratsuka, Kanagawa 259-1293, Japan. E-mail: kaw@kanagawa-u.ac.jp

^b Department of Chemistry, Graduate School of Science, Osaka University, Toyonaka, Osaka 560-0043, Japan

† Electronic supplementary information (ESI) available: Synthesis and characterization of **1**, **2** and **3**. CCDC 898508–898510. For ESI and crystallographic data in CIF or other electronic format see DOI: 10.1039/c2cc36332a



Scheme 2 Formation of *P* and *M* isomers of a Schiff base-type nickel(II) complex.

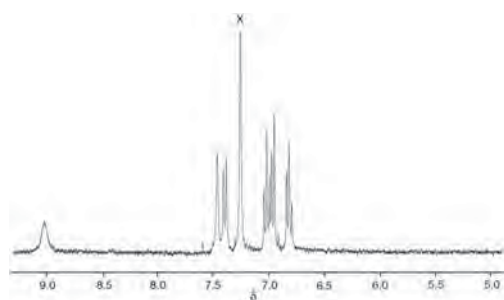


Fig. 1 ^1H NMR spectrum of **1** in CDCl_3 .

several hours, the initial suspension turned to a brown solution, from which violet powder (**2**) was isolated after the chromatographic purification using a silica gel column. Compound **2** exhibits a single set of signals in the ^1H NMR spectrum (Fig. 2a), the spectral feature of which is compatible with that of a proposed non-innocent-type nickel(II) complex. Single-crystals of **2** suitable for X-ray diffraction were obtained by slow evaporation of a pentane solution of **2**. The X-ray analysis established that **2** is indeed a mononuclear nickel(II) complex with a tetradentate- N_2S_2 non-innocent-type ligand (Fig. 3). In **2**, the two carbon atoms adjacent to myrtenyl groups are asymmetric with the *S,S* configuration. This implies that the parental Schiff base-type complex (**1**) has the *M* helical configuration. The averaged Ni–S and Ni–N bond distances are 2.119(3) and 1.809(7) Å, respectively (Table S2, ESI †), which are comparable to those reported for related nickel(II) complexes with non-innocent ligands.^{9,11} The averaged C–S and C–N bond distances are 1.718(10) and 1.356(11) Å, respectively. These values are intermediate between those of single and double bonds and are similar to those found in analogous complexes with *o*-iminothionebenzosemiquinonate ligands.^{9,11} Here it should be noted that **2** is not stable in solution

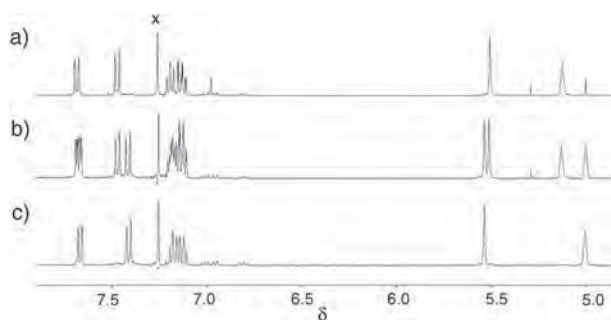


Fig. 2 ^1H NMR spectra of (a) **2**, (b) dark violet powder and (c) **3** in CDCl_3 .

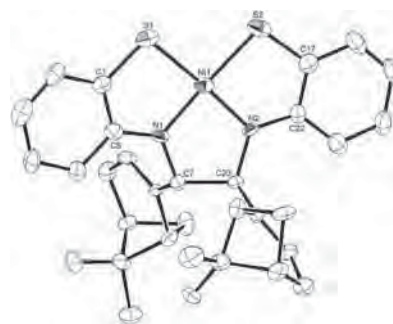


Fig. 3 Ortep drawing of **2**. Ellipsoids represent 30% probability. Hydrogen atoms are omitted for clarity.

and is reverted back to **1**, as evidenced by the ^1H NMR spectral change with time (Fig. S2, ESI †). Thus, it is seen that **2** is a kinetically controlled product of **1** that is thermodynamically more stable.

To check the possibility of the formation of the non-innocent-type nickel(II) complex with another configuration (*R,R* or *R,S*), **1** was treated in toluene under reflux (110–120 °C).¹² Again, the initial suspension turned to a dark brown solution, from which a dark violet powder was isolated. While the absorption spectrum of this powder is essentially the same as that of **2**, its ^1H NMR spectrum gives two sets of signals in a 1 : 1 integration ratio (Fig. 2b), one of which is identical with the signals for **2**. This suggests that another isomer (**3**) of the non-innocent-type nickel(II) complex was produced in this reaction (Fig. 2c), besides **2**. Notably, the signals for **2** decreased with time, with the appearance and growth of the signals of **1**, while the signals for **3** remained intact (Fig. S3, ESI †). In parallel with this observation, dark-violet crystals of **3** were produced by slow evaporation of a pentane solution of the initial dark violet product. Furthermore, dark-brown crystals of **1** were grown, together with dark-violet crystals of **3**, when diethyl ether was diffused into a CH_3CN solution of the dark violet product. The CD spectrum of **3** is enantiomeric to that of **2**, suggesting that **3** has the *R,R* configuration, opposite to the *S,S* configuration of **2** (Fig. S4, ESI †). The molecular structures of **3** and **1** were both determined by X-ray analysis, using the crystals thus obtained.

As shown in Fig. 4, **3** has a mononuclear nickel(II) structure with a tetradentate- N_2S_2 non-innocent-type ligand, which is analogous to **2**. Moreover, the bond distances and angles for **3** are very similar to those for **2** (Table S2, ESI †). However, the two asymmetric carbon atoms adjacent to myrtenyl groups in **3** have the *R,R* configuration. On the other hand, **1** was determined to be an expected mononuclear nickel(II) complex having two bidentate-*N,S* Schiff base

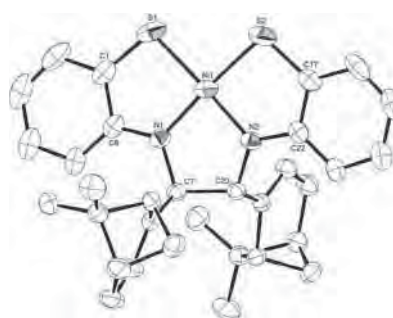


Fig. 4 Ortep drawing of **3**. Ellipsoids represent 30% probability. Hydrogen atoms are omitted for clarity.

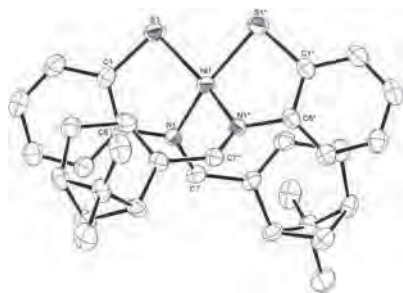
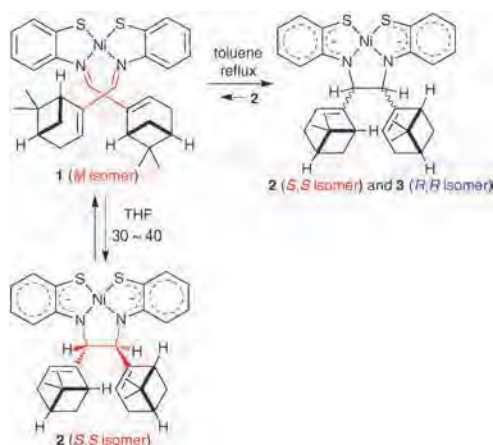


Fig. 5 Ortep drawing of **1**. Ellipsoids represent 50% probability. Hydrogen atoms are omitted for clarity. The asterisk in the atom labels represents symmetry generated atoms ($1 - x, y, 1 - z$).



Scheme 3 Conversion between **1**, **2** and **3**.

ligands (Fig. 5). The metal atom is located on a crystallographic 2-fold axis. In **1**, the two myrtenyl arms of two ligands cross each other to form a single-stranded helical chirality with the *M* configuration. The Ni–S (2.1748(13) Å) and Ni–N (1.904(3) Å) bond distances in **1** are normal for square-planar nickel(II) complexes with an N₂S₂ donor set, and the C–N bond distances (1.299(5) Å) of Schiff base moieties are compatible with a C–N double bond delocalization.^{9,13}

From the structural determinations of **1**, **2** and **3**, it is confirmed that the Schiff base-type nickel(II) complex obtained from (1*R*)-(–)-myrtenal-derived benzothiazoline selectively forms the *M* isomer (**1**), rather than the *P* isomer, and that the reflux of its solution results in the formation of the *S,S* and *R,R* isomers (**2** and **3**) of the non-innocent-type complex, while its moderate heating gives only the *S,S* isomer (**2**). No significant ¹H NMR spectral change with time was noticed for **3**, which is in contrast to the case of **2** (Fig. S2, ESI[†]). The profile of these reactions is summarized in Scheme 3. Molecular model examinations indicate that an unfavorable non-bonding steric interaction exists between the myrtenyl groups and the benzene rings when the Schiff base-type complex has the *P* helical configuration, which seems to account for the selective formation of the *M* isomer. In addition, the stability of **3** toward conversion to the Schiff base-type complex, as well as its formation only under severe reaction conditions, is most likely related to the steric factor, given that **3** is interconvertible to the Schiff base-type complex having the unfavorable *P* configuration.

In summary, we showed that (1*R*)-(–)-myrtenal-derived benzothiazoline readily reacts with nickel(II) to afford only the *M*

isomer of the Schiff base-type nickel(II) complex (**1**). This result indicates that the helical chirality is effectively controlled by asymmetric centers existing in the pendent arms. Remarkably, **1** was found to be converted to the *S,S* isomer of the non-innocent-type complex (**2**) by the moderate heating of its solution, which is easily reverted back to **1** at room temperature. Thus, the information of helical chirality in **1** is kinetically transferred to the central chirality in **2** in the course of the C–C bond formation, while the information of central chirality in **2** is thermodynamically transferred to the helical chirality in **1** in the course of the C–C bond cleavage. Note that the reflux of its solution resulted in the formation of the *R,R* isomer (**3**), together with the *S,S* isomer (**2**). Since **3** is thermodynamically stable and is not converted to the Schiff base-type complex, it is seen that the kinetic control of products is essential for the reversible transfer of chiral information between two isomeric compounds. With this in mind, the development of another chiral coordination system that shows a reversible, chiral selective structural change is currently underway.

Notes and references

- P. Dydio, C. Rubay, T. Gadzikwa, M. Lutz and J. N. H. Reek, *J. Am. Chem. Soc.*, 2011, **133**, 17176–17179; S. J. Wezenberg, G. Salassa, E. C. Escudero-Adan, J. Benet-Buchholz and A. W. Kleij, *Angew. Chem., Int. Ed.*, 2011, **50**, 713–716; J. Wang, D. Ding, L. Zeng, Q. Cao, Y. He and H. Zhang, *New J. Chem.*, 2010, **34**, 1394–1400.
- Y. Imai, K. Kawaguchi, K. Murata, T. Sato, R. Kuroda and Y. Matsubara, *Chem. Lett.*, 2007, 812–813; Y. Tanaka, Y. Murakami and R. Kiko, *Chem. Commun.*, 2003, 160–161.
- R. Vadavi, E. D. Conrad, D. I. Arbuckle, T. S. Cameron, E. Essoun and M. A. S. Aquino, *Inorg. Chem.*, 2011, **50**, 11862–11864; J. Crassous, *Chem. Soc. Rev.*, 2009, **38**, 830–845 and references therein; S. P. Argent, H. Adams, T. Riis-Johannessen, J. C. Jeffery, L. P. Harding, O. Mamula and M. D. Ward, *Inorg. Chem.*, 2006, **45**, 3905–3919; D. Drahoňovský, U. Knof, L. Jungo, T. Belsler, A. Neels, G. C. Labat, H. Stoeckli-Evans and A. von Zelewsky, *Dalton Trans.*, 2006, 1444–1454; P. Biscarini, M. Benedetti, F. Ferranti, R. Kuroda, E. Foresti and P. Sabatino, *Chirality*, 2004, **16**, 251–262; K. Isele, V. Broughton, C. J. Matthews, A. F. Williams, G. Bernardinelli, P. Franz and S. Decurtins, *J. Chem. Soc., Dalton Trans.*, 2002, 3899–3905.
- C. He, Y. Zhao, D. Guo, Z. Lin and C. Duan, *Eur. J. Inorg. Chem.*, 2007, 3451–3463.
- J. Crassous, *Chem. Commun.*, 2012, **48**, 9684–9692.
- Z. Lin, M. A. Celik, C. Fu, K. Harms, G. Frenking and E. Meggers, *Chem.–Eur. J.*, 2011, **17**, 12602–12605.
- R. Lin, H. Zhang, S. Li, L. Chen, W. Zhang, T. B. Wen, H. Zhang and H. Xia, *Chem.–Eur. J.*, 2011, **17**, 2420–2427.
- F. P. Ballistreri, S. Gentile, A. Pappalardo, G. A. Tomaselli, S. Pradhan and L. Di Bari, *Chem.–Eur. J.*, 2011, **17**, 322–328.
- T. Kawamoto, H. Kuma and Y. Kushi, *Bull. Chem. Soc. Jpn.*, 1997, **70**, 1599–1606 The electronic structures of square planar nickel complexes involving non-innocent ligands such as *o*-iminobenzosemiquinonato type ligands have been best described as diradicals with a singlet ground state. See: D. Herebian, E. Bothe, E. Bill, T. Weyhermüller and K. Wieghardt, *J. Am. Chem. Soc.*, 2001, **123**, 10012–10023.
- The *P* isomer has two myrtenyl arms that direct to the upper right and lower left positions from the N donor atoms. The direction of two myrtenyl arms in the *M* isomer is opposite to the *P* isomer.
- T. Kawamoto, K. Takeda, M. Nishiwaki, T. Aridomi and T. Konno, *Inorg. Chem.*, 2007, **46**, 4239–4247; T. Kawamoto and Y. Kushi, *Bull. Chem. Soc. Jpn.*, 2004, **77**, 289–294.
- Reflux of the Schiff base-type complex (**1**) in THF affords the *S,S* and *R,R* isomers (**2** and **3**) of the non-innocent-type complex in ca. 3 : 1 ratio.
- T. Kawamoto and T. Konno, *Bull. Chem. Soc. Jpn.*, 2003, **76**, 127–132; T. Kawamoto and Y. Kushi, *J. Chem. Soc., Dalton Trans.*, 2000, 3022–3026; L. Gomes, E. Pereira and B. de Castro, *J. Chem. Soc., Dalton Trans.*, 2000, 1373–1379; E. Bouwman, R. K. Henderson, A. K. Powell, J. Reedijk, W. J. J. Smeets, A. L. Spek, N. Veldman and S. Wocadlo, *J. Chem. Soc., Dalton Trans.*, 1998, 3495–3499; T. Kawamoto, H. Kuma and Y. Kushi, *Chem. Commun.*, 1996, 2121–2122.



NO_x storage/reduction over alkali-metal-nitrate impregnated titanate nanobelt catalysts and investigation of alkali metal cation migration using XPS

Akihiro Yoshida, Weihua Shen, Tomonori Eda, Ryo Watanabe, Tetsu Ito, Shuichi Naito*

Department of Material and Life Chemistry, Kanagawa University, 3-27-1 Rokkakubashi, Kanagawa-ku, Yokohama 221-8686, Japan

ARTICLE INFO

Article history:

Received 30 July 2011

Received in revised form 18 October 2011

Accepted 18 October 2011

Available online 16 November 2011

Keywords:

NO_x storage/reduction (NSR)

Titanate

X-ray photoelectron spectroscopy

ABSTRACT

We reported earlier that KNO₃- and Pt-impregnated potassium titanate nanobelt (KTN) catalysts exhibit high storage capacity and excellent catalytic cycles for NO_x storage–reduction (NSR) reaction. In the present study, we compared the NSR behavior of various alkali-metal-nitrate impregnated KTN catalysts, which revealed that the KNO₃-impregnated catalyst exhibited superior performance. The XPS and XRD analyses of the NaNO₃-impregnated KTN catalyst showed that the migration of K⁺ from KTN bulk to the surface nitrate salt took place more predominantly than the migration of Na⁺. Probably for this reason, KNO₃-impregnated KTN materials exhibit the best performance for NSR catalytic cycles.

© 2011 Elsevier B.V. All rights reserved.

1. Introduction

Because of recent severe environmental problems, NO_x emissions must be strictly controlled and regulated [1]. Simultaneously, urgent development of highly fuel-efficient vehicles has been sought because of limited crude oil resources in the world and increasingly severe global warming. Conventional three-way catalysts are extremely efficient at reducing NO_x, CO, and unburned hydrocarbon emissions, but only within a narrow window region around the stoichiometric air/fuel ratio (A/F = 14.7), although lean-burn engines (A/F = 20–25) can burn fuel much more efficiently [2]. Therefore, an effective NO_x removal technique for lean-burn exhaust has come to be desired eagerly from both environmental and catalytic perspectives. In fact, NO_x removal technologies under the lean-burn condition include direct catalytic decomposition of NO_x [3], catalytic NO_x storage/reduction (NSR) [1,4–6], and selective catalytic reduction of NO_x with urea/NH₃ [7] or hydrocarbon [8,9].

The NSR catalysts operate under cyclic fuel lean–rich conditions. Under the lean-burn condition, NO_x is absorbed on the catalyst. Under the rich-burn condition, stored NO_x is reduced by H₂, CO, and hydrocarbons. Generally, NSR catalysts contain three compositions: high surface area metal oxides such as Al₂O₃ as a support, basic elements such as Ba and K as a NO_x storage site, and precious metals such as Pt, Pd, and Rh as a redox site for oxidizing NO to NO₂ and for reducing the stored NO_x to regenerate storage capacity. In

actual systems, a storage period of 1–2 min and subsequent 3–5 s rich conditions are typically adopted.

The most popular model NSR catalyst is Pt–Ba/Al₂O₃, which was first developed by Toyota's research group [4–6]. Although considerable amounts of experimental and theoretical investigations of Pt–Ba/Al₂O₃ have been reported, severe problems remain unresolved with respect to sulfur poisoning [5,10–12]. Meanwhile, NSR catalysts with high NO_x storage capacity are desirable because increasing the NO_x storage capacity can decrease the necessary amount of catalyst and thereby decrease the amounts of precious metals and costs. Titanium dioxide has been proposed as an efficient support for NSR reaction instead of Al₂O₃ because of its greater resistance to sulfur poisoning [5]. At the same time, several research groups have demonstrated that potassium based catalyst showed good performance on NO_x storage in a lean-burn atmosphere [13–15].

Recently a Korean research group has reported that Pt/K₂Ti₂O₅ catalysts, prepared through a solid state reaction, exhibited high NO_x storage capacity (1.2 mmol/g) at 550 °C [16,17]. The structural transformation between K₂Ti₂O₅ and K₂Ti₆O₁₃ has been regarded as the mechanism for NO_x storage on Pt/K₂Ti₂O₅ [17]. The lower NO_x storage capacity at lower temperatures (200–400 °C) as well as the slower NO_x storage rate even at higher temperatures (550 °C) has limited the application of K₂Ti₂O₅-based catalysts in wide areas.

Alkali titanate nanomaterials have been widely investigated [18–20]. However, their usual applications have directed the formation of functional materials by neutralizing them with acid [21,22]. Recently we reported the preparation of potassium-titanate nanobelts (KTN) using hydrothermal method. We used them as supports for Pt–KNO₃-impregnated NSR catalysts [23].

* Corresponding author.

E-mail address: naitos01@kanagawa-u.ac.jp (S. Naito).

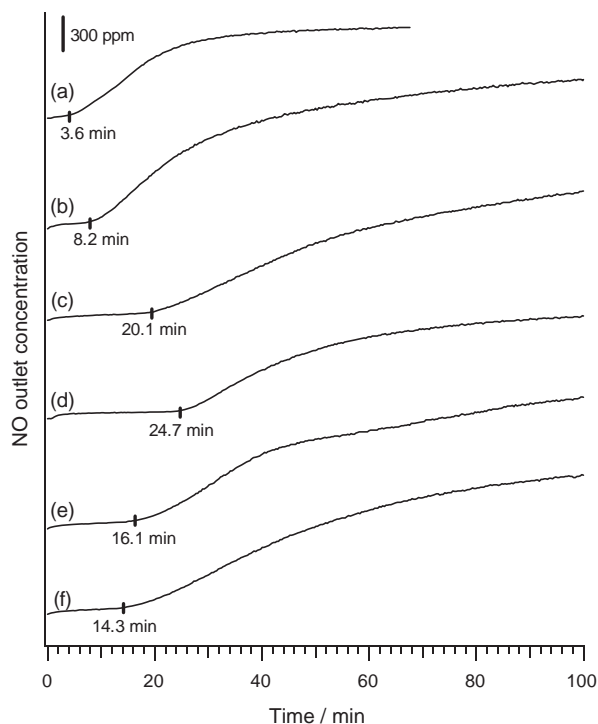


Fig. 1. Time courses of the outlet NO concentration on different catalysts during isothermal NO_x storage tests at 350 °C: (a) KTN, (b) Pt-13LiNO₃/KTN, (c) Pt-17NaNO₃/KTN, (d) Pt-20KNO₃/KTN, (e) Pt-27RbNO₃/KTN, and (f) Pt-33CsNO₃/KTN.

The obtained catalysts exhibited a high NO_x storage capacity (1.27–2.27 mmol/g) at 350 °C, whose maximal value (2.27 mmol) was the highest NO_x storage capacity ever reported in the literature. Results of isothermal NO_x storage and lean-rich cycling experiments, as well as various characterizations of catalysts before and after the reaction, demonstrate that the reduction of stored KNO₃ caused the formation of a K-rich surface layer of KTN. The migration of K⁺ from and back to the K-rich layer might be the mechanism for the storage and reduction of NO_x on those catalysts.

In this study, comparison of NSR behaviors of various alkali-metal-nitrate impregnated KTN catalysts revealed that the KNO₃-impregnated one showed superior performance. The XPS and XRD analyses of NaNO₃-impregnated Pt/KTN catalysts revealed that the migration of K⁺ from KTN bulk to the surface nitrate salts proceeds more predominantly than the migration of Na⁺, which explains why KNO₃-impregnated KTN exhibited the best catalytic performance.

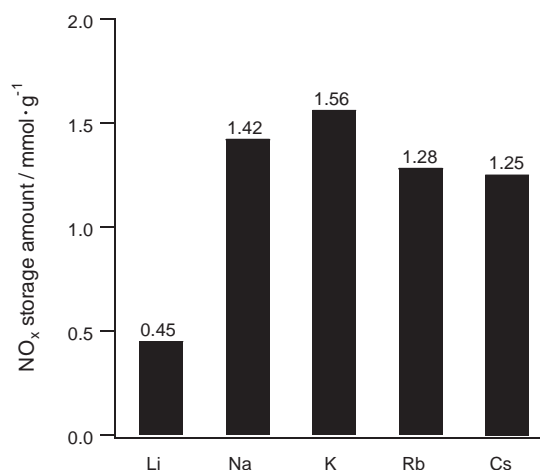


Fig. 2. NO_x storage capacities of Pt-MNO₃/KTN (M=Li, Na, K, Rb, and Cs) during isothermal NO_x storage tests at 350 °C.

2. Experimental

2.1. Catalyst preparation

A KTN was prepared using hydrothermal treatment with TiO₂ and KOH as starting materials. In XRD measurements of the obtained KTN, all reflection peaks were assigned to a monoclinic phase of K₂Ti₈O₁₇ (JCPDS No. 84-2057) (Fig. 5(a)). Nanobelts of several micrometers' length and tens of nanometers width with bending and twisting features were observed using TEM. Details of the preparation method and the results of characterization were described elsewhere [23]. Alkali metal nitrates of various kinds (designated as MNO₃; M=Li, Na, K, Rb, and Cs) and 1.5 wt% Pt were dispersed onto the KTN support using a conventional impregnation method. The impregnation amounts of MNO₃ were, respectively, 13 (M=Li), 17 (Na), 20 (K), 27 (Rb), and 33 wt% (Cs), which corresponded to 2 mmol/g on catalysts. Mixtures of the KTN and aqueous solutions of H₂PtCl₆ and MNO₃ were put into an oven at 70 °C until complete evaporation of water was achieved, with subsequent calcination at 350 °C for 2 h (designated as the as-prepared sample). The catalysts were designated as Pt-xxMNO₃/KTN, where xx signifies the weight percent of MNO₃.

2.2. Catalyst characterization

The XRD patterns were recorded using a diffractometer (MultiFlex; Rigaku Corp.) with a Cu Kα1 X-ray source (50 kV, 30 mA).

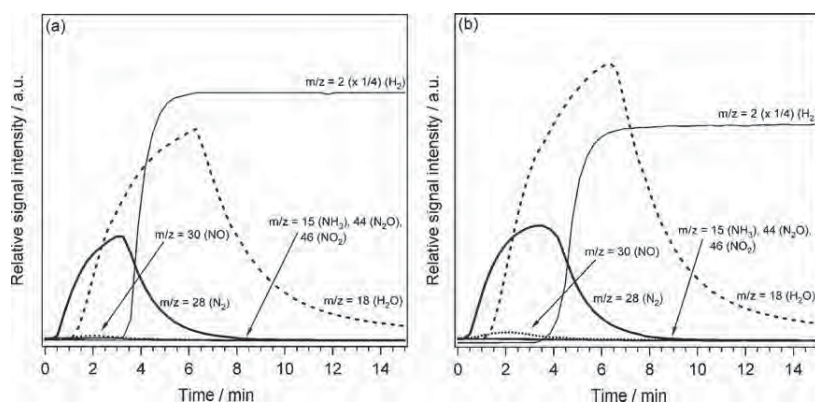


Fig. 3. Time courses of the reduction processes of stored NO_x on (a) Pt-17NaNO₃/KTN and (b) Pt-20KNO₃/KTN catalyst at 350 °C (100 mg of catalyst, 80 mL/min of 4% H₂/He).

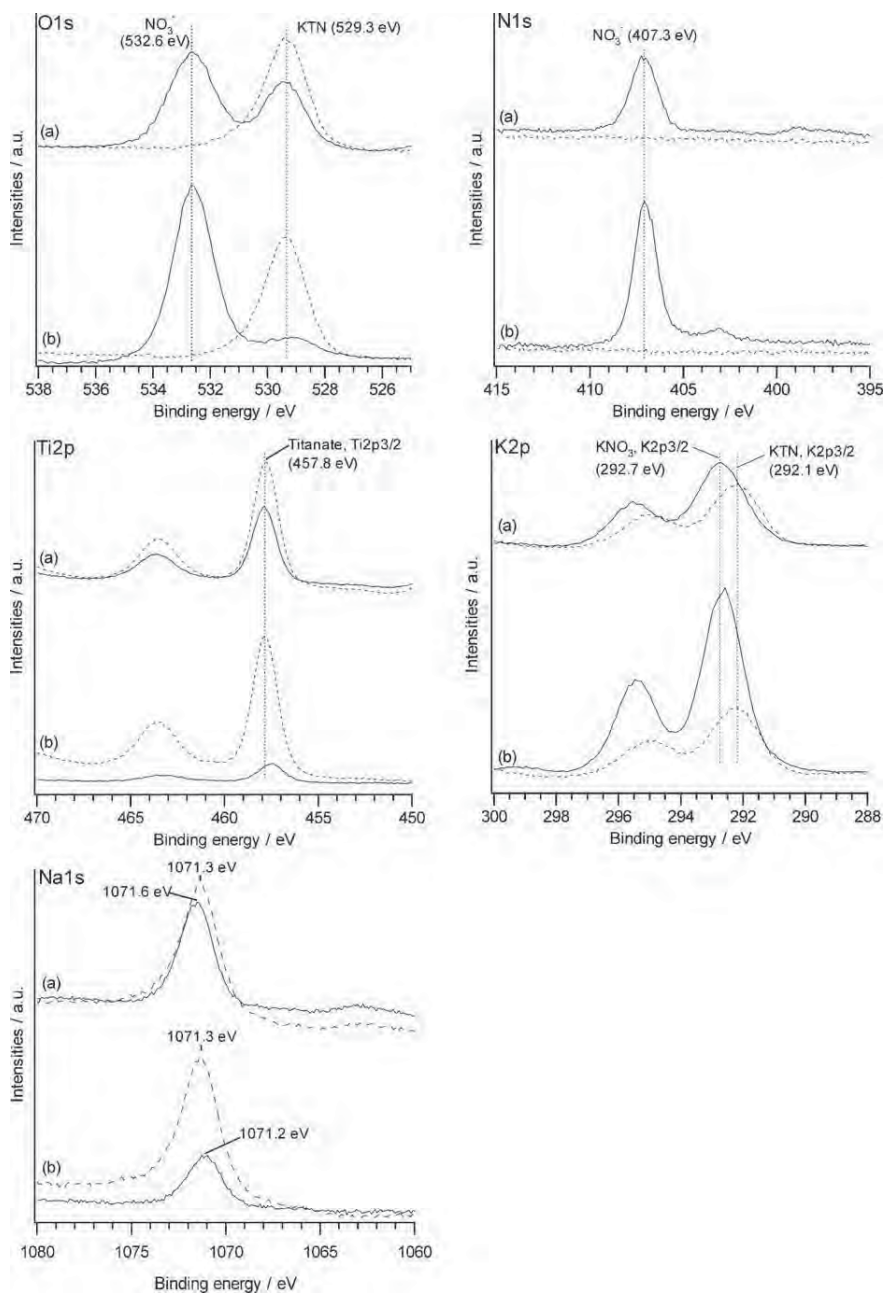


Fig. 4. X-ray photoelectron spectra of (a) as-prepared and (b) NO_x stored Pt-17Na NO_3 /KTN samples. Spectra of both samples before and after *in situ* hydrogen reduction at 350 °C are shown, respectively, as solid and dashed lines.

Then X-ray photoelectron spectroscopy (XPS) was conducted using a spectrometer (JPM-9010MC, JEOL) with a Mg $K\alpha$ X-ray source. The XPS apparatus has a preparation chamber in which a sample can be heated *in situ* and can be reduced by hydrogen (*in situ* hydrogen reduction). The C1s (284.3 eV) peak was used as the standard reference for binding energies.

2.3. Procedure for NO_x storage/reduction

Catalytic tests were performed on a fixed-bed-gas-flow reactor equipped with a pulse gas-feed system. The outlet gas was analyzed using an online quadrupole-mass-spectrometer (QME200;

Pfeiffer Vacuum GmbH). Before each catalytic test, 100 mg of a catalyst was placed in a quartz tube reactor and reduced by 80 mL/min of 8% H_2 /He flow from room temperature to 350 °C with a ramp rate of 10 °C/min. It was maintained at 350 °C for 30 min. For the isothermal NO_x storage test, 80 mL/min of 930 ppm $\text{NO}/7\%\text{O}_2$ /He mixed gas was flowed through the reduced catalyst at 350 °C (designated as a NO_x stored sample). The outlet gas was analyzed using a QMS. After flushing by 80 mL/min of He for 15 min, the NO_x storage catalyst was reduced by 80 mL/min of 4% H_2 /He at 350 °C and the outlet gas was analyzed using a QMS. Then the procedures described above were repeated. Data obtained from the second test were then used for analyses.

3. Results and discussion

3.1. NO_x storage and reduction capability of various alkali-metal-nitrate impregnated potassium titanate catalysts

Fig. 1 shows time courses of isothermal NO_x storage on various alkali-metal-nitrate impregnated KTN catalysts at 350 °C. The storage process includes two stages: at the first stage, NO was trapped completely, with no outlet NO detected; at the second stage, NO was partially trapped, with outlet NO increasing concomitantly with time. As presented in Fig. 1, all alkali-metal-nitrate impregnated Pt/KTN catalysts exhibited better NO trapping capacity than Pt/KTN without impregnation of alkali metal nitrate salts, whereas the periods of the complete NO trapping stage were dependent on impregnating alkali metal nitrate salts of the kind. The potassium and sodium nitrate impregnated ones exhibited excellent performance (24.7 and 20.1 min, respectively). The rubidium- and cesium-impregnated ones exhibited moderate performance (16.1 and 14.3 min, respectively). The lithium-impregnated one exhibited the shortest period (8.2 min). The NO storage capacities calculated from the isothermal NO storage experiment also depended on impregnating alkali metal nitrate salts of the kind, and showed the same trends as the complete NO_x trapping periods (Fig. 2). Our previous report on the potassium nitrate impregnated KTN catalyst revealed that NO trapping facilitates the migration of potassium cations from K-rich titanate layers to surface nitrate salt [23]. The volcano-like trends toward alkali metal cations in NO_x trapping period (Fig. 1) as well as NO_x trapping capacity (Fig. 2) probably arose from the different migration abilities of alkali metal cations between the titanate surface and nitrate salts, which might depend on the size of the cation.

Fig. 3 depicts time courses of the reduction processes of stored NO_x on Pt-17NaNO₃/KNO₃ and Pt-20KNO₃/KNO₃ catalysts at 350 °C. When 4%H₂/He was introduced on both catalysts in the NO_x stored state, the *m/z* = 28 signal derived from N₂ increased after a short period (<30 s) with the subsequent increase of the *m/z* = 18 signal derived from H₂O. This result demonstrates that both catalysts exhibited comparably good responses to hydrogen reduction. The *m/z* = 2 signal derived from H₂ was not observed in the initial stage of reduction (up to 3 min), although a sharp increase of the *m/z* = 2 signal was observed after that period (after 4 min). This result indicates that those catalysts are sufficiently active to consume hydrogen completely in the initial stage and to complete the reduction within a couple of minutes. It is noteworthy that the production of unfavorable byproducts such as NH₃, N₂O and NO₂ was not observed during the reduction process on either catalyst.

3.2. XPS and XRD analyses on sodium nitrate impregnated KTN in NO_x stored/released states

To elucidate the different behavior of various alkali metal cations, which come from impregnating nitrate salts and KTN bulk, XPS and XRD analyses on the NaNO₃-impregnated KTN catalysts under as-prepared and NO_x stored states were conducted. Fig. 4 depicts the X-ray photoelectron spectra of O1s, N1s, Ti2p, K2p, and Na1s transitions of as-prepared (solid line in (a)) and NO_x stored Pt-17NaNO₃/KTN (solid line in (b)) samples, and also the spectra after *in situ* hydrogen reduction of both samples at 350 °C for 1 h (dashed lines in (a) and (b)). In the spectrum of the as-prepared sample, the peaks derived from NO₃⁻ were observed at 407.0 and 532.6 eV in the region of the N1s and O1s transitions, respectively, which disappeared completely after *in situ* reduction and reappeared again after NO_x storage. These results support that NO_x molecules are stored as NO₃⁻ species located on the KTN surface. In contrast to the peaks derived from NO₃⁻, the intensities of the peaks with the binding energies at around 529.3 and 457.8 eV, assignable to the

O1s and Ti2p3/2 transitions of KTN, increased considerably after *in situ* hydrogen reduction. This result is explainable by the fact that the nitrate species that were formed by NO_x storage process and covered the KTN surface were removed after hydrogen reduction, thereby exposing a bare KTN surface.

The K2p3/2 transition of as-prepared sample has a single peak at 292.7 eV, which is assignable to KNO₃, although NaNO₃ was impregnated on the KTN material. This is true probably because the cation exchange reaction between sodium nitrate and potassium cation on KTN surface proceeded to a small degree during the impregnation or calcination process used to prepare NaNO₃/KTN. After *in situ* reduction of the as-prepared sample, K2p3/2 peak was shifted from 292.7 to 292.1 eV, which can be assigned to the K2p3/2 transition of KTN. This result suggests the incorporation of K⁺ of KNO₃ into the bulk of KTN during *in situ* hydrogen reduction. In the NO_x stored sample (spectra (b)), the peak at 292.7 eV, assignable to the K2p3/2 transition of KNO₃, was observed again. The remarkable increase of its intensity indicates that a certain extent of K⁺ migrated from KTN bulk was incorporated into the formation of surface nitrate salt. After *in situ* reduction, its intensity decreased markedly, accompanied with the shift of its binding energy (292.2 eV), suggesting that most of K⁺ was back into the lattice of KTN. On the other hand, the behavior of impregnated Na⁺ differed somewhat from that of K⁺. After *in situ* hydrogen reduction of the as-prepared sample, the intensity of Na1s transition increased slightly with the shift of binding energy from 1071.6 to 1071.3 eV. This result suggests the incorporation of Na⁺ into KTN. In the NO_x stored sample, the intensity of Na1s peak decreased drastically. It was recovered again through *in situ* hydrogen reduction. These observations indicate clearly that potassium cations migrated more predominantly from KTN to surface nitrate salts than sodium cations and covered most of the KTN surface as KNO₃ salts.

Those migration phenomena of potassium cations were also observed using XRD. Fig. 5(b) shows the XRD pattern of Pt-17NaNO₃/KTN catalysts at the NO_x stored state. Strong peaks at 2θ = 23.6, 29.4 and 33.9° can be assigned to KNO₃, although NaNO₃

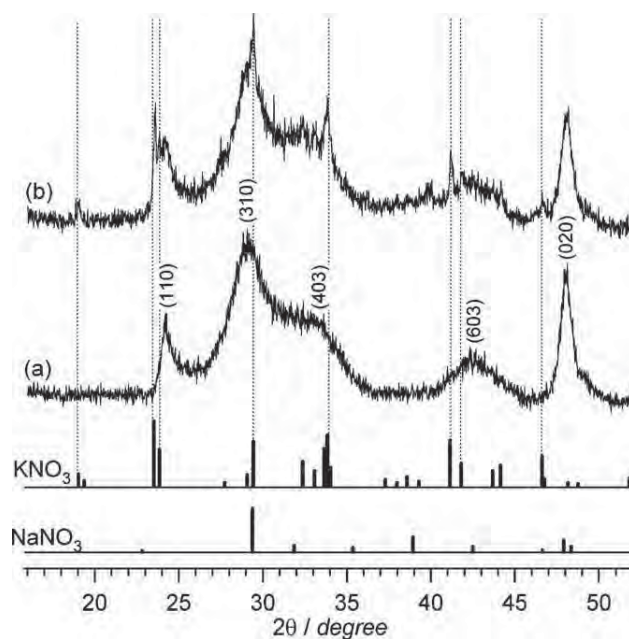


Fig. 5. XRD patterns of (a) KTN and (b) NO_x stored Pt-17NaNO₃/KTN samples. The positions of the reflections from KNO₃ are shown as dashed lines. The indexing of KTN (a) was done according to JCPDS database of a monoclinic K₂Ti₈O₁₇ (No. 84-2057).

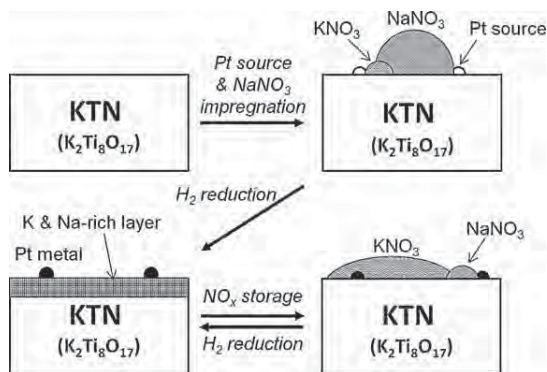


Fig. 6. Proposed mechanistic view of NO_x storage/reduction on Pt- NaNO_3 /KTN.

was impregnated at the beginning. These KNO_3 peaks disappeared completely through hydrogen reduction.

Fig. 6 shows a possible schematic process of the NSR reaction on Pt- NaNO_3 /KTN catalyst. The impregnated H_2PtCl_6 and NaNO_3 (with a small amount of KNO_3) can be reduced during pretreatment by H_2 reduction, and a K- and Na-rich layer and Pt metallic particles can be formed on the surface of KTN. During the NO_x storage process, NO molecules were first oxidized on Pt to NO_2 and then combined predominantly with potassium cations from a K-rich and Na-rich layer, thereby forming KNO_3 on the surface. The formed NO_x storage species might move easily on the surface and eventually cover most of the KTN surface. During the NO_x reduction process, the formed KNO_3 was reduced by hydrogen and the K^+ moved back to the KTN bulk to form the K and Na-rich layer again. The XPS and XRD results revealed that potassium cations can migrate more easily from titanate bulk to surface nitrate salts than sodium cations. Probably for this reason, KNO_3 -impregnated KTN showed the best NO_x storage/reduction performance among various alkali-metal-impregnated KTN catalysts.

4. Conclusion

The NSR activity of KTN was enhanced by the decoration of various alkali metal nitrate salts. Among them, the KNO_3 -impregnated

one showed superior performance and a NaNO_3 -impregnated one showed comparable activity to the KNO_3 -impregnated one. The XPS and XRD analyses of the NaNO_3 -impregnated KTN material revealed that migration of K^+ from the KTN bulk to surface nitrate salts predominated over the migration of Na^+ . Probably for this reason, KNO_3 -impregnated KTN showed the best NO_x storage/reduction performance among the various alkali-metal-impregnated KTN catalysts.

References

- [1] S. Roy, A. Baiker, *Chem. Rev.* 109 (2009) 4054–4091.
- [2] G. Centi, G.E. Arena, S. Perathoner, *J. Catal.* 216 (2003) 443–454.
- [3] M. Iwamoto, S. Yokoo, K. Sakai, S. Kagawa, *J. Chem. Soc., Faraday Trans. 77* (1981) 1629–1638.
- [4] N. Takahashi, H. Shinjoh, T. Suzuki, K. Yamazaki, K. Yokota, H. Suzuki, N. Miyoshi, S. Matsumoto, T. Tanizawa, T. Tanaka, S. Tateishi, K. Kasahara, *Catal. Today* 27 (1996) 63–69.
- [5] S. Matsumoto, Y. Ikeda, H. Suzuki, M. Ogai, N. Miyoshi, *Appl. Catal. B: Environ.* 25 (2000) 115–124.
- [6] K. Tamazaki, T. Suzuki, N. Takahashi, K. Yokota, M. Sugiura, *Appl. Catal. B: Environ.* 30 (2001) 459–468.
- [7] P. Forzatti, *Appl. Catal. A: Gen.* 222 (2001) 221–236.
- [8] R. Burch, J.P. Breen, C.J. Hill, B. Krutzsch, B. Konrad, E. Jobson, L. Cider, K. Eränen, F. Klingstedt, L.-E. Lindfors, *Top. Catal.* 30–31 (2004) 19–25.
- [9] K. Theinnoi, S. Sitshebo, V. Houel, R.R. Rajaram, A. Tsolakis, *Energy Fuels* 22 (2008) 4109–4114.
- [10] F. Frola, M. Manzoli, F. Prinetto, G. Ghiotti, *J. Phys. Chem. C* 112 (2008) 12869.
- [11] M. Happel, A. Desikusumastuti, M. Sobota, M. Laurin, J. Libuda, *J. Phys. Chem. C* 114 (2010) 4568–4575.
- [12] N. Rankovic, A. Nicolle, P.D. Costa, *J. Phys. Chem. C* 114 (2010) 7102–7111.
- [13] K. Yamamoto, R. Kikuchi, T. Takeguchi, K. Eguchi, *J. Catal.* 238 (2006) 449–457.
- [14] T. Lesage, J. Saussey, S. Malo, M. Hervieu, C. Hedouin, G. Blanchard, M. Daturi, *Appl. Catal. B: Environ.* 72 (2007) 166–177.
- [15] A. de Lucas, A. Caravaca, P. Sanchez, F. Dorado, J.L. Valverde, *J. Catal.* 259 (2008) 54–65.
- [16] Q. Wang, Z. Guo, J.S. Chung, *Chem. Comm.* (2009) 5284–5286.
- [17] Q. Wang, J.H. Sohn, J.S. Chung, *Appl. Catal. B: Environ.* 89 (2009) 97–103.
- [18] X. Sun, Y. Li, *Chem. Eur. J.* 9 (2003) 2229–2238.
- [19] Y. Lan, X. Gao, H. Zhu, Z. Zheng, T. Yan, F. Wu, S. Ringer, D. Song, *Adv. Funct. Mater.* 15 (2005) 1310–1318.
- [20] C. Tsai, H. Teng, *Langmuir* 24 (2008) 3434–3438.
- [21] L. Torrente-Murciano, A.A. Lapkin, D.V. Bavykin, F.C. Walsh, K. Wilson, *J. Catal.* 245 (2007) 272–278.
- [22] T.A. Ntho, J.A. Anderson, M.S. Scurrell, *J. Catal.* 261 (2009) 94–100.
- [23] W. Shen, A. Nitta, Z. Chen, T. Eda, A. Yoshida, S. Naito, *J. Catal.* 280 (2011) 161–167.



Enhancement of catalytic activity of Ir/TiO₂ by partially reduced titanium oxide in aerobic oxidation of alcohols

Akihiro Yoshida, Yoshinori Mori, Tsuyoshi Ikeda, Kazuki Azemoto, Shuichi Naito*

Department of Material and Life Chemistry, Kanagawa University, 3-27-1 Rokkakubashi, Kanagawa-ku, Yokohama 221-8686, Japan

ARTICLE INFO

Article history:

Received 25 October 2011
Received in revised form 13 March 2012
Accepted 3 April 2012
Available online 26 May 2012

Keywords:

Alcohol oxidation
Supported Ir catalyst
SMSI effect

ABSTRACT

The catalytic activity of 2 wt% Ir/TiO₂ in alcohol oxidation with molecular oxygen was enhanced by high-temperature reduction (673–873 K) of the catalyst in a hydrogen stream. Wide variety of alcohols were converted efficiently into corresponding carbonyl compounds with 2 wt% Ir/TiO₂ reduced at 723 K. Kinetic analysis revealed that the alcohol adsorption was enhanced by high-temperature reduction of catalysts. Formation of partially reduced titanium oxide by high-temperature hydrogen reduction of TiO₂-supported metal catalysts is a widely known phenomenon as the SMSI effect. The formed TiO_(2-δ) species containing coordinatively unsaturated titanium sites might contribute to the enhancement of catalysis as a coordination site of alcohols.

© 2012 Elsevier B.V. All rights reserved.

1. Introduction

Carbonyl compounds such as aldehydes and ketones comprise an important class of compounds used not only in chemical industries but also in laboratories. The oxidation reaction of alcohols is regarded as a principal process because it is the most common way of producing carbonyl compounds. In spite of the formation of toxic by-products and large amount of heavy metal wastes, the reactions have been performed mainly in non-catalytic systems with stoichiometric amounts of oxidants [1]. From environmental and economic points of view, catalytic systems that can use greener and cheaper oxidants, particularly molecular oxygen, have been desired [2]. To date, catalytic systems of various kinds have been reported in the oxidation of alcohols using transition metal complexes [3–5], nitroxyl radicals [1], heterogeneous catalysts [6–10], and photocatalysts [11,12]. For practical applications, utilization of metal catalysts supported on oxide materials is preferred because of their advantages in separation, recovery and reuse of the catalysts, and ease of catalysts preparation. Therefore, the development of efficient supported metal catalysts for this reaction has been regarded as an attractive research area.

Recently, we reported that TiO₂-supported Ir catalysts prepared using the conventional impregnation method efficiently catalyzed the oxidation of alcohols with molecular oxygen [13]. Although Ir catalysts supported on various oxide materials exhibited catalytic activity to a certain degree, the relations between catalytic activity and metal surface area or acid–base properties of the support were not observed clearly. Investigation of the intrinsic role of TiO₂

support revealed that catalytic activity of Ir/TiO₂ in the alcohol oxidation was enhanced by high-temperature reduction in a hydrogen atmosphere. Strong interaction between metal particles and the TiO₂ support is well known to be induced by high-temperature hydrogen reduction. This phenomenon is known as the Strong-Metal-Support-Interaction (SMSI) effect [14,15]. A well accepted explanation of the SMSI effect is the decoration of metal surface by partially reduced titanium oxide [16–19]. Several reports have described that activity and/or selectivity of the TiO₂ supported catalysts can be tuned by the SMSI effect. For example, Fierro et al. reported enhancement of the catalysis toward the hydrogenation of citral over Ir/TiO₂ by the SMSI effect [20]. They explained that TiO_x species formed by the higher temperature reduction contributed to the polarization of carbonyl group, which made the hydrogenation of citral easier to produce geraniol or nerol. Moon et al. and Panpranot et al. reported that higher temperature reduction of Pd/TiO₂ improved the selectivity in the semi-hydrogenation reactions of alkyne to alkene [21–23]. Moon et al. described that configuration and electronic modification of Pd particles were the key factors for improving the selectivity in the hydrogenation of acetylene to ethylene over Pd/TiO₂ [21]. In the present work, we describe enhancement of the catalytic activity of Ir/TiO₂ in the oxidation of alcohols by high-temperature reduction in a hydrogen stream. Furthermore, we investigated how the SMSI effect participated in the enhancement of the catalytic activity.

2. Experimental

2.1. Instruments

GC analyses were performed using a gas chromatograph (GC-2010; Shimadzu Corp.) with a FID detector equipped with a

* Corresponding author. Tel.: +81 45 481 5661x3903; fax: +81 45 413 9770.
E-mail address: naitos01@kanagawa-u.ac.jp (S. Naito).

TC-WAX capillary column. Mass spectra were recorded on a spectrometer (GCMS2010; Shimadzu Corp.) equipped with a TC-WAX capillary column at an ionization voltage of 70 eV. NMR spectra were recorded on a spectrometer (JNM-ECA-600; JEOL). The ^1H and ^{13}C NMR spectra were measured, respectively, at 600.17 and 150.92 MHz. A transmission electron microscope (JEM2010; JEOL) with an acceleration voltage of 200 kV and a LaB_6 cathode was applied for the observation of the images of supported catalysts. Samples were prepared by suspending the catalyst powder ultrasonically in 2-propanol and depositing a drop of the suspension on a standard copper grid covered with carbon monolayer films. The X-ray photoelectron spectra were recorded on a spectrometer (JPS-9010; JEOL) with a $\text{Mg K}\alpha$ X-ray source (10 kV, 10 mA). Before measurement, a sample was reduced by H_2 at 573 K or 723 K in the preparation chamber and transferred to the analysis chamber without exposure to air. The adsorption amount of carbon monoxide was measured using a static volumetric adsorption apparatus (Omnisorp 100CX; Beckman Coulter, Inc.) at 298 K. Before measurement, a sample was dried at room temperature and reduced for 3 h at varying temperatures in a flow of hydrogen at atmospheric pressure. The dispersion ($D(\%)$; percentage of metal atoms exposed to the surface) of the supported metal was evaluated from the amount of chemisorbed carbon monoxide and adsorption stoichiometry ($\text{CO}/\text{surface metal atom} = 1$).

2.2. Materials and catalyst preparation

The TiO_2 support (P25) was purchased from Nippon Aerosil Co., Ltd. The solvents used for the catalytic reaction were dried with activated molecular sieves 4A. For other materials, commercially available reagents of the highest grade were used without further purification. A TiO_2 -supported Ir catalyst was prepared from aqueous solution of H_2IrCl_6 using the conventional impregnation method. The loading amount of Ir was adjusted in the range of 0.5–15 wt%. The impregnated sample was dried at 373 K and then reduced in a H_2 flow at varying temperature for 3 h.

2.3. Procedures for catalytic oxidation

The oxidation reaction was done in the following procedure: 187 mg of the reduced 2 wt% Ir/ TiO_2 (Ir: 20 μmol , 1.25 mol% to substrates), the solvent (toluene or mesitylene, 1.5 mL), and the substrate (1.5 mmol) were charged into a glass vial (17 mL). The reaction was started by stirring the reaction mixture at 353 K in alcohol oxidation or 423 K in xanthene oxidation under molecular oxygen at atmospheric pressure. The products were identified by

Table 1

Dependence between reduction temperature of catalysts and catalytic activity in the oxidation of 1-phenylethanol at 353 K for 1 h.

Red. temp (K)	Yield of acetophenone (%)	CO chemisorption amount (mL/g)
573	27	1.5
673	62	1.0
723	89	0.35
773	62	0.17
873	57	–

comparison of the mass and NMR spectra with those of authentic samples. The yields of the products were determined using GC analyses with an internal standard technique.

3. Results and discussion

3.1. Characterization of the catalyst

The relation of CO chemisorption amount with hydrogen reduction temperature was examined on 2 wt% Ir/ TiO_2 . When the hydrogen reduction temperature was increased, the CO chemisorption amount was decreased (Table 1) because of the Strong Metal Support Interaction (SMSI) effect. The decrease of chemisorption amount is explained by the decoration of Ir metal surface with partially reduced titanium oxide, which is formed by hydrogen reduction at high temperature [16–19]. After reduction at 873 K, the chemisorption amount of CO was almost zero. A TEM photograph of the catalyst reduced at 723 K is presented in Fig. 1(b). It was rather difficult to distinguish the interface between Ir metal particle and TiO_2 support. In addition, some Ir particles were completely covered with partially reduced titania moieties. On the other hand, the interface between Ir metal particle and support was clearly distinguishable in the case of 573 K reduced catalyst (Fig. 1(a)) and the surfaces of Ir metal particles were well exposed. These observations also support the occurrence of the SMSI effect by the reduction at 723 K. The electronic state of Ir was investigated using XPS analyses. The catalysts reduced in a H_2 atmosphere were transferred to the measurement chamber without exposure to air. In the $\text{Ir}4f_{7/2}$ transition, the similar spectra were obtained for 573 K and 723 K reduced catalysts (Fig. 2). This observation suggests that the electronic state of Ir species formed on the catalyst reduced at 573 K and 723 K are not so different. The observed spectra for $\text{Ir}4f_{7/2}$ transition were separated in two peaks: a major peak centered at 60.2 eV and a minor one at 61.7 or 61.8 eV. Binding energy for the major peak is slightly lower than the reported value for metallic Ir (60.8 eV [24]), indicating that slightly anionic Ir is the major species. The binding

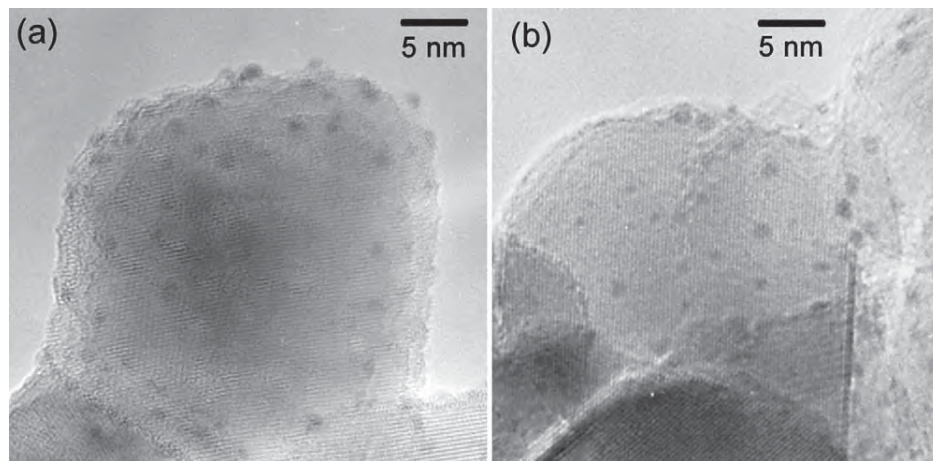


Fig. 1. TEM images of 2 wt% Ir/ TiO_2 reduced at (a) 573 and (b) 723 K.

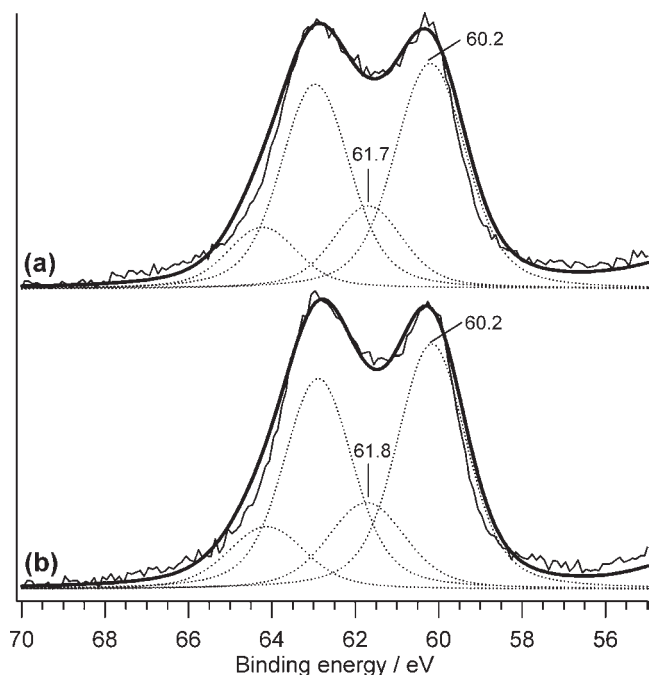


Fig. 2. X-ray photoelectron spectra of the Ir4f transition of 2 wt% Ir/TiO₂ reduced at (a) 573 and (b) 723 K.

energy for the minor peak is approximately equal to that reported for IrO₂ (62.0 eV [24]), indicating that a small amount of Ir species is in an oxidized state even after the reduction.

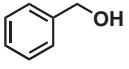
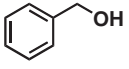
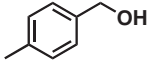
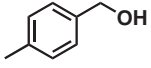
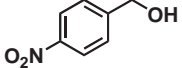
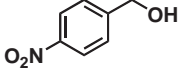
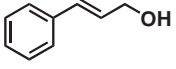
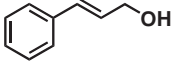
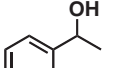
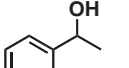
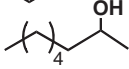
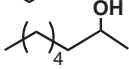
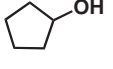
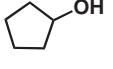
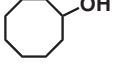
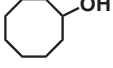
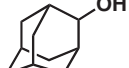
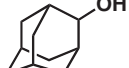
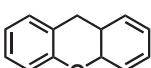
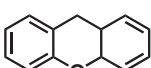
3.2. Enhancement of catalytic activity by higher temperature reduction

The relation between catalytic activity and reduction temperature was investigated in the aerobic oxidation of 1-phenylethanol (Table 1). In spite of the decrease of CO chemisorption amount, the catalysts reduced at higher temperature (673–873 K) showed higher activity than that reduced at 573 K. This result suggests that partially reduced titanium oxide around Ir metal particles enhanced the catalytic activity. The catalyst reduced at 723 K showed the best performance; 94% of acetophenone afforded 98% selectivity after 7 h at 353 K. The lack of detection of a significant amount of by-product indicates that the oxidation proceeded selectively. Low-valent Ir or metallic Ir is expected to be the active species because the catalyst without hydrogen reduction showed almost no activity. The catalysts reduced at 773 and 823 K showed lower activity than the 723 K reduced one. This is probably caused by the too much covering of the Ir surface with partially reduced titania moieties.

The high-temperature reduction enhanced not only 1-phenylethanol, but also the oxidation reactions of a wide variety of alcohols. The catalytic activities of the 723 K reduced catalyst and 573 K reduced catalyst are compared in Table 2. In the oxidation of primary alcohols, the 723 K reduced catalyst showed slightly higher or almost identical activity compared to that of the 573 K reduced catalyst. When benzyl alcohol, 4-methylbenzyl alcohol, and cinnamyl alcohol were applied to the substrates, the 723 K reduced catalyst exhibited excellent catalytic activity to afford corresponding aldehyde quantitatively, whereas the 573 K reduced catalyst also showed good activity to afford aldehydes in around 90% yields. In the oxidation of 4-nitrobenzyl alcohol, the respective catalytic activities of the 723 K reduced catalyst and the 573 K reduced catalyst were almost identical. Enhancement of catalytic activity

Table 2

Oxidation of alcohols and xanthene with molecular oxygen catalyzed by 2 wt% Ir/TiO₂ reduced at 573 K and 723 K.

Entry	Substrate	Time (h)	Yield (%)	Selec. (%)
1 ^a		1	>99	>99
1 ^b			86	>99
2 ^a		1	>99	>99
2 ^b			91	97
3 ^a		30	65	72
3 ^b			65	74
4 ^a		7	>99	>99
4 ^b			93	94
5 ^a		3	>99	>99
5 ^b			65	98
6 ^a		7	92	98
6 ^b			70	95
7 ^a		3	91	92
7 ^b			76	86
8 ^a		7	95	98
8 ^b			84	90
9 ^a		21	94	96
9 ^b			58	91
10 ^{a,c}		12	61	92
10 ^{b,c}			81	88

2 wt% Ir/TiO₂ reduced at ^a273 and ^b573 K were used as catalysts. ^cThe reactions were carried out at 423 K used mesitylene as a solvent.

by high-temperature reduction was observed more clearly in the oxidation of secondary alcohols. For example, the 723 K reduced catalyst afforded 2-adamantanone in 94% yield in the oxidation of 2-adamantanol after 21 h, whereas the 573 K reduced catalyst afforded the product in 58% yield in the same period. For oxidation of other kind of aromatic and aliphatic secondary alcohols, the 723 K reduced catalyst showed efficient catalytic activity to afford the corresponding ketones at more than 92% yields. It is noteworthy that not only the catalytic activity but the selectivity was also improved by the higher-temperature reduction. For oxidation of secondary alcohols, dehydration of substrate to form alkenes was the only detectable side reaction. To consume the substrate in a shorter period might reduce the production of by-products. Therefore the selectivity was improved. We have already reported that Ir/TiO₂ catalyst shows the catalytic activity to the aerobic oxidation of alkylarenes [13]. We also compared the respective catalytic activities of 573 K and 723 K reduced 2 wt% Ir/TiO₂ in the oxidation of xanthene (Table 2, entry 10). It is particularly interesting that the catalytic activity of xanthene oxidation was retarded by the higher-temperature reduction.

As presented in Table 2, catalysis enhancement by high-temperature reduction was observed to a considerable degree in the oxidation of secondary alcohols and moderately in the oxidation of primary alcohols. We reported earlier that primary alcohols reacted predominantly over Ir/TiO₂ catalyst in the presence of both

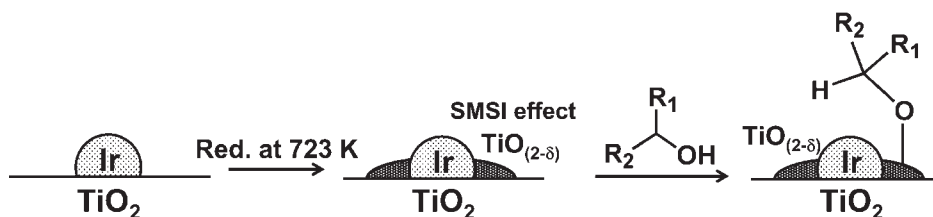


Fig. 3. Schematic representation of the enhancement of catalysis by high-temperature reduction.

primary and secondary alcohols [13]. This result might be explained by the stronger absorption of primary alcohols than secondary alcohols on the active sites. The marked enhancement of the catalytic activity in the oxidation of secondary alcohols by higher temperature reduction suggests that absorption of secondary alcohols on the active sites was improved in the presence of the partially reduced titanium oxide species near the Ir metal particles. On the other hand, the oxidation of primary alcohols was only moderately enhanced by the SMSI effect. This is probably because the adsorption of primary alcohols to the catalyst surfaces is strong enough even in the absence of the SMSI effect is absent. Fierro et al. reported the enhancement of the catalysis toward the hydrogenation of citral over Ir/TiO₂ by the SMSI effect [20]. They explained that TiO_x species formed by the higher temperature reduction activated the substrate by polarizing a carbonyl group. The SMSI effect is known to result from the formation of partially reduced titanium oxide (TiO_{2-δ}) species near the supported precious metals. The partially reduced titanium oxide species contains oxygen vacancies. In other words, it contains coordinatively unsaturated titanium sites, which are able to function as adsorption and/or activation sites of polar molecules, such as carbonyl compounds and alcohols. To bind the alcohol molecules in the vicinity of the iridium metal center is presumed to be an intrinsic role in the enhancement of the catalysis by the SMSI effect (Fig. 3). It is noteworthy that no enhancement was observed in the oxidation of alkylarenes of xanthene (Table 2, entry 10), probably because xanthene does not form alcoholate and has no strong coordination ability.

3.3. Kinetic analysis

To investigate the intrinsic role of the SMSI effect in the enhancement of the catalysis, kinetic analysis using a Langmuir equation was conducted. The Langmuir equation is given as $V = n \cdot k_{\text{reac}} \cdot K \cdot [A] / (1 + K \cdot [A])$ or $1/V = 1/(n \cdot k_{\text{reac}} \cdot K \cdot [A]) + 1/(n \cdot k_{\text{reac}})$ ($K = k_{\text{ads}}/k_{\text{des}}$), where V is the reaction rate, n is the number of reaction sites, k_{reac} is the reaction rate constant of adsorbed species, k_{ads} and k_{des} are the adsorption and desorption rate constants of substrate on catalyst surface, respectively, and $[A]$ is the substrate concentration. The adsorption equilibrium constant K is calculated by dividing intercept of y -axes ($1/(n \cdot k_{\text{reac}})$) by slope ($1/(n \cdot k_{\text{reac}} \cdot K)$) on the plot of $1/V$ vs. $1/[A]$. Fig. 4 presents plots of $1/V$ vs. $1/[A]$ toward the 1-phenylethanol oxidation catalyzed by 573 K and 723 K reduced 2 wt% Ir/TiO₂. Linear correlations were observed on the plots for both 573 K and 723 K reduced catalysts, suggesting that the reaction operated in the Langmuir type kinetics. The K values calculated using the method described above were, respectively, 6.7 and 13.5 for 573 K and 723 K reduced catalysts. Increase of the K value after high-temperature reduction indicates clearly that the SMSI effect enhances adsorption of alcohol on the catalyst surface.

3.4. Recyclability of catalyst

Recyclability of 2 wt% Ir/TiO₂ catalyst reduced at 723 K was examined in oxidation of benzyl alcohol. After the reaction, the catalyst was separated by filtration and subsequently washed with

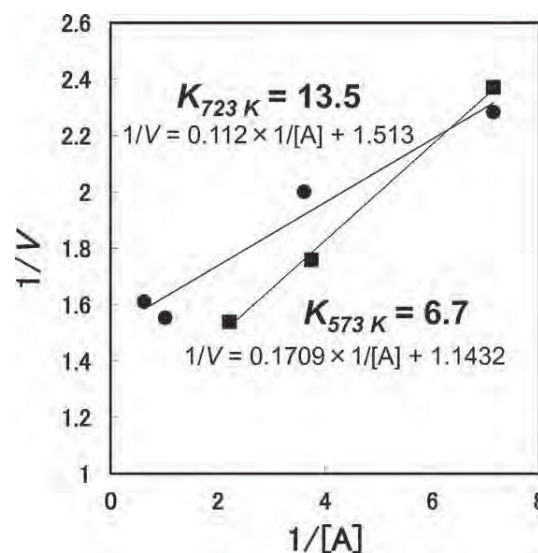


Fig. 4. Plots of $1/V$ vs. $1/[A]$ in the oxidation of 1-phenylethanol catalyzed by 573 K (square symbols) and 723 K (circle symbols) reduced Ir/TiO₂.

toluene. The obtained catalyst was reused without any treatment. During the recycling experiments, the yield of benzaldehyde was only slightly lower than the fresh one in the 2nd and 3rd runs (>99% (fresh catalyst), 90% (2nd run), 92% (3rd run)), although the greater decrease was observed in the 4th run (64% (4th run)). The catalytic activity was almost recovered by hydrogen reduction at 723 K after the 4th run. The activity was maintained in another three reactions (92% (1st run after reduction), 92% (2nd run), and 89% (3rd run)). Tauster et al. discussed from the CO chemisorption results on 2 wt% Pd/TiO₂ that the SMSI effect became ineffective by oxygen treatment at 673 K and recovered again after high-temperature hydrogen reduction [14]. Therefore, the catalyst degradation after several reactions and recovery after high-temperature hydrogen reduction could be explained by ineffectiveness and recovery of the SMSI effect.

4. Conclusion

The catalytic activity of 2 wt% Ir/TiO₂ in alcohol oxidation with molecular oxygen was enhanced by higher-temperature reduction (673–873 K) of the catalyst in a hydrogen stream, even though the chemisorption amount of CO was decreased. Wide variety of alcohols were converted efficiently into corresponding carbonyl compounds with 2 wt% Ir/TiO₂ reduced at 723 K. Kinetic analysis revealed that the reaction operated in Langmuir type kinetics. The adsorption constants in Langmuir equation of 6.7 and 13.5 for 573 K and 723 K reduced catalysts respectively indicate that high-temperature reduction of catalysts enhanced adsorption of alcohols. Formation of partially reduced titanium oxide by high-temperature hydrogen reduction of TiO₂-supported metal catalysts are widely known phenomena referred to the SMSI effect, and the

formed $\text{TiO}_{(2-\delta)}$ species containing coordinatively unsaturated titanium sites might contribute to the enhancement of catalysis as a coordination site of alcohols.

References

- [1] R.A. Sheldon, I.W.C.E. Arends, G.T. Brink, A. Dijkstra, *Accounts of Chemical Research* 35 (2002) 774–781.
- [2] T. Mallat, A. Baiker, *Chemical Reviews* 104 (2004) 3037–3058.
- [3] S.S. Stahl, *Angewandte Chemie International Edition* 43 (2004) 3400–3420.
- [4] M.J. Schultz, M.S. Sigman, *Tetrahedron* 62 (2006) 8227–8241.
- [5] B.A. Steinhoff, S.R. Fix, S.S. Stahl, *Journal of the American Chemical Society* 124 (2002) 766–767.
- [6] K. Mori, K. Yamaguchi, T. Hara, T. Mizugaki, K. Ebitani, K. Kaneda, *Journal of the American Chemical Society* 124 (2002) 11572–11573.
- [7] K. Yamaguchi, N. Mizuno, *Angewandte Chemie International Edition* 41 (2002) 4538–4542.
- [8] K. Yamaguchi, N. Mizuno, *Chemistry – A European Journal* 9 (2003) 4253–4361.
- [9] T. Ishida, M. Nagaoka, T. Akita, M. Haruta, *Chemistry – A European Journal* 14 (2008) 8456–8460.
- [10] T. Matsumoto, M. Ueno, N. Wang, S. Kobayashi, *Chemistry – An Asian Journal* 3 (2008) 196–214.
- [11] S. Higashimoto, N. Kitao, N. Yoshida, T. Sakura, M. Azuma, H. Ohue, Y. Sakata, *Journal of Catalysis* 266 (2009) 279–285.
- [12] S. Higashimoto, N. Suetsugu, M. Azuma, H. Ohue, Y. Sakata, *Journal of Catalysis* 274 (2010) 76–83.
- [13] A. Yoshida, et al., *Catalysis Today* 164 (2011) 332–335.
- [14] S.J. Tauster, S.C. Fung, R.L. Garten, *Journal of the American Chemical Society* 100 (1978) 170–175.
- [15] S.J. Tauster, S.C. Fung, *Journal of Catalysis* 55 (1978) 29–35.
- [16] J. Santos, J. Phillips, J.A. Dumesic, *Journal of Catalysis* 81 (1983) 147–167.
- [17] H.R. Sadeghi, V.E. Henrich, *Journal of Catalysis* 87 (1984) 279–282.
- [18] A.J. Simoens, R.T.K. Baker, D.J. Dwyer, C.R.F. Lund, R.J. Madon, *Journal of Catalysis* 86 (1984) 359–372.
- [19] Y.W. Chung, G. Xiong, C.C. Kao, *Journal of Catalysis* 85 (1984) 237–243.
- [20] P. Reyes, H. Rojas, J.L.G. Fierro, *Applied Catalysis A* 248 (2003) 59–65.
- [21] J.H. Kang, E.W. Shin, W.J. Kim, J.D. Park, S.H. Moon, *Journal of Catalysis* 208 (2002) 310–320.
- [22] J. Panpranot, K. Kontapakdee, P. Praserttham, *Journal of Physical Chemistry B* 110 (2006) 8019–8024.
- [23] P. Weerachawanasak, O. Mekasuwandumrong, M. Arai, S. Fujita, P. Praserttham, J. Panpranot, *Journal of Catalysis* 262 (2009) 199–205.
- [24] NIST X-ray Photoelectron Spectroscopy (XPS) Database, Version 3.5.

1 B 03

炭素材料と水素化リチウムからなる新規水素吸蔵材料の開発とその水素吸放出機構

吉田暁弘・奥山高志・齋藤直樹・内藤周弐

神奈川大学工学部物質生命化学科 〒221-8686 神奈川県横浜市神奈川区六角橋 3-27-1

金属水素化物は水素貯蔵材料として有望な化合物群であるが、高い水素放出温度や再水素化圧、水素吸放出の繰り返しの伴う劣化等の問題により実用化が困難であり、これらの問題の解決が強く望まれている。我々は、グラファイト、フラーレン、ポリアセチレンといった共役構造を有する炭素材料やポリマーと水素化リチウムの複合体が比較的温和な条件で水素を吸放出し、良好な繰り返し特性を示すことを見出した。

[討論したい事項](1)炭素材料の添加による水素吸放出特性の向上、(2)水素吸放出反応機構

1. 緒言

水素は、燃焼時に水以外の物質を副生しない極めてクリーンなエネルギー源であるだけでなく、ガソリンエンジン等の内燃機関の代替燃料として使用でき、燃料電池により高効率で電力に変換可能であるという優れた性質を有している。近年、水素の製造法について様々な技術的な革新もたらされており、従来から行われてきた石油、石炭等の改質といった枯渇が懸念される化石資源に依存した製法だけではなく、可視光による水の光分解¹⁾やバイオマスの改質²⁾といった持続可能な資源やエネルギーからの製法も見出されている。地球温暖化や発展途上国における大気汚染などの環境問題に対する注目が高まる昨今、技術的な革新も相まって、クリーンかつ資源的制約のない究極の次世代エネルギー源として、水素がますます広く注目される状況にある。しかしながら、単体の水素は常温常圧下で気体であることから、単体状態での高密度貯蔵には、極低温下での液化もしくは極高圧下での圧縮のいずれかが必要であり、貯蔵設備の体積や重量が限定される移動体での使用における大きな制約となっている。このような現状から、様々な化合物媒体中への水素の高密度貯蔵が試みられている。金属水素化物を用いた水素貯蔵は有望な手法の一つであり、B, Li, Mg, Al等の軽元素の水素化物や複数の軽元素からなる複合水素化物による水素貯蔵が広く研究されている。例えば、 $\text{NH}_3 \cdot \text{BH}_3$ は 150°C 程度で7.7 wt%の水素を放出するが³⁾、再水素化は著しく困難である。また、 LiNH_2 と LiH の混合物は 400°C 以上で10 wt%の水素を放出し、 200°C 、20気圧の条件で再水素化が可能であるが⁴⁾、繰り返し耐性に乏しい。したがって、金属水素化物系水素貯蔵材料の実用化にあたっては、水素放出温度の低温化、再水素化圧の低減、水素吸放出繰り返し特性の向上が必要である。我々は、グラファイト、フラーレン、ポリアセチレンといった共役構造を有する炭素材料やポリマーと水素化リチウムの複合体が比較的温和な条件で水素を吸放出し、良好な繰り返し特性を示すことを見出した^{5,6)}。特に、フラーレンやポリアセチレンを用いた際は、従来の報告にない新たな機構で水素の吸放出が進行することを明らかとした。

2. 実験

炭素材料と水素化リチウムの複合体は、それぞれ以下に

示す方法により調製した後、水素化を行い、He気流中でのTPD測定により水素放出量を定量した。放出ガス種の同定と定量には四重極質量分析計を使用した。また、TPD測定後には、加圧水素下での水素化を行った後、再度のTPD測定を行うことで水素吸放出サイクル特性について検討した。

i) Li-N/グラファイト複合材料

金属Liの液化 NH_3 溶液にグラファイトを含ませることで、10wt%のLiをグラファイト層間に導入した。これに、 H_2 気流中673 K、6h、He気流中673 K、1hの加熱処理を行うことでグラファイト担持窒化リチウム(Li-N/graphite)とした。得られた試料は、3MPaの H_2 下523 K、2hで水素化した。

ii) Li/フラーレン C_{60} 複合材料

加熱排気処理したフラーレン C_{60} と液体アンモニアに溶解したLiを、195 Kで7h攪拌した後、室温排気でアンモニアの除去を行った。Liの導入量は10 wt%とした。得られた試料について、673 Kの水素気流中で6h、同温のヘリウム気流中で1hの加熱処理を行った後、3MPaの H_2 下523 K、2hで水素化した。

iii) LiH/ポリアセチレン(PA)複合材料

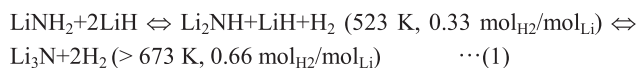
チタノセン触媒の存在下でアセチレンを重合して得たポリアセチレンと水素化リチウムを、 $\text{CH}:\text{LiH}=1:1$ のモル比となるように秤量し、アルゴン加圧下、遊星ボールミル装置を用いて4.5 hミリングした。水素化は、3MPaの H_2 下523 K、12hで行った。

3. 結果と考察

3.1. Li-N/グラファイト複合材料

液体アンモニア中で調製したグラファイトとリチウムの複合体Li-N/graphiteは、3 MPa、523 Kという実用的な雰囲気下で水素化が可能であり、可逆的な水素吸放出特性を示した⁵⁾。⁷Li MAS NMR及びXRDにより検討したところ、調製直後のLi-N/graphite上には Li_3N が生成していることが分かった。Li-N/graphiteの調製時には、金属Liの溶媒として使用したアンモニアを室温下で留去する過程が含まれるが、この際に水素の生成が確認された。したがって、このアンモニア留去の過程で金属Liとアンモニアが反応し、 LiNH_2 と水素が生成したと考えられる。さらに、 LiNH_2 は加熱によりアンモニアを脱離し Li_3N を生成することが知られており、Li-N/graphiteにおいても調製後の加熱処理の過程で同様の反応が進行し、 Li_3N が生成したものと推定さ

れる. Li_3N は, Chen らによって水素吸蔵体として機能することが報告されており, 水素吸蔵後に生成する LiNH_2 と LiH の混合物は, (1)式に示す二段階の反応で可逆的に水素を吸放出することが明らかにされている⁴⁾. したがって, グラファイト上に担持した Li_3N からなる Li-N/graphite も, 同様の機構で可逆的な水素吸放出材料として機能することが期待された.



3 MPa, 523 K で2時間の水素化を行った Li-N/graphite の水素放出特性を TPD により検討したところ, 室温から 673 K までで 1.64 wt% に相当する単一の水素放出ピークが観測された. この水素放出量は, Li 原子当りに換算すると 0.62 $\text{mol}_{\text{H}_2}/\text{mol}_{\text{Li}}$ となり, (1)式の反応が二段階目まで完全に進行した際の 93% に相当する値である. グラファイト担体非存在下で(1)式の二段階目の反応を進行させるためには 673 K 以上の高温が必要とされることから, グラファイト担体の存在により水素放出が低温化していることがわかる. そこで, より低温で LiNH_2 と LiH の物理混合物(モル比 1:2)と Li-N/graphite の水素放出特性を比較した. Li-N/graphite は室温から 523 K までの昇温で(1)式の一段階目の放出量を上回る 0.50 $\text{mol}_{\text{H}_2}/\text{mol}_{\text{Li}}$ の水素を放出したのに対し, LiNH_2 と LiH の物理混合物の水素放出量は(1)式の一段階目と同程度の 0.29 $\text{mol}_{\text{H}_2}/\text{mol}_{\text{Li}}$ であった(Fig. 1). また, Li-N/graphite は物理混合物の約 3 倍程度の水素放出速度を示した. 523 K での水素放出後の試料を ^7Li 固体 NMR で分析したところ,

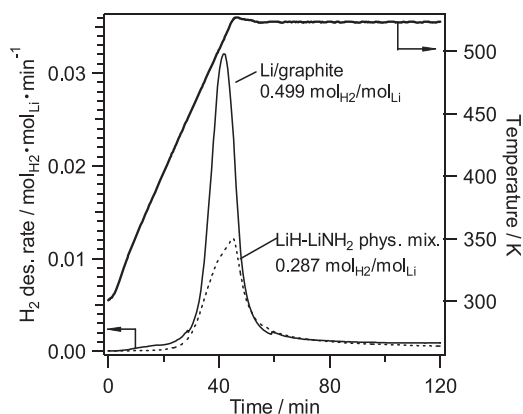


Fig. 1 H_2 -TPD profiles for Li-N/graphite and physical mixture of LiH-LiNH_2 .

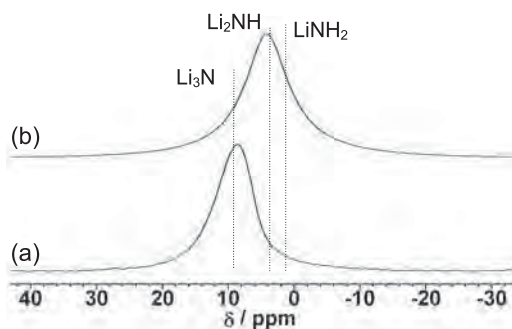


Fig. 2 ^7Li MAS NMR spectra of (a) 10wt% Li-N/graphite and (b) LiH-LiNH_2 physical mixture after hydrogen desorption at 523 K and 673 K, respectively.

物理混合物では 4.19 ppm に Li_3NH のシグナルが観測されたのに対し, Li-N/graphite では 7.96 ppm に Li_3N のシグナルが観測された(Fig. 2). したがって, グラファイト担体の存在により, 担体のない場合に比べてより低温で Li_3N が生成し, Li 当たりの水素放出量と水素放出速度も向上させることに成功した. 現在のところ, (i) LiC_6 等の Li-グラファイト 層間化合物の形成に伴いグラファイト層間に原子レベルで分散した Li がアンモニアと反応した結果, ナノスケールの微細な水素吸放出活性 Li 種 (LiNH_2 , LiH , Li_3N) が生成した, (ii) 水素吸放出に伴う Li-H , Li-N 結合の解離, 生成時の反応中間体が共役構造を持ったグラファイト層との電子の授受により安定化された, という二つの要因によりグラファイト担体が水素放出を促進したと考えている.

3.2. Li/フラーレン C_{60} 複合材料

グラファイト以外の炭素材料についても液体アンモニアを用いたアルカリ金属との複合化を行ったところ, フラーレン C_{60} と Li の複合体も可逆的な水素吸放出能を示した. 従来, NaBH_4 にフラーレンを添加することで, 水素吸放出特性が向上する例は報告されているもの⁷⁾, フラーレンそのものが直接的に水素吸蔵体として機能する例は本研究が初めての例である⁹⁾.

水素化した Li/C_{60} 複合体の TPD 測定では, 557 K に単一の水素放出ピークが観測され, 623 K までの水素放出量は 2.59 wt% (Li 当たり 0.97 $\text{mol}_{\text{H}_2}/\text{mol}_{\text{Li}}$) に達した(Fig. 3). Fig. 4 に各状態における ^{13}C および ^7Li 固体 NMR スペクトルを示す. 水素化後の試料では C_{60}H_n と LiH , 水素放出後では Li_nC_{60} の生成が示唆された. さらに, XRD においても水素

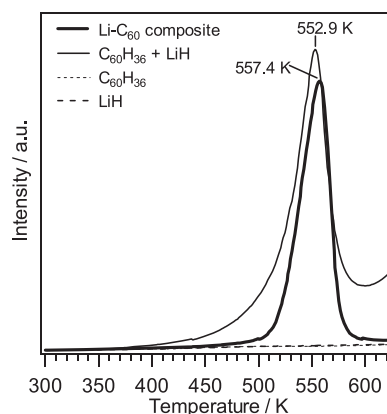


Fig. 3 Hydrogen release profiles up to 623 K for the lithium- C_{60} composite, the physically mixed sample of $\text{C}_{60}\text{H}_{36}$ and LiH (molar ratio, 1:36), LiH and $\text{C}_{60}\text{H}_{36}$ alone.

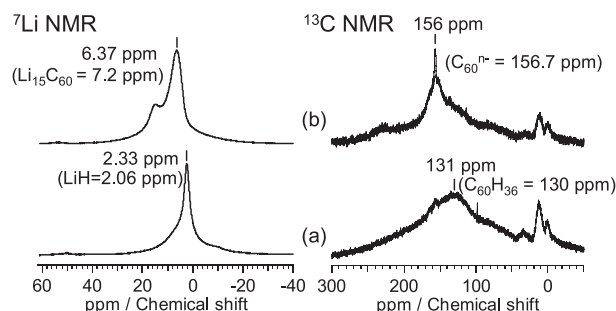


Fig. 4 ^7Li and ^{13}C MAS NMR spectra of lithium- C_{60} composite (a) after hydrogenation and (b) after hydrogen release.

化後試料で LiH 由来のピークが観測され、水素放出によりこのピークは消失した。これらの結果から、 Li_nC_{60} 上での水素吸放出過程は (2) 式で表されるものと推測した。水素放出量が $0.97 \text{ mol}_{\text{H}_2}/\text{mol}_{\text{Li}}$ であり、 H_2 と Li の比がほぼ 1:1 であることも (2) 式の進行を示唆する結果である。この過程では、分子状水素は C_{60} に結合したプロトンと Li^+ に結合したヒドリドとして吸蔵されていると考えられる。なお、水素吸蔵状態に相当する $\text{C}_{60}\text{H}_{36}$ と LiH の混合物を昇温したところ、水素化した Li-C_{60} 複合体とほぼ同様の温度での水素放出が観測されたことより、(2)式に基づいて水素吸放出が進行することが裏付けられた(Fig. 3)。



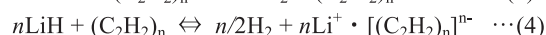
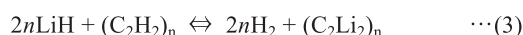
C_{60} と Li の複合体について TPD 測定と水素化を繰り返し、サイクル特性を検討したところ、10 サイクル目においても 1 サイクル目の 76% の水素を放出し、水素放出のピーク温度も大幅に変化せず、良好な特性を示した。このように、サイクルを重ねても (1) 式に基づく水素吸放出が可逆的に進行することが明らかになった。本材料においては、水素放出時に電子を受容することで Li 種を安定化し、水素吸蔵時には自身が水素と結合するという、フラーレンの特異な物性が、 Li-N/graphite とは異なる機構で水素を吸放出し、高い水素吸蔵量を示す上での鍵となっていると考えられる。

3.3. LiH/ポリアセチレン(PA)複合材料

我々は、フラーレンに引き続き、共役構造を有する化合物と金属水素化物からなる水素吸放出材料を探索したところ、ポリアセチレンと水素化リチウムの複合体が新たな水素吸蔵材料となることを見出した。Fig. 5 にポリアセチレンのみ、ボールミリングにより調製した水素化リチウム-ポリアセチレン複合体(LiH-PA)、水素化リチウムのみでの 823 K までの TPD 測定結果を示す。LiH-PA では、450 K 付近から水素由来する $m/z = 2$ の信号強度が増大したが、 $m/z = 16, 28$ 等の水素以外に由来するシグナルはほとんど観測されなかった。水素の放出量は 7.77 wt% に達した。一方、ポリアセチレンのみでは 723 K 以降において $m/z = 2$ と同時に $m/z = 16, 28$ の信号強度が増大した。これは、ポリアセチレンが熱分解し、水素と同時にメタンやエチレンが生成した結果である。なお、水素化リチウムのみでは水素放出はほぼ観測されなかった。これらの結果より、水素化リチウムとポリアセチレンを複合化することで、それぞれが単独の場合に比べてより低温で多量の水素が生成することが明らかとなった。そこで、LiH-PA における可逆的水素吸放出について検討を行った。様々な温度で水素放出を試みたところ、水素放出温度を 573 K とした場合、1 サイクル目に 2.71 wt% の水素放出が観測され、その後、サイクルを重ねても水素放出量はほとんど低下しなかったことから、可逆的な水素吸放出材料として機能することが明らかとなった。なお、623 K で水素放出を行った場合、1 サイクル目の水素放出量は 5.29 wt% と大幅に増大するものの、その後のサイクルではほとんど水素吸放出能を示さなかった。

LiH-PA において推定される水素吸放出機構は、以下の 2 通りである。(3)式は LiH とポリアセチレン鎖の水素原子

から水素分子が生成する反応であり、(4)式は LiH の H^- の電子がポリアセチレンに移動することにより水素分子が生成する反応である。



上記のいずれの機構で水素吸放出が進行するかを検討するため、重水素化したポリアセチレン(C_2D_2) $_n$ と LiH を $\text{CD:LiH} = 1:1$ で複合化した試料の水素放出を行った。(3)式では HD, (4)式では H_2 が主生成物になると推測される。573 K で生成した水素の同位体比は $\text{H}_2:\text{HD}:\text{D}_2 = 63:31:6$ となったことから、主に(4)式の機構で水素が放出されることが明らかとなった。LiH-PA 試料のラマン分光測定より、水素放出前後でポリアセチレン鎖の構造に大きな変化がないことが確認された。また、水素放出後では電荷移動に伴うバンドのシフトが観測された。このように、ラマン分光法からも LiH-PA における水素吸放出機構が(4)式の機構で進行することを示唆する結果が得られた。ポリアセチレンの共役系が電子受容体として機能しヒドリドの電子を受容するだけでなく、電子を受容したポリアセチレンがリチウムカチオンとの相互作用により安定化されることが、本機構で水素放出が進行する上でのドライビングフォースであると考えられる。

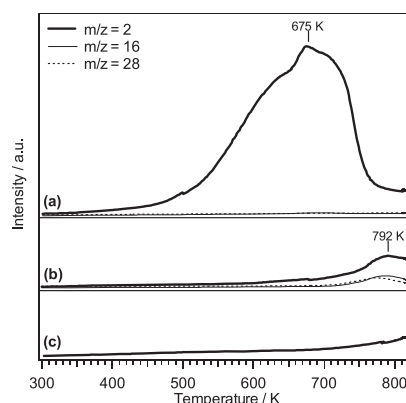


Fig. 5 TPD profiles up to 823 K for (a) PA-LiH composite, (b) polyacetylene, and (c) LiH.

文 献

- 1) 例えば Z. Zou, J. He, K. Sayama, H. Arakawa, *Nature*, **414**, 625 (2001)
- 2) 例えば R. D. Cortright, R. R. Davda, J. A. Dumesic, *Nature*, **418**, 964 (2002)
- 3) V. Sit, R. A. Geanangel, W. W. Wendlandt, *Thermochim. Acta*, **113**, 379 (1987)
- 4) P. Chen, Z. T. Xiong, J. Luo, J. Lin, K. L. Tan, *Nature*, **420**, 302 (2002)
- 5) A. Yoshida, H. Yoshimura, T. Terada, Y. Nakayama, H. Kuno, T. Miyao, S. Naito, *Int. J. Hydrogen Energy*, **36**, 6751 (2011)
- 6) A. Yoshida, T. Okuyama, T. Terada, S. Naito, *J. Mater. Chem.*, **21**, 9480 (2011)
- 7) M. S. Wellons, P. A. Berseth, R. Zidan, *Nanotechnology*, **20**, 204022 (2009)



Reaction products of titanium(IV) sulfate with the two, dimeric precursors, 1,2,3-tri-titanium(IV)- and 1,2-di-titanium(IV)-substituted α -Keggin polyoxometalates (POMs), under acidic conditions. A tetra-titanium(IV) oxide cluster and one coordinated sulfate ion grafted on a di-lacunary Keggin POM

Kenji Nomiya*, Yuki Mouri, Yoshitaka Sakai, Satoshi Matsunaga

Department of Chemistry (formerly Department of Materials Science), Faculty of Science, Kanagawa University, Hiratsuka, Kanagawa 259-1293, Japan

ARTICLE INFO

Article history:

Received 25 November 2011

Accepted 21 January 2012

Available online 31 January 2012

Keywords:

Polyoxometalate

Titanium

Cluster

X-ray structure analysis

ABSTRACT

A novel, monomeric species containing a tetra-titanium(IV) oxide cluster and one coordinated sulfate ion grafted on a di-lacunary Keggin polyoxometalate (POM), $[[\{Ti(H_2O)_3\}_2\{Ti(H_2O)_2\}_2(\mu-O)_3(SO_4)](PW_{10}O_{37})]^-$ **1**, was derived from reactions of $Ti(SO_4)_2$ with two precursors, i.e., $[(\alpha-1,2-PW_{10}Ti_2O_{38})_2O_2]^{10-}$ **2** and $[(\alpha-1,2,3-PW_9Ti_3O_{37})_2O_3]^{12-}$ **3**, under strongly acidic conditions. [Note: the potassium salts of POMs **1–3** are represented as **K1** to **K3**, respectively.] The potassium salt of **1**, which was stable in the solid state, but unstable in water, was unequivocally characterized by complete elemental analysis, TG/DTA, FTIR, X-ray crystallography, and solid-state ^{31}P CP-MAS and solution ^{31}P NMR spectroscopy. Both precursors have been considered as relatively stable forms of titanium(IV)-substituted Keggin POMs. A deposit of crystals from the reaction system consisting of precursor **3**, $Ti(SO_4)_2$, and a strong acid (HCl, HNO_3 , or H_2SO_4) was significantly affected by the conjugate base of the acid, while crystallization from the reaction using precursor **2** was not affected by the base. The Ti_4 center in **1** belongs to a class of a 2-host (di-lacunary site)/4-guest (four Ti atoms) coordination relationship, or a combination of two sets of a 1-host/2-guest coordination.

© 2012 Elsevier B.V. All rights reserved.

Polyoxometalates (POMs) are molecular metal-oxide clusters, which have attracted considerable attention in the fields of catalysis, medicine, surface science and materials science, since POMs are often considered as molecular analogues of metal oxides in terms of structural analogy [1–20]. In the synthesis, structure and behavior in the solid state and in solution of Group IV metal ion (Ti, Zr and Hf)-containing POMs, it has been elucidated that Zr/Hf atoms are very similar to each other, but quite different from Ti atom [20]. Site-selective substitution of W^{VI} atoms in POMs with Ti^{IV} atoms is particularly interesting, because of the formation of multicenter active sites with corner- or edge-sharing TiO_6 octahedra and also the generation of oligomeric species through Ti–O–Ti bonds [21–30]. A number of catalytic reactions of titanium(IV)-containing POMs has also been reported so far [7,13,31,32]. One of the aspects specific to titanium(IV)-substituted POMs is the host-guest relationship observed between the titanium(IV) atom (guest) and the lacunary site (host) of Keggin POMs. Although the relationship is not necessarily based on non-covalent interaction, the use of the term of host-guest is

convenient and useful in classifying and understanding the structures in the myriad titanium(IV)-substituted POMs [33–35].

The ionic radius of Ti^{IV} (0.75 Å) is close to that of W^{VI} (0.74 Å), suggesting that Ti^{IV} should fit nicely into the POM framework. However, there is a significant consequence in terms of oligomeric Ti–O–Ti anhydride formation resulting from substitution with several titanium(IV) atoms. For instance, tri-titanium(IV)-1,2,3- and di-titanium(IV)-1,2-substituted Keggin POMs heretofore reported have been isolated as dimeric, Ti–O–Ti-bridged anhydride forms, e.g., $[(\alpha-1,2-PW_{10}Ti_2O_{38})_2O_2]^{10-}$ **2** [24] and $[(\alpha-1,2,3-PW_9Ti_3O_{37})_2O_3]^{12-}$ **3** [25].

The dimeric species, **2** [24], of a di-titanium(IV)-substituted α -Keggin POM and the dimeric species, **3** [25], of a tri-titanium(IV)-substituted α -Keggin POM have been considered as relatively stable forms of titanium(IV)-substituted Keggin POMs. However, it has recently been found that **3** further reacts with $Ti(SO_4)_2$ to give richer titanium(IV)-containing POMs, such as the dimeric species of a tetra-titanium(IV)-substituted α -Keggin POM $[[\{Ti(H_2O)_3\}_2(\mu-O)](\alpha-PW_9Ti_2O_{38})]_2^{6-}$, **4**, and a monomeric species containing a tetra-titanium(IV) oxide cluster and two coordinated sulfate ions grafted on a tri-lacunary Keggin POM $[[Ti_4(\mu-O)_3(SO_4)_2(H_2O)_8](\alpha-PW_9O_{34})]^{3-}$, **5**, both under HCl-acid conditions [35].

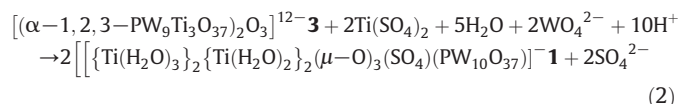
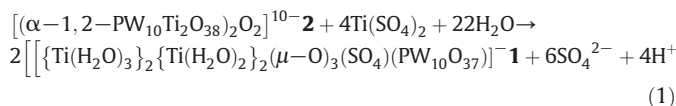
In this work, to further extend the reactions of the dimeric, titanium(IV)-substituted Keggin POM precursors, we have carefully investigated

* Corresponding author. Tel.: +81 463 59 4111; fax: +81 463 58 9684.
E-mail address: nomiya@kanagawa-u.ac.jp (K. Nomiya).

the reaction products under strongly acidic conditions of $\text{Ti}(\text{SO}_4)_2 \cdot 4\text{H}_2\text{O}$ with the two dimeric precursors, **2** and **3**. From the two precursors, a novel, monomeric species containing a tetra-titanium(IV) oxide cluster and one coordinated sulfate ion grafted on a di-lacunary Keggin POM $[\{\{\text{Ti}(\text{H}_2\text{O})_3\}_2\{\text{Ti}(\text{H}_2\text{O})_2\}_2(\mu\text{-O})_3(\text{SO}_4)\}(\text{PW}_{10}\text{O}_{37})]^-$, **1**, was obtained as an analytically pure potassium salt, which was stable in the solid state but unstable in water. The 2-host/4-guest relationship of the Ti_4 center in **1** was in contrast to the 3-host/4-guest relationship of the Ti_4 center in **5** [35]. It should also be noted that a deposit of crystals from the reaction system consisting of **3**, $\text{Ti}(\text{SO}_4)_2$, and strong acid (HCl, HNO_3 , or H_2SO_4) was significantly affected by the conjugate base.

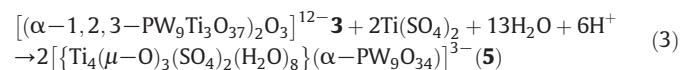
The formula and composition of the monomeric species of a tetra-titanium(IV) oxide cluster and one sulfate ion grafted on the di-lacunary Keggin POM were determined as $\text{K}[\{\{\text{Ti}(\text{H}_2\text{O})_3\}_2\{\text{Ti}(\text{H}_2\text{O})_2\}_2(\mu\text{-O})_3(\text{SO}_4)\}(\text{PW}_{10}\text{O}_{37})] \cdot n\text{H}_2\text{O}$ ($n = 2\text{--}9$) (**K1**) based on complete elemental analysis, TG/DTA, FTIR, X-ray crystallography and solid-state ^{31}P CPMAS NMR spectroscopy. **K1** in analytically pure form was obtained by a reaction of precursor **K2** with $\text{Ti}(\text{SO}_4)_2 \cdot 4\text{H}_2\text{O}$ in a 1 M aqueous HCl solution [36], and also obtained by a reaction of **K3** with $\text{Ti}(\text{SO}_4)_2 \cdot 4\text{H}_2\text{O}$ in a 1 M aqueous HNO_3 solution [37]. A synthetic route of POM **1** from POMs **2** and **3** is shown by arrows of full lines in Fig. 1.

The formation of POM **1** can be represented in Eqs. (1) and (2).



It should be noted that $[\{\{\text{Ti}_4(\mu\text{-O})_3(\text{SO}_4)_2(\text{H}_2\text{O})_8\}(\alpha\text{-PW}_9\text{O}_{34})\}^3]^-$, **5**, was formed by a reaction of precursor **3** with $\text{Ti}(\text{SO}_4)_2$ in a 1 M aqueous HCl solution (Eq. (3)) and its crystals were deposited

under a 1 M aqueous HCl [35]. Formation of **1** or **5** from precursor **3** depends on only the acidic solvents i.e., aqueous HNO_3 or aqueous HCl (Fig. 1).



A deposit of crystals of **K1** from the reaction system consisting of precursor **3**, $\text{Ti}(\text{SO}_4)_2$ and a strong acid (HCl, HNO_3 , or H_2SO_4) was significantly affected by the conjugate bases Cl^- , NO_3^- and SO_4^{2-} ; crystals of **K1** were deposited under 1 M aqueous HNO_3 , but no crystals formed under 1 M aqueous H_2SO_4 . On the other hand, crystal formation of **K1** from the reaction of **2** was not affected by the conjugate bases.

The solid FT-IR spectra, measured on KBr disks of **K1** and the two precursors, **K2** and **K3**, showed the characteristic vibrational bands of the Keggin-type “ $\text{PW}_{12}\text{O}_{40}$ ” polyoxotungstate framework [38]. IR spectra of the two POMs obtained from the two precursors were identical and thus the frameworks of the both POMs were the same. This was also confirmed by X-ray crystallography [39]. In the FT-IR spectra of the two precursors, **K2** and **K3**, the bands based on the Ti–O–Ti vibration between the two Keggin units were observed at 698 and 718 cm^{-1} , respectively, suggesting that they are dimeric species, while in the spectrum of **K1** no Ti–O–Ti vibrational band was observed, suggesting that it is a monomeric species. [Note: the Ti–O–Ti bands between the two Keggin units have been previously reported at 721 cm^{-1} [24] and 731 cm^{-1} [25], respectively.] In the spectrum of **K1**, the bands due to the one coordinated sulfate ion were observed at 1214 and 1100 cm^{-1} , which can be compared with those of the monomeric POM **K5** having two coordinated sulfate ions at 1232, 1200 and 1128 cm^{-1} .

The solid-state ^{31}P CPMAS NMR spectrum of the monomeric POM **K1** showed a single broad signal at -10.8 (the sample obtained from **K2** (Fig. S1)) and -10.4 ppm (the sample obtained from **K3** (Fig. S2)),

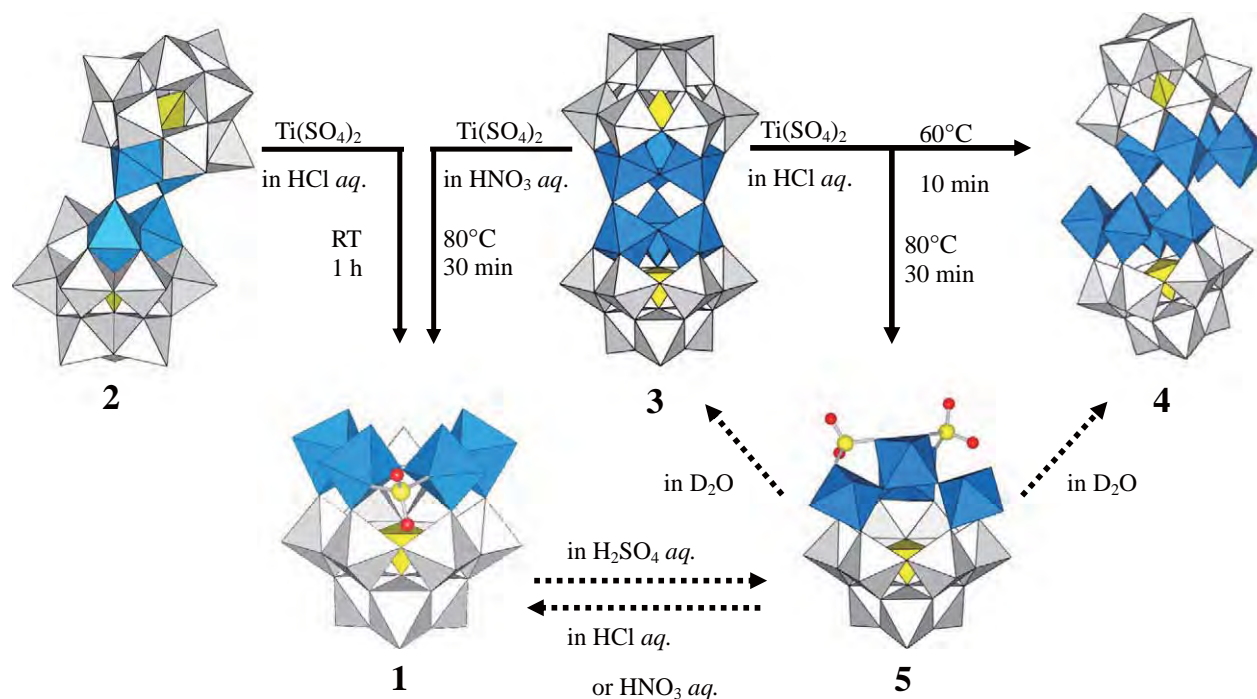


Fig. 1. A synthetic route showing the relation among POMs, **1**, **4** and **5** derived from the two POM precursors, **2** and **3**, is exhibited by arrows of full lines. Behaviors of **1** and **5** in solution are shown by arrows of broken lines. As to colors in polyhedral representations of POMs, the octahedral TiO_6 units are shown in blue, all WO_6 octahedra are shown in gray, and the one central PO_4 group is shown in yellow. Each sulfate ion, bridged between the two titanium(IV) octahedra, is shown by a yellow circle (S atom) and two red circles (O atom).

which can be compared with that of the monomeric POM **K5** at -14.43 ppm and that of the dimeric precursor, **K3**, at -10.64 ppm [35]. These data should correspond to the solid-state structures determined by X-ray crystallography.

K1 was stable in the solid state, but unstable in water and readily decomposed (Fig. S3(a)). POM **1** slowly decomposed in 0.5 M H_2SO_4 aqueous solution to give **5** as one of major species, one week later after dissolving (Fig. S3(b) and (c)). One week later after dissolving in 1 M HCl or 1 M HNO_3 aqueous solution, POM **1** gave major peaks at around -11.1 ppm and minor peaks at around -11.5 ppm (Fig. S3(d) and (e)), and these spectra were not essentially changed even three weeks later [36,37].

POM **5** showed almost unchanged ^{31}P NMR spectra at around -15.0 ppm in 0.5 M H_2SO_4 aqueous solution (Fig. S4(a)) even three weeks later, but in other solutions it gave the ^{31}P NMR spectra containing several minor peaks, in addition to the major peak at around -15.0 ppm, in a couple of days later after dissolving [35]: POM **5** dissolved in D_2O showed the minor peaks due to **4** and **3** at -9.74 and -10.45 ppm, respectively (Fig. S4(c)), and POM **5** dissolved in HCl or HNO_3 aqueous solution showed the minor peaks (probably due to **1** in solution) at -11.13 and -11.03 ppm, respectively (Fig. S4(d) and (e)). In Fig. 1, behaviors of **1** and **5** in solution are shown by arrows of broken lines.

From the reaction system in the absence of SO_4^{2-} ions, i.e., the reaction using *in situ*-generated “ $\text{Ti}(\text{NO}_3)_4$ ”, a POM without coordinated sulfate ions, such as “[$\{\{\text{Ti}(\text{H}_2\text{O})_{3-n}(\text{OH})_n\}_4(\mu\text{-O})_3\}(\alpha\text{-PW}_{10}\text{O}_{37})\}^{-(4n-1)}$ ” ($n=0-3$), was formed, which showed a ^{31}P NMR signal in acidic solution at -11.15 ppm, but it did not crystallize (see Supplementary material). The ^{31}P NMR spectrum of the reaction solution after 1 h stirring, which showed major peaks at -11.07 , -11.10 ppm and a minor peak at -11.51 ppm (Fig. S5(a)), was very similar to those of **1** one week later after dissolving in 1 M HCl or 1 M HNO_3 aqueous solution (Fig. S3(d) and (e)). Probably, coordination of the SO_4^{2-} ion is necessary only for crystallization of the solid. On the other hand, coordination of other bases such as NO_3^- and Cl^- and subsequent crystallization were not realized.

The molecular structure of polyoxoanion **1** in **K1** are shown in Fig. 2. The molecular structure of **1** in the crystals obtained from the precursors **K2** and **K3** was the same. The presented data are of the crystals obtained from **K2** [39] (also see Supplementary material). Selected bond lengths (Å) and angles ($^\circ$) around the Ti_4 centers (Table S1), other bond lengths (Å) and angles ($^\circ$) (Table S2) and the bond valence sum (BVS) calculations of the W, Ti, S, P and O atoms in **1** are deposited in Supplementary material (Table S3).

The composition and formula of **K1** containing one potassium counterion and nine hydrated water molecules were determined by complete elemental analysis and TG/DTA analysis [36]. In X-ray crystallography, POM **1**, one potassium cation, and the oxygen atoms due to 10 coordinated water molecules and three $\mu\text{-O}$ atoms, per formula unit, were identified in the crystal structure, but the location of nine hydrated water molecules, per formula unit, was not determined as a result of disorder.

The molecular structure of **1** is a monomeric POM composed of a Ti_4 cluster and one coordinated sulfate ion constructed on a di-lacunary Keggin unit. Regardless of the coordination of the sulfate ion, the arrangement of the Ti_4 cluster can be considered as a type of host-guest relation, i.e., a 2-host (di-lacunary site)/4-guest (four Ti octahedra) coordination, or a combination of two sets of a 1-host/2-guest coordination. One sulfate ion is bridged between the terminal positions of two Ti octahedra (Fig. 2(b) and (c)). In total, 10 coordinating water molecules in **1** are shown as open circles in Fig. 2(b) and (c). Thus, the whole symmetry of this molecule is approximately exhibited by point group C_s .

Ti–O–Ti bonds and angles in the Ti_4 center supported on the di-lacunary Keggin POM in **1** can be compared with those of the Ti_4 center supported on the tri-lacunary Keggin POM unit in **5** [35], and also

with those of the Ti_4 center accompanied by 4 oxalato ligands supported on the di-lacunary Keggin POM unit in [$\{\{\text{Ti}(\text{ox})(\text{H}_2\text{O})_4(\mu\text{-O})_3\}(\alpha\text{-PW}_{10}\text{O}_{37})\}^{7-}$ ($\text{H}_2\text{ox} = \text{oxalic acid}$) **6** [33].

The Ti–O–Ti skeleton constructed on the di-lacunary Keggin POM in **1** without the ox^{2-} ligands and with the sulfate ligand was very similar to that in **6** without the sulfate ligand and with the ox^{2-} ligands [33]. Three Ti–O–Ti angles ($\text{Ti}_4\text{-O}_3\text{Y-Ti}_2$ 148.9° , $\text{Ti}_2\text{-O}_1\text{Y-Ti}_1$ 147.9° , and $\text{Ti}_1\text{-O}_2\text{Y-Ti}_3$ 147.5°) in **1** are approximately equal, which are not affected by sulfate coordination, whereas in **6**, three Ti–O–Ti angles are different from each other (124.9° , 141.0° and 176.5°). All of the O–Ti–O angles in **1** and **6** are almost equal, i.e., about 100° . The two Ti octahedra (Ti_3 and Ti_4 , equivalent to each other) in **1** are coordinated by three water molecules, and the other two Ti octahedra (Ti_1 and Ti_2 , equivalent to each other) are coordinated by two water molecules and one bridging sulfate ion. On the other hand, each of the four Ti octahedra in **6** has one chelating ox^{2-} ligand and one water oxygen atom. In **5**, composed of four Ti octahedra constructed on a tri-lacunary Keggin POM, the central Ti octahedron does not directly link to any WO_6 octahedra, but connects to three Ti octahedra by corner-sharing. In **5**, the two sulfate ions are bridged between Ti_2 and Ti_4 octahedra and between Ti_1 and Ti_4 octahedra, respectively.

Although the Ti–O–Ti skeleton constructed in **1** is very similar to that in **6**, their stability in solution is considerably different. The instability of **1** in solution and the stability of **6** in acidic media may be attributed to the presence of the ox^{2-} ligand and the unfavorable coordination of the sulfate ion in solution.

The bond valence sum (BVS) calculations [40,41] (Table S3), based on the observed bond lengths, suggest that the 10 doubly protonated oxygen atoms (O1W-O10W : $0.389\text{--}0.517$) are due to water molecules, and that all atoms (W1-W10 , $\text{Ti}_1\text{-Ti}_4$, P1, S1 and O1-O37) maintain formal valences (W^{6+} , Ti^{4+} , P^{5+} , S^{6+} and O^{2-}). No protonation was confirmed in the bridging oxygen atoms in Ti–O–Ti bonds (O1Y-O3Y), i.e., O^{2-} . The BVS of the oxygen atoms bonded to the sulfur atom (O1X-O4X : $1.482\text{--}1.940$) suggest a formal valence O^{2-} , i.e., no protonation of the sulfate ion.

In summary, several titanium(IV)-substituted Keggin POMs such as **K2** and **K3**, but not lacunary Keggin POMs, were used as precursors and the novel titanium(IV)-substituted species, **K1**, was derived under acidic conditions. Precursor **K3** has given so far titanium(IV)-substituted POMs such as **K4** and **K5**, depending upon the conditions [35] (Fig. 1). The present work shows that **K3** gives the novel titanium(IV)-substituted POM, **K1**, under different conditions. Thus, **K3** is found to be a versatile precursor. **K2** has given **K6** by a reaction with an anionic Ti(IV) complex, $[\text{TiO}(\text{ox})_2]^{2-}$ [33]. The present work also shows that **K2** gives **K1** by a reaction with $\text{Ti}(\text{SO}_4)_2$ in an HCl aq. solution. The framework of **K1** with the coordinated SO_4^{2-} ion was similar to that of **K6** with coordinated ox^{2-} ions. From the viewpoint of the host-guest chemistry of Ti-substitution in POMs, the Ti_4 center in **1** comprised a new type of host-guest relation, i.e., 2-host/4-guest coordination. The polyoxoanions containing rich titanium(IV) atoms in the lacunary sites of POM are also of interest as possible solid oxidation catalysts [31,32]. Studies in this direction are in progress.

Acknowledgments

This work was supported by a Grant-in-Aid for Scientific Research (C) No. 22550065 from the Ministry of Education, Culture, Sports, Science and Technology, Japan.

Appendix A. Supplementary data

Further details on the crystal structure investigation may be obtained from the Fachinformationszentrum Karlsruhe, 76344 Eggenstein-Leopoldshafen, Germany (fax: (+49)7247-808-666); e-mail crysdata@fiz-karlsruhe.de, on quoting the depository numbers.

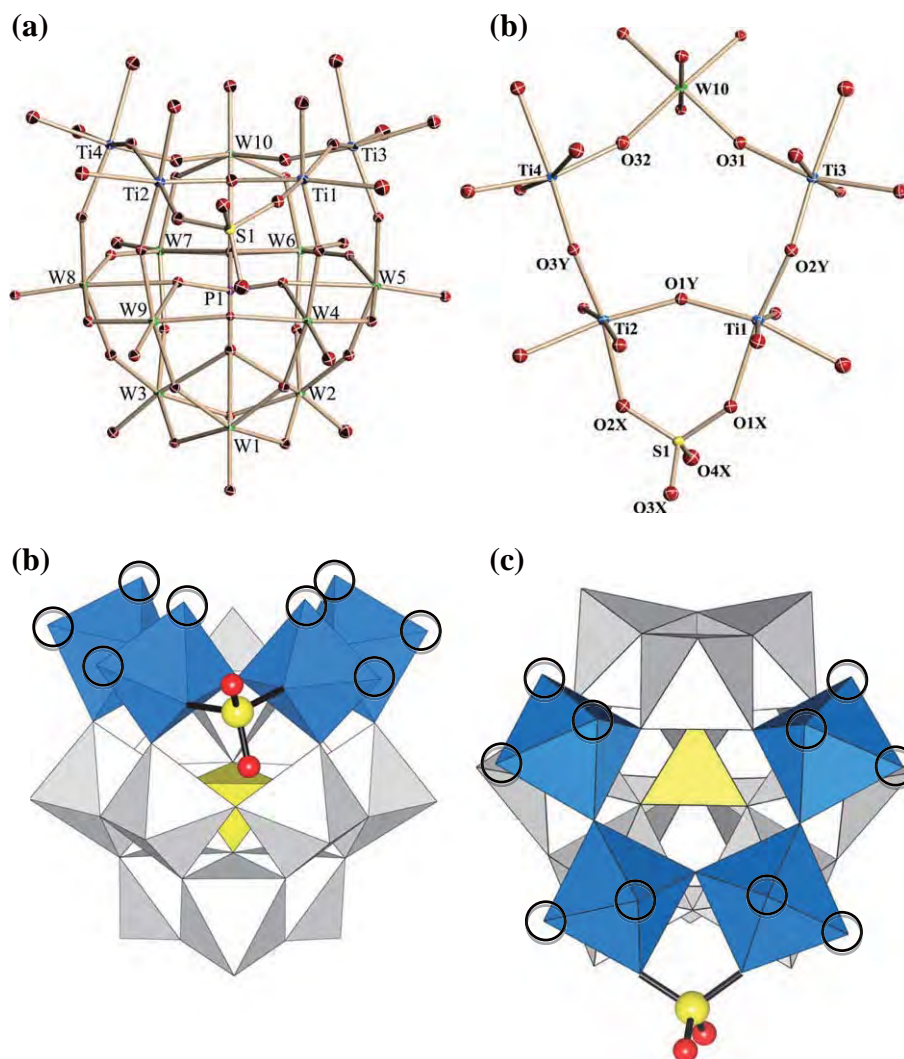


Fig. 2. (a) Molecular structure of monomeric polyoxoanion $[[\{Ti(H_2O)_3\}_2\{Ti(H_2O)_2\}_2(\mu-O)_3(SO_4)](PW_{10}O_{37})]$ (**1**) in **K1**, polyhedral representations ((b) side view and (c) top view), and (d) partial structure around the Ti_4 center. In (b) and (c), the water molecules coordinated to the titanium(IV) octahedra are exhibited as open circles.

CSD reference number 422826 (formula/code: ym005) for **K1**. Supplementary data: General methods, X-ray crystallography, control experiments, the solid-state ^{31}P CPMAS NMR spectra of **K1** (Fig. S1 and S2), the solution ^{31}P NMR spectra of **1** (Fig. S3), **5** (Fig. S4) and the reaction solution of **1** under SO_4^{2-} -free conditions (Fig. S5), selected bond lengths (\AA) and angles ($^\circ$) around the Ti_4 centers for **1** (Table S1), other bond lengths (\AA) and angles ($^\circ$) for **1** (Table S2) and bond valence sum (BVS) calculations of W, Ti, S, P and O atoms for **1** (Table S3) associated with this article can be found in the online version at [doi:10.1016/j.inoche.2012.01.017](https://doi.org/10.1016/j.inoche.2012.01.017).

References

- [1] M.T. Pope, A. Müller, *Angew. Chem. Int. Ed. Engl.* 30 (1991) 34.
- [2] M.T. Pope, *Heteropoly and Isopoly Oxometalates*, Springer-Verlag, New York, 1983.
- [3] V.W. Day, W.G. Klemperer, *Science* 228 (1985) 533.
- [4] C.L. Hill (Ed.), *Chem. Rev.* 98 (1998) 1.
- [5] T. Okuhara, N. Mizuno, M. Misono, *Adv. Catal.* 41 (1996) 113.
- [6] C.L. Hill, C.M. Prosser-McCarthy, *Coord. Chem. Rev.* 143 (1995) 407.
- [7] C.L. Hill (Ed.), *J. Mol. Catal. A: Chem.* 114 (1996) 1.A series of 34 papers in a volume devoted to polyoxoanions in catalysis.
- [8] R. Neumann, *Prog. Inorg. Chem.* 47 (1998) 317.
- [9] M.T. Pope, A. Müller (Eds.), *Polyoxometalate Chemistry from Topology via Self-Assembly to Applications*, Kluwer Academic Publishers, Netherlands, 2001.
- [10] T. Yamase, M.T. Pope (Eds.), *Polyoxometalate Chemistry for Nano-Composite Design*, Kluwer Academic Publishers, Netherlands, 2002.
- [11] M.T. Pope, *Polyoxo anions: synthesis and structure*, *Comprehensive Coordination Chemistry II*, Vol. 4, Elsevier Science, New York, 2004, p. 635.
- [12] C.L. Hill, *Polyoxometalates: Reactivity*, *Comprehensive Coordination Chemistry II*, Vol. 4, Elsevier Science, New York, 2004, p. 679.
- [13] C.L. Hill (Ed.), *J. Mol. Catal. A: Chem.* 262 (2007) 1.A series of 32 recent papers in a volume devoted to polyoxometalates in catalysis.
- [14] A. Proust, R. Thouvenot, P. Gouzerh, *Chem. Commun.* (2008) 1837.
- [15] B. Hasenknopf, K. Micoine, E. Lacôte, S. Thorimbert, M. Malacria, R. Thouvenot, *Eur. J. Inorg. Chem.* (2008) 5001.
- [16] D. Laurencin, R. Thouvenot, K. Boubekeur, F. Villain, R. Villanneau, M.-M. Rohmer, M. Benard, A. Proust, *Organometallics* 28 (2009) 3140.
- [17] D.-L. Long, R. Tsunashima, L. Cronin, *Angew. Chem. Int. Ed.* 49 (2010) 1736.
- [18] A. Dolbecq, E. Dumas, C.R. Mayer, P. Mialane, *Chem. Rev.* 110 (2010) 6009.
- [19] C.P. Pradeep, D.-L. Long, L. Cronin, *Dalton Trans.* 39 (2010) 9443.
- [20] K. Nomiya, Y. Sakai, S. Matsunaga, *Eur. J. Inorg. Chem.* (2011) 179.
- [21] Y. Lin, T.J.R. Weakley, B. Rapko, R.G. Finke, *Inorg. Chem.* 32 (1993) 5095.
- [22] T. Yamase, T. Ozeki, H. Sakamoto, S. Nishiyama, A. Yamamoto, *Bull. Chem. Soc. Jpn.* 66 (1993) 103.
- [23] T. Yamase, X.O. Cao, S. Yazaki, *J. Mol. Catal. A: Chem.* 262 (2007) 119.
- [24] K. Nomiya, M. Takahashi, J.A. Widegren, T. Aizawa, Y. Sakai, N.C. Kasuga, *J. Chem. Soc. Dalton Trans.* (2002) 3679.
- [25] K. Nomiya, M. Takahashi, K. Ohsawa, J.A. Widegren, *J. Chem. Soc. Dalton Trans.* (2001) 2872.
- [26] Y. Goto, K. Kamata, K. Yamaguchi, K. Uehara, S. Hikichi, N. Mizuno, *Inorg. Chem.* 45 (2006) 2347.
- [27] R.X. Tan, D.L. Li, H.B. Wu, C.L. Zhang, X.H. Wang, *Inorg. Chem. Commun.* 11 (2008) 835.

- [28] F. Hussain, B.S. Bassil, L.H. Bi, M. Reicke, U. Kortz, *Angew. Chem. Int. Ed.* 43 (2004) 3485.
- [29] G.A. Al-Kadamany, F. Hussain, S.S. Mal, M.H. Dickman, N. Leclerc-Larozne, J. Marrot, E. Cadot, U. Kortz, *Inorg. Chem.* 47 (2008) 8574.
- [30] Y.H. Ren, S.X. Liu, R.G. Cao, X.Y. Zhao, J.F. Cao, C.Y. Gao, *Inorg. Chem. Commun.* 11 (2008) 1320.
- [31] C.N. Kato, S. Negishi, K. Yoshida, K. Hayashi, K. Nomiya, *Appl. Catal. A* 292 (2005) 97.
- [32] C.N. Kato, K. Hayashi, S. Negishi, K. Nomiya, *J. Mol. Catal. A: Chem.* 262 (2007) 25.
- [33] K. Hayashi, H. Murakami, K. Nomiya, *Inorg. Chem.* 45 (2006) 8078.
- [34] K. Hayashi, M. Takahashi, K. Nomiya, *Dalton Trans.* (2005) 3751.
- [35] Y. Mouri, Y. Sakai, Y. Kobayashi, S. Yoshida, K. Nomiya, *Materials* 3 (2010) 503.
- [36] Synthesis of **K1** from precursor **K2**: $K_{10}[(\alpha-1,2-PW_{10}Ti_2O_{38})_2O_2] \cdot 18H_2O$, **K2**, (1.0 g, 0.16 mmol) was added to a clear colorless solution of $Ti(SO_4)_2 \cdot 4H_2O$ (0.22 g, 0.70 mmol) dissolved in a 1 M aqueous HCl solution (20 mL). The colorless clear solution was stirred for 1 h and was evaporated to a volume of ca. 10 mL with a rotary evaporator at 40 °C. The resulting white suspension was stored in a refrigerator at 4 °C overnight. The white precipitate formed was filtered off through a membrane filter (JG 0.2 μm). The clear filtrate was slowly evaporated at room temperature. After three weeks, clear colorless plate crystals formed, which were subjected to X-ray diffraction measurement. The remaining crystals were collected on a membrane filter (JG 0.2 μm) and dried in vacuo for 2 h. The colorless plate crystals obtained in 52.1% yield (0.53 g scale) were soluble in water but insoluble in most organic solvents. Stability in water was low; it decomposed within a few hours at room temperature to produce several unknown materials (Fig. S3(a)). Anal. {Found: H, 0.81; K, 1.30; O, 27.2; P, 1.03; S, 1.02; Ti, 6.23; W, 60.3; total 97.89%. Calc. for $H_{22}K_1O_{55}P_1S_1Ti_4W_{10}$ or $K[[Ti(H_2O)_3]_2[Ti(H_2O)_2]_2(\mu-O)_3(SO_4)](PW_{10}O_{37}) \cdot H_2O$: H, 0.73 ; K, 1.29; O, 29.00, P, 1.02; S, 1.06; Ti, 6.31; W, 60.59%}. A weight loss of 5.23% (weakly solvated or adsorbed water) was observed during the course of drying at room temperature at 10^{-3} – 10^{-4} torr overnight before analysis, suggesting the presence of 8 water molecules. TG/DTA under atmospheric conditions: a weight loss of 10.61% was observed at below 216.6 °C; calc. 10.77% for a total of 19 water molecules, i.e., 10 coordinated water molecules plus $x = 9$ hydrated water molecules in $K[[Ti(H_2O)_3]_2[Ti(H_2O)_2]_2(\mu-O)_3(SO_4)](PW_{10}O_{37}) \cdot xH_2O$. IR (KBr) (polyoxometalate region): 1214 vw, 1100 m, 1059 m, 1024 w, 971 s, 950 m, 932 m, 896 m, 805 vs, 596 m, 521 m, 472 m cm^{-1} . Solid-state ^{31}P NMR: δ – 10.8 (Fig. S1). ^{31}P NMR (23.7 °C, 0.5 M H_2SO_4 aq., just after dissolving, Fig. S3(b)): δ – 11.02. ^{31}P NMR (23.7 °C, D_2O , just after dissolving, Fig. S3(a)): δ (minor peaks) – 11.02, – 11.23, – 11.35 and (major peaks) – 11.39, – 11.43, – 11.47. ^{31}P NMR (23.7 °C, 1 M HCl aq., one week later after dissolving, Fig. S3(d)): δ (major peaks) – 11.11, – 11.13 and (minor peak) – 11.54 ppm. ^{31}P NMR (23.7 °C, 1 M HNO_3 aq., one week later after dissolving, Fig. S3(e)): δ (major peaks) – 10.97, – 11.02, – 11.04 and (minor peaks) – 11.45 ppm. ^{31}P NMR (23.7 °C, 0.5 M H_2SO_4 aq., one week later after dissolving, Fig. S3(c)): δ (major peaks) – 11.04, – 11.09, – 11.12, (minor peaks) – 11.54, – 13.70 and (major peak due to **5**) – 15.09 ppm.
- [37] Synthesis of **K1** from precursor **K3**: $K_{10}H_2[(\alpha-1,2,3-PW_5Ti_3O_{37})_2O_3] \cdot 15H_2O$, **K3**, (2.0 g, 0.36 mmol) was added to a clear colorless solution of $Ti(SO_4)_2 \cdot 4H_2O$ (0.60 g, 1.92 mmol) dissolved in a 1 M aqueous HNO_3 solution (40 mL). The colorless clear solution was stirred for 30 min in a water bath at 80 °C. To the solution was added solid KCl (0.20 g, 2.68 mmol). After cooling to room temperature, the clear solution was evaporated to a volume of ca. 5 mL with a rotary evaporator at 40 °C. The resulting white suspension was stored in a refrigerator at 4 °C overnight. The white precipitate formed was filtered off through a membrane filter (JG 0.2 μm). The clear filtrate was slowly evaporated at room temperature. After three weeks, clear colorless plate crystals formed, which were subjected to X-ray diffraction measurement. The remaining crystals were collected on a membrane filter (JG 0.2 μm) and dried in vacuo for 2 h. The colorless plate crystals obtained in 29.9% yield (0.67 g scale) were soluble in water but insoluble in most organic solvents. Stability in water was low. TG/DTA under atmospheric conditions: a weight loss of 7.23% was observed at below 200.6 °C; calc. 6.94% for a total of 12 water molecules, i.e., 10 coordinated water molecules plus $x = 2$ hydrated water molecules in $K[[Ti(H_2O)_3]_2[Ti(H_2O)_2]_2(\mu-O)_3(SO_4)](PW_{10}O_{37}) \cdot xH_2O$. IR (KBr) (polyoxometalate region): 1213 vw, 1100 m, 1060 m, 1024 w, 971 s, 950 m, 931 m, 891 m, 806 vs, 595 m, 519 m, 462 s cm^{-1} . Solid-state ^{31}P NMR: δ – 10.4 (Fig. S2). ^{31}P NMR (21.9 °C, 0.5 M H_2SO_4 aq., just after dissolving): δ – 11.03. ^{31}P NMR (22.0 °C, 1 M HNO_3 aq., just after dissolving): δ (major peak) – 11.00 and (minor peaks) – 11.04, – 11.07.
- [38] R. Thouvenot, M. Fournier, R. Franck, C. Rocchiccioli-Deltcheff, *Inorg. Chem.* 23 (1984) 598.
- [39] Crystal data for **K1**: $H_{38}K_1O_{63}P_1S_1Ti_4W_{10}$, $M = 3,140.23$, monoclinic, space group $P2_1$, $a = 14.579(3)$, $b = 13.934(3)$, $c = 14.754(3)$ Å, $\beta = 115.834(3)^\circ$, $V = 2,697.7(10)$ Å³, $Z = 2$, $D_c = 3.866$ Mg m⁻³, $\mu(Mo-K\alpha) = 22.055$ mm⁻¹. $R_1 = 0.0411$, $wR_2 = 0.1031$ (for all data). $R_{int} = 0.0393$, $R_1 = 0.0401$, $wR_2 = 0.1024$, $GOF = 1.057$ (27471 total reflections, 13076 unique reflections where $I > 2\sigma(I)$). The maximum and minimum residual density (8.41 and -3.93 eÅ⁻³) holes were located at 2.73 Å from O(8W) and 0.80 Å from W(1), respectively. One potassium cation and polyoxoanion **1**, which consists of 10 tungsten atoms, four titanium atoms, one phosphorus atom, one sulfur atom, and 54 oxygen atoms (including the oxygen atoms due to 10 coordinated water molecules and three $\mu-O$ atoms) per formula unit were identified, but the location of nine hydrated water molecules per formula unit was not determined as a result of disorder. The molecular structure of **1** has been solved and refined based on the $P2_1$ space group. Since additional symmetry elements m and b (Alert level B in the checkcif report) were indicated, we tried to refine the structure of **1** based on the another space group, $P2_1/m$. However, satisfactory results were not obtained. CSD number 422826.
- [40] I.D. Brown, R.D. Shannon, *Acta Crystallogr. Sect. A* 29 (1973) 266.
- [41] I.D. Brown, *J. Appl. Crystallogr.* 29 (1996) 479.

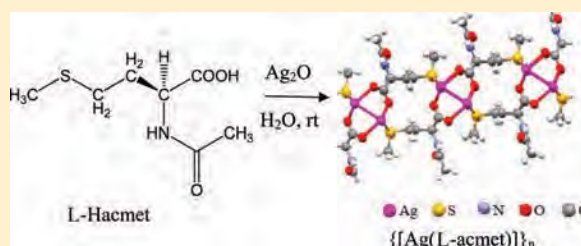
Syntheses, Structures, and Antimicrobial Activities of Remarkably Light-Stable and Water-Soluble Silver Complexes with Amino Acid Derivatives, Silver(I) *N*-Acetylmethioninates

Noriko Chikaraishi Kasuga, Rie Yoshikawa, Yoshitaka Sakai, and Kenji Nomiya*

Department of Chemistry (formerly Materials Science), Faculty of Science, Kanagawa University, Hiratsuka, Kanagawa, 259-1293, Japan

Supporting Information

ABSTRACT: Reaction of *L*- and *DL*-*N*-acetylmethionine (Hacmet) and Ag₂O in water at ambient temperature afforded the remarkably light-stable silver complexes {[Ag(*L*-acmet)]_n} (1) and {[Ag₂(*D*-acmet)(*L*-acmet)]_n} (2), respectively. The color of the solids and aqueous solutions of 1 and 2 did not change for more than 1 month under air without any shields. The light stability of these two silver(I) complexes is much higher than that of silver(I) methioninate {[Ag₂(*D*-met)(*L*-met)]_n} (3) (Hmet = methionine), silver(I) *S*-methyl-*L*-cysteinate {[Ag(*L*-mecys)]_n} (4), and silver(I) *L*-cysteinate {[Ag(*L*-Hcys)]_n} (5). X-ray crystallography of 1 obtained by vapor diffusion revealed that ladder-like coordination polymers with two O- and two S-donor atoms were formed. The acetyl group of acmet[−] prevents chelate formation of the ligand to the metal center, which is frequently observed in amino acid metal complexes, but allows for formation of hydrogen bonds between the ligands in the crystals of 1. These two silver(I) *N*-acetylmethioninates showed a wide spectrum of effective antimicrobial activities against Gram-negative bacteria (*Escherichia coli* and *Pseudomonas aeruginosa*) and yeasts (*Candida albicans* and *Saccharomyces cerevisiae*), the effectiveness of which was comparable to that of water-soluble Ag–O bonding complexes.



INTRODUCTION

Medicinal applications of coinage metal (Cu, Ag, and Au) complexes have been established for years,¹ and among them silver(I) complexes as well as silver clusters² have been known to show antimicrobial activity. It has been said that discovering new compounds that work against Gram-negative bacteria but simultaneously are not toxic to humans is difficult.³ Fortunately, silver materials have been shown to exhibit low toxicity toward human skin,⁴ and silver(I) histidinate formulated with some additives is a practical example.⁵ Notably, silver(I) complexes have been reported to show a different antimicrobial spectrum against microorganisms compared to the activity of the ligand itself and the hydrated silver(I) ion.^{1b,c,6} During investigation of the structural relationship of silver(I) complexes with their antimicrobial activities in aqueous media we noticed that silver(I) complexes with hard donor atoms (i.e., silver(I)–N and/or silver(I)–O bonds) exhibited an effective and a wide spectrum of antimicrobial activity,^{1c,6a–e,h} whereas silver(I) thiolates were shown to have a narrower spectrum of antimicrobial activity.^{6g} From these results we concluded that the nature of the atom that coordinates to the silver(I) center and its bonding properties (rather than the solubility, charge, chirality, or degree of polymerization of the complexes) and the ease of ligand replacement are the key factors that lead to a wide spectrum of antimicrobial activity. The primary targets for inhibition of bacteria and yeasts by the silver(I) complexes are proteins that function as sulfur donor ligands but

not nucleic acids that act as N/O donors. Although Ag–O and Ag–N bonding silver(I) complexes are potential antimicrobial reagents with a wide spectrum of antimicrobial activities, many of them are not light-stable and/or poorly soluble in common solvents, as seen in [Ag(Him)₂]NO₃ (Him = imidazole),^{7a} {[Ag(im)]_n}^{7b} and others, including the silver(I) complexes of amino acids, peptides, and proteins.⁸ Therefore, their characterization, including structural studies, has not been easily carried out.

To investigate the interactions between biomolecules and metal complexes via transmission electron microscopy,⁹ water-soluble coinage metal complexes are desired. However, there are only a few water-soluble silver(I) complexes that can be used as starting materials and are easy to handle. Typical commercial sources are AgClO₄ and AgNO₃, but use of AgClO₄ requires caution, especially in organic solvents, and the NO₃[−] anion is in many cases hard to remove completely during the purification steps. We found that reaction of Ag₂O and acids containing the HOOC–C–X–C=O (X = N or O) moiety gave relatively light-stable (i.e., aqueous solutions containing the silver(I) complexes are stable for a few hours to days at ambient temperature without light shielding) and water-soluble silver(I) complexes, such as silver(I) aspartate,^{6c} silver(I) 2-pyrrolidone-5-carboxylates,^{6b,d} and silver(I) acetyl-

Received: September 6, 2011

Published: January 20, 2012

glycinate.^{6e} Addition of soft ligands, such as phosphines, to a solution containing Ag–O bonding complexes increases the light stability of silver(I) complexes but tends to decrease their antimicrobial activity.¹⁰ Silver(I) thiolate complexes are more light stable, but as described above they exhibit a narrower spectrum of antimicrobial activity against Gram-negative bacteria, and their characterization is difficult, especially for silver(I) complexes with aliphatic thiolate ligands due to their oligomeric nature.^{6f,g,i}

Herein, we report the synthesis, characterization, crystal and solution structures, and properties of novel silver(I) complexes derived from *N*-acetyl-L-methionine (L-Hacmet) and *N*-acetyl-DL-methionine (DL-Hacmet), i.e., {[Ag(L-acmet)]}_n (1) and {[Ag₂(D-acmet)(L-acmet)]}_n (2), the aqueous solutions of which are stable under ambient conditions without shade for several weeks to months. Acetylmethionine was thought to be a potential candidate for forming a water-soluble, light-stable, and effective antimicrobial silver(I) complex for the following reasons: (i) compounds containing the O=C–N–C–COO partial moiety in the backbone have been found to form water-soluble silver(I) complexes (red circle in Figure 1),^{6e} (ii) acetyl

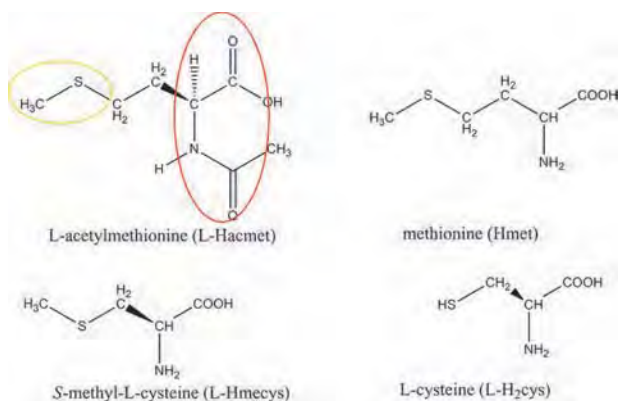


Figure 1. Chemical structure of *N*-acetyl-L-methionine and related ligands. Yellow and red circles show the thioether and O=C–N–C–COO partial moiety of L-Hacmet, respectively.

group substitution changes the zwitterionic nature of the methionine to an acid and also enables the ligands to make interunit hydrogen bonds; (iii) the interaction of the silver(I) ion and the soft S-donor atoms of the thioether groups would be less tight (yellow circle in Figure 1) compared with that of Ag–S (thiolate) bonding silver(I) complexes,¹¹ but it would stabilize silver(I) complexes in aqueous solution; and (iv) the ligand (L-Hacmet or DL-Hacmet) is a derivative of the amino acid methionine, which is easily obtained from natural products and expected to form complexes that are less toxic to human skin. The complexes were characterized using elemental analysis, thermogravimetric (TG) analysis, and differential thermal analysis (DTA), FT-IR, and solution ¹H, ¹³C{¹H}, and ¹⁰⁹Ag NMR spectroscopies, and X-ray crystallography. The antimicrobial activities of complexes 1 and 2, as well as related silver(I) complexes, evaluated by minimum inhibitory concentration (MIC, μg mL⁻¹) in a water or water–suspension system are also presented. The properties of these silver complexes, including light stability, solubility in water, and antimicrobial activity, are compared with those of silver(I) methioninate {[Ag(DL-met)]}_n (3), silver(I) S-methyl-L-cysteinate {[Ag(L-

mecys)]_n (4), and silver(I) L-cysteinate {[Ag(L-Hcys)]_n (5) (Figure 1).

EXPERIMENTAL SECTION

Materials. The following reagent-grade chemicals were used as received: Ag₂O, dimethyl sulfoxide (DMSO), EtOH, Et₂O, CHCl₃, CH₂Cl₂, MeOH, EtOAc, CH₃CN, and acetone (Wako); *N*-acetyl-DL-methionine, *N*-acetyl-L-methionine, L-methionine, DL-methionine, S-methyl-L-cysteine, and L-cysteine (Tokyo Kasei); 4,4-dimethyl-4-silapentane-1-sulfonic acid (DSS) (Aldrich); and D₂O (99.9 D atom %, Isotec).

Instrumentation/Analytical Procedures. CHN elemental analyses were performed using a Perkin-Elmer PE2400 series II CHNS/O analyzer. Thermogravimetric (TG) and differential thermal analyses (DTA) were performed under air with a temperature ramp of 4 °C min⁻¹ using a Rigaku Thermo Plus 2 TG 8120 instrument between 30 and 500 °C. Infrared spectra were recorded on a JASCO FT-IR 4100 spectrometer in KBr disks at room temperature. ¹H, ¹³C{¹H}, and ¹⁰⁹Ag NMR spectra in solution were recorded at ambient temperature on a JEOL EX-400 NMR or a JEOL ECP500 NMR spectrometer. ¹H and ¹³C{¹H} NMR spectra of the complexes were measured in a D₂O solution with reference to an internal DSS. The signals of the two methyl groups and the carbonyl in the acetyl and carboxylate moieties in the ¹H and ¹³C NMR spectra were assigned using 2D NMR, heteronuclear multiple quantum coherence (HMQC), and heteronuclear multiple-bond connectivity (HMBC). ¹⁰⁹Ag NMR spectra of the complexes were measured in D₂O with reference to an external standard solution consisting of saturated AgNO₃–D₂O using a substitution method. Solid-state cross-polarization magic-angle-spinning (CPMAS) ¹³C (75 MHz) NMR spectra were recorded in 6 mm o.d. rotors on a JEOL JNM-ECP 300 FT-NMR spectrometer with a JEOL ECP-300 NMR data processing system. These spectra were referenced to the methyl peak of hexamethylbenzene as an external standard (δ 17.37).

X-ray Crystallography. Crystallization of 1 and 4 was carried out by vapor diffusion of an internal aqueous solution of the silver(I) complex with an external solvent (acetone). Water-soluble colorless crystals of 1 and 4 suitable for single-crystal X-ray analysis were obtained. Colorless crystals of 3 suitable for single-crystal X-ray analysis were grown using a slow-evaporation method.

Each single crystal of the silver(I) complexes (1, 3, and 4) was mounted on a loop and used for measurements of precise cell constants and collection of intensity data at 90 K on a Bruker Smart APEX CCD diffractometer. Structures were solved by direct methods, followed by difference Fourier calculations; they were refined by full-matrix least-squares on *F*² using the SHELXTL program package.¹² All non-hydrogen atoms were refined anisotropically. Hydrogen atoms were placed geometrically or shown on a difference Fourier map and treated using a riding model. Crystal data and structure refinement of complexes 1, 3, and 4 are summarized in Table 1. Details of the crystal data have been deposited with the Cambridge Crystallographic Data Centre as supplementary publication nos. CCDC 842939, 842940, and 842941 for complexes 1, 3, and 4, respectively.

Antimicrobial Activity. Antimicrobial activities were estimated based on the minimum inhibitory concentration (MIC, μg mL⁻¹) by adding an aqueous solution of the silver(I) complexes, as described elsewhere.^{6f–h} Bacteria were inoculated into 5 mL of a liquid medium (soybean casein digest (SCD)) and cultured for 24 h at 35 °C. Yeast was inoculated into 5 mL of a liquid medium (glucose peptone (GP)) and cultured for 48 h at 30 °C. The cultured fluids were diluted, adjusted to a concentration of 10⁶–10⁷ mL⁻¹, and used for inoculation in the MIC test. As for the mold culture, the agar slant (potato dextrose (PD) agar medium), for 1-week cultivation at 27 °C, was gently washed with saline containing 0.05% Tween 80. The spore suspension obtained was adjusted to a concentration of 10⁶ mL⁻¹ and used for inoculation in the MIC test. The test materials were dissolved (silver complexes 1–4 and the “free” ligands) or suspended (complex 5) in water. Such solutions were then diluted with an SCD medium for bacteria and with a GP medium for yeast and mold. Using these 2-fold-

Table 1. Summary of Crystal Data and Structure Refinement Parameters for Crystals 1, 3, and 4^a

	$\{[\text{Ag}(\text{L-acmet})]\}_n$ (1)	$\{[\text{Ag}_2(\text{D-met})(\text{L-met})\cdot 6\text{H}_2\text{O}]\}_n$ (3)	$\{[\text{Ag}(\text{L-mecys})]\}_n$ (4)
empirical formula	$\text{C}_7\text{H}_{12}\text{NO}_3\text{SAg}$	$\text{C}_{10}\text{H}_{32}\text{N}_2\text{O}_{10}\text{S}_2\text{Ag}_2$	$\text{C}_4\text{H}_8\text{NO}_2\text{SAg}$
fw	298.12	620.24	242.04
cryst syst	monoclinic	monoclinic	orthorhombic
space group	C2 (No. 5)	$P2_1/c$ (No. 14)	$P2_12_12_1$ (No. 19)
$a/\text{\AA}$	16.124(5)	12.3891(9)	5.0463(4)
$b/\text{\AA}$	4.7856(14)	7.3815(5)	5.6304(5)
$c/\text{\AA}$	15.443(5)	11.7052(9)	23.2902(19)
α/deg	90	90	90
β/deg	117.911(9)	97.2720(10)	90
γ/deg	90	90	90
$V/\text{\AA}^3$	1053.0(6)	1061.83(13)	661.74(10)
$D_{\text{calcd}}/\text{g}\cdot\text{cm}^{-3}$	1.88	1.94	2.430
Z	4	4	4
μ/mm^{-1}	2.088	2.088	3.281
T/K	90	90	90
no. of total reflns	4188	8112	4923
no. of unique reflns	2463	2631	1641
no. of observations ($I > 2\sigma(I)$)	2342	2531	1638
R_{int}	0.0332	0.0214	0.0235
R_1	0.0361	0.0175	0.0190
wR_2	0.0990	0.0456	0.0446
GOF	1.069	1.102	1.227

^a $R_1 = \sum\{|F_o| - |F_c|\} / \sum|F_o|$, $wR_2 = [\sum\omega(|F_o| - |F_c|)^2 / \sum\omega F_o^2]^{1/2}$, $GOF = [\sum\omega(|F_o| - |F_c|)^2 / (m - n)]^{1/2}$ where m = no. of reflections, n = no. of parameters.

diluted solutions, concentrations from 1000 to 2 $\mu\text{g mL}^{-1}$ were prepared. Each 1 mL of a culture medium containing various concentrations of test materials was inoculated with 0.1 mL of the microorganism suspension prepared above. Bacteria were cultured for 24 h at 35 °C, yeast for 48 h at 30 °C, and mold for 1 week at 25 °C, and then growth of the microorganisms was observed. When no growth was observed in the medium containing the lowest concentration of test materials, the MIC was defined at this point of dilution.

Preparation of $\{[\text{Ag}(\text{L-acmet})]\}_n$ (1). To a suspension of 0.348 g (1.50 mmol) of Ag_2O in 40 mL of water was added 1.15 g (6.02 mmol) of L-Hacmet. During 2 h of stirring, the black suspension changed to a clear pale-yellow solution. Unreacted black powder (Ag_2O) was filtered off through a folded filter paper (Whatman No. 5). The clear yellow filtrate was added dropwise to 500 mL of acetone. The white powder that formed was collected on a membrane filter (JG 0.2 μm), washed with acetone (50 mL \times 2) and diethyl ether (100 mL \times 2), and dried in vacuo. The light-stable and thermally-stable white powder (0.775 g, 87.6% yield) was soluble in water but insoluble in most organic solvents. Crystallization of the obtained powder was carried out by vapor diffusion of an internal aqueous solution of 100 mg of the powder in 10 mL of water with acetone as the external solvent, which gave water-soluble, colorless needle crystals (59.9 mg). The crystals obtained were characterized as below. Anal. Calcd for $\text{C}_7\text{H}_{12}\text{NO}_3\text{SAg}$ or $[\text{Ag}(\text{L-acmet})]$ as a monomer unit: C, 28.20; H, 4.06; N, 4.70. Found: C, 28.30; H, 4.29; N, 4.74. TG/DTA data: no weight loss was observed before the decomposition temperature. Decomposition began at around 192 °C with an endothermic peak at 211 °C. Prominent IR bands in the 1800–400 cm^{-1} region (KBr disk): 1635 vs, 1592 vs, 1442 m, 1399 s, 681 m, 599 m, 549 cm^{-1} . ^1H NMR (D_2O , 17.1 °C): δ 2.03 (CH_3 in acetyl group, s, 3H), 2.06–2.11 and 2.23–2.25 (CH_2CH , two multiplets, 2H), 2.43 (CH_3S , s, 3H),

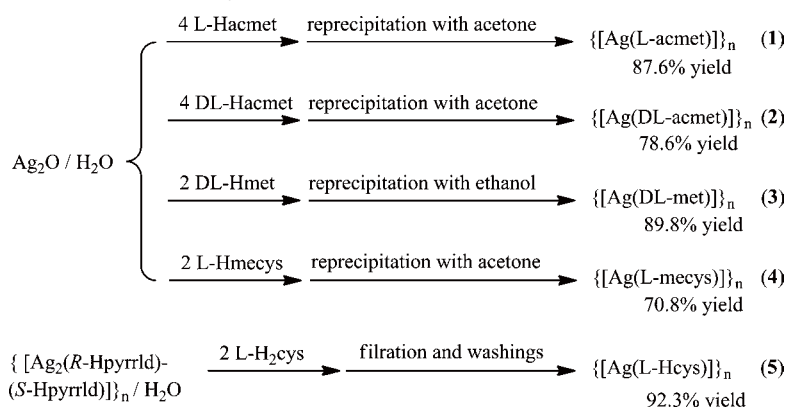
2.82 (CH_2S , t, 2H), 4.32 (CH , double doublet, 1H) ppm. ^{13}C NMR (D_2O , 25.7 °C): δ 20.62 (SCH_3), 24.62 (CH_3 in acetyl group), 34.78 and 35.40 (two CH_2), 56.57 (CH), 176.37 ($\text{C}=\text{O}$ in acetyl group), 180.50 (COO) ppm. ^{109}Ag NMR (D_2O , 19.7 °C, pH 5): δ 352 ppm. No color change was observed for about 1 month in the solid state nor in an aqueous solution. Solubility in water at room temperature was approximately 50 mg mL^{-1} . Even when 4 equiv of L-Hacmet were added to Ag_2O in the reaction mixture instead of 2 equiv, the same silver(I) complex 1 was isolated by adding acetone (confirmed by IR, ^1H and ^{13}C NMR, and elemental analysis data). However, the reaction mixture using 4 equiv of L-Hacmet showed different signals in the ^{109}Ag NMR spectrum (538 ppm, pH 3.0) and was more light stable. The filtrate of the reaction mixture was also more light stable, and the color did not change for several months.

Preparation of $\{[\text{Ag}_2(\text{D-acmet})(\text{L-acmet})]\}_n$ (2). An achiral silver(I) complex, 2, was obtained in a similar manner using 4 equiv of DL-Hacmet instead of L-Hacmet. Anal. Calcd for $\text{C}_{14}\text{H}_{24}\text{N}_2\text{O}_6\text{S}_2\text{Ag}_2$ or $[\text{Ag}_2(\text{D-acmet})(\text{L-acmet})]$ as a monomer unit: C, 28.20; H, 4.06; N, 4.70. Found: C, 28.29; H, 3.80; N, 4.74. TG/DTA data: no weight loss was observed before the decomposition temperature. Decomposition began at around 183 °C with an endothermic peak at 201 °C. Prominent IR bands in the 1800–400 cm^{-1} region (KBr disk): 1637 vs, 1589 vs, 1119 vs, 1043 vs, 966 vs cm^{-1} . ^1H NMR (D_2O , 23.1 °C): δ 2.02 (CH_3 in acetyl group, s, 3H), 2.02–2.09 and 2.16–2.23 (CH_2CH , two multiplets, 2H), 2.42 (CH_3S , s, 3H), 2.83 (CH_2S , t, 2H), 4.32 (CH , dd, 1H) ppm. ^{13}C NMR (D_2O , 25.5 °C): δ 20.46 (SCH_3), 24.66 (CH_3 in acetyl group), 34.83 and 35.14 (two CH_2), 56.62 (CH), 176.43 ($\text{C}=\text{O}$ in acetyl group), 180.62 (COO) ppm. ^{109}Ag NMR (D_2O , 22.0 °C, pH 5): δ 356 ppm. Solubility in water at room temperature was approximately 20 mg mL^{-1} , which is about one-half of that of 1. No color change was observed for about 1 month in the solid state nor in an aqueous solution.

Preparation of $\{[\text{Ag}_2(\text{D-met})(\text{L-met})]\}_n$ (3). To a suspension of 0.580 g (2.50 mmol) of Ag_2O in 100 mL of water was added 0.745 g (5.00 mmol) of DL-Hmet. During 2 h of stirring, the black suspension changed to a clear solution. The unreacted black powder of Ag_2O was filtered off through a folded filter paper (Whatman No. 5). The clear filtrate was added dropwise to 1 L of ethanol, and the resulting mixture was allowed to stand for 1 day. The white powder formed was collected on a membrane filter (JG 0.2 μm), washed with ethanol (50 mL \times 2) and diethyl ether (100 mL \times 2), and dried in vacuo. The light-stable and thermally-stable white powder obtained in 1.15 g (89.8%) yield was soluble in water but insoluble in most organic solvents. The powder (0.300 g) was dissolved in 2.5 mL of warm water. Colorless granular crystals were grown in 1 day while standing at room temperature (0.215 g). Although the powder was soluble in water, the crystals were sparingly soluble in water and insoluble in common organic solvents. The water-soluble powder and crystals obtained were characterized as below. Anal. Calcd for $\text{C}_{10}\text{H}_{20}\text{N}_2\text{O}_4\text{S}_2\text{Ag}_2$ or $[\text{Ag}_2(\text{D-met})(\text{L-met})]$ as a monomer unit: C, 23.45; H, 3.94; N, 5.47. Found: C, 23.41; H, 3.59; N, 5.46. TG/DTA data: no weight loss was observed before the decomposition temperature. Decomposition began at around 148 °C with an endothermic peak at 166 °C. Prominent IR bands in the 1800–400 cm^{-1} region (KBr disk): 1577 vs, 1442 s, 1427 s, 1404 s, 1326 m, 1305 s, 1275 m, 1254 m, 1032 m, 961 m, 620 cm^{-1} . ^1H NMR (D_2O , 22.8 °C): δ 2.04–2.17 (CH_2CH , two multiplets, 2H), 2.45 (CH_3S , s, 3H), 2.90 (CH_2S , t, 2H), 3.58 (CH , t, 1H) ppm. ^{13}C NMR (D_2O , 25.1 °C): δ 20.36 (SCH_3), 34.98 (CH_2), 58.78 (CH), 182.25 (COO) ppm. ^{109}Ag NMR (D_2O , 25.5 °C, 0.08 M): δ 494 ppm. The color of the powder gradually changed to brown in a few days and that of the aqueous solution in a few hours. A chiral silver(I) complex $\{[\text{Ag}(\text{L-met})]\}_n$ was also obtained in a similar manner using 2 equiv of L-Hmet instead of DL-Hmet; however, characterization was too difficult to perform because of its hygroscopic nature. Crystals of complex 3 suitable for X-ray crystallography contained 6 hydrated water molecules.

Preparation of $\{[\text{Ag}(\text{L-mecys})]\}_n$ (4). A chiral silver(I) complex, 4, was obtained in a manner similar to preparation of complex 3 using 2 equiv of L-Hmecys instead of L-Hmet. Crystallization was also carried out by vapor diffusion of an internal aqueous solution of 100 mg of the

Scheme 1. Synthetic Scheme of Silver(I) Complexes 1–5

Table 2. Selected Distances (Angstroms) and Angles (degrees) of Crystals 1, 3, and 4^a

{[Ag(L-acmet)]} _n (1)		{[Ag ₂ (D-met)(L-met)]·6H ₂ O} _n (3)		{[Ag(L-mecys)]} _n (4)	
Ag1–S1	2.4969(13)	Ag1–S1	2.3953(4)	Ag1–S1	2.8436(7)
Ag1–S1 ⁱ	2.9940(14)	Ag1–O1 ^{vii}	2.4530(11)	Ag1–O1 ⁱ	2.590(2)
Ag1–O1 ⁱⁱ	2.345(3)	Ag1–O2 ^{viii}	2.5848(11)	Ag1–O2 ^x	2.188(2)
Ag1–O2 ⁱⁱⁱ	2.209(4)	Ag1 N1 ^{vii}	2.2408(13)	Ag1–N1	2.212(2)
Ag1–Ag1 ^{iv}	2.8987(9)				
N1–O3 ^v	2.909(6)	N1–O1 ^{ix}	2.8982(17)		
		O2–O4	2.6958(16)		
		O3–O4	2.7877(18)		
		O4–O5	2.8795(19)		
O1 ⁱⁱ –Ag1–S1 ⁱ	92.90(9)	O1 ^{vii} –Ag1–S1	123.38(3)	O2 ^x –Ag1–N1	171.80(8)
O2 ⁱⁱⁱ –Ag1–S1 ⁱ	69.96(11)	O2 ^{viii} –Ag1–S1	107.71(3)	O2 ^x –Ag1–O1 ⁱ	94.42(7)
O1 ⁱⁱ –Ag1–O2 ⁱⁱⁱ	131.29(14)	O1 ^{vii} –Ag1–O2 ^{viii}	100.72(4)	N1–Ag1–O1 ⁱ	86.95(8)
O2 ⁱⁱⁱ –Ag1–S1	135.70(11)	N1 ^{vii} –Ag1–S1	152.64(4)	O2 ^x –Ag1–S1	108.75(6)
Ag1 ^{iv} –Ag1–S1	120.29(3)	N1 ^{vii} –Ag1–O1 ^{vii}	70.42(4)	N1–Ag1–S1	78.85(6)
Ag1 ^{iv} –Ag1–O1 ⁱⁱ	73.94(9)	N1 ^{vii} –Ag1–O2 ^{viii}	90.66(4)		
Ag1 ^{iv} –Ag1–O2 ⁱⁱⁱ	81.47(10)				
Ag1–S1–Ag ^{vi}	121.01(5)				

^aSymmetry operations i = x, 1 + y, z; ii = 0.5 + x, 0.5 + y, z; iii = 0.5 – x, 0.5 + y, 1 – z; iv = 1 – x, y, 1 – z; vi = x, –1 + y, z; vii = 1 – x, 1 – y, 2 – z; viii = x, 0.5 – y, 0.5 + z; ix = 1 – x, 0.5 + y, 1.5 – z; X = –1 + x, 1 + y, z.

powder in 10 mL of water with acetone as the external solvent, which gave water-soluble, colorless, granular crystals after standing at room temperature for a few days (yield 70 mg). Anal. Calcd for C₄H₈NO₂SAg or [Ag(L-mecys)] as a monomer unit: C, 19.85; H, 3.33; N, 5.79. Found: C, 19.80; H, 2.90; N, 5.79. Decomposition began at around 112 °C with an endothermic peak at 144 °C. Prominent IR bands in the 1800–400 cm⁻¹ region (KBr disk): 1585 vs, 1398 s, 1357 m cm⁻¹. ¹H NMR (D₂O, 23.5 °C): δ 2.46 (CH₃S, s, 3H), 3.08 and 3.23 (CH₂S, two multiplets, 2H), 3.73 (CH, dd 1H) ppm. ¹³C NMR (D₂O, 25.3 °C): δ 20.86 (SCH₃), 43.14 (CH₂), 56.80 (CH), 180.72 (COO) ppm. ¹⁰⁹Ag NMR (D₂O, 25.5 °C, 0.08 M): δ 549 ppm. The color of the powder and aqueous solution changed to brown in a few days.

Preparation of {[Ag(L-Hcys)]_n (5). To a colorless solution of 0.472 g (1.00 mmol) of silver(I) *R,S*-2-pyrrolidone-5-carboxylates ({[Ag₂(R-Hpyrrld)(S-Hpyrrld)]_n H₂pyrrld = pyrrolidone-5-carboxylic acid)^{6d} in 40 mL of water was added a colorless solution containing 0.242 g (2.00 mmol) of L-cysteine (L-H₂cys) in 40 mL of water. The solution was vigorously stirred overnight to form a suspension. The white powder that formed was collected on a membrane filter (JG 0.2 μm), washed with water (50 mL × 2), acetone (50 mL × 2), and diethyl ether (100 mL × 2), and dried in vacuo. The light-stable and thermally-stable white powder (0.421 g, 92.3% yield) was insoluble in water and most organic solvents. Anal. Calcd for C₃H₆NO₂SAg or [Ag(L-Hcys)] as a monomer unit: C, 15.80; H, 2.65; N, 6.14. Found: C, 15.69; H, 2.37; N, 6.00. TG/DTA

data: no weight loss was observed before the decomposition temperature. Decomposition began at around 118 °C with an endothermic peak at 215 °C. Prominent IR bands in the 1800–400 cm⁻¹ region (KBr disk): 1677 s, 1620 s, 1565 vs, 1485 s, 1390 vs, 1351 m cm⁻¹. Solid ¹³C CP MAS NMR: δ 37.34 (SCH₂), 59.66 (CH), 171.84 (COO) ppm. The color of the white powder gradually changed to yellow in about 1 week.

RESULTS AND DISCUSSION

Preparation and Properties of {[Ag(L-acmet)]_n (1), [Ag₂(D-acmet)(L-acmet)]_n (2), and Other Related Silver(I) Complexes. Water-soluble powder and crystals of silver(I) acetylmethionates 1 and 2 were obtained from reaction of Ag₂O and acetylmethionines (L-Hacmet or DL-Hacmet) in molar ratios of Ag₂O:Hacmet = 1:2 and 1:4 in water at ambient temperature (Scheme 1). The obtained solids were characterized by FT-IR, TG/DTA, NMR, CHN analysis, and X-ray crystallography, confirming that the isolated materials contain Ag and acmet⁻ in a 1:1 ratio in the solid state and in both reaction mixtures. Black particles of Ag₂O disappeared more quickly when higher equivalents of acetylmethionine were employed.

Water-soluble powder and crystals of silver(I) DL-methioninate 3 and silver(I) S-methyl-L-cysteinate 4 were also prepared

from reactions of Ag_2O with DL-Hmet and L-Hmecys, respectively. The synthetic conditions used here gave neutral silver(I) methioninate **3** but not the anionic complex reported previously.¹³ The light stability and water solubility of silver(I) acetylmethioninates **1** and **2** in the solid state and in aqueous solution are more remarkable than those of silver(I) methioninate (**3**), silver(I) S-methyl-L-cysteinate (**4**), and silver(I) L-cysteinate (**5**). Properties such as the solubility in water of **1** and **2** are slightly different depending on whether chiral or achiral ligands were used. Complex **5** is insoluble in most solvents. Judging from elemental analysis, $\{[\text{Ag}_2(\text{R-Hpyrrld})(\text{S-Hpyrrld})]\}_n$ as a silver(I) source for preparation of **5** was superior to AgNO_3 , because the former formed pure polymeric silver(I) cysteinate.¹⁴ In the FT-IR spectrum of **5**, disappearance of the 2552 cm^{-1} band of ν_{SH} in L-H₂cys and an absorption shift of the $\nu_{\text{C=O}}$ band from 1608 to 1677 cm^{-1} were observed. The signal shift of the methine carbon in the ¹³C CP MAS spectrum also suggests that the metal ion of **5** is coordinated by sulfur and nitrogen atoms, so Ag–S (thiolate) bridging coordination may be a cause for the low solubility. These results support our hypothesis of ligand selection for light-stable and water-soluble silver(I) complexes.

Crystal and Molecular Structures of 1, 3 and 4. Crystal data are summarized in Table 1, and selected bond distances and angles with their estimated standard deviations are listed in Table 2.

Structure of $\{[\text{Ag}(\text{L-acmet})]\}_n$ (1**).** The molecular structure of **1** with atom-numbering scheme is depicted in Figure 2a. Ag1 is surrounded by two O (O1ⁱⁱ and O2ⁱⁱⁱ) and two S atoms (S1 and S1ⁱ) in a distorted tetrahedral coordination geometry belonging

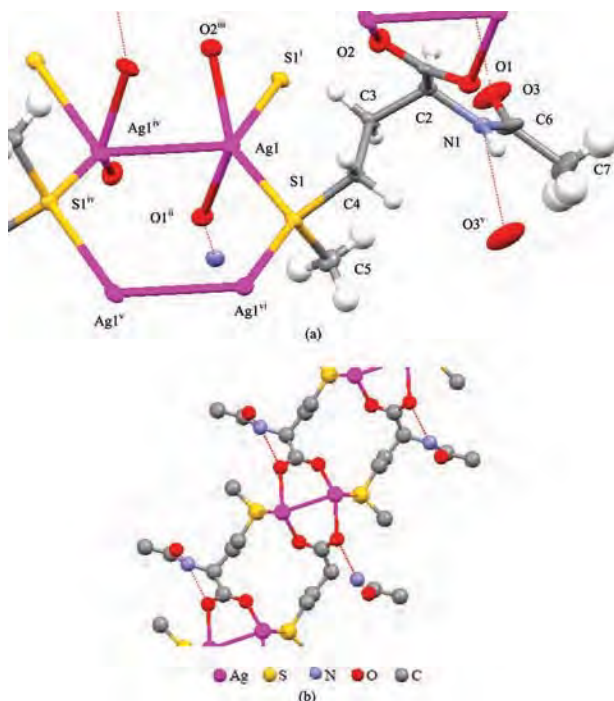


Figure 2. (a) Local structure of $\{[\text{Ag}(\text{L-acmet})]\}_n$ (**1**) with 50% probability thermal ellipsoids, and (b) 3D polymeric structure of crystal **1** viewed along the *b* axis in which hydrogen atoms are omitted for clarity. Symmetry operations: $i = x, 1 + y, z$; $ii = 0.5 + x, 0.5 + y, z$; $iii = 0.5 - x, 0.5 + y, 1 - z$; $iv = 1 - x, y, 1 - z$; $v = 1 - x, -1 + y, 1 - z$; $vi = x, -1 + y, z$.

to four separate L-acmet[−] ligands. A short distance between Ag1 and Ag1^{iv} (symmetry operation $iv = 1 - x, y, 1 - z$) ($2.8987(9)\text{ \AA}$), indicating argentophilic interaction, is also observed in complex **1**.¹⁵ The two close silver(I) atoms are bridged by two carboxylato-*O,O'* groups of acmet[−] ligands to create a syn–syn-type Ag_2O_4 moiety. Two thioether S atoms bridge the Ag_2O_4 moieties, and the S1, Ag1, Ag1^{iv}, S1^{iv}, Ag1^v, and Ag1^{vi} (symmetry operations $v = 1 - x, -1 + y, 1 - z$; $vi = x, -1 + y, z$) atoms form a chairlike 6-membered ring. The rings are connected like ladders as if two infinite linear Ag1^{vi}–S1–Ag1–S1ⁱ are connected by silver(I)–silver(I) separation in the direction of the *b* axis (Figure 2b). No donor atoms of the acetyl group (N1 and O3) coordinate to the silver(I) center. Instead, they form hydrogen bonds between the acmet[−] ligands.

Structure of $\{[\text{Ag}_2(\text{D-met})(\text{L-met})]\}_n$ (3**).** The molecular structure of **3** with atom-numbering scheme is depicted in Figure 3. Unlike that of **1**, none of Ag–Ag interaction, μ -S coordination and Ag_2O_4 moiety was observed in the crystal structure of complex **3**. Ag1 is surrounded by S1, two O atoms

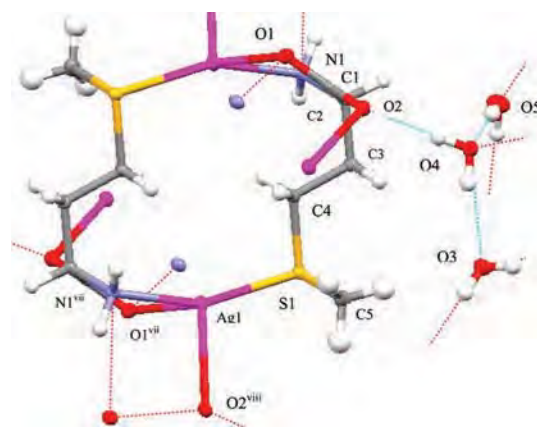


Figure 3. Polymeric structure of crystal $\{[\text{Ag}_2(\text{D-met})(\text{L-met})]\}_n$ (**3**) with 50% probability thermal ellipsoids. Symmetry operations: $vii = 1 - x, 1 - y, 2 - z$; $viii = x, 0.5 - y, 0.5 + z$.

(O1^{vii} and O2^{viii}, symmetry operations $vii = 1 - x, 1 - y, 2 - z$, $viii = x, 0.5 - y, 0.5 + z$), and one N (N1^{vii}) atom in a distorted tetrahedral coordination geometry belonging to three separate met[−] ligands. Coordination of the carboxylato-*O,O'* of the met[−] ligands is in a syn–anti form. The N and O atoms of the α carbon coordinate to silver(I) in a 5-membered, chelated manner. Each met[−] ligand connects three Ag^I atoms, leading to infinite polymeric chains. Intermolecular hydrogen bonds were observed between one water molecule (O4) and one carboxylate (O2), in the three hydrated water molecules (O3, O4, and O5) and met[−] ligands (N1^{vii}⋯O1^{ix} $2.8982(17)\text{ \AA}$, symmetry operations $ix = 1 - x, 0.5 + y, 1.5 - z$).

Structure of $\{[\text{Ag}(\text{L-mecys})]\}_n$ (4**).** The molecular structure of **4** with atom-numbering scheme is depicted in Figure 4. Ag1 is surrounded by S1, two O atoms (O1ⁱ and O2^X, symmetry operations $i = x, 1 + y, z$; $X = 1 + x, 1 + y, z$), and a N1 atom in a distorted tetrahedral coordination geometry belonging to three separate mecys[−] ligands. Coordination of the carboxylato-*O,O'* group of mecys[−] ligands is in a syn–anti form. The N and S atoms coordinate to silver(I) in a 5-membered, chelated manner (Ag1–N1–C2–C3–S1). Each met[−] ligand connects three Ag^I atoms, leading to infinite polymeric chains.

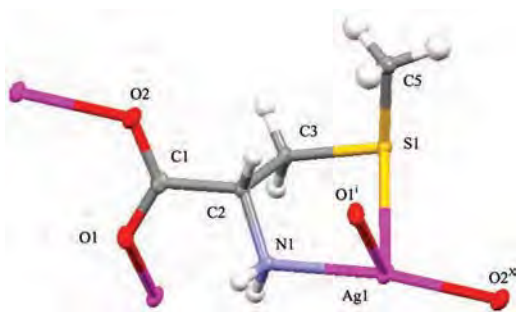


Figure 4. Polymeric structure of crystal $\{[Ag(L\text{-mecys})]\}_n$ (**4**) with 50% probability thermal ellipsoids. Symmetry operations: $i = x, 1 + y, z$; $X = 1 + x, 1 + y, z$.

Solution Behavior of Silver(I) Acetylmethioninate Monitored by ^{109}Ag NMR. Because of poor sensitivity, which stems from very low gyromagnetic ratios γ for ^{109}Ag , relatively highly concentrated samples are required for ^{109}Ag NMR experiments.¹⁶ Silver(I) complexes **1–4** were soluble enough in water for ^{109}Ag NMR measurements.

Solutions of chiral and achiral silver(I) acetylmethioninates **1** and **2** dissolved in D_2O (0.2 M, pH 5) show the same single peak at around 380 ppm in the ^{109}Ag NMR spectra (Figure 5a and 5b), the value of which is larger than those of Ag–O bonding complexes (<100 ppm) such as $\{[Ag_2(R\text{-Hpyrrld})(S\text{-$

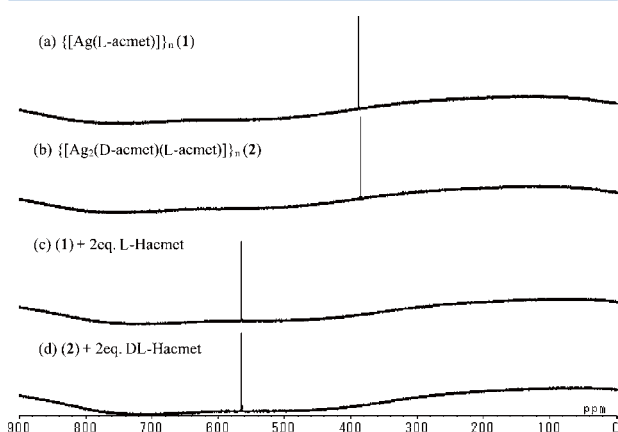


Figure 5. ^{109}Ag NMR spectra of solutions of silver(I) *N*-acetylmethioninate (0.2 M in D_2O at ambient temperature) and a mixture containing 2 equiv of Hacmet.

$Hpyrrld)\}_n$ (^{6d} 48 ppm) but lower than those of water-soluble Ag–S (thiolate) bonding complexes such as $\{Na[Ag(mba)]\}_n$ (H_2mba = 2-mercaptobenzoic acid, 856 ppm),^{6f} $\{Na[Ag(mna)]\}\cdot H_2O\}_n$ (H_2mna = 2-mercaptionicotinic acid, 1029 ppm),^{6g} $\{NaH[Ag(tma)]\}\cdot 0.5H_2O\}_n$ (H_3tma = thiomalic acid, 869 ppm)⁶ⁱ in D_2O , and $[HQ][Ag(pspa)]$ (HQ = diisopropylammonium, H_2pspa = 3-phenyl-2-sulfanylpropenoic acid, 841 ppm in DMSO and 809 ppm in MeOD).¹⁷ No significant difference in the chemical shifts was observed for **1** and **2** under the same conditions in the ^{109}Ag NMR spectra regardless of the chirality of $acmet^-$.

Addition of free Hacmet to the solutions moved the ^{109}Ag NMR signals to a lower field, although no observable changes occurred; the solution remained colorless, and no precipitation was noted. Following addition of 2 equiv of acidic Hacmet, the signal appeared at 565 ppm ($\{[Ag_2(D\text{-acmet})(L\text{-acmet})]\}_n$ (pH

3) (Figure 5c and 5d), and thus, the chemical shift became closer to those of Ag–S (thiolate) bonding complexes, such as silver(I) 2-mercaptionicotinate (856 ppm).^{6f} In water, the S (thioether) and O atoms of $acmet^-$, as well as water oxygen atoms, coordinate to silver(I) because the coordination number of silver(I) is often reported to be more than two.^{1d} Fast ligand exchange between the O atoms of $acmet^-$ and/or water molecules takes place in aqueous solutions of **1** and **2**. Addition of Hacmet to the NMR sample solutions of **1** and **2** increases the concentration of thioether S atoms in the solutions. The lower signal shift of the ^{109}Ag NMR spectra shows that ligand exchange between the O atom and the S atom (thioether) around the silver(I) atom easily takes place in water. As the ratio of Hacmet increases, more sulfur coordination occurs, indicating that the neutral thioether S atom can coordinate to the silver(I) atom more strongly than the O atom, but that is not the case for the thiolate S atom. Addition of Hacmet to aqueous solutions of **1** and **2** causes a decrease in the pH of the solutions, which also increases the light stability of the silver(I) complexes in solution (see Experimental Section, complex (**1**)).

When the Hacmet ligand was added to an aqueous solution of $\{[Ag_2(R\text{-Hpyrrld})(S\text{-Hpyrrld})]\}_n$, the signal in the ^{109}Ag NMR spectrum shifted to around 400 ppm. The opposite reaction did not occur, however. No signal shift was observed when $H_2pyrrld$ was added to the solution of $\{[Ag(L\text{-acmet})]\}_n$. By addition of 2-mercaptobenzoic acid to the aqueous solution of $\{[Ag(L\text{-acmet})]\}_n$, the signal of ^{109}Ag moved to 1000 ppm. Again, the opposite reaction did not take place. These signal shifts clearly show that the affinity of $acmet^-$ for the Ag^+ atom is between the Ag–O bond (<100 ppm) and the Ag–S (thiolate) bond (>800 ppm). The chemical shifts of ^{109}Ag NMR and the ligand exchangeability of the silver(I) thioether complexes, **3** (494 ppm) and **4** (549 ppm), also show that the Ag–S (thioether) bond is between Ag–O and Ag–S (thiolate).

Antibacterial and Antifungal Activities. The antimicrobial activities of complexes **1–5** together with their free ligands and related silver(I) complexes are listed in Table 3, as estimated by the minimum inhibitory concentration (MIC, $\mu g mL^{-1}$). Aqueous solutions of **1–4** were added to the test media. A suspension of **5** was added to the test media because **5** was insoluble in water.

The antimicrobial activities of the free ligands, i.e., DL-Hacmet, DL-Hmet, L-Hmecys, L- H_2cys , $H_2pyrrld$, H_2mba , and H_2mna , were estimated as $>1000 \mu g mL^{-1}$ for selected bacteria, yeast, and mold, indicating no activity. The hydrated Ag^+ ion was reported to show effective activity against Gram-negative bacteria (*E. coli* and *P. aeruginosa*), moderate activity against Gram-positive bacteria (*B. subtilis*), and no activity against yeast and mold.^{6f} Complexes **1** and **2** with Ag–O and Ag–S (thioether) bonds showed effective activities against Gram-negative bacteria (*E. coli* and *P. aeruginosa*) and yeasts (*C. albicans* and *S. cerevisiae*), moderate activities against Gram-positive bacteria (*B. subtilis* and *S. aureus*), and modest activities against mold (*A. niger* and *P. citrinum*). A similar wide spectrum of activity was observed for complex **3**. Complex **4** with Ag–O and Ag–S (thioether) bonds, which has a shorter backbone ligand compared with methionine, also exhibited effective activities against Gram-negative bacteria (*E. coli* and *P. aeruginosa*) and a Gram-positive bacterium (*B. subtilis*), moderate activity against a Gram-positive bacterium (*S. aureus*), modest activities against yeasts, and no activities against molds. The ligand exchangeability of the silver(I) thioether complexes might be influenced by the backbone length of the ligand.

Table 3. Antimicrobial Activities of Silver(I) Complexes 1–5^a

	DL-Hacmet	{[Ag(L-acmet)]} _n (1)	{[Ag ₂ (D-acmet)(L-acmet)] _n (2)	DL-Hmet	{[Ag ₂ (D-met)(L-met)] _n (3)
<i>Escherichia coli</i> (ATCC8739)	>1000	15.7	15.7	>1000	15.7
<i>Bacillus subtilis</i> (ATCC6633)	>1000	62.5	62.5	>1000	62.5
<i>Staphylococcus aureus</i> (ATCC6538)	>1000	125	62.5	>1000	62.5
<i>Pseudomonas aeruginosa</i> (ATCC9027)	>1000	31.3	31.3	>1000	15.7
<i>Candida albicans</i> (ATCC9763)	>1000	15.7	15.7	>1000	15.7
<i>Saccharomyces cerevisiae</i> (ATCC10231)	>1000	31.3	31.3	>1000	15.7
<i>Aspergillus niger</i> (ATCC16404)	>1000	125	250	>1000	125
<i>Penicillium citrinum</i> (NBRC6352)	>1000	>1000	1000	>1000	1000
	S-methyl-L-cysteine (L-Hmecys)	{[Ag(L-mecys)] _n (4)	L-cysteine (L-H ₂ cys)	{[Ag(L-Hcys)] _n (5)	
<i>E. coli</i>	>1000	31.3	>1000	>1000	
<i>B. subtilis</i>	>1000	31.3	>1000	>1000	
<i>S. aureus</i>	>1000	62.5		>1000	
<i>P. aeruginosa</i>	>1000	7.9		>1000	
<i>C. albicans</i>	>1000	250		>1000	
<i>S. cerevisiae</i>	>1000	500		>1000	
<i>A. niger</i>	>1000	>1000		>1000	
<i>P. citrinum</i>	>1000	>1000		>1000	
	{[Ag ₂ (R-Hpyrrld)(S-Hpyrrld)] _n ^{6d}	{Na[Ag(mba)] _n ^{6f}	{Na[Ag(mna)] _n ^{6g}	AgNO ₃ ^{6f}	
<i>E. coli</i>	7.9	<2	12.5	6.3	
<i>B. subtilis</i>	31.3	<2	>1000	100	
<i>S. aureus</i>	15.7	32	>1000	>1600	
<i>P. aeruginosa</i>	7.9	16	31.5	6.3	
<i>C. albicans</i>	7.9	1000	>1000	>1600	
<i>S. cerevisiae</i>	7.9	125	>1000	1600	
<i>A. niger</i>	500	>1000	>1000	>1600	
<i>P. citrinum</i>	125	>1000	>1000	>1600	

^a“Free” ligand and relating silver(I) complexes evaluated by minimum inhibitory concentration (MIC; $\mu\text{g mL}^{-1}$). Compound 5 was added as a suspension in water because it was insoluble in water. H₂pyrrld = pyrrolidone-5-carboxylic acid, Hmba = 2-mercaptobenzoic acid, H₂mna = 2-mercaptonicotinic acid.

As shown in Table 3, water-soluble Ag–S (thiolate) bonding complexes ($\{\text{Na}[\text{Ag}(\text{mba})]\}_n$ and $\{\text{Na}[\text{Ag}(\text{mna})]\}_n$) exhibited effective activity against Gram-negative bacteria but only modest or no activity against yeast and mold.^{6f,g} The pattern of antimicrobial-activity spectra of 1–3 with Ag–O and Ag–S (thioether) bonds is similar to that of water-soluble Ag–O bonding complexes rather than Ag–S (thiolate) complexes. The effectiveness of 1–3 is a little weaker than Ag–O bonding complexes. ¹⁰⁹Ag NMR data and ligand-exchange experiments of 3 and 4 support the fact that the ligand exchangeability of Ag–S (thioether) of silver(I) complexes is between Ag–O and Ag–S (thiolate). The relationship between the ligand-exchange ability of Ag–S (thioether) of 3 and 4 as well as 1 and 2 and antimicrobial activity supports our hypotheses that the antimicrobial activities of silver(I) complexes depend on the nature of the atom that coordinates to the silver(I) center and its bonding properties and the ease of ligand replacement. The antimicrobial activity of 4 was slightly less effective than those of complexes 1–3 with a methionine backbone. Although the bond distances and angles of 4 were normal, the molecular structure of 4 may be strained compared to those of 1–3. These results are in agreement with the fact that the ligand exchangeability of Ag–S (thioether) of silver(I) complexes is between Ag–O and Ag–S (thiolate), consistent with ¹⁰⁹Ag NMR data. Water-insoluble complex 5 showed no activities against the selected bacteria, yeasts and molds.

CONCLUSION

Water-soluble and remarkably light-stable silver(I) acetylmethioninates $\{\text{Ag}(\text{acmet})\}_n$ (1 and 2) were prepared as powder or crystals from Ag₂O and acetylmethionine in water at ambient

temperature. They were fully characterized by CHN elemental analysis, IR, solution ¹H, ¹³C, and ¹⁰⁹Ag NMR, and TG/DTA and compared to related complexes such as silver(I) methioninate (3), silver(I) S-methyl-L-cysteinate (4), and silver(I) cysteinate (5). X-ray crystallography of 1 shows that the O and S atoms of the thioether ligand coordinate to Ag^I but not N atoms. Hydrogen bonds are formed between the acetyl groups of the ligands. The properties of the neutral silver(I) complexes, 1 and 2, are much different from those of silver(I) thiolates, attributable to coordination of the O- and S- (thioether) donor atoms to Ag^I. The silver(I) acetylmethioninates showed effective antimicrobial activities against two Gram-negative bacteria and two yeasts. The remarkable light stability and water solubility and a wide spectrum of antimicrobial activities of silver(I) complexes 1 and 2, compared to those of related silver(I) complexes, indicate that the thioether and a partial ⁻OOC–C–N–C=O moiety, including the acetyl group of acmet⁻, achieve a good balance between stability and antimicrobial activities in silver(I) complexes. These silver(I) acetylmethioninates are easy to handle and would be excellent starting silver(I) materials for synthesis of more complicated metal complexes.

ASSOCIATED CONTENT

Supporting Information

Crystallographic information files (CIF format) of crystals 1, 3, and 4. This material is available free of charge via the Internet at <http://pubs.acs.org>.

■ AUTHOR INFORMATION

Corresponding Author

*Phone: 81-463-59-4111. Fax: 81-463-58-9684. E-mail: nomiya@kanagawa-u.ac.jp.

■ ACKNOWLEDGMENTS

We thank Nippon Soda Co. Ltd., Japan for financial support and also Hiroshi Yokoyama of Kanagawa University for NMR measurements.

■ REFERENCES

- (1) (a) Farrell, N. P. *Uses of Inorganic Chemistry Complexes in Medicine*; RSC: Cambridge, 1999; p 7. (b) Ahmad, S.; Isab, A. A.; Ali, S.; Al-Arfaj, A. R. *Polyhedron* **2006**, *25*, 1633–1645. (c) Farkas, E.; Sovago, I. *Amino acids, Pept. Proteins* **2006**, *35*, 353–434. (d) Gimeno, M. C.; Laguna, A. *Comprehensive Coordination Chemistry II*; Elsevier: Oxford, 2004; Vol. 6, pp 911–1091. (e) Nomiya, K.; Azumaya, I.; Chikaraishi, K. N.; Kato, T. *Curr. Top. Biochem. Res.* **2008**, *10*, 1–11. (f) Tan, S. J.; Yan, Y. K.; Lee, P. P. F.; Lim, K. H. *Future Med. Chem.* **2010**, *2*, 1591–1608. (g) Tisato, F.; Marzano, C.; Porchia, M.; Pelle, M.; Santini, C. *Med. Res. Rev.* **2010**, *30*, 708–749. (h) Lansdown, A. B. G. *Crit. Rev. Toxicol.* **2007**, *37*, 237–250. (i) Shaw, C. F. III *Chem. Rev.* **1999**, *99*, 2589–2600.
- (2) (a) Pakiari, A. H.; Jamshidi, Z. *J. Phys. Chem. A* **2007**, *111*, 14391–4396. (b) Ahang, H.; Chen, G. *Environ. Sci. Technol.* **2009**, *43*, 2905–2910.
- (3) (a) Klasen, H. J. *Burns* **2000**, *2*, 117–130. (b) Silver, S. *FEMS Microbiol. Rev.* **2003**, *27*, 341–353.
- (4) Williams, K. J.; Bax, R. P. *Curr. Opin. Invest. Drugs* **2009**, *10*, 157–163.
- (5) Arai, S.; Kubota, T.; Yabe, M.; Nomiya, K. WO 2009098850, 2009.
- (6) (a) Rowan, R.; Tallon, T.; Sheahan, A. M.; Curran, R.; McCann, M.; Kavanagh, K.; Devereux, M.; McKee, V. *Polyhedron* **2006**, *25*, 1771–1778. (b) Nomiya, K.; Takahashi, S.; Noguchi, R.; Nemoto, S.; Takayama, T.; Oda, M. *Inorg. Chem.* **2000**, *39*, 3301–3311. (c) Nomiya, K.; Yokoyama, H. *J. Chem. Soc., Dalton Trans.* **2002**, 2483–2490. (d) Nomiya, K.; Takahashi, S.; Noguchi, R. *J. Chem. Soc., Dalton Trans.* **2000**, 4369–4373. (e) Kasuga, N. C.; Yamamoto, R.; Hara, A.; Amano, A.; Nomiya, K. *Inorg. Chim. Acta* **2006**, *359*, 4412–4416. (f) Nomiya, K.; Kondoh, Y.; Kasuga, N. C.; Nagano, H.; Oda, M.; Sakuma, S. *J. Inorg. Biochem.* **1995**, *58*, 255–267. (g) Nomiya, K.; Takahashi, S.; Noguchi, R. *J. Chem. Soc., Dalton Trans.* **2000**, 2091–2097. (h) Nomiya, K.; Tsuda, K.; Sudoh, T.; Oda, M. *J. Inorg. Biochem.* **1997**, *68*, 39–44. (i) Nomiya, K.; Onoue, K.; Kondoh, Y.; Kasuga, N. C.; Nagano, H.; Oda, M.; Sakuma, S. *Polyhedron* **1995**, *14*, 1359–1367.
- (7) (a) Antti, C. J.; Lundberg, B. K. S. *Acta Chem. Scand.* **1971**, *25*, 1758–1766. (b) Masciocchi, N.; Moret, M.; Cairati, P.; Sironi, A.; Ardizzoia, G. A.; La Monica, G. *J. Chem. Soc., Dalton Trans.* **1995**, 1671–1675.
- (8) (a) Acland, C. B.; Freeman, H. C. *J. Chem. Soc. D* **1971**, 1016–1017. (b) Kirschenbaum, L. J.; Rush, J. D. *J. Am. Chem. Soc.* **1984**, *104*, 1003–1010.
- (9) (a) Feng, Q. L.; Wu, J.; Chen, G. Q.; Cui, F. Z.; Kim, T. N.; Kim, J. O. *J. Biomed. Mater. Res.* **2000**, *42*, 662–668. (b) Yamanaka, M.; Hara, K.; Kudo, J. *Appl. Environ. Microbiol.* **2004**, *71*, 7589–7593.
- (10) (a) Kasuga, N. C.; Sato, M.; Amano, A.; Hara, A.; Tsuruta, S.; Sugie, A.; Nomiya, K. *Inorg. Chim. Acta* **2008**, *361*, 1267–1273. (b) Noguchi, R.; Sugie, A.; Okamoto, Y.; Hara, A.; Nomiya, K. *Bull. Chem. Soc. Jpn.* **2005**, *78*, 1953–1962.
- (11) Xie, Y.-B.; Zhang, C.; Li, J.-R.; Bu, X.-H. *Dalton Trans.* **2004**, 562–569.
- (12) Sheldrick, G. M. *SHELXTL*, version 5.1; Siemens Analytical X-ray Instruments: Madison, WI, 1998.
- (13) McAuliffe, C. A.; Quagliano, J. V.; Vallarino, L. M. *Inorg. Chem.* **1966**, *5*, 1996–2003.
- (14) Isab, A. A.; Wazer, M. I. M. *Spectrochim. Acta, Part A* **2007**, *66*, 364–370.
- (15) (a) Wells, A. F. *Structural Inorganic Chemistry*, 4th ed.; Oxford University Press: London, 1975; p 101S. (b) Bondi, A. *J. Phys. Chem.* **1964**, *68*, 441–451.
- (16) Penner, G. H.; Liu, X. *Prog. Nucl. Magn. Reson. Spectrosc.* **2006**, *49*, 151–167.
- (17) Barreiro, E.; Casa, J. S.; Couce, M. D.; Sanchez, A.; Seoane, R.; Sordo, J.; Varela, J. M.; Vazquez-Lopez, E. M. *Dalton Trans.* **2007**, 3074–3085.

This paper is published as part of a *Dalton Transactions* themed issue entitled:

Polyoxometalates

Guest Editors: De-Liang Long and Leroy Cronin

Published in issue 33, 2012 of *Dalton Transactions*

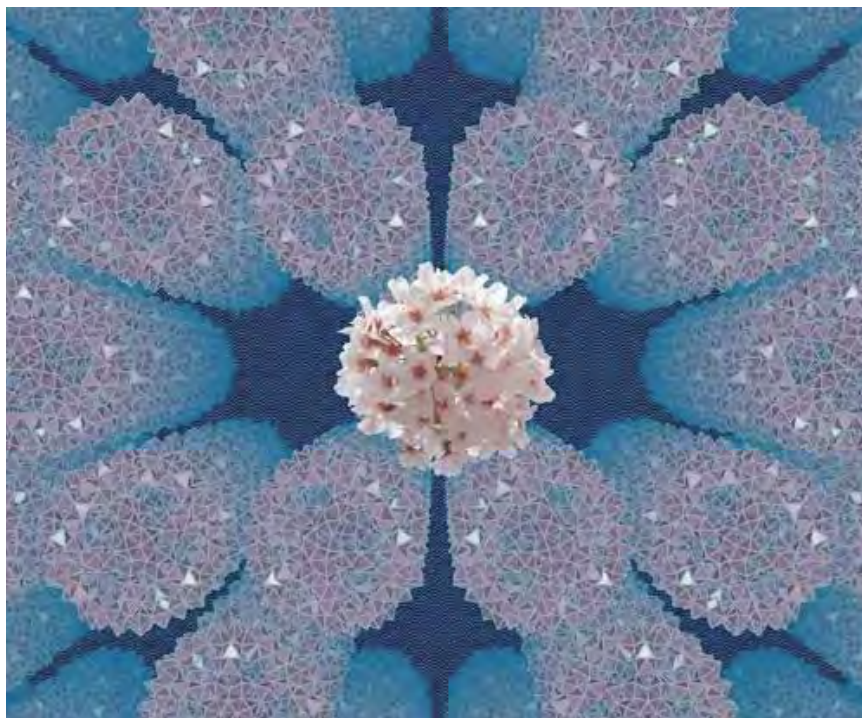


Image reproduced with permission of Tomoji Ozeki

Articles published in this issue include:

[Polyoxometalates as efficient catalysts for transformations of cellulose into platform chemicals](#)

Weiping Deng, Qinghong Zhang and Ye Wang
Dalton Trans., 2012, DOI: 10.1039/C2DT30637A

[Surfactant-encapsulated polyoxometalate building blocks: controlled assembly and their catalytic properties](#)

Amjad Nisar and Xun Wang
Dalton Trans., 2012, DOI: 10.1039/C2DT30470H

[A dodecanuclear Zn cluster sandwiched by polyoxometalate ligands](#)

Guibo Zhu, Yurii V. Geletii, Chongchao Zhao, Djamaladdin G. Musaev, Jie Song and Craig L. Hill
Dalton Trans., 2012, DOI: 10.1039/C2DT30733B

Visit the *Dalton Transactions* website for more cutting-edge inorganic research
www.rsc.org/dalton

Cite this: *Dalton Trans.*, 2012, **41**, 10085

www.rsc.org/dalton

PAPER

Novel intercluster compound between a heptakis{triphenylphosphinegold(i)}-dioxonium cation and an α -Keggin polyoxometalate anion†

Takuya Yoshida, Kenji Nomiya* and Satoshi Matsunaga

Received 25th February 2012, Accepted 1st June 2012

DOI: 10.1039/c2dt30456b

A novel intercluster compound, [$\{\{\text{Au}(\text{PPh}_3)\}_4(\mu_4\text{-O})\}\{\{\text{Au}(\text{PPh}_3)\}_3(\mu_3\text{-O})\}][\alpha\text{-PW}_{12}\text{O}_{40}]\cdot\text{EtOH}$ (**1**) constructed between a heptakis{triphenylphosphinegold(i)}dioxonium cation and an α -Keggin polyoxometalate (POM) is synthesized and unequivocally characterized by elemental analysis, TG/DTA, FTIR, X-ray crystallography, solid-state CPMAS ^{31}P NMR and solution (^1H , $^{31}\text{P}\{^1\text{H}\}$) NMR.

The heptagold(i) cluster was formed during the course of carboxylate elimination of a monomeric phosphinegold(i) carboxylate precursor, *i.e.*, $[\text{Au}(\text{RS-pyrrld})(\text{PPh}_3)]$ ($\text{RS-pyrrld} = (\text{RS})\text{-2-pyrrolidone-5-carboxylic acid}$), in the presence of the sodium salt of an α -Keggin POM, $\text{Na}_3[\alpha\text{-PW}_{12}\text{O}_{40}]\cdot 9\text{H}_2\text{O}$. Compound **1** was formed by ionic interaction between the heptagold(i) cluster cation and the α -Keggin POM anion. The heptagold(i) cluster unit was formed by four inter-cationic aurophilic interactions between the tetragold(i) cluster unit and trigold(i) cluster unit. The tetragold(i) cluster unit and trigold(i) cluster unit contained $\mu_4\text{-O}$ and $\mu_3\text{-O}$ atoms, respectively.

Introduction

Polyoxometalates (POMs) are discrete metal oxide clusters that are of current interest as soluble metal oxides and for their application in catalysis, medicine, and materials science.¹ The preparation of POM-based materials is therefore an active field of research. Some of the intriguing aspects are that a combination of POMs with cluster cations or macrocations has resulted in the formation of various interesting intercluster compounds, from the viewpoints of ionic crystals, crystal growth, crystal engineering, structure, sorption properties, and so on.^{2–4}

Some intercluster compounds have been obtained by a combination of POMs with separately prepared metal cluster cations; for example, $[\text{Au}_9(\text{PPh}_3)_8][\alpha\text{-PW}_{12}\text{O}_{40}]$,^{2a} $\text{Na}_2[\text{Cr}_3\text{O}(\text{OOCH})_6(\text{H}_2\text{O})_3][\alpha\text{-PW}_{12}\text{O}_{40}]\cdot 16\text{H}_2\text{O}$, $\text{K}_3[\text{Cr}_3\text{O}(\text{OOCH})_6(\text{H}_2\text{O})_3][\alpha\text{-SiW}_{12}\text{O}_{40}]\cdot 16\text{H}_2\text{O}$, $\text{Rb}_4[\text{Cr}_3\text{O}(\text{OOCH})_6(\text{H}_2\text{O})_3][\alpha\text{-BW}_{12}\text{O}_{40}]\cdot 16\text{H}_2\text{O}$ and $\text{Cs}_5[\text{Cr}_3\text{O}(\text{OOCH})_6(\text{H}_2\text{O})_3][\alpha\text{-CoW}_{12}\text{O}_{40}]\cdot 7.5\text{H}_2\text{O}$.⁴

Recently, we unexpectedly found clusterization of monomeric phosphinegold(i) $[\text{Au}(\text{PR}_3)]^+$ units during the course of carboxylate elimination of a monomeric phosphinegold(i) carboxylate, $[\text{Au}(\text{RS-pyrrld})(\text{PPh}_3)]$ ($\text{RS-pyrrld} = (\text{RS})\text{-2-pyrrolidone-5-carboxylic acid}$),⁵ in the presence of the free-acid form of the α -Keggin POM, $\text{H}_3[\alpha\text{-PW}_{12}\text{O}_{40}]\cdot 7\text{H}_2\text{O}$.⁶ This reaction resulted in the formation of a novel intercluster compound consisting of a

tetrakis{triphenylphosphinegold(i)}oxonium cation and an α -Keggin POM anion, *i.e.*, $[\{\{\text{Au}(\text{PPh}_3)\}_4(\mu_4\text{-O})\}_3[\alpha\text{-PW}_{12}\text{O}_{40}]]^{7+}$. The formation of such an intercluster compound was strongly dependent upon POMs with bulkiness and high-charge density. In the tetragold(i) cluster, the bridging $\mu_4\text{-O}$ atom comes from water contained in the hydrated water molecules of the POM and/or the reaction system. In relation to the present compound, the field of element-centered gold clusters, $[\text{E}(\text{AuL})_n]^{m+}$ has been extensively studied by Laguna *et al.*^{8a,b} and Schmidbaur *et al.*^{8c–i} For example, the structure of a trigold(i)oxonium cluster, $[\{\{\text{Au}(\text{PMe}_3)\}_3(\mu_3\text{-O})\}]^+$ was a new structural motif for chalcogen-centered gold clusters in that the monomeric units are aggregated through crossed edges.^{8f} In the trigold(i)-sulfonium clusters, $[\{\{\text{Au}(\text{PR}_3)\}_3(\mu_3\text{-S})\}]^+$, the steric and electronic effects of the PR_3 ligands are very similar and have the same structural consequences that the nature of the anion may also play a significant role: the $[\{\{\text{Au}(\text{PPh}_3)\}_3(\mu_3\text{-S})\}]^+$ was a monomer in the BF_4^- salt, but a dimer in the PF_6^- salt.^{8d,e}

The BF_4^- salt of the tetragold(i) cluster cation, $[\{\{\text{Au}(\text{PPh}_3)\}_4(\mu_4\text{-O})\}](\text{BF}_4)_2$ has been synthesized so far by a quite different method, *i.e.*, the reaction of tris{triarylphosphinegold(i)}-oxonium tetrafluoroborate, $[\{\{\text{Au}(\text{PR}_3)\}_3(\mu_3\text{-O})\}]\text{BF}_4^{9a,b}$ with one equivalent of a freshly prepared solution of the monomeric species, $[\text{Au}(\text{PR}_3)]\text{BF}_4$ ($\text{R} = \text{phenyl, } o\text{-tolyl}$) by the Schmidbaur's group.^{9c} It should be noted that tetragold(i) cluster cations with different counterions (BF_4^- vs. POM) have a different geometry. The tetragold(i) cluster cation with a BF_4^- counterion is a regular tetrahedral structure (T_d symmetry), while that with a POM counterion is a trigonal-pyramidal structure (C_{3v} symmetry). Thus, the latter is significantly influenced by POM anions of a larger size and higher-charge density, compared with the BF_4^- anion. Schmidbaur very recently mentions that this

Department of Chemistry (formerly Department of Materials Science), Faculty of Science, Kanagawa University, Hiratsuka, Kanagawa 259-1293, Japan. E-mail: nomiya@kanagawa-u.ac.jp

† Electronic supplementary information (ESI) available: Bond lengths (Å) of the Keggin polyoxoanion in **1** (Table S1). CCDC 867542 for **1**. For ESI and crystallographic data in CIF or other electronic format see DOI: 10.1039/c2dt30456b

distorted structure of the tetragold(i) cluster is an unexpected surprise in structural chemistry.⁸ⁱ

As to applications, several phosphinegold(i) complexes have become known as effective homogeneous catalysts for organic synthesis.¹⁰ For example, $[\{\text{Au}(\text{PPh}_3)\}_3(\mu_3\text{-O})]\text{BF}_4^{9a}$ has been used as an effective catalyst for a Claisen rearrangement of propargyl vinyl ethers,^{10,11} and such a complex has also been utilized as a precursor for the synthesis of novel metal complexes.¹² It is conceivable that the oxonium cations, $[\{\text{Au}(\text{PR}_3)\}_3(\mu_3\text{-O})]^+$ are sources of the catalytically active $[\text{Au}(\text{PR}_3)]^+$ species which can activate both the alkyne and the alkene functions.^{10e}

The POM-mediated clusterization of the monomeric phosphinegold(i) complexes provides effective synthetic routes for novel phosphinegold(i) cluster cations by a combination of the phosphinegold(i) carboxylate and the different POMs. However, the clusterization mechanism of the monomeric phosphinegold(i) unit in the presence of the free-acid form of the α -Keggin POM is still unclear. In this work, we have examined the effects of the acidity of POMs on the formation of the phosphinegold(i) cluster using the sodium salt of an α -Keggin POM, $\text{Na}_3[\alpha\text{-PW}_{12}\text{O}_{40}]\cdot 9\text{H}_2\text{O}$, and found the formation of a novel intercluster compound. Herein, we report the synthesis and characterization of a novel intercluster compound between the heptakis{triphenylphosphinegold(i)}dioxonium cluster cation and the α -Keggin POM, $[\{\{\text{Au}(\text{PPh}_3)\}_4(\mu_4\text{-O})\}\{\{\text{Au}(\text{PPh}_3)\}_3(\mu_3\text{-O})\}][\alpha\text{-PW}_{12}\text{O}_{40}]\cdot \text{EtOH}$ (**1**). This work finds that the $[\{\text{Au}(\text{PPh}_3)\}_3(\mu_3\text{-O})]^+$ cation and the $[\{\text{Au}(\text{PPh}_3)\}_4(\mu_4\text{-O})]^{2+}$ dication can be self-assembled to the $[\{\text{Au}(\text{PPh}_3)\}_7\text{O}_2]^{3+}$ trication in the presence of the sodium salt of the $[\alpha\text{-PW}_{12}\text{O}_{40}]^{3-}$ polyoxoanion. This finding is even relevant to the isolobal protic species $[\text{H}_3\text{O}]^+$ and $[\text{H}_4\text{O}]^{2+}$, which also attracts current interest.¹³

Results and discussion

Synthesis and compositional characterization

The intercluster compound between the heptakis{triphenylphosphinegold(i)}dioxonium cluster cation and the α -Keggin POM anion was obtained as **1** in 50.5% (0.249 g scale) yield. Compound **1** was prepared by a reaction based on liquid–liquid diffusion at room temperature between $[\text{Au}((RS)\text{-pyrrld})(\text{PPh}_3)]$ in CH_2Cl_2 and the sodium salt of an α -Keggin POM in a mixed $\text{EtOH}\text{-H}_2\text{O}$ solvent. Characterization was performed by CHN elemental analysis, TG/DTA, FTIR, X-ray crystallography, solid-state CPMAS ^{31}P NMR and solution (^1H and $^{31}\text{P}\{^1\text{H}\}$) NMR.

The heptagold(i) cluster was directly formed during the course of carboxylate elimination from $[\text{Au}((RS)\text{-pyrrld})(\text{PPh}_3)]$ in the presence of the sodium salt of an α -Keggin POM. This reaction occurs under the reaction space/field of the POM and is significantly influenced by POM anions of a larger size and higher-charge density. The heptagold(i) cluster and the previously reported tetragold(i) cluster⁷ were formed by an α -Keggin POM with different counter cations, *i.e.*, sodium salt and a free-acid form, respectively. The acidity of the POM contributes to the clusterization of the monomeric phosphinegold(i) unit. Compound **1** is an ionic crystal between the heptagold(i) cluster cation and the POM anion, *i.e.*, there is no direct bond between them.

The heptagold(i) cluster containing two bridged-oxygen atoms is a unique structure, and has never been reported before in phosphinegold(i) chemistry.⁸ The two bridged-oxygen atoms come from the water molecules contained in the reaction system and/or the solvated water molecules of the POM. The heptagold(i) cluster is formed only in the presence of POM. When an anion was exchanged from the polyoxoanion to BF_4^- using anion-exchange resin, the tetragold(i) cluster was formed in solution due to decomposition, but the heptagold(i) cluster itself was not found. In fact, the chemical shift observed at 25.18 ppm was in accord with the literature data of the tetragold(i) cluster cation with the BF_4^- counterion (at 25.10 ppm,⁷ 25.4 ppm^{9c}), but not with the trigold(i) cluster cation with the BF_4^- counterion (at 24.0 ppm).^{9b} This fact suggests that the heptagold(i) cluster can exist only in the presence of a POM in the solid-state and even in solution (see the section on solid-state CPMAS ^{31}P and solution $^{31}\text{P}\{^1\text{H}\}$ NMR).

The carboxylate plays only a role of a leaving group.⁷ Thus, not only pyrrolidone carboxylate, but also other carboxylates such as 5-oxotetrahydrofuran-2-carboxylate and acetylglycinate can work in the formation of phosphinegold(i) clusters in the presence of POMs.

The solid-state FTIR spectrum of **1** showed the characteristic vibrational bands based on the coordinating PPh_3 ligands. The FTIR spectrum also showed prominent vibrational bands due to the α -Keggin tungsto-POMs (1078, 977, 895 and 816 cm^{-1}).¹⁴ In this spectrum, the carbonyl vibrational bands at 1696 and 1632 cm^{-1} of the anionic (*RS*)-pyrrld ligand in $[\text{Au}((RS)\text{-pyrrld})(\text{PPh}_3)]$ disappeared, suggesting that the carboxylate ligand is eliminated. Elimination of the carboxylate ligand was also confirmed by ^1H NMR in DMSO-d_6 .

Molecular structure

X-ray crystallography of **1** showed the formation of a discrete intercluster compound between a heptakis{triphenylphosphinegold(i)}dioxonium cluster cation, $[\{\{\text{Au}(\text{PPh}_3)\}_4(\mu_4\text{-O})\}\{\{\text{Au}(\text{PPh}_3)\}_3(\mu_3\text{-O})\}]^{3+}$, and an α -Keggin POM anion. The molecular structure of **1** and the framework of the heptagold(i) cluster cation with an atom numbering scheme are shown in Fig. 1a and 1b, respectively. The heptagold(i) cluster consists of two gold(i) clusters, *i.e.*, the tetragold(i) cluster with a $\mu_4\text{-O}$ atom and the trigold(i) cluster with a $\mu_3\text{-O}$ atom (Fig. 1c). Selected bond lengths (\AA) and angles ($^\circ$) are given in Table 1.

As shown in Fig. 1b, the heptagold(i) cluster unit in **1** was formed by inter-cationic aurophilic interactions (Au2–Au5 3.1028(6) \AA , Au3–Au6 3.0936(7) \AA , Au4–Au5 3.2428(6) \AA , Au4–Au6 3.2732(7) \AA) between the tetragold(i) cluster unit and the trigold(i) cluster unit. The tetragold(i) cluster moiety, $\{\{\text{Au}(\text{PPh}_3)\}_4(\mu_4\text{-O})\}^{2+}$ had a distorted tetrahedron structure composed of three intra-cationic aurophilic interactions (Au1–Au2 3.1381(6) \AA , Au1–Au4 3.1790(7) \AA , Au2–Au3 2.9581(6) \AA) and three longer edges (Au1–Au3 3.411 \AA , Au2–Au4 3.741 \AA , Au3–Au4 3.785 \AA). The three intra-cationic aurophilic interactions (average 3.092 \AA) were longer than the Au–Au distance of metallic gold (2.88 \AA),¹⁵ but shorter than the sum of two van der Waals radii for gold (3.32 \AA).¹⁶ One encapsulated $\mu_4\text{-O}$ atom (O1) was placed within the distorted tetrahedron (Au2–O1–Au3

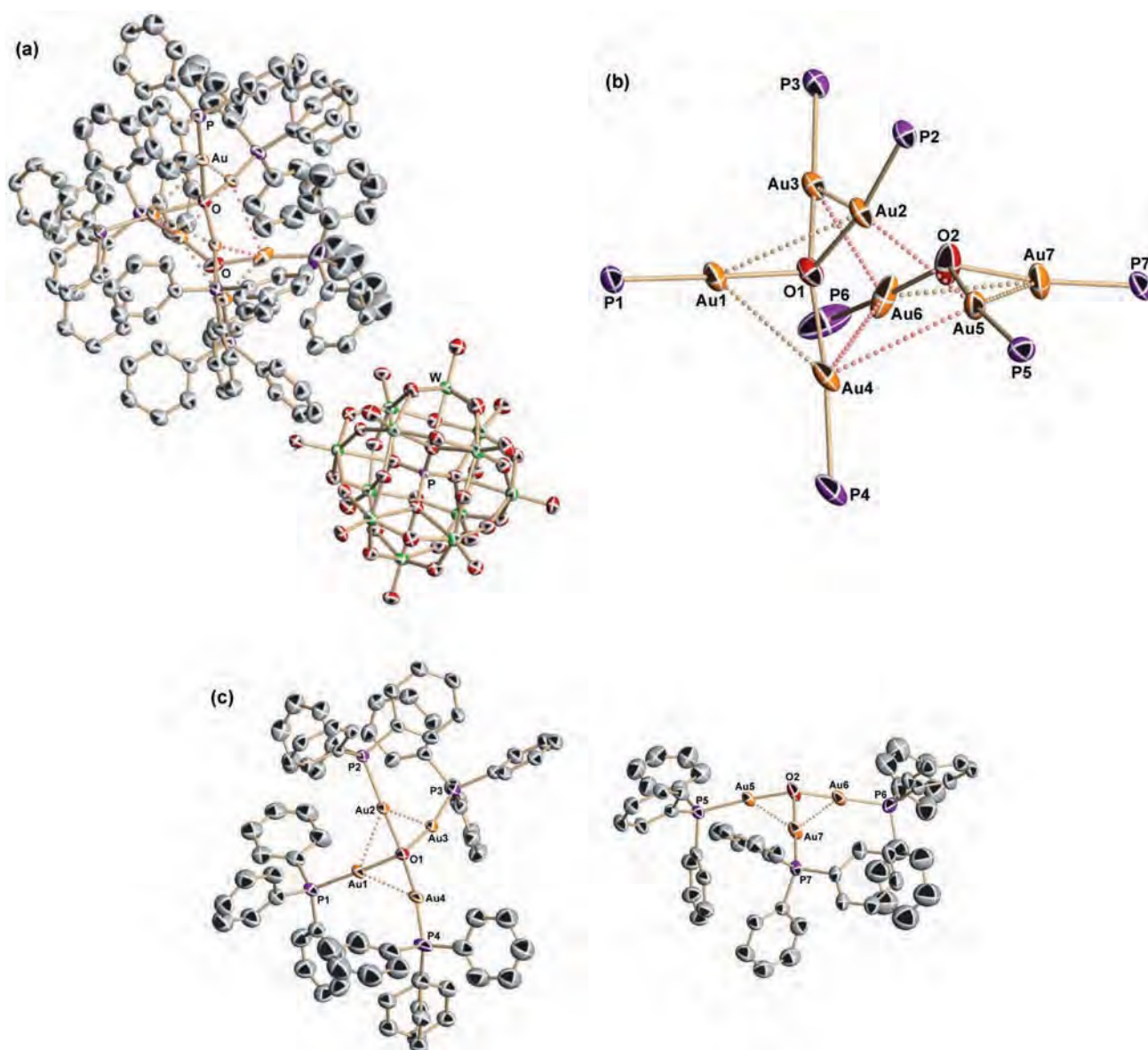


Fig. 1 (a) Molecular structure of $[\{Au(PPh_3)_4(\mu_4-O)\}\{Au(PPh_3)_3(\mu_3-O)\}][\alpha-PW_{12}O_{40}]\cdot EtOH$ (**1**), (b) the partial structure around the heptagold(i) cluster in **1** and (c) the tetragold(i) cluster unit and the trigold(i) cluster unit in the heptagold(i) cluster.

89.2(3)°, Au2–O1–Au4 127.0(4)°, Au3–O1–Au4 128.6(3)°). In the tetragold(i) cluster moiety, one of the phenyl groups was disordered. This tetragold(i) cluster moiety was different from the previously reported tetragold(i) cluster.⁷ In the present compound, an encapsulated μ_4 -O (O1) atom in the tetragold(i) cluster moiety was placed within the distorted tetrahedron, while in the previous tetragold(i) cluster, the μ_4 -O atom is in the basal plane consisting of three gold atoms. On the other hand, in the trigold(i) cluster moiety $\{Au(PPh_3)_3(\mu_3-O)\}^+$, three gold(i) atoms formed a triangular plane composed of the Au5, Au6 and Au7 atoms (Au5–Au7 3.0456(7) Å, Au6–Au7 3.0545(7) Å, Au5–Au6 3.725 Å). One μ_3 -O atom (O2) was placed out-of-plane consisting of the Au5, Au6 and Au7 atoms (Au5–O2–Au6 133.2(5)°, Au5–O2–Au7 97.4(3)°, Au6–O2–Au7 96.7(4)°). In the trigold(i) cluster cation with the BF_4^- counterion, *i.e.*, $[Au(PPh_3)_3(\mu_3-O)]_2(BF_4)_2$ reported as a dimeric form in the

solid-state,^{9a} three gold(i) atoms were arranged in a triangle by three aurophilic interactions (3.032(7) Å, 3.034(7) Å, 3.215(6) Å), and one μ_3 -O atom was placed out-of-plane (Au–O–Au angles 99(3)°, 103(3)°, 108(3)°). In the present trigold(i) cluster moiety, one length (Au5–Au6 3.725 Å) of the triangle formed by three gold(i) atoms was longer than that (3.215(6) Å) of the trigold(i) cluster cation with the BF_4^- counterion, and the present μ_3 -O atom (O2) located closer to the triangle plane. The trigold(i) cluster cation with the BF_4^- counterion existed as a dimeric form in the solid-state,^{9a} while the present trigold(i) cluster moiety with the POM was formed as a part of the heptagold(i) cluster. Therefore, the structure of the trigold(i) cluster moiety is essentially different.

The molecular structure of the α -Keggin POM anion, $[\alpha-PW_{12}O_{40}]^{3-}$ as a counterion in **1**, was identical with that of

Table 1 Selected bond lengths (Å) and angles (°) around the heptagold(i) cluster in **1**

Lengths			
Au(1)–O(1)	2.054(7)	Au(5)–O(2)	2.013(8)
Au(2)–O(1)	2.097(7)	Au(6)–O(2)	2.047(9)
Au(3)–O(1)	2.116(7)	Au(7)–O(2)	2.040(8)
Au(4)–O(1)	2.084(8)	Average	2.064
Au(1)–P(1)	2.220(3)	Au(5)–P(5)	2.217(3)
Au(2)–P(2)	2.230(3)	Au(6)–P(6)	2.204(4)
Au(3)–P(3)	2.220(3)	Au(7)–P(7)	2.219(3)
Au(4)–P(4)	2.218(3)	Average	2.218
Au(1)–Au(2)	3.1381(6)	Au(4)–Au(5)	3.2428(6)
Au(1)–Au(4)	3.1790(7)	Au(4)–Au(6)	3.2732(7)
Au(2)–Au(3)	2.9581(6)	Au(5)–Au(7)	3.0456(7)
Au(2)–Au(5)	3.1028(6)	Au(6)–Au(7)	3.0545(7)
Au(3)–Au(6)	3.0936(7)	Average	3.1209
Angles			
Au(2)–O(1)–Au(3)	89.2(3)	Au(5)–O(2)–Au(6)	133.2(5)
Au(2)–O(1)–Au(4)	127.0(4)	Au(5)–O(2)–Au(7)	97.4(3)
Au(3)–O(1)–Au(4)	128.6(3)	Au(6)–O(2)–Au(7)	96.7(4)

previously reported POMs.¹⁷ The W–O bond lengths of the α -Keggin units were in the normal range (Table S1†).^{1b,17}

Solid-state CPMAS ³¹P and solution ³¹P{¹H} NMR

The solid-state CPMAS ³¹P NMR spectrum (Fig. 2a) of **1** showed two broad signals at –14.2 and 24.6 ppm due to the α -Keggin POM and PPh₃ groups of the heptagold(i) cluster, respectively. The peak at 24.6 ppm due to the PPh₃ groups is observed as one broad signal, because all PPh₃ groups are in an approximately equivalent state, but they are not fluxional in the solid-state. The three broad signals of the tetragold(i) cluster cation with the POM counterion (Fig. 2b) were assignable to the heteroatom phosphorus in the α -Keggin POM anion (–14.6 ppm) and the two nonequivalent phosphorus atoms (15.3, 25.8 ppm) due to the PPh₃ groups in the distorted tetrahedron of the tetragold(i) cluster cation.⁷ The solution ³¹P{¹H} NMR spectrum (Fig. 2c) of **1** in DMSO-d₆ showed two sharp signals at –14.92 and 24.46 ppm. The peak at –14.92 ppm is assignable to the heteroatom phosphorus in the α -Keggin POM. The other peak at 24.46 ppm is an averaged signal of PPh₃ groups due to fluxional motion in the solution of the heptagold(i) cluster, which corresponds to the solid-state broad signal at 24.6 ppm. Probably the heptagold(i) cluster would be present in solution only in the presence of the POM, *i.e.*, it cannot exist without the POM. The solution ³¹P{¹H} NMR signal at 24.46 ppm slightly shifted to a higher field from the single signal observed at 24.84 ppm of the tetragold(i) cluster in solution (Fig. 2d).⁷ In general, the ³¹P NMR signals of phosphinegold(i) clusters are observed in the higher field in comparison with that of the precursor, [Au(*RS*)-pyrrid](PPh₃) at 27.61 ppm in CDCl₃.

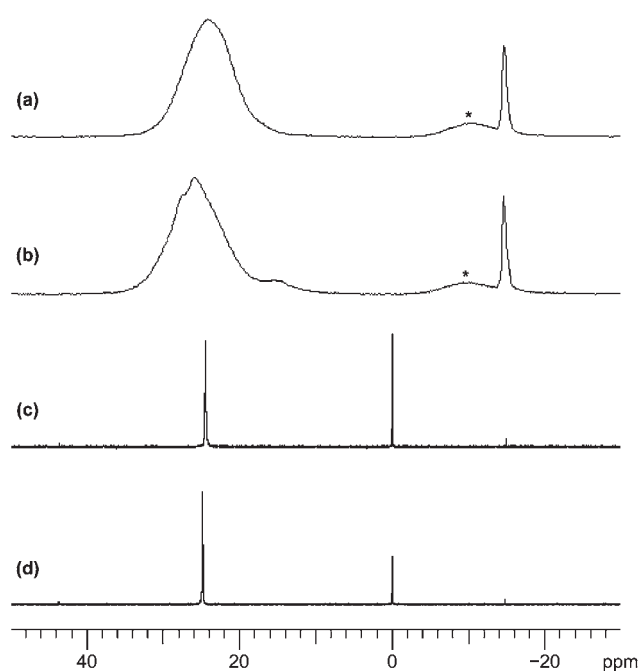


Fig. 2 Solid-state CPMAS ³¹P NMR spectra of (a) **1** and (b) the tetragold(i) cluster,⁷ and solution ³¹P{¹H} NMR spectra in DMSO-d₆ of (c) **1** and (d) the tetragold(i) cluster.⁷ Broad signals denoted by asterisks in the higher field are due to spinning sidebands.

Conclusion

Pale-yellow, block crystals of novel, ionic intercluster compound, [{ { Au(PPh₃)₄(μ_4 -O) } { { Au(PPh₃)₃(μ_3 -O) } }] [α -PW₁₂O₄₀] · EtOH (**1**) were obtained in 50.5% yield by the liquid–liquid diffusion method of a 1 : 7 molar-ratio reaction system of Na₃[α -PW₁₂O₄₀] · 9H₂O and [Au(*RS*)-pyrrid](PPh₃) in CH₂Cl₂ in a solvent mixture of EtOH–H₂O (2 : 1). The heptaphosphinegold(i) cluster species in **1** has never been reported before in phosphinegold(i) chemistry. The formation of **1** significantly depends upon the POM and, in particular, the acidity of [α -PW₁₂O₄₀]³⁻ plays an important role in the clusterization of the monomeric [Au(PPh₃)₃]⁺ unit; the sodium salt of the POM provides the heptagold(i) cluster, while the free-acid form of the POM gives the tetragold(i) cluster.⁷ The heptagold(i) cluster unit, composed of the tetragold(i) cluster unit and the trigold(i) cluster unit, possessed the bridged-oxygen atoms, μ_4 -O and μ_3 -O, respectively, which came from water molecules contained in the reaction system and/or solvated water molecules in the POM. It should be noted that the heptagold(i) cluster can exist only in the presence of a POM in the solid-state and even in solution. In this work, formation of the novel phosphinegold(i) cluster was anticipated by a combination of the phosphinegold(i) carboxylate precursor and a POM with different acidity and charge density. Research in this direction is in progress.

Experimental

Materials

The following reactants were used as received: EtOH, CH₂Cl₂, Et₂O (all from Wako); DMSO-d₆ (Isotec). As for the α -Keggin

POM, $\text{Na}_3[\alpha\text{-PW}_{12}\text{O}_{40}]\cdot 9\text{H}_2\text{O}$ was synthesized according to the literature⁶ and identified by FTIR, TG/DTA and solution ^{31}P NMR spectroscopy. The phosphinegold(i) carboxylate, $[\text{Au}((RS)\text{-pyrrld})(\text{PPh}_3)]$ was synthesized according to the literature⁵ and identified by CHN elemental analysis, FTIR, TG/DTA and solution (^1H , $^{13}\text{C}\{^1\text{H}\}$ and $^{31}\text{P}\{^1\text{H}\}$) NMR spectroscopy.

Instrumentation and analytical procedures

CHN elemental analyses were carried out with a Perkin-Elmer 2400 CHNS Elemental Analyzer II (Kanagawa University). IR spectra were recorded on a Jasco 4100 FT-IR spectrometer in KBr disks at room temperature. Thermogravimetric and differential thermal analyses (TG/DTA) were acquired using a Rigaku Thermo Plus 2 series TG/DTA TG 8120 instrument.

^1H NMR (500.00 MHz) and $^{31}\text{P}\{^1\text{H}\}$ NMR (202.00 MHz) spectra in a DMSO- d_6 solution were recorded in 5 mm outer diameter tubes on a JEOL JNM-ECP 500 FT-NMR spectrometer with a JEOL ECP-500 NMR data processing system. The ^1H NMR spectra were referenced to an internal standard of tetramethylsilane (SiMe_4). The $^{31}\text{P}\{^1\text{H}\}$ NMR spectra were referenced to an external standard of 25% H_3PO_4 in H_2O in a sealed capillary. The ^{31}P NMR data with the usual 85% H_3PO_4 reference are shifted to +0.544 ppm from our data.

Solid-state cross-polarization magic-angle-spinning (CPMAS) ^{31}P NMR (121.00 MHz) spectra were recorded in 6 mm outer diameter rotors on a JEOL JNM-ECP 300 FT-NMR spectrometer with a JEOL ECP-300 NMR data processing system. This spectrum was referenced to an external standard ($\text{NH}_4\text{H}_2\text{PO}_4$ (δ 1.60)).

Synthesis

$\{[\text{Au}(\text{PPh}_3)_4(\mu_4\text{-O})]\{[\text{Au}(\text{PPh}_3)_3(\mu_3\text{-O})]\}[\alpha\text{-PW}_{12}\text{O}_{40}]\cdot \text{EtOH}$ (**1**). $[\text{Au}((RS)\text{-pyrrld})(\text{PPh}_3)]$ (0.329 g, 0.560 mmol) was dissolved in 40 mL of CH_2Cl_2 . A clear solution of $\text{Na}_3[\alpha\text{-PW}_{12}\text{O}_{40}]\cdot 9\text{H}_2\text{O}$ (0.249 g, 0.080 mmol) dissolved in 60 mL of an $\text{EtOH}\text{-H}_2\text{O}$ (2 : 1, v/v) mixed solvent was slowly added along an interior wall of a round-bottom flask containing a colorless clear solution of the gold(i) complex. The round-bottom flask containing two layers, *i.e.*, the gold(i) complex solution in the lower layer and the POM solution in the upper layer, was sealed and left in the dark at room temperature. After 5 days, pale-yellow, clear block crystals formed around the interface of the two layers, which were collected on a membrane filter (JG 0.2 μm), washed with EtOH (20 mL \times 2) and Et_2O (20 mL \times 2), and dried *in vacuo* for 2 h. Yield: 0.249 g (50.5%). The crystalline samples were soluble in DMSO and DMF, but insoluble in H_2O , EtOH and Et_2O . Found: C, 24.97; H, 1.39%. Calc. for $\text{C}_{128}\text{H}_{111}\text{O}_{43}\text{P}_8\text{Au}_7\text{W}_{12}$ or $\{[\text{Au}(\text{PPh}_3)_4(\mu_4\text{-O})]\{[\text{Au}(\text{PPh}_3)_3(\mu_3\text{-O})]\}[\alpha\text{-PW}_{12}\text{O}_{40}]\cdot \text{EtOH}$: C, 24.92; H, 1.81%. TG/DTA under atmospheric conditions: a weight loss of 1.05% due to desorption of EtOH was observed at below 213.7 $^\circ\text{C}$; calc. 0.75% for 1 EtOH molecule. IR (KBr): 1479 w, 1436 s, 1183 vw, 1101 m, 1078 s, 977 vs, 895 s, 816 vs, 742 s, 711 m, 689 s, 538 m, 508 s cm^{-1} . Solid-state CPMAS ^{31}P NMR: δ -14.2, 24.6. $^{31}\text{P}\{^1\text{H}\}$ NMR (24.5 $^\circ\text{C}$, DMSO- d_6): δ -14.92, 24.46. ^1H NMR (23.6 $^\circ\text{C}$, DMSO- d_6): δ 1.09 (t, J = 7.1,

$\text{CH}_3\text{CH}_2\text{OH}$ solvate), 3.39 (q, J = 7.0, $\text{CH}_3\text{CH}_2\text{OH}$ solvate), 7.31–7.51 (m, PPh_3).

X-ray crystallography

A pale-yellow, clear block crystal (0.21 \times 0.20 \times 0.16 mm^3) was surrounded by liquid paraffin to prevent its degradation. Data collection was done by a Bruker SMART APEX CCD diffractometer at 90 K in the range of $0.95^\circ < \theta < 27.50^\circ$. The intensity data were automatically collected for Lorentz and polarization effects during integration. The structure was solved by direct methods (program SHELXS-97)^{18a} followed by subsequent difference Fourier calculation and refined by a full-matrix, least-squares procedure on F^2 (program SHELXL-97).^{18b} Absorption correction was performed with SADABS (empirical absorption correction).^{18c} The composition and formula containing the solvated molecule were determined by CHN elemental analysis, TG/DTA and ^1H NMR. Solvent molecules (EtOH) in the structure were highly disordered and impossible to refine by using conventional discrete-atom models. To resolve these issues, the contribution of the solvent electron density was removed by using the SQUEEZE routine in PLATON.¹⁹ In the refinement, the restraint command 'isor' and 'simu' were employed to keep thermal parameters reasonable. This command led to the restraint number 5154 for the compounds.

Crystal data. $\text{C}_{128}\text{H}_{111}\text{Au}_7\text{O}_{43}\text{P}_8\text{W}_{12}$, M = 6169.89, monoclinic, space group $P2(1)/n$, a = 16.2752(14), b = 39.606(3), c = 25.931(2) \AA , β = 99.623(2) $^\circ$, V = 16 480(2) \AA^3 , Z = 4, D_c = 2.487 Mg m^{-3} , $\mu(\text{Mo-K}\alpha)$ = 14.683 mm^{-1} . R_1 = 0.0660, wR_2 = 0.1279 (for all data). R_{int} = 0.0596, R_1 = 0.0496, wR_2 = 0.1213, GOF = 1.049 (156 542 total reflections, 37 798 unique reflections where $I > 2\sigma(I)$). The maximum and minimum residual density (+7.472 and -7.807 e \AA^{-3}) holes were located at 0.74 \AA from Au(6) and 0.78 \AA from Au(6), respectively. The Keggin polyoxoanion consisting of 12 tungsten atoms, one phosphorus atom, 40 oxygen atoms, and a gold(i) cluster cation consisting of 7 gold atoms, 7 phosphorus atoms, 126 carbon atoms, 105 hydrogen atoms and 2 bridged-oxygen atoms, per formula unit, were identified, but the location of one solvated EtOH molecule per formula unit was not determined as a result of disorder. CCDC 867542.†

Acknowledgements

This work was supported by a Grant-in-Aid for Scientific Research (C) No. 22550065 from the Ministry of Education, Culture, Sports, Science and Technology, Japan.

References

- (a) M. T. Pope and A. Müller, *Angew. Chem., Int. Ed. Engl.*, 1991, **30**, 34; (b) M. T. Pope, *Heteropoly and Isopoly Oxometalates*, Springer-Verlag, New York, 1983; (c) V. W. Day and W. G. Klemperer, *Science*, 1985, **228**, 533; (d) C. L. Hill, *Chem. Rev.*, 1998, **98**, 1; (e) T. Okuhara, N. Mizuno and M. Misono, *Adv. Catal.*, 1996, **41**, 113; (f) C. L. Hill and C. M. Prosser-McCarthy, *Coord. Chem. Rev.*, 1995, **143**, 407; (g) M. T. Pope, Polyoxo Anions: Synthesis and Structure, in *Comprehensive Coordination Chemistry II*, ed. A. G. Wedd, Elsevier Science, New York, 2004, vol. 4, p. 635; (h) C. L. Hill, Polyoxometalates:

- Reactivity, in *Comprehensive Coordination Chemistry II*, ed. A. G. Wedd, Elsevier Science, New York, 2004, vol. 4, p. 679.
- 2 (a) M. Schulz-Dobrick and M. Jansen, *Eur. J. Inorg. Chem.*, 2006, 4498; (b) M. Schulz-Dobrick and M. Jansen, *Z. Anorg. Allg. Chem.*, 2007, **633**, 2326.
 - 3 (a) Q.-G. Zhai, X.-Y. Wu, S.-M. Chen, Z.-G. Zhao and C.-Z. Lu, *Inorg. Chem.*, 2007, **46**, 5046; (b) Y.-F. Song, H. Abbas, C. Ritchie, N. McMillian, D.-L. Long, N. Gadegaard and L. Cronin, *J. Mater. Chem.*, 2007, **17**, 1903.
 - 4 (a) N. Mizuno and S. Uchida, *Chem. Lett.*, 2006, **35**, 688; (b) S. Uchida, R. Kawamoto and N. Mizuno, *Inorg. Chem.*, 2006, **45**, 5136; (c) S. Uchida and N. Mizuno, *Coord. Chem. Rev.*, 2007, **251**, 2537; (d) Y. Ogasawara, S. Uchida and N. Mizuno, *J. Phys. Chem. C*, 2007, **111**, 8218; (e) A. Lesbani, R. Kawamoto, S. Uchida and N. Mizuno, *Inorg. Chem.*, 2008, **47**, 3349; (f) S. Uchida, A. Lesbani, Y. Ogasawara and N. Mizuno, *Inorg. Chem.*, 2012, **51**, 775.
 - 5 R. Noguchi, A. Hara, A. Sugie and K. Nomiya, *Inorg. Chem. Commun.*, 2006, **9**, 355. The representation of H₂pyrrld is changed to Hpyrrld; thus, the formulation of [Au((RS)-Hpyrrld)(PPh₃)] used so far is also changed to [Au((RS)-pyrrld)(PPh₃)].
 - 6 S. Aoki, T. Kurashina, Y. Kasahara, T. Nishijima and K. Nomiya, *Dalton Trans.*, 2011, **40**, 1243; See ESI†
 - 7 K. Nomiya, T. Yoshida, Y. Sakai, A. Nanba and S. Tsuruta, *Inorg. Chem.*, 2010, **49**, 8247.
 - 8 (a) F. Canales, C. Gimeno, A. Laguna and M. D. Villacampa, *Inorg. Chim. Acta*, 1996, **244**, 95; (b) M. C. Gimeno and A. Laguna, *Chem. Soc. Rev.*, 2008, **37**, 1952; (c) E. Zeller, H. Beruda, A. Kolb, P. Bissinger, J. Riede and H. Schmidbaur, *Nature*, 1991, **352**, 141; (d) H. Schmidbaur, A. Kolb, E. Zeller, A. Schier and H. Beruda, *Z. Anorg. Allg. Chem.*, 1993, **619**, 1575; (e) K. Angermaier and H. Schmidbaur, *Chem. Ber.*, 1994, **127**, 2387; (f) K. Angermaier and H. Schmidbaur, *Inorg. Chem.*, 1994, **33**, 2069; (g) H. Schmidbaur, *Z. Naturforsch., B: J. Chem. Sci.*, 2008, **63**, 853; (h) H. Schmidbaur and A. Schier, *Chem. Soc. Rev.*, 2008, **37**, 1931; (i) H. Schmidbaur and A. Schier, *Chem. Soc. Rev.*, 2012, **41**, 370.
 - 9 (a) A. N. Nesmeyanov, E. G. Perevalova, Y. T. Struchkov, M. Y. Antipin, K. I. Grandberg and V. P. Dyadchenko, *J. Organomet. Chem.*, 1980, **201**, 343; (b) Y. Yang, V. Ramamoorthy and P. R. Sharp, *Inorg. Chem.*, 1993, **32**, 1946; (c) H. Schmidbaur, S. Hofreiter and M. Paul, *Nature*, 1995, **377**, 503.
 - 10 (a) A. Fürstner and P. W. Davies, *Angew. Chem., Int. Ed.*, 2007, **46**, 3410; (b) A. S. K. Hashmi, *Chem. Rev.*, 2007, **107**, 3180; (c) E. Jiménez-Núñez and A. M. Echavarren, *Chem. Rev.*, 2008, **108**, 3326; (d) D. J. Gorin, B. D. Sherry and F. D. Toste, *Chem. Rev.*, 2008, **108**, 3351; (e) H. Schmidbaur and A. Schier, *Z. Naturforsch., B: J. Chem. Sci.*, 2011, **66**, 329.
 - 11 (a) B. D. Sherry and F. D. Toste, *J. Am. Chem. Soc.*, 2004, **126**, 15978; (b) K. Sakaguchi, T. Okada, T. Shinada and Y. Ohfuné, *Tetrahedron Lett.*, 2008, **49**, 25; (c) P. Mauleón, J. L. Krinsky and F. D. Toste, *J. Am. Chem. Soc.*, 2009, **131**, 4513.
 - 12 (a) A. Blumenthal, H. Beruda and H. Schmidbaur, *J. Chem. Soc., Chem. Commun.*, 1993, 1005; (b) A. Singh, U. Anandhi, M. A. Cinellu and P. R. Sharp, *Dalton Trans.*, 2008, 2314; (c) A. Singh and P. R. Sharp, *Inorg. Chim. Acta*, 2008, **361**, 3159.
 - 13 (a) H. G. Raubenheimer and H. Schmidbaur, *Organometallics*, 2012, **31**, 2507; (b) E. S. Stoyanov, G. Gunbas, N. Hafezi, M. Mascal, I. V. Stoyanova, F. S. Tham and C. A. Reed, *J. Am. Chem. Soc.*, 2012, **134**, 707.
 - 14 (a) C. Rocchiccioli-Deltcheff, R. Thouvenot and R. Franck, *Spectrochim. Acta*, 1976, **32A**, 587; (b) C. Rocchiccioli-Deltcheff, M. Fournier, R. Franck and R. Thouvenot, *Inorg. Chem.*, 1983, **22**, 207; (c) R. Thouvenot, M. Fournier, R. Franck and C. Rocchiccioli-Deltcheff, *Inorg. Chem.*, 1984, **23**, 598.
 - 15 A. F. Wells, *Structural Inorganic Chemistry*, Clarendon Press, Oxford, 4th edn, 1975, p. 1020.
 - 16 A. Bondi, *J. Phys. Chem.*, 1964, **68**, 441.
 - 17 (a) G. M. Brown, M.-R. Noe-Spirlet, W. R. Busing and H. A. Levy, *Acta Crystallogr., Sect. B: Struct. Crystallogr. Cryst. Chem.*, 1977, **33**, 1038; (b) G. J. Kearley, H. A. Pressman and R. C. T. Slade, *J. Chem. Soc., Chem. Commun.*, 1986, 1801; (c) M.-R. Noe-Spirlet and W. R. Busing, *Acta Crystallogr., Sect. B: Struct. Crystallogr. Cryst. Chem.*, 1978, **34**, 907; (d) M.-R. Noe-Spirlet, G. M. Brown, W. R. Busing and H. A. Levy, *Acta Crystallogr., Sect. A: Cryst. Phys., Diffr., Theor. Gen. Crystallogr.*, 1975, **31**, S80.
 - 18 (a) G. M. Sheldrick, *SHELXS-97, Program for solution of crystal structures*, University of Göttingen, Germany, 1997; (b) G. M. Sheldrick, *SHELXL-97, Program for refinement of crystal structures*, University of Göttingen, Germany, 1997; (c) G. M. Sheldrick, *SADABS, Program for area detector adsorption correction*, Institute for Inorganic Chemistry, University of Göttingen, Germany, 1996.
 - 19 A. L. Spek, *Acta Crystallogr., Sect. A: Found. Crystallogr.*, 1990, **46**, C34.

Characterization of nickel(II)-acylperoxo species relevant to catalytic alkane hydroxylation by nickel complex with *m*CPBA†

Cite this: *Dalton Trans.*, 2013, **42**, 3346

Shiro Hikichi,^{*a} Kento Hanaue,^a Takako Fujimura,^a Hideho Okuda,^a Jun Nakazawa,^a Yoshiko Ohzu,^b Chiho Kobayashi^b and Munetaka Akita^b

Nickel complexes with hydrotris(pyrazolyl)borate (= Tp^R) ligands catalyze alkane oxidation with organic peroxide *meta*-Cl-C₆H₄C(=O)OOH (= *m*CPBA). The electronic and steric hindrance properties of Tp^R affect the catalyses. The complex with an electron-withdrawing group containing a less-hindered ligand, that is, Tp^{Me₂,Br}, exhibits higher alcohol selectivity. Higher selectivity for secondary over tertiary alcohols upon oxidation of methylcyclohexane indicates that the oxygen atom transfer reaction proceeds within the coordination sphere of the nickel centers. A reaction of the catalyst precursor, dinuclear nickel(II)-bis(μ-hydroxo) complexes, with *m*CPBA yields the corresponding nickel(II)-acylperoxo species, as have been characterized by spectroscopy. Thermal decomposition of the nickel(II)-acylperoxo species in CH₂Cl₂ yields the corresponding nickel(II)-chlorido complexes through Cl atom abstraction. Employment of the brominated ligand increases the thermal stability of the acylperoxo species. Kinetic isotope effects observed on decay of the nickel(II)-acylperoxo species indicate concerted O–O breaking of the nickel-bound acylperoxide and H-abstraction from the solvent molecule.

Received 11th October 2012,
Accepted 19th November 2012

DOI: 10.1039/c2dt32419a

www.rsc.org/dalton

Introduction

Selective partial oxidation of alkanes to the corresponding alcohols is an important fundamental chemical transformation.¹ In order to achieve high alcohol selectivity, a free radical-contributed reaction should be prevented because as such reaction will give a mixture of alcohol and the corresponding over-oxidized product (*i.e.* ketone or aldehyde) through the Russel termination mechanism.^{2,3} It therefore remains important to design catalysts that provide a metal-based oxidant showing alkane hydroxylation activity. The most considerable metal-based oxidants are high-valent metal-oxo (or metal-oxyl radical) species. Metal-peroxo species, LM–OO–Z (where L denotes a metal supporting ligand, Z = none, H, alkyl, acyl, metal), are also possible candidates for the metal-based oxidants. Moreover, these species are promising precursors for the metal-oxo species produced by O–O bond activation under mild conditions.⁴

Recently, some experimental^{5–9} and theoretical^{10,11} investigations have revealed the alkane hydroxylation potential of active oxygen complexes of nickel. One of the interesting findings is the selective hydroxylation of cyclohexane catalyzed by nickel(II) complexes with *m*CPBA explored by Itoh and co-workers.^{5a–c} In addition, Balamurugan *et al.* have reported similar catalytic alkane hydroxylation by a series of nickel(II) complexes with *m*CPBA.^{5d} The correlation between the structures of the metal-supporting ligands (shown in Fig. 1) and the catalytic activities of the resulting nickel(II) complexes has been revealed. During the catalytic process, homolytic O–O bond rupture of a putative nickel(II)-acylperoxo intermediate occurs, as has been evidenced by the formation of chlorobenzene from *m*CPBA. Although no reaction intermediates have been detected in these catalytic systems, a related mononuclear nickel(III)-oxygen (oxo and hydroxo) species that is formed through the reaction of the Ni(II) precursor with *m*CPBA has very recently been characterized.⁶

In this study, hydrotris(3,5-dialkyl-4-X-pyrazolyl)borates, Tp^{R₂,X} where R = Me or *i*Pr and X = H or Br (when X = H, H is omitted in the abbreviation shown as Tp^{R₂}; the abbreviation system follows that in the literature:¹² see Fig. 1), have been employed as the nickel-supporting scaffold. The advantage of Tp^{R₂,X} is structural and electronic controllability.¹² In particular, substituent groups on the distal fourth position of the pyrazolyl groups affect the electronic nature of the resulting Tp^{R₂,X}

^aDepartment of Material and Life Chemistry, Faculty of Engineering, Kanagawa University, 3-27-1 Rokkakubashi, Kanagawa-ku, Yokohama 221-8686, Japan.
E-mail: hikichi@kanagawa-u.ac.jp; Fax: +81-45-413-9770

^bChemical Resources Laboratory, Tokyo Institute of Technology, 4259 Nagatsuta, Midori-ku, Yokohama 226-8503, Japan

†Electronic supplementary information (ESI) available. See DOI: 10.1039/c2dt32419a

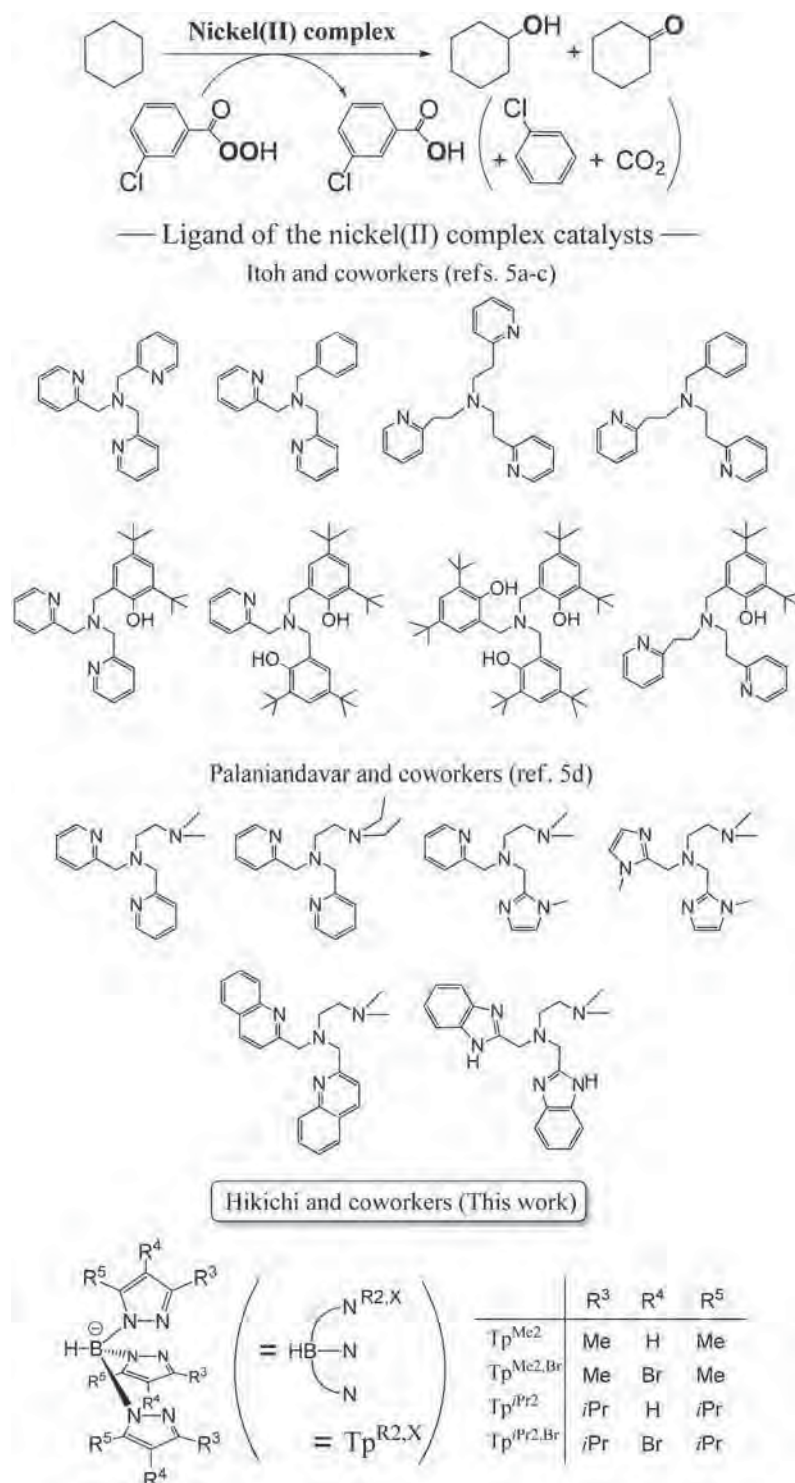


Fig. 1 Cyclohexane oxygenation by the Ni–*m*CPBA system and the ligands used as the support for nickel.

complex, although the structural environment around the metal center is almost the same as that of the prototype compound where X = H. Such electronic tuning leads to control of the stability and reactivity of the nickel(II)-alkylperoxo species.¹³ This strategy is expected to provide insight into the catalytic alkane hydroxylation mechanism of the nickel(II)-

*m*CPBA system. As reported herein, we have explored the catalyses of the Tp^{R²,X} supported nickel(II) complexes toward cyclohexane oxygenation with *m*CPBA. Notably, we have succeeded in detecting thermally unstable nickel(II)-acylperoxo species formed by reaction of the dinuclear nickel(II)-bis-(μ-hydroxo) complexes, [(Ni^{II}Tp^{R²,X})₂(μ-OH)₂] (**1**^X where R = Me

and 1^X where R = iPr, respectively),^{8e,13,14} with *m*CPBA. Product analyses and kinetic studies of the thermal decomposition process of the nickel(II)-acylperoxo species provide insights into the alkane hydroxylation mechanism through the O–O activation process.

Results and discussion

Correlation between catalytic activity and the nature of the metal-supporting ligands

Prior to characterization of a putative nickel(II)-acylperoxo intermediate, trends in cyclohexane oxygenation catalyses of the $\text{Tp}^{\text{R}2,\text{X}}$ -supported nickel complexes were explored (Table 1). The catalysts derived from 1^X , of which the metal-supporting ligands were the less hindered $\text{Tp}^{\text{Me}2,\text{X}}$, yielded the alcohol as the major product. The more hindered $\text{Tp}^{\text{iPr}2,\text{X}}$ ligand analogues 1^X did not exhibit such catalytic activity even in the large excess substrate reaction. In contrast, the alkylperoxo-nickel(II) complex $[\text{Ni}^{\text{II}}(\text{OO}t\text{Bu})\text{Tp}^{\text{iPr}2}]$ can catalyze the oxygenation of cyclohexane with *tert*-butylhydrogenperoxide, but the major product is cyclohexanone because the free-radical reaction occurs predominantly.⁷ As reported previously by Nam and coworkers, a simple nickel(II) salt (an MeCN solution of $\text{Ni}(\text{ClO}_4)_2$) cannot catalyze cyclohexane oxidation with *m*CPBA.¹⁵ Therefore, the catalytic hydroxylation activity of nickel emerges from employment of the appropriate ligands controlling the generation of a metal-based oxidant. In the case of the tris(pyridylmethyl)amine (TPA) ligand system, a cobalt catalyst exhibits selective hydroxylation activity similar

to that of the nickel catalyst.^{5a} Moreover, a cobalt–porphyrinato complex as well as a cobalt–perchlorate salt catalyze cyclohexane hydroxylation with *m*CPBA.^{15,16} In contrast, the cobalt(II) analogues of 1^X were almost inactive under the examined reaction conditions. These findings imply that the combination of a central metal ion and its supporting ligand is dominant.

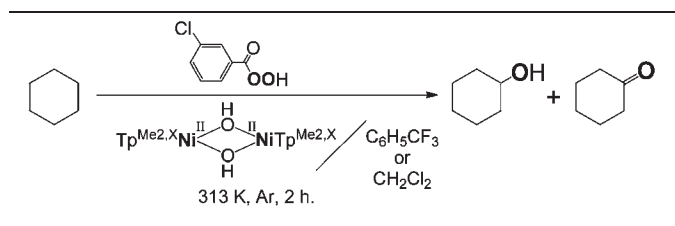
The electron-withdrawing bromine-containing $\text{Tp}^{\text{Me}2,\text{Br}}$ ligand catalyst 1^{Br} showed a higher alcohol yield than that of the non-brominated ligand catalyst 1^{H} when the reaction proceeded in $\text{CF}_3\text{C}_6\text{H}_5$ (Fig. S4†). In the reaction of the mixture of a large excess of substrate and a small amount of CH_2Cl_2 as a solvent for *m*CPBA, an extremely high *A/K* value (= 53) was achieved by 1^{Br} . In this reaction condition, TON of 1^{Br} reached 42 (theoretical maximum is 50). The less electron-withdrawing ligand catalyst 1^{H} exhibited somewhat a higher TON (= 46) but a lower *A/K* (= 32) (Fig. 2).

The formation of chlorobenzene ($\text{C}_6\text{H}_5\text{Cl}$) indicated that homolytic O–O bond cleavage of a putative nickel(II)-acylperoxo intermediate occurred in the present oxidation process.^{5b,d} In the reactions of large excess substrate (entries 3 and 4 in Table 1), 57 μmol of $\text{C}_6\text{H}_5\text{Cl}$ formed when 1^{Br} was used as the catalyst precursor, while 84 μmol of $\text{C}_6\text{H}_5\text{Cl}$ formed when 1^{H} was used. The yield of $\text{C}_6\text{H}_5\text{Cl}$ seems to be correlated with the selectivity of the oxygenated products; a small amount of radical species such as a phenyl radical (generated by decarboxylation of acyloxy radical) might work as a mediator for a free-radical contributed reaction giving a ketone.

When methylcyclohexane was employed as a substrate, 1^X /*m*CPBA systems showed high secondary alcohol selectivity (Table 2). In the absence of 1^X , *i.e.* control reactions (entries 3 and 4 in Table 2), the tertiary C–H bond was oxidized selectively. In the case of substituted cyclohexanes, the tertiary C–H is sterically crowded. Therefore, the bulkiness of the oxidant affects the product selectivity,¹⁷ and selective hydroxylation on secondary C–H bonds results from a sterically demanding $\text{Tp}^{\text{Me}2,\text{X}}$ -supported nickel-based oxidant.

To clarify the nature of the active oxygen species, cyclohexane oxidation in the presence of H_2^{18}O was examined. No ^{18}O -labeled cyclohexanol could be detected, whereas an ^{18}O -labeled cyclohexanone was obtained (Fig. S5†). These

Table 1 Catalytic activity of 1^{H} for cyclohexane oxidation



Entry	Complex	Products ^a /μmol		<i>A/K</i> ^b	TON ^c
Solvent: $\text{C}_6\text{H}_5\text{CF}_3$ (5 mL), amount of 1^X = 26 μmol , Ni : <i>m</i> CPBA : C_6H_{12} = 1 : 5 : 50					
1	1^{H}	10.7	6.4	1.7	0.5
2	1^{Br}	35.9	20.4	1.8	1.5
Solvent: CH_2Cl_2 (1 mL), amount of 1^X = 13 μmol , Ni : <i>m</i> CPBA : C_6H_{12} = 1 : 50 : 2500					
3	1^{H}	227	7.0	32	46
4	1^{Br}	210	4.0	53	42

^a ϵ -Caprolactone, which would form through the reaction of cyclohexanone and *m*CPBA, was not obtained under the examined reaction conditions. ^b *A/K* = yield of cyclohexanol/yield of cyclohexanone. ^c TON = (cyclohexanol + 2 × cyclohexanone)/nickel.

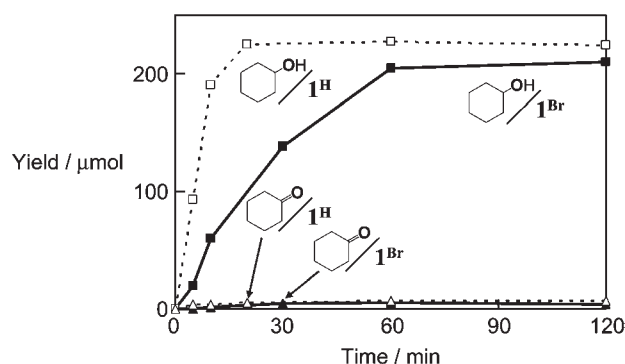
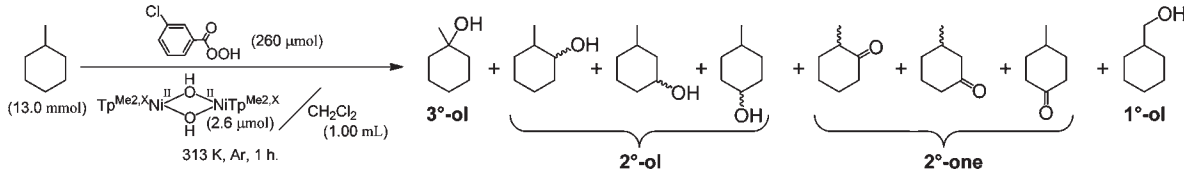
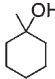
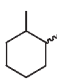
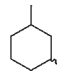
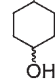
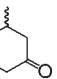
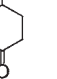
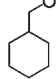


Fig. 2 Time course of cyclohexane oxidation with *m*CPBA mediated by 1^X under a large excess of substrate (corresponding to entries 3 and 4 in Table 1).

Table 2 Catalytic methylcyclohexane oxidation by 1^X with *m*CPBA


Entry	Complex	Products ^a /μmol							3°-ol : 2°-ol ^b	TON ^c
										
1	1^H	74.7	47.1	61.6 ^b	27.9	3.8	0.6	0.9	35 : 65	43
2	1^{Br}	72.3	45.6	62.4 ^b	29.6	3.3	0.5	0.8	34 : 66	42
3	None	6.1	0.9	0.9 ^b	0	0	0	0	77 : 23	2 ^d
4	None ^e	153.6	10.4	11.5 ^b	6.6	1.9	0.5	0.2	84 : 16	36 ^d

^a *ε*-Caprolactones, which would be formed through the reaction of methylcyclohexanones and *m*CPBA, and cyclohexanecarboxaldehyde, which would be formed by oxidation of cyclohexanemethanol (= 1°-ol), were not obtained under the examined reaction conditions. ^b A small amount of 2-methylcyclohexanone was included. ^c TON = (3°-ol + 2°-ol + 1°-ol + 2 × 2°-one)/nickel. ^d Values based on 5.2 μmol of virtual nickel catalyst. ^e Reaction conditions: 353 K, without CH₂Cl₂, 2 h.

findings imply that the ¹⁸O-labeled ketone is not formed from the corresponding alcohol by its over-oxidation, and that the formation pathways of alcohol and ketone are different in our Tp^{R2,X}-supported nickel-*m*CPBA system as well as the previously reported nickel complexes with the amine-based neutral ligands.⁵ In addition, the oxygen atom of the alkane hydroxylating active species of our system (*i.e.* nickel-oxygen species) is not exchangeable with the oxygen atom of the water molecule. Incorporation of the oxygen atom of H₂O into cyclohexanol occurs in the cyclohexane oxidation with *m*CPBA catalyzed by iron and cobalt catalysts (porphyrinato complexes of iron and cobalt, and Co^{II}(ClO₄)₂) reported by Nam and co-workers.^{15,16,18} In these iron and cobalt systems, high-valent metal-oxo species are proposed as the active oxidant and their oxo ligands are exchangeable. Such a difference between our nickel and the other systems may be due to the reaction mechanism and the character of the active species. Possible explanations for our nickel system are: (i) the active oxidant is a putative nickel-oxygen species (such as Ni^{III}=O or Ni^{II}-O[•])^{5b,d,6} and its oxygen atom is readily transferred to the substrate *via* hydrogen atom abstraction and the radical-rebound mechanism, and (ii) a nickel(II)-*m*CPBA complex is the active oxidant and the reaction occurs *via* a concerted mechanism through concomitant O-O rupture and oxygen atom transfer. In the iron-heme system reported by Nam and coworkers, the extent of the ¹⁸O incorporation into the product is varied depending on the nature of the catalysts as well as the reaction conditions, including the choice of solvent.¹⁸

Characterization of nickel(II)-acylperoxy species 2^X

The alkane hydroxylation catalyses of 1^X motivate us to characterize a putative nickel-acylperoxy species that may be a key intermediate formed during the *m*CPBA activation process.

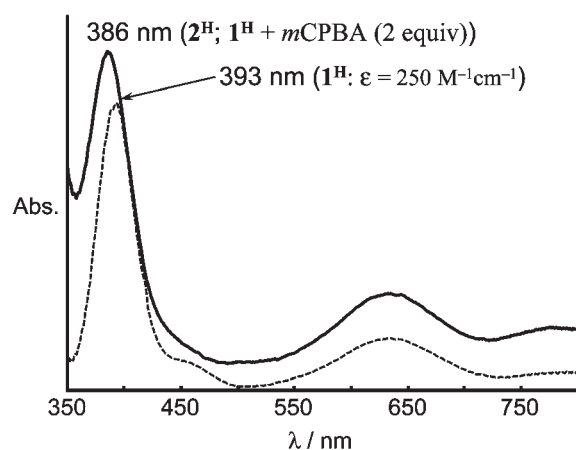


Fig. 3 UV/Vis spectra of *in situ*-generated 2^H (formed by the reaction of the dinuclear nickel(II) complex 1^H with 2 equiv. of *m*CPBA) and the parent 1^H in CH₂Cl₂ at 223 K.

Titration of the reaction of 1^H with *m*CPBA at 223 K monitored by UV/Vis spectra revealed that the increase in the absorption band around 386 nm became saturated when two equivalents of *m*CPBA were added to the CH₂Cl₂ solution of the dinuclear nickel(II)-bis(μ-hydroxo) complex 1^H (Fig. 3 and Table 3). The intensity of this band is not very high, and the spectral pattern of this pale blue solution is clearly different from those of the dinuclear nickel(III)-bis(μ-oxo) and mononuclear nickel(II)-alkylperoxy complexes with Tp^R.^{7,8e,13}

An IR spectrum of this solution exhibited a peak at 1644 cm⁻¹ under low-temperature conditions, and this peak disappeared in response to increases in the solution temperature (Fig. 4). Therefore, the thermally unstable pale blue species could be assigned as the nickel(II)-acylperoxy complex,

Table 3 UV/Vis spectral data of 2^X and 2^{Xa}

	2^{Hb}	2^{Brb}	2^{Hc}	2^{Brc}
λ [nm]	386 (148)	382 (108)	386 (260)	386 (151)
ϵ [$M^{-1} \text{cm}^{-1}$]	633 (42)	628 (22)	654 (68)	654 (50)

^a ϵ values of 2^X and 2^{H} were estimated based on the concentration of nickel in the parent hydroxo complexes 1^X and 1^H , while the ϵ of 2^{Br} was determined based on the used 2^{Br} , which was isolated as a pale blue powder by refrigeration. ^b CH_2Cl_2 solution at 223 K. ^c Et_2O solution at 233 K.

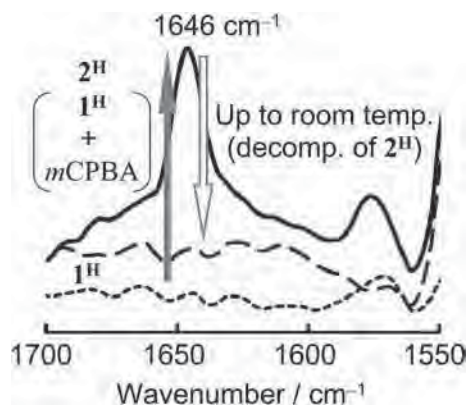


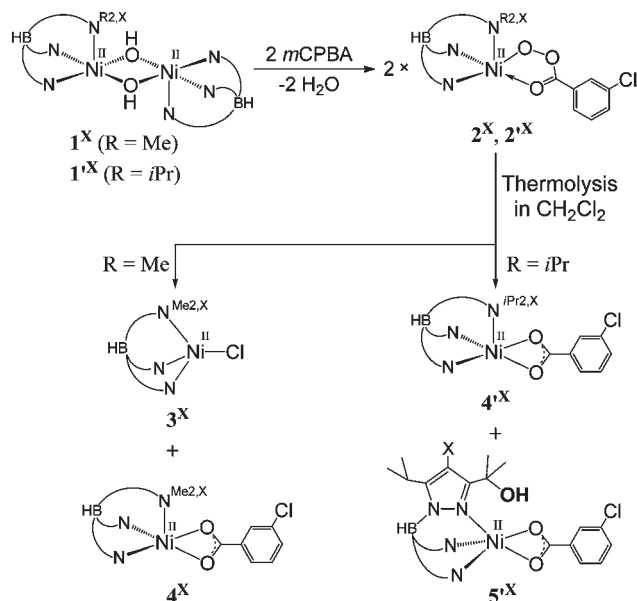
Fig. 4 IR spectra of the CH_2Cl_2 solutions of *in situ*-generated 2^H (formed by the reaction of the dinuclear nickel(II) complex 1^H with 2 equiv. of *mCPBA*; top), the parent 1^H (bottom), and the sample once warmed to room temperature (recorded at 223 K).

Table 4 IR band of $\nu_{\text{C}=\text{O}}$ of the acyl component^a

Compound	$\nu_{\text{C}=\text{O}}$ [cm^{-1}]	Ref.
2^H	1646 ^a	This work
2^{Br}	1661, 1643 ^{a,c}	This work
2^H	1643 ^b	This work
2^{Br}	1637 ^b	This work
$[\text{Fe}^{\text{III}}(\text{OOC}(=\text{O})\text{C}_6\text{H}_4\text{Cl})(\text{TPPPP})]$	1744 ^b	20
$[\text{Cu}^{\text{II}}_2(\text{XYL}-\text{O}-)(\mu-\text{OOC}(=\text{O})\text{C}_6\text{H}_4\text{Cl})]^{2+}$	1745 ^b	21
$[\text{Cu}^{\text{II}}(\text{OOC}(=\text{O})\text{C}_6\text{H}_4\text{Cl})(\text{Tp}^{\text{iPr}2})]$	1640 ^b	22
<i>mCPBA</i>	1738 ^a , 1726 ^b	This work ^d
<i>mCBA</i>	1706 ^a , 1696 ^b	This work ^d

^a CH_2Cl_2 solution. ^b Solid sample (KBr or Nujol). ^c Two peaks appeared. See ESI (Fig. S6†). ^d Measured under the same conditions for 2^X (CH_2Cl_2 solution at 223 K) and for 2^X (KBr pellet at room temperature).

$[\text{Ni}^{\text{II}}(\text{OOC}(=\text{O})\text{C}_6\text{H}_4\text{Cl})(\text{Tp}^{\text{Me}2})]$ (2^H), formed through dehydrative condensation of 1^H with a stoichiometric amount of *mCPBA* (*i.e.*, $\text{Ni}(\text{II})$ -*mCPBA* = 1 : 1).¹⁹ The $\nu_{\text{C}=\text{O}}$ bands of free *mCPBA* and *mCBA* are observed at 1738 and 1706 cm^{-1} , respectively, under the same conditions (*i.e.* CH_2Cl_2 solution at 223 K). To date, a few *meta*-chloroperbenzoate complexes have been characterized, and the wavenumbers of their $\nu_{\text{C}=\text{O}}$ bands (observed in the solid state) are correlated to the binding mode of the acylperoxo moieties, as summarized in Table 4.^{20–22} As found for the structure-determined dinuclear copper(II) complex, the non-coordinating acyl group shows a



Scheme 1 Formation of the nickel(II)-acylperoxo complexes and their thermal decomposition products.

small blue shift of the $\nu_{\text{C}=\text{O}}$ compared to that of the free *mCPBA*.²¹ The observed $\nu_{\text{C}=\text{O}}$ peak at 1644 cm^{-1} of 2^H suggests coordination of the acyl group to the nickel center (see Scheme 1), and the molecular structure of 2^H is probably similar to that of the copper(II) derivative of $\text{Tp}^{\text{iPr}2}$ reported by Kitajima and coworkers.²²

The other nickel(II)-hydroxo complexes, not only the catalytically active $\text{Tp}^{\text{Me}2, \text{Br}}$ but also the inactive $\text{Tp}^{\text{iPr}2, \text{X}}$ derivatives, gave the corresponding acylperoxo complexes 2^{Br} and 2^{X} , respectively. As summarized in Tables 3 and 4, spectral patterns of UV/Vis and wavenumbers of $\nu_{\text{C}=\text{O}}$ of 2^{Br} and 2^{X} are similar to those of 2^H . These findings indicate that the reason for the catalytic inertness of the $\text{Tp}^{\text{iPr}2, \text{X}}$ complexes is the steric hindrance between the substrate and the isopropyl groups surrounding the nickel center. Three isopropyl groups on the third position of the pyrazolyl rings in $\text{Tp}^{\text{iPr}2, \text{X}}$ work as hindered shades surrounding the nickel center, which stabilizes the nickel(II)-acylperoxo species. In fact, the most stable complex 2^{Br} could be isolated, although the C–H hydroxylation potential was retained, as evidenced by the intra-molecular ligand oxygenation (*vide infra*). Unfortunately, our challenge to get single crystals of 2^{Br} (and other ligand derivatives) has not met with success so far.

Characterization of product complexes derived from thermal decomposition of 2^X and 2^{Xa}

The nickel(II)-acylperoxo species 2^X and 2^{Xa} decomposed even at 253 K, and the resulting product nickel(II) complexes were varied depending on conditions such as solvent and temperature as well as R of $\text{Tp}^{\text{R}2, \text{X}}$ (Scheme 1).

(i) **Products from the $\text{Tp}^{\text{Me}2, \text{X}}$ complexes 2^X .** In the case of the CH_2Cl_2 solution of 2^X having the less hindered $\text{Tp}^{\text{Me}2, \text{X}}$, raising the solution temperature from 223 to 253 K resulted in

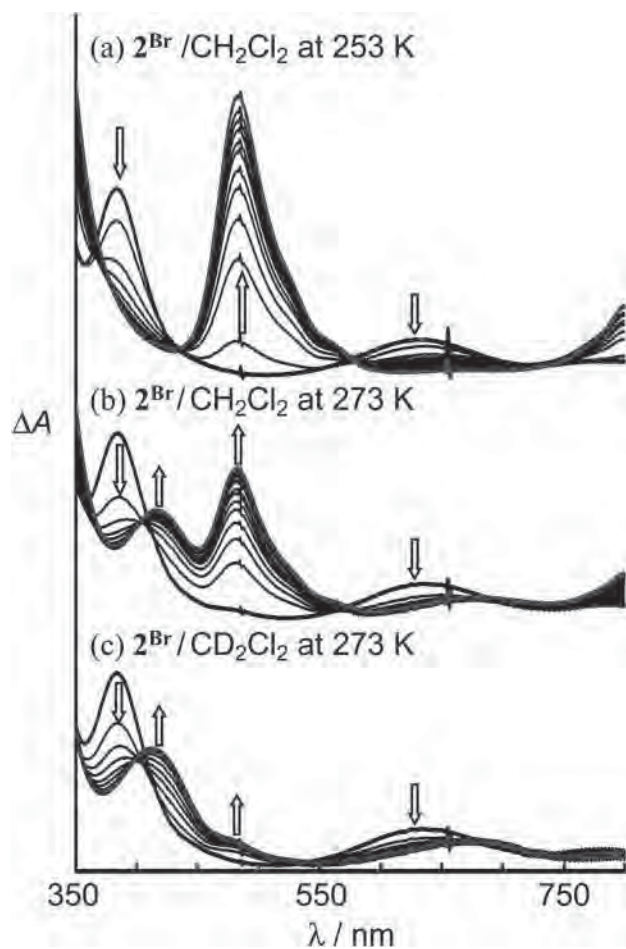


Fig. 5 Decay of 2^{Br} observed by time-course UV/Vis spectra. $[2^{\text{Br}}] = 1 \text{ mM}$. (a) Interval of the spectrum recording was 60 min. (b), (c) Interval of the spectrum recording was 20 min.

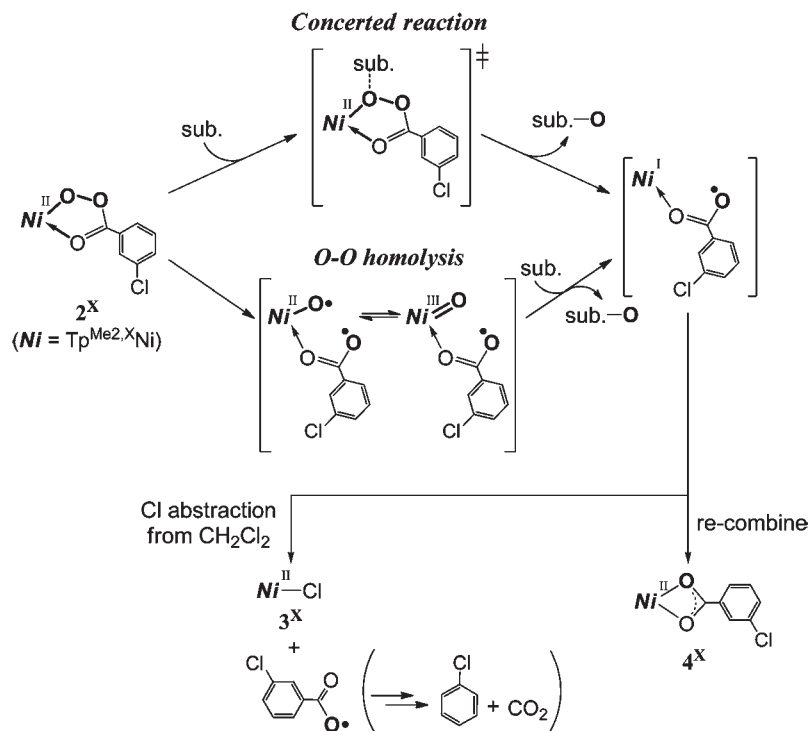
changing the solution color from pale blue-green to pale brown. The resultant pale brown solutions exhibited absorption around 480 nm attributed to the Cl-to-Ni charge transfer band of nickel(II)-chloride complexes, $[\text{Ni}^{\text{II}}(\text{Cl})(\text{Tp}^{\text{Me2,X}})]$ (3^{X} ; see Fig. 5(a): the formed complexes 3^{X} were characterized by comparison to authentic samples synthesized *via* another method).²³ The yields of 3^{X} were over 85% (determined by UV/Vis) when the CH_2Cl_2 solutions of 2^{X} were stored at 253 K for 12 h and then slowly warmed to room temperature. As we have reported previously, thermal decomposition of the nickel(II)-*tert*-butylperoxy complexes with $\text{Tp}^{\text{iPr2,X}}$ in CH_2Cl_2 yields the corresponding chloride complexes $[\text{Ni}^{\text{II}}(\text{Cl})(\text{Tp}^{\text{iPr2,X}})]$ (3^{X}) with a moderate yield (*ca.* 30%).^{7,13} The formation of 3^{X} may proceed through abstraction of the Cl atom from CH_2Cl_2 by a putative nickel(I) species given by the Ni–O bond homolysis of the alkylperoxy complexes. The yielding of 3^{X} from the nickel(II)-acylperoxy complexes 2^{X} suggests the formation of a nickel(I) species through the thermal decomposition process. Itoh and coworkers have proposed formation of the nickel(I) species after the hydroxylation of alkane in the catalytic processes.^{5b} In this context, we can hypothesize that nickel(I)

species with $\text{Tp}^{\text{Me2,X}}$ are formed after the oxidation of CH_2Cl_2 . The formation rates of 3^{X} (3.2×10^{-4} for 3^{H} and $5.2 \times 10^{-5} \text{ s}^{-1}$ for 3^{Br} , respectively, at 253 K) were lower than the decay rates of the corresponding 2^{X} (*vide infra*). Therefore, the conversion from 2^{X} to 3^{X} might proceed by a stepwise process through the decomposition of 2^{X} and the following reaction of the resulting nickel(I) species with CH_2Cl_2 to give 3^{X} , although we have not succeeded in trapping any intermediates so far.

The other products obtained in the decomposition reactions in CH_2Cl_2 were nickel(II)-*meta*-chlorobenzoate complexes, $[\text{Ni}^{\text{II}}(\text{O}_2\text{CC}_6\text{H}_4\text{Cl})(\text{Tp}^{\text{Me2,X}})]$ (4^{X}), having characteristic absorption bands around 420–430 nm (see the Experimental section). Decomposition of 2^{X} in CH_2Cl_2 at 273 K led to an increase in the yield of 4^{X} with a decrease in 3^{X} , as shown in Fig. 5(b). Therefore, the formation of 3^{X} and 4^{X} occurred competitively.

Decomposition of 2^{X} in toluene yielded 4^{X} , with yields of 4^{H} and 4^{Br} of 73 and 77% (determined by UV/Vis), respectively. A possible explanation for the formation of 4^{X} is the coupling of the nickel(I) species with an acyloxy radical resulting from homolysis of the O–O bond of 2^{X} (see Scheme 2). Mass spectral analyses revealed no formation of oxidized $\text{Tp}^{\text{Me2,X}}$ ligand compounds in the case of products derived from either CH_2Cl_2 or toluene solutions. However, decomposition of 2^{Br} in CD_2Cl_2 resulted in the oxidation of $\text{Tp}^{\text{Me2,Br}}$. This result implies that there are competitive reactions between the solvent and the methyl group on $\text{Tp}^{\text{Me2,Br}}$.

(ii) **Ligand hydroxylation on $\text{Tp}^{\text{iPr2,X}}$ complexes 2^{X} .** In the case of more hindered $\text{Tp}^{\text{iPr2,X}}$ systems, the solvent type did not affect the products. UV-vis spectra of the products derived from both CH_2Cl_2 and Et_2O solutions of 2^{X} exhibited peaks around 430 nm, and these spectral patterns were the same as those of the $\text{Tp}^{\text{iPr2,X}}$ analogues of 4^{X} , $[\text{Ni}^{\text{II}}(\text{O}_2\text{CC}_6\text{H}_4\text{Cl})(\text{Tp}^{\text{iPr2,X}})]$ (4^{X}). In mass spectra of the product derived from a CH_2Cl_2 solution, no peak of the chloride complexes 3^{X} existed, whereas peaks consistent with the formula $[4^{\text{X}} + \text{O}]$ ($m/z = 933$) were observed. ^1H NMR spectra of the product mixture showed the existence of 4^{X} and another species, of which the three-fold symmetry of the tris(pyrazolyl)borate ligand moiety was lost. Moreover, the ^1H NMR spectrum derived from 2^{Br} contained a signal at 16.5 ppm, of which the proton was exchangeable with external D_2O . These spectral features suggest the progress of partial oxygenation of the methine portion of the isopropyl groups of $\text{Tp}^{\text{iPr2,X}}$ proximal to the nickel center, and the products were tentatively assigned as nickel(II)-carboxylate complexes with hydroxylated $\text{Tp}^{\text{iPr2,X}}$ ligands, $[\text{Ni}^{\text{II}}(\text{O}_2\text{CC}_6\text{H}_4\text{Cl})\{\text{HB}(3\text{-Me}_2\text{C}(\text{OH})\text{-5-iPrpz})(3,5\text{-iPr}_2\text{pz})_2\}]$ (5^{X} ; see Scheme 1). Such intra-molecular ligand oxygenations have been observed in various transition metal-active oxygen complexes such as $\text{M}_2(\mu\text{-O})_2$ and M-OOR , including the nickel- and cobalt- Tp^{iPr2} complexes.^{7,8d,8e,13,24} Interestingly, the selectivity for the ligand-hydroxylated compounds 5^{X} seems to be correlated with the nature of X on $\text{Tp}^{\text{iPr2,X}}$. The product ratios of $5^{\text{X}} : 4^{\text{X}}$ were 7 : 1 from 2^{Br} and 1 : 2 from 2^{H} , respectively (determined by ^1H NMR). Although the hindered $\text{Tp}^{\text{iPr2,X}}$ complexes cannot catalyze cyclohexane hydroxylation, the higher selectivity toward the intra-molecular alkyl group hydroxylation on 2^{Br} is



Scheme 2 Possible reaction pathways for the thermolysis of 2^X .

consistent with that the alcohol selectivity of the $\text{Tp}^{\text{Me2,Br}}$ ligand catalyst is higher than that of the non-brominated Tp^{Me2} ligand catalyst.

Kinetics of the thermal decomposition process of 2^X

In the absence of an external substrate, both 2^X and 2^{Br} decomposed spontaneously in accord with first-order kinetics. The bromine-containing ligand complexes are more stable than the parent non-brominated complex. Also, 2^{Br} is more stable than 2^{H} (Table 5). These orders illustrate how both the electronic and steric nature of the ligands affect the lifetime of the acylperoxy species and the substrate-oxidizing activities. The bulky alkyl groups (*i.e.* 3-*i*-Pr on $\text{Tp}^{\text{iPr2,X}}$) wrap the O–O moiety of the metal-bound acylperoxide to stabilize 2^X but hinder the reaction with the external substrate. The smaller methyl substituents on $\text{Tp}^{\text{Me2,X}}$ are of an appropriate size to provide substrates-accessible space allowing for the catalyses of 2^X . As well as the previously reported nickel(II)-alkylperoxy complexes with $\text{Tp}^{\text{iPr2,X}}$,¹³ incorporation of the electron-withdrawing bromine at the distal fourth position of the pyrazolyl groups in $\text{Tp}^{\text{R2,X}}$ results in an increase in the stability of the nickel(II)-acylperoxy species.

Interestingly, kinetic isotope effects were observed during the decay of 2^X in CH_2Cl_2 – CD_2Cl_2 . The observed $k_{\text{H}}/k_{\text{D}}$ values at 253 K were 2.5 for 2^{H} and 3.2 for 2^{Br} , respectively. Interestingly, the yields of the chloride complexes 3^X decreased when the deuterated solvent was used (3^{H} : 51% in CH_2Cl_2 → 12% in CD_2Cl_2 at -20°C , 3^{Br} : 36% in CH_2Cl_2 → 7% in CD_2Cl_2 at 0°C). Moreover, the decomposition of 2^{Br} in CD_2Cl_2 led to

Table 5 First order rate for the decomposition of 2^X and 2^{Br}

Solvent (temp.)	Rate/ s^{-1}			
	2^{H}	2^{Br}	2^{H}	2^{Br}
CH_2Cl_2 (273 K)	4.2×10^{-3}	1.7×10^{-3}	— ^a	— ^a
CH_2Cl_2 (253 K)	8.8×10^{-4}	1.6×10^{-4}	— ^a	— ^a
CD_2Cl_2 (253 K)	3.5×10^{-4}	5.0×10^{-5}	— ^a	— ^a
Toluene (273 K)	3.8×10^{-3}	2.3×10^{-3}	— ^a	9.7×10^{-4}
Et_2O (273 K)	— ^a	— ^a	2.5×10^{-3}	5.1×10^{-4}

^a Not measured.

oxygenation of the methyl group of $\text{Tp}^{\text{Me2,Br}}$ (Fig. S9†). These findings indicate an interaction between the solvent molecule and 2^X , and hydrogen atom abstraction from the solvent may occur concomitant with O–O bond rupture of 2^X .²⁵ The large negative values of an activation entropy for the self-decomposition of 2^X in CH_2Cl_2 (Fig. S11 and Table S5†) indicate that the reaction proceeds through an associative transition state, and this is consistent with the interaction between the solvent molecule and 2^X . The observed KIE values are, however, not so large even at low temperatures. Upon decomposition of 2^{Br} (2.0 mM) in the mixture (*v/v* = 1/1) of CD_2Cl_2 and C_6H_{12} or C_6D_{12} at 273 K, the observed KIE was 1.6 ($k(\text{CD}_2\text{Cl}_2/\text{C}_6\text{H}_{12})$ and $k(\text{CD}_2\text{Cl}_2/\text{C}_6\text{D}_{12})$ were $5.2 \times 10^{-4} \text{ s}^{-1}$ and $3.3 \times 10^{-4} \text{ s}^{-1}$, respectively). However, a high concentration of cyclohexane (*v/v* = 1/20 of CD_2Cl_2 and C_6H_{12} or C_6D_{12}) led to a negligible KIE value (decomposition rates of 2 mM of 2^{Br} at 283 K were $k(\text{CD}_2\text{Cl}_2/\text{C}_6\text{H}_{12}) = 2.8 \times 10^{-3} \text{ s}^{-1}$ and $k(\text{CD}_2\text{Cl}_2/\text{C}_6\text{D}_{12}) = 2.5 \times 10^{-3} \text{ s}^{-1}$). Therefore, 2^X themselves have the ability for hydrogen atom

abstraction from an aliphatic C–H group,²⁶ but a putative nickel–oxygen species such as Ni^{III}=O or Ni^{II}–O· resulting from the O–O homolysis of 2^X may work as a major oxidant on catalytic cyclohexane hydroxylation (Scheme 2). Recently, the hydrogen atom abstraction ability of the mononuclear nickel(III)-oxo species, which is generated from the reaction of [Ni^{II}(OTf)(TMG₃tren)]⁺ (TMG₃tren denotes tris[2-(*N*-tetramethylguanidyl)ethyl]amine) with 1 equiv. of *m*CPBA, has been reported.⁶ In the Tp^{R²,X}Ni systems, however, we could not identify any intermediates during decomposition of the nickel(II)-acylperoxo species 2^X by spectroscopy (UV/Vis and EPR), and there is no direct evidence for the contribution of the nickel(III)-oxo and related species.²⁷

Conclusion

The nickel complexes with Tp^{Me²,X} exhibit alkane hydroxylation catalyses with *m*CPBA oxidant. Introduction of an electron-withdrawing group (EWG) into the pyrazolyl backbone of Tp^{Me²,X} leads to an increase in alcohol selectivity. The effectiveness of introduction of EWG into the metal supporting ligand in the selective hydroxylation of alkanes has been demonstrated for iron–heme compounds.²⁸ The electrophilicity of the active oxidant may be enhanced by an EWG-containing ligand, and our results indicate that the common concept for the ligand design, that is, the fine tuning of the electronic property without changing the structure of the metal-supporting scaffold, is applicable to non-heme catalysts. The thermal stability of the nickel(II)-*m*CPBA species is also enhanced by the EWG-containing ligands Tp^{R²,Br}, which might weaken the ability for back-donation from the metal center to the σ* orbital of the peroxide moiety.^{13,29} Kinetic and product analyses of the decomposition of the nickel(II)-*m*CPBA complexes suggest that the nickel(II)-acylperoxo complex, Ni^{II}–OOC(=O)–C₆H₄-*meta*-Cl, is an alternative oxidant. However, the hydrogen atom abstracting potential of nickel(II)-*m*CPBA complexes with Tp^{Me²,Br} is not so high and the previously proposed O–O bond cleaved species (*i.e.* Ni^{II}–O· or Ni^{III}=O) may be a major active oxidant for the catalytic cyclohexane oxygenation.

Experimental section

General

All manipulations were performed under argon by standard Schlenk techniques. THF, Et₂O, pentane, toluene, CH₂Cl₂, MeCN were purified over a Glass Contour Solvent Dispensing System under an Ar atmosphere. CF₃C₆H₅ was distilled using sodium as a drying agent and then stored under argon. *meta*-Chloroperbenzoic acid (*m*CPBA) was washed with a KH₂PO₄–NaOH buffer solution (pH 7.4) and pure water in order to remove *meta*-chlorobenzoic acid. Other reagents of the highest grade commercially available were used without further purification. The catalyst precursors [(Ni^{II}Tp^{R²,X})₂(μ-OH)₂] (1^X (R = Me) and 1^X (R = *i*Pr); X = H, Br) and their starting materials

were prepared by the methods described in the literature.^{8e,13,14,30} Elemental analyses were performed on a Perkin-Elmer CHNS/O Analyzer 2400II. IR measurements of KBr pellets of solid compounds were carried out by using JASCO FT/IR-5300 or FT/IR 4200 spectrometers. IR spectra of the *in situ*-generated solution samples were recorded using a Mettler Toledo ReactIR iC10. NMR spectra were recorded on Bruker AC-200 (¹H, 200.0 MHz) or JEOL ECA-500 (¹H, 500.0 MHz) spectrometers. Chemical shifts (δ) were reported in ppm downfield from internal SiMe₄. UV/Vis spectra were recorded on JASCO V-570, V650 or Agilent 8453 spectrometers equipped with a UNISOKU CoolSpeK USP-203-A for low-temperature measurements. Mass spectra were measured on a JEOL JMS-700 by a field desorption (FD) ionization method or on a JEOL JMS-T100LC by an electrospray ionization (ESI) method. Gas chromatographic (GC) analyses were carried out on a Shimadzu GC-2010 instrument with a flame ionization detector equipped with a RESTEK Rtx-1701 (30 m, 0.25 mm ID, 0.25 μm df) capillary column. GC-MS analyses were carried out on a Shimadzu PARVUM2 system equipped with a RESTEK Rtx-5MS (30 m, 0.25 mm ID, 0.25 μm df) capillary column.

Catalytic cyclohexane oxidation with *m*CPBA

All reactions were carried out at 313 K under Ar, and the products were analyzed by GC and GC–MS with an internal standard. Cyclohexane (0.28 mL, 2.6 mmol) was added to a 5.2 mM CF₃C₆H₅ solution of 1^X or 1^X (5.0 mL, 26 μmol). Next, 45 mg of *m*CPBA (260 μmol) was added to this solution with stirring. The reactions with large excess substrate were carried out as follows. Due to the insolubility of the catalyst precursors (1^X and 1^H) and *m*CPBA toward cyclohexane, a minimal amount of CH₂Cl₂ was used as a solvent: 1.0 mL of a 2.6 mM CH₂Cl₂ solution of 1^X or 1^H (2.6 μmol) was added to 1.4 mL of cyclohexane (13 mmol) under Ar. Then 45 mg of *m*CPBA (260 μmol) was added.

Synthesis of the nickel(II)-*m*CPBA complexes

[Ni^{II}(OOC(=O)C₆H₄Cl)(Tp^{*i*Pr₂,Br})] (2^{Br}). The synthetic procedure for the isolable Tp^{*i*Pr₂,Br} complex 2^{Br} is described as a typical example. The hydroxo complex 1^{Br} (250 mg, 0.16 mmol) was dissolved in Et₂O (15 mL), and the solution was cooled at 233 K. Then 5 mL of an Et₂O solution of *m*CPBA (58.2 mg, 0.33 mmol) was added to the cold solution of 2^{Br}. The resulting pale blue solution was stirred for 10 min at 233 K, and the solvent was then concentrated by evaporation while maintaining a low temperature. Refrigeration of the concentrated solution at 195 K yielded the pale blue powder of 2^{Br}. Almost quantitative oxygenation of Ph₃P to Ph₃P=O (97% yield based on 2^{Br} analyzed by ³¹P NMR) in Et₂O at 293 K (7 equiv. of Ph₃P was applied) indicated that the isolated blue powder compound was a pure acylperoxo complex. UV/Vis (Et₂O 233 K): λ(ε) = 386 (151), 654 nm (50); IR (KBr): ν = 2586 (BH), 1637 cm⁻¹ (CO).

The other ligand complexes 2^X and 2^H could be generated by similar procedures, and spectroscopic characterization by UV/Vis and IR was performed without isolation.

Products analyses of the spontaneous decomposition of the nickel(II)-*m*CPBA complexes

The product complexes derived from the spontaneous decomposition of 2^X and 2^H were characterized by comparison with the UV-vis spectral data of the nickel(II)-chloride and *meta*-chlorobenzoate complexes 3^X , 3^H , 4^X , and 4^H . Except for the previously reported chlorido complexes with Tp^{Me_2} (3^H),²³ Tp^{iPr_2} (3^H),¹⁴ and $\text{Tp}^{\text{iPr}_2,\text{Br}}$ (3^{Br}),¹³ the authentic complexes were synthesized as follows.

$[\text{Ni}^{\text{II}}(\text{Cl})(\text{Tp}^{\text{Me}_2,\text{Br}})]$ (3^{Br}). THF solution (20 mL) of $\text{NaTp}^{\text{Me}_2,\text{Br}}$ (1.00 g, 1.80 mmol) was slowly added to a methanol solution (20 mL) of $\text{NiCl}_2 \cdot 6\text{H}_2\text{O}$ (0.854 g, 3.6 mmol) over 30 min at RT. The green solution was stirred for 30 min, and the solvent was then evaporated. The green residue was re-dissolved in 100 mL of CH_2Cl_2 , and the insoluble green powder was removed by filtration through a celite pad, after which a reddish filtrate was evaporated to dryness to give a green solid. The solid was re-dissolved in 100 mL of MeCN, and the insoluble purple residue was removed by filtration through a celite pad to give a bluish-green filtrate. Evaporation of the solution gave a green solid. Crystallization from toluene gave the title complex as a green platelet crystal (0.498 g, 0.74 mmol, 41% yield). UV/Vis (CH_2Cl_2): $\lambda(\epsilon) = 481$ (360), 801 (105), 900 nm (120); IR (KBr): $\nu = 2532$ cm^{-1} (BH); ^1H NMR (500 MHz, CD_2Cl_2 , r.t.): $\delta = -13.16$ (2H, BH), -8.52 (18H, Me), 3.74 ppm (18H, Me); elemental analysis: calcd (%) for $\text{C}_{18.5}\text{H}_{23}\text{N}_6\text{Br}_3\text{ClNi}$ ($3^{\text{Br}} \cdot 1/2$ toluene): C 32.96, H 3.44, N 12.47; found: C 33.48, H 3.23, N 12.65. The molecular structure was determined by X-ray crystallography, and the details are provided in the ESI.†

$[\text{Ni}^{\text{II}}(\text{O}_2\text{CC}_6\text{H}_4\text{Cl})(\text{Tp}^{\text{R}_2,\text{Br}})]$ (4^X and 4^H). As a typical example, the synthetic procedure for $[\text{Ni}^{\text{II}}(\text{O}_2\text{CC}_6\text{H}_4\text{Cl})(\text{Tp}^{\text{Me}_2,\text{Br}})]$ (4^{Br}) is described. The hydroxo complex 1^{Br} (122 mg, 0.10 mmol) and *meta*-chlorobenzoic acid (*m*CBA, 34.4 mg, 0.22 mmol) were dissolved in 10 mL of CH_2Cl_2 . The green solution was stirred for 30 min at ambient temperature, and the solvent was then evaporated. The green residue was recrystallized from slow evaporation of EtOH to give an ethanol adduct of 4^{Br} , $[\text{Ni}^{\text{II}}(\text{O}_2\text{CC}_6\text{H}_4\text{Cl})(\text{Tp}^{\text{Me}_2,\text{Br}})(\text{C}_2\text{H}_5\text{OH})_2]$, as green block crystals (127 mg, 0.15 mmol, 75% yield). UV/Vis (CH_2Cl_2): $\lambda(\epsilon) = 421$ (210), 682 (47), 843 nm (39); (toluene): $\lambda(\epsilon) = 421$ (180), 685 (38), 851 nm (31); IR (KBr): $\nu = 2544$ (BH), 1591 cm^{-1} (COO); ^1H NMR (500 MHz, CD_2Cl_2 , r.t.): $\delta = -10.51$ (1H, BH), -9.45 (9H, Me), 0.62 (9H, Me), 2.36 (6H; EtOH), 4.28 (4H; EtOH), 6.06 (1H; *m*CBA), 9.39 (1H; *m*CBA), 11.04 (1H; *m*CBA), 11.47 ppm (1H; *m*CBA); elemental analysis: calcd (%) for $\text{C}_{26}\text{H}_{35}\text{Br}_3\text{ClNi}_2\text{O}_4$ ($4^{\text{Br}} \cdot 2\text{EtOH}$): C 37.16, H 4.20, N 10.00; found: C 37.25, H 3.98, N 10.11.

The other nickel(II)-*m*CBA complexes were synthesized by the same procedure.

$[\text{Ni}^{\text{II}}(\text{O}_2\text{CC}_6\text{H}_4\text{Cl})(\text{Tp}^{\text{Me}_2})]$ (4^H). The Tp^{Me_2} complex 4^H is synthesized by the reaction of 1^H (111 mg, 0.15 mmol) and *m*CBA (51.6 mg, 0.33 mmol) in THF. Recrystallization from MeCN

yielded the yellow-green solid of 4^H (60.1 mg, 0.12 mmol, 40% yield). UV/Vis (toluene): $\lambda(\epsilon) = 428$ (213), 686 nm (61); IR (KBr): $\nu = 2514$ (BH), 1591 cm^{-1} (COO); elemental analysis: calcd (%) for $\text{C}_{22}\text{H}_{26}\text{N}_6\text{ClNiO}_2$ (4^H): C 51.67, H 5.12, N 16.43; found: C 51.20, H 4.95, N 16.47.

$[\text{Ni}^{\text{II}}(\text{O}_2\text{CC}_6\text{H}_4\text{Cl})(\text{Tp}^{\text{iPr}_2})]$ (4^H). The hydroxonickel complex with Tp^{iPr_2} 1^H (75.6 mg, 0.0698 mmol) and *m*CBA (21.8 mg, 0.139 mmol) were stirred in 15 mL of Et_2O for 10 min at room temperature. After removal of the volatiles under vacuum, the resulting yellow-green solid of 4^H was recrystallized from pentane (76.5 mg, 0.113 mmol, 81% yield). UV/Vis (CH_2Cl_2): $\lambda(\epsilon) = 429$ (250), 690 (59), 854 nm (47); IR (KBr): $\nu = 2549$ cm^{-1} (BH); ^1H NMR (200 MHz, C_6D_6 , r.t.): $\delta = -3.6$ (3H, br, CH of *i*Pr), 0.07 (18H, s, Me of *i*Pr), 2.61 (21H, s, Me and CH of *i*Pr), 4.80, 9.04, 11.1, 11.5 (1H \times 4, s \times 4, Ph of *m*CBA), 75.4 ppm (3H, s, *pz*-4H); MS (FD): $m/z = 679$ ($[\text{4}^{\text{H}}]^+$); elemental analysis: calcd (%) for $\text{C}_{34}\text{H}_{50}\text{N}_6\text{ClNiO}_2$ (4^H): C 60.08, H 7.41, N 12.36; found: C 59.86, H 7.43, N 12.43.

$[\text{Ni}^{\text{II}}(\text{O}_2\text{CC}_6\text{H}_4\text{Cl})(\text{Tp}^{\text{iPr}_2,\text{Br}})]$ (4^{Br}). Recrystallization of the reaction mixture of 1^{Br} (352 mg, 0.226 mmol) and two equiv. of *m*CBA (70.8 mg, 0.452 mmol) from hexane yielded the yellow-green powder of the $\text{Tp}^{\text{iPr}_2,\text{Br}}$ analogue 4^{Br} (217 mg, 0.120 mmol, 53% yield). UV/Vis (Et_2O): $\lambda(\epsilon) = 416$ (240), 694 nm (52); IR (KBr): $\nu = 2578$ cm^{-1} (BH); ^1H NMR (200 MHz, C_6D_6 , r.t.): $\delta = -11.1$ (1H, BH), -0.75 (br, CH of *i*Pr), 1.78 (18H, s, Me of *i*Pr), 2.12 (21H, br, Me and CH of *i*Pr), 5.10, 9.10 (1H \times 2, s \times 2, Ph of *m*CBA), 13.1 ppm (2H, br, Ph of *m*CBA); MS (FD): $m/z = 917$ ($[\text{4}^{\text{Br}}]^+$); elemental analysis: calcd (%) for $\text{C}_{34}\text{H}_{47}\text{N}_6\text{Br}_3\text{ClNiO}_2$ (4^{Br}): C 44.56, H 5.17, N 9.17; found: C 44.85, H 5.40, N 8.89.

The molecular structures of an EtOH adduct of 4^{Br} and 4^H were determined by X-ray crystallography, and the details are provided in the ESI.†

Acknowledgements

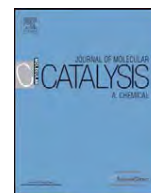
This work was supported in part by a Grant in-Aid for Scientific Research (Nos. 20037063 and 20360367), a Cooperative Research Program of "Network Joint Research Center for Materials and Devices (Nos. 2011169 and 2012216)", a Scientific Frontier Research Project, and a Strategic Development of Research Infrastructure for Private Universities from the Ministry of Education, Culture, Sports, Science, and Technology (MEXT), Japan. S. H. and J. N. also thank Kanagawa University for financial support.

References

- 1 *Metal-Catalyzed Oxidations of Organic Compounds*, ed. R. A. Sheldon and J. K. Kochi, Academic Press, New York, 1981.
- 2 M. Costas, K. Chen and L. Que Jr., *Coord. Chem. Rev.*, 2000, **200–202**, 517–544.

- 3 G. A. Russell, *J. Am. Chem. Soc.*, 1957, **79**, 3871–3877.
- 4 Reviews for example: (a) *Biomimetic Oxidations Catalyzed by Transition Metal Complexes*, ed. B. Meunier, Imperial College Press, London, 2000; (b) Thematic issue: *Homogeneous Biomimetic Oxidation Catalysis*, ed. R. V. Eldik and J. Reedijk, *Adv. Inorg. Chem.*, 2006, vol. 58, pp. 1–290; (c) *Metal-Oxo and Metal-Peroxo Species in Catalytic Oxidations*, ed. B. Meunier, *Struct. Bonding*, 2000, vol. 97, pp. 1–303; (d) L. Que Jr. and W. B. Tolman, *Nature*, 2008, **455**, 333–340.
- 5 Alkane hydroxylation with *m*CPBA catalyzed by nickel complexes with tetradentate ligands: (a) T. Nagataki, Y. Tachi and S. Itoh, *Chem. Commun.*, 2006, 4016–4018; (b) T. Nagataki, K. Ishii, Y. Tachi and S. Itoh, *Dalton Trans.*, 2007, 1120–1128; (c) T. Nagataki and S. Itoh, *Chem. Lett.*, 2007, 748–749; (d) M. Balamurugan, R. Mayilmurugan, E. Sureshb and M. Palaniandavar, *Dalton Trans.*, 2011, **40**, 9413–9424.
- 6 F. F. Pfaff, F. Heims, S. Kundu, S. Mebs and K. Ray, *Chem. Commun.*, 2012, **48**, 3730–3732.
- 7 S. Hikichi, H. Okuda, Y. Ohzu and M. Akita, *Angew. Chem., Int. Ed.*, 2009, **48**, 188–191.
- 8 Intramolecular C–H oxygenation mediated by nickel complexes of active oxygen species: (a) D. Chen and A. E. Martell, *J. Am. Chem. Soc.*, 1990, **112**, 9411–9412; (b) D. Chen, R. J. Motekaitis and A. E. Martell, *Inorg. Chem.*, 1991, **30**, 1396–1402; (c) E. Kimura, R. Machida and M. Kodama, *J. Biol. Inorg. Chem.*, 1997, **2**, 74–82; (d) S. Hikichi, M. Yoshizawa, Y. Sasakura, H. Komatsuzaki, M. Akita and Y. Moro-oka, *Chem. Lett.*, 1999, 979–980; (e) S. Hikichi, M. Yoshizawa, Y. Sasakura, H. Komatsuzaki, Y. Moro-oka and M. Akita, *Chem.–Eur. J.*, 2001, **7**, 5011–5028; (f) S. Itoh, H. Bandoh, S. Nagatomo, T. Kitagawa and S. Fukuzumi, *J. Am. Chem. Soc.*, 1999, **121**, 8945–8946; (g) S. Itoh, H. Bandoh, M. Nakagawa, S. Nagatomo, T. Kitagawa, K. D. Karlin and S. Fukuzumi, *J. Am. Chem. Soc.*, 2001, **123**, 11168–11178; (h) A. Kunishita, Y. Doi, M. Kubo, T. Ogura, H. Sugimoto and S. Itoh, *Inorg. Chem.*, 2009, **48**, 4997–5004; (i) T. Tano, Y. Doi, M. Inosako, A. Kunishita, M. Kubo, H. Ishimaru, T. Ogura, H. Sugimoto and S. Itoh, *Bull. Chem. Soc. Jpn.*, 2010, **83**, 530–538; (j) J. Cho, H. Furutachi, S. Fujinami and M. Suzuki, *Angew. Chem., Int. Ed.*, 2004, **43**, 3300–3303; (k) J. Cho, H. Furutachi, S. Fujinami, T. Tosha, H. Ohtsu, O. Ikeda, A. Suzuki, M. Nomura, T. Uruga, H. Tanida, T. Kawai, K. Tanaka, T. Kitagawa and M. Suzuki, *Inorg. Chem.*, 2006, **45**, 2873–2885; (l) M. Suzuki, *Acc. Chem. Res.*, 2007, **40**, 609–617; (m) K. Honda, J. Cho, T. Matsumoto, J. Roh, H. Furutachi, T. Tosha, M. Kubo, S. Fujinami, T. Ogura, T. Kitagawa and M. Suzuki, *Angew. Chem., Int. Ed.*, 2009, **48**, 3304–3307; (n) A. Company, S. Yao, K. Ray and M. Driess, *Chem.–Eur. J.*, 2010, **16**, 9669–9675; (o) S. Yao, C. Herwig, Y. Xiong, A. Company, E. Bill, C. Limberg and M. Driess, *Angew. Chem., Int. Ed.*, 2010, **49**, 7054–7058; (p) S. Yao and M. Driess, *Acc. Chem. Res.*, 2012, **45**, 276–287.
- 9 D. Schröder and H. Schwarz, *Angew. Chem., Int. Ed. Engl.*, 1995, **34**, 1973–1995.
- 10 Y. Shiota and K. Yoshizawa, *J. Am. Chem. Soc.*, 2000, **122**, 12317–12326.
- 11 A. W. Pierpont and T. R. Cundari, *Inorg. Chem.*, 2010, **49**, 2038–2046.
- 12 (a) S. Trofimenko, *Scorpionates – The Coordination Chemistry of Polypyrazolylborate Ligands*, Imperial College Press, London, 1999; (b) C. Pettinari, *Scorpionates II: Chelating Borate Ligands*, Imperial College Press, London, 2008.
- 13 S. Hikichi, C. Kobayashi, M. Yoshizawa and M. Akita, *Chem.–Asian J.*, 2010, **5**, 2086–2092.
- 14 N. Kitajima, S. Hikichi, M. Tanaka and Y. Moro-oka, *J. Am. Chem. Soc.*, 1993, **115**, 5496–5508.
- 15 W. Nam, J. Y. Ryu, I. Kim and C. Kim, *Tetrahedron Lett.*, 2002, **43**, 5487–5490.
- 16 W. Nam, I. Kim, Y. Kim and C. Kim, *Chem. Commun.*, 2001, 1262–1263.
- 17 K. Kamata, K. Yonehara, Y. Nakagawa, K. Uehara and N. Mizuno, *Nature Chem.*, 2010, **2**, 478–483.
- 18 (a) W. Nam, M. H. Lim, S. K. Moon and C. Kim, *J. Am. Chem. Soc.*, 2000, **122**, 10805–10809; (b) A.-R. Han, Y. J. Jeong, Y. Kang, J. Y. Lee, M. S. Seo and W. Nam, *Chem. Commun.*, 2008, 1076–1078.
- 19 If the nickel(II) centers of 1^X were oxidized to nickel(III) by *m*CPBA at the initial step and the following ligand exchange reaction led to nickel-acylperoxo complexes, the total ratio of Ni to *m*CPBA would be 1 : 1.5 or more as was found for the non-heme iron(II) complex. K. Ray, S. M. Lee and L. Que Jr., *Inorg. Chim. Acta*, 2008, **361**, 1066–1069.
- 20 J. T. Groves and Y. Watanabe, *Inorg. Chem.*, 1987, **26**, 785–786.
- 21 P. Ghosh, Z. Tyeklar, K. D. Karlin, R. R. Jacobson and J. Zubietta, *J. Am. Chem. Soc.*, 1987, **109**, 6889–6891.
- 22 N. Kitajima, K. Fujisawa and Y. Moro-oka, *Inorg. Chem.*, 1990, **29**, 357–358.
- 23 P. J. Desrochers, J. Telser, S. A. Zvyagin, A. Ozarowski, J. Krzystek and D. A. Vacic, *Inorg. Chem.*, 2006, **45**, 8930–8941.
- 24 S. Hikichi, H. Komatsuzaki, M. Akita and Y. Moro-oka, *J. Am. Chem. Soc.*, 1998, **120**, 4699–4710.
- 25 On the basis of the observation of KIE upon thermal decomposition of the copper(II)-alkylperoxo complex in the deuterated solvent (CD_3CN), concerted O–O fission and H abstraction are proposed: T. Tano, M. Z. Ertem, S. Yamaguchi, A. Kunishita, H. Sugimoto, N. Fujieda, T. Ogura, C. J. Cramer and S. Itoh, *Dalton Trans.*, 2011, **40**, 10326–10336.
- 26 In the heme-Fe/*m*CPBA system, both (por)Fe^{III}-acylperoxo and (por[•])Fe^{IV}=O (por[•] denotes 1e[−] oxidized porphyrinate ligand) are proposed as active oxidants for alkane hydroxylation. See ref. 18(a).
- 27 Existence of nickel(IV)-oxo species, which would generate *via* O–O heterolysis of the nickel(II)-acylperoxo species or intramolecular electron transfer from the nickel center of the weakly binding carboxyl radical in the nickel(III)-oxo

- species (O–O homolysis intermediate in Scheme 2), cannot be excluded, although no nickel(IV) complexes with Tp^{R} have been reported so far.
- 28 (a) W. Nam, *Acc. Chem. Res.*, 2007, **40**, 522–531; (b) D. Dolphin, T. G. Traylor and L. Y. Xie, *Acc. Chem. Res.*, 1997, **30**, 251–259.
- 29 Stabilization of $\text{Cu}_2(\mu\text{-}\eta^2\text{:}\eta^2\text{-O}_2)$ species by $\text{Tp}^{\text{CF}_3, \text{Me}}$ has been reported. (a) Z. Hu, R. D. Williams, D. Tran, T. G. Spiro and S. M. Gorun, *J. Am. Chem. Soc.*, 2000, **122**, 3556–3557; (b) Z. Hu, G. N. George and S. M. Gorun, *Inorg. Chem.*, 2001, **40**, 4812–4813; (c) G. Aullón, S. M. Gorun and S. Alvarez, *Inorg. Chem.*, 2006, **45**, 3594–3601.
- 30 S. Hikichi, Y. Sasakura, M. Yoshizawa, Y. Ohzu, Y. Morooka and M. Akita, *Bull. Chem. Soc. Jpn.*, 2002, **75**, 1255–1262.



Iron complex immobilized catalyst based on β -ketiminate ligand: Alkene oxygenation activity depending on the morphology of silica support and the structures of base additives

Takahiro Akashi, Jun Nakazawa, Shiro Hikichi*

Department of Material and Life Chemistry, Faculty of Engineering, Kanagawa University, 3-27-1 Rokkakubashi, Kanagawa-ku, Yokohama 221-8686, Japan

ARTICLE INFO

Article history:

Received 2 September 2012
Received in revised form 23 January 2013
Accepted 26 January 2013
Available online xxx

Keywords:

Immobilized catalyst
Chelating ligand
Support effect
Selective oxidation
Additive effect

ABSTRACT

Novel immobilized iron complex catalysts based on a β -ketiminate ligand have been developed. Dehydrative condensation between β -diketone and the ethylenediamine derivative of silane-coupling reagent yields the silanol ester of the ligand motif which can be anchored on the silica supports through covalent bond. The morphology of the silica supports affects the structures of active sites and catalytic activities on alkene oxygenation with H_2O_2 . The ordered flat surface of SBA-15 allows to immobilize the ligand with highly-dispersion and to form the coordinatively unsaturated iron active site. Addition of small amount of pyrazoles improves the catalytic performance without leaching of iron.

© 2013 Elsevier B.V. All rights reserved.

1. Introduction

Development of heterogeneous catalysts which mediate the selective oxygenation of hydrocarbons with environmentally friendly oxidant such as O_2 and H_2O_2 under mild condition is an attractive and challenging subject from the viewpoint of green chemistry [1]. In nature, iron-containing enzymes catalyze selective hydrocarbon oxygenation under physiological mild condition. The iron centers of these enzymes are supported by organic ligands such as porphyrin in heme enzymes or amino acid residues in non-heme enzymes [2]. From biomimetic viewpoints, various iron complexes with organic supporting ligand (porphyrin, Schiff base, amine, heterocyclic compounds including pyridine and so on, amino acid derivatives, phenols, carboxylic acid derivatives, etc.) have been explored as homogeneous oxidation catalysts so far [3]. Some of these complexes catalyze the oxygenation of hydrocarbons with H_2O_2 at ambient temperature: In these systems, iron-peroxo and/or high-valent iron-oxo species seem to be an active intermediate(s) as well as enzymes [4]. In order to improve catalytic efficiencies, decomposition of the catalyst by leaching of iron, or/and transformation to inactive compounds such as dinuclear Fe(III)- μ -oxo species and coordinatively saturated complex must be avoided.

Immobilization of the non-heme iron complexes on an appropriate support would make possible to construct isolated catalytic active sites [5]. Such immobilized catalyst might hinder the transformation of the iron complex to inactive species and that result in the elongation of catalyst lifetime. In addition, the resulting heterogeneous catalyst would have an advantage for recovering the used catalyst. The most important requirement is no leaching of complex and metal ions. In this context, we have been designing novel immobilized metallocomplex catalysts based on anionic chelating ligands which are anchored to appropriate supports through covalent bond [6].

A family of β -diketonates is one of the well-defined anionic chelating ligands. Importantly, one of two carbonyl groups of the β -diketones (parent of β -diketonate ligands) can be replaced by an imino group giving the corresponding β -ketimine compounds, and their deprotonated form are recognized as β -ketiminate ligands [7]. Recently, metal complexes with *NNO*-chelating β -ketiminate ligands, which are obtained by dehydrative condensation between acetylacetone and ethylenediamine derivatives, are investigated as homogeneous catalysts for coupling reaction and polymerization [8–10]. Especially, the applicability of the *NNO* β -ketiminate complexes toward redox process containing reaction, i.e. the cross-coupling catalysis of the Fe(III) complex [8] and the atom-transfer radical polymerization catalysis of the Cu(II) complexes [9], motivate us to explore oxidation catalysis of the *NNO* β -ketiminate ligands complexes. Herein we report development of β -ketiminate ligand-based immobilized iron complex catalysts. Structures of

* Corresponding author. Tel.: +81 45 481 5661; fax: +81 45 413 9770.
E-mail address: hikichi@kanagawa-u.ac.jp (S. Hikichi).

the immobilized iron complex species and their catalytic activities toward oxygenation of cyclohexene with H_2O_2 depend on the morphology of silica support. In addition, base additives improve the catalytic activity.

2. Experimental

2.1. Instruments

Atomic absorption analysis was performed on a Shimadzu AA-6200. Elemental analysis was performed on a Perkin-Elmer CHNS/O Analyzer 2400II. ESI (electrospray ionization)-MS spectra were measured on a JEOL JMS-T100LC mass spectrometer. Gas chromatographic (GC) analyses were carried out on a Shimadzu GC-2010 (flame ionization detector) equipped with a RESTEK Rtx-5 capillary column (length = 30 m, i.d. = 0.25 mm, thickness = 0.25 μm). IR spectra were recorded on a JASCO FT/IR 4200 spectrometer. NMR spectra were recorded on a JEOL ECA-500 spectrometer. UV-vis spectra were measured on a JASCO V650 spectrometer with a PIN-757 integrating sphere attachment for solid reflectance. Nitrogen sorption studies were performed at liquid nitrogen temperature (77 K) using a Micromeritics TriStar 3000. Before the adsorption experiments, the samples were outgassed under reduced pressure for 3 h at 333 K.

2.2. Materials and methods

All solvents (THF, toluene, CH_2Cl_2 , MeCN) were purified over a Glass Contour Solvent Dispensing System under Ar atmosphere. The reagents of the highest grade commercially available were used without further purification. Merck Silica gel 60 (70–230 mesh; BET surface area = $714 \text{ m}^2 \text{ g}^{-1}$; pore volume: $1.13 \text{ cm}^3 \text{ g}^{-1}$) was employed as an unmodified amorphous silica support (=SiO₂). SBA-15 (BET surface area = $578 \text{ m}^2 \text{ g}^{-1}$; pore volume = $0.76 \text{ cm}^3 \text{ g}^{-1}$) was prepared according to the previously reported procedure [11].

2.3. Catalyst preparation

A linker-attached β -ketimine ligand HL was synthesized as follows. *N*-(3-trimethoxysilylpropyl)ethylenediamine (1.08 g; 5.00 mmol) and one equivalent (0.500 g; 5.00 mmol) of acetylacetone were refluxed in toluene (100 mL) for 3.5 h. Pale yellow oil of HL was obtained by evaporation of volatiles under reduced pressure, and characterized by ¹H NMR. ¹H NMR (CDCl_3): δ 1.61 (m, 2H, CH₂), 3.58 (s, 3H, CH₃), 4.92 (s, 1H, C=CH).

The prepared HL (0.200 g) and SBA-15 (2.00 g) were suspended in toluene and refluxed for 2 h. Filtration of solid and wash with toluene then CH_2Cl_2 yielded pale yellow solid. Elemental analysis data (C, 1.34%; H, 0.40%; N, 0.21%) indicate the loading amount of HL was 0.08 mmol g^{-1} . Remaining silanols on silica were end-capped by trimethylsilyl group. A suspension of the obtained pale yellow solid (1.92 g) and hexamethyldisilazane (10 mL, 42.5 mmol) in toluene (30 mL) was stirred at 50 °C for 1 h. The resulting solid was collected by filtration then washed with toluene and CH_2Cl_2 . Dryness under evacuation yielded 1.89 g of HL-anchored SBA-15 (SBA^L). Elemental analysis data (C, 7.75%; H, 1.07%; N, 0.21%) suggest the retention of L on the support.

The pale yellow colored SBA^L (1.00 g) was suspended in 20 mL of THF under Ar. A hexane solution of *n*-butyllithium (0.12 mL; 0.16 mmol) was added slowly to this THF suspension at 0 °C and stirred at room temperature. After 1 h, methanol solution (20 mL) of FeCl₃ (0.02 g; 0.16 mmol) was added and stirred for 1 h. The resulting pale brown solid was collected by filtration and then washed with MeOH. Dryness by evacuation yielded the desired iron catalyst Fe/SBA^L.

When amorphous silica (abbreviated as SiO₂ in this paper) was employed as the support, the corresponding catalysts were prepared by same procedure. The loading amounts of L on SiO₂^L were controlled by applied amount of HL upon immobilization. A lower ligand loading SiO₂^L was prepared by the reaction of 5.0 g of SiO₂ and 0.50 mmol of HL in refluxing toluene (20 mL). Whereas a higher ligand loading SiO₂^L was obtained by the reaction of 5.0 g of SiO₂ and 3.0 mmol of HL in refluxing toluene (120 mL).

2.4. Synthesis of model compounds [Fe(L')]²⁺ and [Fe(L)₂]⁺

A ligand for model compounds, 4-[2-(ethylamino)ethylamino]-pent-3-en-2-one (HL'), was synthesized via similar procedure for HL. 30 mmol of *N*-ethylethylenediamine and equimolar of acetylacetone were refluxed in toluene (50 mL) for 1 h. Pale yellow oil of HL' was obtained by evaporation, and characterized by ¹H NMR. ¹H NMR (CDCl_3): δ 1.03 (m, 3H, CH₃), 2.63 (t, 2H, CH₂), 2.85 (t, 2H, CH₂), 4.87 (s, 1H, CH). Metalation of L' was achieved by reaction of sodium salt of L', which was obtained by treatment of HL' with sodium hydride in THF, with an appropriate ratio of FeCl₃.

2.5. Catalytic reaction

Typical reaction procedure is as follows: In Schlenk tube, 60 mg of catalyst (Fe/SBA^L) was suspended in 5 mL of MeCN. Cyclohexene (0.25 mL, 2.5 mmol) and nitrobenzene (10 μL , 0.10 mmol; as internal standard) was added to this suspension. All reactions were carried under Ar and the products were analyzed by GC with an internal standard.

3. Results and discussion

3.1. Preparation of catalysts

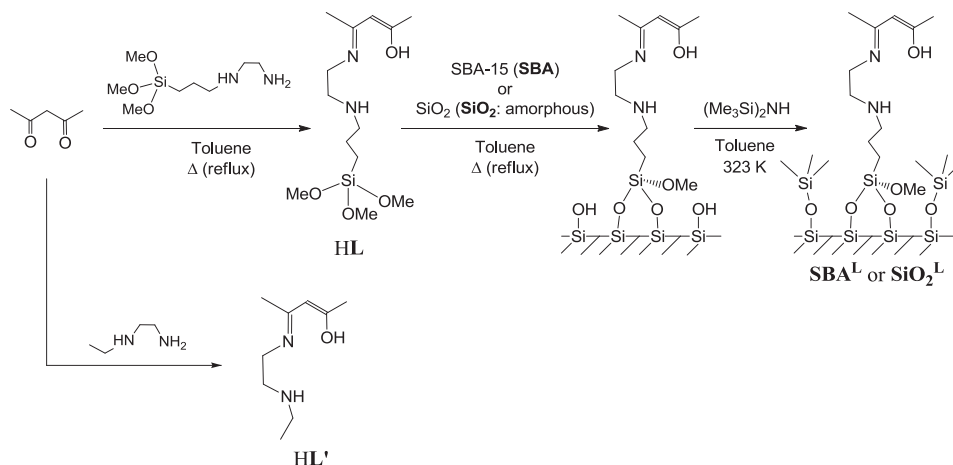
There are two possible procedures for anchoring the *NNO* β -ketimine ligand on silica supports. One is namely "in situ ligand formation" by reaction of an amine-modified silica gel with β -diketone [12]. Another is "grafting of pre-synthesized ligand" which is connected to a linker unit [13]. The analogous metallocomplex immobilized catalysts with a bidentate *NO* β -ketimine ligand motif have been prepared by both procedures so far. We employed the later procedure [13] in order to construct the desired *NNO* β -ketimine ligand certainly. A silanol ester derivative of the *NNO* β -ketimine ligand (=L) was synthesized by dehydrative condensation of *N*-(3-trimethoxysilylpropyl)ethylenediamine with acetylacetone in refluxing toluene. The synthesized linker-attached ligand HL was anchored on pre-dried silica gels (amorphous silica with surface area = $714 \text{ m}^2 \text{ g}^{-1}$ or SBA-15 with surface area = $578 \text{ m}^2 \text{ g}^{-1}$), and remaining surface silanol moieties were end-capped by trimethylsilyl group in order to prevent the immobilization of extra metal ions on the surface of the silica (Scheme 1). Upon amorphous silica (=SiO₂) was employed as the support, amounts of anchored L were varied by changing the amount of applied L to SiO₂. The amounts and densities of anchored L on the supports are summarized in Table 1. L might be densely located on

Table 1
Properties of ligand-immobilized support SBA^L and SiO₂^L.

Ligand-immobilized support	SBA ^L	SiO ₂ ^L ^a	SiO ₂ ^L ^b
BET surface area of support/ $\text{m}^2 \text{ g}^{-1}$	578	714	714
Loading of L/ mmol g^{-1}	0.08	0.11	0.63
Density of L/molecule nm^{-2}	0.08	0.09	0.53
Loading of Fe/ mmol g^{-1}	0.08	0.05	0.31
Ratio of L/Fe	1.0	2.2	2.0

^a Lower ligand loading SiO₂^L.

^b Higher ligand loading SiO₂^L.



Scheme 1. Preparation of NNO β -ketiminate ligands and immobilization on silica gels.

the higher ligand loading SiO_2^{L} . In contrast, the densities of **L** on the lower ligand loading SiO_2^{L} and SBA^{L} were comparable.

Prior to loading iron(III) to the ligand-anchored silica, we checked the coordination behavior of **L** by using model compound **L'** (=4-[2-(ethylamino)ethylamino]-pent-3-en-2-one; obtained via dehydrative condensation of *N*-ethylethylenediamine with acetylacetone, see Scheme 1). Analyses of THF solutions of the reaction mixture of FeCl_3 and sodium salt of **L'** (derived by treatment with NaH prior to reaction with FeCl_3) revealed that the structure of formed complexes were influenced by the ratio of iron(III) to applied **L'**; the observed major ion peak was assigned as $[\text{Fe}(\text{L}')\text{Cl}]^+$ upon the reaction of FeCl_3 with one equiv. of NaL' , whereas the reaction with two equiv. of NaL' gave the major peak attributed to $[\text{Fe}(\text{L}')_2]^+$ as shown in Fig. 1. These observations suggest the density of **L** on the supports should be controlled in order to construct the desired iron complex active sites on the surface of supports. Therefore, the anchoring amount of **L** on the supports kept $<0.1 \text{ mmol g}^{-1}$ because sparsely loaded **L** would yield the isolated coordinatively unsaturated $[\text{Fe}(\text{L})]^{2+}$ species (which might be a favored structure as an active site of catalyst) [14], whereas formation of a coordinatively saturated $[\text{Fe}(\text{L})_2]^+$ might be unavoidable upon densely loading of **L**.

The resulting ligand-anchored silica gels were treated with FeCl_3 to give the corresponding iron-complex immobilized catalysts. The anchored amounts of Fe and **L** on SBA-15 were almost same (i.e. Fe:**L** = 1:1 on $\text{Fe}/\text{SBA}^{\text{L}}$), however, the loadings of iron on the amorphous silica based $\text{Fe}/\text{SiO}_2^{\text{L}}$ were close to half of the anchored **L** (Fe:**L** = 1:2 on) in both higher and lower ligand loading catalysts (Table 1). It should be notable that the density of **L** on the lower ligand loading SiO_2^{L} was comparable with that on SBA^{L} . The difference of loading of iron seems to be correlated with the morphology of the silica supports; relatively flat surface on SBA-15 leads to highly dispersed **L** to give a desired $[\text{Fe}(\text{L})]^{2+}$ species. On the other hand, rugged surface of the amorphous silica support might make the situations that densely located **L** giving $[\text{Fe}(\text{L})_2]^+$ species in addition to iron-inaccessible **L** penetrating into the pores (Fig. 2).

Decreasing of the active $[\text{Fe}(\text{L})]^{2+}$ sites on $\text{Fe}/\text{SiO}_2^{\text{L}}$ reduces the catalytic efficiency (vide infra). Densely located **L** on the higher ligand loading SiO_2^{L} might yield $[\text{Fe}(\text{L})_2]^+$ predominantly. In fact, TON of the iron center of the higher ligand loading $\text{Fe}/\text{SiO}_2^{\text{L}}$ was lower than that of the lower ligand loading $\text{Fe}/\text{SiO}_2^{\text{L}}$ (see Table 2).

3.2. Catalytic activities

Catalytic activities of the prepared iron-complex immobilized catalysts toward oxygenation of cyclohexene with H_2O_2 at

ambient temperature were examined (Table 2). In any case, an allylic oxidized ketone was major product. The SBA-immobilized catalyst $\text{Fe}/\text{SBA}^{\text{L}}$ (Entry 1) exhibited higher activity compared to the lower ligand loading $\text{Fe}/\text{SiO}_2^{\text{L}}$ (Entry 3). Decreasing of TON on the higher ligand loading $\text{Fe}/\text{SiO}_2^{\text{L}}$ (Entry 4) suggests that high density

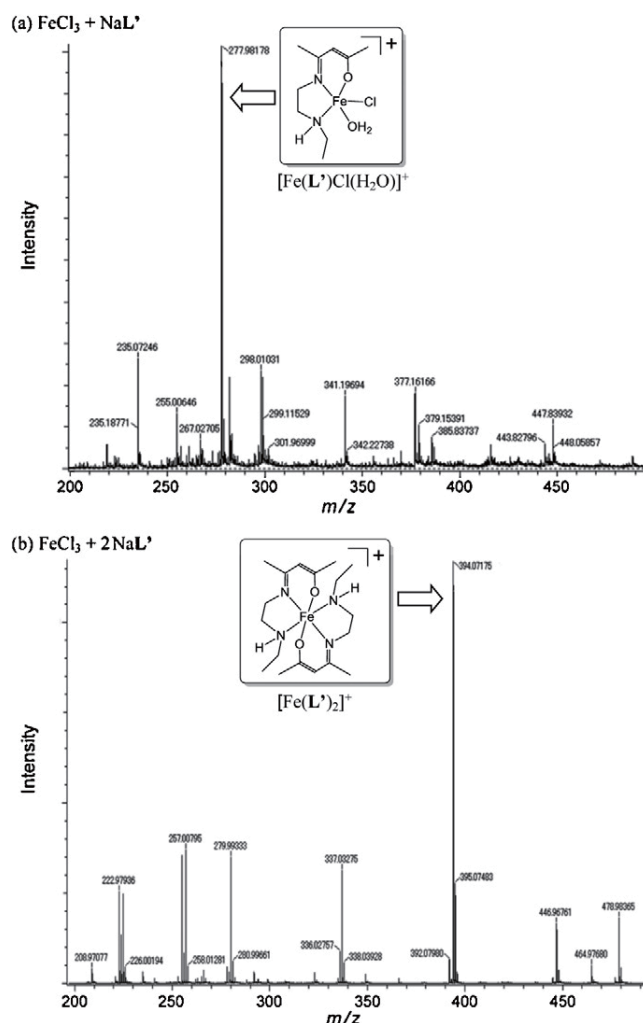
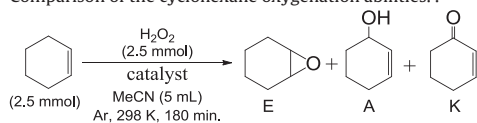


Fig. 1. Mass spectra of reaction mixture of FeCl_3 and 1 equiv. of NaL' (a) and 2 equiv. of NaL' (b).

Table 2
Comparison of the cyclohexane oxygenation abilities.



Entry	Catalyst ^a	Products ^b /μmol			E/(A+K)	TON ^c
		E	A	K		
1	Fe/SBA ^L	7.70	3.30	14.4	0.40	8.3
2 ^d	Fe/SBA ^L	17.0	35.5	109	0.12	57.1
3	Fe/SiO ₂ ^{L,e}	6.11	2.87	8.50	0.54	5.2
4	Fe/SiO ₂ ^{L,f}	8.63	4.01	8.68	0.68	1.0
5	SBA ^L	Trace	0	0	–	–
6	SBA-15	Trace	0	0	–	–
7	[Fe(L')] ^{2+,g,h}	9.49	2.97	5.34	1.14	4.6
8 ^d	[Fe(L)] ^{2+,g,h}	60.3	138	269	0.15	147
9	[Fe(L') ₂] ^{+,g,h}	Trace	Trace	Trace	–	–
10 ^d	[Fe(L') ₂] ^{+,g,h}	7.70	6.02	13.6	0.42	9.6
11	FeCl ₃ ^g	9.40	1.40	5.30	1.73	4.3
12	None	0	0	0	–	–

^a Amount of catalysts: Fe/SBA^L (entries 1 and 2), 60 mg; Fe/SiO₂^L (entries 3 and 4), 100 mg; silica-gel supports (entries 5 and 6), 60 mg; homogeneous iron compounds (entries 7–11), 5.0 μmol of Fe.

^b All reactions yields no or trace amount of *cis*- and *trans*-1,2-cyclohexanediols.

^c TON = (cyclohexen oxide + cyclohexen-1-ol + 2 × cyclohexen-1-one)/iron.

^d Reaction temperature: 353 K.

^e Lower ligand loading SiO₂^L.

^f Higher ligand loading SiO₂^L.

^g Homogeneous reaction.

^h In situ generated complex by reaction of FeCl₃ with appropriate amount of NaL.

of the ligand anchoring leads to increase the inactive [Fe(L)₂]⁺ sites. The SBA-supported iron complex was stable even in the reaction proceeded at 353 K (Entry 2), and no leaching of iron was observed under such hard condition.

We checked the catalytic performances of the parent components of Fe/SBA^L: L-anchored SBA-15 (SBA^L) as well as non-functionalized SBA-15 did not show catalytic activities under heterogeneous condition (Entries 5 and 6). Also, one of the model complexes, [Fe(L')₂]⁺ which was formed by reaction of FeCl₃ with two equiv. of L', was inactive (Entry 9). Even in high temperature

(353 K) condition, activity of [Fe(L')₂]⁺ was low (Entry 10). Therefore, a coordinatively saturated iron center in [Fe(L')₂]⁺ cannot activate H₂O₂. In contrast, cyclohexene epoxidation occurred in homogeneous reactions upon [Fe(L')₂]²⁺ which was generated in situ by reaction of FeCl₃ with one equiv. of L', or FeCl₃ in the absence of L' were used as the catalyst (Entries 7 and 11). The similar activities of the free FeCl₃ and the in situ generated [Fe(L')₂]²⁺ might imply the decomposition of [Fe(L')₂]²⁺ via intermolecular reaction in homogeneous condition. The catalytic activity of Fe/SBA^L was clearly different from those observed on the homogeneous systems. Therefore, heterogenization of the complex seems to shed light on its nature of catalysis due to the prevention of disproportionation of [Fe(L')₂]²⁺ through bimolecular reaction.

In some homogeneous iron complex catalysts system, improvements of catalytic activity by addition of acid [15] or base [16] have been reported. Therefore, we explored additive effect on Fe/SBA^L (Table 3). When AcOH was added (Entry 1), the catalytic activity became almost half of that found in the reaction without additive. In contrast, the catalytic performances were improved by addition of small amount (1.2 equiv. of iron) of base. In case of *tert*-alkylamines, the order of effectiveness seems to be correlated with the basicity (Entries 2–4), and the role of *tert*-alkylamine may play as a proton acceptor from H₂O₂ to give OOH⁻ species. Addition of azoles also influenced the catalytic activity. Alkyl-substitution on azoles led to higher activities compared to the corresponding parent azoles [e.g. imidazole (Entry 5) vs. 1-methylimidazole (Entry 6) and pyrazole (Entry 7) vs. 3,5-dimethylpyrazole (Entry 8)]. Introduction of electron-withdrawing bromine atom at fourth position of the pyrazolyl ring of 3,5-dimethylpyrazole (Entry 9) reduced the efficiency of activity improvement. Although the total TON (180 min) of the 3,5-dimethyl-4-bromopyrazole system (Entry 9) is similar to that observed on the non-additive reaction (Entry 10), the time course of the reaction of these systems are clearly different as shown in Fig. 3. In the no additive system, the substrate oxidation stopped at 60 min. In contrast, the reaction of the 3,5-dimethyl-4-bromopyrazole additive system continued and the total TON reached to 165 after 24 h. In both the presence and absence of

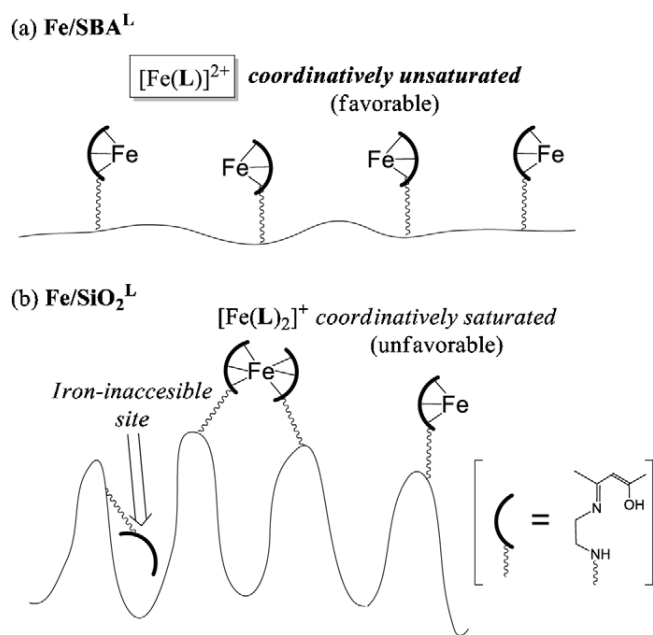
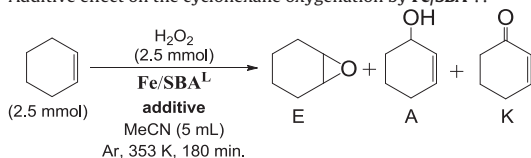


Fig. 2. Plausible models of the surface structures of Fe/SBA^L (a) and Fe/SiO₂^L (b).

Table 3
Additive effect on the cyclohexane oxygenation by Fe/SBA^L.



Entry	Additive ^a	Products/ μmol			E/(A+K)	TON ^b
		E	A	K		
1	AcOH	11.6	14.2	58.1	0.17	28.7
2	Et(<i>i</i> Pr) ₂ N	19.4	41.3	46.7	0.23	30.4
3	Et ₃ N	23.0	42.7	103	0.16	59.0
4	DBU ^c	39.7	53.0	129	0.22	73.3
5		41.6	38.0	105	0.29	60.4
6		42.0	49.5	112	0.26	65.7
7		53.6	62.5	169	0.23	94.7
8		57.1	66.3	192	0.22	105
9		29.4	31.6	97.8	0.23	53.5
10	none	17.0	35.5	108	0.12	57.1

^a 100 equiv. of AcOH (based on Fe) were added. 1.2 equiv. of base compounds were added.

^b TON = (cyclohexen oxide + cyclohexen-1-ol + 2 × cyclohexen-1-one)/iron.

^c DBU denotes 1,8-diazabicyclo[5.4.0]undec-7-ene.

additive, removal of catalyst (by filtration) led to termination of the products formation. Also, the leaching of iron species was negligible because the concentration of the iron species in the solution phase of the reaction mixture was lower than that of the detectable limit. These observations suggest that the observed catalysis is heterogeneous. Therefore, the role of the additive azoles seems to be changing the local structure of the iron center of the immobilized complex by coordination. Notably, pyrazole is less basic compared to imidazole [17], but pyrazole is more effective for activity improvement. A plausible reason for the higher efficiency of pyrazoles compared to imidazoles is a hydrogen bonding ability of N–H group of the metal-coordinating pyrazoles. To date, some transition metal–dioxygen complexes are known to be stabilized by intra-molecular hydrogen bonding between metal-binding peroxides (O_2^{2-} and OOH^-) and the N–H moiety of the pyrazole

ligand [18]. The imidazole ligand also indicates the hydrogen bonding ability with peroxide, but interaction occurs intermolecularly reflecting on the difference of the arrangement of the N–H moieties [19]. In this context, stabilization of a putative Fe(III)–OOH intermediate is considerable effect of the pyrazole additive (Fig. 4). In addition, hydrogen bonding between X–H and the β -oxygen of M–OOH (distal oxygen atom of the hydroperoxide ligand) is suggested to induce the heterolysis of O–O bond giving high-valent M=O active species, whereas the hydrogen bonding on α -oxygen (proximal oxygen of the OOH^- ligand) leads to stabilize O–O bond [20]. In our system, small extent of improvement of epoxide selectivity upon addition of pyrazoles might suggest the

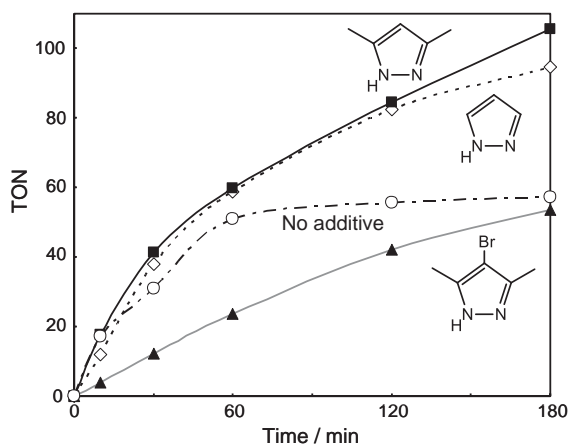


Fig. 3. Comparison of TON varied on the additive pyrazoles.

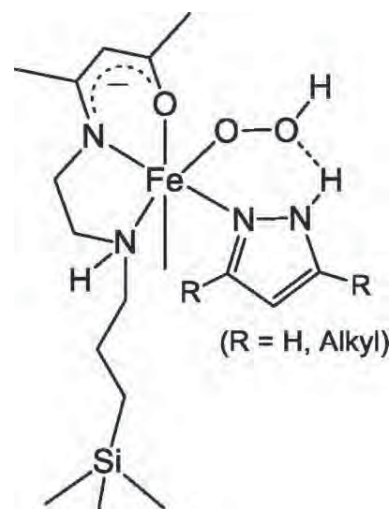


Fig. 4. A putative Fe-OOH intermediate stabilized by pyrazoles.

increasing the contribution of an electrophilic oxidant like Fe–OOH and Fe=O. But the allylic oxidation occurred mainly and the nature of major active oxidant showed radical character.

4. Conclusion

We have developed novel β -ketiminate ligand-based immobilized iron complex catalysts. The precursor of the anchored ligand, the silanol ester derivative of the *NNO* chelating β -ketiminate, can be prepared by dehydrative condensation between acetylacetone and the ethylenediamine derivative of the silane-coupling reagent. The surface morphology of the silica support influences the structure of the formed iron complex and catalytic performance. The ordered flat surface of SBA-15 realizes highly-dispersed ligand immobilization and formation of the coordinatively unsaturated $[\text{Fe}(\text{L})]^{2+}$ active site. The activity of SBA-15 based catalyst Fe/SBA^{L} toward alkene oxygenation with H_2O_2 was improved by addition of small amount of pyrazoles.

The advantage of the present system is high availability of divergent active site structures by modification of the ligand precursors (i.e. combination of carbonyl compounds and amines) and metal sources following the same procedures. Further investigations on screening of an optimum ligand structure as oxidation catalyst and scopes of the present catalyst toward reactions other than oxygenation have been under investigation.

Acknowledgments

This work was supported in part by a Grant in-Aid for a Cooperative Research Program of “Network Joint Research Center for Materials and Devices (Nos. 2011169 and 2012216)”, and a Strategic Development of Research Infrastructure for Private Universities from the Ministry of Education, Culture, Sports, Science, and Technology (MEXT), Japan. S. H. and J. N. also thank Kanagawa University for financial support.

Appendix A. Supplementary data

Supplementary data associated with this article can be found, in the online version, at <http://dx.doi.org/10.1016/j.molcata.2013.01.026>.

References

- [1] L. Alaerts, J. Wahlen, P.A. Jacobs, D.E. De Vos, *Chem. Commun.* (2008) 1727–1737.
- [2] (a) J.T. Groves, *Proc. Natl. Acad. Sci. U. S. A.* 100 (2003) 3569–3574; (b) E.I. Solomon, A. Decker, N. Lehnert, *Proc. Natl. Acad. Sci. U. S. A.* 100 (2003) 3589–3594; (c) I.G. Denisov, T.M. Makris, S.G. Sligar, I. Schlichting, *Chem. Rev.* 105 (2005) 2253–2277; (d) S.V. Kryatov, E.V. Rybak-Akimova, *Chem. Rev.* 105 (2005) 2175–2226, Examples of review articles.
- [3] (a) C. Bolm, J. Legros, J. Le Pailh, L. Zani, *Chem. Rev.* 104 (2004) 6217–6254; (b) B.S. Lane, K. Burgess, *Chem. Rev.* 103 (2003) 2457–2473; (c) M. Costas, M.P. Mehn, M.P. Jensen, L. Que Jr., *Chem. Rev.* 104 (2004) 939–986; (d) E.B. Bauer, *Curr. Org. Chem.* 12 (2008) 1341–1369, Reviews on biomimetic iron oxidation catalyst.
- [4] (a) M.S. Chen, M.C. White, *Science* 318 (2007) 783–787; (b) A. Company, L. Gómez, M. Güell, X. Ribas, J.M. Luis, L. Que Jr., M. Costas, *J. Am. Chem. Soc.* 129 (2007) 15766–15767; (c) V.B. Romakh, B. Therrien, G. Süß-Fink, G.B. Shul'pin, *Inorg. Chem.* 46 (2007) 3166–3175; (d) J. England, G.J.P. Britovsek, N. Rabadia, A.J.P. White, *Inorg. Chem.* 46 (2007) 3752–3767; (e) J. England, C.R. Davies, M. Banaru, A.J.P. White, G.J.P. Britovsek, *Adv. Synth. Catal.* 350 (2008) 883–897; (f) A. Company, L. Gómez, X. Fontrodona, X. Ribas, M. Costas, *Chem. Eur. J.* 14 (2008) 5727–5731; (g) H.-L. Yeung, K.-C. Sham, C.-S. Tsang, T.-C. Lau, H.-L. Kwong, *Chem. Commun.* (2008) 3801–3803; (h) E.V. Kudrik, A.B. Sorokin, *Chem. Eur. J.* 14 (2008) 7123–7126; (i) P.C.A. Bruijninx, I.L.C. Buurmans, S. Gosiewska, M.A.H. Moelands, M. Lutz, A.L. Spek, G.v. Koten, R.J.M. Klein Gebbink, *Chem. Eur. J.* 14 (2008) 1228–1237; (j) Y. Feng, C.-Y. Ke, G. Xue, L. Que Jr., *Chem. Commun.* (2009) 50–52; (k) L. Gómez, I. Garcia-Bosch, A. Company, J. Benet-Buchholz, A. Polo, X. Sala, X. Ribas, M. Costas, *Angew. Chem. Int. Ed.* 48 (2009) 5720–5723; (l) Y. He, J.D. Gorden, C.R. Goldsmith, *Inorg. Chem.* 50 (2011) 12651–12660; (m) Y. Hitomi, K. Arakawa, T. Funabiki, M. Kodera, *Angew. Chem. Int. Ed.* 51 (2012) 3448–3452, Selected reports for hydrocarbon oxygenation with H_2O_2 catalyzed by iron complexes.
- [5] (a) T.J. Terry, G. Dubois, A. Murphy, T.D.P. Stack, *Angew. Chem. Int. Ed.* 46 (2007) 945–947; (b) G.D. Pirngruber, L. Frunzb, M. Luchinger, *Phys. Chem. Chem. Phys.* 11 (2009) 2928–2938; (c) B. Malvi, C. Panda, B.B. Dhar, S.S. Gupta, *Chem. Commun.* 48 (2012) 5289–5291; (d) S. Yamaguchi, T. Fukura, C. Fujita, H. Yahiro, *Chem. Lett.* 41 (2012) 713–715.
- [6] S. Hikichi, M. Kaneko, Y. Miyoshi, N. Mizuno, K. Fujita, M. Akita, *Top. Catal.* 52 (2009) 845–851.
- [7] L. Bourget-Merle, M.F. Lappert, J.R. Severn, *Chem. Rev.* 102 (2002) 3031–3065.
- [8] Y. Yamaguchi, H. Ando, M. Nagaya, H. Hinago, T. Ito, M. Asami, *Chem. Lett.* 40 (2011) 983–985.
- [9] S. Gulli, J.-C. Daran, R. Poli, *Eur. J. Inorg. Chem.* (2011) 1666–1672.
- [10] H.-Y. Tang, H.-Y. Chen, J.-H. Huang, C.-C. Lin, *Macromolecules* 40 (2007) 8855–8860.
- [11] (a) D. Zhao, J. Feng, Q. Huo, N. Melosh, G.H. Fredrickson, B.F. Chmelka, G.D. Stucky, *Science* 279 (1998) 548–552; (b) D. Margolese, J.A. Melero, S.C. Christiansen, B.F. Chmelka, G.D. Stucky, *Chem. Mater.* 12 (2000) 2448–2459.
- [12] C. Pereira, J.F. Silva, A.M. Pereira, J.P. Araújo, G. Blanco, J.M. Pintadoc, C. Freire, *Catal. Sci. Technol.* 1 (2011) 784–793, Immobilization of $[\text{VO}(\text{acac})_2]$ on amino-functionalized silica giving anchored β -ketiminato complex.
- [13] D.-H. Lee, M. Choi, B.-W. Yu, R. Ryo, A. Taher, S. Hossain, M.-J. Jin, *Adv. Synth. Catal.* 351 (2009) 2912–2920.
- [14] (a) J. Nakazawa, T.D.P. Stack, *J. Am. Chem. Soc.* 139 (2008) 14360–14361; (b) J. Nakazawa, B.J. Smith, T.D.P. Stack, *J. Am. Chem. Soc.* 134 (2012) 2750–2759.
- [15] (a) R. Mas-Balleste, L. Que Jr., *J. Am. Chem. Soc.* 129 (2007) 15964–15972; (b) H. Jaafar, B. Vileno, A. Thibon, D. Mandon, *Dalton Trans.* 40 (2011) 92–106; (c) F. Oddon, E. Girgenti, C. Lebrun, C. Marchi-Delapierre, J. Pécaut, S. Ménage, *Eur. J. Inorg. Chem.* (2012) 85–96.
- [16] (a) F.G. Gelalcha, B. Bitterlich, G. Anilkumar, M.K. Tse, M. Beller, *Angew. Chem. Int. Ed.* 46 (2007) 7293–7296; (b) G. Anilkumar, B. Bitterlich, F.G. Gelalcha, M.K. Tse, M. Beller, *Chem. Commun.* (2007) 289–291; (c) B. Bitterlich, G. Anilkumar, F.G. Gelalcha, B. Spilker, A. Grotevendt, R. Jackstell, M.K. Tse, M. Beller, *Chem. Asian J.* 2 (2007) 521–529; (d) B. Bitterlich, K. Schröder, M.K. Tse, M. Beller, *Eur. J. Org. Chem.* 29 (2008) 4867–4870; (e) F.G. Gelalcha, G. Anilkumar, M.K. Tse, A. Brückner, M. Beller, *Chem. Eur. J.* 14 (2008) 7687–7698; (f) K. Schröder, S. Enthaler, B. Join, K. Junge, M. Beller, *Adv. Synth. Catal.* 352 (2010) 1771–1778.
- [17] J. Catalan, M. Menendez, J. Elguero, *Bull. Soc. Chim. Fr.* (1985), I-31–I-33.
- [18] (a) N. Kitajima, H. Komatsuzaki, S. Hikichi, M. Osawa, Y. Moro-oka, *J. Am. Chem. Soc.* 116 (1994) 11596–11597; (b) Y. Takahashi, M. Hashimoto, S. Hikichi, M. Akita, Y. Moro-oka, *Angew. Chem. Int. Ed.* 38 (1996) 3074–3077.
- [19] U.P. Singh, A.K. Sharma, S. Hikichi, H. Komatsuzaki, Y. Moro-oka, M. Akita, *Inorg. Chim. Acta* 359 (2006) 4407–4411.
- [20] T. Matsui, S. Ozaki, E. Liong, G.N. Phillips Jr., Y. Watanabe, *J. Biol. Chem.* 274 (1999) 2838–2844.



Metal-induced decomposition of perchlorate in pressurized hot water

Hisao Hori^{a,*}, Takehiko Sakamoto^a, Takashi Tanabe^a, Miu Kasuya^a, Asako Chino^a, Qian Wu^b, Kurunthachalam Kannan^b

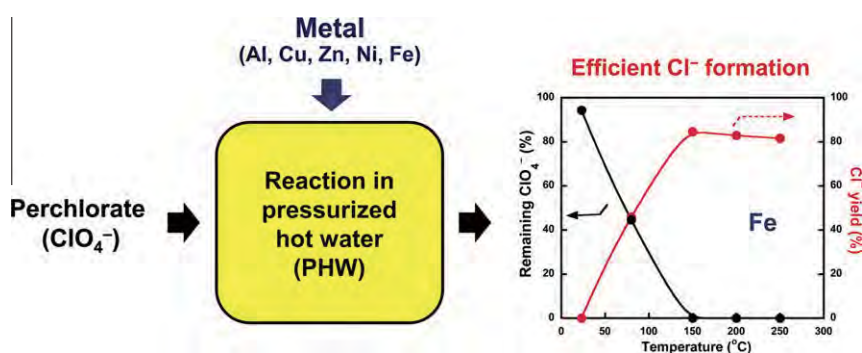
^aDepartment of Chemistry, Faculty of Science, Kanagawa University, 2946 Tsuchiya, Hiratsuka 259-1293, Japan

^bWadsworth Center, New York State Department of Health, and Department of Environmental Health Sciences, School of Public Health, State University of New York at Albany, Empire State Plaza, P.O. Box 509, Albany, NY 12201-0509, USA

HIGHLIGHTS

- ▶ ClO_4^- showed little reactivity in pure pressurized hot water (PHW) up to 300 °C.
- ▶ Metal additive dramatically enhanced the decomposition of ClO_4^- to Cl^- in PHW.
- ▶ Iron led to the most efficient reaction, producing Cl^- with yields of 85–86%.
- ▶ ClO_4^- in water after fireworks display was successfully decomposed by this method.

GRAPHICAL ABSTRACT



ARTICLE INFO

Article history:

Received 30 March 2012
Received in revised form 3 July 2012
Accepted 3 July 2012
Available online 27 July 2012

Keywords:

Perchlorate
Subcritical water
Metal
Fireworks
Supercritical water
Decomposition

ABSTRACT

Decomposition of perchlorate (ClO_4^-) in pressurized hot water (PHW) was investigated. Although ClO_4^- demonstrated little reactivity in pure PHW up to 300 °C, addition of zerovalent metals to the reaction system enhanced the decomposition of ClO_4^- to Cl^- with an increasing order of activity of (no metal) $\approx \text{Al} < \text{Cu} < \text{Zn} < \text{Ni} \ll \text{Fe}$: the addition of iron powder led to the most efficient decomposition of ClO_4^- . When the iron powder was added to an aqueous ClO_4^- solution (104 μM) and the mixture was heated at 150 °C, ClO_4^- concentration fell below 0.58 μM (58 $\mu\text{g L}^{-1}$, detection limit of ion chromatography) in 1 h, and Cl^- was formed with the yield of 85% after 6 h. The decomposition was accompanied by transformation of the zerovalent iron to Fe_3O_4 . This method was successfully used in the decomposition of ClO_4^- in a water sample contaminated with this compound, following fireworks display at Albany, New York, USA.

© 2012 Elsevier Ltd. All rights reserved.

1. Introduction

Perchlorate (ClO_4^-) has recently received much attention because of its ubiquitous occurrence in the aquatic environment and its potential to disrupt thyroid hormone levels. Perchlorate has been reported to occur in aquatic environments (Parker et al., 2008; Rajagopalan et al., 2009; Kannan et al., 2009; Wu

et al., 2011), drinking water and foodstuffs (Dyke et al., 2007; Wu et al., 2010; Guruge et al., 2011), as well as in humans (Zhang et al., 2010; Oldi and Kannan, 2009). The ammonium and potassium salts of ClO_4^- are used as oxidizers in jet and rocket fuels, pyrotechnic devices, explosives, fireworks, vehicle air bag inflators and so forth (Mendiratta et al., 2005). Improper treatment of wastes associated with manufacture and use of these products can act as significant stationary sources of ClO_4^- in the environment (Dasgupta et al., 2006). Furthermore, sources attributable to industrial effluents (Kosaka et al., 2007), fireworks manufacturing

* Corresponding author. Tel.: +1 463 59 4111; fax: +1 463 58 9688.

E-mail address: h-hori@kanagawa-u.ac.jp (H. Hori).

operations (Zhang et al., 2010), and fireworks displays (Wu et al., 2011) were recently indicated. Large doses of ClO_4^- can inhibit iodide uptake by the thyroid gland, which reduces the levels of thyroid hormones in the body; this has resulted in regulatory actions on ClO_4^- levels in drinking water in many countries including the USA (US EPA, 2011). Therefore, development of decomposition technologies for ClO_4^- to harmless Cl^- under mild condition is desired as a measure against stationary sources of emission. As for removal techniques of ClO_4^- in drinking water, biological reduction has widely been investigated (Srinivasan and Sorial, 2009; Bardiyana and Bae, 2011; Ghosh et al., 2011; Boles et al., 2012). However, biological treatment requires nutrient supply (Huang and Sorial, 2007). Zerovalent iron was also employed (Moore et al., 2003; Huang and Sorial, 2007; Xiong et al., 2007), but the removal rate of ClO_4^- was very slow: for example, 66% of the initial amount of ClO_4^- (0.1 mM) was removed after 336 h (Moore et al., 2003), and the rate constants for the removal was $0.001\text{--}0.004\text{ h}^{-1}$ for the initial concentration of $10.1\text{ }\mu\text{M}$ (Huang and Sorial, 2007). To enhance the reactivity towards ClO_4^- , a combination of zerovalent iron with 254-nm light irradiation was examined, at which 5.6% removal of ClO_4^- (initial concentration: $16\text{ }\mu\text{M}$) was observed after 12 h under anaerobic conditions (Im et al., 2011). The combination of zerovalent iron with high energy microwave irradiation was also examined (Oh et al., 2006); in this case, 98% removal of ClO_4^- (initial concentration: 0.5 mM) was achieved in 1 h, whereas the formation of Cl^- was not described. Although the previous reports demonstrated the removal of ClO_4^- from water, many reports did not fully quantify the end products, especially Cl^- ions, which are expected to be formed if the reductive decomposition was complete. Furthermore, zerovalent metals other than iron have been rarely investigated for the removal of ClO_4^- from water (Lee et al., 2011).

Recently, reactions with pressurized hot water (PHW) have been recognized as an innovative and environmentally benign technique in water treatment (Jessop and Leitner, 1999). PHW is defined as hot water at sufficient pressure to maintain the liquid state, below the critical point of water ($374\text{ }^\circ\text{C}$, 22.1 MPa). PHW has many characteristics that are favorable for chemical reactions: high diffusivity, low viscosity, and the ability to accelerate acid- and base-catalyzed reactions. Recently, dechlorination of trinitrotoluene, trichloroethane and polychlorinated biphenyls, via an oxidation (Foy et al., 1996) or reduction (Kubátová et al., 2002, 2003) was investigated with PHW, and a practical-plant-scale decomposition of hazardous compounds was achieved (Hawthorne et al., 2000; Kawasaki et al., 2006). Not only decomposition of chlorinated chemicals, but also perfluorinated surfactants such as perfluorooctane sulfonate was achieved; the reaction of PHW was dramatically enhanced by the introduction of metals (Hori et al., 2006).

In this study, we examined decomposition of ClO_4^- in PHW up to $300\text{ }^\circ\text{C}$, and examined the effect of several zerovalent metals in the reaction system. Among metals we tested, iron led to the most efficient decomposition of ClO_4^- to Cl^- ion, with no formation of other chlorinated species such as chlorate (ClO_3^-) and chlorite (ClO_2^-). We also applied this method to the decomposition of a ClO_4^- contaminated water sample from a man-made reflecting pond, following fireworks display in Albany, New York.

2. Experimental section

2.1. Materials

Potassium perchlorate (>99.5%) and standard solutions of NaClO_3 and NaClO_2 (the concentration of ClO_3^- or ClO_2^- : 1000 mg L^{-1}) were purchased from Wako Pure Chemical Industries (Osaka, Japan). Fine metal powders were used as received: alumi-

num (>99.99% purity, < $75\text{ }\mu\text{m}$ particle size), copper (99.9%, < $75\text{ }\mu\text{m}$), iron [>99.9%, < $53\text{ }\mu\text{m}$, BET (Brunauer, Emmett and Teller) surface area: $0.76\text{ m}^2\text{ g}^{-1}$], nickel (>99.9%, < $53\text{ }\mu\text{m}$), and zinc (99.99%, < $75\text{ }\mu\text{m}$) from Kojundo Chemical Laboratory (Saitama, Japan), and iron (>99.3%, < $180\text{ }\mu\text{m}$, BET surface area: $0.25\text{ m}^2\text{ g}^{-1}$) from Kobe Steel (Tokyo, Japan). Other reagents and solvents were obtained from Wako Pure Chemical Industries. Argon (99.99%) and oxygen (99.999%) were from Taiyo Nippon Sanso (Tokyo, Japan). Collection of ClO_4^- contaminated water from a man-made reflecting pond, following fireworks display (in Albany, New York), was described previously (Wu et al., 2011): the sample was collected 2 d after the July 4th fireworks in 2008, and stored at $5\text{ }^\circ\text{C}$.

2.2. Reaction procedures

A stainless steel high-pressure tube reactor (11 mL volume) equipped with two stainless steel screw caps was used. In a typical run, an argon-saturated aqueous (Milli-Q water) solution (3.5 mL) of ClO_4^- ($101\text{--}204\text{ }\mu\text{M}$) and metal powder (0.91 mmol) were introduced into the reactor under an argon atmosphere by use of a globe bag, and the reactor was sealed. Then the reactor was placed into an oven, and the reactor temperature was raised at a rate of ca $10\text{ }^\circ\text{C min}^{-1}$ to the desired reaction temperature ($80\text{--}300\text{ }^\circ\text{C}$), and the temperature was held constant for a specified time (e.g., 6 h). After the specified time, the reactor was quickly cooled to room temperature using ice water. The reactor was opened under an argon atmosphere, and the reaction mixture was centrifuged to separate the reaction solution and the solid phase (metal powder). The reaction solution was analyzed, by ion chromatography, for the quantification of residual ClO_4^- and the product, Cl^- , as well as other ionic species, if present. The recovered metal powder was dried overnight under vacuum and subjected to X-ray diffractometry (XRD). Control reactions were performed either in the absence of metal or under ambient (air) atmosphere.

The decomposition of ClO_4^- in water from a man-made reflecting pond following fireworks display was also examined. To decompose ClO_4^- in this sample, iron powder (1.82 mmol) was added to the sample (3.5 mL) and the mixture was introduced into the reactor, and then reacted in the same manner as described above. Quantification of ClO_4^- in the samples before and after the reactions was carried out by liquid chromatography-tandem mass spectrometry (LC-MS/MS) at Wadsworth Center, New York State Department of Health, where the samples were analyzed immediately before and after the reaction experiments. Other major ions present in the sample prior to the reaction (Cl^- and SO_4^{2-}) were measured by ion chromatography.

2.3. Analysis

The ion-chromatograph system (Tosoh IC-2001) consisted of an automatic sample injector (injection volume: $30\text{ }\mu\text{L}$), a degasser, a pump, a guard column, a separation column (Tosoh TSKgel Super IC-AP, 4.6-mm id, 7.5-cm length), a column oven, and a conductivity detector with a suppressor device. The mobile phase was an aqueous solution containing NaHCO_3 (1.7 mM), Na_2CO_3 (1.8 mM), and acetonitrile (23 vol%). The detection limit of ClO_4^- was $0.58\text{ }\mu\text{M}$ ($58\text{ }\mu\text{g L}^{-1}$), calculated from a signal-to-noise ratio of 3. An LC-MS/MS system consisting of an HPLC system (Agilent 1100), an anion-exchange column (IonPac AS-21, Dionex), and a mass spectrometer (Micromass Quattro, Waters) was used to quantify ClO_4^- in the water sample from the man-made reflecting pond following fireworks display and its reaction solution. The detection limit of ClO_4^- by this method was 0.20 nM ($0.02\text{ }\mu\text{g L}^{-1}$). Details of the LC-MS/MS procedure have been described elsewhere (Wu et al., 2011). XRD measurement was performed using $\text{Cu K}\alpha$ radiation (Multiflex, Rigaku, Tokyo, Japan).

3. Results and discussion

3.1. Decomposition of ClO_4^- in PHW

Initially, we studied the decomposition of ClO_4^- in PHW in the absence of a metal additive. The densities of the liquid and gas phases of pure water at 300 °C, at which the two phases coexist, are reported to be 0.71214 and 0.046168 g mL⁻¹, respectively (Lemmon et al., 2012). These density values and the water amount (3.5 g) and the internal reactor volume (11 mL) in the present study indicate that the volumes of the liquid and gas phases at 300 °C, the highest temperature tested, were 4.5 and 6.5 mL, respectively. This fact demonstrated that the reactions proceeded in PHW. The effect of temperature on ClO_4^- decomposition, in the absence of a metal, is shown in Fig. 1; the reaction time was 6 h and the initial concentration of ClO_4^- was 103 μM. The residues of ClO_4^- gradually decreased with increasing the temperature and Cl^- was detected in the reaction solution. However, the reactivity of ClO_4^- in PHW was considerably low: when the reaction was carried out at 300 °C, the highest temperature tested, 84% of the initial ClO_4^- remained, accompanied by the formation of a very small concentration of Cl^- , with a yield [(molar concentration of Cl^- formed)/(molar concentration of the initial ClO_4^-)] of 10%. The

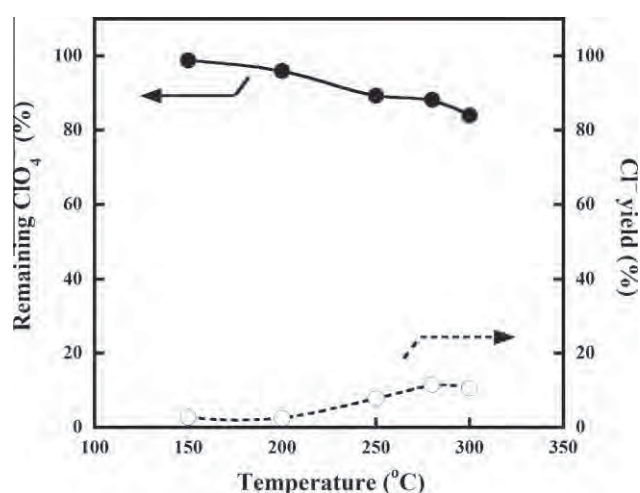


Fig. 1. Effect of temperature on the decomposition of perchlorate (ClO_4^-) in pressurized hot water (PHW) in the absence of metal at a constant reaction time of 6 h. An argon saturated aqueous solution (3.5 mL) of ClO_4^- (103 μM) was introduced in a sealed reactor, then the reactor temperature was raised between 150 and 300 °C [Remaining ClO_4^- (%) = (molar concentration of remaining ClO_4^-)/(initial molar concentration of ClO_4^-) × 100; Cl^- yield (%) = (molar concentration of formed Cl^-)/(initial molar concentration of ClO_4^-) × 100].

low yield reflects the high thermal and chemical stability of ClO_4^- . Total recovery of chlorine, i.e., the molar ratio of total chlorine in Cl^- formed and remaining ClO_4^- to total chlorine atoms in the initial ClO_4^- was 94%, indicating that ClO_4^- and Cl^- were virtually the only chlorinated species present in the reaction solution. Consistently, other chlorinated species such as ClO_3^- and ClO_2^- were not detected in the reaction solution, indicating that these two species are unstable in PHW.

To enhance the decomposition of ClO_4^- in PHW, we carried out reactions in the presence of a metal powder. The results are summarized in Table 1; the reaction was carried out at 150 °C for 6 h. In the absence of a metal (entry 1), most (99%) of the initial ClO_4^- (103 μM) remained, accompanied by a very small yield (3%) of Cl^- . Addition of aluminum did not enhance the formation of Cl^- (entry 2). Alternatively, addition of other metals clearly enhanced the decomposition of ClO_4^- to Cl^- , with an increasing order of, $\text{Cu} < \text{Zn} < \text{Ni} < \text{Fe}$ (entries 3–6). The highest enhancement of decomposition of ClO_4^- to Cl^- was achieved by the addition of iron. After the reaction in PHW with iron for 6 h, no ClO_4^- was detected in the reaction solution, while Cl^- was formed, with a high yield (85%) (entry 6). The enhancement of the decomposition of ClO_4^- to Cl^- was not reflected by the reducing power of the metals, because the order of ClO_4^- reduction (or Cl^- increase) was different from the order of the redox potentials (E_0 , V vs. NHE) of metals in the more negative direction of Cu/Cu^{2+} (0.34) < Ni/Ni^{2+} (-0.26) < Fe/Fe^{2+} (-0.44) < Zn/Zn^{2+} (-0.76) < Al/Al^{3+} (-1.68) (Bard and Faulkner, 2001). This finding suggests that the reduction of ClO_4^- on metal surface is not a simple redox reaction. It appears that specific interaction between ClO_4^- and metal surface (such as adsorption) plays an important role in the decomposition of ClO_4^- . In each case, ClO_3^- and ClO_2^- were not detected in the reaction solution. Iron-induced decomposition was also achieved at high concentrations of ClO_4^- such as 138 and 204 μM, resulted in similar Cl^- yields, i.e., 86% and 85%, respectively (entries 7 and 8).

3.2. Effect of iron

Because the addition of iron powder led to the most efficient Cl^- formation among the metals tested, we further investigated the decomposition of ClO_4^- to Cl^- with iron by changing the reaction conditions. The reaction-time dependence of the residual ClO_4^- ratio and Cl^- yield in the reaction solution is shown in Fig. 2; the initial concentration of ClO_4^- was 104 μM and the reaction temperature was 150 °C. The amount of ClO_4^- remaining in the solution decreased from 100% to 94% after addition of iron at 23 °C: 6% of the initial ClO_4^- was removed from the solution even before heating, with no Cl^- formed. This may be due to the adsorption of ClO_4^- on the iron surface (Moore et al., 2003; Huang and Sorial, 2007). After heating, the concentration of ClO_4^- rapidly decreased

Table 1
Decomposition of perchlorate (ClO_4^-) in pressurized hot water (PHW) with and without metal additives^a.

Entry	Metal additive	Weight of metal additive (mg)	Particle size of metal additive (μm)	Initial ClO_4^- concentration (μM)	Remaining ClO_4^- (%)	Cl^- yield (%)
1	None	–	–	103	99	3
2	Al	24.5	<75	103	93	1
3	Cu	57.7	<75	101	86	13
4	Zn	59.3	<75	102	51	22
5	Ni	53.4	<53	100	46	43
6	Fe	50.8	<53	104	<1 ^b	85 ± 1
7	Fe	50.8	<53	138	0 ^b	86
8	Fe	50.8	<53	204	0 ^b	85

^a An argon saturated aqueous solution (3.5 mL) of ClO_4^- and metal powder (0.91 mmol) were introduced into the reactor under argon, and the reactor was heated to 150 °C for 6 h.

^b Below the detection limit of ion chromatography.

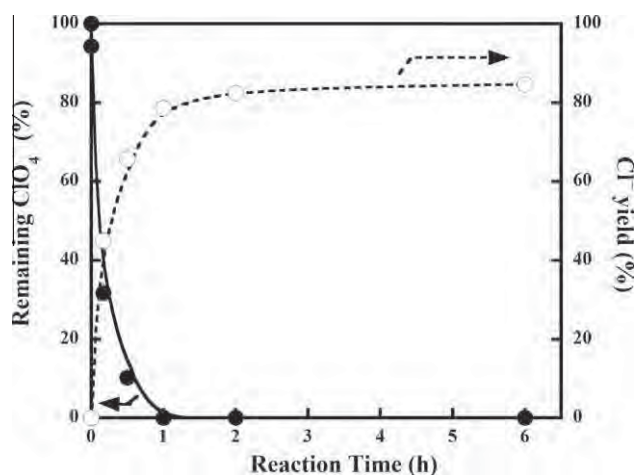


Fig. 2. Reaction-time dependence of the residual ClO_4^- ratio and the Cl^- yield. Iron powder (0.91 mmol; 50.8 mg, $<53 \mu\text{m}$) was added to an argon saturated aqueous solution (3.5 mL) of ClO_4^- (104 μM) under argon atmosphere, and the mixture in the sealed reactor was heated at 150°C for 1–6 h. Two dots for ClO_4^- at time 0 correspond to the values obtained before (higher value) and after (lower value) addition of iron.

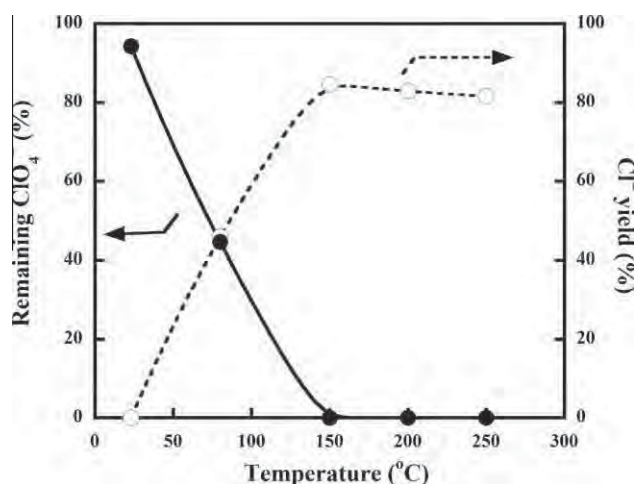


Fig. 3. Effect of temperature on the decomposition of ClO_4^- in PHW in the presence of iron at a constant reaction time of 6 h. An argon saturated aqueous solution (3.5 mL) of ClO_4^- (104 μM) and iron powder (0.91 mmol; 50.8 mg, $<53 \mu\text{m}$) were introduced in the sealed reactor under argon atmosphere, then the reactor temperature was raised between 80 and 250°C .

with increasing reaction time, following pseudo-first-order-kinetics with a rate constant of 4.3 h^{-1} , while Cl^- increased. After 1 h, ClO_4^- was not detected in the reaction solution. The formation of Cl^- showed saturation in 2 h, which indicates that the reaction was almost complete during this period, and the yield of Cl^- reached 85% after 6 h.

Table 2
Effect of iron sort and reaction conditions on the decomposition of ClO_4^- in PHW.^a

Entry	Particle size (μm)	BET surface area ($\text{m}^2 \text{g}^{-1}$)	Initial ClO_4^- concentration (μM)	Atmosphere	Remaining ClO_4^- (%)	Cl^- yield (%)
1	<53	0.76	104	Argon	$<1^b$	85
2	<180	0.25	101	Argon	52	46
3	<53	0.76	105	Air	$<1^b$	68

^a An aqueous solution (3.5 mL) of ClO_4^- and iron powder (0.91 mmol; 50.8 mg) were introduced into the reactor under either argon or air, and the reactor was heated to 150°C for 6 h.

^b Below the detection limit of ion chromatography.

The effect of temperature on ClO_4^- decomposition in the presence of iron is shown in Fig. 3; the reaction time was 6 h and the initial concentration of ClO_4^- was 104 μM . Raising the reaction temperature from 23°C dramatically decreased the residual ClO_4^- and increased Cl^- yield. After the reaction at 80°C for 6 h, 45% of the initial ClO_4^- remained, followed by a Cl^- yield of 46%.

The concentration of ClO_4^- decreased below the detection limit at 150°C , and the Cl^- yield increased to a maximum (85%). Therefore, it was clear that the best reaction temperature for the decomposition of ClO_4^- to Cl^- induced by iron in the present study was 150°C , at which temperature the reaction was almost complete in 2 h (Fig. 2).

In the above experiments, we used iron powder with the particle size of $<53 \mu\text{m}$ and the BET surface area of $0.76 \text{ m}^2 \text{g}^{-1}$. We used another iron powder with the particle size of $<180 \mu\text{m}$ and the BET surface area of $0.25 \text{ m}^2 \text{g}^{-1}$. When iron powder with lower specific surface area was used, the residue of ClO_4^- remained in the reaction solution was 52% and the Cl^- yield was 46% (Table 2, entry 2), after the reaction at 150°C for 6 h. This residual ratio of ClO_4^- was much higher than that when the iron powder with high specific surface area was used (the remaining ClO_4^- was below the detection limit, Table 2, entry 1); the Cl^- yield was considerably lower than that when the iron powder with high specific surface area was used (85%, Table 2, entry 1). These results clearly indicate that the reaction proceeded on the iron surface and that the increase in the specific surface area was a key factor for accelerating the decomposition of ClO_4^- .

We also tested the effect of reaction atmosphere on the decomposition of ClO_4^- . When the reaction was carried out at 150°C for 6 h under ambient atmosphere, the concentration of ClO_4^- reduced to below the detection limit (Table 2, entry 3), similar to that under argon (Table 2, entry 1). On the other hand, the Cl^- yield was 68%, somewhat lower than that under argon (85%, entry 1). In the reaction system under ambient atmosphere, the initial amount of O_2 in the gas phase was calculated to 65 μmol from the reactor volume and O_2 concentration of air. On the other hand, the initial amount of ClO_4^- in the solution was 0.37 μmol : the amount of O_2 was 175 times that the amount of ClO_4^- . Although iron reacted not only with ClO_4^- and water but also with O_2 in the reactor, the presence of O_2 in the reaction system may not cause large interference.

3.3. Fate of iron

To elucidate the fate of iron powder during the reaction, we carried out the XRD measurement of the recovered iron powder after the reaction. The XRD pattern of the recovered iron powder after the reaction at 150°C under argon for 6 h is shown in Fig. 4a. The recovered iron powder showed peaks assigned to Fe_3O_4 . Therefore, iron was transformed into Fe_3O_4 during the decomposition of ClO_4^- in PHW. Alternatively, when the reaction was carried out under ambient atmosphere, the peaks of Fe_3O_4 of the recovered iron powder became outstanding (Fig. 4b). This fact supports that iron reacted not only with ClO_4^- and water but

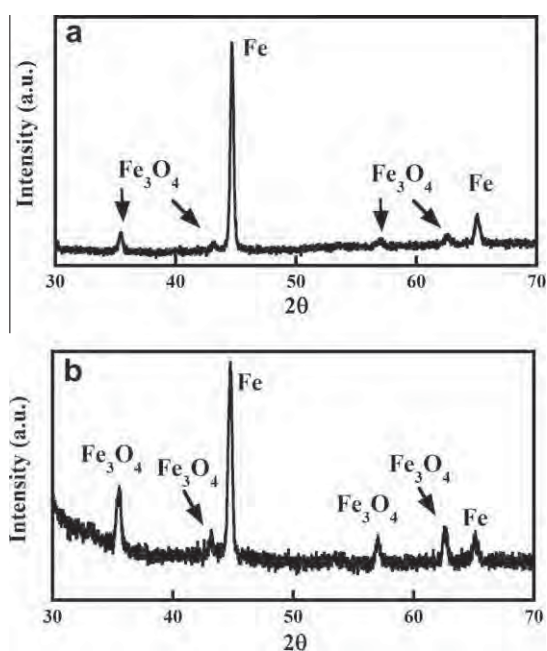


Fig. 4. XRD patterns of the recovered iron powder after the reaction at 150 °C for 6 h under (a) argon or (b) ambient atmosphere. Initial concentration of ClO_4^- was 104 μM and iron amount was 0.91 mmol.

also with O_2 , when the reaction was carried out under ambient atmosphere.

3.4. Application to perchlorate-contaminated water from fireworks display

We used perchlorate-contaminated water from a man-made reflecting pond following a fireworks display, to evaluate the efficiency of the developed method for the remediation of contaminated waters. This sample contained 5.22 μM of ClO_4^- and much higher concentrations of Cl^- (472 μM) and SO_4^{2-} (130 μM), which might interfere with the decomposition of ClO_4^- . Therefore, we prolonged the reaction time to 18 h and increased the amount of iron to 1.82 mmol. Consequently, the concentration of ClO_4^- was dramatically reduced to $0.03 \pm 0.01 \mu\text{M}$ after the reaction at 150 °C: 99% of the initial ClO_4^- was effectively removed from the water.

4. Conclusions

In the present study, we investigated the decomposition of ClO_4^- in PHW. Although ClO_4^- demonstrated low reactivity in pure PHW up to 300 °C, addition of several zerovalent metals to the reaction system enhanced the decomposition of ClO_4^- to Cl^- . The addition of iron powder led to the most efficient decomposition of ClO_4^- : when the iron powder was added to an aqueous ClO_4^- (104 μM) and the mixture was heated at 150 °C, the ClO_4^- concentration was fell below 0.58 μM (detection limit of ion chromatography) in 1 h, and Cl^- ions formed at yield of 85% after 6 h. While the decomposition of ClO_4^- proceeded in PHW, the zerovalent iron was transformed into Fe_3O_4 . This method was successfully applied in the decomposition of ClO_4^- in a water sample contaminated with ClO_4^- from a fireworks display: the initial concentration of ClO_4^- (5.22 μM) was dramatically decreased to $0.03 \pm 0.01 \mu\text{M}$: 99% of the initial ClO_4^- was effectively removed from the water.

Further studies are needed by scaling up and flow configuration of this reaction system at pilot or field scale.

Acknowledgement

This work was supported in part by a Grant-in-Aid for Scientific Research from the Japan Society for the Promotion of Science (JSPS).

References

- Bard, A.J., Faulkner, L.R., 2001. *Electrochemical methods: fundamental and applications*, second ed. John Wiley, New York.
- Bardiya, N., Bae, J.-H., 2011. Dissimilatory perchlorate reduction: a review. *Microbiol. Res.* 166, 237–254.
- Boles, A.R., Conneely, T., McKeever, R., Nixon, P., Nusslein, K.R., Ergas, S.J., 2012. Performance of a pilot-scale packed bed reactor for perchlorate reduction using a sulfur oxidizing bacterial consortium. *Biotechnol. Bioeng.* 109, 637–646.
- Dasgupta, P.K., Dyke, J.V., Kirk, A.B., Jackson, W.A., 2006. Perchlorate in the United States. Analysis of relative source contributions to the food chain. *Environ. Sci. Technol.* 40, 6608–6614.
- Dyke, J.V., Ito, T., Ito, K., Obisu, T., Hisamatsu, Y., Dasgupta, P.K., Blount, B.C., 2007. Perchlorate in dairy milk: comparison of Japan versus the United States. *Environ. Sci. Technol.* 41, 88–92.
- Foy, B.R., Waldthausen, K., Sedillo, M.A., Buelow, S.J., 1996. Hydrothermal processing of chlorinated hydrocarbons in a titanium reactor. *Environ. Sci. Technol.* 30, 2790–2799.
- Ghosh, A., Pakshirajan, K., Ghosh, P.K., Sahoo, N.K., 2011. Perchlorate degradation using an indigenous microbial consortium predominantly *Burkholderia* sp. *J. Hazard. Mater.* 187, 133–139.
- Guruge, K.S., Wu, Q., Kannan, K., 2011. Occurrence and exposure assessment of perchlorate, iodide and nitrate ions from dairy milk and water in Japan and Sri Lanka. *J. Environ. Monitor.* 13, 2312–2320.
- Hawthorne, S.B., Lagadec, A.J.M., Kalderis, D., Lilke, A.V., Miller, D.J., 2000. Pilot-scale destruction of TNT, RDX, and HMX on contaminated soils using supercritical water. *Environ. Sci. Technol.* 34, 3224–3228.
- Hori, H., Nagaoka, Y., Yamamoto, A., Sano, T., Yamashita, N., Taniyasu, S., Kutsuna, S., Osaka, I., Arakawa, R., 2006. Efficient decomposition of environmentally persistent perfluorooctanesulfonate and related fluorochemicals using zerovalent iron in subcritical water. *Environ. Sci. Technol.* 40, 1049–1054.
- Huang, H., Sorial, G.A., 2007. Perchlorate removal in aquatic systems by zero valent iron. *Environ. Eng. Sci.* 24, 917–926.
- Im, J.K., Son, H.S., Zoh, K.D., 2011. Perchlorate removal in $\text{Fe}^0/\text{H}_2\text{O}$ systems: impact of oxygen availability and UV radiation. *J. Hazard. Mater.* 192, 457–464.
- Jessop, P.G., Leitner, W. (Eds.), 1999. *Chemical Synthesis Using Supercritical Fluids*. Wiley-VCH, Weinheim, Germany.
- Kannan, K., Praamsma, M.L., Oldi, J.F., Kunisue, T., Sinha, R.K., 2009. Occurrence of perchlorate in drinking water, ground water, surface water and human saliva from India. *Chemosphere* 76, 22–26.
- Kawasaki, S.-I., Oe, T., Anjoh, N., Nakamori, T., Suzuki, A., Arai, K., 2006. Practical supercritical water reactor for destruction of high concentration polychlorinated biphenyls (PCB) and dioxin waste. *Process Saf. Environ.* 84, 317–324.
- Kosaka, K., Asami, M., Matsuoka, Y., Kamohisa, M., 2007. Occurrence of perchlorate in drinking water sources of metropolitan area in Japan. *Water Res.* 41, 3474–3482.
- Kubátová, A., Herman, J., Steckler, T.S., De Veij, M., Miller, D.J., Klunder, E.B., Wai, C.M., Hawthorne, S.B., 2003. Subcritical (hot/liquid) water dechlorination of PCB (Aroclor 1254) with metal additives and in waste paint. *Environ. Sci. Technol.* 37, 5757–5762.
- Kubátová, A., Lagadec, A.J.M., Hawthorne, S.B., 2002. Dechlorination of lindane, dieldrin, tetrachloroethylene, trichloroethane, trichloroethene, and PVC in subcritical water. *Environ. Sci. Technol.* 36, 1337–1343.
- Lee, C., Batchelor, B., Park, S.H., Han, D.S., Abdel-Wahab, A., Kramer, T.A., 2011. Perchlorate reduction during electrochemically induced pitting corrosion of zero-valent titanium (ZVT). *J. Hazard. Mater.* 197, 183–189.
- Lemmon, E.W., McLinden, M.O., Friend, D.G., 2012. Thermophysical properties of fluid systems in NIST chemistry webbook. In: Linstrom, P.J., Mallard, W.G. (Eds.), *NIST Standard Reference Database Number 69*, National Institute of Standards and Technology, Gaithersburg MD. <<http://webbook.nist.gov>>. (Retrieved 05.16.12)
- Mendiratta, S.K., Dotson, R.L., Brooker, R.T., 2005. *Perchloric Acid and Perchlorates*. John Wiley, New York.
- Moore, A.M., De Leon, C.H., Young, T.M., 2003. Rate and extent of aqueous perchlorate removal by iron surfaces. *Environ. Sci. Technol.* 37, 3189–3198.
- Oh, S.Y., Chiu, P.C., Kim, B.J., Cha, D.K., 2006. Enhanced reduction of perchlorate by elemental iron at elevated temperatures. *J. Hazard. Mater.* B129, 304–307.
- Oldi, J.F., Kannan, K., 2009. Perchlorate in human blood serum and plasma: relationship to concentrations in saliva. *Chemosphere* 77, 43–47.
- Parker, D.R., Seyffarth, A.L., Reese, B.K., 2008. Perchlorate in groundwater: a synoptic survey of “pristine” sites in the coterminous United States. *Environ. Sci. Technol.* 42, 1465–1471.
- Rajagopalan, S., Anderson, T., Cox, S., Harvey, G., Cheng, Q., Jackson, W.A., 2009. Perchlorate in wet deposition across North America. *Environ. Sci. Technol.* 43, 616–622.
- Srinivasan, R., Sorial, G.A., 2009. Treatment of perchlorate in drinking water: a critical review. *Sep. Purif. Technol.* 69, 7–21.

- US EPA, 2011. Drinking water: regulatory determination on perchlorate. Federal Register vol. 76, No. 29. US Environmental Protection Agency, Washington, DC, USA, pp. 7762–7767.
- Wu, Q., Oldi, J.F., Kannan, K., 2011. Fate of perchlorate in a man-made reflecting pond following a fireworks display in Albany, New York, USA. *Environ. Toxicol. Chem.* 30, 2449–2455.
- Wu, Q., Zhang, T., Sun, H.W., Kannan, K., 2010. Perchlorate in tap water, ground water, surface waters, and bottled water from China and its association with other inorganic anions and with disinfection byproducts. *Arch. Environ. Con. Tox.* 58, 543–550.
- Xiong, Z., Zhan, D., Pan, G., 2007. Rapid and complete destruction of perchlorate in water and ion-exchange brine using stabilized zero-valent iron nanoparticles. *Water Res.* 41, 3497–3505.
- Zhang, T., Wu, Q., Sun, H.W., Rao, J., Kannan, K., 2010. Perchlorate and iodide in whole blood samples from infants, children, and adults in Nanchhang, China. *Environ. Sci. Technol.* 44, 6947–6953.

Changes in crustacean hyperglycemic hormones in Pacific whiteleg shrimp *Litopenaeus vannamei* subjected to air-exposure and low-salinity stresses

Junpei Shinji · Bong Jung Kang · Tomoyuki Okutsu · Kota Banzai · Tsuyoshi Ohira · Naoaki Tsutsui · Marcy N. Wilder

Received: 30 January 2012 / Accepted: 21 May 2012 / Published online: 14 June 2012
© The Japanese Society of Fisheries Science 2012

Abstract Changes in crustacean hyperglycemic hormone (CHH)-family peptides in response to stress were investigated in *Litopenaeus vannamei*. Stress treatments consisted of air exposure and low salinity. High-performance liquid chromatography was used to quantify CHH-family peptides in the X-organ–sinus gland complex (XO–SG) in the eyestalks. Among the CHH-family peptides analyzed, only the level of sinus gland peptide-G (SGP-G) in the XO–SG was decreased. SGP-G was also detectable by Western blotting analysis in the hemolymph of animals subjected to stress. These results suggest that SGP-G was secreted from the XO–SG into the hemolymph during stress. Glucose levels in the hemolymph increased under conditions during which SGP-G was detected in the hemolymph. Hyperglycemia was also observed when SGP-G was injected. SGP-G may function to shift energy use to deal with stress.

Keywords Air exposure · Crustacean hyperglycemic hormone · Low salinity · Shrimp · Stress

Electronic supplementary material The online version of this article (doi:10.1007/s12562-012-0514-4) contains supplementary material, which is available to authorized users.

J. Shinji · M. N. Wilder
Department of Global Agricultural Sciences, Graduate School of Agricultural and Life Sciences, The University of Tokyo, Bunkyo-ku, Tokyo 113-0032, Japan

B. J. Kang · T. Okutsu · N. Tsutsui · M. N. Wilder (✉)
Fisheries Division, Japan International Research Center for Agricultural Sciences, Tsukuba, Ibaraki 305-8686, Japan
e-mail: marwil@jircas.affrc.go.jp

K. Banzai · T. Ohira
Department of Biological Science, Faculty of Science, Kanagawa University, Hiratsuka, Kanagawa 259-1293, Japan

Introduction

The supply of energy mediated by an organism's endocrine system is a typical stress response that is used to regulate physiological conditions and protect the body from stress [1–4]. Stress hormones such as cortisol and norepinephrine in vertebrates play a role in satisfying energy demand under these circumstances. However, in crustaceans, a different system exists in which several peptide hormones mediate the maintenance of energy balance under stressful conditions [5].

Crustacean hyperglycemic hormones (CHHs) are neuropeptides that play a central role in the regulation of energy metabolism in response to stress in Crustacea [5, 6]. CHH-family peptides generally consist of 70–80 amino acids and possess 6 cysteine residues that form 3 disulfide bonds [7, 8]. CHH-family peptides are produced mainly by the X-organ–sinus gland complex (XO–SG) in the eyestalk. They have also been found in the pericardial organ, foregut, hindgut, ventral nerve cord, and retina of several crustacean species [5, 6, 9]. However, the CHH-family peptides that are involved in the stress response are secreted mainly from the XO–SG [9]. Stressful conditions may promote signaling via enkephalinergic or serotonergic neurons for the release of CHH-family peptides from the XO–SG into the hemolymph [10–12].

CHH-family peptides are classified into two subtypes: type I, which does not possess glycine at position 12 in the mature peptide, and type II, which exhibits glycine. Immature peptides that belong to type I possess CHH precursor-related peptide between the signal and mature peptides [8]. All molecules associated with hyperglycemic activity have been confirmed to be of type I, and the C-terminal is often amidated [13]. In contrast, type II contains molecules that show vitellogenesis-inhibiting,

molt-inhibiting, or mandibular organ-inhibiting activity [5]. However, it has also been reported that the type I subtype in *Marsupenaeus japonicus* possesses vitellogenesis-inhibiting activity, and that the structural classifications do not always correspond to the functions [14]. CHH-family peptides are therefore often multifunctional. However, the physiological functions of these peptides have still not been sufficiently clarified [9, 15, 16], although the peptides are considered to be secreted to maintain energy metabolism in response to stress. In order to gain better understanding of the mechanisms of energy supply during the stress response in crustaceans, it is considered necessary to identify which CHH-family peptides function in this process.

In this study, therefore, we studied the stress response in terms of CHH-family peptides. We used the penaeid shrimp *Litopenaeus vannamei* as an experimental animal. In this species, 8 CHH-family peptides have been identified in the sinus glands and have been fully or partly sequenced [7, 8]. We therefore considered this species suitable for examining the stress response in relation to CHH-family peptides. For the purpose of screening CHH-family peptides that function under stressful conditions, we utilized two different types of stress that frequently occur, for example, during commercial culture operations. These were air exposure that comprises hypoxia, drying, and handling; and low-salinity exposure that induces the influx of water [5]. Animals were subjected to these stresses, and their responses were analyzed.

Materials and methods

Experimental animals

Whiteleg shrimp *L. vannamei* were purchased from International Mariculture Technology Co. Ltd. (Tokyo, Japan). Carapace length was 26.5 ± 1.6 cm (mean \pm standard deviation, SD) and body weight was 13.8 ± 2.1 g (mean \pm SD). Experimental animals were reared in a 3,000-L tank at 20 °C, under 30–35 parts per thousands (ppt) salinity in artificial seawater (Sea Life, Marinetech, Tokyo, Japan) until the experiments were commenced.

Experimental procedures used for stress treatments

Intermolt or premolt males were used in this study. In the air-exposure experiment, experimental animals were reared in a 3,000-L tank at 20 °C and salinity of 35 parts per thousand (ppt) for 5 days before stress treatment. The animals were fed 0.2 g dry food pellets (Gold Prawn; Higashimaru Co. Ltd., Kagoshima, Japan) per day, except in the 14 h before the experiments. Remaining feed was removed from the tank

10 h after feeding, and the quality of the rearing water was maintained by circulating the water through filters. After the acclimation period, the experimental animals were subjected to air-exposure stress. In the air-exposure experiment, animals were placed on top of a styrofoam box and subjected to air-exposure stress for 0 (control), 15, or 30 min, 30 min being the maximum exposure which would enable the animals to remain alive. The air temperature was maintained at 20 °C using an air conditioner.

In the low-salinity experiment, animals were kept in a 60-L tank at 28 °C and salinity of 28 ppt for 7 days before the stress treatment. They were fed dry food pellets (Gold Prawn; Higashimaru) at a rate of 5 % of body weight per day, except in the 24 h before the experiments. Remaining feed was removed from the tank 5 h after feeding, and the water quality was maintained by circulating the water through filters. After the acclimation period, the experimental animals were subjected to experimental salinities of 0 and 28 (control) ppt for 0, 3, or 6 h at 28 °C, 6 h being the maximum exposure which would enable the animals to remain alive.

Hemolymph was collected in 200 μ L acetonitrile to detect CHH-family peptides in the hemolymph, or in 20 μ L 1 M sodium citrate to analyze glucose levels. The concentration of acetonitrile was adjusted to 50 % with 100 % acetonitrile for samples used in the analysis of CHH. For samples used in glucose analysis, sodium citrate was adjusted to 0.1 M with 1 M sodium citrate after collection.

In vivo bioassay of hyperglycemic activity of SGP-G

The bioassay method used was mainly as described by Katayama et al. [13]. Each experimental animal was kept at salinity of 28 ppt at 28 °C for 7 days. During the experiments, animals were fed dry food pellets (Gold Prawn; Higashimaru) at a rate of 5 % of body weight per day, except in the 24 h before injection. Five days after the beginning of the experimental period, the animals were bilaterally eyestalk-ablated using heated tweezers. After a 7-day total rearing time, sinus gland peptide-G (SGP-G) was injected into the abdomen between the cephalothorax and the tail. SGP-G was identified and obtained from 250 sinus glands by using high-performance liquid chromatography (HPLC) as described below; after freeze-drying, it was then dissolved in phosphate-buffered saline (PBS; pH 7.4, 9.57 mM). The injected concentrations were 0.02, 0.2, 2, 20, and 200 ng, and SGP-G of each concentration was prepared by dilution in 100 μ L PBS. PBS only as a vehicle control, and crude extracts from 2 sinus glands as positive controls were also injected in the same manner. Hemolymph was collected in 20 μ L 1 M sodium citrate 1 h after the injection. The concentration of sodium citrate in the hemolymph samples was adjusted to 0.1 M after collection.

Quantification of CHHs in sinus glands

Peptides in the sinus glands were extracted by the same method as described in our previous study, with several modifications [8]. Eyestalk samples of individuals subjected to air exposure for 0 and 30 min., and of those subjected to all conditions in the low-salinity experiments, were utilized for analysis. The right eyestalks were dissected, and each sinus gland was collected in 200 μ L 30 % acetonitrile containing 0.9 % NaCl. The concentration of acetonitrile was adjusted to 50 % with 100 % acetonitrile, and each sinus gland was homogenized separately. The homogenates were centrifuged at 4 °C and 20,000g for 10 min, and the supernatants were collected. Each supernatant was evaporated to remove the acetonitrile; the volume was then adjusted to 1 mL with 0.05 % trifluoroacetic acid (TFA). The extracts were then applied to a Sep-Pak C₁₈ Cartridge (Waters, MA, USA). The cartridge was washed with 20 % acetonitrile in 0.05 % TFA, and the samples were eluted with 50 % acetonitrile in 0.05 % TFA. The acetonitrile in the eluted samples was evaporated in a centrifugal evaporator, and the sample volume was adjusted to 1 mL with 0.05 % TFA.

Each CHH was quantified by reversed-phase high-performance liquid chromatography (HPLC) in a Shimadzu LC-10 HPLC system (Shimadzu, Kyoto, Japan). The analysis was performed on a Shodex Asahipak ODP-50 2D (2 mm I.D. \times 150 mm; Showa Denko, Tokyo, Japan) with a Shodex Asahipak ODP-50 2A (2 mm I.D. \times 10 mm; Showa Denko, Tokyo, Japan) as a guard column; and 0.05 % TFA and 80 % acetonitrile in 0.05 % TFA was used as a mobile phase. For the air-exposure experiments, ingredients in the samples were separated at 40 °C and flow rate of 0.2 mL/min according to the time program shown in (a) in Table 1. For the low-salinity experiments the experimental conditions were slightly modified because of the use of a different batch of column from the same manufacturer. The time program given in (b) in Table 1 was used at 50 °C for separation. In both experiments, each component was detected at a wavelength of 225 nm.

Human recombinant insulin was used as an external standard for quantification. The quantity of each CHH-family peptide was calculated against the standard curves for insulin and recombinant SGP-G (rSGP-G). In this study, only CHH-family peptides that could be separated to homogeneity by HPLC were targeted for quantification. A CHH-family peptide was regarded as nearly pure in the case that a single peak could be detected by matrix-assisted laser desorption ionization time-of-flight (MALDI-TOF) mass spectrometry (data not shown). The thus targeted CHH-family peptides differed between the experiments; SGP-A, SGP-B, SGP-C, and SGP-G were quantified in animals subjected to air exposure, while SGP-C, SGP-F,

Table 1 Time program for HPLC analysis of CHH-family peptides in eyestalks in experimental air exposure (a) and low salinity (b)

Time (min)	Acetonitrile concentration (%)
(a)	
0	24.8
15	24.8
75	50.0
(b)	
0	22.4
20	22.4
105	39.0

A binary system consisting of 0.05 % TFA and 80 % acetonitrile in 0.05 % TFA was used as the mobile phase in accordance with this time program

and SGP-G were quantified in animals exposed to low salinity. The time programs in these experiments were therefore adjusted for the above purposes.

Identification of each CHH by using MALDI-TOF mass spectrometry

Each HPLC peak was examined by using MALDI-TOF mass spectrometry before the analysis above, in order to identify CHH-family peptides in the peak and to elucidate the purity of each peptide. Sinus gland extract was prepared from 7 to 20 eyestalks by using the method described above. Each HPLC fraction was collected and concentrated to volume of less than 10 μ L. One microliter of each sample was mixed with 1 μ L matrix reagent on the plate used for MALDI-TOF mass spectrometry (AB Sciex, Foster City, CA, USA). The matrix reagent was prepared by dissolving sinapic acid in 50 % acetonitrile in 0.05 % TFA. The mixture on the plate was dried in air, and the plate was then inserted into the mass spectrometer (Voyager-DE STR; AB Sciex). Mass spectra were analyzed in accordance with the instructions in the manual provided by the manufacturer.

Detection of SGP-G in hemolymph

In this study, we analyzed hemolymph samples from animals subjected to 0 and 30 min of air exposure or 3 h of exposure to low salinity. This selection was made on the basis of increases in hemolymph glucose levels when animals were subjected to each type of stress. Hemolymph samples in 50 % acetonitrile were centrifuged at 4 °C and 20,000g for 10 min. The supernatants were collected, and the acetonitrile was evaporated in a centrifugal evaporator. Samples were adjusted to total volume of 1 mL with 0.05 % TFA, and centrifuged again at 4 °C and 20,000g for

10 min. The supernatants were then applied to a Sep-Pak C₁₈ cartridge (Waters) as described above, after the elimination of acetonitrile in a centrifugal evaporator. The fractions of each CHH peptide were collected by HPLC as described above, according to each elution time. Ten microliters of Laemmli buffer (Bio-Rad Laboratory Inc., CA, USA) was added in each fraction, which was then concentrated to 10 μ L and neutralized with 4 μ L 1 M NaHCO₃. Mercaptoethanol was added to each sample; the concentration was adjusted to 10 %, and the samples were heated at 95 °C for 3 min. A standard was prepared by using rSGP-G in the same manner. The samples and standards were subjected to Western blotting analysis.

Sodium dodecyl sulfate (SDS) polyacrylamide gel electrophoresis (PAGE) was performed with commercial 15 % acrylamide gel (Atto, Tokyo, Japan). Running buffer was prepared by dissolving 3.03 g Tris-hydroxymethyl aminomethane (Tris), 14.4 g glycine, and 1 g sodium dodecyl sulfate (SDS) in Milli-Q water (total, 1 L). Electrophoresis was performed at 10 mA for 100 min.

Following SDS-PAGE, peptides in the gel were transferred to a polyvinylidene fluoride (PVDF) membrane. The gel was washed in distilled water for 20 s and then soaked in blotting buffer for 3 min. The PVDF membrane was washed in methanol for 1 min, rinsed in Milli-Q water, and soaked in blotting buffer before use. The blotting buffer was prepared by dissolving 3.03 g Tris, 14.4 g glycine, and 200 mL methanol in Milli-Q water (total, 1 L). The gel and PVDF membrane were each placed between 2 filter papers and treated with a blotting apparatus (Bio-Rad). Transfer was performed at 150 mA for 100 min.

After blotting, the PVDF membrane was soaked in blocking buffer and incubated at 37 °C for 1 h for blocking. Immunoreactions were then performed by an indirect method, using anti-rSGP-G available in our laboratory (Takara Bio Inc., Shiga, Japan) and a second antibody from a commercial kit (Vectastain Elite ABC kit; Vector Laboratories Inc., CA, USA) dissolved in blocking buffer. The PVDF membrane was separately incubated at 37 °C for 1 h in the buffers containing each antibody. The second antibody was labeled with horseradish peroxidase from the kit (Vectastain Elite ABC kit; Vector Laboratories) at 30 °C for 1 h, in accordance with the manufacturer's protocol. The PVDF membrane was washed in washing buffer 3 times for 1 min each time, and 3 times for 5 min each time, between each process. The washing buffer was prepared by dissolving 10 mL 1 M Tris-HCl (pH 8.0), 5.844 g NaCl, and 1 mL Tween 20 in Milli-Q water (total, 1 L). The blocking buffer was prepared by dissolving 2.5 g bovine serum albumin in wash buffer (50 mL total).

The membrane was finally reacted with chemiluminescence reagents (Immunostar LD; Wako Pure Chemical Industries Ltd., Osaka, Japan), and SGP-G on the

membrane was detected using a ChemiDoc XRS molecular imager (Bio-Rad).

Analysis of glucose levels in hemolymph

Hemolymph samples with 0.1 M sodium citrate were heated at 105 °C for 10 min and then centrifuged at 4 °C and 20,000g for 10 min. The supernatants were collected and subjected to glucose assay with a commercial kit (Sigma-Aldrich Inc., MI, USA).

Statistical analysis

For each CHH-family peptide in the eyestalk in the air-exposure experiments, the method of statistical analysis was selected according to the homogeneity of variance examined by the *F* test. Differences between means were compared by using a Student's *t* test or Mann-Whitney *U* test. For each CHH-family peptide in the eyestalk in the low-salinity experiments and for the glucose levels in the hemolymph, the statistical methods were selected according to the homogeneity of variance examined by the Bartlett test. Differences among the mean concentrations of CHH-family peptides in the eyestalk in the low-salinity experiments were compared by using parametric or non-parametric Bonferroni-type multiple comparison. Differences between the means of glucose levels were compared by using Dunnett's method or the Shirley-Williams method.

Results

Responses of CHHs in sinus glands

Under the experimental conditions used in the air-exposure experiments, we found all 8 CHH peptides previously reported in *L. vannamei* (Fig. 1). The fractions of the peaks of SGP-A, SGP-B, SGP-C, and SGP-G were almost pure according to MALDI-TOF mass spectrometry. The chromatogram pattern of 1 sinus gland was similar to that of 20 sinus glands (Fig. 1). The peak area of recombinant SGP-G was one-third as large as that of human recombinant insulin (Fig. 2). Amounts as low as 50 ng of recombinant SGP-G could be detected with this method, with peak area corresponding to that of the standard curve. SGP-A, SGP-B, SGP-C, and SGP-G were quantified by using human recombinant insulin as an external standard and multiplying by one-third. The fractions of the peaks of SGP-C, SGP-F, and SGP-G were almost pure as determined by MALDI-TOF mass spectrometry under the conditions used in the low-salinity experiments (Fig. 3). Similar to those in the air-exposure experiment, the peak area of recombinant

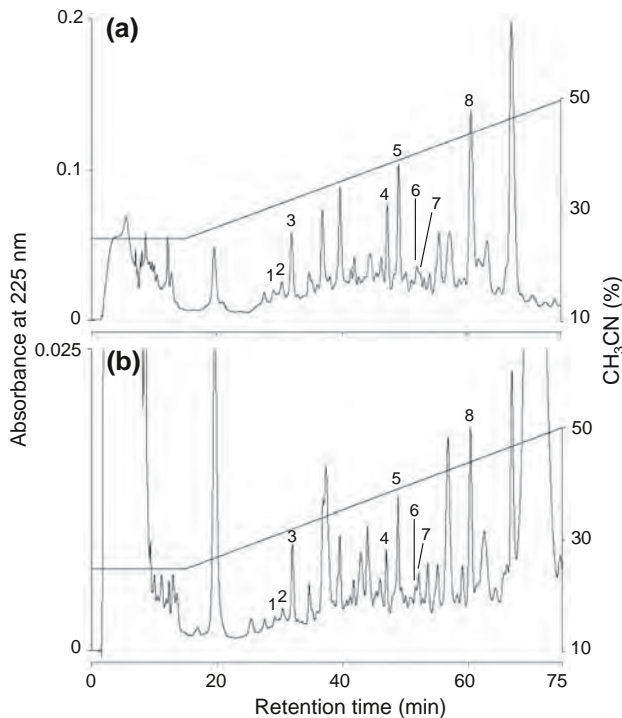


Fig. 1 HPLC chromatograms of sinus glands in animals subjected to air exposure: **a** 20 sinus glands, and **b** one sinus gland extracted from a right eyestalk. Each chromatogram was corrected against the background chromatogram when 1 mL 0.05 % TFA was injected. *Peaks: 1* SGP-A, *2* SGP-B, *3* SGP-C, *4* Pev 26 and impurities, *5* SGP-D and impurities, *6* SGP-E and impurities, *7* SGP-F and impurities, *8* SGP-G. The naming of the CHHs is as described by Tsutsui et al. [8]. The concentration of acetonitrile is indicated by the *solid line*

SGP-G was one-third as large as that of human recombinant insulin (data not shown).

We subjected experimental animals to air-exposure stress and analyzed SGP-A, SGP-B, SGP-C, and SGP-G in the sinus glands by using HPLC. Only the level of SGP-G decreased significantly when the animals were placed in air for 30 min ($P < 0.05$) (Fig. 4). Although the peaks of Pev 26 and SGP-D were not pure, these peaks also showed significant decreases (data not shown). In the low-salinity experiments, SGP-F levels showed a tendency to decrease at 0 ppt after 6 h; however, the decrease was not significant in comparison with the control ($P > 0.05$). Only SGP-G showed a significant decrease in level ($P < 0.05$) when animals were exposed to salinity of 0 ppt for 6 h (Fig. 5). This was similar to the results of the air-exposure experiments.

SGP-G in hemolymph

We confirmed that SGP-G was present in the hemolymph of only those animals that had been subjected to air-exposure stress for 30 min (Fig. 6a). The SGP-G concentration was estimated at 10 ng/mL. The sensitivity of the Western blotting analysis was 0.15 ng. In the air-exposure experiments we

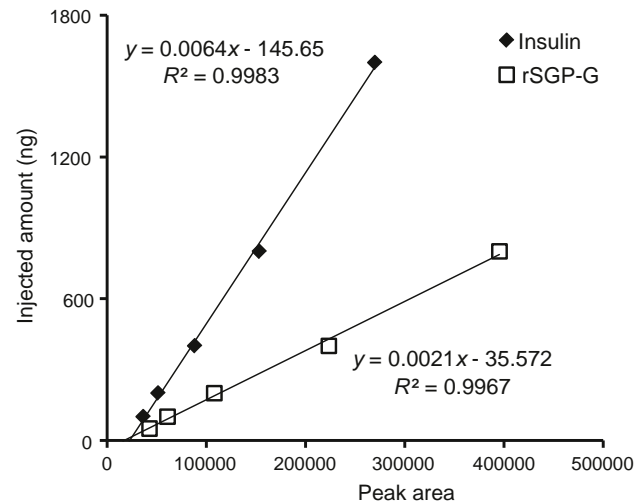


Fig. 2 Standard curve of insulin human recombinant and SGP-G recombinant (rSGP-G). The quantity of rSGP-G per peak area was one-third as large as that of human recombinant insulin, which was used as a standard for CHH quantification

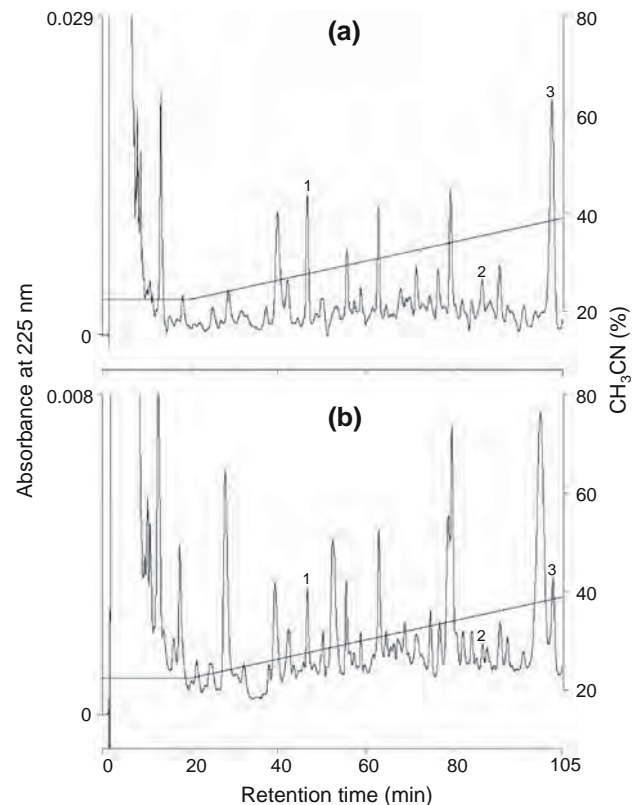


Fig. 3 HPLC chromatograms of sinus glands in animals subjected to low salinity: **a** 7 sinus glands, and **b** 1 sinus gland extracted from a right eyestalk. Each chromatogram was corrected against the background chromatogram when 1 mL 0.05 % TFA was injected. *Peaks: 1* SGP-C, *2* SGP-F, *3* SGP-G. The naming of the CHHs is as described by Tsutsui et al. [8]. The concentration of acetonitrile is indicated by the *solid line*

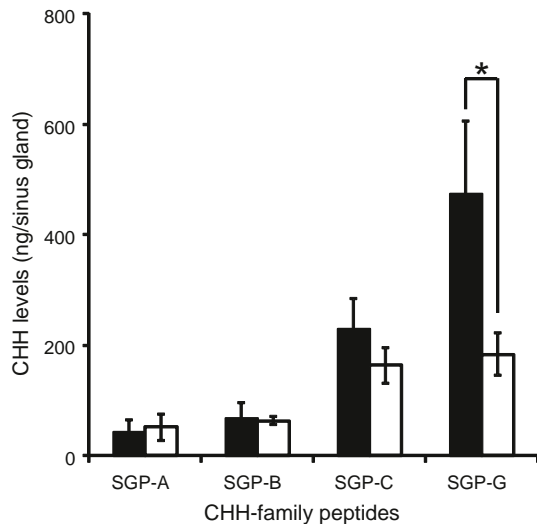


Fig. 4 Levels of the CHHs SGP-A, SGP-B, SGP-C, and SGP-G in the sinus glands of animals subjected to air-exposure stress ($n = 4, 6$). Right sinus glands were individually analyzed. Filled bars indicate control (initial conditions before exposure). Open bars indicate exposure stress for 30 min. Error bars indicate standard errors. Asterisk indicates significant difference ($P < 0.05$)

used 500 μL hemolymph; therefore, the concentration of SGP-G in the hemolymph of animals not subjected to stress was likely to be less than about 0.3 ng/mL. Similarly, SGP-G was detected in the hemolymph of animals exposed to low-salinity stress for 3 h (Fig. 6b), although the quantity was expected to be small. In the low-salinity experiments we used 300 μL hemolymph; therefore, the concentration of SGP-G in the hemolymph of animals not subjected to stress was likely to be less than about 0.5 ng/mL.

Glucose levels in hemolymph

Glucose levels in hemolymph increased significantly in animals subjected to air-exposure stress for 15 or 30 min ($P < 0.05$) (Fig. 7a). Glucose levels also showed a tendency to increase when animals were exposed to low salinity for 3 h, but they recovered to the control levels by 6 h (data not shown). Glucose levels in hemolymph also significantly increased when 200 ng SGP-G or extract of two sinus glands was injected into animals whose sinus glands had been removed by eyestalk ablation ($P < 0.05$) (Fig. 7b). The quantity of SGP-G injected was almost equivalent to the quantity lost from one sinus gland when the animals were subjected to air-exposure stress (Fig. 4).

Discussion

We initially established a method of simultaneously quantifying each CHH-family peptide in the sinus glands by using

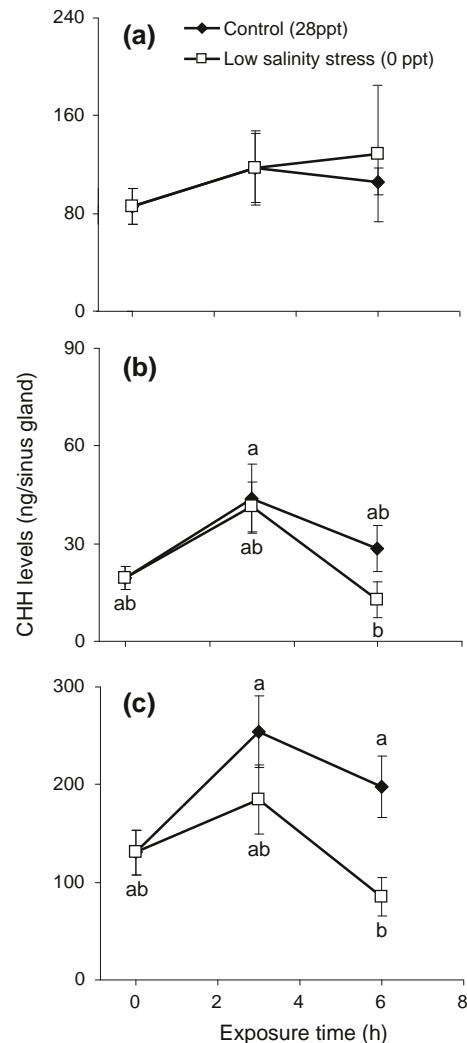


Fig. 5 Levels of the CHHs SGP-C (a), SGP-F (b), and SGP-G (c) in the sinus glands of animals subjected to 0 ppt low-salinity stress for 0, 3, or 6 h ($n = 4-6$). Right sinus glands were individually analyzed. Although the HPLC conditions differed, SGP-G levels decreased when the animals were subjected to low-salinity stress, as when they were subjected to air-exposure stress (Fig. 4). Error bars indicate standard errors. Different letters indicate significant difference ($P < 0.05$)

HPLC. With our method, three or four CHHs from among eight CHH-family peptides already found in *L. vannamei* were separated to almost pure levels. We quantified the peptides, using recombinant insulin as a standard, because recombinant insulin is easy to obtain and has a molecular size similar to those of CHH-family peptides. Use of this method can avoid the overestimation that occurs with analytical methods that use immunoreaction. This point is particularly useful for CHH analysis, because antibodies made from CHH-family peptides often show cross-reaction [17].

All CHH-family peptides that we analyzed are classified as type I [8]. Similarly to in our previous study [8], SGP-G was the most abundant CHH-family peptide in the

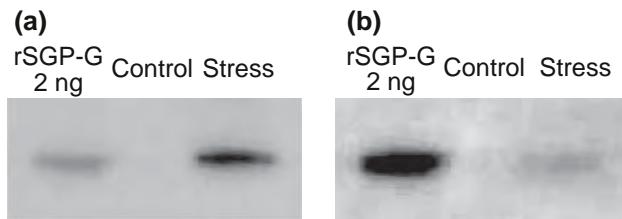


Fig. 6 SGP-G in hemolymph detected by Western blotting analysis. Results for approximately 500 μ L hemolymph from one individual examined in air-exposure experiments (a). Results for approximately 300 μ L hemolymph from one individual examined in low-salinity experiments (b)

eyestalks. When animals were exposed to air, the level of only SGP-G in the eyestalks decreased, whereas the levels of SGP-A, SGP-B, and SGP-C were maintained. Similarly, when animals were exposed to low salinity, the level of only SGP-G in the eyestalks decreased. SGP-G was also detected in hemolymph sampled from animals subjected to air or low salinity. Considering that the XO-SG in eyestalk is the organ that produces and accumulates CHH-family peptides and secretes them into the hemolymph if necessary [18], these results suggest that SGP-G is secreted from the XO-SG into the hemolymph in response to different types of stress, whereas the other hormones analyzed here are probably not.

When the animals were subjected to stressful conditions, hemolymph glucose levels showed an increasing tendency similar to the increase in SGP-G levels in the hemolymph. As described above, CHH-family peptides of type I mostly possess hyperglycemic activity [13]. Hence, we consider that the hyperglycemia observed during air-exposure stress is partly or mostly controlled by SGP-G. This idea is supported by the results of our bioassay of SGP-G. Hemolymph glucose levels were significantly increased by injecting 200 ng SGP-G. This injection amount is close to the amount by which SGP-G levels decreased in one eyestalk during air exposure. These results suggest that SGP-G possesses hyperglycemic activity in the stress response. It has been reported in a related species *M. japonicus* that CHH affects the hepatopancreas, inhibits glycogen synthase, and activates glycogen phosphorylase [6]. Hence, hyperglycemia caused by SGP-G is likely brought about by a similar mechanism. Furthermore, our previous incubation experiments using ovaries in *L. vannamei* revealed that SGP-G has vitellogenesis-inhibiting activity [8]. Inhibition of sexual maturation is a general response when organisms are subjected to stressful conditions. This response is likely caused by a change in energy use, from use in maturation to use in survival. It is possible, therefore, that SGP-G is a hormone that shifts physiological conditions from other activities in order to deal with stress.

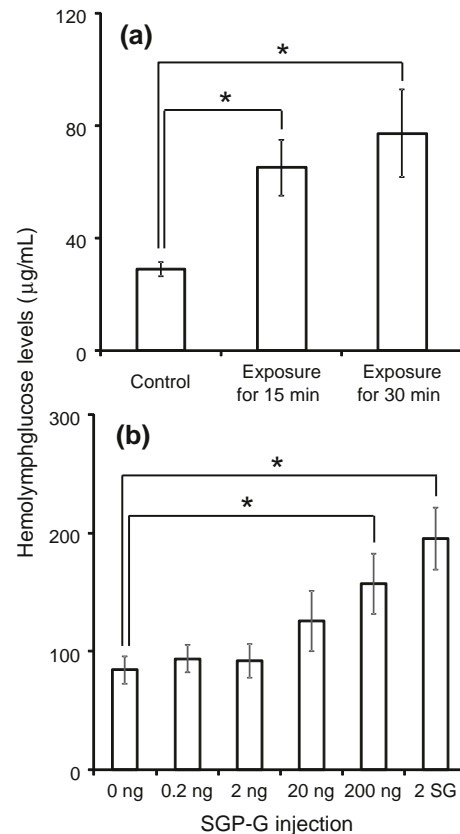


Fig. 7 Hemolymph glucose levels when experimental animals were subjected to exposure stress (a, $n = 4$ or 5) or when SGP-G was injected after bilateral eyestalk ablation (b, $n = 5$ –28). “Control” indicates initial conditions before exposure. “2 SG” indicates the extract from 2 sinus glands. Error bars indicate standard errors. Different letters indicate significant differences ($P < 0.05$)

Our results therefore suggest that, in *L. vannamei* subjected to air-exposure and low-salinity stresses, at least one of the type I CHH-family peptides in the eyestalk is concerned with energy mobilization. Interestingly, the results also implied that not all type I CHH-family peptides function in the stress response. Secretion of CHH-family peptides and increased hemolymph glucose levels have been reported in many crustacean species exposed to various stressful conditions [3, 5, 11, 19, 20]. It may be possible to assume that type I CHH-family peptides that possess similar characteristics to SGP-G in this species also control physiological conditions in the stress response. To support this hypothesis, it would be valuable to compare the dynamics of CHH-family peptides under stressful conditions in other crustacean species. Further studies are necessary in order to better understand the endocrinology of stress response in Crustacea.

Acknowledgments J.S. was supported by a research fellowship from the Japan Society for the Promotion of Science for Young Scientists. We thank Ms. Yoko Furusawa for helpful assistance during the rearing experiments.

References

- Vijayan MM, Pereira C, Grau EG, Iwama GK (1997) Metabolic responses associated with confinement stress in tilapia: the role of cortisol. *Comp Biochem Physiol* 116C:89–95
- Lorenzon S, Giulianini PG, Libralato S, Martinis M, Ferrero EA (2008) Stress effect of two different transport systems on the physiological profiles of the crab *Cancer pagurus*. *Aquaculture* 278:156–163
- Aparicio-Simón B, Piñón M, Racotta R, Racotta IS (2010) Neuroendocrine and metabolic responses of Pacific whiteleg shrimp *Litopenaeus vannamei* exposed to acute handling stress. *Aquaculture* 298:308–314
- Zhou M, Wang AL, Xian JA (2011) Variation of free amino acid and carbohydrate concentrations in white shrimp, *Litopenaeus vannamei*: effects of continuous cold stress. *Aquaculture* 317:182–186
- Chung JC, Zmora N, Katayama H, Tsutsui N (2010) Crustacean hyperglycemic hormone (CHH) neuropeptides family: functions, titer, and binding to target tissues. *Gen Comp Endocrinol* 166:447–454
- Nagai C, Nagata S, Nagasawa H (2011) Effects of crustacean hyperglycemic hormone (CHH) on the transcript expression of carbohydrate metabolism-related enzyme genes in the kuruma prawn, *Marsupenaeus japonicus*. *Gen Comp Endocrinol* 172:293–304
- Wang YJ, Hayes TK, Holman GM, Chavez AR, Keeley LL (2000) Primary structure of CHH/MIH/GIH-like peptides in sinus gland extracts from *Penaeus vannamei*. *Peptides* 21:477–484
- Tsutsui N, Ohira T, Kawazoe I, Takahashi A, Wilder MN (2007) Purification of sinus gland peptides having vitellogenesis-inhibiting activity from the whiteleg shrimp *Litopenaeus vannamei*. *Mar Biotechnol* 9:360–369
- Fanjul-Moles ML (2006) Biochemical and functional aspects of crustacean hyperglycemic hormone in decapod crustaceans: review and update. *Comp Biochem Physiol* 142C:390–400
- Chang ES, Keller R, Chang SA (1998) Quantification of crustacean hyperglycemic hormone by ELISA in hemolymph of the lobster, *Homarus americanus*, following various stresses. *Gen Comp Endocrinol* 111:359–366
- Chung JS, Webster SG (2005) Dynamics of in vivo release of molt-inhibiting hormone and crustacean hyperglycemic hormone in the shore crab, *Carcinus maenas*. *Endocrinology* 146:5545–5551
- Lorenzon S, Edomi P, Giulianini PG, Mettullo R, Ferrero EA (2005) Role of biogenic amines and cHH in the crustacean hyperglycemic stress response. *J Exp Biol* 208:3341–3347
- Katayama H, Ohira T, Aida K, Nagasawa H (2002) Significance of a carboxyl-terminal amide moiety in the folding and biological activity of crustacean hyperglycemic hormone. *Peptides* 23:1537–1546
- Nagai C, Asazuma H, Nagata S, Nagasawa H (2011) Regulation mechanisms of ecdysteroids synthesis in Y-organ. In: Sonobe H, Nagasawa H (eds) *Biology of molting and metamorphosis*. Tokai University Press, Kanagawa, pp 419–430 (in Japanese)
- Lacombe C, Grève P, Martin G (1999) Overview on the sub-grouping of the crustacean hyperglycemic hormone family. *Neuropeptides* 33:71–80
- Chan SM, Chu KH, Tobe SS (2003) Crustacean neuropeptide genes of the CHH/MIH/GIH family: implications from molecular studies. *Gen Comp Endocrinol* 134:214–219
- Giulianini PG, Pandolfelli N, Lorenzon S, Ferrero EA, Edomi P (2002) An antibody to recombinant crustacean hyperglycaemic hormone of *Nephrops norvegicus* cross-reacts with neuroendocrine organs of several taxa of malacostracan Crustacea. *Cell Tissue Res* 307:243–254
- Keller R (1992) Crustacean neuropeptides: structures, functions and comparative aspects. *Experientia* 48:439–448
- Webster SG (1996) Measurement of crustacean hyperglycaemic hormone levels in the edible crab *Cancer pagurus* during emersion stress. *J Exp Biol* 199:1579–1585
- Reddy PS, Sainath SB (2009) Hyperglycemic hormone in freshwater prawn *Macrobrachium rosenbergii*: purification from eyestalk nervous tissue and quantification by ELISA in hemolymph following various stresses. *Aquaculture* 286:290–295

The ex vivo effects of eyestalk peptides on ovarian vitellogenin gene expression in the kuruma prawn *Marsupenaeus japonicus*

Naoaki Tsutsui · Ayano Nagakura-Nakamura ·
Chiaki Nagai · Tsuyoshi Ohira · Marcy N. Wilder ·
Hiromichi Nagasawa

Received: 8 August 2012 / Accepted: 11 October 2012 / Published online: 2 November 2012
© The Japanese Society of Fisheries Science 2012

Abstract Seven major peptides belonging to the crustacean hyperglycemic hormone family were purified from the sinus gland located in the eyestalk of the kuruma prawn *Marsupenaeus japonicus*, and their effects on vitellogenin gene expression were examined using the ex vivo ovary incubation system. Six molecular species of crustacean hyperglycemic hormone, Pej-SGP-I, -II, -III, -V, VI, and VII, displayed significant inhibitory effects on *vg* expression with almost the same efficacies, whereas Pej-SGP-IV (known as molt-inhibiting hormone) did not. Two chromatophoretropic peptides, red pigment-concentrating

hormone and pigment-dispersing hormone, which were also present in the sinus glands, did not have a clear effect on the gene expression levels in this incubation system. These results suggest that the six crustacean hyperglycemic hormones are potentially capable of acting as vitellogenesis-inhibiting hormones in *M. japonicus*.

Keywords Crustacean hyperglycemic hormone · Kuruma prawn · *Marsupenaeus japonicus* · Sinus gland · Vitellogenesis

N. Tsutsui · A. Nagakura-Nakamura · C. Nagai ·
H. Nagasawa (✉)
Department of Applied Biological Chemistry, Graduate School
of Agricultural and Life Sciences, The University of Tokyo,
1-1-1 Yayoi, Bunkyo-ku, Tokyo 113-8657, Japan
e-mail: anagahi@mail.ecc.u-tokyo.ac.jp

Present Address:

N. Tsutsui
Ushimado Marine Institute, Faculty of Science,
Okayama University, 130-17 Kashino, Ushimado,
Setouchi, Okayama 701-4303, Japan

Present Address:

C. Nagai
Department of Molecular Pharmacology, National Cerebral
and Cardiovascular Center Research Institute,
5-7-1 Fujishirodai, Suita, Osaka 565-8565, Japan

T. Ohira
Department of Biological Science, Faculty of Science,
Kanagawa University, 2946 Tsuchiya, Hiratsuka,
Kanagawa 259-1293, Japan

M. N. Wilder
Fisheries Division, Japan International Research Center
for Agricultural Sciences, 1-1 Ohwashi, Tsukuba,
Ibaraki 305-8686, Japan

Introduction

It has been shown that various kinds of neuropeptide hormones are produced in the eyestalks of crustaceans [1]. Most of them are synthesized in the X-organ and transferred to the sinus gland (SG), from where they are released into the hemolymph. Among them, red pigment concentrating hormone (RPCH) was isolated and sequenced from the sinus glands of the pink shrimp *Pandalus borealis* [2]. This molecule was the first neuropeptide to be characterized not only in crustaceans but also in invertebrates. Subsequently, pigment dispersing hormone (PDH), originally identified as distal retinal pigment hormone, was isolated from SG of *P. borealis* and sequenced [3]. A few decades after the discovery of the two chromatophoretropic peptides, four sinus gland neuropeptides—crustacean hyperglycemic hormone (CHH), molt-inhibiting hormone (MIH), vitellogenesis- or gonad-inhibiting hormone (VIH/GIH), and mandibular organ-inhibiting hormone (MOIH)—were purified and sequenced, one after another [4]. Their primary structures are similar to each other, and form a peptide family referred to as the CHH family. CHH-family peptides are mostly 72–78 amino acid residues long with six conserved cysteine residues which form three

intramolecular disulfide bonds. CHH-family peptides are divided into two subgroups based on the absence (type I) or presence (type II) of a glycine residue at position 12 in the mature peptide. According to this grouping, CHHs can be classified as type I peptide, and most MIHs, VIHs, and MOIHs as type II peptides. Additionally, type I peptides are characterized by an amidated C-terminus, although some type II peptides—MIH from the American crayfish *Procambarus clarkii* [5], the South African spiny lobster *Jasus lalandii* [6], and VIH from the American lobster *Homarus americanus* [7, 8]—possess an amidated C-terminus.

In decapod crustaceans, VIH/GIH regulates vitellogenesis by inhibiting vitellogenin (VG) synthesis. The existence of VIH originating in the eyestalks has been suggested based on the results from the earliest studies [9, 10]. However, despite more recent work to characterize VIH using bioassays involving the indirect estimation of inhibition of VG synthesis (reduction in gonadosomatic index or oocyte diameter) or the direct measurement of inhibition of protein synthesis, VG synthesis, or *vg* expression, as reviewed in [1], our knowledge of peptides with vitellogenesis-inhibiting activity is still limited. The primary structure of VIH was first reported in the American lobster *Homarus americanus* [7]. The *Homarus* VIH (Hoa-VIH) was purified and characterized based on an in vivo bioassay using oocyte diameters in grass shrimp *Palaemonetes varians* as indices [11]. That VIH belongs to the type II subfamily as described above. On the other hand, two molecular species of CHH (type I) from the South African spiny lobster *Jasus lalandii* were reported to inhibit protein synthesis in incubated ovary fragments of the green tiger prawn *Penaeus semisulcatus* [12]. In the giant tiger shrimp *Penaeus monodon*, knockdown of the *pem-gih* gene, which encodes a type II peptide, caused the increase in *vg* mRNA levels [13]. Thus, vitellogenesis-inhibiting activities have been recorded for both type I and II peptides.

In the kuruma prawn *Marsupenaeus japonicus*, two PDHs (Pej-PDH-I and -II), Pej-RPCH, and eight molecular species of CHH-family peptides were purified from SG [14–18]. The three chromatophorotropic peptides were characterized by in vivo bioassay [16]. Among the eight CHH-family peptides, six type I molecules, Pej-SGP-I, -II, -III, -V, -VI, and -VII, have been characterized as CHHs [15, 17]. Both Pej-SGP-IV and -MIH-B are type II; Pej-SGP-IV is considered to be an MIH in this species (Pej-MIH) because of its inhibitory effect on the secretion of ecdysteroids by the Y-organ [16] and on the expression of *phantom* (*mj-phm*), whose translation product may be involved in the steroidogenesis in the Y-organ [19]. Pej-MIH-B shows a weaker inhibitory effect on ecdysteroid secretion [18], and its physiological role is still ambiguous. The participation of these CHH-family peptides in vitellogenesis regulation was first examined using incubated *P. semisulcatus* ovary; six type I molecules inhibited the

protein synthesis [20]. For more detailed clarification of their role in vitellogenesis regulation, the cDNA encoding VG was characterized [21, 22]. Then an ex vivo incubation system of the ovary fragment of *M. japonicus* was established, and the effects of three peptides (Pej-SGP-III, -MIH, and -MIH-B) on *vg* mRNA levels were examined [23]. As a result, Pej-SGP-III (type I) exhibited strong inhibitory activity, whereas Pej-MIH and -MIH-B (type II) had no significant effect, which led to the need to assess the inhibitory effects of all type I peptides.

Here, we report the effects of all type I peptides from *M. japonicus* on *vg* mRNA levels, and consider whether they are vitellogenesis-inhibiting hormones. In addition, two chromatophorotropic neuropeptides that accumulate in SG, Pej-PDH-II and Pej-RPCH, were also assayed in the same system in order to study their contribution to vitellogenesis.

Materials and methods

Animals

Adult *M. japonicus* approximately 18 g in body weight were purchased from a local fish market in Tokyo, Japan. For SG collection, animals were kept in the tank with natural seawater and fed with Goldprawn (Higashimaru Co. Ltd., Kagoshima, Japan). The SGs were collected as described previously [14]. For ex vivo ovary incubation, the animals were kept in a tank with natural seawater and used within the day purchased.

Preparation of eyestalk peptides of *M. japonicus*

The preparation of crude SG extract and the separation of CHH-family peptides using reversed-phase high-performance liquid chromatography (RP-HPLC) were carried out according to the method described previously [15, 17]. After HPLC separation, peaks representing Pej-SGP-I to -VII were identified by mass spectral analysis. Mass spectra were measured on a matrix-assisted laser desorption ionization time-of-flight (MALDI-TOF) mass spectrometer (Voyager-DE STR, Applied Biosystems, Foster City, CA, USA) with 3,5-dimethoxy-4-hydroxycinnamic acid used as a matrix in the positive ion mode. The concentration of each purified peptide was determined based on the absorbance at 280 nm and the extinction coefficient at 280 nm, as estimated from the amino acid sequence of each peptide [24].

Pej-PDH-II was synthesized using 9-fluorenylmethyl-oxycarbonyl-protected amino acids on an automated peptide synthesizer (Apex396, AAPPTec, Louisville, KY, USA). Protocols for peptide synthesis, deprotection, and cleavage from the resin were essentially the same as those recommended by the manufacturer. Deprotected peptides were

dissolved in aqueous trifluoroacetic acid and purified by RP-HPLC. Pej-RPCH was purchased from Toray Research Center Inc. (Tokyo, Japan).

Preparation of recombinant peptides

Recombinant peptide of Pej-SGP-IV (rPej-SGP-IV) was prepared according to a previous report [25], and it was confirmed that the biological activity of the rPej-SGP-IV was comparable to the natural one (data not shown). Expression, removal of the tag moiety, the amidating reaction, and the purification of rPej-SGP-I were performed according to methods described previously [26, 27]. The amidating enzyme was a kind gift from Drs. Ohsuye and Furukawa of Asubio Pharma Co. Ltd. (Gunma, Japan).

Bioassay for vitellogenesis-inhibiting activity using an ex vivo incubation system for the ovary

The effects of Pej-PDH-II, Pej-RPCH, and seven CHH-family peptides on *vg* expression were assessed using an ex vivo ovary incubation system [23]. The organic solvent and water in each peptide solution after RP-HPLC purification were removed by vacuum centrifugation, and the dried peptide was dissolved in the incubation medium. Serial dilutions of medium containing each peptide were prepared: 1 nM, 40 pM, and 2 pM for Pej-SGPs (1 nM only for Pej-SGP-IV); 800 nM, 40 nM, 2 nM, and 0.1 nM for Pej-PDH-II and Pej-RPCH. The following peptide concentrations were employed for the combinations of CHH (rPej-SGP-I) and MIH (rPej-SGP-IV): 0.5 nM MIH alone, a combination of 0.5 nM MIH with 50 pM CHH, that of 0.1 nM MIH with 50 pM CHH, and 50 pM CHH alone. For the group containing no peptide (0 nM group), incubation medium alone was used. One ovarian tissue fragment was incubated in 0.2 mL of medium. Preparation of the tissue fragments, incubation conditions, extraction of total RNA, and subsequent relative quantification of *vg* mRNA levels by quantitative reverse transcriptase-polymerase chain reaction (qRT-PCR) were performed as described previously [23], except that a 7300 real-time PCR system (Applied Biosystems) was used instead of an ABI PRISM 7700 sequence detection system (Applied Biosystems) for real-time monitoring of the fluorescence signal generated during PCR.

Statistics

Numerical data are expressed as the mean \pm SEM. *Vg* mRNA levels are expressed as the percentage change relative to each control value (control = 100). One-way ANOVA with Dunnett's post test was performed using GraphPad Prism version 4.03 for Windows (GraphPad Software, Inc., La Jolla, CA, USA).

Results

Effects of CHHs on *vg* expression

The vitellogenesis-inhibiting activities of six CHHs (Pej-SGP-I, -II, -III, -V, -VI, and -VII) were assessed at concentrations ranging from 2 pM to 1 nM. All peptides inhibited *vg* expression in ex vivo incubated ovary fragments in a dose-dependent manner with very similar efficacies (Fig. 1). Significant inhibitory effects were observed at 40 pM and 1 nM; *vg* levels in ovary fragments that received 1 nM CHHs were 19–34 % of those in control ovary fragments. MIH (Pej-SGP-IV) did not show a significant inhibitory effect, even at 1 nM, as reported previously [23].

Effects of PDH and RPCH on *vg* expression

Neither Pej-RPCH nor Pej-PDH-II had a clear effect on *vg* expression in the assay at any of the four concentrations employed. *Vg* mRNA levels were 95–111 % for Pej-RPCH (Fig. 2a) and 94–107 % of the control for Pej-PDH-II (Fig. 2b).

Combined effects of CHH and MIH

To examine the combined effects of CHH and MIH on *vg* expression levels, incubation was performed using medium containing CHH (rPej-SGP-I) or MIH (rPej-SGP-IV) alone or both CHH and MIH. As shown in Fig. 3, CHH alone exhibited 46 % inhibition at 50 pM, which was not reduced by the addition of 100 and 500 pM MIH (47 and 57 %, respectively).

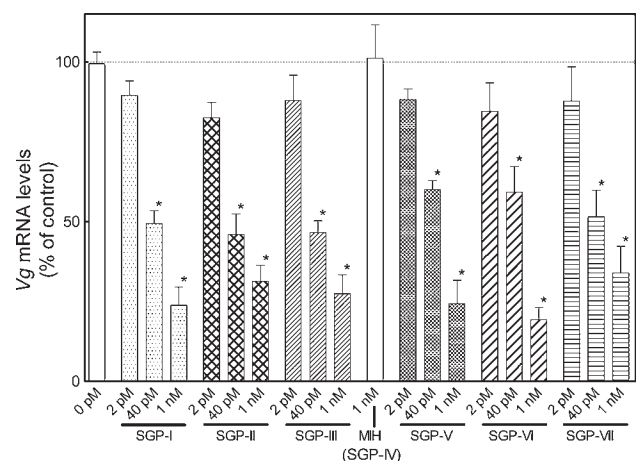


Fig. 1 Effects of CHH-family peptides from *M. japonicus* on *vg* mRNA levels in an ex vivo ovary incubation system. Relative *vg* mRNA levels are expressed as percentage changes relative to control values. The results are presented as the mean \pm SEM of four prawns. Asterisks indicate significant differences compared with 0 pM groups (* $P < 0.01$, Dunnett's test)

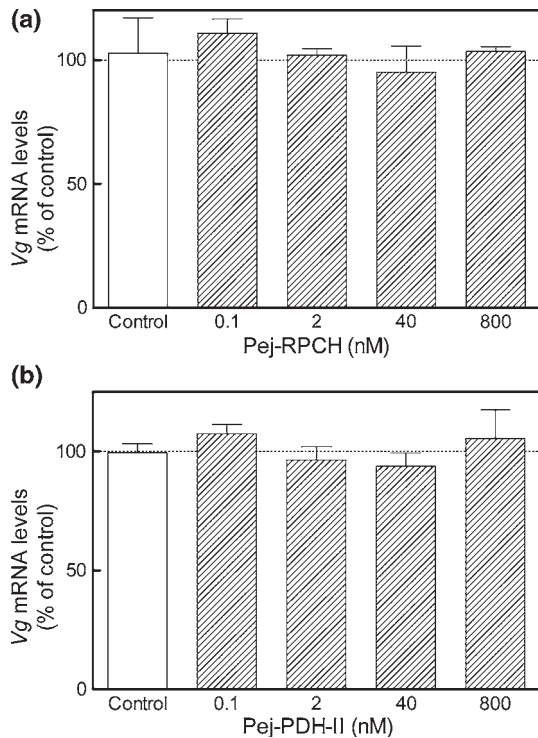


Fig. 2 Effects of Pej-RPCH (a) and Pej-PDH-II (b) on the *vg* mRNA levels in ex vivo incubated ovary fragments. Relative *vg* mRNA levels are expressed as percentage changes relative to control values. The results are presented as the mean \pm SEM of five prawns for a and four prawns for b

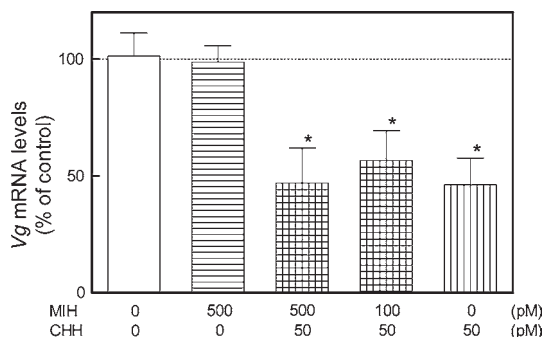


Fig. 3 *Vg* mRNA levels in ex vivo incubated ovary fragments receiving combinations of CHH (rPej-SGP-I) and MIH (rPej-SGP-IV). Relative *vg* mRNA levels are expressed as percentage changes relative to control values. The results are presented as the mean \pm SEM of five prawns. Asterisks indicate significant differences compared with 0 pM groups ($*P < 0.05$, Dunnett's test)

respectively), whereas MIH alone did not affect the *vg* expression level at 500 pM.

Discussion

In recent years, *vg* genes or *vg* cDNAs have been characterized in decapods, and they have been utilized as a reliable tool to understand the process of vitellogenesis. We

previously established an ex vivo bioassay in which *vg* expression levels of incubated ovary fragments were utilized to check the vitellogenesis-inhibiting or -stimulating effects of target molecules, and assessed three CHH-family peptides: Pej-SGP-III, Pej-MIH, and Pej-MIH-B [23]. In the present study, all of the major CHH-family peptides were subjected to this bioassay. The results showed that the six CHHs belonging to the type I peptide group exhibit vitellogenesis-inhibiting activity, but MIH, which belongs to the type II peptide group, does not. Additionally, our preliminary experimental results showed that a non-CHH-family peptide fraction corresponding to the eluate of RP-HPLC, from which CHH-family peptide fractions (Pej-SGP-I to -VII) were removed, did not show a significant inhibitory effect at a concentration of 0.1 SG equivalents/mL (data not shown). Although minor peptides such as a putative CHH, MIH-C, and PDH-3 that were found by performing expressed sequence tag analysis of *M. japonicus* eyestalk [28] or other unknown factors in SG may regulate vitellogenesis, most of the inhibitory activity exerted by the crude extract of SG [23] is considered to be derived from the six CHHs.

In our previous study, vitellogenesis-inhibiting activities of CHH-family peptides of the whiteleg shrimp *Litopenaeus vannamei* were examined by the same ex vivo bioassay; type I peptides showed inhibitory activity, but a C-terminally truncated type I peptide had weaker activity, whereas a type II peptide had no activity [29]. Together with the previous reports [12, 20], we can therefore conclude that vitellogenesis-inhibiting activities of type I peptides are detectable in penaeid shrimp ovarian bioassay, and that their efficacies are affected by the presence or absence of the C-terminal amide moiety, as is the case for hyperglycemic activity [27, 30, 31]. On the other hand, Pem-GIH (a type II peptide) from *P. monodon*, which belongs to the same family (Penaeidae) as *M. japonicus*, was presumed to be a VIH/GIH based on the result that *vg* expression levels were increased by the knockdown of that gene using *pem-gih* dsRNA injection [13]. Thus, the nature of the authentic and biologically relevant VIH within the family Penaeidae is still unclear. In addition to the above work on Pem-GIH, gene silencing by dsRNA administration was also used to characterize the gonad-stimulating hormone (GSH) in *Metapenaeus ensis* [32]. Similarly, dsRNAs that target the six CHHs of *M. japonicus* will be useful for verifying their in vivo vitellogenesis-inhibiting activities. Furthermore, information on the contents of the six CHHs in one SG and their physiological concentrations in the hemolymph during vitellogenesis will provide circumstantial evidence that will aid our understanding of the contribution of each peptide to vitellogenesis regulation.

The C-terminal amide is a characteristic of type I peptides, while the insertion of a glycine residue at position 12

is a characteristic of type II peptides. Mutated type I peptides with a glycine inserted at position 12 showed reduced hyperglycemic activity despite having an amidated C-terminus [33]. As a result of tertiary structural analysis of Pej-MIH (Pej-SGP-IV) and subsequent homology modeling, a common fold has been proposed for both type I and II peptides, because they possess conserved arrangements of the three disulfide bonds [34]. However, the primary structure is not well conserved between the two subgroups, and each group possesses structural characteristics that are essential for its hormonal activity. Therefore, tertiary structural analysis of type I peptides [26] will be required to gain a better understanding of the structural and functional divergence of the CHH family of peptides.

Among chromatophoretic peptides, it has been proposed that RPCH acts as a neurotransmitter in the red swamp crayfish *Procambarus clarkii*, stimulating GSH release from thoracic ganglia [35], and, so far, this is the only report that describes the stimulatory effect of chromatophoretic peptide on vitellogenesis. On the other hand, it was shown that Pej-PDH-I and Pej-RPCH exert no effect on ovarian protein synthesis [20]. In this study, the direct vitellogenesis-regulating activities of both Pej-RPCH and Pej-PDH-II were assessed, and as was expected, they did not show any definite effects on *vg* expression under the experimental conditions employed. In addition to these results, since the non-CHH-family peptide fraction did not show significant vitellogenesis-regulating activity, Pej-PDHs probably do not directly affect *vg* expression. To assess the participation of Pej-RPCH in the regulation of vitellogenesis, *in vivo* injection or *ex vivo* incubation of the ovary and thoracic ganglia will be required.

In the experiment investigating the combined effects of CHH and MIH, MIH acted neither cooperatively nor antagonistically on the vitellogenesis-inhibiting activity of CHH: the inhibitory effect of CHH was unabated in the presence of MIH, the concentration of which was two and ten times higher than that of CHH. These results suggest that the ovarian tissues lack the MIH receptor, or that the MIH molecule has very low affinity for the CHH receptor. In the *M. japonicus* ovary, it was found (using a similar incubation system to that employed in this study) that both cyclic adenosine monophosphate (cAMP) and cyclic guanosine monophosphate (cGMP) mediate the action of VIH, whereas calcium ion and protein kinase C are involved in the inhibition of *vg* expression, irrespective of VIH [36]. Moreover, it was reported that cGMP, rather than cAMP, mediated the signaling pathway of CHH in the hepatopancreas [37], and that intracellular cGMP levels increased upon the stimulation of CHH [38] using rPej-SGP-VII. Therefore, it is presumed that receptors involved in cGMP signaling (i.e., membrane-associated or soluble guanylate cyclase) or in cAMP signaling (i.e., G protein-coupled

receptor) are candidates for the receptor for CHH-family peptides. The cDNA encoding guanylate cyclase has been characterized in some crustacean species [39–41], but the functional receptor for CHH-family peptides has not been identified in any crustacean species. To understand the signal transduction processes activated by VIH, information on its receptor molecule will be needed.

Acknowledgments We are grateful to Dr. Takeshi Kawai of the Department of Applied Biological Chemistry, Graduate School of Agricultural and Life Sciences, The University of Tokyo, for preparing Pej-PDH-II. This work was partly supported by a Fisheries Research Agency project and a Grant-in-Aid for Scientific Research (no. 21780186) from the Ministry of Education, Culture, Sport, Science and Technology of Japan. N.T. and C.N. were supported by a Research Fellowship of the Japan Society for the Promotion of Science for Young Scientists.

References

- Keller R (1992) Crustacean neuropeptides: structures, functions and comparative aspects. *Experientia* 48:439–448
- Fernlund P, Josefsson L (1972) Crustacean color-change hormone: amino acid sequence and chemical synthesis. *Science* 177:173–175
- Fernlund P (1976) Structure of a light-adapting hormone from the shrimp, *Pandalus borealis*. *Biochim Biophys Acta* 439:17–25
- Webster SG, Keller R, Dirksen H (2012) The CHH-superfamily of multifunctional peptide hormones controlling crustacean metabolism, osmoregulation, moulting, and reproduction. *Gen Comp Endocrinol* 175:217–233
- Nagasawa H, Yang WJ, Shimizu H, Aida K, Tsutsumi H, Terauchi A, Sonobe H (1996) Isolation and amino acid sequence of a molt-inhibiting hormone from the American crayfish, *Procambarus clarkii*. *Biosci Biotechnol Biochem* 60:554–556
- Marco HG, Stoeva S, Voelter W, Gäde G (2000) Characterization and sequence elucidation of a novel peptide with molt-inhibiting activity from the South African spiny lobster, *Jasus lalandii*. *Peptides* 21:1313–1321
- Soyez D, Le Caer JP, Noel PY, Rossier J (1991) Primary structure of two isoforms of the vitellogenesis inhibiting hormone from the lobster *Homarus americanus*. *Neuropeptides* 20:25–32
- Soyez D (1997) Occurrence and diversity of neuropeptides from the crustacean hyperglycemic hormone family in arthropods. *Ann NY Acad Sci* 814:319–323
- Panouse JB (1943) Influence de l'ablation du pédoncle oculaire sur la croissance de l'ovaire chez la crevette *Leander serratus*. *C R Acad Sci Paris* 217:553–555
- Brown FA Jr, Jones GM (1948) Ovarian inhibition by a sinus gland principle in the fiddler crab. *Biol Bull* 96:228–232
- Soyez D, Van Deijnen JE, Martin M (1987) Isolation and characterization of a vitellogenesis-inhibiting factor from sinus glands of the lobster *Homarus americanus*. *J Exp Zool* 244:479–484
- Marco HG, Avarre JC, Lubzens E, Gäde G (2002) In search of a vitellogenesis-inhibiting hormone from the eyestalks of the South African spiny lobster, *Jasus lalandii*. *Invert Reprod Dev* 41:143–150
- Treerattrakool S, Panyim S, Chan SM, Withyachumnarnkul B, Udomkit A (2008) Molecular characterization of gonad-inhibiting hormone of *Penaeus monodon* and elucidation of its inhibitory role in vitellogenin expression by RNA interference. *FEBS J* 275:970–980

14. Yang WJ, Aida K, Terauchi A, Sonobe H, Nagasawa H (1996) Amino acid sequence of a peptide with molt-inhibiting activity from the kuruma prawn *Penaeus japonicus*. *Peptides* 17:197–202
15. Yang WJ, Aida K, Nagasawa H (1997) Amino acid sequences and activities of multiple hyperglycemic hormones from the kuruma prawn, *Penaeus japonicus*. *Peptides* 18:479–485
16. Yang WJ, Aida K, Nagasawa H (1999) Characterization of chromatophoretropic neuropeptides from the kuruma prawn *Penaeus japonicus*. *Gen Comp Endocrinol* 114:415–424
17. Nagasawa H, Yang WJ, Aida K, Sonobe H (1999) Chemical and biological characterization of neuropeptides in the sinus glands of the kuruma prawn, *Penaeus japonicus*. In: Shimonishi Y (ed) *Peptide science-present and future*. Kluwer, Dordrecht, pp 453–454
18. Ohira T, Katayama H, Tominaga S, Takasuka T, Nakatsuji T, Sonobe H, Aida K, Nagasawa H (2005) Cloning and characterization of a molt-inhibiting hormone-like peptide from the prawn *Marsupenaeus japonicus*. *Peptides* 26:259–268
19. Asazuma H, Nagata S, Nagasawa H (2009) Inhibitory effect of molt-inhibiting hormone on phantom expression in the Y-organ of the kuruma prawn, *Marsupenaeus japonicus*. *Arch Insect Biochem Physiol* 72:220–233
20. Khayat M, Yang WJ, Aida K, Nagasawa H, Tietz A, Funkenstein B, Lubzens E (1998) Hyperglycaemic hormones inhibit protein and mRNA synthesis in in vitro-incubated ovarian fragments of the marine shrimp *Penaeus semisulcatus*. *Gen Comp Endocrinol* 110:307–318
21. Tsutsui N, Kawazoe I, Ohira T, Jasmani S, Yang WJ, Wilder MN, Aida K (2000) Molecular characterization of a cDNA encoding vitellogenin and its expression in the hepatopancreas and ovary during vitellogenesis in the kuruma prawn, *Penaeus japonicus*. *Zool Sci* 17:651–660
22. Tsutsui N, Kim YK, Jasmani S, Ohira T, Wilder MN, Aida K (2005) The dynamics of vitellogenin gene expression differs between intact and eyestalk ablated kuruma prawn, *Penaeus (Marsupenaeus) japonicus*. *Fish Sci* 71:249–256
23. Tsutsui N, Katayama H, Ohira T, Nagasawa H, Wilder MN, Aida K (2005) The effects of crustacean hyperglycemic hormone family peptides on vitellogenin gene expression in the kuruma prawn, *Marsupenaeus japonicus*. *Gen Comp Endocrinol* 144:232–239
24. Pace CN, Vajdos F, Fee L, Grimsley G, Gray T (1995) How to measure and predict the molar absorption coefficient of a protein. *Protein Sci* 11:2411–2423
25. Ohira T, Nishimura T, Sonobe H, Okuno A, Watanabe T, Nagasawa H, Ichiro K, Aida K (1999) Expression of a recombinant molt-inhibiting hormone of the Kuruma prawn *Penaeus japonicus* in *Escherichia coli*. *Biosci Biotechnol Biochem* 63:1576–1581
26. Inoue H, Tsutsui N, Nagai C, Nagata K, Tanokura M, Nagasawa H (2011) Crystallization and preliminary X-ray analysis of crustacean hyperglycemic hormone from the kuruma prawn *Marsupenaeus japonicus* in its weakly-active precursor form. *Acta Cryst F67*:1586–1589
27. Katayama H, Ohira T, Aida K, Nagasawa H (2002) Significance of a carboxyl-terminal amide moiety in the folding and biological activity of crustacean hyperglycemic hormone. *Peptides* 23:1537–1546
28. Yamano K, Unuma T (2006) Expressed sequence tags from eyestalk of kuruma prawn, *Marsupenaeus japonicus*. *Comp Biochem Physiol Part A Mol Integr Physiol* 143:155–161
29. Tsutsui N, Ohira T, Kawazoe I, Takahashi A, Wilder MN (2007) Purification of sinus gland peptides having vitellogenesis-inhibiting activity from the whiteleg shrimp *Litopenaeus vannamei*. *Mar Biotechnol* 9:360–369
30. Ohira T, Katayama H, Aida K, Nagasawa H (2003) Expression of a recombinant crustacean hyperglycemic hormone of the kuruma prawn *Penaeus japonicus* in methylophilic yeast *Pichia pastoris*. *Fish Sci* 69:95–100
31. Nagai C, Asazuma H, Nagata S, Ohira T, Nagasawa H (2009) A convenient method for preparation of biologically active recombinant CHH of the kuruma prawn, *Marsupenaeus japonicus*, using the bacterial expression system. *Peptides* 30:507–517
32. Tiu SHK, Chan SM (2007) The use of recombinant protein and RNA interference approaches to study the reproductive functions of a gonad-stimulating hormone from the shrimp *Metapenaeus ensis*. *FEBS J* 274:4385–4395
33. Katayama H, Nagasawa H (2004) Effect of a glycine residue insertion into crustacean hyperglycemic hormone on hormonal activity. *Zool Sci* 21:1121–1124
34. Katayama H, Nagata K, Ohira T, Yumoto F, Tanokura M, Nagasawa H (2003) The solution structure of molt-inhibiting hormone from the Kuruma prawn *Marsupenaeus japonicus*. *J Biol Chem* 278:9620–9623
35. Sarojini R, Nagabhushanam R, Fingerman M (1995) A neurotransmitter role for red-pigment-concentrating hormone in ovarian maturation in the red swamp crayfish *Procambarus clarkii*. *J Exp Biol* 198:1253–1257
36. Okumura T (2006) Effects of cyclic nucleotides, calcium ionophore, and phorbol ester on vitellogenin mRNA levels in incubated ovarian fragments of the kuruma prawn *Marsupenaeus japonicus*. *Gen Comp Endocrinol* 148:245–251
37. Nagai C, Asazuma H, Nagata S, Nagasawa H (2009) Identification of a second messenger of crustacean hyperglycemic hormone signaling pathway in the kuruma prawn *Marsupenaeus japonicus*. *Ann NY Acad Sci* 1163:478–480
38. Nagai C, Mabashi-Asazuma H, Nagata S, Nagasawa H (2011) Regulation of ecdysteroidogenesis in the Y-organs of crustaceans (in Japanese). In: Sonobe H, Nagasawa H (eds) *Biology of molting and metamorphosis*. Tokai University Press, Tokyo, pp 419–438
39. Liu HF, Lai CY, Watson RD, Lee CY (2004) Molecular cloning of a putative membrane form guanylyl cyclase from the crayfish *Procambarus clarkii*. *J Exp Zool* 301A:512–520
40. Lee SG, Kim HW, Mykles DL (2007) Guanylyl cyclases in the tropical land crab, *Gecarcinus lateralis*: cloning of soluble (NO-sensitive and -insensitive) and membrane receptor forms. *Comp Biochem Physiol Part D Genomics Proteomics* 2:332–344
41. Zheng J, Nakatsuji T, Roer RD, Watson RD (2008) Studies of a receptor guanylyl cyclase cloned from YO of the blue crab (*Callinectes sapidus*) and its possible functional link to ecdysteroidogenesis. *Gen Comp Endocrinol* 155:780–788

Adhesion and Fusion of Two Kinds of Phospholipid Hybrid Vesicles Controlled by Surface Charges of Vesicular Membranes

Kentaro Suzuki,¹ Ryo Aboshi,² Kensuke Kurihara,² and Tadashi Sugawara*¹

¹Research Center of Life Science as Complex Systems, The University of Tokyo,
3-8-1 Komaba, Meguro-ku, Tokyo 153-8902

²Department of Basic Science, Graduate School of Arts and Sciences, The University of Tokyo,
3-8-1 Komaba, Meguro-ku, Tokyo 153-8902

(Received April 9, 2012; CL-120312; E-mail: suga@pentacle.c.u-tokyo.ac.jp)

Vesicular adhesion and fusion of two kinds of hybrid vesicles composed of zwitterionic and anionic phospholipids were induced by a pH-change that caused a difference in vesicular surface charges. This facile vesicular fusion method can be applied to a substrate-transfer from a conveyer vesicle to a target vesicle.

Recently, giant vesicles (GV), which is a hollow supra-molecular self-assembly of amphiphiles, have played an important role as a nanoreactor in which chemical reactions, including enzymatic reactions, occur efficiently.¹ In general, a GV consists of a semipermeable bilayer membrane which does not pass ions or large molecules. Therefore, development of a new transporting method of a substrate into GVs draws much attention not only from the aspect of construction of a successive model protocell² but also biomedical engineering or applications, e.g., drug delivery,³ gene delivery,⁴ and DNA computing.⁵ However, spontaneous vesicular transport is difficult because of the large energetic barrier arising from the electrostatic repulsion between GVs with homopolar surface charge and the dehydration energy of a substrate required for passing itself through a hydrophobic membrane. In a biological system, smaller substrates like ions or polar molecules can be transported across membranes selectively through an ion channel. In the case of larger substrates, such as sugars, oligonucleotides, and proteins, they are transported by endocytosis. By mimicking these mechanisms from a chemical viewpoint, various transporting methods have been reported.^{6–8} As for vesicular fusion,^{9–11} a vesicular fusion is usually accompanied by adhesion with vesicles carrying a complementary recognition site or an opposite surface charge.

In this paper, we explored a pH-change-triggered vesicular adhesion and fusion caused by two kinds of hybrid vesicles in a certain pH range. In order to transport substrates through this adhesion and fusion event, we are concerned with the acid dissociation equilibrium of the phosphate diester in phospholipids (Figure 1). Since the acid dissociation constant of the phosphate group in water is approximately 3, the phosphate group in basic or neutral water exists as the phosphate anion, and it is protonated in acidic water.¹² Namely, phosphocholine (PC) in 2-oleoyl-1-palmitoyl-*sn*-glycero-3-phosphocholine (POPC) has no effective charge in a neutral solution, but it becomes cationic at pH 3 by protonation, whereas about half of the ester group in 2-oleoyl-1-palmitoyl-*sn*-glycero-3-[phospho-*rac*-(1-glycerol)] (POPG) (sodium salt) remains anionic (Figure 1). Hence, while PC-rich and PG-rich vesicles do not adhere with each other in a neutral dispersion, they do interact and adhere at ca. pH 3.

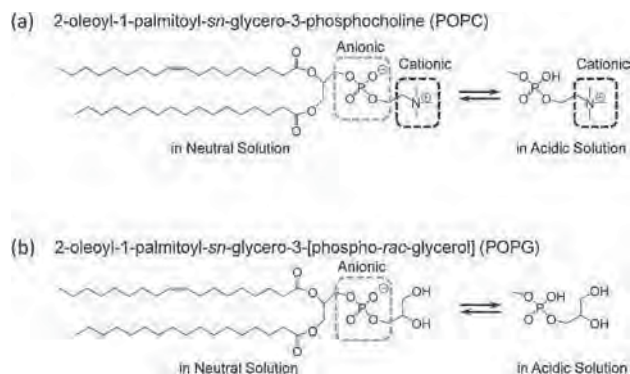


Figure 1. Change of the electric charge of phospholipids (a) POPC is zwitterionic in a neutral dispersion but it becomes cationic in an acidic dispersion. (b) POPG is anionic in neutral but nonionic in acidic dispersions.

The PC-rich GV [target GV] comprising POPC:POPG:cholesterol = 80:10:10 (mol %) was prepared by swelling the film with a 50 mM aqueous NaCl solution and the resulting dispersion was incubated at 23 °C until the adhesion experiment. On the other hand, PG-rich vesicles comprising POPG and cholesterol (POPG:cholesterol = 90:10) were prepared by film swelling as well, being stained by 0.1 mol % of a phospholipid tagged with a lipophilic fluorescent probe (2-(4,4-difluoro-5,7-dimethyl-4-bora-3a,4a-diaza-*s*-indacene-3-dodecaonyl)-1-hexadecanoyl-*sn*-glycero-3-phosphocholine, β -BODIPY FL C12-HPC (Invitrogen)). The dispersion of PG-rich GVs was extruded twice by a syringe with a 0.2- μ m pore membrane filter. By this treatment, the size distribution of the PG-rich GVs was shifted to a large vesicle (LV)-size [conveyer LV], which was unable to be detected under an optical microscope. The pH of the dispersions of target GVs and conveyer LVs stained with the β -BODIPY FL C12-HPC were adjusted to pH 3 and they were mixed in a frame-sealed incubation chamber (17 \times 8 \times 0.25 mm³) from the outlets placed at diagonal corners, respectively, by capillary force. Gentle mixing of both dispersions formed a boundary between two layers (Figure 2a). In the dispersion of target GV at pH 3, no aggregates were observed by phase contrast microscopy (the left-down layer in Figure 2b), or by fluorescent microscopy. The dispersion containing the conveyer LVs emitted green fluorescence as a whole (the right-up layer in Figure 2b); no GVs or aggregates were observed under phase contrast microscopy because the size of conveyer vesicles remained as the LV-size. These results mean that the aggregation between individual phospholipid vesicles did not occur in the separate layers. However, we noticed fluorescent target GVs

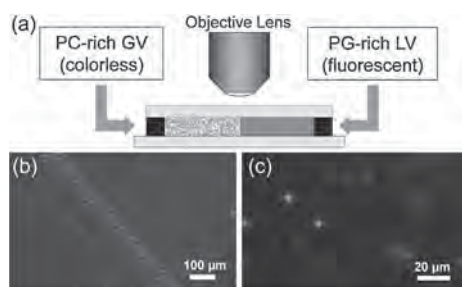


Figure 2. Temporal change of micrograms of a mixed dispersion of target GV and conveyer LVs. (a) Microchamber for mixing dispersions of target GV and conveyer LVs, the latter of which was stained by a fluorescent probe. (b) Fluorescence microgram of the boundary between target GVs and conveyer LVs 2h after mixing. Target GVs became fluorescent due to the adhesion with fluorescent conveyer LVs. (c) A magnified image of target GV adhered by fluorescent conveyer LVs.

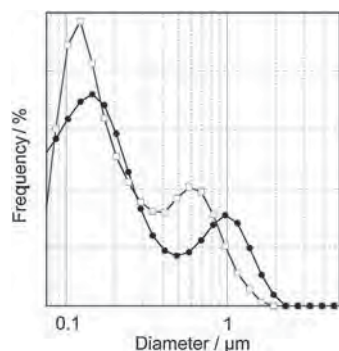


Figure 3. pH dependence of size distribution of target GVs and conveyer LVs in as dispersion Size-distribution obtained by mixing the individual dispersions at pH 7 (solid line connecting open squares) and at pH 3 (thick solid line connecting solid circles).

appeared at the boundary between two layers 2h after the mixing. The expanded micrographic image of the target GV adhered by fluorescent conveyer LVs was shown in Figure 2c. The fluorescent target GV must be formed at least by the vesicular adhesion with fluorescent PG-rich LVs and it could be converted to a fused GV.

In addition, the size distribution of adhered vesicles was measured by dynamic light scattering experiments. The target GVs and the conveyer LVs were extruded by 1.2 and 0.2 μm -membrane filters, respectively, to be distinguished based on the vesicular size. Figure 3 shows the distribution of the target GVs and the conveyer LVs: The horizontal axis of Figure 3 corresponds to the logarithm of the vesicular size and the vertical axis corresponds to the intensity of scattered light which is proportional to a product of the vesicular volume and the frequency. A solid line connecting open circles in Figure 3 shows the vesicular size-distribution of both vesicles when mixed at pH 7. The two maxima correspond to the conveyer LV (ca. 0.12 μm) and to the target GV (ca. 0.6 μm), respectively. The plot drawn by thick lines connecting solid circles shows the size-distribution at pH 3 after 18h. While the maximum in the smaller region remained almost the same, the maximum in the

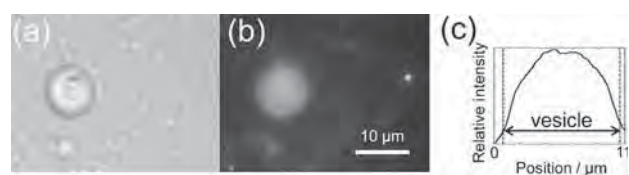


Figure 4. (a) Differential microscope image and (b) fluorescent microscope image of a fused target GV with fluorescent conveyer LVs after fluorescein transport by fusion. (c) Distribution of fluorescent intensity of the fused GV.

larger range was shifted to ca. 1 μm , which means that the adhesion between the target GVs and conveyer LVs, at least occurred.

In order to examine whether the adhesion is followed by the vesicular fusion, we prepared the conveyer LVs the inner pool of which was stained by fluorescein (a hydrophilic fluorescent probe) as follows. The thin PG film was swollen with a 500 mM aqueous solution of fluorescein and the exterior aqueous solution was diluted with water 20 times. This fluorescent PG-vesicular dispersion was filtered through a filter with a mesh of 0.2 μm so that vesicles cannot be observed under an optical microscope. It was then diluted with water 100-fold. Because the fluorescent background from the added outer aqueous solution was diluted about 8000-fold, the fluorescence microscopic observation was not influenced by the outer fluorescent dye. This dispersion of conveyer vesicles was mixed with a dispersion of target GVs (PC-rich GVs), and then 2 mM hydrochloric acid was added to adjust pH 3. When the mixed dispersion was incubated at 23 $^{\circ}\text{C}$ for 18h, the inner pool of the GVs became fluorescent (Figures 4a and 4b). On the other hand, the incubated mixed dispersion of pH 7 did not show any change even after several days. The transport of fluorescein into these GVs at pH 3 was confirmed by the analysis of the fluorescence intensity along the diameter of the GV (Figure 4c). The maximum of the fluorescence intensity was detected at the middle along the diameter (see Supporting Information, Figure S1¹⁵). The result unequivocally indicates that two kinds of phospholipid hybrid vesicles not only adhered but also fused with each other in a specific pH region (ca. pH 3) where the surface charges of one kind of vesicle change to cationic, and the others remain anionic.

Adhesion and fusion events of a large number (50000 GVs) of target (PC-rich) GVs and conveyer (PG-rich) GVs were investigated on the basis of flow cytometric analysis.¹³ Vesicular membranes of the target GV was stained by lipophilic fluorescence probe (2 mol % of BODIPY-red,¹⁴ ethyl 10-[4-(4,4-difluoro-1,7-dimethyl-4-bora-3a,4a-diaza-s-indacene)-3,5-dimethylphenyl]decanate) and that of the conveyer vesicle was doped with a lipophilic quencher (20 mol % of 2,4-dinitro-1-octylbenzene), and the quench of the fluorescence intensity of the target GV was measured in terms of the decrease of the fluorescence intensity of each vesicle caused by the fusion with conveyer LVs. After these two kinds of vesicular dispersions were mixed at pH 7 and 3, respectively, and left standing still for 18h, the forward scattered light (FS) intensity, corresponding to a size of GV, and the fluorescence (FL) intensity, corresponding to amount of the fluorescence probe per GV, of the vesicular mixture were measured (Figure 5). The size distribution of GVs after incubation (23 $^{\circ}\text{C}$) at pH 3 increased slightly compared with that incubated at pH 7 (Figure 5a). On the other hand, the

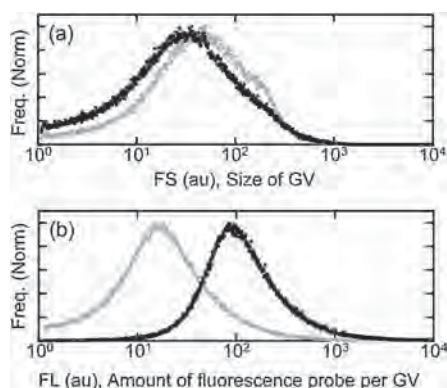


Figure 5. Histograms of the fused GV after incubation at pH 7 (black dots) and pH 3 (gray dots). (a) Size distribution of GV (FS), (b) amount of fluorescence probe per GV (FL). Note that the magnitude of frequencies in the two plots was normalized by the maximum value.

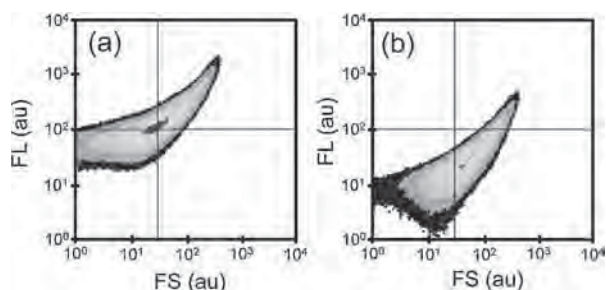


Figure 6. Density plots (2D contour map) of a flow cytometric analysis of dispersions of a mixture of target GV with a lipophilic fluorescent dye and conveyer LV with a lipophilic quencher incubated at pH 7 (a) and pH 3 (b). Cross bars in the both diagrams indicate the highest position in plot (a).

FL intensity of target GV decreased by one tenth after being incubated at pH 3 compared with that at pH 7 (Figure 5b). A control experiment using conveyer LV without the quencher caused almost no difference (Supporting Information, Figure S2¹⁵).

When the two-dimensional density plots of FS and FL intensities after incubation at pH 3 and 7 were examined precisely (Figure 6), the distribution along the FL axis after being incubated at pH 3 apparently broadened compared with that at pH 7. The broadening was not observed in the control experiment without the quencher (Supporting Information, Figure S3¹⁵). The above results mean that the quenching efficiency depends on the lamellarity of GV. This is because conveyer LV coat the surface of the target GV and the quenching occurs only in the outermost vesicular membrane. In the case of multilamellar GV, fluorescent probes buried in the inside membranes are difficult to quench. Thus GV with thin outer membranes are favorable to obtain high performance by our vesicular transport method since the efficiency depends on the lamellarity.

In conclusion, we found that the molecular transport of substrates from the conveyer vesicles to the target GV could be triggered by the pH-change through the vesicular adhesion and

fusion processes. If transport of larger molecules, such as DNA, or enzymes, is feasible, this method will be widely applicable to biochemical or medical purposes.

This work was partially supported by a Grant-in-Aid for Scientific Research (B) (No. 23350060) from Japan Society for the Promotion of Science (JSPS).

References and Notes

- 1 D. M. Vriezema, M. C. Aragonès, J. A. A. W. Elemans, J. J. L. M. Cornelissen, A. E. Rowan, R. J. M. Nolte, *Chem. Rev.* **2005**, *105*, 1445.
- 2 a) V. Noireaux, A. Libchaber, *Proc. Natl. Acad. Sci. U.S.A.* **2004**, *101*, 17669. b) K. Kurihara, M. Tamura, K.-i. Shohda, T. Toyota, K. Suzuki, T. Sugawara, *Nat. Chem.* **2011**, *3*, 775.
- 3 T. M. Allen, P. R. Cullis, *Science* **2004**, *303*, 1818.
- 4 a) E. W. F. W. Alton, P. G. Middleton, N. J. Caplen, S. N. Smith, D. M. Steel, F. M. Munkonge, P. K. Jeffery, D. M. Geddes, S. L. Hart, R. Williamson, K. I. Fasold, A. D. Miller, P. Dickinson, B. J. Stevenson, G. McLachlan, J. R. Dorin, D. J. Porteous, *Nat. Genet.* **1993**, *5*, 135. b) Y. Liu, L. C. Mounkes, H. D. Liggitt, C. S. Brown, I. Solodin, T. D. Heath, R. J. Debs, *Nat. Biotechnol.* **1997**, *15*, 167.
- 5 a) B. Bloom, C. Bancroft, in *DNA Based Computers V in DIMACS Series in Discrete Mathematics and Theoretical Computer Science*, ed. by E. Winfree, D. K. Gifford, The American Mathematical Society Press, New York, **2000**, Vol. 54, pp. 39–48. b) M. Takinoue, D. Kiga, K.-i. Shohda, A. Suyama, *Phys. Rev. E: Stat., Nonlinear, Soft Matter Phys.* **2008**, *78*, 041921.
- 6 G. Das, P. Talukdar, S. Matile, *Science* **2002**, *298*, 1600.
- 7 a) F. M. Menger, D. S. Davis, R. A. Persichetti, J.-J. Lee, *J. Am. Chem. Soc.* **1990**, *112*, 2451. b) Y. Kobuke, K. Ueda, M. Sokabe, *J. Am. Chem. Soc.* **1992**, *114*, 7618. c) M. J. Pregel, L. Jullien, J.-M. Lehn, *Angew. Chem., Int. Ed. Engl.* **1992**, *31*, 1637. d) F. Caschera, T. Sunami, T. Matsuura, H. Suzuki, M. M. Hanczyc, T. Yomo, *Langmuir* **2011**, *27*, 13082.
- 8 M. Mehiri, W.-H. Chen, V. Janout, S. L. Regen, *J. Am. Chem. Soc.* **2009**, *131*, 1338.
- 9 J. M. White, *Science* **1992**, *258*, 917.
- 10 *Membrane Fusion*, ed. by J. Wilschut, D. Hoekstra, Marcel Dekker, New York **1991**.
- 11 a) V. Marchi-Artzner, T. Gulik-Krzywicki, M.-A. Guedeau-Boudeville, C. Gosse, J. M. Sanderson, J.-C. Dedieu, J.-M. Lehn, *ChemPhysChem* **2001**, *2*, 367. b) S. Zellmer, G. Cevc, P. Risse, *Biochim. Biophys. Acta, Biomembr.* **1994**, *1196*, 101. c) N. Maru, K.-i. Shohda, T. Sugawara, *Chem. Lett.* **2008**, *37*, 340. d) D. Papahadjopoulos, W. J. Vail, C. Newton, S. Nir, K. Jacobson, G. Poste, R. Lazo, *Biochim. Biophys. Acta, Biomembr.* **1977**, *465*, 579. e) D. P. Pantazatos, R. C. MacDonald, *J. Membr. Biol.* **1999**, *170*, 27.
- 12 Y. Noda, *Bunseki Kagaku* **1987**, *36*, 403.
- 13 a) K. Sato, K. Obinata, T. Sugawara, I. Urabe, T. Yomo, *J. Biosci. Bioeng.* **2006**, *102*, 171. b) T. Toyota, K. Takakura, Y. Kageyama, K. Kurihara, N. Maru, K. Ohnuma, K. Kaneko, T. Sugawara, *Langmuir* **2008**, *24*, 3037. c) K. Kurihara, K. Takakura, K. Suzuki, T. Toyota, T. Sugawara, *Soft Matter* **2010**, *6*, 1888.
- 14 K. Yamada, T. Toyota, K. Takakura, M. Ishimaru, T. Sugawara, *New J. Chem.* **2001**, *25*, 667.
- 15 Supporting Information is available electronically on the CSJ-Journal Web site, <http://www.csj.jp/journals/chem-lett/index.html>.

pH-Induced Switchable Vesicular Aggregation of Zwitterionic and Anionic Phospholipids

Kentaro Suzuki,^{1,2} Kensuke Kurihara,³ Yusaku Okura,³ Taro Toyota,^{1,3} and Tadashi Sugawara*^{1,2}

¹Research Center of Life Science as Complex Systems, The University of Tokyo,
3-8-1 Komaba, Meguro-ku, Tokyo 153-8902

²Department of Chemistry, Faculty of Science, Kanagawa University,
2946 Tsuchiya, Hiratsuka, Kanagawa 259-1293

³Department of Basic Science, Graduate School of Arts and Sciences, The University of Tokyo,
3-8-1 Komaba, Meguro-ku, Tokyo 153-8902

(Received May 14, 2012; CL-120508; E-mail: suga@pentacle.c.u-tokyo.ac.jp)

Giant vesicles (GVs) comprising zwitterionic and anionic phospholipids (DOPC and POPG, respectively) at a molar ratio of 90:10 formed a sparse network of aggregates that dissociated into isolated GVVs reversibly depending on the pH of the dispersion (pH range, 7.0–2.5). This reversibility was due to the fluctuations in the composition of as-grown GVVs.

Amphiphiles, such as phospholipids, afford three-dimensional structures, belonging to the gyroid and hexagonal phases, under high-temperature,¹ high-concentration,² and high-pressure conditions.¹ On the other hand, they also form vesicles characterized by closed hollow structures with a lipid bilayer.³ Recently, giant vesicles (GVs) with diameters larger than 1 μm have drawn considerable attention in the physical and chemical research fields due to fact that they belong to discrete (zero-dimensional) systems. Aggregation and fusion of GVVs, taking place at high concentrations of electrolytes or in the presence of multivalent inorganic ions, are irreversible processes.⁴ Although the aggregation of GVVs equipped with a specific recognition site, e.g., DNA-tag,⁵ or a coordination site⁶ has been extensively studied, that of phospholipid hybrid GVVs of the same composition but without any specific tag has been scarcely investigated. Since a binary lipid mixture of phosphatidylcholine (PC) and phosphatidylglycerol (PG) in the lamellar phase is uniquely sensitive to the pH change,⁷ we have been interested in examining whether this *intravesicular* response to the pH change influences the *intervesicular* interaction in dispersion. As a result, we conceived PC/PG hybrid GVVs to study the pH-sensitive reversible transformation of the aggregation states of a hybrid GV in dispersion. Here, we found that the switchable aggregation and dissociation of the PC/PG hybrid GVVs can be induced simply by changing the pH of the aqueous dispersion. This phenomenon is caused by the distribution of the positive or negative surface charge of the hybrid GVVs with fluctuating composition of PC and PG. The adhesion of GVVs occurs around pH at which the effective surface charge of the GV membrane becomes zero.

As stated above, vesicles in a colloidal dispersion easily aggregate in the presence of multivalent inorganic ions or at a high concentration of electrolytes.⁴ However, such aggregation often induces fusion between adhering vesicles that are difficult to dissociate reversibly. In this study, we prepared phospholipid hybrid GVVs comprising zwitterionic 1,2-dioleoyl-*sn*-glycero-3-phosphocholine (DOPC) and anionic 2-oleoyl-1-palmitoyl-*sn*-glycero-3-phospho-*rac*-(1-glycerol) (POPG) sodium salt at a ratio of 90:10 (mol %) by a film-swelling method. The mixture

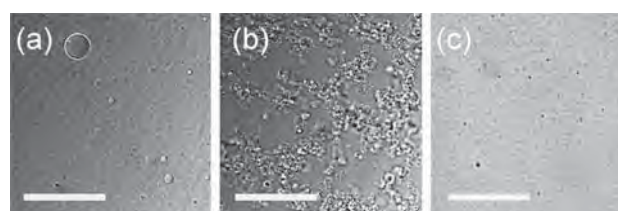


Figure 1. Microscopic images of isolated vesicles or vesicular aggregates in dispersions at (a) pH 7.0, (b) pH 2.5, and (c) pH 2.0. White bars in the micrographs correspond to 100 μm .

of phospholipids was dissolved in chloroform. The solvent was evaporated by dry nitrogen flow. The resulting film was dried under reduced pressure overnight. Deionized water at 25 $^{\circ}\text{C}$ was added to the film to obtain a dispersion of hybrid GVVs with phospholipids at a concentration of 2 mM. Generally, the surface charge of the hybrid GV membrane changes from negative to positive by the protonation of the phosphate groups of PC and PG (vide infra). The surface charge of the GV becomes almost zero at a certain pH and a molar ratio of PC/PG. Since GVVs are damaged due to the complete protonation of the phosphate groups of PC and PG under too low a pH (Figure 1c), the critical pH (pH at which the surface charge of the GV becomes zero) should not be too low. Accordingly, we selected the ratio of PC and PG in the hybrid GV to be 9:1.

The pH of the vesicular dispersion with an average diameter of $5 \pm 1 \mu\text{m}$ (Figure 1a) was decreased by adding aqueous HCl (100 mM) dropwise using a micropipette, following which a sparse network of GVVs appeared at pH 2.4, as observed by differential interference contrast microscopy (OLYMPUS, BX51) (Figure 1b). Incidentally, no aggregation of GVVs was observed at a pH lower than 2.0 (Figure 1c).

To determine whether the observed aggregation is a uniform throughout the whole bulk state, the pH dependence of the particle size distribution was monitored by dynamic light scattering (DLS) analysis (Nikkiso, Microtrac UPA150). The size of the phospholipid hybrid GVVs was maintained less than 100 nm, which was suitable (less than 6.5 μm) for DLS analysis, by filtering the dispersion of GVVs through a membrane filter with pores of 100 nm diameter. Moreover, to prevent the precipitation of large aggregates, DLS analysis was conducted immediately after the adjustment of pH. The pH dependence of the size distribution determined by the DLS measurement is shown in Figure 2. Only the peak centered at 100 nm, which was ascribed to the filtered GVVs, was detected in the pH range of 7–4, which indicated that no size change occurred in this pH

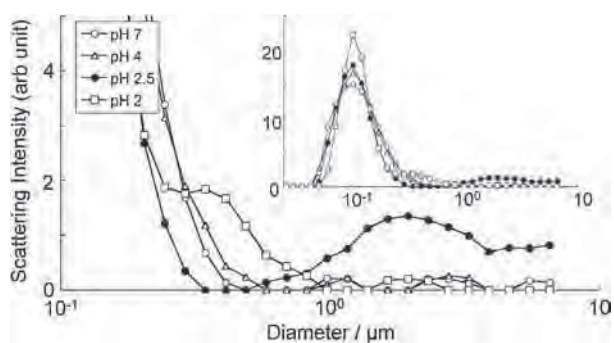


Figure 2. Size distribution of vesicular and their aggregation at several pH. An inset is a whole view.

range. However, a new subpeak with a broad maximum at approximately $2\mu\text{m}$ appeared at pH 2.5, together with the original distribution at 100nm . This subpeak was attributed to aggregates of GVs with sizes in the order of $100\mu\text{m}$, the presence of which was confirmed by optical microscopy. We were not able to observe any micrometer-order aggregates at pH 2. However, we observed a shoulder of the main peak centered at 300nm , the origin of which is not clear at the moment.

The pH of the dispersion containing the vesicular aggregates was neutralized by adding an aqueous NaOH solution (100mM) using a micropipette, and the changes in the aggregates in the dispersion were monitored by differential interference contrast microscopy (Figure 3). As the pH increased, the aggregates dissociated smoothly (Figure 3a), and at pH 7 all the aggregates disappeared (Figure 3b), leaving the vesicular dispersion appearing as it did in the initial state. We confirmed that the aggregation and dissociation of GVs occur reversibly many times using an optical microscope (Figures 3c–3f). Note that this rapid interconversion (30 min) between the dissociated state and the aggregated state of the same GVs can be triggered simply by pH change. The reversibility of the aggregation and dissociation of GVs can be guaranteed for more than one day. A partial breakdown of the reversibility was observed after more than 3 days.

The switchable aggregation and dissociation of GVs were monitored by the aforementioned DLS measurement of the filtered GV ($\phi = 100\text{nm}$) dispersion (Figure 4). The alternating appearance and disappearance of bands corresponding to the micrometer-sized aggregates were clearly observed. This unequivocally showed that the aggregation and dissociation processes occurred not locally in an area observed under the microscope but ubiquitously in the bulk.

Our phospholipid hybrid vesicles comprised zwitterionic DOPC and anionic POPG in a fixed composition. Therefore, how can such a switchable aggregation be rationalized? Because the surface charge of these hybrid vesicles is negative owing to the presence of PG, it generates a repulsive interaction among the hybrid GVs. However, if the pH of the dispersion becomes close to that at the acid dissociation equilibrium of the phospholipid, the number of protonated phosphate groups of the phospholipids (both PC and PG) increases. Assuming that the practical pK_a 's of the phosphate groups of PC and PG were approximately 1 and 3, respectively,⁸ we calculated the pH dependence of the surface charge of the hybrid GV and found

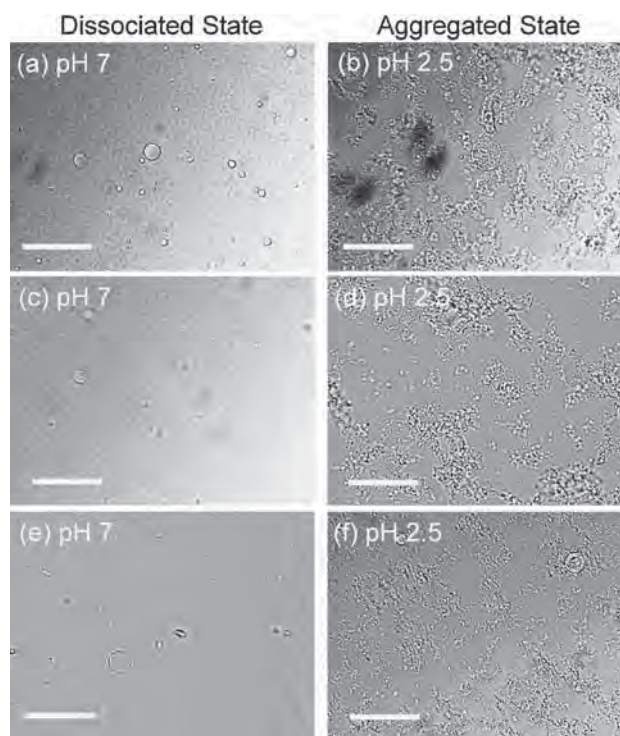


Figure 3. Microscopic images of switchable dynamics between aggregated states and dissociated states depending on the pH of the dispersion. (a) Initial specimen. (b) After the first acidification to pH 2.5 with a diluted HCl(aq). (c) First neutralization with NaOH(aq). (d) Second acidification to pH 2.5 with a diluted HCl(aq). (e) Second neutralization with NaOH(aq). (f) Third acidification to pH 2.5. White bars in the micrographs correspond to $100\mu\text{m}$.

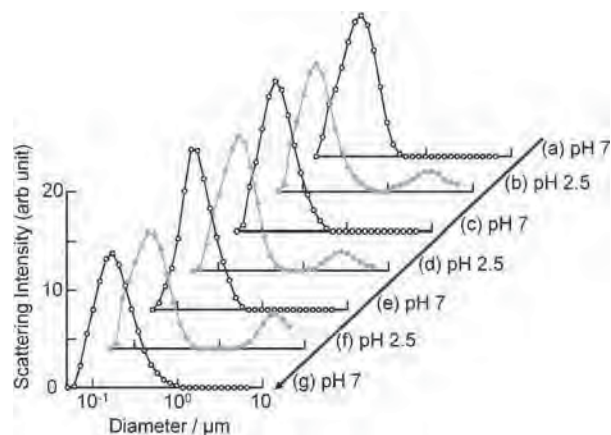


Figure 4. Switching between dissociation (dispersed) and aggregation states in dispersion under neutral or acidic condition observed by dynamic light scattering analysis.

that the surface charge became almost zero at pH of ca. 2.5. This estimation is in accord with our experimental result. As a result, the protonated PC becomes cationic owing to the presence of the choline unit and the protonated PG becomes neutral, which attenuates the anionic characteristic of the surface charge of the hybrid GVs, thereby weakening the repulsive interaction

between the GVs. Note that even though the surface charge of a vesicle composed solely of zwitterionic PC is neutral, PC vesicles never aggregate in the dispersion. If the change in the surface charge of a vesicle is accompanied by the change in the pH of the dispersion, the sign of the surface charge remains the same and only a repulsive interaction would be generated. Consequently, reversible vesicular adhesion cannot occur. However, vesicular adhesion was found to occur at pH 2.4 in the current system. This is the reason why the hybrid phospholipid GV aggregates would originate from the fluctuations in the compositions of PC and PG in each as-grown GV at the time of preparation. Hence, even though the pH was maintained at a value at which the surfaces charges are strictly cancelled, as calculated from the original compositions of PC and PG, there must be a fluctuation in the composition of the as-grown hybrid GVs. If the amount of PG is slightly higher than the estimated value, the surface charge becomes negative, and vice versa. Hence, an attractive interaction can be expected between such GVs.

The pattern of aggregation among vesicles observed in this study correlates well with the structure simulated using a cluster–cluster aggregation (CCA) model based on the adhesive interaction among particles.^{9,10} In this model, the process was assumed such that the adhesive particles encounter and adhere with each other at a random place in the system, and they form small clusters which, in turn, collide and adhere to form larger clusters, and so on; eventually, large clusters with many voids are formed. Indeed, a regular distribution of vesicular aggregates observed by the DLS analysis resembles the initial state of the CCA model.

Moreover, the adhesion force between the vesicles in this study is at a level that prevents fusion that might occur subsequently because fusion prevents the reversible dissociation process. This is in sharp contrast to the studies that reported that tight adhesion is followed by fusion between vesicles.^{4,11–15} In this system, the small ratio of the potential anion source (PG) keeps the adhesion sites few, which guarantees high reversibility of the system. The reason why adhesion does not occur at pHs lower than 2.4 can also be rationalized by the acid dissociation equilibrium. If the pH is low, most of the phosphate groups are protonated, which makes the surface charge of PC-rich vesicles cationic. As a result, the interaction between GVs becomes repulsive.

In this study, we succeeded in switching between the aggregated state and the dissociated state of the phospholipid hybrid vesicles (PC:PG = 90:10 mol %) simply by changing the pH of the dispersion. This reversible process can be repeated many times every 30 min. The key mechanism of this aggregation–dissociation of GVs is derived from the fluctuation of the composition of the as-grown GVs. We have already reported the significant effect of the fluctuation on the responsiveness toward external stimuli (and to the spontaneous movement of soft matter). For example, the self-rewinding motion of the helical structure made of multilamellar tubular

vesicles composed of oleic acid and oleate originates from the fluctuation of effective volume and the charge of the carboxylic group of oleic acid and oleate in the multilamellar membrane.¹⁶ In another instance, curved structures, which can be regarded as a *magneto-elastica* that appear following the application of external magnetic field to the collagen-containing tubular vesicles, originate from the fluctuations of the two components.¹⁷ When a dispersion of PC/PG vesicles is acidified in a thin canal, the vesicles form sparse aggregates, which may precipitate out or form a stack at the bottleneck of the canal. The aggregates can be removed by washing with neutral water. Such vesicular aggregates may work as a “soft valve” or “soft stopper” in a canal. Manipulatable soft matter may lead to new applications along this direction.

Paper based on a presentation made at the International Association of Colloid and Interface Scientists, Conference (IACIS2012), Sendai, Japan, May 13–18, 2012.

References

- 1 R. Winter, *Curr. Opin. Colloid Interface Sci.* **2001**, *6*, 303.
- 2 J. N. Israelachvili, *Intermolecular and Surface Forces*, 3rd ed., Academic Press, Massachusetts, **2011**, Chap. 20, pp. 535–576. doi:10.1016/B978-0-12-375182-9.10020-X.
- 3 *Giant Vesicles in Perspectives in Supramolecular Chemistry*, ed. by P. L. Luisi, P. Walde, Wiley, Chichester, **1999**, Vol. 6. doi:10.1002/9780470511534.
- 4 J. N. Israelachvili, *Intermolecular and Surface Forces*, 3rd ed., Academic Press, Massachusetts, **2011**, Chap. 14, pp. 291–340. doi:10.1016/B978-0-12-375182-9.10014-4.
- 5 N. Maru, K.-i. Shohda, T. Sugawara, *Chem. Lett.* **2008**, *37*, 340.
- 6 S. K. M. Nalluri, J. B. Bultema, E. J. Boekema, B. J. Ravoo, *Chem. Sci.* **2011**, *2*, 2383.
- 7 P. Garidel, C. Johann, L. Mennicke, A. Blume, *Eur. Biophys. J.* **1997**, *26*, 447.
- 8 D. Marsh, *CRC Handbook of Lipid Bilayers*, CRC Press, Florida, **1990**.
- 9 P. Meakin, *Phys. Rev. Lett.* **1983**, *51*, 1119.
- 10 M. Kolb, R. Botet, R. Jullien, *Phys. Rev. Lett.* **1983**, *51*, 1123.
- 11 S. A. Walker, J. A. Zasadzinski, *Langmuir* **1997**, *13*, 5076.
- 12 N. Düzgüneş, R. M. Straubinger, P. A. Baldwin, D. S. Friend, D. Papahadjopoulos, *Biochemistry* **1985**, *24*, 3091.
- 13 M. Johnsson, A. Wagenaar, M. C. A. Stuart, J. B. F. N. Engberts, *Langmuir* **2003**, *19*, 4609.
- 14 L. Stamatatos, R. Leventis, M. J. Zuckermann, J. R. Silvius, *Biochemistry* **1988**, *27*, 3917.
- 15 J. Yao, Y. Feng, Y. Zhao, Z. Li, J. Huang, H. Fu, *J. Colloid Interface Sci.* **2007**, *314*, 523.
- 16 M. Ishimaru, T. Toyota, K. Takakura, T. Sugawara, Y. Sugawara, *Chem. Lett.* **2005**, *34*, 46.
- 17 K. Suzuki, T. Toyota, K. Sato, M. Iwasaka, S. Ueno, T. Sugawara, *Chem. Phys. Lett.* **2007**, *440*, 286.

Cite this: *Phys. Chem. Chem. Phys.*, 2012, **14**, 15412–15420

www.rsc.org/pccp

PAPER

Local electronic properties at organic–metal interfaces: thiophene derivatives on Pt(111)

Hirofumi Sato,^{*a} Shota Ushiyama,^b Mauo Sogo,^a Masaru Aoki,^a Ken-ichi Shudo,^b Tadashi Sugawara,^a Susumu Yanagisawa,^c Yoshitada Morikawa^d and Shigeru Masuda^a

Received 3rd August 2012, Accepted 18th September 2012

DOI: 10.1039/c2cp42700a

The valence electronic states of thiophene (TP), 2-thiophenethiol (TT), 2,2'-bithiophene (BTP), and 2,2'-bithiophene-5-thiol (BTT) on Pt(111) were measured by ultraviolet photoemission spectroscopy (UPS) and metastable atom electron spectroscopy (MAES) to elucidate how the local electronic properties at the organic–metal interface are altered by the extent of π -conjugation and substituent effects. First-principles calculations using density functional theory (DFT) were used to assign the observed spectra. TP and BTP chemisorb weakly on Pt(111), whereas TT and BTT are strongly bound to Pt(111) through the S atom with the cleavage of the S–H bond, forming a thiolate. In the MAES spectra, weak emission just below the Fermi level (E_F) was attributed to a chemisorption-induced gap state (CIGS) produced by orbital mixing between the organic species and Pt(111). The formation of CIGS is responsible for a metallic structure at the organic–metal interface. The relative intensities of CIGSs at E_F were in the order of TP (flat-lying configuration) > TT > TP (inclined configuration), indicating that the spatial distribution of CIGSs is drastically altered by the strength of the organic–metal bond and the adsorption geometry. In other words, TP (flat-lying geometry) and TT serve as good mediators of the extension of the metal wave function at E_F , which would be closely related to charge transport at organic–metal interfaces.

1. Introduction

The nature of thiophene (C₄H₄S, TP) and its derivatives on a metal substrate has attracted considerable attention in several fields, including heterogeneous catalysis, thin-film growth, and electrochemistry. In molecular electronics, oligothiophenes and polythiophenes are widely used because they are promising materials for the fabrication of field-effect transistors,^{1,2} light emitting diodes,³ and molecular junctions.⁴ When organic molecules are chemically bound to the metal substrate, new electronic states may emerge in the highest occupied molecular orbital–lowest unoccupied molecular orbital (HOMO–LUMO) gap. Such a chemisorption-induced gap state (CIGS) is accompanied by charge transfer between the molecules and the substrate, resulting in the formation of an electric dipole layer. The work function change (or vacuum level shift) directly determines the charge injection barrier at the organic–metal interface.⁵

Furthermore, the CIGS mediates the extension of metal wave functions to the molecule, which affects the tunneling probability (and consequently electric conductance) in molecular junctions linked by metal electrodes.⁶ Thus, the CIGS is a key factor in the development of a functional organic–metal system, but it is still unclear how the CIGS is altered by the extent of π -conjugation and substituent effects.

Numerous experimental studies have been performed on the adsorption of TP on metal substrates, including Fe(100),⁷ Ni(100),^{8,9} Cu(100),⁸ Cu(111),¹⁰ Mo(100),¹¹ Rh(111),¹² Pd(110),¹³ Pd(111),¹³ Ag(111),¹⁴ W(110),¹⁵ Pt(111),^{16–19} and Au(111).^{20–22} The adsorption energy and geometry have been estimated using density functional theory (DFT).^{20,23,24} On some substrates such as Pt(111) and Au(111), TP undergoes a coverage-driven phase transition: at low coverage TP adopts a flat-lying conformation, while with increasing coverage a tilted orientation becomes dominant, and these phases are sometimes called “relaxed monolayer” and “compressed monolayer”, respectively. At higher temperatures, TP desulfurizes on reactive substrates, for example, in TP/Pt(111), the C–S bond cleavage begins close to room temperature.¹⁹ Thiophene derivatives such as 2-thiophenethiol (TT) are also candidates for the fabrication of TP monolayers, because they are expected to bind to the substrate through the S atom with the cleavage of the S–H bond, forming a thiolate.^{25–27}

^a Department of Basic Science, Graduate School of Arts and Sciences, The University of Tokyo, Komaba, Meguro, Tokyo 153-8902, Japan

^b Faculty of Engineering, Yokohama National University, Tokiwadai 79-5, Hodogaya, Yokohama 240-8501, Japan

^c Department of Physics and Earth Sciences, Faculty of Science, University of the Ryukyus, Okinawa 903-0213, Japan

^d Division of Precision Science & Technology and Applied Physics, Graduate School of Engineering, Osaka University, 2-1 Yamada-oka, Suita, Osaka 565-0871, Japan

Scanning tunneling microscopy (STM) and X-ray photoemission spectroscopy (XPS) studies of TT on Au(111) have shown that two different sulfur atoms are competitively bound to the substrate, forming a disordered self-assembled monolayer.²⁸ Oligothiophenes such as 2,2'-bithiophene (BTP) are bound in a flat-lying geometry on Ni(110)²⁹ and Ag(111).¹⁴ The valence electronic states of TP on Mo(1001),¹¹ Rh(111),¹² and W(110),¹⁵ and BTP on Ni(110)²⁹ have been measured by ultraviolet photoemission spectroscopy (UPS), but there is little information on the CIGS (in particular, near the Fermi level, E_F) because of the overlap with the substrate bands.

The local electronic states at the outermost layer can be probed by metastable atom electron spectroscopy (MAES), which is based on energy analysis of electrons emitted by thermal collision of rare gas metastable atoms such as He*(1s2s, 2³S) with a solid surface.^{30,31} On a transition-metal surface [e.g., Pt(111)], in which the conduction bands lie opposite the 2s level of He*, the 2s electron tunnels resonantly to the surface, and then, the He⁺(1²S) ion produced is neutralized by an Auger transition; these processes are called resonance ionization (RI) and Auger neutralization (AN), respectively. As the AN process produces two holes in the valence bands, the resulting spectrum shows a broad structure reflecting the self-convolution of the local density of states. On an insulator surface without an empty state opposite the He* 2s level (e.g., ordinary organic film), the RI process is suppressed and Penning ionization (PI), in which an electron in the valence band fills the He* 1s hole and the 2s electron is simultaneously emitted to the vacuum, occurs instead. In PI, a single hole is produced in the valence band, as in the case of photoemission. Extremely high surface sensitivity of MAES has been applied to detect CIGSs near E_F for alkanethiols (C_nH_{2n+1}SH, $n = 1-3$) on Pt(111),^{32,33} benzenethiol (C₆H₅SH) on Pt(111),³⁴ and C₆H₅SH on Au(111).³⁵ The spatial extent of the CIGS (i.e., the extension of metal wave functions to the molecule) is drastically altered by the strength of the organic-metal bond and adsorption geometry, whose character is closely related to transport phenomena in molecular junctions.⁶

In this paper, we report the valence electronic states of TP, TT, BTP, and 2,2'-bithiophene-5-thiol (BTT) on Pt(111) examined by UPS, MAES, and first-principles DFT calculations. The chemical structures of the molecules are shown in Fig. 1. In Sections 4.1 and 4.2, we first show the UPS and MAES spectra of condensed TP and TT on Pt(111) to clarify the native electronic structures. Then, the MAES spectra of the chemisorbed phases are compared with the calculated local density of states. In Section 4.3, we show the MAES spectra of BTP and BTT on Pt(111) in the condensed and chemisorbed phases. Our data indicate that TP and BTP chemisorb weakly on Pt(111), whereas TT and BTT chemisorb strongly on Pt(111) by forming thiolates. In all cases, CIGSs are formed just below E_F , resulting in a metallic structure at the organic-metal interfaces. In Section 4.4, we compare the local density of CIGSs at E_F of the four systems, and address the close relationship of CIGS with transport characteristics.

2. Experimental

The experimental apparatus and related procedure are reported elsewhere.^{32,36} The Pt(111) substrate was cleaned by

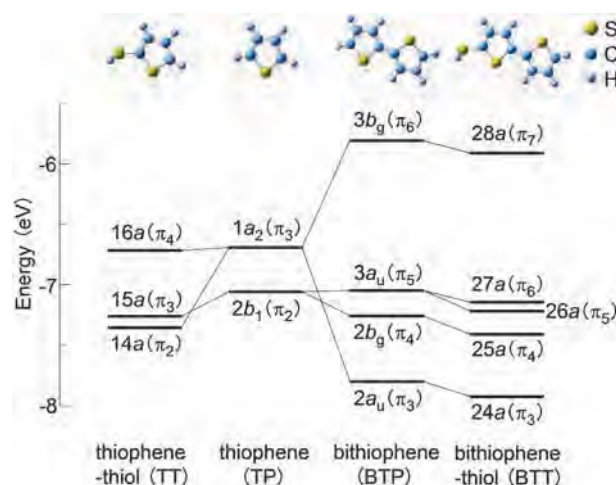


Fig. 1 Energy diagrams of higher-lying occupied π MOs in free thiophene derivatives by *ab initio* calculations at the B3LYP level.

repeated Ar⁺ ion sputtering and heating cycles. The clean substrate showed a well-ordered low-energy electron diffraction pattern and no impurities within the limit of Auger electron spectroscopy. TP and BTP were obtained commercially. TT and BTT were synthesized in our laboratory. Condensed films were prepared by vapor deposition on the clean substrate at 55–205 K cooled by a He-flow cryostat. The film thickness was estimated from the attenuation of photoemission signals from the metal bands and expressed in units of monolayers (ML). Chemisorbed monolayer were obtained by heating the condensed layer. The UPS and MAES spectra were measured by the He I resonance line ($h\nu = 21.21$ eV) and He*(2³S, 19.82 eV) atoms, respectively.

3. Computational details

All calculations based on a generalized gradient approximation (GGA) in DFT were performed using a program package “STATE” (Simulation Tool for Atom TEchnology).³⁷ The pseudopotentials of H 1s, C 2p, and Pt 5d states were constructed with the Vanderbilt’s ultrasoft scheme,³⁸ whereas those of other components were constructed with the norm-conserving scheme.³⁹ The cut-off energy for the wave function and the augmented charge were 25 Ry and 225 Ry, respectively. A periodic slab model was used with each slab composed of three atomic layers separated by a vacuum region of 27.8 Å. Adsorbed molecules were introduced on one side of the slab. Brillouin zone integrations were performed on a $6 \times 6 \times 1$ uniform mesh grid of k -points⁴⁰ for hypothetical (2×2) and ($\sqrt{7} \times \sqrt{7}$)R19.1° unit cells, corresponding to the coverage (θ) of 0.25 and 0.14, respectively. For optimization, adsorbed molecules and the top two layers of the substrate atoms were allowed to relax. The adsorption energy E_{ad} was defined as follows:

$$E_{ad} = E_{tot} - (E_{Pt} + E_{mol}),$$

where E_{tot} , E_{Pt} , and E_{mol} are the total energies of adsorbate-covered Pt(111), bare Pt(111), and an isolated molecular layer, respectively. For the optimized structures, the local density of states (LDOS), projected density of states (PDOS), and crystal orbital overlap population (COOP) were calculated.

4. Results and discussion

Before an analysis of adsorption systems, it is useful to compare the electronic states of free molecules. Fig. 1 shows the energy diagram for the higher-lying occupied π MOs by *ab initio* calculations at the B3LYP level. The notations of MOs are based on the optimized geometries, *i.e.*, a planar structure for TP (C_{2v}) and BTP (C_{2h}), and a non-planar structure, in which the thiol-H atom protrudes out of the ring plane, for TT (C_1) and BTT (C_1). According to our gas-phase UPS spectra (not shown), the ionization energies (IEs) of the higher-lying π bands are 8.85 and 9.64 eV for TP, and 8.83, 9.46, and 9.68 eV for TT. The TT values (in particular the small energy separation between the second and third IEs) support the assumption that TT prefers the non-planar to the planar conformation. Note that the HOMO levels of TP and TT as well as those of BTP and BTT are nearly identical. This feature is drastically altered by chemisorption as mentioned below.

4.1. Thiophene (TP) on Pt(111)

Fig. 2 shows the He I UPS and He*(2^3S) MAES spectra of a TP multilayer (~ 6 ML) on Pt(111) prepared at 55 K. The binding energy (E_B) is referred to the Fermi level (E_F) of the substrate. The UPS spectra of TP in the gas and condensed phases have been measured several times and the following assignment is well established.^{12,41} The first band is assigned to the $1a_2(\pi_3)$ orbital (HOMO) with a nodal plane on the S atom and the $2b_1(\pi_2)$ orbital with a large amount of S 3p (see the isosurface plots in Fig. 2). The second band is assigned to five MOs including $6a_1(n_S)$ and $1b_1(\pi_1)$, and the third band is assigned to three σ MOs. The corresponding bands appear in the MAES spectrum, indicating that the He*(2^3S) atoms decay *via* PI. The Pt 5d bands are observed just below E_F in the UPS spectrum, but are missing in the MAES spectrum, reflecting the limited sensitivity to the topmost layer. In other words, the absence of electron emission near E_F in the MAES spectrum provides direct evidence that the condensed layer (without

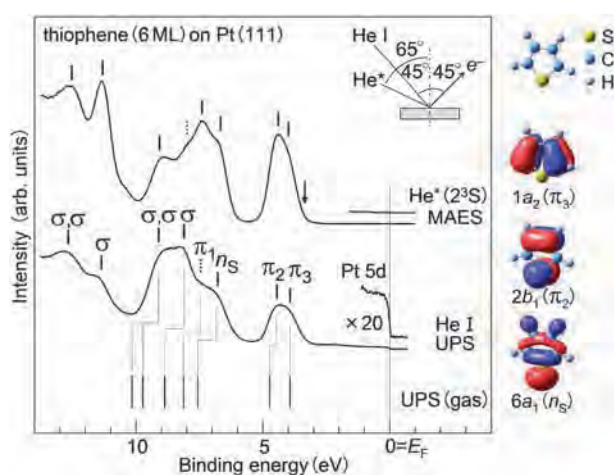


Fig. 2 He I UPS and He*(2^3S) MAES spectra of a TP multilayer (~ 6 ML) on Pt(111) prepared at 55 K, together with the energy levels of gaseous TP determined by He I UPS. The arrow in the spectrum indicates the threshold of electron emission. The isosurface plots of some MOs by *ab initio* calculations are also shown.

direct contact with the Pt substrate) is an insulator with a wide energy gap. The threshold of electron emission for the condensed layer is 3.3 eV below E_F , which corresponds to the hole injection barrier from Pt(111) to the TP film.

Fig. 3 shows the temperature-dependent spectra of a TP multilayer on Pt(111) prepared at 55 K. Upon heating to 120 K, the UPS spectrum shows that the Pt 5d bands increase in intensity, whereas the TP-derived bands are apparently unchanged. In the MAES spectrum, a weak structure due to a chemisorbed species appears just below E_F . According to TDS measurements, with the heating rate of 3 K s^{-1} , the condensed multilayer on Pt(111) desorbs at 152 K, and then, the remaining monolayer partially desorbs at 174 K.¹⁶ Reflection-absorption infrared spectroscopy (RAIRS) studies showed that the condensed molecules desorb by annealing at temperatures above 135 K.¹⁷ Therefore, spectral changes observed at 120 K are not due to thermal desorption but by disorder–crystalline transition.¹⁷ In the latter process, the disordered layers are rearranged at ~ 120 K to form crystalline islands on the chemisorbed layer, as in the case of a benzene (C_6H_6) multilayer on Pt(111).⁴²

With increasing substrate temperature, two types of monolayers are formed,¹⁹ *i.e.*, a compressed (high coverage) monolayer, and then, a relaxed (low coverage) monolayer. The spectra measured at 150 and 200 K shown in Fig. 3 correspond to those for the compressed and relaxed monolayers, respectively. The following remarks can be deduced.

(1) In the UPS spectra, the TP-derived bands show little change in E_B between multilayer and monolayers, indicating that TP chemisorbs weakly on Pt(111).

(2) The MAES spectrum shows that the He*(2^3S) atoms decay on the compressed monolayer predominantly *via* PI, yielding the TP-derived bands. On the relaxed monolayer, PI is considerably suppressed, and RI followed by AN is dominant. The former process yields a weak π -derived band at $E_B \sim 4$ eV, and the latter two-step process yields a broad background (like for the clean substrate). Changes in the branching ratio (Γ_{PI}/Γ_{RI}) are caused by the different molecular orientations in the relaxed and compressed phases, *i.e.*, TP is bound with the ring plane parallel and tilted to the substrate, respectively.¹⁹ In the flat-lying configuration, the He*(2^3S) atoms approach more close to the Pt(111) substrate, leading to the predominant decay *via* RI and AN. A similar feature has been observed in thermal collision of He*(2^3S) with flat-lying C_6H_6 on Pt(111).⁴²

(3) In the MAES spectra, a weak structure just below E_F is attributed to the CIGS formed at the TP–Pt(111) interface, because the corresponding structure is missing in the cases of the bare substrate and multilayer film. The appearance of an edge structure at E_F indicates that the chemisorbed species are metallic in nature.

We also measured the exposure-dependent spectra in the temperature range of 55–295 K (not shown). At saturation, the compressed and relaxed monolayers are formed on Pt(111) at 150 and 200 K, respectively, resulting in a very similar MAES spectrum shown in Fig. 3. According to previous studies of TP on Pt(111),¹⁹ the C–S bond cleavage begins close to room temperature, which is consistent with the MAES spectra.

To examine the local electronic structure at the TP–Pt(111) interface, we performed first-principles DFT calculations using a periodic slab model. Because no order structure has

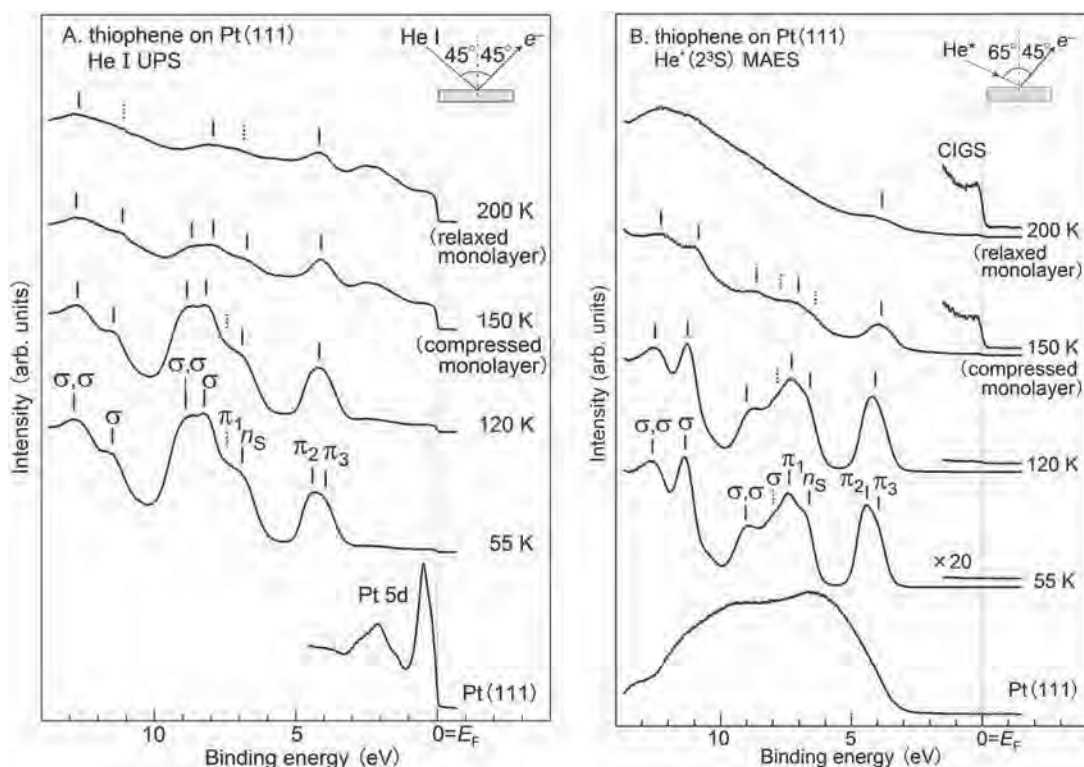


Fig. 3 (A) He I UPS spectra and (B) He*(2^3S) MAES spectra of TP on Pt(111) obtained as a condensed film (~ 6 ML) was prepared at 55 K and then heated to 120–200 K.

been observed for TP on Pt(111), hypothetical $(\sqrt{7} \times \sqrt{7})R19.1^\circ$ and (2×2) overlayers were assumed for the relaxed and compressed monolayers, respectively. The coverages in these overlayers are 0.14 and 0.25, respectively. According to the total energy calculations for the $(\sqrt{7} \times \sqrt{7})R19.1^\circ$ structure, TP adopts a nearly flat geometry on the substrate with the S atom in a terminal position, as schematically shown in Fig. 4A. The adsorption energy is 110 kJ mol^{-1} at a stationary point (which corresponds to the S–Pt distance, $d_{S-Pt} = 3.14 \text{ \AA}$), and finally reaches 132 kJ mol^{-1} at $d_{S-Pt} = 2.28 \text{ \AA}$. For the (2×2) structure, TP is bound to the terminal site *via* the S atom with an inclined configuration (Fig. 5A), where the S–Pt distance is 2.30 \AA and the tilt angle of the molecular plane relative to the surface normal is $\sim 26^\circ$. The adsorption energy is reduced to 83 kJ mol^{-1} . Thus, it is confirmed that the molecular orientation crucially depends on the coverage or molecular packing, in agreement with the MAES feature. According to near-edge X-ray-absorption fine-structure (NEXAFS),¹⁹ the tilt angle in the compressed phase was estimated to be $\sim 50^\circ$, which is somewhat larger than the calculated value.

For the optimized structures, we calculated the LDOS, PDOS, and COOP. Fig. 4B and 5B show the LDOS for the $(\sqrt{7} \times \sqrt{7})R19.1^\circ$ and (2×2) structures, respectively, in which the state density is divided into the Pt, S, and C atomic orbitals. To facilitate comparison, the observed band positions are also shown at the top of the figures. For the $(\sqrt{7} \times \sqrt{7})R19.1^\circ$ structure, the C_1 2p-, C_2 2p-, and S 3p-derived states at $E_B = 2\text{--}3 \text{ eV}$ are much broadened by mixing with the Pt 5d bands, reflecting the flat-lying configuration.

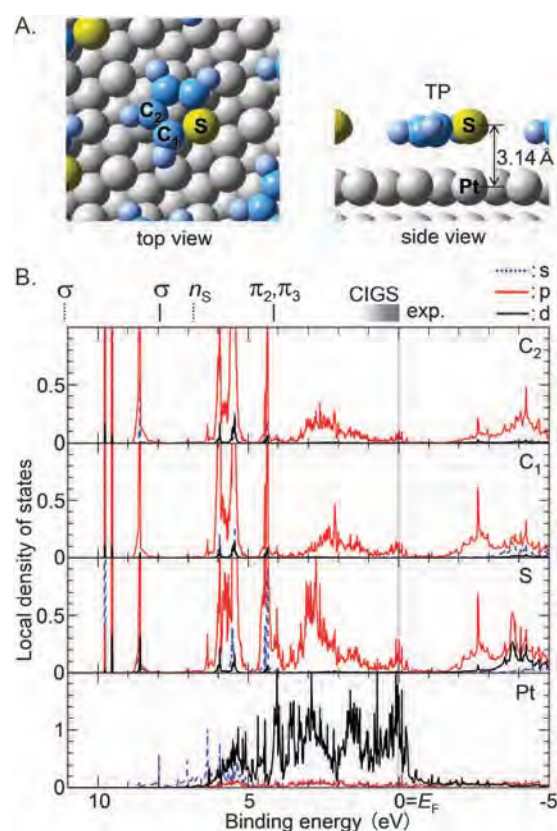


Fig. 4 (A) The structure of Pt(111) $(\sqrt{7} \times \sqrt{7})R19.1^\circ$ -TP obtained from the total energy calculations and (B) LDOS divided into the Pt, S, C and H atomic orbitals. The band positions observed are shown at the top of the panel.

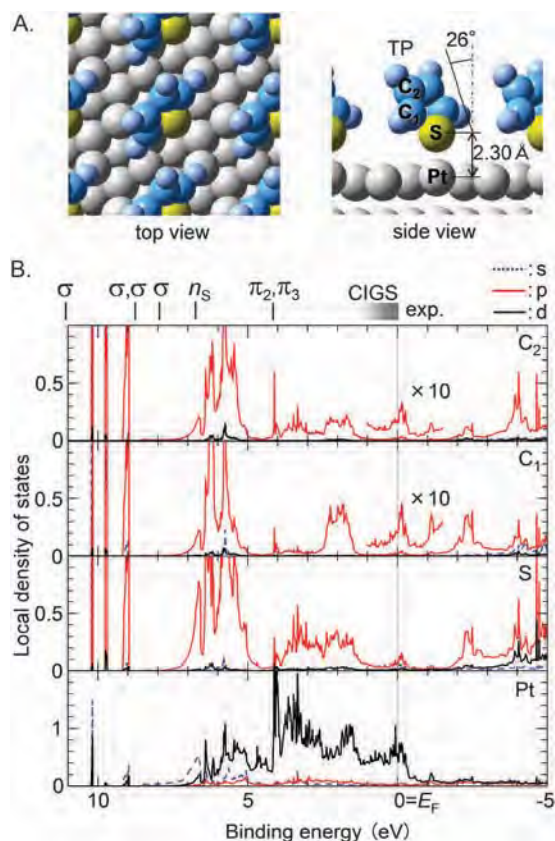


Fig. 5 (A) The structure of Pt(111)(2 × 2)-TP obtained from the total energy calculations and (B) LDOS divided into the Pt, S, C and H atomic orbitals. The band positions observed are shown at the top of the panel.

According to the COOP analysis (not shown), the occupied states below and above $E_B = 2$ eV are composed of the bonding and antibonding couplings between TP π (π_3 and π_2) and Pt 5d, yielding the positive and negative overlap populations, respectively. As a consequence, the sum of the overlap populations below E_F is almost offset, leading to the weak chemisorption of TP on Pt(111). As can be seen in Fig. 4B, the C_1 2p-, C_2 2p-, and S 3p-derived states are distributed below and above E_F , yielding the finite densities at E_F . The filled parts below E_F correspond to CIGS observed in the MAES spectrum. Thus, it is clear that the flat-lying TP species on Pt(111) are wholly metallic in nature. In the region of $E_B = 4$ –10 eV, the C_1 2p-, C_2 2p-, and S 3p-derived states show rather narrow structures because of weak (or negligible) mixing with the Pt 5d bands. These structures correspond to the n_S -, π_1 -, and σ -derived states. Finally, in the energy region far above E_F , broad structures are derived from the $3b_1(\pi_4)$ orbital (LUMO). The overlap population between TP LUMO and Pt 5d is positive but quite low below E_F , meaning that the LUMO plays a minor role in the bond formation. The validities and limitations of the present DFT calculations are discussed in Section 4.4.

For the (2 × 2) structure, the S 3p-derived states are widely distributed below and above E_F by mixing with the Pt 5d bands. The occupied parts just below E_F correspond to the CIGS observed in the MAES spectrum. The state density at

E_F decreases from the terminal S atom to the outer-located C_1 and C_2 atoms, in contrast to the case of the flat-lying configuration. In other words, the metallic nature fades out with increasing distance from the terminal atom. A similar feature has been observed in the LDOS for alkanethiolates ($C_nH_{2n+1}S$, $n = 1$ –3)³³ and benzenethiolate (C_6H_5S)³⁴ on Pt(111), where these species are bound to Pt(111) via the S atom in a tilted orientation and the local densities at E_F attenuate rapidly from the terminal atom to the molecular end.

4.2. 2-Thiophenethiol (TT) on Pt(111)

Fig. 6 shows the He I UPS and He*(2^3S) MAES spectra of TT layers (~ 2 ML) on Pt(111) prepared at 150 K. The MAES spectrum of a chemisorbed layer prepared by heating the condensed layer to 295 K is also shown. In the UPS spectrum, the first band is assigned to three π MOs, in which the $16a(\pi_4)$ and $14a(\pi_2)$ MOs are composed of antibonding and bonding couplings between the TP $1a_2(\pi_3)$ and thiol-S 3p orbitals, respectively, while the $15a(\pi_3)$ MO is derived from TP $2b_1(\pi_2)$ (see Fig. 1 and the isosurface plots in Fig. 6). The second band is assigned to six MOs, including the $13a(n_{S2})$ MO derived from TP $6a_1(n_S)$ and the $12a(n_{S1})$ MO localized at the thiol-S atom. The corresponding bands appear in the MAES spectrum, indicating that PI is the dominant process. Furthermore, electron emission just below E_F is missing because of the insulating nature of the condensed film. The threshold of electron emission for the condensed layer is 2.7 eV below E_F , which is 0.6 eV lower than that for TP on Pt(111). Because the HOMO levels are nearly identical between free TP and TT (see Fig. 1), this reduction is mainly caused by the vacuum level shift induced by the chemisorbed species.

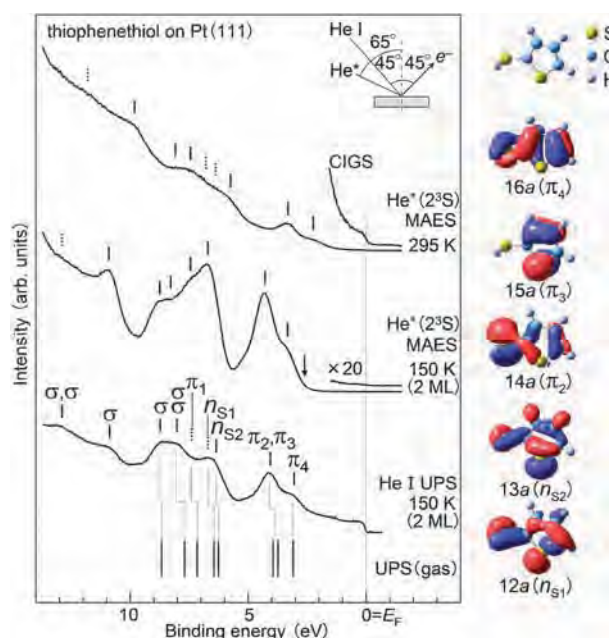


Fig. 6 He I UPS and He*(2^3S) MAES spectra of condensed layers (2 ML) of TT on Pt(111) prepared at 150 K, and He*(2^3S) MAES spectrum of a TT monolayer on Pt(111) at 295 K. The gas-phase energy levels determined by He I UPS and the isosurface plots of some MOs obtained by *ab initio* calculations are also shown. The arrow in the spectrum indicates the threshold of electron emission.

The spectral features of the chemisorbed layer are summarized as follows:

(1) The TT-derived bands are clearly observed above room temperature and shifted by 0.9–1.0 eV to the lower E_B than those in the condensed layer. These features are very different from the case of TP on Pt(111) mentioned above, and strongly suggest that TT is bound to the substrate through the S atom with the cleavage of the S–H bond, forming a thiolate. The high branching ratio ($\Gamma_{\text{PI}}/\Gamma_{\text{RI}}$) indicates that TT is arranged on Pt(111) in the tilted orientation.

(2) The energy splitting of the π -derived bands ($\Delta E_{\pi_4-\pi_2}$) is little changed for the condensed layer and chemisorbed layer, and therefore, the strong ring π -S 3p conjugation is sufficiently preserved after the formation of thiolate.

(3) A weak structure just below E_F is attributed to the CIGS formed at the thiolate–Pt(111) interface. The presence of the Fermi edge clearly indicates the metallic nature of thiolate.

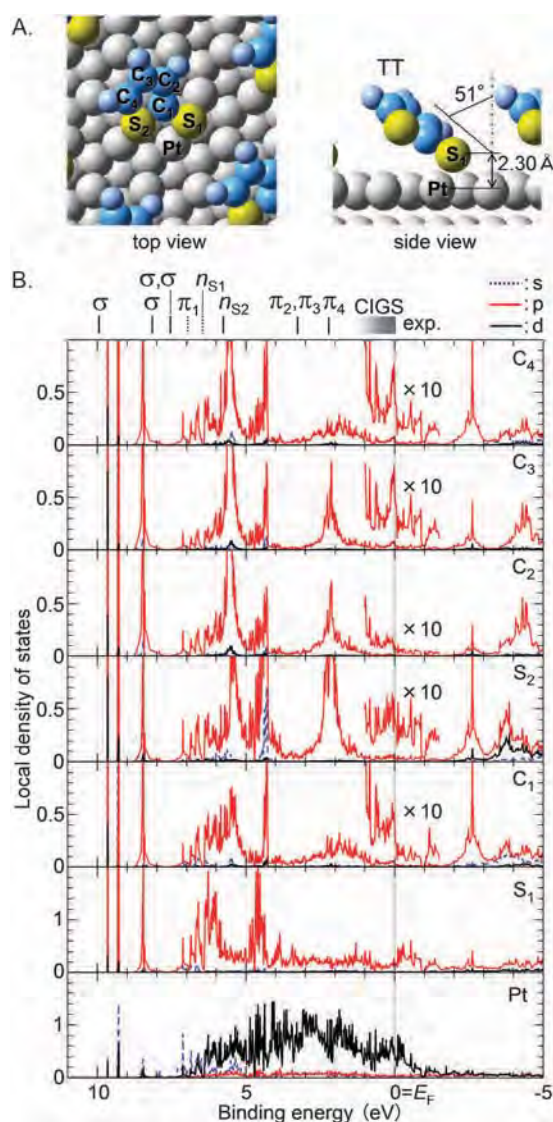


Fig. 7 (A) The structure of Pt(111)($\sqrt{7} \times \sqrt{7}$)R19.1°–TT obtained from the total energy calculations and (B) LDOS divided into the Pt, S, C and H atomic orbitals. The band positions observed are shown at the top of the panel.

According to the first principles DFT calculations for a hypothetical ($\sqrt{7} \times \sqrt{7}$)R19.1° overlayer on Pt(111), thiolate is bound preferentially on the bridge site with an inclined configuration. Fig. 7A shows a schematic view of the optimized structure, where the Pt–S distance is 2.30 Å and the tilted angle of the ring plane relative to the surface normal is 51°. The adsorption energy is 301 kJ mol^{−1}.

Fig. 7B show the LDOS for the ($\sqrt{7} \times \sqrt{7}$)R19.1° structure, in which the state density is divided into the Pt, S, and C atomic orbitals. The observed band positions are also shown at the top of the figure. At the anchor S₁ atom, the 3p-derived states are widely distributed below and above E_F by coupling with the Pt 5d bands, forming a metallic electronic state. The finite density at E_F is discernible not only at the adjacent C₁ atom but also at the outer C₃ and C₄ atoms, indicating that thiolate is wholly metallic in nature. In other words, thiolate is a good mediator of the extension of metal wave functions at E_F . The local DOS at 1–3 eV below E_F are attributed to the π_4 – π_2 states. The sharp structures at the S₂, C₂, and C₃ atoms are derived from the π_4 state, because the native π_3 MO of TT has a nodal plane on the anchor S₁ atom (see Fig. 6) and plays a minor role in the S₁–Pt bond formation. The broad structures at the C₁ and C₄ atoms are caused by the strong couplings of the π_4 and π_2 MOs with the Pt 5d bands. The validities and limitations of the DFT calculations are described in Section 4.4.

4.3. 2,2'-Bithiophene (BTP) and 2,2'-bithiophene-5-thiol (BTT) on Pt(111)

Fig. 8A shows the He I UPS and He*(2³S) MAES spectra of BTP layers (~2 ML) on Pt(111) prepared at 205 K. The MAES spectrum of a chemisorbed layer prepared by heating the condensed layer to 225 K is also shown. The UPS spectra of BTP in the gas and condensed phases have been reported in the literature.^{29,43} The first band is assigned to four π MOs; the 3b_g(π_6) and 2a_u(π_3) MOs are composed of antibonding and bonding couplings of two TP 1a₂(π_3), respectively, while the 3a_u(π_5) and 2b_g(π_4) are derived from the weak coupling of two TP 2b₁(π_2) (see Fig. 1 and the isosurface plots in Fig. 8A). The assignment of the other bands is given in the figure. The corresponding bands are seen in the MAES spectrum, indicating that the He*(2³S) atoms deexcite on the condensed layer *via* PI. The threshold of electron emission for the condensed layer is 2.1 eV below E_F , which is 1.2 eV lower than that for TP on Pt(111), reflecting the HOMO levels in free TP and BTP (see Fig. 1).

For the chemisorbed layer, the BTP-derived bands are clearly seen in the MAES spectrum, indicating that PI is dominant. The binding energies are apparently unchanged upon chemisorption. In addition, a weak emission appears just below E_F and can be attributed to the CIGS formed at the BTP–Pt(111) interface. These features quite well resemble those observed in TP on Pt(111), and suggest that BTP is weakly bound to Pt(111) with an inclined geometry. Angle-resolved UPS for BTP on Ni(110)²⁹ and NEXAFS for BTP on Ag(111)¹⁴ showed that the molecules are bound in a flat-lying geometry, in contrast to the case of BTP on Pt(111).

Fig. 8B shows the relevant spectra of BTT on Pt(111). A chemisorbed layer was prepared by heating the condensed

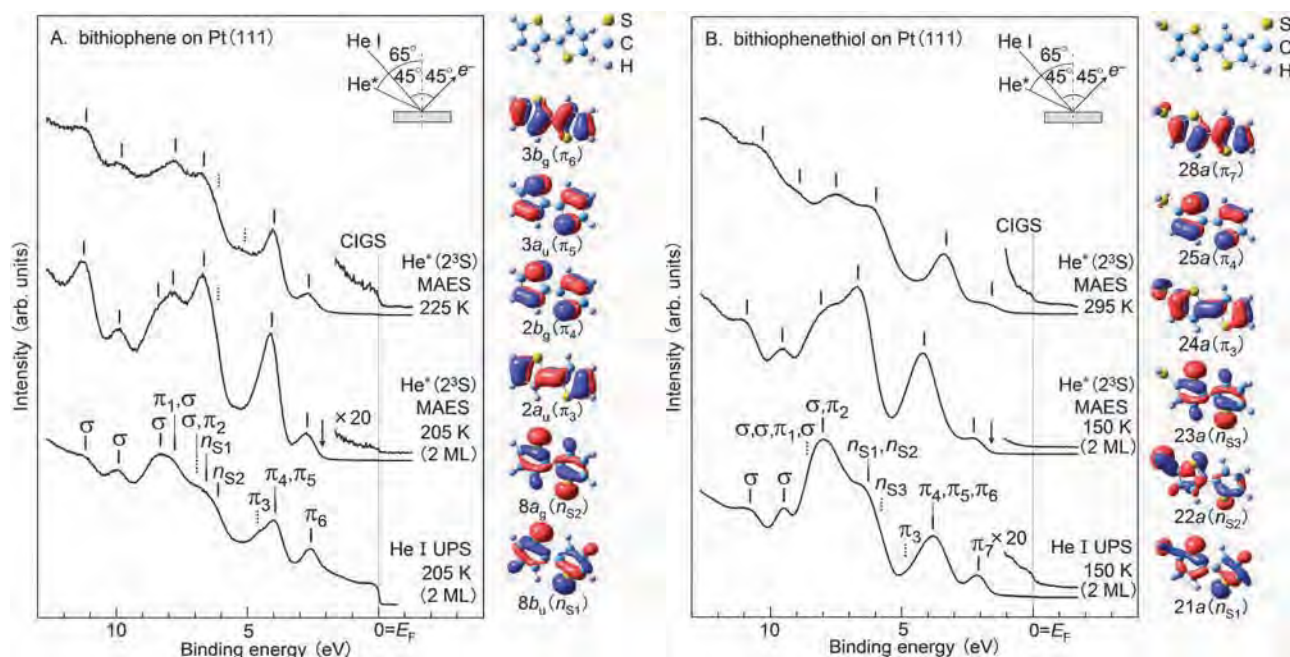


Fig. 8 (A) He I UPS and He*(2^3S) MAES spectra of condensed layers (2 ML) of BTP on Pt(111) at 205 K, and He*(2^3S) MAES spectrum of a BTP monolayer on Pt(111) at 225 K. (B) He I UPS and He*(2^3S) MAES spectra of condensed layers (2 ML) of BTT on Pt(111) at 150 K, and He*(2^3S) MAES spectrum of a BTT monolayer on Pt(111) at 295 K. The arrow in the spectra indicates the threshold of electron emission. The isosurface plots of some MOs obtained by *ab initio* calculations are shown at the right-hand side of the panel.

layer to 295 K. In the UPS spectrum of the condensed layers, the first band is assigned to five π MOs, in which the well-separated $28a(\pi_7)$ MO is derived from the $3b_g(\pi_6)$ MO in BTP (see Fig. 1 and the isosurface plots in Fig. 8B). The assignment of the other bands is given in the figure. The corresponding bands are also observed in the MAES spectra, and indicate that the He*(2^3S) atoms deexcite on the condensed and chemisorbed layers mainly *via* PI. The threshold of electron emission is 1.6 eV below E_F , which is 0.5 eV lower than that for BTP on Pt(111). Because the HOMO levels for free BTP and BTT are nearly identical (see Fig. 1), this reduction is mainly attributed to the increased work function induced at the chemisorbed BTT–Pt(111) interface. As for the chemisorbed layer, the observed bands are uniformly shifted by ~ 0.6 eV to the lower E_B than those in the multilayer. This feature is very similar to the case of TT on Pt(111), suggesting that BTT is also bound to Pt(111) as a thiolate. Furthermore, weak emission just below E_F newly appears and can be attributed to the CIGS formed at the thiolate–Pt(111) interface. A critical comparison of CIGSs observed in these systems is described in the next section.

4.4. Chemisorption-induced gap states (CIGSs)

As mentioned above, TP and the derivatives chemisorb on Pt(111) to form new electronic states in the HOMO–LUMO gap, denoted as CIGSs. Because the CIGS is usually accompanied by charge transfer between the organic molecule and the metal substrate, it plays a crucial role in several phenomena; for example, chemical reactions such as desulfurization and charge injection across the organic–metal interface. Furthermore, CIGSs mediate the extension of the metal wave function to organic species, which determines transport characteristics at the

organic–metal interface. The electric conductance in metal–organic–metal junctions is a typical example.⁶ In this section, we briefly address how the spatial extent of the CIGS is altered by the strength of the organic–metal bond and the adsorption geometry.

Fig. 9 shows the MAES spectra near E_F for the chemisorbed species on Pt(111) at saturation. To facilitate comparison, the first band (hatched area) in each spectrum is normalized in intensity by taking into account the number of the relevant π MOs. The relative intensity of the CIGS at E_F is given in the figure. Fig. 10 shows the calculated DOS at E_F for TP and TT on Pt(111) as a function of distance from the topmost Pt layer. The following features are deduced from Fig. 9 and 10.

(1) For nearly flat-lying TP, the observed CIGS at E_F is greatly enhanced in intensity, indicating that the electron density is sufficiently exposed outside of the molecule. In the calculated DOS at E_F , two maxima at 2.5 and 3.6 Å are derived from the TP π MOs with a node along the ring plane. The charge density is considerably exposed toward the vacuum because of the coupling of TP π with Pt 5d. Thus, it is clear that nearly flat-lying TP acts as a good mediator of the extension of the metal wave function at E_F , in spite of weak chemisorption of TP on Pt(111).

(2) In contrast, the observed CIGS at E_F is rather weak for inclined TP on Pt(111). This result is confirmed by the calculated DOS, in which the charge density at E_F strongly attenuates in the chemisorbed molecule. In other words, inclined TP is a poor mediator of the metal wave function at E_F . This would also be true for inclined BTP on Pt(111), because the CIGS is very suppressed at E_F in the spectrum.

(3) TT chemisorbs strongly on Pt(111) in an inclined fashion, forming a thiolate. The CIGS for TT at E_F is weaker than that

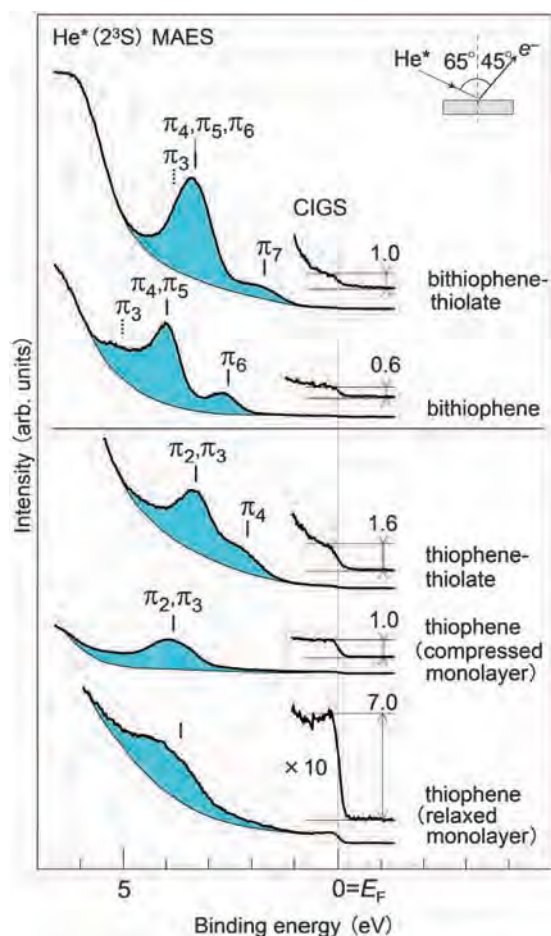


Fig. 9 Comparison of He*(2^3S) MAES spectra of the chemisorbed species on Pt(111) at saturation. The first bands (hatched area) are normalized in intensity to take account of the number of relevant π MOs.

for nearly flat-lying TP and stronger than that for inclined TP. The calculated DOS at E_F is rather high because of strong Pt 5d–S 3p mixing. This would also be the case for BTT on Pt(111), taking into consideration the spectral intensity of the CIGS.

Although the transport characteristics in molecular junctions are beyond the scope of this work, it is appropriate to briefly make some comments. According to current–voltage (I – V) traces for alkanedithiols linked by metal (Ag, Pt, and Au) electrodes,⁴⁴ the conductance at zero bias decreases exponentially with increasing chain length. Such non-resonance tunneling is originated from the fact that the CIGS near E_F is strongly damped from the anchor S atoms to the alkyl chain.³³ Non-resonance tunneling also dominates in metal–benzenedithiol–metal junctions, yielding low conductance at zero bias.^{45–48} This result is closely related to the spatial distribution of the CIGS near E_F ; the benzene π –S 3p conjugation in the free molecule becomes weak upon chemisorption, resulting in the localized CIGS around the S atoms.^{34,35} In contrast, the I – V traces for oligo-thiophenedithiols such as bithiophenedithiol bridged by a pair of Au electrodes showed that the conductance at low bias is dominated by resonance tunneling.⁴ This behavior indicates that the CIGS near E_F is wholly distributed

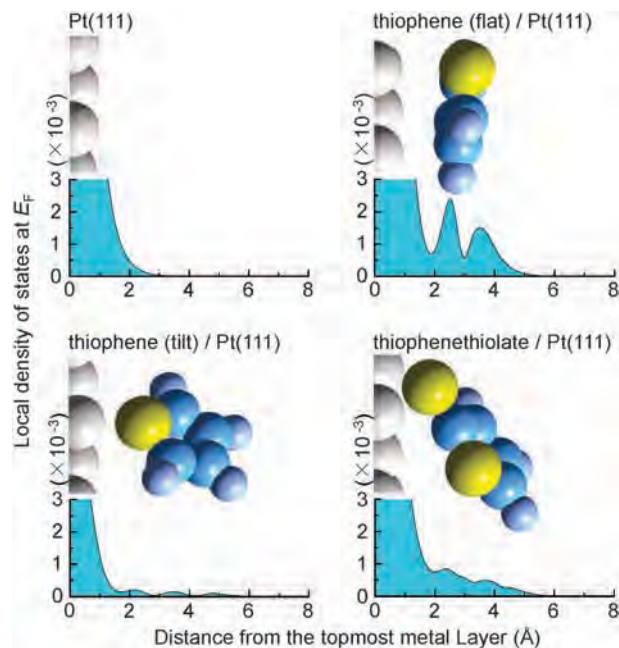


Fig. 10 Calculated DOS at E_F for clean Pt(111), nearly flat-lying and inclined TP on Pt(111), and TT on Pt(111) as a function of the distance from the topmost Pt(111) layer.

in the sandwiched species, similar to the case of BTT on Pt(111), and serves as a so-called resonance state in the tunneling process. The characterization of CIGSs in organic–metal systems and their relationship with charge transport in molecular junctions have been described in our review.⁶

Finally, we comment on the first-principles DFT calculations used in this work. As can be seen in Fig. 4B, 5B, and 7B, the calculated binding energies are much lower than the observed values and they seem inadequate for interpreting the band broadening and splitting. Several limitations in the GGA or local density approximation (LDA) have been pointed out when applied to the description of the organic–metal interface.²³ However, the present calculations aid in qualitative understanding of the molecular orientations and electronic structures, in particular the formation of CIGS.

5. Summary

In this study, we examined the valence electronic states of thiophene derivatives on Pt(111) in the condensed and chemisorbed phases using UPS, MAES, and first-principles DFT calculations. The concluding remarks are summarized as follows.

(i) Condensed films of TP, TT, BTP, and BTT (without direct contact with the substrate) are insulators with a wide energy gap.

(ii) TP chemisorbs weakly on Pt(111) with flat-lying and inclined orientations at low and high coverage, respectively, in agreement with the previous measurements. BTP is weakly bound on Pt(111), whereas TT and BTT are strongly bound on Pt(111) through the S atom with the cleavage of the S–H bond, forming thiolates.

(iii) In the MAES spectra for the chemisorbed species, CIGSs emerge just below E_F , yielding a metallic structure at the organic–metal interface. The formation of CIGSs is responsible for the vacuum level shift, and subsequently, the hole injection barrier at the organic–metal interface.

(iv) In the MAES spectra, the relative intensities of CIGSs at E_F are in the order of TP (flat-lying configuration) > TT > TP (inclined configuration). This indicates that the spatial extent of CIGSs is drastically altered by the strength of the organic–metal bond and the adsorption geometry. In other words, TP (flat-lying geometry) and TT serve as good mediators of the extension of the metal wave function at E_F . Such asymptotic behavior of the metal wave function would be useful for the understanding and fabrication of functional organic-based devices.

References

- H. Sirringhaus, P. J. Brown, R. H. Friend, M. M. Nielsen, K. Bechgaard, B. M. W. Langeveld-Voss, A. J. H. Spiering, R. A. J. Janssen, E. W. Meijer, P. Herwig and D. M. de Leeuw, *Nature*, 1999, **401**, 685.
- F. Garnier, R. Hajlaoui, A. Yassar and P. Srivastava, *Science*, 1994, **256**, 1684.
- R. H. Friend, R. W. Gymer, A. B. Holmes, J. H. Burroughes, R. N. Marks, C. Taliani, D. D. C. Bradley, D. A. Dos Santos, J. L. Brédas, M. Lögdlund and W. R. Salaneck, *Nature*, 1998, **397**, 121.
- N. B. Zhitenev, H. Meng and Z. Bao, *Phys. Rev. Lett.*, 2002, **88**, 226801.
- Conjugated polymer and molecular Interfaces: Science and Technology for Photonic and Optoelectronic Applications*, ed. W. R. Salaneck, K. Seki, A. Kahn and J.-J. Pireaux, Marcel Dekker, New York, 2001.
- S. Masuda, *Appl. Surf. Sci.*, 2010, **256**, 4054 and references therein.
- L. Cheng, A. B. Bocarsly, S. L. Bernasek and T. A. Ramanarayanan, *Surf. Sci.*, 1997, **374**, 357.
- A. Imanishi, S. Yagi, T. Yokoyama, Y. Kitajima and T. Ohta, *J. Electron Spectrosc. Relat. Phenom.*, 1996, **80**, 151.
- J. Stöhr, E. B. Kollin, D. A. Fischer, J. B. Hastings, F. Zaera and F. Sette, *Phys. Rev. Lett.*, 1985, **55**, 1468.
- K. P. Milligan, B. Murphy, D. Lennon, B. C. C. Cowie and M. Kadodwara, *J. Phys. Chem. B*, 2001, **105**, 140.
- J. P. Fulmer, F. Zaera and W. T. Tysoe, *J. Phys. Chem.*, 1988, **92**, 4147.
- F. P. Netzer, E. Bertel and A. Goldmann, *Surf. Sci.*, 1988, **201**, 257.
- S. Terada, T. Yokoyama, M. Sakano, A. Imanishi, Y. Kitajima, M. Kiguchi, Y. Okamoto and T. Ohta, *Surf. Sci.*, 1988, **414**, 107.
- P. Väterlein, M. Schmelzer, J. Taboriski, T. Krause, F. Viczian, M. Bäßler, R. Fink, E. Umbach and W. Wurth, *Surf. Sci.*, 2000, **452**, 20.
- J. E. Whitten, *Surf. Sci.*, 2003, **546**, 107.
- N. A. Khan, H. H. Hwu and J. G. Chen, *J. Catal.*, 2002, **205**, 259.
- H. Haberkern, S. Haq and P. Swiderek, *Surf. Sci.*, 2001, **490**, 160.
- J. F. Lang and R. I. Masel, *Surf. Sci.*, 1987, **183**, 44.
- J. Stöhr, J. L. Gland, E. B. Kollin, R. J. Koestner, A. L. Johnson, E. L. Muettterties and F. Sette, *Phys. Rev. Lett.*, 1984, **53**, 2161.
- J. Zhou, Y. X. Yang, P. Liu, N. Camillone III and M. G. White, *J. Phys. Chem. C*, 2010, **114**, 13670.
- A. Nambu, H. Kondoh, I. Nakai, K. Amemiya and T. Ohta, *Surf. Sci.*, 2003, **530**, 101.
- J. Noh, E. Ito, K. Nakajima, J. Kim, H. Lee and M. Hara, *J. Phys. Chem. B*, 2002, **106**, 7139.
- K. Tonigold and A. Groß, *J. Chem. Phys.*, 2010, **132**, 224701.
- H. Orita and N. Itoh, *Surf. Sci.*, 2004, **550**, 177.
- F. Buonocore and A. di Matteo, *Theor. Chem. Acc.*, 2009, **124**, 217.
- S. Higai, J. Nara and T. Ohno, *Surf. Sci.*, 2006, **600**, 685.
- C. Majumder, H. Mizuseki and Y. Kawazoe, *J. Chem. Phys.*, 2003, **118**, 9809.
- E. Ito, J. Noh and M. Hara, *Surf. Sci.*, 2008, **602**, 3291.
- G. Koller, F. P. Netzer and M. G. Ramsey, *Surf. Sci.*, 1999, **421**, 353.
- Y. Harada, S. Masuda and H. Ozaki, *Chem. Rev.*, 1997, **97**, 1897.
- H. Morgner, *Adv. At., Mol., Opt. Phys.*, 2000, **42**, 387.
- M. Aoki, Y. Koide and S. Masuda, *J. Electron Spectrosc. Relat. Phenom.*, 2007, **156–158**, 383.
- S. Masuda, Y. Koide, M. Aoki and Y. Morikawa, *J. Phys. Chem. C*, 2007, **111**, 11747.
- S. Masuda, T. Kamada, K. Sasaki, M. Aoki and Y. Morikawa, *Phys. Chem. Chem. Phys.*, 2010, **12**, 10914.
- M. Aoki, T. Kamada, K. Sasaki, S. Masuda and Y. Morikawa, *Phys. Chem. Chem. Phys.*, 2012, **14**, 4101.
- M. Aoki, Y. Ohashi, S. Masuda, S. Ojima and N. Ueno, *J. Chem. Phys.*, 2005, **122**, 194508.
- Y. Morikawa, *Phys. Rev. B: Condens. Matter Mater. Phys.*, 1995, **51**, 14802.
- D. Vanderbilt, *Phys. Rev. B: Condens. Matter Mater. Phys.*, 1990, **41**, 7892.
- N. Troullier and J. L. Martins, *Phys. Rev. B: Condens. Matter Mater. Phys.*, 1991, **43**, 1993.
- H. J. Monkhorst and J. D. Pack, *Phys. Rev. B: Solid State*, 1976, **13**, 5188.
- N. Kishimoto, H. Yamakado and K. Ohno, *J. Phys. Chem.*, 1996, **100**, 8204 and references therein.
- M. Sogo, Y. Sakamoto, M. Aoki and S. Masuda, *J. Chem. Phys.*, 2010, **133**, 134704.
- D. Jones, M. Guerra, L. Favaretto, A. Modelli, M. Fabrizio and G. Distefano, *J. Phys. Chem.*, 1990, **94**, 5761.
- V. B. Engelkes, J. M. Beebe and C. D. Frisbie, *J. Am. Chem. Soc.*, 2004, **126**, 14287.
- M. A. Reed, C. Zhou, C. J. Muller, T. P. Burgin and J. M. Tour, *Science*, 1997, **278**, 252.
- X. Xiao, B. Xu and N. J. Tao, *Nano Lett.*, 2004, **4**, 267.
- M. Kiguchi, S. Miura, K. Hara, M. Sawamura and K. Murakoshi, *Appl. Phys. Lett.*, 2006, **89**, 213104.
- M. Kiguchi, S. Miura, K. Hara, M. Sawamura and K. Murakoshi, *Appl. Phys. Lett.*, 2007, **91**, 053110.

Biaxial Alignment Control of Guanine Crystals by Diamagnetic Orientation

Masakazu Iwasaka^{1,2*}, Yuito Miyashita¹, Yuri Mizukawa¹, Kentaro Suzuki³, Taro Toyota⁴, and Tadashi Sugawara³

¹Chiba University, Chiba 263-8522, Japan

²Japan Science and Technology Agency PRESTO, Kawaguchi, Saitama 332-0012, Japan

³Kanagawa University, Hiratsuka, Kanagawa 259-1293, Japan

⁴University of Tokyo, Meguro, Tokyo 153-8902, Japan

E-mail: iwasaka@faculty.chiba-u.jp

Received January 18, 2013; accepted February 17, 2013; published online March 7, 2013

The present study provides evidence that a kind of nucleic acid base crystal, guanine crystal, shows a distinct magnetic orientation. Under the condition where the guanine crystal boards were lying on the glass surface due to gravity, the boards gradually oriented their length to the applied horizontal magnetic fields of 400 mT. On the other hand, the vertical magnetic fields parallel to Earth's gravity caused their width to be oriented along the applied magnetic fields. Moreover, combining both vertical and horizontal magnetic fields produced a rapid alignment of the length to the horizontal magnetic fields. © 2013 The Japan Society of Applied Physics

In previously reported studies, magnetic orientations of organic and inorganic materials were observed under magnetic fields of more than 1 T.^{1–5)} Most of the studies were designed to provide a new finding on the diamagnetic properties of crystals under magnetic fields of 10 T order. However, less attention was paid to the possible effects of mT order fields on diamagnetic crystals with high diamagnetic anisotropy. In the field of polymer science, biaxial magnetic orientations of crystallized organic polymer crystals were observed under magnetic fields of more than 1 T.^{6–9)} The diamagnetic anisotropic energy is expressed using the following equation:

$$E_{d\Delta} = -\frac{\Delta\chi B^2}{2\mu_0},$$

in the cgs system, where $\Delta\chi$ is the difference between magnetic susceptibilities in two axes: B , magnetic fields, and μ_0 , magnetic permeability in vacuum. The diamagnetic orientation becomes obvious when the diamagnetic energy overcomes the thermal energy kT , where k is the Boltzmann constant and T is temperature (K).

Also, it was reported that *Lysozyme* crystals were oriented under 10 T magnetic fields.^{10,11)} However, there was no report on magnetic field effects on the biogenic crystal's orientation. Our previous study focused on the behaviors of guanine crystals, which is a kind of nucleic acid base, showing light-scattering changes under magnetic fields as weak as 260 mT,^{12,13)} by utilizing both in situ high-resolution CCD microscopy and fiber-optic spectroscopy.

The present study focused on the magnetic orientation of goldfish guanine crystals by changing the direction of the magnetic fields. The direction of the magnetic fields was selected as horizontal or vertical depending on the stances standing or lying of guanine crystals on the bottom surface, and exhibited the biaxial alignment of the biogenic crystals.

Figure 1 shows the experimental setup that was utilized for the observation of the biaxial magnetic orientation of guanine crystal boards in an aqueous solution. Figure 1(a) is the configuration of a resistive electromagnet and an inverted optical microscope. Horizontal magnetic fields of up to 500 mT were generated in the gap of two magnetic poles. Figure 1(b) illustrates the permanent magnet that provided 340 mT magnetic fields normal to the bottom of the sample chamber. The magnetic field exposure parallel to Earth's gravity was performed by setting the sample

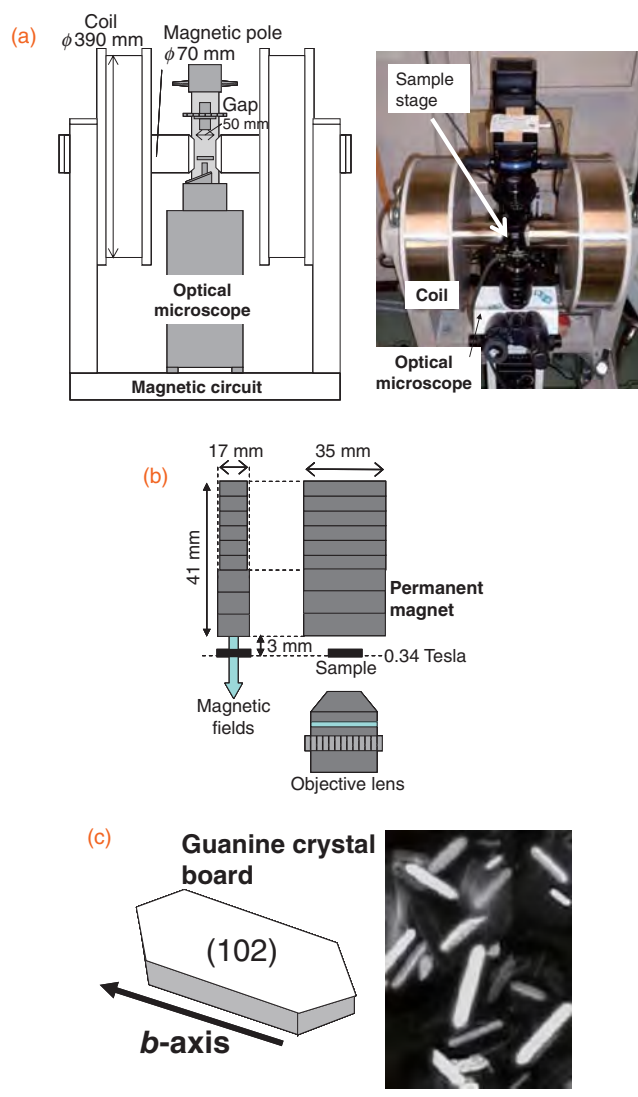


Fig. 1. Experimental system for observing a guanine crystal's orientation by horizontal and vertical magnetic fields. (a) Horizontal magnetic field exposure system for the observation of guanine crystals on an inverted optical microscope. The sizes of the coil and poles of the resistive electromagnet are shown. (b) Configuration of the vertical magnetic field exposure system with a permanent magnet array and the objective lens of the inverted optical microscope. (c) A model of a guanine crystal board showing its b -axis and the broadest surface that is parallel to the (102) plane. The photo on the right shows an image of guanine crystals under dark-field illumination. Bar, 20 μm .

chamber on the permanent magnet where the magnetic field penetrated perpendicular to the bottom of the chamber. The distance between the magnet's surface and the guanine crystals was 3 mm. The sample chamber, about 300 μm in thickness and containing guanine crystal boards, was completely filled with aqueous solution.

The chamber was made of two cover glasses (18 × 18 mm², 0.12–0.17 mm in thickness) bonded by a frame seal (Bio-Rad SLF0201) and set in the stage of an inverted optical microscope (Olympus IX73), as shown in the bottom of Fig. 1(a). In addition, the inverted optical microscope was placed in the space between two coils of the resistive electromagnet. In the case of the horizontal magnetic field exposure, an electric current was introduced into the electromagnet, and the horizontal fields of up to 500 mT were applied parallel to the bottom of the chamber.

The guanine crystals were obtained from chromatophore cells in goldfish scales (and skin). The biological sample preparation procedures were submitted to and approved by the biological ethics committee of Chiba University. The biogenic guanine crystals were thin and their broadest surface represented a long hexagonal pattern, as shown in Fig. 1(c). We carried out X-ray diffraction pattern measurements and obtained data showing that the structure of goldfish guanine crystals was similar to that of anhydrous crystals.^{14,15} According to previous literature on crystallography,¹⁵ the broadest surface corresponds to the (102) plane, and the length of the broadest plane is parallel to the *b*-axis. Within the broadest surface, the lengths in the longitudinal and lateral directions were about 10–20 and 4–8 μm, respectively. The broadest surface of the crystals showed a twinkling light scattering due to the distinct difference in the light reflectivity between guanine crystals and the surrounding aqueous solution.

First, an in situ observation of goldfish guanine crystals was carried out under magnetic fields by utilizing the optical microscope whose stage was set in the gap of poles of an electromagnet. The exposed guanine crystal boards exhibited an orientation directing the length of the (102) plane (*b*-axis) to the applied magnetic fields [Figs. 2(a)–2(d) and its model illustration in Fig. 2(e)]. A random orientation of guanine boards was observed under ambient fields. In contrast, the guanine crystal boards gradually changed their length direction parallel to the applied horizontal magnetic fields. Most of the guanine crystal boards completed their orientation in 5 min. Figure 2(f) shows an example of the angle distribution of the crystal boards which was analyzed on another set of experiments under 500 mT. The number of boards that directed their *b*-axis to the horizontal direction by the angle θ was counted with and without the horizontal magnetic field. It is apparent that the length direction became parallel. The mechanism of this phenomenon is explained in Fig. 2(g), where χ_l and χ_w denotes the diamagnetic susceptibility in the length direction and that in width direction of the (102) plane in guanine crystal board, respectively. The signs of both χ_l and χ_w are minus because guanine is a diamagnetic molecule, and χ_l is larger than χ_w . The values of both diamagnetic energies being deducted from that in the depth direction ($-\chi_d B^2/2\mu_0$) are different; as a result, the diamagnetic energy in the length direction is smaller than that in the width direction. These

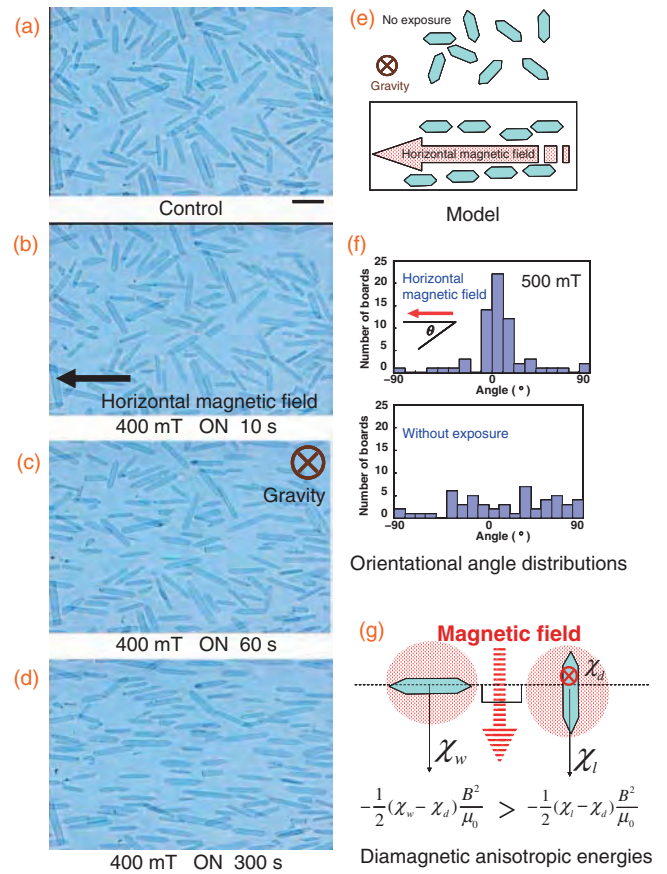


Fig. 2. Primal magnetic orientation of guanine crystal boards. (a) Random orientation of guanine crystal boards under ambient fields. Bar, 20 μm. (b)–(d) Time dependence of the magnetic orientation of guanine crystal boards under 400 mT horizontal magnetic fields. Earth's gravity is normal to the horizontal plane. (e) A model to explain the orientation of guanine crystal boards directing their longest length to the horizontal magnetic fields. (f) An example of the angle distribution of boards directing their *b*-axis to the horizontal direction by angle θ with and without the horizontal magnetic field at 500 mT. (g) A simple model to compare the diamagnetic anisotropic energy of boards when their length or width is directed to the magnetic field.

energy level speculations prove the observed magnetic orientation.

It was speculated that the physical mechanism for the observed orientation under magnetic fields of 400 mT was the same as the pilot study reporting the magnetic orientation of lecithin crystals,¹⁶ which had a similar crystal's morphological size with the goldfish guanine crystal, and was reported to show a magnetic orientation at 160–900 mT. It is considered that the magnetic fields of the sub-Tesla order are enough for diamagnetic crystals to cause orientation versus magnetic fields if the crystals have high diamagnetic anisotropy which can provide enough diamagnetic energy to overcome the thermal energy kT , as described in the introduction. To prove this speculation, a simple estimation of the diamagnetic energy of goldfish guanine crystals was carried out by utilizing the cgs gauss unit system. Depending on this study's DC-SQUID measurements showing that the diamagnetic susceptibility of a goldfish scale with guanine crystals was -4.52×10^{-7} emu/g, it was hypothesized that the maximum $|\Delta\chi|$ in a guanine crystal was 1×10^{-7} emu/g. Also an atomic force microscopy (AFM) analysis

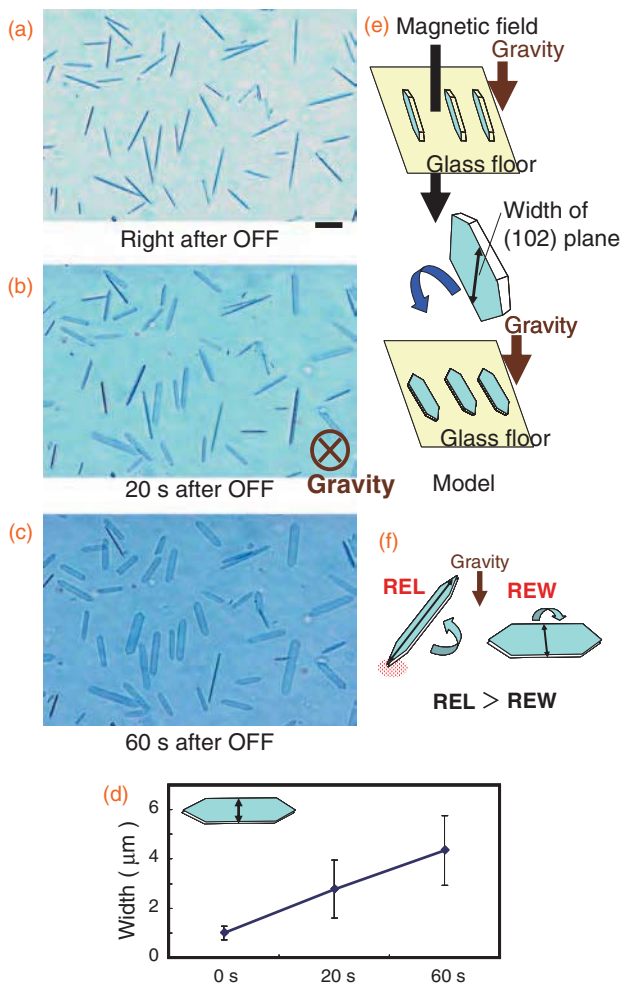


Fig. 3. Secondary magnetic orientation of guanine crystal boards directing the width of the (102) plane to the applied magnetic fields, in other words, magnetic rotation around the *b*-axis. (a) Right after the permanent magnet was removed after applying 340 mT magnetic fields normal to the bottom of the sample chamber in the optical microscope. Bar, 20 μm. (b, c) Guanine crystal boards falling onto the glass floor. (d) Change in the width of the observed shape of a guanine crystal board. Mean ± SD (*n* = 44) are shown. (e) An illustration to explain the alignment of guanine crystal boards directing width of the (102) plane parallel to both magnetic fields and gravity. (f) Comparison of rotational energy when a lying board rotates its length or width to stand up.

suggested that usually the thickness of a goldfish guanine crystal was approximately 0.1 μm. The employed guanine crystal model in the size of 20 × 5 × 0.1 μm³ has a volume of 10⁻¹¹ cm³ (with an assumption of the density ≈ 1 g/cm³) and assumed to have a |Δχ| of 1 × 10⁻¹⁸ emu/g. The diamagnetic energy of this model Δ*E* is estimated to be 8 × 10⁻¹² erg under 400 mT magnetic fields, and is 100 times larger or more than thermal energy *kT* at 300 K, which is 4.14 × 10⁻¹⁴ erg. The estimations quantitatively supported this study's conjecture that the goldfish guanine crystals diamagnetically oriented under 400 mT.

Next, the magnetic orientation of guanine crystal boards directing its width direction in the (102) plane parallel to the magnetic fields was observed. Figure 3(a) shows the guanine crystal boards standing on its long thin plane [(001) plane]¹⁵⁾ and directing their width direction in the (102) plane parallel to both the magnetic fields and gravity. The image that was taken 3 s after removing the permanent magnet shows the

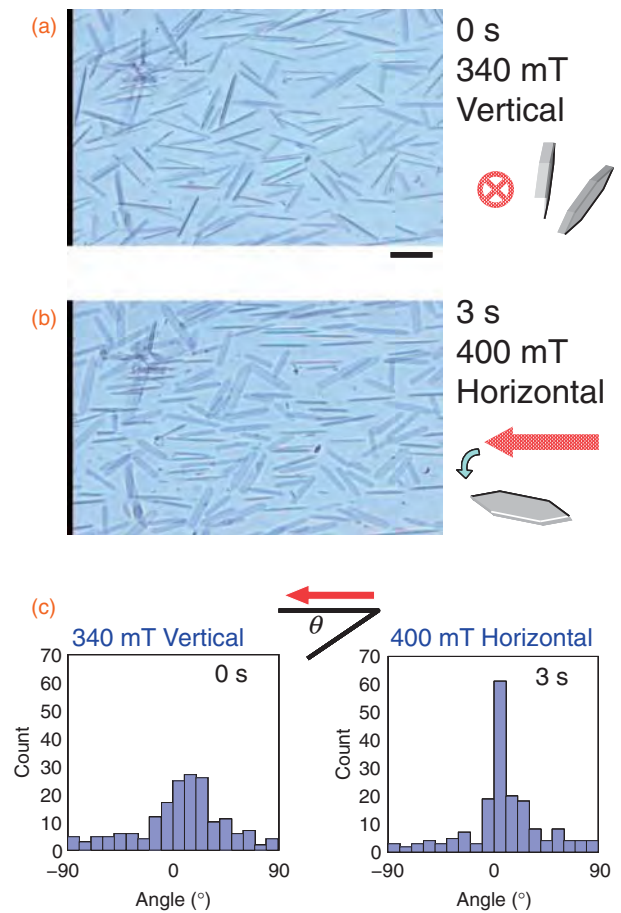


Fig. 4. Rapid horizontal magnetic orientation at 400 mT under an electromagnet, which was achieved by prestanding the guanine crystal boards by the vertical magnetic fields at 340 mT using a permanent magnet. (a) Right after the permanent magnetic was removed from the sample. Bar, 20 μm. (b) 3 s after the 400 mT electromagnetic fields were turned on. (c) Distribution of the angle between the *b*-axis of a board and the horizontal direction in the individual photographs in (a) and (b).

thin line, which is the other long thin plane [(001) plane]. The guanine crystal boards gradually leaned, and in one minute, most of them were lying down, as shown in the photographs [Figs. 3(b) and 3(c)]. The leaning of guanine crystal boards is quantitatively analyzed by measuring the width of boards, as shown in Fig. 3(d). Figure 3(e) illustrates the process of guanine crystal boards directing width of the (102) plane parallel to both magnetic fields and gravity. To explain the mechanism of this kind of orientation, rotational energies with a moment of inertia have to be accounted for. The rotational energy for the rotating length direction [REL in Fig. 3(f)] is larger than that for the rotating width direction (REW). Thus, for the lying board, it is difficult to rotate its length to let it stand up. In the case when the rotational energy of the length rotation is larger than the absolute value of the diamagnetic energy in the length direction, it is possibly easy to rotate the width direction if the rotational energy of the width rotation is small enough. These results indicate that the rotation of the biogenic hexagonal thin crystal boards quickly occurred owing to diamagnetic torque forces around the length direction of the broadest surface (*b*-axis). However, several minutes were needed in order to obtain the magnetic orientation around the depth direction of the guanine crystal board.

Furthermore, this study presents the rapid rotation of the length direction by combining the vertical and horizontal magnetic fields. Figure 4 shows the in situ observation of the time course of the rotation of guanine crystal boards under two kinds of magnetic fields. Figure 4(a) shows a photograph of guanine crystal boards directing their width direction of the broadest surface [(102) plane] to the vertical magnetic fields that were parallel to Earth's gravity. The horizontal magnetic fields were applied by an electromagnet while the boards were still standing. It was observed that the standing guanine crystal boards were twisted by the applied horizontal magnetic fields and the length direction of their (102) plane was quickly oriented to the horizontal direction [Fig. 4(b)]. Some of the boards horizontally rotated while standing, and others fell to make the (102) plane horizontal. The results indicated that the procedure combining the preexposure making the guanine crystal board stand up and the consequent horizontal exposure provided a quick orientation to the horizontal direction. The histogram in Fig. 4(c) indicates that the horizontally aligning guanine crystal boards spontaneously increased in number in 3 s after the horizontal magnetic field of 400 mT was provided.

Along with lecithin crystals,¹⁶⁾ guanine crystal boards exhibited a rapid orientation when the boards oriented their width direction. The physical mechanism depends on the morphological anisotropy which is strongly correlated with the diamagnetic anisotropy. Another morphological axis, the length of guanine crystal boards, rotated relatively slowly versus horizontal magnetic fields, but the developed exposure method with the "vertical + horizontal" sequence exhibited a rapid orientation of the length direction. The obtained technique focusing on the biaxial orientation with a permanent magnet and electromagnet is a new method of aligning the organic crystal plates in micro- to nanometer lengths. The guanine crystal boards with high reflectivity behaved as "micromirrors" in liquid phases, so the magnetic orientation of these organic micromirrors can control the light incidence for micrometer regions noninvasively.

In conclusion, the goldfish guanine crystal boards were exposed to vertical and horizontal magnetic fields. The vertical magnetic fields of 340 mT parallel to Earth's gravity made the guanine crystal boards stand up within dozens of seconds, and directed their width direction of the broadest surface. On the other hand, the horizontal magnetic fields of 400 mT caused the orientation of lying guanine crystal boards, which directed their length direction of the broadest surface within several minutes. The combination of both vertical and horizontal magnetic field exposures resulted in a rapid orientation of their length direction.

Acknowledgments This study was supported by JST, PRESTO, "Creation of Basic Technology for Improved Bioenergy Production through Functional Analysis and Regulation of Algae and Other Aquatic Microorganisms".

- 1) J. Torbet and M. C. Ronzière: *Biochem. J.* **219** (1984) 1057.
- 2) T. Higashi, A. Yamagishi, T. Takeuchi, N. Kawaguchi, S. Sagawa, S. Onishi, and M. Date: *Blood* **82** (1993) 1328.
- 3) J. Torbet, M. Malbouyres, N. Builles, V. Justin, M. Roulet, O. Damour, A. Oldberg, F. Ruggiero, and D. J. S. Hulmes: *Biomaterials* **28** (2007) 4268.
- 4) K. Suzuki, T. Toyota, K. Sato, M. Iwasaka, S. Ueno, and T. Sugawara: *Chem. Phys. Lett.* **440** (2007) 286.
- 5) M. Chabre: *Proc. Natl. Acad. Sci. U.S.A.* **75** (1978) 5471.
- 6) T. Kimura and M. Yoshino: *Langmuir* **21** (2005) 4805.
- 7) T. Kimura, F. Kimura, and M. Yoshino: *Langmuir* **22** (2006) 3464.
- 8) F. Kimura, T. Kimura, K. Matsumoto, and N. Metoki: *Cryst. Growth Des.* **10** (2010) 48.
- 9) F. Kimura, T. Kimura, K. Matsumoto, and N. Metoki: *Cryst. Growth Des.* **11** (2011) 12.
- 10) S. Sakurazawa, T. Kubota, and M. Ataka: *J. Cryst. Growth* **196** (1999) 325.
- 11) T. Sato, Y. Yamada, S. Saijo, T. Hori, R. Hirose, N. Tanaka, G. Sazaki, K. Nakajima, N. Igarashi, M. Tanaka, and Y. Matsuura: *Acta Crystallogr., Sect. D* **56** (2000) 1079.
- 12) M. Iwasaka: *J. Appl. Phys.* **107** (2010) 09B314.
- 13) M. Iwasaka, Y. Miyashita, M. Kudo, S. Kurita, and N. Owada: *J. Appl. Phys.* **111** (2012) 07B316.
- 14) K. Guille and W. Clegg: *Acta Crystallogr., Sect. C* **62** (2006) o515.
- 15) A. Levy-Lior, B. Pokroy, B. Levavi-Sivan, L. Leiserowitz, S. Weiner, and L. Addadi: *Cryst. Growth Des.* **8** (2008) 507.
- 16) I. Sakurai, Y. Kawamura, A. Ikegami, and S. Iwayanagi: *Proc. Natl. Acad. Sci. U.S.A.* **77** (1980) 7232.

ONIOM Study of the Mechanism of Olefin Hydrogenation by the Wilkinson's Catalyst: Reaction Paths and Energy Surfaces of *trans*- and *cis*-Forms

Toshiaki Matsubara,* Ryohei Takahashi, and Saori Asai

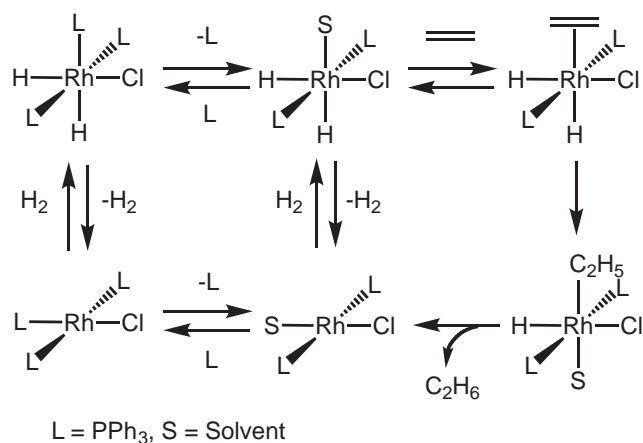
Department of Chemistry, Faculty of Science, Kanagawa University, 2946 Tsuchiya, Hiratsuka, Kanagawa 259-1293

Received April 17, 2012; E-mail: matsubara@kanagawa-u.ac.jp

The mechanism of the olefin hydrogenation by Wilkinson's catalyst is examined by the ONIOM method taking account of the substituents of the phosphine ligands. We optimized the equilibrium and transition state structures involved in the catalytic cycles by both active species, *trans*-[RhCl(PPh₃)₂] (**1Rt**) and *cis*-[RhCl(PPh₃)₂] (**1Rc**), and determined the energy profiles of these catalytic cycles. The steric repulsion between the two phosphine ligands in the *cis*-form was very small throughout the reaction, and in fact **1Rc** was more stable by 3.3 kcal mol⁻¹ than **1Rt** by the stacking interactions between Ph groups, indicating that not only **1Rt** but also **1Rc** is a possible catalytically active species. The entire energy profiles showed that the olefin insertion is a rate-determining step in the case of the *trans* active species **1Rt**. Although the activation energy of the olefin insertion is reduced so much in the case of the *cis* active species **1Rc**, the transition states **TS2** and **TS3** of olefin insertion and isomerization also lie at the highest point of the energy surface. However, the *cis*-form is more favorable than the *trans*-form, since the top of the energy surface is lower for the *cis*-form than for the *trans*-form. The calculations suggested that if we think a large-size substituent of olefin, the *cis*-form that provides a larger space for the reaction will have an energy advantage. The steric or electronic effect of the Ph substituents of the phosphine ligands did not affect the entire energy profile substantially in both cases of *trans*- and *cis*-forms, although the inclusion of the Ph groups is important to evaluate the stability of isomers and to determine the most favorable path.

Recently, we have been able to readily perform quantum chemical calculations of real molecules to examine their structures, properties, reactivities, and so on, without using model molecules, because new methods, for example hierarchical methods such as ONIOM (hybrid method of QM and MM), as well as computer hardware have been developed. The computational methods of quantum chemical calculations are now so reliable that even experimentalists use them for various analyses of molecules. In fact, we know that they are powerful methods to explore and design high-performance homogeneous catalysts with high efficiency, selectivity, and so on. New computational reports concerning catalytic reactions of transition-metal complexes increase year by year giving new insights. In some cases, new information can be abstracted even from previous subjects by revisiting. In this context, we examined the olefin hydrogenation by Wilkinson's complex, which is one of the most well-known catalytic reactions.

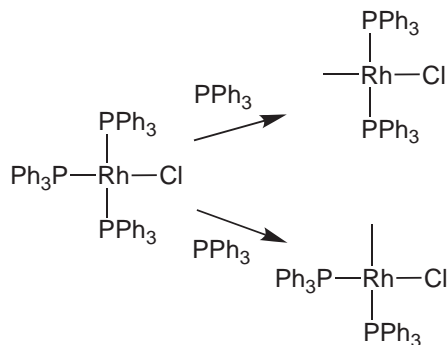
The reaction mechanism of the olefin hydrogenation by Wilkinson's catalyst has been examined in various aspects up to date and proposed as summarized in Scheme 1. Starting from Wilkinson's complex **A**, the oxidative addition of H₂ first occurs to form **C**. Here, two alternative paths depending on the order of H₂ addition and PPh₃ dissociation, i.e., associative: **A** → **B** → **C** and dissociative: **A** → **F** → **C**, are considered. However, it has been thought that the latter is a preferable path, because the addition of H₂ to the active species **F** is much faster than that to the parent complex **A**.¹ We therefore adopted the dissociative path in this study, as Daniel et al. also did in a precedent study.² After the formation of **C**, olefin coordinates to



Scheme 1.

form **D**, which is followed by the olefin insertion into the Rh–H bond. Consequently, an alkyl complex **E** is formed, and then the reductive elimination of alkane takes place to form **F** again. The rate-determining step has been experimentally examined under several conditions using isolated complexes in some cases, and has been generally believed to be the olefin insertion step,³ although there have been contradictions.⁴

Dedieu performed quantum chemical calculations to examine the thermochemical stability of isomers of assumed intermediates in the catalytic cycle and some elementary steps of bond dissociation and association.⁵ Later a quantum chemical calculation was also performed by Daniel et al. for the full



Scheme 2.

catalytic cycle and its energy profile was shown.² This calculation was very meaningful as a first calculation of the full catalytic cycle, because it revealed transition states as well as intermediates of the entire catalytic cycle. However, the electron correlation in the optimizations of structures and the substituent effects of phosphine ligands were ignored due to the undeveloped computational method and computer hardware at that time. Therefore, some structures and the energy profile would be corrected if we recalculate for a real molecule with a present computational method, for example, density functional theory (DFT) and multiscale simulation techniques such as ONIOM method.

In this study, we therefore reexamined the entire process of the olefin hydrogenation by the real Wilkinson's catalyst by means of ONIOM taking account of the electron correlation and the substituent effects of phosphine ligands. We usually describe the catalytic cycle with the *trans*-form by intuition, although the energetic preference of the catalytic cycles of the *trans*- and *cis*-forms has not been squarely discussed so far and also there exist some suggestions of the catalytic cycle with the *cis*-form.^{4a,5} Therefore, we considered both *trans*- and *cis*-forms as the active species of Wilkinson's catalyst, i.e., *trans*-[RhCl(PPh₃)₂] and *cis*-[RhCl(PPh₃)₂] presented in Scheme 2. To determine the most favorable path of the entire catalytic cycle of each *trans*- and *cis*-form, we used ethylene as olefin, and then used propene to discuss the preference of the *trans*- and *cis*-forms.

Following the explanation of the computational details, we will discuss the active species **1**, and then the elementary step of the catalytic cycle, i.e., first step of the oxidative addition of H₂, the second step of the olefin insertion, and the final step of the reductive elimination of alkane. In each section, the model and real complexes, and the *trans*- and *cis*-forms are discussed. In the subsequent section, the entire energy profiles consisting of the most favorable paths of each elementary step for the model and real complexes with the *trans*- and *cis*-forms are discussed. In the last section, the effects of the Ph substituents of the phosphine ligands in the real complexes are discussed.

Computational Details

All calculations by the density functional theory (DFT) and ONIOM methods were performed using the Gaussian 03 program package.⁶ The calculations of energetics as well as geometry optimizations for the model molecules with the H atoms instead of the Ph substituents of phosphine ligands were

carried out at the B3LYP level of theory, which consists of a hybrid Becke + Hartree–Fock exchange and Lee–Yang–Parr correlation functional with nonlocal corrections,⁷ using the basis set BSI. In BSI, we used the 6-31G(d,p) level for the H and C atoms of the H₂, C₂H₄, and C₂H₆ molecules and for the Cl atom, and the 6-31G(d) level for the H and P atoms of the PH₃ ligands. For the Rh atom, we used the lan12dz basis functions, augmented by a single set of f polarization functions⁸ with the exponent of 1.350, for the 17 electrons in the valence shell, and the original effective core potential (ECP) determined by Hay and Wadt⁹ to replace the core electrons except for the valence 17 electrons. For the real molecules, we adopted a two-layered ONIOM methodology,¹⁰ including the Ph substituents of the phosphine ligands in the outer portion of the ONIOM partition. Both geometry optimizations and energy calculations were performed at the ONIOM(B3LYP/BSI:HF/BSII) level. Here, the Hartree–Fock (HF) level was used for the outer part to take account of the electronic effect as well as the steric effect of the Ph substituents. In BSII for the outer part, the lan12dz basis functions were used for all the atoms.

All equilibrium structures and transition states were identified by the number of imaginary frequencies calculated from the analytical Hessian matrix. The reaction coordinates were followed from the transition state to the reactant and the product by the intrinsic reaction coordinate (IRC) technique.¹¹ The thermochemical parameters, enthalpy, entropy, and Gibbs free energy, were calculated at the B3LYP/BSI level for the model complexes and the ONIOM(B3LYP/BSI:HF/BSII) level for the real complexes with a scale factor of 0.9614¹² for calculated vibrational frequencies at the temperature of 298.15 K. The NBO analysis¹³ was performed to obtain the atomic charge.

All the energies presented are relative to the energy of the *trans* active species in both cases of the model and real complexes. We used ethylene as olefin to determine the favorable paths in each *trans*- and *cis*-form and propene to discuss the preference of *trans*- and *cis*-forms including the steric effect between the substituent of olefin and the phenyl groups of the phosphine ligands. The single point energy calculations were also performed at the B3LYP/BSI level for some selected real structures to improve the energy.

To abstract the steric effect of the Ph substituents, we also calculated the energy of the real complexes at the ONIOM-(B3LYP/BSI:MM3) level for the optimized structures at the ONIOM(B3LYP/BSI:HF/BSII) level, treating the outer part of the Ph by the molecular mechanics (MM) method with the MM3 force field parameters. In the MM calculations, the van der Waals parameters reported by Rappé et al. are used for the Rh atom.¹⁴ The torsional contributions associated with dihedral angles involving Rh are set to zero. For the other atoms, the standard MM3 parameters¹⁵ were used. Here, the ONIOM energy is expressed by the sum of the QM(B3LYP) and MM(MM3) energies for the inner and outer parts, and the energy of the outer part is defined as follows.

$$E(\text{ONIOM}) = E(\text{QM,inner}) + E(\text{MM,outer}) \quad (1)$$

$$E(\text{MM,outer}) = E(\text{MM,entire}) - E(\text{MM,inner}) \quad (2)$$

Therefore, the energy of the outer part calculated by eq 2 represents the steric effect of the Ph substituents in this case. When the HF method is used instead of the MM method for the

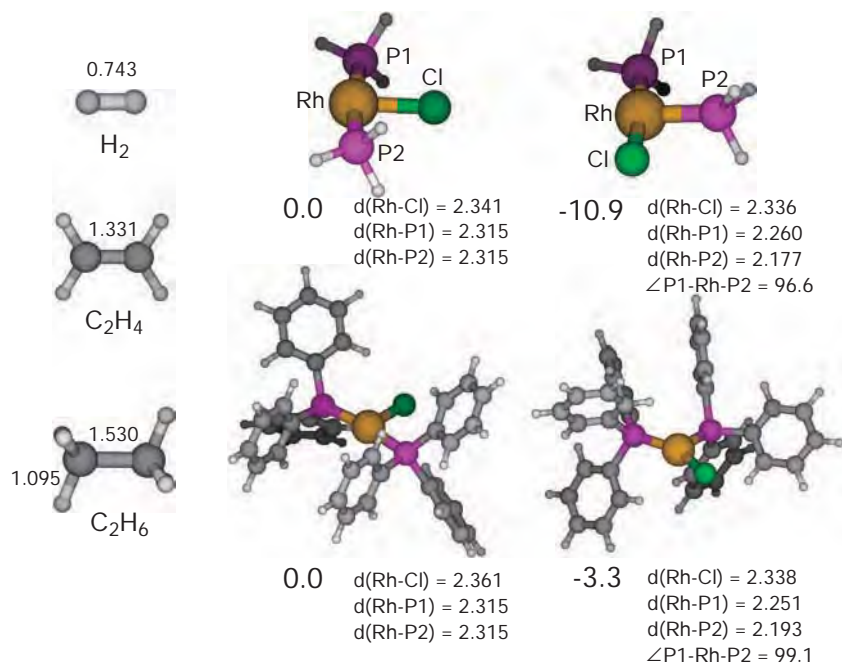


Figure 1. Optimized structures (in Å and degree) of the active species **1** of the model complex at the B3LYP/BSI level and of the real complex at the ONIOM(B3LYP/BSI:HF/BSII) level with those of H₂, C₂H₄, and C₂H₆ at the B3LYP/BSI level. The relative potential energies (in kcal mol⁻¹) are also presented together.

outer part, both steric and electronic effects are considered by eq 2. However, it should be noted that the steric effects of the MM method and the HF method are not completely the same. For the MM3 calculations, we used the TINKER program package.¹⁶

We added **M** and **R** as suffixes to the labels of the equilibrium and transition state structures to distinguish the model and real complexes and also added **t** and **c** to distinguish the *trans*- and *cis*-forms.

Results and Discussion

Active Species. The optimized structures of the active species for the model and real complexes in the *trans*- and *cis*-forms are presented in Figure 1. *Cis* form as well as *trans*-form are T-shaped. In the *cis*-form, the ∠P1-Rh-P2 angle is 96.6° in the model complex and is increased only by 2.5° even in the real complex. This suggests that the steric effect between the Ph groups is small enough to keep the T-shape even in the *cis*-form. The two Rh-P distances are also not affected by the steric effect of the Ph groups. These Rh-P distances in the *cis*-form are shortened by 0.055–0.138 Å compared to those in the *trans*-form by the *trans* influence. As shown in Table S1, the NBO analysis indicates that the electron donation of the P(1)H₃ ligand is larger for **1Mc** than for **1Mt**, and then the bond population of the Rh-P1 becomes larger for **1Mc** than for **1Mt**. The electron donative character of the Ph group, which was shown by the MO energy of the lone electron pair of PR₃ higher for R = Ph (-0.21424 au) than for R = H (-0.27565 au), is reflected in the Rh-P1 distance shorter for **1Rc** than for **1Mc**.

The *trans* influence is also reflected in the stability of the complex; **1Mc** is more stable by 10.9 kcal mol⁻¹ than **1Mt**. However, in the real complex, this preference of the *cis*-form is

reduced, as **1Rc** is only 3.3 kcal mol⁻¹ more stable than **1Rt**. This fact would be ascribed to the electronic effect of the Ph groups rather than the steric effect, because the energy of the Ph groups is 4.2 kcal mol⁻¹ more stable in *cis* than in *trans* by the stacking interaction between the Ph groups when the energy of the outer part of the Ph groups are calculated at the MM3 level (see below). At the ONIOM(B3LYP/BSI:MM3) level, the energy of the entire molecule was 16.4 kcal mol⁻¹ more stable in *cis* than in *trans* (Figure 9). Thus, the *cis*-form which can provides more space for the reaction is more stable in energy than the *trans*-form.

Oxidative Addition of H₂. The first step of the catalytic reaction is the oxidative addition of H₂ to the *trans*- or *cis*-form of the active species **1**. The H₂-coordinated complex **2** is formed first in the side-on manner, and then the H-H bond activation occurs to form the dihydrido complex **3** through the transition state **TS1**, as presented in Figure 2. In both *trans*- and *cis*-forms of the model and real complexes, all the equilibrium and transition state structures, **2**, **TS1**, and **3**, are Y-shaped structure as previously presented² except for **3Rc** with the T-shaped structure.

Model Complex: In **2Mt** with the *trans*-form, the H-H bond of H₂ is already stretched to 0.957 Å (Table 1) by its coordination to the Rh atom. This is further stretched up to 1.120 Å in **TS1Mt** with the very small energy barrier of 0.2 kcal mol⁻¹ and is broken in **3Mt**. The reaction **2Mt** → **TS1Mt** → **3Mt** was slightly exothermic.

On the other hand, in **2Mc** with the *cis* form, the H-H bond of 0.815 Å is not so stretched compared to that in **2Mt** with the *trans*-form due to the *trans* influence. The $d\sigma(d_{x^2-y^2})$ orbital of the Rh of the fragment **1Mc** with the PH₃ ligand *trans* to H₂ lies lower in energy as shown in Table S1, which makes the

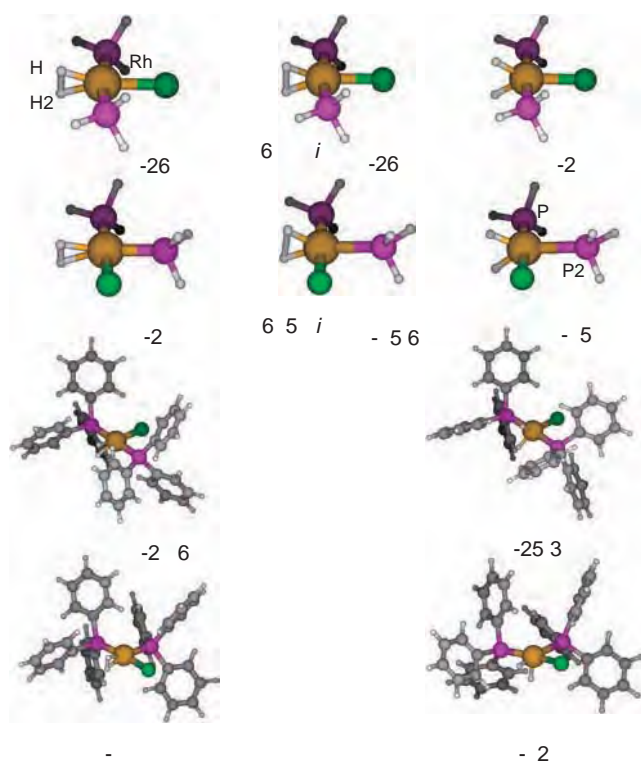


Figure 2. Optimized structures of the H₂-coordinated complexes **2**, transition states **TS1**, and the dihydrido complexes **3** of the oxidative addition of H₂ to the active species **1**, **2** → **TS1** → **3**, for the model complex at the B3LYP/BSI level and for the real complex at the ONIOM(B3LYP/BSI:HF/BSII) level. The relative potential energies (in kcal mol⁻¹) together with the imaginary frequencies (in cm⁻¹) of the transition states are also presented. See Table 1 for the geometric parameters.

electron donation from the H₂ σ orbital to the dσ orbital of the Rh difficult. Thereby, the Rh–H bonds are longer for **2Mc** than for **2Mt**, consistently. The long H–H distance of 1.314 Å in **TS1Mc** is product-like, because the reaction **2Mc** → **TS1Mc** → **3Mc** is 6.3 kcal mol⁻¹ endothermic. This H–H distance is much longer than that in the case of *trans*-form where the reaction is exothermic.

Real Complex: In the real complex, the H–H distance is also shorter for **2Rc** with the *cis*-form than for **2Rt** with the *trans*-form, which is similar to the case of the model complex. As to the energy, **2Rc** is destabilized by 11.1 kcal mol⁻¹ by the electronic effect of the Ph groups compared to **2Mc**. As a result, the reaction **2Rc** → **3Rc** becomes exothermic. For both *trans*- and *cis*-forms of the real complex, we were not able to find the transition state **TS1** due to unsteadiness of the coordinates of the reaction part by the steric contact with the Ph groups. Therefore, we searched the transition state plotting the energy against the H–H distance. As a result, it was found that the H₂ oxidative addition step is almost downhill energetically for *trans* whereas it has the small energy barrier of about 4 kcal mol⁻¹ for *cis* (Figure S1).

Ethylene Insertion. The second step of the catalytic cycle is the ethylene insertion. After the coordination of ethylene to

Table 1. Optimized Geometric Parameters (in Å) of the Equilibrium and Transition State Structures of the Oxidative Addition of H₂ to the Active Species, **2** → **TS1** → **3**^{a)}

	2	TS1	3
Model, <i>trans</i>			
d(H1–H2)	0.957	1.120	1.640
d(Rh–H1)	1.624	1.577	1.535
d(Rh–H2)	1.624	1.577	1.535
Model, <i>cis</i>			
d(H1–H2)	0.815	1.314	1.631
d(Rh–H1)	1.769	1.537	1.523
d(Rh–H2)	1.769	1.555	1.523
Real, <i>trans</i>			
d(H1–H2)	0.940		1.739
d(Rh–H1)	1.664		1.526
d(Rh–H2)	1.661		1.526
Real, <i>cis</i>			
d(H1–H2)	0.832		1.974
d(Rh–H1)	1.724		1.535
d(Rh–H2)	1.725		1.507

a) See Figure 2 for the structures.

the dihydrido complex **3**, the ethylene insertion into the Rh–H bond takes place to produce the ethyl complex.

Model Complex: In the *trans*-form of the model complex, ethylene approaches the Rh parallel to the Rh–Cl axis and an octahedral complex is formed as shown in Figure 3. After passing through the transition state **TS2Mt**, the ethyl complex **6Mt1** is directly formed without undergoing an intermediate with an agostic interaction between the ethyl C–H bond and the Rh atom that has been found at the Hartree–Fock level.² Although both energy and structure of **TS2Mt** is far from those of the product **6Mt1**, the short distance of C1–H1 (1.171 Å) and the long distances of Rh–H1 (1.996 Å) and Rh–C1 (2.533 Å) in **TS2Mt** (Table 2) suggests that the ethylene insertion actually is almost completed. Therefore, the large activation barrier of 18.6 kcal mol⁻¹ from **4Mt** to **TS2Mt** is consistent with the Hammond postulate.¹⁷

In the *cis*-form, there exist two isomers **4Mc1** and **4Mc2** for the ethylene-coordinated complex. Here, the energy barrier for the formation of **4Mc2** from **3Mc** was only 0.8 kcal mol⁻¹ as shown in Figure S2. We also assumed the solvation of **3Mc** to examine the influence of the solvation on the energy profile. As shown in Figure S3, the displacement of the solvent (ethylene was used as the solvent benzene experimentally used) by the substrate ethylene to form **4Mc1** was found to take place by a dissociative mechanism. This suggests that the solvation is actually out of the catalytic cycle as previously reported.¹⁸

Starting from **4Mc1** and **4Mc2**, two paths of ethylene insertion exist, i.e., **4Mc1** → **TS2Mc1** → **5Mc1** and **4Mc2** → **TS2Mc2** → **5Mc2**. The products **5Mc1** and **5Mc2** in each path are intermediates with an agostic interaction between the ethyl C–H bond and the Rh atom. Although the stability of the

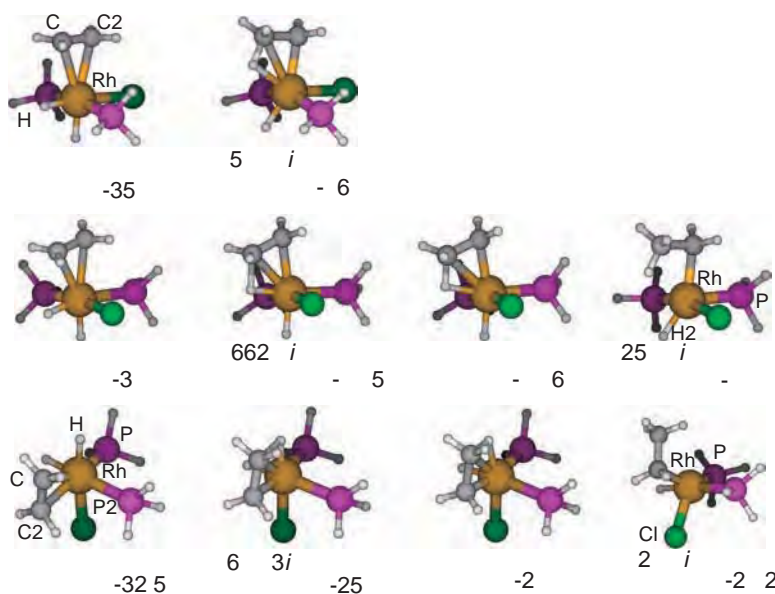


Figure 3. Optimized structures of the ethylene-coordinated complexes **4**, transition states **TS2**, and the ethyl complexes **5** of the ethylene insertion into the Rh–H bond, **4** → **TS2** → **5**, and the transition states **TS3** of the isomerization from **5** to **6** for the model complex at the B3LYP/BSI level. The relative potential energies (in kcal mol⁻¹) together with the imaginary frequencies (in cm⁻¹) of the transition states are also presented. See Table 2 for the geometric parameters.

Table 2. Optimized Geometric Parameters (in Å) of the Equilibrium and Transition State Structures of the Ethylene Insertion into the Rh–H Bond, **4** → **TS2** → **5**^{a)}

	4	TS2	5
Model, <i>trans</i>			
d(C1–C2)	1.356	1.478	
d(Rh–C1)	2.490	2.533	
d(Rh–C2)	2.480	2.163	
d(C1–H1)	2.623	1.171	
d(Rh–H1)	1.560	1.996	
Model, <i>cis1/cis2</i>			
d(C1–C2)	1.360/1.375	1.422/1.423	1.472/1.483
d(Rh–C1)	2.437/2.315	2.344/2.260	2.397/2.346
d(Rh–C2)	2.484/2.284	2.271/2.155	2.193/2.083
d(C1–H1)	2.554/2.369	1.437/1.551	1.213/1.201
d(Rh–H1)	1.558/1.555	1.665/1.615	1.842/1.828
Real, <i>trans</i>			
d(C1–C2)	1.357	1.476	
d(Rh–C1)	2.472	2.551	
d(Rh–C2)	2.492	2.169	
d(C1–H1)	2.523	1.167	
d(Rh–H1)	1.540	2.001	
Real, <i>cis1/cis2</i>			
d(C1–C2)	1.352/1.371	1.421/1.420	1.462/1.482
d(Rh–C1)	2.516/2.343	2.348/2.278	2.395/2.368
d(Rh–C2)	2.580/2.339	2.276/2.167	2.218/2.082
d(C1–H1)	2.807/2.336	1.403/1.538	1.217/1.191
d(Rh–H1)	1.545/1.554	1.659/1.620	1.812/1.848

a) See Figures 3 and 4 for the structures.

starting complex **4Mc1** and **4Mc2** are nearly the same in energy, the transition state and the product are 7–9 kcal mol⁻¹ more stable for **TS2Mc2** and **5Mc2** than for **TS2Mc1** and **5Mc1**. This would be ascribed to the *trans* influence, because the energy of the d orbitals of the Rh atom participating the C–H bond formation will depend on the Cl and PH₃ ligands at the *trans* position as shown by Table S1. In contrast to the case of *trans*, the transition states, **TS2Mc1** and **TS2Mc2**, are reactant-like, as shown by the long distance of C1–H1 and the short distances of Rh–H1 and Rh–C1 (Table 2). Therefore, the activation barriers of 13.2 kcal mol⁻¹ for **4Mc1** → **TS2Mc1** and of 6.7 kcal mol⁻¹ for **4Mc2** → **TS2Mc2** are smaller than in the case of *trans*. The produced **5Mc1** and **5Mc2** isomerize and become the starting complex of the reductive elimination **6Mc1** and **6Mc2** passing through the transition states **TS3Mc1** and **TS3Mc2**, respectively. The angle, ∠H2–Rh–P1 or ∠Cl–Rh–P, increase to 120–130° to break the agostic interactions in **TS3Mc1** and **TS3Mc2**, and the structures finally change to square-pyramid in **6Mc1** and **6Mc2**. This isomerization path is more facile for **5Mc1** → **TS3Mc1** → **6Mc1** than for **5Mc2** → **TS3Mc2** → **6Mc2**, as shown by the activation energy of each step. The larger activation barrier for the latter originates from the energetically stable **5Mc2** with the hydride *trans* to the Cl ligand.

Real Complex: We have found the same paths for the ethylene insertion and the subsequent isomerization also for the real complex in both cases of *trans* and *cis* forms (Figure 4). As shown in Table 2, in the geometric parameters of **4**, **TS2**, and **5** in the *trans*- and *cis*-forms, we do not find any significant difference compared to the corresponding ones for the model complex. However, in **4Rc1**, the coordinated ethylene is twisted from the H–Rh–P axis due to the steric effects of the surrounding Ph groups. This destabilizes **4Rc1** and then reduces the energy barrier in the step from **4Rc1** to **TS2Rc1** up

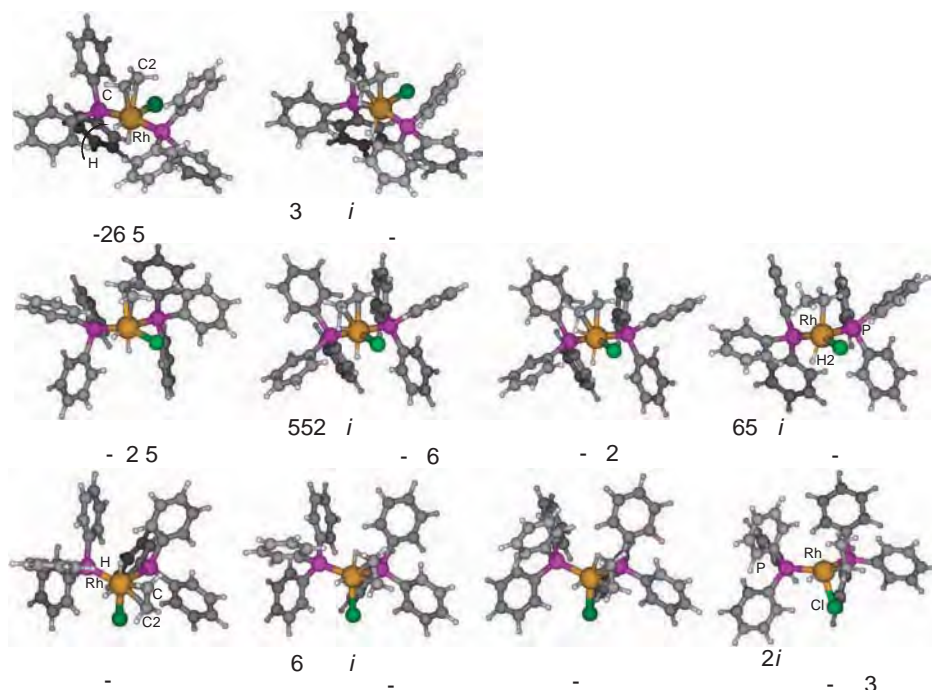


Figure 4. Optimized structures of the ethylene-coordinated complexes **4**, transition states **TS2**, and the ethyl complexes **5** of the ethylene insertion into the Rh–H bond, $4 \rightarrow \text{TS2} \rightarrow 5$, and the transition states **TS3** of the isomerization from **5** to **6** for the real complex at the ONIOM(B3LYP/BSI:HF/BSII) level. The relative potential energies (in kcal mol⁻¹) together with the imaginary frequencies (in cm⁻¹) of the transition states are also presented. See Table 2 for the geometric parameters.

to 3.9 kcal mol⁻¹. On the other hand, the energy barrier of 6.3 kcal mol⁻¹ in the step from **4Rc2** to **TS2Rc2** is nearly the same as the corresponding one of 6.7 kcal mol⁻¹ in the model complex. Thus, the steric effect of the Ph groups would be small in the reaction $4\text{Rc2} \rightarrow \text{TS2Rc2} \rightarrow 5\text{Rc2}$ compared to the case of the reaction $4\text{Rc1} \rightarrow \text{TS2Rc1} \rightarrow 5\text{Rc1}$, because the space for the reaction is far from the Ph groups. The energy surface in the *cis*-form was more stable for $4\text{Rc2} \rightarrow \text{TS2Rc2} \rightarrow 5\text{Rc2} \rightarrow \text{TS3Rc2} \rightarrow 6\text{Rc1}$ than for $4\text{Rc1} \rightarrow \text{TS2Rc1} \rightarrow 5\text{Rc1} \rightarrow \text{TS3Rc1} \rightarrow 6\text{Rc1}$, which is similar to the case of the model complex.

Reductive Elimination of Ethane. The final step of the catalytic cycle is the reductive elimination of ethane. The optimized equilibrium and transition state structures of the model and real complexes in the *trans*- and *cis*-forms are presented in Figures 5 and 6.

Model Complex: In the *trans*-form of the model complex, the ethyl complex **6Mt1** is formed from **TS2Mt** directly without passing through the equilibrium structure with a C–H agostic interaction as mentioned above. The ethyl complex **6Mt1** as well as the dihydrido complex **3Mt** has a Y-shaped structure. Here, the ethyl ligand of **6Mt1** turns outside from the C2–Rh–Cl plane, which is different from the precedent report.² In the other isomer **6Mt2**, the ethyl ligand turns up. The switch between these two isomers would possibly occur by the rotation of the ethyl ligand. In both isomers, **6Mt1** and **6Mt2**, the reductive elimination of ethane takes place, keeping the orientation of the ethyl ligand in the transition states, **TS4Mt1** and **TS4Mt2**. The energy of the transition state was slightly lower for **TS4Mt1** and the activation energy was smaller for path **6Mt1** \rightarrow **TS4Mt1**.

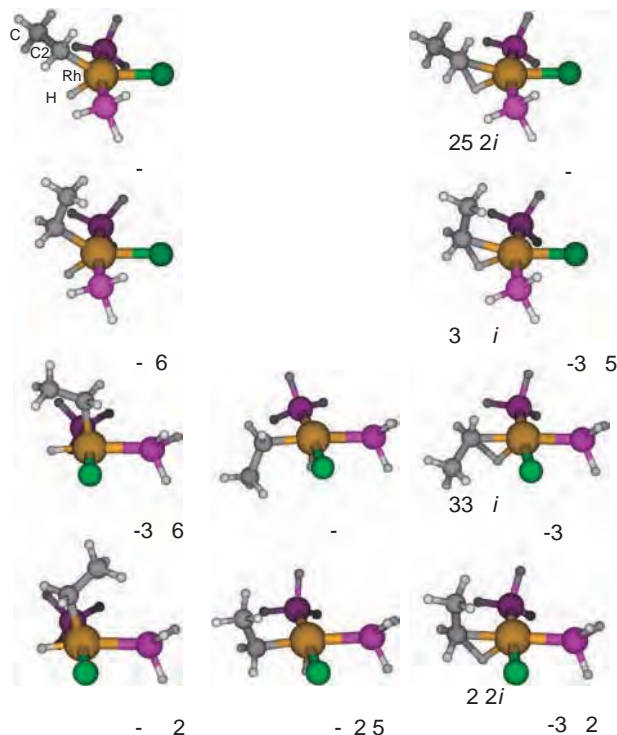


Figure 5. Optimized structures of the ethyl complexes **6** and **7** and the transition states **TS4** of the reductive elimination of ethane, $6 \rightarrow (7 \rightarrow) \text{TS4}$, for the model complex at the B3LYP/BSI level. The relative potential energies (in kcal mol⁻¹) together with the imaginary frequencies (in cm⁻¹) of the transition states are also presented. See Table 3 for the geometric parameters.

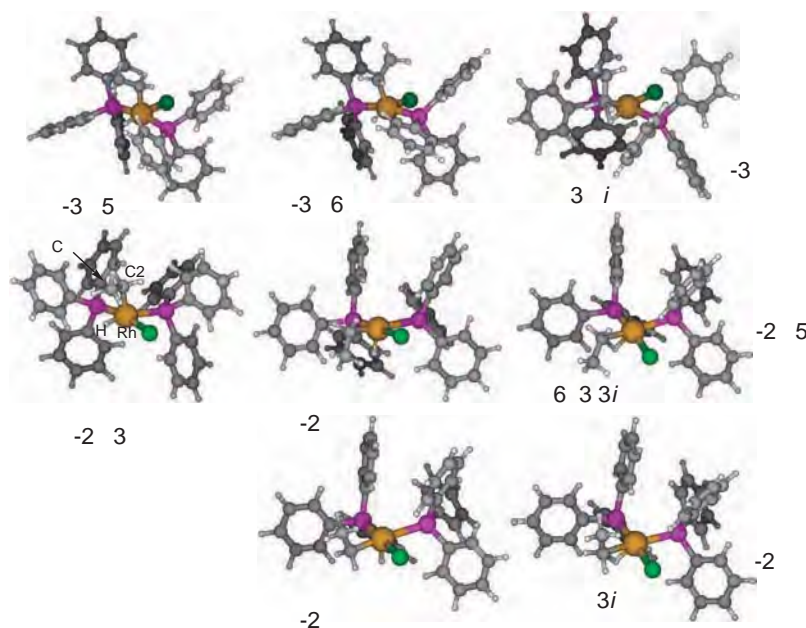


Figure 6. Optimized structures of the ethyl complexes **6** and **7** and the transition states **TS4** of the reductive elimination of ethane, $6 \rightarrow 7 \rightarrow \text{TS4}$, for the real complex at the ONIOM(B3LYP/BSI:HF/BSII) level. The relative potential energies (in kcal mol⁻¹) together with the imaginary frequencies (in cm⁻¹) of the transition states are also presented. See Table 3 for the geometric parameters.

Also in the *cis*-form, there are two isomers of ethyl complex, **6Mc1** and **6Mc2**, which are produced from **5Mc1** and **5Mc2** through the transition states **TS3Mc1** and **TS3Mc2**, respectively. Here, it is notable that these ethyl complexes are T-shaped and their energies are higher than the corresponding *trans*-forms. Each ethyl complex, **6Mc1** and **6Mc2**, isomerizes to **7Mc1** and **7Mc2**, and then eliminates ethane through each transition state, **TS4Mc1** and **TS4Mc2**. Other isomerizations between **6Mc1** and **6Mc2** and between **7Mc1** and **7Mc2** would also occur by the rotation of the ethyl ligand. The C2–H1 distances in the transition states, **TS4Mc1** and **TS4Mc2**, are stretched by 0.15 Å compared to the *trans*-form by the *trans* influence, as shown in Table 3, which is similar to the case of the oxidative addition of H₂. Although the energies of the transition states, **TS4Mc1** and **TS4Mc2**, were nearly the same, the activation energy was smaller for the path passing through **TS4Mc1** with ethyl ligand turned downward, which is similar to the case of the *trans*-form. However, their activation energies were larger than the corresponding ones for the *trans* form, because the structural change from T shape to Y shape is required to reach the transition state in the case of the *cis*-form.

We also optimized **7Mc1**, **7Mc2**, **TS4Mc1**, and **TS4Mc2** with the solvent ethylene and the additional PH₃ ligand to examine the associative mechanism in the reductive elimination for the *cis*-form. As shown in Figure S4, the PH₃ ligand coordinated to the Rh atom whereas the solvent ethylene did not except for **7Mc1**. However, this coordination of the PH₃ ligand did not lower the energy barrier in both steps from **7Mc1** to **TS4Mc1** and from **7Mc2** to **TS4Mc2**, suggesting that the associative mechanism is not important.

Real Complex: All the ethyl complexes in the real complex have a T-shaped structure as presented in Figure 6. **6Rt** in

Table 3. Optimized Geometric Parameters (in Å) of the Equilibrium and Transition State Structures of the Reductive Elimination of Ethane, $6 \rightarrow (7 \rightarrow) \text{TS4}^a$

	6	7	TS4
Model, <i>trans1/trans2</i>			
d(Rh–C2)	2.096/2.091		2.182/2.214
d(Rh–H1)	1.531/1.530		1.554/1.563
d(C2–H1)	2.226/2.237		1.586/1.487
Model, <i>cis1/cis2</i>			
d(Rh–C2)	2.082/2.076	2.102/2.083	2.166/2.176
d(Rh–H1)	1.549/1.545	1.506/1.511	1.537/1.546
d(C2–H1)	2.560/2.412	2.577/2.505	1.740/1.633
Real, <i>trans</i>			
d(Rh–C2)	2.078	2.083	2.215
d(Rh–H1)	1.544	1.537	1.571
d(C2–H1)	2.510	2.393	1.474
Real, <i>cis1/cis2</i>			
d(Rh–C2)	2.081	2.094/2.083	2.172/2.195
d(Rh–H1)	1.527	1.507/1.509	1.534/1.543
d(C2–H1)	2.454	2.548/2.478	1.696/1.604

a) See Figures 5 and 6 for the structures.

the *trans*-form produced from **4Rt** through **TS2Rt** also has a T-shaped structure with the ethyl ligand at the apical position due to the steric and/or electronic effects of the Ph groups, which is different from the corresponding ethyl complex **6Mt1** in the model complex. Since the transition state with the ethyl group turned down does not exist due to the steric effect of the

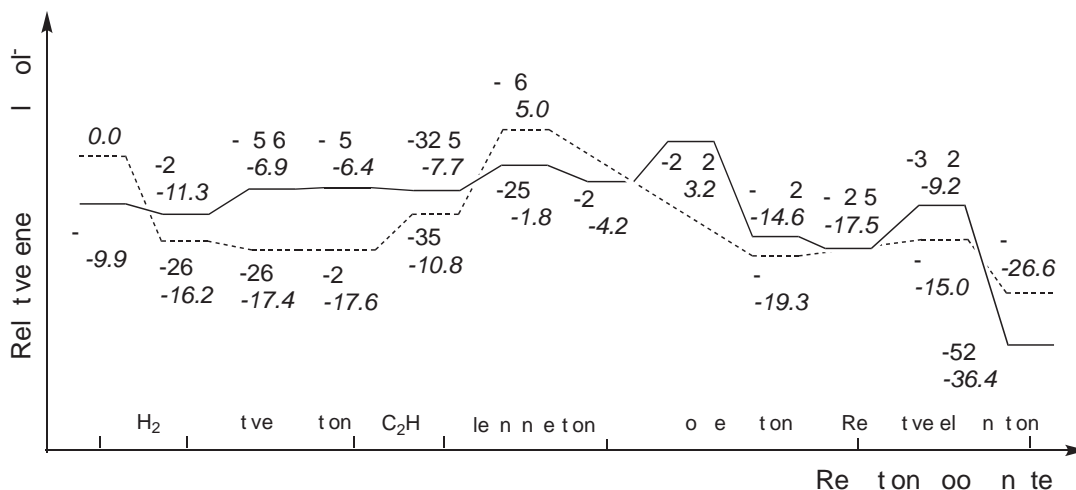


Figure 7. Energy profiles of the ethylene hydrogenation by the model complexes at the B3LYP/BSI level. Normal and dotted lines are for the *cis*-[RhCl(PH₃)₂] and *trans*-[RhCl(PH₃)₂] active species, respectively. Numbers in plain and italic type are for the potential and Gibbs free energies, respectively.

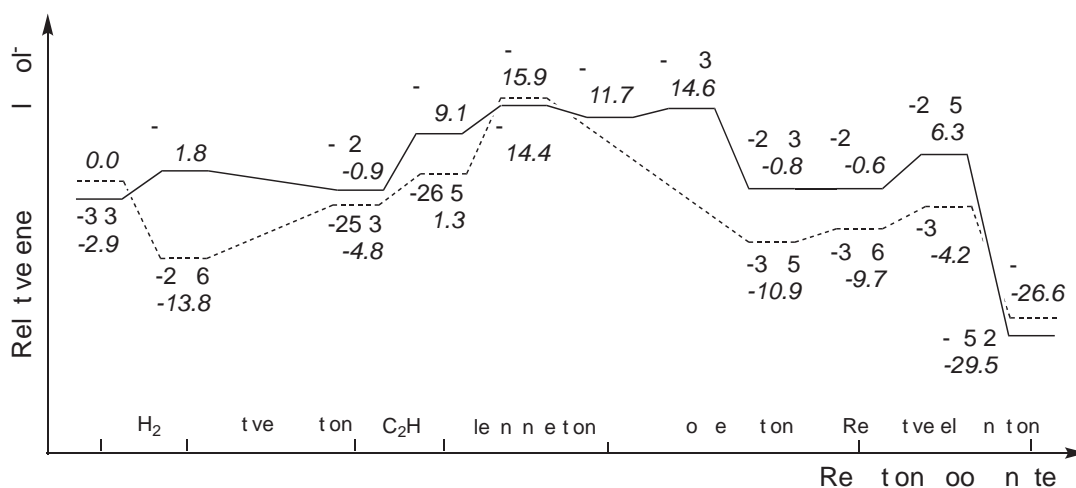


Figure 8. Energy profiles of the ethylene hydrogenation by the real complexes at the ONIOM(B3LYP/BSI:HF/BSII) level. Normal and dotted lines are for the *cis*-[RhCl(PPh₃)₂] and *trans*-[RhCl(PPh₃)₂] active species, respectively. Numbers in plain and italic type are for the potential and Gibbs free energies, respectively.

Ph groups, **6Rt** is first transformed to another isomer **7Rt** and then the ethane reductive elimination takes place through the transition state **TS4Rt**.

In **6Rc1** in the *cis*-form, the ethyl ligand at the apical position is oriented to the less crowded space in order to avoid the steric repulsion with the Ph groups. Other isomers, **7Rc1** and **7Rc2**, have the ethyl ligand at the equatorial position, where the ethyl group is turned down in **7Rc1** and turned up in **7Rc2**. **7Rc1** is transformed from **6Rc1**, and **7Rc2** is transformed from **7Rc1**. Then, the reductive elimination of ethane occurs from **7Rc1** through the transition state **TS4Rc1** and from **7Rc2** through the transition state **TS4Rc2**, the former being energetically slightly favorable.

All the C–H distances in the transition states in the real complex are shorter compared to those in the corresponding transition states in the model complex by the effects of the Ph groups. However, as to the activation energy, the *cis*-form as well as the *trans*-form exhibits values similar to those in the case of the model complex.

Energy Profile of the Catalytic Cycle. The energy profiles of the entire catalytic cycle consisting of the most favorable paths of each elementary step for the model and real complexes are displayed in Figures 7 and 8, respectively.

Model Complex: We first discuss the potential energy profile for the model complex. In the case of the *trans*-form, the H₂-coordinated complex **2Mt** is stabilized by 26.9 kcal mol⁻¹ by the H₂ coordination. The oxidative addition of H₂, **2Mt** → **TS1Mt** → **3Mt**, has a small energy barrier of only 0.2 kcal mol⁻¹. After the ethylene coordination to form **4Mt**, the ethylene insertion, **4Mt** → **TS2Mt** → **6Mt1**, takes place with the large energy barrier of 18.6 kcal mol⁻¹, which is the rate-determining step. Since the final step, the reductive elimination of ethane has two alternative paths, **6Mt1** → **TS4Mt1** → **1Mt** and **6Mt1** → **6Mt2** → **TS4Mt2** → **1Mt**, we adopted the former, of which energy surface is lower. The activation barrier of this step was 4.7 kcal mol⁻¹ and much smaller than that of ethylene insertion. The entire catalytic reaction was 41.8 kcal mol⁻¹ exothermic.

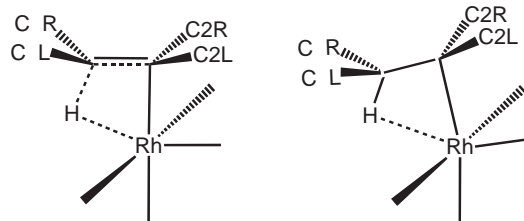
On the other hand, in the *cis*-form, the active species **1Mc** is more stable by 10.9 kcal mol⁻¹ than that in the *trans*-form. However, the energy surface of the oxidative addition of H₂, **2Mc** → **TS1Mc** → **3Mc**, is less stable compared to the case of the *trans*-form by the *trans* effect as mentioned above. From the ethylene-coordinated complex **4**, there exist two paths, **4Mc1** → **TS2Mc1** → **5Mc1** → **TS3Mc1** → **6Mc1** and **4Mc2** → **TS2Mc2** → **5Mc2** → **TS3Mc2** → **6Mc2**, and further two paths from the ethyl complex **6**, **6Mc1** → **7Mc1** → **TS4Mc1** → **1Mt** and **6Mc2** → **7Mc2** → **TS4Mc2** → **1Mc**, are possible. We therefore selected the energetically favorable path with a lower energy surface for this process, **4Mc2** → **TS2Mc2** → **5Mc2** → **TS3Mc2** → **6Mc2** → **7Mc2** → **TS4Mc2** → **1Mc**. The large activation energy of the ethylene insertion in the *trans*-form was reduced to 6.7 kcal mol⁻¹ in the *cis*-form.

The Gibbs free energy did not change so much the entire energy profiles, although the small energy barrier of the oxidative addition of H₂ in the case of *trans*-form disappears. However, the entropy term affects the stability of the energy surface when a molecule associates or dissociates.¹⁸ In fact, the energy surface of **2** → **TS1** → **3** is about 10 kcal mol⁻¹ destabilized by the H₂ addition and the subsequent energy surface of **4** → **TS2** → (**5** → **TS3** → **6** → (**7** → **TS4**) is 20–25 kcal mol⁻¹ destabilized by the H₂ and C₂H₄ addition in both cases of *trans*- and *cis*-forms. In accordance with the previous report,² the ethylene insertion with the large energy barrier of 15.8 kcal mol⁻¹ is the rate-determining step in the *trans*-form. However, in the *cis*-form, its energy barrier is reduced so that the entire energy surface becomes smoother and the top of the energy surface is lower for the *cis*-form than for the *trans*-form, suggesting that the catalytic reaction in the *cis*-form is more favorable, which is similar to the case of the potential energy surface.

Real Complex: Also in the case of the real complex in the *cis*-form, we have alternative paths, **4Rc1** → **TS2Rc1** → **5Rc1** → **TS3Rc1** → **6Rc1** and **4Rc2** → **TS2Rc2** → **5Rc2** → **TS3Rc2** → **6Rc1**, in the ethylene insertion and the subsequent isomerization, and **6Rc1** → **7Rc1** → **TS4Rc1** → **1Rc** and **6Rc1** → **7Rc1** → **7Rc2** → **TS4Rc2** → **1Rc**, in the reductive elimination. To describe the entire energy profiles in Figure 8, we adopted the path, **4Rc2** → **TS2Rc2** → **5Rc2** → **TS3Rc2** → **6Rc1** → **7Rc1** → **TS4Rc1** → **1Rc**, which has a lower energy surface. As presented in Figure 8, the potential and Gibbs free energy surfaces of the entire catalytic reaction showed a similar feature to each other, although the entropy term destabilized or stabilized the energy surface when the H₂ and C₂H₄ molecules are added or the C₂H₆ molecule is eliminated.

The active species **1** is more stable in energy for the *cis*-form than for the *trans*-form also in the real complex. However, after the H₂ coordination in **2**, the energy surface for the *cis*-form is less stable, which is similar to the case of the model complex, except for the transition state **TS2**. Since the energy barriers of the steps, **4** → **TS2** → **5** for the ethylene insertion and **5** → **TS3** → **6** for the isomerization, are small in the *cis*-form, the energy surface of **4** → **TS2** → **5** → **TS3** → **6** as well as that of **1** → **2** → **3** of the H₂ oxidative addition is very flat. As a result, the entire energy surface is smoother and the top of the

Table 4. Potential Energies (in kcal mol⁻¹) of the Transition States in the Olefin Insertion and Isomerization Steps, **TS2Rt**, **TS2Rc2**, and **TS3Rc2**, Relative to the Active Species **1Rt** in the Case of Propene at the ONIOM-(B3LYP/BSI:HF/BSII) and B3LYP/BSI^(a) Levels



Position of Me group	TS2Rt		TS2Rc2		TS3Rc2	
	ONIOM	B3LYP	ONIOM	B3LYP	ONIOM	B3LYP
C1L	-5.4	-7.9	-9.4	-12.0	-6.7	-8.4
C1R	-4.2	-6.9	-7.0	-9.9	-7.5	-9.4
C2L	-4.6	-7.8	-9.2	-12.5	-6.9	-9.6
C2R	-2.7	-6.6	-3.0	-7.1	-7.5	-11.5

a) 6-31G(d,p) was used for the phenyl groups of phosphine ligands.

energy surface is lower for the *cis*-form than for the *trans*-form, suggesting that the catalytic reaction in the *cis*-form is more favorable.

We also performed single point energy calculations of the entire molecule at the B3LYP/BSI level for the highest points of the energy surfaces to improve the energies. Although in both cases of the *trans*- and *cis*-forms the energy is stabilized by 2–3 kcal mol⁻¹, the tendency that the top of the energy surface is lower for the *cis* than for the *trans* form did not change (Table S2).

We further examined the case of representative propene with the methyl substituent, since the steric contact between the substituent of olefin and phenyl groups of the PPh₃ ligands is expected to affect the energy surface of the reaction. We optimized the transition states at the highest points of the energy surfaces of the reaction for both cases of *trans* and *cis* forms, **TS2R** and **TS3R**, at the ONIOM(B3LYP/BSI:HF/BSII) level including the Me group of propene in the outer part. Here, the positions of the atoms for the 4-membered ring of the reaction part RhHCC were fixed. The potential energies of four possible structures depending on the position of the methyl group in each transition states, **TS2Rt**, **TS2Rc2**, and **TS3Rc2**, are shown in Table 4. The ONIOM(B3LYP/BSI:HF/BSII) calculations showed that C1L is the most favorable in energy in the case of the *trans*-form, on the other hand, C1R in the case of the *cis*-form, and the *cis*-form is more stable than the *trans*-form at the highest point of energy surface. As mentioned earlier, the single point energy calculations of the entire molecule at the B3LYP/BSI level stabilized the transition states by 2–4 kcal mol⁻¹ similarly, but the energetic advantage of the *cis* form did not change. Only the favorable position of the methyl group changed from C1R to C2L. This advantage would be responsible for the *cis* form providing a larger space for the reaction (Figure S5).

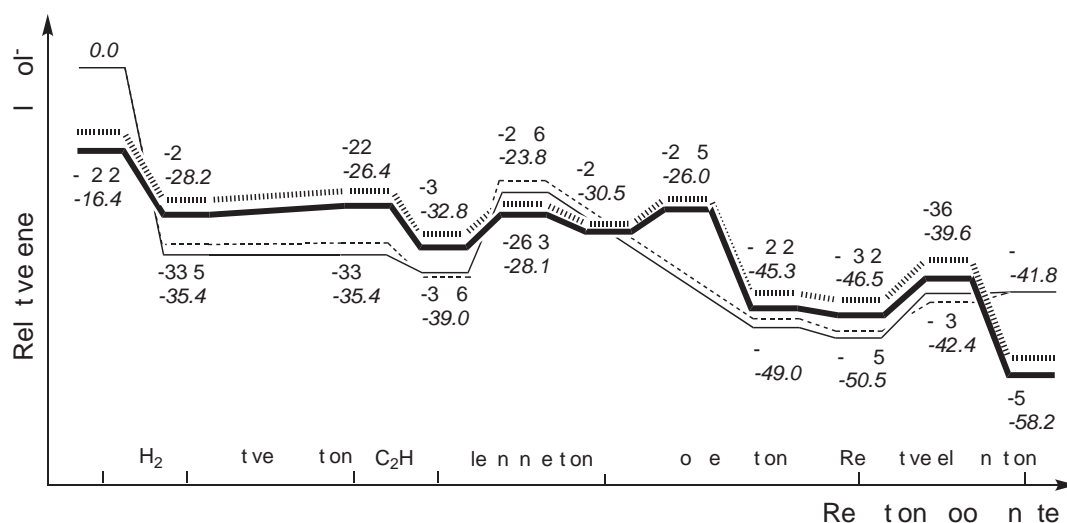


Figure 9. Potential energy profiles of the ethylene hydrogenation by the real complexes. The sets of the normal and dotted lines and of the bold and bold dotted lines are for the *trans*-[RhCl(PPh₃)₂] and *cis*-[RhCl(PPh₃)₂] active species, respectively. Numbers in plain and italic type represent the energies of the inner part and entire molecule calculated at the ONIOM(B3LYP/BSI:MM3)//ONIOM(B3LYP/BSI:HF/BSII) level and correspond to the dotted and normal lines or the bold dotted and bold lines, respectively. See the **Computational Details** for the details of the calculations.

Steric and Electronic Effects of the Ph Groups on the Energy Profile of the Catalytic Cycle.

The energy profiles in Figure 8 include both steric and electronic effects, since the Ph groups in the outer part are calculated at the Hartree–Fock level. Therefore, to examine the steric effect of the Ph groups, we calculated the outer part by the molecular mechanics method using the MM3 force field for the optimized structure at the ONIOM(B3LYP/BSI:HF/BSII) level. Using the calculated MM3 energy for the outer part and the original B3LYP energy for the inner part (See the **Computational Details** for the details.), we obtained the energy at the ONIOM(B3LYP/BSI:MM3) level. The ONIOM(B3LYP/BSI:MM3) energy of the entire molecule and its component of the B3LYP energy of the inner part for the equilibrium and transition state structures of the entire catalytic reaction are presented in Figure 9. As one can see, in the case of the *cis*-form, the relative energy of the entire molecule is stabilized by the MM3 energy of 1–4 kcal mol⁻¹ for the outer part. This indicates that the steric repulsion between the PPh₃ ligands is quite small even in the *cis*-form and the stacking interaction of Ph groups stabilizes the entire molecule. The steric repulsion between the PPh₃ ligands in the *trans*-form is also small as we expected.

The ONIOM(B3LYP/BSI:HF/BSII) energy of the entire molecule and its component of the B3LYP energy of the inner part for the equilibrium and transition state structures of the entire catalytic reaction are presented in Figure 10. The shapes of the energy surfaces for the inner part and the entire molecule in Figure 10 are very similar to those in Figure 9 except for the reductive elimination in the *trans*-form, indicating that the electronic effect of the Ph groups does not affect so much the elementary step. In the step, 7 → TS4 → 1, in the *trans* form, the shapes of the energy surfaces for both the inner part and the entire molecule in Figure 10 differ from those in Figure 9, due to the electronic effect of the Ph groups.

Concluding Remarks

We theoretically reexamined the entire process of the olefin hydrogenation by Wilkinson's catalyst by the ONIOM method including the substituent effects of phosphine ligands. As active species, we considered both *trans*- and *cis*-forms of [RhCl(PPh₃)₂] (**1**). The steric repulsion between the two PPh₃ ligands in the active species **1** was small even in the *cis*-form, and the *cis*-form **1Rc** was more stable by 3.3 kcal mol⁻¹ than the *trans*-form **1Rt** due to the stacking interaction between the Ph groups, suggesting that not only **1Rt** but also **1Rc** is one of candidates of catalytically active species.

The entire energy profiles of the catalytic reaction showed that the olefin insertion with the largest energy barrier is a rate-determining step in the case of the *trans*-form. On the other hand, in the case of the *cis*-form, the energy barrier in the olefin insertion is much reduced. As a result, the entire energy profile for the *cis*-form is smooth and lower than that for the *trans*-form, suggesting that the *cis*-form is more favorable than the *trans*-form. The steric repulsion between the Ph groups of the phosphine ligands was small even in the *cis*-form throughout the catalytic reaction. Moreover, the *cis*-form can provide a large space for the reaction and has an advantage in energy toward the olefin with a large-size substituent compared to the *trans*-form. The steric and electronic effects of the Ph groups did not affect substantially each energy profile of the *trans*- and *cis*-forms, although the inclusion of the Ph groups is important to evaluate the stability of isomers and to determine the most favorable path.

Part of the computations was performed at the Research Center for Computational Science, Okazaki, Japan. This study was supported in part by grants from the Ministry of Education, Culture, Sports, Science and Technology, Japan.

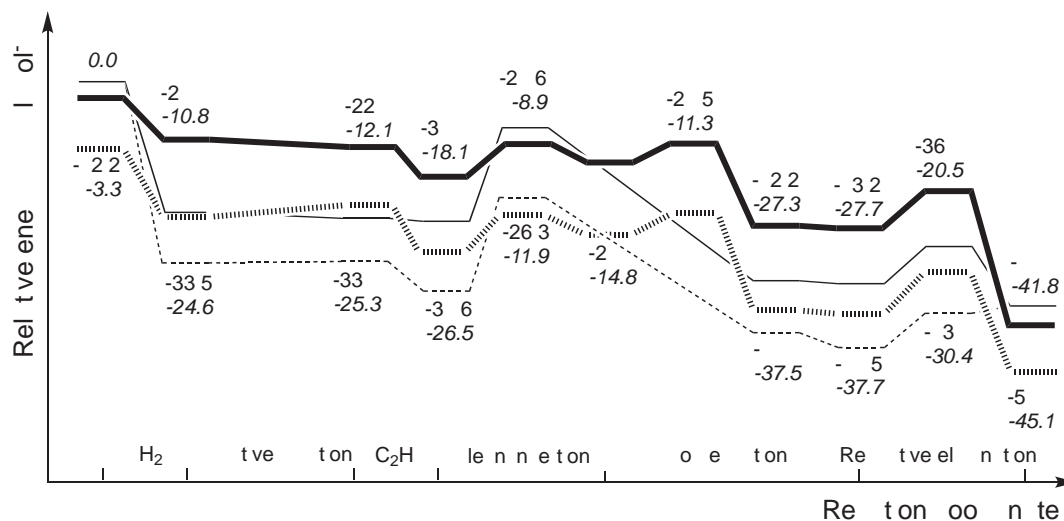


Figure 10. Potential energy profiles of the ethylene hydrogenation by the real complexes. The sets of the normal and dotted lines and of the bold and bold dotted lines are for the *trans*-[RhCl(PPh₃)₂] and *cis*-[RhCl(PPh₃)₂] active species, respectively. Numbers in plain and italic type represent the energies of the inner part and entire molecule calculated at the ONIOM(B3LYP/BSI:HF/BSII) level and correspond to the dotted and normal lines or the bold dotted and bold lines, respectively. See the **Computational Details** for the details of the calculations.

Supporting Information

Listings giving the optimized Cartesian coordinates of all equilibrium structures and transition states presented in this paper, Table S1: Bond distance, bond population, and NBO analysis of the Rh–P bond and the molecular orbital (MO) energies of **1Mt** and **1Mc** at the B3LYP/BSI level, Table S2: Relative energies of the transition states, **TS2Rt**, **TS2Rc2**, and **TS3Rc2**, at the ONIOM(B3LYP/BSI:HF/BSII) and B3LYP/BSI levels, Figure S1: Plots of the energy and the Rh–H distance against the H–H distance from **2Rc** to **3Rc** at the B3LYP/BSI level, Figure S2: Plots of the energy and the Rh–(ethylene) distance against the \angle Cl–Rh–P1 angle from **3Mc** to **4Mc2** at the B3LYP/BSI level, Figure S3: Plots of the energy and the Rh–(substrate ethylene) distance against the Rh–(solvent ethylene) distance in the displacement of the solvent ethylene by the substrate ethylene to form **4Mc1** from the solvated **3Mc(=4Mc1)** at the B3LYP/BSI level, Figure S4: Optimized structures and the relative energies of **7Mc1**, **7Mc2**, **TS4Mc1**, and **TS4Mc2** with the solvent ethylene and the additional PH₃ ligand at the B3LYP/BSI level, Figure S5: Optimized structures of the transition states, **TS2Rt**, **TS2Rc2**, and **TS3Rc2**, in the case of propene at the ONIOM(B3LYP/BSI:HF/BSII) level. This material is available free of charge on the Web at <http://www.csj.jp/journals/bcsj/>.

References

- 1 J. Halpern, C. S. Wong, *J. Chem. Soc., Chem. Commun.* **1973**, 629.
- 2 a) N. Koga, C. Daniel, J. Han, X. Y. Fu, K. Morokuma, *J. Am. Chem. Soc.* **1987**, *109*, 3455. b) C. Daniel, N. Koga, J. Han, X. Y. Fu, K. Morokuma, *J. Am. Chem. Soc.* **1988**, *110*, 3773.
- 3 a) S. Siegel, D. Ohrt, *Inorg. Nucl. Chem. Lett.* **1972**, *8*, 15. b) Y. Ohtani, M. Fujimoto, A. Yamagishi, *Bull. Chem. Soc. Jpn.* **1976**, *49*, 1871. c) J. Halpern, T. Okamoto, A. Zakhariev, *J. Mol. Catal.* **1977**, *2*, 65. d) Y. Ohtani, M. Fujimoto, A. Yamagishi, *Bull. Chem. Soc. Jpn.* **1977**, *50*, 1453. e) Y. Ohtani, A. Yamagishi, M. Fujimoto, *Bull. Chem. Soc. Jpn.* **1979**, *52*, 69.
- 4 a) J. A. Osborn, F. H. Jardine, J. F. Young, G. Wilkinson, *J. Chem. Soc. A* **1966**, 1711. b) M. H. J. M. de Croon, P. F. M. T. van Nesselrooij, H. J. A. M. Kuipers, J. W. E. Coenen, *J. Mol. Catal.* **1978**, *4*, 325.
- 5 a) A. Dedieu, *Inorg. Chem.* **1980**, *19*, 375. b) A. Dedieu, *Inorg. Chem.* **1981**, *20*, 2803.
- 6 M. J. Frisch, G. W. Trucks, H. B. Schlegel, G. E. Scuseria, M. A. Robb, J. R. Cheeseman, J. A. Montgomery, Jr., T. Vreven, K. N. Kudin, J. C. Burant, J. M. Millam, S. S. Iyengar, J. Tomasi, V. Barone, B. Mennucci, M. Cossi, G. Scalmani, N. Rega, G. A. Petersson, H. Nakatsuji, M. Hada, M. Ehara, K. Toyota, R. Fukuda, J. Hasegawa, M. Ishida, T. Nakajima, Y. Honda, O. Kitao, H. Nakai, M. Klene, X. Li, J. E. Knox, H. P. Hratchian, J. B. Cross, V. Bakken, C. Adamo, J. Jaramillo, R. Gomperts, R. E. Stratmann, O. Yazyev, A. J. Austin, R. Cammi, C. Pomelli, J. W. Ochterski, P. Y. Ayala, K. Morokuma, G. A. Voth, P. Salvador, J. J. Dannenberg, V. G. Zakrzewski, S. Dapprich, A. D. Daniels, M. C. Strain, O. Farkas, D. K. Malick, A. D. Rabuck, K. Raghavachari, J. B. Foresman, J. V. Ortiz, Q. Cui, A. G. Baboul, S. Clifford, J. Cioslowski, B. B. Stefanov, G. Liu, A. Liashenko, P. Piskorz, I. Komaromi, R. L. Martin, D. J. Fox, T. Keith, M. A. Al-Laham, C. Y. Peng, A. Nanayakkara, M. Challacombe, P. M. W. Gill, B. Johnson, W. Chen, M. W. Wong, C. Gonzalez, J. A. Pople, *Gaussian 03 (Revision E.01)*, Gaussian, Inc., Wallingford CT, **2004**.
- 7 a) A. D. Becke, *Phys. Rev. A* **1988**, *38*, 3098. b) C. Lee, W. Yang, R. G. Parr, *Phys. Rev. B* **1988**, *37*, 785. c) A. D. Becke, *J. Chem. Phys.* **1993**, *98*, 5648.
- 8 A. W. Ehlers, M. Böhme, S. Dapprich, A. Gobbi, A. Höllwarth, V. Jonas, K. F. Köhler, R. Stegmann, A. Veldkamp, G. Frenking, *Chem. Phys. Lett.* **1993**, *208*, 111.
- 9 P. J. Hay, W. R. Wadt, *J. Chem. Phys.* **1985**, *82*, 299.

- 10 a) F. Maseras, K. Morokuma, *J. Comput. Chem.* **1995**, *16*, 1170. b) T. Matsubara, S. Sieber, K. Morokuma, *Int. J. Quantum Chem.* **1996**, *60*, 1101. c) T. Matsubara, F. Maseras, N. Koga, K. Morokuma, *J. Phys. Chem.* **1996**, *100*, 2573. d) M. Svensson, S. Humbel, R. D. J. Froese, T. Matsubara, S. Sieber, K. Morokuma, *J. Phys. Chem.* **1996**, *100*, 19357. e) S. Dapprich, I. Komáromi, K. S. Byun, K. Morokuma, M. J. Frisch, *THEOCHEM* **1999**, 461–462, 1. f) T. Vreven, K. Morokuma, *J. Comput. Chem.* **2000**, *21*, 1419. g) K. Morokuma, *Bull. Korean Chem. Soc.* **2003**, *24*, 797.
- 11 K. Fukui, S. Kato, H. Fujimoto, *J. Am. Chem. Soc.* **1975**, *97*, 1.
- 12 A. P. Scott, L. Radom, *J. Phys. Chem.* **1996**, *100*, 16502.
- 13 E. D. Glendening, A. E. Reed, J. E. Carpenter, F. Weinhold, *NBO Version 3.1*.
- 14 A. K. Rappé, C. J. Casewit, K. S. Colwell, W. A. Goddard, III, W. M. Skiff, *J. Am. Chem. Soc.* **1992**, *114*, 10024.
- 15 a) N. L. Allinger, Y. H. Yuh, J.-H. Lii, *J. Am. Chem. Soc.* **1989**, *111*, 8551. b) J.-H. Lii, N. L. Allinger, *J. Am. Chem. Soc.* **1989**, *111*, 8566. c) J.-H. Lii, N. L. Allinger, *J. Am. Chem. Soc.* **1989**, *111*, 8576. d) J.-H. Lii, N. L. Allinger, *J. Phys. Org. Chem.* **1994**, *7*, 591. e) J.-H. Lii, N. L. Allinger, *J. Comput. Chem.* **1998**, *19*, 1001.
- 16 J. W. Ponder, *TINKER, Software Tools for Molecular Design, version 4.2*, Department of Chemistry and Department of Biochemistry and Molecular Biophysics, Washington University, St. Louis, MO, 63130.
- 17 a) G. S. Hammond, *J. Am. Chem. Soc.* **1955**, *77*, 334. b) W. J. le Noble, A. R. Miller, S. D. Hamann, *J. Org. Chem.* **1977**, *42*, 338. c) A. R. Miller, *J. Am. Chem. Soc.* **1978**, *100*, 1984.
- 18 T. Matsubara, N. Koga, Y. Ding, D. G. Musaev, K. Morokuma, *Organometallics* **1997**, *16*, 1065.



Synthesis of bicyclic dioxetanes tethering a fluororescer through an ω -carbamoyle-substituted linker and their high-performance chemiluminescence in an aqueous system

Nobuko Watanabe^{a,*}, Hidetoshi Kino^a, Shinichiro Watanabe^a, Hisako K. Ijuin^a, Masashi Yamada^b, Masakatsu Matsumoto^a

^a Department of Chemistry, Kanagawa University, Tsuchiya, Hiratsuka, Kanagawa 259-1293, Japan

^b Tosoh AIA, Inc. Iwase, Koshi-machi, Toyama 931-8510, Japan

ARTICLE INFO

Article history:

Received 24 March 2012
Received in revised form 19 April 2012
Accepted 20 April 2012
Available online 7 May 2012

Keywords:

Dioxetane
Chemiluminescence
Charge-transfer-induced decomposition
Fluorescein

ABSTRACT

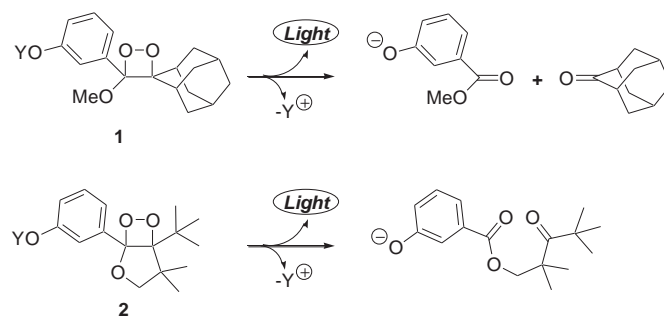
Bicyclic dioxetanes **3** and **4** tethering a fluorescein or 4-(benzothiazol-2-yl)-3-hydroxyphenyl moiety through a linker were synthesized by the use of dihydrofuran-intermediate **5** or its advanced intermediate **6**. These dioxetanes underwent base-induced decomposition to effectively give light due to intramolecular energy-transfer from an excited oxidobenzoate to a tethered fluorophore. Although the chemiluminescence efficiency ϕ^{CL} values for **3** and **4** were only ca. 2-fold greater than that for parent **2** in a TBAF/acetonitrile system, these values were 30–550-fold greater than that for **2** in a NaOH/H₂O system. Such marked increase of ϕ^{CL} was hardly observed by the simple addition of **25** or **26** as a model of a tethered fluorescer.

© 2012 Elsevier Ltd. All rights reserved.

1. Introduction

The intramolecular charge-transfer-induced decomposition (CTID) of oxidophenyl-substituted dioxetanes has received considerable attention due to interest in the mechanisms of bioluminescence and chemiluminescence and because of possible applications in modern biological and clinical analyses using chemiluminescence.^{1–4} Typical examples of such CTID-active dioxetanes are adamantylidene-substituted dioxetane **1** and bicyclic dioxetane **2** (Scheme 1).^{2,5,6} Although these dioxetanes effectively emit light in an aprotic polar solvent, they give light in quite poor yield in an aqueous medium. This significant defect has been considerably improved through the addition of a fluorescer such as fluorescein and/or a surfactant such as quaternary ammonium or phosphonium salt for practical use in an aqueous system.^{7,8}

This situation prompted us to realize new CTID-active dioxetanes tethering a fluorescer that show highly effective chemiluminescence without any additives in an aqueous system.^{9,10} Since it is more appropriate than **1** to structural modification for the present purpose, dioxetane **2** was selected as a basic skeleton.^{11,12} To modify the structure of **2** with a minimal decrease in thermal stability and minimal change in the structure around the dioxetane ring, we planned to functionalize a methyl of the



a: Y = H, b: Y = *tert*-Bu(Me₂)Si-, c: Y = Na₂O₂P(O)-

Scheme 1. Base-induced chemiluminescent decomposition of 3-oxophenyl-substituted dioxetanes **1** and **2**.

tert-butyl group in **2**. The resulting dioxetanes **3** and **4** tethered a fluorescein or 4-(benzothiazol-2-yl)-3-hydroxyphenyl moiety as a highly efficient fluorescer (Fig. 1).

We report here that **3** and **4** were effectively synthesized by using dihydrofuran-intermediate **5** bearing an ω -carboxy-substituted linker,^{13,14} which was prepared from the key building block **7** or by using advanced intermediate **6** bearing an *N*-hydroxysuccinimide (HOSu) ester moiety (Fig. 1).¹⁵ We also report that dioxetanes **3** and **4** gave light far more efficiently than the parent **2a** in an aqueous medium.

* Corresponding author. E-mail address: nwatanab@kanagawa-u.ac.jp (N. Watanabe).

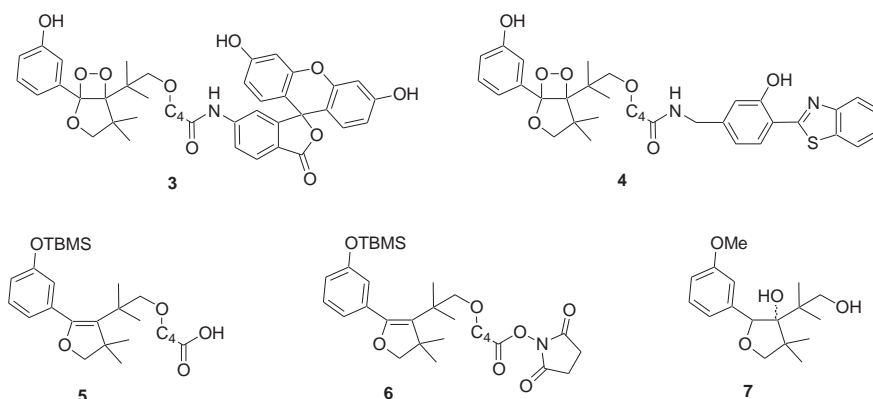


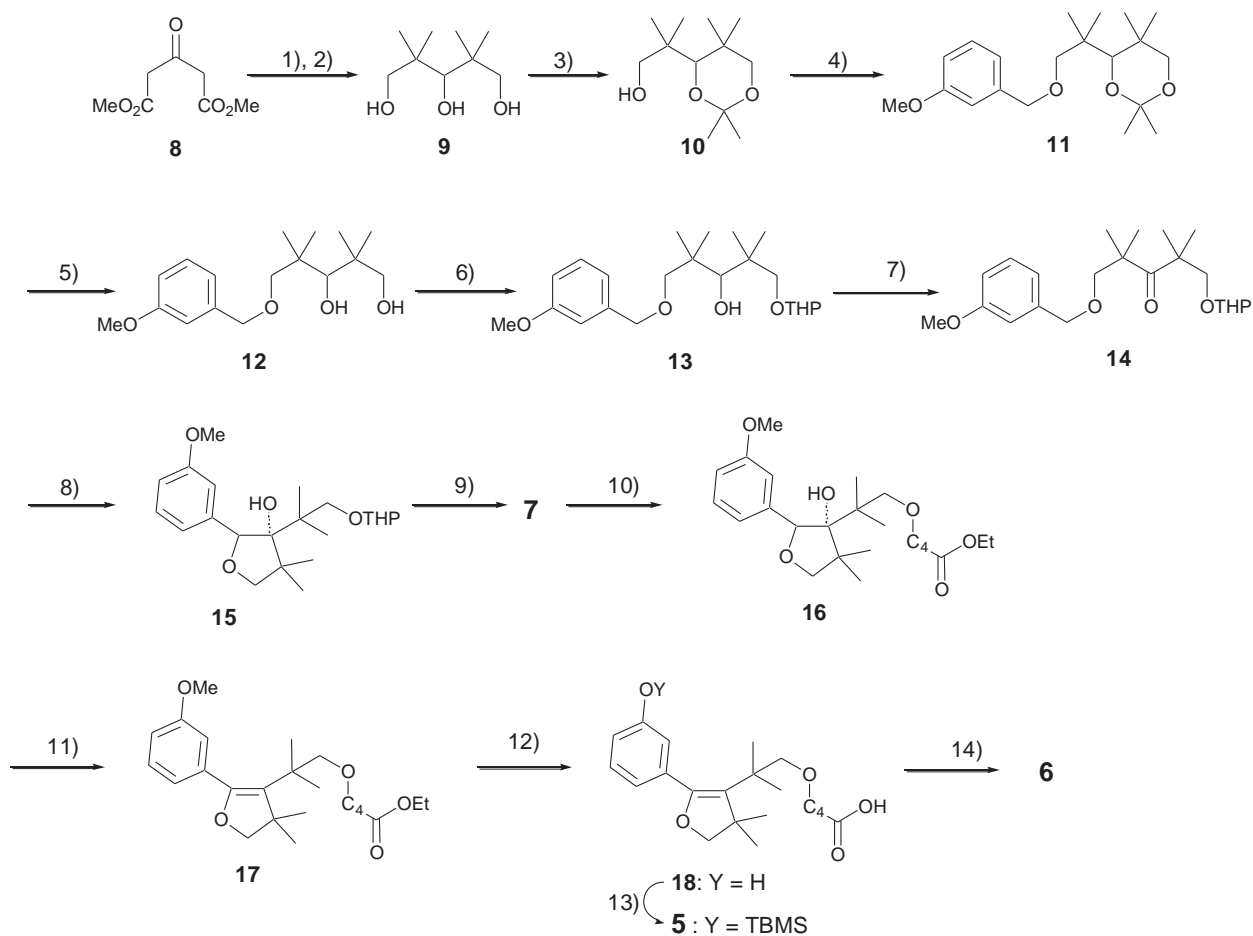
Fig. 1. Bicyclic dioxetanes **3** and **4** tethering a fluorescer and their synthetic intermediates **5**–**7**.

2. Results and discussion

2.1. Synthesis of bicyclic dioxetanes tethering a fluorescer through a linker

First, we synthesized a key building block **7** for the preparation of dihydrofuran-intermediate **5** starting from 2,2,4,4-tetramethylpentane-1,3,5-triol (**9**). The triol **9** was prepared from dimethyl

3-oxopentanedioate **8** through the introduction of four methyl groups followed by reduction with LiAlH_4 (Scheme 2). Two hydroxy groups in triol **9** were protected as cyclic acetal **10**, which was in turn subjected to Williamson synthesis with 3-methoxybenzyl chloride to selectively give benzyl ether **11**. Compound **11** was then deprotected to give diol **12**, in which only the primary OH was protected to give tetrahydropyranyl (THP) ether **13**. The remaining secondary OH in **13** was oxidized with PCC to give



Reagents: 1) NaH/MeI , 2) LiAlH_4 ; 3) $\text{Me}_2\text{C}(\text{OMe})_2/\text{PPTS}$; 4) $3\text{-MeOC}_6\text{H}_4\text{CH}_2\text{Cl}/\text{NaH}$; 5) $\text{H}_2\text{O}/\text{MeOH}/1\text{N HCl}$; 6) DHP/PPTS ; 7) PCC ; 8) LDA ; 9) $\text{MeOH}/1\text{N HCl}$; 10) $\text{Br}(\text{CH}_2)_4\text{CO}_2\text{Et}/\text{NaH}$; 11) $\text{SOCl}_2/\text{pyridine}$; 12) $\text{MeSNa}/\text{DMF}/\Delta$; 13) $t\text{-BuMe}_2\text{SiCl}/\text{DMAP}$; 14) di(*N*-hydroxysuccinidyl) carbonate

Scheme 2. Synthetic pathway starting from dimethyl 3-oxopentanedioate **8** to intermediate **5** and advanced intermediate **6** through key building block **7**.

1-benzyloxypentan-3-one **14**. LDA-mediated cyclization¹⁶ of **14** effectively took place at low temperature to give 3-hydroxytetrahydrofuran **15** bearing a THP-oxy group, deprotection of which quantitatively gave the desired key building block **7** as a mixture of stereoisomers.

Key building block **7** was condensed with ethyl 5-bromopentanoate to selectively give ester **16**. The hydroxytetrahydrofuran **16** was dehydrated with SOCl_2 /pyridine to give the corresponding dihydrofuran **17** (Scheme 2). When **17** was treated with MeSNa in hot DMF, both demethylation and saponification took place to give 5-(3-hydroxyphenyl)-2,3-dihydrofuran **18** bearing an ω -carboxy-substituted linker. Then, a phenolic hydroxyl group in **18** was protected with *tert*-butyldimethylsilyl (TBMS) chloride to give the desired dihydrofuran-intermediate **5**. Condensation of **5** with bis(*N*-hydroxysuccinimidyl) carbonate gave HOSu ester **6** as an advanced intermediate.

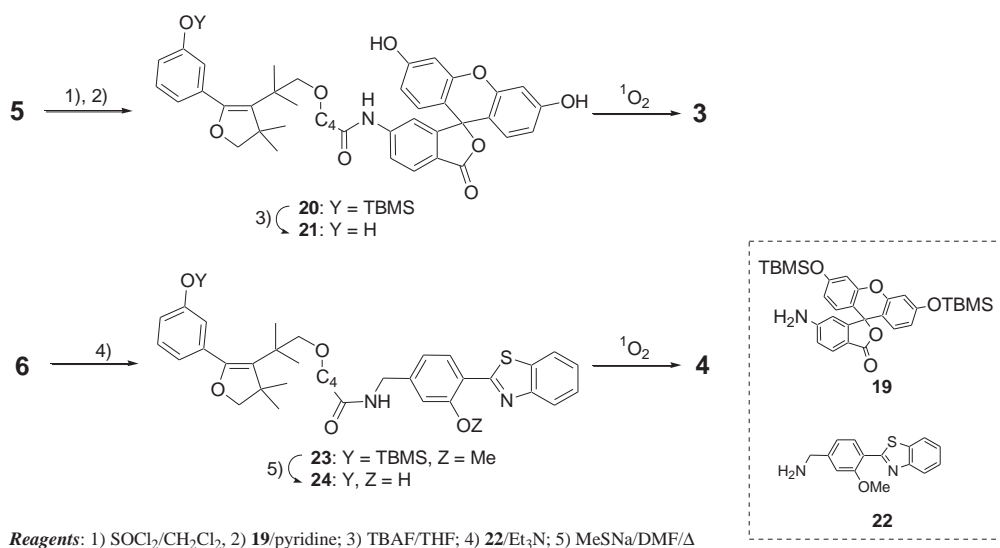
Intermediate **5** was transformed to its acid chloride in situ, which was coupled with TBMS-protected 5-aminofluorescein **19** in pyridine to give dihydrofuran **20** bearing a fluorescein moiety (Scheme 3). Deprotection of a silyloxy group in **20** with tetrabutylammonium fluoride (TBAF) gave precursor **21** of dioxetane tethering a fluorescein. On the other hand, condensation of **6** with 4-(benzothiazol-2-yl)-3-methoxybenzylamine **22** gave dihydrofuran **23** tethering a 4-(benzothiazol-2-yl)-3-methoxyphenyl moiety

through an amide linkage. Amide **23** was further treated with hot MeSNa in DMF gave precursor **24** leading to dioxetane **4**.

Finally, dihydrofurans **21** and **24** were individually irradiated together with a catalytic amount of tetraphenylporphyrin (TPP) in CH_2Cl_2 with a Na-lamp under an oxygen atmosphere at 0 °C. Thus, 1,2-addition of singlet oxygen to **21** and **24** smoothly took place to selectively give the corresponding dioxetanes **3** and **4**. The structures of these dioxetanes were determined by ^1H NMR, ^{13}C NMR, IR, and HRMass spectral analyses.

2.2. Chemiluminescent decomposition of bicyclic dioxetanes tethering a fluorescein or 4-(benzothiazol-2-yl)-3-hydroxyphenyl moiety through a linker

First of all, we investigated CTID of dioxetanes **3** and **4** in a TBAF/acetonitrile system, since this triggering system has been often used to evaluate chemiluminescence properties of CTID-active dioxetanes.^{3–6} When **3** was treated with a large excess of TBAF in acetonitrile at 25 °C, **3** decomposed according to pseudo-first-order kinetics to effectively give light with $\lambda_{\text{max}}^{\text{CL}} = 535 \text{ nm}$ (Fig. 2A), rate of CTID $k^{\text{CTID}} = 4.7 \times 10^{-3} \text{ s}^{-1}$ and chemiluminescence efficiency $\phi^{\text{CL}} = 0.19$,^{17,18} the value of which was 1.7 times larger than that for **2a** (Table 1, entries 1 and 2). This chemiluminescence spectrum coincided with fluorescence spectrum of acetamidofluorescein **25**



Scheme 3. Synthesis of dioxetanes **3** and **4** through precursors **21** and **24**.

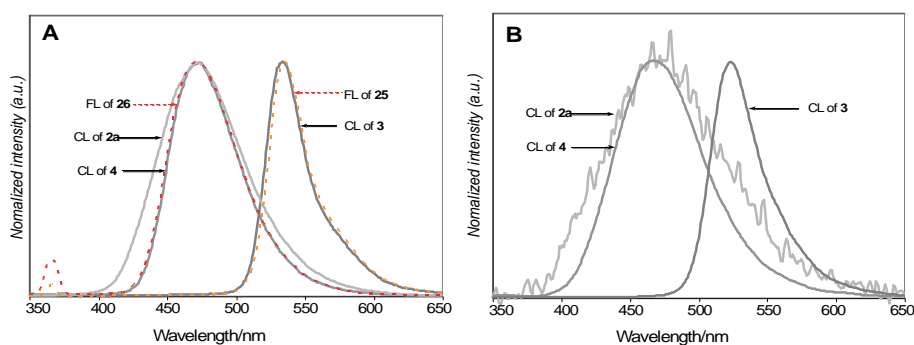


Fig. 2. (A) Chemiluminescence (CL) spectra of dioxetanes **2a**, **3**, and **4**, and fluorescence (FL) spectra of **25** and **26** in TBAF/acetonitrile. (B) Chemiluminescence (CL) spectra of dioxetanes **2a**, **3**, and **4** in NaOH/ H_2O .

Table 1
Base-induced chemiluminescent decomposition of dioxetane **2a** and dioxetanes **3** and **4** tethering a fluorescer^a

Entry	Dioxetane	System ^b	Additive	$\lambda_{\text{max}}^{\text{CL}}/\text{nm}$	ϕ^{CLc}	$k^{\text{CTID}}/\text{s}^{-1}$	Relative ϕ^{CLd}
1 ^e	2a	A	—	467	0.11	2.8×10^{-2}	1
2	3	A	—	535	0.19	4.7×10^{-3}	1.7
3	4	A	—	469	0.21	2.6×10^{-2}	1.9
4 ^e	2a	B ^e	—	467	1.1×10^{-5}	8.6×10^{-4}	1
5	2a	B	25	542	1.3×10^{-4}	8.7×10^{-3}	12
6	2a	B	26	481	3.2×10^{-5}	8.4×10^{-3}	3
7	3	B	—	525	6.0×10^{-3}	1.3×10^{-3}	550
8	4	B	—	468	3.7×10^{-4}	1.2×10^{-3}	30
9	3	B	27	535	4.4×10^{-3}	3.6×10^{-4}	400
10	4	B	27	473	2.6×10^{-2}	1.1×10^{-3}	2400

^a All reactions were carried out at 25 °C.

^b A: TBAF/acetonitrile system, B: NaOH/H₂O system.

^c Based on a value reported for the chemiluminescent decomposition of 3-adamantylidene-4-(3-*tert*-butyldimethylsiloxy)phenyl-4-methoxy-1,2-dioxetane **1b** in TBAF/DMSO.¹⁸

^d Values for entries 2 and 3 were based on the ϕ^{CL} in entry 1, while values for entries 5–10 were based on the ϕ^{CL} in entry 4.

^e Ref. 6a.

(Fig. 3) as a model of a tethered fluorescein moiety, which showed maximum wavelength $\lambda_{\text{max}}^{\text{fl}} = 535$ nm, but was significantly different from that for **2a** ($\lambda_{\text{max}}^{\text{CL}} = 467$ nm, Table 1, entry 1) in a TBAF/acetonitrile system (Fig. 2A). These results strongly suggested that CTID of **3** showed chemiluminescence due to energy-transfer from initially formed excited oxidobenzoate to fluorescein moiety.¹⁹ Similarly to the case of **3**, dioxetane **4** underwent CTID on treatment with TBAF/acetonitrile to give light. As shown in Table 1 (entry 3), $\lambda_{\text{max}}^{\text{CL}}$ and k^{CTID} for **4** were only a little different from those for **2**, though ϕ^{CL} was 1.9 times increased. The chemiluminescence spectrum of **4** was somewhat narrower than that for **2a** but coincided with fluorescence spectrum ($\lambda_{\text{max}}^{\text{fl}} = 469$ nm) of *N*-[4-(benzothiazol-2-yl)-3-hydroxybenzyl]acetamide **26** (Fig. 3) as a model of a tethered fluorescer in **4** in TBAF/acetonitrile (Fig. 2A). From these results, we can see that energy-transfer most likely occurred for **4** similarly to the case of **3** (Scheme 4).

Singlet-chemiexcitation efficiency $\phi_{\text{S}} = \phi^{\text{CL}} \times \phi^{\text{fl}}$ (ϕ^{fl} : fluorescence efficiency of emitter) has been estimated to be 0.46 for **2a** in TBAF/acetonitrile.^{6a} Here, the ϕ_{S} for **2a** is presumably maintained even for both **3** and **4**. On the other hand, ϕ^{fl} s were estimated to be 0.52 for **25** and 0.48 for **26** in TBAF/acetonitrile. These values are

also expected to be not so much different from those for fluorescein moiety of **3** and benzothiazolylphenol moiety of **4**, respectively. Thus, we can estimate formally that singlet-chemiexcitation energy generated from the dioxetane moiety transferred to the tethered fluorescer in efficiency of 80% for **3** and 95% for **4**.

The results described above encouraged us to investigate chemiluminescent decomposition of **3** and **4** in an aqueous system. When **3** was treated with 0.1 M NaOH/H₂O, **3** decomposed with the accompanying emission of yellow light with $\lambda_{\text{max}}^{\text{CL}} = 525$ nm, $\phi^{\text{CL}} = 6.0 \times 10^{-3}$ and $k^{\text{CTID}} = 1.3 \times 10^{-3} \text{ s}^{-1}$ [Fig. 2B, Table 1 (entry 7)]. This ϕ^{CL} value was 550-fold greater than that for **2a**. Similarly, **4** decomposed to give light with $\lambda_{\text{max}}^{\text{CL}} = 468$ nm, $\phi^{\text{CL}} = 3.7 \times 10^{-4}$ and $k^{\text{CTID}} = 1.2 \times 10^{-3} \text{ s}^{-1}$ [Fig. 2B, Table 1 (entry 8)]. In this case, ϕ^{CL} value was 30-fold greater than that for **2a**.^{6a}

Such marked enhancement of ϕ^{CL} was not observed when the chemiluminescent decomposition of **2a** was carried out by simply adding fluorescer **25** or **26** in NaOH/H₂O system. When **2a** (1.0×10^{-4} M, 1 mL) was treated with NaOH/H₂O (0.1 M, 2 mL) including **25** (1.0×10^{-3} M) at 25 °C,²⁰ **2a** decomposed with the accompanying emission of yellow light ($\lambda_{\text{max}}^{\text{CL}} = 542$ nm), but not blue light ($\lambda_{\text{max}}^{\text{CL}} = 467$ nm), the spectrum of which is shown in Fig. 2B. Table 1 (entry 5) shows that the value of ϕ^{CL} for **2a** increased

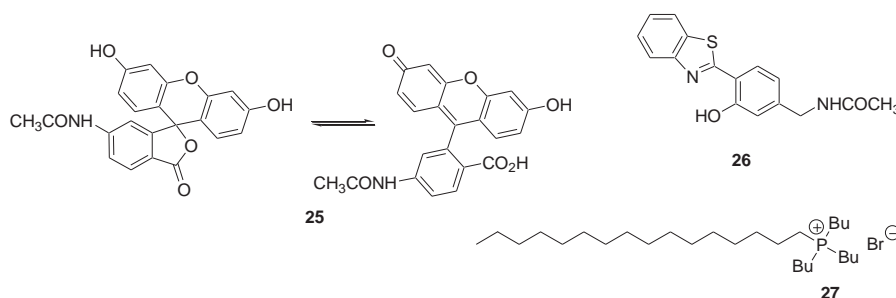
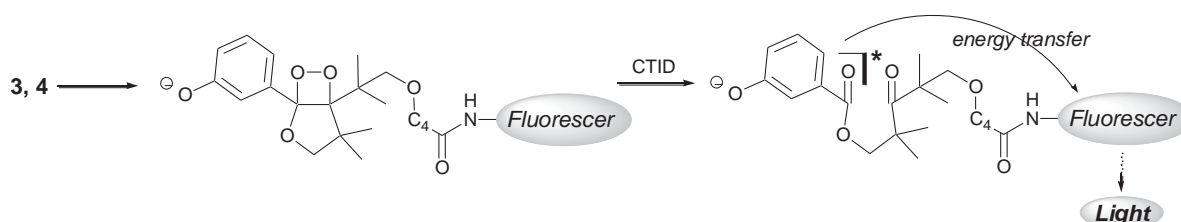


Fig. 3. Fluorescers **25** and **26** and surfactant **27**.



Scheme 4. Chemiluminescence based on energy-transfer for dioxetanes **3** and **4**.

12 times by the addition of **25**, though it was only 1/50 of that for **3**. On the other hand, the CTID of **2a** in the presence of **26** gave light only three times more than the case of **2a** without any additive fluorescer (Table 1, entry 6).

The results described above showed that ϕ^{CL} was markedly increased by tethering a fluorescer to dioxetane **2** skeleton in NaOH/H₂O system. However, the magnitude of enhancement of ϕ^{CL} for **4** was only 1/16 of that for **3**, though model **26** was yet an effective fluorescer like as **25** in NaOH/H₂O: $\phi^{\text{fl}}=0.73$ for **25**, and 0.36 for **26**. This suggested that the energy-transfer did not operate well for the CTID of **4** in an aqueous system differently from a non-aqueous system such as TBAF/acetonitrile.

Although it was unclear the reason why the fluorescer moiety did not act well in **4** in an aqueous system, a hydrophobic circumstance appeared to be favorable to the energy-transfer chemiluminescence for the CTID of **4**. Thus, we finally attempted to use a surfactant with expectation that it should provide more or less a hydrophobic microenvironment in an aqueous system. A surfactant selected as a representative was tributylhexadecylphosphonium bromide **27** (Fig. 3), since it was used for a chemiluminescent clinical analysis using dioxetane **2c** (phosphate form).⁸ When **4** was treated with NaOH/H₂O including an equimolar amount of **27** (Fig. 3), emission of light markedly increased. As shown in Table 1 (entry 10), the value of ϕ^{CL} became 2400-fold greater than that for innocent **2**. On the other hand, **27** rather did not act to increase ϕ^{CL} for CTID of **3** in NaOH/H₂O system (Table 1, entry 9).²¹

3. Conclusion

Bicyclic dioxetanes **3** and **4** tethering a fluorescein or 4-(benzothiazol-2-yl)-3-hydroxyphenyl moiety were synthesized through the preparation of dihydrofuran-intermediate **5** and its advanced intermediate **6**. These dioxetanes underwent base-induced decomposition to effectively give light due to intramolecular energy-transfer from an excited oxidobenzoate to a fluorescein or 4-(benzothiazol-2-yl)-3-hydroxyphenyl moiety. Although the values of chemiluminescence efficiency (ϕ^{CL}) for **3** and **4** were only slightly larger than that for parent **2a** in a TBAF/acetonitrile system, these values were 30–550-fold greater than that for **2a** in a NaOH/H₂O system. A comparison of the chemiluminescent decomposition of **3** and **4** to that of parent **2a** with additive model fluorescer **25** or **26** in an aqueous system showed that tethering a fluorophore was 10–50 times more effective to increase ϕ^{CL} than a simple combination of dioxetane and fluorescer in a NaOH/H₂O system.

4. Experimental

4.1. General

Melting points were uncorrected. IR spectra were taken on an FT/IR infrared spectrometer. ¹H and ¹³C NMR spectra were recorded on a 400 MHz and 500 MHz spectrometers. Mass spectra were obtained by using double-focusing mass spectrometers and an ESI-TOF mass spectrometer. Column chromatography was carried out using SiO₂ or NH–SiO₂.

4.2. Data for compounds

4.2.1. 2,2,4,4-Tetramethylpentane-1,3,5-triol (9). A solution of dimethyl 2,2,4,4-tetramethyl-3-oxopentanedioate (40.1 g, 0.174 mol), prepared from dimethyl 3-oxopentanedioate (**8**), in dry THF (40 mL) was added dropwise to a suspension of LiAlH₄ (10.2 g, 0.269 mol) in dry THF (110 mL) under a N₂ atmosphere at 0 °C and stirred overnight. After the usual workup, the crude product was chromatographed on SiO₂ and eluted with AcOEt/hexane (3:1) to give triol **9** in 53% yield (16.2 g). Colorless needles; mp 61.0–61.5 °C

(from hexane); ¹H NMR (400 MHz, CDCl₃): δ_{H} 1.01 (s, 6H), 1.09 (s, 6H), 2.11 (br s, 3H), 3.50 (q_{AB}, $J=10.7$ Hz, 4H), 3.64 (s, 1H) ppm; ¹³C NMR (125 MHz, CDCl₃): δ_{C} 20.3, 24.7, 40.3, 75.4, 85.7 ppm; IR (KBr): $\tilde{\nu}$ 3305, 2988, 2960, 2875, 1043 cm⁻¹; HRMS (ESI): 199.1266, calcd for C₉H₂₀O₃Na [M+Na]⁺ 199.1310.

4.2.2. 4-(2-Hydroxy-1,1-dimethylethyl)-2,2,5,5-tetramethyl-1,3-dioxane (10). 2,2-Di-methoxypropane (7.10 mL, 56.6 mmol) and pyridinium *p*-toluenesulfonate (PPTS) (1.41 g, 5.61 mmol) were added to a solution of triol **9** (9.76 g, 55.4 mmol) in CH₂Cl₂ (60 mL) under N₂ atmosphere at room temperature and stirred overnight. The reaction mixture was poured into aq NaHCO₃ and was extracted with CH₂Cl₂. The organic layer was washed three times with aq NaCl, dried over anhydrous MgSO₄, and concentrated in vacuo. The residue was chromatographed on SiO₂ and eluted with AcOEt/hexane (1:3) to give 1,3-dioxane **10** in 97% yield (11.6 g). Colorless oil; ¹H NMR (400 MHz, CDCl₃): δ_{H} 0.89 (s, 3H), 1.02 (s, 3H), 1.02 (s, 3H), 1.21 (s, 3H), 1.42 (s, 6H), 3.01 (br s, 1H), 3.11 (d, $J=11.1$ Hz, 1H), 3.33 (d, $J=11.1$ Hz, 1H), 3.50–3.57 (m, 2H), 3.59 (s, 1H) ppm; ¹³C NMR (100 MHz, CDCl₃): δ_{C} 18.7, 20.3, 21.2, 24.1, 24.5, 29.0, 35.4, 40.2, 73.0, 74.4, 83.2, 98.5 ppm. IR (liquid film): $\tilde{\nu}$ 3451, 2991, 2958, 2873, 1201, 1091, 738 cm⁻¹. HRMS (ESI): 239.1589, calcd for C₁₂H₂₄O₃Na [M+Na]⁺ 239.1623.

4.2.3. 4-[2-(3-Methoxybenzyloxy)-1,1-dimethylethyl]-2,2,5,5-tetramethyl-1,3-dioxane (11). A solution of 1,3-dioxane **10** (11.6 g, 53.6 mmol) in dry THF/DMF (4:3, 70 mL) was added to a suspension of NaH (60% in oil, 2.45 g, 61.3 mmol) in dry THF (80 mL) under a N₂ atmosphere at 0 °C and then stirred at room temperature for 1 h. To the solution, 3-methoxybenzyl chloride (8.0 mL, 53.4 mmol) was added at 0 °C and stirred at room temperature overnight. The reaction mixture was quenched with aq NH₄Cl, and extracted with AcOEt. The organic layer was dried over anhydrous MgSO₄ and concentrated in vacuo. The residue was chromatographed on SiO₂ and eluted with AcOEt/hexane (1:20 → 1:9) to give benzyl ether **11** in 91.7% yield (16.6 g). Colorless oil; ¹H NMR (400 MHz, CDCl₃): δ_{H} 0.88 (s, 3H), 0.95 (s, 3H), 1.05 (s, 3H), 1.14 (s, 3H), 1.34 (s, 3H), 1.37 (s, 3H), 3.01 (d, $J=8.4$ Hz, 1H), 3.08 (d, $J=11.4$ Hz, 1H), 3.37 (d, $J=8.4$ Hz, 1H), 3.51 (d, $J=11.4$ Hz, 1H), 3.65 (s, 1H), 3.81 (s, 3H), 4.45 (q_{AB}, $J=12.5$ Hz, 2H), 6.82 (d with fine coupling, $J=8.2$ Hz, 1H), 6.88–6.92 (m, 2H), 7.25 (t, $J=8.2$ Hz, 1H) ppm; ¹³C NMR (125 MHz, CDCl₃): δ_{C} 19.0, 20.9, 21.9, 23.4, 24.2, 29.1, 35.3, 40.5, 55.1, 72.9, 74.7, 78.4, 78.5, 98.5, 112.7 (×2), 119.5, 129.2, 140.6, 159.6 ppm; IR (liquid film): $\tilde{\nu}$ 2991, 2941, 2871, 1602, 1092 cm⁻¹; Mass (m/z , %): 336 (M⁺, 15), 222 (72), 143 (14), 137 (39), 121 (100). HRMS (ESI): 359.2181, calcd for C₂₀H₃₂O₄Na [M+Na]⁺ 359.2198.

4.2.4. 5-(3-Methoxybenzyloxy)-2,2,4,4-tetramethylpentane-1,3-diol (12). Benzyl ether **11** (15.8 g, 47.0 mmol) was heated in refluxing dioxane (160 mL) and 1 N HCl (40 mL) for 3 h. The reaction mixture was poured into aq NaHCO₃ and extracted with AcOEt. The organic layer was washed with aq NaCl, dried over anhydrous MgSO₄, and concentrated in vacuo. The residue was chromatographed on SiO₂ and eluted with AcOEt/hexane (1:9 → 1:1) to give benzyloxy-pentanediol **12** in 86.1% yield (12.0 g). Colorless oil; ¹H NMR (400 MHz, CDCl₃): δ_{H} 0.98 (s, 3H), 1.02 (s, 3H), 1.05 (s, 3H), 1.11 (s, 3H), 3.33 (s, 2H), 3.37 (d with fine coupling, $J=10.7$ Hz, 1H), 3.48 (dd, $J=10.7$ and 2.2 Hz, 1H), 3.58 (d, $J=2.2$ Hz, 1H), 3.61 (br s, 1H), 3.81 (s, 3H), 4.26 (br s, 1H), 4.49 (s, 2H), 6.83–6.90 (m, 3H), 7.24–7.30 (m, 1H) ppm; ¹³C NMR (125 MHz, CDCl₃): δ_{C} 20.1, 21.1, 24.7, 25.0, 40.4, 40.4, 55.1, 73.5, 75.4, 83.0, 85.3, 112.9, 113.3, 119.8, 129.5, 139.0, 159.7 ppm; IR (liquid film): $\tilde{\nu}$ 3412, 2959, 2914, 2874, 1602, 1267, 1080 cm⁻¹; Mass (m/z , %): 296 (M⁺, 31), 138 (100), 121 (92), 97 (14), 91 (10); HRMS (ESI): 319.1856, calcd for C₁₇H₂₈O₄Na [M+Na]⁺ 319.1885.

4.2.5. 1-(3-Methoxybenzyloxy)-2,2,4,4-tetramethyl-5-(tetrahydro-2H-pyran-2-yloxy)-pentan-3-ol (13). PPTS (540 mg, 2.15 mmol) and 3,4-dihydro-2H-pyran (4.8 mL, 51.0 mmol) were added to a solution of benzyloxy-pentanediol **12** (12.0 g, 40.5 mmol) in dry CH₂Cl₂ (120 mL) under a N₂ atmosphere at room temperature and stirred at room temperature for 3 h. The reaction mixture was poured into satd aq NaHCO₃ and extracted with AcOEt. The organic layer was washed with aq NaCl, dried over anhydrous MgSO₄, and concentrated in vacuo. The residue was chromatographed on SiO₂ and eluted with AcOEt/hexane (1:9) to give THP-ether **13** in 92.1% yield (14.2 g). Colorless oil; ¹H NMR (400 MHz, CDCl₃): δ_H 1.02 (s, 1.5H), 1.04 (s, 1.5H), 1.04 (s, 1.5H), 1.05 (s, 1.5H), 1.06 (s, 1.5H), 1.09 (s, 1.5H), 1.10 (s, 1.5H), 1.11 (s, 1.5H), 1.47–1.85 (m, 6H), 3.14–3.70 (m, 7H), 3.76–3.86 (m, 1H), 3.81 (s, 3H), 4.45–4.53 (m, 2H), 4.54–4.59 (m, 1H), 6.82 (d with fine coupling, J=8.2 Hz, 1H), 6.88–6.92 (m, 2H), 7.25 (t, J=8.2 Hz, 1H) ppm; ¹³C NMR (125 MHz, CDCl₃): δ_C 19.3, 19.6, 21.6, 21.9, 21.9, 22.0, 24.4, 24.7, 24.9, 25.0, 25.3, 25.4, 30.5, 30.6, 40.4, 40.5, 40.8 (×2), 55.1 (×2), 61.9, 62.4, 73.1 (×2), 77.7, 78.2, 80.4, 80.5, 80.6, 81.1, 99.0, 99.3, 112.7 (×2), 112.9, 113.0, 119.6 (×2), 129.3, 129.3, 140.1, 140.2, 159.6 (×2) ppm; IR (liquid film): ν̄ 3500, 2942, 2871, 1602, 1266, 1119, 1034 cm⁻¹; Mass (m/z, %): 380 (M⁺, trace), 295 (3), 138 (31), 136 (22), 121 (100), 109 (17); HRMS (ESI): 403.2434, calcd for C₂₂H₃₆O₅Na [M+Na]⁺ 403.2460.

4.2.6. 1-(3-Methoxybenzyloxy)-2,2,4,4-tetramethyl-5-(tetrahydro-2H-pyran-2-yloxy)-pentan-3-one (14). Alcohol **13** (7.90 g, 20.8 mmol) in CH₂Cl₂ (20 mL) was added to a suspension of PCC (6.90 g, 32.0 mmol), pyridine (2.7 mL, 33.4 mmol), and Celite (15.7 g) in CH₂Cl₂ (60 mL) at room temperature and refluxed for 4 h. After the usual workup, the crude product was chromatographed on SiO₂ and eluted with AcOEt/hexane (1:16→1:2) to give ketone **14** in 85.9% yield (6.76 g). Colorless oil; ¹H NMR (400 MHz, CDCl₃): δ_H 1.23 (s, 3H), 1.28 (s, 6H), 1.32 (s, 3H), 1.42–1.80 (m, 6H), 3.46 (d, J=9.2 Hz, 1H), 3.43–3.54 (m, 1H), 3.51 (q_{AB}, J=8.8 Hz, 2H), 3.72 (d, J=9.2 Hz, 1H), 3.77–3.84 (m, 1H), 3.80 (s, 3H), 4.47 (s, 2H), 4.55 (s with fine coupling, 1H), 6.80 (d with fine coupling, J=8.1 Hz, 1H), 6.85–6.89 (m, 2H), 7.23 (t, J=8.1 Hz, 1H) ppm; ¹³C NMR (100 MHz, CDCl₃): δ_C 19.3, 23.3, 23.5, 23.6, 23.7, 25.5, 30.5, 50.1, 50.3, 55.1, 61.8, 73.0, 76.0, 78.3, 98.9, 112.5, 112.9, 119.5, 129.1, 140.1, 159.5, 215.9 ppm; IR (liquid film): ν̄ 2940, 2870, 1686, 1602, 1266 cm⁻¹; Mass (m/z, %): 378 (M⁺, 2), 294 (12), 138 (42), 137 (13), 121 (100); HRMS (ESI): 401.2279, calcd for C₂₂H₃₄O₅Na [M+Na]⁺ 401.2304.

4.2.7. 3-[1,1-Dimethyl-2-(tetrahydro-2H-pyran-2-yloxy)ethyl]-3-hydroxy-2-(3-methoxyphenyl)-4,4-dimethyltetrahydrofuran (15). Ketone **14** (12.6 g, 33.2 mmol) in dry THF (50 mL) was added to a solution of LDA, prepared from BuLi (1.61 M solution, 48.0 mL, 77.3 mmol) and diisopropylamine (12 mL), in THF (80 mL) at -78 °C and stirred for 5 h. The reaction mixture was poured into aq NH₄Cl, and extracted with AcOEt. The organic layer was washed with aq NaCl, dried over anhydrous MgSO₄, and concentrated in vacuo. The crude hydroxytetrahydrofuran **15** (3.20 g, an oil) as a stereoisomeric mixture was used for the next reaction without purification.

4.2.8. 3-Hydroxy-3-(2-hydroxy-1,1-dimethylethyl)-2-(3-methoxyphenyl)-4,4-dimethyl-2,3,4,5-tetrahydrofuran (7). HCl (1 N, 5 mL) was added to a solution of tetrahydrofuran **15** (12.9 g) in MeOH (120 mL) at room temperature and stirred overnight. The reaction mixture was poured into aq NaHCO₃ and extracted with AcOEt. The organic layer was washed with aq NaCl, dried over anhydrous MgSO₄, and concentrated in vacuo. The residue was chromatographed on SiO₂ and eluted with AcOEt/hexane (1:4) to give hydroxytetrahydrofuran **7** in 97.4% yield (2.33 g) (a mixture of *trans*-3-hydroxy form and *cis*-3-hydroxy form, *trans/cis*=95:5). Colorless oil; ¹H NMR (500 MHz, CDCl₃): δ_H 0.78 (br s, 2.85H), 0.93

(s, 0.15H), 1.02 (s, 2.85H), 1.20 (s, 0.15H), 1.22 (s, 0.15H), 1.25 (s, 2.85H), 1.37 (s, 2.85H), 1.39 (s, 0.15H), 2.22 (br s, 1H), 3.21 (dd, J=11.0 and 5.1 Hz, 1H), 3.33 (d, J=5.1 Hz, 0.1H), 3.45–3.65 (m, 0.95H), 3.50 (d, J=7.2 Hz, 0.05H), 3.70 (d, J=8.1 Hz, 0.95H), 3.81 (s, 2.85H), 3.82 (s, 0.15H), 3.89 (d, J=8.1 Hz, 0.95H), 4.09 (d, J=7.2 Hz, 0.05H), 4.57 (br s, 0.95H), 5.04 (s, 0.95H), 5.27 (s, 0.05H), 6.81 (d with fine coupling, J=8.0 Hz, 0.95H), 6.86 (d with fine coupling, J=8.2 Hz, 0.05H), 7.04–7.10 (m, 0.1H), 7.13 (s, 0.95H), 7.16 (d, J=7.8 Hz, 0.95H), 7.20–7.25 (m, 0.05H), 7.22 (dd, J=8.0 and 7.8 Hz, 1H) ppm; ¹³C NMR (125 MHz, CDCl₃): δ_C 20.3, 22.7 (×2), 22.8, 23.2, 23.2, 25.4, 26.6, 40.6, 41.4, 47.9, 48.3, 55.2 (×2), 72.0, 73.1, 80.4, 81.3, 84.0, 86.7, 89.6, 93.7, 113.0, 113.6, 114.5, 115.2, 121.3, 122.0, 128.6, 128.9, 141.4, 142.2, 159.0, 159.2 ppm; IR (liquid film): ν̄ 3295, 2938, 2877, 1607, 1284, 1043 cm⁻¹; Mass (m/z, %): 294 (M⁺, 20), 276 (33), 236 (45), 190 (33), 159 (20), 136 (100), 126 (68); HRMS (ESI): 377.1703, calcd for C₁₇H₂₆O₄Na [M+Na]⁺ 377.1729.

4.2.9. 3-(7-Ethoxycarbonyl-1,1-dimethyl-3-oxaheptyl)-3-hydroxy-2-(3-methoxyphenyl)-4,4-dimethyl-2,3,4,5-tetrahydrofuran (16). 3-Hydroxy-3-(2-hydroxy-1,1-dimethylethyl)tetrahydrofuran **7** (1.00 g, 3.40 mmol) was added to a suspension of NaH (60% in oil, 255 mg, 6.38 mmol) in dry DMF (7 mL) under a N₂ atmosphere at 0 °C and stirred at room temperature for 30 min. To the solution, ethyl 5-bromopentanoate (0.81 mL, 7.16 mmol) was added at 0 °C and stirred at room temperature for 2 h. The reaction mixture was poured into aq NH₄Cl and extracted with AcOEt. The organic layer was washed with aq NaCl, dried over anhydrous MgSO₄, and concentrated in vacuo. The residue was chromatographed on SiO₂ and eluted with AcOEt/hexane (1:6) to give ester **16** in 94.7% yield (1.36 g) as a mixture of stereoisomers (*cis/trans*=93:7), from which a small amount of pure isomers were isolated.

3-r-(7-Ethoxycarbonyl-1,1-dimethyl-3-oxaheptyl)-3-hydroxy-2-trans-(3-methoxyphenyl)-4,4-dimethyl-2,3,4,5-tetrahydrofuran (16-trans): Colorless oil; ¹H NMR (400 MHz, CDCl₃): δ_H 0.80 (br s, 3H), 1.06 (s, 3H), 1.19 (s, 3H), 1.26 (t, J=7.1 Hz, 3H), 1.35 (s, 3H), 1.55–1.73 (m, 4H), 2.32 (t, J=7.1 Hz, 2H), 2.80 (d, J=9.3 Hz, 1H), 3.10–3.30 (m, 3H), 3.68 (d, J=7.9 Hz, 1H), 3.80 (s, 3H), 3.87 (d, J=7.9 Hz, 1H), 4.13 (q, J=7.1 Hz, 2H), 4.89 (br s, 1H), 5.04 (s, 1H), 6.80 (d with fine coupling, J=7.8 Hz, 1H), 7.10–7.17 (m, 2H), 7.21 (t, J=7.8 Hz, 1H) ppm; ¹³C NMR (125 MHz, CDCl₃): δ_C 14.1, 21.6, 23.4 (br×3), 25.3, 28.8, 33.7, 41.5, 47.7, 55.1, 60.1, 70.6, 80.1, 81.7, 88.4, 92.3 (br), 112.8, 114.0 (br), 120.8 (br), 128.4, 142.2, 159.0, 173.2 ppm; IR (liquid film): ν̄ 3447, 2936, 2873, 1734, 1603, 1093 cm⁻¹; Mass (m/z, %): 422 (M⁺, 8), 258 (22), 245 (100), 243 (53), 135 (64), 129 (60); HRMS (ESI): 445.2562, calcd for C₂₄H₃₈O₆Na [M+Na]⁺ 445.2566. **3-r-(7-Ethoxycarbonyl-1,1-dimethyl-3-oxaheptyl)-3-hydroxy-2-cis-(3-methoxyphenyl)-4,4-dimethyl-2,3,4,5-tetrahydrofuran (16-cis):** Colorless oil; ¹H NMR (400 MHz, CDCl₃): δ_H 1.01 (s, 3H), 1.16 (s, 3H), 1.21 (s, 3H), 1.26 (t, J=7.2 Hz, 3H), 1.37 (s, 3H), 1.30–1.40 (m, 2H), 1.45–1.55 (m, 2H), 2.23 (t, J=7.3 Hz, 2H), 2.54 (dt, J=9.3 and 6.4 Hz, 1H), 2.82 (d, J=9.3 Hz, 1H), 2.94 (dt, J=9.3 and 6.4 Hz, 1H), 3.08 (d, J=9.3 Hz, 1H), 3.44 (d, J=7.1 Hz, 1H), 3.81 (s, 3H), 4.08–4.15 (m, 3H), 4.87 (s, 1H), 5.23 (s, 1H), 6.83 (d with fine coupling, J=8.3 Hz, 1H), 7.10 (d with fine coupling, J=7.6 Hz, 1H), 7.16 (s with fine coupling, 1H), 7.21 (dd with fine coupling, J=8.3 and 7.6 Hz, 1H) ppm; ¹³C NMR (100 MHz, CDCl₃): δ_C 14.3, 20.5, 21.6, 23.7 (×2), 26.9, 28.7, 33.9, 40.4, 48.4, 55.2, 60.2, 70.5, 81.0, 81.7, 83.9, 86.4, 113.5, 115.5, 122.5, 128.3, 142.4, 159.0, 173.1 ppm; IR (liquid film): ν̄ 3403, 2963, 2873, 1734, 1599, 1372, 1094 cm⁻¹; Mass (m/z, %): 422 (M⁺, 21), 245 (24), 147 (28), 140 (32), 136 (92), 129 (100); HRMS (ESI): 445.2563, calcd for C₂₄H₃₈O₆Na [M+Na]⁺ 445.2566.

4.2.10. 4-(7-Ethoxycarbonyl-1,1-dimethyl-3-oxaheptyl)-5-(3-methoxyphenyl)-3,3-dimethyl-2,3-dihydrofuran (17). SOCl₂ (0.53 mL, 7.27 mmol) was added to a solution of hydroxytetrahydrofuran **16** (2.55 g, 6.02 mmol) and pyridine (5.0 mL, 61.8 mmol) in dry CH₂Cl₂

(30 mL) under a N₂ atmosphere at 0 °C and stirred for 3 h. The reaction mixture was poured into satd aq NaHCO₃ and extracted with CH₂Cl₂. The organic layer was washed twice with satd aq NaCl, dried over anhydrous MgSO₄, and concentrated in vacuo. The residue was chromatographed on SiO₂ and eluted with AcOEt/hexane (1:6) to give dihydrofuran **17** in 85.7% yield (2.09 g). Colorless oil; ¹H NMR (400 MHz, CDCl₃): δ_H 1.04 (s, 6H), 1.25 (t, *J*=7.2 Hz, 3H), 1.31 (s, 6H), 1.51–1.59 (m, 2H), 1.63–1.72 (m, 2H), 2.31 (t, *J*=7.3 Hz, 2H), 3.10 (s, 2H), 3.24 (t, *J*=6.2 Hz, 2H), 3.80 (s, 3H), 3.87 (s, 2H), 4.12 (q, *J*=7.2 Hz, 2H), 6.83–6.87 (m, 2H), 6.90 (d with fine coupling, *J*=7.5 Hz, 1H), 7.20–7.25 (m, 1H) ppm; ¹³C NMR (100 MHz, CDCl₃): δ_C 14.3, 21.9, 27.3 (×2), 27.4 (×2), 29.1, 34.1, 37.0, 47.0, 55.2, 60.1, 70.4, 79.5, 83.0, 113.9, 115.1, 122.3, 122.3, 128.7, 137.0, 150.9, 158.9, 173.5 ppm; IR (liquid film): ν̄ 2956, 2866, 1735, 1596, 1048 cm⁻¹; Mass (*m/z*, %): 404 (M⁺, 2), 259 (12), 258 (19), 246 (20), 245 (100), 243 (43), 135 (20). HRMS (ESI): 427.2420, calcd for C₂₄H₃₆O₅Na [M+Na]⁺ 427.2460.

4.2.11. 4-(7-Carboxy-1,1-dimethyl-3-oxaheptyl)-5-(3-hydroxyphenyl)-3,3-dimethyl-2,3-dihydrofuran (**18**). CH₃SO₃Na (95%, 988 mg, 13.5 mmol) was added to a solution of dihydrofuran (**17**) (1.19 g, 2.94 mmol) in dry DMF (10 mL) under a N₂ atmosphere at room temperature and stirred at 140 °C for 2 h. The reaction mixture was poured into diluted aq HCl and extracted with AcOEt. The organic layer was washed three times with satd aq NaCl, dried over anhydrous MgSO₄, and concentrated in vacuo. The residue was chromatographed on SiO₂ and eluted with AcOEt/hexane (1:1) to give carboxylic acid **18** in 92.7% yield (1.09 g). Colorless oil; ¹H NMR (400 MHz, CDCl₃): δ_H 1.03 (s, 6H), 1.30 (s, 6H), 1.54–1.62 (m, 2H), 1.68–1.77 (m, 2H), 2.41 (t, *J*=7.2 Hz, 2H), 3.10 (s, 2H), 3.26 (t, *J*=6.0 Hz, 2H), 3.86 (s, 2H), 6.77 (d with fine coupling, *J*=8.1 Hz, 1H), 6.83–6.87 (m, 2H), 7.16 (t with fine coupling, *J*=8.1 Hz, 1H) ppm; ¹³C NMR (100 MHz, CDCl₃): δ_C 21.9, 27.3 (×2), 27.5 (×2), 28.9, 33.7, 37.1, 47.0, 70.5, 79.5, 82.9, 115.3, 116.9, 122.0, 122.1, 128.9, 136.9, 150.7, 155.2, 178.8 ppm; IR (liquid film): ν̄ 3376, 2957, 2869, 1709, 1595, 1047 cm⁻¹; Mass (*m/z*, %): 362 (M⁺, 3), 244 (22), 232 (28), 231 (100), 230 (12), 229 (46), 121 (37), 55 (10); HRMS (ESI): 385.1954, calcd for C₂₁H₃₀O₅Na [M+Na]⁺ 385.1991.

4.2.12. 5-(3-*tert*-Butyldimethylsilyloxyphenyl)-4-(7-carboxy-1,1-dimethyl-3-oxaheptyl)-3,3-dimethyl-2,3-dihydrofuran (**5**). Imidazole (1.53 g, 22.5 mmol) and TBMSCl (97%, 3.17 g, 21.0 mmol) were added to a solution of carboxylic acid **18** (2.70 g, 7.45 mmol) in dry DMF (6.8 mL) under a N₂ atmosphere at room temperature and stirred for 2 h. The reaction mixture was poured into satd aq NH₄Cl and extracted with AcOEt. The organic layer was washed three times with satd aq NaCl, dried over anhydrous MgSO₄, and concentrated in vacuo. K₂CO₃ (484 mg, 3.50 mmol) in H₂O (10 mL) was added to a solution of the residue in CH₃OH (40 mL) at room temperature and stirred for 1 h. The reaction mixture was poured into satd aq NH₄Cl and extracted with AcOEt. The organic layer was washed twice with satd aq NaCl, dried over anhydrous MgSO₄, and concentrated in vacuo. The residue was chromatographed on SiO₂ and eluted with AcOEt/hexane (1:5) to give dihydrofuran **5** in 92.6% yield (3.29 g). Colorless oil; ¹H NMR (400 MHz, CDCl₃): δ_H 0.18 (s, 6H), 0.98 (s, 9H), 1.04 (s, 6H), 1.30 (s, 6H), 1.54–1.62 (m, 2H), 1.65–1.75 (m, 2H), 2.38 (t, *J*=7.5 Hz, 2H), 3.10 (s, 2H), 3.25 (t, *J*=6.1 Hz, 2H), 3.86 (s, 2H), 6.76–6.81 (m, 2H), 6.90 (d with fine coupling, *J*=7.6 Hz, 1H), 7.14–7.19 (m, 1H) ppm; ¹³C NMR (125 MHz, CDCl₃): δ_C -4.4 (×2), 18.1, 21.6, 25.7 (×3), 27.2 (×2), 27.4 (×2), 28.9, 33.8, 37.0, 47.0, 79.6, 83.0, 119.8, 121.7, 122.4, 123.0, 128.7, 137.1, 151.0, 155.0, 179.6 ppm; IR (liquid film): ν̄ 2956, 2930, 2860, 1711, 1595, 1262, 1118 cm⁻¹; Mass (*m/z*, %): 476 (M⁺, trace), 358 (35), 343 (100), 309 (13), 231 (10); HRMS (ESI): 499.2815, calcd for C₂₇H₄₄O₅SiNa [M+Na]⁺ 499.2856.

4.2.13. *N*-Hydroxysuccinimide ester of 5-(3-*tert*-butyldimethylsilyloxyphenyl)-4-(7-carboxy-1,1-dimethyl-3-oxaheptyl)-3,3-dimethyl-2,3-dihydrofuran (**6**). Di(*N*-succinimidyl) carbonate (760 mg, 2.97 mmol) and Et₃N (0.64 mL, 4.59 mmol) were added to a solution of carboxylic acid **5** (445 mg, 0.932 mmol) in dry CH₃CN (8 mL) under a nitrogen atmosphere at room temperature and stirred for 1 h. The reaction mixture was concentrated in vacuo. The residue was chromatographed on silica gel and eluted with ether/hexane (2:1) to give 1.30 g of *N*-hydroxysuccinimide ester **6** as a colorless oil in 99.8% yield; ¹H NMR (400 MHz, CDCl₃): δ_H 0.18 (s, 6H), 0.98 (s, 9H), 1.04 (s, 6H), 1.31 (s, 6H), 1.59–1.67 (m, 2H), 1.76–1.85 (m, 2H), 2.63 (t, *J*=7.5 Hz, 2H), 2.83 (br s, 4H), 3.10 (s, 2H), 3.26 (t, *J*=6.1 Hz, 2H), 3.86 (s, 2H), 6.75–6.81 (m, 2H), 6.90 (d with fine coupling, *J*=7.3 Hz, 1H), 7.14–7.20 (m, 1H) ppm; ¹³C NMR (125 MHz, CDCl₃): δ_C -4.4 (×2), 18.1, 21.6, 25.5 (×2), 25.6 (×3), 27.2 (×2), 27.4 (×2), 28.6, 30.6, 36.9, 47.0, 70.0, 79.6, 83.0, 119.8, 121.6, 122.3, 123.0, 128.7, 137.1, 151.0, 155.0, 168.5, 169.1 (×2) ppm. IR (liquid film): ν̄ 2956, 2930, 2860, 1816, 1746, 1480, 1206, 1068, 840 cm⁻¹; Mass (*m/z*, %): 573 (M⁺, trace), 359 (12), 358 (33), 345 (19), 344 (37), 343 (100), 309 (10), 231 (10), 99 (23), 75 (14), 73 (17), 57 (17), 56 (26), 55 (11). HRMS (ESI): 596.2974, calcd for C₃₁H₄₇NO₇SiNa [M+Na]⁺ 596.3020.

4.2.14. 5-[3-(*tert*-Butyldimethylsilyloxy)phenyl]-4-[7-(fluorescein-5-yl)carbamoyl-1,1-dimethyl-3-oxaheptyl]-3,3-dimethyl-2,3-dihydrofuran (**20**). SOCl₂ (0.02 mL, 0.27 mmol) was added to a solution of carboxylic acid **5** (99.7 mg, 0.209 mmol) in dry CH₂Cl₂ (1 mL) at room temperature under a N₂ atmosphere and stirred for 3 h. The solution was concentrated, and then the residue was dissolved in dry THF (1 mL) and stirred at room temperature under a N₂ atmosphere. To the solution [3',6'-bis(*tert*-butyldimethylsilyloxy)-5-aminofluorescein (**19**) (120 mg, 0.208 mmol) and pyridine (0.02 mL, 0.247 mmol) were added and stirred for 24 h. The reaction mixture was poured into satd aq NH₄Cl and extracted with AcOEt. The organic layer was washed three times with satd aq NaCl, dried over anhydrous MgSO₄, and concentrated in vacuo. The residue was chromatographed on SiO₂ and eluted with AcOEt/hexane (1:1) to give dihydrofuran (**20**) in 79.5% yield (111 mg). Amorphous orange solid; ¹H NMR (500 MHz, CD₃OD): δ_H 0.19 (s, 6H), 0.98 (s, 9H), 1.05 (s, 6H), 1.31 (s, 6H), 1.61–1.69 (m, 2H), 1.76–1.85 (m, 2H), 2.46 (t, *J*=7.3 Hz, 2H), 3.14 (s, 2H), 3.28–3.35 (m, 2H), 3.84 (s, 2H), 6.51–6.58 (m, 4H), 6.60–6.70 (m, 4H), 6.75 (s with fine coupling, 1H), 6.81 (d with fine coupling, *J*=8.2 Hz, 1H), 6.89 (d with fine coupling, *J*=7.6 Hz, 1H), 7.14 (d, *J*=8.2 Hz, 1H), 7.20 (dd, *J*=8.2 and 7.6 Hz, 1H), 7.83–7.90 (m, 1H), 8.29 (br s, 1H) ppm; ¹³C NMR (125 MHz, CD₃OD): δ_C -3.8, -3.6, 19.3, 24.0, 26.5 (×3), 28.0 (×2), 28.3 (×2), 30.6, 38.1, 38.4, 48.3, 49.6, 71.9, 81.0, 84.3, 103.9 (×2), 111.8 (×2), 113.9 (×2), 116.3, 121.3, 123.2, 124.2, 124.7, 126.0, 128.3, 129.4, 130.2, 130.4 (×2), 138.8, 142.1, 149.0, 152.5, 154.4 (×2), 156.6, 161.7 (br×2), 171.6, 175.0 ppm; IR (KBr): ν̄ 3338, 2956, 2930, 2860, 1738, 1609, 1259, 1179, 1114 cm⁻¹; HRMS (ESI): 828.3565, calcd for C₄₇H₅₅NO₉SiNa [M+Na]⁺ 828.3544.

4.2.15. 4-[7-(Fluorescein-5-yl)carbamoyl-1,1-dimethyl-3-oxahept-1-yl]-5-(3-hydroxyphenyl)-3,3-dimethyl-2,3-dihydrofuran (**21**). Tetrabutylammonium fluoride (1 M in THF, 2.08 mL, 2.08 mmol) was added to a solution of dihydrofuran **20** (508 mg, 0.630 mmol) in dry THF (4 mL) at 0 °C under a N₂ atmosphere and stirred for 0.5 h. The reaction mixture was poured into diluted aq HCl and extracted with AcOEt. The organic layer was washed three times with satd aq NaCl, dried over anhydrous MgSO₄, and concentrated in vacuo. The residue was chromatographed on SiO₂ and eluted with AcOEt/hexane (9:1) to give phenolic dihydrofuran **21** in 81.7% yield (356 mg). Amorphous orange solid; ¹H NMR (500 MHz, CD₃OD): δ_H 1.06 (s, 6H), 1.30 (s, 6H), 1.60–1.70 (m, 2H), 1.76–1.84 (m, 2H), 2.46 (t, *J*=7.3 Hz, 2H), 3.13 (s, 2H), 3.27–3.32 (m, 2H), 3.82 (s, 2H), 6.53 (dd, *J*=8.7 and 2.3 Hz, 2H), 6.62 (d, *J*=8.7 Hz, 2H), 6.66

(d, $J=2.3$ Hz, 2H), 6.72–6.73 (m, 1H), 6.75 (dd, $J=7.8$ and 1.8 Hz, 2H), 7.11–7.16 (m, 2H), 7.85 (dd, $J=8.2$ and 1.8 Hz, 1H), 8.31 (d, $J=1.4$ Hz, 1H) ppm; ^{13}C NMR (125 MHz, CD_3OD): δ_{C} 24.0, 28.0 ($\times 2$), 28.2 ($\times 2$), 30.5, 38.0, 38.3, 48.3, 50.1, 71.8, 80.9, 84.2, 103.8 ($\times 2$), 111.8 ($\times 2$), 114.0 ($\times 2$), 116.4 ($\times 2$), 118.3, 122.7, 123.9, 126.0, 128.3, 129.3, 130.1, 130.5 ($\times 2$), 138.5, 142.0, 148.9 (br), 152.7, 154.4 ($\times 2$), 158.1, 161.7 ($\times 2$), 171.6, 175.2 ppm; IR (KBr): $\tilde{\nu}$ 3393, 2957, 2869, 1735, 1607, 1313, 1179, 1115 cm^{-1} ; HRMS (ESI): 692.2869, calcd for $\text{C}_{41}\text{H}_{42}\text{NO}_9$ $[\text{M}+\text{H}]^+$ 692.2860, 714.2687, calcd for $\text{C}_{41}\text{H}_{41}\text{NO}_9\text{Na}$ $[\text{M}+\text{Na}]^+$ 714.2679.

4.2.16. 4-{7-[N-(4-Benzothiazol-2-yl)-3-hydroxyphenyl]methyl-carbamoyl}-1,1-dimethyl-3-oxahept-1-yl}-5-(3-tert-butyl-dimethylsilyloxyphenyl)-3,3-dimethyl-2,3-dihydrofuran (**23**). 2-(4-Aminomethyl-2-methoxyphenyl)benzothiazole (320 mg, 1.18 mmol) and Et_3N (0.20 mL, 1.43 mmol) were added to a solution of *N*-hydroxy-succinimide ester **6** (602 mg, 1.05 mmol) in CH_3CN (6 mL) under a nitrogen atmosphere at room temperature and stirred for 5 h. The reaction mixture was concentrated in vacuo. The residue was chromatographed on silica gel and eluted with AcOEt /hexane (1:2) to give amide **23** as a colorless oil in 86.3% yield (661 mg); ^1H NMR (400 MHz, CDCl_3): δ_{H} 0.17 (s, 6H), 0.97 (s, 9H), 1.03 (s, 6H), 1.29 (s, 6H), 1.55–1.64 (m, 2H), 1.71–1.80 (m, 2H), 2.30 (t, $J=7.4$ Hz, 2H), 3.10 (s, 2H), 3.27 (t, $J=6.1$ Hz, 2H), 3.84 (s, 2H), 4.02 (s, 3H), 4.49 (d, $J=5.9$ Hz, 2H), 5.95 (br s, 1H), 6.74–6.79 (m, 1H), 6.77 (s, 1H), 6.89 (d with fine coupling, $J=7.7$ Hz, 1H), 6.98 (s, 1H), 7.00 (d, $J=7.9$ Hz, 1H), 7.15 (t, $J=7.7$ Hz, 1H), 7.37 (dd with fine coupling, $J=8.2$ and 7.2 Hz, 1H), 7.49 (dd with fine coupling, $J=8.2$ and 7.2 Hz, 1H), 7.92 (d with fine coupling, $J=7.9$ Hz, 1H), 8.07 (d with fine coupling, $J=8.2$ Hz, 1H), 8.47 (d with fine coupling, $J=7.9$ Hz, 1H) ppm; ^{13}C NMR (125 MHz, CDCl_3): δ_{C} -4.4 ($\times 2$), 18.1, 22.9, 25.6 ($\times 3$), 27.2 ($\times 2$), 27.4 ($\times 2$), 29.0, 36.4, 37.0, 43.3, 47.0, 55.7, 70.7, 79.7, 83.0, 111.0, 119.8, 120.2, 121.2, 121.4, 121.7, 122.3, 122.7, 123.0, 124.6, 125.9, 128.7, 129.7, 136.0, 137.1, 142.8, 151.0, 152.1, 155.0, 157.3, 162.8, 172.9 ppm; IR (liquid film): $\tilde{\nu}$ 3299, 2955, 2930, 2859, 1649, 1577, 1463, 1419, 1264, 1125, 940 cm^{-1} ; Mass (m/z , %): 728 (M^+ , 1), 346 (31), 345 (100), 254 (10), 235 (13); HRMS (ESI): 729.3747, calcd for $\text{C}_{42}\text{H}_{57}\text{N}_2\text{O}_5\text{Si}$ $[\text{M}+\text{Na}]^+$ 729.3757.

4.2.17. 4-{7-[N-(4-Benzothiazol-2-yl)-3-hydroxyphenyl]methyl-carbamoyl}-1,1-dimethyl-3-oxahept-1-yl}-5-(3-hydroxyphenyl)-3,3-dimethyl-2,3-dihydrofuran (**24**). CH_3SNa (95%, 211 mg, 2.86 mmol) was added to a solution of amide **23** (493 mg, 0.676 mmol) in dry DMF (5 mL) under a nitrogen atmosphere at room temperature and stirred at 140 °C for 1 h. The reaction mixture was poured into satd aq NH_4Cl and extracted with AcOEt . The organic layer was washed three times with satd aq NaCl, dried over anhydrous MgSO_4 , and concentrated in vacuo. The residue was chromatographed on silica gel and eluted with AcOEt /hexane (2:1) to give amide **24** in 94.8% yield (385 mg). Colorless granules mp 132.5–133.0 °C (from AcOEt /hexane); ^1H NMR (500 MHz, CDCl_3): δ_{H} 1.01 (s, 6H), 1.29 (s, 6H), 1.57–1.64 (m, 2H), 1.77–1.90 (m, 2H), 2.35 (t, $J=7.2$ Hz, 2H), 3.10 (s, 2H), 3.29 (t, $J=5.7$ Hz, 2H), 3.85 (s, 2H), 4.50 (d, $J=5.8$ Hz, 2H), 5.91 (br s, 1H), 6.77–6.83 (m, 1H), 6.83 (d with fine coupling, $J=8.2$ Hz, 1H), 6.90 (dd, $J=7.9$ and 1.5 Hz, 1H), 7.00 (s with fine coupling, 1H), 7.03 (s with fine coupling, 1H), 7.16 (t, $J=7.9$ Hz, 1H), 7.42 (t with fine coupling, $J=7.9$ Hz, 1H), 7.51 (t with fine coupling, $J=7.9$ Hz, 1H), 7.66 (d, $J=8.2$ Hz, 1H), 7.91 (d, $J=7.9$ Hz, 1H), 7.99 (d, $J=7.9$ Hz, 1H), 8.32 (s, 1H), 12.60 (br s, 1H) ppm; ^{13}C NMR (125 MHz, CDCl_3): δ_{C} 22.9, 27.2 ($\times 2$), 27.7 ($\times 2$), 29.2, 36.1, 37.1, 43.3, 46.9, 70.3, 79.3, 82.9, 115.4, 115.8, 116.4, 117.3, 118.9, 121.1, 121.4, 121.4, 122.0, 125.5, 126.6, 128.7, 128.8, 132.5, 136.9, 143.2, 151.2, 151.6, 156.3, 157.9, 168.9, 173.9 ppm; IR (KBr): $\tilde{\nu}$ 3316, 2955, 2929, 2865, 1634, 1578, 1481, 1440, 1215, 759 cm^{-1} ; Mass (m/z , %): 600 (M^+ , 1), 255 (13), 244 (15), 232 (17), 231 (100); HRMS (ESI): 623.2517, calcd for $\text{C}_{35}\text{H}_{40}\text{N}_2\text{O}_5\text{SNa}$ $[\text{M}+\text{Na}]^+$ 623.2556.

4.2.18. 5-[7-(Fluorescein-5-yl)carbamoyl]-1,1-dimethyl-3-oxaheptyl]-1-(3-hydroxyphenyl)-4,4-dimethyl-2,6,7-trioxabicyclo[3.2.0]heptane (**3**). Dihydrofuran **21** (100 mg, 0.145 mmol) was irradiated in the presence of TPP (1.0 mg) externally with a 940 W Na-lamp in CH_2Cl_2 (10 ml) and CH_3OH (10 drops) under an O_2 atmosphere at 0 °C for 1 h. The photolysate was concentrated in vacuo. The residue was chromatographed on SiO_2 and eluted with CH_2Cl_2 /ether to give dioxetane **3** in 84.6% yield (88.8 mg). Amorphous orange solid; ^1H NMR (500 MHz, CD_3OD): δ_{H} 0.87 (s, 3H), 1.13 (s, 3H), 1.17 (s, 3H), 1.39 (s, 3H), 1.56–1.66 (m, 2H), 1.72–1.84 (m, 2H), 2.45 (t, $J=7.3$ Hz, 2H), 3.25 (d, $J=9.2$ Hz, 1H), 3.33–3.40 (m, 3H), 3.38 (d, $J=9.2$ Hz, 1H), 3.79 (d, $J=8.0$ Hz, 1H), 4.47 (d, $J=8.0$ Hz, 1H), 6.53 (dd, $J=8.7$ and 2.3 Hz, 2H), 6.63 (d, $J=8.7$ Hz, 2H), 6.60 (d, $J=2.3$ Hz, 2H), 6.80–6.85 (m, 1H), 7.05 (s, 1H), 7.06 (d, $J=7.9$ Hz, 1H), 7.14 (d, $J=8.2$ Hz, 1H), 7.22 (dd, $J=8.2$ and 7.9 Hz, 1H), 7.86 (dd, $J=8.2$ and 1.8 Hz, 1H), 8.31 (d, $J=1.8$ Hz, 1H) ppm; ^{13}C NMR (125 MHz, CD_3OD): δ_{C} 18.5, 21.6, 23.3, 24.0 ($\times 2$), 25.3, 30.3, 38.0, 42.5, 46.9, 72.1, 77.7, 81.4, 103.8 ($\times 2$), 106.6, 111.8 ($\times 2$), 114.0 (br, $\times 2$), 116.4 (br), 116.8, 117.8, 118.5, 121.0, 126.0, 128.4, 129.4, 130.3, 130.5 ($\times 2$), 138.9, 142.1, 149.0 (br), 154.5 ($\times 2$), 158.5, 161.7 (br $\times 2$), 171.6, 175.1 ppm; IR (KBr): $\tilde{\nu}$ 3353, 2925, 2871, 1735, 1671, 1606, 1312, 1114 cm^{-1} ; HRMS (ESI): 746.2553, calcd for $\text{C}_{41}\text{H}_{41}\text{NO}_{11}\text{Na}$ $[\text{M}+\text{Na}]^+$ 746.2577.

4.2.19. 5-{7-[N-(4-Benzothiazol-2-yl)-3-hydroxyphenyl]methyl-carbamoyl}-1,1-dimethyl-3-oxahept-1-yl}-1-(3-hydroxyphenyl)-4,4-dimethyl-2,6,7-trioxabicyclo[3.2.0]heptane (**4**). A solution of dihydrofuran **24** (150 mg, 0.250 mmol) and TPP (3 mg) in CH_2Cl_2 (10 ml) was irradiated externally with 940 W Na-lamp under an oxygen atmosphere at 0 °C for 1 h. The photolysate was concentrated in vacuo. The residue was chromatographed on silica gel and eluted with CH_2Cl_2 and ether/ CH_2Cl_2 (1:1) to give dioxetane **4** in quantitative yield. Compound **4**: Colorless amorphous solid; ^1H NMR (400 MHz, CDCl_3): δ_{H} 0.87 (s, 3H), 1.04 (s, 3H), 1.12 (s, 3H), 1.35 (s, 3H), 1.50–1.82 (m, 4H), 2.27–2.43 (m, 2H), 3.23 (d, $J=9.3$ Hz, 1H), 3.29–3.42 (m, 2H), 3.57 (d, $J=9.3$ Hz, 1H), 3.80 (d, $J=8.0$ Hz, 1H), 4.45–4.55 (m, 2H), 4.54 (d, $J=8.0$ Hz, 1H), 6.35 (t, $J=5.6$ Hz, 1H), 6.89 (d with fine coupling, $J=8.1$ Hz, 1H), 6.96 (d with fine coupling, $J=8.1$ Hz, 1H), 7.06–7.10 (m, 2H), 7.22–7.28 (m, 2H), 7.41 (dd with fine coupling, $J=7.9$ and 7.3 Hz, 1H), 7.51 (dd with fine coupling, $J=8.1$ and 7.3 Hz, 1H), 7.67 (d, $J=8.1$ Hz, 1H), 7.90 (d with fine coupling, $J=7.9$ Hz, 1H), 7.99 (d with fine coupling, $J=8.1$ Hz, 1H), 12.72 (br s, 1H) ppm; ^{13}C NMR (125 MHz, CDCl_3): δ_{C} 18.0, 20.9, 22.4, 23.5, 24.6, 28.2, 36.0, 40.8, 43.2, 45.5, 71.5, 76.9, 80.0, 105.6, 115.7, 115.8, 116.6, 116.8, 116.9, 119.2, 119.9, 121.4, 122.0, 125.5, 126.6, 128.7, 129.2, 132.5, 136.9, 143.8, 151.6, 156.4, 157.7, 169.0, 174.1 ppm; IR (KBr): $\tilde{\nu}$ 3342, 2948, 2872, 1632, 1583, 1481, 1316, 1216, 759 cm^{-1} ; Mass (m/z , %): 632 (M^+ , 89), 482 (12), 356 (22), 355 (10), 340 (12), 339 (58), 326 (11), 278 (35), 257 (17), 256 (30), 255 (100), 241 (12), 240 (14), 228 (11), 227 (18), 221 (26), 121 (26), 100 (45), 94 (55), 83 (24), 71 (10), 56 (11); HRMS (ESI): 655.2434, calcd for $\text{C}_{35}\text{H}_{40}\text{N}_2\text{O}_7\text{SNa}$ $[\text{M}+\text{Na}]^+$ 655.2454.

4.3. Measurement of chemiluminescence and time-course of the base-induced decomposition of dioxetanes: general procedure

Chemiluminescence was measured using a JASCO FP-750 and/or FP-6500 spectrometer, and a Hamamatsu Photonics PMA-11 multi-channel detector.

4.3.1. TBAF/acetonitrile system. A freshly prepared solution (2.00 mL) of TBAF (1.0×10^{-2} mol/L) in acetonitrile was transferred to a quartz cell ($10 \times 10 \times 50$ mm), which was placed in a spectrometer that was thermostated with stirring at 25 °C. After 3–5 min, a solution of dioxetane **3** or **4** in acetonitrile (1.0×10^{-4} mol/L, 1.00 mL) was added by means of a syringe, and measurement was

started immediately. The time-course of the intensity of light emission was recorded and processed according to first-order kinetics. The total light emission was estimated by comparing it with that of an adamantylidene dioxetane, the chemiluminescent efficiency ϕ^{CL} of which has been reported to be 0.29 and which was used here as a standard.^{17,18}

4.3.2. NaOH/H₂O system. A freshly prepared solution (2.00 mL) of NaOH (0.1 M) in H₂O was transferred to a quartz cell (10×10×50 mm), which was placed in a spectrometer that was thermostated with stirring at 25 °C. After 3–5 min, a solution of dioxetane **3** or **4** in H₂O containing acetonitrile (9:1) (1.0×10⁻⁴ mol/L, 1.00 mL) was added by means of a syringe, and measurement was started immediately. The time-course of the intensity of light emission was recorded and processed according to first-order kinetics. The total light emission was estimated as in the case of solvent-promoted decomposition described above.

4.3.3. NaOH/H₂O system including a fluorescer. Except for the use of NaOH in H₂O (0.1 M) including acetamidofluorescein **25** (1.0×10⁻³ M) or *N*-[4-(benzothiazol-2-yl)-3-hydroxybenzyl]acetamide **26** (1.0×10⁻³ M) in place of NaOH in H₂O (0.1 M) without any additive, the chemiluminescent reaction was carried out as in the NaOH/H₂O system described above.

4.3.4. NaOH/H₂O system including a surfactant. Except for the use of NaOH in H₂O (0.1 M) including tributylhexadecylphosphonium bromide **27** (1.0×10⁻³ M) in place of NaOH in H₂O (0.1 M) without any additive, the chemiluminescent reaction was carried out as in the NaOH/H₂O system described in Section 4.3.2.

Acknowledgements

The authors gratefully acknowledge financial assistance provided by Grants-in aid (No. 17550050 and No. 21550052) for Scientific Research from the Ministry of Education, Culture, Sports, Science, and Technology, Japan.

Supplementary data

Supplementary data associated with this article can be found in the online version, at doi:10.1016/j.tet.2012.04.078.

References and notes

- Schaap, A. P.; Gagnon, S. D. *J. Am. Chem. Soc.* **1982**, *104*, 3504–3506.
- (a) Schaap, A. P.; Handley, R. S.; Giri, B. P. *Tetrahedron Lett.* **1987**, *28*, 935–938; (b) Schaap, A. P.; Chen, T. S.; Handley, R. S.; DeSilva, R.; Giri, B. P. *Tetrahedron Lett.* **1987**, *28*, 1155–1158.
- Reviews of dioxetane-based chemiluminescence, see: (a) Beck, S.; Köster, H. *Anal. Chem.* **1990**, *62*, 2258–2270; (b) Adam, W.; Reihardt, D.; Saha-Möller, C. R. *Analyst* **1996**, *121*, 1527–1531; (c) Matsumoto, M. *J. Photochem. Photobiol., C: Photochem. Rev.* **2004**, *5*, 27–53; (d) Matsumoto, M.; Watanabe, N. *Bull. Chem. Soc. Jpn.* **2005**, *78*, 1899–1920.
- (a) Adam, W.; Trofimov, A. V. In *The Chemistry of Peroxides*; Rappoport, Z., Ed.; Wiley: New York, NY, 2006; Vol. 2, pp 1171–1209; (b) Baader, W. J.; Stevani, C. V.; Bastos, E. L. In *The Chemistry of Peroxides*; Rappoport, Z., Ed.; Wiley: New York, NY, 2006; Vol. 2, pp 1211–1278.
- (a) Trofimov, A. V.; Vasil'ev, R. F.; Mielke, K.; Adam, W. *Photochem. Photobiol.* **1995**, *62*, 35–43; (b) Adam, W.; Bronstein, I.; Edwards, B.; Engel, T.; Reinhardt, D.; Schneider, F. W.; Trofimov, A. V.; Vasil'ev, R. F. *J. Am. Chem. Soc.* **1996**, *118*, 10400–10407; (c) Adam, W.; Bronstein, I.; Trofimov, T.; Vasil'ev, R. F. *J. Am. Chem. Soc.* **1999**, *121*, 958–961.
- (a) Matsumoto, M.; Mizoguchi, Y.; Motoyama, T.; Watanabe, N. *Tetrahedron Lett.* **2001**, *42*, 8869–8872; (b) Matsumoto, M.; Watanabe, N.; Kasuga, N. C.; Hamada, F.; Tadokoro, K. *Tetrahedron Lett.* **1997**, *38*, 2863–2866; (c) Adam, W.; Matsumoto, M.; Trofimov, T. *J. Am. Chem. Soc.* **2000**, *122*, 8631–8634.
- (a) Bronstein, I.; Edwards, B.; Voyta, J. C. *J. Biolumin. Chemilumin.* **1989**, *4*, 99–111; (b) Schaap, A. P.; Akhavan, H.; Romano, R. J. *Clin. Chem.* **1989**, *35*, 1863–1864.
- Yamada, M.; Kitaoka, K.; Matsumoto, M.; Watanabe, N. In *Bioluminescence and Chemiluminescence*; Tsuji, A., Matsumoto, M., Maeda, M., Kricka, L. J., Stanley, P. E., Eds.; World Scientific: Singapore, 2004; pp 487–490.
- It has been reported in a patent 10 that a dioxetane tethering a fluorescein through an ω,ω' -dioxyalkylene linker instead of a methoxy group in **1** shows enhanced chemiluminescence.
- Schaap, A. P.; Akhavan-Tafti, H. PCT/US89/05741, WO 90/07511.
- Although the methoxy group of parent dioxetane **1** can easily be modified to a substituted alkoxy, aryloxy or alkylsulfanyl group, such modification directly affects chemiluminescence properties.^{10,12} On the other hand, structural modification of the adamantylidene would not easily be attained: even if such modification is attained, the thus-synthesized analogs of **1** decompose to two molecules, i.e., an oxidobenzoate in the excited state and a modified adamantanone, which would rapidly separate from each other.
- Akhavan-Tafti, H.; Eickholt, R. A.; Arghavani, Z.; Schaap, A. P. *J. Am. Chem. Soc.* **1997**, *119*, 245–246.
- We attempted to use ω -oxypentanoic acid unit as a representative of linker, since ω -oxy- or ω -amino-substituted C₅ or C₆ carboxylic acid has been often used as a linker for fluorescent probes.¹⁴
- (a) Walter, N. G.; Burke, J. M.; Millar, D. P. *Nat. Struct. Biol.* **1999**, *6*, 544–549; (b) Tsybul'sky, D. A.; Kvach, M. V.; Stepanova, I. A.; Korshun, V. A. *J. Org. Chem.* **2012**, *77*, 977–984; (c) Tiancheng, L.; Nedrow-Byers, J. R.; Hopkins, M. R.; Berkman, C. E. *Bioorg. Med. Chem. Lett.* **2011**, *21*, 7013–7016; (d) See also Haugland, R. P. In *A Guide to Fluorescent Probes and Labeling Technologies*, 10th ed.; Spence, M. T. Z., Ed.; Invitrogen: Carlsbad, 2005.
- Advanced intermediate **6** could lead, under mild reaction conditions, to dioxetanes tethering a various functional auxiliary or junctioning a biomacromolecule or a modified solid surface. Key building block **7** was also useful to synthesize various analogs of dioxetane **2** functionalized on a methyl of a *tert*-butyl group, since a primary OH group in **7** was far more reactive than another OH group for nucleophilic displacements. The results will be reported elsewhere in near future.
- Matsumoto, M.; Watanabe, N.; Ishikawa, A.; Murakami, H. *Chem. Commun.* **1997**, 2395–2396.
- ϕ^{CL} was estimated based on the value 0.29 for the chemiluminescent decomposition of 3-adamantylidene-4-methoxy-4-(3-oxidophenyl)-1,2-dioxetane in a TBAF/DMSO system.¹⁸
- Trofimov, A. V.; Mielke, K.; Vasil'ev, R. F.; Adam, W. *Photochem. Photobiol.* **1996**, *63*, 463–467.
- Turro, N. J.; Ramamurthy, V.; Scaiano, J. C. *Modern Molecular Photochemistry of Organic Chemistry*; University Science: Sausalito, 2010, pp 383–481.
- Effect of concentration of fluorescer **25** or **26** on ϕ^{CL} was preliminarily examined in the range of 10⁻⁵–10⁻² M and 10⁻³ M of the fluorescer (**25**/**26**)/**2a** ≈ 20) was found to be the most effective to improve ϕ^{CL} for CTID of **2a** in NaOH/H₂O system. On the other hand, in a TBAF/acetonitrile system, even 10⁻⁴ M of the fluorescer (**25**/**2a** ≈ 200) was insufficient for the intermolecular energy-transfer chemiluminescence.
- Surfactant **27** was initially expected not to improve ϕ^{I} of a fluorescein moiety, since ϕ^{I} of acetamidofluorescein **25** as a model fluorophore in **3** was higher in an aqueous medium rather than in an aprotic medium: 0.73 in NaOH/H₂O versus 0.52 in TBAF/acetonitrile.



N-Acyl group-directed color modulation in the *t*-BuOK-mediated chemiluminescent decomposition of hydroxyaryl-substituted dioxetanes fused with a pyrrolidine ring

Nobuko Watanabe, Kairi Matsumoto, Teruhiko Tanaka, Haruna Suzuki, Hisako K. Ijuin, Masakatsu Matsumoto*

Department of Chemistry, Kanagawa University, Tsuchiya, Hiratsuka, Kanagawa 259-1293, Japan

ARTICLE INFO

Article history:

Received 9 June 2012

Revised 12 July 2012

Accepted 20 July 2012

Available online 27 July 2012

Keywords:

Dioxetane

Chemiluminescence

Color modulation

ABSTRACT

Bicyclic dioxetanes, 1-(hydroxyaryl)-2-aza-6,7-dioxabicyclo[3.2.0]heptanes, bearing a *syn*-*N*-acyl or *anti*-*N*-acyl group underwent TBAF (tetrabutylammonium fluoride)-induced decomposition in DMSO or THF accompanied by the emission of bright light, the maximum wavelengths ($\lambda_{\text{max}}^{\text{CL}}$) of which were similar to each other. On the other hand, upon treatment with *t*-BuOK in THF, the dioxetanes bearing a *syn*-*N*-acyl group emitted light that showed a dramatic red-shift compared to that in a TBAF/THF system, while the dioxetanes bearing an *anti*-*N*-acyl group showed light with a blue-shift. For oxidoaryl-substituted dioxetanes bearing a *syn*-*N*-acyl group, *t*-BuOK most likely coordinated with both a *syn*-*N*-acyl and an oxygen of the dioxetane ring, so that two imide carbonyls in the produced emitter possessed a considerably regulated structure leading to a red-shift in the chemiluminescence. Such coordination of K^+ was hardly expected for the case of the dioxetanes bearing an *anti*-*N*-acyl group, for which the strong contact of K^+ to an oxidoaryl group presumably caused a blue-shift in chemiluminescence.

© 2012 Elsevier Ltd. All rights reserved.

A dioxetane bearing an electron-rich aromatic substituent undergoes intramolecular charge-transfer-induced decomposition (CTID) accompanied by the emission of light. This phenomenon has received considerable attention due to interest in the mechanism of bioluminescence and chemiluminescence and in its possible application to high-performance biological and clinical analysis.^{1–6} Thus, a wide variety of CTID-active dioxetanes have been designed and synthesized. One of these dioxetanes is *N*-acylamino-substituted bicyclic dioxetane **1**.^{7–9}

Dioxetane **1** possesses unique stereochemical characteristics due to the presence of an *N*-acyl group, in contrast to the related dioxetane **2**, which is fused with a tetrahydrofuran ring. First, large steric interaction between *N*-acyl and aryl groups at the C_1 causes rotational isomerism between the *syn*-aryl form and *anti*-aryl form⁷ around the axis that joins an aryl to the C_1 carbon, when the aryl group has a hydroxyl group at an asymmetrical position, as shown in Figure 1 (type A isomerism).^{8,9} This *syn*-aryl/*anti*-aryl isomerism has very recently been found to significantly affect the chemiluminescence efficiency ϕ^{CL} for CTID of dioxetanes **1**.⁹ Second, the *N*-acyl group would cause another isomerism between the *syn*-acyl form and *anti*-acyl form,⁷ though only the *anti*-acyl form has been observed to date (type B isomerism in Fig. 1). We

report here that, in addition to the *anti*-acyl form, dioxetanes **1** with the *syn*-acyl form were observed and that the *syn*/*anti* stereochemistry of the *N*-acyl group could lead to a new type of color modulation for CTID-active dioxetanes.^{10,11}

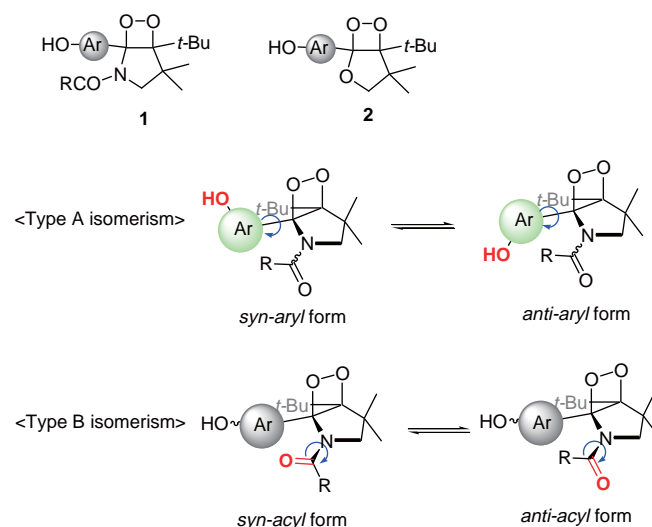


Figure 1. Conformational isomers for hydroxyaryl-substituted dioxetanes fused with an *N*-acylpyrrolidine ring.

* Corresponding author. Tel.: +81 463 59 4111; fax: +81 463 58 9684.

E-mail address: matsumo-chem@kanagawa-u.ac.jp (M. Matsumoto).

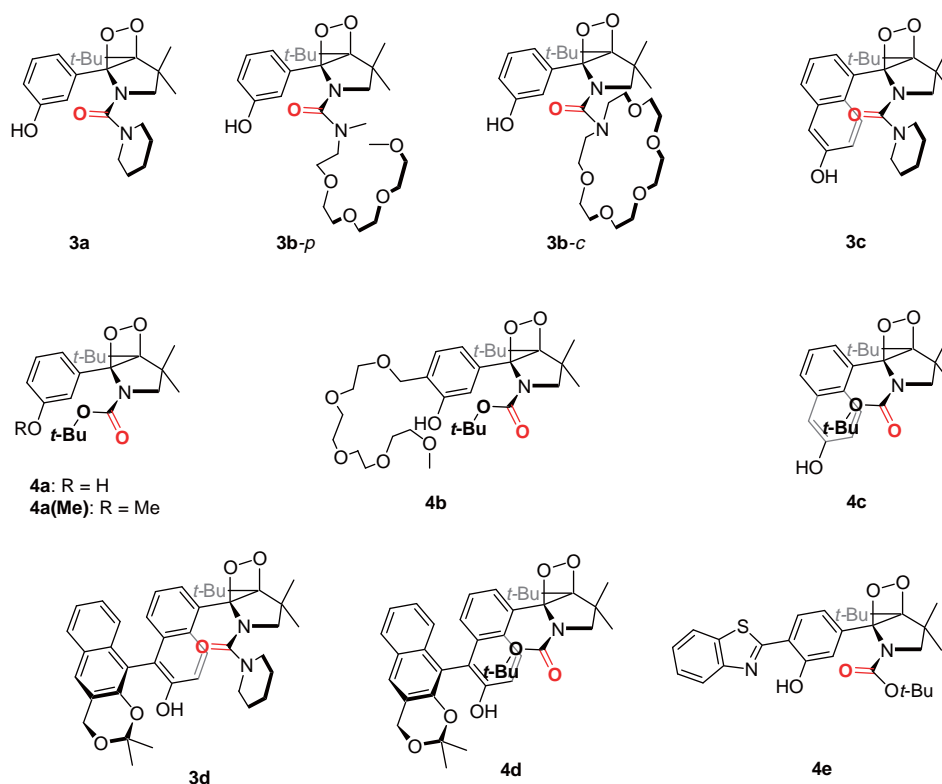


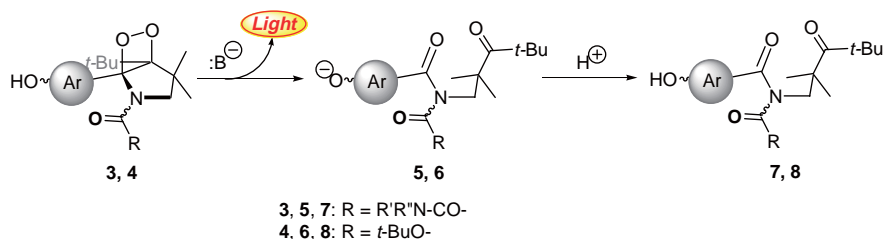
Figure 2. Hydroxyaryl-substituted dioxetanes **3** and **4** fused with an *N*-acylpyrrolidine ring.

The new type of color modulation for chemiluminescence that will be described here was developed for *N*-acyl-substituted dioxetanes **3a–d** and **4a–e**: the former possessed a urea-type substituent, while the latter possessed an *N*-Boc as a representative carbamate-type substituent (Fig. 2). This work started from a casual finding. We had preliminarily investigated CTID of dioxetanes **3b-p** and **3b-c** bearing an *N*-acyl group functionalized as a podand or crown ether, respectively, and dioxetane **4b** as their reference, to understand whether or not dioxetanes bearing such a functionalized *N*-acyl group could become a new chemiluminescence system for recognizing molecules and/or ions.

When **3b-p**, **3b-c**, and their reference **4b** were individually treated with a large excess of TBAF (tetrabutylammonium fluoride) in DMSO at 25 °C, they decomposed according to pseudo-first order kinetics with an accompanying effective emission of yellow light, the maximum wavelength ($\lambda_{\text{max}}^{\text{CL}}$) of which was 563, 569, and 566 nm, respectively (Scheme 1). Their chemiluminescence properties, that is, $\lambda_{\text{max}}^{\text{CL}}$, chemiluminescence efficiency (ϕ^{CL}) and rate of CTID (k^{CTID}), are shown in Table 1.^{12,13} These $\lambda_{\text{max}}^{\text{CL}}$ values were similar to those of the parent dioxetanes **3a** possessing an *N*-(piperidin-1-yl)carbonyl group and **4a** possessing an *N*-Boc group.

Upon treatment with TBAF in THF instead of TBAF in DMSO, **3b-p**, **3b-c**, and **4b** similarly underwent CTID to give yellow light, though their $\lambda_{\text{max}}^{\text{CL}}$ values showed a red-shift of 10–18 nm (Table 1, Fig. 3). The chemiluminescence properties ($\lambda_{\text{max}}^{\text{CL}}$, ϕ^{CL} and k^{CTID}) for **3b-p**, **3b-c**, and **4b** quite resembled those of the parent dioxetanes **3a** and **4a** in both TBAF/DMSO and TBAF/THF systems. Notably, all of the spent reaction mixtures for **3a**, **3b-p**, **3b-c**, and **4a–b** in both TBAF/DMSO and TBAF/THF exclusively gave the corresponding ketoimides **7a**, **7b-p**, **7b-c**, and **8a–b** after careful neutralization. Thus, the CTID of **3a**, **3b-p**, **3b-c**, and **4a–b** was strongly suggested to give the corresponding anionic ketoimides **5a**, **5b-p**, **5b-c**, and **6a–b** in the excited state, as shown in Scheme 1.

As described above, the functionalized *N*-substituent on a pyrrolidine ring for **3b-p** or **3b-c** did not practically affect the change in the color of chemiluminescence when TBAF was used as a base. However, CTID of these dioxetanes showed characteristic changes in chemiluminescence in a *t*-BuOK/THF system. When **3b-p** and **3b-c** were treated with *t*-BuOK in THF, they emitted orange–red light with $\lambda_{\text{max}}^{\text{CL}} = 616$ and 599 nm, respectively (Fig. 3 and Table 1). Thus, the change in the base from TBAF to *t*-BuOK caused a considerable red-shift of the chemiluminescence spectra (20–40 nm)



Scheme 1. Base-induced chemiluminescent decomposition of hydroxyaryl-substituted dioxetanes.

Table 1
Chemiluminescence properties of dioxetanes **3a–d** and **4a–e** in a TBAF/DMSO, TBAF/THF or *t*-BuOK/THF system^{a,b}

	TBAF/DMSO ^c			TBAF/THF ^d			<i>t</i> -BuOK/THF ^e		
	$\lambda_{\text{max}}^{\text{CL}}(\text{nm})$	ϕ^{CL}	$k^{\text{CTID}}(\text{s}^{-1})$	$\lambda_{\text{max}}^{\text{CL}}(\text{nm})$	ϕ^{CL}	$k^{\text{CTID}}(\text{s}^{-1})$	$\lambda_{\text{max}}^{\text{CL}}(\text{nm})$	ϕ^{CL}	$k^{\text{CTID}}(\text{s}^{-1})$
3a	564	1.8×10^{-2}	2.7×10^{-3}	578	8.3×10^{-3}	2.6×10^{-3}	620 [†]	1.4×10^{-3}	6.7×10^{-2}
3b-p	563	1.6×10^{-2}	2.2×10^{-3}	576	7.4×10^{-3}	1.5×10^{-3}	616 [†]	5.0×10^{-4}	5.7×10^{-3}
3b-c	569	2.4×10^{-2}	2.1×10^{-3}	579	9.5×10^{-3}	2.1×10^{-3}	599 [†]	2.1×10^{-3}	4.5×10^{-3}
3c^f	650	1.3×10^{-3}	2.8×10^{-3}	685	6.5×10^{-4}	7.4×10^{-4}	770 [†]	6.7×10^{-5}	1.4×10^{-2}
3d	662	1.4×10^{-3}	2.0×10^{-3}	683	3.7×10^{-4}	3.4×10^{-3}	766 [†]	9.2×10^{-5}	2.9×10^{-3}
4a	571	8.5×10^{-3}	4.2×10^{-2}	590	2.9×10^{-3}	5.8×10^{-3}	565 [‡]	1.1×10^{-3}	2.5×10^{-3}
4b	566	1.1×10^{-2}	5.5×10^{-2}	584	3.8×10^{-3}	2.7×10^{-3}	522 [‡]	2.3×10^{-3}	3.3×10^{-3}
4c^h	678	2.8×10^{-4}	3.2×10^{-2}	693	6.1×10^{-4}	8.3×10^{-3}	685 [‡]	2.3×10^{-4}	6.8×10^{-3}
4d^h	680	2.2×10^{-4}	1.6×10^{-1}	682	4.3×10^{-5}	2.2×10^{-1}	660 [‡]	3.7×10^{-4}	6.2×10^{-3}
4e^h	542	0.15	1.2×10^{-4}	544	0.19	2.9×10^{-2}	588 [†]	0.11	1.4×10^{-2}
9ⁱ	582	1.7×10^{-2}	3.7×10^{-2}	607	6.2×10^{-3}	1.1×10^{-2}	583 [‡]	2.2×10^{-3}	5.6×10^{-3}

^a Unless stated otherwise, the base-induced decomposition of dioxetanes was carried out at 25 °C.

^b Chemiluminescence efficiencies ϕ^{CL} were based on a value reported for the chemiluminescent decomposition of 3-adamantylidene-4-(3-*tert*-butyldimethylsilyloxyphenyl)-4-methoxy-1,2-dioxetane in TBAF/DMSO.¹³

^c A solution of dioxetane in DMSO (1.0×10^{-4} – 1.0×10^{-5} M, 1 mL) was added to a solution of TBAF in DMSO (1.0×10^{-2} M, 2 mL).

^d A solution of dioxetane in THF (1.0×10^{-4} , 1 mL) was added to a solution of TBAF in THF (1.0×10^{-2} M, 2 mL).

^e A solution of dioxetane in THF (1.0×10^{-4} , 1 mL) was added to a solution of *t*-BuOK in THF (1.0×10^{-2} M, 2 mL).

^f The symbol [†] indicates that $\lambda_{\text{max}}^{\text{CL}}$ showed a red-shift when the triggering system changed from TBAF/THF to *t*-BuOK/THF, while [‡] indicates a blue-shift $\lambda_{\text{max}}^{\text{CL}}$.

^g At 45 °C for both the TBAF/DMSO and *t*-BuOK/THF systems.

^h At 45 °C for the *t*-BuOK/THF system.

ⁱ Ref. 11.

for **3b-p** and **3b-c**. On the other hand, upon treatment with *t*-BuOK in THF, dioxetane **4b** gave light, the spectrum of which showed a blue-shift of 62 nm compared to that in the TBAF/THF system.

The opposite trend (red-shift/blue-shift) seen between the chemiluminescence spectra of **3b** and **4b** in a *t*-BuOK/THF system was thought to be due to the crown ether or podand moiety attached to the *N*-acyl group for **3b-p** and **3b-c**. However, even the parent dioxetane **3a** exhibited chemiluminescence in a *t*-BuOK/THF system, which also showed a large red-shift compared to the case in TBAF/THF. In contrast, the parent dioxetane **4a** showed chemiluminescence with a blue-shift (Fig. 3 and Table 1). These results showed that, for CTID in a *t*-BuOK/THF system, the red-shift in

chemiluminescence was likely common among dioxetanes **3a** and **3b** with a urea-type *N*-acyl group, while the blue-shift in chemiluminescence was likely common among dioxetanes **4a** and **4b** with an *N*-Boc (carbamate-type *N*-acyl) group.

To clarify whether or not this phenomenon has greater applicability, we further investigated the chemiluminescent decomposition of related dioxetanes in a *t*-BuOK/THF system. We considered two pairs of dioxetanes bearing an *N*-Boc or a urea-type *N*-acyl group: one was a pair of dioxetanes bearing a 6-hydroxy-1-naphthyl group **3c** vs **4c**, while the other was a pair bearing a 2-hydroxy-1,1'-binaphthyl-5-yl group **3d** vs **4d**. As expected, when the base for triggering was changed from TBAF to *t*-BuOK in THF, the

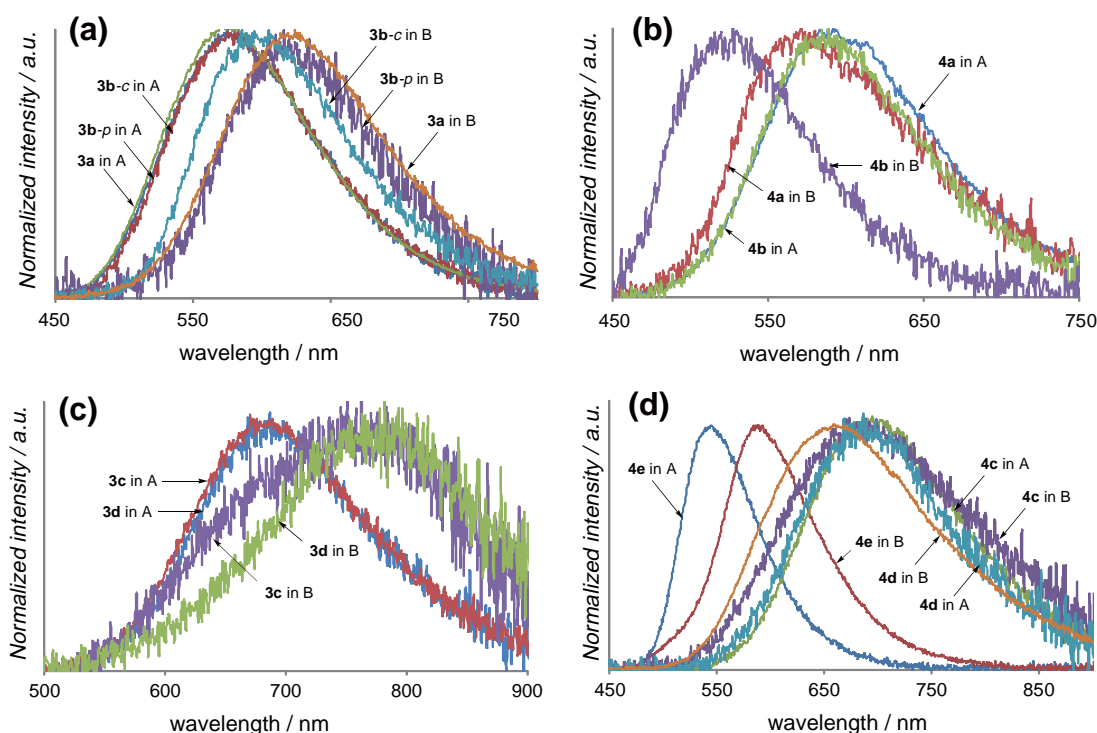


Figure 3. Chemiluminescence spectra for the base-induced decomposition of dioxetanes **3a–d** and **4a–e**: (a) **3a–b**, (b) **4a–b**, (c) **3c–d**, (d) **4c–e**; A refers to a TBAF/THF system, while B refers to a *t*-BuOK/THF system.

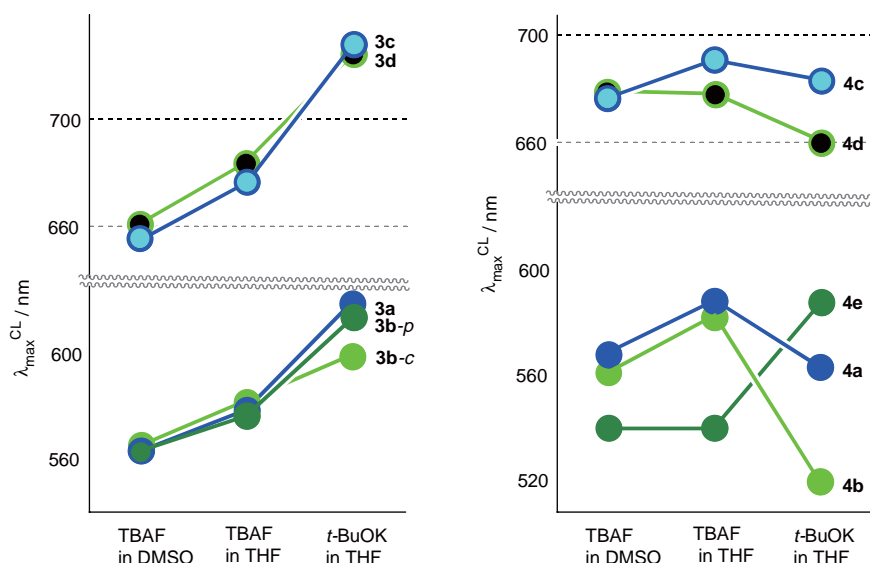


Figure 4. Color modulation in the base-induced chemiluminescent decomposition of dioxetanes **3** and **4**.

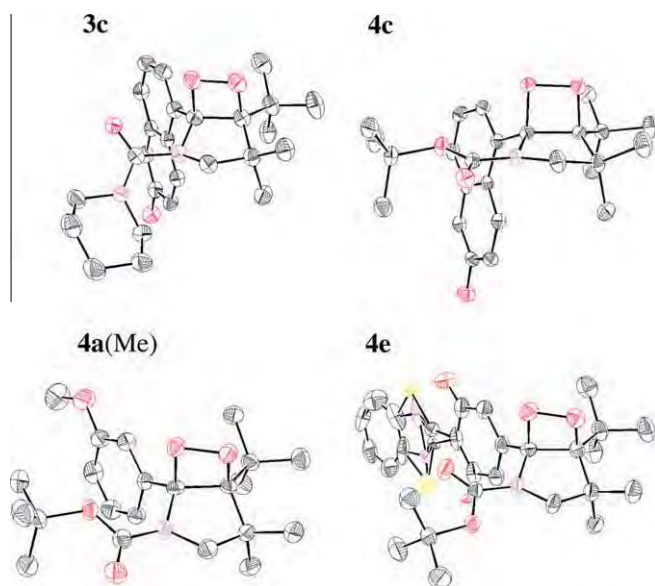


Figure 5. ORTEP structures of dioxetanes.

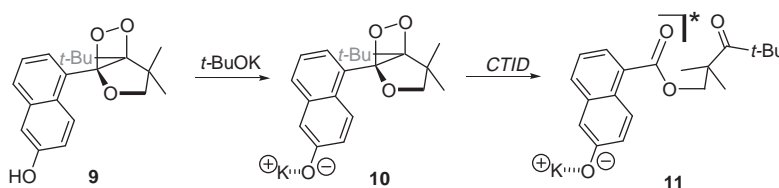
chemiluminescence spectra for both **3c** and **3d** showed a considerable red-shift, while those for **4c** and **4d** showed a blue-shift (Fig. 3 and Table 1). The overall trend in color modulation described above for **3** and **4** is shown in Figure 4.

Among the *N*-substituted bicyclic dioxetanes **3a–d** and **4a–d** investigated here, the structures of **3c** and **4c** were determined by X-ray single crystallographic analysis, as illustrated in Figure

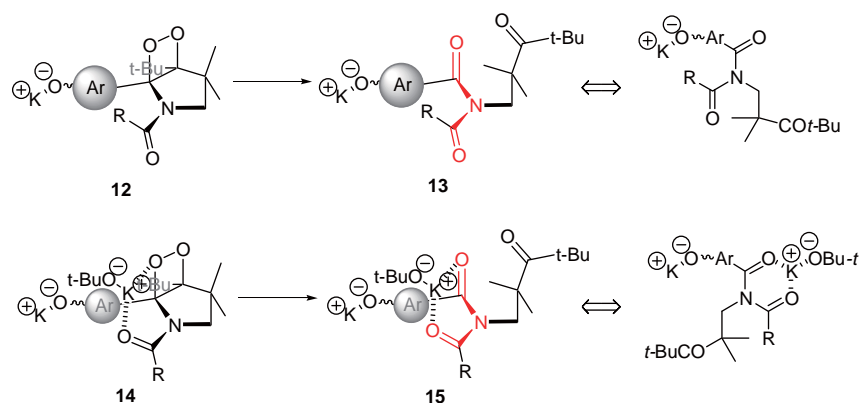
5.^{14–16} As shown, dioxetane **3c** with an *N*-(piperidin-1-yl)carbonyl group possesses a *syn*-acyl form, while **4c** with an *N*-Boc group possesses an *anti*-acyl form. Furthermore, if we consider that the 3-methoxy-analog **4a(Me)** of **4a** has an *anti*-acyl form observed by X-ray single crystallographic analysis,⁸ **4a** should also possess an *anti*-acyl form. These findings suggest that the red-shift/blue-shift color modulation caused by *t*-BuOK was presumably due to the difference in the orientation of the *N*-acyl carbonyl group between dioxetanes **3a–d** and **4a–d**.

Tetrahydrofuran-analog **9** underwent CTID to give light, the $\lambda_{\max}^{\text{CL}}$ of which showed a blue-shift, as in the case of **4c**, when the triggering system changed from TBAF/THF to *t*-BuOK/THF (Table 1). This blue-shift was thought to be due to the strong interaction between K^+ ion and naphthoxido anion to form a contact ion pair for both the intermediate dioxetane **10** and emitter **11**, in contrast to the case with TBAF, as illustrated in Scheme 2. This would be also the case with the blue-shifted chemiluminescence for dioxetanes **4a–d** with an *anti*-acyl form. Thus, dioxetanes **4a–d** produce oxidoaryl anion **12** with K^+ which decomposes to ketoimide **13** in the excited state (Scheme 3).

For dioxetanes **3a–d** with a *syn*-acyl form, the contact ion pair between K^+ and an aryloxido anion would also form as in the case of **4a–d** in a *t*-BuOK/THF system. However, their chemiluminescence showed a red-shift, in contrast to the case with **4a–d**. Thus, the red-shift of chemiluminescence for **3a–d** can be attributed to some factor that is stronger than the effect of the contact ion pair between K^+ and an oxidoaryl anion. A strong candidate to explain this phenomenon is the participation of an *N*-acyl group in the presence of *t*-BuOK, which is characteristic for a *syn*-acyl form, but not an *anti*-acyl form. A difference in coordination with K^+ between the *syn*-acyl and *anti*-acyl conformations is that the former carbonyl can presumably coordinate with *t*-BuOK (or K^+) together



Scheme 2. *t*-BuOK-mediated CTID of dioxetane **9**.



Scheme 3. Coordination of K^+ and/or $t\text{-BuOK}$ to dioxetanes and imides.

with an oxygen of dioxetane O–O to form the intermediate dioxetane **14**, as illustrated in Scheme 3. Dioxetane **14** decomposes to ketoimide **15** in the excited state, to which $t\text{-BuOK}$ (or K^+) coordinates as it is, so that two imide carbonyls lie in the same orientation. Notably, ketoimide **13** produced from dioxetane **12** would possess two imide carbonyls which lie in opposite directions relative to each other. An MO calculation suggested that the $\pi \rightarrow \pi^*$ transition energy ($E_{\pi \rightarrow \pi^*}$) for **15** was considerably smaller than that for **13**.¹⁷

We found that 4-(benzothiazol-2-yl)-3-hydroxyphenyl-substituted dioxetane **4e** possessing an *N*-Boc group has a *syn-acyl* form by X-ray single crystallographic analysis, in contrast to its analog **4a–d**, as illustrated in Figure 5. When dioxetane **4e** was treated with TBAF in DMSO or THF, it emitted light with $\lambda_{\text{max}}^{\text{CL}}$ at 542–544 nm. On the other hand, upon treatment with $t\text{-BuOK}$ in THF, **4e** emitted light that was red-shifted ca 45 nm, as shown in Table 1 and Figure 3. This result further strengthened the notion that the *syn-N-acyl* group caused a red-shift of chemiluminescence for *N-acyl*-substituted bicyclic dioxetanes **3** and **4** in a $t\text{-BuOK}$ /THF system.

Acknowledgement

The authors gratefully acknowledge financial assistance in the form of Grants-in-aid (Nos. 21550052 and 22550046) for Scientific Research from the Ministry of Education, Culture, Sports, Science, and Technology, Japan.

Supplementary data

Supplementary data associated with this article can be found, in the online version, at <http://dx.doi.org/10.1016/j.tetlet.2012.07.086>.

References and notes

- Schaap, A. P.; Gagnon, S. D. *J. Am. Chem. Soc.* **1982**, *104*, 3504–3506.
- Schaap, A. P.; Chen, T.-S.; Handley, R. S.; DeSilva, R.; Giri, B. P. *Tetrahedron Lett.* **1987**, *28*, 1155–1158.
- Beck, S.; Köster, H. *Anal. Chem.* **1990**, *62*, 2258–2270.
- Adam, W.; Reihardt, D.; Saha-Möller, C. R. *Analyst* **1996**, *121*, 1527–1531.
- Matsumoto, M. *J. Photochem. Photobiol. C: Photochem. Rev.* **2004**, *5*, 27–53.
- Adam, W.; Trofimov, A. V. Contemporary trends in dioxetane chemistry In *The Chemistry of Peroxides*; Rappoport, Z., Ed.; Wiley: New York, 2006; Vol. 2.
- For convenience, we refer to an isomer as the *syn-acyl* form when the *N*-acyl carbonyl faces the dioxetane O–O, while in the *anti-acyl* form the acyl carbonyl faces the opposite side. On the other hand, we refer to a rotamer as the *syn-aryl* form when the dioxetane O–O and a hydroxyl group on an aromatic ring are on the same side of the pyrrolidine ring, while in the *anti-aryl* form the dioxetane O–O and a hydroxyl group on an aromatic ring are on opposite sides of the pyrrolidine ring.
- Watanabe, N.; Sano, Y.; Suzuki, H.; Tanimura, M.; Ijuin, H. K.; Matsumoto, M. *J. Org. Chem.* **2010**, *75*, 5920–5926.
- Matsumoto, M.; Suzuki, H.; Watanabe, N.; Ijuin, H. K.; Tanaka, J.; Tanaka, C. *J. Org. Chem.* **2011**, *76*, 5006–5017.
- Color modulation of chemiluminescence is an important subject in the investigation of CTID-active dioxetanes from the perspective of interest in the mechanism of bioluminescence as well as regarding the design of high-performance chemiluminescent compounds.¹¹ Thus, several attempts have been made to realize CTID-active dioxetanes for which chemiluminescence changes depending on the anisotropic microenvironment represented by a coordination sphere of a crown ether complex with an alkaline metal ion: the steric interaction between the crown ether and a dioxetane molecule affects the stereochemistry of the dioxetane so that color modulation occurs for chemiluminescence.
- Matsumoto, M.; Watanabe, N.; Hoshiya, N.; Ijuin, H. K. *Chem. Rec.* **2008**, *8*, 213–228.
- All of the ϕ^{CL} values presented here were estimated, based on the value reported for the chemiluminescent decomposition of 3-adamantylidene-4-(3-*tert*-butyldimethylsilyloxyphenyl)-4-methoxy-1,2-dioxetane ($\phi^{\text{CL}} = 0.29$) in TBAF/DMSO.¹³
- Trofimov, A. V.; Mielke, K.; Vasil'ev, R. F.; Adam, W. *Photochem. Photobiol.* **1996**, *63*, 463–467.
- Crystal data for **3c**, **4a(Me)**, **4c**, and **4e** were submitted to CCDC, with deposition numbers 875575, 297571, 687258, and 875576, respectively. These data can be obtained free of charge via www.ccdc.cam.ac.uk/conts/retrieving.html (or from the Cambridge Crystallographic Data Center, 12 Union Road, Cambridge CB21EZ, UK; fax: / (+44)1223 336 033; or deposit@ccdc.cam.ac.uk).
- Matsumoto, M.; Suzuki, H.; Sano, Y.; Watanabe, N.; Ijuin, H. K. *Tetrahedron Lett.* **2008**, *49*, 5372–5375.
- Matsumoto, M.; Sano, Y.; Watanabe, N.; Ijuin, H. K. *Chem. Lett.* **2006**, *35*, 882–883.
- An MO calculation with HF/6-31G suggested that the $\pi \rightarrow \pi^*$ transition energy ($E_{\pi \rightarrow \pi^*}$) was 8.65 eV for a model of **15** and 10.72 eV for a model of **13**: the model emitter was the potassium salt of *N*-methyl-acetyl-(3-oxidobenzoyl)imide.

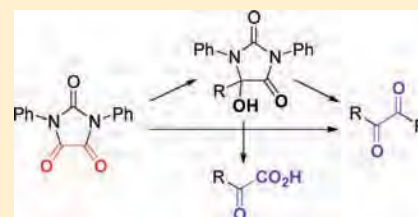
Diphenylparabanic Acid as a Synthron for the Synthesis of α -Diketones and α -Ketocarboxylic Acids

Nobuko Watanabe, Mitsutaka Hamano, Shota Todaka, Takahiro Asaeda, Hisako K. Ijuin, and Masakatsu Matsumoto*

Department of Chemistry, Kanagawa University, Tsuchiya, Hiratsuka, Kanagawa 259-1293, Japan

Supporting Information

ABSTRACT: Diphenylparabanic acid was found to react with >2 equiv of organolithiums at $-78\text{ }^{\circ}\text{C}$ to effectively give the corresponding symmetrical α -diketones. However, upon treatment with 1 equiv of organolithium, the parabanic acid gave mainly 5-substituted 5-hydroxyimidazolidine-2,4-diones. On the other hand, Grignard reagents were less reactive toward the parabanic acid at low temperature, and selectively gave the corresponding 5-hydroxyimidazolidine-2,4-diones even if more than 1 equiv of the reagents was used. A tandem process in which the parabanic acid was first reacted with a Grignard reagent and then reacted in one-pot with an organolithium effectively gave the unsymmetrical α -diketone. 5-Substituted 5-hydroxyimidazolidine-2,4-diones were useful as versatile precursors for preparing α -ketocarboxylic acids as well as unsymmetrical α -diketones.



INTRODUCTION

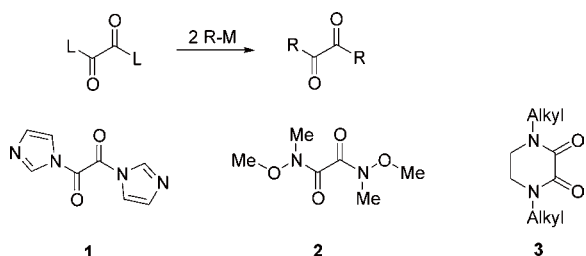
α -Diketones, an important class of compounds as versatile intermediates for organic synthesis, can be synthesized by various methods, such as the oxidation of acetylenic compounds,^{1–5} acyloins⁶ or enamines,⁷ the base-mediated homologation of dimethyldihydropyrazines,⁸ and the nucleophilic substitution (addition–elimination) of oxalic acid derivatives.^{9–12} Among these methods, the latter shows a considerably wide scope for the synthesis of dialkyl-, diaryl-, and unsymmetrically substituted α -diketones, though it could be made even more versatile with the development of a new effective synthron.

α -Diketone synthons that have been described thus far include oxalyldiimidazole (**1**),⁹ oxalamide of *N,O*-dimethylhydroxylamine (**2**),¹⁰ *N,N'*-dialkylpiperazine-2,3-diones (**3**)¹¹ and oxalyl chloride (Chart 1).¹² Each synthron offers characteristic

well as double nucleophilic substitution with aromatic organolithiums to give α -diketones in moderate yields. However, there have been no reports of the synthesis of unsymmetrical α -diketones from **2**. Cyclic oxalamide **3** undergoes double nucleophilic substitution with organolithiums or Grignard reagents to give the corresponding α -diketones in good yields, while there have been no reports of single substitution. The reaction of oxalyl chloride with organocopper reagents is apparently limited to the synthesis of ω,ω' -disubstituted hexa-1,5-diyne-3,4-diones.

We report here that readily available diphenylparabanic acid (*N,N'*-diphenylimidazolidine-2,4,5-trione) (**4**)¹³ acts as a new synthron¹⁴ to effectively prepare symmetrical and unsymmetrical α -diketones **5** and **6**, and provides stable precursors **7**, which can be successively transformed to α -ketocarboxylic acids **8** as well as α -diketones **5** and **6** (Scheme 1).

Chart 1. Oxalamide Derivatives as α -Diketone Synthons



advantages and disadvantages. Oxalamide **1** reacts even with sterically crowded aromatic Grignard reagents to give α -diketones at low temperature, while its effectiveness for the synthesis of unsymmetrical α -diketones is unclear. Oxalamide **2** undergoes nucleophilic substitution with Grignard reagents to give the corresponding α -ketoamides in low to high yields, as

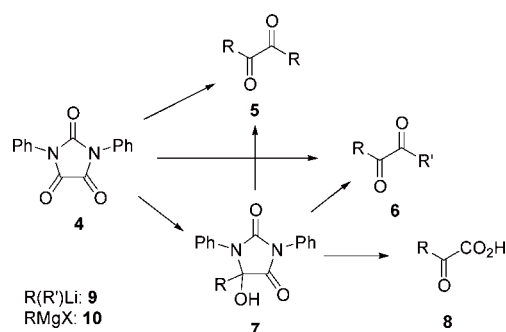
RESULTS AND DISCUSSION

1. Reaction of Diphenylparabanic acid with Organolithiums or Grignard Reagents: Formation of Symmetrical α -Diketones or 5-Substituted 5-Hydroxyimidazolidine-2,4-diones. Diphenylparabanic acid **4** is an oxalic acid derivative that has the characteristics of an α -diketone synthron as follows. First, **4** is formally a cyclic imide of oxalic acid, so that the carbons of $-\text{CO}-\text{CO}-$ would be more electron-deficient, and thus more reactive, toward nucleophiles than simple oxalamides **1–3**. Second, a fixed cisoid $-\text{CO}-\text{CO}-$ structure presumably stabilizes the metal salt of monoadduct **7** produced from organolithium or Grignard reagent by forming a chelate, so that it preferably inhibits side reactions such as a

Received: November 8, 2011

Published: December 2, 2011

Scheme 1. Synthesis of α -Diketones 5 and 6, 5-Substituted 5-Hydroxyimidazolidine-2,4-diones 7 and α -Ketocarboxylic Acids 8



double nucleophilic attack on the same carbon. Third, it may be possible to isolate intermediate, a certain cyclic hemiaminal, **7** produced by the reaction of **4** with a nucleophile, since it has been reported that certain *N,N',S*-trisubstituted 5-hydroxyimidazolidine-2,4-diones are isolable.¹⁵

First, we treated diphenylparabanic acid **4** with >2 equiv of phenyllithium (**9a**) in THF at $-78\text{ }^{\circ}\text{C}$ for 3 h. A usual workup of the reaction mixture gave 1,2-diphenylethane-1,2-dione (**5a**), as expected, in 84% isolated yield along with *N,N'*-diphenylurea. Similar treatment of **4** with 1-naphthyllithium (**9b**) or 2-naphthyllithium (**9c**) gave the corresponding 1,2-diarylethane-1,2-diones **5b** and **5c** in good yields, as shown in Table 1. These results suggest that, as expected, aryllithium **9**

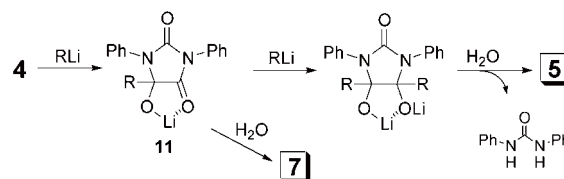
Table 1. Synthesis of α -Diketones 5 or 5-Substituted 5-Hydroxyimidazolidine-2,4-diones 7 by the Reaction of Diphenylparabanic Acid (4) with Organolithiums 9^a

Organolithium 9	Product	Yield / %	Organolithium 9	Product	Yield / %
R			R		
9a	5a	84	9e	7e	90
	7a ^b	73 ^b	9f	5f	62
9b	5b	84	9g	5g	77
9c	5c	89		7g ^c	85 ^c
9d	7d	96	9h	5h	87

^aUnless otherwise stated, all of the reactions were carried out by using 2.0–2.5 equiv of organolithium **9** in THF at $-78\text{ }^{\circ}\text{C}$ for 1–3 h. ^b1.1 equiv of **9a** was used. ^c1.1 equiv of **9g** was used.

attacked a $-\text{CO}-\text{CO}-$ of **4** to initially produce lithium salt **11**, in which a remaining carbonyl was presumably coordinated with Li^+ and subsequently reacted with the second aryllithium (Scheme 2). In fact, when **4** was treated with 1 equiv of phenyllithium **9a** as a representative compound at $-78\text{ }^{\circ}\text{C}$, 1:1 adduct, that is, 5-hydroxy-*N,N',S*-triphenylimidazolidine-2,4-dione (**7a**), was obtained in 73% yield together with a trace amount of **5a**. In contrast to the results with **9a–c**, the reaction of **4** with 9-anthryllithium (**9d**), even with the use of >2 equiv, did not give the desired α -diketone **5d**, and instead gave 1:1 adduct **7d**. Sterically congested 2,4,6-trimethylphenyllithium (**9e**) also gave only 1:1 adduct **7e** (Table 1).

Scheme 2. Reaction of Diphenylparabanic Acid with Organolithiums



BuLi (**9f**), as a representative aryllithium, also gave α -diketone **5f**, though the isolated yield was somewhat low (62%). We also attempted to synthesize hexa-1,5-diyne-3,4-diones, since they have only been synthesized by the reaction of oxalyl chloride with copper acetylides.¹¹ Treatment of **4** with >2 equiv of (4-methylphenyl)ethynyllithium (**9g**) at $-78\text{ }^{\circ}\text{C}$ gave the desired diyne **5g** in 77% yield, while the reaction of **4** with 1 equiv of **9g** gave 1:1 adduct **7g** in 85% yield. Notably, benzothiophen-2-ylolithium (**9h**), as a representative heteroaromatic lithium reagent, effectively underwent addition to **4** to give α -diketone **5h**. These results are summarized in Table 1.

Next, we investigated the reactivity of **4** with Grignard reagents **10**. When **4** was treated with >1 equiv of phenylmagnesium bromide (**10a**) in THF at $-78\text{ }^{\circ}\text{C}$ for 1 h, only 1:1 adduct **7a** was selectively obtained. A use of excess **10** and/or a prolonged reaction time at $-78\text{ }^{\circ}\text{C}$ had little effect on the production of α -diketone **5a**. Various Grignard reagents **10b**, **10c** and **10i–k** were found to react similarly with **4** to give the corresponding 5-substituted 5-hydroxyimidazolidine-2,4-diones **7b**, **7c** and **7i–k** in high yields, as shown in Table 2. However, at higher

Table 2. Synthesis of 5-Substituted 5-Hydroxyimidazolidine-2,4-diones 7 by the Reaction of Diphenylparabanic Acid (4) with Grignard Reagents 10^a

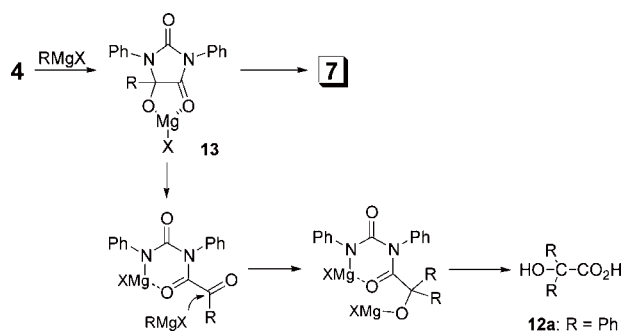
Grignard reagent	Product	Yield / %	Grignard reagent	Product	Yield / %
R			R		
10a	7a	97	10i	7i	98
10b	7b	94	10j	7j	90
10c	7c	95	10k	7k	93

^aReactions were carried out in THF at $-78\text{ }^{\circ}\text{C}$ for 1 h.

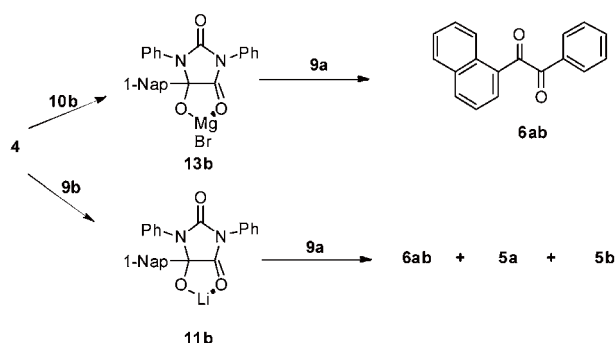
temperature (room temp), 2 equiv of **10a** reacted with **4** to give hydroxydiphenylacetic acid (**12a**) in high yield, but not **5a**. These results suggest that Grignard reagents were not sufficiently reactive to cause double nucleophilic attack to two carbons of **4**, though the initially formed **Mg** salt **13** could not retain its structure at room temperature and presumably exposed a reactive α -ketoamide moiety, as illustrated in Scheme 3.

2. Synthesis of Unsymmetrical α -Diketones and α -Ketocarboxylic Acids. The results described in the previous section suggest that the tandem reaction of **4** would proceed with the use of two different organometallic reagents to give unsymmetrical α -diketone **6**. There are two possible types of tandem method: the addition of organolithium **9** to a solution of magnesium salt **13** prepared from **4** and Grignard reagent **10**, and the successive addition of organolithium **9** to an initially prepared solution of lithium salt **11**. Thus, we examined these two types of reactions using Grignard reagent

Scheme 3. Reaction of Diphenylparabanic Acid with Grignard Reagents 10



10b, and organolithiums 9a and 9b as representative reagents. When 4 was first treated with 1.5 equiv of Grignard reagent 10b in THF at $-78\text{ }^{\circ}\text{C}$ for 1 h, and successively treated in one-pot with organolithium 9a at $-78\text{ }^{\circ}\text{C}$ for 1 h, unsymmetrical α -diketone 6ab was obtained in 90% yield. On the other hand, a tandem reaction with a combination of two organolithiums was less effective for synthesizing unsymmetrical α -diketones 6: treatment of 4 with 1.1 equiv of 9b and then with 9a in THF at $-78\text{ }^{\circ}\text{C}$ gave the desired 6ab in only 44% yield along with a small amount of symmetrical α -diketone 5a and 5b (Scheme 4).

Scheme 4. Synthesis of Unsymmetrical α -Diketone 6ab by a Tandem Reaction

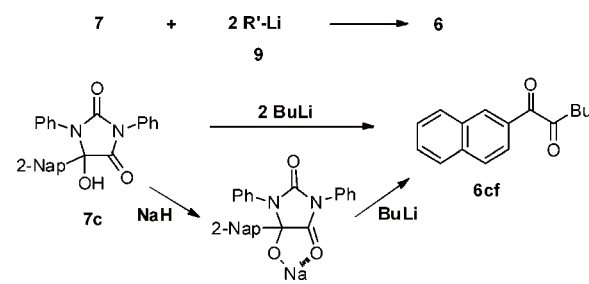
We further attempted to use 5-substituted 5-hydroxyimidazolidine-2,4-diones 7 as a versatile precursor for the synthesis of unsymmetrical α -diketones 6. When 7a was treated with >2 equiv of 9b in THF at $-78\text{ }^{\circ}\text{C}$ for 1 h, unsymmetrical α -diketone 6ab was obtained in 99% yield. The inverse combination, that is, the addition of 9a to 7b, also gave 6ab in 88% yield, as shown in Table 3. Other representative combinations of 7 and 9 also gave the expected unsymmetrical α -diketones 6 in high yields, as shown in Table 3.

The synthetic method that uses precursor 7 as described above would be useful as a library for the synthesis of unsymmetrical α -diketones 6, though it requires more than 2 equiv of organolithium reagent 9: half of 9 is consumed just to form a lithium salt 11. Thus, we attempted to use an inexpensive sodium salt of 7 instead of 11 for the synthesis of 6. A representative reaction sequence was as follows. Precursor 7c was treated with NaH in THF to give a sodium salt, which was then treated in one-pot with 1.2 equiv of BuLi 9f at $-78\text{ }^{\circ}\text{C}$ for 1 h. After workup, unsymmetrical α -diketone 6cf was obtained in 92% yield (Scheme 5).

Table 3. Synthesis of Unsymmetrical α -Diketones 6 by the Reaction of 5-Substituted 5-Hydroxyimidazolidine-2,4-diones 7 with Organolithium 9^a

Combination	Unsymmetrical α -diketone	Product Yield / %
7a + 9b	6ab	99
7b + 9a	6ab	88
7b + 9c	6bc	83
7b + 9f	6bf	91
7c + 9f	6cf	97
7g + 9a	6ag	98
7k + 9a	6ak	62

^aReactions were carried out using 2.3 equiv of organolithium 9 in THF at $-78\text{ }^{\circ}\text{C}$ for 1 h.

Scheme 5. Synthesis of Unsymmetrical α -Diketones 6 from 5-Substituted 5-Hydroxyimidazolidine-2,4-diones 7

Finally, we investigated whether or not hydroxyimidazolidinediones 7 could be effectively hydrolyzed to the corresponding α -ketocarboxylic acids 8. When 7a was heated in NaOH/H₂O-MeOH at $50\text{ }^{\circ}\text{C}$ for 1 h, the hydrolysis of 7a proceeded to give 2-oxo-2-phenylethanoic acid 8a in 89% yield together with diphenylurea after acidification. Similarly, hydroxyimidazolidinediones 7b–e, 7g, 7i and 7k were effectively hydrolyzed to the corresponding α -ketocarboxylic acids 8b–e, 8g, 8i and 8k, as shown in Table 4.

CONCLUSION

Diphenylparabanic acid 4 was found to react with >2 equiv of organolithiums at $-78\text{ }^{\circ}\text{C}$ to effectively give the corresponding symmetrical α -diketones 5, though 4 gave mainly 5-substituted 5-hydroxyimidazolidine-2,4-diones 7 when treated with 1 equiv of organolithiums. On the other hand, Grignard reagents were less reactive toward 4 at low temperature, and selectively gave 7 even if more than 1 equiv of the reagents were used. A tandem reaction of 4 by the successive addition of two different organolithiums gave an unsymmetrical α -diketone 6 in moderate yields. However, a tandem process in which 4 was first reacted with a Grignard reagent and then with an organolithium was effective for producing an unsymmetrical α -diketone 6. 5-Substituted 5-hydroxyimidazolidine-2,4-diones

Table 4. Synthesis of α -Ketocarboxylic Acids 8 from 5-Substituted 5-Hydroxyimidazolidine-2,4-diones 7^a

Imidazolidine-2,4-dione	α -Ketocarboxylic acid	Yield / %	Imidazolidine-2,4-dione	α -Ketocarboxylic acid	Yield / %
7a	8a	98	7e	8e	39 ^{b)}
7b	8b	94	7g	8g	80 ^{c)}
7c	8c	89	7i	8i	84
7d	8d	78	7k	8k	96

^aReactions were carried out by using 4 M NaOH in H₂O/MeOH at 50 °C for 1 h. ^b*N*-Phenyl-2-(2,4,6-trimethylphenyl)-2-oxoacetamide (14) was concomitantly produced in 54% yield. ^c8g was isolated as a lactone form, 5-(4-methylphenyl)furan-2,3-dione.

7 were useful as versatile precursors for preparing unsymmetrical α -diketones 6 and α -ketocarboxylic acids 8.

Finally, synthon 4 could be easily modified to a copolymer with *N*-phenyl-*N'*-(4-vinylphenyl)parabanic acid and styrene, and further studies of this process are now underway.

EXPERIMENTAL SECTION

Preparation of Diphenylparabanic Acid (4). According to the procedure reported,¹³ 4 was prepared as follows, though CH₂Cl₂ was used as a solvent instead of diethyl ether. Oxalyl chloride (12.0 mL, 0.14 mol) was added dropwise to a solution of *N,N'*-diphenylurea (25.2 g, 0.12 mol) in CH₂Cl₂ (400 mL) and refluxed for 1.5 h. The reaction mixture was washed with sat. aq. NaCl, dried over anhydrous Na₂SO₄ and concentrated in vacuo. The residue was crystallized from CH₂Cl₂–hexane to give 4 as colorless needles (31.5 g, 99% yield).

4: colorless needles melted at 208.0–209.0 °C (from CH₂Cl₂–hexane). (lit.,¹³ 202 °C). ¹H NMR (400 MHz, CDCl₃): δ_{H} 7.44–7.51 (m, 6H), 7.52–7.58 (m, 4H) ppm.

Synthesis of 1,2-Diphenylethane-1,2-dione (5a) by the Reaction of Diphenylparabanic Acid (4) with Phenyllithium (9a). *Typical Procedure.* A solution of 4 (1.02 g, 3.83 mmol) in dry THF (5 mL) was added to a solution of phenyllithium (9a) (1.13 M in THF, 7.80 mL, 8.81 mmol, 2.30 equiv) in dry THF (5 mL) at –78 °C under a N₂ atmosphere and stirred for 1 h. The reaction mixture was poured into sat. aq. NH₄Cl and then extracted with AcOEt. The organic layer was washed with sat. aq. NaCl, dried over anhydrous Na₂SO₄ and concentrated in vacuo. The residue was rinsed with CHCl₃ and *N,N'*-diphenylurea was removed by filtration. The filtrate was concentrated in vacuo, and the residue was chromatographed on silica gel and eluted with hexane–AcOEt (4:1) to give 5a as a yellow solid (675 mg, 84% yield).

5a: yellow needles melted at 96.5–97.0 °C (from AcOEt–hexane) (lit.,¹⁶ 95–97 °C from AcOEt–hexane). ¹H NMR (500 MHz, CDCl₃): δ_{H} 7.52 (dd, *J* = 8.2 and 7.3 Hz, 4H), 7.66 (t, *J* = 7.3 Hz, 2H), 7.98 (d with fine coupling, *J* = 8.2 Hz, 4H) ppm. ¹³C NMR (125 MHz, CDCl₃): δ_{C} 129.0 (×2), 129.9 (×2), 133.0, 134.9, 194.5 ppm. IR (KBr): $\tilde{\nu}$ 3063, 1677, 1660, 1594, 1579 cm^{–1}. Mass (*m/z*, %): 210 (M⁺, 6), 105 (100), 77 (54). HRMS (ESI): 233.0583, calcd for C₁₄H₁₀O₂Na [M + Na]⁺ 233.0579.

According to the procedure described above, 4 was reacted with 1-naphthyllithium (9b), 2-naphthyllithium (9c), butyllithium (9f), (4-methylphenyl)ethynyllithium (9g), or benzothiofen-2-ylithium (9h) to give the corresponding symmetrical α -diketones 5b (84%), 5c (89%), 5f (62%), 5g (77%) and 5h (87%); organolithiums 9b and 9c were prepared by the metal–halogen exchange reaction of the corresponding bromide with butyllithium, while 9g and 9h were prepared by the lithiation of (4-methylphenyl)ethyne or benzothiofen with butyllithium.

5b: yellow granules melted at 192.0–194.0 °C (from CH₂Cl₂) (lit.,¹⁷ 192–194 °C from AcOEt–hexane). ¹H NMR (500 MHz, CDCl₃): δ_{H} 7.47 (dd, *J* = 8.2 and 7.3 Hz, 2H), 7.63 (ddd, *J* = 8.2, 7.1, and 1.1 Hz, 2H), 7.75 (ddd, *J* = 8.5, 7.1, and 1.4 Hz, 2H), 7.95 (d with fine coupling, *J* = 8.2 Hz, 2H), 8.02 (dd, *J* = 7.3 and 1.1 Hz, 2H), 8.12 (d, *J* = 8.2 Hz, 2H), 9.36 (d, *J* = 8.5 Hz, 2H) ppm. ¹³C NMR (125 MHz, CDCl₃): δ_{C} 124.4, 126.0, 127.1, 128.8, 128.9, 129.4, 131.1, 134.1, 135.0, 135.8, 196.9 ppm. IR (KBr): $\tilde{\nu}$ 3055, 1662, 1571 cm^{–1}. Mass (*m/z*, %): 310 (M⁺, 10), 156 (11), 155 (100), 128 (10), 127 (96), 126 (18). HRMS (ESI): 333.0901, calcd for C₂₂H₁₄O₂Na [M + Na]⁺ 333.0892.

5c: colorless needles melted at 160.0–161.0 °C (from CH₂Cl₂) (lit.,¹⁸ 156–157 °C from AcOEt–hexane). ¹H NMR (500 MHz, CDCl₃): δ_{H} 7.55 (dd with fine coupling, *J* = 8.0 and 7.1 Hz, 2H), 7.65 (dd with fine coupling, *J* = 8.0 and 7.1 Hz, 2H), 7.91 (d, *J* = 8.0 Hz, 2H), 7.91 (d, *J* = 8.0 Hz, 2H), 7.99 (d, *J* = 8.7 Hz, 2H), 8.16 (d with fine coupling, *J* = 8.7 Hz, 2H), 8.46 (s, 2H) ppm. ¹³C NMR (125 MHz, CDCl₃): δ_{C} 123.7, 127.1, 127.9, 129.1, 129.5, 129.9, 130.4, 132.3, 133.6, 136.4, 194.7 ppm. IR (KBr): $\tilde{\nu}$ 3061, 1664, 1628, 1596 cm^{–1}. Mass (*m/z*, %): 310 (M⁺, 12), 156 (12), 155 (100), 127 (85), 126 (15). HRMS (ESI): 333.0901, calcd for C₂₂H₁₄O₂Na [M + Na]⁺ 333.0892.

5f: yellow oil. ¹H NMR (500 MHz, CDCl₃): δ_{H} 0.92 (t, *J* = 7.3 Hz, 6H), 1.30–1.38 (m, 4H), 1.53–1.60 (m, 4H), 2.74 (t, *J* = 7.3 Hz, 4H) ppm. ¹³C NMR (125 MHz, CDCl₃): δ_{C} 13.7, 22.2, 25.1, 35.7, 200.1 ppm. (lit.,^{3a} 100 MHz, CDCl₃ δ_{C} 13.8, 22.2, 25.1, 35.8, 200.2 ppm). IR (liquid film): $\tilde{\nu}$ 2961, 1713 cm^{–1}. Mass (*m/z*, %): 170 (M⁺, 7), 85 (100), 71 (12), 57 (66).

5g: orange columns melted at 154.5–156.0 °C (from CH₂Cl₂). ¹H NMR (400 MHz, CDCl₃): δ_{H} 2.42 (s, 6H), 7.23 (d, *J* = 8.1 Hz, 4H), 7.60 (d, *J* = 8.1 Hz, 4H) ppm.; ¹³C NMR (125 MHz, CDCl₃): δ_{C} 21.9, 86.2, 100.8, 116.1, 129.6 (×2), 133.9 (×2), 142.9, 172.6 ppm. IR (KBr): $\tilde{\nu}$ 3033, 2190, 1659, 1603, 1508 cm^{–1}. Mass (*m/z*, %): 286 (M⁺, 0.8), 230 (37), 144 (11), 143 (100), 115 (13), 89 (11). HRMS (ESI): 309.0894 calcd for C₂₀H₁₄O₂Na [M + Na]⁺ 309.0892.

5h: yellow needles melted at 236.0–236.5 °C (from CH₂Cl₂) (lit.,¹⁹ 239–240 °C). ¹H NMR (400 MHz, CDCl₃): δ_{H} 7.44 (dd, *J* = 8.5 and 6.8 Hz, 2H), 7.53 (dd, *J* = 8.5 and 6.8 Hz, 2H), 7.93 (d, *J* = 8.5 Hz, 4H), 8.32 (s, 2H) ppm. ¹³C NMR (125 MHz, CDCl₃): δ_{C} 123.0, 125.4, 126.9, 128.7, 135.4, 138.8, 139.0, 143.8, 184.3 ppm. IR (KBr): $\tilde{\nu}$ 1647, 1592 cm^{–1}. Mass (*m/z*, %): 322 (M⁺, 19), 162 (11), 161 (100), 133 (31), 89 (55). HRMS (ESI): 345.0002, calcd for C₁₈H₁₀O₂S₂Na [M + Na]⁺ 345.0020.

Synthesis of 5-Hydroxy-*N,N'*-5-triphenylimidazolidine-2,4-dione (7a) by the Reaction of Diphenylparabanic Acid (4) with Phenyllithium (9a). A solution of 4 (1.00 g, 3.76 mmol) in dry THF (5 mL) was added dropwise to a solution of phenyllithium (9a) (1.1 equiv) in dry THF under a N₂ atmosphere at –78 °C and stirred for 1 h. The reaction mixture was poured into sat. aq. NH₄Cl and then extracted with AcOEt. The organic layer was washed with sat. aq. NaCl, dried over anhydrous Na₂SO₄ and concentrated in vacuo. The crude product was crystallized from CHCl₃ to give 7a (174 mg, 13%). The filtrate was concentrated in vacuo, and chromatographed on silica gel with hexane–AcOEt (4:1) to further give 7a (772 mg, 60%) as a yellow solid. Total yield of 7a was 73%.

7a: colorless granules melted at 208.0–209.0 °C (from CHCl₃). ¹H NMR (500 MHz, CDCl₃): δ_{H} 4.20 (s, 1H), 7.18 (t, *J* = 7.6 Hz, 1H), 7.23–7.28 (m, 2H), 7.34–7.52 (m, 12H) ppm. ¹³C NMR (125 MHz, DMSO-*d*₆): δ_{C} 88.5, 125.4 (×2), 126.6, 126.6 (×2), 127.4 (×2), 128.8, 128.9 (×2), 129.0 (×2), 129.4 (×3), 131.9, 135.2, 136.3, 153.4, 170.9 ppm. IR (KBr): $\tilde{\nu}$ 3378, 3062, 3034, 1779, 1706, 1596 cm^{–1}. Mass (*m/z*, %): 344 (M⁺, 23), 225 (26), 197 (15), 119 (34), 105 (100), 91 (12), 77 (37). HRMS (ESI): 367.1073, calcd for C₂₁H₁₆N₂O₃Na [M + Na]⁺ 367.1059. Anal. Calcd for C₂₁H₁₆N₂O₃: C, 73.24; H, 4.68; N, 8.13. Found: C, 73.06; H, 4.67; N, 8.14.

Synthesis of 5-(9-Anthryl)-5-hydroxy-*N,N'*-diphenylimidazolidine-2,4-dione (7d). BuLi (1.63 M in hexane, 5.30 mL, 8.64 mmol) was added to a solution of 9-bromoanthracene (2.44 g, 9.49 mmol) in dry THF (20 mL) at –78 °C under a N₂ atmosphere and stirred for

30 min. To the thus-prepared solution of 9-anthryllithium, a solution of **4** (1.00 g, 3.76 mmol) in dry THF (10 mL) was added dropwise under a N₂ atmosphere at -78 °C and stirred for 1 h. The reaction mixture was poured into sat. aq. NH₄Cl and then extracted with AcOEt. The organic layer was washed with sat. aq. NaCl, dried over anhydrous Na₂SO₄ and concentrated in vacuo. The crude product was purified by chromatography on silica gel and eluted with hexane-AcOEt (4:1) to give **7d** (1.61 g, 96%) as a yellow solid.

7d: yellow granules melted at 192.0–194.0 °C (from CH₂Cl₂-hexane). ¹H NMR (500 MHz, CDCl₃): δ_H 4.15 (s, 1H), 7.09–7.19 (m, 6H), 7.27–7.31 (m, 1H), 7.42 (t with fine coupling, *J* = 7.3 Hz, 1H), 7.45–7.61 (m, 6H), 7.88 (d, *J* = 8.2 Hz, 1H), 7.94 (d, *J* = 9.2 Hz, 1H), 8.03 (d, *J* = 8.2 Hz, 1H), 8.40 (d, *J* = 9.2 Hz, 1H), 8.46 (s, 1H) ppm. ¹³C NMR (125 MHz, CDCl₃): δ_C 90.3, 122.4, 123.9, 124.6, 124.8, 125.9, 125.9 (×2), 126.0, 127.4, 128.4, 128.7, 129.0 (×2), 129.1 (×2), 129.2, 129.2 (×2), 129.6, 130.0, 130.9, 131.5, 131.8, 132.0, 132.1, 133.6, 154.1, 171.8 ppm. IR (KBr): $\tilde{\nu}$ 3461, 3046, 1778, 1726, 1624, 1597 cm⁻¹. Mass (35 eV, *m/z*, %): 444 (M⁺, 1), 325 (18), 206 (16), 205 (100), 177 (33), 119 (12). HRMS (ESI): 467.1376, calcd for C₂₉H₂₀N₃O₃Na [M + Na]⁺ 467.1372.

Synthesis of 5-Hydroxy-5-(2,4,6-trimethylphenyl)-N,N'-diphenylimidazolidine-2,4-dione (7e). BuLi (1.64 M in hexane, 5.30 mL, 8.69 mmol) was added to a solution of 1-bromo-2,4,6-trimethylbenzene (1.41 mL, 9.42 mmol) in dry THF (5 mL) at -78 °C under a N₂ atmosphere and stirred for 30 min. To the thus-prepared solution of 2,4,6-trimethylphenyllithium in dry THF, a solution of **4** (1.02 g, 3.83 mmol) in dry THF (5 mL) was added dropwise under a N₂ atmosphere at -78 °C and stirred for 1.5 h. The reaction mixture was poured into sat. aq. NH₄Cl and then extracted with AcOEt. The organic layer was washed with sat. aq. NaCl, dried over anhydrous Na₂SO₄ and concentrated in vacuo. The crude product was crystallized from hexane-AcOEt to give **7e** (1.06 g, 72%) as colorless granules. The filtrate was concentrated in vacuo and chromatographed on silica gel with hexane-AcOEt (4:1) to further give **7e** (275 mg, 18%) as a colorless solid. Total yield of **7e** was 90%.

7e: colorless granules melted at 170.0–171.0 °C (from CH₂Cl₂). ¹H NMR (500 MHz, CDCl₃): δ_H 2.16 (s, 3H), 2.23 (s, 3H), 2.35 (s, 3H), 3.92 (s, 1H), 6.72 (s, 1H), 6.85 (s, 1H), 7.11–7.17 (m, 2H), 7.24–7.30 (m, 3H), 7.37–7.44 (m, 1H), 7.38–7.52 (m, 4H) ppm. ¹³C NMR (125 MHz, DMSO-*d*₆): δ_C 20.3, 20.8, 24.7, 90.6, 125.8 (×2), 126.8 (×2), 127.1, 128.6, 128.9 (×2), 128.9, 129.3 (×2), 131.1, 131.8, 132.5, 134.8, 135.4, 137.8, 139.9, 153.2, 170.8 ppm. IR (KBr): $\tilde{\nu}$ 3356, 3065, 2973, 2924, 1783, 1715, 1598 cm⁻¹. Mass (*m/z*, %): 386 (M⁺, 1), 212 (14), 148 (11), 147 (100), 119 (19), 93 (44), 91 (14), 77 (10). HRMS (ESI): 409.1527, calcd for C₂₄H₂₂N₂O₃Na [M + Na]⁺ 409.1528.

Synthesis of 5-Hydroxy-5-(4-methylphenylethynyl)-N,N'-diphenylimidazolidine-2,4-dione (7g). BuLi (1.61 M in hexane, 2.50 mL, 4.03 mmol) was added to a solution of 4-methylphenylacetylene (0.57 mL, 4.5 mmol) in dry THF (5 mL) at -78 °C under a N₂ atmosphere and stirred for 30 min. To the solution of 2-(4-methylphenyl)ethynyllithium in dry THF, a solution of **4** (1.02 g, 3.83 mmol) in dry THF (5 mL) was added dropwise under N₂ atmosphere at -78 °C and stirred for 1 h. The reaction mixture was poured into sat. aq. NH₄Cl and then extracted with AcOEt. The organic layer was washed with sat. aq. NaCl, dried over anhydrous Na₂SO₄ and concentrated in vacuo. The crude product was crystallized from CH₂Cl₂-hexane to give **7g** (1.25 g, 85%) as a colorless solid.

7g: colorless granules melted at 168.0–169.0 °C (from CH₂Cl₂). ¹H NMR (500 MHz, CDCl₃): δ_H 2.32 (s, 3H), 4.85 (s, 1H), 7.07 (d, *J* = 7.8 Hz, 2H), 7.22 (d, *J* = 7.8 Hz, 2H), 7.33–7.39 (m, 2H), 7.40–7.47 (m, 6H), 7.65 (d, *J* = 7.8 Hz, 2H) ppm. ¹³C NMR (125 MHz, CDCl₃): δ_C 21.5, 80.5, 80.7, 90.0, 117.1, 126.1 (×2), 126.9 (×2), 128.0, 128.5, 129.1 (×6), 130.9, 131.9 (×2), 133.7, 140.2, 152.4, 167.9 ppm. IR (KBr): $\tilde{\nu}$ 3387, 2227, 1787, 1728, 1596 cm⁻¹. Mass (*m/z*, %): 382 (M⁺, 0.6), 266 (50), 119 (100), 116 (17), 115 (19), 91 (52), 64 (20), 63 (12). HRMS (ESI): 405.1221, calcd for C₂₄H₁₈N₂O₃Na [M + Na]⁺ 405.1215. Anal. Calcd for C₂₄H₁₈N₂O₃: C, 75.38; H, 4.74; N, 7.33. Found: C, 75.03; H, 4.49; N, 7.30.

Synthesis of 5-Hydroxy-N,N',5-triphenylimidazolidine-2,4-dione (7a) by the Reaction of N,N'-Diphenylparabanic Acid (4) with Phenylmagnesium Bromide (10a). *Typical Procedure.* To the solution of phenylmagnesium bromide (**10a**), which was prepared from bromobenzene (11.3 mmol) and Mg (13.0 mmol) in dry THF, a solution of **4** (2.01 g, 7.55 mmol) in dry THF (10 mL) was added dropwise over 5 min at -78 °C and stirred for 1 h. The reaction mixture was poured into sat. aq. NH₄Cl and extracted with AcOEt. The reaction mixture was poured into sat. aq. NH₄Cl and then extracted with AcOEt. The organic layer was washed with sat. aq. NaCl, dried over anhydrous Na₂SO₄ and concentrated in vacuo. The crude product was chromatographed on silica gel and eluted with hexane-AcOEt (4:1) to give **7a** (2.53 g, 97%) as colorless granules.

According to the procedure described above, the reaction of diphenylparabanic acid (**4**) with 1-naphthylmagnesium bromide (**10b**), 2-naphthylmagnesium bromide (**10c**), 1-pyrenylmagnesium bromide (**10i**), ethylmagnesium chloride (**10j**) or tert-butylmagnesium chloride (**10k**) gave the corresponding 5-substituted 5-hydroxyimidazolidine-2,4-diones **7b** (94%), **7c** (95%), **7i** (98%), **7j** (90%) and **7k** (93%).

7b: colorless granules melted at 191.0–192.0 °C (from CH₂Cl₂-hexane). ¹H NMR (300 MHz, CDCl₃): δ_H 4.64 (s, 1H), 7.02–7.18 (m, 5H), 7.29–7.57 (m, 8H), 7.78–7.97 (m, 4H) ppm. ¹³C NMR (125 MHz, DMSO-*d*₆): δ_C 87.4 (br), 121.6 (br), 125.1, 125.4 (×2), 125.9, 126.8 (br), 127.1 (×2), 127.8 (br), 128.4 (br), 128.7 (×3), 128.8, 129.4, 129.4, 129.8 (br), 130.2 (br), 130.8, 131.8, 133.8 (br), 134.6 (br), 153.4, 170.9 ppm. IR (KBr): $\tilde{\nu}$ 3383, 3094, 3058, 3019, 1784, 1726, 1596 cm⁻¹. Mass (*m/z*, %): 394 (M⁺, 6), 275 (23), 156 (13), 155 (100), 127 (43), 119 (25), 91 (10). HRMS (ESI): 417.1230, calcd for C₂₅H₁₈N₂O₃Na [M+Na]⁺ 417.1215.

7c: colorless needles melted at 204.0–205.0 °C (from CH₂Cl₂-hexane). ¹H NMR (500 MHz, CDCl₃): δ_H 4.69 (s, 1H), 7.14 (t, *J* = 7.3 Hz, 1H), 7.22 (dd, *J* = 8.2 and 7.3 Hz, 2H), 7.38–7.55 (m, 10H), 7.80–7.86 (m, 3H), 8.11 (s with fine coupling, 1H) ppm. ¹³C NMR (125 MHz, DMSO-*d*₆): δ_C 88.5, 123.6, 125.3 (×2), 126.4, 126.5, 126.7, 127.1, 127.3 (×2), 127.7, 128.6 (×2), 128.7, 128.8 (×2), 129.2 (×2), 131.8, 132.7, 133.1, 133.7, 135.1, 153.3, 170.7 ppm. IR (KBr): $\tilde{\nu}$ 3350, 3063, 1785, 1723, 1596 cm⁻¹. Mass (*m/z*, %): 394 (M⁺, 4), 275 (22), 156 (13), 155 (100), 127 (63), 126 (10), 119 (16), 77 (13). HRMS (ESI): 417.1224, calcd for C₂₅H₁₈N₂O₃Na [M + Na]⁺ 417.1215. Anal. Calcd for C₂₅H₁₈N₂O₃: C, 76.13; H, 4.60; N, 7.10. Found: C, 75.90; H, 4.37; N, 7.10.

7i: pale yellow granules melted at 218.5–219.5 °C (from CHCl₃). ¹H NMR (500 MHz, CDCl₃): δ_H 4.74 (s, 1H), 6.95–7.03 (m, 3H), 7.13–7.17 (m, 2H), 7.41–7.53 (m, 3H), 7.57 (d, *J* = 7.3 Hz, 2H), 7.95 (d, *J* = 8.7 Hz, 1H), 7.99 (d, *J* = 8.2 Hz, 1H), 8.03 (dd, *J* = 7.8 and 7.3 Hz, 2H), 8.07 (d, *J* = 9.2 Hz, 1H), 8.16 (d, *J* = 7.3 Hz, 1H), 8.21 (d with fine coupling, *J* = 7.8 Hz, 2H), 8.36 (br-s, 1H) ppm. ¹³C NMR (125 MHz, CDCl₃): δ_C 124.5, 124.6, 125.1, 125.8, 126.1 (×2), 126.2 (×4), 126.3 (×2), 127.0, 127.2 (×2), 128.5, 128.6 (×3), 128.6, 129.1 (br), 129.3 (×3), 130.1, 131.1, 131.3, 132.6, 133.6, 153.8, 171.8 ppm. IR (KBr): $\tilde{\nu}$ 3380, 3044, 1780, 1722, 1597 cm⁻¹. Mass (35 eV, *m/z*, %): 468 (M⁺, 2), 349 (20), 230 (18), 229 (100), 201 (46), 119 (11). HRMS (ESI): 491.1388, calcd for C₃₁H₂₀N₂O₃Na [M + Na]⁺ 491.1372. Anal. Calcd for C₃₁H₂₀N₂O₃: C, 79.47; H, 4.30; N, 5.98. Found: C, 79.15; H, 4.15; N, 5.99.

7j: colorless amorphous solid. ¹H NMR (500 MHz, CDCl₃): δ_H 0.84 (t, *J* = 7.3 Hz, 3H), 1.87 (dq, *J* = 14.4 and 7.3 Hz, 1H), 2.06 (dq, *J* = 14.4 and 7.3 Hz, 1H), 4.33 (s, 1H), 7.32 (t, *J* = 7.3 Hz, 1H), 7.35–7.47 (m, 7H), 7.55 (d, *J* = 8.2 Hz, 2H) ppm. ¹³C NMR (125 MHz, CDCl₃): δ_C 7.3, 27.3, 89.1, 126.1 (×2), 126.2 (×2), 127.3, 128.3, 129.0 (×4), 130.8, 133.6, 153.5, 171.8 ppm. IR (KBr): $\tilde{\nu}$ 3388, 3065, 2974, 2939, 2882, 1781, 1714, 1596 cm⁻¹. Mass (*m/z*, %): 296 (M⁺, 60), 268 (16), 267 (100), 149 (11), 120 (62), 119 (31), 93 (29), 91 (20), 77 (36), 57 (12). HRMS (ESI): 297.1258, calcd for C₁₇H₁₇N₂O₃ [M + H]⁺ 297.1239.

7k: colorless granules melted at 145.0–146.0 °C (from AcOEt-hexane). ¹H NMR (500 MHz, CDCl₃): δ_H 0.98 (s, 9H), 4.14 (s, 1H), 7.29 (t, *J* = 7.3 Hz, 1H), 7.32–7.38 (m, 5H), 7.40–7.45 (m, 2H), 7.51 (d, *J* = 7.8 Hz, 2H) ppm. ¹³C NMR (125 MHz, CDCl₃): δ_C 24.9 (×3), 40.2, 91.9, 126.2 (×2), 127.5, 127.8 (×2), 128.3, 128.8 (×2), 129.0

($\times 2$), 131.1, 136.1, 153.8, 171.9 ppm. IR (KBr): $\tilde{\nu}$ 3421, 3065, 2963, 2874, 1775, 1711, 1597 cm^{-1} . Mass (m/z , %): 324 (M^+ , 4), 269 (17), 268 (100), 267 (94), 120 (56), 119 (34), 92 (11), 91 (22), 77 (28), 57 (29). HRMS (ESI): 347.1380, calcd for $C_{19}H_{20}N_2O_3Na$ [$M + Na$] $^+$ 347.1372.

Synthesis of 1-Naphthyl-2-phenylethane-1,2-dione (6ab) by the Reaction of 5-Hydroxy-*N,N'*,5-triphenylimidazolidine-2,4-dione (7a) with 1-Naphthyllithium (9b). *Typical Procedure.* To the solution of 1-naphthyllithium (9b) prepared from BuLi (1.63 M in hexane, 4.10 mL, 6.68 mmol) and 1-bromonaphthalene in dry THF (10 mL), a solution of 5-hydroxy-*N,N'*,5-triphenylimidazolidine-2,4-dione (7a) (1.01 g, 2.93 mmol) in dry THF (5 mL) was added dropwise under a N_2 atmosphere at -78°C and stirred for 1 h. The reaction mixture was poured into sat. aq. NH_4Cl and then extracted with AcOEt. The organic layer was washed with sat. aq. NaCl, dried over anhydrous Na_2SO_4 and concentrated in vacuo. The crude product was dissolved in $CHCl_3$ (15 mL) including Et_3N (catalytic amount), stirred at 50°C for 30 min and concentrated in vacuo. The residue was rinsed with $CHCl_3$ to remove *N,N'*-diphenylurea by filtration and the filtrate was concentrated in vacuo. The residue was chromatographed on silica gel and eluted with hexane–AcOEt (4:1) to give **6ab** (753 mg, 99% yield) as a yellow solid.

6ab: pale-yellow granules melted at 103.0 – 104.0°C (from CH_2Cl_2) (lit.,²⁰ 101.5 – 102°C). 1H NMR (400 MHz, $CDCl_3$): δ_H 7.44–7.54 (m, 3H), 7.58–7.68 (m, 2H), 7.74 (ddd, $J = 8.6, 6.8,$ and 1.3 Hz, 1H), 7.91 (dd, $J = 7.3$ and 1.2 Hz, 1H), 7.93 (d with fine coupling, $J = 8.3$ Hz, 1H), 8.03 (d with fine coupling, $J = 8.3$ Hz, 2H), 8.11 (d, $J = 8.2$ Hz, 1H), 9.31 (d with fine coupling, $J = 8.6$ Hz, 1H) ppm. ^{13}C NMR (125 MHz, $CDCl_3$): δ_C 124.4, 125.9, 127.1, 128.5, 128.7, 129.0 ($\times 2$), 129.4, 129.9 ($\times 2$), 130.9, 133.3, 134.0, 134.7, 135.0, 135.9, 194.5, 197.1 ppm. IR (KBr): $\tilde{\nu}$ 3065, 1673, 1661, 1594, 1572 cm^{-1} . Mass (m/z , %): 260 (M^+ , 9), 156 (11), 155 (100), 127 (68), 126 (14), 105 (17), 77 (29). HRMS (ESI): 283.0740, calcd for $C_{18}H_{12}O_2Na$ [$M + Na$] $^+$ 283.0735.

According to the procedure described above, unsymmetrical diketones **6ab**, **6bc**, **6bf**, **6cf**, **6ag** and **6ak** were synthesized by the reaction of 5-hydroxy-5-(1-naphthyl)-*N,N'*-diphenylimidazolidine-2,4-dione (**7b**) with phenyllithium (**9a**), **7b** with 2-naphthyllithium (**9c**), **7b** with butyllithium (**9f**), 5-hydroxy-5-(2-naphthyl)-*N,N'*-diphenylimidazolidine-2,4-dione (**7c**) with butyllithium (**9f**), 5-hydroxy-5-(4-methylphenyl)ethynyl-*N,N'*-diphenylimidazolidine-2,4-dione (**7g**) with **9a**, 5-tert-butyl-5-hydroxy-*N,N'*-diphenylimidazolidine-2,4-dione (**7k**) with phenyllithium (**9a**), respectively. The yields were 88% for **6ab** (from **7b** with **9a**), 83% for **6bc**, 91% for **6bf**, 97% for **6cf**, 98% for **6ag**, and 62% for **6ak**.

6bc: yellow granules melted at 140.0 – 141.5°C (from CH_2Cl_2). 1H NMR (500 MHz, $CDCl_3$): δ_H 7.46 (dd, $J = 8.0$ and 7.6 Hz, 1H), 7.53 (dd, $J = 8.2$ and 7.1 Hz, 1H), 7.60–7.66 (m, 2H), 7.76 (dd with fine coupling, $J = 8.7$ and 6.9 Hz, 1H), 7.88 (d, $J = 8.2$ Hz, 1H), 7.89 (d, $J = 8.2$ Hz, 1H), 7.92–7.98 (m, 3H), 8.11 (d, $J = 8.0$ Hz, 1H), 8.14 (dd with fine coupling, $J = 8.7$ and 1.6 Hz, 1H), 8.48 (s, 1H), 9.37 (d, $J = 8.7$ Hz, 1H) ppm. ^{13}C NMR (125 MHz, $CDCl_3$): δ_C 123.9, 124.4, 126.0, 127.1, 127.1, 127.9, 128.8, 128.8, 129.1, 129.4 ($\times 2$), 129.9, 130.7, 131.0, 132.4, 133.4, 134.1, 135.2, 135.9, 136.3, 194.7, 197.1 ppm. IR (KBr): $\tilde{\nu}$ 3380, 3044, 1780, 1722, 1597 cm^{-1} . Mass (m/z , %): 310 (M^+ , 11), 156 (12), 155 (100), 128 (11), 127 (97), 126 (20). HRMS (ESI): 333.0898, calcd for $C_{22}H_{14}O_2Na$ [$M + Na$] $^+$ 333.0892.

6bf: yellow oil. 1H NMR (500 MHz, $CDCl_3$): δ_H 0.97 (t, $J = 7.3$ Hz, 3H), 1.41–1.50 (m, 2H), 1.71–1.78 (m, 2H), 2.97 (t, $J = 7.4$ Hz, 2H), 7.53 (dd, $J = 8.2$ and 7.3 Hz, 1H), 7.59 (ddd, $J = 8.2, 6.9,$ and 1.1 Hz, 1H), 7.68 (ddd, $J = 8.5, 6.9,$ and 1.4 Hz, 1H), 7.87 (dd, $J = 7.3$ and 1.4 Hz, 1H), 7.92 (d with fine coupling, $J = 8.2$ Hz, 1H), 8.10 (d, $J = 8.2$ Hz, 1H), 8.96 (d, $J = 8.5$ Hz, 1H) ppm. ^{13}C NMR (125 MHz, $CDCl_3$): δ_C 13.8, 22.4, 25.1, 38.6, 124.2, 125.7, 126.9, 128.1, 128.7, 129.0, 131.1, 133.6, 134.1, 135.3, 195.6, 204.0 ppm. IR (liquid film): $\tilde{\nu}$ 2959, 1710, 1666 cm^{-1} . Mass (m/z , %): 240 (M^+ , 89), 197 (16), 169 (19), 157 (11), 156 (100), 155 (99), 128 (95), 127 (97), 126 (94), 101 (44), 85 (16), 77 (50), 76 (14), 75 (25), 74 (12), 57 (31), 51 (14). HRMS (ESI): 263.1037, calcd for $C_{16}H_{16}O_2Na$ [$M + Na$] $^+$ 263.1048.

6cf: yellow oil. 1H NMR (500 MHz, $CDCl_3$): δ_H 0.96 (t, $J = 7.3$ Hz, 3H), 1.39–1.48 (m, 2H), 1.69–1.77 (m, 2H), 2.94 (t, $J = 7.3$ Hz, 2H), 7.57 (dd, $J = 8.2$ and 6.9 Hz, 1H), 7.64 (dd, $J = 8.2$ and 6.9 Hz, 1H), 7.88 (d, $J = 8.2$ Hz, 1H), 7.92 (d, $J = 8.7$ Hz, 1H), 7.96 (d, $J = 8.2$ Hz, 1H), 8.03 (dd, $J = 8.7$ and 1.8 Hz, 1H), 8.51 (s with fine coupling, 1H) ppm. ^{13}C NMR (125 MHz, $CDCl_3$): δ_C 13.8, 22.3, 25.0, 38.6, 124.2, 127.0, 127.9, 128.9, 129.2, 129.4, 130.0, 132.3, 133.5, 136.2, 192.5, 203.7 ppm. IR (liquid film): $\tilde{\nu}$ 2959, 1711, 1668, 1626 cm^{-1} . Mass (m/z , %): 240 (M^+ , 7), 156 (12), 155 (100), 127 (66), 126 (12). HRMS (ESI): 263.1061, calcd for $C_{16}H_{16}O_2Na$ [$M + Na$] $^+$ 263.1048.

6ag: yellow oil. 1H NMR (500 MHz, $CDCl_3$): δ_H 2.40 (s, 3H), 7.22 (d, $J = 7.8$ Hz, 2H), 7.51–7.57 (m, 4H), 7.67 (t with fine coupling, $J = 7.3$ Hz, 1H), 8.08 (d with fine coupling, $J = 7.3$ Hz, 2H) ppm. ^{13}C NMR (125 MHz, $CDCl_3$): δ_C 21.9, 87.1, 100.1, 116.1, 128.9 ($\times 2$), 129.6 ($\times 2$), 130.5 ($\times 2$), 131.7, 133.7 ($\times 2$), 134.8, 142.7, 178.6, 188.6 ppm. IR (liquid film): $\tilde{\nu}$ 2186, 1679, 1657, 1601 cm^{-1} . Mass (m/z , %): 248 (M^+ , 2), 192 (27), 144 (11), 143 (100), 115 (13), 105 (58), 77 (55). HRMS (ESI): 271.0738, calcd for $C_{17}H_{12}O_2Na$ [$M + Na$] $^+$ 271.0735.

6ak: yellow oil. 1H NMR (400 MHz, $CDCl_3$): δ_H 1.31 (s, 9H), 7.50 (dd, $J = 7.9$ and 7.4 Hz, 2H), 7.64 (t with fine coupling, $J = 7.4$ Hz, 1H), 7.83 (d with fine coupling, $J = 7.9$ Hz, 2H) ppm. ^{13}C NMR (125 MHz, $CDCl_3$): δ_C 26.2 ($\times 3$), 42.6, 128.9 ($\times 2$), 129.5 ($\times 2$), 132.9, 134.5, 195.4, 210.9 ppm. (lit.,^{3a} 100 MHz, $CDCl_3$, δ_C 26.2, 42.6, 128.9, 129.5, 132.8, 134.5, 195.4, 210.9 ppm). IR (liquid film): $\tilde{\nu}$ 2969, 1704, 1676, 1597 cm^{-1} . Mass (m/z , %): 190 (M^+ , 3), 105 (100), 77 (51), 57 (23).

Synthesis of 2-Oxo-2-naphthylethanoic Acid (8c) from 5-Hydroxy-5-(2-naphthyl)-*N,N'*-diphenylimidazolidine-2,4-dione (7c). *Typical Procedure.* NaOH in H_2O (4 M, 3 mL) was added to a solution of 5-hydroxy-5-(2-naphthyl)-*N,N'*-diphenylimidazolidine-2,4-dione (**7c**) (1.16 g, 2.94 mmol) in MeOH (10 mL) at room temperature and heated 50°C for 1 h. The reaction mixture poured into H_2O and extracted with AcOEt to give organic layer including *N,N'*-diphenylurea. The thus-obtained aqueous layer was acidified with 1N HCl, and then extracted with AcOEt. The AcOEt solution was washed with sat. aq. NaCl, dried over anhydrous Na_2SO_4 and concentrated in vacuo. The residue was crystallized from hexane– CH_2Cl_2 to give **8c** (525 mg, 89% yield) as a yellow solid.

8c: yellow granules melted at 92.0 – 93.0°C (from AcOEt–hexane) (lit.,²¹ 92 – 93°C from xylene). 1H NMR (500 MHz, $CDCl_3$): δ_H 7.59 (dd with fine coupling, $J = 8.2$ and 6.9 Hz, 1H), 7.68 (dd with fine coupling, $J = 8.2$ and 6.9 Hz, 1H), 7.89 (d, $J = 8.2$ Hz, 1H), 7.93 (d, $J = 8.7$ Hz, 1H), 8.02 (d, $J = 8.2$ Hz, 1H), 8.18 (d with fine coupling, $J = 8.7$ Hz, 1H), 8.95–9.17 (m, 1H), 9.09 (s, 1H) ppm. ^{13}C NMR (125 MHz, $CDCl_3$): δ_C 124.4, 127.2, 127.8, 128.9, 129.0, 130.0, 130.3, 132.2, 135.2, 136.5, 163.3, 184.3 ppm. IR (KBr): $\tilde{\nu}$ 3062, 3006, 2964, 1747, 1653, 1616, 1588 cm^{-1} . HRMS (ESI negative): 199.0345, calcd for $C_{12}H_8O_3$ [$M - H$] $^-$ 199.0395.

According to the procedure described above, 5-substituted 5-hydroxyimidazolidine-2,4-diones (**7a**, **7b**, **7d**, **7e**, **7i** and **7k**) were individually hydrolyzed to give the corresponding α -ketocarboxylic acids **8a** (98%), **8b** (94%), **8d** (78%), **8e** (39%), **8i** (84%), and **8k** (96%); for hydrolysis of **7e**, **8e** was produced along with 2-oxo-*N*-phenyl-2-(2,4,6-trimethylphenyl)acetamide (**14**) (54%). Hydroxyimidazolidinedione **7g** was similarly hydrolyzed to give 5-(4-methylphenyl)furan-2,3-dione in 80% yield instead of the expected keto carboxylic acid (**8g**).

8a: yellow oil. 1H NMR (500 MHz, $CDCl_3$): δ_H 7.53 (dd, $J = 8.2$ and 7.6 Hz, 2H), 7.70 (td, $J = 7.6$ and 1.1 Hz, 1H), 8.23 (dd, $J = 8.2$ and 1.1 Hz, 2H), 9.77 (s, 1H) ppm. (lit.,²¹ $CDCl_3$, δ_H 7.51 (t, $J = 7.8$ Hz, 2H), 7.65 (t, $J = 7.8$ Hz, 1H), 8.14 (d, $J = 7.8$ Hz, 2H), 12.47 (s, 1H) ppm). ^{13}C NMR (125 MHz, $CDCl_3$): δ_C 129.0 ($\times 2$), 130.9 ($\times 2$), 131.7, 135.6, 163.8, 184.9 ppm. IR (liquid film): $\tilde{\nu}$ 3496, 1741, 1686, 1596 cm^{-1} . HRMS (ESI negative): 299.0570, calcd for $C_{16}H_{11}O_6$ [$2M - H$] $^-$ 299.0556.

8b: colorless needles melted at 102.0 – 103.0°C (from CH_2Cl_2 –hexane) (lit.,²² 112 – 114°C). 1H NMR (500 MHz, $CDCl_3$): δ_H 7.51–7.62 (m, 2H), 7.68 (dd, $J = 8.2$ and 6.9 Hz, 1H), 7.90 (d, $J = 7.8$ Hz, 1H), 8.12 (d, $J = 7.3$ Hz, 1H), 8.32 (d, $J = 6.9$ Hz, 1H), 8.93 (d, $J = 8.7$ Hz, 1H), 10.51–11.06 (m, 1H) ppm. ^{13}C NMR (125 MHz,

CDCl₃): δ_{C} 124.3, 125.3, 127.1, 127.2, 128.9, 129.5, 131.0, 133.8, 134.9, 136.5, 165.4, 187.0 ppm. IR (KBr): $\tilde{\nu}$ 3142, 1701, 1681, 1573 cm⁻¹. HRMS (ESI negative): 199.0346, calcd for C₁₂H₇O₃ [M - H]⁻ 199.0395.

8d: pale yellow solid melted at >300 °C. ¹H NMR (500 MHz, DMSO-*d*₆): δ_{H} 7.49–7.56 (m, 4H), 8.07–8.15 (m, 2H), 8.18–8.27 (m, 2H), 8.64 (s, 1H) ppm. ¹³C NMR (125 MHz, DMSO-*d*₆): δ_{C} 125.7 (×2), 126.1 (×2), 126.4 (×2), 127.9, 128.0 (×2), 128.5 (×2), 130.8 (×2), 136.4, 169.1, 203.6 ppm. IR (KBr): $\tilde{\nu}$ 3399, 3052, 1673, 1645 cm⁻¹. HRMS (ESI negative): 249.0534, calcd for C₁₆H₉O₃ [M - H]⁻ 249.0552.

8e: pale yellow columns melted at 119.0–120.0 °C (from CH₂Cl₂–hexane) (lit.²³ 118.8–119.4 °C from hexane). ¹H NMR (500 MHz, CDCl₃): δ_{H} 2.25 (s, 6H), 2.30 (s, 3H), 6.89 (s, 2H), 10.4 (s, 1H) ppm. ¹³C NMR (125 MHz, CDCl₃): δ_{C} 19.6 (×2), 21.2, 129.1 (×2), 131.6, 136.4 (×2), 141.5, 163.4, 192.0 ppm. IR (KBr): $\tilde{\nu}$ 3042, 2961, 2926, 1721, 1692, 1609 cm⁻¹. HRMS (ESI negative): 191.0695, calcd for C₁₁H₁₁O₃ [M - H]⁻ 191.0708.

14: colorless needles melted at 136.0–137.5 °C (from CH₂Cl₂). ¹H NMR (300 MHz, CDCl₃): δ_{H} 2.23 (s, 6H), 2.31 (s, 3H), 6.90 (s, 2H), 7.19 (t with fine coupling, *J* = 7.4 Hz, 1H), 7.39 (dd with fine coupling, *J* = 8.7 and 7.4 Hz, 2H), 7.70 (d with fine coupling, *J* = 8.7 Hz, 2H), 8.87 (s, 1H) ppm. ¹³C NMR (125 MHz, CDCl₃): δ_{C} 19.5 (×2), 21.2, 119.6 (×2), 125.2, 128.7 (×2), 129.2 (×2), 132.6, 135.6 (×2), 136.6, 140.4, 158.0, 197.3 ppm. IR (KBr): $\tilde{\nu}$ 3287, 3135, 3060, 3018, 2975, 2920, 1685, 1674, 1674, 1600, 1542 cm⁻¹. Mass (*m/z*, %): 267 (M⁺, 3), 148 (11), 147 (100), 119 (17), 91 (10). HRMS (ESI): 268.1324, calcd for C₁₇H₁₈NO₂ [M + H]⁺ 268.1338, 290.1154, calcd for C₁₇H₁₇NO₂Na [M + Na]⁺ 290.1157. Anal. Calcd for C₁₇H₁₇NO₂: C, 76.38; H, 6.41; N, 5.24. Found: C, 76.09; H, 6.29; N, 5.13.

5-(4-Methylphenyl)furan-2,3-dione as a Cyclized Form of 8g. Colorless needles were melted at 142.5–144.0 °C (from CHCl₃) (lit.²⁴ 136–137 °C (decom.)). ¹H NMR (500 MHz, CDCl₃): δ_{H} 2.45 (s, 3H), 7.15 (s, 1H), 7.32 (d, *J* = 8.2 Hz, 2H), 7.92 (d, *J* = 8.2 Hz, 2H) ppm. ¹³C NMR (125 MHz, CDCl₃): δ_{C} 21.8, 95.3, 128.1 (×2), 129.8 (×2), 130.6, 145.6 (×2), 162.6, 187.6 ppm. IR (KBr): $\tilde{\nu}$ 1700, 1604 cm⁻¹. Mass (*m/z*, %): 188 (M⁺, 1), 162 (11), 161 (100), 119 (17).

8i: orange granules melted at 183.0–185.0 °C (from AcOEt–hexane) (lit.²⁵ 170–172 °C from ethanol). ¹H NMR (500 MHz, CDCl₃): δ_{H} 8.09–8.15 (m, 2H), 8.23 (d, *J* = 8.2 Hz, 1H), 8.28 (d, *J* = 8.7 Hz, 1H), 8.31–8.38 (m, 3H), 8.90 (d, *J* = 8.2 Hz, 1H), 9.17 (d, *J* = 9.6 Hz, 1H) ppm. ¹³C NMR (125 MHz, CDCl₃): δ_{C} 123.8, 123.9, 124.0, 124.2, 124.9, 126.8, 127.2, 127.3, 127.6, 130.3, 130.9, 131.4 (×2), 131.5, 132.3, 136.4, 161.5, 186.4 ppm. IR (KBr): $\tilde{\nu}$ 3466, 3013, 1712, 1666, 1592 cm⁻¹. HRMS (ESI negative): 273.0600, calcd for C₁₈H₉O₃ [M - H]⁻ 273.0552.

8k: colorless oil. ¹H NMR (300 MHz, CDCl₃): δ_{H} 1.34 (s, 9H), 7.81–8.47 (m, 1H) ppm. ¹³C NMR (125 MHz, CDCl₃): δ_{C} 25.6 (×3), 42.5, 164.2, 202.0 ppm. (lit.²⁶ 100 MHz, CDCl₃, 25.6 (×3), 42.5, 163.7, 201.9 ppm. IR (liquid film): $\tilde{\nu}$ 3538, 2977, 1717 cm⁻¹. HRMS (ESI negative): 259.1185, calcd for C₁₂H₁₉O₆ [2M - H]⁻ 259.1182.

ASSOCIATED CONTENT

Supporting Information

¹H NMR/¹³C NMR spectra of **5g**, **7a**, **7b**, **7c**, **7d**, **7e**, **7g**, **7i**, **7j**, **7k**, **6bc**, **6bf**, **6cf**, **6ag** and **14**. This material is available free of charge via the Internet at <http://pubs.acs.org>.

AUTHOR INFORMATION

Corresponding Author

*E-mail: matsumo-chem@kanagawa-u.ac.jp.

ACKNOWLEDGMENTS

We gratefully acknowledge financial assistance provided by Grants-in-aid (No. 22550046 and No. 21550052) for Scientific Research from the Ministry of Education, Culture, Sports, Science, and Technology, Japan.

REFERENCES

- (a) Wan, Z.; Jones, C. D.; Mitchell, D.; Pu, J. Y.; Zhang, T. Y. *J. Org. Chem.* **2006**, *71*, 826–828. (b) Yasubov, M. S.; Zholobova, G. A.; Vasilievsky, S. F.; Tretyakov, E. V.; Knight, D. W. *Tetrahedron* **2002**, *58*, 1607–1610. (c) Chen, M.; Zhao, Q.; She, D. B.; Yang, M. Y.; Hui, H. H.; Huang, G. S. *J. Chem. Sci.* **2008**, *119*, 347–351. (d) Giraud, O.; Provot, O.; Peyrat, J.-F.; Alami, M.; Brion, J.-D. *Tetrahedron* **2006**, *62*, 7667–7673. (e) Mousset, C.; Provot, O.; Hamze, A.; Bignon, J.; Brion, J.-D. *Tetrahedron* **2008**, *64*, 4287–4294.
- (2) (a) Lai, S.; Lee, D. G. *Tetrahedron* **2002**, *58*, 9879–9887. (b) Mader, M.; Dios, A.; de; Shih, C.; Bonjouklian, R.; Li, T.; White, W.; Uralde, B. L.; de; Sánchez-Martinez, C.; Prado, M.; Jaramillo, C.; Diego, E.; de; Cabrejas, L. M. M.; Dominguez, C.; Montero, C.; Shepherd, T.; Dally, R.; Toth, J. E.; Chatterjee, A.; Pleite, S.; Blanco-Urgoiti, J.; Perez, L.; Barberis, M.; Lorite, M. J.; Jambriña, E.; Nevill, P. C. R. Jr.; Lee, A.; Schultz, R. C.; Wolos, J. A.; Li, L. C.; Campbell, R. M.; Anderson, D. *Bioorg. Med. Chem. Lett.* **2008**, *18*, 179–183. (c) Walsh, C. J.; Mandal, B. K. *J. Org. Chem.* **1999**, *64*, 6102–6105.
- (3) (a) Rei, W.; Liu, J.; Chen, L.; Wan, X. *Adv. Synth. Catal.* **2010**, *352*, 1424–1428. (b) Ryu, J. Y.; Heo, S.; Park, J.; Nam, W.; Kim, J. *Inorg. Chem. Commun.* **2004**, *7*, 534–537.
- (4) (a) Chandrasekhar, S.; Reddy, N. K.; Kumer, V. P. *Tetrahedron Lett.* **2010**, *51*, 3623–3625. (b) Che, C.-M.; Yu, W.-Y.; Chan, P.-M.; Cheng, W.-C.; Peng, S.-M.; Lau, K.-C.; Li, W.-K. *J. Am. Chem. Soc.* **2000**, *122*, 11380–11392.
- (5) (a) Ren, W.; Xia, Y.; Ji, S.-J.; Zhang, Y.; Wan, X.; Zhao, J. *Org. Lett.* **2009**, *11*, 1841–1844. (b) Tan, K. J.; Wille, U. *Chem. Commun.* **2008**, 6239–6241. (c) Nobuta, T.; Tada, N.; Hattori, K.; Hirashima, S.; Miura, T.; Itoh, A. *Tetrahedron Lett.* **2011**, *52*, 875–877.
- (6) (a) Muthupandi, P.; Sekar, G. *Tetrahedron: Asymmetry* **2011**, *22*, 512–517. (b) Karimi, B.; Farhabgi, E. *Chem.—Eur. J.* **2011**, *17*, 6056–6060. (c) Tochtermann, W.; Kirrstetter, R. G. H. *Chem. Ber.* **1978**, *111*, 1228–1230. (d) Macainoe, D. P.; Wentworth, S. E. *Synthesis* **1974**, 716. (e) Weiss, M.; Appel, M. J. *J. Am. Chem. Soc.* **1948**, *70*, 3666–3667.
- (7) Wasserman, H. H.; Ives, J. L. *J. Org. Chem.* **1985**, *50*, 3573–3580.
- (8) Gopal, D.; Nadekarni, D. V.; Sayre, L. M. *Tetrahedron Lett.* **1998**, *39*, 1877–1880.
- (9) Mitchell, R. H.; Iyer, V. S. *Tetrahedron Lett.* **1993**, *34*, 3683–3686.
- (10) (a) Sibi, M. P.; Sharma, R.; Paulson, K. L. *Tetrahedron Lett.* **1992**, *33*, 1941–1944. (b) Sibi, M. P.; Marvin, M.; Sharma, R. *J. Org. Chem.* **1995**, *60*, 5616–5023.
- (11) (a) Mueller-Westerhoff, U. T.; Zhou, M. *Tetrahedron Lett.* **1993**, *34*, 571–574. (b) Mueller-Westerhoff, U. T.; Zhou, M. *J. Org. Chem.* **1994**, *59*, 4988–4992.
- (12) (a) Fault, R.; Bruhn, C.; Rossi, S. *Acta. Cryst. Sect. C* **2005**, *61*, 253–255. (b) Castro, C. E.; Gaughan, E. J.; Owsley, C. J. *J. Org. Chem.* **1966**, *31*, 4071–4078. (c) Mitzel, F.; FitzGerald, S.; Beeby, A.; Fault, R. *Chem.—Eur. J.* **2003**, *9*, 1233–1241. (d) Faust, R.; Weber, C.; Fiandanese, V.; Marchese, G.; Punzi, A. *Tetrahedron* **1997**, *53*, 14655–14670. (e) Kashiwabara, T.; Tanaka, M. *J. Org. Chem.* **2009**, *74*, 3958–3961. (f) Merkul, E.; Dohl, J.; Gers, C.; Rominger, F.; Müller, T. J. *J. Angew. Chem., Int. Ed.* **2011**, *50*, 2966–2969.
- (13) Biltz, H.; Topp, E. *Chem. Ber.* **1913**, *46*, 1387–1404.
- (14) Although analogs of **4** with *N,N'*-dialkyl groups such dimethyl and diethyl also acted as α -diketone synthons, they were inferior to **4** in terms of reactivity with organolithiums and Grignard reagents, solubility, and ease of isolating the product(s).
- (15) Marsili, A.; Nuti, V.; Saettone, M. F. *Tetrahedron* **1969**, *25*, 3267–3275.
- (16) Katritzky, A. R.; Zhang, D.; Kirichenko, K. *J. Org. Chem.* **2005**, *70*, 3271–3274.
- (17) Nudelman, N. S.; Outumuro, P. *J. Org. Chem.* **1982**, *47*, 4347–4348.
- (18) Shimakawa, Y.; Morikawa, T.; Sakaguchi, S. *Tetrahedron Lett.* **2010**, *51*, 1786–1789.
- (19) Schuetz, R. D.; Nilles, G. P. *J. Org. Chem.* **1971**, *36*, 2486–2489.
- (20) Ruggli, P.; Reinert, M. *Helvetica Chem. Acta.* **1926**, *9*, 67–79.

- (21) Blick, F. F.; Feldkamp, R. F. *J. Am. Chem. Soc.* **1944**, *66*, 1087–1091.
- (22) Crich, D.; Zou, Y. *J. Org. Chem.* **2005**, *70*, 3309–3311.
- (23) Dauben, W. G.; Rogan, J. B. *J. Am. Chem. Soc.* **1956**, *78*, 4135–4139.
- (24) Igidov, N. M.; Koz'minykh, E. N.; Sofina, O. A.; Shironina, T. M.; Koz'minykh, V. O. *Chem. Heterocycl. Compd.* **1999**, *35*, 1276–1285.
- (25) Cymerman-Craig, J.; Loder, J. W.; Moore, B. *Aust. J. Chem.* **1956**, *9*, 222–227.
- (26) Koch, C.-J.; Šimonyiova, S.; Pabel, J.; Kärtner, A.; Polborn, K.; Wanner, K. T. *Eur. J. Org. Chem.* **2003**, 1244–1263.

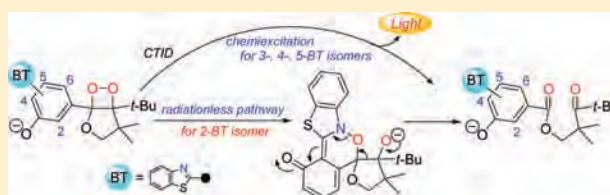
Base-Induced Chemiluminescent Decomposition of Bicyclic Dioxetanes Bearing a (Benzothiazol-2-yl)-3-hydroxyphenyl Group: A Radiationless Pathway Leading to Marked Decline of Chemiluminescence Efficiency

Masatoshi, Tanimura, Nobuko Watanabe, Hisako K. Ijuin, and Masakatsu Matsumoto*

Department of Chemistry, Kanagawa University, Tsuchiya, Hiratsuka, Kanagawa 259-1293, Japan

Supporting Information

ABSTRACT: Charge-transfer-induced decomposition (CTID) of bicyclic dioxetanes **1b–d** bearing a 3-hydroxyphenyl moiety substituted with a benzothiazol-2-yl group at the 2-, 6-, or 5-position was investigated, and their chemiluminescence properties were compared to each other, based on those for a 4-benzothiazolyl analogue **1a**. Dioxetanes **1c** and **1d** underwent CTID to give the corresponding oxido anions of keto esters **8c** or **8d** in the singlet excited state with high efficiencies similarly to the case of **1a**. On the other hand, **1b** showed chemiluminescence with quite low efficiency, though it gave exclusively keto ester **2b**. The marked decline of chemiluminescence efficiency for **1b** was attributed to **1b** mainly being decomposed to **8b** through a radiationless pathway, in which intramolecular nucleophilic attack of nitrogen in the benzothiazolyl group to dioxetane O–O took place to give cyclic intermediate *cis*-**11**.



INTRODUCTION

Dioxetanes substituted with an aromatic electron donor such as the phenoxide anion undergo intramolecular charge-transfer-induced decomposition (CTID) with an accompanying emission of bright light.^{1–4} The phenomenon has received considerable attention from the viewpoints of mechanistic interest related to bioluminescence and application to clinical and biological analysis.^{5–7} Thus, up to the present, a wide variety of CTID-active dioxetanes have been designed and synthesized. One such dioxetane is bicyclic dioxetane **1a** bearing a 4-(benzothiazol-2-yl)-3-hydroxyphenyl group, which effectively emits light even in an aqueous system.^{8,9} To understand how the benzothiazol-2-yl group functioned to achieve high-performance chemiluminescence, we investigated CTID of three isomeric dioxetanes **1b–d**, in which a benzothiazolyl group was attached at the 2-, 6-, or 5-position on the 3-hydroxyphenyl group. We report here that these isomeric dioxetanes **1b–d** showed characteristic chemiluminescence depending on the structure of the aromatic electron donor, and that a radiationless decomposition of dioxetane **1b** concurrently took place with the chemiluminescent CTID, though both decompositions gave the same keto ester **2b** (Chart 1).

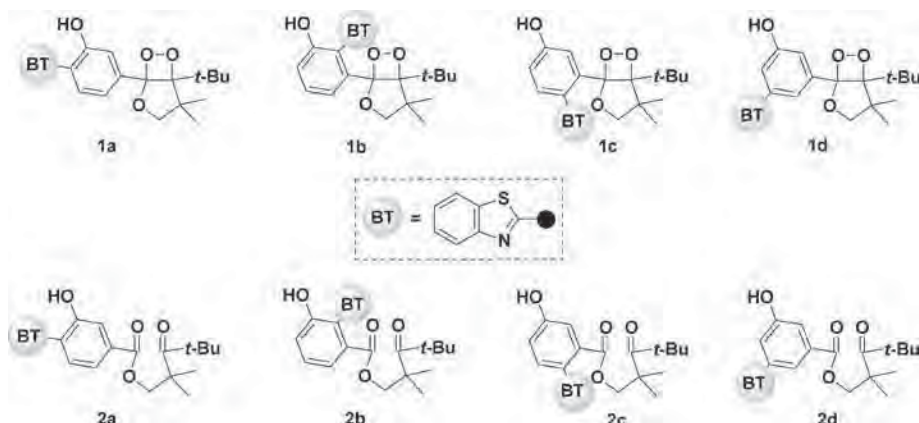
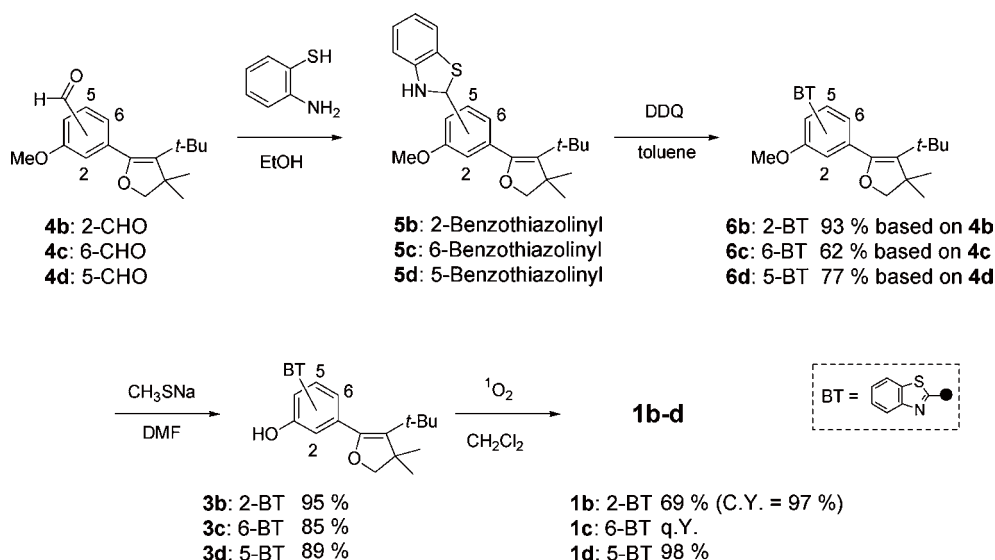
RESULTS AND DISCUSSION

Synthesis of Bicyclic Dioxetanes 1b–d Bearing a 3-Hydroxyphenyl Moiety Substituted with a Benzothiazol-2-yl Group. All of the dioxetanes **1b–d** investigated here were prepared by singlet oxygenation of the corresponding 4-*tert*-butyl-3,3-dimethyl-2,3-dihydrofurans **3b–d** bearing a 5-(3-

hydroxyphenyl) group, to which a benzothiazolyl group was attached at the 2-, 5-, or 6-position. These precursors **3b–d** were synthesized according to the synthetic process of **1a**⁹ through several steps starting from the corresponding 4-*tert*-butyl-3,3-dimethyl-2,3-dihydrofurans **4b–d** bearing a 5-(formyl-3-methoxyphenyl) group, as illustrated in Scheme 1. The initial step was condensation of **4b–d** with 2-aminobenzethiol to give exclusively the corresponding benzothiazolyl derivatives **5b–d**, which were used for the next reaction without further purification. The oxidation of benzothiazolines **5b–d** was achieved by the use of 2,3-dichloro-5,6-dicyano-1,4-benzoquinone (DDQ) in toluene to give dihydrofurans **6b–d** in high yields. Dihydrofurans **6b–d** were finally demethylated with sodium methanethiolate in hot DMF to give the desired precursors **3b–d** in 95, 85, and 89% yields, respectively. All of **3b–d** underwent 1,2-addition of singlet oxygen to selectively give the corresponding dioxetanes **1b–d** in 69 (conversion yield 97%), 100, and 98% yields. The structures of dioxetanes **1b–d** were determined by ¹H NMR, ¹³C NMR, IR, mass spectral data, and elemental analyses. Furthermore, X-ray single crystallographic analysis was successfully achieved for all dioxetanes **1b–d**. ORTEP views of dioxetanes **1b–d** are shown in the Supporting Information. All of these benzothiazolyl-substituted dioxetanes **1b–d** were thermally stable enough to permit handling at room temperature, though they decomposed into the corresponding keto esters **2b–d** when heated in refluxing *p*-xylene.

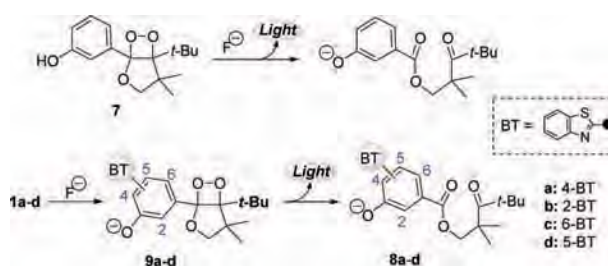
Received: March 13, 2012

Published: April 23, 2012

Chart 1. Bicyclic Dioxetanes **1a–d** Bearing a 3-Hydroxyphenyl Moiety Substituted with a Benzothiazol-2-yl Group and Their Decomposition Products **2a–d**Scheme 1. Synthetic Pathway of Dioxetanes **1b–d**

Chemiluminescent Decomposition of Bicyclic Dioxetanes Bearing a 3-Hydroxyphenyl Moiety Substituted with a Benzothiazol-2-yl Group in a TBAF/Acetonitrile System. Dioxetane **1a** has been reported to decompose according to the pseudo-first-order kinetics to give bright green light (maximum wavelength $\lambda_{\max}^{\text{CL}} = 492 \text{ nm}$) with chemiluminescence efficiency $\Phi^{\text{CL}} = 0.28$ and rate constant of CTID $k^{\text{CTID}} = 4.2 \times 10^{-4} \text{ s}^{-1}$ at $45 \text{ }^\circ\text{C}$ (half-life $t_{1/2} = \ln 2 / k^{\text{CTID}} = 1600 \text{ s}$) when treated with a large excess of tetrabutylammonium fluoride (TBAF) in acetonitrile.^{8,9} Comparing chemiluminescence properties for **1a** with those for parent dioxetane **7** bearing an unsubstituted 3-hydroxyphenyl group ($\lambda_{\max}^{\text{CL}} = 467 \text{ nm}$, $\Phi^{\text{CL}} = 0.11$, and $t_{1/2} = 25 \text{ s}$ in TBAF/acetonitrile at $25 \text{ }^\circ\text{C}$) (Scheme 2),¹⁰ we can see that the benzothiazolyl group acts to considerably improve Φ^{CL} , while decreasing $t_{1/2}$ by 2 orders.

Dioxetane **1b** has a π -electron system of *o*-(benzothiazol-2-yl)phenol formally the same as that of **1a**, though the benzothiazolyl group suffers the steric hindrance of the adjacent dioxetane ring and a hydroxy group at the opposite side. On treatment with TBAF (large excess) in acetonitrile at $25 \text{ }^\circ\text{C}$, dioxetane **1b** decomposed far more rapidly than **1a** with the

Scheme 2. Base-Induced Decomposition of Dioxetanes **1b–d** and **7**

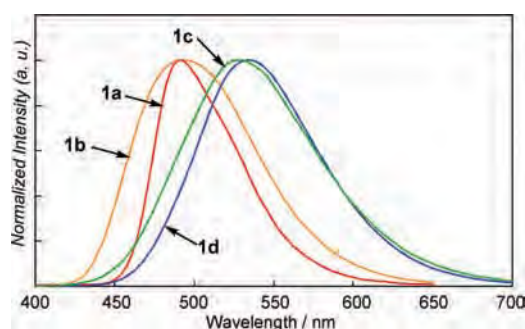
accompanying chemiluminescence, the $\lambda_{\max}^{\text{CL}}$ of which was the same as that for **1a**, as shown in Table 1, though the spectrum was broader than that for **1a**, as shown in Figure 1. However, Φ^{CL} for **1b** was unexpectedly low ($\Phi^{\text{CL}} = 0.0036$)^{11,12} and only 1/80 of that for **1a**.

Careful neutralization of the spent reaction mixture of **1b** gave selectively keto ester **2b** as in the case of **1a** giving **2a**. Oxido anion **8b** generated from **2b** in situ in TBAF/acetonitrile showed fluorescence, the spectrum of which practically

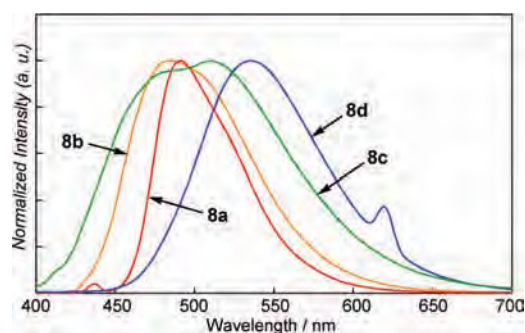
Table 1. TBAF-Induced Chemiluminescence of Dioxetanes **1a–d** and **7^a**

dioxetane	$\lambda_{\text{max}}^{\text{CL}}/\text{nm}$	Φ^{CLb}	Φ^{fl}	Φ_{S}	$k^{\text{CTID}}/\text{s}^{-1}$	$t_{1/2}/\text{s}$
1a^c	492	0.28	0.66	0.42	4.2×10^{-4}	1600
1b	493	0.0036	0.67	0.0054	2.0×10^{-2}	34
1c	528	0.011	0.024	(0.46)	6.9×10^{-5}	11000
1d	535	0.044	0.060	0.73	7.2×10^{-3}	96
7^d	467	0.11	0.24 ^e	0.46	2.8×10^{-2}	25

^aUnless otherwise stated, reactions were carried out in a TBAF/ acetonitrile system at 45 °C. ^bBased on a value reported for the chemiluminescent decomposition of 3-adamantylidene-4-(3-*tert*-butyldimethylsilyloxyphenyl)-4-methoxy-1,2-dioxetane in TBAF/DMSO.^{11,12} ^cFrom ref 9. ^dFrom ref 10. Chemiluminescent decomposition was carried out at 25 °C. ^eFrom ref 13.

**Figure 1.** Chemiluminescence spectra of dioxetanes **1a–d**.

coincided with chemiluminescence spectrum of **1b** (Figure 2). This result showed that **8b** was the emitter produced through

**Figure 2.** Fluorescence spectra of authentic **8a–d** generated from **2a–d** in TBAF/acetonitrile.

9b from **1b** (Scheme 2). On the basis of fluorescence efficiency $\Phi^{\text{fl}} = 0.67$ measured for **8b**, singlet chemiexcitation efficiency $\Phi_{\text{S}} (= \Phi^{\text{CL}}/\Phi^{\text{fl}})$ for **1b** was estimated to be only 0.0054 and 1/80 of that for **1a**. Therefore, unexpected decline of Φ^{CL} for **1b** was attributed to quite low Φ_{S} . Thus, we decided to investigate TBAF-induced decomposition of analogous dioxetanes **1c** and **1d** to understand why **1b** gave such a poor chemiluminescence.

Benzothiazolyl group of dioxetane **1c** lies in a π -conjugation system with a hydroxy group, though at the *para*-position differently from the case of **1a** and **1b**, and receives steric effect of the adjacent dioxetane ring as **1b**. When **1c** was treated in a TBAF/acetonitrile system similarly to the case of **1b**, **1c** showed chemiluminescence, the spectrum of which shifted to a longer wavelength region from the case of **1a** and **1b**, as shown

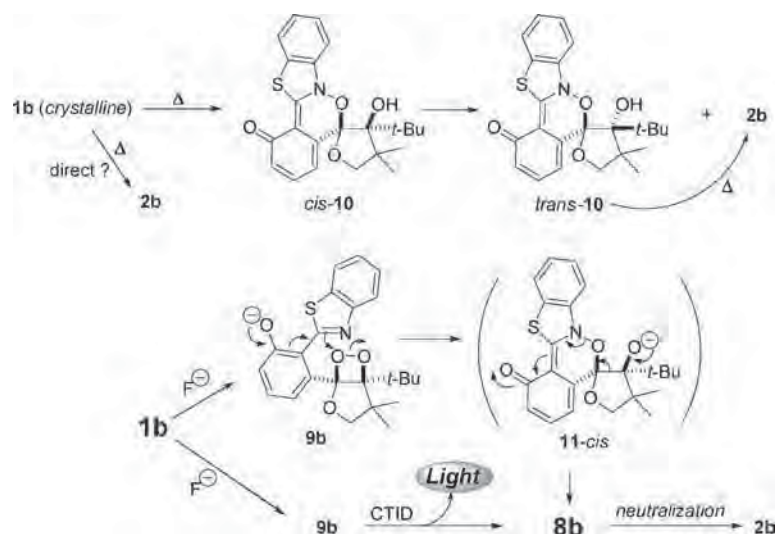
in Figure 1 and Table 1. Value of Φ^{CL} for **1c** was considerably higher than that for **1b**, though the rate of CTID markedly decreased.

Benzothiazolyl group of dioxetane **1d** does not directly lie in π -conjugation system with a hydroxy group and receives steric effect from neither a dioxetane ring nor a hydroxyl group since these three groups are in *meta*-relation among each other. Therefore, the aromatic system of **1d** lies in a different situation from those for **1a**, **1b**, and **1c**. Dioxetane **1d** also underwent TBAF-induced decomposition to give light, the spectrum of which is shown in Figure 1. As shown in Table 1 and Figure 1, comparing that for dioxetane **7** rather than **1a**, the chemiluminescence spectrum shifted to a longer wavelength region, but both Φ^{CL} and k^{CTID} decreased for **1d**: low Φ^{CL} was attributed to low Φ^{fl} of the emitter (*vide infra*). Such a tendency has been observed for various dioxetanes bearing a 5-aryl-3-hydroxyphenyl group (1,3,5-trisubstitution pattern).¹⁴

Both dioxetanes **1c** and **1d** gave also the corresponding keto esters **2c** and **2d** in high yields after careful neutralization of spent reaction mixtures, as in the case of **1a** and **1b**. Fluorescence spectrum of authentic emitter **8d** generated from **2d** coincided with the chemiluminescence spectrum of dioxetane **1d** (Figure 2). On the basis of fluorescence efficiency Φ^{fl} (0.060) for **8d**, singlet chemiexcitation efficiency Φ_{S} for **1d** was estimated to be as high as or rather higher than for **1a**, as shown in Table 1. On the other hand, authentic emitter **8c** generated from **2c** showed fluorescence ($\Phi^{\text{fl}} = 0.024$), the spectrum of which did not coincide with the chemiluminescence spectrum of **1c** and showed two peaks, differently from the case of **8a**, **8b**, and **8d** (Figure 2). Notably, the concentration of **8c** did not affect the shape of the spectrum. Thus, the fluorescence spectrum of **8c** was analyzed to comprise two fluorescence spectra: the first coincided with the chemiluminescence spectrum of **1c** ($\lambda_{\text{max}}^{\text{fl}} = 528 \text{ nm}$), and the second was one with $\lambda_{\text{max}}^{\text{fl}} = 466 \text{ nm}$ (Figure 2 and the Supporting Information). This finding suggests that **8c** should exist as an equilibrium mixture of at least two species.¹⁵ Here, chemiexcitation efficiency Φ_{S} for **1c** was formally estimated to be as high as that for **1a** (Table 1), though it could not reliably be estimated because of a discrepancy in the spectrum between chemiluminescence of **1c** and the fluorescence of **8c**.

As described above, singlet chemiexcitation effectively occurred for CTID of **1a**, **1c**, and **1d** but not for **1b**. Considering that **1a** and **1b** both have an *ortho*-benzothiazolyl-substituted phenol group as an important aromatic electron donor as well as a fluorophore and that the authentic emitters **8a** and **8b** both effectively show fluorescence, the marked decrease in Φ_{S} for CTID of **1b** was unexpected. Thus, we thought that **1b** may decompose to keto ester **8b** through a new concurrent pathway(s) that did not lead to chemiluminescence. A clue to understanding this radiationless decomposition was found when we measured the melting point of **1b**.

After a sample of crystalline **1b** was heated to melting (100 °C), we found the unusual decomposition product *trans*-**10** in addition to intact dioxetane **1b** and keto ester **2b**. Chromatographic purification (SiO_2) gave crystalline *trans*-**10**, the structure of which was determined by X-ray single crystallographic analysis (Supporting Information). However, the ¹H NMR and ¹³C NMR spectra of pure *trans*-**10** could not be measured because of its instability: *trans*-**10** was contaminated by ca. 10% of keto ester **2b**. Notably, crystalline **1a**, **1c**, and **1d** exclusively gave the corresponding keto esters **2a**, **2c**, and **2d** when heated to melting.

Scheme 3. Radiationless Decomposition of Dioxetane **1b** to Keto Ester **2b**

The unusual decomposition product *trans*-**10** was thought to be derived from an intramolecular redox reaction between the benzothiazolyl nitrogen and the O–O in dioxetane **1b**. A redox reaction between an amine and a dioxetane has been reported by Adam and his co-workers: a *primary* or *secondary* amine attacks a dioxetane to give the corresponding 2-aminoxyethanol, while *tertiary* amine catalyzes the decomposition of dioxetane to two carbonyl fragments through an as-yet-undetected aminoxy intermediate.¹⁶ Thus, *trans*-**10** was the first example of an aminoxy intermediate for the *tert*-amine-catalyzed decomposition of dioxetane. In fact, when heated at >100 °C, *trans*-**10** changed exclusively to **2b**. However, such a redox reaction would directly give isomeric *cis*-**10** but not *trans*-**10**. Although product *cis*-**10** could not be isolated in pure form after thermolysis of crystalline **1b** (vide infra),¹⁷ its structure was fortunately determined by X-ray single crystallographic analysis of a eutectic crystal of **1b** and *cis*-**10** (1:1) obtained during the recrystallization of **1b** (Supporting Information).

The results described above encouraged us to investigate whether or not **1b** produced **10** or its anion *cis*-**11** even in TBAF/acetonitrile. Upon treatment with even only 1 equiv of TBAF in acetonitrile at 45 °C, **1b** exclusively gave **2b** after 30 min. However, when the amount of TBAF was further decreased to 0.3 equiv, **1b** was found to produce *cis*-**10** (29%) and **2b** (64%) along with a trace amount of **1b** and *trans*-**10** after 10 h. Thus, *cis*-**10** contaminated with ca. 10% of **2b** was obtained as yellow crystals by rinsing from a reaction mixture after usual workup. The product *cis*-**10** was, of course, rapidly and exclusively transformed to **2b** on further treatment with TBAF.

The results described above showed that the decomposition of **9b** (oxido anion of **1b**) to **8b** (isolated as **2b**) through intermediate *cis*-**11** (isolated as *cis*-**10**) should occur concurrently with chemiluminescent CTID to give **8b** in TBAF/acetonitrile. Scheme 3 offers a plausible process, in which nucleophilic attack of the nitrogen in the benzothiazolyl group takes place on O–O of dioxetane **9b** to give intermediate *cis*-**11**, which spontaneously undergoes cleavage of a C–C bond of the tetrahydrofuran ring to finally give keto ester **8b**. This process would not cause chemiexcitation of any carbonyl fragment, in

contrast to CTID of **9b**. Hence, the base-induced decomposition of **1b** gave only weak light.

CONCLUSION

CTID of bicyclic dioxetanes **1b–d** bearing a benzothiazolyl-substituted 3-hydroxyphenyl group was investigated, and their chemiluminescence properties were compared, based on those for **1a**. While dioxetanes **1c** and **1d** underwent CTID to give the corresponding keto esters **8c** and **8d** in a singlet excited state with high efficiencies as with **1a**, **1b** led to singlet chemiexcitation with quite low efficiency. The unusually low singlet chemiexcitation efficiency for **1b** was attributed to the decomposition of oxido anion **9b** to **8b** mainly through a radiationless pathway in which intramolecular nucleophilic attack of the nitrogen of benzothiazolyl group took place on the dioxetane O–O to give *cis*-**11**.

EXPERIMENTAL SECTION

General. Melting points were uncorrected. IR spectra were taken on a FT/IR infrared spectrometer. ¹H and ¹³C NMR spectra were recorded on a 400 and 500 MHz spectrometers. Mass spectra were obtained by using double-focusing mass spectrometers and an ESI-TOF mass spectrometer. X-ray diffraction data were collected on a CCD diffractometer with graphite monochromated MoK α ($\lambda=0.71070$ Å) radiation. Column chromatography was carried out using silica gel.

4-tert-Butyl-5-(2-formyl-3-methoxyphenyl)-3,3-dimethyl-2,3-dihydrofuran (4b): Pale yellow oil; ¹H NMR (400 MHz, CDCl₃) δ_{H} 1.01 (s, 9H), 1.35 (s, 6H), 3.92 (s, 2H), 3.93 (s, 3H), 6.94 (dd, $J=7.6$ and 1.0 Hz, 1H), 6.99 (d, $J=8.4$ Hz, 1H), 7.48 (dd, $J=8.4$ and 7.6 Hz, 1H), 10.35 (s, 1H) ppm; ¹³C NMR (125 MHz, CDCl₃) δ_{C} 27.0, 32.0, 32.5, 47.2, 55.9, 83.5, 112.1, 123.5, 124.0, 127.1, 134.1, 140.0, 146.1, 160.6, 190.8 ppm; IR (liquid film) ν 2957, 2867, 2762, 1698, 1652, 1587, 1577 cm⁻¹; mass (m/z , %) 288 (M⁺, 8), 273 (12), 232 (16), 231 (100), 217 (24), 201 (17), 189 (11), 163 (11); HRMS (ESI) 311.1656, calcd for C₁₈H₂₄O₃Na [M + Na⁺] 311.1623.

4-tert-Butyl-5-(2-formyl-5-methoxyphenyl)-3,3-dimethyl-2,3-dihydrofuran (4c): Colorless plates, mp 61.5–62.0 °C (from hexane); ¹H NMR (500 MHz, CDCl₃) δ_{H} 1.03 (s, 9H), 1.37 (s, 6H), 3.89 (s, 3H), 3.94 (s, 2H), 6.84 (d, $J=2.4$ Hz, 1H), 6.97 (dd, $J=8.8$ and 2.4 Hz, 1H), 7.93 (d, $J=8.8$ Hz, 1H), 10.04 (s, 1H) ppm; ¹³C NMR (125 MHz, CDCl₃) δ_{C} 27.1, 32.1, 32.5, 47.4, 55.5, 83.4, 114.7, 116.1, 128.0, 129.0, 129.1, 141.7, 144.9, 163.5, 190.5 ppm; IR (KBr) ν 2981, 2861, 2763, 1655, 1690, 1601 cm⁻¹; mass (m/z , %) 288 (M⁺, 7),

233 (58), 232 (16), 231 (68), 217 (35), 201 (17), 189 (17), 163 (100); HRMS (ESI) 311.1613, calcd for $C_{18}H_{24}O_3Na$ [$M + Na^+$] 311.1623.

4-tert-Butyl-5-(3-formyl-5-methoxyphenyl)-3,3-dimethyl-2,3-dihydrofuran (4d): Colorless oil; 1H NMR (400 MHz, $CDCl_3$) δ_H 1.06 (s, 9H), 1.35 (s, 6H), 3.87 (s, 3H), 3.89 (s, 2H), 7.11 (s with fine coupling, 1H), 7.35 (s with fine coupling, 1H), 7.41 (s, 1H), 9.96 (s, 1H) ppm; ^{13}C NMR (125 MHz, $CDCl_3$) δ_C 27.3, 32.5, 32.6, 47.3, 55.6, 83.3, 112.0, 122.8, 125.2, 126.8, 137.4, 138.4, 148.2, 159.8, 191.8 ppm; IR (liquid film) ν 2958, 2868, 2729, 1700, 1463, 1335, 1054 cm^{-1} ; mass (m/z , %) 288 (M^+ , 24), 274 (19), 273 (100), 217 (14), 163 (32); HRMS (ESI) 311.1653, calcd for $C_{18}H_{24}O_3Na$ [$M + Na^+$] 311.1623.

Synthesis of 5-[2-(Benzothiazol-2-yl)-3-methoxyphenyl]-4-tert-butyl-3,3-dimethyl-2,3-dihydrofuran (6b). Typical Procedure: A solution of 4-tert-butyl-5-(2-formyl-3-methoxyphenyl)-3,3-dimethyl-2,3-dihydrofuran (**4b**) (7.12 g, 24.7 mmol) and 2-amino-benzenethiol (2.90 mL, 27.2 mmol, 1.1 equiv) in dry EtOH (140 mL) was mixed under a nitrogen atmosphere at room temperature and stirred for 5 h. The reaction mixture was concentrated in vacuo to give 10.5 g of crude 4-tert-butyl-5-[2-(2,3-dihydrobenzothiazol-2-yl)-3-methoxyphenyl]-3,3-dimethyl-2,3-dihydrofuran **5b** as a pale yellow oil. The crude **5b** was used for the next reaction without further purification.

A solution of crude **5b** and 2,3-dichloro-5,6-dicyano-1,4-benzoquinone (DDQ) (5.60 g, 24.7 mmol, 1.00 equiv) in dry toluene (80 mL) was refluxed for 50 min. After cooling, the reaction mixture was filtered and concentrated in vacuo. The residue was chromatographed on silica gel and eluted with AcOEt–hexane (1:4) to give 9.01 g of 5-[2-(benzothiazol-2-yl)-3-methoxyphenyl]-4-tert-butyl-3,3-dimethyl-2,3-dihydrofuran (**6b**) as a colorless solid in 93% yield based on **4b**.

According to the procedure described above, 5-[2-(benzothiazol-2-yl)-5-methoxyphenyl]-4-tert-butyl-3,3-dimethyl-2,3-dihydrofuran (**6c**) and 5-[3-(benzothiazol-2-yl)-5-methoxyphenyl]-4-tert-butyl-3,3-dimethyl-2,3-dihydrofuran (**6d**) were synthesized by using the corresponding benzaldehydes **4c** and **4d** instead of **4b** in **6c** and 77% yield, respectively.

6b: Colorless granules, mp 120.0–120.5 °C (from AcOEt–hexane); 1H NMR (400 MHz, $CDCl_3$) δ_H 0.88 (s, 9H), 0.75–1.40 (m, 6H), 3.77 (s, 2H), 3.82 (s, 3H), 6.98–7.04 (m, 2H), 7.38 (ddd, $J = 7.9, 7.2$, and 1.2 Hz, 1H), 7.41 (dd, $J = 8.3$ and 7.8 Hz, 1H), 7.47 (ddd, $J = 8.2, 7.2$, and 1.2 Hz, 1H), 7.92 (d with fine coupling, $J = 7.9$ Hz, 1H), 8.09 (d with fine coupling, $J = 8.2$ Hz, 1H) ppm; ^{13}C NMR (125 MHz, $CDCl_3$) δ_C 26.9 (broad), 31.7, 32.4, 46.7, 56.0, 82.8, 111.3, 121.1, 123.1, 123.2, 123.6, 124.7, 125.5, 126.1, 130.4, 136.4, 137.9, 146.7, 152.9, 157.5, 162.6 ppm; IR (KBr) ν 3434, 2989, 2924, 2864, 1654, 1577, 1468, 1429 cm^{-1} ; mass (m/z , %) 393 (M^+ , 0.2), 378 (16), 337 (22), 336 (100), 322 (15); HRMS (ESI) 394.1852, calcd for $C_{24}H_{28}NO_2S$ [$M + H^+$] 394.1841, 416.1673, calcd for $C_{24}H_{27}NO_2SNa$ [$M + Na^+$] 416.1660. Anal. Calcd for $C_{24}H_{27}NO_2S$: C, 73.25; H, 6.92; N, 3.56. Found: C, 73.18; H, 7.07; N, 3.67.

6c: Colorless oil; 1H NMR (400 MHz, $CDCl_3$) δ_H 0.94 (s, 9H), 1.37 (s, 6H), 3.88 (s, 3H), 3.92–4.20 (m, 2H), 6.89 (d, $J = 2.7$ Hz, 1H), 7.01 (dd, $J = 8.8$ and 2.7 Hz, 1H), 7.36 (ddd, $J = 7.9, 7.2$, and 1.2 Hz, 1H), 7.47 (ddd, $J = 8.2, 7.2$, and 1.2 Hz, 1H), 7.90 (d with fine coupling, $J = 7.9$ Hz, 1H), 8.06 (d with fine coupling, $J = 8.2$ Hz, 1H), 8.11 (d, $J = 8.8$ Hz, 1H) ppm; ^{13}C NMR (125 MHz, $CDCl_3$) δ_C 26.2 (broad), 28.4 (broad), 31.8, 32.6, 47.2, 55.5, 83.3, 114.6, 117.2, 121.2, 123.0, 124.6, 125.9, 126.5, 126.6, 131.5, 136.1, 136.4, 147.2, 153.1, 160.5, 166.1 ppm; IR (liquid film) ν 2957, 2934, 2868, 1602, 1566, 1482, 1463, 1433 cm^{-1} ; mass (m/z , %) 393 (M^+ , 0.7), 378 (15), 337 (22), 336 (100), 322 (15), 268 (9). HRMS (ESI): 394.1854, calcd for $C_{24}H_{28}NO_2S$ [$M + H^+$] 394.1841, 416.1673, calcd for $C_{24}H_{27}NO_2SNa$ [$M + Na^+$] 416.1660.

6d: Pale yellow granules, mp 139.0–140.0 °C (from AcOEt–hexane); 1H NMR (400 MHz, $CDCl_3$) δ_H 1.10 (s, 9H), 1.37 (s, 6H), 3.91 (s, 2H), 3.92 (s, 3H), 6.98 (dd, $J = 2.6$ and 1.3 Hz, 1H), 7.39 (ddd, $J = 7.9, 7.2$, and 1.2 Hz, 1H), 7.49 (ddd, $J = 8.2, 7.2$, and 1.3 Hz, 1H), 7.59 (dd, $J = 1.6$ and 1.3 Hz, 1H), 7.64 (dd, $J = 2.6$ and 1.6 Hz, 1H), 7.90 (d with fine coupling, $J = 7.9$ Hz, 1H), 8.08 (d with fine

coupling, $J = 8.2$ Hz, 1H) ppm; ^{13}C NMR (125 MHz, $CDCl_3$) δ_C 27.4, 32.5, 32.5, 47.2, 55.6, 83.2, 112.0, 118.6, 121.5, 121.8, 123.2, 125.2, 126.3, 126.3, 134.5, 135.0, 138.2, 148.8, 154.0, 159.6, 167.6 ppm; IR (KBr) ν 3442, 2982, 2955, 2924, 2854, 1605, 1584, 1508, 1458, 1422, 1337 cm^{-1} ; mass (m/z , %) 394 (M^+ , 1, 7), 393 (M^+ , 25), 379 (24), 378 (100), 322 (26). HRMS (ESI): 394.1844, calcd for $C_{24}H_{28}NO_2S$ [$M + H^+$] 394.1841, 416.1666, calcd for $C_{24}H_{27}NO_2SNa$ [$M + Na^+$] 416.1660. Anal. Calcd for $C_{24}H_{27}NO_2S$: C, 73.25; H, 6.92; N, 3.56. Found: C, 73.25; H, 7.08; N, 3.57.

Synthesis of 5-[2-(Benzothiazol-2-yl)-3-hydroxyphenyl]-4-tert-butyl-3,3-dimethyl-2,3-dihydrofuran (3b). Typical Procedure: A solution of 5-[2-(benzothiazol-2-yl)-3-methoxyphenyl]-4-tert-butyl-3,3-dimethyl-2,3-dihydrofuran (**6b**) (537 mg, 1.36 mmol) and sodium thiomethoxide (200 mg, 2.85 mmol, 2.09 equiv) in dry DMF (5 mL) was stirred under a nitrogen atmosphere at 140 °C for 10 min. The reaction mixture was poured into saturated aqueous NH_4Cl and extracted with AcOEt. The organic layer was washed three times with saturated aqueous NaCl, dried over anhydrous $MgSO_4$, and concentrated in vacuo. The residue was chromatographed on silica gel and eluted with AcOEt–hexane (1:9) to give 493 mg of 5-[2-(benzothiazol-2-yl)-3-hydroxyphenyl]-4-tert-butyl-3,3-dimethyl-2,3-dihydrofuran (**3b**) as a pale yellow solid in 95% yield.

(Benzothiazol-2-yl)-3-methoxyphenyl-substituted dihydrofurans **6c** and **6d** were similarly demethylated with sodium thiomethoxide to give 5-[2-(benzothiazol-2-yl)-5-hydroxyphenyl]-4-tert-butyl-3,3-dimethyl-2,3-dihydrofuran (**3c**) and 5-[3-(benzothiazol-2-yl)-5-hydroxyphenyl]-4-tert-butyl-3,3-dimethyl-2,3-dihydrofuran (**3d**) in 85 and 89% yield, respectively.

3b: Pale yellow granules, mp 171.0–171.5 °C (from AcOEt–hexane); 1H NMR (400 MHz, $CDCl_3$) δ_H 1.05 (s, 9H), 1.42 (s, 3H), 1.51 (s, 3H), 4.03 (d, $J = 8.3$ Hz, 1H), 4.17 (d, $J = 8.3$ Hz, 1H), 6.87 (dd, $J = 7.3$ and 1.3 Hz, 1H), 7.13 (dd, $J = 8.3$ and 1.3 Hz, 1H), 7.33 (dd, $J = 8.3$ and 7.3 Hz, 1H), 7.42 (ddd, $J = 7.9, 7.2$, and 1.2 Hz, 1H), 7.51 (ddd, $J = 8.2, 7.2$, and 1.2 Hz, 1H), 7.93 (d with fine coupling, $J = 7.9$ Hz, 1H), 8.01 (d with fine coupling, $J = 8.2$ Hz, 1H), 13.93 (s, 1H) ppm; ^{13}C NMR (125 MHz, $CDCl_3$) δ_C 25.7, 29.0, 31.7, 32.9, 47.6, 83.4, 116.2, 118.7, 121.1, 121.9, 123.5, 125.4, 126.5, 127.7, 131.3, 133.9, 135.4, 147.7, 149.4, 159.4, 167.3 ppm; IR (KBr) ν 3435, 2984, 2952, 2928, 2866, 2700, 2586, 1575, 1466, 1454, 1444 cm^{-1} ; mass (m/z , %) 379 (M^+ , 0.3), 364 (20), 323 (21), 322 (100), 308 (17), 254 (10), 57 (12). HRMS (ESI): 380.1682, calcd for $C_{23}H_{26}NO_2S$ [$M + H^+$] 380.1684, 402.1512, calcd for $C_{23}H_{25}NO_2SNa$ [$M + Na^+$] 402.1504. Anal. Calcd for $C_{23}H_{25}NO_2S$: C, 72.79; H, 6.64; N, 3.69. Found: C, 72.79; H, 6.75; N, 3.78.

3c: Colorless columns, mp 206.5–207.0 °C (from AcOEt–hexane); 1H NMR (400 MHz, $CDCl_3$) δ_H 0.94 (s, 9H), 1.36 (s, 6H), 3.90–4.20 (m, 2H), 5.77 (s, 1H), 6.85 (d, $J = 2.7$ Hz, 1H), 6.91 (dd, $J = 8.5$ and 2.7 Hz, 1H), 7.37 (ddd, $J = 7.9, 7.2$, and 1.2 Hz, 1H), 7.47 (ddd, $J = 8.2, 7.2$, and 1.2 Hz, 1H), 7.90 (d with fine coupling, $J = 7.9$ Hz, 1H), 8.03 (d, $J = 8.5$ Hz, 1H), 8.06 (d with fine coupling, $J = 8.2$ Hz, 1H) ppm; ^{13}C NMR (125 MHz, $CDCl_3$) δ_C 26.1 (broad), 28.4 (broad), 31.8, 32.6, 47.2, 83.2, 116.3, 119.0, 121.3, 122.8, 124.8, 126.0, 126.0, 127.0, 131.6, 135.9, 136.6, 146.8, 152.7, 157.4, 166.7 ppm; IR (KBr) ν 3388, 3058, 2966, 2929, 2908, 2864, 2777, 2677, 2586, 1608, 1568, 1465, 1432 cm^{-1} ; mass (m/z , %) 379 (M^+ , 0.3), 364 (14), 323 (20), 322 (100), 308 (15), 254 (11). HRMS (ESI): 380.1696, calcd for $C_{23}H_{26}NO_2S$ [$M + H^+$] 380.1684, 402.1517, calcd for $C_{23}H_{25}NO_2SNa$ [$M + Na^+$] 402.1504. Anal. Calcd for $C_{23}H_{25}NO_2S$: C, 72.79; H, 6.64; N, 3.69. Found: C, 72.79; H, 6.83; N, 3.75.

3d: Colorless granules, mp 190.0–191.0 °C (from CH_2Cl_2 –hexane); 1H NMR (400 MHz, $CDCl_3$) δ_H 1.06 (s, 9H), 1.33 (s, 6H), 3.89 (s, 2H), 6.95 (t, $J = 1.8$ Hz, 1H), 7.32 (s, 1H), 7.34 (ddd, $J = 8.0, 7.3$, and 1.1 Hz, 1H), 7.44 (ddd, $J = 8.2, 7.3$, and 1.1 Hz, 1H), 7.53 (d, $J = 1.8$ Hz, 2H), 7.82 (d with fine coupling, $J = 8.0$ Hz, 1H), 8.04 (d, $J = 8.2$ Hz, 1H) ppm; ^{13}C NMR (125 MHz, $CDCl_3$) δ_C 27.3, 32.5, 32.5, 47.2, 83.1, 114.2, 120.3, 121.5, 121.6, 123.0, 125.3, 126.4, 126.6, 134.2, 134.8, 138.3, 148.5, 153.6, 156.3, 168.1 ppm; IR (KBr) ν 3494, 2980, 2967, 2910, 2869, 1608, 1597, 1465, 1438, 1429 cm^{-1} ; mass (m/z , %) 380 (M^+ , 1, 7), 379 (M^+ , 26), 365 (25), 364 (100), 308 (27), 254 (10), 226 (8); HRMS (ESI) 380.1691, calcd for $C_{23}H_{26}NO_2S$ [$M +$

H⁺ 380.1684, 402.1509, calcd for C₂₃H₂₅NO₂SNa [M + Na⁺] 402.1504. Anal. Calcd for C₂₃H₂₅NO₂S: C, 72.79; H, 6.64; N, 3.69. Found: C, 72.79; H, 6.77; N, 3.72.

Singlet Oxygenation of 5-[2-(Benzothiazol-2-yl)-3-hydroxyphenyl]-4-tert-butyl-3,3-dimethyl-2,3-dihydrofuran (3b). Typical Procedure: A solution of dihydrofuran **3b** (202 mg, 0.532 mmol) and tetraphenylporphyrin (TPP) (1.5 mg) in CH₂Cl₂ (10 mL) was irradiated externally with a 940 W Na lamp under an oxygen atmosphere at 0 °C for 8.5 h. After the concentration of the photolysate in vacuo, the residue was chromatographed on silica gel and eluted with CH₂Cl₂–hexane (4:1) and then with AcOEt–hexane (1:1) to give intact **3b** (60 mg, 30%) and 1-[2-(benzothiazol-2-yl)-3-hydroxyphenyl]-5-tert-butyl-4,4-dimethyl-2,6,7-trioxabicyclo[3.2.0]heptane (**1b**) as a pale yellow solid (150 mg, 69% yield (CY = 97%)).

Dihydrofurans **3c** and **3d** were similarly oxygenated with singlet oxygen to give the corresponding dioxetanes **1c** and **1d** in 100 and 98% yields, respectively.

1b: Colorless granules, mp 100.5–101.0 °C (dec) (from CH₂Cl₂–hexane); ¹H NMR (500 MHz, CDCl₃) δ_H 0.95 (s, 9H), 1.03 (broad s, 3H), 1.06 (s, 3H), 3.81 (d, J = 8.2 Hz, 1H), 4.55 (d, J = 8.2 Hz, 1H), 7.14 (dd, J = 8.2 and 1.1 Hz, 1H), 7.28–7.36 (m, 1H), 7.42 (dd, J = 8.2 and 7.8 Hz, 1H), 7.43 (ddd, J = 8.0, 7.3, and 1.1 Hz, 1H), 7.52 (ddd, J = 8.0, 7.3, and 1.1 Hz, 1H), 7.92 (d, J = 8.0 Hz, 1H), 8.10 (d, J = 8.0 Hz, 1H), 8.36 (s, 1H) ppm; ¹³C NMR (125 MHz, CDCl₃) δ_C 19.0, 24.6, 26.9, 36.7, 45.1, 80.4, 106.1, 117.0, 118.1, 118.7, 121.2, 122.2, 123.0, 125.4, 126.1, 130.5, 135.1, 136.8, 151.8, 155.4, 165.5 ppm; IR (KBr) ν 3493, 3314, 3218, 3065, 2974, 2919, 2806, 2681, 1586, 1463 cm⁻¹; mass (m/z, %) 412 (M⁺ + 1, 14), 411 (M⁺, 57), 271 (13), 255 (17), 254 (100), 253 (33), 227 (27), 198 (12), 57 (15); HRMS (ESI) 412.1597, calcd for C₂₃H₂₆NO₄S [M + H⁺] 412.1583, 434.1422, calcd for C₂₃H₂₅NO₄SNa [M + Na⁺] 434.1402. Anal. Calcd for C₂₃H₂₅NO₄S·1/2CH₂Cl₂: C, 62.17; H, 5.77; N, 3.09. Found: C, 62.19; H, 6.08; N, 3.19.

1c: Colorless granules, mp 181.0–181.5 °C (dec) (from AcOEt–hexane); ¹H NMR (500 MHz, CDCl₃) δ_H 0.89 (broad s, 3H), 1.00 (s, 3H), 1.01 (s, 9H), 3.61 (d, J = 8.2 Hz, 1H), 4.42 (d, J = 8.2 Hz, 1H), 6.85 (dd, J = 8.5 and 2.7 Hz, 1H), 7.25 (d, J = 8.5 Hz, 1H), 7.31 (broad s, 1H), 7.40 (ddd, J = 8.0, 7.3, and 1.1 Hz, 1H), 7.47 (ddd, J = 8.0, 7.3, and 1.1 Hz, 1H), 7.63 (broad s, 1H), 7.87 (d, J = 8.0 Hz, 1H), 8.04 (d, J = 8.0 Hz, 1H) ppm; ¹³C NMR (125 MHz, CDCl₃) δ_C 19.1, 24.4 (broad), 27.0, 36.7, 45.2, 80.3, 106.1, 116.5, 116.8, 117.9, 121.1, 123.0, 125.1, 125.1, 126.0, 133.7, 136.3, 136.5, 151.9, 157.1, 169.3 ppm; IR (KBr) ν 3441, 3067, 3007, 2982, 2959, 2896, 1605, 1479, 1432, 1306 cm⁻¹; mass (m/z, %) 411 (M⁺, 8), 355 (11), 255 (17), 254 (100), 227 (40), 57 (16); HRMS (ESI) 412.1594, calcd for C₂₃H₂₆NO₄S [M + H⁺] 412.1583, 434.1420, calcd for C₂₃H₂₅NO₄SNa [M + Na⁺] 434.1402. Anal. Calcd for C₂₃H₂₅NO₄S: C, 67.13; H, 6.12; N, 3.40. Found: C, 67.11; H, 6.23; N, 3.45.

1d: Colorless columns, mp 141.0–141.5 °C (dec) (from CH₂Cl₂–hexane); ¹H NMR (400 MHz, CDCl₃) δ_H 1.02 (s, 9H), 1.17 (s, 3H), 1.39 (s, 3H), 3.84 (d, J = 8.3 Hz, 1H), 4.60 (d, J = 8.3 Hz, 1H), 6.35 (s, 1H), 7.27 (dd, J = 2.4 and 1.5 Hz, 1H), 7.40 (ddd, J = 8.1, 7.2, and 1.2 Hz, 1H), 7.49 (ddd, J = 8.2, 7.2, and 1.3 Hz, 1H), 7.71 (dd, J = 2.4 and 1.5 Hz, 1H), 7.84 (dd, J = 1.5 and 1.5 Hz, 1H), 7.89 (d with fine coupling, J = 8.1 Hz, 1H), 8.08 (d with fine coupling, J = 8.2 Hz, 1H) ppm; ¹³C NMR (100 MHz, CDCl₃) δ_C 18.5, 25.2, 27.0, 36.8, 45.7, 80.3, 105.2, 115.1, 116.0, 118.3, 120.2, 121.6, 123.2, 125.4, 126.4, 134.5, 135.0, 138.7, 153.7, 156.1, 167.3 ppm; IR (KBr) ν 3388, 3073, 2979, 2967, 2696, 1600, 1488, 1433, 1346 cm⁻¹; mass (m/z, %) 411 (M⁺, 5), 355 (39), 354 (10), 272 (10), 271 (19), 255 (15), 254 (100), 227 (30), 226 (28), 57 (20); HRMS (ESI) 412.1598, calcd for C₂₃H₂₆NO₄S [M + H⁺] 412.1583, 434.1409, calcd for C₂₃H₂₅NO₄SNa [M + Na⁺] 434.1402. Anal. Calcd for C₂₃H₂₅NO₄S: C, 67.13; H, 6.12; N, 3.40. Found: C, 67.03; H, 6.19; N, 3.43.

Thermal Decomposition of 1-[2-(Benzothiazol-2-yl)-3-hydroxyphenyl]-5-tert-butyl-4,4-dimethyl-2,6,7-trioxabicyclo[3.2.0]heptane (1b). Typical Procedure: A solution of dioxetane **1b** (168 mg, 0.408 mmol) in *p*-xylene (4 mL) was refluxed under a nitrogen atmosphere for 4 h. After cooling, the reaction mixture was concentrated in vacuo. The residue was chromatographed on silica gel

and eluted with AcOEt–hexane (1:9) to give 2,2,4,4-tetramethyl-3-oxopentyl 2-(benzothiazol-2-yl)-3-hydroxybenzoate (**2b**) as a pale yellow oil (165 mg, 98% yield).

Dioxetanes **1c** and **1d** were similarly decomposed to give the corresponding keto esters **2c** and **2d** in 98 and 97% yields, respectively.

2b: Colorless oil; ¹H NMR (500 MHz, CDCl₃) δ_H 1.12 (s, 9H), 1.28 (s, 6H), 4.40 (s, 2H), 7.10 (dd, J = 7.4 and 1.4 Hz, 1H), 7.22 (dd, J = 8.4 and 1.4 Hz, 1H), 7.38 (dd, J = 8.4 and 7.4 Hz, 1H), 7.45 (ddd, J = 7.8, 7.3, and 1.2 Hz, 1H), 7.53 (ddd, J = 8.1, 7.3, and 1.4 Hz, 1H), 7.93 (d with fine coupling, J = 7.8 Hz, 1H), 8.04 (d with fine coupling, J = 8.1 Hz, 1H), 12.68 (s, 1H) ppm; ¹³C NMR (125 MHz, CDCl₃) δ_C 23.5, 27.8, 45.7, 48.7, 73.7, 114.7, 120.3, 120.6, 121.3, 122.3, 125.8, 126.7, 131.7, 133.1, 134.2, 150.4, 158.1, 166.1, 168.7, 215.6 ppm; IR (liquid film) ν 3351, 2974, 2872, 1724, 1685, 1579, 1477, 1454 cm⁻¹; mass (m/z, %) 412 (M⁺ + 1, 11), 411 (M⁺, 40), 255 (17), 254 (100), 253 (32), 227 (29), 198 (12), 57 (20); HRMS (ESI) 412.1598, calcd for C₂₃H₂₆NO₄S [M + H⁺] 412.1583, 434.1415, calcd for C₂₃H₂₅NO₄SNa [M + Na⁺] 434.1402.

2c: Colorless oil; ¹H NMR (500 MHz, CDCl₃) δ_H 1.04 (s, 6H), 1.10 (s, 9H), 4.23 (s, 2H), 6.92 (dd, J = 8.4 and 2.6 Hz, 1H), 7.13 (d, J = 2.6 Hz, 1H), 7.39 (ddd, J = 8.0, 7.2, and 1.1 Hz, 1H), 7.47 (d, J = 8.4 Hz, 1H), 7.48 (ddd, J = 8.1, 7.2, and 1.2 Hz, 1H), 7.88 (d with fine coupling, J = 8.0 Hz, 1H), 8.02 (d, J = 8.1 Hz, 1H), 8.76 (broad s, 1H) ppm; ¹³C NMR (125 MHz, CDCl₃) δ_C 23.1, 27.9, 45.7, 48.7, 72.8, 117.1, 118.5, 121.5, 122.9, 124.3, 125.2, 126.3, 132.1, 133.0, 135.6, 153.1, 158.6, 167.5, 167.7, 217.0 ppm; IR (liquid film) ν 3355, 3060, 2976, 2934, 2873, 2793, 2683, 2607, 1726, 1685, 1605, 1576, 1479, 1434, 1367 cm⁻¹; mass (m/z, %) 411 (M⁺, 6), 355 (10), 255 (16), 254 (100), 227 (42), 57 (23); HRMS (ESI) 434.1414, calcd for C₂₃H₂₅NO₄SNa [M + Na⁺] 434.1402.

2d: Colorless needles, mp 185.5–186.0 °C (from AcOEt–hexane); ¹H NMR (400 MHz, CDCl₃) δ_H 1.33 (s, 9H), 1.43 (s, 6H), 4.44 (s, 2H), 6.01 (s, 1H), 7.41 (ddd, J = 8.1, 7.2, and 1.2 Hz, 1H), 7.50 (ddd, J = 8.2, 7.2, and 1.2 Hz, 1H), 7.56 (dd, J = 2.6 and 1.3 Hz, 1H), 7.86 (dd, J = 2.6 and 1.6 Hz, 1H), 7.91 (d with fine coupling, J = 8.1 Hz, 1H), 8.06 (d with fine coupling, J = 8.2 Hz, 1H), 8.16 (dd, J = 1.6 and 1.3 Hz, 1H) ppm; ¹³C NMR (125 MHz, CDCl₃) δ_C 23.7, 28.1, 46.0, 49.2, 72.6, 118.1, 119.2, 120.9, 121.6, 123.1, 125.6, 126.5, 132.1, 134.7, 134.9, 153.4, 157.0, 165.4, 167.1, 216.7 ppm; IR (KBr) ν 3434, 2973, 1696, 1685, 1614, 1601, 1437, 1374, 1334 cm⁻¹; mass (m/z, %) 411 (M⁺, 5), 355 (39), 354 (10), 272 (10), 271 (19), 255 (16), 254 (100), 227 (28), 226 (25), 57 (22); HRMS (ESI) 412.1605, calcd for C₂₃H₂₆NO₄S [M + H⁺] 412.1583, 434.1411, calcd for C₂₃H₂₅NO₄SNa [M + Na⁺] 434.1402. Anal. Calcd for C₂₃H₂₅NO₄S: C, 67.13; H, 6.12; N, 3.40. Found: C, 67.06; H, 6.11; N, 3.44.

Time Course of Thermal Decomposition of Crystalline 1b at 80 °C. Crystalline **1b** (20.0 mg) was heated at 80 °C, and after 1, 2, 3, and 4 h, product distribution was monitored by ¹H NMR in CDCl₃ (Figure S1).

Thermal Decomposition of Crystalline 1b To Isolate *trans*-10. Crystalline **1b** (21.5 mg) was heated at 90 °C for 45 min to give a mixture of **2b** and *trans*-**10**. After cooling, the crude product was chromatographed on NH–silica gel and eluted with AcOEt–MeOH (9: 1) to give a mixture of **2b** and *trans*-**10** (37:63) as a pale yellow oil (13.2 mg), which was crystallized from CHCl₃–hexane to give colorless plates of *trans*-**10** including 10% of **1b**. Further purification of *trans*-**10** was unsuccessful because of its thermal and chemical (silica gel) instability: *trans*-**10** gradually decomposed to **2b** during isolation and purification process even though at low temperature.

***trans*-10:** ¹H NMR (500 MHz, CDCl₃) δ_H 1.19 (s, 9H), 1.38 (s, 3H), 1.89 (s, 3H), 2.47 (s, 1H), 3.88 (d, J = 8.7 Hz, 1H), 4.01 (d, J = 8.7 Hz, 1H), 6.84 (d, J = 8.9 Hz, 1H), 7.13 (d, J = 7.3 Hz, 1H), 7.34 (dd, J = 8.9 and 7.3 Hz, 1H), 7.47 (dd with fine coupling, J = 8.0 and 7.3 Hz, 1H), 7.61 (dd with fine coupling, J = 8.0 and 7.3 Hz, 1H), 7.66 (d, J = 8.0 Hz, 1H), 7.89 (d, J = 8.0 Hz, 1H) ppm; ¹³C NMR (125 MHz, CDCl₃) δ_C 25.2, 28.7, 29.1, 39.3, 46.8, 82.2, 90.9, 107.5, 110.8, 111.4, 117.5, 123.9, 124.0, 125.5, 126.3, 127.9, 130.0, 135.3, 136.7, 151.0, 174.4 ppm.

TBAF-Induced Decomposition of Crystalline 1b To Isolate cis-10. A solution of **1b** (61.4 mg) and TBAF (0.3 equiv) in acetonitrile (15 mL) was heated at 45 °C for 10 h. The reaction mixture was poured in aqueous NH₄Cl and extracted with AcOEt. The organic layer was washed with aqueous NaCl, dried over MgSO₄, and concentrated in vacuo. The residue was rinsed with CH₂Cl₂ to give *cis*-**10** as a yellow solid (14.0 mg).

cis-10: ¹H NMR (500 MHz, CDCl₃) δ_H 0.68 (broad s, 9H), 1.25 (s, 3H), 1.51 (s, 3H), 2.61 (s, 1H), 3.76 (d, *J* = 8.6 Hz, 1H), 4.33 (d, *J* = 8.6 Hz, 1H), 6.61 (d, *J* = 7.1 Hz, 1H), 6.85 (d, *J* = 9.0 Hz, 1H), 7.35 (dd, *J* = 9.0 and 7.1 Hz, 1H), 7.47 (dd with fine coupling, *J* = 8.0 and 7.3 Hz, 1H), 7.61 (dd with fine coupling, *J* = 8.2 and 7.3 Hz, 1H), 7.79 (d, *J* = 8.2 Hz, 1H), 7.85 (d, *J* = 8.0 Hz, 1H) ppm; ¹³C NMR (125 MHz, CDCl₃) δ_C 21.3, 25.9, 27.8 (broad), 39.5, 49.3, 80.4, 91.9, 107.9, 110.5, 111.7, 119.3, 123.7, 125.1, 125.5, 125.7, 128.1, 131.6, 134.8, 136.4, 153.0, 174.3 ppm.

Measurement of Chemiluminescence and Time Course of the Charge-Transfer-Induced Decomposition of Dioxetanes 1. General Procedure: Chemiluminescence was measured using a JASCO FP-750 and/or FP-6500 spectrometer and/or Hamamatsu Photonics PMA-11 multichannel detector.

A freshly prepared solution (2.0 mL) of TBAF (1.0 × 10⁻² mol/L) in acetonitrile was transferred to a quartz cell (10 × 10 × 50 mm) and was placed in the spectrometer, which was thermostatted with stirring at an appropriate temperature range of 45 °C. After 3–5 min, a solution of the dioxetane **1** in acetonitrile (1.0 × 10⁻⁵ mol/L, 1.0 mL) was added by means of a syringe and measurement was started immediately. The intensity of the light emission time-course was recorded and processed according to first-order kinetics. The total light emission was estimated by comparing it with that of an adamantylidene dioxetane, whose chemiluminescent efficiency Φ^{CL} has been reported to be 0.29 and was used here as a standard.^{11,12}

■ ASSOCIATED CONTENT

● Supporting Information

¹H NMR/¹³C NMR spectra of **1b–d**, **2b–d**, **3b–d**, **4b–d**, **6b–d**, *trans*-**10**, *cis*-**10**, and ORTEP views and crystallographic information files for **1b–d**, *trans*-**10**, and *cis*-**10**. This material is available free of charge via the Internet at <http://pubs.acs.org>.

■ AUTHOR INFORMATION

Corresponding Author

*E-mail: matsumo-chem@kanagawa-u.ac.jp.

Notes

The authors declare no competing financial interest.

■ ACKNOWLEDGMENTS

We gratefully acknowledge financial assistance provided by Grants-in-Aid (No. 22550046 and No. 21550052) for Scientific Research from the Ministry of Education, Culture, Sports, Science, and Technology, Japan.

■ REFERENCES

- (1) (a) Schaap, A. P.; Gagnon, S. D. *J. Am. Chem. Soc.* **1982**, *104*, 3504–3506. (b) Schaap, A. P.; Handley, R. S.; Giri, B. P. *Tetrahedron Lett.* **1987**, *28*, 935–938. (c) Schaap, A. P.; Chen, T. S.; Handley, R. S.; DeSilva, R.; Giri, B. P. *Tetrahedron Lett.* **1987**, *28*, 1155–1158.
- (2) (a) Koo, J.-Y.; Schuster, G. B. *J. Am. Chem. Soc.* **1977**, *99*, 6107–6109. (b) Koo, J.-Y.; Schuster, G. B. *J. Am. Chem. Soc.* **1978**, *100*, 4496–4503. (c) Zaklika, K. A.; Kissel, T.; Thayer, A. L.; Burns, P. A.; Schaap, A. P. *Photochem. Photobiol.* **1979**, *30*, 35–44. (d) Catalani, L. H.; Wilson, T. *J. Am. Chem. Soc.* **1989**, *111*, 2633–2639. (e) McCapra, F. *J. Photochem. Photobiol. A* **1990**, *51*, 21–28. (f) McCapra, F. In *Chemiluminescence and Bioluminescence*; Hastings, J. W., Kricka, L. J., Stanley, P. E., Eds.; Wiley: New York, 1996; pp 7–15. (g) Adam, W.; Bronstein, I.; Trofimov, T.; Vasil'ev, R. F. *J. Am. Chem. Soc.* **1999**, *121*, 958–961. (h) Adam, W.; Matsumoto, M.; Trofimov, T. *J. Am. Chem.*

Soc. **2000**, *122*, 8631–8634. (i) Nery, A. L. P.; Weiss, D.; Catalani, L. H.; Baader, W. *J. Tetrahedron* **2000**, *56*, 5317–5327.

(3) (a) Catalani, L. H.; Wilson, T. *J. Am. Chem. Soc.* **1989**, *111*, 2633–2639. (b) McCapra, F. *J. Photochem. Photobiol. A* **1990**, *51*, 21–28. (c) Wilson, T. *Photochem. Photobiol.* **1995**, *62*, 601–606.

(4) (a) Takano, Y.; Tsunesada, T.; Isobe, H.; Yoshioka, Y.; Yamaguchi, K.; Saito, I. *Bull. Chem. Soc. Jpn.* **1999**, *72*, 213–225. (b) Tanaka, J.; Tanaka, C.; Matsumoto, M. In *Bioluminescence and Chemiluminescence*; Tsuji, A., Matsumoto, M., Maeda, M., Kricka, L. J., Stanley, P. E., Eds.; World Scientific: Singapore, 2004; pp 205–208. (c) Tanaka, C.; Tanaka, J.; Matsumoto, M. In *Bioluminescence and Chemiluminescence*; Tsuji, A., Matsumoto, M., Maeda, M., Kricka, L. J., Stanley, P. E., Eds.; World Scientific: Singapore, 2004; pp 209–212. (d) Isobe, H.; Takano, Y.; Okumura, M.; Kuramitsu, S.; Yamaguchi, K. *J. Am. Chem. Soc.* **2005**, *127*, 8667–8679.

(5) (a) Beck, S.; Köster, H. *Anal. Chem.* **1990**, *62*, 2258–2270. (b) Adam, W.; Reihardt, D.; Saha-Möller, C. R. *Analyst* **1996**, *121*, 1527–1531. (c) Matsumoto, M. *J. Photochem. Photobiol. C* **2004**, *5*, 27–53. (d) Matsumoto, M.; Watanabe, N. *Bull. Chem. Soc. Jpn.* **2005**, *78*, 1899–1920.

(6) (a) Bronstein, I.; Edwards, B.; Voyta, J. C. *J. Biolumin. Chemiluminescence* **1989**, *4*, 99–111. (b) Schaap, A. P.; Akhavan, H.; Romano, R. *J. Clin. Chem.* **1989**, *35*, 1863–1864. (c) Edwards, B.; Sparks, A.; Voyta, J. C.; Bronstein, I. *J. Biolumin. Chemiluminescence* **1990**, *5*, 1–4. (d) Martin, C.; Bresnick, L.; Juo, R. R.; Voyta, J. C.; Bronstein, I. *BioTechniques* **1991**, *11*, 110–113. (e) Mariscal, A.; Garcia, A.; Carnero, M.; Gomez, M.; Fernandez-Crehuet, J. *BioTechniques* **1994**, *16*, 888–893. (f) Trofimov, A. V.; Vasil'ev, R. F.; Mielke, K.; Adam, W. *Photochem. Photobiol.* **1995**, *62*, 35–43. (g) Adam, W.; Bronstein, I.; Edwards, B.; Engel, T.; Reinhardt, D.; Schneider, F. W.; Trofimov, A. V.; Vasil'ev, R. F. *J. Am. Chem. Soc.* **1996**, *118*, 10400–10407. (h) Buxton, R. C.; Edwards, B.; Juo, R. R.; Voyta, J. C.; Bethell, R. *Anal. Biochem.* **2000**, *280*, 291–300. (i) Sabelle, S.; Renard, P.-Y.; Pecorella, K.; de Suzzoni-Dezard, S.; Creminon, C.; Grassi, J.; Mioskowski, C. *J. Am. Chem. Soc.* **2002**, *124*, 4874–4880.

(7) Edwards, B.; Sparks, A.; Voyta, J. C.; Bronstein, I. In *Bioluminescence and Chemiluminescence, Fundamentals and Applied Aspects*; Campbell, A. K., Kricka, L. J., Stanley, P. E., Eds.; Wiley: Chichester, 1994; pp 56–59.

(8) Matsumoto, M.; Akimoto, T.; Matsumoto, Y.; Watanabe, N. *Tetrahedron Lett.* **2005**, *46*, 6075–6078.

(9) (a) Tanimura, M.; Watanabe, N.; Ijuin, H. K.; Matsumoto, M. *J. Org. Chem.* **2010**, *75*, 3678–3684. (b) Tanimura, M.; Watanabe, N.; Ijuin, H. K.; Matsumoto, M. *J. Org. Chem.* **2011**, *75*, 902–908.

(10) Matsumoto, M.; Mizoguchi, Y.; Motoyama, T.; Watanabe, N. *Tetrahedron Lett.* **2001**, *42*, 8869–8872.

(11) Value of Φ^{CL} was estimated based on the value 0.29 for the chemiluminescent decomposition of 3-adamantylidene-4-(3-*tert*-butyldimethylsilyloxyphenyl)-4-methoxy-1,2-dioxetane in a TBAF/DMSO system.¹²

(12) Trofimov, A. V.; Mielke, K.; Vasil'ev, R. F.; Adam, W. *Photochem. Photobiol.* **1996**, *63*, 463–467.

(13) Adam, W.; Matsumoto, M.; Trofimov, A. V. *J. Org. Chem.* **2000**, *65*, 2078–2082.

(14) (a) Matsumoto, M.; Kasai, D.; Yamada, K.; Fukuda, N.; Watanabe, N.; Ijuin, H. K. *Tetrahedron Lett.* **2004**, *45*, 8079–8082. (b) Matsumoto, M.; Yamada, K.; Ishikawa, H.; Hoshiya, N.; Watanabe, N.; Ijuin, H. K. *Tetrahedron Lett.* **2006**, *47*, 8407–8411. (c) Matsumoto, M.; Yamada, K.; Watanabe, N.; Ijuin, H. K. *Luminescence* **2007**, *22*, 420–429.

(15) **8c** presumably exists as an equilibrium mixture of *syn*- and *anti*-isomers in regard to an ester C=O group.

(16) Adam, W.; Heil, M. *J. Am. Chem. Soc.* **1992**, *114*, 5591–5598.

(17) ¹H NMR analysis showed that the crystalline was composed of **1b** (21%), **2b** (35%), *cis*-**10** (23%), and *trans*-**10** (22%) after heating at 80 °C for 2 h, while composed of **1b** (7%), **2b** (49%), *cis*-**10** (9%), and *trans*-**10** (35%) after heating for 4 h (Supporting Information).

HETEROCYCLES, Vol. 87, No. 1, 2013, pp. 65 - 78. © 2013 The Japan Institute of Heterocyclic Chemistry
Received, 9th October, 2012, Accepted, 31st October, 2012, Published online, 8th November, 2012
DOI: 10.3987/COM-12-12602

SYNTHESIS OF BICYCLIC DIOXETANES BEARING A 4-(BENZIMIDAZOL-2-YL)-3-HYDROXYPHENYL GROUP AND THEIR BASE-INDUCED CHEMILUMINESCENT DECOMPOSITION IN AN APROTIC MEDIUM AND IN AN AQUEOUS MEDIUM

Hiromasa Hagiwara, Nobuko Watanabe, Hisako K. Ijuin, Masashi Yamada,¹
and Masakatsu Matsumoto*

*Department of Chemistry, Kanagawa University, Tsuchiya, Hiratsuka,
Kanagawa 259-1293, Japan ¹Tosoh AIA, Inc. Iwase, Koshi-machi, Toyama
931-8510, Japan *E-mail*: matsumo-chem@kanagawa-u.ac.jp

Abstract – Bicyclic dioxetane, 5-*tert*-butyl-4,4-dimethyl-2,6,7-trioxabicyclo[3.2.0]heptane, bearing a 4-(benzimidazol-2-yl)-3-hydroxyphenyl group at the 1-position and its *N*-substituted benzimidazolyl-analogs were synthesized. *N*-Methylbenzimidazolyl-analog and *N*-phenylbenzimidazolyl-analog were found to undergo charge-transfer-induced decomposition (CTID) to effectively give light in both TBAF/MeCN and in NaOH/H₂O. The CTID of *N*-(4-carboxybutyl)benzimidazolyl-analog gave also effectively light both in MeCN and in H₂O. On the other hand, chemiluminescent CTID of the unsubstituted benzimidazolyl-analog changed depending on the base used: TBAF/MeCN induced weak emission of yellow light due to a dianion of the dioxetane, while TMG(tetramethylguanidine)/MeCN induced strong emission of blue light due to a monoanion of the dioxetane.

INTRODUCTION

Upon treatment with a base, a hydroxyphenyl-substituted dioxetane is deprotonated to give an unstable oxidophenyl-substituted dioxetane which rapidly decomposes with an accompanying emission of light by intramolecular charge-transfer-induced decomposition (CTID) mechanism. This phenomenon has received considerable attention from the viewpoints of application to clinical and biological analysis as well as of mechanistic interest related to bioluminescence and chemiluminescence.¹⁻⁷ One of such CTID-active dioxetanes is bicyclic compound **1** bearing a 4-(benzothiazol-2-yl)-3-hydroxyphenyl group, which effectively emits light in an aqueous system as well as in an aprotic polar solvent.⁸ Furthermore,

dioxetane **1** has very recently been found to undergo solvent-promoted decomposition, which is an entropy-controlled reaction leading to effective chemiluminescence.⁹

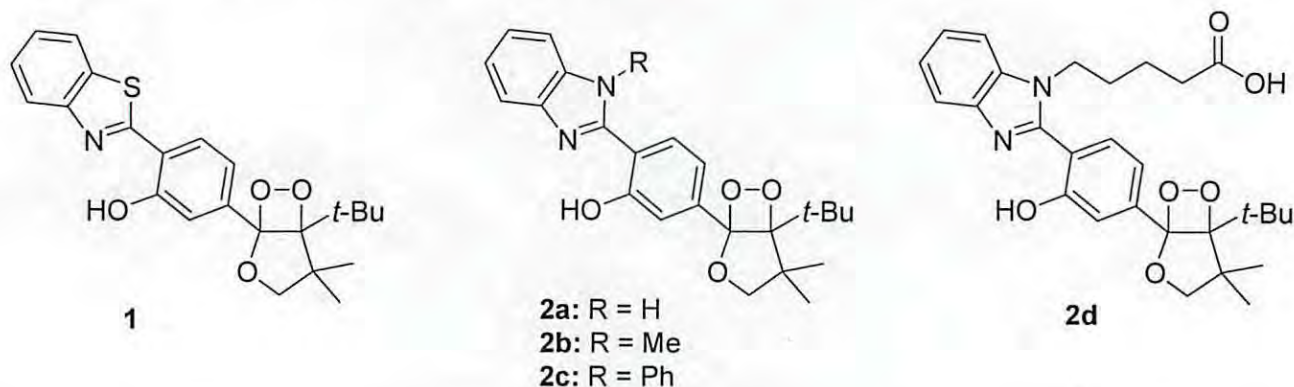


Figure 1. Dioxetanes bearing a 3-hydroxyphenyl group substituted with a 4-(benzothiazol-2-yl) **1** or 4-(benzimidazol-2-yl) group **2a–d**

These facts prompted us to realize bicyclic dioxetanes **2** bearing a 4-(benzimidazol-2-yl)-3-hydroxyphenyl group with expectation that the skeleton of **2** could be developed to novel chemiluminescence substrates bearing various auxiliaries, since a saturated nitrogen of benzimidazolyl group could be easily functionalized or tethered, differently from benzothiazolyl or benzoxazolyl group. Thus, we basically investigated here whether or not dioxetanes **2** showed effective chemiluminescence in an aqueous medium as well as in an aprotic medium. Dioxetanes investigated here were parent **2a** bearing a 4-(benzimidazol-2-yl)-3-hydroxyphenyl group and its *N*-methylbenzimidazolyl- **2b**, *N*-phenylbenzimidazolyl- **2c** and *N*-(4-carboxybutyl)benzimidazolyl-analog **2d** (Figure 1).

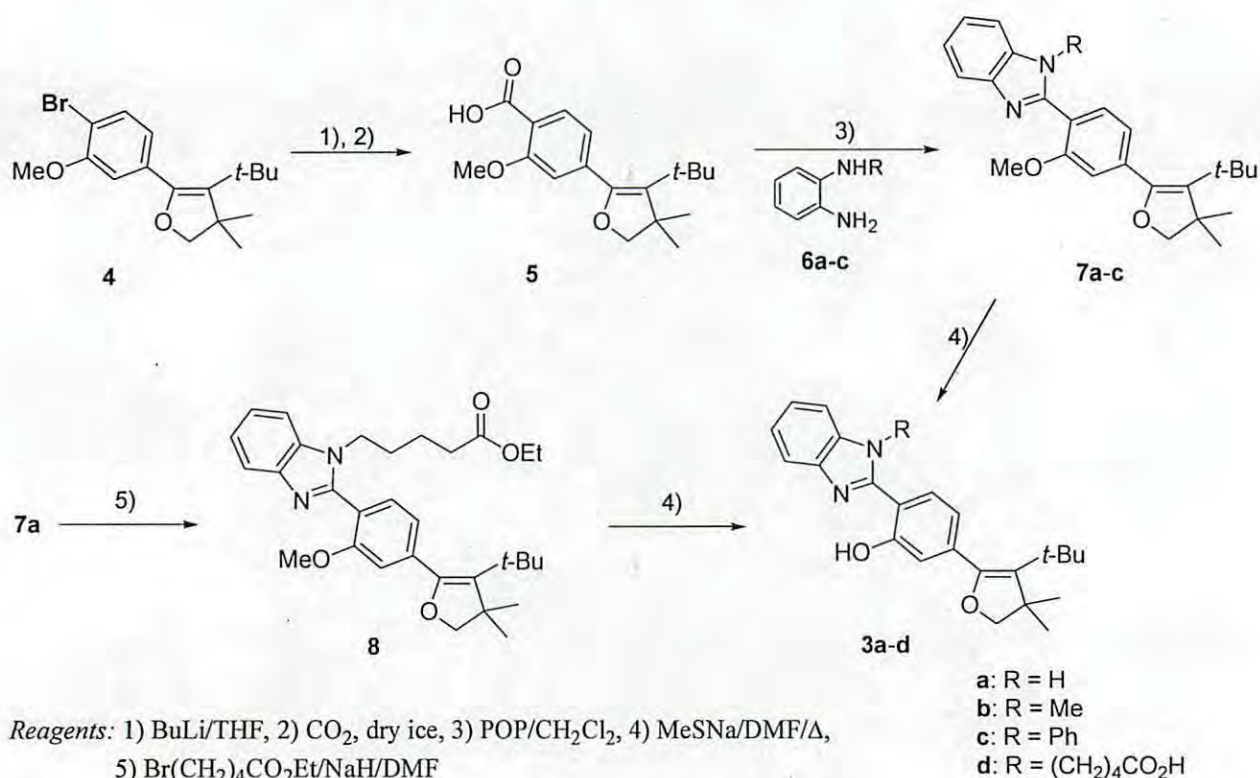
RESULTS AND DISCUSSION

Synthesis of bicyclic dioxetanes bearing a 4-(benzimidazol-2-yl)-3-hydroxyphenyl group

All of the dioxetanes **2a–d** investigated here were prepared by singlet oxygenation of the corresponding 5-[4-(benzimidazol-2-yl)-3-hydroxyphenyl]-4-*tert*-butyl-3,3-dimethyl-2,3-dihydrofurans **3a–d**. These precursors were synthesized through several steps starting from 4-*tert*-butyl-5-(4-carboxy-3-methoxyphenyl)-3,3-dimethyl-2,3-dihydrofuran (**5**), which was synthesized from 5-(4-bromo-3-methoxyphenyl)-4-*tert*-butyl-3,3-dimethyl-2,3-dihydrofuran (**4**),¹⁰ as illustrated in Scheme 1.

The initial step was condensation of carboxylic acid **5** with benzene-1,2-diamines **6a–c**, which smoothly proceeded by using triphenylphosphonium anhydride trifluoromethanesulfonate (POP)¹¹ in CH₂Cl₂ at room temperature to give the corresponding benzimidazoles **7a–c**. Nucleophilic substitution of benzimidazole **7a** with ethyl 5-bromopentanoate gave ester **8**. These 4-benzimidazolyl-3-methoxyphenyl-substituted dihydrofurans **7a–c** and **8** were demethylated effectively with sodium methylthiolate to give the desired precursors **3a–d**: for the case of **8**, saponification of the ester function

also proceeded. All of dihydrofurans **3a–d** were individually irradiated with Na-lamp in the presence of catalytic amount of tetraphenylporphin (TPP) in acetone or CH_2Cl_2 under O_2 atmosphere at $0\text{ }^\circ\text{C}$ to selectively give the corresponding dioxetanes **2a–d**. The structures of dioxetanes **2a–d** were determined by ^1H NMR, ^{13}C NMR, IR, MS and HRMass spectral analyses.



Scheme 1. Synthetic pathway of dihydrofurans **3a–d** bearing a 4-(benzimidazol-2-yl)-3-hydroxyphenyl group

Base-induced chemiluminescent decomposition of dioxetanes bearing a 4-(benzimidazol-2-yl)-3-hydroxyphenyl group

When a solution of dioxetane **2a** in MeCN was added to a solution of tetrabutylammonium fluoride (TBAF, large excess) in MeCN at $45\text{ }^\circ\text{C}$, **2a** decomposed according to the pseudo-first order kinetics independent of the TBAF concentration to emit yellow light, the spectrum of which is shown in Figure 2(A). The chemiluminescence properties of **2a** were as follows: maximum wavelength $\lambda_{\text{max}}^{\text{CL}} = 510\text{ nm}$, chemiluminescence efficiency $\phi^{\text{CL}} = 0.065$,^{12,13} rate of CTID $k^{\text{CTID}} = 4.6 \times 10^{-3}\text{ s}^{-1}$, and half-life $t_{1/2}^{\text{CTID}} = 150\text{ s}$ (Table 1). On similar treatment with TBAF, **2b** and **2c** showed bright chemiluminescence, the properties of which are shown in Table 1 (Figure 2(A)). We can see from Table 1 that **2b** and **2c** emitted light as effectively as benzothiazolyl-analog **1**, while, in contrast, parent **2a** gave light in poor yield, and the $\lambda_{\text{max}}^{\text{CL}}$ was considerably longer for **2a** than those for **2b** and **2c**.

Next, we carried out CTID of dioxetanes **2a–c** in an aqueous system. When dioxetanes **2a–c** were individually treated with 0.1 M NaOH aqueous solution at 45 °C, they decomposed with the accompanying chemiluminescence. Their chemiluminescence properties and spectra are summarized in Table 1 and Figure 2(B), respectively. Table 1 shows that all of three dioxetanes **2a–c** emitted light in high yields, which were >1000 times higher than that for simple bicyclic dioxetane, 5-*tert*-butyl-1-(3-hydroxyphenyl)-4,4-dimethyl-2,6,7-trioxabicyclo[3.2.0]heptane (**9**),¹⁴ though they were somewhat lower than that for **1**. If we compare here features of CTID for **2a–c** in a NaOH/H₂O system to those in a TBAF/MeCN, we can see that only parent dioxetane **2a** showed the noticeable differences in $\lambda_{\max}^{\text{CL}}$ and in Φ^{CL} between these two systems. The $\lambda_{\max}^{\text{CL}}$ for **2a** was 33 nm shorter in an aqueous system than in a MeCN system, though those for **2b** and **2c** were not so much different between in these two systems. Chemiluminescence efficiency for **2a** was unexpectedly higher in the aqueous system than in the MeCN system, while those for **2b** and **2c** somewhat decreased in an aqueous system. Notably, **2a** was the first example that a CTID-active dioxetane emitted light more effectively in an aqueous system than in an aprotic polar solvent system.

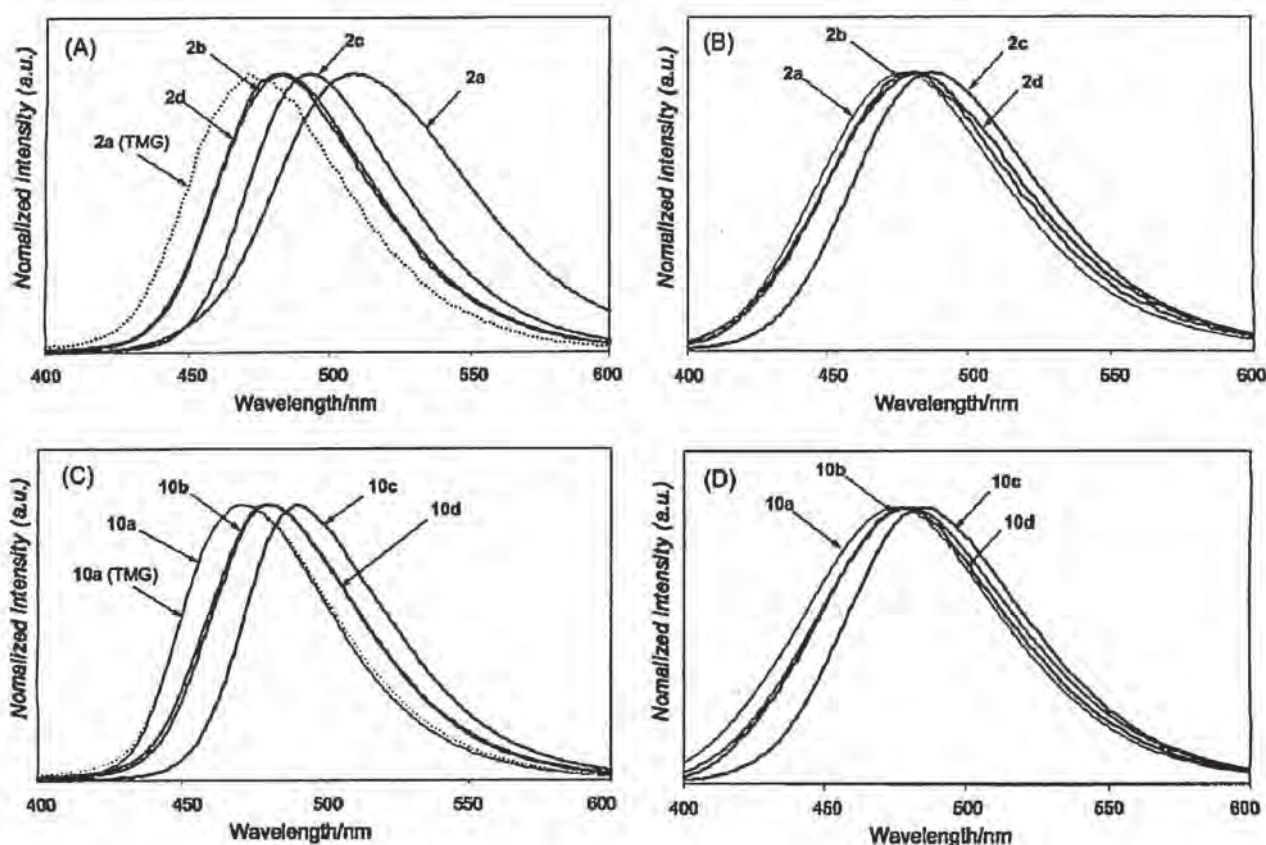
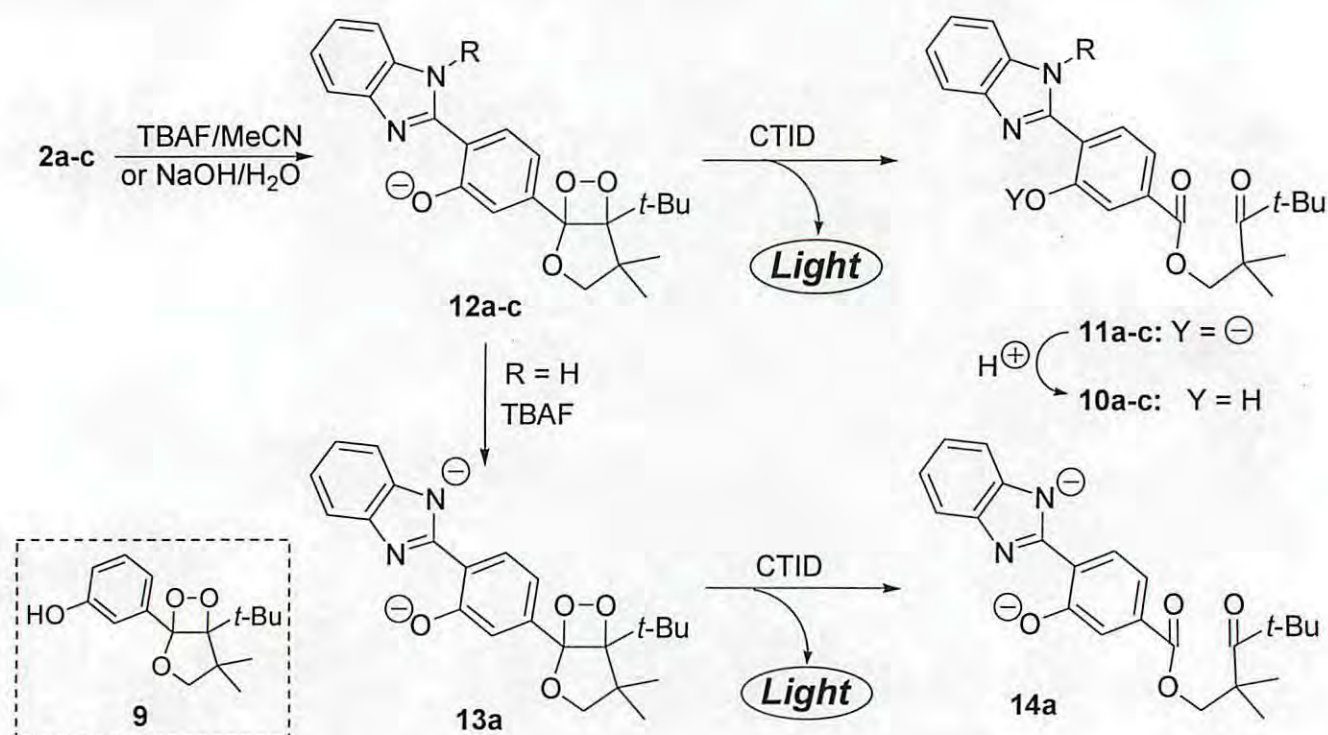


Figure 2. Chemiluminescence spectra of dioxetanes **2a–d** in TBAF/MeCN (A) and in NaOH/H₂O (B) and fluorescence spectra of keto esters **10a–d** in TBAF/MeCN (C) and in NaOH/H₂O (D)

The freshly spent reaction mixture for **2a–c** in both base systems effectively gave the corresponding keto

ester **10a–c** after careful neutralization. Authentic oxido anions **11a–c** generated by dissolving **10a–c** in NaOH/H₂O gave fluorescences, the spectra of which coincided with the corresponding chemiluminescence spectra of **2a–c** (Figure 2(D)). The results suggest that **11a–c** were undoubtedly emitters for CTID of the corresponding dioxetanes **2a–c** in a NaOH/H₂O system (Scheme 2). On the other hand, in a TBAF/MeCN system, fluorescence spectrum of **11a** generated from **10a** did not coincide with chemiluminescence spectrum from **2a**, though fluorescence spectra of authentic **11b** and **11c** coincided with the corresponding chemiluminescence spectra of **2b** and **2c** (Figure 2(C)).



Scheme 2. Base-Induced decomposition of dioxetanes **2a–c**

We carried out several experiments to understand the discrepancy between fluorescence spectrum of **11a** and chemiluminescence spectrum of **2a** in a TBAF/MeCN. Prominent difference in the structure between **2a** and **2b** or **2c** was that only benzimidazolyl group in **2a** possesses a weakly acidic NH. This structural difference suggested that **2a** would decompose in different manner depending on a base system. Thus, we attempted to use tetramethylguanidine (TMG, pK_a = 13.6) as a base far weaker than TBAF (pK_a >> 15) though strong enough for CTID of **2a** in MeCN. When a solution of **2a** in MeCN was added to a solution of MeCN including a large excess of TMG instead of TBAF at 45 °C, **2a** showed chemiluminescence with $\lambda_{\max}^{\text{CL}} = 471 \text{ nm}$, $\Phi^{\text{CL}} = 0.22$, $k^{\text{CTID}} = 1.9 \times 10^{-4}$ and $t_{1/2} = 3700 \text{ s}$. This $\lambda_{\max}^{\text{CL}}$ was 39 nm shorter than that in a TBAF/MeCN, and coincided with $\lambda_{\max}^{\text{fl}}$ of fluorescence from

authentic **11a** in TBAF/MeCN as well as in TMG/MeCN (Figure 2(C)). We can understand from Table 1 that Φ^{CL} of **2a** in a TMG/MeCN system increased more than 3 times from that in a TBAF/MeCN system, and was same as that for **2b** in a TBAF/MeCN. These results suggested that a strong base TBAF produced dianion **14a** of keto ester in the excited state through dianion **13a** of dioxetane **2a**, whereas TMG could abstract only a phenolic proton of **2a** to produce monoanion of dioxetane **12a** which decomposed into monoanion **11a** in the excited state (Scheme 2).

Table 1. Base-induced chemiluminescent decomposition of bicyclic dioxetanes **2a–2d** bearing a 4-(benzimidazol-2-yl)-3-hydroxyphenyl moiety in TBAF/MeCN and in NaOH/H₂O^{a)}

Dioxetane	TBAF/MeCN			NaOH/H ₂ O		
	$\lambda_{\text{max}}^{\text{CL}}$ / nm	Φ^{CL} b)	$t_{1/2}$ / s	$\lambda_{\text{max}}^{\text{CL}}$ / nm	Φ^{CL} b)	$t_{1/2}$ / s
2a	510	0.065	150	477	0.070	246
2b	483	0.22	90	480	0.024	361
2c	492	0.23	36	485	0.086	164
2d	483	0.20	63	483	0.017	396
1	492	0.28	1600	492	0.12	280
9^{c)}	467	0.11	25	467	1.1×10^{-5}	810
2a^{d)}	471	0.22	3700	-----	-----	-----

a) Reactions were carried out at 45 °C. b) Chemiluminescence efficiencies were based on the reported value for 3-(3-*tert*-butyldimethylsiloxyphenyl)-3-methoxy-4-(2'-spiroadamantane)-1,2-dioxetane ($\Phi^{\text{CL}} = 0.29$).¹³ c) ref. 14 d) TMG was used as a base instead of TBAF.

As described above, dioxetane **2b** bearing a 3-hydroxy-4-(*N*-methylbenzimidazol-2-yl)phenyl group underwent CTID to effectively give light in both TBAF/MeCN and NaOH/H₂O systems. Thus, we investigated whether or not the substitution with ω -functionalized alkyl group instead of *N*-methyl in **2b** could keep up chemiluminescence properties, especially high Φ^{CL} , for base-induced decomposition. As a representative of ω -functionalized alkyl group, we selected 4-carboxybutyl group, which could tether various auxiliaries or pendants (Figure 1). Dioxetane bearing an 4-[*N*-(4-carboxybutyl)-benzimidazol-2-yl]-3-hydroxyphenyl group **2d** decomposed to effectively emit light in both TBAF/MeCN and NaOH/H₂O systems (Figure 2). The results summarized in Table 1 show that chemiluminescence properties for **2d** were practically similar to those for **2b**.

CONCLUSION

Bicyclic dioxetane bearing a 4-(benzimidazol-2-yl)-3-hydroxyphenyl group **2a** and its *N*-substituted benzimidazolyl-analogs **2b–2d** were synthesized. *N*-Methylbenzimidazolyl-analog **2b** and *N*-phenylbenzimidazolyl-analog **2c** were found to undergo CTID to effectively give light in both

TBAF/MeCN and in NaOH/H₂O. On the other hand, Φ^{CL} , $\lambda_{\text{max}}^{\text{CL}}$ and k^{CTID} for CTID of unsubstituted benzimidazolyl-analog **2a** changed depending on the base used: especially Φ^{CL} in TBAF/MeCN system was quite low and was only <1/3 of Φ^{CL} in TMG/MeCN system. CTID of *N*-(4-carboxybutyl)-benzimidazolyl-analog **2d** gave also effectively light both in MeCN and in H₂O. The results presented here show that design of new CTID-dioxetanes tethering various auxiliaries through an *N*-spacer can become possible.

EXPERIMENTAL

General

Melting points were uncorrected. IR spectra were taken on a FT/IR infrared spectrometer. ¹H and ¹³C NMR spectra were recorded on a 400 MHz and 500 MHz spectrometers. Mass spectra were obtained by using a double-focusing mass spectrometer and an ESI-TOF mass spectrometer. Column chromatography was carried out using SiO₂.

Synthesis of 5-(4-carboxy-3-methoxyphenyl)-4-*tert*-butyl-3,3-dimethyl-2,3-dihydrofuran (5): BuLi (4.30 mL, 1.62 M in hexane, 6.97 mmol) was added to a solution of 5-(4-bromo-3-methoxyphenyl)-4-*tert*-butyl-3,3-dimethyl-2,3-dihydrofuran (**4**) (2.22 g, 6.56 mmol) in dry THF (20 mL) under a nitrogen atmosphere at -78 °C. After stirring for 30 min, dry ice was added to the solution and the reaction mixture was warmed slowly to room temperature. The reaction mixture was poured into 1 M HCl and extracted with AcOEt. The organic layer was washed twice with sat. aq. NaCl, dried over anhydrous MgSO₄, and concentrated in vacuo. The residue was chromatographed on silica gel and eluted with AcOEt–hexane (1:9~1:1) to give **5** (1.73 g, 5.69 mmol, 87%). **5**: colorless needles, mp 103.0–104.0 °C (from AcOEt–hexane). ¹H NMR (400 MHz, CDCl₃): δ_{H} 1.07 (s, 9H), 1.35 (s, 6H), 3.90 (s, 2H), 4.09 (s, 3H), 6.98 (d, $J = 1.1$ Hz, 1H), 7.11 (dd, $J = 7.9$ and 1.1 Hz, 1H), 8.15 (d, $J = 7.9$ Hz, 1H), 10.60 (br s, 1H) ppm. ¹³C NMR (125 MHz, CDCl₃): δ_{C} 27.3, 32.5, 32.5, 47.4, 56.8, 83.4, 113.2, 117.1, 124.1, 127.2, 133.4, 143.4, 148.0, 157.5, 165.0 ppm. IR (KBr): 3448, 2956, 1687, 1604, 1561 cm⁻¹. Mass (*m/z*, %): 304 (*M*⁺, 22), 289 (100), 245 (22), 215 (30), 179 (29), 52 (21). HRMS (ESI): 327.1554 calcd for C₁₈H₂₄O₄Na [*M*+Na⁺] 327.1572.

Synthesis of 5-[4-(benzimidazol-2-yl)-3-methoxyphenyl]-4-*tert*-butyl-3,3-dimethyl-2,3-dihydrofuran (7a): Typical procedure. Triphenylphosphonium anhydride trifluoromethanesulfonate (POP) was prepared by adding trifluoromethanesulfonic anhydride (2.19 mL, 13.0 mmol) to a solution of triphenylphosphine oxide (7.26 g, 26.1 mmol) in dry CH₂Cl₂ (15 mL) under a nitrogen atmosphere at room temperature and stirring for 20 min. To the POP solution, 5-(4-carboxy-3-methoxyphenyl)-4-*tert*-butyl-3,3-dimethyl-2,3-dihydrofuran (**5**) (1.00 g, 3.29 mmol) and 1,2-phenylenediamine (353 mg, 3.26 mmol) in dry CH₂Cl₂ (10 mL) were added and stirred at room temperature over night. The reaction mixture was poured into sat. aq. NaHCO₃ and extracted with AcOEt. The organic layer was washed twice

with sat. aq. NaCl, dried over anhydrous MgSO₄, and concentrated *in vacuo*. The residue was chromatographed on silica gel and eluted with AcOEt–hexane (1:2) to give **7a** (753 mg, 2.00 mmol, 62%) as a pale yellow solid. **7a**: colorless needles, mp 233.5–234.0 °C (from AcOEt). ¹H NMR (400 MHz, CDCl₃): δ_H 1.09 (s, 9H), 1.36 (s, 6H), 3.92 (s, 2H), 4.11 (s, 3H), 7.01 (s with fine coupling, 1H), 7.12 (d with fine coupling, *J* = 7.9 Hz, 1H), 7.23–7.30 (m, 2H), 7.42–7.58 (m, 1H), 7.72–7.90 (m, 1H), 8.56 (d, *J* = 7.9 Hz, 1H), 10.60 (br s, 1H) ppm. ¹³C NMR (125 MHz, DMSO-*d*₆): δ_C 27.3, 32.3, 32.5, 47.0, 56.1, 82.5, 112.2, 113.4, 118.1, 118.7, 121.8, 122.4, 122.8, 125.8, 129.5, 134.9, 139.0, 142.9, 148.7, 149.1, 156.3 ppm. IR (KBr): 3435, 3056, 2962, 2870, 1646, 1611, 1570 cm⁻¹. Mass (*m/z*, %): 377 (M⁺+1, 13), 376 (M⁺, 43), 362 (28), 361 (100), 305 (30), 251 (13). HRMS (ESI): 377.2206 calcd for C₂₄H₂₉N₂O₂ [M+H⁺] 377.2229. Anal. Calcd for C₂₄H₂₈N₂O₂: C, 76.56; H, 7.50; N, 7.44. Found: C, 76.32; H, 7.69; N, 7.42.

4-tert-Butyl-5-[3-methoxy-4-(*N*-methylbenzimidazol-2-yl)phenyl]-3,3-dimethyl-2,3-dihydrofuran (7b): 79% yield. Colorless plates, mp 158.0–158.5 °C (from CH₂Cl₂–hexane). ¹H NMR (400 MHz, CDCl₃): δ_H 1.10 (s, 9H), 1.37 (s, 6H), 3.64 (s, 3H), 3.83 (s, 3H), 3.93 (s, 2H), 6.96 (d, *J* = 1.2 Hz, 1H), 7.07 (dd, *J* = 7.6 and 1.2 Hz, 1H), 7.26–7.35 (m, 2H), 7.38–7.41 (m, 1H), 7.55 (d, *J* = 7.6 Hz, 1H), 7.80–7.83 (m, 1H) ppm. ¹³C NMR (125 MHz, CDCl₃): δ_C 27.3, 30.8, 32.4, 32.5, 47.3, 55.6, 83.2, 109.3, 112.5, 119.4, 119.7, 121.9, 122.4, 122.7, 126.4, 131.8, 136.0, 139.6, 143.1, 149.1, 151.7, 157.0 ppm. IR (KBr): 3049, 2958, 2871, 1655, 1609, 1563 cm⁻¹. Mass (*m/z*, %): 391 (M⁺+1, 16), 390 (M⁺, 53), 376 (29), 375 (100), 319 (35), 265 (8). HRMS (ESI) : 391.2401 calcd for C₂₅H₃₁N₂O₂ [M+H⁺] 391.2386. Anal. Calcd for C₂₅H₃₀N₂O₂: C, 76.89; H, 7.74; N, 7.17. Found: C, 76.98; H, 7.93; N, 7.19.

4-tert-Butyl-5-[3-methoxy-4-(*N*-phenylbenzimidazol-2-yl)phenyl]-3,3-dimethyl-2,3-dihydrofuran (7c): 56% yield. Colorless amorphous solid. ¹H NMR (400 MHz, CDCl₃): δ_H 1.04 (s, 9H), 1.33 (s, 6H), 3.33 (s, 3H), 3.89 (s, 2H), 6.66 (d, *J* = 1.2 Hz, 1H), 7.01 (dd, *J* = 7.6 and 1.2 Hz, 1H), 7.20–7.40 (m, 8H), 7.63 (d, *J* = 7.6 Hz, 1H), 7.88 (d, *J* = 7.6 Hz, 1H) ppm. ¹³C NMR (125 MHz, CDCl₃): δ_C 27.3, 32.4, 32.4, 47.2, 54.7, 83.2, 110.2, 112.4, 119.7, 119.9, 122.5, 123.1, 125.8, 126.3, 127.5, 129.0, 131.6, 136.0, 137.1, 139.3, 143.1, 149.1, 150.9, 156.4 ppm. IR (KBr): 3057, 2956, 2865, 1652, 1604, 1565, 1499 cm⁻¹. Mass (*m/z*, %): 453 (M⁺+1, 24), 452 (M⁺, 70), 438 (34), 437 (100), 381 (29), 327 (13), 298 (12). HRMS (ESI): 453.2520 calcd for C₃₀H₃₃N₂O₂ [M+H⁺] 453.2542.

Synthesis of 4-tert-butyl-5-[4-[*N*-(4-ethoxycarbonylbutyl)benzimidazol-2-yl]-3-methoxyphenyl]-3,3-dimethyl-2,3-dihydrofuran (8): 4-tert-Butyl-5-[4-(benzimidazol-2-yl)-3-methoxyphenyl]-3,3-dimethyl-2,3-dihydrofuran (**7a**) (500 mg, 1.33 mmol) was added to a suspension of NaH (60% in oil, 70.2 mg, 1.76 mmol) in dry DMF (10 mL) under a nitrogen atmosphere at room temperature. After stirring for 30 min, ethyl 5-bromopentanoate (0.32 mL, 2.0 mmol) was added to the solution at room temperature and stirred for 2 days. The reaction mixture was poured into sat. aq. NH₄Cl and extracted with AcOEt. The organic layer was washed twice with sat. aq. NaCl, dried over anhydrous MgSO₄, and concentrated *in vacuo*. The residue was chromatographed on silica gel and eluted with AcOEt–hexane (1:1) to give **8**

(666 mg, 1.32 mmol, 99%). **8**: Yellow oil. $^1\text{H NMR}$ (400 MHz, CDCl_3): δ_{H} 1.09 (s, 9H), 1.21 (t, $J = 7.1$ Hz, 3H), 1.37 (s, 6H), 1.42–1.52 (m, 2H), 1.69–1.79 (m, 2H), 2.16 (t, $J = 7.3$ Hz, 2H), 3.81 (s, 3H), 3.93 (s, 2H), 4.01–4.11 (m, 4H), 6.96 (s, 1H), 7.06 (dd, $J = 7.6$ and 1.2 Hz, 1H), 7.23–7.33 (m, 2H), 7.38–7.43 (m, 1H), 7.47 (d, $J = 7.6$ Hz, 1H), 7.78–7.84 (m, 1H) ppm. $^{13}\text{C NMR}$ (125 MHz, CDCl_3): δ_{C} 14.1, 22.0, 27.3, 28.7, 32.4, 32.5, 33.6, 44.1, 47.3, 55.6, 60.3, 83.2, 109.8, 112.6, 119.7, 120.0, 121.9, 122.4, 122.7, 126.5, 131.7, 135.0, 139.5, 143.3, 149.0, 151.2, 156.9, 172.8 ppm. IR (liquid film): 3055, 2957, 2868, 1732, 1651, 1609, 1563 cm^{-1} . Mass (m/z , %): 505 ($M^+ + 1$, 23), 504 (M^+ , 60), 490 (37), 489 (100), 459 (11). HRMS (ESI): 505.3039 calcd for $\text{C}_{31}\text{H}_{41}\text{N}_2\text{O}_4$ [$M + \text{H}^+$] 505.3066.

Synthesis of 5-[4-(benzimidazol-2-yl)-4-*tert*-butyl-3-hydroxyphenyl]-3,3-dimethyl-2,3-dihydrofuran (3a): Typical procedure. MeSNa (95%, 120 mg, 1.63 mmol) was added to a solution of **7a** (210 mg, 0.56 mmol) in dry DMF (5 mL) under a nitrogen atmosphere at room temperature and stirred for 30 min at 140 °C. The reaction mixture was poured into 1 M aq. HCl and sat. aq. NaCl, and extracted with AcOEt. The organic layer was washed twice with sat. aq. NaCl, dried over anhydrous MgSO_4 , and concentrated *in vacuo*. The residue was chromatographed on silica gel and eluted with AcOEt–hexane (1:4) to give **3a** (200 mg, 0.552 mmol, 99%) as a pale yellow solid. **3a**: Colorless needles, mp 284.5–285.0 °C (from AcOEt). $^1\text{H NMR}$ (400 MHz, CDCl_3): δ_{H} 1.09 (s, 9H), 1.35 (s, 6H), 3.90 (s, 2H), 6.91 (dd, $J = 8.0$ and 1.5 Hz, 1H), 7.08 (d, $J = 1.5$ Hz, 1H), 7.28–7.34 (m, 2H), 7.46–7.53 (m, 1H), 7.52 (d, $J = 8.0$ Hz, 1H), 7.71–7.78 (m, 1H), 9.45 (br s, 1H), 13.09 (br s, 1H) ppm. $^{13}\text{C NMR}$ (125 MHz, $\text{DMSO-}d_6$): δ_{C} 27.2, 32.3, 32.4, 47.0, 82.5, 111.7 (br), 112.6, 118.1 (br), 118.5, 121.0, 122.7 (br), 123.4 (br), 125.6, 126.0, 133.4 (br), 139.5, 141.1 (br), 149.0, 151.5, 157.5 ppm. IR (KBr): 3302, 2958, 2868, 2630, 1630, 1580 cm^{-1} . Mass (m/z , %): 363 ($M^+ + 1$, 11), 362 (M^+ , 39), 348 (27), 347 (100), 291 (38). HRMS (ESI): 363.2043 calcd for $\text{C}_{23}\text{H}_{27}\text{N}_2\text{O}_2$ [$M + \text{H}^+$] 363.2073. Anal. Calcd for $\text{C}_{23}\text{H}_{26}\text{N}_2\text{O}_2$: C, 76.21; H, 7.23; N, 7.73. Found: C, 76.47; H, 7.43; N, 7.72.

4-*tert*-Butyl-5-[3-hydroxy-4-(*N*-methylbenzimidazol-2-yl)phenyl]-3,3-dimethyl-2,3-dihydrofuran (3b): 97% yield. Colorless columns, mp 136.0–137.0 °C (from AcOEt). $^1\text{H NMR}$ (400 MHz, CDCl_3): δ_{H} 1.11 (s, 9H), 1.35 (s, 6H), 3.90 (s, 2H), 4.07 (s, 3H), 6.93 (dd, $J = 8.1$ and 1.7 Hz, 1H), 7.13 (d, $J = 1.7$, 1H), 7.31–7.39 (m, 2H), 7.41–7.44 (m, 1H), 7.70 (d, $J = 8.1$ Hz, 1H), 7.75–7.78 (m, 1H), 12.92 (br s, 1H) ppm. $^{13}\text{C NMR}$ (125 MHz, CDCl_3): δ_{C} 27.3, 32.5, 32.5, 33.0, 47.3, 83.2, 109.5, 112.7, 118.8, 119.6, 120.2, 123.0, 123.3, 126.1, 126.5, 135.6, 139.6, 140.3, 149.0, 151.4, 158.6 ppm. IR (KBr): 3417, 2956, 2867, 1624, 1566, 1466 cm^{-1} . Mass (m/z , %): 377 ($M^+ + 1$, 14), 376 (M^+ , 48), 362 (28), 361 (100), 305 (40). HRMS (ESI): 377.2212 calcd for $\text{C}_{24}\text{H}_{29}\text{N}_2\text{O}_2$ [$M + \text{H}^+$] 377.2229. Anal. Calcd for $\text{C}_{24}\text{H}_{28}\text{N}_2\text{O}_2$: C, 76.56; H, 7.50; N, 7.44. Found: C, 76.52; H, 7.68; N, 7.46.

4-*tert*-Butyl-5-[3-hydroxy-4-(*N*-phenylbenzimidazol-2-yl)phenyl]-3,3-dimethyl-2,3-dihydrofuran (3c): 82% yield. Pale yellow plates, mp 180.5–181.5 °C (from CH_2Cl_2). $^1\text{H NMR}$ (400 MHz, CDCl_3): δ_{H} 1.05 (s, 9H), 1.30 (s, 6H), 3.83 (s, 2H), 6.49 (dd, $J = 8.3$ and 1.7 Hz, 1H), 6.79 (d, $J = 8.3$ Hz, 1H), 7.06 (d, $J = 1.7$ Hz, 1H), 7.08 (d, $J = 8.1$ Hz, 1H), 7.23–7.29 (m, 1H), 7.32–7.42 (m, 3H), 7.56–7.63 (m, 3H), 7.80

(d, $J = 8.1$ Hz, 1H), 13.48 (br s, 1H) ppm. ^{13}C NMR (125 MHz, CDCl_3): δ_{C} 27.2, 32.4, 32.4, 47.2, 83.1, 110.3, 111.9, 118.6, 119.5, 119.7, 123.4, 123.8, 126.0, 126.7, 127.9, 129.5, 130.3, 136.5, 137.1, 139.4, 140.0, 149.0, 150.6, 159.1 ppm. IR (KBr): 3431, 3065, 2955, 2867, 1623, 1596, 1565 cm^{-1} . Mass (m/z , %): 439 ($\text{M}^+ + 1$, 20), 438 (M^+ , 60), 424 (33), 423 (100), 381 (13), 368 (11), 367 (40), 285 (12). HRMS (ESI): 439.2363 calcd for $\text{C}_{29}\text{H}_{31}\text{N}_2\text{O}_2$ [$\text{M} + \text{H}^+$] 439.2386.

4-*tert*-Butyl-5-{4-[*N*-(4-carboxybutyl)benzimidazol-2-yl]-3-hydroxyphenyl}-3,3-dimethyl-2,3-dihydrofuran (3d): 89% yield. Pale yellow columns, mp 174.0–175.0 °C (from CH_2Cl_2 –hexane). ^1H NMR (400 MHz, CDCl_3): δ_{H} 1.11 (s, 9H), 1.35 (s, 6H), 1.73–1.82 (m, 2H), 1.99–2.09 (m, 2H), 2.44 (t, $J = 7.1$ Hz, 2H), 3.90 (s, 2H), 4.39–4.48 (m, 2H), 6.94 (dd, $J = 8.1$ and 1.7 Hz, 1H), 7.13 (d, $J = 1.7$ Hz, 1H), 7.30–7.38 (m, 2H), 7.40–7.45 (m, 1H), 7.58 (d, $J = 8.1$ Hz, 1H), 7.73–7.80 (m, 1H) ppm. ^{13}C NMR (125 MHz, CDCl_3): δ_{C} 21.8, 27.3, 29.1, 32.5, 32.5, 33.2, 45.2, 47.2, 83.2, 109.7, 112.8, 118.9, 119.9, 120.5, 123.1, 123.4, 125.9, 126.3, 134.9, 139.6, 140.3, 148.8, 150.7, 158.4, 178.4 ppm. IR (KBr): 3386, 3061, 2955, 2865, 1723, 1654, 1618, 1558 cm^{-1} . Mass (m/z , %): 463 ($\text{M}^+ + 1$, 25), 462 (M^+ , 77), 448 (36), 447 (100), 445 (21), 403 (17), 391 (30), 389 (20), 347 (32), 291 (18), 57 (18). HRMS (ESI): 463.2591 calcd for $\text{C}_{28}\text{H}_{35}\text{N}_2\text{O}_4$ [$\text{M} + \text{H}^+$] 463.2597.

Synthesis of 1-[4-(benzimidazol-2-yl)-3-hydroxyphenyl]-5-*tert*-butyl-4,4-dimethyl-2,6,7-trioxabicyclo[3.2.0]heptane (2a): Typical procedure. A solution of **3a** (164 mg, 0.45 mmol) and tetraphenylporphine (TPP) (2.0 mg) in acetone (10 mL) was irradiated externally with 940W Na lamp under an oxygen atmosphere for 1.5 h at 0 °C. The reaction mixture was concentrated *in vacuo*. The photolysate was rinsed with CH_2Cl_2 to give dioxetane **2a** (139 mg, 78%). **2a**: Pale yellow granules, mp 284.0–285.0 °C (dec.) (from THF–hexane). ^1H NMR (400 MHz, $\text{DMSO}-d_6$): δ_{H} 0.99 (s, 9H), 1.10 (s, 3H), 1.38 (s, 3H), 3.92 (d, $J = 8.1$ Hz, 1H), 4.38 (d, $J = 8.1$ Hz, 1H), 7.18 (d, $J = 1.5$, 1H), 7.22 (dd, $J = 8.3$ and 1.5 Hz, 1H), 7.26–7.34 (m, 2H), 7.60–7.77 (m, 2H), 8.14 (d, $J = 8.3$ Hz, 1H), 13.24 (br s, 1H) ppm. ^{13}C NMR (125 MHz, $\text{THF}-d_8$): δ_{C} 18.7, 25.2, 27.3, 37.5, 46.4, 80.9, 105.7, 111.7, 114.4, 117.0, 118.8, 119.3, 119.5, 123.4, 124.3, 125.5, 134.3, 140.6, 142.7, 152.5, 159.7 ppm. IR (KBr): 3417, 3288, 2969, 2901, 1630, 1588, 1543 cm^{-1} . Mass (m/z , %): 395 ($\text{M}^+ + 1$, 19), 394 (M^+ , 67), 338 (20), 294 (15), 255 (11), 254 (27), 238 (19), 237 (100), 210 (27), 209 (28), 181 (19), 57 (22). HRMS (ESI): 395.1947 calcd for $\text{C}_{23}\text{H}_{27}\text{N}_2\text{O}_4$ [$\text{M} + \text{H}^+$] 395.1971. Anal. Calcd for $\text{C}_{23}\text{H}_{26}\text{N}_2\text{O}_4$: C, 70.03; H, 6.64; N, 7.10. Found: C, 69.98; H, 6.75; N, 7.02.

5-*tert*-Butyl-1-[3-hydroxy-4-(*N*-methylbenzimidazol-2-yl)phenyl]-4,4-dimethyl-2,6,7-trioxabicyclo[3.2.0]heptane (2b): 94% yield. Pale yellow needles, mp 162.5–163.0 °C (dec.) (from CH_2Cl_2 –hexane). ^1H NMR (400 MHz, CDCl_3): δ_{H} 1.05 (s, 9H), 1.17 (s, 3H), 1.41 (s, 3H), 3.85 (d, $J = 8.3$ Hz, 1H), 4.09 (s, 3H), 4.61 (d, $J = 8.3$ Hz, 1H), 7.28 (dd, $J = 8.5$ and 1.8 Hz, 1H), 7.33–7.46 (m, 4H), 7.76–7.80 (m, 2H), 13.07 (br s, 1H) ppm. ^{13}C NMR (125 MHz, CDCl_3): δ_{C} 18.4, 25.0, 26.9, 33.1, 36.7, 45.6, 80.3, 105.2, 109.6, 113.9, 116.2, 118.2, 118.4, 118.9, 123.1, 123.5, 126.4, 135.6, 139.2, 140.2, 150.9, 158.7 ppm. IR (KBr): 3428, 2969, 2893, 1625, 1577 cm^{-1} . Mass (m/z , %): 409 ($\text{M}^+ + 1$, 23), 408 (M^+ , 97), 352 (10), 308

(21), 278 (12), 268 (14), 267 (23), 252 (19), 251 (100), 224 (37), 223 (39), 195 (18), 57 (36). HRMS (ESI): 409.2114 calcd for $C_{24}H_{29}N_2O_4$ $[M+H]^+$ 409.2127. Anal. Calcd for $C_{24}H_{28}N_2O_4$: C, 70.57; H, 6.91; N, 6.86. Found: C, 70.26; H, 7.01; N, 6.85.

5-tert-Butyl-1-[3-hydroxy-4-(*N*-phenylbenzimidazol-2-yl)phenyl]-4,4-dimethyl-2,6,7-trioxabicyclo[3.2.0]heptane (2c): 96% yield. Colorless plates, mp 164.0–165.0 °C (dec.) (from CH_2Cl_2 –hexane). 1H NMR (500 MHz, $CDCl_3$): δ_H 0.99 (s, 9H), 1.13 (s, 3H), 1.34 (s, 3H), 3.78 (d, $J = 8.4$ Hz, 1H), 4.54 (d, $J = 8.4$ Hz, 1H), 6.81 (dd, $J = 8.5$ and 1.7 Hz, 1H), 6.87 (d, $J = 8.5$ Hz, 1H), 7.10 (d, $J = 8.2$ Hz, 1H), 7.25–7.30 (m, 5H), 7.58–7.64 (m, 3H), 7.81 (d, $J = 7.9$ Hz, 1H), 13.61 (br s, 1H) ppm. ^{13}C NMR (125 MHz, $CDCl_3$): δ_C 18.4, 25.0, 26.9, 36.7, 45.6, 80.3, 105.1, 110.4, 113.1, 116.1, 117.9, 118.1, 118.7, 123.6, 124.0, 126.6, 127.8, 129.7, 130.4, 136.5, 136.9, 139.1, 139.9, 150.1, 159.2 ppm. IR (KBr): 3433, 3065, 2993, 2969, 2898, 1631, 1595, 1574 cm^{-1} . Mass (m/z , %): 471 ($M^+ + 1$, 36), 470 (M^+ , 100), 414 (13), 370 (17), 330 (15), 329 (16), 314 (19), 313 (77), 286 (40), 285 (47), 257 (12), 256 (22), 255 (14), 57 (23). HRMS (ESI): 471.2279 calcd for $C_{29}H_{31}N_2O_4$ $[M+H]^+$ 471.2284.

5-tert-Butyl-1-{4-[*N*-(4-carboxybutyl)benzimidazol-2-yl]-3-hydroxyphenyl}-4,4-dimethyl-2,6,7-trioxabicyclo[3.2.0]heptane (2d): 99% yield. Pale yellow amorphous solid. 1H NMR (500 MHz, $CDCl_3$): δ_H 1.05 (s, 9H), 1.17 (s, 3H), 1.41 (s, 3H), 1.74–1.83 (m, 2H), 2.01–2.10 (m, 2H), 2.44 (t, $J = 7.3$ Hz, 2H), 3.84 (d, $J = 8.2$ Hz, 1H), 4.41–4.49 (m, 2H), 4.60 (d, $J = 8.2$ Hz, 1H), 7.28 (dd, $J = 8.2$ and 1.8 Hz, 1H), 7.32–7.39 (m, 2H), 7.41–7.46 (m, 2H), 7.66 (d, $J = 8.2$ Hz, 1H), 7.76–7.79 (m, 1H) ppm. ^{13}C NMR (125 MHz, $CDCl_3$): δ_C 18.4, 21.7, 25.0, 26.9, 29.1, 33.1, 36.7, 45.3, 45.6, 80.3, 105.3, 109.8, 114.0, 116.2, 118.5, 118.6, 119.0, 123.3, 123.7, 125.8, 135.0, 139.4, 140.2, 150.3, 158.6, 178.4 ppm. IR (KBr): 3448, 2965, 1716, 1625, 1542 cm^{-1} . Mass (m/z , %): 495 ($M^+ + 1$, 31), 494 (M^+ , 100), 478 (17), 477 (49), 435 (36), 422 (24), 421 (67), 409 (23), 408 (30), 394 (27), 338 (29), 337 (78), 319 (40), 310 (46), 309 (61), 281 (45), 254 (27), 237 (56), 181 (47), 57 (88). HRMS (ESI): 495.2485 calcd for $C_{28}H_{35}N_2O_6$ $[M+H]^+$ 495.2495.

Thermal decomposition of 2a to 2,2,4,4-tetramethyl-3-oxopentyl 4-(benzimidazol-2-yl)-3-hydroxybenzoate (10a): Typical procedure. A solution of 2a (48.0 mg, 0.12 mmol) in *p*-xylene was stirred under a nitrogen atmosphere at 140 °C for 3 h. After cooling, the reaction mixture was concentrated *in vacuo*. The residue was chromatographed on silica gel and eluted with hexane–AcOEt to give 10a (47.4 mg, 99%). **10a:** Colorless granules, mp 285.0–286.0 °C (dec.) (from THF–hexane). 1H NMR (400 MHz, $DMSO-d_6$): δ_H 1.23 (s, 9H), 1.35 (s, 6H), 4.35 (s, 2H), 7.28–7.35 (m, 2H), 7.48 (d, $J = 1.5$ Hz, 1H), 7.53 (dd, $J = 8.1$ and 1.5 Hz, 1H), 7.66–7.74 (m, 2H), 8.21 (d, $J = 8.1$ Hz, 1H), 13.34 (br s, 1H) ppm. ^{13}C NMR (125 MHz, $DMSO-d_6$): δ_C 23.3, 28.0, 45.4, 48.8, 71.9, 112.3 (br), 117.1, 117.6, 118.2 (br), 119.6, 123.4 (br), 126.9, 131.9, 133.7 (br), 140.9 (br), 150.5, 157.8, 164.9, 215.5 ppm. IR (KBr): 3347, 3318, 2969, 1709, 1681, 1612, 1582 cm^{-1} . Mass (m/z , %) 395 ($M^+ + 1$, 19), 394 (M^+ , 70), 338 (18), 294 (14), 255 (11), 254 (27), 238 (18), 237 (100), 210 (25), 209 (25), 181 (19), 57 (24). HRMS (ESI): 395.1980 calcd for $C_{23}H_{27}N_2O_4$ $[M+H]^+$ 395.1971. Anal. Calcd for $C_{23}H_{26}N_2O_4$: C, 70.03; H, 6.64; N, 7.10. Found:

C, 70.02; H, 6.78; N, 7.08.

2,2,4,4-Tetramethyl-3-oxopentyl 3-hydroxy-4-(*N*-methylbenzimidazol-2-yl)benzoate (10b): 94% yield. Pale yellow columns, mp 174.0–175.0 °C (from CH₂Cl₂–hexane). ¹H NMR (400 MHz, CDCl₃): δ_H 1.31 (s, 9H), 1.41 (s, 6H), 4.09 (s, 3H), 4.43 (s, 2H), 7.34–7.47 (m, 3H), 7.59 (dd, *J* = 8.3 and 1.7 Hz, 1H), 7.74 (d, *J* = 1.7 Hz, 1H), 7.76–7.82 (m, 2H), 13.13 (br s, 1H) ppm. ¹³C NMR (125 MHz, CDCl₃): δ_C 23.6, 28.1, 33.1, 45.9, 49.1, 72.2, 109.6, 116.7, 118.9, 119.0, 119.3, 123.2, 123.8, 126.7, 132.3, 135.6, 140.0, 150.4, 158.9, 165.5, 215.9 ppm. IR (KBr): 3423, 3071, 2961, 1712, 1680, 1573 cm⁻¹. Mass (*m/z*, %): 409 (M⁺+1, 29), 408 (M⁺, 100), 352 (11), 308 (17), 268 (12), 267 (19), 252 (16), 251 (87), 224 (27), 223 (30), 195 (11), 57 (16). HRMS (ESI): 409.2139 calcd for C₂₄H₂₉N₂O₄ [M+H⁺] 409.2127. Anal. Calcd for C₂₄H₂₈N₂O₄: C, 70.57; H, 6.91; N, 6.86. Found: C, 70.28; H, 6.98; N, 6.91.

2,2,4,4-Tetramethyl-3-oxopentyl 3-hydroxy-4-(*N*-phenylbenzimidazol-2-yl)benzoate (10c): 97% yield. Pale yellow columns, mp 180.5–181.0 °C (from CH₂Cl₂–hexane). ¹H NMR (400 MHz, CDCl₃): δ_H 1.27 (s, 9H), 1.37 (s, 6H), 4.37 (s, 2H), 6.89 (d, *J* = 8.4 Hz, 1H), 7.10–7.15 (m, 2H), 7.28–7.44 (m, 4H), 7.62–7.66 (m, 3H), 7.68 (d, *J* = 1.6 Hz, 1H), 7.84 (d, *J* = 7.9 Hz, 1H), 13.67 (br s, 1H) ppm. ¹³C NMR (125 MHz, CDCl₃): δ_C 23.6, 28.2, 45.8, 49.1, 72.1, 110.5, 116.1, 118.8, 118.9, 119.0, 123.7, 124.3, 127.1, 127.8, 129.8, 130.5, 132.2, 136.5, 136.8, 139.8, 149.7, 159.4, 165.6, 215.9 ppm. IR (KBr): 3431, 3060, 2971, 2874, 1724, 1685, 1579 cm⁻¹. Mass (*m/z*, %): 471 (M⁺+1, 36), 470 (M⁺, 100), 414 (14), 370 (24), 330 (18), 329 (22), 314 (21), 313 (86), 287 (11), 286 (53), 285 (64), 257 (20), 256 (34), 255 (20), 57 (30). HRMS (ESI): 471.2278 calcd for C₂₉H₃₁N₂O₄ [M+H⁺] 471.2284.

2,2,4,4-Tetramethyl-3-oxopentyl 4-[*N*-(4-carbonylbutyl)benimidazol-2-yl]-3-hydroxybenzoate (10d): 82% yield. Pale yellow amorphous solid. ¹H NMR (500 MHz, CDCl₃): δ_H 1.30 (s, 9H), 1.41 (s, 6H), 1.75–1.83 (m, 2H), 2.02–2.10 (m, 2H), 2.45 (t, *J* = 7.1 Hz, 2H), 4.42 (s, 2H), 4.42–4.49 (m, 2H), 7.33–7.40 (m, 2H), 7.43–7.47 (m, 1H), 7.59 (dd, *J* = 8.2 and 1.8 Hz, 1H), 7.69 (d, *J* = 8.2 Hz, 1H), 7.73 (d, *J* = 1.8 Hz, 1H), 7.77–7.80 (m, 1H) ppm. ¹³C NMR (125 MHz, CDCl₃): δ_C 21.7, 23.6, 28.1, 29.1, 33.1, 45.3, 45.9, 49.1, 72.2, 109.9, 116.9, 119.1, 119.2, 119.6, 123.4, 123.9, 126.4, 132.4, 135.0, 140.0, 149.8, 158.7, 165.5, 178.1, 216.1 ppm. IR (KBr): 2970, 2932, 2877, 1719, 1704, 1684, 1525, cm⁻¹. Mass (*m/z*, %): 495 (M⁺+1, 34), 494 (M⁺, 100), 493 (41), 477 (54), 435 (36), 421 (64), 408 (25), 337 (58), 319 (84), 309 (37), 292 (39), 237 (34), 57 (60). HRMS (ESI): 495.2481 calcd for C₂₈H₃₅N₂O₆ [M+H⁺] 495.2495.

Measurement of chemiluminescence and time-course of the base-induced decomposition of dioxetanes; General Procedure: Chemiluminescence was measured using a JASCO FP-750 and/or FP-6500 spectrometer, and a Hamamatsu Photonics PMA-11 multi-channel detector.

TBAF/MeCN system. A freshly prepared solution (2.00 mL) of TBAF (1.0 × 10⁻² mol/L) in MeCN was transferred to a quartz cell (10 × 10 × 50 mm), which was placed in a spectrometer that was thermostated with stirring at 45 °C. After 3–5 min, a solution of dioxetane 2 in MeCN (1.0 × 10⁻⁵ mol/L, 1.00 mL)

was added by means of a syringe, and measurement was started immediately. The time-course of the intensity of light emission was recorded and processed according to first-order kinetics. The total light emission was estimated by comparing it with that of an adamantylidene dioxetane, the chemiluminescent efficiency Φ^{CL} of which has been reported to be 0.29 and which was used here as a standard.^{12,13}

NaOH/H₂O system. A solution of NaOH (0.1 M, 2.90 mL) in H₂O was transferred to a quartz cell (10 x 10 x 50 mm), which was placed in a spectrometer that was thermostated with stirring at 45 °C. After 3–5 min, a solution of dioxetane **2** in MeCN (1.0 x 10⁻⁴ mol/L, 0.10 mL) was added by means of a syringe, and measurement was started immediately. The time-course of the intensity of light emission was recorded and processed according to first-order kinetics.

ACKNOWLEDGEMENTS

The authors gratefully acknowledge financial assistance in the form of Grants-in-aid (No. 21550052 and No. 22550046) for Scientific Research from the Ministry of Education, Culture, Sports, Science, and Technology, Japan.

REFERENCES AND NOTES

- (a) A. P. Schaap and S. D. Gagnon, *J. Am. Chem. Soc.*, 1982, **104**, 3504; (b) A. P. Schaap, R. S. Handley, and B. P. Giri, *Tetrahedron Lett.*, 1987, **28**, 935; (c) A. P. Schaap, T. S. Chen, R. S. Handley, R. DeSilva, and B. P. Giri, *Tetrahedron Lett.*, 1987, **28**, 1155.
- (a) J.-Y. Koo and G. B. Schuster, *J. Am. Chem. Soc.*, 1977, **99**, 6107; (b) J.-Y. Koo and G. B. Schuster, *J. Am. Chem. Soc.*, 1978, **100**, 4496; (c) W. Adam, I. Bronstein, T. Trofimov, and R. F. Vasil'ev, *J. Am. Chem. Soc.*, 1999, **121**, 958; (d) W. Adam, M. Matsumoto, and T. Trofimov, *J. Am. Chem. Soc.*, 2000, **122**, 8631; (e) A. L. P. Nery, D. Weiss, L. H. Catalani, and W. J. Baader, *Tetrahedron*, 2000, **56**, 5317.
- (a) L. H. Catalani and T. Wilson, *J. Am. Chem. Soc.*, 1989, **111**, 2633; (b) F. J. McCapra, *Photochem. Photobiol. A Chem.*, 1990, **51**, 21; (c) T. Wilson, *Photochem. Photobiol.*, 1995, **62**, 601.
- (a) Y. Takano, T. Tsunesada, H. Isobe, Y. Yoshioka, K. Yamaguchi, and I. Saito, *Bull. Chem. Soc. Jpn.*, 1999, **72**, 213; (b) J. Tanaka, C. Tanaka, and M. Matsumoto, *PCCP*, 2011, **13**, 16005; (c) H. Isobe, Y. Takano, M. Okumura, S. Kuramitsu, and K. Yamaguchi, *J. Am. Chem. Soc.*, 2005, **127**, 8667.
- (a) S. Beck and H. Köster, *Anal. Chem.*, 1990, **62**, 2258; (b) W. Adam, D. Reihardt, and C. R. Saha-Möller, *Analyst*, 1996, **121**, 1527.
- (a) M. Matsumoto, *J. Photochem. Photobiol. C: Photochem. Rev.*, 2004, **5**, 27; (b) M. Matsumoto and N. Watanabe, *Bull. Chem. Soc. Jpn.*, 2005, **78**, 1899.
- B. Edwards, A. Sparks, J. C. Voyta, and I. Bronstein, 'Bioluminescence and Chemiluminescence, Fundamentals and Applied Aspects', ed. by A. K. Campbell, L. J. Kricka, and P. E. Stanley, Wiley,

Chichester, 1994, pp. 56–59.

8. (a) M. Matsumoto, T. Akimoto, Y. Matsumoto, and N. Watanabe, *Tetrahedron Lett.*, 2005, **46**, 6075; (b) M. Tanimura, N. Watanabe, H. K. Ijuin, and M. Matsumoto, *J. Org. Chem.*, 2010, **75**, 3678.
9. M. Tanimura, N. Watanabe, H. K. Ijuin, and M. Matsumoto, *J. Org. Chem.*, 2011, **75**, 902.
10. M. Matsumoto, T. Sakuma, and N. Watanabe, *Luminescence*, 2001, **16**, 275.
11. (a) A. R. Katrizky, *Tetrahedron*, 1980, **36**, 679; (b) A. R. Katrizky and C. M. Marson, *Angew. Chem. Int. Ed. Engl.*, 1984, **23**, 420; (c) A. R. Katrizky and G. Musumara, *Chem. Soc. Rev.*, 1984, **13**, 47; (d) A. R. Katrizky, K. Sakizadeh, and G. Musumara, *Heterocycles*, 1985, **23**, 1765.
12. Φ^{CL} was estimated based on the value 0.29 for the chemiluminescent decomposition of 3-(3-*tert*-butyldimethylsiloxyphenyl)-3-methoxy-4-(2'-spiroadamantane)-1,2-dioxetane in a TBAF/DMSO system.¹³
13. A. V. Trofimov, K. Mielke, R. F. Vasil'ev, and W. Adam, *Photochem. Photobiol.*, 1996, **63**, 463.
14. M. Matsumoto, Y. Mizoguchi, T. Motoyama, and N. Watanabe, *Tetrahedron Lett.*, 2001, **42**, 8869.

Magnesium methoxide-induced chemiluminescent decomposition of bicyclic dioxetanes bearing a 2'-alkoxy-2-hydroxy-1,1'-binaphthyl-7-yl moiety

Hidehisa Kawashima, Nobuko Watanabe, Hisako K. Ijuin and Masakatsu Matsumoto*

ABSTRACT: Bicyclic dioxetanes **2a–c** bearing a 2'-alkoxy-2-hydroxy-1,1'-binaphthyl-7-yl moiety were effectively synthesized and their base-induced chemiluminescent decomposition was investigated by the use of alkaline metal (Na⁺ and K⁺) or Mg²⁺ alkoxide in MeOH. When **2a–c** were treated with tetrabutylammonium fluoride (TBAF) in dimethyl sulfoxide (DMSO) as a reference system, they showed chemiluminescence as a flash of orange light (maximum wavelength $\lambda_{\max}^{\text{CL}} = 573\text{--}577\text{ nm}$) with efficiency $\Phi^{\text{CL}} = 6\text{--}8 \times 10^{-2}$. On the other hand, for an alkaline metal (Na⁺ or K⁺) alkoxide/MeOH system, **2a–c** decomposed slowly to emit a glow of chemiluminescence, the spectra of which were shifted slightly toward red from the TBAF/DMSO system, and $\Phi^{\text{CL}} (= 1.4\text{--}2.3 \times 10^{-3})$ was considerably decreased. In addition, Mg(OMe)₂ was found to play a characteristic role as a base for the chemiluminescent decomposition of **2a–c** through coordination to the intermediary oxidoaryl-substituted dioxetanes **13**. Thus, Mg²⁺ increased Φ^{CL} to more than twice those with Na⁺ or K⁺, while it shifted $\lambda_{\max}^{\text{CL}}$ considerably toward blue ($\lambda_{\max}^{\text{CL}} = 550\text{--}566\text{ nm}$). Copyright © 2012 John Wiley & Sons, Ltd.

Keywords: 2'-alkoxy-2-hydroxy-1,1'-binaphthyl; chemiluminescence; dioxetane; magnesium methoxide

Introduction

Upon treatment with a base, a dioxetane bearing a hydroxyaryl moiety produces an unstable oxidoaryl-substituted dioxetane, which rapidly decomposes with the accompanying emission of light by an intramolecular charge-transfer-induced decomposition (CTID) mechanism. This phenomenon has received considerable attention due to interest in the mechanism of bioluminescence and its potential application to modern chemiluminescent biological analysis (1–5). Recently, it has been reported that, for CTID of bicyclic dioxetane **1** bearing a 2-hydroxy-1,1'-binaphthyl-5-yl moiety, the color of chemiluminescence varies with changes in the twisted angle of the binaphthyl moiety in an anisotropic microenvironment, such as the coordination sphere of crown ether complexes (6).

In the course of our studies to design dioxetanes of this type, we synthesized bicyclic dioxetanes **2a–c** bearing a 2'-alkoxy-2-hydroxy-1,1'-binaphthyl-7-yl moiety, the structures of which were more congested than that of **1** (Fig. 1). We report here that dioxetanes **2a–c** underwent CTID effectively accompanied by the emission of light in methanol and that Mg(OMe)₂ acted as a unique base to cause a change in the color of chemiluminescence as well as to enhance the efficiency of chemiluminescence.

Experimental

Synthesis of bicyclic dioxetanes **2a–c** bearing a 2'-alkoxy-2-hydroxy-1,1'-binaphthyl-7-yl moiety

Dioxetanes **2a–c** were prepared by singlet oxygenation of the corresponding dihydrofurans **3a–c** (Scheme 1). These precursors were

synthesized through several steps starting from 7-hydroxy-2-naphthyl-substituted dihydrofuran **4** (7). First, oxidative cross-coupling of **4** with methyl naphthoate **5** was carried out in an O₂/Cu₂Cl₂/pyridine/MeOH system at room temperature to give binaphthyl-substituted dihydrofuran **6** in 94% yield. Hydrolysis of the ester group in **6** exclusively gave carboxylic acid **7**, which was, in turn, decarboxylated with Cu₂Cr₂O₅ in hot quinoline to give the desired bisnaphthol **8** in 77% yield. Williamson ether synthesis of **8** with methyl iodide gave precursor **3a** and its isomer **3a'**. The isomer **3a'** was converted to neopentyl ether **3ab**, which was, in turn, demethylated with MeSnA to give precursor **3b**. On the other hand, reduction of **6** with LiAlH₄ gave alcohol **9**, which was successively reacted with 2,2-dimethoxypropane in the presence of acid catalyst to give precursor acetal **3c**. When these precursors **3a–c** were individually irradiated in the presence of a catalytic amount of tetraphenylporphyrin in CH₂Cl₂ with a Na lamp under an O₂ atmosphere at 0°C, the desired dioxetanes **2a–c** were effectively produced as a mixture of diastereomers. The structures of dioxetanes **2a–c** were determined by ¹H NMR, ¹³C NMR, IR, Mass and HRMass spectral data. For **2c**, diastereomers **2c(a)** and **2c(b)** were separated in pure form and their stereochemistries were tentatively assigned by reference to the ¹H NMR spectral data of **1** and its related dioxetanes (7): **2c(a)** possessed (*RaR/SaS*) form, while **2c(b)** possessed (*RaS/SaR*) form.

Detailed synthetic procedures are described below.

* Correspondence to: M. Matsumoto, Department of Chemistry, Kanagawa University, Tsuchiya, Hiratsuka, Kanagawa 259-1293, Japan. E-mail: matsumo-chem@kanagawa-u.ac.jp

Department of Chemistry, Kanagawa University, Tsuchiya, Hiratsuka, Kanagawa 259-1293, Japan

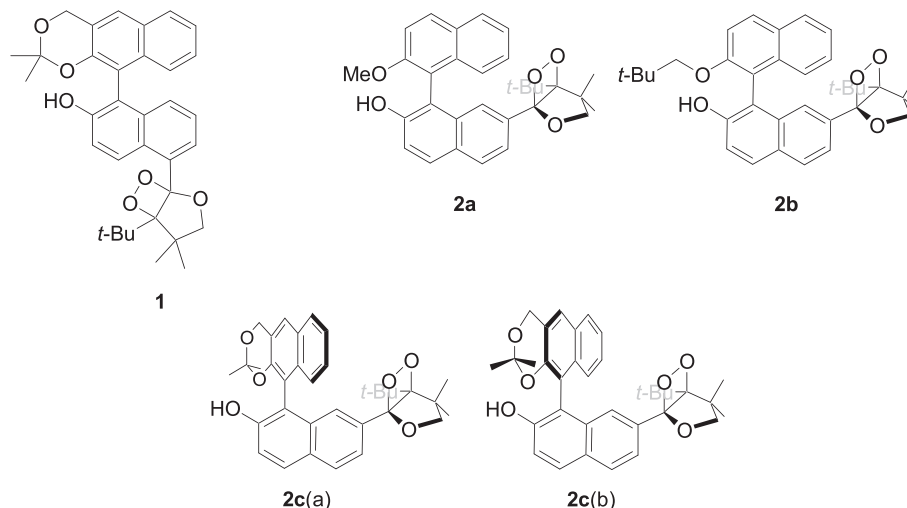
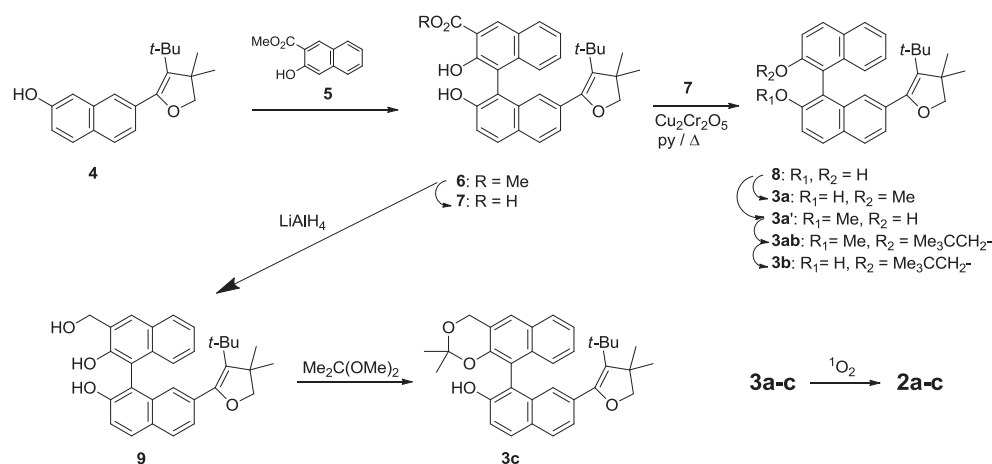


Figure 1. Bicyclic dioxetanes **1** and **2a–c** bearing a 2-hydroxy-1,1'-binaphthyl-7-yl moiety.



Scheme 1. Synthesis of bicyclic dioxetanes **2a–c** through key precursors **3a–c**.

Synthesis of 4-tert-butyl-5-(2,2'-dihydroxy-3'-methoxycarbonyl-1,1'-binaphthyl-7-yl)-3,3-dimethyl-2,3-dihydrofuran (**6**)

A solution of 4-tert-butyl-5-(7-hydroxy-2-naphthyl)-3,3-dimethyl-2,3-dihydrofuran (**4**) (5.03 g, 17.0 mmol) and 3-hydroxy-2-naphthoic acid methyl ester (**5**) (5.17 g, 25.5 mmol) were stirred together with CuCl (1.69 g, 17.1 mmol) and pyridine (14 mL) in MeOH (100 mL) at room temperature under O₂ atmosphere for 5 h. The reaction mixture was poured into 1 M HCl and extracted with ethyl acetate (AcOEt). The organic layer was washed with saturated aqueous NaHCO₃ and saturated aqueous NaCl, dried over anhydrous MgSO₄ and concentrated *in vacuo*. The residue was chromatographed on silica gel and eluted with hexane–AcOEt (4:1), then with hexane–CH₂Cl₂ (1:2) to give dihydrofuran **6** (7.94 g, 94%) as an amorphous solid. **6**: Yellow granules, m.p. 193.0–194.0°C (from AcOEt–hexane); ¹H NMR (500 MHz, CDCl₃): δ_H 0.82 (s, 9H), 1.19 (s, 3H), 1.21 (s, 3H), 3.74 (s, 2H), 4.07 (s, 3H), 4.98 (s, 1H), 6.99 (s with fine coupling, 1H), 7.16–7.20 (m, 1H), 7.23 (dd, *J* = 8.2 and 1.5 Hz, 1H), 7.33–7.39 (m, 3H), 7.82 (d, *J* = 8.2 Hz, 1H), 7.90 (d, *J* = 8.9 Hz, 1H), 7.90–7.95 (m, 1H), 8.72 (s, 1H), 10.78 (s, 1H) p.p.m.; ¹³C NMR (125 MHz, CDCl₃): δ_C 27.4, 27.4, 32.2, 32.3 (× 3), 47.1, 52.8, 83.0, 114.3, 114.3, 114.4, 118.0, 124.4, 124.9 (× 2), 125.9, 126.2, 127.3, 127.8, 128.8, 129.7, 129.9, 130.2, 132.9, 133.9, 134.1, 137.4, 150.2, 151.6, 154.8, 170.3 p.p.m.; IR (KBr): ν 3530, 3249, 3062, 2953, 2924, 1688, 1622, 1604 cm⁻¹; Mass (*m/z*, %): 496

(M⁺, 27), 482 (M⁺, 32), 481 (M⁺, 100), 393 (M⁺, 19); HRMS (ESI): 497.2347, calculated for C₃₂H₃₃O₅ [M + H⁺] 497.2328, 519.2144, calculated for C₃₂H₃₂O₅Na [M + Na⁺] 519.2147.

Synthesis of 4-tert-butyl-5-(3'-carboxy-2,2'-dihydroxy-1,1'-binaphthyl-7-yl)-3,3-dimethyl-2,3-dihydrofuran (**7**)

Dihydrofuran **6** (3.92 g, 7.88 mmol) was dissolved in a solution of KOH (1.58 g, 28.2 mmol) in EtOH (40 mL) and heated at refluxing temperature under N₂ atmosphere for 15 min. The reaction mixture was poured into 1 M HCl and extracted with AcOEt. The organic layer was washed with saturated aqueous NaCl, dried over anhydrous MgSO₄ and concentrated *in vacuo*. The residue was rinsed with hexane to give naphthalenecarboxylic acid **7** (3.80 g, quantitative yield) as a pale brown solid. **7**: Yellow granules m.p. 205.0–207.0°C (AcOEt–hexane); ¹H NMR (500 MHz, CDCl₃): δ_H 0.82 (s, 9H), 1.19 (s, 3H), 1.23 (s, 3H), 3.76 (s, 2H), 7.02 (s, 1H), 7.15–7.19 (m, 1H), 7.25 (dd, *J* = 8.2 and 1.4 Hz, 1H), 7.33–7.39 (m, 3H), 7.84 (d, *J* = 8.2 Hz, 1H), 7.89–7.94 (m, 1H), 7.92 (d, *J* = 8.9 Hz, 1H), 8.73 (s, 1H), 10.45 (br-s, 1H) p.p.m.; ¹³C NMR (125 MHz, CDCl₃): δ_C 27.3, 27.5, 32.2, 32.3 (× 3), 47.1, 82.9, 113.3, 114.3, 114.4, 118.1, 124.6, 124.9, 125.1, 126.2, 126.2, 127.4, 127.9, 128.9, 130.0, 130.0, 130.5, 133.0, 134.1, 135.2, 138.0, 149.9, 151.5, 155.0, 172.8 p.p.m.; IR (KBr): ν 3444, 3212, 3060,

2957, 1680, 1623 cm^{-1} ; Mass (m/z , %): 482 (M^+ , 36), 468 (M^+ , 34), 467 (M^+ , 100), 438 (M^+ , 33), 437 (M^+ , 81), 423 (M^+ , 27), 57 (M^+ , 39); HMRS (ESI): 505.1994, calculated for $\text{C}_{31}\text{H}_{30}\text{O}_3\text{Na}$ [$M + \text{Na}^+$] 505.1991.

Synthesis of 4-tert-butyl-5-(2,2'-dihydroxy-1,1'-binaphthyl-7-yl)-3,3-dimethyl-2,3-dihydrofuran (8)

A solution of naphthalenecarboxylic acid **7** (2.16 g 4.47 mmol) in AcOEt (2 mL) was added dropwise over 1 min to a solution of $\text{Cu}_2\text{Cr}_2\text{O}_5$ (185 mg, 0.594 mmol) in quinoline (4 mL) and stirred at 230°C under N_2 atmosphere for 5 h. The reaction mixture was cooled to room temperature and then was diluted with diethyl ether (6 mL). The mixture was filtered through celite, and the filtrate was poured into 3 M HCl and extracted with AcOEt. The organic layer was washed with saturated aqueous NaCl, dried over anhydrous MgSO_4 and concentrated *in vacuo*. The residue was chromatographed on silica gel and eluted with hexane–AcOEt (4:1) to give 2,2'-dihydroxy-1,1'-binaphthyl **8** (1.51 g, 77%) as a pale brown amorphous solid.

8: Colorless needles m.p. 141.0–142.0°C (from AcOEt–hexane); ^1H NMR (500 MHz, CDCl_3): δ_{H} 0.82 (s, 9H), 1.19 (s, 3H), 1.22 (s, 3H), 3.74 (s, 2H), 5.15 (br-s, 2H), 7.05 (s, 1H), 7.09 (d, $J=8.2$ Hz, 1H), 7.21–7.34 (m, 5H), 7.80 (d, $J=8.2$ Hz, 1H), 7.83 (d, $J=8.2$ Hz, 1H), 7.86 (d, $J=9.2$ Hz, 1H), 7.89 (d, $J=9.2$ Hz, 1H) p.p.m.; ^{13}C NMR (125 MHz, CDCl_3): δ_{C} 27.3, 27.4, 32.2, 32.3 ($\times 3$), 47.1, 83.0, 110.8, 111.3, 117.7, 118.0, 123.9, 124.4, 125.6, 125.7, 126.2, 127.4, 127.9, 128.2, 128.9, 129.3, 130.9, 131.3, 132.9, 133.5, 135.0, 149.7, 152.7, 152.8 p.p.m.; IR (KBr): ν 3473, 3419, 2957, 2868, 1619, 1598 cm^{-1} ; Mass (m/z , %): 438 (M^+ , 27), 436 (M^+ , 10), 424 (M^+ , 29), 423 (M^+ , 100), 421 (M^+ , 16), 313 (M^+ , 14); HRMS (M^+ , ESI): 461.2085, calculated for $\text{C}_{30}\text{H}_{30}\text{O}_3\text{Na}$ [$M + \text{Na}^+$] 461.2093.

Synthesis of 4-tert-butyl-5-(2-hydroxy-2'-methoxy-1,1'-binaphthyl-7-yl)-3,3-dimethyl-2,3-dihydrofuran (3a) and 4-tert-butyl-5-(2'-hydroxy-2-methoxy-1,1'-binaphthyl-7-yl)-3,3-dimethyl-2,3-dihydrofuran (3a')

2,2'-Dihydroxy-1,1'-binaphthyl **8** (801 mg, 1.83 mmol) and K_2CO_3 (253 mg, 1.83 mmol) were added to N,N-dimethylformamide (DMF) (6 mL) and stirred under a N_2 atmosphere at room temperature for 1 h. To the solution, methyl iodide (MeI) (0.225 mL, 3.63 mmol) was added and stirred at room temperature for 1 h. The reaction mixture was poured into 1 M HCl and extracted with AcOEt. The organic layer was washed with saturated aqueous NaCl, dried over anhydrous MgSO_4 and concentrated *in vacuo*. The residue was chromatographed on silica gel and eluted with hexane– CH_2Cl_2 (1:4–1:2) to give 2-hydroxy-2'-methoxy-1,1'-binaphthyl **3a** (170 mg, 21%) as a colorless solid and its 2'-hydroxy-2-methoxy-1,1'-binaphthyl isomer **3a'** (298 mg, 36%) as a pale yellow solid. **3a**: Colorless granules, m.p. 163.0–164.0°C (from AcOEt–hexane); ^1H NMR (500 MHz, CDCl_3): δ_{H} 0.83 (s, 9H), 1.21 (s, 3H), 1.22 (s, 3H), 3.74 (s, 2H), 3.78 (s, 3H), 4.90 (s, 1H), 6.98 (s, 1H), 7.18 (d, $J=8.5$ Hz, 1H), 7.22 (dd, $J=8.2$ and 1.4 Hz, 1H), 7.24–7.28 (m, 1H), 7.33–7.37 (m, 2H), 7.47 (d, $J=9.2$ Hz, 1H), 7.81 (d, $J=8.2$ Hz, 1H), 7.88 (d, $J=8.7$ Hz, 1H), 7.89 (d, $J=8.0$ Hz, 1H), 8.05 (d, $J=9.2$ Hz, 1H) p.p.m.; ^{13}C NMR (125 MHz, CDCl_3): δ_{C} 27.4, 27.4, 32.2, 32.3 ($\times 3$), 47.1, 56.3, 82.9, 113.3, 114.9, 115.3, 117.7, 124.0, 124.8, 125.0, 125.7, 126.4, 127.4, 127.7, 128.0, 128.6, 129.3, 129.5, 131.0, 133.2, 133.9, 134.0, 150.2, 151.4, 155.8 p.p.m.; IR (KBr): ν 3486, 3056, 2956, 2867, 1592 cm^{-1} ; Mass (m/z , %): 452 (M^+ , 27), 438 (M^+ , 31), 437 (M^+ , 100), 327 (M^+ , 12); HRMS (ESI): 475.2254, calculated for $\text{C}_{31}\text{H}_{32}\text{O}_3\text{Na}$ [$M + \text{Na}^+$] 475.2249. **3a'**: pale yellow granules, m.p. 175.0–176.0°C (from AcOEt–hexane); ^1H NMR (500 MHz, CDCl_3): δ_{H} 0.80 (s, 9H), 1.19 (s, 3H), 1.22 (s, 3H), 3.75 (s, 2H), 3.80 (s, 3H), 4.90 (s, 1H), 7.01 (d, $J=8.5$ Hz, 1H), 7.09 (s with fine coupling, 1H), 7.19 (dd with fine coupling, $J=8.5$ and 6.9 Hz, 1H), 7.25–7.30 (m, 2H), 7.34 (d, $J=8.9$ Hz, 1H), 7.48 (d, $J=8.9$ Hz, 1H), 7.82–7.87 (m, 2H), 7.89 (d, $J=8.9$ Hz, 1H), 8.03 (d, $J=8.9$ Hz, 1H) p.p.m.; ^{13}C NMR (125 MHz, CDCl_3): δ_{C} 27.2, 27.5, 32.2, 32.3 ($\times 3$), 47.1, 56.6, 83.0, 114.0, 114.7, 115.6, 117.4, 123.1, 124.9, 125.7, 126.1, 126.3, 126.4, 127.7, 127.9, 128.9, 129.0, 129.7, 130.7, 133.5, 133.8, 134.9, 149.7, 151.2, 156.1 p.p.m.; IR (KBr): ν 3379, 3058, 2955, 2870, 1619, 1596 cm^{-1} ; Mass (m/z , %): 452 (M^+ ,

28), 438 (M^+ , 31), 437 (M^+ , 100), 327 (M^+ , 13); HRMS (ESI): 475.2250, calculated for $\text{C}_{31}\text{H}_{32}\text{O}_3\text{Na}$ [$M + \text{Na}^+$] 475.2249.

Synthesis of 4-tert-butyl-5-(2-hydroxy-2'-neopentyloxy-1,1'-binaphthyl-7-yl)-3,3-dimethyl-2,3-dihydrofuran (3b)

2'-Hydroxy-2-methoxy-1,1'-binaphthyl **3a'** (501 mg, 1.11 mmol) was added to a suspension of NaH (60% in oil, 99.7 mg, 2.49 mmol) in dry DMF (5 mL) at 0°C under a N_2 atmosphere and stirred for 30 min at room temperature. To the solution, neopentyl iodide (0.29 mL, 2.2 mmol) was added at room temperature and refluxed for 2 h. The reaction mixture was poured into saturated aqueous NH_4Cl and extracted with AcOEt. The organic layer was washed with saturated aqueous NaCl, dried over anhydrous MgSO_4 and concentrated *in vacuo*. The residue was chromatographed on silica gel and eluted with hexane–AcOEt (9:1) to give 2-methoxy-2'-neopentyloxy-1,1'-binaphthyl **3ab** (531 mg, 92%) as a pale yellow solid. **3ab**: Colorless granules, m.p. 151.0–152.0°C (from AcOEt–hexane); ^1H NMR (500 MHz, CDCl_3): δ_{H} 0.57 (s, 9H), 0.81 (s, 9H), 1.20 (s, 3H), 1.20 (s, 3H), 3.54 (q_{AB}, $J=8.1$ Hz, 2H), 3.73 (s, 2H), 3.74 (s, 3H), 7.02 (s with fine coupling, 1H), 7.15–7.22 (m, 3H), 7.29 (ddd, $J=8.2$, 6.2 and 1.8 Hz, 1H), 7.37 (d, $J=8.9$ Hz, 1H), 7.41 (d, $J=8.9$ Hz, 1H), 7.80 (d, $J=8.5$ Hz, 1H), 7.84 (d, $J=8.2$ Hz, 1H), 7.92 (d, $J=8.9$ Hz, 2H) p.p.m.; ^{13}C NMR (125 MHz, CDCl_3): δ_{C} 26.2 ($\times 3$), 27.4, 27.5, 31.8, 32.2, 32.4 ($\times 3$), 47.1, 56.6, 79.3, 82.9, 114.0, 115.4, 120.0, 120.1, 123.3, 124.9, 125.5, 125.6, 126.2, 126.8, 127.3, 127.7, 128.5, 128.8, 129.1, 129.1, 133.7, 133.8, 134.2, 150.4, 154.7, 155.2 p.p.m.; IR (KBr): ν 3054, 2954, 2902, 2866, 1621, 1594 cm^{-1} ; Mass (m/z , %): 523 (M^+ + 1, 13), 522 (M^+ , 33), 508 (M^+ , 38), 507 (M^+ , 100), 437 (M^+ , 12); HRMS (ESI): 523.3220, calculated for $\text{C}_{36}\text{H}_{43}\text{O}_3$ [$M + \text{H}^+$] 523.3212, 545.3036, calculated for $\text{C}_{36}\text{H}_{42}\text{O}_3\text{Na}$ [$M + \text{Na}^+$] 545.3032.

MeSNa (52.0 mg, 0.742 mmol) was added to a solution of 2-methoxy-2'-neopentyloxy-1,1'-binaphthyl **3ab** (164 mg, 0.314 mmol) in dry DMF (2 mL) at 0°C under a N_2 atmosphere and stirred at refluxing temperature for 5 h. The reaction mixture was poured into saturated aqueous NH_4Cl and extracted with AcOEt. The organic layer was washed with saturated aqueous NaCl, dried over anhydrous MgSO_4 and concentrated *in vacuo*. The residue was chromatographed on silica gel and eluted with hexane–AcOEt (9:1) to give 2-hydroxy-2'-neopentyloxy-1,1'-binaphthyl **3b** (139 mg, 96%) as a pale yellow solid. **3b**: Colorless columns, m.p. 178.0–178.5°C (from AcOEt–hexane); ^1H NMR (500 MHz, CDCl_3): δ_{H} 0.63 (s, 9H), 0.81 (s, 9H), 1.19 (s, 3H), 1.21 (s, 3H), 3.59 (q_{AB}, $J=8.1$ Hz, 2H), 3.73 (s, 2H), 4.95 (s, 1H), 6.96 (s with fine coupling, 1H), 7.20 (dd, $J=8.2$ and 1.4 Hz, 1H), 7.21 (d with fine coupling, $J=8.5$ Hz, 1H), 7.26 (dd with fine coupling, $J=8.5$ and 6.6 Hz, 1H), 7.33 (d, $J=8.7$ Hz, 1H), 7.35 (dd with fine coupling, $J=8.0$ and 6.6 Hz, 1H), 7.41 (d, $J=8.9$ Hz, 1H), 7.80 (d, $J=8.2$ Hz, 1H), 7.84–7.89 (m, 2H), 8.01 (d, $J=8.9$ Hz, 1H) p.p.m.; ^{13}C NMR (125 MHz, CDCl_3): δ_{C} 26.2 ($\times 3$), 27.4 ($\times 2$), 31.9, 32.2, 32.4 ($\times 3$), 47.1, 79.4, 82.9, 115.2, 115.5, 115.9, 117.6, 124.0, 124.7, 125.2, 125.6, 126.3, 127.3, 127.6, 128.0, 128.5, 129.3, 129.4, 130.8, 133.5, 133.8, 134.3, 150.4, 151.5, 155.6 p.p.m.; IR (KBr): ν 3471, 3060, 2954, 2865, 1620, 1590 cm^{-1} ; Mass (m/z , %): 509 (M^+ + 1, 10), 508 (M^+ , 26), 494 (M^+ , 34), 493 (M^+ , 100), 239 (M^+ , 10). HRMS (ESI): 509.3079, calculated for $\text{C}_{35}\text{H}_{41}\text{O}_3$ [$M + \text{H}^+$] 509.3056, 531.2882, calculated for $\text{C}_{35}\text{H}_{40}\text{O}_3\text{Na}$ [$M + \text{Na}^+$] 531.2875.

Synthesis of 4-tert-butyl-5-(2,2'-dihydroxy-3'-hydroxymethyl-1,1'-binaphthyl-7-yl)-3,3-dimethyl-2,3-dihydrofuran (9)

A solution of naphthalenecarboxylate **6** (517 mg, 1.04 mmol) in dry tetrahydrofuran (THF) (3 mL) was added dropwise to a suspension of LiAlH_4 (64.2 mg, 1.69 mmol) in dry THF (2 mL) at 0°C under a N_2 atmosphere and stirred at room temperature for 1 h. The reaction mixture was quenched with H_2O in THF, poured into 3 M HCl and extracted with AcOEt. The organic layer was washed with saturated aqueous NaCl, dried over anhydrous MgSO_4 and concentrated *in vacuo*. The residue was chromatographed on silica gel and eluted with hexane–AcOEt (2:1) to give 2,2'-dihydroxy-3'-hydroxymethylbinaphthyl **9** (447 mg, 92%) as a

colorless solid. **9**: Colorless granules, m.p. 223.0–224.0°C (from AcOEt–hexane). ^1H NMR (500 MHz, CDCl_3): δ_{H} 0.82 (s, 9H), 1.20 (s, 3H), 1.22 (s, 3H), 2.48 (t, $J=6.2$ Hz, 1H), 3.75 (s, 2H), 4.91–4.99 (m, 2H), 5.14 (s, 1H), 5.83 (s, 1H), 7.04 (s with fine coupling, 1H), 7.11 (d, $J=8.2$ Hz, 1H), 7.24–7.30 (m, 2H), 7.34–7.39 (m, 2H), 7.83–7.87 (m, 2H), 7.91 (s, 1H), 7.94 (d, $J=8.9$ Hz, 1H) p.p.m.; ^{13}C NMR (125 MHz, CDCl_3): δ_{C} 27.2, 27.4, 32.2, 32.3 ($\times 3$), 47.1, 62.8, 83.0, 111.8, 111.9, 118.2, 124.2, 124.4, 125.4, 125.8, 126.2, 127.2, 127.9, 128.1, 128.5, 128.8, 129.0, 129.0, 130.8, 133.0, 133.3, 134.8, 149.7, 151.3, 152.8 p.p.m.; IR (KBr): ν 3525, 3212, 2956, 2862, 1624 cm^{-1} ; Mass (m/z , %): 469 ($\text{M}^+ + 1$, 14), 468 (M^+ , 40), 454 (M^+ , 32), 453 (M^+ , 100), 451 (M^+ , 14), 435 (M^+ , 15), 379 (M^+ , 15), 239 (M^+ , 10); HRMS (ESI): 491.2197, calculated for $\text{C}_{31}\text{H}_{32}\text{O}_4\text{Na}$ [$\text{M} + \text{Na}^+$] 491.2198.

Synthesis of 4-tert-butyl-5-[1-(2,2-dimethyl-1,3-dioxo-1,2,3,4-tetrahydro-anthracen-9-yl)-2-hydroxy-7-naphthyl]-3,3-dimethyl-2,3-dihydrofuran (**3c**)

2,2'-Dihydroxy-3'-hydroxymethylbinaphthyl **9** (1.51 g, 3.23 mmol), acetone dimethyl acetal (1.59 mL, 12.9 mmol) and pyridinium *p*-toluenesulfonate (84 mg, 0.33 mmol) were dissolved in acetone (15 mL) and refluxed under N_2 atmosphere for 3 h. The reaction mixture was poured into saturated aqueous NaHCO_3 and extracted with AcOEt. The organic layer was washed with saturated aqueous NaCl, dried over anhydrous MgSO_4 and concentrated *in vacuo*. The residue was chromatographed on silica gel and eluted with hexane–AcOEt (4:1) to give cyclic acetal **3c** (1.38 g, 84%) as a pale brown solid. **3c**: Colorless needles, m.p. 201.5–202.0°C (from AcOEt–hexane); ^1H NMR (500 MHz, CDCl_3): δ_{H} 0.82 (s, 9H), 1.20 (s, 3H), 1.22 (s, 3H), 1.41 (s, 3H), 1.46 (s, 3H), 3.74 (q_{AB} , $J=8.0$ Hz, 2H), 4.90 (s, 1H), 5.16 (q_{AB} with fine coupling, $J=15.3$ Hz, 2H), 6.99 (s with fine coupling, 1H), 7.12 (d, $J=8.7$ Hz, 1H), 7.21 (dd with fine coupling, $J=8.7$ and 6.6 Hz, 1H), 7.22 (dd, $J=8.3$ and 1.6 Hz, 1H), 7.33 (d, $J=8.9$ Hz, 1H), 7.33 (dd with fine coupling, $J=8.0$ and 6.6 Hz, 1H), 7.68 (s, 1H), 7.80 (d, $J=8.0$ Hz, 1H), 7.81 (d, $J=8.3$ Hz, 1H), 7.87 (d, $J=8.9$ Hz, 1H) p.p.m. ^{13}C NMR (125 MHz, CDCl_3): δ_{C} 24.7, 24.8, 27.2, 27.5, 32.2, 32.4 ($\times 3$), 47.1, 61.2, 82.9, 100.4, 114.6, 114.6, 117.7, 121.3, 124.3, 124.8, 124.9, 124.9, 125.6, 126.3, 126.8, 127.6, 127.6, 128.6, 128.7, 129.4, 133.3, 133.4, 134.0, 148.7, 150.2, 151.5 p.p.m.; IR (KBr): ν 3484, 3049, 2981, 2962, 2866, 1618, 1602 cm^{-1} ; Mass (m/z , %): 509 ($\text{M}^+ + 1$, 10), 508 (M^+ , 26), 451 (M^+ , 26), 450 (M^+ , 77), 436 (M^+ , 32), 435 (M^+ , 100), 379 (M^+ , 12); HRMS (ESI): 509.2718, calculated for $\text{C}_{34}\text{H}_{37}\text{O}_4$ [$\text{M} + \text{H}^+$] 509.2692, 531.2515, calculated for $\text{C}_{34}\text{H}_{36}\text{O}_4\text{Na}$ [$\text{M} + \text{Na}^+$] 531.2511.

Singlet oxygenation of 4-tert-butyl-5-(2-hydroxy-2'-methoxy-1,1'-binaphthyl-7-yl)-3,3-dimethyl-2,3-dihydrofuran (**3a**)

Typical procedure: a solution of 2-hydroxy-2'-methoxy-1,1'-binaphthyl **3a** (50.7 mg, 0.112 mmol) and tetraphenylporphyrin (1.0 mg) in CH_2Cl_2 (5 mL) was irradiated externally with 940 W Na lamp under an O_2 atmosphere at 0°C for 30 min. The photolysate was concentrated *in vacuo*. The residue was chromatographed on silica gel and eluted with hexane–AcOEt (4:1) to give a diastereomeric mixture (50:50) of 5-tert-butyl-1-(2-hydroxy-2'-methoxy-1,1'-binaphthyl-7-yl)-4,4-dimethyl-2,4,7-trioxabicyclo[3.2.0]heptane (**2a**) (52.8 mg, 97%) as a pale yellow solid. **2a**: Colorless needles, m.p. 161.0–162.0°C (dec.) (from CH_2Cl_2 –hexane) (50:50 mixture of stereoisomers). ^1H NMR (500 MHz, CDCl_3): δ_{H} 0.75 (s, 9H), 0.86 (s, 9H $\times 0.50$), 1.04 (s, 3H $\times 0.50$), 1.05 (s, 3H $\times 0.50$), 1.10 (s, 3H $\times 0.50$), 1.25 (s, 3H $\times 0.50$), 3.66 (d, $J=8.0$ Hz, 1H $\times 0.5$), 3.69 (d, $J=8.2$ Hz, 1H $\times 0.5$), 3.73 (s, 3H $\times 0.50$), 3.77 (s, 3H $\times 0.50$), 4.41–4.46 (m, 1H), 4.94 (s, 1H $\times 0.50$), 4.95 (s, 1H $\times 0.50$), 7.08 (d, $J=8.5$ Hz, 1H $\times 0.50$), 7.14 (d, $J=8.5$ Hz, 1H $\times 0.50$), 7.18–7.27 (m, 1H), 7.30–7.37 (m, 2H), 7.39 (d, $J=8.8$ Hz, 1H), 7.42–7.49 (m, 2H), 7.83–7.93 (m, 3H), 8.05 (d, $J=8.8$ Hz, 1H) p.p.m. ^{13}C NMR (125 MHz, CDCl_3): δ_{C} 18.4, 24.6 and 24.8, 26.7 and 26.8, 36.5 and 36.6, 45.4 and 45.4, 56.2 and 56.4, 80.1 and 80.1, 104.8 and 104.8, 113.2 and 113.4, 114.3 and 114.5, 116.0 and 116.1, 116.7, 118.6, 122.6 and 122.6, 124.0 and 124.0, 124.5 and 124.7, 125.6 and 125.7, 127.2 and 127.3, 127.7 and 127.8, 128.1 and 128.1, 129.3, 129.3 and 129.3, 129.3 and 129.4, 131.3 and 131.3, 132.9 and 133.0, 133.5

and 133.6, 133.9 and 134.0, 151.7 and 151.7, 155.9 and 155.9 p.p.m.; IR (KBr): ν 3497, 3448, 3060, 2962, 2894, 1623, 1593 cm^{-1} ; Mass (m/z , %): 485 ($\text{M}^+ + 1$, 16), 484 (M^+ , 47), 428 (M^+ , 30), 344 (M^+ , 31), 328 (M^+ , 24), 327 (M^+ , 100), 268 (M^+ , 27), 267 (M^+ , 23), 266 (M^+ , 11), 255 (M^+ , 10), 239 (M^+ , 26), 226 (M^+ , 13), 57 (M^+ , 44); HRMS (ESI): 507.2155, calculated for $\text{C}_{31}\text{H}_{32}\text{O}_5\text{Na}$ [$\text{M} + \text{Na}^+$] 507.2147.

5-tert-Butyl-1-(2-hydroxy-2'-neopentyl-1,1'-binaphthyl-7-yl)-4,4-dimethyl-2,4,7-trioxabicyclo[3.2.0]heptane (**2b**)

Singlet oxygenation of 4-tert-butyl-5-(2-hydroxy-2'-neopentyl-1,1'-binaphthyl-7-yl)-3,3-dimethyl-2,3-dihydrofuran (**3b**) was carried out similarly to the case of **3a** to give dioxetane **2b** as a mixture of diastereomer (50:50) in 96% yield. **2b**: Colorless needles, m.p. 176.0–177.0°C (dec.) (from CH_2Cl_2 –hexane) (50:50 mixture of stereoisomers). ^1H NMR (500 MHz, CDCl_3): δ_{H} 0.58 (s, 9H $\times 0.50$), 0.62 (s, 9H $\times 0.50$), 0.73 (s, 9H $\times 0.50$), 0.82 (s, 9H $\times 0.50$), 1.02 (s, 3H $\times 0.50$), 1.04 (s, 3H), 1.25 (s, 3H $\times 0.50$), 3.47–3.53 (m, 1H), 3.60–3.71 (m, 2H), 4.40–4.46 (m, 1H), 5.02 (s, 1H $\times 0.50$), 5.03 (s, 1H $\times 0.50$), 7.13 (d, $J=8.2$ Hz, 1H $\times 0.50$), 7.17–7.26 (m, 1.5 H), 7.27–7.42 (m, 4.5 H), 7.48 (dd, $J=8.5$ and 1.6 Hz, 1H $\times 0.50$), 7.81–7.90 (m, 3H), 8.00 (d, $J=8.9$ Hz, 1H) p.p.m.; ^{13}C NMR (125 MHz, CDCl_3): δ_{C} 18.3 and 18.4, 24.4 and 24.8, 26.1 and 26.1, 26.7 and 26.8, 31.8 and 31.9, 36.5 and 36.6, 45.4 and 45.4, 79.2 and 79.3, 80.1 and 80.2, 104.8 and 104.9, 114.9 and 115.0, 115.1 and 115.4, 116.2 and 116.3, 116.8 and 116.8, 118.4 and 118.4, 122.3 and 122.4, 123.9 and 124.0, 124.8 and 124.8, 125.7 and 125.8, 127.1 and 127.2, 127.6 and 127.7, 128.1 and 128.1, 129.1 and 129.1, 129.1 and 129.2, 129.3 and 129.4, 131.1 and 131.1, 133.1 and 133.2, 133.4 and 133.4, 134.2 and 134.2, 151.9 and 151.9, 155.6 and 155.6 p.p.m.; IR (KBr): ν 3492, 3059, 2957, 2870, 1623, 1603, 1592 cm^{-1} ; Mass (m/z , %): 541 ($\text{M}^+ + 1$, 38), 540 (M^+ , 100), 384 (M^+ , 27), 383 (M^+ , 85), 330 (M^+ , 40), 314 (M^+ , 20), 313 (M^+ , 92), 312 (M^+ , 90), 295 (M^+ , 17), 285 (M^+ , 16), 284 (M^+ , 18), 268 (M^+ , 23), 267 (M^+ , 41), 266 (M^+ , 18), 256 (M^+ , 11), 255 (M^+ , 26), 240 (M^+ , 14), 239 (M^+ , 56), 228 (M^+ , 12), 227 (M^+ , 10), 226 (M^+ , 19), 57 (M^+ , 89); HRMS (ESI): 541.2991, calculated for $\text{C}_{35}\text{H}_{41}\text{O}_5$ [$\text{M} + \text{H}^+$] 541.2954, 563.2776, calculated for $\text{C}_{35}\text{H}_{40}\text{O}_5\text{Na}$ [$\text{M} + \text{Na}^+$] 563.2773.

Synthesis of 5-tert-butyl-1-[1-(2,2-dimethyl-1,3-dioxo-1,2,3,4-tetrahydro-anthracen-9-yl)-2-hydroxy-7-naphthyl]-4,4-dimethyl-2,4,7-trioxabicyclo[3.2.0]heptane [**2c(a)**] and [**2c(b)**]

Singlet oxygenation of 4-tert-butyl-5-[1-(2,2-dimethyl-1,3-dioxo-1,2,3,4-tetrahydroanthracen-9-yl)-2-hydroxy-7-naphthyl]-3,3-dimethyl-2,3-dihydrofuran (**3c**) (305 mg) was carried out similarly to the case of **3a**. The photolysate was concentrated *in vacuo*, and the residue was chromatographed on silica gel and eluted with hexane– CH_2Cl_2 (1:4) to give **2c(b)** (178 mg, 54.8%) as a colorless solid and its isomer **2c(a)** (111 mg, 34.1%) as a colorless solid. **2c(b)**: Colorless needles, m.p. 153.0–154.0°C (dec.) (from CH_2Cl_2 –hexane). ^1H NMR (500 MHz, CDCl_3): δ_{H} 0.69 (s, 9H), 1.04 (s, 3H), 1.29 (s, 3H), 1.34 (s, 3H), 1.38 (s, 3H), 3.72 (d, $J=8.2$ Hz, 1H), 4.46 (d, $J=8.2$ Hz, 1H), 5.03 (s, 1H), 5.12 (q_{AB} , $J=15.2$ Hz, 2H), 7.08 (d, $J=8.5$ Hz, 1H), 7.18 (dd, $J=8.5$ and 6.9 Hz, 1H), 7.31 (dd, $J=8.0$ and 6.9 Hz, 1H), 7.37–7.42 (m, 3H), 7.65 (s, 1H), 7.78 (d, $J=8.0$ Hz, 1H), 7.84 (d, $J=9.2$ Hz, 1H), 7.88 (d, $J=8.9$ Hz, 1H) p.p.m.; ^{13}C NMR (125 MHz, CDCl_3): δ_{C} 18.4, 23.8, 24.9, 25.8, 26.7, 36.5, 45.5, 61.2, 80.2, 100.4, 104.8, 114.1, 115.5, 116.8, 118.6, 121.3, 122.5, 124.2, 124.6, 125.2, 125.7, 126.6, 127.8, 127.8, 128.7, 129.2, 129.3, 133.0, 133.4, 133.4, 148.9, 151.9 p.p.m.; IR (KBr): ν 3539, 3060, 2981, 2895, 1627, 1604 cm^{-1} ; Mass (m/z , %): 540 (M^+ , 11), 483 (M^+ , 28), 482 (M^+ , 83), 426 (M^+ , 10), 383 (M^+ , 10), 342 (M^+ , 17), 327 (M^+ , 12), 326 (M^+ , 28), 325 (M^+ , 100), 324 (M^+ , 21), 298 (M^+ , 14), 297 (M^+ , 13), 296 (M^+ , 14), 271 (M^+ , 14), 269 (M^+ , 21), 268 (M^+ , 19), 267 (M^+ , 12), 252 (M^+ , 16), 250 (M^+ , 10), 240 (M^+ , 12), 239 (M^+ , 39), 57 (M^+ , 70); HRMS (ESI): 563.2414, calculated for $\text{C}_{34}\text{H}_{36}\text{O}_6\text{Na}$ [$\text{M} + \text{Na}^+$] 563.2410. **2c(a)**: Colorless needles, m.p. 166.0–167.0°C (dec.) (from CH_2Cl_2 –hexane); ^1H NMR (500 MHz, CDCl_3): δ_{H} 0.81 (s, 9H), 1.02 (s, 6H), 1.37 (s, 3H), 1.46 (s, 3H), 3.62 (d, $J=8.2$ Hz, 1H), 4.42 (d, $J=8.2$ Hz, 1H), 5.04 (s, 1H), 5.13 (q_{AB} , $J=15.4$ Hz, 2H), 6.96 (d, $J=8.5$ Hz, 1H), 7.12

(ddd, $J = 8.5, 6.9$ and 1.1 Hz, 1H), 7.27 (s with fine coupling, 1H), 7.28 (ddd, $J = 8.2, 6.9$ and 1.1 Hz, 1H), 7.38 (d, $J = 8.9$ Hz, 1H), 7.50 (dd, $J = 8.5$ and 1.8 Hz, 1H), 7.64 (s, 1H), 7.75 (d, $J = 8.2$ Hz, 1H), 7.86 (d, $J = 8.5$ Hz, 1H), 7.89 (d, $J = 8.9$ Hz, 1H) p.p.m.; ^{13}C NMR (125 MHz, CDCl_3): δ_{C} 18.4, 24.3, 24.5, 25.3, 26.9, 36.6, 45.4, 61.2, 80.1, 100.4, 104.9, 114.1, 115.3, 116.8, 118.6, 121.2, 122.5, 124.2, 124.7, 125.1, 125.5, 126.7, 127.6 ($\times 2$), 128.6, 129.3, 129.3, 133.1, 133.4, 133.6, 148.7, 151.9 p.p.m.; IR (KBr): ν 3391, 3060, 2984, 2960, 2894, 1629, 1604 cm^{-1} ; Mass (m/z , %): 540 (M^+ , 11), 483 (M^+ , 27), 482 (M^+ , 82), 426 (M^+ , 10), 383 (M^+ , 10), 342 (M^+ , 16), 327 (M^+ , 13), 326 (M^+ , 27), 325 (M^+ , 100), 324 (M^+ , 21), 298 (M^+ , 14), 297 (M^+ , 14), 296 (M^+ , 15), 271 (M^+ , 15), 269 (M^+ , 22), 268 (M^+ , 20), 267 (M^+ , 13), 252 (M^+ , 16), 251 (M^+ , 10), 250 (M^+ , 12), 240 (M^+ , 13), 239 (M^+ , 44), 226 (M^+ , 10), 57 (M^+ , 71); HRMS (ESI): 563.2417, calculated for $\text{C}_{34}\text{H}_{36}\text{O}_6\text{Na}$ [$\text{M} + \text{Na}^+$] 563.2410.

Thermal decomposition of 5-*tert*-butyl-1-(2-hydroxy-2'-methoxy-1,1'-binaphthyl-7-yl)-4,4-dimethyl-2,4,7-trioxabicyclo[3.2.0]heptane (2a)

Typical procedure: Dioxetane **2a** (69.4 mg, 0.143 mmol) was stirred in *p*-xylene (0.7 mL) for 2 h at reflux temperature. After the concentration *in vacuo*, the reaction mixture was chromatographed on silica gel and eluted with AcOEt–hexane (1:9) to give 2,2,4,4-tetramethyl-3-oxopentyl 2-hydroxy-2'-methoxy-1,1'-binaphthyl-7-carboxylate (**12a**) (63.8 mg, 92% yield) as a colorless solid. The other dioxetanes **2b** and **2c** were similarly decomposed in hot *p*-xylene to give keto ester **12b** in 99% yield and **12c** in 92% yield, respectively.

12a: Colorless granules, m.p. 190.5–191.0 °C (from AcOEt–hexane). ^1H NMR (500 MHz, CDCl_3): δ_{H} 1.03 (s, 9H), 1.14 (s, 3H), 1.17 (s, 3H), 3.80 (s, 3H), 4.24 (q_{AB} , $J = 10.8$ Hz, 2H), 4.97 (br-s, 1H), 7.11 (d, $J = 8.5$ Hz, 1H), 7.27 (dd with fine coupling, $J = 8.5$ and 6.9 Hz, 1H), 7.36 (dd with fine coupling, $J = 8.0$ and 6.9 Hz, 1H), 7.45 (d, $J = 8.9$ Hz, 1H), 7.50 (d, $J = 9.2$ Hz, 1H), 7.77 (s with fine coupling, 1H), 7.84 (dd, $J = 8.5$ and 1.6 Hz, 1H), 7.87–7.95 (m, 3H), 8.08 (d, $J = 9.2$ Hz, 1H) p.p.m.; ^{13}C NMR (125 MHz, CDCl_3): δ_{C} 23.4, 23.6, 26.0 ($\times 3$), 27.9 ($\times 3$), 31.7, 45.6, 48.9, 71.7, 78.9, 114.6, 114.7, 116.8, 119.8, 122.5, 124.0, 124.4, 127.4, 127.5, 128.1, 128.2, 128.3, 129.3, 129.4, 131.2, 131.2, 133.1, 133.8, 151.9, 155.6, 166.5, 215.7 p.p.m.; IR (KBr): ν 3452, 3057, 2962, 2933, 2839, 1703, 1687, 1620, 1602 cm^{-1} ; Mass (m/z , %): 485 ($\text{M}^+ + 1$, 14), 484 (M^+ , 25), 428 (M^+ , 25), 344 (M^+ , 28), 328 (M^+ , 23), 327 (M^+ , 100), 268 (M^+ , 23), 237 (M^+ , 20), 239 (M^+ , 22), 226 (M^+ , 11), 57 (M^+ , 24); HRMS (ESI): 507.2157, calculated for $\text{C}_{31}\text{H}_{32}\text{O}_5\text{Na}$ [$\text{M} + \text{Na}^+$] 507.2147.

12b: Colorless viscous oil. ^1H NMR (500 MHz, CDCl_3): δ_{H} 0.55 (s, 9H), 1.02 (s, 9H), 1.13 (s, 3H), 1.16 (s, 3H), 3.59 (q_{AB} , $J = 8.2$ Hz, 2H), 4.23 (s, 2H), 5.06 (br-s, 1H), 7.20 (d, $J = 8.5$ Hz, 1H), 7.28 (dd with fine coupling, $J = 8.5$ and 6.8 Hz, 1H), 7.35 (dd with fine coupling, $J = 8.0$ and 6.8 Hz, 1H), 7.39–7.45 (m, 2H), 7.79 (s with fine coupling, 1H), 7.82 (dd, $J = 8.8$ and 1.6 Hz, 1H), 7.85–7.91 (m, 3H), 8.01 (d, $J = 8.9$ Hz, 1H) p.p.m.; ^{13}C NMR (125 MHz, CDCl_3): δ_{C} 23.4, 23.6, 27.9 ($\times 3$), 45.6, 49.0, 56.5, 71.8, 113.6, 114.2, 116.5, 119.9, 122.7, 124.2, 124.4, 127.5, 127.8, 127.8, 128.3, 128.4, 129.5, 129.5, 131.3, 131.5, 133.0, 133.7, 151.8, 156.0, 166.5, 215.7 p.p.m.; IR (KBr): ν 3423, 3058, 2957, 2869, 1714, 1686, 1622, 1592 cm^{-1} ; Mass (m/z , %): 541 ($\text{M}^+ + 1$, 39), 540 (M^+ , 20), 384 (M^+ , 20), 383 (M^+ , 66), 330 (M^+ , 32), 314 (M^+ , 16), 313 (M^+ , 73), 312 (M^+ , 80), 295 (M^+ , 11), 285 (M^+ , 20), 284 (M^+ , 22), 268 (M^+ , 13), 267 (M^+ , 23), 255 (M^+ , 14), 239 (M^+ , 29), 57 (M^+ , 45); HRMS (ESI): 563.2777, calculated for $\text{C}_{35}\text{H}_{40}\text{O}_5\text{Na}$ [$\text{M} + \text{Na}^+$] 563.2773.

12c: Colorless granules, m.p. 206.0–207.0 °C (from AcOEt–hexane). ^1H NMR (500 MHz, CDCl_3): δ_{H} 1.02 (s, 9H), 1.16 (s, 3H), 1.18 (s, 3H), 1.39 (s, 3H), 1.41 (s, 3H), 4.25 (q_{AB} , $J = 10.5$ Hz, 2H), 5.00 (s, 1H), 5.18 (q_{AB} , $J = 15.4$ Hz, 2H), 7.10 (d, $J = 8.5$ Hz, 1H), 7.23 (dd, $J = 8.5$ and 6.4 Hz, 1H), 7.35 (dd, $J = 8.2$ and 6.4 Hz, 1H), 7.44 (d, $J = 8.9$ Hz, 1H), 7.70 (s, 1H), 7.79–7.86 (m, 3H), 7.89 (d, $J = 8.5$ Hz, 1H), 7.92 (d, $J = 8.9$ Hz, 1H) p.p.m.; ^{13}C NMR (125 MHz, CDCl_3): δ_{C} 23.4, 23.7, 23.8, 25.9, 27.9 ($\times 3$), 45.6, 49.0, 61.2, 71.8, 100.5, 113.6, 115.9, 120.0, 121.4, 122.7, 124.3, 124.4, 125.4, 126.9, 126.9, 127.6, 128.0 ($\times 2$), 128.4, 128.8, 129.5, 131.3, 133.0, 149.0, 152.0, 166.5, 215.7 p.p.m.; IR (KBr): ν 3421, 3061, 2970, 2871,

1715, 1685, 1627, 1602 cm^{-1} ; Mass (m/z , %): 540 (M^+ , 13), 483 (M^+ , 36), 482 (M^+ , 100), 426 (M^+ , 14), 383 (M^+ , 11), 342 (M^+ , 20), 327 (M^+ , 12), 326 (M^+ , 28), 325 (M^+ , 99), 324 (M^+ , 27), 298 (M^+ , 13), 297 (M^+ , 13), 296 (M^+ , 13), 271 (M^+ , 11), 269 (M^+ , 17), 268 (M^+ , 15), 252 (M^+ , 12), 239 (M^+ , 28), 57 (M^+ , 38); HMS (ESI): 563.2413, calculated for $\text{C}_{34}\text{H}_{36}\text{O}_6\text{Na}$ [$\text{M} + \text{Na}^+$] 563.2410.

Chemiluminescence measurement: general procedure

Chemiluminescence was measured by a Hamamatsu Photonics PMA-11 (detection limit, 200–900 nm) and/or JASCO FP-6500 spectrometer (detection limit 200–900 nm).

Tetrabutylammonium fluoride/dimethyl sulfoxide system

A freshly prepared solution (2.00 mL) of tetrabutylammonium fluoride (TBAF) (1.0×10^{-2} mol/L) in DMSO was transferred to a quartz cell ($10 \times 10 \times 50$ mm), which was placed in a spectrometer that was thermostated with stirring at 25 °C. After 3–5 min, a solution of dioxetane **2** in DMSO (1.0×10^{-4} mol/L, 1.00 mL) was added by means of a syringe, and measurement was started immediately. The time-course of the intensity of light emission was recorded and processed according to first-order kinetics. The total light emission was estimated by comparing it with that of 3-adamantylidene-4-[3-(*tert*-butyldimethylsiloxy)phenyl]-4-methoxy-1,2-dioxetane, the chemiluminescence efficiency Φ^{CL} of which has been reported to be 0.29 and was used here as a standard (9,10).

NaOMe/MeOH system, typical procedure

A freshly prepared solution (2.00 mL) of NaOMe (0.1 M) in MeOH was transferred to a quartz cell ($10 \times 10 \times 50$ mm), which was placed in a spectrometer that was thermostated with stirring at 45 °C. After 3–5 min, a solution of dioxetane **2** in MeOH (1.0×10^{-4} mol/L, 1.00 mL, 45 °C) was added by means of a syringe, and measurement was started immediately. The time-course of the intensity of light emission was recorded and processed according to first-order kinetics. The total light emission was estimated as in the TBAF/DMSO system described above.

When tetrabutylammonium methoxide (TBAOMe), potassium *t*-butoxide (KO t -Bu), or Mg(OMe) $_2$ was used in place of NaOMe, chemiluminescent decomposition was carried out according to the procedure described above.

Results and discussion

First, we investigated the chemiluminescent decomposition of **2a**, **2b** and the two diastereomers **2c(a)** and **2c(b)** in a TBAF/DMSO system, which is a typical triggering system that produces a naked oxido anion for the base-induced decomposition of hydroxyaryl-substituted dioxetanes (3,4). When dioxetanes **2a** and **2b** were individually treated with a large excess of TBAF in DMSO at 25 °C, **2a** and **2b** rapidly decomposed according to pseudo-first-order kinetics to effectively give light with maximum wavelength $\lambda_{\text{max}}^{\text{CL}} = 576$ and 577 nm and chemiluminescence efficiency $\Phi^{\text{CL}} = 7.0$ and 5.7×10^{-2} , respectively (Table 1) (9,10). Notably, the Φ^{CL} values for **2a** and **2b** were about five times higher than those for **1** in the TBAF/DMSO system, as shown in Table 1. Diastereomeric dioxetanes **2c(a)** and **2c(b)** similarly underwent TBAF-induced decomposition to show chemiluminescence, for

Table 1. TBAF-induced chemiluminescent decomposition of binaphthyl-substituted dioxetanes in DMSO^a

	$\lambda_{\max}^{\text{CL}}/\text{nm}$	Φ^{CL} ^b	$k^{\text{CTID}}/\text{s}^{-1}$	$t_{1/2}/\text{s}$
2a	576	7.0×10^{-2}	4.3×10^{-2}	16
2b	577	5.7×10^{-2}	9.8×10^{-2}	7.1
2c(a)	573	7.9×10^{-2}	4.0×10^{-2}	17
2c(b)	573	7.9×10^{-2}	5.0×10^{-2}	14
(<i>RaR/SaS</i>)- 1 ^c	600	1.1×10^{-2}	1.8×10^{-1}	3.9
(<i>RaR/SaS</i>)- 1 ^c	600	9.2×10^{-3}	1.8×10^{-1}	3.9

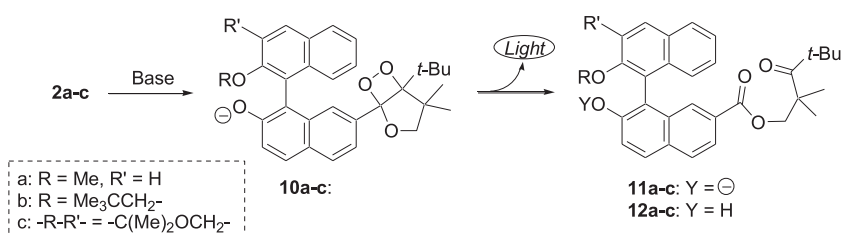
DMSO, dimethyl sulfoxide; TBAF, tetrabutylammonium fluoride.
^aAll reactions were carried out at 25°C.
^bBased on a value reported for the chemiluminescent decomposition of 3-adamantylidene-4-(3-*tert*-butyldimethylsilyloxyphenyl)-4-methoxy-1,2-dioxetane in TBAF/DMSO (9,10).
^cRef. 8.

which the Φ^{CL} s and $\lambda_{\max}^{\text{CL}}$ s resembled those for **2a** and **2b**, though these two isomers showed slightly different rates of CTID, k^{CTID} , as shown in Table 1. For these TBAF-induced decompositions of

2a–c, freshly spent reaction mixtures exclusively gave the corresponding keto esters **12a–c** after neutralization. Thus, the chemiluminescent decomposition of **2a–c** was undoubtedly thought to proceed through oxido anion **10a–c**, which rapidly decomposed to give keto ester **11a–c** in the excited state (Scheme 2).

The 2'-alkoxy-2-hydroxy-1,1'-binaphthyl-7-yl moiety in **2a–c** can act as a bidentate ligand for chelation to an appropriate metal ion. If CTID takes place under the metal ion-chelation of an oxidoaryl group as an electron donor, such chelation should become a new entry to controlling the color and/or efficiency of chemiluminescence and the rate of the CTID through regulation of the stereochemistry of an oxidoaryl-substituted dioxetane. For this purpose, we sought to preliminarily investigate CTID of **2a–c** in MeOH, as MeOH is the neutral solvent in which a metal ion is soluble as in water, though it has been known to often significantly decrease Φ^{CL} for CTID of oxidoaryl-substituted dioxetanes in MeOH (3,4).

When dioxetane **2a** was treated with a large excess of NaOMe in MeOH at 45°C, **2a** underwent CTID to emit chemiluminescence (Fig. 2), the properties of which are summarized in Table 2. Comparing the result for NaOMe/MeOH (Table 2) to that for a TBAF/DMSO system (Table 1), we can see several characteristic



Scheme 2. Tetrabutylammonium fluoride-induced chemiluminescent decomposition of dioxetanes **2a–c**.

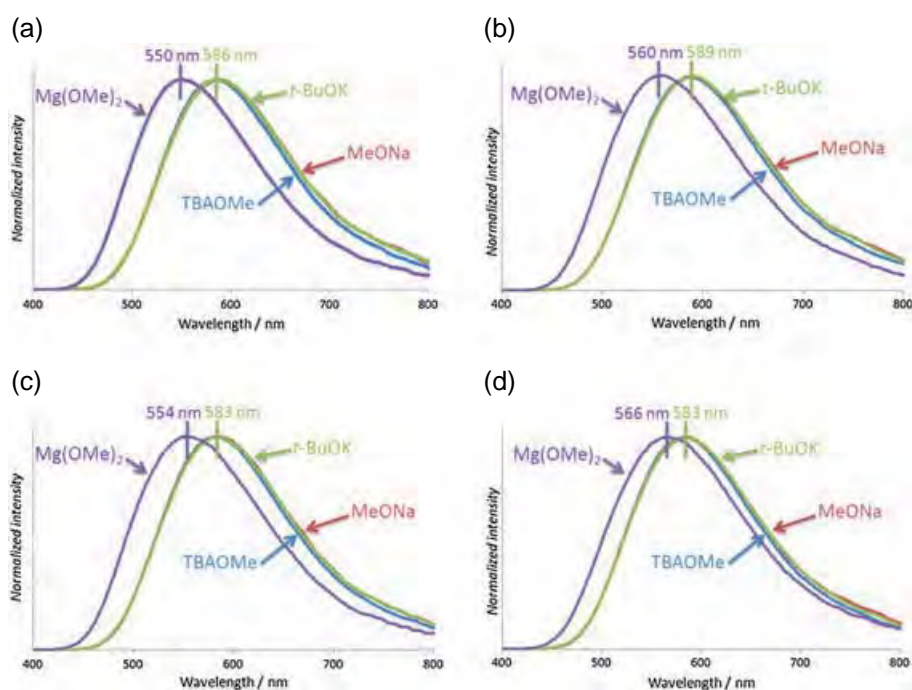


Figure 2. Chemiluminescence spectra of dioxetanes **2a–c** in a tetrabutylammonium methoxide, MeONa, *t*-BuOK, or Mg(OMe)₂/MeOH system: (a) for **2a**, (b) for **2b**, (c) for **2c(a)** and (d) **2c(b)**.

Table 2. Base-induced chemiluminescent decomposition of binaphthyl-substituted dioxetanes in MeOH^a

	Base	$\lambda_{\max}^{\text{CL}}/\text{nm}$	Φ^{CL} ^b	Relative Φ^{CL}	$k^{\text{CTID}}/\text{s}^{-1}$	$t_{1/2}/\text{s}$
2a	NaOMe	586	2.1×10^{-3}	1	2.2×10^{-3}	320
	KOt-Bu	586	2.0×10^{-3}	1.0	2.2×10^{-3}	320
	Mg(OMe) ₂	550	5.0×10^{-3}	2.4	4.5×10^{-4}	1500
	TBAOMe	583	2.6×10^{-3}	1.2	1.9×10^{-3}	370
2b	NaOMe	589	1.4×10^{-3}	1	4.6×10^{-3}	150
	KOt-Bu	589	1.4×10^{-3}	1.0	4.7×10^{-3}	150
	Mg(OMe) ₂	560	3.5×10^{-3}	2.5	6.1×10^{-4}	1100
	TBAOMe	587	1.9×10^{-3}	1.4	4.2×10^{-3}	170
2c(a)	NaOMe	583	2.3×10^{-3}	1	2.6×10^{-3}	270
	KOt-Bu	583	2.3×10^{-3}	1.0	2.7×10^{-3}	260
	Mg(OMe) ₂	554	5.1×10^{-3}	1.7	4.4×10^{-4}	1600
	TBAOMe	581	3.0×10^{-3}	1.3	2.6×10^{-3}	270
2c(b)	NaOMe	583	2.2×10^{-3}	1	1.9×10^{-3}	370
	KOt-Bu	583	2.3×10^{-3}	1.0	1.9×10^{-3}	370
	Mg(OMe) ₂	566	4.7×10^{-3}	2.1	2.6×10^{-4}	2700
	TBAOMe	581	2.9×10^{-3}	1.3	1.8×10^{-3}	380

^aAll reactions carried out at 45°C.

^bBased on a value reported for the chemiluminescent decomposition of 3-adamantylidene-4-(3-*tert*-butyldimethylsiloxyphenyl)-4-methoxy-1,2-dioxetane in tetrabutylammonium fluoride/dimethyl sulfoxide (9,10).

features for CTID in a NaOMe/MeOH system. First, the $\lambda_{\max}^{\text{CL}}$ in the NaOMe/MeOH system was shifted slightly (≈ 10 nm) to a longer wavelength region from the case in the TBAF/DMSO system. Second, the Φ^{CL} value for the NaOMe/MeOH system decreased to 1/30 of that for the TBAF/DMSO system. Third, the k^{CTID} significantly decreased. When KOt-Bu was used as a base in place of NaOMe in MeOH, CTID also took place to show chemiluminescence, the spectrum and properties of which were very similar to those for NaOMe (Fig. 2, Table 2).

We examined the chemiluminescent decomposition of **2a** using tetrabutylammonium methoxide TBAOMe as a representative base with little coordination ability, to evaluate the effect of alkaline metal ions on the chemiluminescence of **2a** in MeOH (Fig. 2, Table 2). The Φ^{CL} value increased to some extent and chemiluminescence spectrum showed a slight blue-shift. This result suggested that Na⁺ and K⁺ more or less affected the CTID of dioxetane **2a** through coordination to oxido anion **10a** and **11a** (Scheme 2). This suggestion prompted us to investigate the CTID of **2a** induced by a metal alkoxide with stronger chelation ability, with the expectation that it could become a new system based on metal-chelation for triggering the chemiluminescence of dioxetanes.

Our choice of metal alkoxide was Mg(OMe)₂, which is soluble in MeOH and has been reported to show characteristic activity as a base that is different from those of alkaline metal alkoxides for base-mediated reactions such as stereoselective aldol and Claisen reactions (11,12); methoxides of alkaline earth metal other than Mg are hardly soluble in MeOH. When treated with a large excess of Mg(OMe)₂ in MeOH at 45°C, dioxetane **2a** decomposed more slowly than with NaOMe and KOt-Bu to show chemiluminescence with $\lambda_{\max}^{\text{CL}}$ (550 nm), which was 36 nm shorter than those for NaOMe and KOt-Bu. In addition to the color change, the most prominent finding was that the Φ^{CL} value for the Mg(OMe)₂ system was 2.4 times greater than those with NaOMe or KOt-Bu and even larger than that with TBAOMe in MeOH (Table 2).

Next, we investigated CTID of **2b** triggered by NaOMe, KOt-Bu, TBAOMe or Mg(OMe)₂ in MeOH similarly to the cases of **2a** (Fig. 2, Table 2). The results show that Mg(OMe)₂ also characteristically affected CTID of **2b**. The chemiluminescence spectrum with Mg(OMe)₂ showed a blue-shifted peak, while those with NaOMe, KOt-Bu or TBAOMe shifted to red from the case in a TBAF/DMSO system. The Φ^{CL} value for the Mg(OMe)₂ system was greater than those with NaOMe, KOt-Bu or TBAOMe. To better understand the characteristic features of CTID for **2a** and **2b** induced by Mg(OMe)₂, Fig. 3 shows the changes in the values of $\lambda_{\max}^{\text{CL}}$ and Φ^{CL} depending on the metal alkoxide used as a base in MeOH.

The blue-shift of $\lambda_{\max}^{\text{CL}}$ and the decrease of k^{CTID} are presumably attributed to strong coordination of Mg²⁺ ion to an oxidoaryl anion on the metal alkoxide used as a base in MeOH. However, the increase of Φ^{CL} could not simply be explained by such coordination of Mg²⁺ ion. Referring that the stereochemistry around an aromatic electron donor has been reported to strongly affect chemiluminescence properties such as Φ^{CL} (3,4,13), coordination of Mg²⁺ ion to a 2-oxido-1,1'-binaphthyl group as a bidentate ligand was presumed to regulate stereochemistry of the biaryl to increase Φ^{CL} for CTID of **2a** and **2b**.

Finally, we investigated the decomposition of diastereomeric **2c(a)** and **2c(b)** in NaOMe, KOt-Bu, TBAOMe or Mg(OMe)₂ system (Figs 2 and 3, Table 2). Upon treatment with Mg(OMe)₂ in MeOH, **2c(a)** decomposed slowly to show chemiluminescence, for which the $\lambda_{\max}^{\text{CL}}$ (554 nm) was 29 nm shorter and the Φ^{CL} value was 1.7 times greater than those for NaOMe and KOt-Bu. Diastereomer **2c(b)** also showed chemiluminescence in NaOMe, KOt-Bu or TBAOMe system, for which the Φ^{CL} values and the $\lambda_{\max}^{\text{CL}}$ s were practically same as those for isomeric **2c(a)**. In contrast, chemiluminescence properties of **2c(b)** in the Mg(OMe)₂ system were considerably different from those for isomeric **2c(a)**. These discrepancies in $\lambda_{\max}^{\text{CL}}$, Φ^{CL} and k^{CTID} between diastereomers indicated that Mg(OMe)₂ diastereoselectively induced the chemiluminescent decomposition of **2c(a)** and **2c(b)**. Thus,

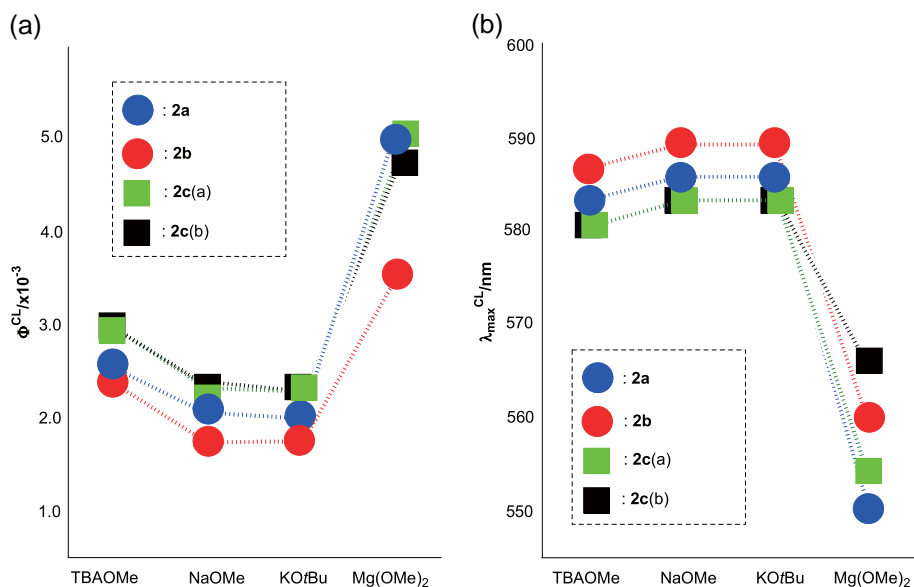
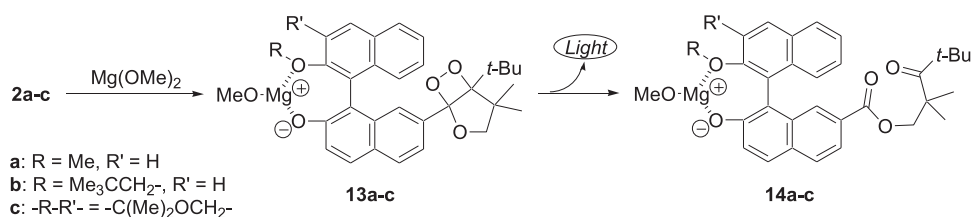


Figure 3. Base-dependency of (a) Φ^{CL} and (b) λ_{max}^{CL} for the chemiluminescent decomposition of dioxetanes **2a**, **2b**, **2c(a)** and **2c(b)** in MeOH.



Scheme 3. Mg(OMe)₂-induced chemiluminescent decomposition of dioxetanes **2a–c**.

as suggested already, Mg(OMe)₂ presumably coordinated to a 2-oxido-1,1'-binaphthyl group as a bidentate ligand for CTID of the present dioxetanes. Scheme 3 illustrates CTID of **2** induced by Mg(OMe)₂, in which Mg²⁺ ion coordinates to **2** to form Mg complex **13** with intermediary oxidoaryl-substituted dioxetanes, the stereochemistry of which is considerably regulated by the chelation.

Conclusions

Bicyclic dioxetanes **2a–c** bearing a 2'-alkoxy-2-hydroxy-1,1'-binaphthyl-7-yl moiety underwent base-induced decomposition accompanied by the emission of light, the yield and spectrum of which varied depending on the base/solvent system used. When **2a–c** were treated with TBAF in DMSO they effectively emitted flashes of orange light. In the case of alkaline metal (Na⁺ or K⁺) alkoxide/MeOH systems, **2a–c** decomposed slowly to show glowing chemiluminescence, the spectra of which were slightly shifted toward red from those in the TBAF/DMSO system, and Φ^{CL} decreased considerably. In addition, Mg(OMe)₂ was found to play a characteristic role as a base for the chemiluminescent decomposition of **2a–c** through coordination to the intermediary oxidoaryl-substituted dioxetane **13**. Thus, Mg²⁺ increased Φ^{CL} to more than twice those for Na⁺ or K⁺, while it shifted λ_{max}^{CL} considerably to blue.

Acknowledgements

We gratefully acknowledge financial assistance provided by Grants-in-aid (No. 22550046 and No. 21550052) for Scientific Research from the Ministry of Education, Culture, Sports, Science, and Technology, Japan.

References

- Schaap AP, Chen T-S, Handley RS, DeSilva R, Giri BP. Chemical and enzymatic triggering of 1,2-dioxetanes. 2-Fluoride-induced chemiluminescence from tert-butyl dimethylsiloxy-substituted dioxetanes. *Tetrahedron Lett* 1987;28:1155–8.
- Beck S, Köster H. Applications of dioxetane chemiluminescent probes to molecular biology. *Anal Chem* 1990;62:2258–70.
- Matsumoto M. Advanced chemistry of dioxetane-based chemiluminescent substrates originating from bioluminescence. *J Photochem Photobiol C* 2004;5:27–53.
- Matsumoto M, Watanabe N. Structural aspects of 1,2-dioxetanes active toward intramolecular charge-transfer-induced chemiluminescent decomposition. *Bull Chem Soc Jpn* 2005;78:1899–920.
- Edwards B, Sparks A, Voyta JC, Bronstein I. New chemiluminescent dioxetane enzyme substrates. In: Campbell AK, Kricka LJ, Stanley PE, editors. *Bioluminescence and chemiluminescence, fundamentals and applied aspects*. Chichester: Wiley, 1994:56–9.
- Matsumoto M, Hamaoka K, Takashima Y, Yokokawa M, Yamada K, Watanabe N, Ijuin HK. Chemiluminescence in molecular recognition: base-induced decomposition of optically active dioxetanes

- bearing a bisnaphthol moiety with a complex of optically active crown ether-potassium tert-butoxide. *Chem Commun* 2005;808–10.
- Hoshiya N, Fukuda N, Maeda H, Watanabe N, Matsumoto M. Synthesis and fluoride-induced chemiluminescent decomposition of bicyclic dioxetanes substituted with a 2-hydroxynaphthyl group. *Tetrahedron* 2006;62:5808–20.
 - Hoshiya N, Watanabe N, Ijuin KH, Matsumoto M. Synthesis of bicyclic dioxetanes bearing a 2-hydroxy-1,1'-binaphthyl-5-yl moiety active toward intramolecular charge-transfer-induced chemiluminescent decomposition. *Tetrahedron* 2006;62:12424–37.
 - Relative chemiluminescence efficiencies estimated were based on the value ($\Phi^{\text{CL}} = 0.29$) for 3-adamantylidene-4-(3-tert-butyl dimethylsiloxyphenyl)-4-methoxy-1,2-dioxetane in TBAF/DMSO system.(10)
 - Trofimov AV, Mielke K, Vasil'ev RF, Adam W. Chemically initiated electron exchange luminescence of siloxyaryl-substituted spiroadamantyl dioxetanes: kinetics and excited state yields. *Photochem Photobiol* 1996;63:463–7.
 - Paquette LA. ed. *Encyclopedia of reagents for organic synthesis*, Vol. 5. New York: Wiley, 1995:3204–5.
 - Crombie L, Games DE, Knight MH. Base-catalyzed cyclization of highly enolizable systems: diversion of pathway by magnesium chelation. *J Chem Soc Chem Comm* 1966;355–7.
 - Matsumoto M, Suzuki H, Watanabe N, Ijuin HK, Tanaka J, Tanaka C. Crucial dependence of chemiluminescence efficiency on the syn/anti conformation for intramolecular charge-transfer-induced decomposition of bicyclic dioxetanes bearing an oxidoaryl group. *J Org Chem* 2011;76:5006–17.

Crystal structure and electrical properties of new brownmillerite-type composition $\text{Ba}_2\text{In}_{2-x}(\text{Zn,Zr})_x\text{O}_5$ system

S. Ito*, M. Watanabe, M. Saito, H. Yamamura

Department of Material and Life Chemistry, Faculty of Engineering, Kanagawa University

3-27-1, Rokkakubashi, Kanagawa-ku, Yokohama 221-8686, Japan

E-mail: r201070298ji@kanagawa-u.ac.jp

ABSTRACT

To design the new proton conductor, the relationship between the proton conductivity in $\text{Ba}_2\text{In}_{2-x}(\text{Zn}_{1/2}\text{Zr}_{1/2})_x\text{O}_5$ compounds and the crystallographic parameters (i.e. lattice constant, unit cell volume, phase transformation temperature between brownmillerite phase and perovskite phase) was investigated. $\text{Ba}_2\text{In}_{2-x}(\text{Zn}_{1/2}\text{Zr}_{1/2})_x\text{O}_5$ ($0.4 \leq x \leq 2.0$) consisted of single phase of cubic perovskite-type cubic structure. And single phase of orthorhombic brownmillerite-type structure was obtained in the composition range of $\text{Ba}_2\text{In}_{2-x}(\text{Zn}_{1/2}\text{Zr}_{1/2})_x\text{O}_5$ ($0.0 \leq x \leq 0.3$). The temperature dependence of electrical conductivity observed for $\text{Ba}_2\text{In}_{1.7}(\text{Zn}_{1/2}\text{Zr}_{1/2})_{0.3}\text{O}_5$ which consists of single orthorhombic phase corresponded to the temperature dependence of electrical conductivity observed for $\text{Ba}_2\text{In}_2\text{O}_5$ which is high temperature form of $\text{Ba}_2\text{In}_2\text{O}_5$. The phase analysis by means of high temperature XRD analysis indicates that the aforementioned temperature dependence of electrical conductivity observed for $\text{Ba}_2\text{In}_{1.7}(\text{Zn}_{1/2}\text{Zr}_{1/2})_{0.3}\text{O}_5$ was attributable to the conducting behavior in tetragonal $\text{Ba}_2\text{In}_{1.7}(\text{Zn}_{1/2}\text{Zr}_{1/2})_{0.3}\text{O}_5$ sample which phase was observed above 800K. Also, the proton conductivity in $\text{Ba}_2\text{In}_{1.7}(\text{Zn}_{1/2}\text{Zr}_{1/2})_{0.3}\text{O}_5$ sample was observed in humidified condition below 723K. Based on all experimental data, it is concluded that co-doping of Zr cation and Zn cation into In site of $\text{Ba}_2\text{In}_2\text{O}_5$ is effective for design of high quality oxide proton conductor.

1 Introduction

The perovskite-type oxides which show high oxide ion conducting property have attracted much attention from the perspective of application for solid oxide fuel cells (SOFCs), oxygen sensors, oxygen pumps and so on. Goodenough and coworkers [1] have found that $\text{Ba}_2\text{In}_2\text{O}_5$ which consists of the orthorhombic brownmillerite-type structure transforms to the cubic perovskite-type structure above 1203K, and this phase transformation is related to the order-disorder transition of oxygen vacancies in the $\text{Ba}_2\text{In}_2\text{O}_5$. Also they showed a sharp increase in electrical conductivity above this phase transformation temperature. Yamamura et al. [2, 3] reported that a partial substitution of tri-valent cation in place of In^{3+} site of $\text{Ba}_2\text{In}_2\text{O}_5$ lowered the aforementioned phase transition temperature. Kakinuma et al. showed that La and Sr co-doped ($\text{Ba}_{0.3}\text{Sr}_{0.2}\text{La}_{0.5}$) $\text{In}_2\text{O}_{5.2}$ revealed higher conductivity such as 0.3 S/cm at 1093K and it is higher than that of stabilized ZrO_2 [4]. Also, Shimura and Yogo [5] reported that the partial substitution of W cation in place of In^{3+} site of $\text{Ba}_2\text{In}_2\text{O}_5$ stabilized the high-temperature cubic perovskite-type $\text{Ba}_2\text{In}_2\text{O}_5$ down to room temperature. Alternatively, the authors prepared new brownmillerite-type compounds $\text{Ba}_2(\text{Zn}_{1/2}\text{M}^{4+})_{1/2}\text{O}_5$ ($\text{M} = \text{Zr, Hf, Ce}$) which consist of single cubic perovskite-type structures and examined temperature dependence of their conductivities [6]. However, the conductivities in the $\text{Ba}_2(\text{Zn}_{1/2}\text{M}^{4+})_{1/2}\text{O}_5$ ($\text{M} = \text{Zr, Hf, Ce}$) samples with single cubic perovskite-type structures were lower than that in the high-temperature cubic perovskite-type $\text{Ba}_2\text{In}_2\text{O}_5$ above 1203K. In order to maximize the conductivity and find out new aspect of $\text{Ba}_2(\text{Zn}_{1/2}\text{M}^{4+})_{1/2}\text{O}_5$ ($\text{M} = \text{Zr, Hf, Ce}$) samples, $\text{Ba}_2\text{In}_{2-x}(\text{Zn}_{1/2}\text{Zr}_{1/2})_x\text{O}_5$ ($0.0 \leq x \leq 2.0$) compounds were prepared and its proton conducting property was

observed as well as oxide ionic conducting property.

2 Experimental

Powder samples of $\text{Ba}_2\text{In}_{2-x}(\text{Zn}_{1/2}\text{Zr}_{1/2})_x\text{O}_5$ were synthesized by using solid-state method. BaCO_3 (99.9%, Wako Pure Chemical), In_2O_3 (99.99%, Kojundo Chemical), ZnO (99.999%, Kojundo Chemical), and ZrO_2 (99.7%, TOSOH) were used as the starting materials. The weighed powders were mixed in a ball mill for 24h with ethanol as a dispersive medium. The mixtures were dried at 373K for several hours, and calcined at 1273K for 10h. The powders, which were sieved under 54 μm , were uniaxially pressed at 5 MPa into rectangular shape or pellets. Compacts thus obtained were isostatically pressed again at 200MPa. The samples were sintered at 1673K for 10h in air. The relative densities of all the single phased specimens, which were estimated from their dimensions and weights, were higher than 90% to X-ray density.

The tolerance factor was used for preparation of cubic perovskite-type structure. The tolerance factor (t) is defined by following equation (1):

$$t = (r_O + r_A) / \sqrt{2}(r_O + r_B), \quad (1)$$

where r_O , r_A , and r_B are the ionic radii of O, A, and B in ABO₃-type perovskite structure, respectively. This tolerance factor is equal to unity for an ideal perovskite structure, and a deviation from unity induces a distortion from the ideal structure. In the present work, it was assumed that the phase transition from brownmillerite to perovskite might have a closerelation with this tolerance factor.

The crystal phases of prepared powders were characterized

by using X-ray diffraction (XRD) (Multiflex, Rigaku Co.) with $CuK\alpha$ radiation (monochromated with graphite). To characterize the high temperature phase of $Ba_2In_{2-x}(Zn,Zr)_xO_5$, the XRD measurements were carried out from room temperature (303 K) to 1223 K in air.

The electrical conductivities in the single phased samples were measured by the DC four-probe method under various conditions in the temperatures range from 773K to 1173K in air.

The thermal properties of samples were measured by Thermogravimetric-Differential thermal analysis (TG-DTA) (model : TG8192, Rigaku).

Moreover, the temperature dependence of proton conductivity in the samples was observed in the temperature ranging from 573 to 1173K in dry and wet Ar atmosphere by using ac two-probe method. The wet Ar atmosphere was obtained by flowing Ar (70 dm^3/min) saturated with water vapor at 343 K. The impedance analyzer (4192A LF, Yokogawa-Hewlett-Packard) was used for the ac conductivity measurement in the frequency ranging from 5Hz to 13MHz. The dimension of sintered disk for the ac conductivity measurements was 2 mm in thickness. For the all measurements, Pt electrode was applied to both sides of specimen by firing at 1223K for 30min in air.

3 Results and Discussion

3-1 Crystal structure

XRD profiles in Fig.1 shows that $Ba_2In_{2-x}(Zn_{1/2}Zr_{1/2})_xO_5$ ($0.0 \leq x \leq 0.3$) consists of single phase of orthorhombic brownmillerite-type structure. The intensity of ordered lines which are the characteristic small peaks of orthorhombic structure became unclear when the x value in the composition of $Ba_2In_{2-x}(Zn_{1/2}Zr_{1/2})_xO_5$ increased from 0.0 to 0.3. This suggests that the distortion from ideal cubic perovskite-type structure is getting small. And the lattice constants ($a = 5.993$, $b = 16.77$, and $c = 6.056$ Å) observed for $Ba_2In_{2-x}(Zn_{1/2}Zr_{1/2})_xO_5$ ($x=0.0$, i.e. $Ba_2In_2O_5$) agreed with the previously reported data (i.e. $a = 5.89$, $b = 16.79$, and $c = 6.08$ Å) [1]. To examine the relationship between observed lattice constants and x values in the composition of

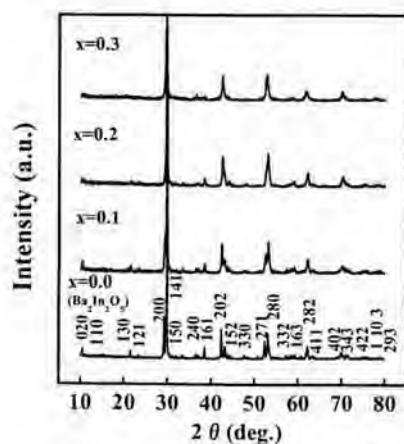


Fig.1 XRD patterns of $Ba_2In_{2-x}(Zn,Zr)_xO_5$ ($x=0.0-0.3$).

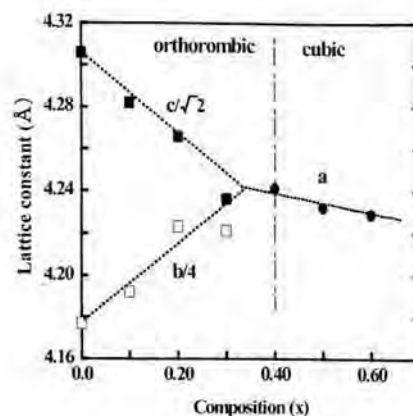


Fig.2 Lattice parameters as a function of x.

$Ba_2In_{2-x}(Zn_{1/2}Zr_{1/2})_xO_5$, the composition dependence of lattice constant (a) of cubic structure compared with the composition dependence of lattice constants (b/√2 and c/4) of orthorhombic structure as shown in Fig.2. Both lattice constants becomes the same when the x value in the composition of $Ba_2In_{2-x}(Zn_{1/2}Zr_{1/2})_xO_5$ is equal to 0.4. This suggests that the lattice distortion of orthorhombic structure decreased with increasing x value in the composition of $Ba_2In_{2-x}(Zn_{1/2}Zr_{1/2})_xO_5$ and it is minimized around $x=0.4$ of $Ba_2In_{2-x}(Zn_{1/2}Zr_{1/2})_xO_5$. In addition, the lattice constant (a) monotonously decreased with increasing x value in the region of composition of $Ba_2In_{2-x}(Zn_{1/2}Zr_{1/2})_xO_5$ ($0.4 \leq x \leq 2.0$). Since Zn^{2+} cation and Zr^{4+} cation (the average ionic radius of $(Zn_{1/2}Zr_{1/2})$: 0.73 Å) partially substituted into In^{3+} (ionic radius: 0.8 Å) site of cubic perovskite type $Ba_2In_2O_5$, the observed lattice constant (a) would be changed by following Vegard's rule.

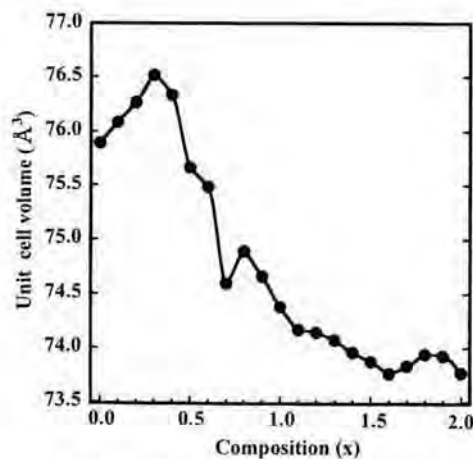


Fig. 3 Unit cell lattice volume as a function of x.

Also, the tolerance factor (t) which is calculated for $Ba_2In_2O_5$ is 0.967. This t increased with increasing x value in the composition of $Ba_2In_{2-x}(Zn_{1/2}Zr_{1/2})_xO_5$ and it got close to unity when x value in the composition of $Ba_2In_{2-x}(Zn_{1/2}Zr_{1/2})_xO_5$ became 0.4. This clearly indicates that the phase transition from brownmillerite to perovskite has a close relation with this tolerance factor (t). The unit cell volume as a function of x value in the composition of $Ba_2In_{2-x}(Zn_{1/2}Zr_{1/2})_xO_5$ is

displayed in Fig.3. The unit cell volume increased with increasing x value up to $x=0.3$. As mentioned in the conclusion part about the results in Fig.2, the lattice distortion of orthorhombic type structure decreased with an increase of x value up to $x=0.4$. However, the observed increase of unit cell volume reached maximum at $x=0.3$. Also the decrease of unit cell volume in the composition region of $\text{Ba}_2\text{In}_{2-x}(\text{Zn}_{1/2}\text{Zr}_{1/2})_x\text{O}_5$ ($0.4 \leq x \leq 2.0$) was not so monotonous. This implies that the composition dependence of unit cell volume doesn't simply follow the classical Vegard's rule. The careful analysis of actual crystal structure of $\text{Ba}_2\text{In}_{2-x}(\text{Zn}_{1/2}\text{Zr}_{1/2})_x\text{O}_5$ samples is required in the future.

3-2 Electrical conductivity

Temperature dependence, Arrhenius type $\log\sigma$ - $1/T$ plots, of the electrical conductivity in $\text{Ba}_2\text{In}_{2-x}(\text{Zn}_{1/2}\text{Zr}_{1/2})_x\text{O}_5$ ($0.0 \leq x \leq 0.3$) sintered bodies is shown in Fig.4. The electrical conductivity observed for $\text{Ba}_2\text{In}_2\text{O}_5$ ($x = 0.0$) showed the sharp increase in the temperature ranging from 1073K to 1223K. This discontinuity of electrical conductivity would be attributed to the order-disorder transition for oxygen vacancies which corresponds to the phase transition from the orthorhombic brownmillerite-type structure to the cubic perovskite-type structure. The transition temperature observed for $\text{Ba}_2\text{In}_2\text{O}_5$ ($x = 0.0$) almost agrees with the transition temperature in the literature [1]. Also, this figure indicates that the transition temperatures decreased with increasing x value in the composition of $\text{Ba}_2\text{In}_{2-x}(\text{Zn}_{1/2}\text{Zr}_{1/2})_x\text{O}_5$. The temperature dependence of conductivity observed for $\text{Ba}_2\text{In}_{2-x}(\text{Zn}_{1/2}\text{Zr}_{1/2})_x\text{O}_5$ ($0.0 \leq x \leq 0.3$) sintered bodies which is appeared above the respective phase transition temperature follows the temperature dependence of conductivity in $\text{Ba}_2\text{In}_2\text{O}_5$ which is high temperature phase of $\text{Ba}_2\text{In}_2\text{O}_5$ with disordered oxygen vacancy well. Unfortunately, the conductivity in the $\text{Ba}_2\text{In}_{2-x}(\text{Zn}_{1/2}\text{Zr}_{1/2})_x\text{O}_5$ ($0.4 \leq x$) which consists of cubic phase at room temperature could not be observed because of the low relative densities of the sintered bodies.

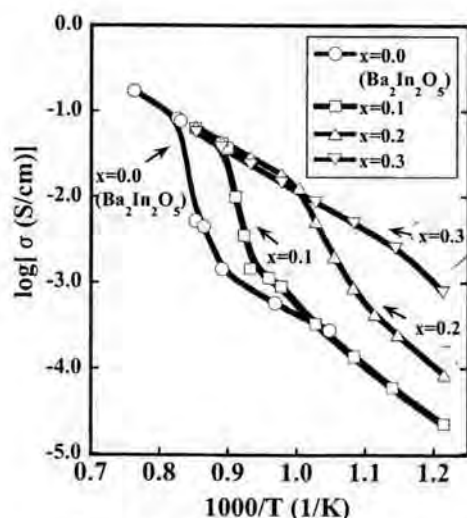


Fig. 4 Arrhenius plots of electrical conductivity for $\text{Ba}_2\text{In}_{2-x}(\text{Zn,Zr})_x\text{O}_5$ ($x=0.0-0.3$).

Figure 5 presents the onset- and end-temperatures of phase transition from brownmillerite phase to cubic phase, which corresponds to onset- and end-temperatures of sharp increase of the electrical conductivity in the Arrhenius plots, as a function of x value in the composition of $\text{Ba}_2\text{In}_{2-x}(\text{Zn}_{1/2}\text{Zr}_{1/2})_x\text{O}_5$. This suggests that the partial substitution of Zn and Zr cations into In_{3+} site of $\text{Ba}_2\text{In}_2\text{O}_5$ is effective for a lowering of order-disorder transition temperature of oxygen vacancy which corresponds to the aforementioned phase transition temperature.

In the temperature ranging from 1073K to 1223K, the conductivity in $\text{Ba}_2(\text{Zn}_{1/2}\text{Zr}_{1/2})_2\text{O}_5$ which consists of the cubic single phase at room temperature was lower than that of $\text{Ba}_2\text{In}_2\text{O}_5$ which is high temperature form of $\text{Ba}_2\text{In}_2\text{O}_5$. It would be attributable to the localization of oxygen vacancies around Zn site. It is because the localization of oxygen vacancies around Zn tetrahedral site gives rise to the decrease of oxygen vacancy concentration for the mobile oxide ion.

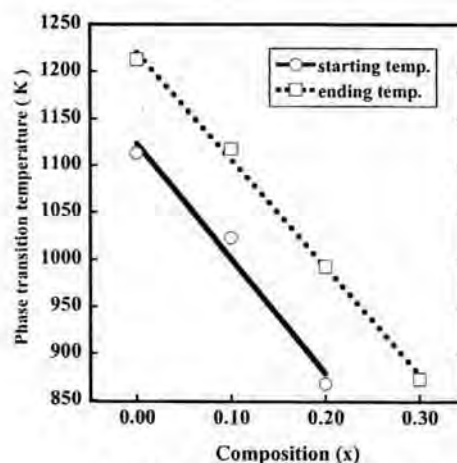


Fig.5 Phase transition temperature as a function of x ($0.0 \leq x \leq 0.3$).

3-3 High temperature X-ray diffraction

In order to clarify the relationship among the phase transition temperature, crystal phases and the level of electrical conductivity in the samples, the high-temperature XRD analysis was performed from room temperature (303K) to 973K. The typical XRD patterns taken from $\text{Ba}_2\text{In}_{1.7}(\text{Zn}_{1/2}\text{Zr}_{1/2})_{0.3}\text{O}_5$ sintered body was shown in Fig.6. The observed phase at 973K was assigned by the tetragonal perovskite-type structure. To examine the phase transition phenomenon observed for $\text{Ba}_2\text{In}_{1.7}(\text{Zn}_{1/2}\text{Zr}_{1/2})_{0.3}\text{O}_5$ in detail, the lattice parameters ($a/\sqrt{2}$, $b/4$, and $c/\sqrt{2}$) as a function of temperature was observed as shown in Fig.7. In this figure, the lattice parameters a , b and c were converted as well as the analysis of lattice parameters in Fig.2 for a comparison of lattice parameters between orthorhombic phase and tetragonal phase. The lattice parameters $b/4$ and $c/\sqrt{2}$ observed for orthorhombic phase became the lattice parameter c of tetragonal phase above 800K. Also another lattice parameter 'a' agreed with the lattice parameter 'a' of the tetragonal phase above same temperature. This suggests that the crystal of $\text{Ba}_2\text{In}_{1.7}(\text{Zn}_{1/2}\text{Zr}_{1/2})_{0.3}\text{O}_5$ was extended along b axis at elevated temperature. Also lattice distortion around octahedral

site and tetrahedral site in the brownmillerite-type structure would be minimized above 800K.

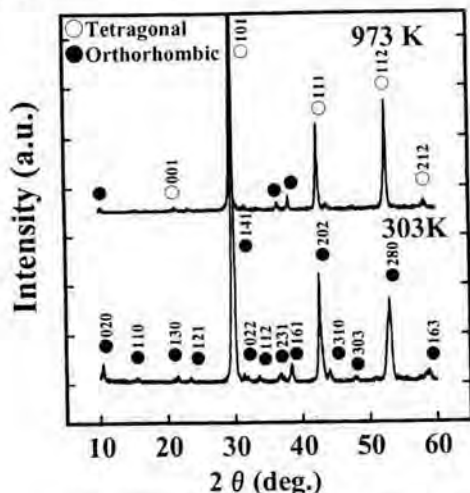


Fig.6 High temperature XRD patterns of $Ba_2In_{1.7}(ZnZr)_{0.3}O_5$.

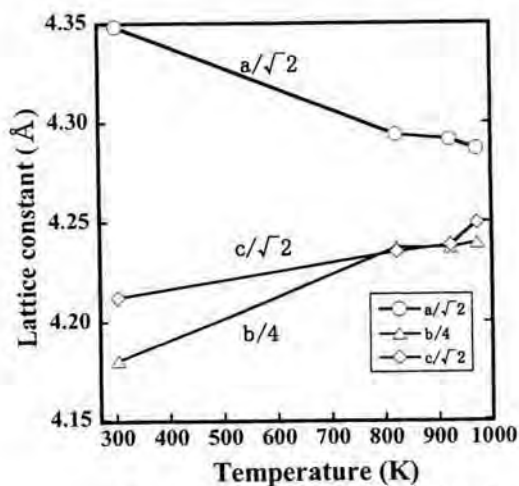


Fig.7 Lattice constant as a function of temperature ($x=0.3$).

Based on those results, it is concluded that the sharp increase of electrical conductivity observed in Fig.4 has a close relation to the phase transition between orthorhombic phase and cubic/ tetragonal phase.

3-4 Proton conduction

The temperature dependence of weight loss recorded from $Ba_2In_{2-x}(Zn_{1/2}Zr_{1/2})_xO_5$ ($0.0 \leq x \leq 0.3$) samples was analyzed by using TG-DTA experiments (Fig.8). In Fig.8, typical three steps of weight loss were observed. The first step was appeared in the temperature ranging from R.T. to 500K. The weight loss at second step was observed around 800K. The last step was observed from 900K to 1100K. The weight loss in the first and second step was assigned by desorption of H_2O molecule from samples. And the weight loss in the third

step was due to desorption of CO_2 molecule from the samples. And aforementioned weight loss at each step observed for $Ba_2In_{2-x}(Zn_{1/2}Zr_{1/2})_xO_5$ samples was greater than that of $Ba_2In_2O_5$ ($x=0.0$).

Since the proton conductivity in oxide can be enhanced by adsorption of H_2O molecule, the temperature dependence of the electrical conductivity in $Ba_2In_{1.7}(Zn_{1/2}Zr_{1/2})_{0.3}O_5$ sintered body was observed in dry- and wet-Ar atmospheres (Fig.9). The observed conductivity in wet-Ar atmosphere was one order of magnitude higher than that in dry Ar atmosphere at 573K. This indicates that $Ba_2In_{1.7}(Zn_{1/2}Zr_{1/2})_{0.3}O_5$ can be proton conductor below 573K because the electrical conductivity in the sample increased with increasing relative humidity in the measurement condition. Also it can be highlighted that the observed temperature of proton conducting phenomena corresponds to the temperature region of H_2O molecule desorption in DTA-TG analysis (Fig.8) and the crystal structural feature of $Ba_2In_{2-x}(Zn_{1/2}Zr_{1/2})_xO_5$ ($0.0 \leq x \leq 0.3$) might affect the adsorption-desorption behavior of H_2O molecule and proton conducting phenomenon.

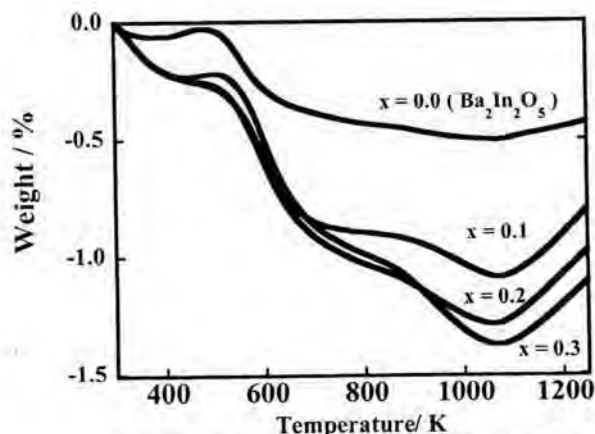


Fig.8 TG curve of $Ba_2In_{2-x}(ZnZr)_xO_5$ ($x=0.0-0.3$).

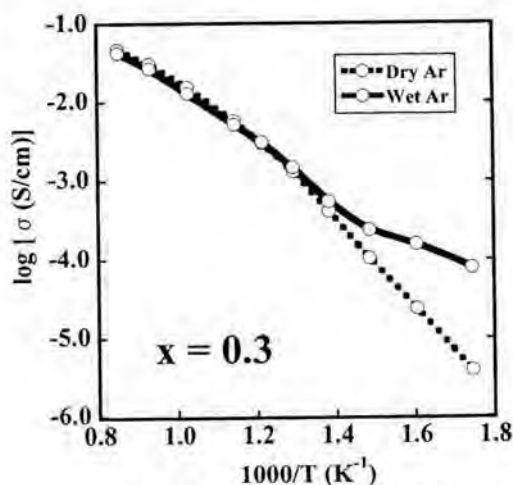


Fig.9 Arrhenius plots of conductivity in AC impedance measurement of $Ba_2In_{1.7}(Zn,Zr)_{0.3}O_5$ system in dry and humid Ar.

4 Conclusion

The relationship between phase transition and electrical conductivities in $\text{Ba}_2\text{In}_{2-x}(\text{Zn}_{1/2}\text{Zr}_{1/2})_x\text{O}_5$ system was examined. $\text{Ba}_2\text{In}_{2-x}(\text{Zn}_{1/2}\text{Zr}_{1/2})_x\text{O}_5$ ($0.0 \leq x \leq 0.3$) consisted of orthorhombic brownmillerite-type structure and $\text{Ba}_2\text{In}_{2-x}(\text{Zn}_{1/2}\text{Zr}_{1/2})_x\text{O}_5$ ($0.4 \leq x \leq 2.0$) consisted of cubic perovskite-type structure at room temperature. The phase transition temperature from orthorhombic phase to tetragonal phase shifted to a lower temperature side when x value in the composition of $\text{Ba}_2\text{In}_{2-x}(\text{Zn}_{1/2}\text{Zr}_{1/2})_x\text{O}_5$ ($0.0 \leq x \leq 0.3$) was increased. The temperature dependence of conductivity observed for $\text{Ba}_2\text{In}_{2-x}(\text{Zn}_{1/2}\text{Zr}_{1/2})_x\text{O}_5$ ($0.0 \leq x \leq 0.3$) sintered bodies which is appeared above the respective phase transition temperature agrees with the temperature dependence of conductivity in BaInO_3 which is high temperature phase of $\text{Ba}_2\text{In}_2\text{O}_5$ with disordered oxygen vacancy well. Also, the proton coning phenomenon was observed in $\text{Ba}_2\text{In}_{1.7}(\text{Zn}_{1/2}\text{Zr}_{1/2})_{0.3}\text{O}_5$ in wet-Ar atmosphere below 573K. The authors suspect that the crystal structural feature of $\text{Ba}_2\text{In}_{2-x}(\text{Zn}_{1/2}\text{Zr}_{1/2})_x\text{O}_5$ ($0.0 \leq x \leq 0.3$) affects the adsorption-desorption behavior of H_2O molecule and proton conducting phenomenon.

References

- [1] J. B. Goodenough, J.E.Ruiz-Diaz and Y.S. Zhen, *Solid State Ionics*, **44** (1990) 21-31.
- [2] H. Yamamura, Y. Yamada, T. Mori, and T. Atake, *Solid State Ionics*, **108** (1998) 377-381.
- [3] H. Yamamura, H. Hamazaki, K. Kakinuma and J. Korean Phys. Soc., **35** (1999) S200-S204.
- [4] K. Kakinuma, H. Yamamura, H. Haneda and T. Atake, *Solid State Ionics*, **154** (2002) 571-576.
- [5] T. Shimura and T. Yogo, *Solid State Ionics*, **175** (2004) 345-348.
- [6] S. Ito, M. Saito, T. Takayama and H. Yamamura, *Trans. Mater. Res. Soc. Japan*, **35**[3](2010) 507-509.

(Received 28 March 2012; Accepted 22 July 2012)

Lattice distortion and thermoelectric property for $Zn_{1-(x+y)}Ga_xIn_yO$ system ($x + y = 0.007$, $0 \leq x \leq 0.007$, $0 \leq y \leq 0.007$)

H. Takemoto*, H. Kawakami, M. Saito, and H. Yamamura

Department of Material and Life Chemistry, Faculty of Engineering, Kanagawa University

3-27-1 Rokkakubashi, Kanagawa-ku, Yokohama, 221-8686, Japan

* hironao.earth@gmail.com

ABSTRACT

The intermetallic compounds which are mainly used for the thermoelectric power generation system are unstable at high temperature. Therefore, we studied thermoelectric property of ZnO doped with group 3B elements periodic table, which can be expected to be a good candidate of thermoelectric material with high performance. The electrical conductivity (σ) and Seebeck coefficient (S) were evaluated under He atmosphere from 673 to 1073K. Although the electrical conductivity was showed maximum value for sample with $r_{av.} = 0.054$ nm, the Seebeck coefficient did not change for all samples. This fact was considered that the increase in electrical conductivity was caused by improvement of carrier mobility, and the improvement of carrier mobility may be ascribed to the decrease in lattice distortion which caused by co-doping. Power factor ($S^2\sigma$) of $Zn_{9.993}A_{0.007}O$ ($A = Ga, In$) showed higher value than that of $Zn_{9.993}A_{0.007}O$ ($A = Ga, In$). Thus, the co-doping was effective for the improvement of power factor.

Key word : $Zn_{1-(x+y)}Ga_xIn_yO$, electrical conductivity, Seebeck coefficient, ionic radius, lattice distortion

1 Introduction

Recently, the development of next generation energy systems is desired due to the exhaustion problem of fossil fuel. As a consequence of this, the thermoelectric generation system is focused. However, the system can be used in the limited temperature range (from 300K to 700K) because of use of the intermetallic alloys such as $PbTe$ [1] and $Bi_2Te_{2.85}Se_{0.15}$ [2]. To overcome this limited temperature problem, thermoelectric properties of ZnO which has high thermal stability in the temperature ranging from 600K to 1100K has been examined for development of high quality thermoelectric materials. Tsubota et al and Fujishiro et al reported that Al (1 to 2mol%) doped ZnO developed as transparent electrode material showed excellent n-type thermoelectric properties.[3-4] Also, our research group has reported that the Ga and In co-doped ZnO system showed the minimum resistivity around the mean ionic radius of 0.054 nm.[5] In the present work, the relationship among the mean ionic radius of Zn site in co-doped system, lattice distortion ($\Delta d/d$), and power factor ($S^2\sigma$) was examined for development design paradigm for fabrication of high quality ZnO thermoelectric material.

2 Experimental

$Zn_{1-(x+y)}Ga_xIn_yO$ ($x+y=0.007$) compounds were prepared by using solid-state reaction method. The starting materials used were ZnO powder (99.999 %, Koujundo chemical co ltd.), Ga_2O_3 powder (99.9 %, Koujond chemical co ltd.), and In_2O_3 powder (99.99 %, Koujundo chemical co ltd.). The mean ionic radius of dopant ($r_{av.}$) was calculated by using Equation (1)

$$r_{av.} = r_1 \times (x / x + y) + r_2 \times (y / x + y), \quad (1)$$

where r_1 and r_2 are the dopant ionic radius, and x and y are the molar concentration of the dopant component. The ionic radii of Zn^{2+} , Ga^{3+} , and In^{3+} which were estimated as four oxygen coordination around cations by Shannon [6] are presented in Table 1. The relationship between $r_{av.}$ and composition of $Zn_{1-(x+y)}Ga_xIn_yO$ are summarized in Table 2. The total amount of dopant in composition of $Zn_{1-(x+y)}Ga_xIn_yO$ was fixed to 0.007. The compositions of examined samples shown in Table 2. The starting reagents were weighted by using a weighing bottle and were mixed in ball mill for 24h. The mixed powders were calcined at 1073K, 5h. After the calcination, the mixed powders were pressed into a rectangular-shaped specimen, and sintered at 1673K, 10h in air. The crystal phases of sintered samples were identified at room temperature by using X-ray powder diffraction (XRD, Multiflex, Rigaku Company) equipment. In order to calculate the lattice distortions of samples, the structural parameters of samples were refined using Rietveld analysis [7]. The Seebeck coefficient and the electrical conductivity of samples were measured using ZEM-3 (ULVAC, Japan) under He atmosphere from 673 to 1073K. The power factor was calculated by using the electrical conductivity and Seebeck coefficient.

Table 1 Ionic radius in tetrahedrally coordination.

ion	ionic radius / nm
Zn^{2+}	0.060
Ga^{3+}	0.047
In^{3+}	0.062

3 Results and discussion

3.1 XRD

The XRD patterns observed for $Zn_{1-(x+y)}Ga_xIn_yO$ sintered samples are shown in Fig.1. The figure indicates that all observed samples consist of single phase of hexagonal ZnO and no other phases are observed. The relative densities which were measured using all sintered samples were more than 95% to theoretical one which was calculated by using lattice constants and crystallographic data.

Table 2 The relationship between r_{av} and composition of $Zn_{1-(x+y)}Ga_xIn_yO$ ($x+y=0.007$) system.

composition	mean ionic radius (r_{av})/nm
$Zn_{0.993}Ga_{0.007}O$	0.047
$Zn_{0.993}Ga_{0.0065}In_{0.0005}O$	0.048
$Zn_{0.993}Ga_{0.0051}In_{0.0019}O$	0.051
$Zn_{0.993}Ga_{0.0037}In_{0.0033}O$	0.054
$Zn_{0.993}Ga_{0.0023}In_{0.0047}O$	0.057
$Zn_{0.993}Ga_{0.0009}In_{0.0061}O$	0.060
$Zn_{0.993}In_{0.007}O$	0.062

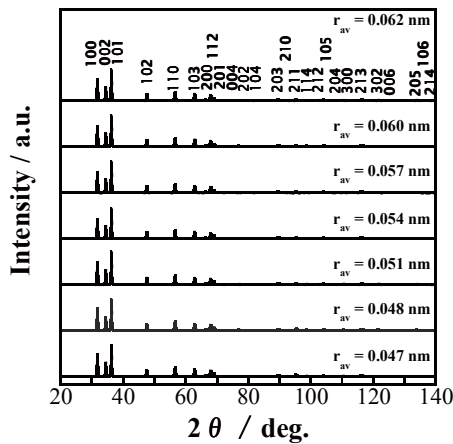


Fig.1 XRD patterns observed for $Zn_{1-(x+y)}Ga_xIn_yO$ ($x+y=0.007$) sintered bodies; $x+y=0.007, 0 \leq x \leq 0.007, 0 \leq y \leq 0.007$.

3.2 Electrical properties

Figure 2 presents the electrical conductivity as a function of temperature. The conductivities observed for co-doped system were higher than the conductivities observed for the single doped samples (i.e. $Zn_{0.993}Ga_{0.007}O$ and $Zn_{0.993}In_{0.007}O$). And the observed conductivity reached the maximum in the composition of $Zn_{0.993}Ga_{0.0037}In_{0.0033}O$ which r_{av} is equal to 0.054nm. The temperature dependence of Seebeck coefficient observed for sintered samples is shown in Fig.3. The observed Seebeck coefficients linearly increased with increasing temperature. The Seebeck coefficient observed for the sample which r_{av} is equal to 0.060nm was the highest (i.e. $151 \times 10^{-6} \text{VK}^{-1}$ at 1073K) in all data observed for co-doped samples. Also, Seebeck coefficient of $Zn_{0.993}In_{0.007}O$ was higher than $Zn_{0.993}Ga_{0.007}O$. The electrical conductivity (σ) and the

Seebeck coefficient (S) is given by the following Equations:

$$\sigma = en\mu, \quad (2)$$

$$S = \mp k_B / e [(r + 2) + \ln \{ 2\pi m^* k_B T^{3/2} / h^3 n \}], \quad (3)$$

where μ , k_B , e , r , m^* , h , and n presents the mobility of conduction carrier, the Boltzmann's constant, the elementary electric charge, the scattering parameter, the effective mass, Planck's content, and carrier concentration, respectively. Equations (2) and (3) indicate that the enhancement of conduction carrier correspond to an increase of the electrical conductivity and a decrease of the Seebeck coefficient. In the present work, however, the enhancement of observed Seebeck coefficient did not correspond to the increase of electrical conductivity at each observed temperature. Based on this result, it is concluded that the carrier concentration in the present co-doped system was not changed at observed temperature. Figure 4 shows the Seebeck coefficient as a function of the electrical conductivity. The straight line observed for co-doped samples in Fig.4 shifted to higher temperature side as compared with single dope samples, while the Seebeck coefficient was not changed in those co-dope samples. It is considered that the carrier mobility in the co-dope samples is higher than that of single dope sample. The improvement of carrier mobility in co-dope samples might be attributable to lowering of the lattice distortion by means of solid solution of Ga cation and In cation and into Zn sub-lattice site.

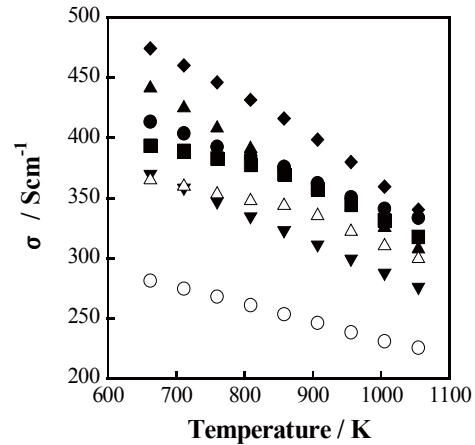


Fig.2 The electrical conductivity of $Zn_{1-(x+y)}Ga_xIn_yO$ system ($x+y=0.007, 0 \leq x \leq 0.007, 0 \leq y \leq 0.007$) as a function of temperature for $r_{av} = 0.048 \text{ nm}$ (\bullet), 0.051 nm (\blacksquare), 0.054 nm (\blacklozenge), 0.057 nm (\blacktriangle), 0.060 nm (\blacktriangledown), $Zn_{0.993}Ga_{0.007}O$ (\triangle), $Zn_{0.993}In_{0.007}O$ (\circ).

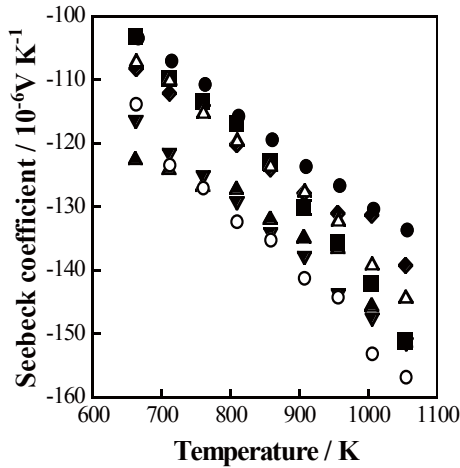


Fig.3 The Seebeck coefficient of $Zn_{1-(x+y)}Ga_xIn_yO$ system ($x+y=0.007$, $0 \leq x \leq 0.007$, $0 \leq y \leq 0.007$) as a function of temperature for $r_{av} = 0.048$ nm (●), 0.051 nm (■), 0.054 nm (◆), 0.057 nm (▲), 0.060 nm (▼), $Zn_{0.993}Ga_{0.007}O$ (Δ), $Zn_{0.993}In_{0.007}O$ (○).

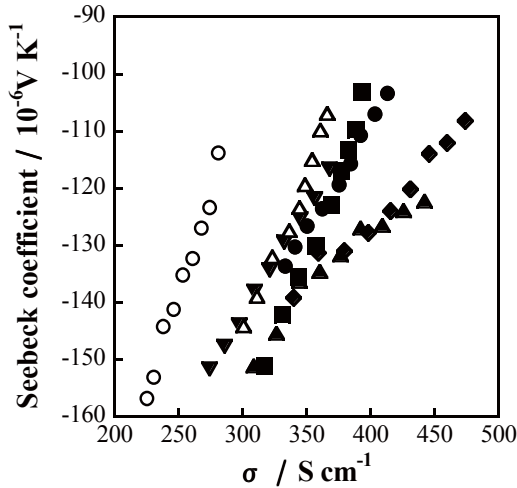


Fig.4 The Seebeck coefficient of $Zn_{1-(x+y)}Ga_xIn_yO$ system ($x+y=0.007$, $0 \leq x \leq 0.007$, $0 \leq y \leq 0.007$) as a function of electrical conductivity for $r_{av} = 0.048$ nm (●), 0.051 nm (■), 0.054 nm (◆), 0.057 nm (▲), 0.060 nm (▼), $Zn_{0.993}Ga_{0.007}O$ (Δ), $Zn_{0.993}In_{0.007}O$ (○).

3.3 $\beta \cos \theta - \sin \theta$ plot

$\beta \cos \theta - \sin \theta$ plot was used to estimate the lattice distortion ($\Delta d/d$) in observed samples. In case of co-doped system, the full width at half maximum (FWHM) of XRD patterns observed for co-dope samples become broad or narrow due to the change of crystalline size and lattice distortion. Therefore, the observed FWHM of XRD pattern can be expressed by the following Equation (4).

$$\beta = \beta_c + \beta_s \tag{4}$$

where β , β_c and β_s present the observed FWHM of

X-ray diffraction pattern, the FWHM of XRD pattern by crystallite with distortion free and the FWHM of XRD pattern by crystallite with lattice distortion, respectively. The β_c is expressed by using Equation (5) (i.e. Scherrer's Equation):

$$\beta_c = K\lambda / D \cos \theta \tag{5}$$

where K , λ , D , and θ presents Scherrer constant, wavelength of X-ray source, crystallite size, and Bragg angle, respectively. The β_s is shown the following equation by Bragg's equation:

$$\beta_s = (\Delta d/d) \sin \theta / \cos \theta \tag{6}$$

where $\Delta d/d$ and θ presents lattice distortion and Bragg angle. Therefore, Equation (4) can convert to Equation (7).

$$\beta \cos \theta = (\Delta d/d) \sin \theta + K\lambda / D \tag{7}$$

Figure 5 presents $\beta \cos \theta - \sin \theta$ plot for $Zn_{1-(x+y)}Ga_xIn_yO$ system ($x+y=0.007$). The FWHM values which were estimated by Rietveld analysis [7] were used for the calculation of β values. This figure clearly indicates that $\beta \cos \theta - \sin \theta$ plot shows high linearity and lattice distortion can be correctly estimated using the observed data in Fig.5. Figure 6 demonstrates the relationship between lattice distortion ($\Delta d/d$) and mean ionic radii (r_{av}) observed for the samples. The lattice distortion values observed for samples which r_{av} values become 0.048 and 0.054 nm reached minimum in all observed lattice distortion values. Figure 7 shows the electrical conductivity as a function of $\Delta d/d$. From the result of Fig.7, the electrical conductivity tends to increase with decreasing lattice distortion. Based on all observed results, it is concluded that the carrier mobility is enhanced by a lowering of lattice distortion and the electrical conductivity is also improved by aforementioned enhancement of carrier mobility in the samples.

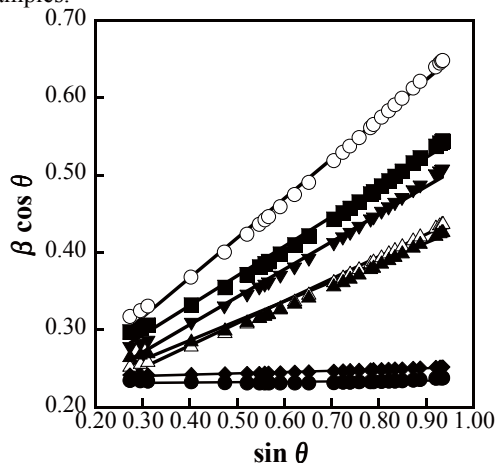


Fig.5 The $\beta \cos \theta - \sin \theta$ plot of $Zn_{1-(x+y)}Ga_xIn_yO$ system by Rietveld analysis ($x+y=0.007$, $0 \leq x \leq 0.007$, $0 \leq y \leq 0.007$) as a function of electrical conductivity for $r_{av} = 0.048$ nm (●), 0.051 nm (■), 0.054 nm (◆), 0.057 nm (▲), 0.060 nm (▼), $Zn_{0.993}Ga_{0.007}O$ (Δ), $Zn_{0.993}In_{0.007}O$ (○).

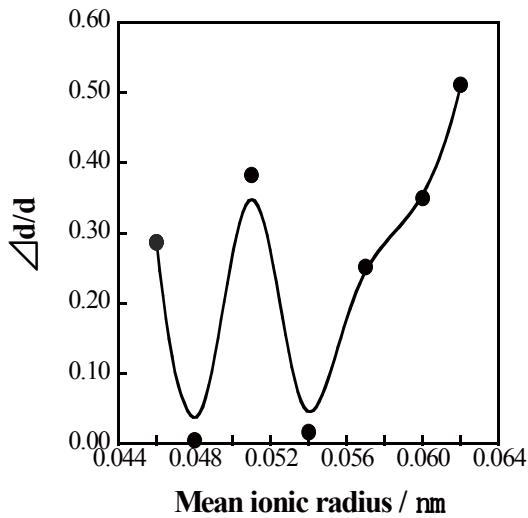


Fig.6 The relationship between mean ionic radius and lattice distortion ($\Delta d/d$) for $Zn_{1-(x+y)}Ga_xIn_yO$ system ($x+y=0.007$, $0 \leq x \leq 0.007$, $0 \leq y \leq 0.007$).

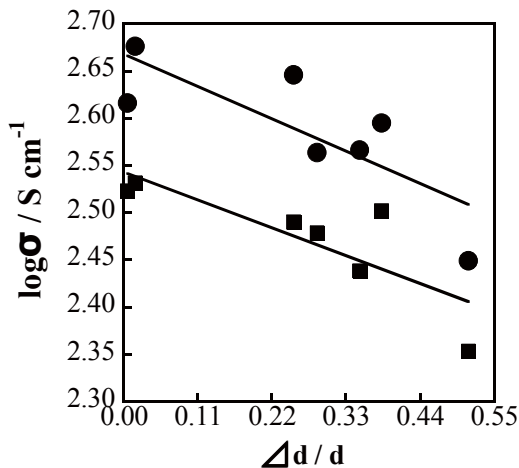


Fig.7 The relationship between electrical conductivity (at 673K (●) and 1073K (■)) and lattice distortion ($\Delta d/d$) for $Zn_{1-(x+y)}Ga_xIn_yO$ system ($x+y=0.007$, $0 \leq x \leq 0.007$, $0 \leq y \leq 0.007$) with various ionic radii.

3.4 Power factor

The calculated values of $S^2\sigma$ for ZnO and $Zn_{1-(x+y)}Ga_xIn_yO$ samples are shown in Fig.8. The $S^2\sigma$, which is generally called power factor, shows the electrical contribution to the overall thermoelectric performance. The $S^2\sigma$ values for all the samples increased with increasing temperature. The power factors calculated for $Zn_{1-(x+y)}Ga_xIn_yO$ samples which r_{av} values become 0.054 and 0.057nm were 6.6×10^{-4} and $7.0 \times 10^{-4} \text{ Wm}^{-1}\text{K}^{-2}$ at 1073K, respectively. Those values were higher than the calculated power factors for single cation dope $Zn_{0.993}Ga_{0.007}O$ (power factor: $6.2 \times 10^{-4} \text{ Wm}^{-1}\text{K}^{-2}$ at 1073K) and single cation dope $Zn_{0.993}In_{0.007}O$ (power factor: $5.5 \times 10^{-4} \text{ Wm}^{-1}\text{K}^{-2}$ at

1073K). This result clearly indicates that co-doping of Ga and In cations into ZnO lattice is effective for the improvement of the power factors of ZnO system.

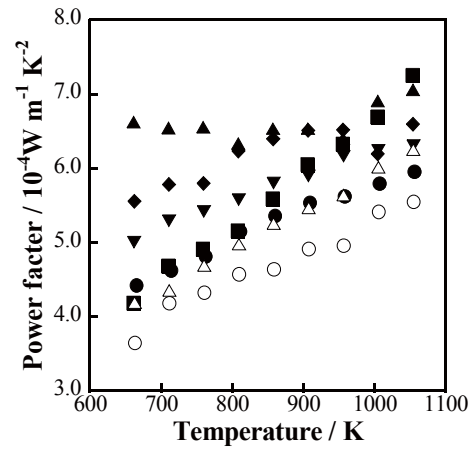


Fig.8 The power factor of $Zn_{1-(x+y)}Ga_xIn_yO$ system ($x+y=0.007$, $0 \leq x \leq 0.007$, $0 \leq y \leq 0.007$) as a function of electrical conductivity for $r_{av} = 0.048 \text{ nm}$ (●), 0.051 nm (■), 0.054 nm (◆), 0.057 nm (▲), 0.060 nm (▼), $Zn_{0.993}Ga_{0.007}O$ (△), $Zn_{0.993}In_{0.007}O$ (○).

4 Conclusions

The Ga and In co-doped ZnO ($Zn_{1-(x+y)}Ga_xIn_yO$) samples consisted of single phase of hexagonal ZnO. The co-doping was effective way for the improvement of electrical conductivity in ZnO system. The electrical conductivity in co-dope system was higher than that of single dope system. The Seebeck coefficient observed for $Zn_{0.993}Ga_{0.0023}In_{0.0047}O$ which r_{av} is equal to 0.057nm was the highest (i.e. $151 \times 10^{-6} \text{ VK}^{-1}$ at 1073K) in all examined co-dope samples. Although the electrical conductivity of co-doped systems were higher than single doped system, the Seebeck coefficient showed almost the same value as the single doped system. This result indicates that the carrier mobility in co-dope samples is higher than that in the single dope samples. And the improvement of carrier mobility would be attributable to a lowering of lattice distortion by means of co-doping of Ga and In cations into ZnO lattice. To conclude the relationship between lattice distortion and electrical conductivity, the lattice distortion was calculated by using $\beta \cos \theta - \sin \theta$ plot. This analysis indicates that $Zn_{0.993}Ga_{0.0051}In_{0.0019}O$ (r_{av} : 0.048nm) and $Zn_{0.993}Ga_{0.0037}In_{0.0033}O$ (r_{av} : 0.054nm) show the lowest lattice distortion in all examined samples. Also the improvement of electrical conductivity corresponds to a lowering of lattice distortion and aforementioned two samples show higher electrical conductivity as compared with other examined samples. Based on all observed results, it is concluded that the carrier mobility is enhanced by a lowering of lattice distortion. Moreover, the power factors of $Zn_{1-(x+y)}Ga_xIn_yO$ were calculated by using electrical conductivity and Seebeck coefficient. The power factors calculated for

$\text{Zn}_{0.993}\text{Ga}_{0.0037}\text{In}_{0.0033}\text{O}$ (r_{av} : 0.054nm) and $\text{Zn}_{0.993}\text{Ga}_{0.0023}\text{In}_{0.0047}\text{O}$ (r_{av} : 0.057nm) were 6.6×10^{-4} and $7.0 \times 10^{-4} \text{ Wm}^{-1}\text{K}^{-2}$ at 1073K, respectively. The aforementioned values were higher than single dope $\text{Zn}_{0.993}\text{Ga}_{0.007}\text{O}$ (power factor: $6.2 \times 10^{-4} \text{ Wm}^{-1}\text{K}^{-2}$ at 1073K) and $\text{Zn}_{0.993}\text{In}_{0.007}\text{O}$ (power factor: $5.5 \times 10^{-4} \text{ Wm}^{-1}\text{K}^{-2}$ at 1073K). This clearly indicates that the co-doping of Ga and In cation into ZnO lattice was effective for the improvement of the power factor.

References

- [1] Z.H. Dughaish, *Physica B*, **332**, 205 (2002)
- [2] XA Fan et. Al., *J.Phys. D*, **40**, 5727 (2007)
- [3] T. Tsubota et al., *J. Mater. Chem.*, **7(1)**, 85-90 (1997)
- [4] Y. Fujishiro et al., *J. Am. Ceram. Soc.*, **86**, 2063 (2003)
- [5] K. Kakinuma et al., *Ceramics International*, **33(4)**, 589-593 (2007)
- [6] R.D. Shannon, *Acta Cryst.*, **A32**, 751 (1976)
- [7] F. Izumi and K. Momma, *Solid State Phenom.*, **130**, 15-20 (2007)

(Received 14 June 2012; Accepted 18 July 2012)

Influence of average ionic radius of dopants in Zn site on thermal conductivity and dimensionless figure of merit for $Zn_{1-(x+y)}Ga_xIn_yO$ system ($0.0 \leq x + y \leq 0.007$)

H. Takemoto*, M. Saito, and H. Yamamura

Department of Material and Life Chemistry, Faculty of Engineering,
Kanagawa University 3-27-1 Rokkakubashi, Kanagawa-ku, Yokohama, 221-8686, Japan

* hironao.earth@gmail.com

Abstract

$Zn_{1-(x+y)}Ga_xIn_yO$ ($x+y=0.005, 0.007$ and 0.009) compounds which consist of single phase of hexagonal ZnO were prepared using solid state reaction method. To develop the design paradigm for fabrication of high quality thermoelectric ZnO based materials, the relationship between the average ionic radius of dopants in Zn site of samples and ZT values was examined. The experimental results indicated that the ZT value was improved by using concept of average ionic radius of dopants for development of high quality thermoelectric ZnO based materials.

Key words; co-doped ZnO system, average ionic radius of dopants, lattice thermal conductivity, lattice vibration in the defect structure, ZT,

1. Introduction

The intermetallic alloys such as PbTe[1] and $Bi_2Te_{2.85}Se_{0.15}$ [2] mainly have been used in the thermoelectric generation system. However, Pb, Bi and Te which are the main components in those intermetallic alloys are toxic metals. Also, the thermoelectric properties of aforementioned intermetallic alloys become low over $600^\circ C$ in air. As a consequence, the thermoelectric oxides such as $CaMnO_3$ [3], $SrTiO_3$ [4] and ZnO[5] have attracted much attention from the perspective of sustainable material design and high efficiency system engineering in high temperature region (i.e. over $600^\circ C$). Especially, ZnO based oxides (i.e. mono-doped ZnO, co-doped ZnO and homologous phase $(In_2O_3)ZnO_k$; $k=3,4$, and 5) are one of promising oxide series because the charge transfer in ZnO based oxides are faster than that of other oxides.

Tsubota et al. and Fujishiro et al. reported that Al (1 to 2mol%) doped ZnO which was developed as one of transparent electrode materials showed the excellent n-type thermoelectric properties[6]. Ohotaki et al. revealed that the dimensionless figure of merit (ZT) observed for Al and Ga co-doped ZnO system reached 0.65[7]. Also, the authors examined the influence of lattice distortion on conductivity (σ) and Seebeck coefficient (S) using Ga and In co-doped ZnO system. This work suggested that the lattice distortion can be important parameter for improvement of σ and S [8]. In the present work, influence of the average ionic radius of dopants in Zn site into Ga and In co-doped ZnO system on the thermal conductivity (κ) and ZT is examined and key crystallographic parameter for design of ZnO as high quality thermoelectric material is discussed.

2. Experimental

$Zn_{1-(x+y)}Ga_xIn_yO$ ($x+y=0, 0.005, 0.007$ and 0.009) compounds were prepared by using solid-state reaction method. The starting materials used were ZnO powder (purity:99.999 %, Koujundo chemical Co. ltd.), Ga_2O_3 powder (purity:99.9 %, Koujond chemical Co. ltd.), and In_2O_3 powder (purity: 99.99 %, Koujundo chemical Co. ltd.). The average ionic radius of dopant (r_{av}) was calculated by using Equation (1)

$$r_{av} = r_{Ga} \times (x / x + y) + r_{In} \times (y / x + y), \quad (1)$$

where r_{Ga} and r_{In} are ionic radii of Ga and In, respectively, x and y are the dopant concentration (mol%) in the composition of $Zn_{1-(x+y)}Ga_xIn_yO$. The ionic radii of Ga^{3+} and In^{3+} which are used for calculation of r_{av} are shown in Table I [9]. Also, the relationship between calculated r_{av} and composition of $Zn_{1-(x+y)}Ga_xIn_yO$ are summarized in Table II. The starting powders were mixed using ball mill for 24h. The mixed powders were calcined at 1073K, 5h. The calcined powders were pressed into a rectangular-shaped specimen and sintered at 1673K, 10h in air. The crystal phases taken from the sintered samples were identified at room temperature by using X-ray powder diffraction (XRD, Multiflex, Rigaku Company) analysis. S and σ of samples were measured using ZEM-3 (ULVAC, Japan) in He atmosphere from 673 to 1073K. The thermal conductivity (κ) was observed by using steady state method [10]. The reference material in this method was quartz crystal (Joint Research Centre, BCR-724A). ZT was calculated by using following Equation (2).

$$ZT = \sigma S^2 T / \kappa \quad (2)$$

Table I ionic radius of dopants in Zn site.

ion	ionic radius / nm
Zn ²⁺	0.060
Ga ³⁺	0.047
In ³⁺	0.062

Table II Relationship between r_{av} and composition of $Zn_{1-(x+y)}Ga_xIn_yO$ ($x+y=0.005, 0.009$) systems.

Sample No.	r_{av}	composition	relative density
x+y=0.005	1	Zn _{0.995} Ga _{0.0047} In _{0.0003} O	94.8%
	2	Zn _{0.995} Ga _{0.0037} In _{0.0013} O	93.2%
	3	Zn _{0.995} Ga _{0.0027} In _{0.0023} O	96.8%
	4	Zn _{0.995} Ga _{0.0017} In _{0.0033} O	94.7%
	5	Zn _{0.995} Ga _{0.0007} In _{0.0043} O	93.4%
x+y=0.009	6	Zn _{0.991} Ga _{0.0084} In _{0.0006} O	95.8%
	7	Zn _{0.991} Ga _{0.0066} In _{0.0024} O	97.2%
	8	Zn _{0.991} Ga _{0.0048} In _{0.0042} O	92.8%
	9	Zn _{0.991} Ga _{0.0039} In _{0.0060} O	96.6%
	10	Zn _{0.991} Ga _{0.0012} In _{0.0078} O	95.4%

3. Results and discussion

The XRD patterns observed for $Zn_{1-(x+y)}Ga_xIn_yO$ ($x+y=0.005$ and 0.009) sintered samples are shown in Fig.1. Figure 1 indicates that all observed samples consist of single phase of hexagonal ZnO and no other phases are observed. The XRD profiles taken from $Zn_{1-(x+y)}Ga_xIn_yO$ ($x+y=0.07$) were already reported in our previously published paper [11]. The $Zn_{1-(x+y)}Ga_xIn_yO$ ($x+y=0.07$) consists of hexagonal ZnO single phase as well. Based on the data of Table 2 and crystal phase analysis, it is concluded that the single phase of hexagonal ZnO can be prepared when the calculated average ionic radius (r_{av}) varied from 0.48 to 0.60nm in the composition of $Zn_{1-(x+y)}Ga_xIn_yO$ ($x+y=0.005, 0.07,$ and 0.009). Also, the relative densities of all sintered samples were more than 95% to theoretical one which was calculated by the estimated lattice constants in Fig.1 and crystallographic data of hexagonal ZnO.

Figure 2 presents the electrical conductivity as a function of average ionic radius in Zn site. The conductivities observed for the samples which r_{av} is equal to 0.054nm were higher than that of other samples. Since the average ionic radius r_{av} dependence of conductivity σ reached the maximum in the present work, the relationship between the power factor (σS^2) which is one of important parameters for design of high quality thermoelectric oxides and r_{av} was

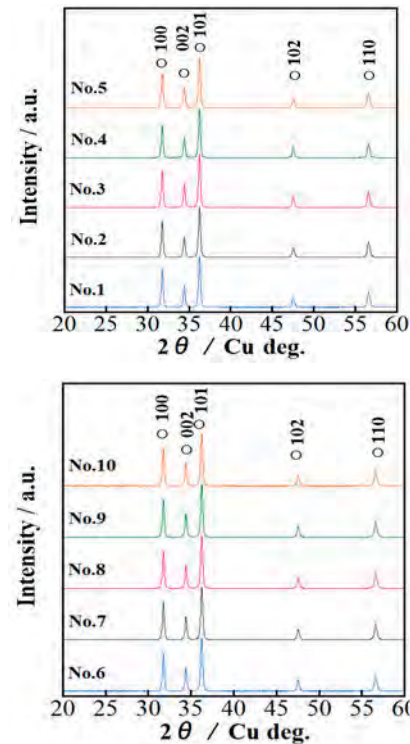


Fig.1 XRD patterns taken from $Zn_{1-(x+y)}Ga_xIn_yO$ ($0.005 \leq x+y \leq 0.009$) sintered bodies.

examined as shown in Fig.3. The calculated σS^2 in Fig.3 were scattered in the range from 4.0×10^{-4} to 8.0×10^{-4} ($Wm^{-1}K^{-2}$). This suggests that the observed relationship between the average ionic radius and the conductivity (or power factor) isn't useful factor for design of thermoelectric properties in ZnO.

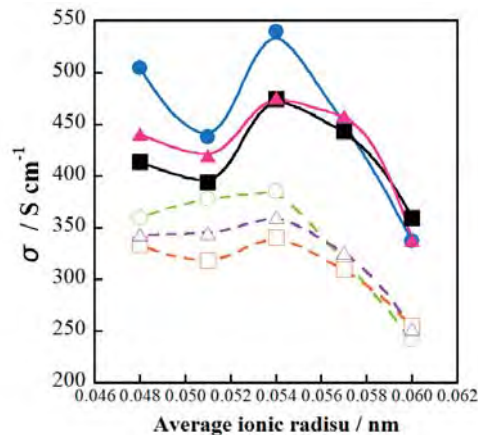


Fig.2 The electrical conductivity of $Zn_{1-(x+y)}Ga_xIn_yO$ systems ($0.005 \leq x+y \leq 0.009$) as a function of average ionic radius for $x+y=0.005$ at 673K(●), $x+y=0.007$ at 673K(■), $x+y=0.009$ at 673K(▲), $x+y=0.005$ at 1073K(○), $x+y=0.007$ at 1073K(□), $x+y=0.009$ at 1073K(Δ).

To develop the design paradigm for fabrication of high quality thermoelectric ZnO, relationship between the thermal conductivity which is denominator of Eq.(2) and average ionic radius of dopants in Zn site was examined.

In general, the thermal conductivity (κ) is given by following Equation (3):

$$\kappa = \kappa_{ph} + \kappa_{el} \quad (3)$$

where κ_{ph} and κ_{el} present the lattice thermal conductivity and carrier thermal conductivity, respectively.

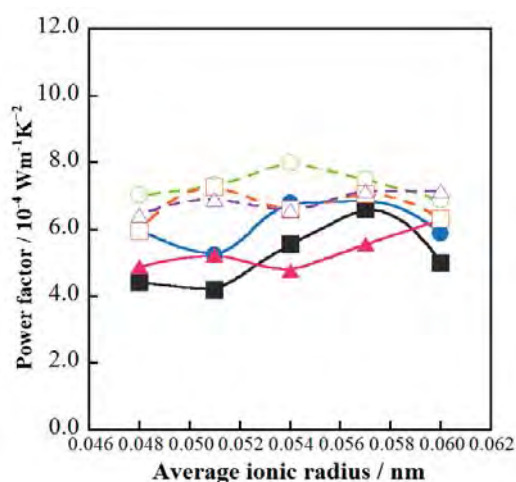


Fig.3 Power factor of $Zn_{1-(x+y)}Ga_xIn_yO$ systems ($0.005 \leq x+y \leq 0.009$) as a function of ionic radius for $x+y=0.005$ at 673K(\bullet), $x+y=0.007$ at 673K(\blacksquare), $x+y=0.009$ at 673K(\blacktriangle), $x+y=0.005$ at 1073K(\circ), $x+y=0.007$ at 1073K(\square), $x+y=0.009$ at 1073K(Δ).

Fig. 4 demonstrates the lattice thermal conductivity (κ_{ph}) as a function of average ionic radius of dopants in Zn site of $Zn_{1-(x+y)}Ga_xIn_yO$ ($x+y=0.005$ and 0.007). The κ_{ph} clearly decreased with increasing r_{av} and reached the minimum as shown in Fig.4. This indicates that there is the optimum average ionic radius which contributes to a lowering of κ_{ph} and improvement of ZT in Eq.(2). Also, this figure suggests that the relationship between r_{av} of dopants in Zn site of $Zn_{1-(x+y)}Ga_xIn_yO$ ($x+y=0.009$) and κ_{ph} would shift to the higher κ_{ph} side which is not suitable for the design of high quality thermoelectric ZnO.

Since κ_{ph} observed for monolithic ZnO which r_{av} is equal to 0.06nm appeared around $12Wm^{-1}K^{-2}$, it is concluded that the relationship between r_{av} and κ_{ph} in Fig.4 guides us to the best research direction for a lowering of κ_{ph} .

Alternatively, the carrier thermal conductivity

κ_{el} dependence of the average ionic radius of dopants in Zn site of $Zn_{1-(x+y)}Ga_xIn_yO$ ($x+y=0.005$ and 0.007) is shown in **Fig.5**. This figure didn't provide us the best research direction as well as the results in Fig.4. Therefore, it is concluded that the magnitude of lattice vibration in the ZnO lattice which corresponds to the level of κ_{ph} can be depressed for improvement of ZT based on the results in Fig.4.

Figure 6 presents the dimensionless figure of merit of $Zn_{1-(x+y)}Ga_xIn_yO$ systems ($x+y=0.005, 0.007$) as a function of average ionic radius

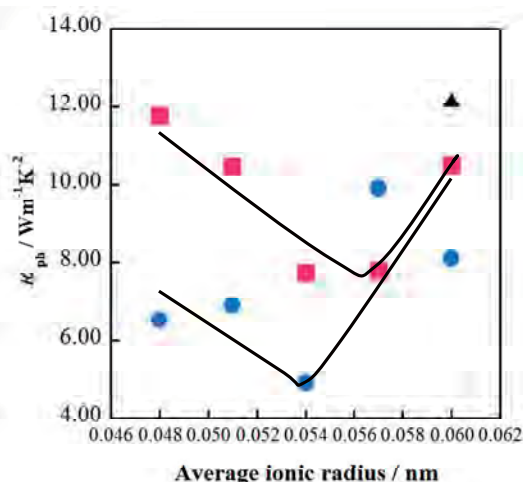


Fig.4 Lattice thermal conductivity of $Zn_{1-(x+y)}Ga_xIn_yO$ systems ($x+y=0.005, 0.007$) as a function of average ionic radius at 673K for $x+y=0.005$ (\bullet), $x+y=0.007$ (\blacksquare), ZnO (\blacktriangle).

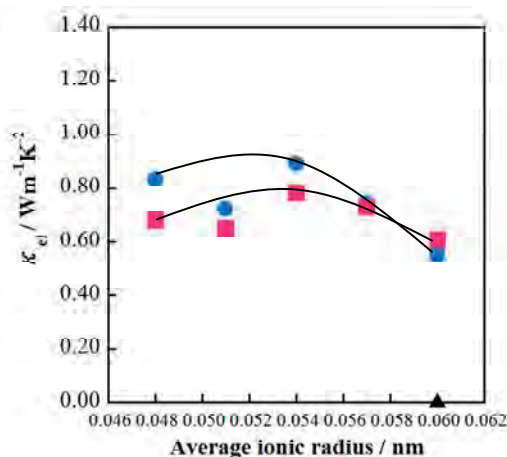


Fig.5 Carrier thermal conductivity of $Zn_{1-(x+y)}Ga_xIn_yO$ systems ($x+y=0.005, 0.007$) as a function of average ionic radius at 673K for $x+y=0.005$ (\bullet), $x+y=0.007$ (\blacksquare), ZnO (\blacktriangle).

observed at 673K. This figure clearly indicates that the observed tendency in Fig.4 apparently corresponds to the tendency observed in Fig.6. Based on all data in the present work, it is concluded that the lattice vibration in the $Zn_{1-(x+y)}Ga_xIn_yO$ ($x+y=0.005, 0.007$ and 0.009) which consists of the defect Wurtzitic structure can be minimized and ZT value observed for the samples can be maximized by using the concept of average ionic radius of dopants in Zn site. Also, Fig.6 would indicate the ideal defect crystal structure for design of high quality thermoelectric ZnO with high ZT and low κ .

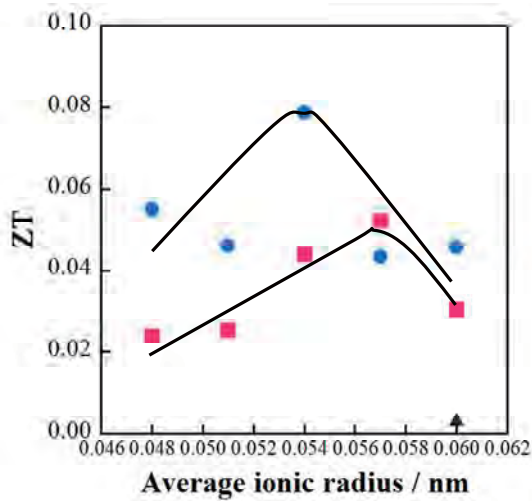


Fig.6 Dimensionless figure of merit of $Zn_{1-(x+y)}Ga_xIn_yO$ systems ($x+y=0.005, 0.007$) as a function of average ionic radius at 673K for $x+y=0.005$ (●), $x+y=0.007$ (■), ZnO (▲).

4. Conclusions

Ga and In co-doped ZnO ($Zn_{1-(x+y)}Ga_xIn_yO$: $x+y=0.005, 0.007$ and 0.009) system which consists of single phase of hexagonal ZnO was prepared. The average ionic radius of dopants in Zn site of $Zn_{1-(x+y)}Ga_xIn_yO$ ($x+y=0.005, 0.007$ and 0.009) dependence of power factor didn't show the useful research direction, while the conductivity vs. the average ionic radius dopants in ZnO site shows the maximum value in the present work. This result suggests that the other crystallographic factor has to be clarified for design of high quality thermoelectric ZnO. To develop the design paradigm for fabrication of high quality thermoelectric ZnO based materials, the relationship between the average ionic radius of dopants in Zn site of the samples and the lattice thermal conductivity observed for the $Zn_{1-(x+y)}Ga_xIn_yO$ ($x+y=0.005$ and 0.007) was

examined. Surprisingly, the average ionic radius of dopants in Zn of co-doped ZnO samples has close relation to the changes of lattice thermal conductivity and dimensionless figure of merit in the present work.

According to Pauling's first rule, the crystallographic coordination number of the cation is decided by the radius ratio between cation and anion. The crystal structure is dominated by the coordination number of the cation in the case of the oxide [12]. The crystal structure of ZnO is the wurtzitic structure with hexagonal symmetry, where the coordination number of cation is four. This one is the polymorph of ZnS type structure. Another type of polymorph of ZnS is sphalerite structure with cubic symmetry, where the coordination number of cations is also four.

The ionic radius ratio between the cation (r_c) and anion (r_a) ranges from 0.225 to 0.414 in the case of four-fold coordination. Since ZnO consists of the distorted structure, the ionic radius ratio (r_c/r_a) of ZnO becomes 0.435 which slightly deviates from Pauling's 1st rule. And the ionic radius ratio (r_c/r_a) of the sphalerite structure (i.e. cubic ZnS) which structure is similar to cubic diamond becomes 0.326, where the coordination number of Zn cations in ZnS is four as well.

Since the cubic ZnS can be seen as anti-fluorite compound when Zn cation occupies the anion site in the fluorite structure and the coordination number of S around Zn is six. In this case, half of all cation sites in the cubic defect ZnS which can be seen as anti-fluorite structure are vacant. And the ionic radius ratio (r_c/r_a) of the cubic ZnS structure which the coordination number of Zn cations is six becomes 0.405.

In the present work, the ionic radius ratio (average r_c/r_a) of co-doped ZnO which average ionic radius is approximately 0.056nm becomes 0.400 and it is very close to the calculated ionic radius ratio ($r_c/r_a = 0.405$) of aforementioned cubic ZnS which has large number of lattice defect.

In general, it is well known that the phonon scattering is enhanced in the defect lattice and the thermal conductivity becomes low level.

As mentioned above, it is concluded that the lattice thermal conductivity observed for co-doped ZnO which average ionic radius is approximately 0.056nm became low level due to the formation of large amount of lattice defects.

Based on above conclusions, it is concluded that the magnitude of lattice vibration in the defect structure of ZnO and the lattice thermal

conductivity can be minimized using the concept of average ionic radius of dopants in Zn suite of co-doped ZnO system. Also, ZT value observed for ZnO based materials can be maximized using aforementioned concept based on crystallography. And it is expected that the combination analysis of defect structure simulation and microanalysis at atomic scale will clarify the detail defect structure in the prepared co-dope ZnO and support our concept for design of high quality thermoelectric ZnO based materials in the near future.

References

- [1] Z.H. Dughaish, *Physica B*, **332**, pp.205 - 223 (2002).
- [2] X.A.Fan¹, J.Y.Yang, W.Zhu, S.Q.Bao, X. K. Duan, C. J. Xiao and K.Li., *J.Phys. D*, **40**, pp.5727 - 5732(2007).
- [3] D.Flahaut, T.Mihara, R.Funahashi, N.Nabeshima, K.Lee, H.Ohta, K.Koumoto, *J.Appl. Phys.*, **100**, 084911 (2006).
- [4] K.Kato, M.Yamamoto, S.Ohata, H. Muta, K.Kurosaki, S. Yamanaka, H.Iwasaki, H.Ohata, K.Koumoto, *J.Appl. Phys.*, **102**, 116107 (2007).
- [5] T.Tsubota, M.Ohtaki, K.Eguchi, H.Arai, 16th International Conference on Thermoelectrics, pp.240 - 243 (1997).
- [6] T.Tsubota, M.Ohtaki, K.Eguchi, H.Arai, *J. Mater. Chem.*, **7(1)**, pp.85 - 90 (1997).
- [7] M.Ohtaki, K Araki, K.Yamamoto, *J. Elec. Materials*, **38**, pp.1234 - 1238 (2009).
- [8] I.Nisida, K.Sugi, R.Ryou, K.Takeda., *Thermoelectrics: principles and applications*, pp.60 - 65 (2001).
- [9] R.D. Shannon, *Acta Cryst.*, **A32**, pp.751- 767 (1976).
- [10] T. kazikawa, *Thermoelectric conversion handbook*, pp.341- 342 (2008).
- [11] H.Takemoto, H.Kawakami, M.Saito, H.Yamamura, *Transactions of the Materials Research Society of Japan*, (accepted for publication, 2012).
- [12] Y. M. Chiang, D. Birnie III, and W. D. Kingery, *Physical Ceramics, -Principles for Ceramic Science and Engineering*, Chap. 1, pp. 13-18, John Wiley & Sons, Inc., New York (1996).

(Received 30 July 2012; Accepted 30 August 2012)

シアノバクテリアの光生物学的な水素生産実用化に向けた研究開発： バイオリアクターの低コスト化と培養気相

櫻井英博*¹、増川一^{1,2}、北島正治³、井上和仁^{1,3}

¹神奈川大学光合成水素生産研究所、²JST さきがけ、³神奈川大学理学部

E-mail: sakurai@waseda.jp

R & D for Practical Application of Photobiological Hydrogen Production by Cyanobacteria: the Cost Reduction of Bioreactors and of the Gas for Cultivation

Hidehiro Sakurai, Hajime Masukawa, Masaharu Kitashima, Kazuhito Inoue

¹Research Institute for Photobiological Hydrogen Production, ³Department of Biological Sciences, Faculty of Science, Kanagawa University, and ²PRESTO, JST

Abstract

We have proposed large-scale photobiological H₂ production by cyanobacteria in large flexible plastic bags as the bioreactors floating on the sea surface in the future. The H₂ production is based on the photosynthesis and nitrogenase activities of nitrogen-fixing cyanobacteria, and we have created more than 50 hydrogenase- and nitrogenase-related mutants of *Nostoc* species by genetic engineering. Some of the mutants accumulated H₂ for more than 60 days in the presence of O₂ evolved by photosynthesis. In order that our proposed system is put into practice, one of the issues is the cost reduction of photobioreactors. In laboratory experiments, we have shown that flexible transparent plastic bags (Wakhy bags) are good barriers to H₂. The escape of the photobiologically produced H₂ from large plastic photobioreactors is estimated to be about 0.2% in 60 days. For the sustained H₂ production, the N₂ concentration in the gas phase should be low. The H₂ production activities of some of the nitrogenase mutants are not inhibited by N₂, and N₂ gas can be used in place of Ar as the gas mixture for H₂ production by such mutants.

Keywords: Cyanobacteria, Hydrogen production, Photobioreactor, Photosynthesis, Solar energy

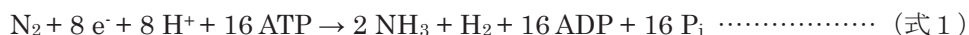
1. まえがき

1. 1 海面を利用した大規模光生物学的な水素生産の構想

地表が受ける太陽光エネルギーは、人類が消費する化石燃料エネルギーの 6000 倍にも達する。生物の光合成を利用した再生可能エネルギーとして、サトウキビやトウモロコシ由来のバイオエタノールが一部地域では市場競争力を持っているが、その大量生産は食料価格の高騰を招くおそれがある。また、人類の化石燃料エネルギー消費量は莫大であり、食物摂取エネルギー(1 人 1 日 2000 kcal)の 20 倍(米国は約 100 倍、日本は約 50 倍)にも達するから、陸上農作物だけで化石燃料を大規模に代替することは困難だと考えられる。そこでわれわれは、海面上でシアノバクテリアの光合成系とニトロゲナーゼを利用して水素を大規模に生産する構想を発表し、将来の実現に向けて研究開発を行っている¹⁻³⁾。

1. 2 改良シアノバクテリア(別名:ラン藻、ラン色細菌)の水素生産系 — 光合成系とニトロゲナーゼ

水素生産に利用する酵素は、ニトロゲナーゼである。ニトロゲナーゼの生化学的役割は窒素固定であるが、反応の必然的副産物として不可逆的に水素が発生する:



この反応に必要な電子は光合成によって生産された糖質の分解などによって得られ、ATP は光リン

酸化および糖質の酸化的リン酸化によって供給される。また、Ar(アルゴン)気相下などの窒素ガス非存在下では、式2のように、ニトロゲナーゼに投入された電子はすべてが水素生産に向けられる：



ヒドロゲナーゼと比較して、ニトロゲナーゼはATP(生体の高エネルギー物質)を消費するため理論的最大エネルギー変換効率が低い、反応が不可逆的に水素の放出方向に向いているという利点がある。窒素固定シアノバクテリアは一般にヒドロゲナーゼを持っているが、その遺伝子を遺伝子工学的に破壊した株はH₂の再吸収活性が実質上なくなり、O₂存在下でもH₂を蓄積できる。われわれが作成した *Nostoc* sp. PCC 7422 ΔHup 株は、水素を濃度約30%に蓄積でき、実験室条件下での光-H₂エネルギー変換効率は3.7%(対可視光)、1.7%(対太陽光換算)であった⁴⁾。

ニトロゲナーゼは酸素感受性であり、われわれが利用する *Nostoc/Anabaena* 属のシアノバクテリアはO₂発生型光合成と両立させるために、通常の光合成を行い糖質を合成してO₂を発生する栄養細胞と、O₂発生型光合成を行わずN₂固定に特化したヘテロシスト(異型細胞)の共同により、全体としてH₂Oを電子供与体としてH₂生産とO₂発生を行うことができる。

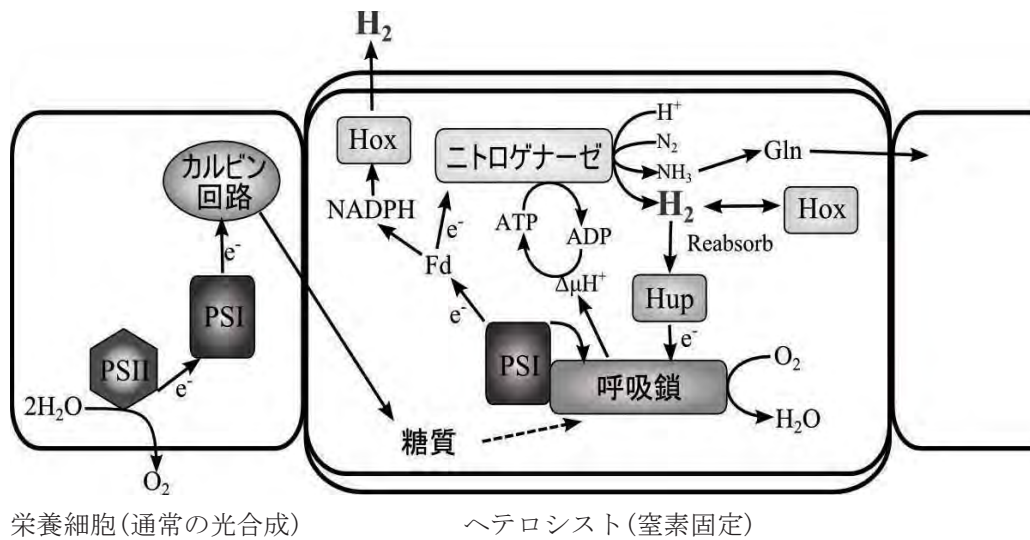


図1 シアノバクテリアのH₂生産を中心とする代謝系

生産されたH₂はヒドロゲナーゼにより再吸収されるので、その活性除去が有効である。(Hup: 取込み型ヒドロゲナーゼ、Hox: 双方向性ヒドロゲナーゼ、PSIおよびPSII: 光化学系I及びII)

2. 将来の低コスト化のための検討

2. 1 将来のプロセスフロー

洋上における大規模光生物学的水素生産の実施にはまだ多くの年月を要するものと考えられ、不確定な要素が多々ある。想定されるプロセスを図2に示すが、その一部についてわれわれが行ったコスト低減のための研究開発について述べる。

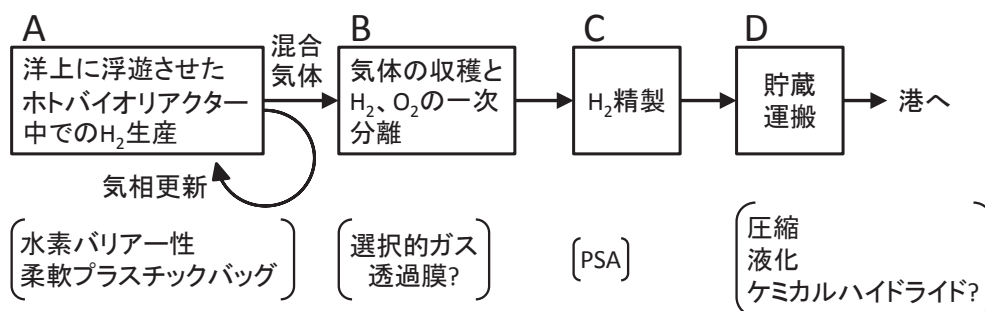


図2 光生物学的水素大規模生産のプロセスフロー図

2. 2 バイオリアクターの低コスト化

われわれは、改良シアノバクテリアを洋上で3層のプラスチックバッグからなるホットバイオリアクター内で、水素を数10日にわたり生産させ、収穫するという構想を描いている。Amos(2004)⁵⁾のコスト分析によれば、ホットバイオリアクターのコスト低廉化は実用化に当って必須の課題であり、100ドル/m²では経済的生産は不可能であり、約20ドル/m²以下が求められる。われわれは、ガスバリアー層としてポリアクリル酸系樹脂(PBeタイプ)または酸化アルミニウム(PG1タイプ)を持つ透明プラスチックバッグ(Wakhyバッグ、GLサイエンス)の水素バリアー性が、相当程度高いことを確認した(Km: 22-87 cm³ m⁻² d⁻¹ atm⁻¹)。これらを用いて改良シアノバクテリアによるH₂の蓄積を測定した。H₂の蓄積と共にO₂も発生するが、シアノバクテリアのニトロゲナーゼはO₂の傷害から相当程度保護されているが、その保護は完璧ではない。図3の結果は、ガスの発生によりプラスチックバッグは気体の内

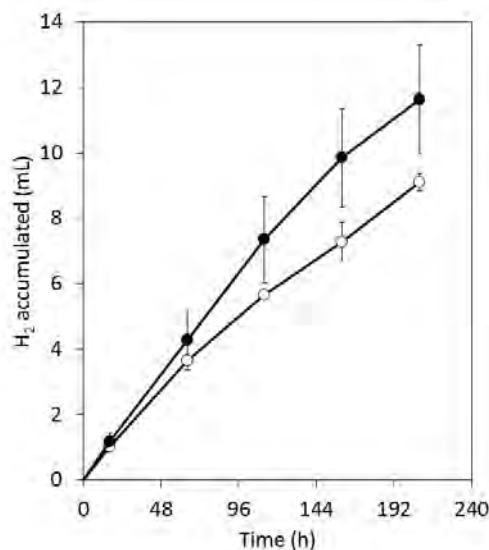


図3 シアノバクテリアによるH₂蓄積時間経過の柔軟プラスチックバッグ(PBe-Eタイプ、●)と密閉ガラスボトル(ブチルゴム栓、○)との比較。

圧が常圧に保たれるのに対して、ガラスボトルでは上昇する。したがって、ガラスボトルではO₂分圧の上昇がより高いため、こうした差が生じたと説明される⁶⁾。

将来、巨大なプラスチックバッグ(例、幅25m、長さ200m)を、波浪の静かな無風帯と呼ばれる海域(1か所につき数km²以上)に多数浮かべる構想であるが、Kubota⁷⁾らによれば、海上漂流物の移動を、海流、風等の影響を考慮してシミュレートすると、漂流物は南北緯30度付近の無風帯と呼ばれる海域に集積するという。このような海域では、バイオリアクターを係留せずに設置することが可能だと考えられる。なお、初期気相の厚みを50cmとし、シアノバクテリアがエネルギー変換効率1.2%でH₂を生産したときのH₂の漏れは、Kmを50 cm³ m⁻² d⁻¹ atm⁻¹とすれば、60日間で総生産量の約0.2%程度と試算される。

2. 3. 培養気相

2. 3. 1 ヒドロゲナーゼ遺伝子破壊株(ΔHup)

ニトロゲナーゼを利用した水素生産ではN₂の分圧が高いと多くの電子が窒素固定に向けられ、H₂の生産が低下する(式1、2)。長期培養では、窒素固定により窒素化合物の栄養が充足されると、NH₃の必要性もなくなるためニトロゲナーゼタンパク質合成の抑制も起こり、ニトロゲナーゼ活性、およびこれに連動するH₂生産活性が低下していく。Arをベースにした5% CO₂、0.5% N₂では長期間高いH₂生産活性を維持できるが、N₂が10%を超えると活性は急速に低下する。

2. 3. 2 ニトロゲナーゼ部位特異的変異株の作成と水素生産活性

ニトロゲナーゼ反応は、触媒作用を持つジニトロゲナーゼとそれに電子を渡すジニトロゲナーゼレダクターゼの共同により営まれる(一般的には、両者を合わせて単にニトロゲナーゼという)。前者の活性中心はFe, Mo, Sから成る金属クラスター(FeMo-co)で、ここにホモクエン酸が配位している(なお、Moの位置に、VまたはFeが置き換わったものもあり、それぞれV型、Fe-only型ニトロゲナーゼと呼ばれる)。アゾトバクテリアのニトロゲナーゼの立体構造はX線結晶解析により明らかにされており、他の生物(シアノバクテリアを含む)のニトロゲナーゼのアミノ酸配列も相同性が高く、特にFeMo-co付近に配位するアミノ酸残基は相同性が高い(図4)。アゾトバクテリアの立体構造を参考に、シアノバクテリア *Nostoc/Anabaena* PCC 7120 ΔHup株を親株として、FeMo-coの近くに位置して触媒機能に影響すると考えられるアミノ酸残基の部位特異的変異株を46種作成した⁸⁾。その中には、N₂存在下で培養してもH₂生産活性が低下しないものいくつかあり、またホモクエン酸合成酵素破壊株もN₂によるH₂生産阻害の程度が低かった⁹⁾。

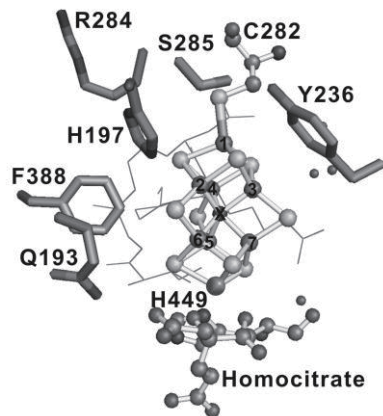


図4 (左) ニトロゲナーゼFeMo-coとその近傍に位置すると推定されるアミノ酸残基。数字：*Nostoc* sp. PCC 7120株のアミノ酸配列上の番号。C:システイン、F:フェニルアラニン、H:ヒスチジン、Q:グルタミン、R:アルギニン、S:セリン、Y:チロシン。Homocitrate:ホモクエン酸

図5(下) 親株(Δ Hup)およびR284H変異株株の H_2 蓄積活性の経日変化

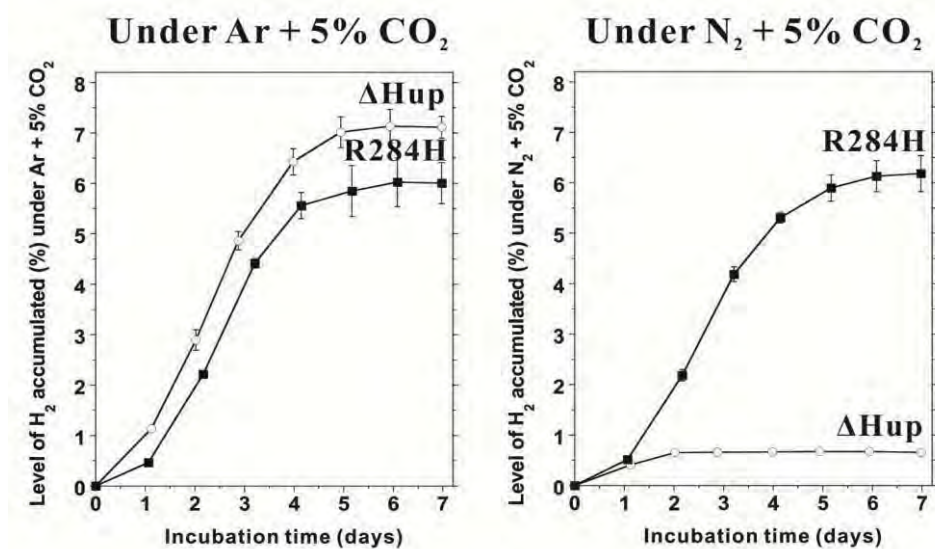


図5に示すように、親株 Δ Hup株の H_2 生産はAr気下では高いが、 N_2 存在下では低い。これに対しR284H(284番目のアルギニンをヒスチジンに置換)変異株は、 N_2 存在下でもArの場合と同程度の H_2 生産活性を示した。このような変異株は、 H_2 生産時のガスのコスト削減に有用だと考えられる。

謝辞

本研究の研究費の一部は文科省私大戦略的研究基盤支援事業 (K. I)、科研費(基盤研究 (B) 課題番号 21380200, H. S.), 新学術領域研究 課題番号 24107004, K. I.), JST さきがけ (M. H.) 等による。

参考文献

- 1) 櫻井 英博、増川 一 : 燃料電池, 6, 46-52 (2006)
- 2) H. Sakurai, H. Masukawa: Mar. Biotechnol. 9, 128-145 (2007)
- 3) H. Sakurai, H. Masukawa, M. Kitashima, K. Inoue: Adv. Exp. Med. Biol. 675, 291-303 (2010)
- 4) F. Yoshino, H. Ikeda, H. Masukawa, H. Sakurai: Mar. Biotechnol. 9, 101-112 (2007)
- 5) W.A. Amos: NREL Milestone Report, www.nrel.gov/docs/fy04osti/35593.pdf (2004)
- 6) M. Kitashima et al.: Biosci. Biochem. Biotechnol. 76, 831-833 (2012)
- 7) M. Kubota, K. Takayama, D. Namimoto: Appl. Microbiol. Biotechnol. 67, 469-476 (2005)
- 8) H. Masukawa, et al.: Appl. Env. Microbiol. 76, 6741-6750 (2010)
- 9) H. Masukawa, K. Inoue, H. Sakurai: Appl. Environ. Microbiol. 73, 7562-7570 (2007)

■報告書■

シアノバクテリアのニトロゲナーゼを利用した水素の光生物学的生産性
に関する研究

—2011年度神奈川大学大学院理学研究科博士論文概要—

北島正治^{1,2,3} 井上和仁^{1,2}

Studies for the improvement of nitrogenase-Based photobiological hydrogen
production by cyanobacteria

Masaharu Kitashima^{1,2,3} and Kazuhito Inoue^{1,2}

¹ Research Institute for Integral Science, Kanagawa University, Hiratsuka City 259-1293 Kanagawa, Japan

² Department of Biological Sciences, Faculty of Science, Kanagawa University, Hiratsuka City, 259-1293 Kanagawa, Japan

³ To whom correspondence should be addressed. E-mail: pt125536zy@kanagawa-u.ac.jp

Abstract: In order to decrease CO₂ emission from burning fossil fuels, we need to exploit renewable energy on a large scale, and solar energy is the strongest candidate for this energy source. In this study, the H₂ production system is based on photosynthetic and nitrogenase activities of the uptake hydrogenase mutant of cyanobacteria that can accumulate H₂ for extended periods even in the presence of evolved O₂. This report describes basic studies aiming at putting this technology to practical use in the future.

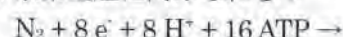
Keywords: cyanobacteria, hydrogen, photosynthesis, nitrogenase, bioreactor

序論

表1に示すように、人類社会(約65億人)が消費するエネルギーは、食物摂取エネルギー(1人、2,000kcal/日)と比較して世界平均で20倍、日本は約50倍、米国は約100倍に達している。一方で、地表が受ける太陽光エネルギーは、人類が消費する化石燃料エネルギーの6,000倍を超えるほど莫大である。しかし、その光強度は地球平均で約1,500 kWh/m²/年程度と低く、ソーラーパネルにしる、植物の光合成を利用するバイオ燃料にしる、経済性を確保しながら太陽エネルギーを利用する大規模なシステムをいかにして構築するかが大きな課題である。

シアノバクテリアは、高等植物や藻類と同様に水を電子供与体として、酸素発生型光合成をおこなう原核生物であり、水素生産に利用できる酵素は、ニトロゲナーゼとヒドロゲナーゼである¹⁾。ニトロゲナーゼは、空気中の窒素(N₂)ガスを固定する酵素で、マメ科植物の根に共生する根粒菌など一部の原核生物がその活性を持つ。水を電子供与体として利用できる光合成生物のうちニトロゲナーゼを持つのは、一部のシアノバクテリアに限られ、クロレラなどの真核光合成生物は持たない。ニトロゲナーゼ反応で

は、水素が必然的副産物として発生するので、ニトロゲナーゼを水素生産に利用することができる。窒素固定の効率が最も高いとき(N₂濃度が十分高いとき)、その反応は、次式のように表され、電子の1/4が水素生産に向けられる:

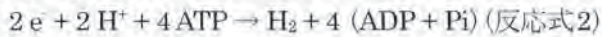


窒素ガスが存在しない条件下(例:Ar気相)では、

表1. 太陽光エネルギーと社会的エネルギー消費

	数量	比率
世界		
一次エネルギー消費(2006)	(494)	(1.22)
(うち化石エネルギー)	404	1.00
光合成純生産	4,200	11
太陽光エネルギー	2,700,000	6,700
食物と摂取エネルギー	20	0.05
日本		
一次エネルギー消費(2005)	(23.8)	(1.21)
(うち化石エネルギー)	19.7	1.00
太陽光エネルギー(陸地)	2,100	107
同上(含排他的経済水域)	33,000	1,700
日本のバイオマス利用可能量	1.26	0.064

全ての電子が水素生産に向かう。



ニトロゲナーゼは、上記反応式に示されるように大量の ATP (生体の高エネルギー物質) を消費するので理論的最高エネルギー変換効率は低い²⁾、水素生産が不可逆的に起こることが、その利点である^{3,4)}。

これに対しヒドロゲナーゼは、水素生産の理論的最高エネルギー変換効率が非常に高いが、反応は可逆的なため、光合成により生成する酸素の存在下では生産された水素の再吸収が起こりやすい。再吸収を避けるためには、水素を毎日収穫する必要があり、曇天下での再吸収の懸念も残る。このような総合的判断から、我々はニトロゲナーゼを基礎とする水素生産方式を採用し、その研究開発に取り組んでいる。北島の博士論文は、3つの研究課題についてまとめたものである。

本研究は、Yoshino らによって作成された、取り込み型ヒドロゲナーゼ遺伝子 (*hupL*) を破壊した *Nostoc* sp. PCC 7422 Δ HupL 株⁵⁾ を用いて、ニトロゲナーゼに基づく光生物学的水素生産の持続性向上を目的とした培養気相組成の検討と、水素生産の長期的持続性の実証及び柔軟プラスチック膜のバイオリクターとしての利用可能性について研究を行った。

材料と方法

シアノバクテリア *Nostoc* sp. PCC 7422 Δ HupL 株
本研究で用いた糸状性シアノバクテリア *Nostoc* sp. PCC 7422 株では、窒素栄養欠乏条件下で、ヘテロ

シストと呼ばれる窒素固定に特化した細胞が、栄養細胞と呼ばれる通常の細胞 10 細胞に 1 つ程度の割合で分化する。ヘテロシストは、細胞壁が肥厚しており、加えて酸素発生の源となる光化学系 II が不活性化されているので、細胞内部は酸素濃度の低い状態に保たれている。この時系状態全体としては、栄養細胞で酸素発生型光合成による糖質合成が行われ、その糖質がヘテロシストへ運ばれ、ニトロゲナーゼを駆動する還元力の源となる。ヘテロシストで窒素固定によって作られたアンモニアはグルタミンに変換されて栄養細胞へと輸送され、光合成と窒素固定が空間的に分離されることにより全体として酸素発生型光合成とニトロゲナーゼ反応の両立が可能となる (図 1)。

Nostoc sp. PCC 7422 Δ HupL 株の培養条件

前培養は、窒素栄養を含む培地である BG11⁶⁾ を用いて、二酸化炭素ガスを培養気相中の濃度が 5% となるように添加し、植物育成用蛍光灯 (NEC、ピオルクス) 約 $100 \mu\text{mol photons m}^{-2}\text{s}^{-1}$ の 12 時間毎の明暗周期光照射下、26°C で、マグネチックスターラー (HANNA、HI-190M) を用いて緩やかに培養液を攪拌しながら培養した。

窒素栄養制限条件下での培養には、BG11 培地から硝酸塩を除去した BG11₀ 培地を用い、植物育成用蛍光灯を用いて約 $100 \mu\text{mol photons m}^{-2}\text{s}^{-1}$ の 12 時間毎の明暗周期光照射下、26°C の条件で行った。

水素生産性への窒素ガス及び二酸化炭素ガス濃度の影響に関する実験、水素生産の長期的持続性に関する実験では、窒素欠乏培地へ移した *Nostoc* sp.

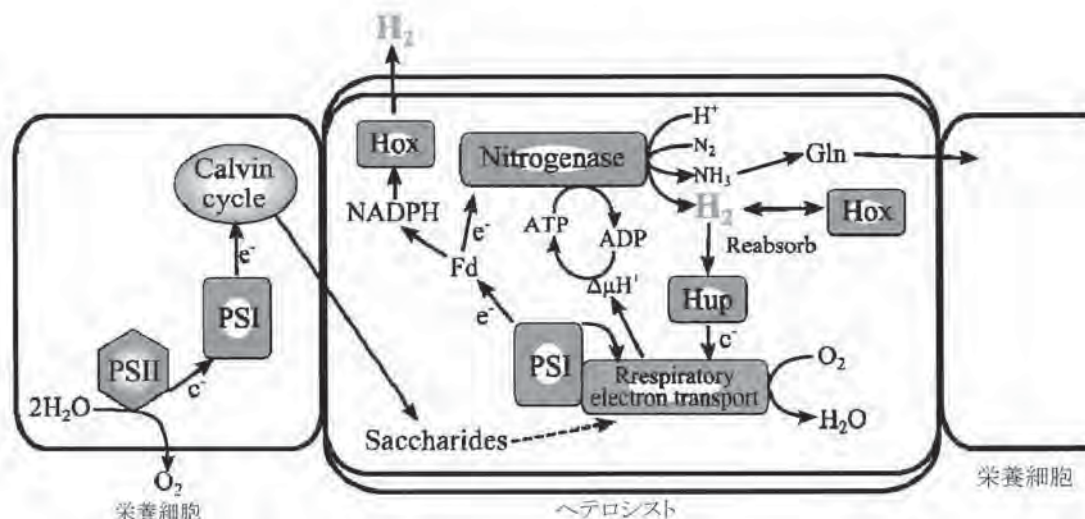


図 1. シアノバクテリアにおける栄養細胞とヘテロシストによる光合成とニトロゲナーゼ反応の空間的分離。栄養細胞が光合成により生産した糖質が、ヘテロシストへと輸送され、ニトロゲナーゼによる窒素固定反応の還元力の源となる。反応全体としては、水を原料として、光合成により酸素が、窒素固定反応の副産物として水素が生産される。

PCC 7422 Δ HupL株をブチルゴム製の中蓋を付けたガスクロバイアル(日電理化硝子)に封入した後、培養気相をアルゴンガスで置換した後に、実験内容に応じて窒素ガス及び二酸化炭素ガスをガスタイトシリンジ(SGE)で注入して培養気相組成を調整した。その後、植物育成用蛍光灯を用いて約 $100 \mu\text{mol photons m}^{-2} \text{s}^{-1}$ の12時間毎の明暗周期光照射下、 26°C の条件下で培養を行った。

プラスチックバッグ内(常圧下)と密閉ガラス容器での水素生産性の比較実験では、窒素欠乏培地へ移した *Nostoc* sp. PCC 7422 Δ HupL株を50 mLあるいは100 mL容のガスクロバイアルへと50 mLずつ分注した後、前者はガスサンプリングポートを装着した水素バリアー性フィルムで作成したバッグ内に入れ四辺を溶着し、後者はブチルゴム製の中蓋をつけて密閉した。両者とも培養気相をアルゴンガスで置換した後、培養気相の体積が同等となるようにアルゴンガスで調整し、窒素ガスを1% (v/v)、二酸化炭素ガスを5% (v/v)となるように添加し、約 $100 \mu\text{mol photons m}^{-2} \text{s}^{-1}$ の12時間毎の明暗周期光照射下で培養を行った。

培養気相組成の分析方法

培養気相中の窒素、酸素、水素の体積比組成分析はガスクロマトグラフィー(Shimadzu, GC-2014)を用い、ゼオライト皮膜キャピラリーカラム(RESTEK, Rt-MSieve5A PLOT: $30 \text{ m} \times 0.32 \text{ mm} \times 30 \mu\text{m}$)による気体の分離により行った。キャリアーガスにはアルゴンガスを用い(圧力220 kPa)、カラムの温度は 50°C 、インジェクター及び検出器の温度は 80°C 、検出器には、加熱されたフィラメントの電気抵抗変化を検出する熱伝導度検出器(TCD)を用いた。

培養気相体積の算出方法

プラスチックバッグ内の総気体体積の算出は、バッグ内に注入したヘリウムガスの濃度を測定することによって行った。バッグ内にヘリウムガスを注入し、濃度平衡後(60分後)、TCD検出器を用いたガスクロマトグラフィー(Shimadzu, GC-2010 Plus)によりバッグ内混合ガスの組成分析を行った。その測定値のヘリウムガスとの比率から、各成分ガスの常圧下での体積を算出した。気体の分離はゼオライト皮膜キャピラリーカラム(RESTEK, Rt-MSieve5A PLOT: $50 \text{ m} \times 0.32 \text{ mm} \times 30 \mu\text{m}$)を用いて、キャリアーガスにアルゴンガス(圧力209.6 kPa)、カラムの温度は 50°C 、インジェクター及び検出器の温度は 80°C で行った。

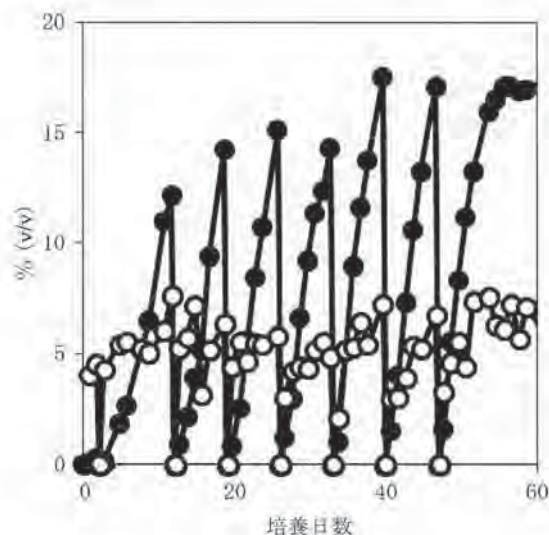


図2. 長期間にわたる持続的水素生産の実証, 窒素栄養欠乏状態に移した *Nostoc* sp. PCC 7422 Δ HupL株を, 密閉ガラス容器に分注し, 26°C , $100 \mu\text{mol photons m}^{-2} \text{s}^{-1}$ の12時間明暗周期光下で培養した. 2日目までの, 培養気相中の窒素ガス濃度は0.5%, 二酸化炭素ガス濃度は5%とした. それ以降の培養気相の組成はヘテロシスト誘導期と同様にし, およそ1週間毎に気相の更新を行った. ○は酸素, ●は水素の濃度.

結果と討論

培養気相の組成と水素の生産活性

ニトロゲナーゼに基づく水素生産では、窒素栄養欠乏状態によってヘテロシストの分化とニトロゲナーゼの誘導が起こり、反応の副産物としての水素が生産される。ニトロゲナーゼによる窒素固定が進み、窒素栄養が充足すると酵素活性が低下し、それにとまって水素生産も低下する。そこで、*Nostoc* sp. PCC 7422 Δ HupL株の細胞を、硝酸塩類を含むBG11培地からこれを除いた培地(BG11₀培地)へと移してからガラス容器に分注し、ブチルゴム栓で密閉した後に培養気相の組成を変えて、12時間ごとの明暗周期光下での水素生産性に対する影響を調べた。まず、窒素ガス濃度が水素生産持続性と、水素ガス蓄積濃度に及ぼす影響について調べた。窒素栄養欠乏条件培地に細胞を移してから期間を、数日(2-4日)間(ヘテロシスト形成と水素生産の開始期)とそれ以降(水素生産期)に分け、それぞれの培養気相中の窒素ガス濃度を1-80% (v/v)と変えて、水素生産性への影響を調べた。また、ニトロゲナーゼを駆動するための還元力の源となる糖質の原料となる二酸化炭素ガスの濃度を0.03-5% (v/v)と変えて水素生産に対する影響を調べた。二酸化炭素ガスの影響についても、窒素栄養欠乏培地に細胞を移してから2日目までと、それ以降とのそれぞれについて

ガス濃度を変えて検討を行った。その結果、培養気相中の窒素ガス濃度は、ヘテロシスト形成期では影響が低かったが、水素生産期では高濃度で水素生産に強く阻害的に働き、濃度 1% 程度の時に水素生産の持続性がよく、最終的な水素ガスの蓄積濃度も高かった。二酸化炭素ガスの濃度の影響はそれほど大きくなかったが、本研究の条件下では 5% 程度の時に水素生産の持続性がよく、最終的な水素ガスの蓄積濃度も有意に高かった。

水素生産の長期的持続性

光合成微細藻類を利用したエネルギー生産では、細胞の成長に窒素栄養などの栄養塩類と炭素源となる二酸化炭素ガスのエネルギーコストがかかることが指摘されており、その克服が経済的で正味のエネルギー生産を実現する上での課題だと指摘されている⁷⁾。この課題を念頭に、ヘテロシストが分化し水素生産が可能となったシアノバクテリアが、培養液を交換することなく長期間にわたって持続して水素生産が可能かどうかについて調べた。*Nostoc sp. PCC 7422 ΔHupL* 株の細胞を、BG11 培地から BG11₀ 培地へと移してからガラス容器へと分注し、ブチルゴム栓で密閉した後に培養気相の組成を変えて、12 時間ごとの明暗周期光下での水素生産持続性への影響を調べた。第 2 章の結果を参考に、培養気相中の窒素ガス濃度を 0.5%、二酸化炭素ガス濃度を 5% として誘導期を 2 日間取った後、同じ組成の気相に更新して、およそ 1 週間ごとに気相を更新しながら培養気相の組成を分析し続けたところ、60 日以上にわたって 15-20% の水素ガスを含む培養気相が得られ、活性の低下は見られなかった (図 2)。この時水素と酸素の体積比は約 2 : 1 で、光合成とニトロゲナーゼの連携により、水を基質として水素と酸素が発生するという予測と合致する結果が得られた。なお、60 日程度の水素生産持続性は、窒素ガス濃度 0.5%、0% とほぼ同等の水素生産性を示したが、より長期の場合窒素ガス濃度 0% では水素蓄積濃度が徐々に低下していった。以上の結果は、シアノバクテリアによる光生物学的な水素生産において、栄養塩類を追加することなく長期間にわたって水素生産が可能であることを示しており、低コストでの大規模な水素生産を実現できる可能性を持つことが示された。

バイオリクター素材としての水素低透過性プラスチック膜の利用とガスサンプリングポートの開発

Amos は藻類の光合成を利用した大規模エネルギー生産において、経済性を確保するためにはバイオリクターのコスト低減が重要な課題だと指摘し、

受光面 1 m² 当たり \$10 以下のバイオリクターが必要だと結論している⁸⁾。当研究室では水素バリアー性プラスチック膜を含む 3 層のプラスチックバックを用いることで、安価なバイオリクターの作成が可能であると提案している^{9,10,11,12,13)}。水素バリアー性プラスチック膜を用いた実験用にガスサンプリングポートの開発を行った。ガスサンプリングポートは、バッグ内にブチルゴムセプタムを付けたインナーパッドを入れ、プラスチックフィルムの外からブチルゴムセプタムを付けた押しネジもしくはニードルポートで挟み込み、ナットホイールで押しネジを繰り出すことで、プラスチックフィルムの内側と外側からブチルゴムセプタムで挟み込む構造のものを設計した (公開特許; 公開番号: 2011-085571)。水素バリアー性プラスチック膜として、市販品の Besela フィルム (クレハ社) および GL フィルム (凸版社) を選択し、水素のバリアー性について検討した。両者とも PET 樹脂フィルムをベースとしたラミネート膜で、水素ガスバリアー層は前者がアクリル酸樹脂系高分子コート、後者が酸化アルミニウムコートとなっている。どちらも水素ガスバリアー層の上に、二軸延伸ナイロン層、さらに無延伸ポリプロピレン (CPP) または直鎖状低密度ポリエチレン (LLDPE) 層がラミネートされている。これら 4 種類のバッグ、Besela-CPP (Be-P)、Besela-LLDPE (Be-E)、GL-CPP (Gl-P)、GL-LLDPE (Gl-E) をオートクレーブ滅菌処理 (120°C、20min)、間歇滅菌処理 (100°C、20min、3 回) したもの、及び未加熱処理のものを、熱融着によって密閉バッグを作り、内部に封入した水素ガスの透過性を測定した。一例を挙げると、ガスサンプリングポートを付けた Gl-E バッグに 17.1% (v/v) となるように水素ガスを注入し、ニードルポートから適時サンプリングを行い、内部水素ガス濃度の測定を行ったところ、15 日目には 16.2% となった。同様の測定を 4 種類の未加熱および加熱処理済みフィルムで行い、水素透過性を算出した。これらプラスチックバッグの水素透過性は 20-90 cm³ m⁻² day⁻¹ atm⁻¹ 程度であり、将来の実用化の材料として候補となりうることを示された。

次に、未加熱処理の Gl-E を用いて、密閉容器内での水素生産量とプラスチックバッグ内での水素生産量を比較した。BG11 培地から BG11₀ 培地へと移した *Nostoc sp. PCC 7422 ΔHupL* 株の細胞培養液を、同じ直径の、容量 100 および 75 mL のガラス容器に 50 mL ずつ分注し、100 mL 容器はブチルゴム栓で密封、50 mL 容器はガスサンプリングポートを付けたプラスチックバッグに入れた。プラスチックバッグ内の気相容積をおよそ 50 mL に調節した後、

共に気相中の窒素ガス濃度が1%、二酸化炭素ガス濃度が5%となるようにそれぞれを加え、12時間ごとの明暗周期光照射を行いながら水素の蓄積量を測定した。後者の気体体積は、添加した希ガスの濃度分析により求めた。その結果、3日目まではどちらの水素蓄積量もほぼ同等であったが、それ以降ではプラスチックバッグの水素蓄積量が多く、光照射後10日目で密閉容器での水素生産量は約8 mL、プラスチックバッグでは約11 mLとなった。これは、密閉容器と比較してプラスチックバッグの方が内部の酸素分圧の上昇が緩やかであるため、酸素感受性の高いニトロゲナーゼへの影響が低かったためだと考えられる。

結論

本研究によってシアノバクテリアが培地を代えることなく、長期間にわたる持続的な水素生産が可能であること、また将来、改良シアノバクテリアを海上で培養し水素を大規模に、低コストで生産するために柔軟プラスチック製バイオリクターの利用可能性を示す結果が得られた¹⁴⁾。水素の経済的な大規模生産を実現するためには、今後、野外環境下での光・水素エネルギー変換効率の向上や、生産後の水素精製・貯蔵・運搬に関連する技術開発、諸コスト低減など多くの課題が残っている。前者の課題に対する生物学的アプローチとしては、遺伝子工学的手法によるシアノバクテリアの持つ巨大なアンテナ色素蛋白複合体の削減による培養液全体としての水素生産活性の向上、水素発生への電子配分比率の高い活性中心金属の異なるニトロゲナーゼの利用、プロトクロロフィドリダクターゼを参考にしたニトロゲナーゼの酸素感受性の低減^{15,16)}に向けた改良などが考えられる。

謝辞

本研究を遂行するにあたり、多大なる御助言を賜りました櫻井英博神奈川大学光合成水素生産研究所客員教授、同客員研究員増川一博士に感謝いたします。実験における助言を頂きました神奈川大学総合理学研究所客員研究員鈴木温博士に感謝いたします。

文献

- 1) Tamagnini P, Axelsson R, Lindberg P, Oxelfelt F, Wünschiers R and Lindblad P (2002) Hydrogenases and hydrogen metabolism of cyanobacteria. *Microbial. Mol. Biol. Rev.* **66**: 1-20.
- 2) Burris RH (1991) Nitrogenases. *J. Biol. Chem.* **266**: 9339-9342.
- 3) Benemann JR and Weare NM (1974) Hydrogen

evolution by nitrogen-fixing *Anabaena cylindrica* cultures. *Science* **184**: 174-175.

- 4) Mitsui A, Philips EJ, Kumazawa S, Reddy KJ, Ramachandran S, Matsunaga T, Haynes L and Ikemoto H (1983) Progress in research toward outdoor biological hydrogen production using solar energy, sea water, and marine photosynthetic microorganisms. *Ann. New York Acad. Sci.* **413**: 514-530.
- 5) Yoshino F, Ikeda H, Masukawa H and Skurai H (2007) High photobiological hydrogen production activity of a *Nostoc* sp. PCC 7422 uptake hydrogenase-deficient mutant with high nitrogenase activity. *Mar. Biotechnol.* **9**: 101-112.
- 6) Rippka, R. (1988) Isolation and purification of cyanobacteria. *Methods Enzymol.* **167**: 3-27.
- 7) Clarens AF, Resurreccion EP, White MA and Colosi LM (2010) Environmental life cycle comparison of algae to other bioenergy feedstocks. *Env. Sci. Tech.* **44**: 1813-1819.
- 8) Amos WA (2004) Updated cost analysis of photobiological hydrogen production from *Chlamydomonas reinhardtii* green algae. In: *Milestone Completion Report (2004) National Renewable Energy Laboratory*. <http://www.nrel.gov/docs/fy04osti/35593.pdf> (電子出版)
- 9) Sakurai H and Masukawa H (2007) Invited review: Promoting R & D in photobiological hydrogen production utilizing mariculture-rised cyanobacteria. *Mar. Biotechnol.* **9**: 128-145.
- 10) Sakurai H, Kitashima M, Masukawa H and Inoue K (2009) Research and development of large-scale hydrogen production on the sea surface utilizing photosynthetic systems and nitrogenase of cyanobacteria. *Sci. J. Kanagawa Univ.* **20**: 287-290.
- 11) 北島正治, 櫻井英博, 井上和仁 (2011) シアノバクテリアを利用した海面上での水素の大規模生産. *水環境学会誌* **34**: 108-112.
- 12) Masukawa H, Kitashima M, Inoue K, Sakurai H and Hausinger RP (2012) Genetic engineering of cyanobacteria to enhance biohydrogen production from sunlight and water. *AMBIO* **41** (Suppl. 2): 169-173.
- 13) 増川 一, 北島正治, 櫻井英博, 井上和仁 (2012) ラン藻の窒素固定酵素ニトロゲナーゼを利用した大規模な水素生産構想. CMC 出版. (印刷中)
- 14) Kitashima M, Masukawa H, Sakurai H and Inoue K (2012) Flexible plastic bioreactors for photobiological hydrogen production by hydrogenase-deficient cyanobacteria. *Biosci. Biotech. Biochem.* **76**: 831-833.
- 15) Nomata J, Kitashima M, Inoue K and Fujita Y (2006) Nitrogenase Fe protein-like Fe-S cluster is conserved in L-protein (BchL) of dark-operative protochlorophyllide reductase from *Rhodobacter capsulatus*. *FEBS Lett.* **580**: 6151-6154.
- 16) Nomata J, Ogawa T, Kitashima M, Inoue K and Fujita Y (2008) NB-protein (BchN-BchB) of dark-operative protochlorophyllide reductase is the catalytic component containing oxygen-tolerant Fe-S clusters. *FEBS Lett.* **582**: 1346-1350.

■原 著■ 2011 年度神奈川大学総合理学研究所共同研究助成論文

Keggin 型ヘテロポリアニオンと金 (I) 多核クラスターからなる 新規クラスター間化合物の合成

野宮健司^{1,2} 吉田拓也¹ 伊能小百合¹ 保田裕太¹ 力石紀子¹ 松永 諭¹

Novel Intercluster Compounds between a Multinuclear - Gold(I) Cluster Cation and a Keggin Polyoxometalate (POM): Formation during the Course of Carboxylate Elimination of a Monomeric Triphenylphosphinegold(I) Carboxylate in the Presence of POMs

Kenji Nomiya^{1,2}, Takuya Yoshida¹, Sayuri Iyoku¹, Yuta Yasuda¹,
Noriko Chikaraishi Kasuga¹ and Satoshi Matsunaga¹

¹ Department of Chemistry, Faculty of Science, Kanagawa University, Hiratsuka City, Kanagawa 259-1293, Japan

² To whom correspondence should be addressed. E-mail: nomiya@kanagawa-u.ac.jp

Abstract: Preparation and structural characterization of novel intercluster compounds, i.e., $[\{\text{Au}(\text{PPh}_3)_4(\mu_4\text{-O})\}_3[\alpha\text{-PW}_{12}\text{O}_{40}]_2 \cdot 4\text{EtOH}$ (**1**), $[\{\text{Au}(\text{PPh}_3)_4(\mu_4\text{-O})\}_2[\alpha\text{-SiW}_{12}\text{O}_{40}] \cdot 2\text{H}_2\text{O}$ (**2**) and $[\{\text{Au}(\text{PPh}_3)_4(\mu_4\text{-O})\}_3[\alpha\text{-PMo}_{12}\text{O}_{40}]_2 \cdot 3\text{EtOH}$ (**3**), constructed between a tetrakis(triphenyl phosphinegold(I))oxonium cation and a saturated α -Keggin polyoxometalate (POM), are described. The tetragold(I) cluster oxonium cation was formed during the course of carboxylate elimination of a monomeric phosphinegold(I) carboxylate complex, i.e., $[\text{Au}(\text{R},\text{S})\text{-pyrrld}(\text{PPh}_3)][(\text{R},\text{S})\text{-Hpyrrld} = (\text{R},\text{S})\text{-2-pyrrolidone-5-carboxylic acid}]$, in the presence of the free acid form of a Keggin POM, $\text{H}_n[\alpha\text{-XM}_{12}\text{O}_{40}] \cdot m\text{H}_2\text{O}$ ($n = 3, \text{X} = \text{P}, \text{M} = \text{W}, \text{Mo}; n = 4, \text{X} = \text{Si}, \text{M} = \text{W}; m = 7\text{-}14$). The tetragold(I) cluster cation in **1** was composed of four $\text{PPh}_3\text{Au}^{\text{I}}$ units bridged by a central μ_4 -oxygen atom in a distorted tetrahedron. On the other hand, by using sodium salt of Keggin POM, $\text{Na}_3[\text{PW}_{12}\text{O}_{40}] \cdot 9\text{H}_2\text{O}$, the heptagold(I) cluster cation was formed, i.e., in the form of $[\{\{\text{Au}(\text{PPh}_3)_4(\mu_4\text{-O})\}\{\text{Au}(\text{PPh}_3)_3(\mu_3\text{-O})\}}[\alpha\text{-PW}_{12}\text{O}_{40}] \cdot \text{EtOH}$ (**4**). The heptagold(I) cluster unit in **4** was formed by four inter-aurophilic interactions between the tetragold(I) cluster unit and trigold(I) cluster unit, which contained $\mu_4\text{-O}$ and $\mu_3\text{-O}$ atoms, respectively. The POM anion in **1** can be exchanged with the BF_4^- anion using an anion-exchange resin (Amberlyst A-27) in BF_4^- form, resulting in the formation of $[\{\text{Au}(\text{PPh}_3)_4(\mu_4\text{-O})\}(\text{BF}_4)_2$. On the other hand, when the POM anion in **4** was exchanged with BF_4^- , the heptagold(I) cluster was decomposed and a tetragold(I) cluster was formed. This suggests that the heptagold(I) cluster can exist only in the presence of POM. These compounds were characterized by elemental analysis, thermogravimetric and differential thermal analyses, Fourier transform IR, X-ray crystallography, and solid-state (CPMAS ^{31}P and ^{29}Si) and solution ($^{31}\text{P}\{^1\text{H}\}$ and ^1H) NMR spectroscopy.

Keywords: polyoxometalate, intercluster compound, multinuclear gold(I) triphenylphosphine cluster cation, NMR, X-ray crystallography

序論

分子性の酸化物クラスターであるポリ酸塩（ポリオキソメタレート：POM）は、強酸性、耐酸性、豊富な酸化還元特性などの極めて多彩な性質を有しているため、触媒、表面化学、材料科学、医薬など様々

な観点から広く研究がなされている¹⁾。近年、POMの対カチオンとして様々なクラスターを用いた、いわゆる「クラスター間化合物」が注目を集めている。水野ら²⁾は、 $[\text{Cr}_3\text{O}(\text{O}_2\text{CH})_6(\text{H}_2\text{O})_3]^+$ と Keggin 型

POM $[\alpha\text{-XW}_{12}\text{O}_{40}]^n$ (X = P, Si, B, Co; n = 3-6) とのクラスター間化合物が、結晶構造中に大きなチャンネル構造を有していることを明らかにしている。このチャンネル構造は、炭素原子 1 つの違いを識別できる吸着能・分離能を示し、新たな吸着材料として有望である。また、Jansen ら³⁾は、Keggin 型 POM $(\text{Bu}_4\text{N})_3[\alpha\text{-PW}_{12}\text{O}_{40}]$ と別途合成した金 (I) 9 核クラスター $[\text{Au}_9(\text{PPh}_3)_8](\text{NO}_3)_3$ との反応により、二種類のクラスター間化合物の合成を報告している。これらは合成溶媒の違いにより $[\text{Au}_9(\text{PPh}_3)_8]^{3+}$ 部位が butterfly 型および crown 型の異なった構造をとり、同じ組成でありながらクラスターサイズの違いに起因する異なるパッキング構造 (NaCl 型と CsCl 型) を作り別けることに成功している。

本報告では、単核の金 (I) / カルボン酸 / ホスフィン系錯体 $[\text{Au}((R,S)\text{-pyrrld})(\text{PPh}_3)]$ ($(R,S)\text{-pyrrld} = (R,S)\text{-2-ピロリドン-5-カルボキシレート}$) と各種 Keggin POM との反応から、新規クラスター間化合物の合成・構造解析を行った⁴⁾。単核金 (I) / カルボン酸 / ホスフィン系錯体 $[\text{Au}((R,S)\text{-pyrrld})(\text{PPh}_3)]$ とフリーアシッド型 Keggin POM $\text{H}_n[\text{XM}_{12}\text{O}_{40}] \cdot m\text{H}_2\text{O}$ (n = 3, X = P, M = W, Mo; n = 4, X = Si, M = W; m = 7-14) との反応からは、金 (I) 4 核クラスターを対カチオンに持つ $\{[\text{Au}(\text{PPh}_3)]_4(\mu_4\text{-O})\}_3[\alpha\text{-PW}_{12}\text{O}_{40}]_2 \cdot 4\text{EtOH}$ (**1**), $\{[\text{Au}(\text{PPh}_3)]_4(\mu_4\text{-O})\}_2[\alpha\text{-SiW}_{12}\text{O}_{40}] \cdot 2\text{H}_2\text{O}$ (**2**) および $\{[\text{Au}(\text{PPh}_3)]_4(\mu_4\text{-O})\}_3[\alpha\text{-PMo}_{12}\text{O}_{40}]_2 \cdot 3\text{EtOH}$ (**3**) が得られた。一方、ナトリウム塩の Keggin POM $\text{Na}_3[\text{PW}_{12}\text{O}_{40}] \cdot 9\text{H}_2\text{O}$ との反応からは金 (I) 7 核クラスターを対カチオンに持つ $\{[\text{Au}(\text{PPh}_3)]_4(\mu_4\text{-O})\}\{[\text{Au}(\text{PPh}_3)]_3(\mu_3\text{-O})\}[\alpha\text{-PW}_{12}\text{O}_{40}] \cdot \text{EtOH}$ (**4**) が得られた。これらの合成は、前駆体の Keggin POM の酸性度 (フリーアシッド型とナトリウム塩型) に大きく依存し、それぞれ異なる核数と構造を有する金 (I) クラスターを与えた。また、前述の Jansen らのクラスター間化合物は別途合成した金 (I) 9 核クラスター $[\text{Au}_9(\text{PPh}_3)_8](\text{NO}_3)_3$ と POM の間での対イオン交換反応であったが³⁾、本合成法では POM 存在下で単核金 (I) / カルボン酸 / ホスフィン系錯体 $[\text{Au}((R,S)\text{-pyrrld})(\text{PPh}_3)]$ のカルボキシレート配位子 ($(R,S)\text{-pyrrld}$) が脱離し、金 (I) クラスターを形成する点で異なっている。この様な、POM を介して単核金 (I) 錯体から多核金 (I) クラスターを合成する手法はこれまでに例が無く、新しいクラスター合成法として非常に興味深い。

材料と方法

材料

$\text{H}[\text{AuCl}_4] \cdot 4\text{H}_2\text{O}$, エタノール, ジクロロメタン, ジエ

チルエーテル, (和光純薬工業株), アセトニトリル (関東化学), PPh_3 (Aldrich), $(R,S)\text{-2-ピロリドン-5-カルボン酸}$ [$(R,S)\text{-Hpyrrld}$] (TCI) は、精製せずに購入したものをそのまま用いた。単核金 (I) 錯体 $[\text{Au}((R,S)\text{-pyrrld})(\text{PPh}_3)]$ ⁵⁾、及び Keggin POM 前駆体 $\text{H}_3[\alpha\text{-PW}_{12}\text{O}_{40}] \cdot 7\text{H}_2\text{O}$ ⁶⁾, $\text{H}_3[\alpha\text{-PMo}_{12}\text{O}_{40}] \cdot 14\text{H}_2\text{O}$ ⁶⁾, $\text{H}_4[\alpha\text{-SiW}_{12}\text{O}_{40}] \cdot 10\text{H}_2\text{O}$ ⁶⁾, $\text{Na}_3[\text{PW}_{12}\text{O}_{40}] \cdot 9\text{H}_2\text{O}$ ⁷⁾ は既報に従い合成した。

測定方法

単結晶 X 線構造解析は Bruker SMART APEX CCD 回折計を使用した。

結果と討論

合成

$[\text{Au}((R,S)\text{-pyrrld})(\text{PPh}_3)]$ を CH_2Cl_2 に溶解し、ガラス製試験管に加えた。そこに $\text{H}_3[\alpha\text{-PW}_{12}\text{O}_{40}] \cdot 7\text{H}_2\text{O}$ を $\text{EtOH}/\text{H}_2\text{O}$ 混合溶媒 (5 : 1, v/v) に溶解した溶液をゆっくり二層になるよう加え、暗所室温にて反応させた。5 日後、 $\{[\text{Au}(\text{PPh}_3)]_4(\mu_4\text{-O})\}_3[\alpha\text{-PW}_{12}\text{O}_{40}]_2 \cdot 4\text{EtOH}$ (**1**) を淡黄色柱状結晶として得た (収率 42.1%)。また、前駆体にそれぞれ $\text{H}_4[\alpha\text{-SiW}_{12}\text{O}_{40}] \cdot 10\text{H}_2\text{O}$, $\text{H}_3[\alpha\text{-PMo}_{12}\text{O}_{40}] \cdot 14\text{H}_2\text{O}$ を用いて **1** の合成と同様の操作を行うことで、ヘテロ原子が Si の $\{[\text{Au}(\text{PPh}_3)]_4(\mu_4\text{-O})\}_2[\alpha\text{-SiW}_{12}\text{O}_{40}] \cdot 2\text{H}_2\text{O}$ (**2**) を淡黄色ブロック状結晶、周辺金属が Mo である $\{[\text{Au}(\text{PPh}_3)]_4(\mu_4\text{-O})\}_3[\alpha\text{-PMo}_{12}\text{O}_{40}]_2 \cdot 3\text{EtOH}$ (**3**) を黄色透明結晶として得ることに成功した (収率 **2**, 50.6%; **3**, 50.1%)。

一方、 $[\text{Au}((R,S)\text{-pyrrld})(\text{PPh}_3)]$ の CH_2Cl_2 溶液の上部に、ナトリウム塩 Keggin POM $\text{Na}_3[\alpha\text{-PW}_{12}\text{O}_{40}] \cdot 9\text{H}_2\text{O}$ の $\text{EtOH}/\text{H}_2\text{O}$ (2 : 1, v/v) 溶液をゆっくりと二層になるように加え、暗所室温で 5 日間放置することで、 $\{[\text{Au}(\text{PPh}_3)]_4(\mu_4\text{-O})\}\{[\text{Au}(\text{PPh}_3)]_3(\mu_3\text{-O})\}[\alpha\text{-PW}_{12}\text{O}_{40}] \cdot \text{EtOH}$ (**4**) を淡黄色ブロック状結晶として得た (収率 50.5%)。

これらの錯体は、全元素分析 (4 は CHN 元素分析)、FTIR、TG/DTA、固体 CPMAS (³¹P および ²⁹Si) NMR、溶液 (¹H および ³¹P{¹H}) NMR、単結晶 X 線構造解析 (**1**, **2**, **4**) により同定を行った。**3** は良質な単結晶が得られず X 線構造解析は完了していないが、**1**, **2** と同様の金 (I) 4 核クラスターカチオンを有していることは明らかとなった。

単結晶 X 線構造解析

化合物 **1**, **2** は、金 (I) 4 核クラスター $\{[\text{Au}(\text{PPh}_3)]_4(\mu_4\text{-O})\}^{2+}$ と Keggin POM $[\text{XW}_{12}\text{O}_{40}]^n$ (n = 3, X = P (**1**); n = 4, X = Si (**2**)) から構成されるク

ラスターストック化合物であった (図 1(a) (b))。1 の金 (I) クラスターストック部位は、4 つの金 (I) 原子 (Au1, Au2, Au3, Au4) が歪んだ四面体の頂点に位置し、その内の 3 つの金 (I) 原子からなる底辺のほぼ中心に酸素原子 (O1) が存在していた (図 1(c))。この中心の酸素原子は 4 つの金 (I) 原子をつなぐ $\mu_4\text{-O}$ であった。また、クラスターストック内には 3 つの Au-Au 相互作用 (Au1-Au2, Au1-Au3, Au1-Au4) が存在し、それらの Au-Au 原子間距離は平均 2.962 Å であった。この原子間距離 (2.962 Å) は、金属状態の Au-Au 距離 (2.88 Å) より長い、Au の van der Waals 半径の和 (3.32 Å) よりも短く、明確な相互作用の存在を示している。このような構造の金 (I) 4 核ホスフィン錯体は、1995 年に Schmidbauer らによって BF_4 塩すなわち $[\{\text{Au}(\text{P}(\text{o-tolyl})_3)_4(\mu_4\text{-O})\}(\text{BF}_4)_2]$ として単離されている⁸⁾。Schmidbauer らの金 (I) 4 核クラスターストックは、4 つの金 (I) 原子が正四面体の頂点に配置しており、我々の金 (I) クラスターストックの様な歪みは見られない。金 (I) 4 核クラスターストックと Keggin POM の存在比は POM の電荷に依存し、ヘテロ原子が P である 1, 3 は Keggin POM の電荷が 3- であるため 3 : 2、ヘテロ原子が Si である 2 は電荷が 4- のため 2 : 1 であった。

一方、化合物 4 は金 (I) 7 核クラスターストック $[\{\{\text{Au}(\text{PPh}_3)_4(\mu_4\text{-O})\}\{\{\text{Au}(\text{PPh}_3)_3(\mu_3\text{-O})\}\}]^{3+}$ と Keggin POM $[\text{PW}_{12}\text{O}_{40}]^{3-}$ から構成され、1, 2 とは金 (I) クラスターストック部位の構造が大きく異なっていることが明らかとなった (図 2(a) (b))。この金 (I) 7 核クラスターストックは、金 (I) 4 核クラスターストック $\{\text{Au}(\text{PPh}_3)_4(\mu_4\text{-O})\}^{2+}$ と金 (I) 3 核クラスターストック $\{\text{Au}(\text{PPh}_3)_3(\mu_3\text{-O})\}^+$ が Au-Au 相互作用によって連結された構造と見なすことが可能である (図 2(b))。金 (I) 4 核クラスターストック部位は、歪んだ四面体構造の頂点に 4 つの金 (I) 原子 (Au1, Au2, Au3, Au4) が配置され、3 つの Au-Au 相互作用 (Au1-Au2, Au1-Au4, Au2-Au3) が存在する。3 つの Au-Au 原子間距離の平均値 (3.092 Å) は、van der Waals 半径の和 (3.32 Å) よりも短く、明確な相互作用が存在する。4 つの金 (I) 原子をつなぐ酸素原子 ($\mu_4\text{-O}$; O1) が歪んだ四面体の内部に存在している。化合物 1, 2 の金 (I) 4 核クラスターストックでは、 $\mu_4\text{-O}$ 原子は歪んだ四面体の底辺に位置しており、4 の金 (I) 4 核クラスターストックは異なる構造を有していた。金 (I) 3 核クラスターストック部位は、3 つの金 (I) 原子 (Au5, Au6, Au7) が三角形に配列し、これら 3 つの金 (I) をつなぐ $\mu_3\text{-O}$ 原子 (O2) が三角平面外に存在していた。また、この三角形の 2 つの辺は短く (Au5-Au7 3.0451(11) Å, Au6-Au7 3.0532(11) Å)、Au-Au 相互作用の存在が確認できるのに対し、もう 1 つの辺

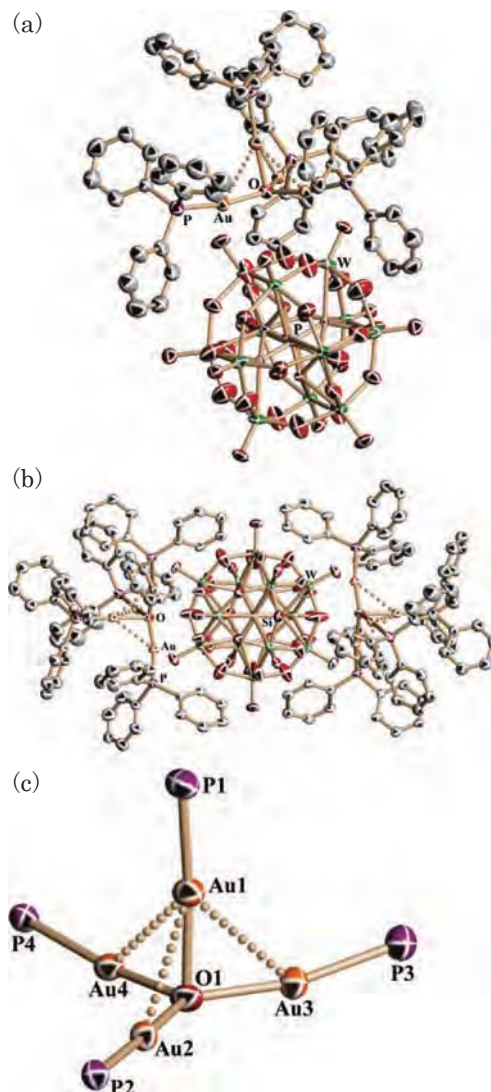


図 1. 単結晶 X 線構造解析から得られた (a) 化合物 1 および (b) 化合物 2 の分子構造と (c) 化合物 1 の金 (I) 4 核クラスターストック部位の構造. 図の簡略化のため、(a) (b) では水素原子を、(c) ではフェニル基を省略してある。

は van der Waals 半径の和より長く (Au5-Au6 3.723 Å)、Au-Au 相互作用は確認されなかった。このような金 (I) 4 核クラスターストック $\{\text{Au}(\text{PPh}_3)_4(\mu_4\text{-O})\}^{2+}$ と金 (I) 3 核クラスターストック $\{\text{Au}(\text{PPh}_3)_3(\mu_3\text{-O})\}^+$ が、4 つの Au-Au 相互作用により連結されることで金 (I) 7 核クラスターストック $[\{\{\text{Au}(\text{PPh}_3)_4(\mu_4\text{-O})\}\{\{\text{Au}(\text{PPh}_3)_3(\mu_3\text{-O})\}\}]^{3+}$ が形成されていた。

化合物 1-4 の POM アニオン部位は、いずれも一般的な飽和型 Keggin POM アニオンであった。

その他のキャラクターゼーション

化合物 1, 2, 3 は全元素分析、化合物 4 は CHN 元素分析を行い、TG/DTA の測定結果と合わせてそれぞれの組成を決定した。この結果は単結晶 X 線構造解

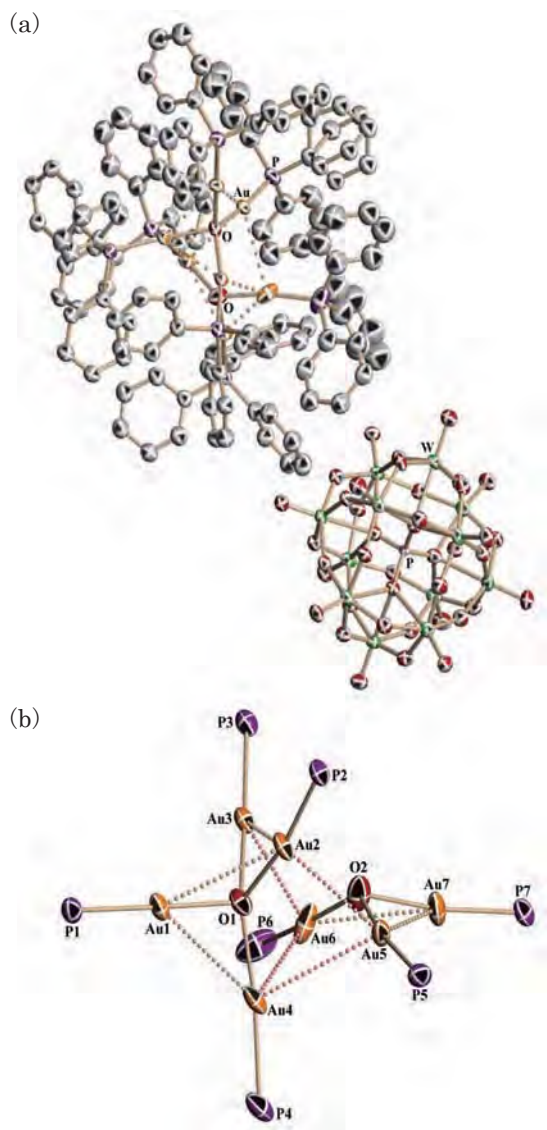


図2. 化合物4の(a)分子構造と(b)金(I)7核クラスター部位. 図の簡略化のため, (a)では水素原子を, (b)ではフェニル基を省略してある.

析の結果とも一致していた。金(I)4核クラスターおよび金(I)3核クラスター中の $\mu_4\text{-O}$ 原子および $\mu_3\text{-O}$ 原子は、いずれも反応系に存在する水およびPOMの結晶水の水に由来しているものと思われる。

FTIRの結果、これら4種類の化合物で飽和型Keggin POM構造に基づく吸収($800\text{-}1100\text{ cm}^{-1}$)と PPh_3 に基づく吸収が観測された。また、前駆体である単核金(I)錯体 $[\text{Au}((R,S)\text{-pyrrld})(\text{PPh}_3)]$ の $(R,S)\text{-pyrrld}$ 配位子のカルボニル基に基づく吸収($1696, 1632\text{ cm}^{-1}$)が観測されなかったことから、POMとの反応において $(R,S)\text{-pyrrld}$ 配位子は脱離していることが示唆され、X線構造解析の結果と対応している。

固体CPMAS ^{31}P NMRの結果、いずれの化合物も25 ppm付近にブロードなシグナルが観測さ

れ、金(I)ホスフィンクラスターの PPh_3 に由来するシグナルと帰属できる。また、化合物1では15.3 ppm、2では19.2 ppmにもピークが観測された。これらは、固体状態において金(I)4核クラスターが歪んだ四面体構造をとっているため、非等価な PPh_3 がクラスター中に存在することに由来する。一方、溶液中($\text{DMSO-}d_6$)の $^{31}\text{P}\{^1\text{H}\}$ NMR測定では、いずれの化合物も一本のシグナル(24.87 (1), 24.76 (2), 25.5 (3), 24.46 (4) ppm)として観測された。溶液中では、分子運動により PPh_3 の環境が平均化され、鋭い一本線ピークとして観測されたためである。また、化合物4では24.46 ppmに観測され、1の24.87 ppmに比べて僅かではあるが高磁場シフトしている。このことから、4における金(I)7核クラスターは溶液中でも7核構造を保っていると推測される。

イオン交換による金(I)4核および7核クラスターカチオンの BF_4 塩としての単離の試み

金(I)の4核および7核クラスターとPOMから構成されるクラスター間化合物1, 4のPOMアニオン部位を、陰イオン交換樹脂を用いて BF_4 アニオンへと交換することを試みた。陰イオン交換樹脂には BF_4 型のAmberlyst A-27を用いバッチ法で行った。1ではPOMアニオンが BF_4 アニオンに置き換わった $[\{\text{Au}(\text{PPh}_3)\}_4(\mu_4\text{-O})](\text{BF}_4)_2$ を得ることが出来た。溶液の ^{31}P NMRでは25.10 ppmにシグナルが観測され、Schmidbaurらが報告している錯体 $[\{\text{Au}(\text{PPh}_3)\}_4(\mu_4\text{-O})](\text{BF}_4)_2$ の25.4 ppmとほぼ一致していた。Schmidbaurらは、金(I)3核ホスフィン錯体 $[\{\text{Au}(\text{PPh}_3)\}_3(\mu_3\text{-O})]\text{BF}_4$ を合成した後、金(I)単核ホスフィン錯体 $[\text{Au}(\text{PPh}_3)]\text{BF}_4$ を反応させ4核錯体へと二段階で導いているが⁸⁾、我々の合成法では金(I)単核錯体からPOM存在下で直接4核錯体を合成する点で大きく異なっている。

一方、4ではアニオンを BF_4 へと交換すると7核構造を保つことが出来ず、1と同様の4核クラスターへと変換してしまうことが ^{31}P NMRより示唆された。これは金(I)7核クラスターカチオン $[\{\{\text{Au}(\text{PPh}_3)\}_4(\mu_4\text{-O})\}\{\{\text{Au}(\text{PPh}_3)\}_3(\mu_3\text{-O})\}]^{3+}$ は、固体状態と溶液状態共にPOMアニオンの存在下のみ安定化されることを示唆している。このことより、本報告で提唱するPOMアニオンを介した金(I)クラスターカチオンの合成法を用いることで、これまでに合成・単離されていない新たな金(I)クラスターを合成することが可能と考えている。

まとめ

単核の金 (I) / カルボン酸 / ホスフィン系錯体 $[\text{Au}((R,S)\text{-pyrrld})(\text{PPh}_3)]$ ($(R,S)\text{-pyrrld} = (R,S)\text{-2-ピロリドン-5-カルボキシレート}$) と各種 Keggin POM との反応により、新規クラスター間化合物の合成・構造解析に成功した。単核金 (I) ホスフィン錯体 $[\text{Au}((R,S)\text{-pyrrld})(\text{PPh}_3)]$ とフリーアシッド型 Keggin POM $\text{H}_n[\text{XM}_{12}\text{O}_{40}]$ ($n = 3, \text{X} = \text{P}, \text{M} = \text{W}, \text{Mo}; n = 4, \text{X} = \text{Si}, \text{M} = \text{W}$) との反応からは、金 (I) 4 核クラスターをカチオンに持つ化合物 **1**, **2**, **3** が、ナトリウム塩 Keggin POM $\text{Na}_3[\text{PW}_{12}\text{O}_{40}]$ との反応からは金 (I) 7 核クラスターを対カチオンに持つ化合物 **4** が得られた。従来の合成法では多段階反応により金 (I) ホスフィン多核クラスターを得ていたのに対し、本方法では単核金 (I) ホスフィン錯体 $[\text{Au}((R,S)\text{-pyrrld})(\text{PPh}_3)]$ から POM 存在下で直接多核クラスターを合成することが可能であった。また、生成する金 (I) クラスターの核数や構造は、合成に用いた前駆体の Keggin POM の種類に依存しており、**4** で見られた金 (I) 7 核クラスターカチオンは POM 存在下でのみ安定に存在する。金 (I) ホスフィンクラスターは有機合成における触媒としての観点からも最近注目されており、本方法の POM アニオンを用いた金 (I) ホスフィンクラスター合成法は、新規で多様な金 (I) クラスターを合成する新しい手法となりうる。

謝辞

本研究は、平成 22 年度～ 24 年度科学研究費補助金 (基盤 (C) 22550065) および平成 23 年度神奈川大学総合理学研究所共同研究の研究助成を受けた。

文献

- Hill CL, Ed. (1998) Polyoxometalates. *Chem. Rev.* **98**: 1-390.
- Mizuno N and Uchida S (2006) Structures and sorption properties of ionic crystal of polyoxometalates with macrocation. *Chem. Lett.* **35**: 688-693.
- Schulz-Dobrick M and Jansen M (2006) Supramolecular intercluster compounds consisting of gold clusters and Keggin anions. *Eur. J. Inorg. Chem.* **2006**: 4498-4502.
- Nomiya K, Yoshida T, Sakai Y, Nanba A and Tsurutata S (2010) Intercluster compound between a tetrakis{triphenylphosphinegold (I)}oxonium cation and a Keggin polyoxometalate (POM): formation during the course of carboxylate elimination of a monomeric triphenylphosphinegold (I) carboxylate in the presence of POMs. *Inorg. Chem.* **49**: 8247-8254.
- Noguchi R, Hara A, Sugie A and Nomiya K (2006) Synthesis of novel gold (I) complexes derived by AgCl-elimination between $[\text{AuCl}(\text{PPh}_3)]$ and silver (I) heterocyclic carboxylates, and their antimicrobial activities. Molecular structure of $[\text{Au}(R,S\text{-Hpyrrld})(\text{PPh}_3)]$ (H2pyrrld = 2-pyrrolidone-5-carboxylic acid). *Inorg. Chem. Commun.* **9**: 355-359.
- North EO and Haney W (1939) 47. Silicomolybdic Acid. 48. Silicotungstic Acid. 49. Phosphotungstic Acid. *Inorg. Synth.* **1**: 127-133.
- Aoki S, Kurashina T, Kasahara Y, Nishijima T and Nomiya K (2011) Polyoxometalate (POM)-based, multi-functional, inorganic-organic, hybrid compounds: syntheses and molecular structures of silanol-and/or siloxane bond-containing species grafted on mono- and tri-lacunary Keggin POMs. *Dalton Trans.* **40**: 1243-1253.
- Schmidbaur H, Hofreiter S and Paul M (1995) Synthesis of the gold analogue of the elusive doubly protonated water molecule. *Nature* **377**: 503-504.